INFLUENCE OF IMPACT AND EJECTA ENVIRONMENTS ON PLANETARY GEOCHRONOLOGY

by

JENNIFER REYNÉ DAVIS

B.S., Miami University, 2020

A dissertation submitted to the

Faculty of the Graduate School of the

University of Colorado in partial fulfillment

of the requirement for the degree of

Doctor of Philosophy

Department of Geological Sciences

2025

Committee Members:

Dr. Carolyn Crow

Dr. Rebecca Flowers

Dr. Timmons Erickson

Dr. Leah Morgan

Dr. Ann-Marie Madigan

Abstract

Jennifer Reyné Davis (Ph.D., Geological Sciences)

Influence of Impact and Ejecta Environments on Planetary Geochronology

Dissertation directed by Associate Professor Carolyn Crow

Impact events are a ubiquitous geologic phenomenon across the Universe affecting all planetary bodies, yet aspects of their geologic ramifications remain poorly understood. Impacts can generate extremely high temperatures and pressures that profoundly alter impacted materials, both within the crater and material ejected during the impact process. Additionally, impact events can partially and fully reset host rock geochronologic systems, often introducing complexities and uncertainties in constraining the timing of discrete impact events. A clearer understanding of how impact processes affect host rock material properties and the geochronology record is essential to refine our knowledge of planetary histories.

This dissertation investigates the effects of impacts on rock materials and radiometric systematics through microtextural and geochronologic analyses of impact crater rocks (host and newly created from host rocks) and ejecta. Project 1 examines materials within the Kamestastin Lake crater, using shock microtextural analysis of thin sections and bulk rock $^{40}Ar/^{39}Ar$ geochronology to explore the relationship between temperature, pressure, and microtextures, and how these factors influence ^{40}Ar diffusion, retentivity, and ultimately $^{40}Ar/^{39}Ar$ ages. Projects 2 and 3 shift focus to ejecta materials, specifically investigating how the mineral zircon is altered from the high pressure-temperature environment of an impact event and how U-Pb ages derived from these altered zircons are affected in the ejecta environment. Project 2 analyzes Chicxulub

impact ejecta, while project 3 examines Apollo sample 14311, an impact melt breccia, and also evaluates zircon mineral separation processing techniques to optimize lunar zircon recovery.

Collectively, this dissertation advances our understanding of the pressure-temperature complexities of impact cratering and the impact environmental effects on rocks, mineral material properties, and geochronologic systems. The findings demonstrate that high temperatures, evidenced by specific microtextures, can result in fully resetting geochronometers, therefore producing true impact ages. However, the impact cratering process is highly heterogeneous and produces heterogeneous temperature and pressure conditions, resulting in variable effects across an impact structure and different geochronologic systems (e.g., U-Pb, $^{40}Ar/^{39}Ar$). By elucidating these processes in this dissertation, this research enhances our ability to interpret and date materials from impact events across the Solar System.

Dedication

This dissertation is dedicated to all the mountain goats in Colorado I have met and have yet to meet. To you, I wish you all the salt on Mount Blue Sky.

Acknowledgements

So many people have helped and supported me throughout this graduate program, and I am deeply grateful to each of them.

Thank you to my entire dissertation committee (Drs. Carolyn Crow, Rebecca Flowers, Timmons Erickson, Leah Morgan, and Ann-Marie Madigan) for your time and support throughout the past 5 years. I am very grateful for the roles that each of you have played during my graduate student career. Additional thanks to Dr. Gordon Osinski for his advice and co-authorship on chapter 2 of this dissertation regarding the Kamestastin impact structure and to Dr. Jeff Benowitz for your many contributions and helpful discussions that elevated my dissertation work.

I have had the loveliest support from those around me that have helped contribute to my success over the past few years. I first off thank Lucy for being the best buddy that I could ever have who got me through undergraduate program and was there as long as she could be for my graduate degree. To her I say she earned her honorary dogterate dogree alongside me.

Enormous gratitude is owed to my lab mates: Master Lydia Pinkham, Connor Antonio Diaz, Marcus Richards, Patrick Harper, Dr. Amanda Alexander, Autumn Roberts, and many others along the way. I am so lucky to have met such amazing scientists and people, and I am so honored to be a part of your lives and to have had your support along the way. Lydia Pinkham, you quickly became one of my all-time best friends, and I owe so much of my PhD success to your support—and, of course, our countless Lego adventures over the years.

A special shout out to some of the amazing graduate student friends I have made along the way at CU including my lovely office mates Spencer and Vanessa for the “no windows, all vibes”

office. Special love to so many other amazing graduate student friends in the department and at the university for making this a great graduate student experience with some of the best people.

I thank the support I received as an undergraduate at Miami University, in particular under the support of Drs. Claire McLeod and Carrie Tyler. You both pushed me to be the best scientist and geologist that I could be. Your guidance allowed me to gain confidence and experience that pushed me to become the scientist that I am today. An additional thank you to my amazing friends in both the geology department (Wilnelly, Aleks, Trez) and on the women's ice hockey team at Miami for the most amazing experiences and memories. I cherish my time as an undergraduate at Miami.

A wonderful thank you for the support from my amazing Colorado friends including Randall, Am, Doug, Taylor, Natasha, Vlad, Bailey, Hedy, Darcy, Rubarbara, Cashew, the 2x back-to-back championship winning Icemen Cometh hockey team, among so many others. Thank you to many other friends (both new and old) for their indefatigable love including Christina, Annette, Erica, Isaac, Sam, and Devin. Your love has made my heart feel nothing short of full.

I owe my family the most gratitude of them all. My dad, Ron, has been my inspiration from the beginning, teaching me about all kinds of science, especially planetary science, on countless walks, car rides to hockey practice, and Sunday morning donuts runs to Bizy Bee. Dad, you single handedly inspired me to become a scientist and to pursue my PhD. My mom, Reyné, has been there for support every single step of the way in every way possible. She is and will always be my biggest cheerleader and supporter, essentially my twin. My brother Adam always has my back, and my brother Ronnie has always been supportive. Grandma Yunker and Grandma Davis, you always made me feel so loved, and I can finally say I'm now smart thanks to your spearmint candies. My amazing family Archer, Ezra, and Ivy have never failed to make me laugh. Dexter,

you were always my little dude and our snuggles made the late night work not feel so bad. An EXTRA special shout out to Goatconut, Dr. MG, Nacho, Nugget, Nimbus, and all the other beloved buddies out there for being my buddies that helped give me that extra push to the finish line. A world of thanks to KBJC, so much inspiration for my PhD work and for the future.

Dr. Daniel Blakemore, you have helped me through the entire way. You've given me so many laughs, crazy experiences, and unwavering support. You know I couldn't let you be the only doctor. I'm eager to embark on our next adventure.

Table of Contents

Chapter 1: Introduction 1

1.1 Impact Cratering 1
1.2 The Effects of Impacts 4
1.3 Geochronology in Impact Settings 8
1.3.1 Radiometric Dating 10
1.3.2 $^{40}Ar/^{39}Ar$ Dating 13
1.3.3 U-Pb Dating 17
1.4 Dissertation Overview 19
1.5 References 22

Chapter 2: Impactful Dates: Coordinated $^{40}Ar/^{39}Ar$ Geochronology and Shock Study of the Kamestastin Lake Impact Structure, Canada 27

2.1 Abstract 27
2.2 Introduction 28
2.3 Geologic Context and Samples 31
2.4 Methods 34
2.4.1 Optical Microscopy 34
2.4.2 Raman Spectroscopy 35
2.4.3 $^{40}Ar/^{39}Ar$ Geochronology 36
2.5 Results 39
2.5.1 Mangerite 40
2.5.2 Anorthosite 41
2.5.3 Impact Glass 42
2.5.4 Granite 42
2.6 Discussion 47
2.6.1 Investigating Pre-Impact Age Resetting 48
2.6.2 Partial Resetting and Impact Glasses 49
2.6.3 Full Resetting and Age of Kamestastin Lake Impact 51
2.6.4 Thermal History of Kamestastin Granite Clast Reset Samples 52
2.7 Summary and Conclusions 55
2.8 Acknowledgements 57
2.9 References 58

Chapter 3: The Effects of Impacts on Ejecta: Correlating U-Pb Geochronology and Shock Microtextural Study of Ejecta Zircons from the Chicxulub Impact 65

3.1 Abstract 65
3.2 Introduction 66
3.3 Geologic Context and Previous Studies of Chicxulub Ejecta 70
3.4 Methods 74
3.4.1 Refining Zircon Extraction Methodology 74
3.4.2 Microstructural Characterization 75
3.4.3 U-Pb Geochronology 76
3.5 Results 76
3.5.1 Unshocked Grains 78

3.5.2 Crystal Plastic Deformation 78
3.5.3 Shock Twins 79
3.5.4 Reidite 79
3.5.5 FRIGN zircon 80
3.5.6 Granular Texture Recrystallization 80
3.5.7 Metamict/Amorphous 81
3.6 Discussion 88
3.6.1 Screening for Contributions from Local Detrital Zircons in the Ejecta Layer 89
3.6.2 Pressure-Temperature Conditions Experienced by Distal Ejecta 90
3.6.3 U-Pb Age Resetting in Distal Ejecta Zircons 93
3.6.3.1 Comparison of Chicxulub Ejecta Zircons to Previous Impact Ejecta Studies 93
3.6.3.2 New Insights into Chicxulub Ejecta Zircons 97
3.6.3.3 Granular Zircons in Chicxulub Ejecta Accurately Date the Impact 102
3.7 Conclusions 107
3.8 References 110

Chapter 4: The Lost Lunar Zircons: How Sample Processing has Biased the Apollo Zircon Record 122

4.1 Abstract 122
4.2 Introduction 123
4.3 Apollo Sample 14311 127
4.4 Methods 130
4.4.1 Zircon Extraction Methodology Testing 130
4.4.2 Microtextural Characterization 130
4.4.3 U-Pb Geochronology and Ti-in Zircon Thermometry 131
4.5 Results 132
4.5.1 $^{207}Pb/^{206}Pb$ Ages of Less Dense Zircons 133
4.5.2 Microtextures of Less Dense Zircons 133
4.5.3 Ti-in-Zircon Thermometry 137
4.6 Discussion 150
4.6.1 Characterization of Previously Missing Grains and Suggested Mineral Separation Methodology for Maximizing Zircon Yield from Lunar Samples 150
4.6.1.1 Causes for Density Changes in Zircon Grains through Microstructural Analysis 151
4.6.1.2 Chemical Variation and Ultraviolet Light Fluorescence Response 155
4.6.1.3 Suggested Lunar Zircon Separation Methods 156
4.6.2 Zircon Crystallization Temperatures 157
4.6.3 History of 14311 160
4.6.3.1 Missing Zircon Ages – What's the Full Story of 14311? 160
4.6.3.2 14311 Breccia Formation 166
4.6.3.3 Timing of Breccia Annealing and Metamictization in 14311,58 Zircons 166
4.6.3.4 Summary of 14311 Sample History 167
4.7 Conclusions 172
4.8 References 175

Chapter 5: Conclusions 184

All Dissertation References 188

Appendix A: $^{40}Ar/^{39}Ar$ data tables 214
Appendix B: Supporting figures from Kamestastin impact structure study (Chapter 2) ..227
Appendix C: Diffusion Parameter and Fractional Loss Calculations for Granite Clasts ..260
Appendix D: U-Pb, Ti-in-zircon thermometry, and U concentration data tables 264
Appendix E: Chicxulub zircon images (excluding unshocked grains).....285
Appendix F: Apollo 14311, 58 zircon images 402

Tables

Table 1.1 Common geochronometers for radiometric dating 12

Table 2.1 Summary of geochronology completed at the Kamestastin impact structure.....33

Table 2.2 Summary of shock metamorphic features and $^{40}Ar/^{39}Ar$ geochronology of Kamestastin samples.....43

Table 4.1 Total grains that contain each microtexture in Apollo 14311,58 zircons from this study 138

Table A1 Overview of $^{40}Ar/^{39}Ar$ analyses 214

Table A2 $^{40}Ar/^{39}Ar$ geochronology data 214

Table C1 Summary of diffusion parameter and T-t results 262

Table D1 U-Pb geochronology data from Chicxulub zircons.....264

Table D2 U-Pb geochronology data from Apollo 14311,58 zircons 270

Table D3 Apollo 14311,58 Ti-in-zircon thermometry.....278

Table D4 U concentrations, alpha dose, and amorphization fraction for Apollo 14311,58 zircons 280

Figures

Figure 1.1 Impact cratering process for simple and complex craters 4

Figure 1.2 Map of impact craters across the lunar surface 10

Figure 1.3 Example age spectra for $^{40}Ar/^{39}Ar$ geochronology.....16

Figure 1.4 Lunar zircon showing spatial resolution using secondary ionization mass spectrometry (BSE).....19

Figure 2.1 Map of the Kamestastin impact structure 31

Figure 2.2 Thin section images of major shock features in the Kamestastin samples.....40

Figure 2.3 Raman spectra from plagioclase crystals depicting the range of shock in Kamestastin samples.....45

Figure 2.4 $^{40}Ar/^{39}Ar$ age spectra and K/Ca plots for each sample from Kamestastin.....46

Figure 2.5 Combined $^{40}Ar/^{39}Ar$ age spectra from all samples from Kamestastin.....47

Figure 3.1 Cross-section of the Chicxulub impact crater during excavation.....73

Figure 3.2 World map of Chicxulub ejecta sites where shocked zircons have been identified and U-Pb studies have been conducted 73

Figure 3.3 Unshocked zircon from the Chicxulub ejecta (EBSD and CL).....81

Figure 3.4 Probability density function of surrounding detrital zircon grain U-Pb age populations compared to U-Pb ages of Chicxulub ejecta zircons 82

Figure 3.5 Plastically deformed zircons from the Chicxulub ejecta (EBSD) 83

Figure 3.6 U-Pb ages of Chicxulub ejecta zircons grouped by primary microtexture.....84

Figure 3.7 Reidite from the Chicxulub ejecta (EBSD) 85

Figure 3.8 Granular (both FRIGN and non-FRIGN) zircons and shock twinning in Chicxulub ejecta zircons (EBSD, pole figures, misorientation axis figures) 86

Figure 3.9 Pie chart showing abundances of zircons with each microtexture in Chicxulub ejecta 87

Figure 3.10 Metamict zircon from the Chicxulub ejecta (EBSD, CL) 88

Figure 3.11 Tera-Wasserburg concordia diagram of U-Pb ratios from Chicxulub ejecta 96

Figure 3.12 Wetherill concordia diagram of U-Pb ratios from Chicxulub ejecta grouped by microtexture (excluding unshocked grains).....97

Figure 3.13 U-Pb ages of Chicxulub ejecta zircons grouped by locality from this study and previous studies.....102

Figure 3.14 Ages of only granular zircons (both FRIGN and non-FRIGN) in Chicxulub ejecta 105

Figure 3.15 Youngest largest single age population (Y-LSP) of granular zircon ages from Chicxulub ejecta.....106

Figure 3.16 Youngest single age population (YSP) of granular zircon ages from Chicxulub ejecta 107

Figure 4.1 Map of Apollo landing sites on the Moon and a map of the traverse during the Apollo 14 mission with the location of the Apollo sample 14311 collection site 129

Figure 4.2 Probability density function of $^{207}Pb/^{206}Pb$ ages from the 14311,58 zircons in this study 139

Figure 4.3 Wetherill concordia diagram of U-Pb ratios from 14311,58 zircons 140

Figure 4.4 Tera-Wasserburg concordia diagram of U-Pb ratios from 14311,58 zircons.....141

Figure 4.5 Unshocked zircon from 14311,58 (EBSD, FSD, SE).....142

Figure 4.6 Zircon with evidence of primary igneous zonation from 14311,58 (EBSD, SE, FSD) 143

Figure 4.7 Zircon with a curviplanar feature from 14311,58 (FSD, EBSD, SE).....144

Figure 4.8 Plastically deformed zircons from 14311,58 (EBSD, SE, FSD) 145

Figure 4.9 Complex plastic deformation in a 14311,58 zircon (EBSD, FSD, SE).....146

Figure 4.10 Granular recrystallization in zircons from 14311,58 (EBSD, SE, FSD).....147

Figure 4.11 U ppm concentration relative to degree of metamictization (none, partial, full) in 14311,58 zircons 148

Figure 4.12 Shock twinning in 14311,58 zircons (EBSD, SE, FSD) 149

Figure 4.13 Ti-in-zircon thermometry plots of crystallization temperature vs. age and $^{57}Fe/^{94}Zr2O$ vs. crystallization temperature 159

Figure 4.14 Ti-in-zircon thermometry crystallization temperatures grouped by study from this study, other 14311,58 zircons from Trail et al. (2020), and other Apollo 14 zircons 160

Figure 4.15 Probability density function of $^{207}Pb/^{206}Pb$ ages from the 14311,58 zircons in this study (MI float) compared to the $^{207}Pb/^{206}Pb$ ages from the 14311,58 zircons in Trail et al. (2020) (MI sink) 169

Figure 4.16 Probability density function of $^{207}Pb/^{206}Pb$ ages from the 14311,58 zircons from both this study and Trail et al. (2020) 170

Figure 4.17 Probability density function of $^{207}Pb/^{206}Pb$ ages from 14311,58 zircons compared to other 14311 zircon ages and probability density function of $^{207}Pb/^{206}Pb$ ages from all 14311 zircons combined 171

Figure B1-B5 Outcrop images of sample localities (Kamestastin)..... 227-231

Figure B6-B14 Thin section images with circled areas of focus for Raman analyses (Kamestastin) 232-240

Figure B15-B18 Representative Raman spectra from plagioclase crystals analyzed in each sample (Kamestastin)..... 241-244

Figure B19 Raman spectra of hydrothermal minerals from sample MM10-028 (Kamestastin) 245

Figure B20-B22 Full scale age spectra (not zoomed) for samples 2021-3163, MM10-016, and MM09-035 (Kamestastin)..... 246-248

Figure B23 All glass age spectra figures from the $^{40}Ar/^{39}Ar$ analyses of four subsamples of impact glass (Kamestastin) 249

Figure B24 Overview of geochronology impact age determinations regarding the Kamestastin impact (this study and previous studies).....250

Figure B25-B33 Inverse isochron figures from each sample that $^{40}Ar/^{39}Ar$ analyses were completed on (Kamestastin) 251-259

Figure C1 Arrhenius plot for granite clast diffusion parameter and fractional loss modeling ...261

Chapter 1

Introduction

1.1 Impact Cratering

Impact cratering is a ubiquitous geologic process that affects all solid bodies in our Solar System—both rocky and icy (Osinski and Pierazzo, 2012). Since impact cratering plays such a significant and widespread role in our Solar System, studying it is essential for gaining deeper insight into the conditions and effects of this geologic process. Impact events excavate material, form craters on planetary surfaces, and physically alter the target rock material (Melosh, 1989; Osinski and Pierazzo, 2012). Impacted target materials undergo shock and alteration, making them valuable for analyzing the extent of the extreme temperature and pressure conditions generated by the impact event (e.g., Schmieder et al., 2015; Timms et al., 2017; Stöffler et al., 2018; Rasmussen et al., 2020). Determining the timing of impact events is crucial for reconstructing planetary evolution and understanding how impact flux has evolved over time. Accurate impact dating provides constraints on planetary surface ages, aids in the calibration of crater-based chronologies, and helps correlate impact events with potential global consequences, such as mass extinctions on Earth or resurfacing events on other planetary bodies (Kelley and Sherlock, 2012). By dating impact structures and associated shocked minerals, geoscientists can also assess the role of impacts in planetary evolution and their influence on crustal evolution and geologic modification over time.

The impact record on Earth serves as a critical resource for studying hypervelocity impact processes and their effects on target rock materials (Osinski and Pierazzo, 2012). Currently, the 188 confirmed impact craters on Earth provide valuable opportunities to investigate impact

cratering mechanics, shock metamorphism, and post-impact processes (Osinski et al., 2022). These craters vary in size from meters to hundreds of kilometers in diameter and span ages from the present day to billions of years (Osinski et al., 2022). However, Earth's dynamic geological activity—including erosion, volcanic resurfacing, tectonics (e.g., subduction), and biological processes—can obfuscate or completely erase impact structures over time, limiting the long-term preservation of impact evidence.

To develop a more complete understanding of impact cratering, it is essential to study both terrestrial and extraterrestrial impact structures, such as those on the Moon. The Moon has different environmental dynamics than Earth such as a minimal atmosphere and a lack of active plate tectonics, allowing its impact record to be preserved for billions of years (Stöffler et al., 2006). As a result, the lunar surface provides a nearly continuous record of impact events, making it an invaluable reference for studying crater formation, impact flux over time, and planetary surface evolution. Additionally, the Moon has been so extensively bombarded that all surface materials have been affected by at least one impact event, with many samples originating from impact craters or ejecta blankets (Taylor, 1982). However, this extensive bombardment of the lunar surface has resulted in a complex and overlapping geologic history, where older impact features are continuously reworked by subsequent impacts, making it challenging to precisely date individual events and unravel the intricate timeline of lunar surface evolution. By integrating studies of impact craters on both Earth and the Moon, researchers can better understand the fundamental processes and effects of impact cratering across planetary bodies, refine impact chronologies, and improve interpretations of impact-modified materials across the Solar System.

To understand how to study impact cratering on various planetary surfaces, it is imperative to examine and comprehend the process itself. Impact cratering is grouped into three separate steps

that then produce the resulting impact structure: 1) the contact and compression stage, 2) the excavation stage, and 3) the modification stage (Figure 1.1) (Collins et al., 2012; Osinski and Pierazzo, 2012). The contact and compression stage can produce extremely high temperature and pressure conditions (>3000°C and >100 GPa) in large impact events (impacts with craters that are 10s to 100s of kilometers in diameter) (Osinski and Pierazzo, 2012). During the excavation stage, material is ejected from the impact site and deposited within the crater and outside of the crater rim as proximal (<5 crater radii from point of impact) and distal ejecta (>5 crater radii) (Osinski et al., 2012). The modification stage is where the crater takes its final form as the impact produces a simple or complex impact structure, and the rock within the crater collapses and settles in response to the release of pressure and excavation during the cratering process. A simple crater forms during smaller impact events (craters of <2-4 km on Earth and <15-27 km on the Moon; Osinski and Pierazzo, 2012) and results in a bowl shape depression, while a complex crater forms in larger impact events resulting in a structure with a central uplift in the center of the crater and, if large enough, multiple rings within the crater structure (Figure 1.1) (Pike, 1980; Osinski and Pierazzo, 2012).

The impact cratering process alters materials both within the crater and in the surrounding ejecta deposits. Impact induced deformation and alteration provide valuable insights into the conditions experienced during impact events and the subsequent modifications to rock properties. Examining both terrestrial and lunar impact sites allows researchers to better characterize the pressures, temperatures, and deformation histories associated with impact cratering across planetary bodies. By analyzing the physicochemical alterations that occur during impact events, scientists can gain further clarifications on how these processes modify planetary surfaces, refine

our understanding of dating these complex events, and better interpret the broader evolution of planetary bodies in our Solar System.

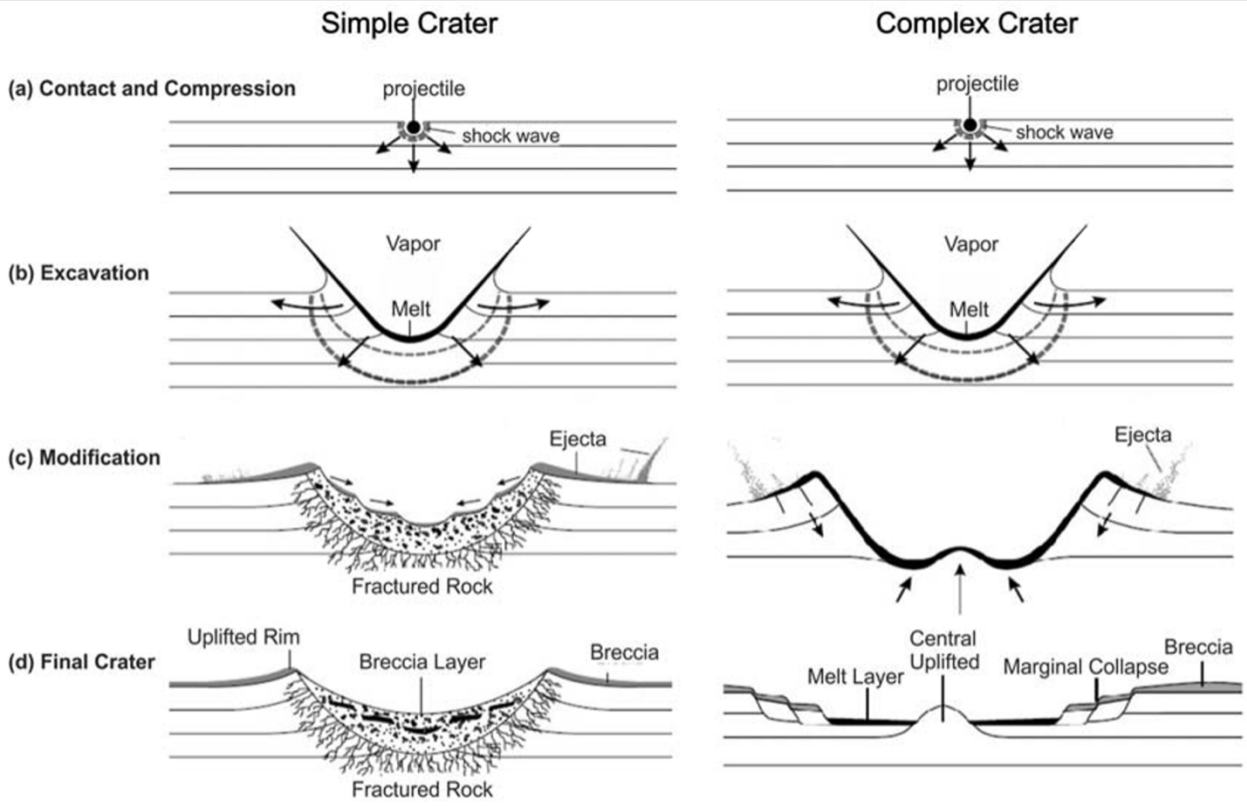

Figure 1.1: Illustration of the impact cratering process through the various stages of a) contact and compression, b) excavation, c) modification, and d) the final resulting crater. The combination of steps a-d display the steps of how the impact process occurs, the displacement, alteration, and ejection of material, and how the cratering process produces the final crater structure that is left on the surface of a planetary body in both simple craters and complex craters. (Figure modified from Ferreira et al., 2015)

1.2 The Effects of Impacts

The high temperatures and high pressures that occur in an impact event produce a wide array of conditions that can vaporize, melt, shock, metamorphose, and deform target rock material (Osinski et al., 2022). The rocks that are involved in and produced by impact events are called impactites. Impactites are typically classified into three major groups: 1) shocked rocks, 2) impact

melt rocks, and 3) impact breccias (Osinski and Pierazzo, 2012). Shocked rocks are non-brecciated, melt-free rocks that display evidence of shock metamorphism (Osinski and Pierazzo, 2012). Impact melt rocks experience melting as a result of the impact and are subclassified based on the crystallinity and clast content (Osinski and Pierazzo, 2012). Impact breccias form when rocks are shattered and fragmented from an impact and are cemented via fine-grained rock or impact melt. These are further classified according to the degree of mixing of target lithologies and melt content (Osinski and Pierazzo, 2012).

Beyond classifying impactites, it is also crucial to examine how extreme temperature and pressure conditions modify the physical and chemical properties of affected rocks and minerals (Melosh, 2012). These alterations can create diagnostic shock features that provide definitive evidence of an impact event. While certain macro- and micro-textural features in minerals may suggest an impact event, some shock features form exclusively through impact processes, making them reliable diagnostic indicators (Cavosie et al., 2024). These diagnostic impact-related textures occur at both macro and micro scales. At the macro scale, shatter cones are cone-shaped structures characterized by radiating striations originating from a central apex (Osinski et al., 2022; Cavosie et al., 2024). At the micro scale, diagnostic features include planar deformation features (PDFs) and planar features (PFs) in quartz grains. Additionally, high-pressure mineral phases such as reidite ($ZrSiO_4$), akaogiite (TiO_2), riesite (TiO_2), stöfflerite ($(Ca,Na)(Si,Al)_4O_8$), tissintite ($(Ca,Na)AlSi_2O_6$), wangdaodeite ($FeTiO_3$), liuite ($FeTiO_3$), and maohokite ($MgFe_2O_4$) serve as key indicators of shock metamorphism. Minerals that preserve evidence of former high-pressure phases, such as formerly reidite-in-granular neoblastic (FRIGN) zircon or granular ilmenite, further support an impact origin (Osinski et al., 2022; Cavosie et al., 2024).

Impact events can also produce other microtextural features that, while associated with shock metamorphism, are not yet widely accepted as definitive diagnostic indicators. Some of these features can form in other geologic or tectonic settings, or their exclusivity to impact processes remains under investigation. These include crystal plastic deformation in minerals such as zircon and apatite, granular zircon (excluding FRIGN), diaplectic plagioclase glass (maskelynite), melt inclusions, and shock twinning in zircon (Thomas et al., 2003; Jaret et al., 2015; Cavosie et al., 2016, Cavosie et al., 2018; Cavosie et al., 2024; Crow et al., 2024). Some of these features, such as shock twins in zircon (misorientation between host and twin of 65° about the <110> axis) and maskelynite, are generally accepted as impact produced features by the impact community but their exclusivity to impact settings is still under review by the impact cratering research community (e.g., French and Koeberl, 2010; Timms et al., 2011). Committees such as the Impact Cratering Committee (ICC) continue to evaluate these features to determine their reliability as diagnostic impact evidence (Cavosie et al., 2016; Cavosie et al., 2024).

Specific temperature and pressure conditions give rise to distinct microstructures, which serve as indicators of the temperature-pressure environment created during an impact. Impact microtextures can be observed in impactites that are found both within the impact crater and exterior to the crater in the ejecta environment and through a variety of different minerals such as quartz, feldspars, and zircons (Cavosie et al., 2015; Stöffler et al., 2018; Xie et al., 2020). Certain microtextures, such as impact shock twinning in zircon, can indicate elevated pressures (~20+ GPa in the case of shock twinning), while other microtextures, such as ballen silica, can indicate elevated temperatures (in this case >1150°C), and some impact features such as maskelynite can indicate both elevated temperature and pressures (in this case 35 GPa and temperatures ~300°C) (Ostertag, 1983; Fritz et al., 2005; Ferrière et al., 2009; Ferrière et al., 2010; Morozova, 2015;

Cavosie et al., 2016; Stöffler et al., 2018). The impact features and microtextures from a large impact event are therefore critical to identify to give insight into the effects of an impact and what that implies about the larger impact environmental conditions.

Impact microtextural features can be observed through a variety of analytical methodologies. Common techniques to observe microtextural features in different minerals include observing shock through a polarized or cross-polarized light microscope, cathodoluminescence (CL) via instruments such as the scanning electron microscope (SEM), the electron microprobe (EPMA), or the transmission electron microscope (TEM), electron backscatter diffraction (EBSD) via the SEM, or Raman spectroscopy (e.g., French and Koeberl, 2010; Moser et al., 2011; Yin and Dai, 2020). The polarized and cross-polarized light microscope is the traditional, time-efficient technique for identifying evidence of shock features such as planar deformation features (PDFs) in quartz, mosaicism, fracturing, evidence of planar features (PFs) and shock twins, and diaplectic glass like maskelynite (Short, 1970; Goltrant et al., 1992; Jaret et al., 2015). However, features like shock twins and PFs often require confirmation through methods that analyze crystallographic orientation relationships like EBSD. CL imaging reveals changes in luminescence patterns, indicating zonation, defects, and recrystallization in important rock forming minerals and accessory minerals such as feldspars, quartz, and zircon (Götze, 2012). EBSD identifies crystal orientations, revealing deformation, misorientations, and high-pressure polymorphs caused by impacts (Erickson et al., 2013). Raman spectroscopy determines crystal structure and lattice disorder, detecting high-pressure polymorphs and diaplectic glass (e.g., maskelynite), and also quantifying shock levels in minerals like plagioclase feldspar (Xie et al., 2020). These techniques are often used together to identify shock microtextures and understand the effects of impacts on minerals, as demonstrated by their widespread application in studies of

terrestrial and extraterrestrial impact rocks, including Apollo samples and meteorites, to characterize shock microtextures and quantify impact processes (e.g., Erickson et al., 2013; Crow et al., 2017; Jaret et al., 2018; Xie et al., 2020).

1.3 Geochronology in Impact Settings

In addition to physically transforming target rock material, the extreme heat and pressure of an impact can alter the chemical properties of minerals and influence the behavior of certain elements within individual crystals. Depending on the extent of the pressure and temperature conditions, this can cause diffusion of certain elements and therefore affect geochronometric systems and reset isotopic ages. The extent of age resetting in a mineral during an impact event depends on factors such as impact size, pressure, temperature, timescales of the conditions, and the specific conditions required to reset a specific geochronometer. This can result in no age resetting, partial age resetting (which is geologically meaningless), or full age resetting to the age of the impact event.

Impact events often create heterogeneous impact conditions (wide variety of temperature and/or pressure experienced throughout an impact structure and within individual impactites), and therefore this can cause varying degrees of age resetting throughout an impact, depending on the conditions experienced by a dated sample. As a result of variability in isotope resetting, it can be difficult to extrapolate geologically meaningful ages from impacted rocks since impactites throughout an impact structure or in impact ejecta can produce a wide range of ages (Osinski et al., 2022). This is apparent through the fact that most impact structures on Earth have very poor to no age constraints, and only 20% of identified hypervelocity impact structures have ages with uncertainties of less than 2% (at 2σ) (Osinski et al., 2022). The absence of age constraints for most

impact events highlights the extreme difficulty of dating these complex materials and underscores the need to determine how to extract geologically meaningful ages from impactites.

Impact ages have significance beyond their parent bodies, playing a crucial role in unraveling the history and evolution of the Solar System. Accurate dating of impact events provides critical insights into planetary formation, surface evolution, and Solar System dynamics. In particular, impact ages help refine models of planetary bombardment, constraining the timing and frequency of collisions that shaped planetary crusts (Morbidelli et al., 2012; Marchi et al., 2013; Osinski et al., 2022). On heavily cratered bodies such as the Moon, impact cratering is a dominant geological process, making reliable impact dating essential for interpreting planetary surface histories and dating returned samples (Figure 1.2) (Jaumann et al., 2012; Grieve et al., 2014; Barlow, 2015). Without robust ages from impactites, reconstructing planetary evolution, tracking changes in impact flux over time, and assessing the broader influence of these events on planetary environments becomes increasingly difficult. Refining impact geochronology will not only enhance our understanding of Earth's impact history but also improve future studies dating impactites from the Moon, Mars, and beyond.

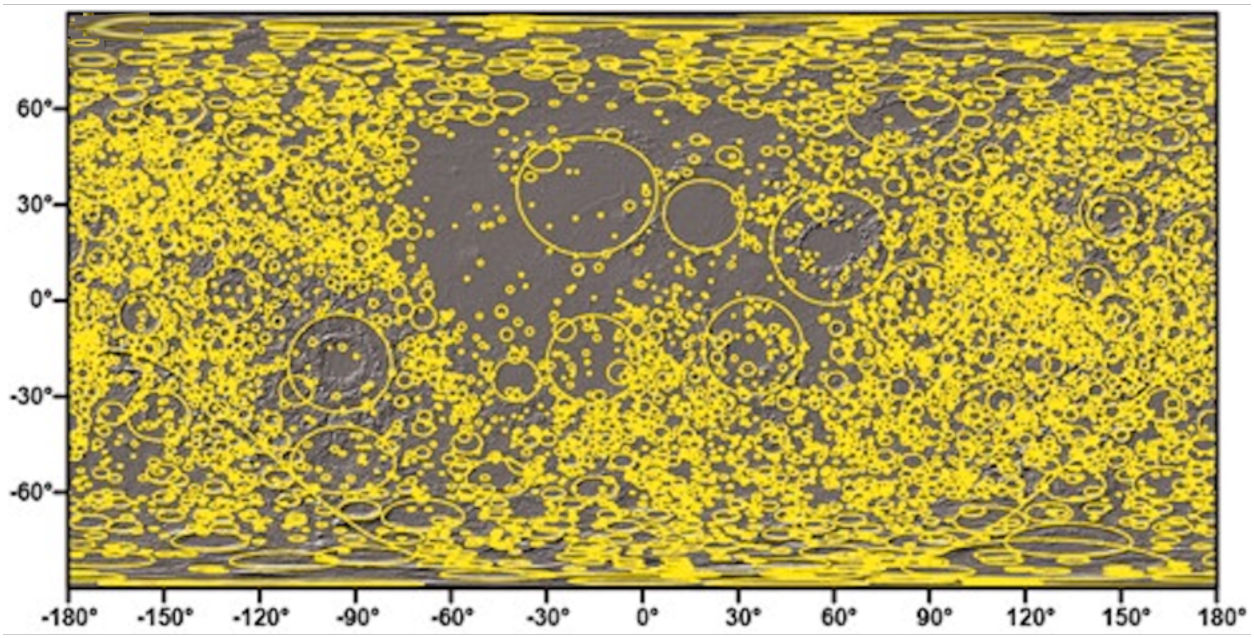

Figure 1.2: Impact crater map of the lunar surface from LOLA (Lunar Orbiter Laser Altimeter) data depicting the heavily cratered surface. Each of the impact craters has an associated ejecta blanket relative to the size of each impact event. This depicts the dominance of this geologic process on the lunar surface and the need to better understand how impact cratering shocks rocks and affects various geochronometers to determine how to reliably date a complex planetary surface. (Figure modified from Head et al., 2010)

1.3.1 Radiometric Dating

Geochronology is fundamental to determining the absolute age of geological materials, providing insights into the timing and history of geological events and processes. Some minerals within rocks can be dated by analyzing the radioactive decay of certain elements, which occurs at a known rate, or half-life. By measuring the ratio of parent to daughter isotopes in a sample, geologists can calculate its age with precision. However, several conditions must be met for a rock to yield a reliable radiometric date. It must contain radioactive parent isotopes, and there must be a sufficient quantity of both parent and daughter isotopes to ensure accurate measurement. Additionally, the initial conditions of the system must be well constrained, meaning the starting concentration of daughter isotopes must be known or estimable. Most importantly, the rock must

have remained a closed system, meaning that isotopes have not been lost or gained due to diffusion since a significant geological event such as crystallization, impact, or metamorphism.

Different minerals are better suited for specific geochronologic methods based on their chemical composition, the elements they incorporate during formation, and the time scales they can effectively measure (Table 1). For example, zircon is a widely used mineral for U-Pb dating because it incorporates uranium (U) and strongly rejects lead (Pb), making it ideal for obtaining precise ages. Similarly, feldspar can be used for K-Ar and Ar/Ar dating due to its higher potassium content. However, minerals only record meaningful isotopic ages if they retain their isotopic signatures, which is dependent on the thermal and chemical conditions they have experienced throughout their history.

Crucial to interpreting radiometric ages is understanding how temperature affects isotopic retention. Each geochronometer has a specific temperature range at which it becomes an open system, meaning prolonged exposure to elevated temperatures can cause isotopes to diffuse out of the crystal structure, effectively resetting the isotopic clock. If a mineral has been subjected to high temperatures over an extended period, it may yield an apparent age that reflects the timing of thermal resetting rather than its original formation. This relationship between temperature and diffusion must be considered when selecting a geochronologic method, as it influences whether the recorded age represents crystallization, metamorphism, or another geological event.

Because the thermal history of a mineral/rock can impact the accuracy of age determinations, it is essential to consider the relative timing of the event being dated in relation to the sample's metamorphic or impact history. Elevated temperatures from events such as regional metamorphism, magmatic intrusion, or shock metamorphism can reset certain isotopic systems

while leaving others unaffected. Therefore, selecting an appropriate geochronometer requires careful evaluation of the sample's mineralogy, isotopic system behavior, and thermal history to ensure that the measured age corresponds to the geological event of interest (Table 1). This dissertation focuses on the bulk rock $^{40}Ar/^{39}Ar$ and U-Pb in zircon geochronometers to date impactites as these are common geochronometers used in dating planetary materials (e.g., Stöffler et al., 2006; Schmieder and Kring, 2020).

Table 1.1: Common geochronometers for radiometrically dating materials

Isotope		Half-life of parent isotope (years)	Useful age range (years)	Common materials of utility
Parent	Daughter			
Carbon 14	Nitrogen 14	5,730	100-30,000	Organic materials (wood, bone, plants)
Potassium 40	Argon 40	1.3 billion	10,000-4.5 billion	K-rich minerals (feldspars, micas, amphiboles, pyroxenes), volcanic glass
Rubidium 87	Strontium 87	48 billion	10 million-4.5 billion	Feldspars, micas, pegmatite rocks, carbonate minerals
Uranium 238 Uranium 235	Lead 206 Lead 207	4.5 billion 710 billion	1 million-4.6 billion	Zircon, apatite, titanite, monazite, baddeleyite, xenotime

1.3.2 $^{40}Ar/^{39}Ar$ Dating

Argon-40/Argon-39 ($^{40}Ar/^{39}Ar$) geochronology is based on the naturally occurring ^{40}K-^{40}Ar decay system. ^{40}K decays to ^{40}Ar with a half-life of 1,250 Ma (Lee, 2015). However, since Ar is a (noble) gas and K is a solid, K and Ar need to be measured using separate instrumentation techniques on separate sample aliquots. To eliminate instrumentation and sample heterogeneity concerns during the K-Ar dating technique, K-bearing samples are now irradiated with neutrons to convert ^{39}K to ^{39}Ar (Lee, 2015). Since the ratio of ^{40}K to ^{39}K is known and constant, ^{39}Ar can, therefore, be used as a proxy for ^{40}K and $^{40}Ar/^{39}Ar$ ratios are measured on one sample aliquot.$^{40}Ar/^{39}Ar$ dating is done using minerals that either readily incorporate K into their crystal structures (e.g. feldspars, micas, amphiboles, K-rich clays) or minerals that may not have K as a dominant element but can contain sufficient K content for dating (e.g. plagioclase, pyroxene). Many minerals useful for $^{40}Ar/^{39}Ar$ are often dominant, rock-forming minerals and are therefore $^{40}Ar/^{39}Ar$ datable minerals can be found nearly ubiquitously on rocky planetary bodies (e.g., plagioclase, pyroxene). A variety of geological and planetary materials contain rocks with K-bearing minerals and pairing this with the strong temperature dependence of Ar diffusion in minerals allows for the widespread application of $^{40}Ar/^{39}Ar$ geochronology (Lee, 2015).

$^{40}Ar/^{39}Ar$ step heating experiments incrementally heat and therefore incrementally release Ar gas throughout the sample to determine Ar distribution (Lee, 2015). $^{40}Ar/^{39}Ar$ analyses can be done via bulk rock, individual mineral, and in situ methods. When a sample is step-heated, its resulting age for each step relative to the cumulative fraction of ^{39}Ar released from the sample is plotted and referred to as age spectra diagrams (Figure 1.3). Often for $^{40}Ar/^{39}Ar$, “plateau ages”, or incremental heating steps that yield similar ages and appear as a flat line on age spectra, are used to interpret the age of the geologic event during which the sample crystallized or was reset

(Figure 1.3A). Typically, a plateau is defined as having at least three or more consecutive steps that comprise >50% of the ^{39}Ar release with an MSWD <2.5 (McDougall and Harrison, 1999). Some age spectra do not have similar ages in each step as ^{39}Ar is released (no "plateau" with steps of similar age) and therefore this is evidence indicative of Ar-loss and partial $^{40}Ar/^{39}Ar$ resetting of a sample (Figure 1.3B). Age spectra that exhibit a stair-stepping pattern (Figure 1.3B), rather than a well-defined plateau, indicate Ar-loss or redistribution. In these cases, lower-temperature steps often yield younger apparent ages due to Ar-loss from less retentive phases and grain boundaries, while higher-temperature steps retain older ages from more retentive domains. The degree of age increase across steps reflects the fraction of Ar-loss, with steeper trends indicating more significant disturbance. If there is partial age resetting, it can be difficult to interpret sample ages as the age spectra may not converge on a single age. Complex, partially reset age spectra are often seen in extra-terrestrial samples which makes our current interpretations of lunar age spectra difficult (e.g. Norman et al., 2006; Cassata et al., 2010).

$^{40}Ar/^{39}Ar$ dating has widespread utility to determine ages and timing of geologic events throughout nearly the entirety of Earth's history (Table 1.1). Additionally, since $^{40}Ar/^{39}Ar$ can be used to date a wide variety of K-bearing minerals, this allows for the broad use of this geochronometer across a wide array of minerals, rocks, and geologic settings. Depending on the minerals analyzed, Ar diffusion occurs at a variety of different temperatures where minerals such as potassium feldspar open to diffusion at lower temperatures than other minerals such as muscovite (Lee, 2015). As a result, some minerals are more easily reset in complex environments, such as impact settings, where extreme temperatures are distributed unevenly. Temperature variations occur over a wide range of timescales, from fractions of a second to hours, depending on factors like shock intensity and post-impact thermal conditions. This heterogeneity can lead to

partial or complete Ar-loss in different parts of a sample, producing complex resetting patterns in the $^{40}Ar/^{39}Ar$ geochronometer and making age interpretations more challenging. Therefore, the $^{40}Ar/^{39}Ar$ geochronometer can be a critical tool in dating and understanding impact environments, but careful attention needs to be given to determine the reliability and geologic significance of the resulting ages.

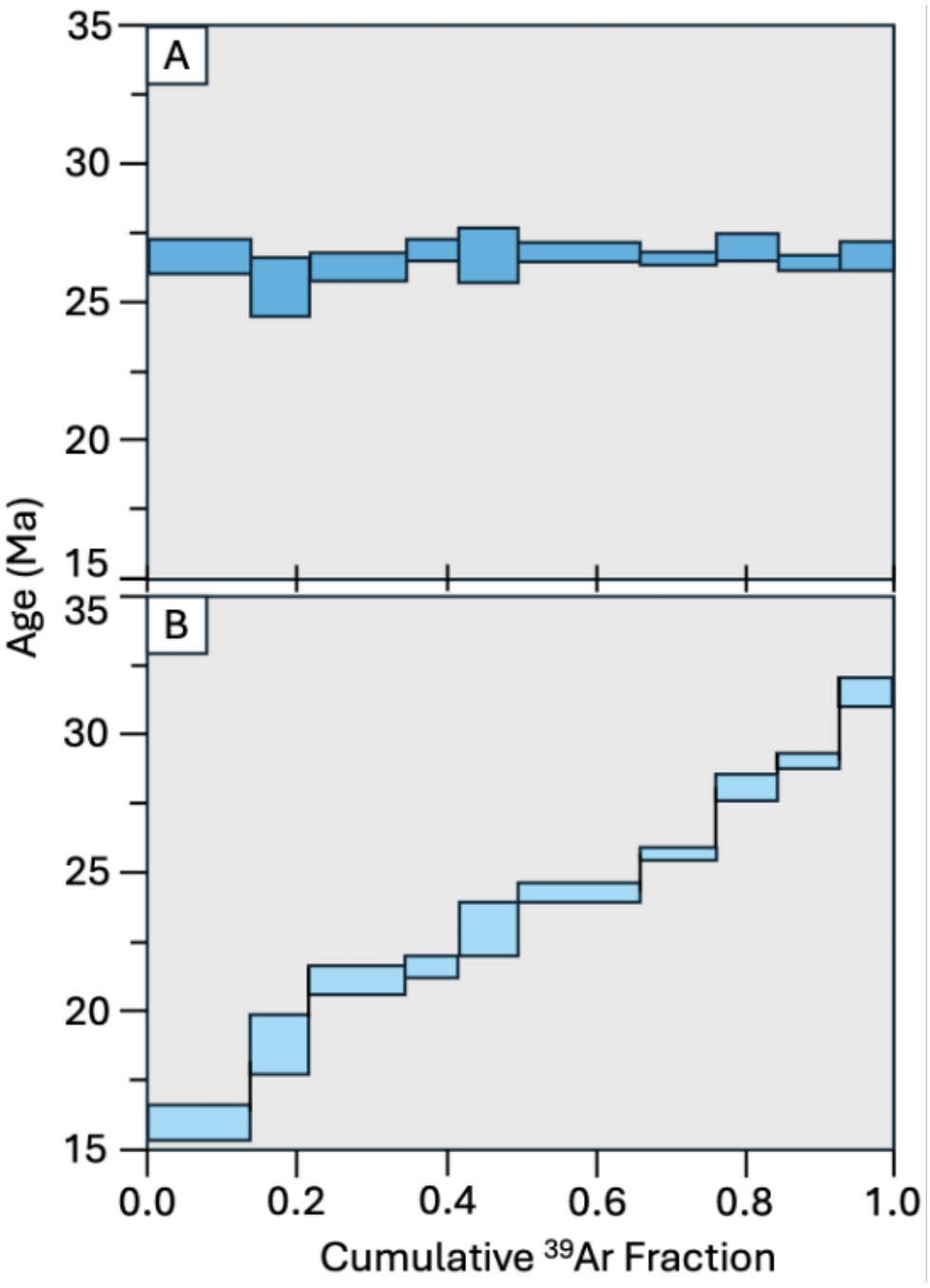

Figure 1.3: Examples of hypothetical $^{40}Ar/^{39}Ar$ age spectra figures that show how ages are displayed as samples are incrementally step heated and Ar is released from the sample. Each colored rectangle represents a single heating step. Figure A depicts an age spectrum that displays a relatively flat line considered a "plateau". Figure B shows an age spectrum that does not have a flat line that converges on an age and therefore depicts a disturbed age spectrum. It is difficult to determine geologic significance to the $^{40}Ar/^{39}Ar$ ages from this spectrum since it displays a wide range of ages.

1.3.3 U-Pb Dating

Uranium (U)-Lead (Pb) geochronology is based on the decay of radioactive ^{238}U and ^{235}U to stable ^{206}Pb and ^{207}Pb, respectively. Many U-bearing minerals can be used for U-Pb dating but zircon ($ZrSiO_4$) is one of the most commonly used minerals for the U-Pb geochronometer because zircon is a very common and widespread accessory mineral; is quite resistant to destruction and isotopic resetting during weathering, metamorphic, and igneous processes; and readily incorporates U with little-to-no initial Pb into its crystal structure at its time of formation, resulting in higher precision ages (Corfu, 2015). U-Pb geochronology can date samples as old as the age of the Solar System to samples less than 1 Ma (Parrish, 2015).

U-Pb dating utilizes the decay of ^{238}U-^{206}Pb and the decay of ^{235}U-^{207}Pb to determine the age of a zircon. By comparing these two independent decay systems, geochronologists can compare and assess the reliability of the measured ages. U-Pb ages are often reported as either a ^{238}U-^{206}Pb age, ^{235}U-^{207}Pb age, or a $^{207}Pb/^{206}Pb$ age, primarily dependent on the age of what is being dated. U/Pb and Pb/Pb isotope ratios are commonly plotted on concordia diagrams, such as the Wetherill ($^{206}Pb/^{238}U$ vs. $^{207}Pb/^{235}U$) or Tera-Wasserburg ($^{207}Pb/^{206}Pb$ vs. $^{238}U/^{206}Pb$) concordia plots. These diagrams help assess whether samples fall along the concordia line—representing equal ages as defined by the ^{238}U-^{206}Pb and ^{235}U-^{207}Pb geochronometers—or if they exhibit discordance due to open-system behavior, which indicates post-formational disturbance of the U-Pb system (Parrish, 2015). If temperatures in an impact event exceed that at which diffusion of Pb in zircon typically occurs (~900°C), the U-Pb age can become partially or fully reset, depending on the exact extent of the impact conditions (i.e., temperature, pressure, time) (Cherniak and Watson, 2001; Osinski et al., 2022).

U-Pb ages can be measured using a variety of geochemical instrumentation including secondary ionization mass spectrometry (SIMS/nanoSIMS), sensitive high-resolution ion microprobe (SHRIMP), thermal ionization mass spectrometry (TIMS), and laser ablation inductively coupled plasma mass spectrometry (LA-ICP-MS), depending on the needs such as sample size, number of analyses needed, analysis spot size, precision, and analytical time. SIMS is used in this dissertation because it holds several key advantages in comparison with the aforementioned techniques: it is a relatively fast analysis technique (~15 minutes per spot) which allows time for an abundance of measurement and its small spot size (~10 μm diameter, ~1–2 μm depth) enables analysis across various grain sizes, while the ability to target specific grain regions provides high spatial resolution (Figure 1.4). The high spatial resolution of SIMS analyses is particularly useful for shocked samples, where microtextures can range from a few microns to pervasive shock effects throughout the crystal, allowing for precise age differentiation in impact-shocked regions.

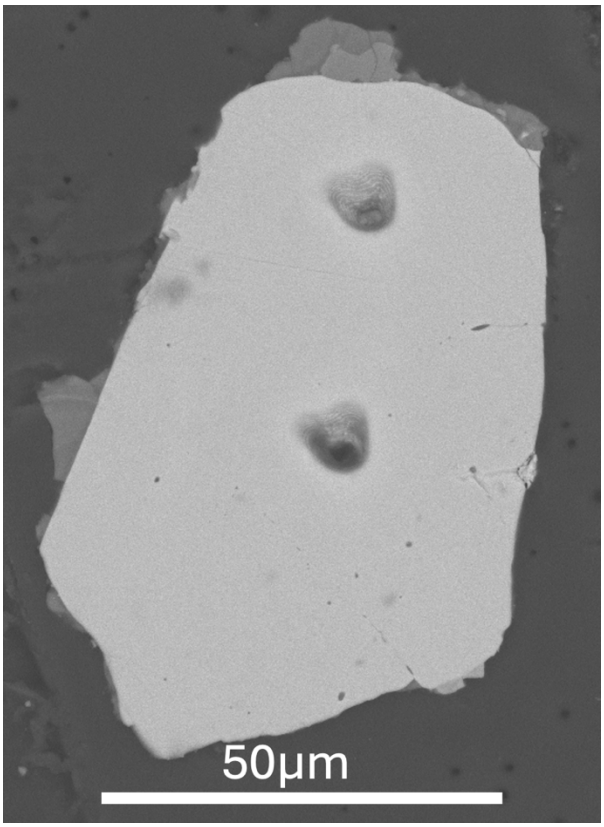

Figure 1.4: Backscattered electron image of a lunar zircon from this dissertation (Chapter 4, M_M2_z12) with two SIMS pits on the grain. The spatial resolution using the SIMS allows for measurements targeting certain grain regions for analyses. This allows for measurements targeting microtextures in zircons affected by impact cratering events.

1.4 Dissertation Overview

This dissertation investigates the physical effects and geochronologic age resetting in complex impact cratering environments by analyzing different impact sites on Earth and the Moon using various microtextural, elemental, and isotopic analysis techniques.

Chapter 2 addresses the extent and nature of shock induced resetting of the $^{40}Ar/^{39}Ar$ geochronometer in impact environments. This study uses the Kamestastin (formerly "Mistastin") Lake impact structure in Labrador, Canada to understand the effects and extent of shock in impactites from various locations within the impact crater from a large impact (28 km diameter).

The shock effects in these samples are paired with bulk rock $^{40}Ar/^{39}Ar$ geochronology to better understand the range of shock and temperature in an impact event to cause age resetting and give insight into conditions that produce geologically meaningful ages in an impact setting. Anorthosite, a key rock type in this impact setting, serves as an analog for impact effects on the lunar surface.

Chapters 3 and 4 address the extent of impact shock and alteration in zircon crystals and how impact microtextures and temperature-pressure conditions relate to age resetting in the U-Pb geochronometer in distal ejecta environments. Chapter 3 focuses on terrestrial impact cratering through the study of distal ejecta in Colorado and New Mexico from the Chicxulub impact structure, also known as the K/Pg and K/T boundary impact. This chapter explores how an impact ejecta blanket, derived from target rocks of known ages, records the temperature and pressure conditions of a large impact, how these conditions shock and alter zircon crystals, and what ages are preserved in ejecta zircons. These analyses provide insight into the complexities of dating ejecta material.

Chapter 4 examines impact and ejecta blanket environments on the Moon to study the effects on zircon crystals on an extra-terrestrial planetary body where impact cratering is the dominant geologic process. Rather than studying one single impact cratering event as done in chapters 2 and 3, this chapter focuses on unraveling the complex impact history encapsulated within Apollo 14 sample 14311, a zircon rich impact melt breccia. The abundance of zircons in this sample allows for a comprehensive survey of microtextures as well as elemental and isotopic measurements to understand the range of histories recorded in this impact breccia. However, traditional zircon mineral separation techniques for lunar materials failed to recover a significant portion of zircons from 14311. This chapter evaluates the best processing methods for zircon

separation and examines how incorporating the missing zircon ages and microtextures refine our understanding of sample 14311.

As a whole, this dissertation furthers our understanding of the complexities of impact cratering and how these events affect the geochronology and datable minerals of target rocks.

1.5 References

Barlow, N.G., 2015. Constraining geologic properties and processes through the use of impact craters. Geomorphology, Planetary Geomorphology: Proceedings of the 45th Annual Binghamton Geomorphology Symposium, held 12-14 September 2014 in Knoxville, Tennessee, USA 240, 18–33. https://doi.org/10.1016/j.geomorph.2014.08.027

Cassata, W.S., Shuster, D.L., Renne, P.R., Weiss, B.P., 2010. Evidence for shock heating and constraints on Martian surface temperatures revealed by 40Ar/39Ar thermochronometry of Martian meteorites. Geochimica et Cosmochimica Acta 74, 6900–6920. https://doi.org/10.1016/j.gca.2010.08.027

Cavosie, A.J., Erickson, T.M., Timms, N.E., Reddy, S.M., Talavera, C., Montalvo, S.D., Pincus, M.R., Gibbon, R.J., Moser, D., 2015. A terrestrial perspective on using ex situ shocked zircons to date lunar impacts. Geology 43, 999–1002. https://doi.org/10.1130/G37059.1

Cavosie, A.J., Timms, N.E., Erickson, T.M., Hagerty, J.J., Hörz, F., 2016. Transformations to granular zircon revealed: Twinning, reidite, and ZrO2 in shocked zircon from Meteor Crater (Arizona, USA). Geology 44, 703–706. https://doi.org/10.1130/G38043.1

Cavosie, A.J., Timms, N.E., Ferrière, L., Rochette, P., 2018. FRIGN zircon—The only terrestrial mineral diagnostic of high-pressure and high-temperature shock deformation. Geology 46, 891–894. https://doi.org/10.1130/G45079.1

Cavosie, A.J., Alwmark, S., Baratoux, D., Consolmagno, G., Ferrière, L., Hauser, N., Kenkmann, T., Koeberl, C., Osinski, G.R., PickersgilL, A.E., 2024. A Diagonstic Impact Criteria List to Confirm Terrestrial Impact Craters by the Meteoritical Society Impact Cratering Committee - Work in Progress. Presented at the 86th Annual Meeting of the Meteoritical Society.

Cherniak, D.J., Watson, E.B., 2001. Pb diffusion in zircon. Chemical Geology, What are we dating? Understanding the Crystallogernesis of U-Pb 172, 5–24. https://doi.org/10.1016/S0009-2541(00)00233-3

Collins, G.S., Melosh, H.J., Osinski, G.R., 2012. The Impact-Cratering Process. Elements 8, 25–30. https://doi.org/10.2113/gselements.8.1.25

Corfu, F., 2015. Uranium–Lead, Zircon, in: Jack Rink, W., Thompson, J.W. (Eds.), Encyclopedia of Scientific Dating Methods, Encyclopedia of Earth Sciences Series. Springer Netherlands, Dordrecht, pp. 914–918. https://doi.org/10.1007/978-94-007-6304-3_23

Crow, C.A., McKeegan, K.D., Moser, D.E., 2017. Coordinated U–Pb geochronology, trace element, Ti-in-zircon thermometry and microstructural analysis of Apollo zircons. Geochimica et Cosmochimica Acta 202, 264–284. https://doi.org/10.1016/j.gca.2016.12.019

Crow, C.A., Tong, C., Erickson, T.M., Moser, D.E., Bell, A.S., Kelly, N.M., Prissel, T.C., Hyde, B.C., 2024. Impact origin of lunar zircon melt inclusions in Apollo impact melt breccia 14311. Meteoritics & Planetary Science 59, 1509–1522. https://doi.org/10.1111/maps.14162

Erickson, T.M., Cavosie, A.J., Moser, D.E., Barker, I.R., Radovan, H.A., 2013. Correlating planar microstructures in shocked zircon from the Vredefort Dome at multiple scales: Crystallographic modeling, external and internal imaging, and EBSD structural analysis. American Mineralogist 98, 53–65. https://doi.org/10.2138/am.2013.4165

Ferreira, J., Leite, E., Vasconcelos, M., Crósta, A., 2015. 3D gravity modeling of impact structures in basaltic formations in Brazil: Part I – Vargeão, Santa Catarina. Revista Brasileira de Geofísica 33, 319. https://doi.org/10.22564/rbgf.v33i2.723

Ferrière, L., Koeberl, C., Reimold, W.U., 2009. Characterisation of ballen quartz and cristobalite in impact breccias: new observations and constraints on ballen formation. European Journal of Mineralogy 21, 203–217. https://doi.org/10.1127/0935-1221/2009/0021-1898

Ferrière, L., Koeberl, C., Libowitzky, E., Reimold, W.U., Greshake, A., Brandstätter, F., 2010. Ballen quartz and cristobalite in impactites: New investigations, in: Large Meteorite Impacts and Planetary Evolution IV. Geological Society of America, pp. 609–618. https://doi.org/10.1130/2010.2465(29)

French, B.M., Koeberl, C., 2010. The convincing identification of terrestrial meteorite impact structures: What works, what doesn't, and why. Earth-Science Reviews 98, 123–170. https://doi.org/10.1016/j.earscirev.2009.10.009

Fritz J., Greshake A., Stoffler D., 2005. Micro-Raman spectroscopy of plagioclase and maskelynite in Martian meteorites: Evidence of progressive shock metamorphism. Antarctic meteorite research 18, 96–116. https://doi.org/10.15094/00006067

Goltrant, O., Leroux, H., Doukhan, J.-C., Cordier, P., 1992. Formation mechanisms of planar deformation features in naturally shocked quartz. Physics of the Earth and Planetary Interiors 74, 219–240. https://doi.org/10.1016/0031-9201(92)90012-K

Götze, J., 2012. Application of Cathodoluminescence Microscopy and Spectroscopy in Geosciences. Microscopy and Microanalysis 18, 1270–1284. https://doi.org/10.1017/S1431927612001122

Grieve, R.A.F., Osinski, G.R., Tornabene, L.L., 2014. Chapter 4 - Planetary Impacts, in: Spohn, T., Breuer, D., Johnson, T.V. (Eds.), Encyclopedia of the Solar System (Third Edition). Elsevier, Boston, pp. 83–99. https://doi.org/10.1016/B978-0-12-415845-0.00004-9

Head, J.W., Fassett, C.I., Kadish, S.J., Smith, D.E., Zuber, M.T., Neumann, G.A., Mazarico, E., 2010. Global Distribution of Large Lunar Craters: Implications for Resurfacing and Impactor Populations. Science 329, 1504–1507. https://doi.org/10.1126/science.1195050

Jaret, S.J., Woerner, W.R., Phillips, B.L., Ehm, L., Nekvasil, H., Wright, S.P., Glotch, T.D., 2015. Maskelynite formation via solid-state transformation: Evidence of infrared and X-ray anisotropy. Journal of Geophysical Research: Planets 120, 570–587. https://doi.org/10.1002/2014JE004764

Jaumann, R., Hiesinger, H., Anand, M., Crawford, I.A., Wagner, R., Sohl, F., Jolliff, B.L., Scholten, F., Knapmeyer, M., Hoffmann, H., Hussmann, H., Grott, M., Hempel, S., Köhler, U., Krohn, K., Schmitz, N., Carpenter, J., Wieczorek, M., Spohn, T., Robinson, M.S., Oberst, J., 2012. Geology, geochemistry, and geophysics of the Moon: Status of current understanding. Planetary and Space Science, Scientific Preparations For Lunar Exploration 74, 15–41. https://doi.org/10.1016/j.pss.2012.08.019

Kelley, S.P., Sherlock, S.C., 2012. The geochronology of impact craters, in: Impact Cratering: Processes and Products. John Wiley & Sons, Ltd.

Lee, J.K.W., 2015. Ar–Ar and K–Ar Dating, in: Jack Rink, W., Thompson, J.W. (Eds.), Encyclopedia of Scientific Dating Methods, Encyclopedia of Earth Sciences Series. Springer Netherlands, Dordrecht, pp. 58–73. https://doi.org/10.1007/978-94-007-6304-3_40

Marchi, S., Bottke, W.F., Cohen, B.A., Wünnemann, K., Kring, D.A., McSween, H.Y., De Sanctis, M.C., O'Brien, D.P., Schenk, P., Raymond, C.A., Russell, C.T., 2013. High-velocity collisions from the lunar cataclysm recorded in asteroidal meteorites. Nature Geosci 6, 303–307. https://doi.org/10.1038/ngeo1769

McDougall, I., Harrison, T.M., 1999. Geochronology and Thermochronology by the 40Ar/39Ar Method. Oxford University Press.

Melosh, H.J., 1989. Impact cratering : a geologic process. New York : Oxford University Press ; Oxford : Clarendon Press.

Melosh, J., 2012. The contact and compression stage of impact cratering, in: Impact Cratering: Processes and Products. John Wiley & Sons, Ltd.

Morbidelli, A., Lunine, J.I., O'Brien, D.P., Raymond, S.N., Walsh, K.J., 2012. Building Terrestrial Planets. Annu. Rev. Earth Planet. Sci. 40, 251–275. https://doi.org/10.1146/annurev-earth-042711-105319

Morozova, I., 2015. Strength Study of Zircon Under High Pressure (M.Sc.). The University of Western Ontario (Canada), Canada -- Ontario, CA.

Moser, D.E., Cupelli, C.L., Barker, I.R., Flowers, R.M., Bowman, J.R., Wooden, J., Hart, J.R., 2011. New zircon shock phenomena and their use for dating and reconstruction of large impact structures revealed by electron nanobeam (EBSD, CL, EDS) and isotopic U–Pb and (U–Th)/He analysis of the Vredefort domeThis article is one of a series of papers published in this Special Issue on the theme of Geochronology in honour of Tom Krogh. Canadian Journal of Earth Sciences 48, 117–139. https://doi.org/10.1139/E11-011

Norman, M.D., Duncan, R.A., Huard, J.J., 2006. Identifying impact events within the lunar cataclysm from 40Ar–39Ar ages and compositions of Apollo 16 impact melt rocks. Geochimica et Cosmochimica Acta, A Special Issue Dedicated to Larry A. Haskin 70, 6032–6049. https://doi.org/10.1016/j.gca.2006.05.021

Osinski, G., Grieve, R.A.F., Tornabene, L.L., 2012. Excavation and impact ejecta emplacement, in: Impact Cratering: Processes and Products. John Wiley & Sons, Ltd.

Osinski, G., Pierazzo, E., 2012. Impact cratering: processes and products, in: Impact Cratering: Processes and Products. John Wiley & Sons, Ltd.

Osinski, G.R., Grieve, R.A.F., Ferrière, L., Losiak, A., Pickersgill, A.E., Cavosie, A.J., Hibbard, S.M., Hill, P.J.A., Bermudez, J.J., Marion, C.L., Newman, J.D., Simpson, S.L., 2022. Impact Earth: A review of the terrestrial impact record. Earth-Science Reviews 232, 104112. https://doi.org/10.1016/j.earscirev.2022.104112

Ostertag, R., 1983. Shock experiments on feldspar crystals. Journal of Geophysical Research: Solid Earth 88, B364–B376. https://doi.org/10.1029/JB088iS01p0B364

Parrish, R., 2015. Uranium–Lead Dating, in: Jack Rink, W., Thompson, J.W. (Eds.), Encyclopedia of Scientific Dating Methods, Encyclopedia of Earth Sciences Series. Springer Netherlands, Dordrecht, pp. 848–857. https://doi.org/10.1007/978-94-007-6304-3_193

Pike, R.J., 1980. Control of crater morphology by gravity and target type: Mars, Earth, Moon. Presented at the Lunar and Planetary Science Conference XI, pp. 2159–2189.

Rasmussen, C., Stockli, D.F., Erickson, T.M., Schmieder, M., 2020. Spatial U-Pb age distribution in shock-recrystallized zircon – A case study from the Rochechouart impact structure, France. Geochimica et Cosmochimica Acta 273, 313–330. https://doi.org/10.1016/j.gca.2020.01.017

Schaen, A.J., Jicha, B.R., Hodges, K.V., Vermeesch, P., Stelten, M.E., Mercer, C.M., Phillips, D., Rivera, T.A., Jourdan, F., Matchan, E.L., Hemming, S.R., Morgan, L.E., Kelley, S.P., Cassata, W.S., Heizler, M.T., Vasconcelos, P.M., Benowitz, J.A., Koppers, A.A.P., Mark, D.F., Niespolo, E.M., Sprain, C.J., Hames, W.E., Kuiper, K.F., Turrin, B.D., Renne, P.R., Ross, J., Nomade, S., Guillou, H., Webb, L.E., Cohen, B.A., Calvert, A.T., Joyce, N., Ganerød, M., Wijbrans, J., Ishizuka, O., He, H., Ramirez, A., Pfänder, J.A., Lopez-Martínez, M., Qiu, H., Singer, B.S., 2020. Interpreting and reporting 40Ar/39Ar geochronologic data. GSA Bulletin 133, 461–487. https://doi.org/10.1130/B35560.1

Schmieder, M., Tohver, E., Jourdan, F., Denyszyn, S., Haines, P., 2015. Zircons from the Acraman impact melt rock (South Australia): Shock metamorphism, U–Pb and 40Ar/39Ar systematics, and implications for the isotopic dating of impact events. Geochimica et Cosmochimica Acta 161, 71–100. https://doi.org/10.1016/j.gca.2015.04.021

Schmieder, M., Kring, D., 2020. Earth's Impact Events Through Geologic Time: A List of Recommended Ages for Terrestrial Impact Structures and Deposits | Astrobiology. Astrobiology 20, 91–141.

Short, N.M., 1970. Progressive Shock Metamorphism of Quartzite Ejecta from the Sedan Nuclear Explosion Crater. The Journal of Geology 78, 705–732. https://doi.org/10.1086/627572

Stöffler, D., Ryder, G., Ivanov, B.A., Artemieva, N.A., Cintala, M.J., Grieve, R.A.F., 2006. Cratering History and Lunar Chronology. Reviews in Mineralogy and Geochemistry 60, 519–596. https://doi.org/10.2138/rmg.2006.60.05

Stöffler, D., Hamann, C., Metzler, K., 2018. Shock metamorphism of planetary silicate rocks and sediments: Proposal for an updated classification system. Meteoritics & Planetary Science 53, 5–49. https://doi.org/10.1111/maps.12912

Taylor, S.R., 1982. Planetary science : a lunar perspective. Publishers Production International.

Thomas, J.B., Bodnar, R.J., Shimizu, N., Chesner, C.A., 2003. Melt Inclusions in Zircon. Reviews in Mineralogy and Geochemistry 53, 63–87. https://doi.org/10.2113/0530063

Timms, N.E., Kinny, P.D., Reddy, S.M., Evans, K., Clark, C., Healy, D., 2011. Relationship among titanium, rare earth elements, U–Pb ages and deformation microstructures in zircon: Implications for Ti-in-zircon thermometry. Chemical Geology 280, 33–46. https://doi.org/10.1016/j.chemgeo.2010.10.005

Timms, N.E., Erickson, T.M., Pearce, M.A., Cavosie, A.J., Schmieder, M., Tohver, E., Reddy, S.M., Zanetti, M.R., Nemchin, A.A., Wittmann, A., 2017. A pressure-temperature phase diagram for zircon at extreme conditions. Earth-Science Reviews 165, 185–202. https://doi.org/10.1016/j.earscirev.2016.12.008

Xie, T., Osinski, G.R., Shieh, S.R., 2020. Raman study of shock features in plagioclase feldspar from the Mistastin Lake impact structure, Canada. Meteoritics & Planetary Science 55, 1471–1490. https://doi.org/10.1111/maps.13523

Yin, F., Dai, D., 2020. A Study of Shock-Metamorphic Features of Feldspars from the Xiuyan Impact Crater. Minerals 10, 231. https://doi.org/10.3390/min10030231

Chapter 2

Impactful Dates: Coordinated $^{40}Ar/^{39}Ar$ Geochronology and Shock Study of the Kamestastin Lake Impact Structure, Canada

2.1 Abstract

The $^{40}Ar/^{39}Ar$ geochronometer is susceptible to resetting due to the high pressures and temperatures produced during meteorite impact events. These conditions can also alter minerals and produce textural and structural features indicative of the pressure-temperature conditions experienced. This study investigates correlations between mineral shock indicators, identified via optical microscopy and Raman spectroscopy, and $^{40}Ar/^{39}Ar$ resetting behaviors in impactites from the Kamestastin (Mistastin Lake) impact structure in Labrador, Canada. This is a well-preserved 28 km diameter complex impact structure, in ~1.4 Ga target rock (primarily anorthosite), with a previously determined putative age of ~38 Ma (U-Pb of impact grown zircon). Our results show that mangerite with no or minimal shock features showed no impact-related $^{40}Ar/^{39}Ar$ age resetting. Anorthosite with shock metamorphic features and no evidence of high-temperature heating (≳1150°C) yielded complex age spectra and no determinable meaningful ages. An impact glass sample yielded a weighted average age (~77 Ma) that is not coeval with any known regional event suggesting the age reflects the incorporation of excess ^{40}Ar during the impact event. Granite clasts, from within the impact melt rocks, that have shock features and evidence of impact heating to above 1450°C, displayed near full $^{40}Ar/^{39}Ar$ age resetting at the time of the impact. Fractional loss calculations indicate maximum impact heating lasted for seconds to hours for the two granite clast samples and they were not affected by post-impact hydrothermal heating. These $^{40}Ar/^{39}Ar$

results together indicate an impact age of 38.12 ± 0.07 Ma, consistent with the previous U-Pb zircon determination.

2.2 Introduction

Impact cratering is a widespread geologic process that occurs across all rocky and icy bodies in our Solar System and is the dominant surface process on most terrestrial planetary bodies (Osinski and Pierazzo, 2012). In planetary science, impacts serve as benchmarks for determining the ages of surfaces, constrain the timing of geologic events, and provide a connection between remote sensing and returned sample data (e.g., Taylor, 1982a; Morbidelli et al., 2012; Marchi et al., 2013). Impact events can produce extremely high temperatures and high pressures that may partially or fully reset rock sample geochronometers (Osinski et al., 2022). However, in many terrestrial impact structures, samples exhibit a wide range of shock pressures and temperatures resulting in heterogeneous age resetting on the outcrop to hand sample scale, which can complicate interpretations of impact event ages (e.g., Jourdan et al., 2009; Osinski et al., 2022).

Experimental studies have demonstrated that a hypervelocity impact produces varied age resetting for geochronologic systems such as Rb-Sr, Sm-Nd, and Pb-Pb (e.g., Gaffney et al., 2011). Analyses of planetary materials have also shown that shock heating can produce unique age resetting patterns, such as high-temperature Ar-loss in $^{40}Ar/^{39}Ar$ age spectra (e.g., Cassata et al., 2010). Due in part to the complex nature of age resetting, the majority of terrestrial impact craters have very poor age constraints (Osinski et al., 2022). Partial isotopic resetting makes interpreting geochronologic data difficult unless there is context to the isotopic resetting, such as the extent of shock damage and heating (Bogard, 1995). To better interpret and constrain the ages of both terrestrial and planetary impactites (samples produced by impacts), it is imperative to better

understand correlations between the level of physical and chemical alteration and the extent or nature of age resetting.

$^{40}Ar/^{39}Ar$ geochronology is one of the main methods used to constrain impact ages (Jourdan, 2012; Schmieder and Kring, 2020), and age reliability or open system behavior can also be assessed by performing step-heating analyses (Jourdan, 2012; Schmieder and Kring, 2020; Schaen et al., 2020). $^{40}Ar/^{39}Ar$ geochronology, when paired with physical characterization of samples to identify shock defects indicative of temperature and pressure conditions, is a promising approach to place constraints on the influence of impacts on bulk sample Ar diffusion. While there have been studies that investigated the relationships between the extent of $^{40}Ar/^{39}Ar$ age resetting and the level of shock in the mineral plagioclase feldspar (e.g., Jaret et al., 2018), these studies mainly focused on end member samples – e.g., crystalline, unshocked plagioclase and highly shocked maskelynite (diaplectic glass) – and the full range of shock conditions typically observed in impact structures and planetary materials have not been investigated. It is also important to investigate $^{40}Ar/^{39}Ar$ geochronology on bulk impactite samples (i.e., whole rock) in addition to mineral separates as an analog for planetary materials since many extraterrestrial samples have grain sizes that are too small for mineral separation.

Optical microscopy combined with Raman spectroscopy is effective in identifying and characterizing shocked minerals (Fritz et al., 2005; Jaret et al., 2018; Xie et al., 2020). Optical microscopy is useful in identifying shock features in a variety of different minerals such as quartz and feldspars. Common shock features include planar features (PFs), diaplectic glass, and undulose extinction, as well as fracturing, and optical mosaicism, which are not necessarily unique to hypervelocity impacts (Ferrière and Osinski, 2012). These features can help to assess relative shock conditions within and between samples (Singleton et al., 2011). Raman spectroscopy is a

non-destructive technique that is sensitive to crystallinity and deformation, making it an ideal method for determining structural variation and crystal lattice damage within a mineral resulting from impact shock (Fritz et al., 2005; Kayama et al., 2009; Xie et al., 2020). For example, in plagioclase feldspar, with increasing shock pressure, there is a progressive loss in crystallinity which is identified in Raman spectra via peak weakening, peak broadening, and the presence of new, broad peaks at certain peak positions (Xie et al., 2020; Xie et al., 2021).

To better understand the effects of impact pressure and temperature conditions on $^{40}Ar/^{39}Ar$ geochronology, we have conducted a paired geochronology, petrologic, and shock metamorphic survey of samples from the Kamestastin (also known as Mistastin Lake) impact structure in Newfoundland and Labrador, Canada (55°53'N, 63°18'W) (Figure 2.1) that have experienced a wide range of peak shock pressures and thermal histories (Mader and Osinski, 2018). Kamestastin is a complex impact structure of ~28 km in diameter. This impact structure was chosen because of the wide variety of impactites found at the structure (Mader and Osinski, 2018), the dominantly anorthositic target rock (~54-71%) making it useful as a lunar analog (Grieve, 1975), and the large age spread between the target rock age (~1.4 Ga; Marion and Sylvester, 2010; zircon U-Pb) and the putative age of the impact (~38 Ma; Sylvester et al., 2013; zircon U-Pb) which provides a framework for evaluating age resetting behaviors.

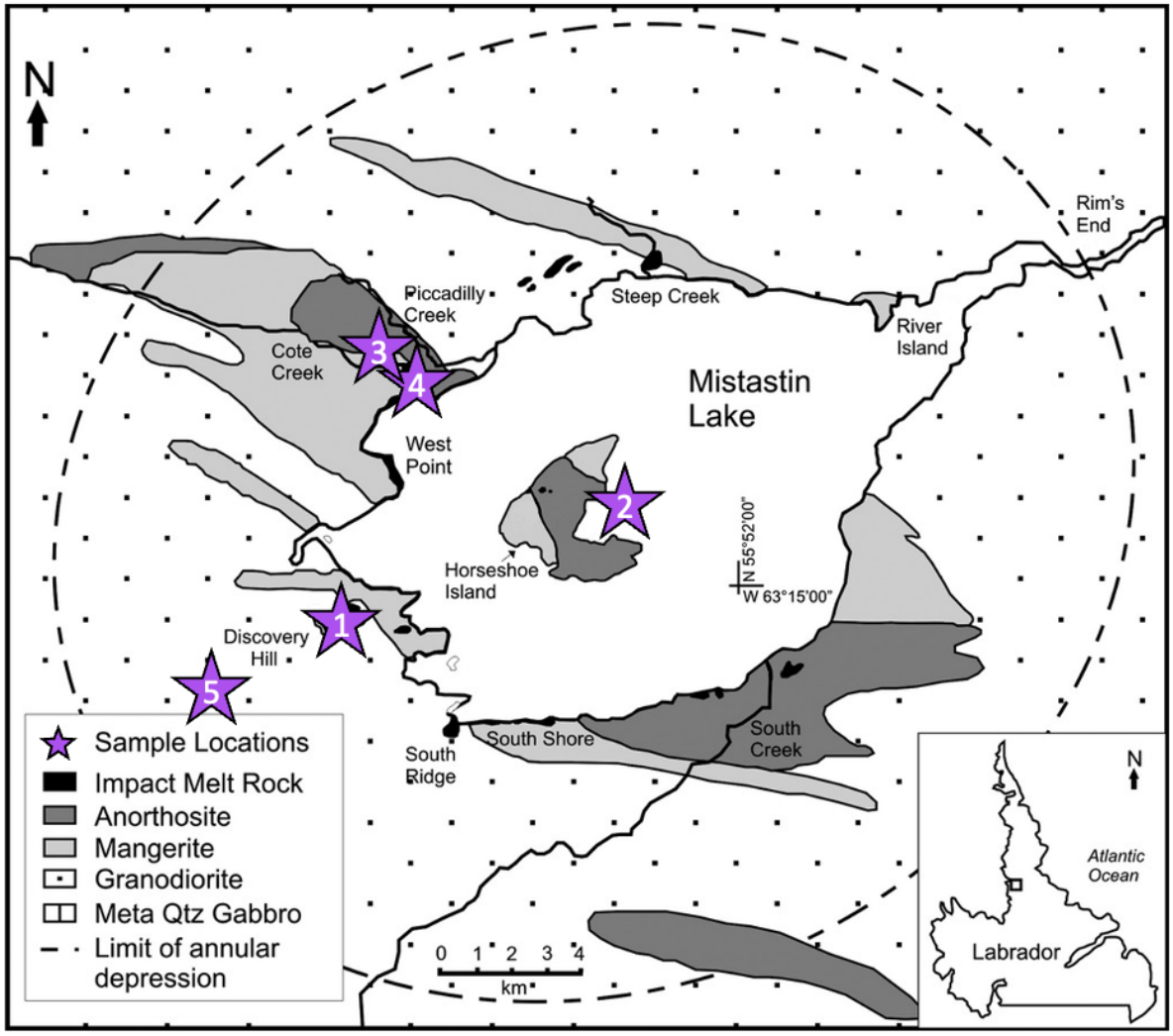

Figure 2.1: Map of the Kamestastin impact structure and the location of sample collection sites. Sample CM09-05 (impact glass) was collected from site 1, sample MM09-021b (anorthosite) was collected from site 2, samples MM10-028 (anorthosite) and MM10-016 (granite) were collected near site 3, sample MM09-035 (granite) collected from site 4, and sample 2021-3163 (mangerite) collected from site 5. Figure modified from Pickersgill et al. (2015).

2.3 Geologic Context and Samples

The Kamestastin Lake impact structure formed within the Mistastin Lake batholith, which is a part of the Canadian Shield and is composed of three main lithologies: anorthosite, mangerite (pyroxene-rich quartz monzonite), and granodiorite (Currie, 1971; Pickersgill et al., 2015).

Kamestastin has been previously used as a lunar analog site for impact studies (e.g., Antonenko et al., 2013; Young, 2014; Mader and Osinski, 2018) because of the dominance of plagioclase feldspar in the target rocks, which makes for a good analog for the anorthositic lunar highlands (Pickersgill et al., 2015). Kamestastin is one of only two known impact structures with anorthosite as a major target rock, the other being the Manicouagan impact structure, Quebec, Canada (Spray et al., 2010).

Previous geochronology studies of the Kamestastin structure have primarily focused on determining the age of the impact from melt rocks. There is some disagreement regarding the age of the impact, with age estimates ranging from 39.6 ± 8.8 Ma to 30.8 ± 1.4 Ma (Table 2.1; Figure B24) (Mak et al., 1976; Storzer and Wagner, 1977; Sylvester et al., 2013; Young, 2014). A wide array of plagioclase shock characteristics have previously been identified in Kamestastin samples from unshocked, crystalline materials to maskelynite (e.g., Pickersgill et al., 2015; Mader and Osinski, 2018; Xie et al., 2020). With such a wide array of documented plagioclase shock features, this impact crater is ideal for this study of the effects of shock conditions on the $^{40}Ar/^{39}Ar$ ages of impactites.

The samples analyzed in this study include unaltered target rock material, moderately to heavily shock-metamorphosed anorthosite, large granitic clasts (10's of cm size) in impact melt rocks, and impact glass that were collected from six locations within the Kamestastin structure (Figure 2.1). Samples were collected from the central uplift of the impact structure, terraces within the crater rim, and the near rim of the impact crater.

Table 2.1: Summary of Geochronology Completed at the Kamestastin Lake Impact Structure

Age	Location	Event	Material for Geochronology	Geochronologic technique	Study
36.0 ± 0.9 Ma	Discovery Creek	Impact age	Impact melt rock	$^{40}Ar/^{39}Ar$ in situ	Young, 2014
30.8 ± 1.4 Ma	Coté Creek	Impact age	Impact melt rock	$^{40}Ar/^{39}Ar$ in situ	Young, 2014
35.4 ± 0.6 Ma	Discovery Creek	Impact age	Zircon in mangerite boulders	(U-Th)/He	Young, 2014
37.2 ± 1.1 Ma	Coté Creek	Impact age	Zircon in impact melt	(U-Th)/He	Young, 2014
39.6 ± 8.8 Ma	Unknown	Impact age	Apatite	Fission track	Storzer and Wagner, 1977
37.8 ± 0.1 Ma	Discovery Hill	Impact age	Zircon in impact melt rock	U-Pb (TIMS)	Sylvester et al., 2013
36.0 ± 4.0 Ma	Unknown	Impact age	Impact glass	K-Ar	Wanless et al., 1974
38.0 ± 6.0 Ma	Unknown	Impact age	Impact glass	K-Ar	Wanless et al., 1974
37.8 ± 0.9 Ma	Unknown	Impact age	Impact glass	K-Ar	Mak et al., 1976
36.0 ± 4.0 Ma	Discovery Hill region?	Impact age	Impact glass	$^{40}Ar/^{39}Ar$	Mak et al., 1976; recalculated by Grieve, 2006
1451.0 ± 12.0 Ma	Horseshoe island	Target rock age	Zircon in mangerite	U-Pb (LA-(MC)-ICP-MS)	Marion and Sylvester, 2010
1438.7 ± 8.9 Ma	Horseshoe island	Target rock age	Zircon in anorthosite	U-Pb (LA-(MC)-ICP-MS)	Marion and Sylvester, 2010
1429.0 ± 10.0 Ma	Steep Creek and NE shore of lake	Target rock age	Zircon in granodiorite	U-Pb (LA-(MC)-ICP-MS)	Marion and Sylvester, 2010
1440.0 ± 13.0 Ma	Steep Creek and NE shore of lake	Target rock age	Zircon in granodiorite gneiss	U-Pb (LA-(MC)-ICP-MS)	Marion and Sylvester, 2010
1435.0 ± 12.0 Ma	Coté Creek	Target rock age	Zircon in melt rock	U-Pb (LA-(MC)-ICP-MS)	Marion and Sylvester, 2010
1431.0 ± 21.0 Ma	Steep Creek	Target rock age	Zircon in melt rock	U-Pb (LA-(MC)-ICP-MS)	Marion and Sylvester, 2010

1413.0 ± 13.0 Ma	South Ridge on SW bay of lake	Target rock age	Zircon in melt rock	U-Pb (LA-(MC)-ICP-MS)	Marion and Sylvester, 2010
1347.0 ± 30 Ma	Unknown	Target rock age	Unknown	Rb-Sr	Marchand and Crocket, 1974

2.4 Methods

One thin section was made from each sample, except for MM09-035 from which four thin sections were made. Sample classification was initially determined using a petrographic microscope. In general, the analysis protocol included (1) searching thin sections for optical shock features, (2) Raman spectroscopy on individual plagioclase feldspar crystals to quantify the level of shock deformation, and (3) $^{40}Ar/^{39}Ar$ geochronology of small aliquots of sample to assess the degree and characteristics of age resetting in each sample. The details of each analysis are included below.

2.4.1 Optical Microscopy

Initial characterization of thin sections was conducted at the University of Western Ontario, London, Canada. Plane-polarized and cross-polarized light were used to assess mineralogy and composition, identify impact shock features and alteration minerals, and develop a description for each sample. Sections were subsequently investigated at the University of Colorado Boulder to constrain the overall level of impact shock metamorphism across each sample. In particular, samples were examined for shock induced features in quartz, potassium feldspar, and plagioclase feldspar. Samples were also evaluated for evidence of thermal metamorphism, such as toasted

quartz (translucent brown "toasted" appearing quartz as a result of elevated temperatures and the pressure release after an impact, Ferrière et al., 2010).

2.4.2 Raman Spectroscopy

Raman spectroscopy was conducted at the University of Colorado Boulder using a Horiba LabRAM HR Evolution Raman spectrometer equipped with a 532 nm, 100mW frequency-doubled Nd:YAG laser excitation source, 600 mm^{-1} diffraction grating, 256x1024 pixel CCD detector, and 100x microscope objective (N.A. 0.9). A laser power of 50 or 100% was applied to a 1 μm spot size for 10 second acquisitions with three spectra accumulations each. Spectra were collected from 50 cm^{-1} to 1800 cm^{-1} by integrating the counts in the undiffracted, 256-pixel direction of the detector, such that each spectrum contains 1024 points. The resulting spectra were corrected using an 8th order polynomial baseline using LabSpec 6 software (Horiba Scientific, Inc.). The spectrometer was calibrated using the 520.7 cm^{-1} Raman peak of a silicon reference sample prior to analysis.

To determine the representative shock level across each sample, 3-6 grains of plagioclase that optically appeared to represent various degrees of shock (e.g., various degrees of fracturing and/or extinction) were analyzed on each section and multiple spectra (2-10) were collected on each targeted grain. Relative shock level was quantified using the procedures and shock level characterization (S1-S5) outlined in Xie et al. (2020) where shock level is assigned based on the observed changes in Raman peak position, intensity, and width, which are a result of microstructural deformation and loss of crystallinity. S1 is unshocked, S2 is weakly shocked, S3 is moderately shocked, S4 is strongly shocked, and S5 is very strongly shocked. Diagnostic two to

three prominent Raman peaks between 460 and 515 cm^{-1} identify the spectra as feldspar and the exact position, number of peaks, and distance between these peaks vary with composition. Peaks near the approximate following wavelengths of 185, 200, 285, 408, 480, 510, 568, 765, 795, 984, 1186, and 1216 cm^{-1} are considered to be unshocked and are classified as shock stage S1. When the main diagnostic peaks between 460 and 515 cm^{-1} begin to show slight broadening and peaks under 350 cm^{-1} have slight weakening, the sample is considered to be weakly shocked and classified as shock stage S2. Once there is a more significant broadening of the main peaks between 460 and 515 cm^{-1} and a diminishing of less prominent peaks, the sample is considered to be moderately shocked and is classified as shock stage S3. When there is a broad band near approximately 510 cm^{-1}, a shoulder near 580 cm^{-1}, the presence of a broad peak centered around 1050 cm^{-1}, and varying intensity of peaks, the sample is considered to be strongly shocked and is classified as shock stage S4. Once a sample reaches the very strongly shocked stage, it is considered to be composed entirely of glass material, as it no longer produces a discernable spectrum pattern and, therefore, is classified as shock stage S5. These changes in Raman spectra are a result of distortion and breaking of bonds, in particular in the tetrahedral bonds, within the crystal structure with increasing amorphization (Xie et al., 2020).

2.4.3 $^{40}Ar/^{39}Ar$ Geochronology

Small fragments of each sample, 2.22-12.38 mg, were used for bulk (or whole) rock and impact glass $^{40}Ar/^{39}Ar$ geochronology analyses. In general, the analytical methods follow those described in Sanders et al. (2006), however, details are included here that are specific to this study. Target (country) rock outcrop and clasts within melt rocks were degassed using a resistance furnace and impact glasses were degassed using a diode laser.

$^{40}Ar/^{39}Ar$ analyses were conducted at the New Mexico Institute of Mining and Technology. The samples were irradiated in machined Al disks in two separate irradiations. NM-324 was irradiated for 21 hours at the OSU reactor in the CLOCIT position, whereas NM-327 was irradiated for 20 hours at the USGS Denver reactor in the central thimble. Neutron flux gradients were measured using Fish Canyon sanidine (FC-2) placed in holes of known geometry in the Al disks. All ages and J-factors are calculated using the FC-2 at 28.201 Ma (Kuiper et al., 2008) and a total ^{40}K decay constant of 5.463e-10 yr^{-1} (Min et al., 2000). Respectively, six and eight single flux monitor crystals from eight positions of a 24-hole, 2.54 cm diameter tray were analyzed to determine the J-value. Mean values for each location were fit with a sine curve and J-values for unknowns were extrapolated based on their geometric relation to the monitors. J-factor uncertainties are determined at 0.02 to 0.05% (1σ). Correction factors for interfering reactions were measured using CaF_2 and K-glass included with the samples during irradiation. $^{40}Ar/^{39}Ar$ isotopic information and plots are in Appendix A and Appendix B.

All samples except the impact glass samples were step heated in a double vacuum molybdenum resistance furnace. Samples were wrapped in Cu-foil and heated with high resolution (30-35 steps) heating schedules, and isothermal replicate steps were conducted to help determine ^{39}Ar-derived kinetic parameters. Heating times for steps less than 1100°C were 10 and 20 minutes with the 1100°C step as long as 4 hours. Gas clean up used a SAES GP-50 getter operated at 1.54 A during the heating, followed by a second stage clean up for 60 seconds using an additional SAES GP-50 getter operated at 1.54 A. Several replicates of the impact glass were incrementally heated with a diode laser with a heating time of 60 seconds followed by 45 seconds of gas clean up using a SAES GP-50 getter operated at 1.54 A. Gas was also exposed to a cold finger operated at -140°C to remove water. Argon isotopes were measured using a Thermo-Fisher Scientific Helix MC-plus

multi-collector mass spectrometer. ^{40}Ar and ^{37}Ar was measured on the H2 and L2 Faradays, respectively, using a 10^{12} Ohm resistor, ^{39}Ar on the H1 Faraday with a 10^{13} Ohm resistor, and ^{38}Ar on the Axial Faraday with a 10^{14} Ohm resistor. ^{36}Ar was measured on a CDD ion counter with a dead time of 20 ns. The furnace thermocouple was calibrated by melting Cu-foil. Furnace blank and background values were determined by running a 10 minute, 800°C hot blank before each analysis. Blank values are nearly insignificant (less than 1%) compared to the measured sample gas.

Calibration gases of air and a gas mixture enriched in radiogenic ^{40}Ar along with ^{39}Ar were analyzed interspersed with the unknowns to monitor instrument drift and determine detector intercalibration factors. All data collection was conducted with Pychron software and data reduction using MassSpec version 7.875. Flux monitors were degassed with a CO_2 laser and isotopes were collected for 120 seconds followed by 30-45 seconds of baseline measurement using the ARGUS VI mass spectrometer. Isotopes for the samples were measured for 340 seconds followed by a 60 second baseline measurement.

Plateau ages (criteria based weighted mean ages) are commonly defined by three or more consecutive heating steps representing >50% of ^{39}Ar release with an MSWD <2.5 (McDougall and Harrison, 1999). Due to the high-precision of multi-collector noble gas spectrometry (Schaen et al., 2020), samples that produced a "flat" age spectrum reflecting minimum age dispersion between heating steps had high MSWD values due to the high-precision analytical results. Hence, we report a "mini" plateau age for sample MM10-016 to isolate the most statistically significant age population (i.e., lower MSWD values) (Table 2.2) (Matchan et al., 2018; Heath et al., 2020). Mini plateau and weighted average ages are calculated based on a weighted mean with the weighting factor being the inverse variance (e.g., Taylor, 1982b) and the uncertainty is the square root of the

sum of $1/\sigma^2$ values. The reported uncertainty is multiplied by the square root of the MSWD for MSWD greater than 1 and uncertainties are reported at 2σ. J-uncertainty and irradiation correction factor uncertainties are included for all weighted mean age uncertainties.

2.5 Results

In general, samples displayed a wide range of shock metamorphism and age resetting behaviors (Figure 2.2), and the age resetting behaviors vary with different shock metamorphic features. Below is a description of the results for each sample and a summary of the findings is given in Table 2.2. Inverse isochron plots are presented in Appendix B (Figure B25-B33) for completeness but do not provide valid regressions to initial $^{40}Ar/^{36}Ar$ because of the generally radiogenic (~100%) and homogenous nature of the individual incremental radiogenic ^{40}Ar step heating gas composition and the overall high precision (<0.1%) of the isotopic data.

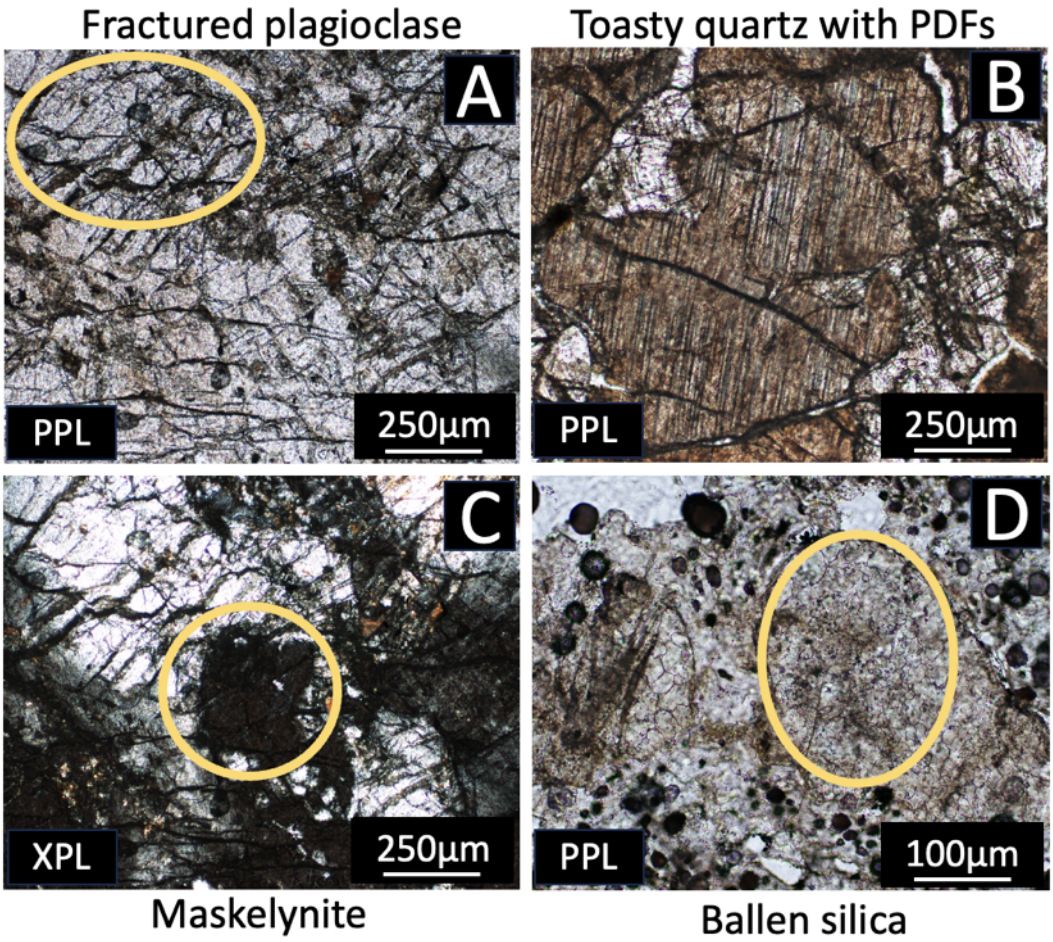

Figure 2.2: Thin section images illustrating major shock features (circled in light orange) observed in Kamestastin samples. Images are in plane-polarized light (PPL) or cross-polarized light (XPL). (A) Heavily fractured plagioclase suggests low shock pressures (1-5 GPa) and temperatures (MM09-021B) (Stöffler et al., 2018; Hu and Sharp, 2022) (B) Toasted quartz with planar features indicates rapid high temperatures after an impact event and pressures of ~10-30 GPa (MM09-021B) (Ferrière et al., 2010, Stöffler et al., 2018) (C) Maskelynite, or diaplectic glass, requires shock pressures ~35 GPa and a lack of extended periods of elevated temperatures (MM09-021B) (Ostertag, 1983; Fritz et al., 2005; Stöffler et al., 2018) (D) Ballen silica suggests very high peak temperatures exceeding 1200°C for hours (MM09-035) (Ferrière et al., 2009; Ferrière et al., 2010).

2.5.1 Mangerite

Mangerite collected near the west rim of the impact structure (sample 2021-3163; Figure 2.1, Site 5, Figure B1) is considered a relatively unaltered target rock and serves as a baseline for the pre-impact $^{40}Ar/^{39}Ar$ age. This sample is fractured suggesting minimal impact related

metamorphism (Figure 2.2; Figure B6). Raman spectra from individual plagioclase crystals are consistent with shock stages S1-S2 (Figure 2.3; Figure B15). The $^{40}Ar/^{39}Ar$ analysis produced a slightly jagged age spectrum with an integrated (total gas) age of 1342.25 ± 0.92 Ma (Figure 4A, B20, B25, and Table 2.2).

2.5.2 Anorthosite

One sample collected from the central uplift (Horseshoe Island, sample MM09-021B; Figure 2.1, Site 2; Figure B2) and one sample from an inner terrace (Piccadilly Creek, MM10-028; Figure 2.1, Site 3; Figure B5) are classified as anorthosite. Sample MM09-021B displayed a variety of optical shock features including fracturing, toasted quartz, planar features (PFs) in quartz, undulose extinction in some plagioclase crystals, and maskelynite (Figure 2 and B7). The Raman spectra are consistent with shock stages S3-S4 (Figure 3 and B16), and the $^{40}Ar/^{39}Ar$ analysis from this sample did not yield an age determination. The first step has an age of 133.01 ± 1.60 Ma, and each step has a progressively older age until it reaches a maximum age of 1227.87 ± 11.05 Ma (Figure 4B and B26).

Sample MM10-028 is fractured but otherwise does not display additional shock features in thin section (Figure 2 and B10). Raman spectra in plagioclase from this sample are classified as shock level S3 (Figure 3 and B18). Additional Raman spectra of visually altered minerals identified these minerals as prehnite, chabazite, and grossular (Figure B19). The $^{40}Ar/^{39}Ar$ age spectrum has a similar pattern to that of sample MM09-021B. The first step from this sample has an age of 34.75 ± 2.09 Ma and the last step has an age of 1352.61 ± 16.47 Ma (Figure 4C, B22,

and B29). Due to the stepping up nature of the release pattern, no age determination was possible for samples MM10-028 and MM09-021B.

2.5.3 Impact Glass

Impact glass was collected from an inner terrace area of the crater (CM09-05; Figure 2.1, Site 1). This sample primarily consists of whole rock impact glass with lithic clasts ranging from 150 µm-1 mm in size (Figure B14). Some mineral clasts are visible in the prepared thin section. These are fractured, but no plagioclase crystals were identified for Raman spectra analyses. $^{40}Ar/^{39}Ar$ ages from four aliquots of one impact glass sample yielded spectra with relatively flat regions reflecting >60% of gas released. Weighted mean ages for the flat regions of these spectra yield ages of 80.22 ± 0.55 Ma, 78.93 ± 0.84 Ma, 78.84 ± 0.42 Ma, and 77.42 ± 0.24 Ma (Figure 2.4D, B20, B23, and Table 2.2).

2.5.4 Granite

Two granite clast samples were collected from impact melt rocks from an inner terrace region of the structure at different localities along Coté Creek (MM09-035 and MM10-016; Figure 2.1, Site 4 and Site 3, respectively; Figure B3 and B4 respectively). Fractures, ballen silica, and undulose extinction in potassium feldspar were found in sample MM09-035 (Figure 2, B8, and B11-B13). Raman spectra of this sample suggest a shock stage of S2-S3 (Figure 3 and B17) and the $^{40}Ar/^{39}Ar$ age spectrum produced a weighted average age (28.7% of ^{39}Ar; MSWD = 10) of 37.95 ± 0.06 Ma (Figure 4E, B27, and Table 2.2). Sample MM10-016 displayed the same optical shock features as sample MM09-035 with the addition of minor amounts of glass (Figure 2 and

B9). No plagioclase feldspar crystals were identified in this sample for plagioclase Raman shock analyses. This sample produced a mini plateau age (35.8% of ^{39}Ar; MSWD = 2) of 38.20 ± 0.04 Ma (Figure 4F, B21, B28, and Table 2.2) with a weighted average K/Ca ratio of 6.93 ± 1.58. The higher temperature steps also produced a mini plateau age of (24.5% of ^{39}Ar; MSWD = 1) of 37.83 ± 0.04 Ma, but since the weighted average K/Ca ratio is 2.33 ± 0.43 we prefer to use the higher K phases of the gas release for the age determination for this sample. To better constrain the thermal histories of these granite clasts and the conditions required for age resetting, thermal resetting calculations were conducted of samples MM10-016 and MM09-035 and is discussed in section 2.6.2.

Table 2.2: Summary of Shock Metamorphic Features and ^{40}Ar/^{39}Ar Geochronology

Geographic Location	Rock Type	Sample ID	Shock features	^{40}Ar/^{39}Ar Age spectra characteristics	Age spectra ages	T and P conditions
Discovery Hill (Figure 1, Site 1)	Impact glass	CM09-05	Hyaline matrix, fractured clasts, possible alteration to phyllosilicates	Partially reset age is geologically meaningless (between target rock and true impact age) (Figure 4, panel F)	**Integrated age**: 81.42 ± 0.09 Ma **Weighted average age**: 77.42 ± 0.24 Ma **%^{39}Ar released**: 83.4 **MSWD**: 2.7 **N**=4 (of 10)	T: >2370°C P: >60 GPa
Horseshoe Island (Figure 1, Site 2)	Shocked anorthosite	MM09-021B	Fractures, "toasted" quartz, PFs in quartz, undulose extinction in plagioclase, maskelynite	No plateau age, "stair-stepping" age spectra, geologically meaningless ages (Figure 4, panel B)	**Integrated age**: 762.39 ± 0.94 Ma **Plateau age**: none	T: at least 300°C P: ~35 GPa

Coté Creek (Figure 1, Site 3)	Shocked and baked granite	MM10-016	Fractures, ballen silica, undulose extinction in k-spar, glass	Mini plateau age of consistent with the putative age of impact (Figure 4, panel C)	**Integrated age**: 39.13 ± 0.09 Ma **Mini plateau age**: 38.20 ± 0.04 Ma **%^{39}Ar released**: 35.8 **MSWD**: 2 **N**=6 (of 30)	T: >1150°C P: >45 GPa
Piccadilly Creek (Figure 1, Site 3)	Anorthosite	MM10-028	Fractures, presence of hydrothermal minerals (prehnite, chabazite, and grossular)	No plateau age, "stair-stepping" age spectra, geologically meaningless ages (Figure 4, panel D)	**Integrated age**: 527.69 ± 0.74 Ma **Plateau age**: none	T: <200-350°C P: <1 GPa
Coté Creek (Figure 1, Site 4)	Shocked and baked granite	MM09-035	Fractures, ballen silica, undulose extinction in k-spar	Mini plateau age consistent with putative age of impact (Figure 4, panel E)	**Integrated age**: 50.33 ± 0.12 Ma **Weighted average age**: 37.95 ± 0.06 Ma **%^{39}Ar released**: 28.7 **MSWD**: 10 **N**=5 (of 35)	T: >1150°C P: >~5-10 GPa
Near west rim (Fig .1, Site 5)	Mangerite	2021-3163	Fractures	Integrated age consistent with target rock age (Figure 4, panel A)	**Integrated age**: 1342.25 ± 0.92 Ma **Plateau age**: none	T: <25°C P: <1 GPa

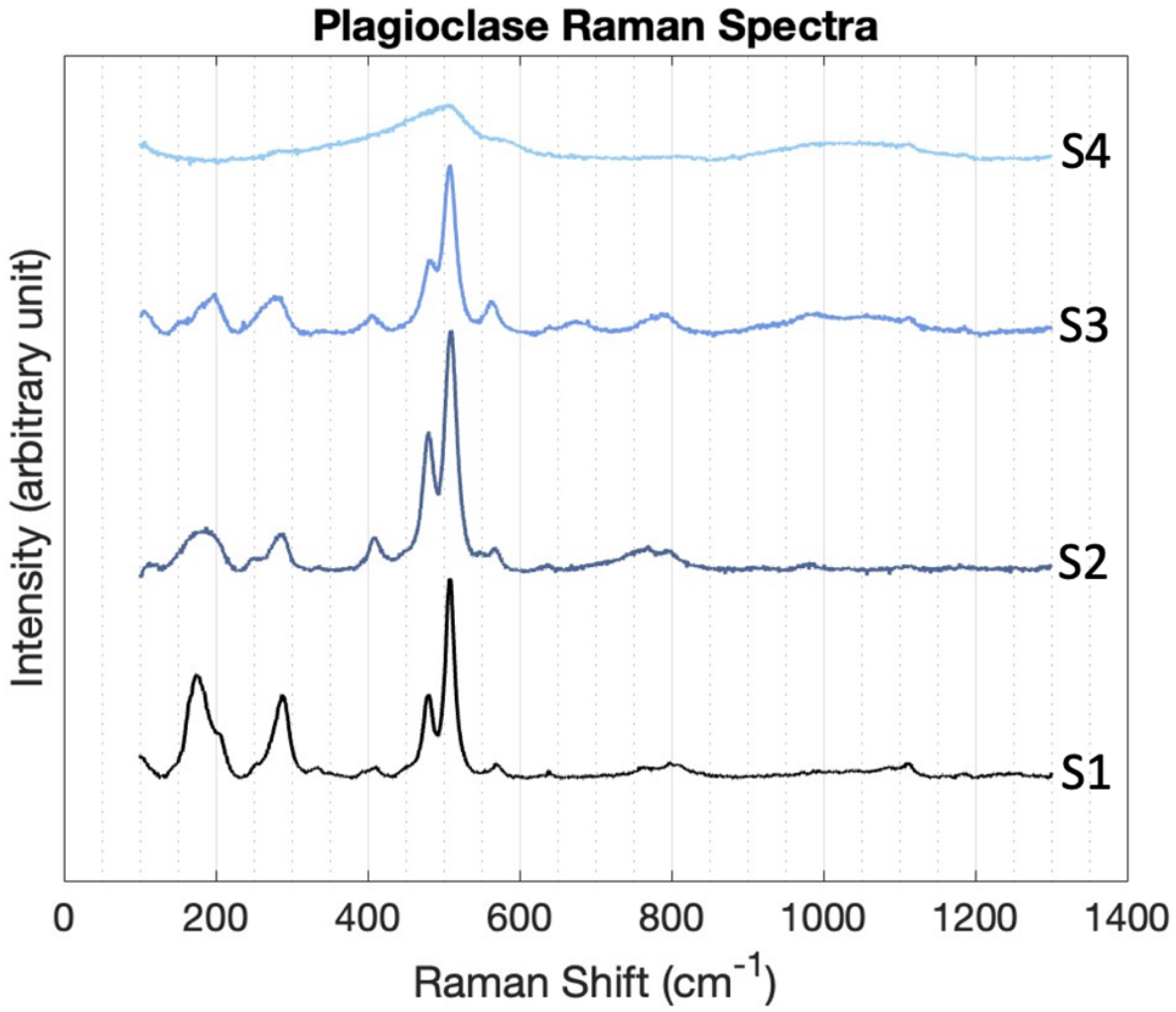

Figure 2.3: Raman spectra from plagioclase crystals displaying the range of shock seen across samples. There is a range from unshocked (S1), weak shock (S2), moderately shocked (S3), and strongly shocked (S4) spectra present in these samples. There is a general trend of peak broadening and peak loss with increasing shock as well as an increased presence of a broad shoulder around 1000-1050 cm^{-1}.

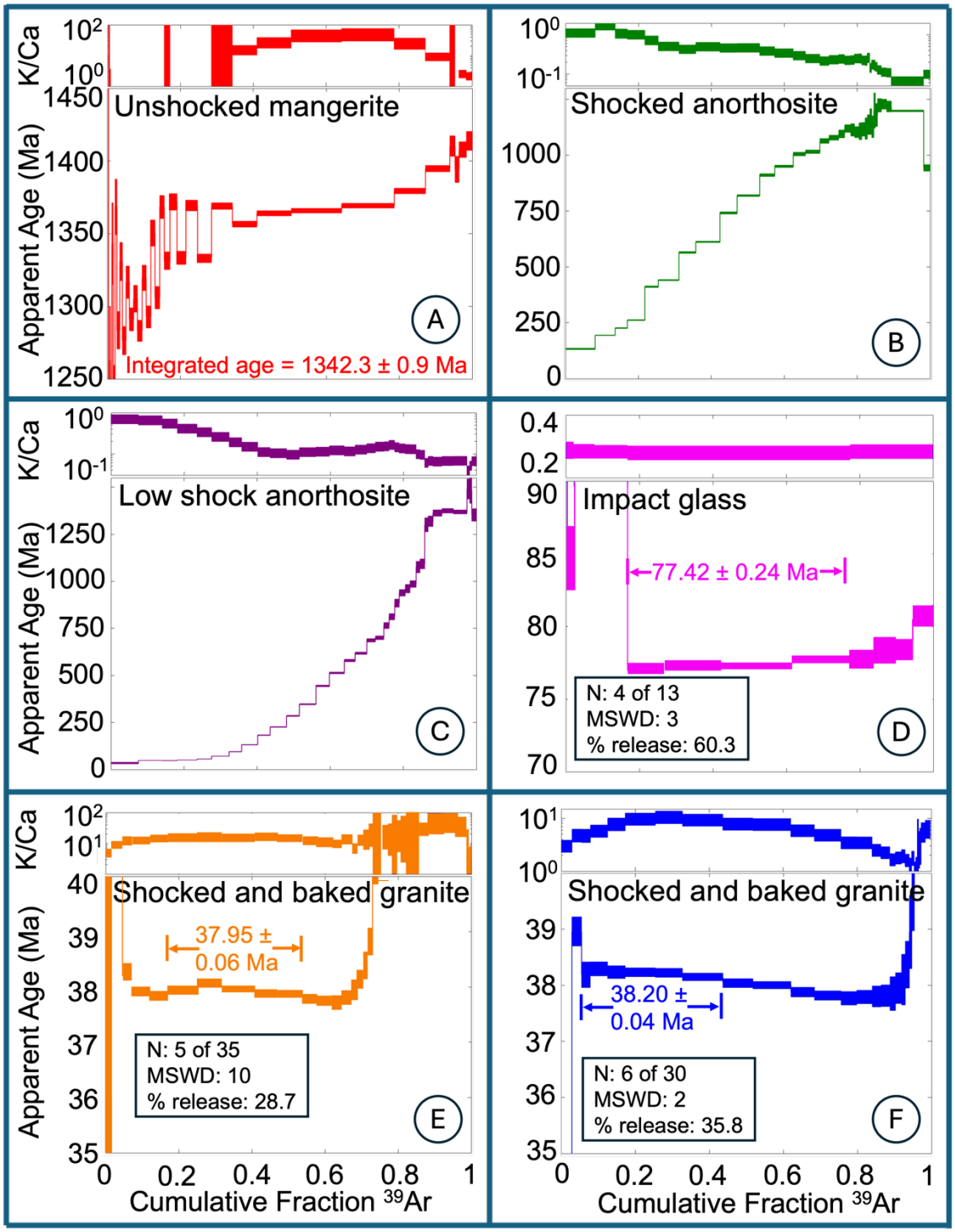

Figure 2.4: $^{40}Ar/^{39}Ar$ age spectra and K/Ca graphs for each rock type in this study. Samples show a variety of age resetting from no resetting of age in unshocked materials (A) to near full resetting during the impact event in samples that were exposed to extended elevated temperatures (B, C) as well as some partial resetting seen in shocked rocks (D, E) and impact glass (F). 2σ uncertainty reported. A = 2021-3163, B = MM10-016, C = MM09-035, D = MM09-021b, E = MM10-028, F = CM09-05.

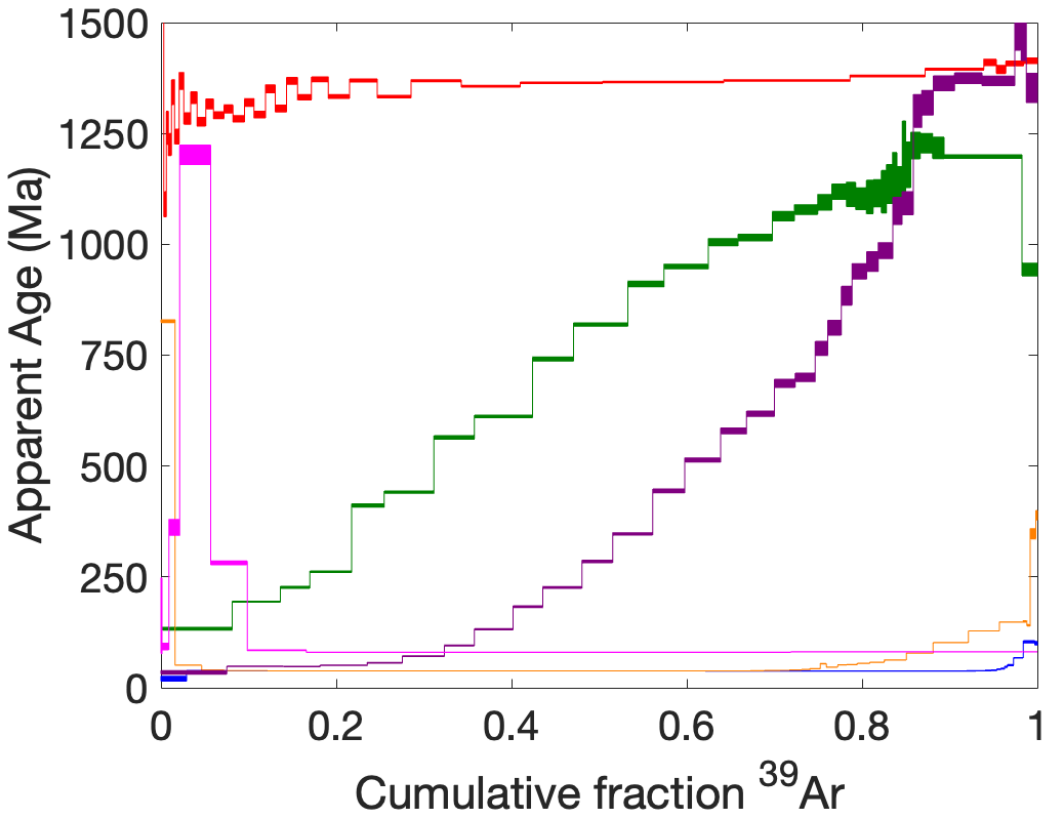

Figure 2.5: Combined $^{40}Ar/^{39}Ar$ age spectra from all samples in this study to better illustrate the various degrees of $^{40}Ar/^{39}Ar$ age resetting observed across the samples. Red = 2021-3163 (unshocked mangerite), green = MM09-021b (shocked anorthosite), purple = MM10-028 (anorthosite), pink = CM09-05 (impact glass), orange = MM09-035 (shocked and baked granite), blue = MM10-016 (shocked and baked granite). 2σ uncertainty reported.

2.6 Discussion

Since impact events can produce extremely high temperatures and pressures that may partially or fully reset geochronometers (Osinski et al., 2022), our ability to date an impact and interpret geochronologic data for impactites relies on determining relationships between petrologic indicators and age resetting behaviors. These observations can then be scaled up to include field context that could inform and improve sample selection in the field for impact craters in general on Earth and other planetary bodies. The Kamestastin samples in this study display a wide range

of shock features and $^{40}Ar/^{39}Ar$ age resetting behaviors (Figure 2.5 and Table 2.2) that can be used to probe these relationships. In the following section, we summarize the observed correlations between optical shock features, Raman analyses, and $^{40}Ar/^{39}Ar$ geochronology. These attributes are then used to better understand the range in impact ages for the Kamestastin impact structure and provide a recommended age for this impact event. All samples were found to contain fracturing which suggests that all samples were exposed to at least low shock pressures (<1 GPa) and low temperature heating of up to ~25°C (Stöffler et al., 2018; Hu and Sharp, 2022).

2.6.1 Investigating Pre-Impact Age Resetting

The mangerite sample, which is the least-shocked target rock sample, shows evidence of exposure to low shock pressures (<1 GPa). This minimally altered target rock material resulted in an integrated $^{40}Ar/^{39}Ar$ age of 1342.25 ± 0.92 Ma (Table 2.2 and Figure 2.4A). This age approximates the previously measured target rock ages of 1451 ± 12 Ma (2σ) to 1347 ± 30 Ma (2σ) determined by U-Pb zircon and bulk rock Rb-Sr geochronology, respectively (Marion and Sylvester, 2010). While some features in this sample, like fractures, may be the result of the Kamestastin impact, these impact conditions do not appear to alter the resulting $^{40}Ar/^{39}Ar$ geochronometer of this sample significantly. This result confirms that there were no post-crystallization and pre-impact events that influenced $^{40}Ar/^{39}Ar$ systematics in the region surrounding Kamestastin.

2.6.2 Partial Resetting and Impact Glasses

The two shocked anorthosite samples (MM09-021b and MM10-028) were affected by partial age resetting and show stair-step age spectra (Figure 4B and 4C) similar to what can be seen in $^{40}Ar/^{39}Ar$ age spectra from Apollo samples (e.g., Dalrymple and Ryder, 1996; Norman et al., 2006). It is typically thought that geologically meaningful ages cannot be recovered from these types of age spectra (McDougal and Harrison, 1999). This is best illustrated by sample MM09-021b (Figure 2.4B). Maskelynite was observed in this sample, indicating shock pressures near 35 GPa and temperatures ~300°C (Ostertag, 1983; Fritz et al., 2005; Stöffler et al., 2018). Jaret et al. (2018) found that analyses of maskelynite at the Manicouagan impact crater resulted in plateau age determinations yielding geologically meaningless ages, therefore implying possible widespread complexities in age interpretations of maskelynite ages. Our results further suggest the pressure and temperature conditions necessary to form and retain maskelynite result in only partial Ar-loss both in individual grains and bulk samples.

The other anorthosite sample, MM10-028, produced a similar stair-step age spectrum (Figure 2.4C). This sample is less shocked but also contains the minerals prehnite, chabazite, and grossular, determined via Raman spectra, which are produced from hydrothermal alteration (Figure B19) (Naumov, 2002; Naumov, 2005; Kring et al., 2020). Prehnite, chabazite, and grossular typically form in hydrothermal systems with temperatures ranging from <200-350°C (Naumov, 2002; Naumov, 2005). The oldest step ages derived from this sample are consistent with the age of the mangerite target rock samples. The lowest temperature step for this sample is 34.75 ± 2.09 Ma which is below the weighted average ages for our granite clast samples, which speculatively suggests this sample may have experienced age resetting by post-impact processes. While hydrothermal alteration has been noted at Kamestastin, it is not pervasive throughout the

structure (Bermudez et al., 2022). However, previous $^{40}Ar/^{39}Ar$ analyses of impact melt rock and (U-Th)/He geochronology of zircons from a variety of rock types at Kamestastin yielded numerous single grain ZHe and $^{40}Ar/^{39}Ar$ spot ages (Young, 2014) younger than the ~38 Ma age of the impact (this study). These results, along with our identification of hydrothermal minerals suggest hydrothermal systems may be playing a role in geochronology resetting. However, further work is needed to confirm the extent and duration of impact induced hydrothermal activity at Kamestastin.

Impact glasses, in general, form under high temperatures and pressures of >60 GPa and post-shock temps of >1500°C (French, 1998; Osinski et al., 2018). The glass in this study is different than most previously dated terrestrial impact glasses, which consist of clasts within impact melt-bearing breccia ("suevite") samples or ejecta products like tektites and spherules (Schmieder and Kring, 2020 and references therein). The Kamestastin impact glass we analyzed came from a unique glassy sample in which previous studies identified cubic zirconia suggesting it was superheated to temperatures above 2370°C (Timms et al., 2017; Tolometti et al., 2022). The $^{40}Ar/^{39}Ar$ ages of these impact glass samples yielded weighted average ages of ~77-80 Ma, significantly older than the ~38 Ma impact age (this study) for the Kamestastin impact event and younger than the oldest target rock (1451 ± 12 Ma (2σ); Marion and Sylvester, 2010). The high temperatures implied by the cubic zirconia are high enough for full resetting of the $^{40}Ar/^{39}Ar$ geochronometer in Kamestastin target rock materials (Goldsmith, 1980; Section 2.6.4). Thus, the age of the Kamestastin glass may reflect the incorporation of radiogenic Ar degassed from surrounding rock material during melt sheet formation during the impact event (Jourdan et al., 2007; Schwarz and Lippolt, 2014). Additionally, the possible presence of impact-induced hydrothermal activity at the Kamestastin site can introduce excess Ar into impact glass samples through fluid interactions, as was noted in previous studies of other impact structures (e.g.,

Schmieder and Jourdan, 2013; Schwarz and Lippolt, 2014; Schmieder et al., 2018). This inherited or excess Ar scenario can be amplified when there is a large age spread between the target rock age and the impact rock age (Jourdan et al., 2007) as is the case of the Kamestastin impact event. Though impact glass has been used to date impact events (e.g., Mark et al., 2014; Mercer et al., 2015; Pickersgill et al., 2020), careful consideration needs to be made when determining geologically significant ages from glassy impact material (Jourdan et al., 2011).

2.6.3 Full Resetting and Age of Kamestastin Lake Impact

The granite clasts samples (MM10-016 and MM09-035) collected within impact melt rocks were fully or nearly (~90%) reset in the $^{40}Ar/^{39}Ar$ geochronology system (Table 2.2 and Figure 4E and 4F). The pressures associated with the formation of ballen silica are debated, but undulatory extinction in potassium feldspar suggests shock pressures of ≳5-10 GPa and glass suggests shock pressures of >45 GPa (French, 1998; Ferrière et al., 2009; Ferrière et al., 2010; Chanou et al., 2015; Stöffler et al., 2018). The presence of ballen silica suggests temperatures over 1150°C for timescales of seconds to hours (French, 1998; Ferrière et al., 2009; Ferrière et al., 2010; Stöffler et al., 2018). These two granite clast samples yielded a consistent mini plateau age of 38.20 ± 0.04 Ma (MM10-016) and a weighted average age of 37.95 ± 0.06 Ma (MM09-035), which is concordant with previous estimates of the impact age using U-Pb dating of zircon (37.83 ± 0.05 Ma; Sylvester et al., 2013). Jaret et al. (2018) made a similar observation at the Manicouagan impact structure where clasts within the impact melt sheet had fully reset $^{40}Ar/^{39}Ar$ ages consistent with the impact age. However, these samples differ from our granite samples in that the clasts in this study are significantly larger (10's of cm vs. 1.5-2 cm).

2.6.4 Thermal History of Kamestastin Granite Clast Reset Samples

While the petrologic constraints suggest pressures of >5-10 GPa and/or exposure to temperatures above ~1150°C, fractional loss calculations can place more refined constraints on the time-temperature conditions required to fully or partially reset $^{40}Ar/^{39}Ar$ ages. We constrained diffusion parameters (activation energy and frequency factor) based on Arrhenius plots from the $^{40}Ar/^{39}Ar$ temperature-time controlled diffusion experimental results and performed fractional loss calculations to determine the temperature-time histories necessary to fully reset the $^{40}Ar/^{39}Ar$ ages of feldspars in the granitic samples. Both plagioclase and potassium feldspar (K-spar) were identified in the sections of sample MM09-035. While only K-spar was observed in the one thin section sample MM10-016, granodiorite from Kamestastin typically contains a mixture of both plagioclase (30%) and K-spar (25%) (Marion, 2009). As such, we assume that most of the Ar within the granitic clasts resides in a mixture of plagioclase and K-spar. The K/Ca ratios in Figure 2.4E and 2.4F are also consistent with this conclusion, with K/Ca values between 1 and 20 for the two granite clast samples. Typical plagioclase has $^{40}Ar/^{39}Ar$ analysis K/Ca ratios of <0.5 and K-feldspar has K/Ca ratios of >10 (e.g., Schaen et al., 2020), further supporting the granite clasts $^{40}Ar/^{39}Ar$ results are reflecting a mixture of the degassing of plagioclase and K-feldspar.

Arrhenius plots of samples MM09-035 and MM10-016 are shown in Figure C1 (summary of diffusion parameter and fractional loss calculations provided in Appendix C; plane sheet geometry was assumed). Both samples are consistent with mixing between two diffusion domains. A single phase is visualized as a line on an Arrhenius plot where activation energy (E_a) is proportional to the slope and the frequency factor (D_0/r^2) is the y-intercept. To constrain the diffusion kinetics of these samples we fit the data using the multiple diffusion domain (MDD) program from Lovera et al. (1989), and we also constrained diffusion parameters assuming E_a of

crystalline plagioclase and orthoclase (the major Ar-hosting phases) and solving for D_0/r^2. The Lovera program determines the best fit E_a and D_0/r^2 for the lowest temperature steps assuming they are consistent with a single phase. The steps fit by the Lovera program are those that yielded impact ages for both samples. The best fit for both samples has an E_a of 31.9 ± 1.9 kcal/mol, which is lower than crystalline plagioclase. To further assess the influence of this lower E_a, we calculated the diffusion kinetics for these same steps assuming the measured activation energy of crystalline plagioclase from the Nain Complex (Cassata et al., 2013) and manually fit D_0/r^2; this sample has a similar plagioclase composition as is observed in the Kamestastin samples (Xie et al., 2020) (see Table C1). We also conducted similar calculations for the more retentive phase using the E_a of Benson Mines orthoclase (Cassata et al., 2013).

We next used these diffusion parameters to constrain the temperature-time conditions required to reset the ages of the granite clast samples (Appendix C). We used the following assumptions for the fractional loss calculations: (1) plagioclase loses 100% of Ar; (2) orthoclase loses 90% Ar since the higher temperature steps for the two granite clasts are not fully reset and orthoclase (350°C; e.g., Schaen et al., 2020) has a higher maximum closure temperature than plagioclase (~225-300°C; Cassata et al., 2013); (3) a single pulse heating event of constant temperature. These assumptions are further supported by the increase in K/Ca at the high temperature steps in Figure 2.4F. We calculated the resetting time at 1150°C, 1450°C, and 2000°C. The lower temperatures are consistent with experiments that produced ballen silica (Ferrière et al., 2009), and the highest temperature is consistent with shock heating observed in meteorite samples (Cassata et al., 2010). At 1150°C, it takes ~10-40 minutes to degas the plagioclase and ~40 days to degas orthoclase. At 1450°C, degassing is significantly faster; ~1 minute or less to reset the

plagioclase and ~7.6 hours for the orthoclase. If temperatures were to exceed 2000°C, it would take seconds to fully reset the plagioclase domains and minutes to reset orthoclase.

While our calculations suggest it is possible to reset the $^{40}Ar/^{39}Ar$ ages at the minimum temperature of 1150°C, petrologic constraints do not support this heating scenario. The fractional loss calculations suggest the 1150°C temperature would need to be maintained for over a month. We would expect to see significant melting and/or recrystallization of the feldspars in this sample if it were kept near the melting temperature of orthoclase (1170°C; Tuttle and Bowen, 1958) for this long duration. However, only a minimal amount of melting (~2% glass) was seen in one of the granite clast samples. As such, a higher temperature (≥1450°C) and shorter duration (≤1 minute to ~8 hours) heating pulse best explains both the petrologic and thermochronologic observations. These conditions are consistent with interpretations of zircon microstructures from Kamestastin of rapid cooling from peak temperatures >2370°C (Tolometti et al., 2022). Our observation of a range of Ar-loss behavior between the different samples at Kamestastin also agrees with the heterogeneity in peak temperatures observed in zircons microstructures as well as observations of heterogeneous melting and microstructures in impactites representing an array of conditions in other terrestrial impact structures (e.g., Osinski et al., 2022).

In summary, the most robust $^{40}Ar/^{39}Ar$ constraint of the Kamestastin impact age was obtained from samples with evidence of exposure to elevated temperatures (granite clasts in impact melt), but not present in a reservoir of impact released ^{40}Ar (impact glass). A unique feature of these granite clast samples was the presence of ballen silica. The presence of this impact induced texture may be indicative of exposure to conditions adequate to reset $^{40}Ar/^{39}Ar$ geochronology. Furthermore, the overall degree of shock pressure does not seem to be correlated with age resetting. Notably, the one sample with high pressure/low temperature maskelynite produced a complicated,

uninterpretable age spectrum (Figure 2.4B). It appears the high shock pressures necessary to form maskelynite and the lack of significant heating required to retain maskelynite are not sufficient to fully reset $^{40}Ar/^{39}Ar$ ages. Additionally, caution should be taken when dating impact glass as excess or inherited ^{40}Ar within quenched glass can produce geologically meaningless ages.

2.7 Summary and Conclusions

Combined optical microscopy and Raman spectroscopy can be advantageous for assessing impactites prior to $^{40}Ar/^{39}Ar$ geochronologic studies and placing the data in a framework of shock pressures and thermal constraints. Since previous studies also found heterogeneous pressure, temperature, and time conditions across the Kamestastin impact structure (Tolometti et al., 2022), this study furthered this understanding via determining shock and thermal conditions necessary for understanding ages of impactites through microtextural analysis. Kamestastin samples that experienced only brief exposure to high shock pressures, and associated temperatures, exhibited complicated age spectra (Figure 2.4B and 2.4C), making it difficult to interpret any geologically meaningful ages from these samples. This further emphasizes the importance of detailed petrology in assessing the cause of age resetting. Kamestastin impact glass samples yielded $^{40}Ar/^{39}Ar$ weighted average ages (~77-80 Ma) that were younger than the target rock age (~1440 Ma; Marion and Sylvester, 2010), but also older than the true impact age (~38 Ma; this study). These Kamestastin glass dates likely reflect incorporation of degassed radiogenic ^{40}Ar from surrounding rock material during the impact event as observed in other impact events (Jourdan et al., 2007; Schwarz and Lippolt, 2014). Kamestastin impact glass weighted average ages, without other geochronology context, would appear to reflect the age of the Kamestastin impact event.

The Kamestastin granite clasts that were exposed to high temperatures (≥ 1450°C) during the impact and contained ballen silica yielded ages of the impact event suggesting that samples do not need to fully recrystallize to give a reliable impact age. Based on our overall $^{40}Ar/^{39}Ar$ geochronology application, in the context of previous U-Pb geochronology zircon work (Sylvester et al., 2013), we assign an age of 38.12 ± 0.07 Ma (2σ) to the Kamestastin impact event. Furthermore, we constrained the Kamestastin impact event led to high temperature (≥1450°C) conditions that lasted for seconds to hours at this sample site. Younger ages from other studies reported for this structure (Table 2.1) may be due in part to post-impact hydrothermal systems as demonstrated at other impact sites (e.g., Schmieder and Jourdan, 2013; Schmieder et al., 2018).

Overall, caution must be taken during impact geochronology analysis, because shock, temperature, post-impact hydrothermal conditions, and available rock materials vary between impact events. In terms of best practice for dating impact events, we recommend:

1) Collecting and analyzing diverse rock materials including unaltered target rock, crystalline melt rocks, clasts within impact melt rocks that were heated, but not fully recrystallized, and authigenic impact zircons if present, as others have suggested (Buchner et al., 2010).
2) Impact temperature conditions more so than maximum shock pressure appear to have a greater influence on Ar diffusion in rock material. While petrologic studies of impactites to identify shock features are important, samples investigated for geochronology should be further assessed for evidence of thermal and hydrothermal alteration. In particular, the presence of ballen silica may be a useful indicator of appropriate pressure-temperature conditions needed to reset $^{40}Ar/^{39}Ar$ geochronology.

3) Applying a range of radiometric systems (e.g., U-Pb, $^{40}Ar/^{39}Ar$, U-Th/He) to multiple impactites at a single impact site is likely required to distinguish between partial resetting/inheritance, post-impact hydrothermal system effects, and the true age of the impact event.

2.8 Acknowledgments

The authors would like to thank Dr. Matt Heizler of the New Mexico Bureau of Geology and Mineral Resources for his assistance in collecting and processing $^{40}Ar/^{39}Ar$ data. An additional thanks to Dr. Tianqi Xie for discussion of Raman analyses and interpretation. Raman measurements were completed in the Raman Microscopy Laboratory at the University of Colorado Boulder (RRID: SCR_019305) and was supported by internal University of Colorado Boulder funding. The authors also thank the Innu Nation on whose lands the Kamestastin Lake impact structure lie for their permission and support to conduct fieldwork.

2.9 References

Antonenko, I., Osinski, G.R., Battler, M., Beauchamp, M., Cupelli, L., Chanou, A., Francis, R., Mader, M.M., Marion, C., McCullough, E., Pickersgill, A.E., Preston, L.J., Shankar, B., Unrau, T., Veillette, D., 2013. Issues of geologically-focused situational awareness in robotic planetary missions: Lessons from an analogue mission at Mistastin Lake impact structure, Labrador, Canada. Advances in Space Research, Lunar Exploration - II 52, 272–284. https://doi.org/10.1016/j.asr.2012.11.024

Bermudez, J.P., Osinski, G.R., Tolometti, G.D., Chinchalkar, N.S., 2022. Impact-Generated Hydrothermal Alteration at the Mistastin Lake Impact Structure, Canada 2678, 2671.

Bogard, D.D., 1995. Impact ages of meteorites: A synthesis. Meteoritics 30, 244–268. https://doi.org/10.1111/j.1945-5100.1995.tb01124.x

Buchner, E., Schwarz, W.H., Schmieder, M., Trieloff, M., 2010. Establishing a 14.6 ± 0.2 Ma age for the Nördlinger Ries impact (Germany)—A prime example for concordant isotopic ages from various dating materials. Meteoritics & Planetary Science 45, 662–674. https://doi.org/10.1111/j.1945-5100.2010.01046.x

Cassata, W.S., Shuster, D.L., Renne, P.R., Weiss, B.P., 2010. Evidence for shock heating and constraints on Martian surface temperatures revealed by 40Ar/39Ar thermochronometry of Martian meteorites. Geochimica et Cosmochimica Acta 74, 6900–6920. https://doi.org/10.1016/j.gca.2010.08.027

Cassata, W.S., Renne, P.R., 2013. Systematic variations of argon diffusion in feldspars and implications for thermochronometry. Geochimica et Cosmochimica Acta 112, 251–287. https://doi.org/10.1016/j.gca.2013.02.030

Chanou, A., Grieve, R.A.F., Osinski, G.R., 2015. Formation of Ballen in Silica by Thermal Shock. Presented at the Bridging the Gap III: Impact Cratering In Nature, Experiments, and Modeling.

Currie, K.L., 1971. Geology of the Resurgent Cryptoexplosion Crater at Mistastin Lake, Labrador. Geological Survey of Canada Bulletin: Department of energy, mines, and resources.

Dalrymple, G.B., Ryder, G., 1996. Argon-40/argon-39 age spectra of Apollo 17 highlands breccia samples by laser step heating and the age of the Serenitatis basin. Journal of Geophysical Research: Planets 101, 26069–26084. https://doi.org/10.1029/96JE02806

Ferrière, L., Koeberl, C., Reimold, W.U., 2009. Characterisation of ballen quartz and cristobalite in impact breccias: new observations and constraints on ballen formation. European Journal of Mineralogy 21, 203–217. https://doi.org/10.1127/0935-1221/2009/0021-1898

Ferrière, L., Koeberl, C., Libowitzky, E., Reimold, W.U., Greshake, A., Brandstätter, F., 2010. Ballen quartz and cristobalite in impactites: New investigations, in: Large Meteorite Impacts

and Planetary Evolution IV. Geological Society of America, pp. 609–618. https://doi.org/10.1130/2010.2465(29)

Ferrière, L., Osinski, G.R., 2012. Shock Metamorphism. In: Osinski, G.R., Pierazzo, E. (Eds.), Impact Cratering: Processes and Products, 1st ed., 106-124, John Wiley & Sons, Ltd. https://doi.org/10.1002/9781118447307

French, B.M., 1998. Traces of Catastrophe: A Handbook of Shock-Metamorphic Effects in Terrestrial Meteorite Impact Structures.

Fritz J., Greshake A., Stoffler D., 2005. Micro-Raman spectroscopy of plagioclase and maskelynite in Martian meteorites: Evidence of progressive shock metamorphism. Antarctic meteorite research 18, 96–116. https://doi.org/10.15094/00006067

Gaffney, A.M., Borg, L.E., Asmerom, Y., Charles K. Shearer, Burger, P.V., 2011. Disturbance of isotope systematics during experimental shock and thermal metamorphism of a lunar basalt with implications for Martian meteorite chronology. Meteoritics & Planetary Science 46, 35–52. https://doi.org/10.1111/j.1945-5100.2010.01137.x

Goldsmith, J.R., 1980. The melting and breakdown reactions of anorthite at high pressures and temperatures. American Mineralogist 65, 272–284.

Grieve, R.A.F., 1975. Petrology and chemistry of the impact melt at Mistastin Lake crater, Labrador. GSA Bulletin 86, 1617–1629. https://doi.org/10.1130/0016-7606(1975)86<1617:PACOTI>2.0.CO;2

Grieve, Richard A. F., 2006. Mistastin, in: Impact Structures in Canada. Earth Science Sector Natural Resources Canada, Geological Association of Canada, pp. 115–120.

Heath, M., Phillips, D., Matchan, E.L., 2020. Basalt lava flows of the intraplate Newer Volcanic Province in south-east Australia (Melbourne region): 40Ar/39Ar geochronology reveals ~8 Ma of episodic activity. Journal of Volcanology and Geothermal Research 389, 106730. https://doi.org/10.1016/j.jvolgeores.2019.106730

Hu, J., Sharp, T.G., 2022. Formation, preservation and extinction of high-pressure minerals in meteorites: temperature effects in shock metamorphism and shock classification. Prog Earth Planet Sci 9, 6. https://doi.org/10.1186/s40645-021-00463-2

Jaret, S.J., Hemming, S.R., Rasbury, E.T., Thompson, L.M., Glotch, T.D., Ramezani, J., Spray, J.G., 2018. Context matters – Ar–Ar results from in and around the Manicouagan Impact Structure, Canada: Implications for martian meteorite chronology. Earth and Planetary Science Letters 501, 78–89. https://doi.org/10.1016/j.epsl.2018.08.016

Jourdan, F., Renne, P.R., Reimold, W.U., 2007. The problem of inherited 40Ar* in dating impact glass by the 40Ar/39Ar method: Evidence from the Tswaing impact crater (South Africa).

Geochimica et Cosmochimica Acta 71, 1214–1231. https://doi.org/10.1016/j.gca.2006.11.013

Jourdan, F., Renne, P.R., Reimold, W.U., 2009. An appraisal of the ages of terrestrial impact structures. Earth and Planetary Science Letters 286, 1–13. https://doi.org/10.1016/j.epsl.2009.07.009

Jourdan, F., Moynier, F., Koeberl, C., Eroglu, S., 2011. 40Ar/39Ar age of the Lonar crater and consequence for the geochronology of planetary impacts. Geology 39, 671–674. https://doi.org/10.1130/G31888.1

Jourdan, F., 2012. The 40Ar/39Ar dating technique applied to planetary sciences and terrestrial impacts. Australian Journal of Earth Sciences 59, 199–224. https://doi.org/10.1080/08120099.2012.644404

Kayama, M., Gucsik, A., Nishido, H., Ninagawa, K., Tsuchiyama, A., 2009. Cathodoluminescence and Raman Spectroscopic Characterization of Experimentally Shocked Plagioclase. American Institute of Physics Conference Proceedings 1163, 86–95. https://doi.org/10.1063/1.3222897

Kring, D.A., Tikoo, S.M., Schmieder, M., Riller, U., Rebolledo-Vieyra, M., Simpson, S.L., Osinski, G.R., Gattacceca, J., Wittmann, A., Verhagen, C.M., Cockell, C.S., Coolen, M.J.L., Longstaffe, F.J., Gulick, S.P.S., Morgan, J.V., Bralower, T.J., Chenot, E., Christeson, G.L., Claeys, P., Ferrière, L., Gebhardt, C., Goto, K., Green, S.L., Jones, H., Lofi, J., Lowery, C.M., Ocampo-Torres, R., Perez-Cruz, L., Pickersgill, A.E., Poelchau, M.H., Rae, A.S.P., Rasmussen, C., Sato, H., Smit, J., Tomioka, N., Urrutia-Fucugauchi, J., Whalen, M.T., Xiao, L., Yamaguchi, K.E., 2020. Probing the hydrothermal system of the Chicxulub impact crater. Science Advances 6, eaaz3053. https://doi.org/10.1126/sciadv.aaz3053

Kuiper, K.F., Deino, A., Hilgen, F.J., Krijgsman, W., Renne, P.R., Wijbrans, J.R., 2008. Synchronizing Rock Clocks of Earth History. Science 320, 500–504. https://doi.org/10.1126/science.1154339

Lovera, O.M., Richter, F.M., Harrison, T.M., 1989. The 40Ar/39Ar thermochronometry for slowly cooled samples having a distribution of diffusion domain sizes - Lovera - 1989 - Journal of Geophysical Research: Solid Earth - Wiley Online Library. Journal of Geophysical Research: Solid Earth 94, 17917–17935. https://doi.org/10.1029/JB094iB12p17917

Mader, M.M., Osinski, G.R., 2018. Impactites of the Mistastin Lake impact structure: Insights into impact ejecta emplacement. Meteoritics & Planetary Science 53, 2492–2518. https://doi.org/10.1111/maps.13173

Mak, E.K., York, D., Grieve, R.A.F., Dence, M.R., 1976. The age of the Mistastin Lake crater, Labrador, Canada. Earth and Planetary Science Letters 31, 345–357. https://doi.org/10.1016/0012-821X(76)90116-3

Marchand, M., Crocket, J.H., 1974. The Mistastin Lake pluton and meteorite crater, northern Labrador. Presented at the Geological Association of Canada/Mineral Association of Canada Joint Annual Meeting, St. John's, Newfoundland, p. 58.

Marchi, S., Bottke, W.F., Cohen, B.A., Wünnemann, K., Kring, D.A., McSween, H.Y., De Sanctis, M.C., O'Brien, D.P., Schenk, P., Raymond, C.A., Russell, C.T., 2013. High-velocity collisions from the lunar cataclysm recorded in asteroidal meteorites. Nature Geosci 6, 303–307. https://doi.org/10.1038/ngeo1769

Marion, C.L., 2009. Geology, distribution and geochemistry of impact melt at the Mistastin lake impact crater, Labrador (masters). Memorial University of Newfoundland.

Marion, C.L., Sylvester, P.J., 2010. Composition and heterogeneity of anorthositic impact melt at Mistastin Lake crater, Labrador. Planetary and Space Science, Exploring other worlds by exploring our own: The role of terrestrial analogue studies in planetary exploration 58, 552–573. https://doi.org/10.1016/j.pss.2009.09.018

Mark, D.F., Lindgren, P., Fallick, A.E., 2014. A high-precision 40Ar/39Ar age for hydrated impact glass from the Dellen impact, Sweden. Geological Society, London, Special Publications 378, 349–366. https://doi.org/10.1144/SP378.22

Matchan, E.L., Phillips, D., Traine, E., Zhu, D., 2018. 40Ar/39Ar ages of alkali feldspar xenocrysts constrain the timing of intraplate basaltic volcanism. Quaternary Geochronology 47, 14–28. https://doi.org/10.1016/j.quageo.2018.04.009

McDougall, I., Harrison, T.M., 1999. Geochronology and Thermochronology by the 40Ar/39Ar Method. Oxford University Press.

Mercer, C.M., Young, K.E., Weirich, J.R., Hodges, K.V., Jolliff, B.L., Wartho, J.-A., van Soest, M., 2015. Refining lunar impact chronology through high spatial resolution 40Ar/39Ar dating of impact melts | Science Advances. Science Advances 1. https://doi.org/DOI: 10.1126/sciadv.1400050

Min, K., Mundil, R., Renne, P.R., Ludwig, K.R., 2000. A test for systematic errors in 40Ar/39Ar geochronology through comparison with U/Pb analysis of a 1.1-Ga rhyolite. Geochimica et Cosmochimica Acta 64, 73–98. https://doi.org/10.1016/S0016-7037(99)00204-5

Morbidelli, A., Lunine, J.I., O'Brien, D.P., Raymond, S.N., Walsh, K.J., 2012. Building Terrestrial Planets. Annu. Rev. Earth Planet. Sci. 40, 251–275. https://doi.org/10.1146/annurev-earth-042711-105319

Naumov, M.V., 2002. Impact-Generated Hydrothermal Systems: Data from Popigai, Kara, and Puchezh-Katunki Impact Structures, in: Plado, J., Pesonen, L.J. (Eds.), Impacts in Precambrian Shields. Springer, Berlin, Heidelberg, pp. 117–171. https://doi.org/10.1007/978-3-662-05010-1_6

Naumov, M.V., 2005. Principal features of impact-generated hydrothermal circulation systems: mineralogical and geochemical evidence. Geofluids 5, 165–184. https://doi.org/10.1111/j.1468-8123.2005.00092.x

Norman, M.D., Duncan, R.A., Huard, J.J., 2006. Identifying impact events within the lunar cataclysm from 40Ar–39Ar ages and compositions of Apollo 16 impact melt rocks. Geochimica et Cosmochimica Acta, A Special Issue Dedicated to Larry A. Haskin 70, 6032–6049. https://doi.org/10.1016/j.gca.2006.05.021

Osinski, G., Pierazzo, E., 2012. Impact cratering: processes and products, in: Impact Cratering: Processes and Products. John Wiley & Sons, Ltd.

Osinski, G.R., Grieve, R.A.F., Bleacher, J.E., Neish, C.D., Pilles, E.A., Tornabene, L.L., 2018. Igneous rocks formed by hypervelocity impact. Journal of Volcanology and Geothermal Research 353, 25–54. https://doi.org/10.1016/j.jvolgeores.2018.01.015

Osinski, G.R., Grieve, R.A.F., Ferrière, L., Losiak, A., Pickersgill, A.E., Cavosie, A.J., Hibbard, S.M., Hill, P.J.A., Bermudez, J.J., Marion, C.L., Newman, J.D., Simpson, S.L., 2022. Impact Earth: A review of the terrestrial impact record. Earth-Science Reviews 232, 104112. https://doi.org/10.1016/j.earscirev.2022.104112

Ostertag, R., 1983. Shock experiments on feldspar crystals. Journal of Geophysical Research: Solid Earth 88, B364–B376. https://doi.org/10.1029/JB088iS01p0B364

Pickersgill, A.E., Osinski, G.R., Flemming, R.L., 2015. Shock effects in plagioclase feldspar from the Mistastin Lake impact structure, Canada. Meteoritics & Planetary Science 50, 1546–1561. https://doi.org/10.1111/maps.12495

Pickersgill, A.E., Mark, D.F., Lee, M.R., Osinski, G.R., 2020. 40Ar/39Ar systematics of melt lithologies and target rocks from the Gow Lake impact structure, Canada. Geochimica et Cosmochimica Acta 274, 317–332. https://doi.org/10.1016/j.gca.2020.01.025

Sanders, R.E., Heizler, M.T., Goodwin, L.B., 2006. 40Ar/39Ar thermochronology constraints on the timing of Proterozoic basement exhumation and fault ancestry, southern Sangre de Cristo Range, New Mexico. GSA Bulletin 118, 1489–1506. https://doi.org/10.1130/B25857.1

Schaen, A.J., Jicha, B.R., Hodges, K.V., Vermeesch, P., Stelten, M.E., Mercer, C.M., Phillips, D., Rivera, T.A., Jourdan, F., Matchan, E.L., Hemming, S.R., Morgan, L.E., Kelley, S.P., Cassata, W.S., Heizler, M.T., Vasconcelos, P.M., Benowitz, J.A., Koppers, A.A.P., Mark, D.F., Niespolo, E.M., Sprain, C.J., Hames, W.E., Kuiper, K.F., Turrin, B.D., Renne, P.R., Ross, J., Nomade, S., Guillou, H., Webb, L.E., Cohen, B.A., Calvert, A.T., Joyce, N., Ganerød, M., Wijbrans, J., Ishizuka, O., He, H., Ramirez, A., Pfänder, J.A., Lopez-Martínez, M., Qiu, H., Singer, B.S., 2020. Interpreting and reporting 40Ar/39Ar geochronologic data. GSA Bulletin 133, 461–487. https://doi.org/10.1130/B35560.1

Schmieder, M., Jourdan, F., 2013. The Lappajärvi impact structure (Finland): Age, duration of crater cooling, and implications for early life. Geochimica et Cosmochimica Acta 112, 321–339. https://doi.org/10.1016/j.gca.2013.02.015

Schmieder, M., Kennedy, T., Jourdan, F., Buchner, E., Reimold, W.U., 2018. A high-precision 40Ar/39Ar age for the Nördlinger Ries impact crater, Germany, and implications for the accurate dating of terrestrial impact events. Geochimica et Cosmochimica Acta 220, 146–157. https://doi.org/10.1016/j.gca.2017.09.036

Schmieder, Martin, Kring, David, 2020. Earth's Impact Events Through Geologic Time: A List of Recommended Ages for Terrestrial Impact Structures and Deposits | Astrobiology. Astrobiology 20, 91–141.

Schwarz, W.H., Lippolt, H.J., 2014. 40Ar-39Ar step-heating of impact glasses from the Nördlinger Ries impact crater—Implications on excess argon in impact melts and tektites. Meteoritics & Planetary Science 49, 1023–1036. https://doi.org/10.1111/maps.12309

Singleton, A.C., Osinski, G.R., McCausland, P.J.A., Moser, D.E., 2011. Shock-induced changes in density and porosity in shock-metamorphosed crystalline rocks, Haughton impact structure, Canada. Meteoritics & Planetary Science 46, 1774–1786. https://doi.org/10.1111/j.1945-5100.2011.01290.x

Spray, J.G., Thompson, L.M., Biren, M.B., O'Connell-Cooper, C., 2010. The Manicouagan impact structure as a terrestrial analogue site for lunar and martian planetary science. Planetary and Space Science, Exploring other worlds by exploring our own: The role of terrestrial analogue studies in planetary exploration 58, 538–551. https://doi.org/10.1016/j.pss.2009.09.010

Stöffler, D., Hamann, C., Metzler, K., 2018. Shock metamorphism of planetary silicate rocks and sediments: Proposal for an updated classification system. Meteoritics & Planetary Science 53, 5–49. https://doi.org/10.1111/maps.12912

Storzer, D., Wagner, G.A., 1977. Fission Track Dating of Meteorite Impacts. Meteoritics 12, 368–369.

Sylvester, P.J., Crowley, J.L., Schmitz, M.D., 2013. U-Pb zircon age of Mistastin Lake crater, Labrador, Canada - implications for high-precision dating of small impact melt sheets and the end Eocene extinction, in: Mineralogical Magazine. Presented at the Goldschmidt, p. 2295.

Taylor, S.R., 1982a. Planetary science: a lunar perspective. Publishers Production International.

Taylor, J.R., 1982b. An introduction to error analysis: the study of uncertainties in physical measurements. University science books, Mill Valley, CA.

Timms, N.E., Erickson, T.M., Zanetti, M.R., Pearce, M.A., Cayron, C., Cavosie, A.J., Reddy, S.M., Wittmann, A., Carpenter, P.K., 2017. Cubic zirconia in >2370 °C impact melt records

Earth's hottest crust. Earth and Planetary Science Letters 477, 52–58. https://doi.org/10.1016/j.epsl.2017.08.012

Tolometti, G.D., Erickson, T.M., Osinski, G.R., Cayron, C., Neish, C.D., 2022. Hot rocks: Constraining the thermal conditions of the Mistastin Lake impact melt deposits using zircon grain microstructures. Earth and Planetary Science Letters 584, 117523. https://doi.org/10.1016/j.epsl.2022.117523

Tuttle, O.F., Bowen, N.L. (Eds.), 1958. Origin of Granite in the Light of Experimental Studies in the System NaAlSi3O8–KAlSi3O8–SiO2–H2O, in: Origin of Granite in the Light of Experimental Studies in the System NaAlSi3O8–KAlSi3O8–SiO2–H2O. Geological Society of America, p. 0. https://doi.org/10.1130/MEM74-p1

Wanless, R.K., Stevens, R.D., Lachance, G.R., Delabio, R.M.D., 1974. Age Determinations and Geological Studies K-Ar Isotopic Ages, Report 12. Geological Survey of Canada 145–148.

Xie, T., Osinski, G.R., Shieh, S.R., 2020. Raman study of shock features in plagioclase feldspar from the Mistastin Lake impact structure, Canada. Meteoritics & Planetary Science 55, 1471–1490. https://doi.org/10.1111/maps.13523

Xie, T., Osinski, G.R., Shieh, S.R., 2021. Raman study of shock effects in lunar anorthite from the Apollo missions. Meteoritics & Planetary Science 56, 1633–1651. https://doi.org/10.1111/maps.13728

Young, K., 2014. The use of terrestrial analogs in preparing for planetary surface exploration: sampling and radioisotopic dating of impactites and deployment of in situ analytical technologies. Arizona State University.

Chapter 3

The Effects of Impacts on Ejecta: Correlating U-Pb Geochronology and Shock Microtextural Study of Ejecta Zircons from the Chicxulub Impact

3.1 Abstract

Impact events generate extreme temperature and pressure conditions that can significantly alter both target rock material within the crater and ejected materials. These conditions have the potential to partially or fully reset geochronometers. The U-Pb system in zircon, a common accessory mineral, is particularly valuable for investigating impact ages and effects. This study examines zircons ejected from the Chicxulub impact (~66 Ma, Mexico) and deposited in the Raton Basin ~2,300 km away in southern Colorado and northern New Mexico (USA). Shock microtextures in these zircons were analyzed using electron backscatter diffraction (EBSD) and paired with U-Pb dating via secondary ionization mass spectrometry (SIMS). Our results indicate that the ejecta environment encompasses a wide range of temperature and pressure conditions, as inferred from the diversity of identified microtextures that form under certain temperature and/or pressure conditions (0–30 GPa and/or temperatures exceeding 1673°C). High-pressure shock features (e.g., plastic deformation, shock twinning, reidite) do not lead to U-Pb age resetting, whereas high-temperature microtextures (e.g., granular textures, former reidite in granular neoblastic (FRIGN) zircon) can result in complete resetting to the impact age. Since granular and FRIGN zircons can reliably record the impact age, these grains should be preferentially targeted for dating impact events. However, caution is necessary when dating impacts of unknown age, as not all granular or FRIGN zircons undergo complete resetting. The youngest single population of

ages of granular grains resulted in an accurate determination of the Chicxulub impact age within uncertainty and has potential to be used as a methodology for determining the age of an unknown impact.

3.2 Introduction

During large impact events, the intense temperature and pressure conditions that occur over extremely short periods of time (fractions of a second) can heavily alter the affected material. Depending on the mineral and the geochronometer, these high temperature and pressure shock conditions can variably reset ages. The extent of resetting can often be challenging to determine, making it difficult to accurately interpret measured dates and assign an age to impact structures. As a result, there is a need to better understand the effects of these impact conditions on the physicochemical behavior and changes within individual mineral grains and their resulting ages. Conducting an extensive survey of geochronology and impact induced microtextures in individual mineral grains from an impact and target rock material of known age can elucidate our understanding of how geochronometers are reset in impact settings (Ross et al., 2021a).

The U-Pb geochronometer in zircon ($ZrSiO_4$) is commonly used for dating impact materials on Earth as well as impact samples from other planetary bodies, including the Moon and meteorites (Corfu et al., 2015; Nemchin et al., 2015; Schmieder and Kring, 2020). While zircons are relatively resistant to shock processes compared to other minerals, the U-Pb geochronometer may be affected if shocked to sufficiently high pressures or temperatures (Moser et al., 2011). This has been observed in multiple studies of variably shocked zircons in both terrestrial and extra-terrestrial samples (i.e., Grange et al., 2013a; Cavosie et al., 2015; Schmieder et al., 2017; Rasmussen et al., 2020). Impacts can create moderate shock defects including microstructures such

as microfractures, planar features (PFs), curviplanar features (CFs), shock twins, high pressure polymorphs (i.e., reidite), plastic deformation, and granules. These all have the potential to provide pathways for accelerated Pb diffusion through the zircon crystal and result in partial resetting of the U-Pb geochronometer (Erickson et al., 2013; Grange et al., 2013a; Timms et al., 2017; Crow et al., 2019). Zircon grains that show the best potential for determining impact age are the newly crystallized or recrystallized zircons since this crystallization process is thought to reset the geochronologic clock (Moser et al., 2011; Cavosie et al., 2015; Kenny et al., 2017; Kenny et al., 2019). Shock pressures of less than ~20 GPa can produce fractures/planar features and high strain in zircons that can result in plastic deformation, and at ~20 GPa shock twinning can occur (Leroux et al., 1999; Morozova, 2015; Rasmussen et al., 2020). Plastic deformation in zircons is typically <5° in most tectonic settings but can reach up to 20° in high-grade metamorphic conditions. In contrast, impact-related zircons that exhibit plastic deformation exceeding 5° and show no evidence of high-grade metamorphism since deposition are generally assumed to be attributed to impact processes (Reddy et al., 2007; Crow et al., 2024). Both plastic deformation and shock twinning can produce variable U-Pb resetting ranging from no age resetting to full resetting (Grange et al., 2013a; Timms et al., 2017, Rasmussen et al., 2020). Very high shock pressures (~30 GPa) can result in the formation of reidite, the high pressure polymorph of zircon (Kusaba et al., 1985, Glass et al., 2002, Wittmann et al., 2006, Timms et al., 2017; Rasmussen et al., 2020). The transition to reidite has been shown to locally mobilize and concentrate trace elements in reidite lamellae but overall is seen to cause minimal to no disturbance in the U-Pb system (Montalvo et al., 2019; Szumila et al., 2023). High-temperature conditions (≥1200°C) following the passage of a shock wave can lead to the formation of FRIGN (former reidite in granular neoblastic) zircon, where reidite reverts to granular zircon (polycrystalline aggregates of micro-sized granules) as

pressures decrease (Rasmussen et al., 2020). This process can sometimes result in complete age resetting, depending on factors such as potential contamination of interstitial material around small granules or subsequent Pb-loss experienced by the neoblasts (Timms et al., 2017; Cavosie et al., 2018). When high shock temperature (>1200-1673°C) results in granular recrystallization of zircons, the U-Pb system is often seen to be partially to entirely reset as Pb can be lost during the recrystallization process (Kamo and Krogh, 1995; Deloule et al., 2001; Schmieder et al., 2015; Schmieder et al., 2017; Timms et al., 2017; Cavosie et al., 2018; Rasmussen et al., 2020). Granularization is not considered to be a texture that is unique to impact deformation (e.g., Cavosie et al., 2015), however, FRIGN zircons are a diagnostic indicator of impact shock deformation (Cavosie et al., 2018). In general, samples that experience high strain and higher temperatures over longer timescales are correlated with the extent of age resetting (Schmieder et al., 2015; Timms et al., 2017).

Material exposed to high temperatures and/or pressures from an impact can be found both within the resulting crater structure and ejected outside of the crater rim (Osinski et al., 2022). Dating impact ejecta can be crucial for correlating it with the specific impact event from which it originated. Some ejecta can be stratigraphically intermixed when deposited during turbulent events as a result of impacts, such as mass gravity flows induced by earthquakes and impact generated tsunamis, making it difficult to constrain an age based solely on stratigraphical superposition (e.g., Schulte et al., 2006; Keller et al., 2007; Pierazzo and Melosh, 2012; Ross et al., 2021a). Some impact deposits (i.e., spherules, ejecta layers) have been discovered, but the associated impact that produced the impact deposits has not been identified (e.g., Huber et al., 2014; Armor et al., 2019). Therefore, the ability to independently date ejecta deposits, separate from the impact structure, can

help identify the impact structure of origin (e.g., Walkden et al., 2002; Pinto and Warme, 2007; Glass and Simonson, 2012).

Dating ejecta deposits independently of their source impact structure can help identify the structure of origin (e.g., Walkden et al., 2002; Pinto and Warme, 2007; Glass and Simonson, 2012). This is particularly valuable for dating samples from the Moon and other planetary bodies where impact cratering is the dominant geologic process. The lunar surface, for example, is continually bombarded by impacts, and ejecta material is repeatedly deposited across the surface (Taylor, 1982). To improve age interpretations, it is essential to constrain the extent to which impact resetting affects ejected materials independently of the crater. Additionally, understanding how ejecta materials are shocked or altered during impact—and whether these processes correlate with reliable age resetting—is crucial. Insights from terrestrial zircon studies can assist in refining interpretations of extra-terrestrial zircon ages.

The Chicxulub impact is an ideal case for studying distal ejecta materials due to the widespread preservation of ejecta worldwide (Smit, 1999; James et al., 2023) and the impact's large size (~180–200 km diameter crater; Gulick et al., 2008; Schmieder and Kring, 2020), which generated a wide range of temperature and pressure conditions. This impact and its large scale make it a useful analog for the large impacts on the lunar surface. Since similarly sized and smaller craters on the Moon (e.g., Tycho–85 km diameter; Margot et al., 1999) have been shown to have global ejecta deposits, understanding how geochronometers are affected in ejecta is critical to our understanding of lunar chronology (Hayne et al., 2017).

3.3 Geologic Context and Previous Studies of Chicxulub Ejecta

The Chicxulub impact structure is one of Earth's largest preserved impacts (preservation level 2 on a 1-7 scale where level 1 is most preserved; Osinski et al., 2022) and is associated with the extinction that marks the boundary between the Cretaceous and Paleogene periods in Earth history (K-Pg) (Alvarez et al., 1980; Izett 1991; Arenillas et al., 2006). It occurred 66.052 ± 0.043 Ma (2σ), as determined via $^{40}Ar/^{39}Ar$ of impact melt from the Chicxulub crater (C-1 well) and glassy microtektites from ejecta in Beloc, Haiti and Arroyo de Mimbral, Mexico (Swisher et al., 1992; Schmieder and Kring, 2020). The impact of the estimated ~10-12 km diameter asteroid (Morgan et al., 1997; Schulte et al., 2010) resulted in a ~180-200 km diameter crater (Gulick et al., 2008; Schmieder and Kring, 2020). The resulting complex, peak-ring basin impact structure is in present day Yucatán peninsula, Mexico (Kring et al., 2017). The target rock consisted of ~3 km thick Jurassic-Cretaceous carbonate platform sediments overlying a structurally complex network of granitoid, amphibolite, dolerite, gneiss, and paragneiss basement (Kring, 2005; Keppie et al., 2011; Morgan et al., 2016; Schmieder et al., 2017; de Graaff et al., 2021, Ross et al., 2021b). These target rock ages contain zircon age populations of 334 ± 2.3 Ma (2σ), 400-435 Ma, 500-635 Ma, and 940-1400 Ma (see compilation of Ross et al., 2021b and references therein). The impact excavated material up to 25 km in depth during the impact cratering process based on the size of the crater (Figure 3.1) (Sharpton et al., 1994, Sharpton et al., 1996; Salguero-Hernández et al., 2020; Kring et al., 2020). As a result of the large size and therefore high energy from the impact event, ejected material from the impact containing shocked minerals can be found as far as New Zealand (paleodistance ~12,600 km) (Hildebrand and Boynton 1990, Smit 1990; James et al., 2023). This global ejecta layer was linked to the Chicxulub impact via the ejecta's distribution,

composition, estimated age, impact shock and deformation characteristics, and depositional mode (Hildebrand et al., 1991; Schulte et al., 2010).

Previous studies have analyzed K/Pg (also referred to as K/T or KTB in some literature) boundary materials to confirm a Chicxulub impact origin of this material (Figure 3.2) (e.g., Krogh et al., 1993a; Krogh et al., 1993b; Kamo and Krogh, 1995; Kamo et al., 2011). These studies primarily assessed the impact and shock microtextures of individual zircon grains using a binocular microscope or by acid etching zircon grains, often with NaOH, and viewing grains via secondary electron microscopy (SE). U-Pb dating in these studies was performed using thermal ionization mass spectrometry (TIMS), which measures whole grain ages by dissolving the zircon crystal and measuring isotope ratios. One potential limitation of this method is that it measures the averaged U-Pb of the entire grain, obscuring age heterogeneities that may exist in the heterogeneously shocked grains. From a practical perspective, TIMS analyses involve a more time and resource intensive sample preparation process than other analytical techniques, thus, past studies of Chicxulub ejecta have been limited to 15 or fewer zircon analyses per study.

This study integrates correlated U-Pb dating and impact-induced microstructure analysis of distal ejecta zircons from the Chicxulub ejecta blanket to better understand the temperature and pressure conditions experienced by ejected zircon grains and how the resulting microtextures relate to the degree of resetting in the U-Pb geochronometer. In contrast to the preceding studies, this work uses electron backscatter diffraction (EBSD) to identify impact features based on grain orientation and misorientation relationships, which has been used to identify a wide range of shock microstructure in zircon (e.g., Erickson et al., 2013; Timms et al., 2017; Cavosie et al., 2018). Our study tests the effectiveness of spatially resolved U-Pb dating in targeting specific microstructures to determine geologically meaningful ages from impact ejecta. Using secondary ionization mass

spectrometry (SIMS) enables a much larger survey compared to TIMS, as it is a more time-efficient analytical method while also preserving spatial context.

The Chicxulub ejecta zircons for this study were collected from the shocked mineral rich, ~1-5 mm thick impact ejecta layer of the K/Pg boundary in southern Colorado and northern New Mexico. This layer is colloquially referred to in the literature as the "fireball layer." The K/Pg boundary localities in this region are all nestled within the Raton Basin and outcrop similarly in the same stratigraphic sequence (Pillmore and Flores, 1987). The K/Pg boundary layer in this region is found within the Raton Formation and consists of a lower claystone unit (1.5-2.5 cm thick; Pollastro and Pillmore, 1987; Bohor and Glass, 1995) and an upper impact layer unit that is often referred to as the "fireball layer" with a sharp contact between these two units (Izett, 1987). The lower claystone unit represents the ballistic ejecta curtain that was transported primarily within the atmosphere, while the upper fireball layer represents the fallout of the vertically rising vapor plume from the impact (Bohor and Glass, 1995). The fireball layer is known to primarily contain the majority of shocked minerals and host the iridium anomaly (Izett, 1987; Bohor and Glass, 1995). The lower claystone unit hosts spherules, a faint iridium anomaly, and a very low concentration of shocked grains (Izett, 1987; Bohor et al., 1989; Bohor, 1990; Bohor and Glass, 1995).

The K/Pg boundary units can be identified by locating the 1.5-2.5 cm claystone layer that outcrops as a bright white-to-light gray layer. Above that, the fireball layer outcrops as a finely laminated, dark colored (dark brown to dark gray in appearance) layer about 1-5 mm thick above the claystone layer. The top of the fireball layer is truncated by a coal bed, denoting the end of the Chicxulub ejecta deposits (Pillmore and Flores, 1987). Outcrops sampled for this study include the Madrid site in Trinidad, Colorado (37.125° N, 104.622° W) and the Raton site in Raton, New

Mexico (36.903° N, 104.451° W). These sites are located at a paleodistance of approximately 2,300 km from the Chicxulub impact (Figure 3.2) (Kamo and Krogh, 1995).

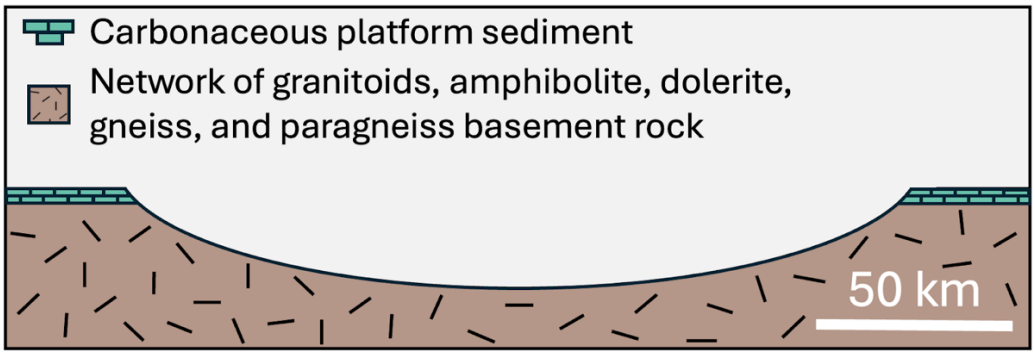

Figure 3.1: Cross-section of the impact crater showing the depth of excavation upon impact. This represents the transient cavity formed during the excavation stage of crater formation, depicting the maximum depth of excavated material. The final crater differs from this stage due to the rock's response to rapid compression and decompression, with excavated material partially re-filling the structure.

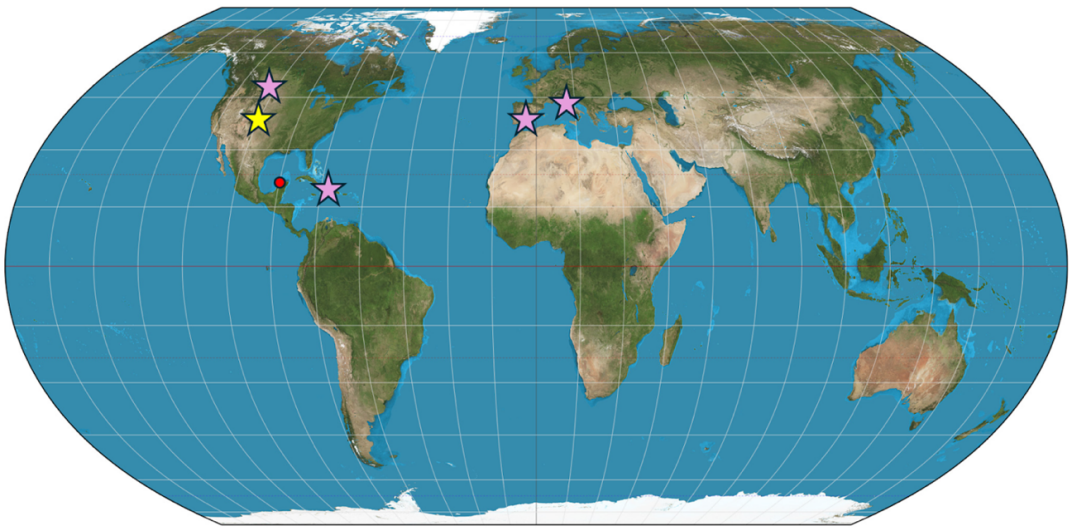

Figure 3.2: World map showing sample locations for Chicxulub ejecta where shocked zircons have been identified and U-Pb studies have been conducted. The Chicxulub crater is denoted by a red dot, which is slightly larger than the impact crater for visibility. The yellow star denotes the sampling location for this study and purple stars are locations of previous studies of distal ejecta zircons from Beloc, Haiti; Saskatchewan, Canada; Caravaca, Spain; and Petriccio, Italy (Krogh et al., 1993a; Krogh et al., 1993b; Kamo and Krogh, 1995; Kamo et al., 2011).

3.4 Methods

3.4.1 Refining Zircon Extraction Methodology

Mineral separation was completed on the fireball layer ejecta material to isolate zircon grains for further analysis. This included processing material using a variety of techniques to determine the best method for maximizing the zircon extraction yield. Initial processing methods were completed on ~9 g of fireball layer material. Samples were hand crushed using an agate mortar and pestle. Following crushing, samples were processed using heavy liquid density separation with lithium metatungstate (LMT) (density: 2.95 g/cm^3). Grains were then hand picked under a binocular microscope, and zircons were confirmed via energy dispersive X-ray spectroscopy (EDS) using a Hitachi SU3500 Variable Pressure Scanning Electron Microscope in the Colorado Shared Instrumentation in Nanofabrication and Characterization (COSINC) facility at the University of Colorado Boulder. The carbonaceous and clay material in this sample reacted with the LMT solution, forming secondary minerals with optical properties similar to zircon, which made it challenging to identify zircons using the petrographic microscope. This processing methodology yielded only two zircon crystals.

In the next iteration of this process, ~275 g of sample was panned in water multiple times to remove lighter clays and carbonaceous material to minimize possible sample reactions during subsequent density separation. Heavy liquid density separation was conducted using methylene iodide (MI) that was diluted to near LMT density (2.8 g/cm^3) using acetone. The heavy separate was sieved to 150 μm to remove larger fragments that were not crushed, and zircons were hand picked from the remaining material under a binocular microscope and confirmed via EDS. The addition of panning, change in heavy liquid medium, and processing a larger amount of material significantly increased the yield to 226 zircons. Diluted MI is favored since it may have helped

increase yield since shocked grains with lower densities would not be missed. The 228 recovered zircons were mounted in Buehler EpoxiCure2 epoxy and polished using 3 µm, 1µm, and 0.25 µm diamond slurry for further microstructural characterization and geochronology.

We recommend the following refined sample processing methodology to maximize the extraction of zircons from clay-rich and/or impact ejecta materials: 1) crush via mortar and pestle, 2) pan in water, 3) sieve dense material from MI at 150 µm to remove larger material, 4) density separation of dense material from panning with MI diluted to (2.8 g/cm^3), 5) pick suspected zircons under a binocular microscope, and 6) confirm zircons via SEM-EDS.

3.4.2 Microstructural Characterization

Epoxy disks were further polished with a vibratory polisher using colloidal silica for EBSD analyses at NASA Johnson Space Center at the Astromaterials Research and Exploration Science Division. EBSD analyses were performed on 224 grains using a JEOL 7900F Field Emission Scanning Electron Microscope (FE-SEM). Data was collected using a 20 kV, ~20 mm working distance, and 70° sample tilt relative to the beam incidence. Maps were collected with a 0.05 µm step size. Electron backscatter diffraction patterns were collected with the Oxford Instruments Symmetry S2 EBSD detector and indexed using match units for zircon (Hazen and Finger, 1979) and reidite (Farnan et al., 2003). Post-processing and creating of EBSD maps and pole figures of EBSD data was completed using the Oxford Instruments Aztec Crystal software package. All EBSD data were given a wild-spike noise reduction and a seven nearest neighbor zero-solution correction. EBSD images were exported as phase color maps, inverse pole figure maps (IPF) maps, and grain rotation orientation distribution (GROD) function maps. Zircon pole plots are equal area,

lower hemisphere projections. All images of zircons with visible deformation or microtextures are in Appendix E.

3.4.3 U-Pb Geochronology

One hundred and nineteen SIMS U-Pb analysis spots were collected across 94 total grains. Some grains were targeted for multiple SIMS spots in order to investigate shock features or textures of interest. U-Pb measurements were collected using the UCLA CAMECA ims-1290 secondary ion mass spectrometer equipped with the Hyperion II ion source over two sessions. In the first analytical session, a primary O^{3-} beam without oxygen flooding was used. In the second session, a primary O^{-} beam and oxygen flooding were used. In both sessions, the spot side was ~10 μm. Instrumental mass fractionation of U and Pb was calibrated using the AS3 and Fish Canyon (FC) zircon age standards, and trace element (U, Th) concentrations were calculated using the 91500 zircon standard (Paces and Miller, 1993; Schmitz and Bowring, 2001; Wiedenbeck et al., 2004). A common-Pb correction was applied to all data (standards and unknowns) assuming all ^{204}Pb is from terrestrial surface contamination and a Pb-isotope composition of San Diego sewage water (Sañudo-Wilhelmy and Flegal, 1994). Post-processing was completed using the in-house ZIPS software (created by C. Coath) and IsoplotR (Vermeesch, 2018). Table of all SIMS analyses and U-Pb data is in Appendix D, Table D1.

3.5 Results

The Chicxulub ejecta zircon grains range from euhedral to anhedral and vary in size from approximately 35 to 150 μm. Zircons extracted from the ejecta material exhibit a variety of shock

microtextures and age-resetting behaviors, with the extent of age resetting depending on the specific microtexture.

Shock microtextures indicative of a wide range of pressure, temperature, and time conditions were observed in the ejecta zircons. These include unshocked grains with no detectable presence of shock characteristics, fractures, planar features, shock twins, plastic deformation, granular texture recrystallization, reidite, or FRIGN zircon. Some grains contained multiple microstructures. The locations of individual SIMS spots were chosen to target single shock features for U-Pb analyses, however, in some grains, it was difficult to isolate one single shock feature, and therefore some spots overlap multiple shock features. This was the case for 31 analysis spots and is denoted in the figures and data tables. Each SIMS spot was categorized via the primary shock feature that the spot targeted. If multiple shock features had a significant presence in the spot, then the analysis was labeled as the higher order shock feature that would represent higher temperature and pressure conditions. The analysis spots that contained more than one feature were denoted as such in all figures and plots. Planar features are not discussed separately below because, although planar features were present, they were not the dominant, highest order shock feature present in any of the analysis spots.

Isotopic data for both U and Pb were measured, however, the ages of many zircons are young (ages as young as ~49 Ma), resulting in low concentrations of radiogenic ^{207}Pb. We opted to use ^{206}Pb/^{238}U ages for our analysis since there were large uncertainties on ^{207}Pb/^{235}U and ^{207}Pb/^{206}Pb ages. A majority of the SIMS analyses (~62%) contained significant fractions (10% or more) of non-radiogenic ^{206}Pb, which was not surprising as zircon deformation could induce Pb mobilization and produce shock features that can act as a conduit for common-Pb (Corfu, 2013; Schwarz et al., 2020; Zhang et al., 2021). As such, we included all grains with shock features

regardless of percent radiogenic ^{206}Pb to avoid removing any shocked zircon analyses from further interpretation. Unshocked grains were expected to be less susceptible to Pb-loss and common Pb contamination compared to shock grains since they lack shock related deformation and, therefore, do not have pathways that facilitate Pb-loss or deformation that hosts excessive common-Pb (Grange et al., 2013a; Timms et al., 2017). Consequently, only unshocked grains with ≥90% radiogenic ^{206}Pb were considered for data interpretation. Further discussion of the source of the non-radiogenic ^{206}Pb in shocked grains is included in section 3.6.3.1.

3.5.1 Unshocked Grains

One hundred and nine zircons contained no evidence of shock microstructures or alteration (Figure 3.3). Of the 109 grains, 43 were analyzed to determine U-Pb ages and 25 had >90% radiogenic ^{206}Pb. These grains appear euhedral to subhedral and exhibit U-Pb ages between 1850 ± 84 Ma to 81.6 ± 4.0 Ma (2σ) (n=25, Figure 3.4). There is no significant age clustering (Figure 3.4).

3.5.2 Crystal Plastic Deformation

Plastic deformation is presented as partial grain twisting, full grain twisting, and planar deformation banding (Figure 3.5; Timms et al., 2018). Thirty-nine zircons exhibited impact crystal plastic deformation that ranged from ~5°-38°. These samples had U-Pb ages that ranged from 591.6 ± 50.4 Ma to 126.9 ± 8.8 Ma (2σ) (n=28) (Figure 3.6). There is no correlation between age and the maximum degree of plastic deformation.

3.5.3 Shock Twins

Five zircon grains contained shock twins. Shock twins were identified and confirmed via EBSD by identifying misorientation angles between 60-70° about the <110>. This relationship of the shock twins relative to the host zircon crystal is diagnostic of shock twinning (Moser et al., 2011; Erickson et al., 2013). Four SIMS analysis spots overlapped shock twins, however the shock twins are thin (μm to sub-μm scale thickness) and elongate (often 10s of μm) and therefore cannot be completely isolated from other portions of the zircon crystal (Figure 3.5, M45). In the case of all of the analysis spots on shock twins, both shock twins and plastic deformation shock features were present in each analysis spot. These four spots had ages of 527.8 ± 43.4 Ma, 405.1 ± 28.6 Ma, 361.3 ± 25.6 Ma, and 395.3 ± 22.8 Ma (2σ) with 89-93% radiogenic ^{206}Pb.

3.5.4 Reidite

Reidite was found in seven grains. Reidite presented itself as: (1) nearly full grain transition to reidite structure with small amounts of zircon present mainly around the rim, (2) predominantly zircon with granular reidite found throughout the crystal and surrounding the rim of the grain, (3) mostly zircon with some reidite regions that are not granular, or (4) primarily zircon with reidite as lamellae (Figure 3.7). The three SIMS spots that contained reidite have ages of 237.5 ± 22.2 Ma, 211.0 ± 15.7 Ma, and 118.9 ± 39.8 Ma (2σ). These spots have radiogenic ^{206}Pb percentages of 75.8%, 84.7%, and 30.24%, respectively. The reidite with 30.24% radiogenic ^{206}Pb is from the granular reidite grain.

3.5.5 FRIGN zircon

Fifty-four FRIGN zircons were identified. Most zircons that exhibited granular texture were determined to be FRIGN zircons (86%). Grains were confirmed FRIGN zircon if granules were systematically misoriented by 90° about the <110> with three dominant orientations, which can be determined via equal area, lower hemisphere pole figures of the (001) and {110} poles, and misorientation axis angles between 85-95° about the <110> (Figure 3.8) (Cavosie et al., 2018). This process identifies the residual crystal structure change from the backformation of reidite, confirming the former presence of the reidite crystal structure. Granules range from <1-25 μm in size, with a majority of granules smaller than 10 μm (Figure 3.8). A large percentage (43 of 54) of FRIGN zircons also contain misorientations consistent with shock twins (i.e., 65° about the <110> misorientations). Granular zircons range from fully granular, partially granular, to containing only a few granules (granules making up 1-2% of the crystal). The FRIGN zircon grains range in age from 481.6 ± 51.2 Ma to 48.7 ± 14.7 Ma (2σ) (n=35). There is no correlation between granule size and age. Few FRIGN zircon analysis spots (n=4) have 90% or greater radiogenic ^{206}Pb.

3.5.6 Granular Texture Recrystallization

Of the 54 granular zircon grains identified, nine granular zircons lack evidence for back reversion from reidite (i.e., 90° about the <110> misorientations), three of which were analyzed for U-Pb. These grains range from fully granular to only containing a few granules (1-2% of the exposed crystal) and the granule sizes for non-FRIGN zircons are 1-8 μm (Figure 3.8). Ages from granular SIMS spots are 318.8 ± 19.9 Ma, 224.6 ± 14.7 Ma, and 84.4 ± 8.7 Ma (2σ). These grains reported 93.6%, 86.9%, and 70.6% radiogenic ^{206}Pb, respectively.

3.5.7 Metamict/Amorphous

One zircon did not produce electron backscatter diffraction patterns and is interpreted as being metamict at the scale of the EBSD analyses (50 nm) (Figure 3.10). The age of this sample was 119.4 ± 24.8 Ma (2σ), and the sample had a low percent radiogenic ^{206}Pb (61%).

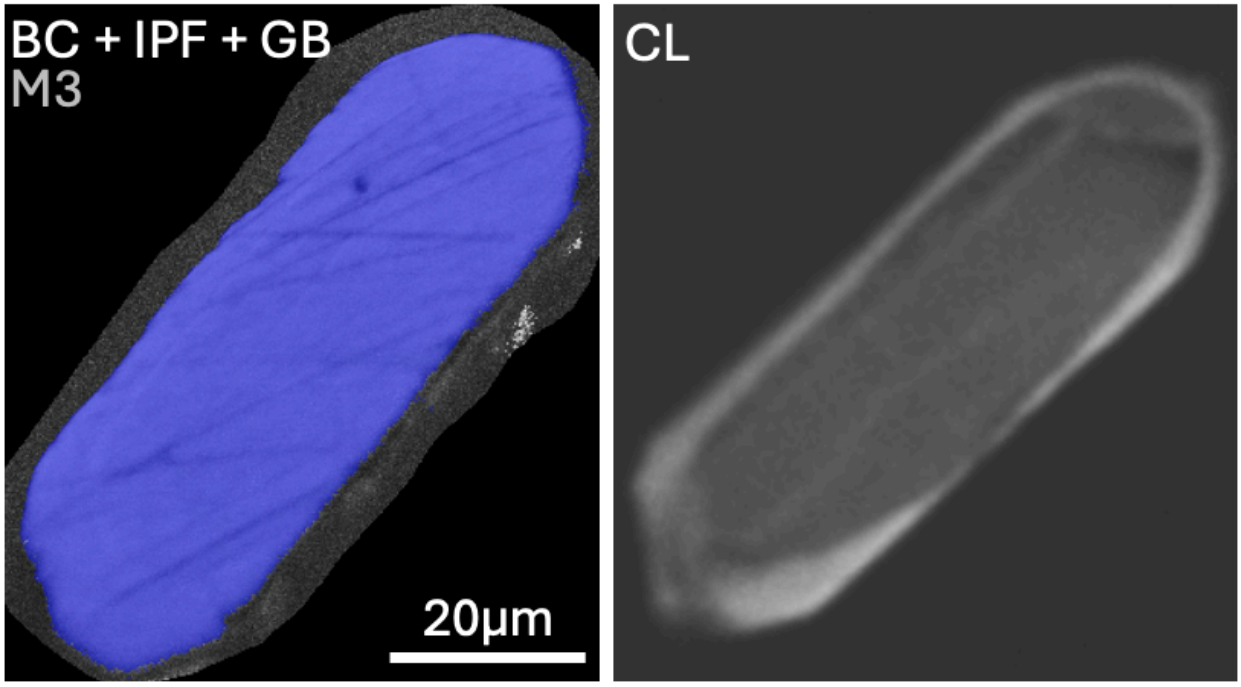

Figure 3.3: Unshocked zircon from the Chicxulub ejecta layer denoting no shock features in EBSD or CL. Surface features on BC+IPF+GB image are remnant scratches from polishing. CL image shows possible zonation.

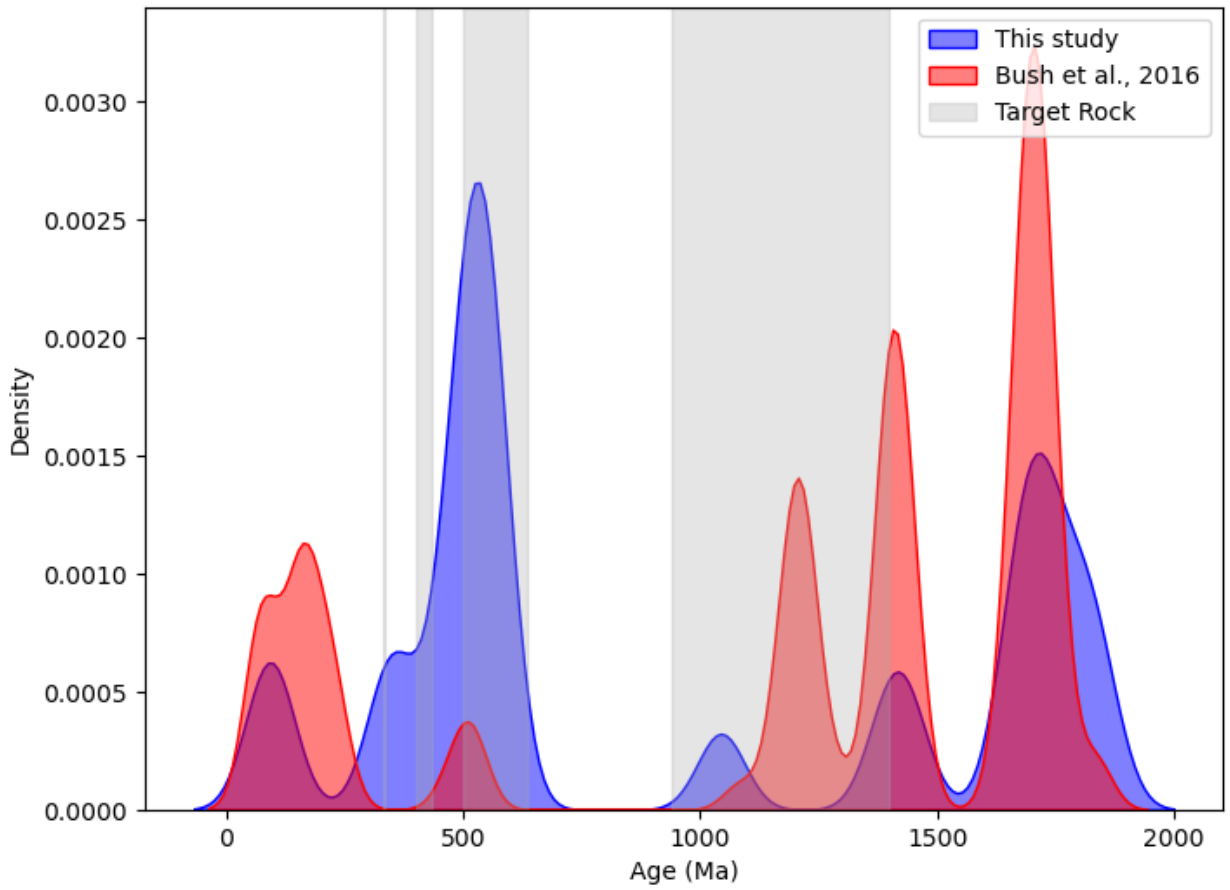

Figure 3.4: Probability density function of the ages of detrital zircon grains from the portion of the Raton formation immediately above the Chicxulub ejecta layer (red, n=105) compared to the most reliable ages of the unshocked grains from this study (ages with ≥90% radiogenic ^{206}Pb) (blue, n=23). Most unshocked grains come from surrounding material but some can only be explained as originating from the impact target rock depicting a mix of sources for unshocked grains in the impact layer.

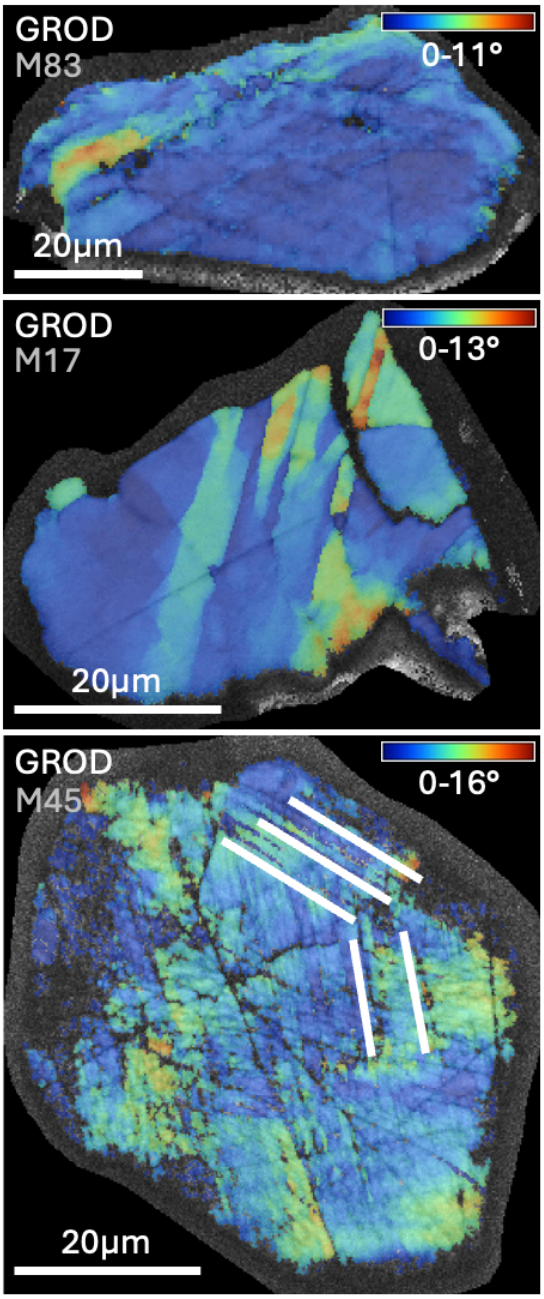

Figure 3.5: EBSD (GROD) images depicting the variety of plastic deformation textures in Chicxulub ejecta zircons. Zircon M83 denotes partial grain twisting in the left central region of the crystal, where the crystal is dark red and represents ~11° of twisting. Zircon M17 represents planar deformation banding, where bands of plastic deformation are found roughly parallel to one another in a crystal. These regions run from the top right to the bottom left of the crystal image and represent up to 13° of twisting in the crystal. Zircon M45 shows twisting that can be found distributed throughout the entire grain and is not concentrated in bands. These regions are randomly located throughout the grain with a maximum of 16° of crystal twisting. Zircon M45 also includes shock twinning which is indicated by white lines. BSE images of each grain in this figure are included in supplemental appendix E.

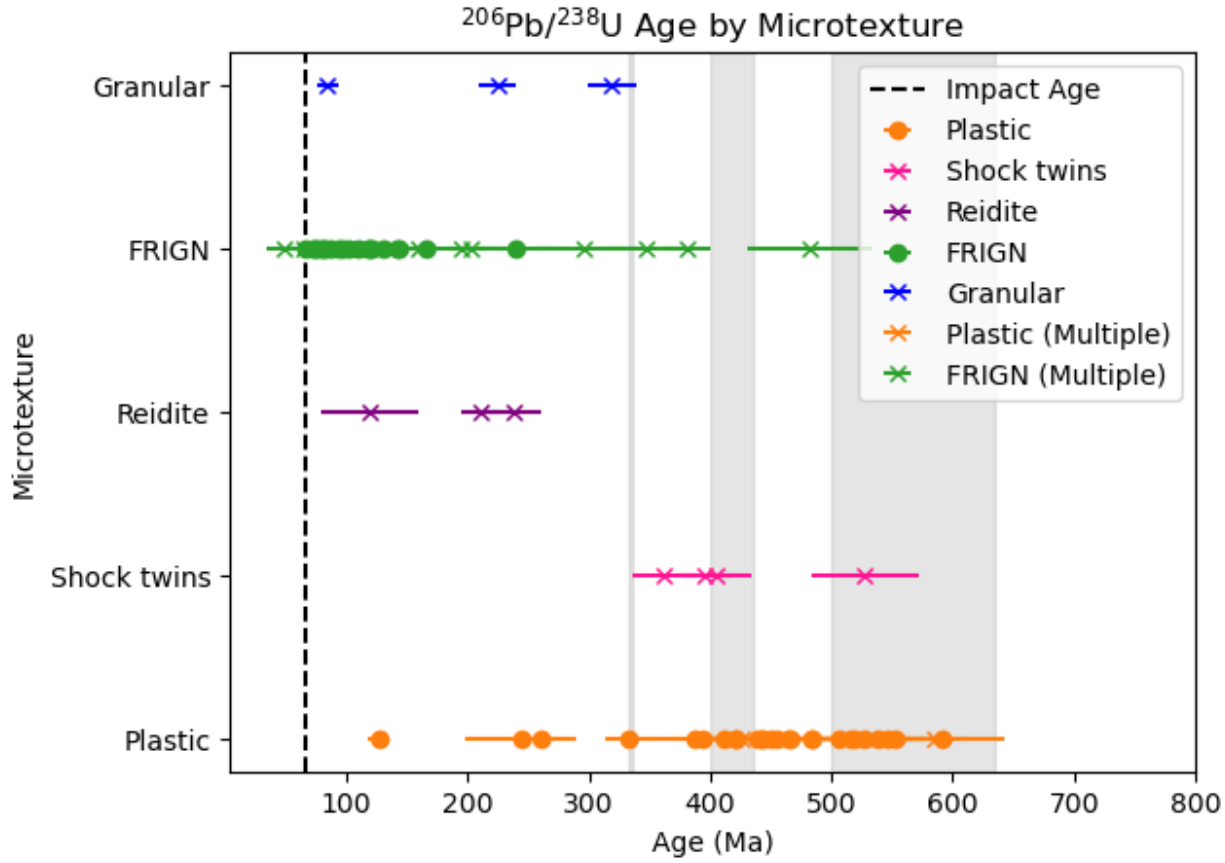

Figure 3.6: U-Pb ages grouped by the primary microtexture within each SIMS analysis spot (ages of unshocked zircons are reported in Figure 3.4). All ages are reported in this figure regardless of the percentage of radiogenic ^{206}Pb with 2σ uncertainty. When analysis spots contain one shock feature, these are labeled as o's. When analysis spots contain multiple shock textures, these are labeled as x's. Target rock ages of rock for the Chicxulub impact structure are denoted by vertical gray bars (Ross et al., 2021b). Each shock feature correlates with a certain degree of Pb-loss and, therefore, age resetting. Some microtextures experienced no discernable resetting (target rock age), some experienced no discernable resetting (target rock age) and partial resetting, some only experienced partial resetting, and some experienced the entire range of no discernable resetting (target rock age) to fully reset to impact age. (n=76)

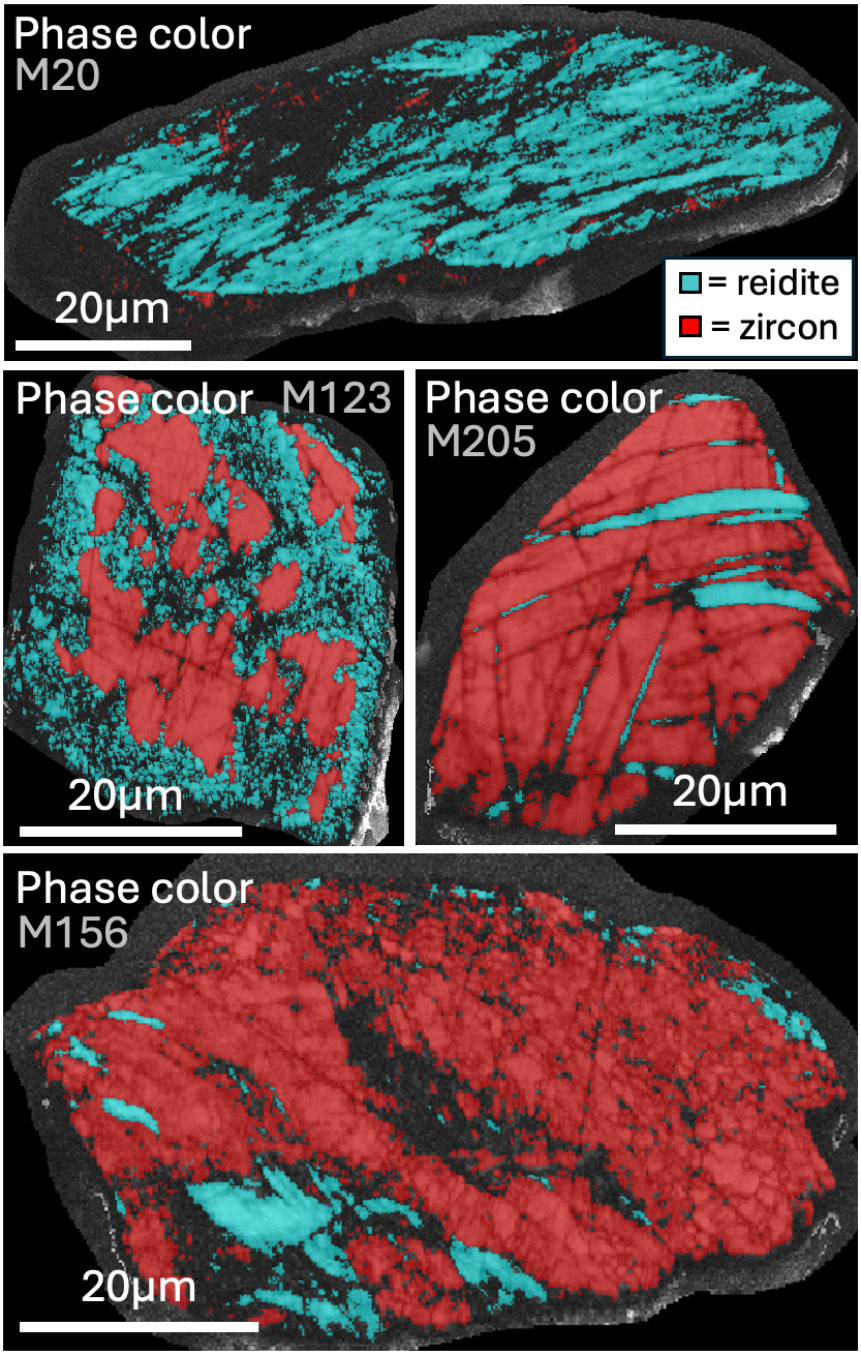

Figure 3.7: Phase color EBSD images that contained reidite and zircon. Zircon M20 represents a crystal that has converted almost entirely to reidite with small regions (≤1µm) of zircon around the rim. Zircon M123 retains a host zircon crystal with granular reidite throughout and around the edge of the zircon crystal. Zircon M205 is primarily zircon with reidite lamellae that range from <1-2 µm in width. Zircon 156 is a zircon crystal with regions throughout the crystal that are reidite (not granular). BSE images of each grain in this figure are included in supplemental appendix E.

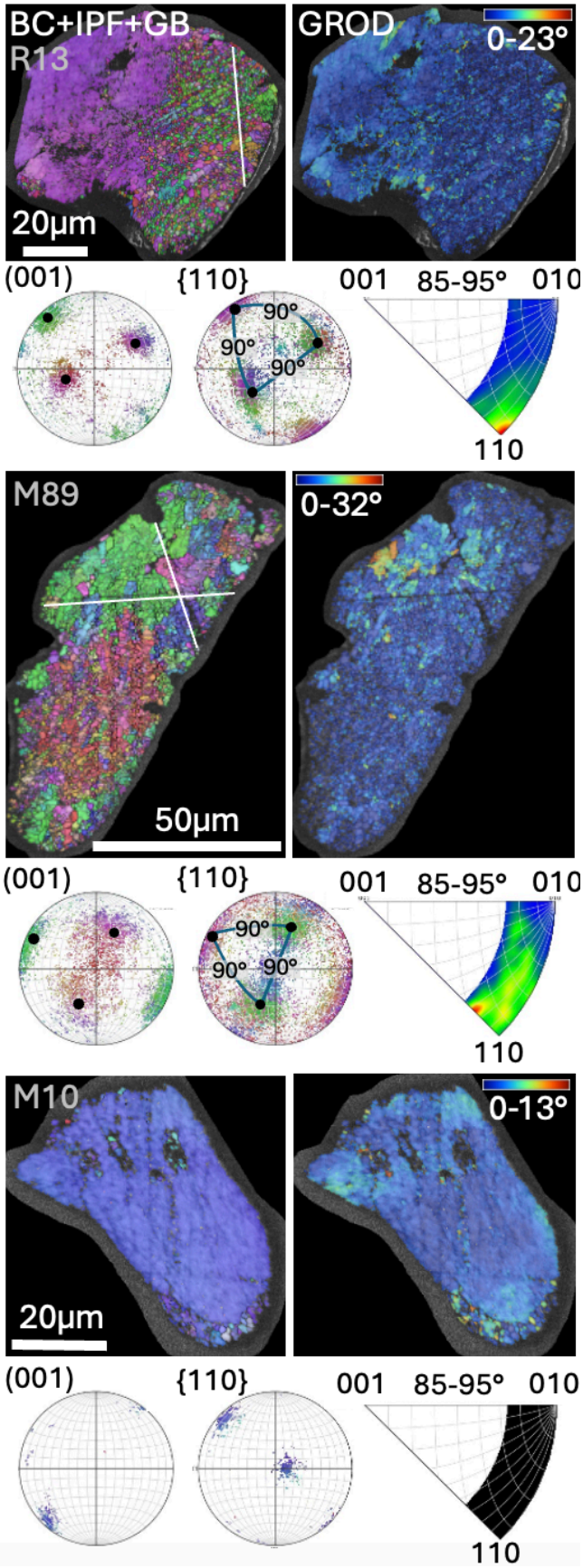

Figure 3.8: GROD and BC+IPF+GB EBSD images of granular zircons (both FRIGN and non-FRIGN) showing various degrees of granularization. Granules are confirmed FRIGN through the identification of systematic three dominant orientations by 90° about the <110> via equal area, lower hemisphere pole figures of the (001) and {110} poles, and misorientation axis angles between 85-95° with a maxima at the <110>. Grain R13 is a grain with FRIGN granules that shows that some crystals are only partially FRIGN and can contain multiple shock features. In this case, this crystal contains the shock features FRIGN granules, plastic deformation, and shock twinning (denoted as a white line parallel to a shock twin in BC+IPF+GB). Grain M89 is a FRIGN zircon that is fully granular. It also contains shock twinning which is seen in 85% of FRIGN zircons and is denoted with white lines parallel to shock twins in BC+IPF+GB. Grain M10 has granules that are not FRIGN since there is a lack of three orientations by 90° about the <110>. This is an example of a grain that has very few granules. BSE images of each grain in this figure are included in supplemental appendix E.

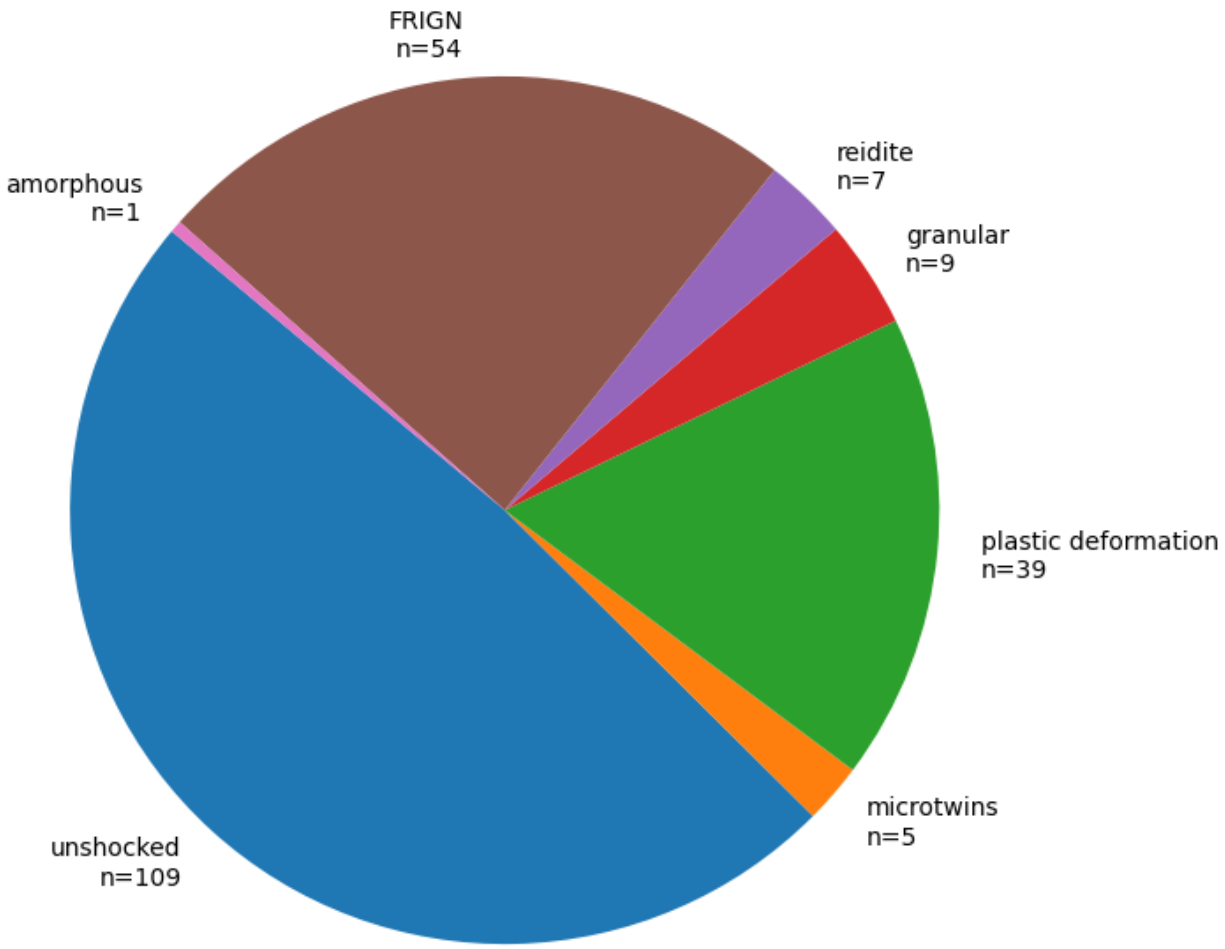

Figure 3.9: Pie chart showing the abundances of zircons with each texture. Samples were classified by the highest order shock feature present within the grain. The "unshocked" section of this figure contains all of the unshocked grains identified since it is difficult to determine if unshocked grains originated from the impact or from local detrital sources in the depositional area. (n=224)

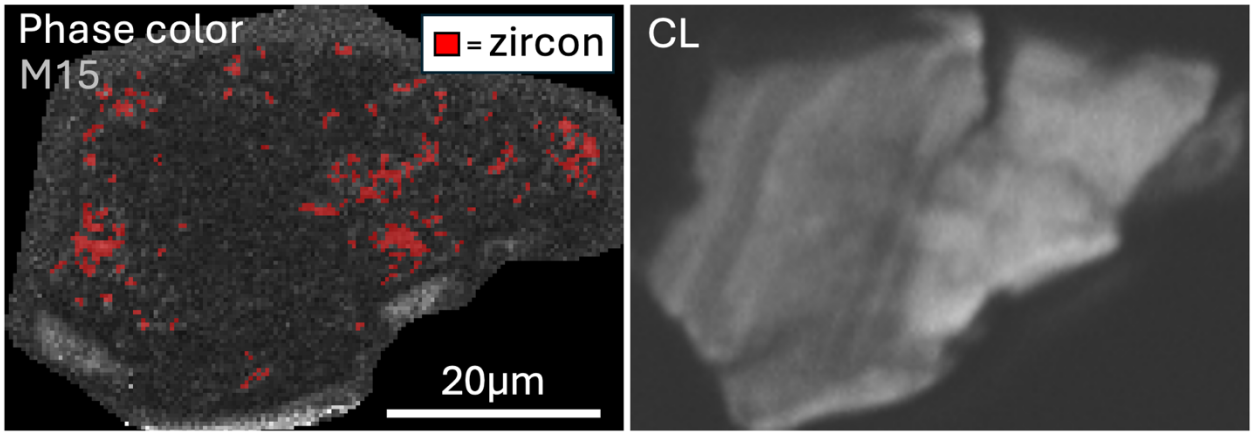

Figure 3.10: Metamict zircon in phase color EBSD showing areas that index as zircon in red and regions that do not index (metamict) are gray, indicating that this grain is mostly metamict. CL image of the grain depicts zonation that is not observed in EBSD. BSE image of this grain is included in supplemental appendix E. (grain M15)

3.6 Discussion

The temperature and pressure paths of ejected material from an impact event can be assessed by analyzing shock microtextures in zircon (e.g., Timms et al., 2012; Timms et al., 2017). These conditions can disturb U-Pb ages in zircon if the temperatures and pressures are sufficient to cause appreciable Pb-loss. Earlier studies have correlated U-Pb age resetting with shock microtexture in zircons to better decipher geologically meaningful ages, demonstrating a need for pairing these methods to interpret ages of impacted materials (e.g., Grange et al., 2013a, Grange et al., 2013b; Cavosie et al., 2015; Crow et al., 2017; Rasmussen et al., 2020). In this study, we conducted microstructural analysis via EBSD to assess shock microtextures of ejected material to determine how ejecta material is physically affected by an impact. Age resetting in relation to microtexture can provide critical insights into analyzing ejecta material for determining geologically significant ages from impact ejecta material. The ejecta zircons in this study display an array of shock microtextures and age resetting behaviors that suggest a wide range of P-T-t

conditions. Here we assess the correlation of shock microtexture and U-Pb ages to better elucidate the impact ejecta environment and provide recommendations for using ejecta zircons to date impacts.

3.6.1 Screening for Contributions from Local Detrital Zircons in the Ejecta Layer

The thin (1-5 mm) Chicxulub shocked mineral ejecta layer, the fireball layer, is sandwiched between sedimentary units within the Raton Basin, and the ejecta layer is exposed to weathering at the surface (Pillmore and Flores, 1987). As a result, it is important to determine if unshocked zircons extracted from ejecta material at this location are sourced from the ejecta or from weathering of the surrounding sedimentary units. Since unshocked, crystalline grains do not have significant lattice defects that provide easier pathways for diffusion, it is expected that the ages of these grains will likely have minimal Pb-loss and therefore reflect their crystallization ages, or at least a lower limit on crystallization ages (Grange et al., 2013a; Timms et al., 2017; Kenny et al., 2019; Rasmussen et al., 2020). The uncertainties on U-Pb ages are inversely correlated with percentages of radiogenic ^{206}Pb, i.e., those with higher radiogenic Pb contributions have lower uncertainties. Since unshocked grains made up half the zircons in this study and we were not sample limited in this population, we only considered unshocked zircons with ages ≥90% radiogenic ^{206}Pb (removing 42% of unshocked grain analyses). The grains analyzed in this study are a 2D slice of grains and since many of the zircons exhibited heterogeneous shock features, it is possible that grains that appear unshocked may contain shock features in other portions of the crystal.

A comparison between the shocked zircon ages from this study and the detrital zircon ages in the unit directly above the fireball layer in the Raton formation is shown in Figure 3.4 (Bush et

al., 2016). Many of the zircons in this study are consistent with detrital zircon age peaks in the Raton Basin (~70, 510, 1200, 1410, and 1690 Ma) (Bush et al., 2016, Sylvester et al., 2022). However, multiple peaks in the unshocked grains overlap with Chicxulub impact target rock ages and cannot be explained by sampling of surrounding stratigraphic units, indicating that some of the unshocked zircons originate from the impact structure. These peaks include those at the ages of 337.6 ± 18.8 (2σ) and ~1050 Ma, which correspond with Chicxulub target rock ages of ~334 Ma and 940-1400 Ma, respectively (Ross et al., 2021b). Other peaks are more ambiguous. For example, there is an age peak around ~510 Ma and ~1410 Ma in both zircons from this study and local detrital zircons, however, zircons of this age have been found in target rock at the Chicxulub impact site. Without the presence of shock features in these zircons, it proves difficult to determine the original source of this zircon population. It is clear from Figure 3.4 that there is a mix of both impact ejecta and local detrital unshocked zircon grains in the material sampled.

3.6.2 Pressure-Temperature Conditions Experienced by Distal Ejecta

The presence of certain microstructures in zircon implies a particular set of pressure and/or temperature conditions. At pressures below ~20 GPa, zircon forms brittle fractures including planar features (PFs), curviplanar features (CFs), and crystal plastic microstructural deformation within zircon grains (Leroux et al., 1999; Erickson et al., 2013; Morozova, 2015; Cavosie et al., 2016; Crow et al., 2019; Rasmussen et al., 2020). While plastic deformation is not exclusive to impact settings, plastic deformation in most tectonic settings is typically <5°, and therefore 5°+ of plastic deformation is the threshold considered in this paper to be associated with impact deformation processes (Reddy et al., 2007; Crow et al., 2024). As shock pressures increase to ~20 GPa these conditions cause zircon deformation shock twinning (Leroux et al., 1999; Morozova,

2015; Cavosie et al., 2016; Rasmussen et al., 2020). Once shock twins are formed, they are found to be quite robust and are preserved even through extreme levels of shock metamorphism (>40 GPa; Moser et al., 2011). At ~30 GPa, the transformation of zircon to reidite, its high pressure polymorph, can occur (Kusaba et al., 1985, Glass et al., 2002, Wittmann et al., 2006, Timms et al., 2017; Rasmussen et al., 2020). Reidite can revert back into zircon as FRIGN zircon if temperatures are ≥1200°C after initial high shock pressures recede to near atmospheric pressures (Kusaba et al., 1985; Cavosie et al., 2018, Rasmussen et al., 2020). Granular zircon can be formed by this FRIGN process, however, this texture can also form via the annealing of dissociated zircon when ZrO_2 grains react with Si-saturated melt to reconstitute zircon (Wittmann et al., 2006; Wittmann et al., 2009; Timms et al., 2017; Zhao et al., 2024). Dissociation of zircon into ZrO_2 and liquid SiO_2 can occur as low as 1673°C at low pressures (<<1 GPa) and, once dissociated the dissociated ZrO_2 and liquid SiO_2, can recrystallize into granular neoblasts at temperatures <1673°C (Timms et al., 2017; Rasmussen et al., 2020; Zhao et al., 2024). It is important to consider that granular zircons are not unique to impact events as they can also form during regional metamorphism and, therefore, the presence of a granular texture does not necessarily denote impact origin (Cavosie et al., 2015). FRIGN zircons, which have distinctive phase heritage signature recorded in their disorientation axes (e.g., 90° <110>), however, are a diagnostic indicator of impact origin (Cavosie et al., 2018). The presence of all of these shock features in the Chicxulub zircons from this study demonstrates the impact ejecta environment is very heterogeneous and the ejecta zircons experience a large range of temperature and pressure from 0-30 GPa and temperatures exceeding 1673°C.

Other studies have assessed shock microtextures in distal ejecta zircons from the Chicxulub impact in Haiti, Colorado, Saskatchewan, Spain, and Italy to determine shock characteristics via secondary electron (SE) imaging (Krogh et al., 1993a; Krogh et al., 1993b, Kamo and Krogh,

1995; Kamo et al., 2011). SE imaging can be used to identify many shock features such as fractures (non-PFs, PFs, CFs) and granular textures but is not capable of discerning and quantifying strain such as plastic deformation in a crystal structure, and therefore plastic deformation is not discussed in these other studies. These studies have found the presence of zircons with crystals that contain no shock features, PFs, and/or granular microtextures. The granular microtextures were not possible to distinguish FRIGN from non-FRIGN granules since EBSD analyses were not conducted on these grains. Additionally, with the lack of EBSD analyses to confirm shock features such as shock twins and reidite, these features are not identified in these samples but they may be present. The presence of planar features in previous studies constrains pressures to less than ~20 GPa, and granularization suggests temperatures ≥1200°C for some zircons. The microtextures in zircons from these other studies also show heterogeneous shock environment conditions in the Chicxulub ejecta deposits at these other localities, regardless of the distance from the impact. The inclusion of EBSD analyses in this study enables the identification of shock features that were not easily identifiable in previous studies, providing a more comprehensive understanding of impact-induced textures and conditions in zircons.

Zircon crystal microtextures have been extensively analyzed from within the Chicxulub crater to assess shock experienced within the crater environment (e.g., Timms et al., 2019; Rasmussen et al., 2019; Cox et al., 2020; Wittmann et al., 2021; Zhao et al., 2021; Zhao et al., 2024). Hundreds of zircons were analyzed across these studies from drill cores from the peak ring structure within the impact crater primarily from the International Ocean Discovery Program (IODP)/International Continental Drilling Project (IODO-ICDP) expedition 364. The cores from this expedition represent rock that had a pre-impact depth of 8-10 km that was uplifted to form the peak ring during crater modification (Morgan et al., 2016; Kring et al., 2020; Wittman et al., 2021).

The studies on these cores found a wide range of shock features present in these zircons from fractures, planar features, plastic deformation, reidite, to granular zircon, some of which were confirmed FRIGN zircon by EBSD (Timms et al., 2019; Rasmussen et al., 2019; Cox et al., 2020; Wittmann et al., 2021; Zhao et al., 2021). Not every study of Chicxulub peak ring zircons has identified all of these shock features, as different studies analyze a variety of cores from Expedition 364, with the resulting variation in shock textures likely reflecting the extensive heterogeneity of the impact cratering process, often driven by shock pressure isobars cross-cutting excavation flow lines (e.g., Stöffler et al., 1971; Schmieder et al., 2015; Cox et al., 2020). Since all of the same shock features are found within the Chicxulub impact structure as are found in the ejected material, this implies that the impact structure experienced similar pressure (0-30 GPa) and temperature conditions (≥1200°C) as experienced in the ejecta environment.

3.6.3 U-Pb Age Resetting in Distal Ejecta Zircons

3.6.3.1 Comparison of Chicxulub Ejecta Zircons to Previous Impact Ejecta Studies

Microtextures in the Chicxulub ejecta from this study were found to correlate with various degrees of age resetting within zircon grains (Figure 3.6). Previous studies have found that the presence of any shock features, including fracturing, plastic deformation, shock twinning, formation of reidite, and granular recrystallization textures may introduce fast-diffusion pathways and can affect the U-Pb geochronometer in zircon (Timms et al., 2017; Kenny et al., 2019; Rasmussen et al., 2020). These fast diffusion pathways do not necessarily affect the age of the crystals during impact and impact alteration but can make them more susceptible to Pb-loss during any subsequent geologic events (Rasmussen et al., 2020). While shock twinning can provide diffusion pathways, many shock twinned crystals have no impact related Pb-loss and preserve host

rock ages, denoting that the process of forming these features during an impact is not correlated with Pb-loss (Deutsch and Schärer, 1990; Cavosie et al., 2010; Moser et al., 2011; Grange et al., 2013a). Plastically deformed crystals have been associated with a range of behavior from no resetting (i.e., ages representing target rock age) to partial resetting with ages falling between target rock and impact age. Similar to shock twins, the formation process of plastic deformation does not necessarily cause Pb-loss, but this deformation is susceptible to at least some Pb-loss either during impact formation or post-impact processes (Moser et al., 2011; Grange et al., 2013a; Rasmussen et al., 2020). The transition to reidite has been found to result in minimal-to-no disturbance of the U-Pb geochronometer as it inherits the primary U and Pb elemental and isotopic ratios from zircon (Szumila et al., 2023). The granular recrystallization process to produce both FRIGN and non-FRIGN granular zircons has often been seen to partially to entirely reset U-Pb ages in zircon making these grains the most likely to indicate impact age (Kamo and Krogh, 1995; Deloule et al., 2001; Schmieder et al., 2015; Schmieder et al., 2017; Timms et al., 2017; Cavosie et al., 2018; Rasmussen et al., 2020). Zircons can experience post-impact events, such as thermal and/or hydrothermal events, that can cause subsequent Pb-loss facilitated by the presence of the shock features that create fast diffusion pathways (Rasmussen et al., 2020). These shock features can also produce defects where common-Pb can concentrate, causing shocked zircons to be susceptible to common-Pb contamination. Our study found that only 29% of shocked grains contained ≥90% radiogenic ^{206}Pb values, signifying significant common-Pb contamination. Therefore, all analysis spots regardless of the percent of radiogenic ^{206}Pb were considered for further interpretation. Other studies of impact shocked zircons have also found that a significant portion of the measured zircon U-Pb ages had low radiogenic ^{206}Pb values (e.g., Kalleson et al., 2009; Tohver et al., 2012; Kenny et al., 2019). When the analyses from this study were plotted on a Tera-Wasserburg concordia plot,

116 of 119 SIMS analyses plotted on concordia at 2σ uncertainty, giving us confidence in our common-Pb correction for this data (Figure 3.11).

Nearly all age analyses from this study plot as concordant within 2σ uncertainty on a Wetherill concordia diagram (Figure 3.12). However, all samples likely plot on concordia since the uncertainties on these ages are quite large, and so their large uncertainties intersect concordia. Other studies of Chicxulub ejecta at different localities (Haiti, Saskatchewan, Colorado, Spain, and Italy) have analyzed U-Pb in zircon via higher-precision methods such as TIMS and achieved significantly smaller uncertainties on ages (Krogh et al., 1993a; Krogh et al., 1993b, Kamo and Krogh, 1995; Kamo et al., 2011). These studies using higher-precision methods like TIMS were able to resolve Pb-loss discordance, showing that zircons with no shock features or planar deformation features primarily plotted as concordant near the target rock age, with a few ages ranging between target rock and impact ages where some appear discordant. Granular zircons primarily plotted along a discord between the crystallization age and the impact age, with a few plotting as concordant near impact age (Figure 3.13, Krogh et al., 1993a; Krogh et al., 1993b; Kamo and Krogh, 1995; Kamo et al., 2011). While studies of impact generated granular zircon textures from other impacts events/structures have reported some concordant granular ages, often it is reported that the granular texture grains have discordant U-Pb ages that plot on a discord or plot on concordia at impact age (e.g., Kalleson et al., 2009; Tohver et al., 2012; Cavosie et al., 2015; Erickson et al., 2020).

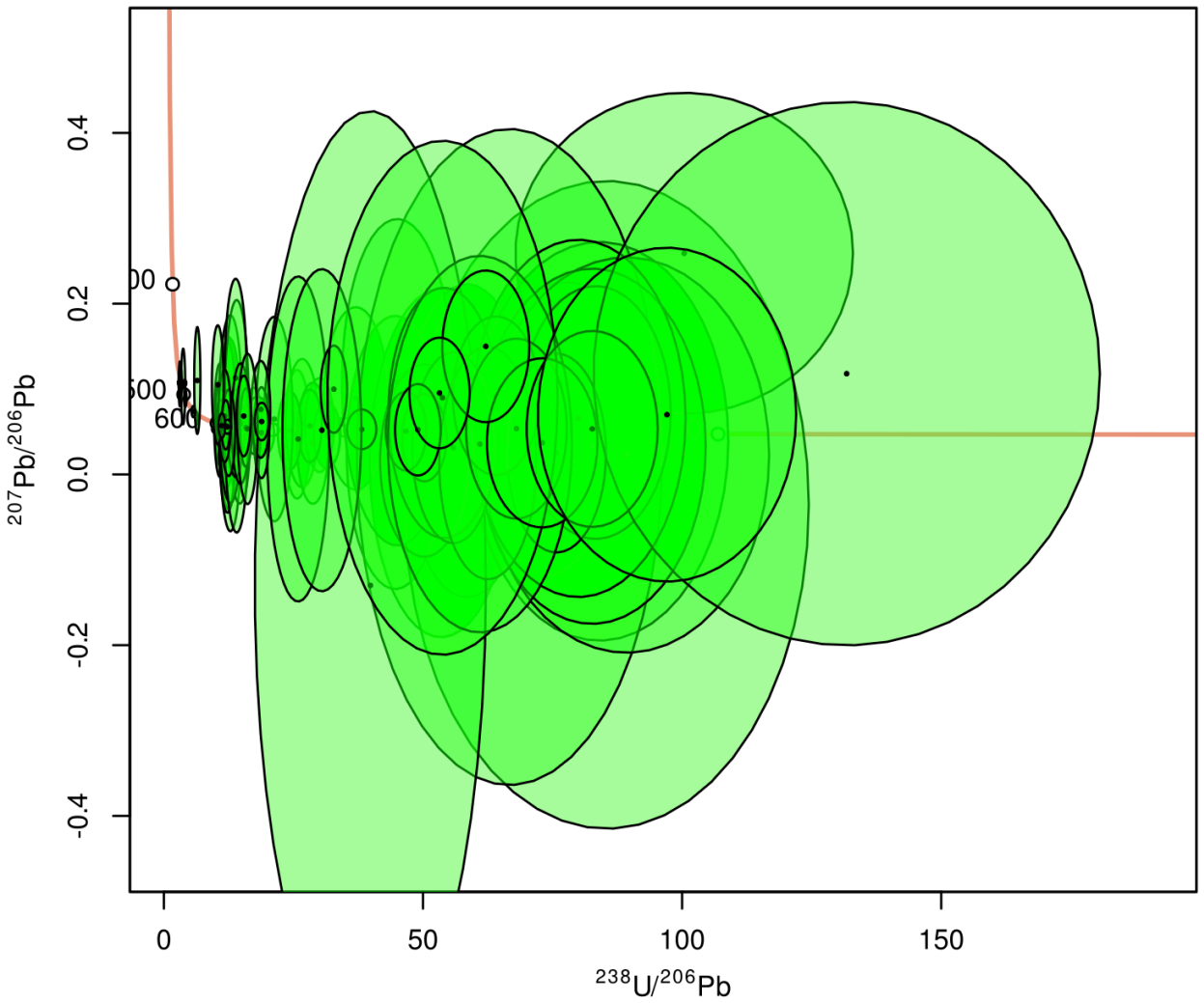

Figure 3.11: Tera-Wasserburg concordia diagram of all of the common Pb corrected U-Pb ratios from zircons from this study (n=119). Nearly all analysis spots plotted as concordant (116 of 119), signifying confidence in our common-Pb correction for this data. Uncertainty reported as 2σ.

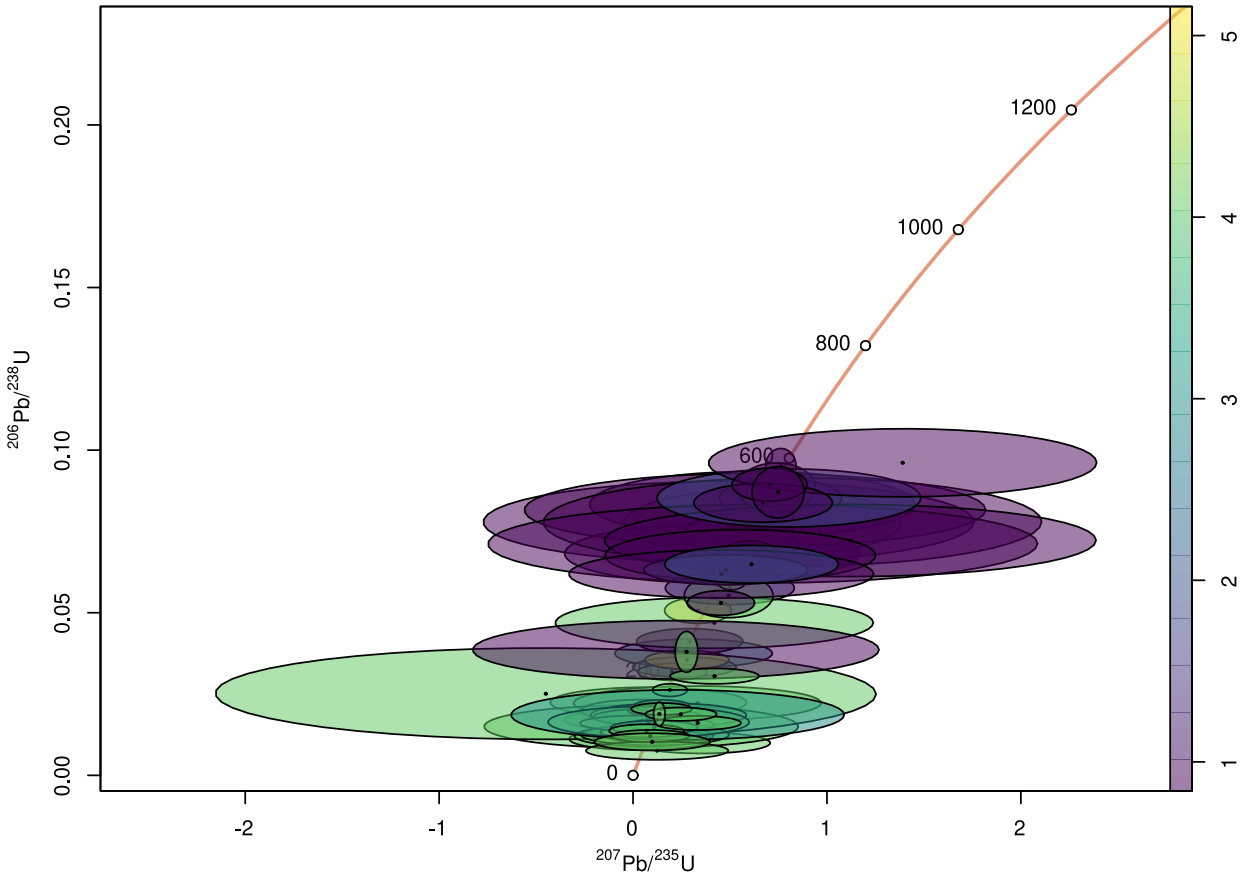

Figure 3.12: Wetherill concordia diagram of the common-Pb corrected U-Pb ratios of impact shocked zircons from this study (all zircons except unshocked). All shocked zircon ages are plotted on this figure. Data points are organized by microtexture: (1) purple = plastic deformation, (2) dark blue = shock twins, (3) light blue = reidite, (4) green = FRIGN zircon, (5) yellow = granular (non-FRIGN). All but one age plots as concordant at 1σ uncertainty, and all ages are concordant at 2σ. Uncertainty reported as 1σ for ease of viewing. (n=77)

3.6.3.2 New Insights into Chicxulub Ejecta Zircons

U-Pb ages were paired with primary microtextures to assess the effectiveness of targeting microstructures via SIMS surveying for dating impacts. The presence of plastic deformation (a less than ~20 GPa microtexture) resulted in either no age resetting or partial age resetting of U-Pb in zircon since some ages match target rock ages while other ages plot between the youngest target

rock age and impact age (Figure 3.6). There is, therefore, variable partial Pb-loss in zircons with crystal plastic deformation, but not full Pb-loss to reset to impact age. There is no correlation between the degree of plastic deformation and age resetting in these grains. Previous studies of both terrestrial and lunar shocked zircons found that both within and external to the impact crater, plastically deformed zircon is sometimes reset and is only found to be fully reset when it is subsequently exposed to prolonged high temperatures (longer than the rapid fraction of a second to seconds long heating during impact) (Moser et al., 2011; Grange et al., 2013a; Grange et al., 2013b; Rasmussen et al., 2020).

Shock twins (misorientation between host and twin of 65° about the <110> axis) were observed primarily in conjunction with other microstructures such as plastic deformation, reidite, non-FRIGN granules, and/or FRIGN granules. However, the shock twins are mostly found in association with FRIGN zircon where ~81% of shock twins are in FRIGN zircon grains (n=44). However, four analysis spots were collected on some grains where the highest order shock feature in the analysis spot was shock twins and these yielded ages consistent with target rock ages. This suggests that the shock twins did not result in any detectable Pb-loss (Figure 3.6). This aligns with previous studies that found twinning is typically associated with minimal to partial age resetting (Moser et al., 2011; Grange et al., 2013a; Timms et al., 2017; Kenny et al., 2019).

Granular zircons are present as both FRIGN and non-FRIGN zircons. These granular grains have ages ranging from 481.6 ± 51.2 Ma to 48.7 ± 14.7 Ma (2σ), spanning the entire range of target rock age to impact age (Figure 3.6 and 3.14). Some zircons are entirely granular, while other grains are partially granular (~1%-80% granular). Some granular analysis spots overlapped multiple shock features and these are denoted as such in Figure 3.6 (x symbol). Many of the older granular zircons, both FRIGN and non-FRIGN, have ages that are closer to the target rock age, while the

FRIGN zircons age tend to be younger with one that is younger than the accepted impact age (48.7 ± 14.7 Ma (2σ)). Previous studies have shown that granular zircon formation can significantly reset U-Pb ages and, in some cases, record the impact age (e.g., Krogh et al., 1993b; Kamo and Krogh, 1995; Moser et al., 2011; Grange et al., 2013b; Cavosie et al., 2015; Timms et al., 2017; Rasmussen et al., 2020). This resetting is likely driven by high-temperature conditions (≥1200°C), which can mobilize U and Pb and induce Pb-loss during granule recrystallization (Wittmann et al., 2006; Cavosie et al., 2015; Schmieder et al., 2015; Cavosie et al., 2016; Timms et al., 2017; Kenny et al., 2019; Rasmussen et al., 2020). However, granular zircons do not always yield fully reset ages, which could result from multiple reasons. The granular neoblasts are often very small, making it difficult to isolate individual granules for SIMS age measurements without contamination of the variably reset interstitial material between granules (e.g., Deloule et al., 2001; Tohver et al., 2012; Schmieder et al., 2015; Timms et al., 2017). In addition to resetting from the impact, the small size of these granules (<15 μm with a vast majority of granules in the <1-5 μm range) can make them more susceptible to later Pb-loss after the impact event, such as subsequent thermal events, which can lead to spurious young ages that post-date the impact (Schmieder et al., 2015; Kenny et al., 2019; Rasmussen et al., 2020). This could explain the one granular/FRIGN zircon that has an age of 48.7 ± 14.7 Ma (2σ) that is not within uncertainty of the impact age (66.052 ± 0.043 Ma (2σ)). Since only 1 of the 40 (or 2.5%) of the granular grains produced this spuriously young age, it is not conclusive evidence of a post-depositional thermal event. Instead, it is more likely due to the contamination of the interstitial material between granules during SIMS analyses (e.g., Deloule et al., 2001; Tohver et al., 2012; Schmieder et al., 2015; Timms et al., 2017). Overall, this study supports the idea that granular zircons are the microtexture that is most associated with age resetting and typically represents the youngest ages relative to other microstructures (Krogh et al.,

1993a; Krogh et al., 1993b; Kamo et al., 1996; Kalleson et al., 2009; Tohver et al., 2012; Schmieder et al., 2015; Rasmussen et al., 2020).

U-Pb ages of reidite were found to be partially reset with ages between the target rock age and impact age. A study by Szumila et al. (2023) on experimentally produced reidite found that the transformation of zircon to reidite typically does not result in any change to the U-Pb geochronometer, so this partial resetting appears unusual in the ejecta zircons. However, the SIMS analyses on these samples had significantly lower percent radiogenic ^{206}Pb components (30-84%) than the reidite in Szumila et al. (2023), which had 99% radiogenic ^{206}Pb, indicating a higher common-Pb contamination in our analyses. In the case of our reidite crystals, ages are taken on granular reidite and on a reidite crystal with widespread amorphization throughout the crystal. Therefore, reidite was not fully isolated in our study and the SIMS spots contained a significant portion of interstitial material (~15-50%). This could cause similar measurement issues to that seen in FRIGN and non-FRIGN granular zircon, where interstitial material can host common-Pb and result in spurious U-Pb ages (e.g., Deloule et al., 2001; Tohver et al., 2012; Schmieder et al., 2015; Schmieder et al., 2015; Timms et al., 2017; Kenny et al., 2019). The analysis on reidite that consisted of a mixture of reidite crystals and amorphized domains produced ages of 237.5 ± 22.2 Ma and 211.0 ± 15.7 Ma (2σ). The analysis spot on the granular reidite produced an age of 118.9 ± 39.8 Ma (2σ) (Figure 3.6). Similar to granular zircon (both FRIGN and non-FRIGN zircon), granular reidite also produced younger ages, further supporting granularization as a mechanism that causes significant U-Pb age resetting.

Overall, the shock features of plastic deformation, shock twinning, and reidite all resulted in target rock age (presumed no Pb-loss) and partial Pb-loss that produced partially reset ages. These shock features are all pressure dependent, signifying that pressure is not a driving factor for

full age resetting during an impact event. Reidite exhibits more Pb-loss and therefore age resetting than expected, despite previous studies not associating its formation with age resetting (Szumila et al., 2023). The degree of resetting may depend on the specific type of reidite (massive, granular, lamellae), as different phase transformations among these types could result in variable Pb-loss (Plan et al., 2021). The presence of granular texture and amorphization in the reidite grains, both of which are associated with Pb-loss, suggests that these features may explain the young age measured in this grain. Additionally, the significant proportion of interstitial material (up to ~50% of the analysis spot) could further contribute to the observed Pb-loss, as amorphous interstitial material is more susceptible to resetting.

Granular zircons, both FRIGN and non-FRIGN zircons, showed significant resetting, with full resetting in some grains consistent with the target rock age (Figure 3.6). FRIGN zircons are the only ejecta zircons in our study found to record the impact age of the Chicxulub impact. Since granular zircon is the only impact shock feature in zircon found in this study of ejecta materials that is dependent on extreme temperatures to form (≥1200°C), it is clear that U-Pb age resetting of zircons in impact settings is most facilitated by high temperatures and recrystallization, and not just high pressures, to reset to impact age (Kusaba et al., 1985; Cavosie et al., 2018, Rasmussen et al., 2020). Deutsch and Schärer (1990) conducted studies on experimentally shocked zircons shocked to pressures of 35-59 GPa and found that shock alone does not disturb the U-Pb system in zircon, further supporting high temperatures as critical for significant age resetting. Since granular zircons are a temperature dependent, and not purely shock dependent, system, this shock feature can be associated with being able to preserve full age resetting (Figure 3.13).

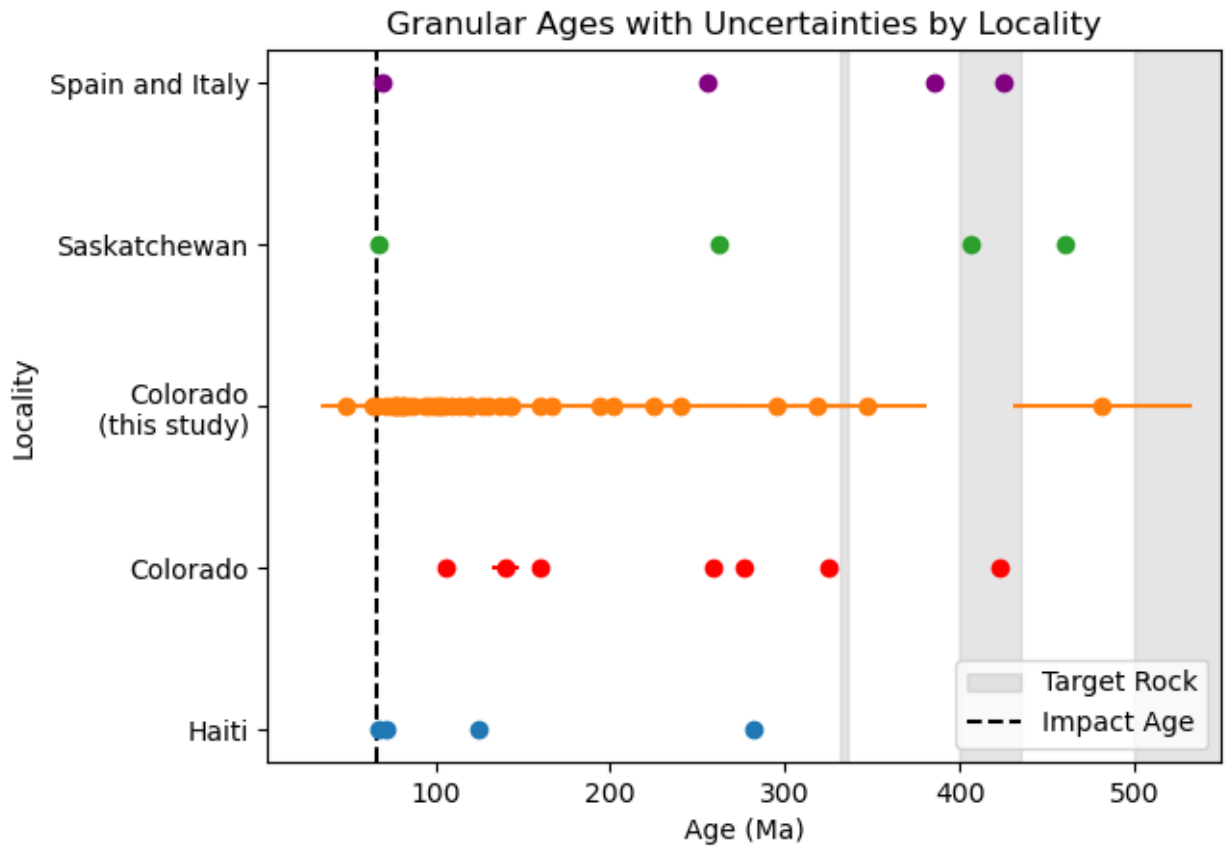

Figure 3.13: U-Pb ages of granular zircons (both FRIGN and non-FRIGN) from various localities at different distances from the impact structure from this study (orange) and Krogh et al., 1993a (red) (Colorado) (paleodistance ~2,300 km), and studies of ejecta from Spain and Italy (paleodistance ~6,700-7,900 km) (Kamo et al., 2011), Saskatchewan (paleodistance ~3,600 km) (Kamo and Krogh, 1995), and Haiti (paleodistance ~880 km) (Krogh et al., 1993b). Uncertainty reported as 2σ.

3.6.3.3 Granular Grains in Chicxulub Ejecta Accurately Date the Impact

The distribution of U-Pb ages in this study of both FRIGN and non-FRIGN granular zircons form an asymptotic curve from ~500 Ma and approach a flat line of late Cretaceous-early Cenozoic ages (Figure 3.14). This type of age distribution is common for a population of zircons that have experienced different degrees of Pb-loss and/or recrystallization (Hoskin and Black, 2000; Cherniak and Watson, 2001; Sharman and Malkowski, 2024). The Chicxulub impact site has been well dated to 66.052 ± 0.043 Ma (2σ) (Swisher et al., 1992; Schmieder and Kring, 2020)

and therefore the youngest zircon grain (48.7 ± 14.7 Ma (2σ)) dated in this study is possibly reflecting a single spurious, unreproducible age. Previous studies of detrital zircon ages also have shown low confidence in the youngest single grain age producing a geologically significant and reliable age and instead, this may be attributed to issues such as low temperature Pb-loss (well documented in detrital zircons) or analytical errors (i.e. matrix effects) (e.g., Dickinson and Gehrels, 2009; Herriott et al., 2019; Howard et al., 2025).

There are numerous other methods to obtain a maximum depositional age from a set of U-Pb zircon ages (Dickinson and Gehrels, 2009; Coutts et al., 2019; Herriott et al., 2019) that are designed to parse young zircon ages that could be reflecting Pb-loss and/or analytical concerns. The youngest largest single population (Y-LSP) method allows for the elimination of young zircons that may be reflecting post depositional Pb-loss (Trop et al., 2019; Fiorillo et al., 2024). Applying the single largest population method results in a population of eight grains yielding an age of 76.8 ± 3.5 Ma (2σ; MSWD = 0.30; Figure 3.15). This age is not within uncertainty of the known Chicxulub ~66 Ma impact age (Swisher et al., 1992; Schmieder and Kring, 2020), but roughly approximates the true age of this impact event.

Since the conditions of the Raton Basin that hosts the Chicxulub ejecta layer in this region have indicated minimum burial/reheating/fluid flow we infer limited post-depositional Pb-loss in our zircons (Rautman et al., 2004; Cooper et al., 2007; Bush et al., 2016). This inference is also supported by the preservation of zircon ages that approximate the zircon ages of the country rock of the Chicxulub impact site (Ross et al., 2021b). Hence, any young zircon populations may capture the true age of the Chicxulub impact event. Applying the youngest single population (YSP; Herriot et al., 2019) method results in an estimated impact age of 66.8 ± 9.1 Ma (2σ, MSWD = 0.23; 3 grains) that is within uncertainty of the impact age of 66.052 ± 0.043 Ma (2σ) (Figure 3.16,

Swisher et al., 1992; Schmieder and Kring, 2020). The YSP, defined as the youngest population of two or more grains with an MSWD of ≲1, has been shown to be an accepted and effective estimate of geologically significant zircon age populations in detrital zircon material (e.g., Spencer et al., 2016; Herriott et al., 2019). Although the uncertainty in the age of the YSP grains is large (± 9.1 Ma), if the Chicxulub impact age were unknown, this estimate would still provide valuable insight into its relative timing. Therefore, when determining an unknown impact age from granular zircon populations, it may prove helpful to utilize the YSP method if post depositional conditions do not favor Pb-loss. When post depositional Pb-loss may have occurred applying the Y-LSP method may be preferred.

Overall, we demonstrate that analyzing zircon microtexture through EBSD is important for identifying zircons that will approximate the age of the target rock (shock twin, plastic), impact age (FRIGN), or age in between these events (plastic, reidite, granular non-FRIGN, granular FRIGN). FRIGN granular zircon and non-FRIGN granular zircons provide variable degrees of resetting and some ages from FRIGN zircons provide the impact age, within 2σ uncertainty (n=6, Figure 3.14). FRIGN zircons make up a majority of granular zircons in the Chicxulub ejecta and are found to be the only granular grains in this study that dated the Chicxulub impact event. Therefore, it is useful to identify FRIGN zircons via EBSD to preferentially date these zircon grains.

The results between granular zircon measurements from TIMS analyses and SIMS analyses draw similar conclusions, showing both of these analytical techniques are effective for dating granular zircons. While our SIMS data does not have small enough uncertainties to determine discordance in individual analyses, our results suggest that it is arguably more important to conduct a large geochronology survey of granular grains via SIMS supplemented by microtextural

information to effectively constrain an impact age. The spatial resolution of SIMS can also isolate granular regions of a crystal to best target regions of a grain that would result in age resetting, rather than averaging the age across the entire grain via TIMS analyses. After the SIMS survey of FRIGN zircons, the YSP method can be applied to determine the impact age, as it has been shown to be effective in determining the Chicxulub impact age in this study.

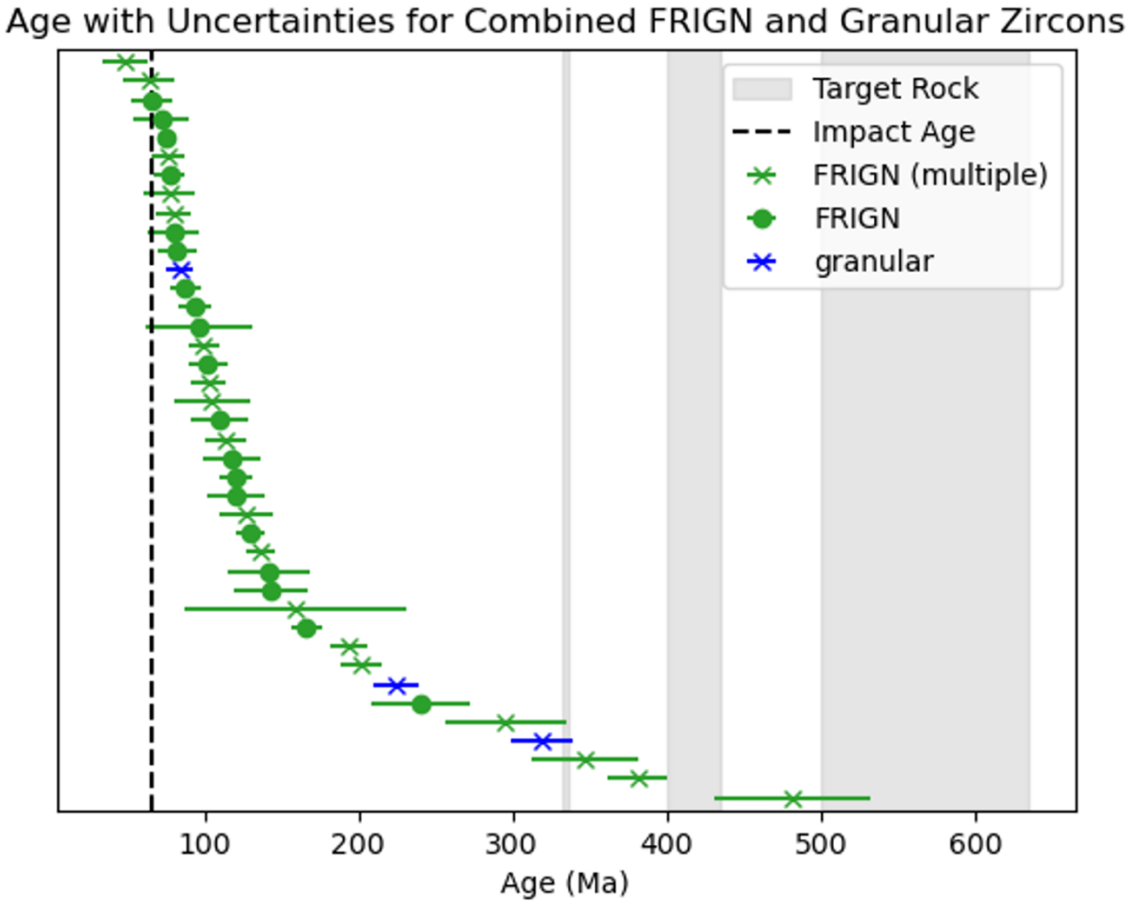

Figure 3.14: Ages of all granular zircons both FRIGN (green) with FRIGN as the only shock texture in the analysis spot (o's) and FRIGN with multiple microtextures (x's) as well as non-FRIGN (blue) granular zircons. Uncertainty reported as 2σ. Target rock ages of rock for the Chicxulub impact structure are denoted by vertical gray bars (Ross et al., 2021b). Ages represent the entire range (within 2σ uncertainty) from target rock age to slightly beyond impact age. Ages with multiple shock features represent a variety of ages. The oldest ages in this sample set, which includes the only ages that reach the target rock age, contain multiple shock textures in the analysis spot, including plastic deformation and amorphous regions. Uncertainty reported as 2σ. (n=40)

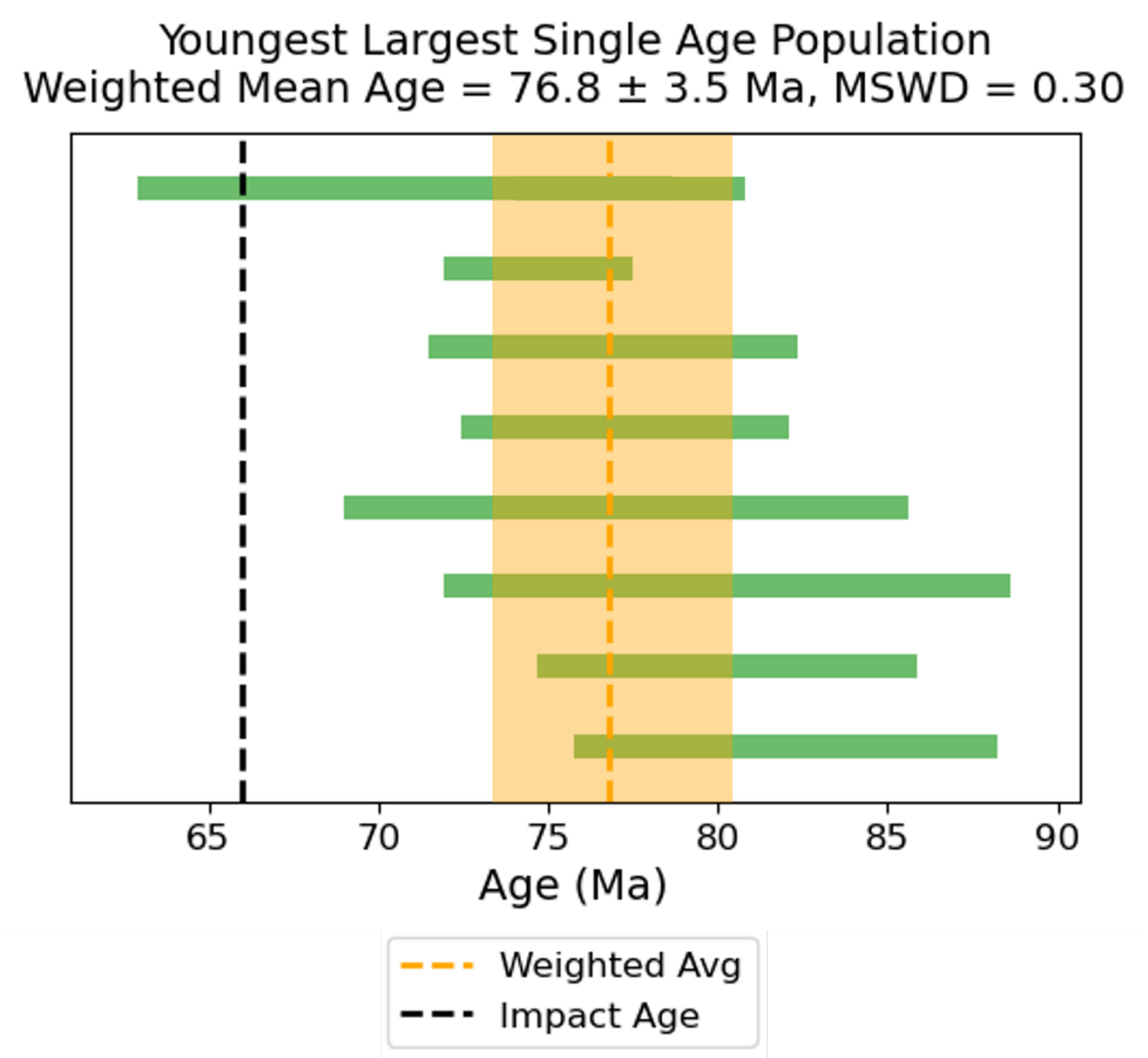

Figure 3.15: The youngest largest single population (Y-LSP) of granular zircon ages showing the weighted mean of these grains does not accurately calculate the impact age within uncertainty. The uncertainty on the age using the Y-LSP method is shaded in orange (2σ). However, if the impact age was unknown, this method closely approximates the general timing of this impact.

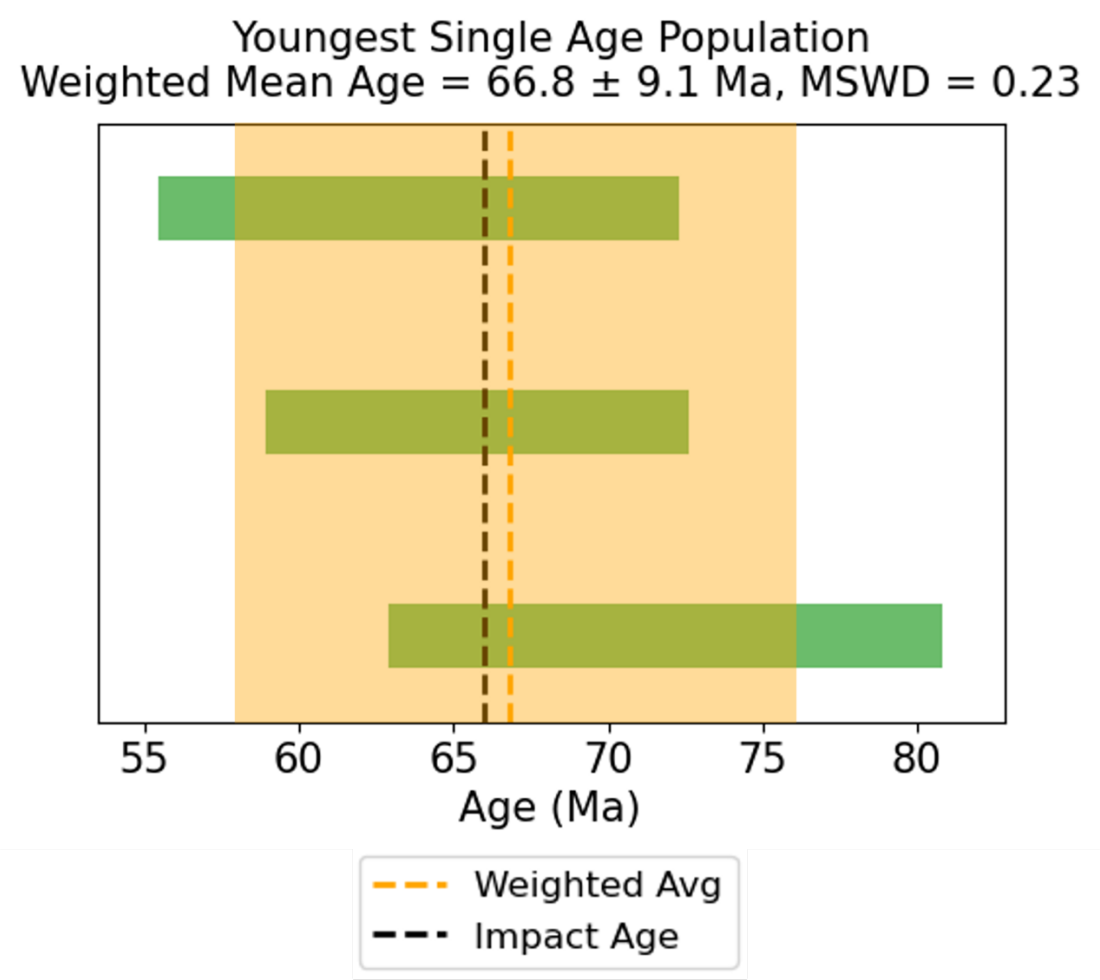

Figure 3.16: The youngest single age population (YSP) of granular zircon ages showing that the weighted mean age of these grains accurately comes within uncertainty of the Chicxulub impact age. The uncertainty on the age using the YSP method is shaded in orange (2σ). This serves as a reliable methodology for determining the age of Chicxulub and could prove useful in determining the age of an unknown impact through the analysis of granular zircons.

3.7 Conclusions

Material can be ejected to extreme distances as a result of an impact event, such as the globally distributed K-Pg layer associated with the Chicxulub impact. The distal ejecta blanket contains zircons with microstructures representing a wide array of temperature and pressure conditions experienced during the excavation and ejection process. This includes unshocked grains, plastic deformation, shock twinning, reidite, FRIGN zircons, and granular (non-FRIGN)

zircons. These represent extremely heterogeneous conditions in the ejecta environment requiring pressures ranging from 0-30 GPa and/or temperatures to exceed 1673°C.

Certain impact microtextures are found to be associated with specific degrees of U-Pb age resetting in zircon. Shock twinning is associated with minimal age resetting and therefore hosts target rock age. Plastically deformed zircons are found to produce minimal to partial resetting resulting in a range of ages from the target rock age to intermediate ages between the target rock and impact age. Reidite ages are found to be partially reset between impact age and target rock age, likely because of the lack of isolation of crystalline reidite in these samples and presence of other microstructures like amorphous domains and granular recrystallization which are known to cause Pb-loss. Further studies of fully crystalline reidite analysis spots would be helpful for determining resetting in reidite. Unshocked zircons could originate from the impact target rock, or they could originate from local, detrital grains where ejecta is deposited, and careful analysis into the depositional rock record of surrounding geologic units relative to these grains in the ejecta layer is essential in order to confirm the zircons that are impact in origin.

Granular zircons displayed a range of resetting from target rock age to impact age with some FRIGN zircons (n=6) measuring within uncertainty (2σ) of the impact age of Chicxulub. Since shock twinning, plastic deformation, and reidite formation are all pressure dependent shock textures (~20 to 30+ GPa) and granularization (both FRIGN and non-FRIGN) is a temperature driven recrystallization process (≥1200°C), this shows that U-Pb age resetting in zircon is a temperature dependent process that is facilitated by the zircon recrystallization. A large sampling of granular zircon ages (n=40 in this study) was found to asymptotically converge on the age on the impact with the youngest largest single population of ages from granular zircons produced a weighted mean age that is within uncertainty of the impact age. These methods could prove useful

for dating ejecta deposits from an unknown impact crater. A time-efficient methodology like SIMS is advantageous because sample preparation and age measurement are less labor-intensive than methods like TIMS. As a result, ages can be measured more efficiently and at a finer spatial resolution, allowing for targeted analyses of granular microtextures to determine an impact age. In general, analytical spots that contained only granules produced more reset ages, signifying that using the small SIMS spot size (~10 μm), rather than methods that have a much larger spot size or average an entire grain (i.e., LA-ICP-MS, TIMS), may be more likely to yield impact ages. As FRIGN zircons were the only type of microtexture to produce the impact age, when determining an impact age it is recommended conduct EBSD analyses on granular grains to identify FRIGN zircons for preferential dating.

3.8 References

Alvarez, L.W., Alvarez, W., Asaro, F., Michel, H.V., 1980. Extraterrestrial Cause for the Cretaceous-Tertiary Extinction. Science 208, 1095–1108. https://doi.org/10.1126/science.208.4448.1095

Amor, K., Hesselbo, S.P., Porcelli, D., Price, A., Saunders, N., Sykes, M., Stevanović, J., MacNiocaill, C., 2019. The Mesoproterozoic Stac Fada proximal ejecta blanket, NW Scotland: constraints on crater location from field observations, anisotropy of magnetic susceptibility, petrography and geochemistry. Journal of the Geological Society 176, 830–846. https://doi.org/10.1144/jgs2018-093

Arenillas, I., Arz, J.A., Grajales-Nishimura, J.M., Murillo-Muñetón, G., Alvarez, W., Camargo-Zanoguera, A., Molina, E., Rosales-Domínguez, C., 2006. Chicxulub impact event is Cretaceous/Paleogene boundary in age: New micropaleontological evidence. Earth and Planetary Science Letters 249, 241–257. https://doi.org/10.1016/j.epsl.2006.07.020

Bohor, B.F., Foord, E.E., Betterton, W.J., 1989. Trace minerals in K-T boundary clays. Meteoritics 24.

Bohor, B.F., 1990. Shock-induced microdeformations in quartz and other mineralogical indications of an impact event at the Cretaceous-Tertiary boundary. Tectonophysics, Cryptoexplosions and catastrophes in the geological record, with a special focus on the Vredefort structure 171, 359–372. https://doi.org/10.1016/0040-1951(90)90110-T

Bohor, B.F., Glass, B.P., 1995. Origin and diagenesis of K/T impact spherules—From Haiti to Wyoming and beyond. Meteoritics & Planetary Science 30, 182–198.

Bush, M.A., Horton, B.K., Murphy, M.A., Stockli, D.F., 2016. Detrital record of initial basement exhumation along the Laramide deformation front, southern Rocky Mountains. Tectonics 35, 2117–2130. https://doi.org/10.1002/2016TC004194

Cavosie, A.J., Erickson, T.M., Timms, N.E., Reddy, S.M., Talavera, C., Montalvo, S.D., Pincus, M.R., Gibbon, R.J., Moser, D., 2015. A terrestrial perspective on using ex situ shocked zircons to date lunar impacts. Geology 43, 999–1002. https://doi.org/10.1130/G37059.1

Cavosie, A.J., Timms, N.E., Erickson, T.M., Hagerty, J.J., Hörz, F., 2016. Transformations to granular zircon revealed: Twinning, reidite, and ZrO2 in shocked zircon from Meteor Crater (Arizona, USA). Geology 44, 703–706. https://doi.org/10.1130/G38043.1

Cavosie, A.J., Timms, N.E., Ferrière, L., Rochette, P., 2018. FRIGN zircon—The only terrestrial mineral diagnostic of high-pressure and high-temperature shock deformation. Geology 46, 891–894. https://doi.org/10.1130/G45079.1

Cherniak, D.J., Watson, E.B., 2001. Pb diffusion in zircon. Chemical Geology, What are we dating? Understanding the Crystallogernesis of U-Pb 172, 5–24. https://doi.org/10.1016/S0009-2541(00)00233-3

Cooper, J.R., Crelling, J.C., Rimmer, S.M., Whittington, A.G., 2007. Coal metamorphism by igneous intrusion in the Raton Basin, CO and NM: Implications for generation of volatiles. International Journal of Coal Geology, TSOP 2005 71, 15–27. https://doi.org/10.1016/j.coal.2006.05.007

Corfu, F., 2013. A century of U-Pb geochronology: The long quest towards concordance. GSA Bulletin 125, 33–47. https://doi.org/10.1130/B30698.1

Corfu, F., 2015. Uranium–Lead, Zircon, in: Jack Rink, W., Thompson, J.W. (Eds.), Encyclopedia of Scientific Dating Methods, Encyclopedia of Earth Sciences Series. Springer Netherlands, Dordrecht, pp. 914–918. https://doi.org/10.1007/978-94-007-6304-3_23

Coutts, D.S., Matthews, W.A., Hubbard, S.M., 2019. Assessment of widely used methods to derive depositional ages from detrital zircon populations. Geoscience Frontiers 10, 1421–1435. https://doi.org/10.1016/j.gsf.2018.11.002

Cox, M.A., Erickson, Timmons M., Schmieder, M., Christoffersen, R., Ross, D., Cavosie, A.J., Bland, P.A., Kring, D.A., 2020. High-resolution microstructural and compositional analyses of shock deformed apatite from the peak ring of the Chicxulub impact crater. Meteoritics & Planetary Science 55.

Crow, C.A., McKeegan, K.D., Moser, D.E., 2017. Coordinated U–Pb geochronology, trace element, Ti-in-zircon thermometry and microstructural analysis of Apollo zircons. Geochimica et Cosmochimica Acta 202, 264–284. https://doi.org/10.1016/j.gca.2016.12.019

Crow, C.A., Moser, D.E., McKeegan, K.D., 2019. Shock metamorphic history of >4 Ga Apollo 14 and 15 zircons. Meteoritics & Planetary Science 54, 181–201. https://doi.org/10.1111/maps.13184

Crow, C.A., Tong, C., Erickson, T.M., Moser, D.E., Bell, A.S., Kelly, N.M., Prissel, T.C., Hyde, B.C., 2024. Impact origin of lunar zircon melt inclusions in Apollo impact melt breccia 14311. Meteoritics & Planetary Science 59, 1509–1522. https://doi.org/10.1111/maps.14162

de Graaff, S.J., Kaskes, P., Déhais, T., Goderis, S., Debaille, V., Ross, C.H., Gulick, S.P.S., Feignon, J.-G., Ferrière, L., Koeberl, C., Smit, J., Mattielli, N., Claeys, P., 2021. New insights into the formation and emplacement of impact melt rocks within the Chicxulub impact structure, following the 2016 IODP-ICDP Expedition 364. GSA Bulletin 134, 293–315. https://doi.org/10.1130/B35795.1

Deloule, E., Chaussidon, M., Glass, B.P., Koeberl, C., 2001. U–Pb isotopic study of relict zircon inclusions recovered from Muong Nong-type tektites. Geochimica et Cosmochimica Acta 65, 1833–1838. https://doi.org/10.1016/S0016-7037(01)00548-8

Deutsch, A., Schärer, U., 1990. Isotope systematics and shock-wave metamorphism: I. U-Pb in zircon, titanite and monazite, shocked experimentally up to 59 GPa. Geochimica et Cosmochimica Acta 54, 3427–3434. https://doi.org/10.1016/0016-7037(90)90295-V

Dickinson, W.R., Gehrels, G.E., 2009. Use of U–Pb ages of detrital zircons to infer maximum depositional ages of strata: A test against a Colorado Plateau Mesozoic database. Earth and Planetary Science Letters 288, 115–125. https://doi.org/10.1016/j.epsl.2009.09.013

Erickson, T.M., Cavosie, A.J., Moser, D.E., Barker, I.R., Radovan, H.A., 2013. Correlating planar microstructures in shocked zircon from the Vredefort Dome at multiple scales: Crystallographic modeling, external and internal imaging, and EBSD structural analysis. American Mineralogist 98, 53–65. https://doi.org/10.2138/am.2013.4165

Erickson, T.M., Kirkland, C.L., Timms, N.E., Cavosie, A.J., Davison, T.M., 2020. Precise radiometric age establishes Yarrabubba, Western Australia, as Earth's oldest recognised meteorite impact structure. Nat Commun 11, 300. https://doi.org/10.1038/s41467-019-13985-7

Farnan, I., Balan, E., Pickard, C.J., Mauri, F., 2003. The effect of radiation damage on local structure in the crystalline fraction of ZrSiO4: Investigating the 29Si NMR response to pressure in zircon and reidite. American Mineralogist 88, 1663–1667. https://doi.org/10.2138/am-2003-11-1205

Fiorillo, A.R., McCarthy, P.J., Shimer, G., Suarez, M.B., Takasaki, R., Chinzorig, T., Kobayashi, Y., O'Sullivan, P., Orphys, E., 2024. New Dinosaur Ichnological, Sedimentological, and Geochemical Data from a Cretaceous High-Latitude Terrestrial Greenhouse Ecosystem, Nanushuk Formation, North Slope, Alaska. Geosciences 14, 36. https://doi.org/10.3390/geosciences14020036

Glass, B.P., Liu, S., Leavens, P.B., 2002. Reidite: An impact-produced high-pressure polymorph of zircon found in marine sediments. American Mineralogist 87, 562–565. https://doi.org/10.2138/am-2002-0420

Glass, B.P., Simonson, B.M., 2012. Distal Impact Ejecta Layers: Spherules and More. Elements 8, 43–48. https://doi.org/10.2113/gselements.8.1.43

Grange, M.L., Pidgeon, R.T., Nemchin, A.A., Timms, N.E., Meyer, C., 2013a. Interpreting U–Pb data from primary and secondary features in lunar zircon. Geochimica et Cosmochimica Acta 101, 112–132. https://doi.org/10.1016/j.gca.2012.10.013

Grange, M.L., Nemchin, A.A., Pidgeon, R.T., 2013b. The effect of 1.9 and 1.4 Ga impact events on 4.3 Ga zircon and phosphate from an Apollo 15 melt breccia. Journal of Geophysical Research: Planets 118, 2180–2197. https://doi.org/10.1002/jgre.20167

Gulick, S.P.S., Barton, P.J., Christeson, G.L., Morgan, J.V., McDonald, M., Mendoza-Cervantes, K., Pearson, Z.F., Surendra, A., Urrutia-Fucugauchi, J., Vermeesch, P.M., Warner, M.R., 2008. Importance of pre-impact crustal structure for the asymmetry of the Chicxulub impact crater. Nature Geosci 1, 131–135. https://doi.org/10.1038/ngeo103

Hayne, P.O., Bandfield, J.L., Siegler, M.A., Vasavada, A.R., Ghent, R.R., Williams, J.-P., Greenhagen, B.T., Aharonson, O., Elder, C.M., Lucey, P.G., Paige, D.A., 2017. Global Regolith Thermophysical Properties of the Moon From the Diviner Lunar Radiometer Experiment. Journal of Geophysical Research: Planets 122, 2371–2400. https://doi.org/10.1002/2017JE005387

Hazen, R.M., Finger, L.W., 1979. Crystal structure and compressibility of zircon at high pressure. American Mineralogist 64, 196–201.

Herriott, T.M., Crowley, J.L., Schmitz, M.D., Wartes, M.A., Gillis, R.J., 2019. Exploring the law of detrital zircon: LA-ICP-MS and CA-TIMS geochronology of Jurassic forearc strata, Cook Inlet, Alaska, USA. Geology 47, 1044–1048. https://doi.org/10.1130/G46312.1

Hildebrand, A.R., Boynton, W.V., 1990. Proximal Cretaceous-Tertiary Boundary Impact Deposits in the Caribbean. Science 248, 843–847. https://doi.org/10.1126/science.248.4957.843

Hildebrand, A.R., Penfield, G.T., Kring, D.A., Pilkington, M., Camargo Z., A., Jacobsen, S.B., Boynton, W.V., 1991. Chicxulub Crater: A possible Cretaceous/Tertiary boundary impact crater on the Yucatán Peninsula, Mexico. Geology 19, 867–871. https://doi.org/10.1130/0091-7613(1991)019<0867:CCAPCT>2.3.CO;2

Hoskin, P. w. o., Black, L. p., 2000. Metamorphic zircon formation by solid-state recrystallization of protolith igneous zircon. Journal of Metamorphic Geology 18, 423–439. https://doi.org/10.1046/j.1525-1314.2000.00266.x

Howard, B.L., Sharman, G.R., Crowley, J.L., Wersan, E.R., 2025. The leaky chronometer: Evidence for systematic cryptic Pb loss in laser ablation U-Pb dating of zircon relative to CA-TIMS. Terra Nova 37, 19–25. https://doi.org/10.1111/ter.12742

Huber, M.S., Črne, A.E., McDonald, I., Hecht, L., Melezhik, V.A., Koeberl, C., 2014. Impact spherules from Karelia, Russia: Possible ejecta from the 2.02 Ga Vredefort impact event. Geology 42, 375–378. https://doi.org/10.1130/G35231.1

Izett, G.A., 1987. The Cretaceous-Tertiary (K-T) boundary interval, Raton Basin, Colorado and New Mexico, and its content of shock-metamorphosed minerals; implication concerning the K-T boundary impact-extinction theory (No. 87–606), Open-File Report. U.S. Geological Survey,. https://doi.org/10.3133/ofr87606

Izett, G.A., 1991. Tektites in Cretaceous-Tertiary boundary rocks on Haiti and their bearing on the Alvarez Impact Extinction Hypothesis. Journal of Geophysical Research: Planets 96, 20879–20905. https://doi.org/10.1029/91JE02249

James, S., Chandran, S.R., Aswathi, J., Padmakumar, D., Sajinkumar, K.S., 2023. Geologic, geomorphic, tectonic, and paleoclimatic controls on the distribution and preservation of Chicxulub distal ejecta: A global perspective. Earth-Science Reviews 244, 104545. https://doi.org/10.1016/j.earscirev.2023.104545

Kalleson, E., Corfu, F., Dypvik, H., 2009. U–Pb systematics of zircon and titanite from the Gardnos impact structure, Norway: Evidence for impact at 546 Ma? Geochimica et Cosmochimica Acta 73, 3077–3092. https://doi.org/10.1016/j.gca.2009.02.020

Kamo, S.L., Krogh, T.E., 1995. Chicxulub crater source for shocked zircon crystals from the Cretaceous-Tertiary boundary layer, Saskatchewan: Evidence from new U-Pb data. Geology 23, 281–284. https://doi.org/10.1130/0091-7613(1995)023<0281:CCSFSZ>2.3.CO;2

Kamo, S.L., Reimold, W.U., Krogh, T.E., Colliston, W.P., 1996. A 2.023 Ga age for the Vredefort impact event and a first report of shock metamorphosed zircons in pseudotachylitic breccias and Granophyre. Earth and Planetary Science Letters 144, 369–387. https://doi.org/10.1016/S0012-821X(96)00180-X

Kamo, S.L., Lana, C., Morgan, J.V., 2011. U–Pb ages of shocked zircon grains link distal K–Pg boundary sites in Spain and Italy with the Chicxulub impact. Earth and Planetary Science Letters 310, 401–408. https://doi.org/10.1016/j.epsl.2011.08.031

Keller, G., Adatte, T., Berner, Z., Harting, M., Baum, G., Prauss, M., Tantawy, A., Stueben, D., 2007. Chicxulub impact predates K–T boundary: New evidence from Brazos, Texas. Earth and Planetary Science Letters 255, 339–356. https://doi.org/10.1016/j.epsl.2006.12.026

Kenny, G.G., Morales, L.F., Whitehouse, M.J., Petrus, J.A., Kamber, B.S., 2017. The formation of large neoblasts in shocked zircon and their utility in dating impacts. Geology 45, 1003–1006. https://doi.org/10.1130/G39328.1

Kenny, G.G., Schmieder, M., Whitehouse, M.J., Nemchin, A.A., Morales, L.F.G., Buchner, E., Bellucci, J.J., Snape, J.F., 2019. A new U-Pb age for shock-recrystallised zircon from the Lappajärvi impact crater, Finland, and implications for the accurate dating of impact events. Geochimica et Cosmochimica Acta 245, 479–494. https://doi.org/10.1016/j.gca.2018.11.021

Keppie, J.D., Dostal, J., Norman, M., Urrutia-Fucugauchi, J., Grajales-Nishimura, M., 2011. Study of melt and a clast of 546 Ma magmatic arc rocks in the 65 Ma Chicxulub bolide breccia, northern Maya block, Mexico: western limit of Ediacaran arc peripheral to northern Gondwana. International Geology Review 53, 1180–1193. https://doi.org/10.1080/00206810903545527

Kring, D.A., 2005. Hypervelocity collisions into continental crust composed of sediments and an underlying crystalline basement: comparing the Ries (~24 km) and Chicxulub (~180 km) impact craters. Geochemistry 65, 1–46. https://doi.org/10.1016/j.chemer.2004.10.003

Kring, D.A., Claeys, P., Gulick, S.P.S., Morgan, J.V., Collins, G.S., 2017. Chicxulub and the Exploration of Large Peak-Ring Impact Craters through Scientific Drilling. GSAT 4–8. https://doi.org/10.1130/GSATG352A.1

Kring, D.A., Tikoo, S.M., Schmieder, M., Riller, U., Rebolledo-Vieyra, M., Simpson, S.L., Osinski, G.R., Gattacceca, J., Wittmann, A., Verhagen, C.M., Cockell, C.S., Coolen, M.J.L., Longstaffe, F.J., Gulick, S.P.S., Morgan, J.V., Bralower, T.J., Chenot, E., Christeson, G.L., Claeys, P., Ferrière, L., Gebhardt, C., Goto, K., Green, S.L., Jones, H., Lofi, J., Lowery, C.M., Ocampo-Torres, R., Perez-Cruz, L., Pickersgill, A.E., Poelchau, M.H., Rae, A.S.P., Rasmussen, C., Sato, H., Smit, J., Tomioka, N., Urrutia-Fucugauchi, J., Whalen, M.T., Xiao, L., Yamaguchi, K.E., 2020. Probing the hydrothermal system of the Chicxulub impact crater. Science Advances 6, eaaz3053. https://doi.org/10.1126/sciadv.aaz3053

Krogh, T. E., Kamo, S.L., Bohor, B.F., 1993a. Fingerprinting the K/T impact site and determining the time of impact by U-Pb dating of single shocked zircons from distal ejecta. Earth and Planetary Science Letters 119, 425–429. https://doi.org/10.1016/0012-821X(93)90150-8

Krogh, Thomas E., Kamo, S.L., Sharpton, V.L., Marin, L.E., Hildebrands, A.R., 1993b. U–Pb ages of single shocked zircons linking distal K/T ejecta to the Chicxulub crater. Nature 366, 731–734. https://doi.org/10.1038/366731a0

Kusaba, K., Syono, Y., Kikuchi, M., Fukuoka, K., 1985. Shock behavior of zircon: phase transition to scheelite structure and decomposition. Earth and Planetary Science Letters 72, 433–439. https://doi.org/10.1016/0012-821X(85)90064-0

Leroux, H., Reimold, W.U., Koeberl, C., Hornemann, U., Doukhan, J.-C., 1999. Experimental shock deformation in zircon: a transmission electron microscopic study. Earth and Planetary Science Letters 169, 291–301. https://doi.org/10.1016/S0012-821X(99)00082-5

Margot, J.-L., Campbell, D.B., Jurgens, R.F., Slade, M.A., 1999. The topography of Tycho Crater. Journal of Geophysical Research: Planets 104, 11875–11882. https://doi.org/10.1029/1998JE900047

Montalvo, S.D., Reddy, S.M., Saxey, D.W., Rickard, W.D.A., Fougerouse, D., Quadir, Z., Johnson, T.E., 2019. Nanoscale constraints on the shock-induced transformation of zircon to reidite. Chemical Geology 507, 85–95. https://doi.org/10.1016/j.chemgeo.2018.12.039

Morgan, J., Warner, M., the Chicxulub Working Group, Brittan, J., Buffler, R., Camargo, A., Christeson, G., Denton, P., Hildebrand, A., Hobbs, R., Macintyre, H., Mackenzie, G., Maguire, P., Marin, L., Nakamura, Y., Pilkington, M., Sharpton, V., Snyder, D., Suarez, G., Trejo, A., 1997. Size and morphology of the Chicxulub impact crater. Nature 390, 472–476. https://doi.org/10.1038/37291

Morgan, J.V., Gulick, S.P.S., Bralower, T., Chenot, E., Christeson, G., Claeys, P., Cockell, C., Collins, G.S., Coolen, M.J.L., Ferrière, L., Gebhardt, C., Goto, K., Jones, H., Kring, D.A., Le Ber, E., Lofi, J., Long, X., Lowery, C., Mellett, C., Ocampo-Torres, R., Osinski, G.R.,

Perez-Cruz, L., Pickersgill, A., Poelchau, M., Rae, A., Rasmussen, C., Rebolledo-Vieyra, M., Riller, U., Sato, H., Schmitt, D.R., Smit, J., Tikoo, S., Tomioka, N., Urrutia-Fucugauchi, J., Whalen, M., Wittmann, A., Yamaguchi, K.E., Zylberman, W., 2016. The formation of peak rings in large impact craters. Science 354, 878–882. https://doi.org/10.1126/science.aah6561

Morozova, I., 2015. Strength Study of Zircon Under High Pressure (M.Sc.). The University of Western Ontario (Canada), Canada -- Ontario, CA.

Moser, D.E., Cupelli, C.L., Barker, I.R., Flowers, R.M., Bowman, J.R., Wooden, J., Hart, J.R., 2011. New zircon shock phenomena and their use for dating and reconstruction of large impact structures revealed by electron nanobeam (EBSD, CL, EDS) and isotopic U–Pb and (U–Th)/He analysis of the Vredefort domeThis article is one of a series of papers published in this Special Issue on the theme of Geochronology in honour of Tom Krogh. Canadian Journal of Earth Sciences 48, 117–139. https://doi.org/10.1139/E11-011

Nemchin, A., 2015. Uranium–Lead, Extraterrestrial, Planetary Materials, in: Jack Rink, W., Thompson, J.W. (Eds.), Encyclopedia of Scientific Dating Methods, Encyclopedia of Earth Sciences Series. Springer Netherlands, Dordrecht, pp. 890–894. https://doi.org/10.1007/978-94-007-6304-3_255

Osinski, G.R., Grieve, R.A.F., Ferrière, L., Losiak, A., Pickersgill, A.E., Cavosie, A.J., Hibbard, S.M., Hill, P.J.A., Bermudez, J.J., Marion, C.L., Newman, J.D., Simpson, S.L., 2022. Impact Earth: A review of the terrestrial impact record. Earth-Science Reviews 232, 104112. https://doi.org/10.1016/j.earscirev.2022.104112

Paces, J.B., Miller Jr., J.D., 1993. Precise U-Pb ages of Duluth Complex and related mafic intrusions, northeastern Minnesota: Geochronological insights to physical, petrogenetic, paleomagnetic, and tectonomagmatic processes associated with the 1.1 Ga Midcontinent Rift System. Journal of Geophysical Research: Solid Earth 98, 13997–14013. https://doi.org/10.1029/93JB01159

Pierazzo, E., Melosh, J., 2012. Environmental effects of impact events, in: Impact Cratering: Processes and Products. John Wiley & Sons, Ltd.

Pillmore, C.L., Flores, R.M., 1987. Stratigraphy and depositional environments of the Cretaceous-Tertiary boundary clay and associated rocks, Raton basin, New Mexico and Colorado, in: Fassett, J.E., Rigby, J.K., Jr. (Eds.), The Cretaceous-Tertiary Boundary in the San Juan and Raton Basins, New Mexico and Colorado. Geological Society of America, p. 0. https://doi.org/10.1130/SPE209-p111

Pinto, J.A., Warme, J.E., 2007. Alamo Event, Nevada: Crater stratigraphy and impact breccia Realms, in: Evans, K.R., Horton, J.W., Jr., King, D.T., Jr., Morrow, J.R. (Eds.), The Sedimentary Record of Meteorite Impacts. Geological Society of America, p. 0. https://doi.org/10.1130/2008.2437(07)

Plan, A., Kenny, G.G., Erickson, T.M., Lindgren, P., Alwmark, C., Holm-Alwmark, S., Lambert, P., Scherstén, A., Söderlund, U., 2021. Exceptional preservation of reidite in the Rochechouart impact structure, France: New insights into shock deformation and phase transition of zircon. Meteoritics & Planetary Science 56, 1795–1828. https://doi.org/10.1111/maps.13723

Rasmussen, C., Stockli, D.F., Ross, C.H., Pickersgill, A., Gulick, S.P., Schmieder, M., Christeson, G.L., Wittmann, A., Kring, D.A., Morgan, J.V., 2019. U-Pb memory behavior in Chicxulub's peak ring — Applying U-Pb depth profiling to shocked zircon. Chemical Geology 525, 356–367. https://doi.org/10.1016/j.chemgeo.2019.07.029

Rasmussen, C., Stockli, D.F., Erickson, T.M., Schmieder, M., 2020. Spatial U-Pb age distribution in shock-recrystallized zircon – A case study from the Rochechouart impact structure, France. Geochimica et Cosmochimica Acta 273, 313–330. https://doi.org/10.1016/j.gca.2020.01.017

Rautman, C.A., Herrin, J.M., Cooper, S.P., Basinski, P.M., Olsson, W.A., Arnold, B.W., Broadhead, R.F., Knight, C.D., Keefe, R.G., McKinney, C., Holm, G., Holland, J.F., Larson, R., Engler, T.W., Lorenz, J.C., 2004. Natural gas production problems : solutions, methodologies, and modeling. (No. SAND2004-4859). Sandia National Laboratories (SNL), Albuquerque, NM, and Livermore, CA (United States). https://doi.org/10.2172/919653

Reddy, S.M., Timms, N.E., Pantleon, W., Trimby, P., 2007. Quantitative characterization of plastic deformation of zircon and geological implications. Contrib Mineral Petrol 153, 625–645. https://doi.org/10.1007/s00410-006-0174-4

Ross, C., Stockli, D.F., Gulick, S.P.S., Kaskes, P., Smit, J., Artemieva, N.A., 2021a. Finding a Specific Needle in a Haystack: Tracing Ejected Zircon from the Chicxulub Impact in K-Pg Boundary Sections, in: 6. Presented at the Geological Society of America. https://doi.org/doi:10.1130/abs/2021AM-370733

Ross, C.H., Stockli, D.F., Rasmussen, C., Gulick, S.P.S., de Graaff, S.J., Claeys, P., Zhao, J., Xiao, L., Pickersgill, A.E., Schmieder, M., Kring, D.A., Wittmann, A., Morgan, J.V., 2021b. Evidence of Carboniferous arc magmatism preserved in the Chicxulub impact structure. GSA Bulletin 134, 241–260. https://doi.org/10.1130/B35831.1

Salguero-Hernández, E., Pérez-Cruz, L., Urrutia-Fucugauchi, J., 2020. Seismic attribute analysis of Chicxulub impact crater. Acta Geophys. 68, 627–640. https://doi.org/10.1007/s11600-020-00442-z

Sañudo-Wilhelmy, S.A., Flegal, A.R., 1994. Temporal variations in lead concentrations and isotopic composition in the Southern California Bight. Geochimica et Cosmochimica Acta 58, 3315–3320. https://doi.org/10.1016/0016-7037(94)90060-4

Schmieder, M., Tohver, E., Jourdan, F., Denyszyn, S., Haines, P., 2015. Zircons from the Acraman impact melt rock (South Australia): Shock metamorphism, U–Pb and 40Ar/39Ar

systematics, and implications for the isotopic dating of impact events. Geochimica et Cosmochimica Acta 161, 71–100. https://doi.org/10.1016/j.gca.2015.04.021

Schmieder, M., Shaulis, B.J., Lapen, T.J., Kring, D.A., 2017. U–Th–Pb systematics in zircon and apatite from the Chicxulub impact crater, Yucatán, Mexico. Geological Magazine 155, 1330–1350. https://doi.org/10.1017/S0016756817000255

Schmieder, M., Kring, D., 2020. Earth's Impact Events Through Geologic Time: A List of Recommended Ages for Terrestrial Impact Structures and Deposits | Astrobiology. Astrobiology 20, 91–141.

Schmitz, M.D., Bowring, S.A., 2001. U-Pb zircon and titanite systematics of the Fish Canyon Tuff: an assessment of high-precision U-Pb geochronology and its application to young volcanic rocks. Geochimica et Cosmochimica Acta 65, 2571–2587. https://doi.org/10.1016/S0016-7037(01)00616-0

Schulte, P., Speijer, R., Mai, H., Kontny, A., 2006. The Cretaceous–Paleogene (K–P) boundary at Brazos, Texas: Sequence stratigraphy, depositional events and the Chicxulub impact. Sedimentary Geology 184, 77–109. https://doi.org/10.1016/j.sedgeo.2005.09.021

Schulte, P., Alegret, L., Arenillas, I., Arz, J.A., Barton, P.J., Bown, P.R., Bralower, T.J., Christeson, G.L., Claeys, P., Cockell, C.S., Collins, G.S., Deutsch, A., Goldin, T.J., Goto, K., Grajales-Nishimura, J.M., Grieve, R.A.F., Gulick, S.P.S., Johnson, K.R., Kiessling, W., Koeberl, C., Kring, D.A., MacLeod, K.G., Matsui, T., Melosh, J., Montanari, A., Morgan, J.V., Neal, C.R., Nichols, D.J., Norris, R.D., Pierazzo, E., Ravizza, G., Rebolledo-Vieyra, M., Reimold, W.U., Robin, E., Salge, T., Speijer, R.P., Sweet, A.R., Urrutia-Fucugauchi, J., Vajda, V., Whalen, M.T., Willumsen, P.S., 2010. The Chicxulub Asteroid Impact and Mass Extinction at the Cretaceous-Paleogene Boundary. Science 327, 1214–1218. https://doi.org/10.1126/science.1177265

Schwarz, W.H., Hanel, M., Trieloff, M., 2020. U-Pb dating of zircons from an impact melt of the Nördlinger Ries crater. Meteoritics & Planetary Science 55, 312–325. https://doi.org/10.1111/maps.13437

Sharman, G.R., Malkowski, M.A., 2024. Modeling apparent Pb loss in zircon U–Pb geochronology. Geochronology 6, 37–51. https://doi.org/10.5194/gchron-6-37-2024

Sharpton, V.L., Marín, L.E., Schuraytz, B.C., Spudis, P.D., Ryder, G., 1994. Constraints on Excavation and Mixing During the Chicxulub Impact Event. Presented at the 25th Lunar and Planetary Science Conference, pp. 1255–1256.

Sharpton, V.L., Marin, L.E., Carney, J.D., Lee, S., Ryder, G., Schuraytz, B.C., Sikora, P., Spudis, P.D., 1996. A Model of the Chicxulub Impact Basin Based on Evaluation of Geophysical Data, Well Logs, and Drill Core Samples (No. LPI-Contrib-873).

Smit, J., 1990. Meteorite impact, extinctions and the Cretaceous-Tertiary Boundary. Geologie en Mijnbouw 69, 187–204.

Smit, J., 1999. The Global Stratigraphy of the Cretaceous-Tertiary Boundary Impact Ejecta. Annual Review of Earth and Planetary Sciences 27, 75–113. https://doi.org/10.1146/annurev.earth.27.1.75

Spencer, C.J., Kirkland, C.L., Taylor, R.J.M., 2016. Strategies towards statistically robust interpretations of in situ U–Pb zircon geochronology. Geoscience Frontiers 7, 581–589. https://doi.org/10.1016/j.gsf.2015.11.006

Stöffler, D., 1971. Progressive metamorphism and classification of shocked and brecciated crystalline rocks at impact craters. Journal of Geophysical Research (1896-1977) 76, 5541–5551. https://doi.org/10.1029/JB076i023p05541

Swisher, C.C., Grajales-Nishimura, J.M., Montanari, A., Margolis, S.V., Claeys, P., Alvarez, W., Renne, P., Cedillo-Pardoa, E., Maurrasse, F.J.-M.R., Curtis, G.H., Smit, J., McWilliams, M.O., 1992. Coeval 40Ar/39Ar Ages of 65.0 Million Years Ago from Chicxulub Crater Melt Rock and Cretaceous-Tertiary Boundary Tektites. Science 257, 954–958. https://doi.org/10.1126/science.257.5072.954

Sylvester, P.J., Souders, A.K., Liu, R., 2022. Significance of U-Pb detrital zircon geochronology for mudstone provenance. Geology 50, 670–675. https://doi.org/10.1130/G49684.1

Szumila, I., Trail, D., Erickson, T., Simon, J.I., Wielicki, M.M., Lapen, T., Nakajima, M., Fries, M., Bell, E.A., 2023. Microstructural changes and Pb mobility during the zircon to reidite transformation: Implications for planetary impact chronology. American Mineralogist 108, 1516–1529. https://doi.org/10.2138/am-2022-8604

Taylor, S.R., 1982. Planetary science : a lunar perspective. Publishers Production International.

Timms, N.E., Reddy, S.M., Healy, D., Nemchin, A.A., Grange, M.L., Pidgeon, R.T., Hart, R., 2012. Resolution of impact-related microstructures in lunar zircon: A shock-deformation mechanism map. Meteoritics & Planetary Science 47, 120–141. https://doi.org/10.1111/j.1945-5100.2011.01316.x

Timms, N.E., Erickson, T.M., Pearce, M.A., Cavosie, A.J., Schmieder, M., Tohver, E., Reddy, S.M., Zanetti, M.R., Nemchin, A.A., Wittmann, A., 2017. A pressure-temperature phase diagram for zircon at extreme conditions. Earth-Science Reviews 165, 185–202. https://doi.org/10.1016/j.earscirev.2016.12.008

Timms, N.E., Healy, D., Erickson, T.M., Nemchin, A.A., Pearce, M.A., Cavosie, A.J., 2018. Role of Elastic Anisotropy in the Development of Deformation Microstructures in Zircon, in: Microstructural Geochronology. American Geophysical Union (AGU), pp. 183–202. https://doi.org/10.1002/9781119227250.ch8

Timms, N.E., Pearce, M.A., Erickson, T.M., Cavosie, A.J., Rae, Auriol S. P., Wheeler, J., Wittmann, Axel, Ferrière, Ludovic, Poelchau, Michael H., Tomioka, Naotaka, Collins, G.S., Gulick, Sean P. S., Rasmussen, Cornelia, Morgan, Joanna V., Gulick, S. P. S., Morgan, J. V., Chenot, E., Christeson, G.L., Claeys, P., Cockell, C.S., Coolen, M.J.L., Ferrière, L., Gebhardt, C., Goto, K., Green, S., Jones, H., Kring, D.A., Lofi, J., Lowery, C.M., Ocampo-Torres, R., Perez-Cruz, L., Pickersgill, A.E., Poelchau, M. H., Rae, A. S. P., Rasmussen, C., Rebolledo-Vieyra, M., Riller, U., Sato, H., Smit, J., Tikoo, S.M., Tomioka, N., Urrutia-Fucugauchi, J., Whalen, M.T., Wittmann, A., Xiao, L., Yamaguchi, K.E., IODP-ICDP Expedition 364 Scientists, 2019. New shock microstructures in titanite (CaTiSiO5) from the peak ring of the Chicxulub impact structure, Mexico. Contrib Mineral Petrol 174, 38. https://doi.org/10.1007/s00410-019-1565-7

Tohver, E., Lana, C., Cawood, P.A., Fletcher, I.R., Jourdan, F., Sherlock, S., Rasmussen, B., Trindade, R.I.F., Yokoyama, E., Souza Filho, C.R., Marangoni, Y., 2012. Geochronological constraints on the age of a Permo–Triassic impact event: U–Pb and 40Ar/39Ar results for the 40 km Araguainha structure of central Brazil. Geochimica et Cosmochimica Acta 86, 214–227. https://doi.org/10.1016/j.gca.2012.03.005

Trop, J.M., Benowitz, J., Cole, R.B., O'Sullivan, P., 2019. Cretaceous to Miocene magmatism, sedimentation, and exhumation within the Alaska Range suture zone: A polyphase reactivated terrane boundary. Geosphere 15, 1066–1101. https://doi.org/10.1130/GES02014.1

Vermeesch, P., 2018. IsoplotR: A free and open toolbox for geochronology. Geoscience Frontiers, SPECIAL ISSUE: Frontiers in geoscience:A tribute to Prof. Xuanxue Mo 9, 1479–1493. https://doi.org/10.1016/j.gsf.2018.04.001

Walkden, G., Parker, J., Kelley, S., 2002. A Late Triassic Impact Ejecta Layer in Southwestern Britain. Science 298, 2185–2188. https://doi.org/10.1126/science.1076249

Wittmann, A., Kenkmann, T., Schmitt, R.T., Stöffler, D., 2006. Shock-metamorphosed zircon in terrestrial impact craters. Meteoritics & Planetary Science 41, 433–454. https://doi.org/10.1111/j.1945-5100.2006.tb00472.x

Wittmann, A., Schmitt, R.T., Kring, D.A., Reimold, W.U., Povenmire, H., 2009. The ICDP-USGS Deep Drilling Project in the Chesapeake Bay Impact Structure: Results from the Eyreville Core Holes. Geological Society of America.

Wittmann, A., Cavosie, A.J., Timms, N.E., Ferrière, L., Rae, A., Rasmussen, C., Ross, C., Stockli, D., Schmieder, M., Kring, D.A., Zhao, J., Xiao, L., Morgan, J.V., Gulick, S.P.S., 2021. Shock impedance amplified impact deformation of zircon in granitic rocks from the Chicxulub impact crater. Earth and Planetary Science Letters, 117201 575, 1–13. https://doi.org/10.1016/j.epsl.2021.117201

Zhang, B., Lin, Y., Moser, D.E., Hao, J., Liu, Y., Zhang, J., Barker, I.R., Li, Q., Shieh, S.R., Bouvier, A., 2021. Radiogenic Pb mobilization induced by shock metamorphism of zircons

in the Apollo 72255 Civet Cat norite clast. Geochimica et Cosmochimica Acta 302, 175–192. https://doi.org/10.1016/j.gca.2021.03.012

Zhao, J., Xiao, L., Xiao, Z., Morgan, J.V., Osinski, G.R., Neal, C.R., Gulick, S.P.S., Riller, U., Claeys, P., Zhao, S., Prieur, N.C., Nemchin, A., Yu, S., IODP 364 Science Party, 2021. Shock-deformed zircon from the Chicxulub impact crater and implications for cratering process. Geology 49, 755–760. https://doi.org/10.1130/G48278.1

Zhao, Jiawei, Zhang, X., Xiao, L., Cavosie, A.J., Timms, N.E., Nemchin, A., Xiao, Z., Hu, W., Chang, Y., Shu, J., He, Q., Zhao, S., Wang, J., Zhao, Jiannan, 2024. Nanoscale constraints on the nucleation and evolution of granular zircon from reidite in impactites at the Chicxulub impact structure. Earth and Planetary Science Letters 626, 118507. https://doi.org/10.1016/j.epsl.2023.118507

Chapter 4

The Lost Lunar Zircons: How Sample Processing has Biased the Apollo Zircon Record

4.1 Abstract

The lunar surface preserves a complex history of impact cratering spanning nearly its entire ~4.5 Ga history. Among the minerals crucial for reconstructing this history is zircon, which is typically analyzed in lunar materials either through thin section investigations to maintain petrologic context or via mineral separation from bulk rock to extract a larger number of grains. However, standard zircon separation techniques using heavy liquid density separations and ultraviolet (UV) light-assisted picking have been shown to result in ineffective zircon separation with 75% (249 of 330) zircons remaining unseparated from the bulk material in the case of Apollo sample 14311,58—necessitating a revision of separation methodologies for lunar zircon extraction. To address this issue, the missing zircons from 14311,58 were analyzed for microtextures using electron backscatter diffraction (EBSD), secondary electron imaging (SE), and forescatter electron imaging (FSD), with additional analyses including Ti-in-zircon crystallization temperature and U-Pb dating via secondary ionization mass spectrometry (SIMS) to determine how the addition of the zircon data from this population effects our understanding of impact melt breccia 14311. Our results indicate that heavy liquid separations and UV light picking should be modified (i.e., lower heavy liquid density) or all together discontinued in favor of alternative methods, including sieving (optional), hand magnet separation, sprinkling non-magnetic separates onto tape, and chemical mapping (e.g., EDS) to locate zircons. The analyzed zircons were predominantly fractured or unshocked, though some exhibited metamict textures, plastic deformation, shock twins, or granular textures. Ti-in-zircon thermometry crystallization

temperatures from these zircons matched 14311 temperatures from previous studies. U-Pb dating revealed age peaks at 4.34, 4.25, and 3.95 Ga, as well as a continuous distribution between 4.25 and 3.95 Ga, confirming the presence of the 3.95 Ga peak and filling a previously missing segment of the lunar zircon age record.

4.2 Introduction

The entirety of the lunar surface has experienced meteorite impacts, ranging in scale from micrometeorites (micron scale impactor) to large events such as the South Pole-Aitken basin impact (1500-2000 km diameter crater, Citron et al., 2024), which has caused the breakdown and reworking of crustal material. Elucidating the geologic and impact history of the Moon requires comprehensive geochronological studies of return samples (i.e., Apollo, Luna, Chang'e) and of terrestrial collected lunar meteorites. Dated lunar rocks and meteorites often yield complex ages in a variety of radiogenic systems, suggesting multiple shock re-melting events on the lunar surface that can contribute to the complexity in interpreting geochronometric data (e.g., Fernandes et al., 2013; Hopkins and Mojzsis, 2015). Therefore, the effects of impact conditions on geochronologic systems must be considered to accurately interpret ages from lunar material.

Because impacts can physically deform the crystal structure of individual minerals, lunar sample studies must evaluate the resulting changes to their physical and chemical properties by interpreting geochronology in the context of microtextural features (e.g., Grange et al., 2013a; Crow et al., 2017; Zhang et al., 2021; Vanderliek et al., 2021). While some studies have successfully identified datable minerals in situ within lunar sample petrographic thin sections, obtaining a larger yield of datable minerals for analysis and thus therefore a more statistically robust dataset is more effectively achieved by crushing and separating bulk rock material. Zircon

($ZrSiO_4$), an accessory mineral (i.e., present in small quantities alongside the major minerals composing a rock), is routinely dated in both terrestrial and lunar rocks. It is typically extracted from bulk rock material using standard techniques that exploit its distinctive physical and chemical properties, such as density, fluorescence, and magnetism. However, if the physicochemical properties of zircons are altered due to meteorite impacts, this could hinder their effective separation from the bulk rock, potentially introducing sample bias and influencing our understanding of lunar chronology.

Zircon has been identified at each of the Apollo mission landing sites on the Moon, though its prevalence varies depending on the target lithology—for example, KREEP-rich materials (enriched in potassium [K], rare earth elements [REEs], and phosphorus [P]) typically host a greater abundance of zircons (e.g., Rasmussen et al., 2008; Nemchin et al., 2008; Taylor et al., 2009; Moser et al., 2011; Thiessen et al., 2018; Crow et al., 2019; Joy et al., 2020). Zircon is generally resistant to the destructive effects of impacts, and as a result, zircon is sometimes the only surviving physical record available for dating large impact events. When exposed to sufficient temperatures and/or pressures, it can become shocked and the crystal structure can open to diffusion, potentially resulting in age resetting (Moser et al., 2011; Timms et al., 2017). When conditions are sufficient to reset the U-Pb geochronometer in zircon, the isotopic compositions of zircon reflect the age of these large, resetting events. The ages, chemistries, and physical characteristics (i.e. shock features) of lunar zircons have been previously analyzed to constrain the formation and evolution history of the Moon (e.g., Nemchin et al., 2008; Grange et al., 2009; Grange et al., 2013b; Crow et al., 2017; Trail et al., 2020; Barboni et al., 2024). Previous studies of U-Pb in lunar zircons at various Apollo landing sites have found a majority of zircon ages are distributed between ~3.9 to 4.4 Ga (e.g., Meyer et al., 1996; Pidgeon et al., 2007; Nemchin et al.,

2008; Nemchin et al., 2010; Hopkins and Mojzsis, 2015; Crow et al., 2017; Trail et al., 2020). U-Pb geochronology has also been used to identify the potential of multiple large lunar impact events, mostly before 3.9 Ga, that may have produced conditions to form zircons with ages around 4.35-4.30 Ga and 4.25-4.20 Ga (e.g., Nemchin et al., 2008; Grange et al., 2009; Hopkins and Mojzsis, 2015; Crow et al., 2017; Trail et al., 2020). In contrast to the $^{40}Ar/^{39}Ar$ data, the zircon U-Pb record includes some grains with ages around ~3.9 Ga, but overall does not exhibit a significant spike in impact ages at that time. This lack of a pronounced peak around ~3.9 suggests limited support for the Late Heavy Bombardment (LHB) hypothesis in the zircon record (e.g., Cohen et al., 2000; Grange et al., 2009; Nemchin et al., 2010; Hopkins and Mojzsis, 2015; Crow et al., 2017; Michael et al., 2018). This further denotes that the zircons likely were not exposed to temperatures required for age resetting of their U-Pb geochronometer during the proposed 3.9 Ga impact spike (Grange et al., 2009). Additionally, microtextural analyses in lunar zircons have been used to determine shock effects from impacts and have revealed that many of the lunar zircons display a few shock features such as shock twins, plastic deformation, and granules but on the whole are minimally shocked (Pidgeon et al., 2011; Grange et al., 2013a; Crow et al., 2017). Analyzing an array of zircons from the lunar surface for their age and shock features can piece together the Moon's complex impact history.

Ideally, zircons are analyzed in petrographic thin sections in order to retain petrologic context. Zircons have been successfully identified and analyzed in Apollo sections (e.g., Hopkins and Mojzsis, 2015; Thiessen et al., 2018; Zhang et al., 2019; Vanderliek et al., 2021) however, they are relatively rare in most lunar samples and thin sections. To obtain a larger population of zircons to then analyze for statistically meaningful results such as age populations, some studies have extracted zircons from samples using mineral separation techniques commonly used for

terrestrial samples which typically includes crushing, heavy liquid density separations, and ultraviolet light fluorescence assisted picking (e.g., Taylor et al., 2009; Hopkins and Mojzsis, 2015; Crow et al., 2017; Kelly et al., 2018; Trail et al., 2020).

The processing techniques to extract lunar zircons assume the standard properties of unshocked terrestrial zircons such as morphology, density (4.6 g/cm^3), lack of magnetism, and fluorescence under certain wavelengths of ultraviolet light (254 nm). When reprocessing material for phosphate separation from Apollo 14311,58 for an ongoing study of lunar phosphates, which had previously gone through these processing methods to extract zircons for Trail et al. (2020), it was discovered that hundreds of zircons were not recovered from the processed material that should have had all zircons already removed. This brought into question the effectiveness of zircon mineral separation methods and what information may be missing in the zircon record with a significant portion of zircons that were not previously analyzed. Therefore, the methodology of these processing techniques required reassessment of effectiveness in zircon extraction to determine the reliability of these extraction methods on lunar zircons. It is known that zircons can be both physically altered (i.e., shock deformation) and susceptible to age resetting as a result of impacts, therefore zircons may not present the expected physicochemical properties which would allow for effective extraction using previous standard methods on non-impacted, terrestrial zircons. It is critical to determine how these zircons that appear to have non-standard zircon properties may be physically altered and what potential affects these missing ages might have on age spreads and age interpretations of zircons from 14311,58 through microstructural and age studies of the previously missing zircons.

4.3 Apollo Sample 14311

Sample 14311 is a polymict impact melt breccia with an unusually high zirconium (Zr) concentration (1240 μg/g Zr; Warren et al., 1983). This sample has been extensively characterized (Scoon, 1972; Kesson 1975; Simonds et al., 1977; Stöffler and Knöll, 1977), and contains hundreds of zircons that have systematically dated via U-Pb SIMS (secondary ionization mass spectrometry), SHRIMP (sensitive high resolution ion microprobe), and TIMS (thermal ionization mass spectrometry) in both thin sections and extracted from bulk rock material through mineral separation (Meyer et al., 1989; Meyer et al., 1996; Hopkins and Mojzsis, 2015; Pigeon et al., 2016; Merle et al., 2017; Trail et al., 2020; Barboni et al., 2024). Some subsamples of 14311 have been previously processed for zircons following the methods in Taylor et al. (2009) (e.g., Hopkins and Mojzsis, 2015; Trail et al., 2020).

The U-Pb ages of zircons within 14311 range from approximately 3.93-4.40 Ga throughout all studies (Hopkins and Mojzsis, 2015; Merle et al., 2017; Trail et al., 2020). These ages are interpreted to represent a mix of igneous crystallization ages and (partially or fully) impact reset ages. There are multiple age peaks observed in probability density plots of 14311 zircon $^{207}Pb/^{206}Pb$ ages. These peaks have been interpreted by Hopkins and Mojzsis (2015) as impact in origin while other studies such as Pidgeon et al. (2016) and Merle et al. (2017) interpret these as a mix of impact events and lunar crustal magma crystallization. The breccia itself is hypothesized to have formed by an impact at approximately 3.938 Ga, incorporating zircons older than this age, but explaining why there are no zircon ages younger than 3.938 Ga present in this sample (Merle et al., 2014; Merle et al., 2017); this interpretation is further supported by an $^{40}Ar/^{39}Ar$ age record of ~3.9 Ga (Stadermann et al., 1991). After breccia formation, temperatures were raised between ~230-500°C at 3410 ± 80 Ma (2σ), resulting in annealing within zircon crystals (Pidgeon et al.,

2016). The exposure age of this sample is ~550-660 Ma (via Kr and Ar noble gas clocks) which is the relative timing it was exposed to the surface at the Apollo 14 site where it was collected (Figure 4.1) (Crozaz et al., 1972; Drozd et al., 1974; Stadermann et al., 1991, Merle et al., 2017)

Subsample 14311,58 was processed to extract zircons via crushing, density separation with methylene iodide (MI), and ultraviolet (UV) light aided picking of the dense sink or separate in Trail et al. (2020). The float material from density separations was further processed for phosphate separation which identified hundreds of remaining zircons in the process (methods for separations detailed in section 4.4.1). Thus, the large abundance of zircons missing from previous analyses by Trail et al. (2020) necessitated a study of these zircons to determine what information may be missing from our understanding of the zircon cargo of 14311,58. Trail et al. (2020) reports that there are age peaks in these zircon ages at approximately 4.33, 4.23, and 3.94 Ga, which is consistent with the U-Pb zircon age peaks from other subsamples of 14311 (Hopkins and Mojzsis, 2015; Merle et al., 2017). However, the peak at 3.94 Ga is significantly more prominent in the zircons from Trail et al. (2020) than the zircons from Hopkins and Mojzsis (2015) and Merle et al. (2017). It is important to assess if the additional zircons identified during the reprocessing of the MI float has a similar or different age distribution relative to the original study of 14311,58 (Trail et al., 2020), and other studies from this parent sample (e.g., Hopkins and Mojzsis, 2015; Merle et al., 2017).

Since our identified zircons do not behave as expected of zircons in density separations, it necessitates a study of their microtextures to determine physical properties of these zircons that may inform why these zircons deviate from the expected density. One possible explanation for the reduced density of these zircons is shock damage, so microstructural analyses are critical to determine why these grains were missed and to assess the extensive impact histories of 14311

proposed by Hopkins and Mojzsis (2015) and Merle et al. (2017). Electron backscatter diffraction (EBSD) is known to be an effective method of analyzing zircons for shock features that can be interpreted to infer shock conditions experienced by these zircons (e.g., Grange et al., 2013a; Crow et al., 2017; Davis et al., in prep (Chapter 3 of this dissertation)). Pairing this methodology investigation with a shock and geochronology study to determine grain anomalies will allow for a more comprehensive understanding of lunar zircons: how to process lunar samples to extract the full yield of zircons, what shock features are present in altered zircons on the lunar surface, and how this relates to ages determined via U-Pb in zircon. This investigation of 14311,58 will determine if sample processing is biasing our overall understanding of 14311 and the results of microtextural studies and age analyses will contribute to a more holistic understanding of an important, zircon rich Apollo sample.

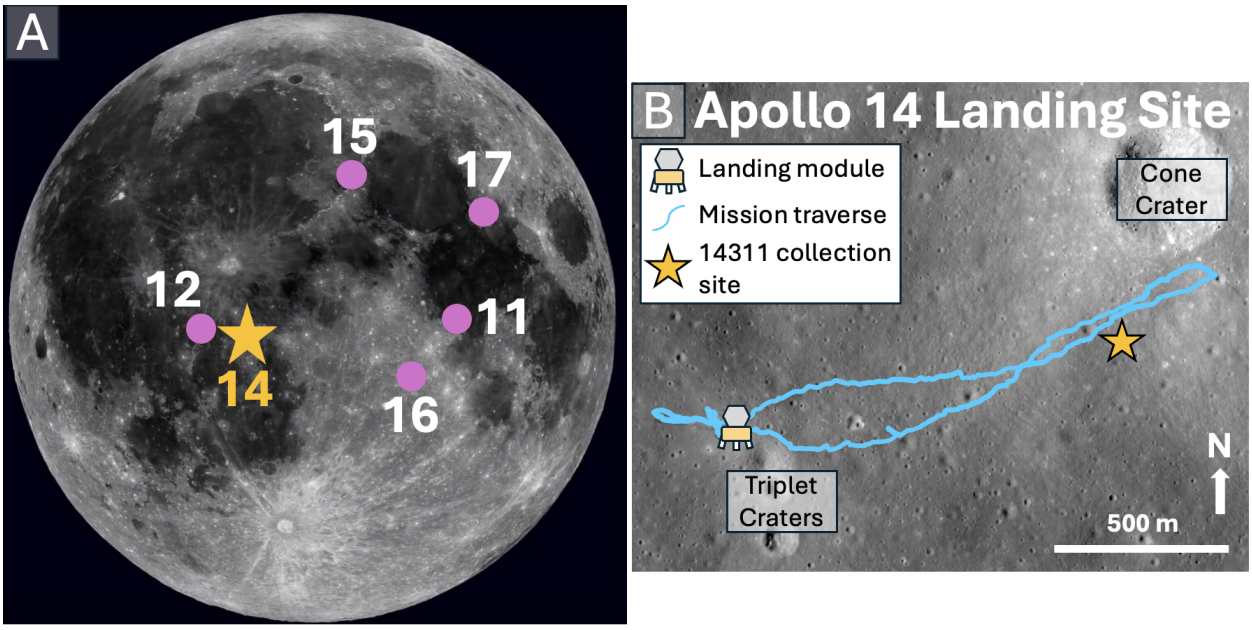

Figure 4.1: A) Map of the Apollo landing sites on the Moon's near side. Apollo 14 site labeled as an orange star and all other Apollo sites are labeled with magenta dots. B) Map of the Apollo 14 landing site depicting the location of the lunar module landing, traverse, and location of the collection site of Apollo sample 14311 (orange star).

4.4 Methods

4.4.1 Zircon Extraction Methodology Testing

Material that floated in MI density separations in Trail et al. (2020) was further magnetically separated with a neodymium hand magnet, which removed 99% of material. The remaining non-magnetic material was sprinkled onto double sided tape and was mapped via backscattered electron (BSE) and energy dispersive X-ray spectroscopy (EDS) at Southern Methodist University using a JEOL IT500 HR Field Emission SEM with a ThermoFischer EDS detector using the Pathfinder software to identify zircon grains. Zr/P and Ca maps were collected at 15kV with an ~8 nA beam current to collect ~100 counts per pixel for maps with 4 μm pixels. Even though the Zr and P peaks are not resolvable with EDS, the comparison of the Zr/P and Ca maps allowed for accurate discrimination of zircons from phosphates Each zircon was then analyzed to determine the effectiveness of the UV light picking method. Zircon UV fluorescence was tested using a 254 nm wavelength light under a petrographic microscope.

4.4.2 Microtextural Characterization

Once zircons were identified, grains were mounted in Buehler EpoxiCure2 epoxy and polished using 3 μm, 1μm, and 0.25 μm diamond slurry and subsequently polished via colloidal silica for EBSD analyses. EBSD, secondary electron imaging (SE), and forescatter electron imaging (FSD) was acquired on 244 zircons at the NASA Johnson Space Center at the Astromaterials Research and Exploration Science Division using a JEOL 7900F Field Emission Scanning Electron Microscope (FE-SEM) equipped with an Oxford Instruments Symmetry S2 EBSD detector. Data was collected using a 20 kV, ~20 mm working distance, and 70° sample tilt relative to the beam incidence. Maps were collected with a 0.25 μm step size. Electron backscatter diffraction patterns were captured with the Oxford Symmetry S2 EBSD detector and indexed using

match units for zircon (Hazen and Finger, 1979), reidite (Farnan et al., 2003), and monoclinic ZrO_2 (Howard et al., 1988). Post processing and creating of EBSD maps and pole figures of EBSD data was completed using the Oxford Instruments Aztec Crystal software package. All EBSD data were given a wild-spike noise reduction and seven nearest neighbor zero-solution correction. EBSD images were exported as phase color maps, inverse pole figure maps (IPF) maps, and grain rotation orientation distribution (GROD) function maps. Zircon pole plots are equal area, lower hemisphere projections. All images of 14311,58 zircons from this study are in Appendix F.

4.4.3 U-Pb Geochronology and Ti-in-zircon Thermometry

U-Pb geochronology was analyzed on individual zircon grains (sometimes multiple analyses per grain) using the UCLA CAMECA ims-1290 secondary ion mass spectrometer equipped with the Hyperion II ion source. We used an O^{3-} primary beam without oxygen flooding, which resulted in a spot size of ~10 μm. Instrumental mass fractionation of U and Pb was calibrated using the AS3 zircon age standard and trace element (U, Th, Ti) concentrations were calculated using the 91500 zircon standard (Paces and Miller, 1993; Schmitz and Bowring, 2001; Wiedenbeck et al., 2004). A total of 136 SIMS U-Pb analysis spots were taken and Ti was measured for 66 analytical spots. A common-Pb correction was applied to all data (standards and unknowns) assuming all ^{204}Pb is from terrestrial surface contamination and assuming the Pb-isotope composition of San Diego Sewage Water (Sañudo-Wilhelmy and Flegal, 1994). Post processing was completed using the in-house ZIPS software (created by C. Coath) and IsoplotR (Vermeesch, 2018). Tables of all SIMS analyses and U-Pb data, Ti-in-zircon thermometry temperatures, and U concentrations and metamictization is in Appendix D, Table D2, D3, and D4.

4.5 Results

Two-hundred and forty-nine zircons were identified in the reprocessed MI float material from 14311,58. These grains ranged in size from approximately 30-300 μm. UV light fluorescence was tested on the 249 remaining grains to determine the effectiveness of this method for zircon identification and it was found that only 119 (or ~48%) of grains displayed fluorescence under 254 nm wavelength UV light exposure. EBSD analyses were conducted for microtextural assessment on 119 (48%) of the 249 zircon grains that remained in the float after MI density separation methods to better understand the microtextures of these missing grains. Several microtextures were identified including unshocked, partially metamict, and fully metamict grains. Fracturing including curviplanar features (CF), planar features (PF), trapped melt veins and blebs, plastic deformation, shock twins, and granular texture recrystallization were also observed (Table 4.1). Additionally, not all zircons were isolated as single crystals and many grains (at least 60%) were found to have adhering phases attached. In total, 136 SIMS U-Pb analysis spots across 112 zircon grains were collected. Seven grains were excluded as a result of either unsuccessful SIMS analyses, such as missing the grain entirely or unreliable measurements, or as a result of some zircons having too small of a grain size to isolate zircon for analyses. Individual SIMS analysis spots primarily targeted one microtexture (87%) with only a few analysis spots overlapping multiple shock features. Small microstructures such as fractures, complex patterns of partially metamict and unshocked regions, trapped melt domains, and shock twins are typically 1-2 μm in size and, therefore, cannot be isolated with the 10 μm SIMS spot in this study.

4.5.1 $^{207}Pb/^{206}Pb$ Ages of Less Dense Zircons

The $^{207}Pb/^{206}Pb$ ages of the 14311,58 float zircons extracted in this study range from 3920 ± 26 Ma to 4381 ± 23 Ma (2σ) (Figure 4.2). The probability density distribution shows that the ages span nearly this entire age range with peaks in abundance at approximately 3.96 Ga, 4.24, and 4.34 Ga (Figure 4.2). $^{207}Pb/^{206}Pb$ ages were preferentially used for further analyses and interpretation since there is appreciable Pb present from both the ^{238}U-^{206}Pb and ^{235}U-^{207}Pb decay in these samples and since nearly all (130 of 136) of the ages plot as concordant (at 2σ uncertainty) in both Wetherill concordia and Tera-Wasserburg concordia plots, and therefore $^{207}Pb/^{206}Pb$ ages are preferred since this age will have smaller uncertainties as a result of not needing to correct for instrumental mass fractionation with Pb (Figure 4.3 and 4.4) (Spencer et al., 2016).

4.5.2 Microtextures of Less Dense Zircons

The 14311 zircon crystals in this study are anhedral and have highly irregular crystal shapes. This is presumably due to either the impact bombardment on these grains prior to their incorporation into the breccia or from the sample crushing process that may separate the zircon into irregular shapes based on fractures or areas of weakness within the crystal. A majority of crystals (62%) contain no clear diagnostic shock features visible in EBSD, FSD, or SE and appear relatively unaltered other than slight fracturing (Figure 4.5). Some zircons display primary igneous textures such as oscillatory zonation. Various impact induced microtextures are present in these zircons including potential impact melt inclusions, high degrees of crystal plastic deformation, shock twins, and granular recrystallization. Thirty-four zircons have a combination of two or more of these microtextural features. It was found that 29% of the grains (34 in total) were either partially to fully amorphous at the resolution of the EBSD analyses, 0.25 μm. When unshocked, crystalline

regions were present, these domains were targeted for SIMS analyses. However, for 42% of the grains, these regions did not exist or were too small to target, so SIMS analysis locations were selected to include the least number of microtextures to allow for comparison between geochronology and texture. The following is a comparison between the geochronology and microtextures that will be used to assess the significance of the $^{207}Pb/^{206}Pb$ ages.

One grain had evidence of primary igneous zonation (Figure 4.6), which is evident by the light and dark oscillatory zoning in the FSD image. This zonation is visible in EBSD images where some zoned regions are preferentially metamict while others index as zircon and are not metamict. The zonation is possibly due to variations in U concentration incorporated into some zones during crystallization since higher U concentration can result in higher degrees of metamictization and result in preferential metamictization in some zones as seen in this zircon (Corfu, 2013). The SIMS analysis spot mostly overlapped metamict regions of the crystal with only a small portion of the analysis spot targeting crystalline regions. This grain has a $^{207}Pb/^{206}Pb$ age of 4340 ± 7 Ma (2σ).

Fracturing, planar features, and curviplanar features are all deformation induced structures in zircon that make up the types of thin (≤1 μm), cross cutting features seen in these zircons. These features represent various phases of impact deformation and the degree of crystallographic influence of shock and microstructural formation in zircon where fracture represents non-crystallographically influenced (i.e., brittle) deformation, planar features represent crystallographic controlled deformation, and curviplanar features represent the formation crystallographically influenced in their formation (Erickson et al., 2013). Fracturing was the most common form of deformation seen within these grains and was observed in 69 of the 119 grains. Fewer grains had evidence for planar and curviplanar features with each of those microtextures found in 32 grains and eight grains, respectively (Figure 4.7). Eleven SIMS spots overlapped at

least one fracture when targeting otherwise unshocked zircons, and no planar or curviplanar features had age measurements taken. SIMS spots over some fractures yield $^{207}Pb/^{206}Pb$ ages from 4335 ± 7 - 3929 ± 27 Ma (2σ), denoting no clear correlation between fracture and age.

Crystal plastic deformation was found in 18 grains. EBSD grain rotation orientation distribution (GROD) maps revealed between 2-21° cumulative crystal plastic strain within individual grains. Seven zircon grains exhibited crystal plastic deformation of ≥5° within a single, cohesive unit of the crystal—distinct from rotation between zircon fragments. Such deformation has been suggested to result from impact-related processes, as tectonic settings typically produce plastic deformation of <5°, except under conditions of high-grade metamorphism (Reddy et al., 2007; Crow et al., 2024). Therefore, this study follows the threshold from other studies (e.g., Crow et al., 2024) and considers ≥5° of plastic deformation as the threshold for identifying impact-related deformation in lunar zircon. Crystal plastic deformation is found in localized regions of individual grains or widespread throughout a single crystal (Figure 4.8, Crow et al., 2024 Figure 6). One grain displayed a unique plastic deformation microtexture that displayed parallel plastic deformation bands oriented along larger plastic deformation bands, showing two preferential plastic deformation orientations within the crystal (Figure 4.9). Five analysis spots on four different grains included plastically deformed regions and did not show definitive evidence of a direct correlation with plastic deformation and resetting. The $^{207}Pb/^{206}Pb$ ages from these spots are 4271 ± 33, 4240 ± 24, 4208 ± 37, 4165 ± 45, 4115 ± 25 (2σ).

Two crystals showed evidence of granular recrystallization textures (Figure 4.10). One grain is fully granular (Figure 4.10, grain S_M2_16) and has 2-8 μm granules that partially index as zircon, primarily near the center of the granules. The indexed zircon regions of the granules appear to be associated with potential topography in the SE and FSD images. This zircon is largely

amorphous and, therefore, most of the grain does not index by EBSD. Two 1-2 μm granules in this grain index as monoclinic ZrO_2 (baddeleyite). The SIMS analysis spot overlaps both the granular zircon and baddeleyite and yields a $^{207}Pb/^{206}Pb$ age of 3933 ± 16 Ma (2σ). The other crystal that contained evidence of granular zircon crystallization is a small, 10-20 μm, granular zircon fragment attached to a larger clast of primarily anorthite and pigeonite (Figure 4.10, grain M_M2_15). The granules range from ~2-5 μm in the longest dimension. Similarly to the other granular crystal, a portion of this granular region indexes as zircon (~50%) while the other portion does not index in EBSD and granules are clearly visible in FSD and SE images. An age was not collected from this granular region.

Over 35% of the zircon crystals analyzed (44 of the 119) contained some degree of metamictization (Figure 4.6). The extent of metamictization ranged from partially to fully metamict. Thirty-four of these grains were visually estimated (based on the lack of indexing in EBSD images) to be at least half metamict and 14 grains were fully metamict. Highly metamict grains (a visually estimated 50% or greater) typically have elevated U ppm, with most having concentrations above 100 ppm (Figure 4.11). There is no correlation between metamictization and age, as SIMS spots on metamict regions of zircon crystals resulted in $^{207}Pb/^{206}Pb$ ages ranging from 4371 ± 18 - 3933 ± 16 Ma (2σ).

Mechanical {112} shock twins were identified in three crystals (Figure 4.12). These are visible as narrow bands in the EBSD images and were confirmed as shock twins via EBSD through the diagnostic misorientation relationship between host and twin of 65° about the <110>. The shock twins range in thickness from less than 1 μm to ~2 μm. Two analysis spots were taken on shock twins, however, since the shock twins are thin (<1-2 μm), they were not isolated, and

unshocked regions of the grain are also included in the SIMS analysis spot. These $^{207}Pb/^{206}Pb$ ages of analyses including shock twins are 4052 ± 71 Ma and 4025 ± 103 Ma (2σ).

Crow et al. (2024) conducted an extensive analysis of melt inclusions seen in some of the 14311,58 grains analyzed in this study. These melts range from small, isolated, randomly distributed blebs of a few microns in size to extensive melt networks spanning the entire crystal. The previous work by Crow et al. (2024) on these grains suggests that the trapped melt forms from decompression melts of adjacent phases during the impact shock wave refraction. As such, most of these melts are coming from minerals that don't have significant Pb or U, and therefore they should not significantly affect the geochronology. These melt inclusions can, however, have the ability to influence the common-Pb correction. This is likely not a significant factor as 96% of zircons plot as concordant on a Tera-Wasserburg concordia plot (2σ) (Figure 4.4).

4.5.3 Ti-in-Zircon Thermometry

For 66 of the analyses (on 44 grains), measurements of Ti and Fe concentrations were included in addition to geochronology. The concentration of Ti in zircon is a function of crystallization temperature and the activities of SiO_2 (a_{SiO2}) and TiO_2 (a_{TiO2}) in the parent melt with little to no influence from variations in pressure or oxygen fugacity (fO_2) (Watson and Harrison, 2005; Ferry and Watson, 2007; Ferriss et al., 2007; Fu et al., 2008, Burnham and Berry, 2012). Ti-in-zircon temperatures were calculated for the MI float 14311,58 zircons in this study following the methods of Ferry and Watson (2007) using the estimates of a_{SiO2} and a_{TiO2} constrained by Trail et al. (2020) of 0.6 and 0.55, respectively, to directly compare the temperatures of the 14311,58 grains in this study to the 14311, 58 grains in Trail et al. (2020). Fe is used as a filter for Ti data to

assist in determining accurate measurements and identifying instrumental effects and interferences as well as contaminants (e.g., inclusions, epoxy) that could result in inaccurate Ti measurements and interpretations. Therefore, Ti temperatures were filtered by plotting the measurement of $^{57}Fe/^{94}ZrO_2$ vs. temperature from Ti-in-zircon thermometry calculations (as a proxy for Ti concentration since crystallization temperature is calculated from Ti concentration) and removing anomalously high $^{57}Fe/^{94}ZrO_2$ measurements that would be associated with possible inaccurate measurements (Hopkins and Mojzsis, 2015; Crow et al., 2017; Trail et al., 2020). This filtering resulted in the removal of one datapoint, colored in red in the plots in Figure 4.13. The calculated Ti crystallization temperatures range from 882-1221°C (Figure 4.14).

Table 4.1: Total grains that contain each microtexture

Zircon microtexture	**Total grains with texture**
Unshocked	95
Partially metamict	30
Fully metamict	14
Fracture	69
Planar feature	32
Curviplanar feature	8
Plastic deformation (any)	18
Plastic deformation (>5°)	7
Shock twins	3
Granules	2
Igneous zonation	1

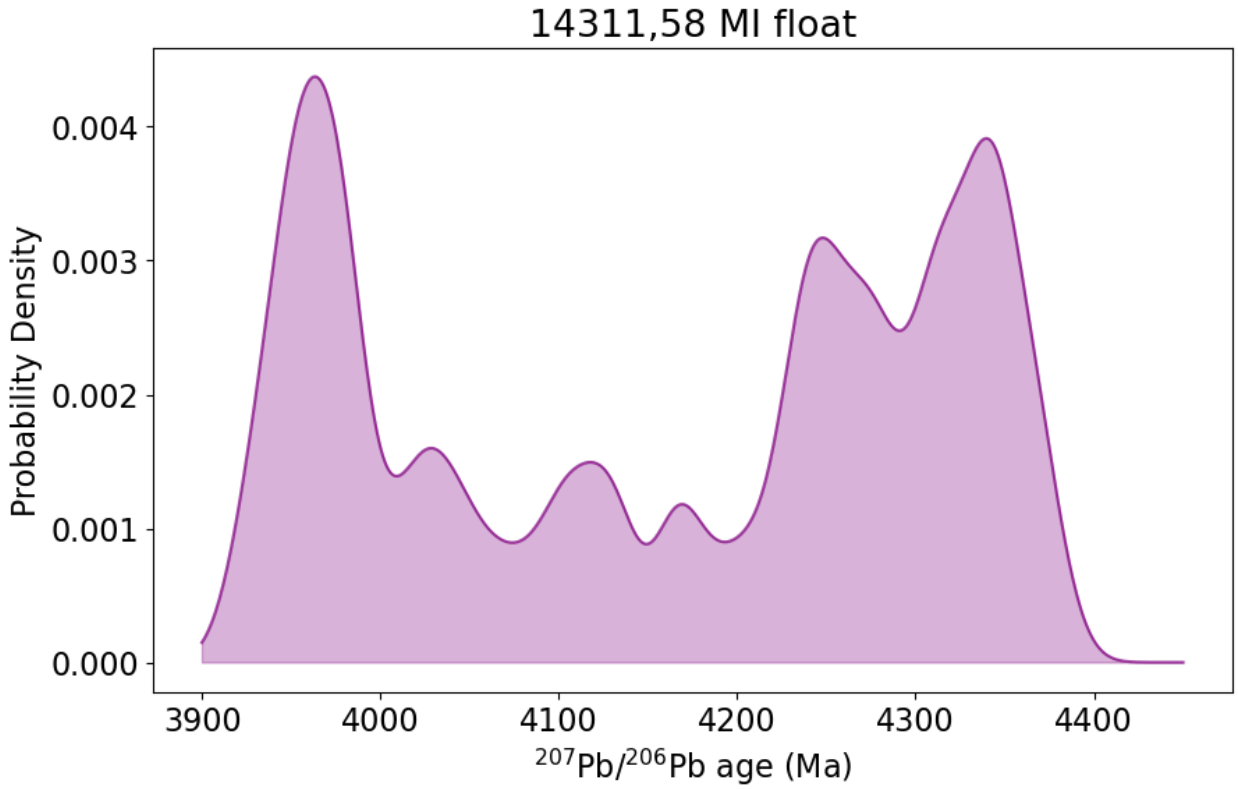

Figure 4.2: Probability density function of $^{207}Pb/^{206}Pb$ ages from zircons that floated in MI density separations from 14311,58 (this study). There are three main peaks in probability near ~3.96, 4.25, and 4.34 Ga with several less dominant peaks near ~4.02, ~4.12, and ~4.17 Ma. The ages span the entire range of 3.93-4.40 Ga. (n=136)

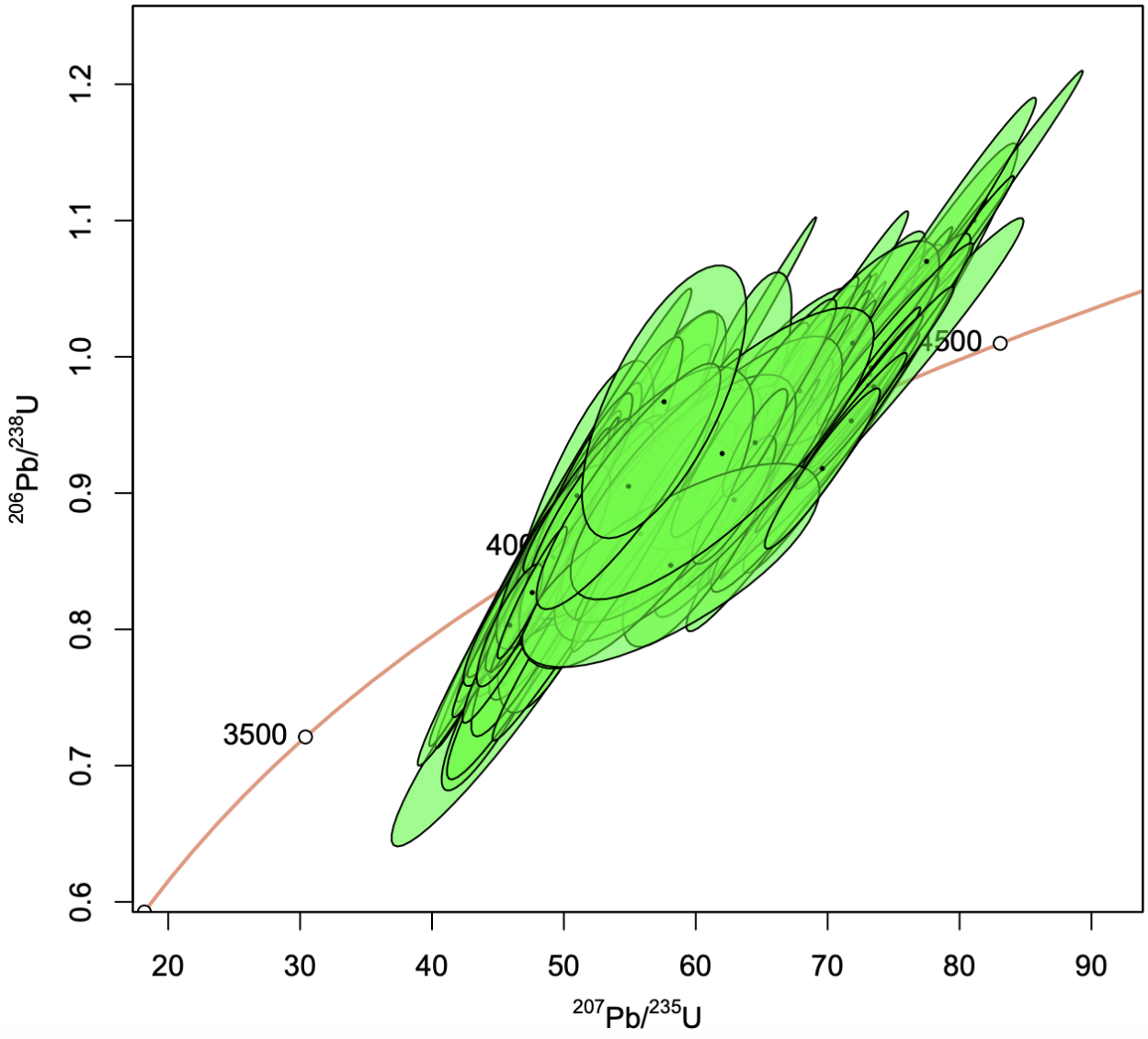

Figure 4.3: Wetherill concordia diagram of the common-Pb corrected U-Pb ratios of the zircons from this study. All but six ages plot as concordant at 2σ uncertainty. (n=136)

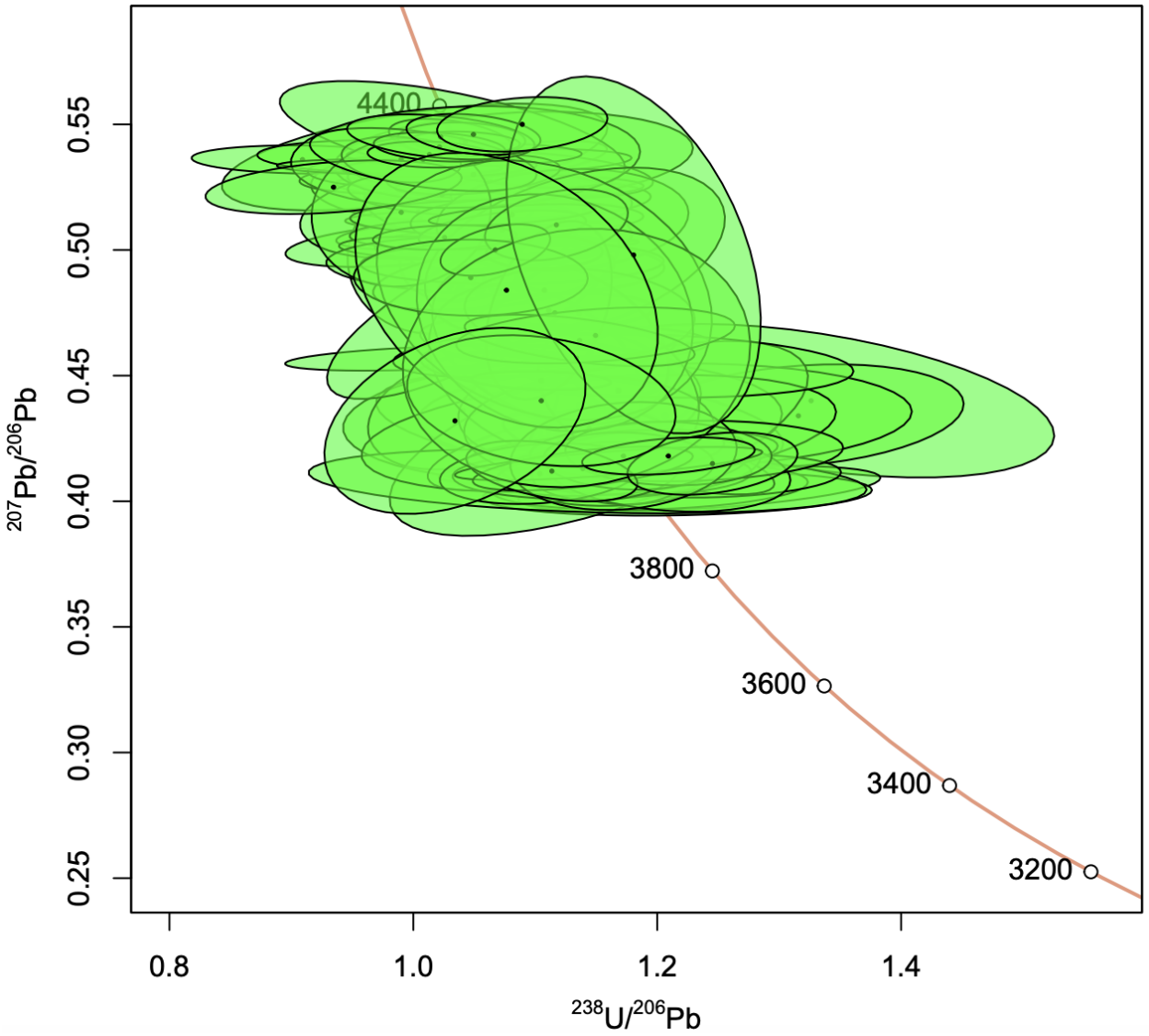

Figure 4.4: Tera-Wasserburg concordia diagram of all of the common-Pb corrected U-Pb ratios from zircons from this study (n=136). All but six ages plot as concordant at 2σ uncertainty, signifying confidence in our common-Pb correction for this data.

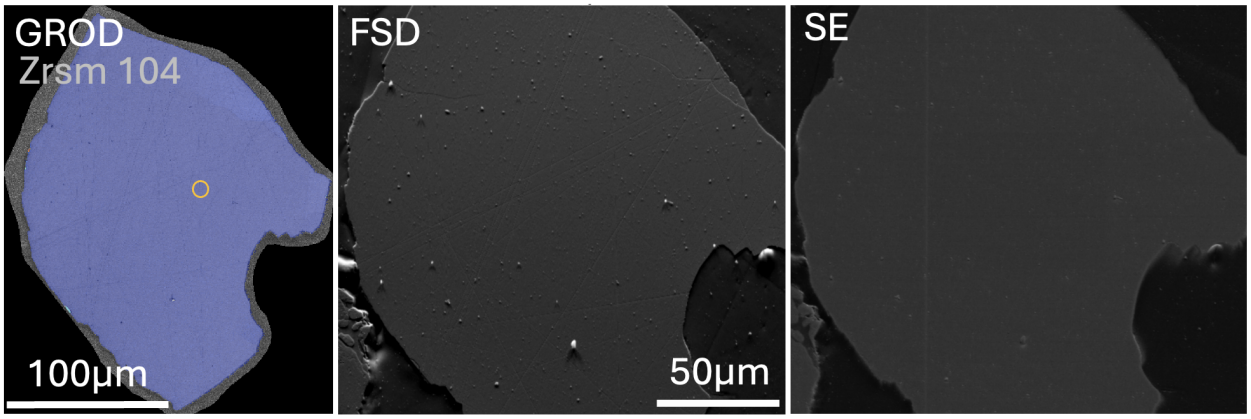

Figure 4.5: GROD, FSD, and SE images of a representative zircon crystal that appears unshocked, crystalline, and relatively unaltered. There is no evidence of shock features seen in GROD, FSD, or SE images. The age from this analysis spot (circled in orange) is 3969 ± 38 Ma (2σ).

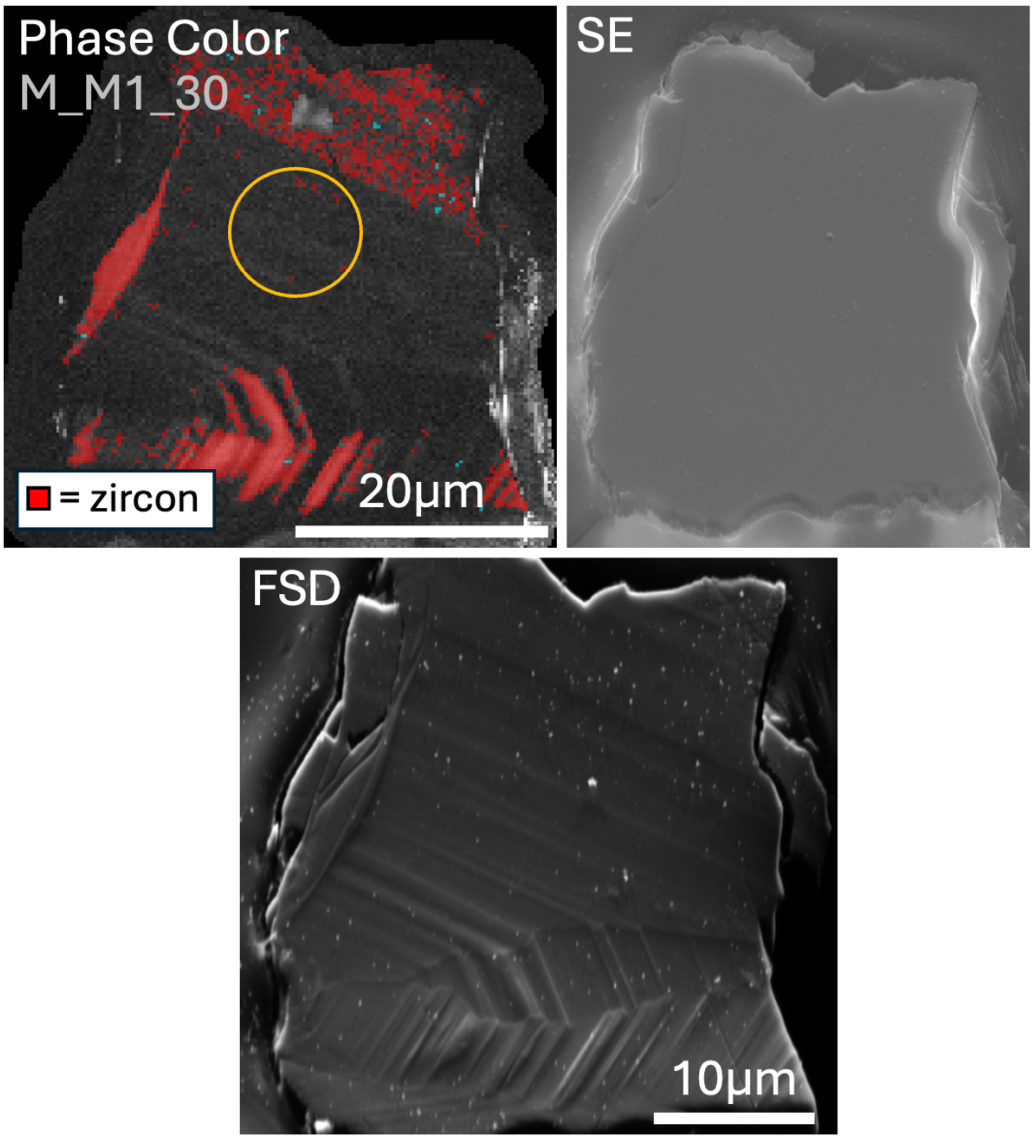

Figure 4.6: The only zircon crystal in this study that has evidence of primary igneous zonation, which is visible in the EBSD phase color and FSD images. This type of zonation typically results from changing elemental concentrations (such as U concentrations) in the melt during growth, resulting in light and dark banding in the FSD image. Regions with higher U are preferentially metamict and do not index in the EBSD phase color image. This zonation is not visible in SE suggesting there is no preferential polishing between the crystalline and metamict domains. The age from this analysis spot (circled in orange) is 4340 ± 7 Ma (2σ).

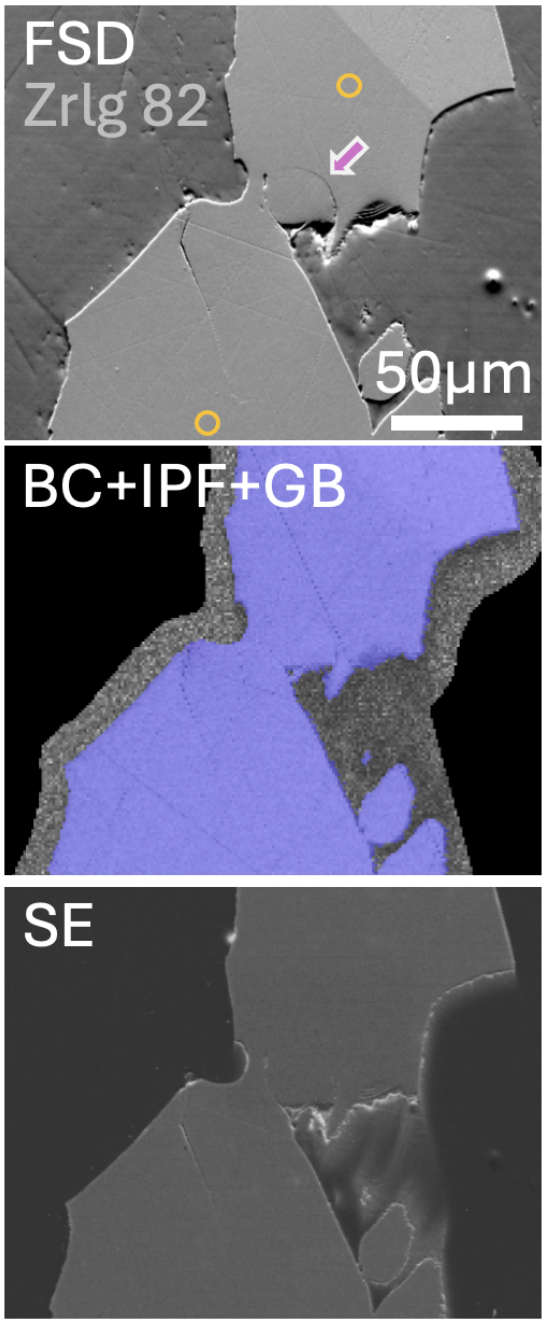

Figure 4.7: Zircon crystal that has a curviplanar feature denoted by a pink arrow in the FSD image. This is not as prominent in EBSD BC+IPF+GF and SE images. Evidence of curviplanar features is found in 15 zircon crystals and can be as large as 10s of microns in length. The ages from these analysis spots (circled in orange) are 3976 ± 62 Ma and 3954 ± 35 Ma (2σ).

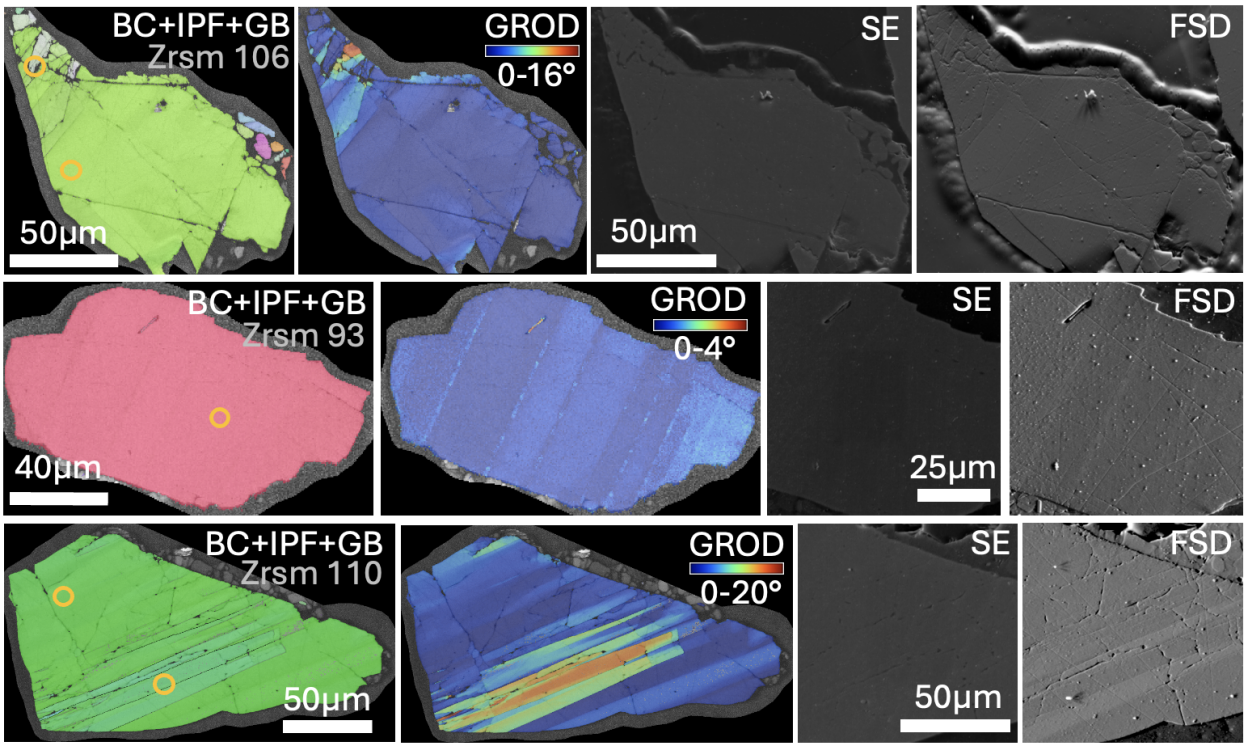

Figure 4.8: Zircon crystals that illustrate the different forms of plastic deformation observed ranging from regional plastic deformation in Zrsm 108 to full grain deformation seen in Zrsm 93 and Zrsm 110. The plastic deformation is identified in the GROD image. Grains Zrsm 108 and Zrsm 110 are likely impact in origin since the plastic deformation is ≥5°. Zrsm 93 shows variation in the thickness of the low-degree plastic deformation banding throughout the crystal. Adhering, non-zircon phases can be seen attached to the top right of Zrsm 110. Grains Zrsm 108 and Zrsm 110 are analyzed and imaged in Crow et al. (2024), Figure 6. The ages from Zrsm 106 are 4265 ± 18 Ma and 4098 ± 34 Ma. The age from Zrsm 93 is 4237 ± 80 Ma. The ages from Zrsm 110 are 4165 ± 45 Ma and 4255 ± 11 Ma. All SIMS U-Pb analysis spots are circled in orange. All uncertainties are reported as 2σ.

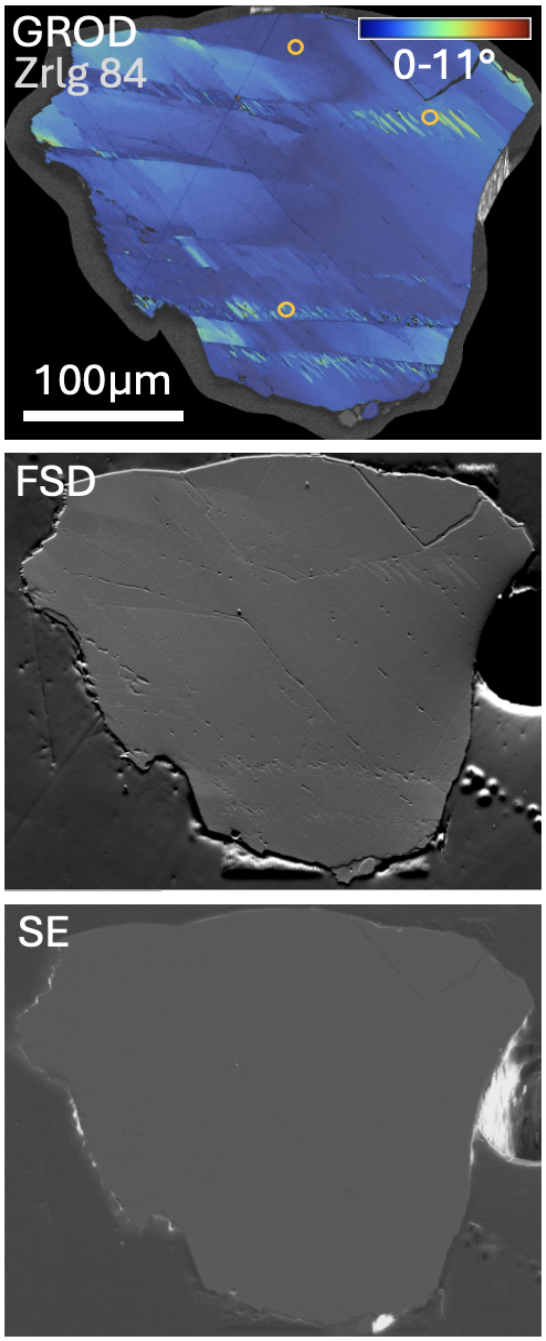

Figure 4.9: Zircon Zrlg 84 displays a complex plastically deformed texture where there are parallel plastic deformation bands oriented along larger subparallel plastic deformation bands. This shows two preferential plastic deformation orientations. This deformation is clearly visible in GROD and faintly visible in FSD. This texture is now known to be previously reported in lunar zircon. The ages from these analysis spots (circled in orange) are 4271 ± 33 Ma, 4208 ± 37 Ma, and 4240 ± 24 Ma (2σ).

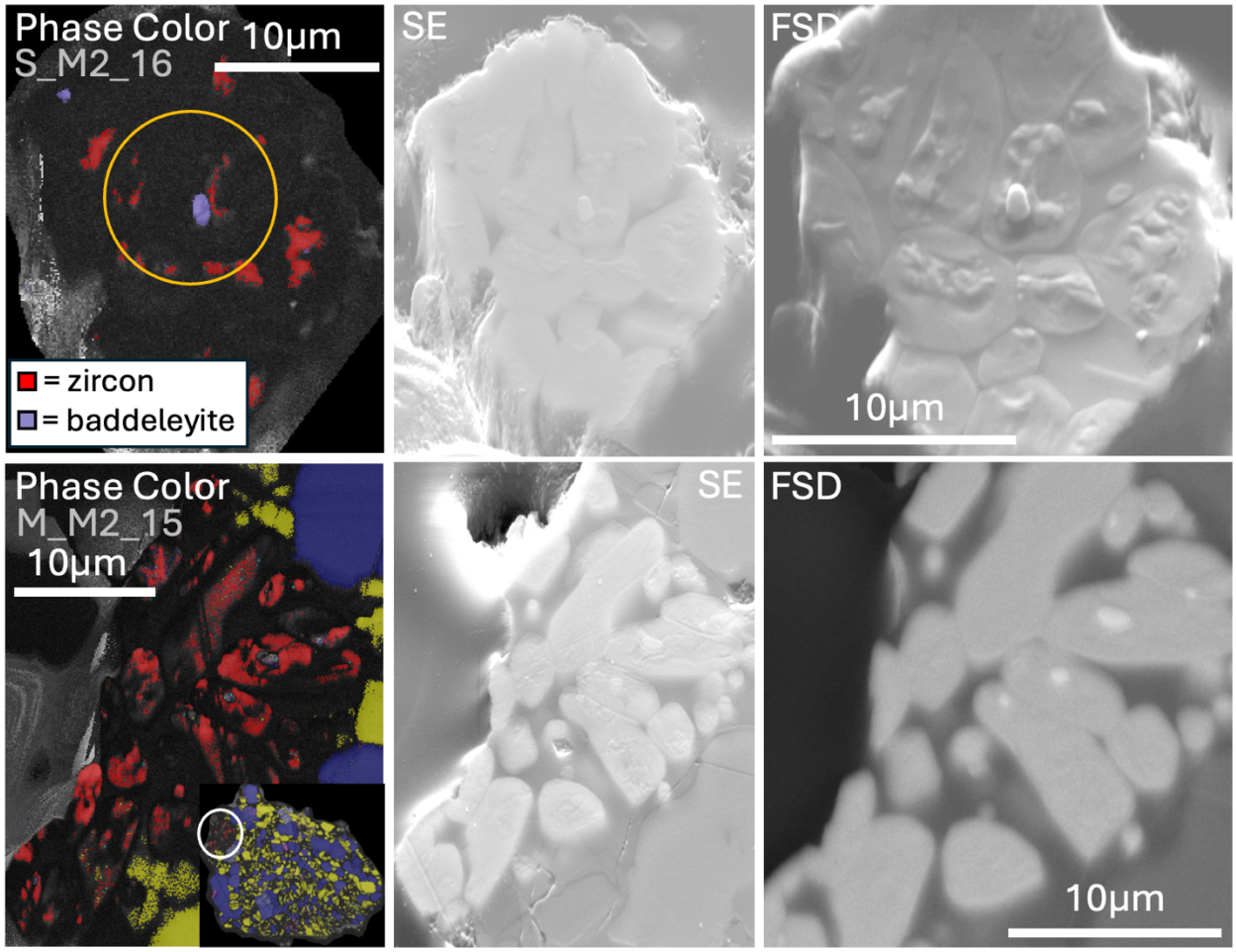

Figure 4.10: Two zircons that display granular recrystallization textures. These granular zircons do not index well in EBSD (phase color) and therefore depict some form of amorphization, possibly from metamictization. The granules can more clearly be seen in SE and FSD images. In zircon S_M2_16, baddeleyite is identified showing dissociation of zircon. These baddeleyite blebs can be seen in SE and FSE as a slightly lighter region. The age from this analysis spot (circled in orange) is 3922 ± 16 Ma (2σ). Zircon M_M2_15 is a granular region on a larger clast of anorthite (yellow) and pigeonite (dark blue). While baddeleyite is not identified via EBSD, there are lighter regions that do not index in EBSD but are seen in SE and FSD which may also signify the decomposition of this zircon into baddeleyite, similar to what is seen in S_M2_16. No SIMS analysis spots were taken on zircon M_M2_15.

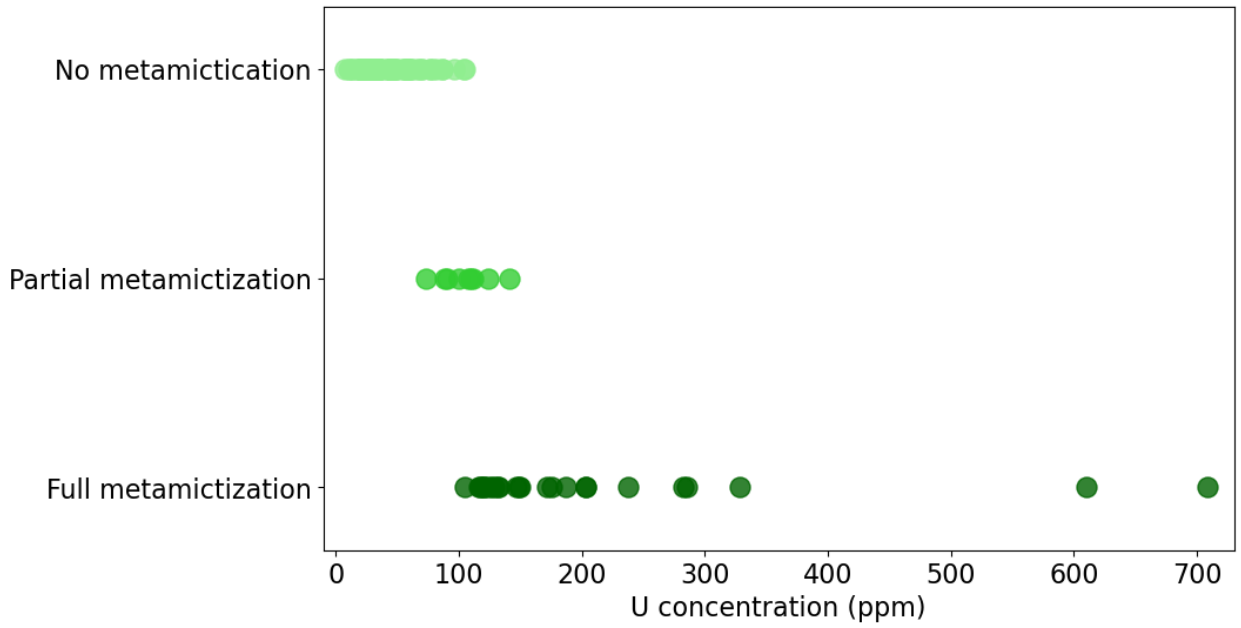

Figure 4.11: Concentration of U (ppm) relative to the metamictization present at the SIMS analysis spot from the zircons in this study. The metamictization is grouped into no metamictization, partial metamictization, and full metamictization. There is a correlation of increasing U concentration relative to the degree of metamictization. Zircons with partial metamictization have a U ppm of >73 and fully metamictized zircons have a U ppm of >105.

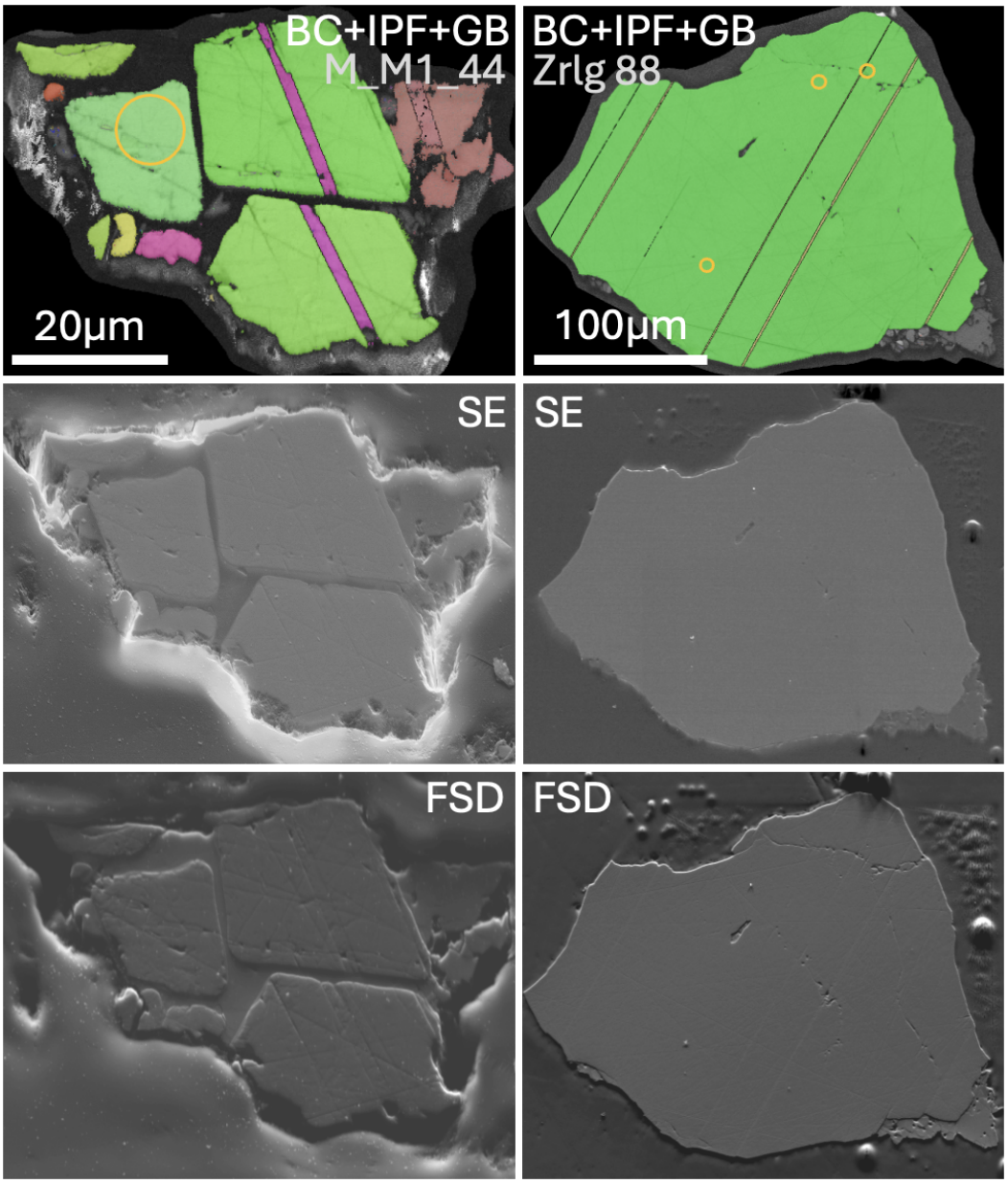

Figure 4.12: Zircons with shock twins that are clearly visible in BC+IPF+GB images. These shock twins are seen as the thick magenta bands in M_M1_44 that run from top left to bottom right of the grain and yellow-orange bands in Zrlg 88 that run from top right to bottom left of the grain. These are most easily identified in EBSD images but can also be seen in FSD. The shock twins are not easily visible in SE. A non-zircon adhering phase(s) can be seen on the right of M_M1_44 and to the bottom right of Zrlg 88. Grains Zrlg 88 is analyzed and imaged in Crow et al. (2024), Figure 5. The age from M_M1_44 is 4024 ± 67 Ma. The ages from Zrlg 88 are 4193 ± 134 Ma, 4052 ± 71 Ma, and 4025 ± 103 Ma. All SIMS U-Pb analysis spots are circled in orange. All uncertainties are reported as 2σ.

4.6 Discussion

Previous lunar zircon studies analyzed grains both in thin sections and extracted using standard zircon mineral separation methods. While the former method allows petrologic information to be retained, the latter increases zircon yield. As evident by the large number of zircons recovered from the previously processed sample from Trail et al. (2020), the traditional extraction methods used in this study were not fully effective. These methods depend on zircon properties such as crystal shape, density, or fluorescence, and our results signify that many of the lunar grains do not have the standard zircon features and characteristics. Geochemical and geochronologic datasets from these previous lunar zircon studies that analyzed extracted zircons (Taylor et al., 2009; Hopkins and Mojzsis, 2015; Crow et al., 2017; Trail et al., 2020) may therefore be incomplete. This study explores potential bias introduced by previous extraction methods by assessing the "missed" zircons in Apollo sample 14311, subsample 58 (also used in Trail et al. 2020). We also report on the comprehensive geochronology, geochemical, and microstructural survey of the 14311 zircons to assess the full igneous and impact history recorded in these grains. Lastly, in this section, we suggest a separation procedure for lunar samples that maximizes the zircon yield.

4.6.1 Characterization of Previously Missing Grains and Suggested Mineral Separation Methodology for Maximizing Zircon Yield from Lunar Samples

Trail et al. (2020) was able to extract 81 zircons from subsample 14311,58 using traditional methylene iodide (MI) heavy liquid methods. In this study, we were able to extract an additional 249 zircons from the MI float material. This means that the traditional MI density separation method missed at least 75% of the zircons from this subsample. Many previous studies also used

UV light fluorescence to aid in hand picking zircons (e.g., Taylor et al., 2009; Valley et al., 2014; Crow et al., 2017, Crow et al., 2019). As such, we also investigated the fluorescence properties of the 249 zircons and found that 52% of the grains did not have visible fluorescence even when using an optical microscope equipped with a camera at maximum exposure (10 second exposure time). As a result, we do not recommend using separation methods using density separation in MI at standard MI density (3.3 g/cm^3) and picking aided by UV light fluorescence for mineral separation of lunar materials because of the large proportion of zircon crystals that can be missed.

Zircons found to float in MI density separations must therefore either have average grain densities less than that of MI (3.3 g/cm^3) or are influenced by other factors such as grain shape (e.g., high surface area) which inhibits them from sinking in heavy liquid. Zircon typically has a density of ~4.6-4.7 g/cm^3 which means that a majority of the grains in this sample may have densities that are at least 28% less dense than expected of typical zircons. This density difference in zircon could be a result of chemical and/or physical differences in these less dense zircons. Here we use the results of the EBSD analyses for 119 of the 249 zircons to investigate the likely source(s) of these differences.

4.6.1.1 Causes for Density Changes in Zircon Grains through Microstructural Analysis

One cause of the density reduction could be the result of less dense, adhering phases that are not completely separated from zircon crystals during the crushing process. Adhering phases could contribute to density changes to the individual grains. There is evidence of adhering phases on at least 60% of the zircons imaged with EBSD, demonstrating that this is a widespread occurrence within this population of grains (Figure 4.8 and 4.12). This may be an underestimate

of the number of zircons affected by adhering phases because the epoxy grain mounts expose a two-dimensional slice of a three-dimensional zircon crystal. As such, adhering phases may not be visible in the current grain orientation. Some of the adhering phases are identified as anorthite, pyroxene, merrillite, and ilmenite which have densities of ~2.7, 3.2-3.3, 3.1, and 4.3-4.8 g/cm^3, respectively. Most of these adhering phases have densities that are below zircon and MI. Therefore, if there is a significant amount of these phases or other common lunar rock forming minerals such as olivine (density = 3.2-3.3 g/cm^3), which has previously been identified in the bulk rock 14311 sample, then the average density of the grains/grain aggregates may be lowered enough for it to float during MI density separation (MI density = 3.3 g/cm^3) (Meyer, 2008). If adhering phases is the only factor in lowering the density of these zircons, a significant portion would need to be adhering phases. For the endmember case of anorthite, there would need to be at least 69% anorthite by volume or 57% by mass relative to a zircon crystal. However, zircons that have adhering material often do not appear to have such a high percentage of adhering material that it would require to cause substantial density changes. Since it would require a such significant amount of adhering material to the zircon crystal to lower the density of zircon by at least 28%, this is likely a large contributing factor, but it may not be the only factor contributing to the significant density decrease.

Other factors, such as metamictization, may also be contributing to the lowering of the zircon density seen in these grains. Metamictization is caused by the decay of U to its daughter products and the expulsion of alpha particles during radioactive decay, which can cause radiation damage to these crystals and can be attributed to structural changes and abnormalities (Woodhead et al., 1991; Ewing, 1994; Salje et al., 1999). Many of the zircons produced indexable electron backscattered diffraction patterns (EBSPs), thus, at the 0.25 μm step size of the EBSD analyses,

these zircons appear to have normal, crystalline structures. However, 37% of the zircons showed non-indexing regions, likely due to partial metamictization, indicating that they have damaged crystal lattices. Metamictization in these zircons generally correlates with slightly elevated U concentrations of ~50-221 ppm with even slight metamictization occurring in grains with U concentrations as low as 31 ppm. The partially metamict zircons have generally lower U ppm concentrations than the fully metamict zircon crystals (Figure 4.11). Since other studies of 14311, such as Trail et al. (2020), did not include crystal structure analyses such as EBSD or Raman, it is difficult to determine if other metamict crystals were present. However, metamict grains are present in studies from other Apollo zircons denoting the widespread presence of metamictization in lunar zircon grains (Wopenka et al., 1996; Timms et al., 2012; Grange et al., 2013a; Crow et al., 2019). This may attribute enough damage to have a significant effect on the zircon density in these grains as an increase in radiation damage has been correlated to considerable density decreases (Nasdala et al., 1995; Zhang et al., 2000). It is also possible that small, nanometer scale structural differences or abnormalities could be present in the crystalline, indexing zircons that are not detectable at the 0.25 μm step size and could contribute to zircon density decreases.

The shock induced damage during impact has been previously determined to lower the density of bulk rock samples (Singleton et al., 2011). Singleton et al. (2011) analyzed bulk impact melt rock material from the Haughton impact structure and found that with increasing shock state, there is a general decrease in density and an increase in porosity as a result of fracturing and differential mineral melting during shock wave passage. This has been seen to lower the bulk rock density by less than 1 g/cm^3 (Singleton et al., 2011). To the author's knowledge, there has been no study on density changes within individual mineral grains due to impact shock, however, it is possible that density and porosity changes could also occur on the individual crystal scale and

influence impacted zircon properties. Pressure induced microtextural features such as fracturing, impact melt blebs, plastic deformation, and shock twinning were found to be present in these zircons, indicating structural damage and deformation to a significant portion of the grains (58%). This type of structural deformation could potentially affect the crystal structure and contribute to the lowering of the density of zircon crystals, although these effects would likely not be the only contributing factor to the lowering of zircon density.

Some variations to the original zircons through structural changes (e.g. polymorphs) or recrystallization could cause significant changes to the density of the crystal. High pressure polymorphs of minerals can increase the density of grains and can sometimes be found in impact settings. However, reidite, the high pressure polymorph of zircon, was not found to be present in any of the grains in this study. In fact, no Apollo zircons have been found to contain evidence of reidite or reidite reversion (FRIGN), further supporting no density increases (Crow et al., 2019). Recrystallization textures such as granularization and decomposition of zircon into baddeleyite (ZrO_2) can also affect the density of grains. The granularization process is a temperature driven process where zircons are heated, to a temperature that can cause zircons to decompose and/or recrystallize (>900-1000°C in damaged zircons) (Weber 1990; Weber et al., 1994; Reimold and Gibson, 1996; Gibson et al., 1997; Crow et al., 2019). Granular textured grains are one of the least common shock features in the grains from this study with only 2% of grains containing this texture. The granular grains in this study primarily index as zircon with only a few small (1-2 μm) regions of baddeleyite present, therefore indicating the grains did not fully decompose into ZrO_2 and SiO_2. Both baddeleyite and reidite have densities of 5.4-6.0 and 5.2 g/cm^3 respectively and so the lack of a significant presence of baddeleyite and any presence of reidite shows that there is minimal to no density increases to the zircon crystals. When zircons decompose and/or recrystallize in a

granular texture, this process can introduce porosity and therefore result in a decrease in the overall density of the grain.

4.6.1.2 Chemical Variation and Ultraviolet Light Fluorescence Response

Fluorescence properties of minerals are a result of both chemical and physical makeup within a single crystal (Foster, 1948). Chemically, UV light fluorescence in zircon is influenced by the concentration of trace element fluorescence activators (such as Mn, many rare earth elements (REES)) and quenching agents (such as Fe or Co) within the crystal (Budd et al., 2000; Waychunas and Kempe, 2024). Different concentrations of activators relative to quenching agents affect whether a mineral will fluoresce under UV light. Structural damage to zircon that can occur as a result of impact deformation or metamictization can create disorder in the crystal structure, and this disorder has the ability to reduce the resulting UV light fluorescence (Kumar et al., 2024; Waychunas and Kempe, 2024). The metamictization seen in EBSD analyses reveals a significant degree of structural damage to over a third of the 14311 zircons, and more fine scale disorder is possible. Therefore, since only 48% of zircons fluoresce under 254 nm wavelength UV light, more than half of zircon grains in this study have either a lack of fluorescence activator elements and/or an excess of quenching agents that fluoresce under UV light or have structural alterations (i.e. metamictization) that affect their fluorescence. Further analysis into trace elemental concentrations in the zircons could give further insight into the chemical composition effects of fluorescence in these zircons and whether there is a chemical or physical driven effect to fluorescence.

4.6.1.3 Suggested Lunar Zircon Separation Methods

Since the lunar zircons from 14311,58 did not effectively separate all the zircons from this sample, there is a need to determine a more effective methodology. Likely, a combination of factors such as adhering phases, metamictization, and damage induced density decreases in zircon all contribute to the significant lowering of the 14311 zircon densities. We therefore propose the following methodology for maximizing zircon yield from a sample. To begin processing, if a sample is a bulk rock, it can be crushed to separate individual minerals and an optional step of sieving a sample can assist in removing grains that are not of a size of interest. We then suggest magnetic separation (we used a neodymium hand magnet) as a key step in the process, since it was effective at removing most non-zircon minerals from the crushed 14311 material (99% of material). This amount may vary depending on the sample based on how much non-magnetic material is present, but our lab has had success using the method on multiple lunar soil and breccia samples. The next step in our process was to sprinkle the non-magnetic portion onto double sided kapton tape and map the sprinkle mounts via SEM EDS for P/Zr and Ca to determine the location of individual zircons. Phosphates, such as apatite and merrillite, can also be found in the non-magnetic materials using this method. When chemical mapping, it is important to map for both P and Ca peaks. The Zr Lα and P Kα peaks overlap and therefore P can be used as a proxy for Zr. If there is a Ca peak present along with P, then the mineral is a phosphate, while the presence of P and lack of Ca denotes zircon. The benefit of EDS mapping is it allows for rapid chemical confirmation of zircons and phosphates. This results in a more accurate, reliable method for zircon identification rather than relying on zircon identification by their expected chemical and/or physical characteristics such as shape or UV fluorescence, which has been seen to vary in lunar

samples. Furthermore, this methodology omits separation with heavy liquid, which can be toxic/carcinogenic, challenging to handle, and make it difficult to use samples for subsequent analyses. As all of the zircons in this study had a density decrease and/or had possible separation issues as a result of grain shape (e.g., high surface area) since this material floated in MI separations, density separation is not ideal for extracting all zircons grains from a lunar sample. However, if density separations are needed (i.e. if there is a significant amount of non-magnetic material after magnetic separations) then lowering the density of the heavy liquid for density separation (via dilution) may be effective. As such, we recommend this revised methodology to maximize yields in future lunar zircon separation efforts.

4.6.2 Zircon Crystallization Temperatures

Ti-in-zircon thermometry is used to infer zircon crystallization temperatures and parent melt conditions based on Ti concentrations (Watson and Harrison, 2005; Ferry and Watson, 2007; Ferriss et al., 2007; Fu et al., 2008, Burnham and Berry, 2012; Crow et al., 2017). The zircons in subsample 14311,58 were found to have crystallization temperatures of 882-1221°C (Figure 4.14). These temperatures are, on average, slightly higher than the temperatures of 777-1123°C calculated by Trail et al. (2020) on the 14311,58 zircons that sank in the density separations (Figure 4.14). A majority of the temperatures lie within the same range of ~900-1150°C but each dataset has outliers that lie outside of this range of temperatures that are present in both datasets; there are a few high temperature outliers in this study and a few low temperature outliers in Trail et al. (2020). Temperatures of other 14311 zircons from other subsamples in Hopkins and Mojzsis (2015) have a similar average temperature to the Trail et al. (2020) 14311 zircons but the temperatures span a larger range of temperatures (771-1846°C) than the 14311,58 zircons from

this study and Trail et al. (2020). Even with the outliers, the temperatures calculated from the zircons in this study are found to be within the range of Apollo 14 zircon temperatures (Figure 4.14) (Taylor et al., 2009; Valley et al., 2014; Hopkins and Mojzsis, 2015; Crow et al., 2017; Trail et al., 2020). The <4.0 Ga zircons have crystallization temperatures that cluster primarily around 1000-1100°C, which suggests the zircons formed from a homogenized melt compared to zircons >4.0 Ga (Figure 4.13). This was also observed by Trail et al. (2020). Overall, there is no significant correlation between the temperature of formation and the age of the zircon for grains that are >4.0 Ga, consistent with what was seen in Trail et al. (2020) (Figure 4.13). This study suggested that a majority these older zircons likely formed from either endogenic magmas or impact derived magmas of two main types: 1) magma of hot Mg-rich melt or impact induced melt interacting with urKREEP and ferroan anorthosites or 2) urKREEP magma. Trail et al. (2020) interprets these >4.0 Ga ages as a mixture of KREEP basalts and feldspathic highlands terrane-like rocks consistent with the thorough mixing and re-melting of the upper crust (~15 km) during basin forming impacts occurring at this time. The results of the Ti-in-zircon thermometry from the missing zircons that were not included in Trail et al. (2020) do not significantly change the understanding and interpretation of the temperatures of formation and source magmas. Additionally, there does not appear to be any correlation between age, microtexture, and T-in-zircon thermometry temperatures.

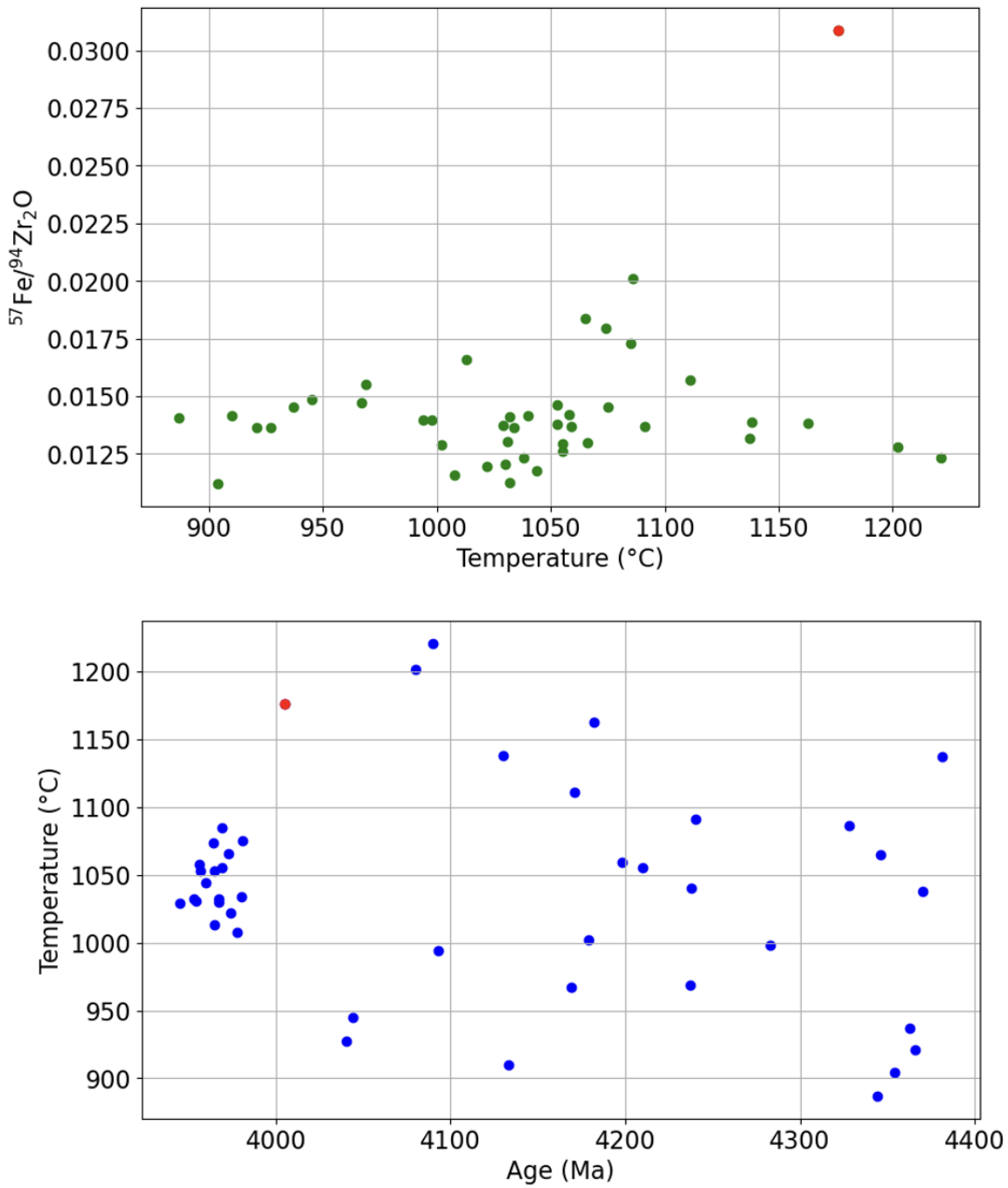

Figure 4.13: The top plot is $^{57}Fe/^{96}Zr_2O$ plotted against crystallization temperature (as a proxy for Ti concentration) to filter out anomalously high Fe measurements that would be associated with possible contamination. The only point (red in both panels) that was found to have anomalously high iron was filtered out. The bottom plot is crystallization temperatures plotted against the $^{207}Pb/^{206}Pb$ ages of the zircons. When multiple sample spots were taken on the zircons from this study, the temperatures were averaged across all the spots to get an average temperature for the entire grain. Most of the zircons >4 Ga do not have significant age and temperature clustering. Samples <4000 Ma cluster around 1000-1100°C. (n=44)

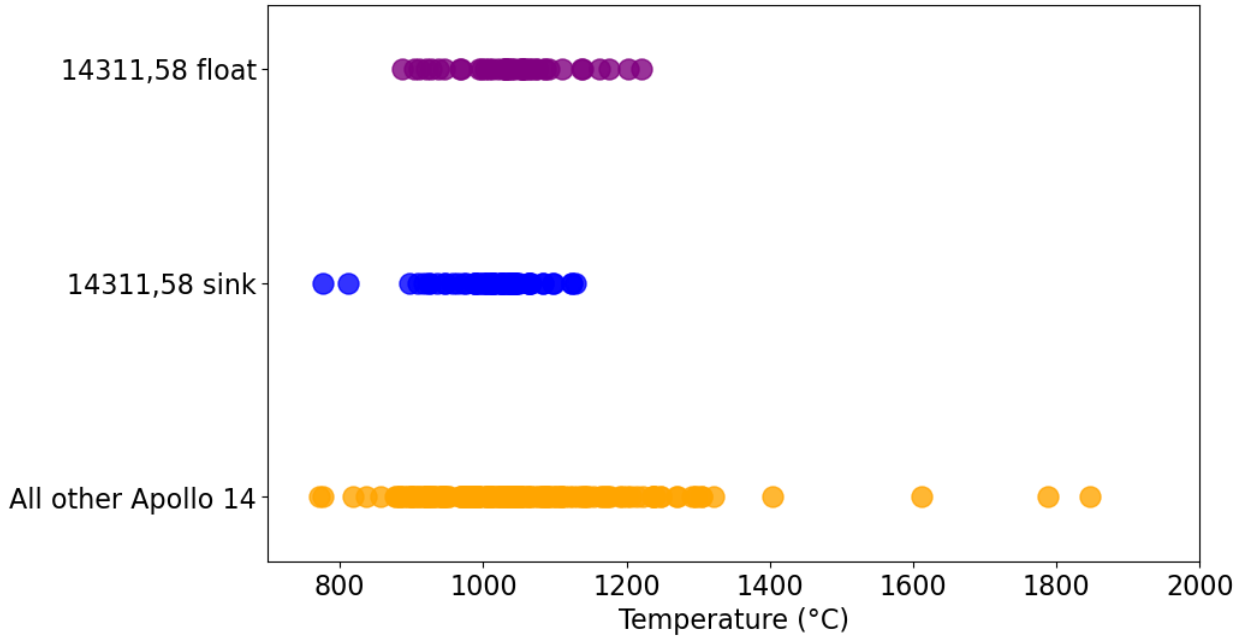

Figure 4.14: Crystallization temperatures calculated via Ti-in-zircon thermometry. These temperatures are separated by the 14311,58 zircons that floated in MI density separations (this study) (n=44), 14311,58 zircons that sank in MI density separations (Trail et al., 2020) (n=70), and a comparison to all other calculated temperatures in all other Apollo 14 samples (n=191) (Taylor et al., 2009; Valley et al., 2014; Hopkins and Mojzsis, 2015; Crow et al., 2017, Trail et al., 2020). When multiple sample spots were taken on the zircons from this study, the temperatures were averaged across all the spots to get an average temperature for the entire grain. The zircon temperatures for the zircons from this study are on average slightly higher than the zircons from Trail et al., 2020. All of the 14311,58 zircon temperatures (from both this study and Trail et al., 2020) are within the range of temperatures calculated from all Apollo 14 zircons.

4.6.3 History of 14311

4.6.3.1 Missing Zircon Ages – What's the Full Story of 14311?

Apollo sample 14311 has been extensively studied through a variety of methods to characterize and determine the history of this sample. Previous studies include geochronologic measurements of zircon, apatite, and bulk rock (Stadermann et al., 1991; Merle et al., 2014; Hopkins and Mojzsis, 2015; Merle et al., 2017; Kelly et al., 2018; Trail et al., 2020; Diaz et al.,

2024); assessing annealing of zircon damage (Pidgeon et al., 2016); investigating formational conditions (e.g., crystallization temperature) of the zircons within the sample (Hopkins and Mojzsis, 2015; Trail et al., 2020); and exposure age dating to determine how long the sample has been on the lunar surface (Crozaz et al., 1972; Drozd et al., 1974; Stadermann et al., 1991, Merle et al., 2017). The zircons that have previously been studied from 14311 include grains analyzed in both thin and thick sections and through the mineral separation methods that were analyzed for effectiveness in this study (Hopkins and Mojzsis, 2015; Pidgeon et al., 2016; Merle et al., 2017; Kelly et al., 2018; Trail et al., 2020). It has been suggested that the source of the sample is likely located within the Procellarum KREEP terrane (PKT) based on its high content of incompatible elements such as zirconium, which in turn form a high abundance of zircons (Dickenson and Hess, 1982; Jolliff et al., 2000; Merle et al., 2017). This is supported by the large abundance of zircon grains and fragments found in this study (at least several 100s of zircons in the 9.92 g 14311,58). Building on the extensive studies of 14311 and incorporating the new insights from this study, these findings will be examined to assess their impact on and contribute to a comprehensive summary of the history of 14311.

With over 75% of zircons being missed in the previous study of Trail et al. (2020), we were curious to see how these additional zircons expanded the full history of Apollo impact melt breccia 14311. Overall, the observed $^{207}Pb/^{206}Pb$ age range (~3.9-4.4 Ga) for the MI float grains from this study is similar to the age range of the MI sink grains reported in Trail et al. (2020). However, the distribution of ages (i.e., the location and intensity of peaks in probability density) varies between the two samples (Figure 4.15). In the MI sink material from Trail et al. (2020), there is a large spike at ~3.94, and a few slightly smaller peaks at 4.25 and 4.33 Ga, whereas the zircons from this study (MI float zircons) display age clusters near ~3.96, 4.25, and 4.34 Ga, but there were

proportionally fewer grains in the ~3.96 Ga population compared to Trail et al. (2020) (Figure 4.15). When all of the 14311,58 zircon ages from both this study and Trail et al. (2020) are combined, the three dominant peaks are present at ~3.95, 4.25, and 4.34 Ga (Figure 4.16). An important addition in this study is the ages of 67% more 14311,58 zircons than that analyzed in Trail et al. (2020) to create a significantly larger dataset of ages from this subsample (total of 217 zircons when combined). With the addition of significantly more ages, smaller peaks between the 3.95 and 4.25 Ga that were present in Trail et al. (2020) are no longer present and are instead replaced by a continuum of ages between this range, with no notable, individual peaks present (Figure 4.16). This is significant as other studies with smaller datasets have assigned significance to these age peaks between 4.25 and 3.95 Ga, which this study now denotes are not necessarily representing individual events at those times (Hopkins and Mojzsis, 2015). As a result, in smaller datasets, over-interpretation of smaller age populations can occur. Therefore, the addition of this data emphasizes that when a large dataset can be collected on a sample, this gives a better understanding of when age peaks are significant.

The microtextures recorded in the 4.33-4.35 Ga 14311,58 zircons from this study all show either unshocked or metamict grains, with no evidence of shock features such as plastic deformation, shock twinning, or granularization. With evidence of primary igneous zonation in one grain with an age of 4340 ± 7.4 Ma (2σ) and lack of significant shock evidence in grains in this age peak, this suggests a possible magmatic crystallization origin (Figure 4.6). However, impacts can produce vast melt sheets that can crystallize and produce unshocked zircon, making it difficult to determine if these zircons at this age crystallized from primary magma crystallization or impact produced melt crystallization. The zircon chemistries (e.g., alumina activity environment) as seen in Trail et al. (2020) provides evidence for possible ferroan anorthosite

(FAN) crystallization from the magma ocean that goes as far back as 4.42 Ga, for Mg-suite magmatism that could form these zircons, or for impact melt origin (Figure 4.17) (Meyer et al., 1996; Pidgeon et al., 2007; Nemchin et al., 2008; Grange et al., 2009; Grange et al., 2011; Hopkins and Mojzsis, 2015; Merle et al., 2017; Trail et al., 2020). Between the results of this study and other studies of 14311 zircons, it is difficult to further constrain the origin of the 4.34 Ga grains as primary magma crystallization, Mg-suite magmatism, or impact melt crystallization.

The next prominent peak of 14311 zircon ages is at ~4.25 Ga. The zircons at this age display a range of textures from unshocked, fracturing, and plastic deformation. With the presence of some shock features such as plastic deformation (>5° of deformation), this is evidence of possible impact deformation and age resetting of this zircon at 4.25 Ga. The assessment of zircons of this age by Trail et al. (2020) found that these zircons are considered to be a suite of related samples by their relative activity parameters. These zircons may then have assimilated anorthosite material or Mg-suite rocks to form these 14311 zircons in Trail et al. (2020), however, high temperature endogenous melts that can assimilate these assemblages become harder to produce as the Moon cools, making this a possible, but not necessarily a decisive formation history to have these zircons form from endogenic magmatism. Instead, it is proposed that these zircons may have formed in an exogenous event such as an impact event to explain the related activity parameters and the anomalously wide range of U and Th concentrations meaning a complex formational environment such as an impact (Hopkins and Mojzsis, 2015; Trail et al., 2020). While there is evidence for possible impact origin, it is difficult to confidently determine the exact origin of the 4.25 Ga zircons as magmatic or impact produced zircons.

There is a range of less prominent ages between larger age peaks at ~4.25 and 3.95 Ga. These ages have relatively similar lower probability densities at this range, showing there is no distinct peak in ages in this range (Figure 4.16).

A range of less prominent ages is present between the two major age peaks at ~4.25 and 3.95 Ga. These ages exhibit relatively uniform, lower probability densities across this interval, indicating the absence of a distinct peak (Figure 4.16). The microtextures associated with the ages in this range are a majority unshocked with only a few grains containing pressure induced shock features such as plastic deformation or shock twins and several grains either partially or fully metamict. While these shock features are evidence of impacts, plastic deformation has been associated with partial Pb-loss, and therefore these grains with impact microtextures in this range may represent partial resetting either during this time range or after this age range, possibly during the 3.95 Ga impact spike (Cavosie et al., 2018; Rasmussen et al., 2020; Davis et al., in prep (Chapter 3 of this dissertation)). Since most zircons in this range are unshocked, they likely represent zircons that have not been involved in significant impact events that would shock the crystals and produce shock microtextures. Although the zircons appear relatively unshocked, this is determined via a 2D slice of an otherwise 3D crystal, leaving the possibility that the zircons may unknowingly be shocked. With no significant spikes in ages between 4.25 and 3.95 Ga, this is likely signifying no large, individual geologic events such as an impact at this time. Therefore, the results of this study lack significant evidence for the “picket fence” multiple cataclysm theory of large impact bombardment during this time range from Hopkins and Mojzsis (2015).

An age peak at ~3.95 Ga is found to be extremely prominent in the 14311,58 zircons from both this study and Trail et al. (2020). In fact, the 14311,58 zircon ages have the highest concentration of ages at this 3.95 Ga age. While some previous studies have had zircon ages ~3.9

Ga, lunar zircons have not commonly had a significant age population at this age (e.g., Nemchin et al., 2006; Pidgeon et al., 2007; Nemchin et al., 2008; Grange et al., 2013a; Grange et al., 2013b; Hopkins and Mojzsis, 2015; Crow et al., 2017). This observation illustrates the heterogeneity that can be found within impact breccia samples (Haskin et al., 2010; Grieve and Therriault, 2012). Granular zircon, which represents zircon recrystallization from high temperatures (>900-1000°C in damaged zircons) and pressures often produced during impact events, was found to have an age of 3933 ± 16 Ma (2σ) (Weber 1990; Weber et al., 1994; Reimold and Gibson, 1996; Gibson et al., 1997; Grange et al., 2013a; Merle et al., 2017). Similar to the age of a granular grain from this study (3933 ± 16 (2σ)), the ages of the granular grains from Hopkins and Mojzsis (2015) are 3954 ± 26 and 3927 ± 16 (2σ). This is further supported by all of the granular ages representing the youngest ages found in 14311 zircons. Since the granular grains can be formed through impact cratering causing recrystallization (Grange et al., 2013a; Cavosie et al., 2016; Cavosie et al., 2018), and impact cratering is a common process on the lunar surface, this points towards the 14311 zircon ages near ~3.93-3.95 Ga may represent impact ages (Hopkins and Mojszis, 2015; Trail et al., 2020). Additionally, similar to what has been seen in Trail et al. (2020), the zircons from this study show relatively constrained formation temperatures and conditions in the <4.0 Ga grains (1000-1100°C from this study) (Figure 4.13). This represents a relatively homogeneous crystallization environment which is proposed to be the result of a single large, basin-forming sized impact that may have formed a large melt sheet from which these zircons crystallized (Figure 4.13) (Hopkins and Mojzsis, 2015; Trail et al., 2020).

4.6.3.2 14311 Breccia Formation

Merle et al. (2014) measured U-Pb ages of 14311 phosphates, which have a weighted average age of 3938 ± 4 Ma (2σ). The U-Pb geochronometer in phosphates resets at lower temperatures (~500°C) than in zircon (~900°C), therefore, phosphates, such as apatite and merrillite, often preserve younger impact ages than zircon within a sample (Cherniak et al., 1991; Krogstad and Walker 1994; Lee et al., 1997; Chamberlain and Bowring, 2000; Cherniak and Watson, 2001; Merle et al., 2014; Snape et al., 2016; Pidgeon et al., 2016). The well constrained, young age of 3938 ± 4 Ma (2σ) in Merle et al. (2014) pre-dates the Imbrium impact which is determined by Snape et al. (2016) to be 3927 ± 2 Ma (2σ). Although some of the zircons measured in this study have ages that are younger than the proposed breccia formation age of 3938 ± 4 (2σ), all the samples are within the uncertainty of the breccia formation age and therefore further support this age as an accepted formation age of the breccia (Merle et al., 2014; Merle et al., 2017). It is then theorized by Merle et al. (2017) that either 14311 formed in the PKT by an impact at 3938 Ma and then became integrated into the Fra Mauro Formation during the deposition of the Imbrium impact ejecta at 3927 Ma or alternatively that the breccia formed at an unknown location by an impact at 3938 Ma and was transported to its current location by an impact at 660 Ma (based on the exposure age) (Snape et al., 2016; Merle et al., 2017).

4.6.3.3 Timing of Breccia Annealing and Metamictization in 14311,58 Zircons

An annealing age of 3410 ± 80 Ma (2σ) was measured for zircons in 14311 (Pidgeon et al., 2016). This study determined the amount of radiation damage through Raman spectra analyses on 14311 zircons. Based on U concentrations, the grains are more crystalline (less radiation damaged)

than expected if they had crystallized ≥3938 Ma, therefore they must have experienced subsequent annealing since their original formation. This means that the zircons were heated above the annealing temperature of ~230°C at 3410 ± 80 Ma (2σ) (stage 1 annealing of short range order detectable in Raman spectroscopy) (Murakami et al., 1991; Pidgeon et al., 2016). However, since the U-Pb phosphate ages are not reset to this annealing age, the temperature did not exceed the temperature needed to reset the U-Pb apatite system of ~500°C at this time (Cherniak et al., 1991; Krogstad and Walker 1994; Chamberlain and Bowring, 2000; Merle et al., 2014; Snape et al., 2016; Pidgeon et al., 2016).

We conducted a similar analysis to that of Pidgeon et al. (2016) and calculated alpha-doses for zircons using measured U concentration and the expected annealing age of 3410 ± 80 Ma (2σ). We next assumed a ~10^{16} α/mg dose is needed to cause complete metamictization of zircon (Wopenka et al., 1996) and used EBSD indexing as a proxy for radiation damage. Some grains that display higher degrees of metamictization in EBSD have α/mg doses of ~10^{16}, which is close to the metamictization dose. Other grains that display no metamictization contain α/mg doses of ~10^{14}-10^{15}. This agreement suggests that the annealing age of Pidegon et al. (2016) of 3410 ± 80 Ma (2σ) is also realistic for the zircons in this study. This annealing has been proposed to be a result of elevated temperatures in close proximity to Mare volcanism basalt flows occurring during this time (Pidgeon et al., 2016; Merle et al., 2017).

4.6.3.4 Summary of 14311 Sample History

Overall, this sample experienced periodic geologic events denoting either magmatic pulses and/or impact events throughout its history both before and after the 14311 breccia formation. At ~4.34 Ga, either initial magma ocean crystallization, Mg-suite volcanism, or an impact produced

the oldest zircon ages in this sample (Hopkins and Mojzsis, 2015; Merle et al., 2017; Trail et al., 2020). Next, at ~4.25 Ga, either a magmatic pulse or an impact event occurred to produce a large U-Pb age population at this time (Hopkins and Mojzsis, 2015; Merle et al., 2017; Trail et al., 2020). After a relatively geologically quiescent period between 4.25-3.95 Ga that did not result in notable age resetting events, at ~3.95, a large basin forming impact likely occurred to notably reset a significant portion of zircon ages (Figure 4.16) (Merle et al., 2017; Trail et al., 2020). At 3.938 Ga, the 14311 breccia formed as a result of an impact (pre-Imbrium) (Merle et al., 2014; Merle et al., 2017). Subsequent annealing of zircons occurred at 3410 Ga when temperatures were elevated within the sample from proximal Mare volcanism basalt flows (Pidgeon et al., 2016; Merle et al., 2017). It is theorized that this sample was deposited in its current location either 1) during the deposition of Imbrium impact ejecta (3927 Ma) and exhumed by a smaller impact at 660 Ma or 2) that it was at an unknown location until it was transported by an impact at 660 Ma to its current location (Snape et al., 2016; Merle et al., 2017).

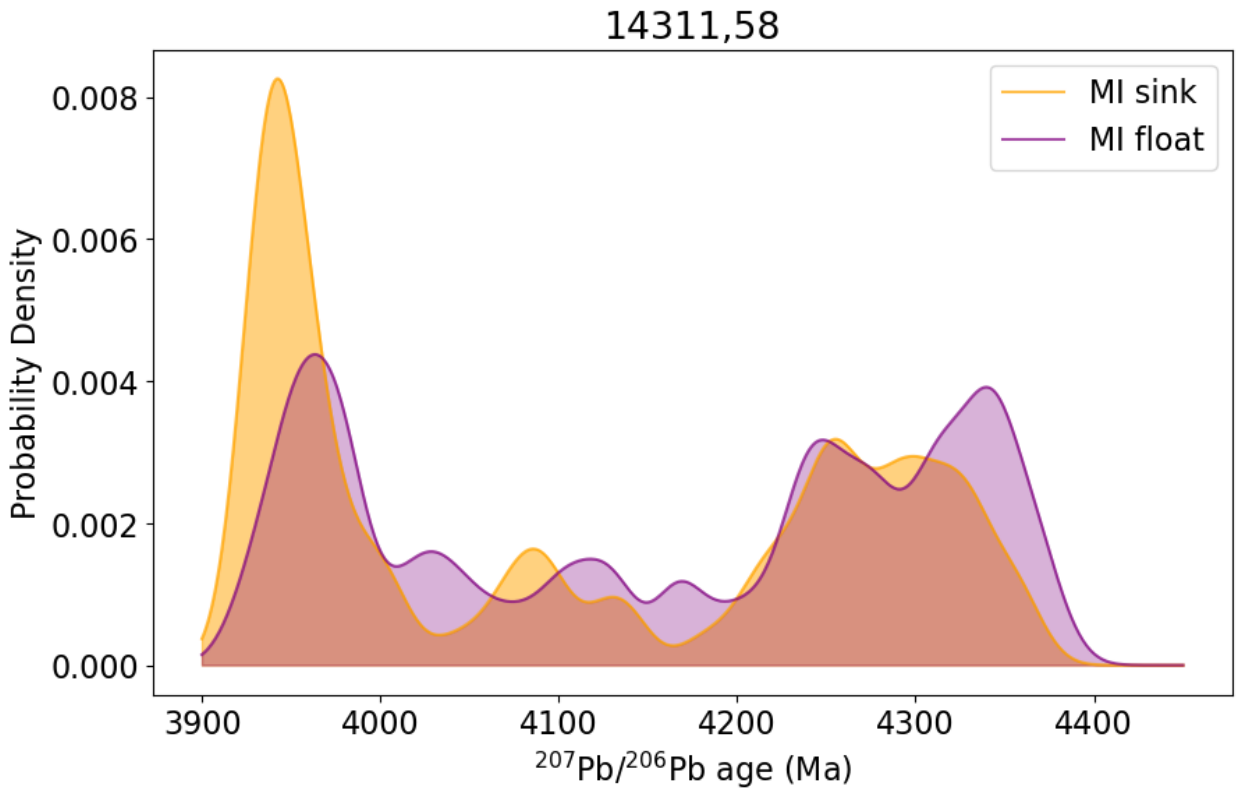

Figure 4.15: Probability density function for $^{207}Pb/^{206}Pb$ ages from zircons that sank in MI density separations from 14311,58 in Trail et al. (2020) (n=75) compared to the $^{207}Pb/^{206}Pb$ ages from zircons in the reprocessed MI float material from the same subsection in this study; n=136. This shows how the two age distributions compare between these samples and the minor variations in dominant age peaks around ~3.94-3.96, 4.25, and 4.33-4.34 Ga. Small age peaks between these three dominant peaks vary slightly between the two subsamples depicting no single, significant age peak.

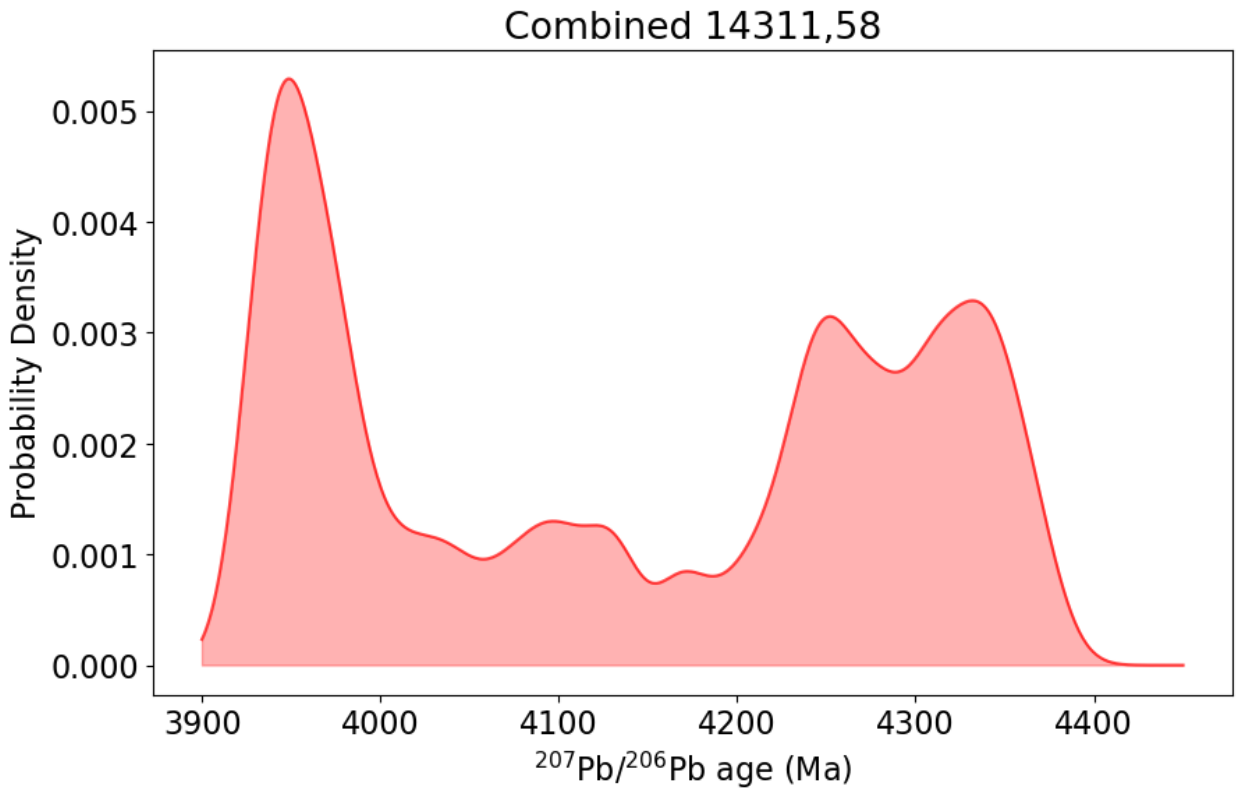

Figure 4.16: Probability density function for the combined $^{207}Pb/^{206}Pb$ zircon ages from subsection 14311,58 (Trail et al., 2020, and this study). The largest age peak is at ~3.95 Ga with two smaller predominant peaks around ~4.25 and 4.34 Ga. There is a continuum of ages between the larger age peaks. (n=211)

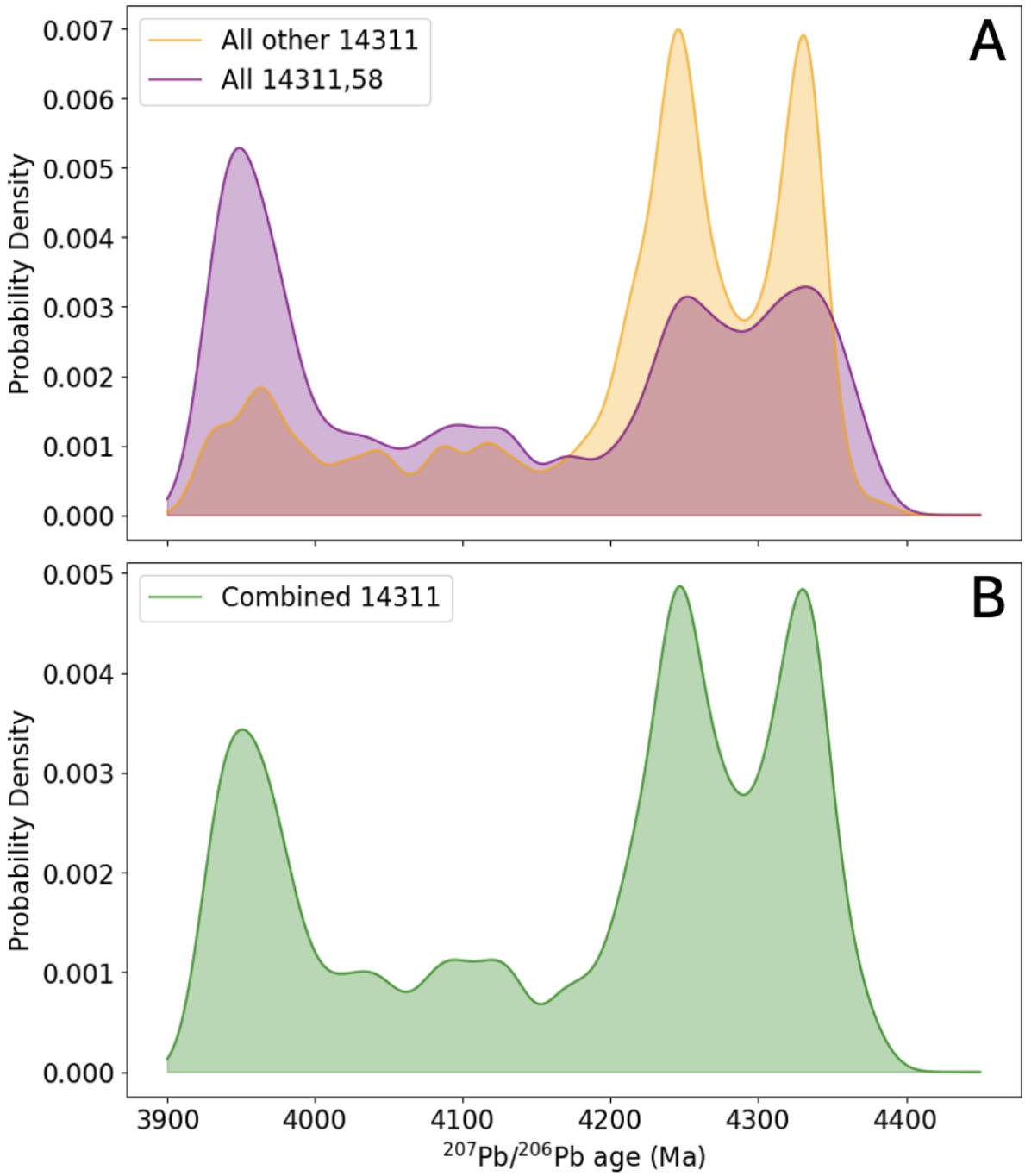

Figure 4.17: Probability density functions (PDFs) of the $^{207}Pb/^{206}Pb$ ages of 14311 zircons. A) PDF of all Apollo 14311,58 (n=211) (this study and Trail et al., 2020) relative to all other 14311 zircons that are not from subsample 58 (n=240) (Hopkins and Mojzsis, 2015; Merle et al., 2017). The 14311,58 zircons have more zircons with ages near ~3.94-3.96 Ga while the other 14311 ages have a much lower density at this age. The 14311 ages (excluding 14311,58 ages from this study and Trail et al. (2020)) have two significant age peaks near 4.25 and 4.33-4.35 Ga, which are present in the 14311,58 grains but less probable. B) Combined age PDF for the full population of 14311 zircons (n=451) showing three significant age peaks at ~3.94-3.96, 4.25, and 4.33-4.35 Ga and a continuum in the range of 4.40-3. 93Ga.

4.7 Conclusions

U-Pb dating, Ti-in-zircon thermometry, and microtextural analysis of zircon allow for critical insights into elucidating our understanding of the history and evolution of a sample and the overall lunar surface. Zircon is studied in either thin or thick sections or through individual minerals that are isolated from bulk material through mineral separation to increase zircon yields, as was done in this study. These separation methods have previously included steps such as crushing bulk rock, density separation, and UV light picking. Since it is now known that these sample processing methods are not efficient and miss large fractions of grains, we have given careful attention to developing more effective extraction methods.

To more effectively extract lunar zircons from bulk rock material, we suggest adjusting processing procedures to 1) crushing the sample (if bulk rock), 2) an optional step of sieving the sample to remove difficult-to-process grains or grains not of target size, 3) magnetically separating via hand magnet separations, 4) sprinkling non-magnetic separates onto tape, and 5) chemical mapping (such as EDS) to locate zircons. This eliminates the use of density separations with heavy liquid, such as MI, which has been seen to miss 75% of 14311,58 zircons. Likely, a combination of less dense, adhering phases, metamictization, and impact induced zircon density changes affected the overall density of these zircons for the grains from this study to unexpectedly float in MI density separation. Additionally, this new processing procedure removes the method of UV light fluorescence aided picking (at 254 nm wavelength) which missed an additional 48% of 14311,58 zircon grains. Fluorescence can be affected by chemical variations in trace elemental concentrations (e.g., low concentrations of activator elements, high concentrations of quenching elements) as well as physical disorder to the structure. This new methodology has proven to effectively extract zircons from bulk lunar material.

The addition of ages of these previously overlooked zircon grains in this study resulted in additions to our understanding of 14311 that were previously missing. The ages of the 14311,58 zircons in this study displayed a similar age distribution to the 14311,58 zircons from Trail et al. (2020) and other studies of 14311 zircons with peaks at ~4.34, 4.25, and 3.95 Ga (i.e., Hopkins and Mojzsis, 2015; Merle et al., 2017). However, our large survey of additional 14311,58 zircons (45% more 14311 ages and 168% more 14311,58 ages, n=136 from this study) displayed a continuum of ages between 4.25 and 3.95 Ga that was previously not present. Instead, studies that consisted of smaller populations of 14311 zircons had small age peaks in this range, which likely resulted in overinterpretation of these peaks (Hopkins and Mojzsis, 2015; Trail et al., 2020). Instead, these peaks likely signify partially reset ages from other events, and this period did not consist of any geologically significant events (i.e., large impacts) for the sources of the 14311 constituents. Our study also reinforced the presence of the 3.95 Ga age peak that was present in Trail et al. (2020) but has been previously missing from many lunar zircon analyses, documenting a large age resetting event at this time. The addition of the Ti-in-zircon thermometry crystallization temperatures further confirmed similar crystallization temperatures measured from other 14311 zircons.

Textural analyses through EBSD assisted in better understanding the history of these zircons through the observation of microtextural features such as igneous zonation, metamictization, fractures, melt inclusions, plastic deformation, shock twins, and granules. Although more than half of the grains (62%) did not present signs of any microtextural features, the textures that were observed significantly contributed to the understanding of the zircon histories recorded in 14311. Impact induced microtextures such as plastic deformation (>5° deformation), shock twinning, and granules further supported impact processes occurring to affect

these zircons. The presence of granules in the zircon with an age of 3933 ± 16 Ma (2σ) supports the impact hypothesis for the spike in ages at ~3.95 Ga. Metamictization was found to occur in 37% of grains, depicting significant radiation damage to a large number of these zircons, supporting the annealing age of 3410 Ga. The addition of microtextural analyses greatly enhanced our understanding of the history of these zircons.

Overall, the results from this study gave a new understanding of the age distribution of 14311 zircons to fill out the previously overlooked zircon history as well as further confirmed the formation and evolution history of the 14311 breccia sample. The zircons in this sample likely represent various periods of either magmatic crystallization or impact events at 4.34 and 4.25 Ga, followed by a large impact at 3.95 Ga prior to breccia formation by an impact at 3.938 Ga. At 3410 Ma, the sample experienced elevated temperatures that allowed for zircon annealing but no age resetting in the U-Pb zircon or phosphate systems. Eventually, at 660 Ma, the breccia was exhumed to the surface where it remained until collection during the Apollo 14 mission.

4.8 References

Barboni, M., Szymanowski, D., Schoene, B., Dauphas, N., Zhang, Z.J., Chen, X., McKeegan, K.D., 2024. High-precision U-Pb zircon dating identifies a major magmatic event on the Moon at 4.338 Ga. Science Advances 10, eadn9871. https://doi.org/10.1126/sciadv.adn9871

Budd, D.A., Hammes, U., Ward, W.B., 2000. Cathodoluminescence in Calcite Cements: New Insights on Pb and Zn Sensitizing, Mn Activation, and Fe Quenching at Low Trace-Element Concentrations. Journal of Sedimentary Research 70, 217–226. https://doi.org/10.1306/2DC4090C-0E47-11D7-8643000102C1865D

Burnham, A.D., Berry, A.J., 2012. An experimental study of trace element partitioning between zircon and melt as a function of oxygen fugacity. Geochimica et Cosmochimica Acta 95, 196–212. https://doi.org/10.1016/j.gca.2012.07.034

Cavosie, A.J., Timms, N.E., Erickson, T.M., Hagerty, J.J., Hörz, F., 2016. Transformations to granular zircon revealed: Twinning, reidite, and ZrO2 in shocked zircon from Meteor Crater (Arizona, USA). Geology 44, 703–706. https://doi.org/10.1130/G38043.1

Cavosie, A.J., Timms, N.E., Ferrière, L., Rochette, P., 2018. FRIGN zircon—The only terrestrial mineral diagnostic of high-pressure and high-temperature shock deformation. Geology 46, 891–894. https://doi.org/10.1130/G45079.1

Chamberlain, K.R., Bowring, S.A., 2000. Apatite–feldspar U–Pb thermochronometer: a reliable, mid-range (~450°C), diffusion-controlled system. Chemical Geology, What are we dating? Understanding the Crystallogernesis of U-Pb 172, 173–200. https://doi.org/10.1016/S0009-2541(00)00242-4

Cherniak, D.J., Lanford, W.A., Ryerson, F.J., 1991. Lead diffusion in apatite and zircon using ion implantation and Rutherford Backscattering techniques. Geochimica et Cosmochimica Acta 55, 1663–1673. https://doi.org/10.1016/0016-7037(91)90137-T

Cherniak, D.J., Watson, E.B., 2001. Pb diffusion in zircon. Chemical Geology, What are we dating? Understanding the Crystallogernesis of U-Pb 172, 5–24. https://doi.org/10.1016/S0009-2541(00)00233-3

Citron, R.I., Smith, D.E., Stewart, S.T., Hood, L.L., Zuber, M.T., 2024. The South Pole-Aitken Basin: Constraints on Impact Excavation, Melt, and Ejecta. Geophysical Research Letters 51, e2024GL110034. https://doi.org/10.1029/2024GL110034

Cohen, B.A., Swindle, T.D., Kring, D.A., 2000. Support for the Lunar Cataclysm Hypothesis from Lunar Meteorite Impact Melt Ages. Science 290, 1754–1756. https://doi.org/10.1126/science.290.5497.1754

Crow, C.A., McKeegan, K.D., Moser, D.E., 2017. Coordinated U–Pb geochronology, trace element, Ti-in-zircon thermometry and microstructural analysis of Apollo zircons. Geochimica et Cosmochimica Acta 202, 264–284. https://doi.org/10.1016/j.gca.2016.12.019

Crow, C.A., Moser, D.E., McKeegan, K.D., 2019. Shock metamorphic history of >4 Ga Apollo 14 and 15 zircons. Meteoritics & Planetary Science 54, 181–201. https://doi.org/10.1111/maps.13184

Crow, C.A., Tong, C., Erickson, T.M., Moser, D.E., Bell, A.S., Kelly, N.M., Prissel, T.C., Hyde, B.C., 2024. Impact origin of lunar zircon melt inclusions in Apollo impact melt breccia 14311. Meteoritics & Planetary Science 59, 1509–1522. https://doi.org/10.1111/maps.14162

Crozaz, G., Drozd, R., Hohenberg, C.M., Hoyt, Jr., H.P., Ragan, D., Walker, R.M., Yuhas, D., 1972. Solar flare and galactic cosmic-ray studies of Apollo 14 and 15 samples. Presented at the 3rd Lunar Science Conference.

Diaz, C.A., Flowers, R.M., Crow, C., Metcalf, J.R., Economos, R., Erickson, T., Boyce, J.W., Davis, J., Brounce, M., Lehman-Franco, K., Schoene, B., n.d. Phosphate (U-Th)/He Thermochronology of Apollo 14 Melt Breccia 14311. Presented at the 55th Lunar and Planetary Science Conference (LPSC), The Woodlands, TX.

Dickinson, J.E., Hess, P.C., 1982. Zircon saturation in lunar basalts and granites. Earth and Planetary Science Letters 57, 336–344. https://doi.org/10.1016/0012-821X(82)90154-6

Drozd, R.J., Hohenberg, C.M., Morgan, C.J., Ralston, C.E., 1974. Cosmic-ray exposure history at the Apollo 16 and other lunar sites: lunar surface dynamics. Geochimica et Cosmochimica Acta 38, 1625–1642. https://doi.org/10.1016/0016-7037(74)90178-1

Ewing, R.C., 1994. The metamict state: 1993 — the centennial. Nuclear Instruments and Methods in Physics Research Section B: Beam Interactions with Materials and Atoms 91, 22–29. https://doi.org/10.1016/0168-583X(94)96186-7

Farnan, I., Balan, E., Pickard, C.J., Mauri, F., 2003. The effect of radiation damage on local structure in the crystalline fraction of ZrSiO4: Investigating the 29Si NMR response to pressure in zircon and reidite. American Mineralogist 88, 1663–1667. https://doi.org/10.2138/am-2003-11-1205

Fernandes, V.A., Fritz, J., Weiss, B.P., Garrick-Bethell, I., Shuster, D.L., 2013. The bombardment history of the Moon as recorded by 40Ar-39Ar chronology. Meteoritics & Planetary Science 48, 241–269. https://doi.org/10.1111/maps.12054

Ferriss, E.D.A., Essene, E.J., Becker, U., 2008. Computational study of the effect of pressure on the Ti-in-zircon geothermometer. European Journal of Mineralogy 20, 745–755. https://doi.org/10.1127/0935-1221/2008/0020-1860

Ferry, J.M., Watson, E.B., 2007. New thermodynamic models and revised calibrations for the Ti-in-zircon and Zr-in-rutile thermometers. Contrib Mineral Petrol 154, 429–437. https://doi.org/10.1007/s00410-007-0201-0

Foster, W.R., 1948. Useful aspects of the fluorescence of accessory-mineral-zircon*. American Mineralogist 33, 724–735.

Fu, B., Page, F.Z., Cavosie, A.J., Fournelle, J., Kita, N.T., Lackey, J.S., Wilde, S.A., Valley, J.W., 2008. Ti-in-zircon thermometry: applications and limitations. Contrib Mineral Petrol 156, 197–215. https://doi.org/10.1007/s00410-008-0281-5

Gibson, R.L., Armstrong, R.A., Reimold, W.U., 1997. The age and thermal evolution of the Vredefort impact structure: A single-grain U-Pb zircon study. Geochimica et Cosmochimica Acta 61, 1531–1540. https://doi.org/10.1016/S0016-7037(97)00013-6

Grange, M.L., Nemchin, A.A., Pidgeon, R.T., Timms, N., Muhling, J.R., Kennedy, A.K., 2009. Thermal history recorded by the Apollo 17 impact melt breccia 73217. Geochimica et Cosmochimica Acta 73, 3093–3107. https://doi.org/10.1016/j.gca.2009.02.032

Grange, M.L., Nemchin, A.A., Timms, N., Pidgeon, R.T., Meyer, C., 2011. Complex magmatic and impact history prior to 4.1Ga recorded in zircon from Apollo 17 South Massif aphanitic breccia 73235. Geochimica et Cosmochimica Acta 75, 2213–2232. https://doi.org/10.1016/j.gca.2011.01.036

Grange, M.L., Pidgeon, R.T., Nemchin, A.A., Timms, N.E., Meyer, C., 2013a. Interpreting U–Pb data from primary and secondary features in lunar zircon. Geochimica et Cosmochimica Acta 101, 112–132. https://doi.org/10.1016/j.gca.2012.10.013

Grange, M.L., Nemchin, A.A., Pidgeon, R.T., 2013b. The effect of 1.9 and 1.4 Ga impact events on 4.3 Ga zircon and phosphate from an Apollo 15 melt breccia. Journal of Geophysical Research: Planets 118, 2180–2197. https://doi.org/10.1002/jgre.20167

Grieve, R.A.F., Therriault, A.M., 2012. Impactites: their characteristics and spatial distribution, in: Impact Cratering: Processes and Products. John Wiley & Sons, Ltd.

Haskin, L.A., Korotev, R.L., Rockow, K.M., Jolliff, B.L., 2010. The case for an Imbrium origin of the Apollo thorium-rich impact-melt breccias. Meteoritics & Planetary Science 33, 959–975. https://doi.org/10.1111/j.1945-5100.1998.tb01703.x

Hazen, R.M., Finger, L.W., 1979. Crystal structure and compressibility of zircon at high pressure. American Mineralogist 64, 196–201.

Hopkins, M.D., Mojzsis, S.J., 2015. A protracted timeline for lunar bombardment from mineral chemistry, Ti thermometry and U–Pb geochronology of Apollo 14 melt breccia zircons. Contrib Mineral Petrol 169, 1–18. https://doi.org/10.1007/s00410-015-1123-x

Howard, C.J., Hill, R.J., Reichert, B.E., 1988. Structures of ZrO2 polymorphs at room temperature by high-resolution neutron powder diffraction. Acta Cryst B 44, 116–120. https://doi.org/10.1107/S0108768187010279

Jolliff, B.L., Gillis, J.J., Haskin, L.A., Korotev, R.L., Wieczorek, M.A., 2000. Major lunar crustal terranes: Surface expressions and crust-mantle origins. Journal of Geophysical Research: Planets 105, 4197–4216. https://doi.org/10.1029/1999JE001103

Joy, K.H., Snape, J.F., Nemchin, A.A., Tartèse, R., Martin, D.M., Whitehouse, M.J., Vishnyakov, V., Pernet-Fisher, J.F., Kring, D.A., 2020. Timing of geological events in the lunar highlands recorded in shocked zircon-bearing clasts from Apollo 16. Royal Society Open Science 7, 200236. https://doi.org/10.1098/rsos.200236

Kelly, N.M., Flowers, R.M., Metcalf, J.R., Mojzsis, S.J., 2018. Late accretion to the Moon recorded in zircon (U–Th)/He thermochronometry. Earth and Planetary Science Letters 482, 222–235. https://doi.org/10.1016/j.epsl.2017.11.009

Kesson, S.E., 1975. Experimental investigation of reaction coronas on olivine in Apollo 14 high-grade breccias. Earth and Planetary Science Letters 28, 65–68. https://doi.org/10.1016/0012-821X(75)90074-6

Krogstad, E.J., Walker, R.J., 1994. High closure temperatures of the U-Pb system in large apatites from the Tin Mountain pegmatite, Black Hills, South Dakota, USA. Geochimica et Cosmochimica Acta 58, 3845–3853. https://doi.org/10.1016/0016-7037(94)90367-0

Kumar, Y., Tripathi, S., Sengupta, P., Jha, S.N., Nand, M., Trivedi, A., Sagdeo, A., Sharma, A., Tiwari, M.K., Sathe, V.G., Arya, A., 2024. Local Structure, Structural, Vibrational, and Optical Properties of Natural Zircon. physica status solidi (b) 261, 2400032. https://doi.org/10.1002/pssb.202400032

Lee, J.K.W., Williams, I.S., Ellis, D.J., 1997. Pb, U and Th diffusion in natural zircon. Nature 390, 159–162. https://doi.org/10.1038/36554

Merle, R.E., Nemchin, A.A., Grange, M.L., Whitehouse, M.J., Pidgeon, R.T., 2014. High resolution U-Pb ages of Ca-phosphates in Apollo 14 breccias: Implications for the age of the Imbrium impact. Meteoritics & Planetary Science 49, 2241–2251. https://doi.org/10.1111/maps.12395

Merle, R.E., Nemchin, A.A., Whitehouse, M.J., Pidgeon, R.T., Grange, M.L., Snape, J.F., Thiessen, F., 2017. Origin and transportation history of lunar breccia 14311. Meteoritics & Planetary Science 52, 842–858. https://doi.org/10.1111/maps.12835

Meyer, C., Williams, I.S., Compston, W., 1989. Workshop on Moon in Transition: Apollo 14, KREEP, and Evolved Lunar Rocks. Zircon-containing Rock Fragments within Apollo 14 Breccia Indicate Serial Magmatism from 4350 to 4000 Million Years 75–78.

Meyer, C., Williams, I.S., Compston, W., 1996. Uranium-lead ages for lunar zircons: Evidence for a prolonged period of granophyre formation from 4.32 to 3.88 Ga. Meteoritics & Planetary Science 31, 370–387. https://doi.org/10.1111/j.1945-5100.1996.tb02075.x

Meyer, C., 2008. 14311, in: The Lunar Sample Compendium. NASA.

Michael, G., Basilevsky, A., Neukum, G., 2018. On the history of the early meteoritic bombardment of the Moon: Was there a terminal lunar cataclysm? Icarus 302, 80–103. https://doi.org/10.1016/j.icarus.2017.10.046

Moser, D.E., Cupelli, C.L., Barker, I.R., Flowers, R.M., Bowman, J.R., Wooden, J., Hart, J.R., 2011. New zircon shock phenomena and their use for dating and reconstruction of large impact structures revealed by electron nanobeam (EBSD, CL, EDS) and isotopic U–Pb and (U–Th)/He analysis of the Vredefort domeThis article is one of a series of papers published in this Special Issue on the theme of Geochronology in honour of Tom Krogh. Canadian Journal of Earth Sciences 48, 117–139. https://doi.org/10.1139/E11-011

Murakami, T., Chakoumakos, B.C., Ewing, R.C., Lumpkin, G.R., Weber, W.J., 1991. Alpha-decay event damage in zircon. American Mineralogist 76, 1510–1532.

Nasdala, L., Irmer, G., Wolf, D., 1995. The degree of metamictization in zircon; a Raman spectroscopic study. European Journal of Mineralogy 7, 471–478.

Nemchin, A.A., Whitehouse, M.J., Pidgeon, R.T., Meyer, C., 2006. Oxygen isotopic signature of 4.4–3.9 Ga zircons as a monitor of differentiation processes on the Moon. Geochimica et Cosmochimica Acta 70, 1864–1872. https://doi.org/10.1016/j.gca.2005.12.009

Nemchin, A.A., Pidgeon, R.T., Whitehouse, M.J., Vaughan, J.P., Meyer, C., 2008. SIMS U–Pb study of zircon from Apollo 14 and 17 breccias: Implications for the evolution of lunar KREEP. Geochimica et Cosmochimica Acta 72, 668–689. https://doi.org/10.1016/j.gca.2007.11.009

Nemchin, A.A., Pidgeon, R.T., Healy, D., Grange, M.L., Whitehouse, M.J., Vaughan, J., 2010. The comparative behavior of apatite-zircon U-Pb systems in Apollo 14 breccias: Implications for the thermal history of the Fra Mauro Formation. Meteoritics & Planetary Science 44, 1717–1734. https://doi.org/10.1111/j.1945-5100.2009.tb01202.x

Paces, J.B., Miller Jr., J.D., 1993. Precise U-Pb ages of Duluth Complex and related mafic intrusions, northeastern Minnesota: Geochronological insights to physical, petrogenetic, paleomagnetic, and tectonomagmatic processes associated with the 1.1 Ga Midcontinent Rift System. Journal of Geophysical Research: Solid Earth 98, 13997–14013. https://doi.org/10.1029/93JB01159

Pidgeon, R.T., Nemchin, A.A., van Bronswijk, W., Geisler, T., Meyer, C., Compston, W., Williams, I.S., 2007. Complex history of a zircon aggregate from lunar breccia 73235.

Geochimica et Cosmochimica Acta 71, 1370–1381. https://doi.org/10.1016/j.gca.2006.11.021

Pidgeon, R.T., Nemchin, A.A., Kamo, S.L., 2011. Comparison of structures in zircons from lunar and terrestrial impactites. Can. J. Earth Sci. 48, 107–116. https://doi.org/10.1139/E10-037

Pidgeon, R.T., Merle, R.E., Grange, M.L., Nemchin, A.A., Whitehouse, M.J., 2016. Annealing of radiation damage in zircons from Apollo 14 impact breccia 14311: Implications for the thermal history of the breccia. Meteoritics & Planetary Science 51, 155–166. https://doi.org/10.1111/maps.12572

Rasmussen, B., Fletcher, I.R., Muhling, J.R., 2008. Pb/Pb geochronology, petrography and chemistry of Zr-rich accessory minerals (zirconolite, tranquillityite and baddeleyite) in mare basalt 10047. Geochimica et Cosmochimica Acta 72, 5799–5818. https://doi.org/10.1016/j.gca.2008.09.010

Rasmussen, C., Stockli, D.F., Erickson, T.M., Schmieder, M., 2020. Spatial U-Pb age distribution in shock-recrystallized zircon – A case study from the Rochechouart impact structure, France. Geochimica et Cosmochimica Acta 273, 313–330. https://doi.org/10.1016/j.gca.2020.01.017

Reddy, S.M., Timms, N.E., Pantleon, W., Trimby, P., 2007. Quantitative characterization of plastic deformation of zircon and geological implications. Contrib Mineral Petrol 153, 625–645. https://doi.org/10.1007/s00410-006-0174-4

Reimold, W.U., Gibson, R.L., 1996. Geology and evolution of the Vredefort impact structure, South Africa. Journal of African Earth Sciences 23, 125–162. https://doi.org/10.1016/S0899-5362(96)00059-0

Salje, E.K.H., Chrosch, J., Ewing, R.C., 1999. Is "metamictization" of zircon a phase transition? American Mineralogist 84, 1107–1116. https://doi.org/10.2138/am-1999-7-813

Sañudo-Wilhelmy, S.A., Flegal, A.R., 1994. Temporal variations in lead concentrations and isotopic composition in the Southern California Bight. Geochimica et Cosmochimica Acta 58, 3315–3320. https://doi.org/10.1016/0016-7037(94)90060-4

Schmitz, M.D., Bowring, S.A., 2001. U-Pb zircon and titanite systematics of the Fish Canyon Tuff: an assessment of high-precision U-Pb geochronology and its application to young volcanic rocks. Geochimica et Cosmochimica Acta 65, 2571–2587. https://doi.org/10.1016/S0016-7037(01)00616-0

Scoon, J.H., 1972. Chemical analyses of lunar samples. Presented at the Proceedings of the Third Lunar Science Conference, pp. 1335–1336.

Simonds, C.H., Phinney, W.C., Warner, J.L., McGee, P.E., Geeslin, J., Brown, R.W., Rhodes, J.M., 1977. Apollo 14 revisited, or breccias aren't so bad after all.

Singleton, A.C., Osinski, G.R., McCausland, P.J.A., Moser, D.E., 2011. Shock-induced changes in density and porosity in shock-metamorphosed crystalline rocks, Haughton impact structure, Canada. Meteoritics & Planetary Science 46, 1774–1786. https://doi.org/10.1111/j.1945-5100.2011.01290.x

Snape, J.F., Nemchin, A.A., Grange, M.L., Bellucci, J.J., Thiessen, F., Whitehouse, M.J., 2016. Phosphate ages in Apollo 14 breccias: Resolving multiple impact events with high precision U–Pb SIMS analyses. Geochimica et Cosmochimica Acta 174, 13–29. https://doi.org/10.1016/j.gca.2015.11.005

Spencer, C.J., Kirkland, C.L., Taylor, R.J.M., 2016. Strategies towards statistically robust interpretations of in situ U–Pb zircon geochronology. Geoscience Frontiers 7, 581–589. https://doi.org/10.1016/j.gsf.2015.11.006

Stadermann, F.J., Heusser, E., Jessberger, E.K., Lingner, S., Stöffler, D., 1991. The case for a younger Imbrium basin: New 40Ar-39Ar ages of Apollo 14 rocks. Geochimica et Cosmochimica Acta 55, 2339–2349. https://doi.org/10.1016/0016-7037(91)90108-H

Stöffler, D., Knöll, H.-D., 1977. Composition and origin of plagioclase, pyroxene, and olivine clasts of lunar breccias 14006, 14063, 14066, 14311, 14320, and 14321. Presented at the Proceedings of the Eighth Lunar Science Conference, pp. 1849–1867.

Taylor, G.J., 2009. Ancient Lunar Crust: Origin, Composition, and Implications. Elements 5, 17–22. https://doi.org/10.2113/gselements.5.1.17

Thiessen, F., Nemchin, A.A., Snape, J.F., Bellucci, J.J., Whitehouse, M.J., 2018. Apollo 12 breccia 12013: Impact-induced partial Pb loss in zircon and its implications for lunar geochronology. Geochimica et Cosmochimica Acta 230, 94–111. https://doi.org/10.1016/j.gca.2018.03.023

Timms, N.E., Reddy, S.M., Healy, D., Nemchin, A.A., Grange, M.L., Pidgeon, R.T., Hart, R., 2012. Resolution of impact-related microstructures in lunar zircon: A shock-deformation mechanism map. Meteoritics & Planetary Science 47, 120–141. https://doi.org/10.1111/j.1945-5100.2011.01316.x

Timms, N.E., Erickson, T.M., Pearce, M.A., Cavosie, A.J., Schmieder, M., Tohver, E., Reddy, S.M., Zanetti, M.R., Nemchin, A.A., Wittmann, A., 2017. A pressure-temperature phase diagram for zircon at extreme conditions. Earth-Science Reviews 165, 185–202. https://doi.org/10.1016/j.earscirev.2016.12.008

Trail, D., Barboni, M., McKeegan, K.D., 2020. Evidence for diverse lunar melt compositions and mixing of the pre-3.9 Ga crust from zircon chemistry. Geochimica et Cosmochimica Acta 284, 173–195. https://doi.org/10.1016/j.gca.2020.06.018

Valley, J.W., Spicuzza, M.J., Ushikubo, T., 2014. Correlated δ18O and [Ti] in lunar zircons: a terrestrial perspective for magma temperatures and water content on the Moon. Contrib Mineral Petrol 167, 956. https://doi.org/10.1007/s00410-013-0956-4

Vanderliek, D.M., Becker, H., Rocholl, A., 2021. Impact-related crystallization and modification of small zircons in Apollo 15 and 16 impactites at 4.2 Ga. Earth and Planetary Science Letters 576, 117216. https://doi.org/10.1016/j.epsl.2021.117216

Vermeesch, P., 2018. IsoplotR: A free and open toolbox for geochronology. Geoscience Frontiers, SPECIAL ISSUE: Frontiers in geoscience:A tribute to Prof. Xuanxue Mo 9, 1479–1493. https://doi.org/10.1016/j.gsf.2018.04.001

Warren, P.H., Taylor, G.J., Keil, K., Kallemeyn, G.W., Shirley, D.N., Wasson, J.T., 1983. Seventh Foray: Whitlockite-rich lithologies, a diopside-bearing troctolitic anorthosite, Ferroan anorthosites, and KREEP. Journal of Geophysical Research: Solid Earth 88, B151–B164. https://doi.org/10.1029/JB088iS01p0B151

Watson, E.B., Harrison, T.M., 2005. Zircon Thermometer Reveals Minimum Melting Conditions on Earliest Earth. Science 308, 841–844. https://doi.org/10.1126/science.1110873

Waychunas, G., Kempe, U., 2024. Activators in Minerals and the Role of Electronic Defects. Elements 20, 293–298. https://doi.org/10.2138/gselements.20.5.293

Weber, W.J., 1990. Radiation-induced defects and amorphization in zircon. Journal of Materials Research 5, 2687–2697. https://doi.org/10.1557/JMR.1990.2687

Weber, W.J., Ewing, R.C., Wang, L.-M., 1994. The radiation-induced crystalline-to-amorphous transition in zircon. Journal of Materials Research 9, 688–698. https://doi.org/10.1557/JMR.1994.0688

Wiedenbeck, M., Hanchar, J.M., Peck, W.H., Sylvester, P., Valley, J., Whitehouse, M., Kronz, A., Morishita, Y., Nasdala, L., Fiebig, J., Franchi, I., Girard, J.-P., Greenwood, R. c., Hinton, R., Kita, N., Mason, P. r. d., Norman, M., Ogasawara, M., Piccoli, P. m., Rhede, D., Satoh, H., Schulz-Dobrick, B., Skår, O., Spicuzza, Mj., Terada, K., Tindle, A., Togashi, S., Vennemann, T., Xie, Q., Zheng, Y.-F., 2004. Further Characterisation of the 91500 Zircon Crystal. Geostandards and Geoanalytical Research 28, 9–39. https://doi.org/10.1111/j.1751-908X.2004.tb01041.x

Woodhead, J.A., Rossman, G.R., Silver, L.T., 1991. The metamictization of zircon: Radiation dose-dependent structural characteristics. American Mineralogist 76, 74–82.

Wopenka, B., Jolliff, B.L., Zinner, E., Kremser, D.T., 1996. Trace element zoning and incipient metamictization in a lunar zircon; application of three microprobe techniques. American Mineralogist 81, 902–912. https://doi.org/10.2138/am-1996-7-813

Zhang, M., Salje, E.K.H., Farnan, I., Graeme-Barber, A., Daniel, P., Ewing, R.C., Clark, A.M., Leroux, H., 2000. Metamictization of zircon: Raman spectroscopic study. Journal of Physics: Condensed Matter 12, 1915–1925.

Zhang, B., Lin, Y., Moser, D.E., Hao, J., Shieh, S.R., Bouvier, A., 2019. Imbrium Age for Zircons in Apollo 17 South Massif Impact Melt Breccia 73155. Journal of Geophysical Research: Planets 124, 3205–3218. https://doi.org/10.1029/2019JE005992

Zhang, B., Lin, Y., Moser, D.E., Hao, J., Liu, Y., Zhang, J., Barker, I.R., Li, Q., Shieh, S.R., Bouvier, A., 2021. Radiogenic Pb mobilization induced by shock metamorphism of zircons in the Apollo 72255 Civet Cat norite clast. Geochimica et Cosmochimica Acta 302, 175–192. https://doi.org/10.1016/j.gca.2021.03.012

Chapter 5

Conclusions

The results of this dissertation unequivocally support the understanding that impact cratering can induce a range of shock microtextures in rocks both within the impact crater and ejected during the impact process. The variety of shock microtextures represent the heterogeneous temperature and pressures experienced by the target rock material during an impact. Additionally, this dissertation assists in determining how impact induced pressures and temperatures affect various planetary geochronometers.

The study of the Kamestastin Impact Structure in Chapter 2 addressed the complexities of bulk rock $^{40}Ar/^{39}Ar$ dating of impacted rocks that underwent various temperature and/or pressure conditions. The Kamestastin impact event produced a complex impact structure in Labrador, Canada that has anorthosite as a dominant target rock, making this site an analog for the anorthositic lunar surface. Macro- and micro-textural analyses via thin sections of various impactites within the crater structure were paired with $^{40}Ar/^{39}Ar$ step-heating analyses to determine what impact conditions were present in the impactites and how this relates to $^{40}Ar/^{39}Ar$ age results. When samples experienced high pressure conditions (35 GPa) and only slightly elevated temperatures (300°C), determined by the presence of shock microtextures that are only formed in high pressure conditions without temperature dependence, these samples were found to display complex, partially reset ages. However, when samples contained minerals that had mineralogical evidence of high temperatures (>1150°C), these samples had the highest probability of determining the true age of the Kamestastin impact event. Impact melt glass from the Kamestastin

crater was found to produce geologically meaningless ages, signifying this material at times cannot be reliably dated. Overall, this study proves the utility of pairing microtextural assessment of a sample with $^{40}Ar/^{39}Ar$ dating to more accurately determine the geologic significance of impactite ages.

Analyses of shock microtextures combined with the U-Pb geochronometer were applied to two different impact ejecta environments in chapters 3 and 4 to address the question if shock microtextures are associated with U-Pb age resetting. Individual zircons were isolated from Chicxulub ejecta in chapter 3 and the Apollo 14311 impact melt breccia in chapter 4. These individual zircons were then analyzed for microtextures via EBSD and CL imaging and were analyzed via SIMS for U-Pb ages and Ti-in-zircon thermometry (Ti-in-zircon thermometry was completed for chapter 4 only). Zircon microtextures had a dependence on elevated pressures and/or temperatures for formation which generally correlated with age resetting, similar to what was determined in chapter 2 on bulk rock samples from the Kamestastin impact structure ($^{40}Ar/^{39}Ar$ geochronometer). Zircon microtextures that signified only elevated pressures for formation showed unreliable age resetting. Zircons with microtextures that reflect elevated temperature environments, such as granular and FRIGN granular zircon (>900°C), were able to be fully reset to the timing of the impact events. The spatially resolved methodology of SIMS U-Pb dating also allowed for the targeting of impact shock features, which assisted in targeting granular regions of zircon crystals to attempt to determine the true impact age of the sample.

Additionally, while processing Apollo sample 14311 to extract zircon and apatite crystals in chapter 4, it was determined that a significant percentage of zircons were missed using standard zircon processing techniques, therefore bringing to light the complexities of processing extra-terrestrial materials. Therefore, chapter 4 addressed the sample processing methodology to

maximize zircon extraction from lunar materials. Zircon crystals, when extracted from heavily impacted materials from the lunar surface can be altered from impacts that affect their standard physical and/or chemical properties, can be difficult to crush and isolate zircon crystals without having adhering phases, and can be metamict which can cause damage to the crystal structure. A combination of these factors likely resulted in the lack of effectiveness of standard zircon processing techniques of density separation and UV light-assisted picking. I, therefore, suggest instead using a revised method of magnetic separations and chemical mapping via EDS in place of these previous standard mineral separation techniques. Assessing the microtextures of these previously missing zircons and adding the zircon U-Pb ages and Ti-in-zircon thermometry temperatures from these grains helped fill out the U-Pb history of a ~3.95 Ga age peak and a smearing of ages between 4.25-3.95 Ga from 14311 that was previously overlooked, determining the importance of analyzing a full dataset without sample extraction bias.

We add these results to the canon of studies combining microtextural analysis with geochronology applications to date impact crater environments. As we advance our exploration of planetary materials from Mars, asteroids, and the Moon in future sample return missions, this dissertation provides an additional framework on how to best process, understand, and date planetary materials. The variety of shock microtextures presented in this dissertation reflect the heterogeneous temperatures and pressures experienced by the target rock material during an impact event. Overall, these results provide a framework for determining which microtextures can be targeted to obtain possible geologically meaningful ages from multiple planetary geochronometers. While it will likely always be difficult to determine the age of an unknown impact event, by dating materials that have microtextural evidence of high temperature conditions, results from different radiometric dating systems (i.e. U-Pb, $^{40}Ar/^{39}Ar$) can converge towards the

true age of an undated impact event. With the complex heterogeneous conditions present in impact cratering environments, continual research and assessment of impactites is needed to keep furthering our understanding of impact cratering pressure, thermal, and petrological-mineralogical effects and, how impact craters can best be dated.

All Dissertation References

Alvarez, L.W., Alvarez, W., Asaro, F., Michel, H.V., 1980. Extraterrestrial Cause for the Cretaceous-Tertiary Extinction. Science 208, 1095–1108. https://doi.org/10.1126/science.208.4448.1095

Amor, K., Hesselbo, S.P., Porcelli, D., Price, A., Saunders, N., Sykes, M., Stevanović, J., MacNiocaill, C., 2019. The Mesoproterozoic Stac Fada proximal ejecta blanket, NW Scotland: constraints on crater location from field observations, anisotropy of magnetic susceptibility, petrography and geochemistry. Journal of the Geological Society 176, 830–846. https://doi.org/10.1144/jgs2018-093

Antonenko, I., Osinski, G.R., Battler, M., Beauchamp, M., Cupelli, L., Chanou, A., Francis, R., Mader, M.M., Marion, C., McCullough, E., Pickersgill, A.E., Preston, L.J., Shankar, B., Unrau, T., Veillette, D., 2013. Issues of geologically-focused situational awareness in robotic planetary missions: Lessons from an analogue mission at Mistastin Lake impact structure, Labrador, Canada. Advances in Space Research, Lunar Exploration - II 52, 272–284. https://doi.org/10.1016/j.asr.2012.11.024

Arenillas, I., Arz, J.A., Grajales-Nishimura, J.M., Murillo-Muñetón, G., Alvarez, W., Camargo-Zanoguera, A., Molina, E., Rosales-Domínguez, C., 2006. Chicxulub impact event is Cretaceous/Paleogene boundary in age: New micropaleontological evidence. Earth and Planetary Science Letters 249, 241–257. https://doi.org/10.1016/j.epsl.2006.07.020

Barboni, M., Szymanowski, D., Schoene, B., Dauphas, N., Zhang, Z.J., Chen, X., McKeegan, K.D., 2024. High-precision U-Pb zircon dating identifies a major magmatic event on the Moon at 4.338 Ga. Science Advances 10, eadn9871. https://doi.org/10.1126/sciadv.adn9871

Barlow, N.G., 2015. Constraining geologic properties and processes through the use of impact craters. Geomorphology, Planetary Geomorphology: Proceedings of the 45th Annual Binghamton Geomorphology Symposium, held 12-14 September 2014 in Knoxville, Tennessee, USA 240, 18–33. https://doi.org/10.1016/j.geomorph.2014.08.027

Bermudez, J.P., Osinski, G.R., Tolometti, G.D., Chinchalkar, N.S., 2022. Impact-Generated Hydrothermal Alteration at the Mistastin Lake Impact Structure, Canada 2678, 2671.

Bogard, D.D., 1995. Impact ages of meteorites: A synthesis. Meteoritics 30, 244–268. https://doi.org/10.1111/j.1945-5100.1995.tb01124.x

Bohor, B.F., Foord, E.E., Betterton, W.J., 1989. Trace minerals in K-T boundary clays. Meteoritics 24.

Bohor, B.F., 1990. Shock-induced microdeformations in quartz and other mineralogical indications of an impact event at the Cretaceous-Tertiary boundary. Tectonophysics, Cryptoexplosions and catastrophes in the geological record, with a special focus on the Vredefort structure 171, 359–372. https://doi.org/10.1016/0040-1951(90)90110-T

Bohor, B.F., Glass, B.P., 1995. Origin and diagenesis of K/T impact spherules—From Haiti to Wyoming and beyond. Meteoritics & Planetary Science 30, 182–198.

Buchner, E., Schwarz, W.H., Schmieder, M., Trieloff, M., 2010. Establishing a 14.6 ± 0.2 Ma age for the Nördlinger Ries impact (Germany)—A prime example for concordant isotopic ages from various dating materials. Meteoritics & Planetary Science 45, 662–674. https://doi.org/10.1111/j.1945-5100.2010.01046.x

Budd, D.A., Hammes, U., Ward, W.B., 2000. Cathodoluminescence in Calcite Cements: New Insights on Pb and Zn Sensitizing, Mn Activation, and Fe Quenching at Low Trace-Element Concentrations. Journal of Sedimentary Research 70, 217–226. https://doi.org/10.1306/2DC4090C-0E47-11D7-8643000102C1865D

Burnham, A.D., Berry, A.J., 2012. An experimental study of trace element partitioning between zircon and melt as a function of oxygen fugacity. Geochimica et Cosmochimica Acta 95, 196–212. https://doi.org/10.1016/j.gca.2012.07.034

Bush, M.A., Horton, B.K., Murphy, M.A., Stockli, D.F., 2016. Detrital record of initial basement exhumation along the Laramide deformation front, southern Rocky Mountains. Tectonics 35, 2117–2130. https://doi.org/10.1002/2016TC004194

Cassata, W.S., Shuster, D.L., Renne, P.R., Weiss, B.P., 2010. Evidence for shock heating and constraints on Martian surface temperatures revealed by 40Ar/39Ar thermochronometry of Martian meteorites. Geochimica et Cosmochimica Acta 74, 6900–6920. https://doi.org/10.1016/j.gca.2010.08.027

Cassata, W.S., Renne, P.R., 2013. Systematic variations of argon diffusion in feldspars and implications for thermochronometry. Geochimica et Cosmochimica Acta 112, 251–287. https://doi.org/10.1016/j.gca.2013.02.030

Cavosie, A.J., Erickson, T.M., Timms, N.E., Reddy, S.M., Talavera, C., Montalvo, S.D., Pincus, M.R., Gibbon, R.J., Moser, D., 2015. A terrestrial perspective on using ex situ shocked zircons to date lunar impacts. Geology 43, 999–1002. https://doi.org/10.1130/G37059.1

Cavosie, A.J., Timms, N.E., Erickson, T.M., Hagerty, J.J., Hörz, F., 2016. Transformations to granular zircon revealed: Twinning, reidite, and ZrO2 in shocked zircon from Meteor Crater (Arizona, USA). Geology 44, 703–706. https://doi.org/10.1130/G38043.1

Cavosie, A.J., Timms, N.E., Ferrière, L., Rochette, P., 2018. FRIGN zircon—The only terrestrial mineral diagnostic of high-pressure and high-temperature shock deformation. Geology 46, 891–894. https://doi.org/10.1130/G45079.1

Cavosie, A.J., Alwmark, S., Baratoux, D., Consolmagno, G., Ferrière, L., Hauser, N., Kenkmann, T., Koeberl, C., Osinski, G.R., PickersgilL, A.E., 2024. A Diagonstic Impact Criteria List to

Confirm Terrestrial Impact Craters by the Meteoritical Society Impact Cratering Committee - Work in Progress. Presented at the 86th Annual Meeting of the Meteoritical Society.

Chamberlain, K.R., Bowring, S.A., 2000. Apatite–feldspar U–Pb thermochronometer: a reliable, mid-range (~450°C), diffusion-controlled system. Chemical Geology, What are we dating? Understanding the Crystallogernesis of U-Pb 172, 173–200. https://doi.org/10.1016/S0009-2541(00)00242-4

Chanou, A., Grieve, R.A.F., Osinski, G.R., 2015. Formation of Ballen in Silica by Thermal Shock. Presented at the Bridging the Gap III: Impact Cratering In Nature, Experiments, and Modeling.

Cherniak, D.J., Lanford, W.A., Ryerson, F.J., 1991. Lead diffusion in apatite and zircon using ion implantation and Rutherford Backscattering techniques. Geochimica et Cosmochimica Acta 55, 1663–1673. https://doi.org/10.1016/0016-7037(91)90137-T

Cherniak, D.J., Watson, E.B., 2001. Pb diffusion in zircon. Chemical Geology, What are we dating? Understanding the Crystallogernesis of U-Pb 172, 5–24. https://doi.org/10.1016/S0009-2541(00)00233-3

Citron, R.I., Smith, D.E., Stewart, S.T., Hood, L.L., Zuber, M.T., 2024. The South Pole-Aitken Basin: Constraints on Impact Excavation, Melt, and Ejecta. Geophysical Research Letters 51, e2024GL110034. https://doi.org/10.1029/2024GL110034

Cohen, B.A., Swindle, T.D., Kring, D.A., 2000. Support for the Lunar Cataclysm Hypothesis from Lunar Meteorite Impact Melt Ages. Science 290, 1754–1756. https://doi.org/10.1126/science.290.5497.1754

Collins, G.S., Melosh, H.J., Osinski, G.R., 2012. The Impact-Cratering Process. Elements 8, 25–30. https://doi.org/10.2113/gselements.8.1.25

Cooper, J.R., Crelling, J.C., Rimmer, S.M., Whittington, A.G., 2007. Coal metamorphism by igneous intrusion in the Raton Basin, CO and NM: Implications for generation of volatiles. International Journal of Coal Geology, TSOP 2005 71, 15–27. https://doi.org/10.1016/j.coal.2006.05.007

Corfu, F., 2013. A century of U-Pb geochronology: The long quest towards concordance. GSA Bulletin 125, 33–47. https://doi.org/10.1130/B30698.1

Corfu, F., 2015. Uranium–Lead, Zircon, in: Jack Rink, W., Thompson, J.W. (Eds.), Encyclopedia of Scientific Dating Methods, Encyclopedia of Earth Sciences Series. Springer Netherlands, Dordrecht, pp. 914–918. https://doi.org/10.1007/978-94-007-6304-3_23

Coutts, D.S., Matthews, W.A., Hubbard, S.M., 2019. Assessment of widely used methods to derive depositional ages from detrital zircon populations. Geoscience Frontiers 10, 1421–1435. https://doi.org/10.1016/j.gsf.2018.11.002

Cox, M.A., Erickson, Timmons M., Schmieder, M., Christoffersen, R., Ross, D., Cavosie, A.J., Bland, P.A., Kring, D.A., 2020. High-resolution microstructural and compositional analyses of shock deformed apatite from the peak ring of the Chicxulub impact crater. Meteoritics & Planetary Science 55.

Crow, C.A., McKeegan, K.D., Moser, D.E., 2017. Coordinated U–Pb geochronology, trace element, Ti-in-zircon thermometry and microstructural analysis of Apollo zircons. Geochimica et Cosmochimica Acta 202, 264–284. https://doi.org/10.1016/j.gca.2016.12.019

Crow, C.A., Moser, D.E., McKeegan, K.D., 2019. Shock metamorphic history of >4 Ga Apollo 14 and 15 zircons. Meteoritics & Planetary Science 54, 181–201. https://doi.org/10.1111/maps.13184

Crow, C.A., Tong, C., Erickson, T.M., Moser, D.E., Bell, A.S., Kelly, N.M., Prissel, T.C., Hyde, B.C., 2024. Impact origin of lunar zircon melt inclusions in Apollo impact melt breccia 14311. Meteoritics & Planetary Science 59, 1509–1522. https://doi.org/10.1111/maps.14162

Crozaz, G., Drozd, R., Hohenberg, C.M., Hoyt, Jr., H.P., Ragan, D., Walker, R.M., Yuhas, D., 1972. Solar flare and galactic cosmic-ray studies of Apollo 14 and 15 samples. Presented at the 3rd Lunar Science Conference.

Currie, K.L., 1971. Geology of the Resurgent Cryptoexplosion Crater at Mistastin Lake, Labrador. Geological Survey of Canada Bulletin: Department of energy, mines, and resources.

Dalrymple, G.B., Ryder, G., 1996. Argon-40/argon-39 age spectra of Apollo 17 highlands breccia samples by laser step heating and the age of the Serenitatis basin. Journal of Geophysical Research: Planets 101, 26069–26084. https://doi.org/10.1029/96JE02806

de Graaff, S.J., Kaskes, P., Déhais, T., Goderis, S., Debaille, V., Ross, C.H., Gulick, S.P.S., Feignon, J.-G., Ferrière, L., Koeberl, C., Smit, J., Mattielli, N., Claeys, P., 2021. New insights into the formation and emplacement of impact melt rocks within the Chicxulub impact structure, following the 2016 IODP-ICDP Expedition 364. GSA Bulletin 134, 293–315. https://doi.org/10.1130/B35795.1

Deloule, E., Chaussidon, M., Glass, B.P., Koeberl, C., 2001. U–Pb isotopic study of relict zircon inclusions recovered from Muong Nong-type tektites. Geochimica et Cosmochimica Acta 65, 1833–1838. https://doi.org/10.1016/S0016-7037(01)00548-8

Deutsch, A., Schärer, U., 1990. Isotope systematics and shock-wave metamorphism: I. U-Pb in zircon, titanite and monazite, shocked experimentally up to 59 GPa. Geochimica et Cosmochimica Acta 54, 3427–3434. https://doi.org/10.1016/0016-7037(90)90295-V

Diaz, C.A., Flowers, R.M., Crow, C., Metcalf, J.R., Economos, R., Erickson, T., Boyce, J.W., Davis, J., Brounce, M., Lehman-Franco, K., Schoene, B., n.d. Phosphate (U-Th)/He

Thermochronology of Apollo 14 Melt Breccia 14311. Presented at the 55th Lunar and Planetary Science Conference (LPSC), The Woodlands, TX.

Dickinson, J.E., Hess, P.C., 1982. Zircon saturation in lunar basalts and granites. Earth and Planetary Science Letters 57, 336–344. https://doi.org/10.1016/0012-821X(82)90154-6

Dickinson, W.R., Gehrels, G.E., 2009. Use of U–Pb ages of detrital zircons to infer maximum depositional ages of strata: A test against a Colorado Plateau Mesozoic database. Earth and Planetary Science Letters 288, 115–125. https://doi.org/10.1016/j.epsl.2009.09.013

Drozd, R.J., Hohenberg, C.M., Morgan, C.J., Ralston, C.E., 1974. Cosmic-ray exposure history at the Apollo 16 and other lunar sites: lunar surface dynamics. Geochimica et Cosmochimica Acta 38, 1625–1642. https://doi.org/10.1016/0016-7037(74)90178-1

Erickson, T.M., Cavosie, A.J., Moser, D.E., Barker, I.R., Radovan, H.A., 2013. Correlating planar microstructures in shocked zircon from the Vredefort Dome at multiple scales: Crystallographic modeling, external and internal imaging, and EBSD structural analysis. American Mineralogist 98, 53–65. https://doi.org/10.2138/am.2013.4165

Erickson, T.M., Kirkland, C.L., Timms, N.E., Cavosie, A.J., Davison, T.M., 2020. Precise radiometric age establishes Yarrabubba, Western Australia, as Earth's oldest recognised meteorite impact structure. Nat Commun 11, 300. https://doi.org/10.1038/s41467-019-13985-7

Ewing, R.C., 1994. The metamict state: 1993 — the centennial. Nuclear Instruments and Methods in Physics Research Section B: Beam Interactions with Materials and Atoms 91, 22–29. https://doi.org/10.1016/0168-583X(94)96186-7

Farnan, I., Balan, E., Pickard, C.J., Mauri, F., 2003. The effect of radiation damage on local structure in the crystalline fraction of ZrSiO4: Investigating the 29Si NMR response to pressure in zircon and reidite. American Mineralogist 88, 1663–1667. https://doi.org/10.2138/am-2003-11-1205

Fernandes, V.A., Fritz, J., Weiss, B.P., Garrick-Bethell, I., Shuster, D.L., 2013. The bombardment history of the Moon as recorded by 40Ar-39Ar chronology. Meteoritics & Planetary Science 48, 241–269. https://doi.org/10.1111/maps.12054

Ferreira, J., Leite, E., Vasconcelos, M., Crósta, A., 2015. 3D gravity modeling of impact structures in basaltic formations in Brazil: Part I – Vargeão, Santa Catarina. Revista Brasileira de Geofísica 33, 319. https://doi.org/10.22564/rbgf.v33i2.723

Ferrière, L., Koeberl, C., Reimold, W.U., 2009. Characterisation of ballen quartz and cristobalite in impact breccias: new observations and constraints on ballen formation. European Journal of Mineralogy 21, 203–217. https://doi.org/10.1127/0935-1221/2009/0021-1898

Ferrière, L., Koeberl, C., Libowitzky, E., Reimold, W.U., Greshake, A., Brandstätter, F., 2010. Ballen quartz and cristobalite in impactites: New investigations, in: Large Meteorite Impacts and Planetary Evolution IV. Geological Society of America, pp. 609–618. https://doi.org/10.1130/2010.2465(29)

Ferrière, L., Osinski, G.R., 2012. Shock Metamorphism. In: Osinski, G.R., Pierazzo, E. (Eds.), Impact Cratering: Processes and Products, 1st ed., 106-124, John Wiley & Sons, Ltd. https://doi.org/10.1002/9781118447307

Ferriss, E.D.A., Essene, E.J., Becker, U., 2008. Computational study of the effect of pressure on the Ti-in-zircon geothermometer. European Journal of Mineralogy 20, 745–755. https://doi.org/10.1127/0935-1221/2008/0020-1860

Ferry, J.M., Watson, E.B., 2007. New thermodynamic models and revised calibrations for the Ti-in-zircon and Zr-in-rutile thermometers. Contrib Mineral Petrol 154, 429–437. https://doi.org/10.1007/s00410-007-0201-0

Fiorillo, A.R., McCarthy, P.J., Shimer, G., Suarez, M.B., Takasaki, R., Chinzorig, T., Kobayashi, Y., O'Sullivan, P., Orphys, E., 2024. New Dinosaur Ichnological, Sedimentological, and Geochemical Data from a Cretaceous High-Latitude Terrestrial Greenhouse Ecosystem, Nanushuk Formation, North Slope, Alaska. Geosciences 14, 36. https://doi.org/10.3390/geosciences14020036

Foster, W.R., 1948. Useful aspects of the fluorescence of accessory-mineral-zircon*. American Mineralogist 33, 724–735.

French, B.M., 1998. Traces of Catastrophe: A Handbook of Shock-Metamorphic Effects in Terrestrial Meteorite Impact Structures.

French, B.M., Koeberl, C., 2010. The convincing identification of terrestrial meteorite impact structures: What works, what doesn't, and why. Earth-Science Reviews 98, 123–170. https://doi.org/10.1016/j.earscirev.2009.10.009

Fritz J., Greshake A., Stoffler D., 2005. Micro-Raman spectroscopy of plagioclase and maskelynite in Martian meteorites: Evidence of progressive shock metamorphism. Antarctic meteorite research 18, 96–116. https://doi.org/10.15094/00006067

Fu, B., Page, F.Z., Cavosie, A.J., Fournelle, J., Kita, N.T., Lackey, J.S., Wilde, S.A., Valley, J.W., 2008. Ti-in-zircon thermometry: applications and limitations. Contrib Mineral Petrol 156, 197–215. https://doi.org/10.1007/s00410-008-0281-5

Gaffney, A.M., Borg, L.E., Asmerom, Y., Charles K. Shearer, Burger, P.V., 2011. Disturbance of isotope systematics during experimental shock and thermal metamorphism of a lunar basalt with implications for Martian meteorite chronology. Meteoritics & Planetary Science 46, 35–52. https://doi.org/10.1111/j.1945-5100.2010.01137.x

Gibson, R.L., Armstrong, R.A., Reimold, W.U., 1997. The age and thermal evolution of the Vredefort impact structure: A single-grain U-Pb zircon study. Geochimica et Cosmochimica Acta 61, 1531–1540. https://doi.org/10.1016/S0016-7037(97)00013-6

Glass, B.P., Liu, S., Leavens, P.B., 2002. Reidite: An impact-produced high-pressure polymorph of zircon found in marine sediments. American Mineralogist 87, 562–565. https://doi.org/10.2138/am-2002-0420

Glass, B.P., Simonson, B.M., 2012. Distal Impact Ejecta Layers: Spherules and More. Elements 8, 43–48. https://doi.org/10.2113/gselements.8.1.43

Goldsmith, J.R., 1980. The melting and breakdown reactions of anorthite at high pressures and temperatures. American Mineralogist 65, 272–284.

Goltrant, O., Leroux, H., Doukhan, J.-C., Cordier, P., 1992. Formation mechanisms of planar deformation features in naturally shocked quartz. Physics of the Earth and Planetary Interiors 74, 219–240. https://doi.org/10.1016/0031-9201(92)90012-K

Götze, J., 2012. Application of Cathodoluminescence Microscopy and Spectroscopy in Geosciences. Microscopy and Microanalysis 18, 1270–1284. https://doi.org/10.1017/S1431927612001122

Grange, M.L., Nemchin, A.A., Pidgeon, R.T., Timms, N., Muhling, J.R., Kennedy, A.K., 2009. Thermal history recorded by the Apollo 17 impact melt breccia 73217. Geochimica et Cosmochimica Acta 73, 3093–3107. https://doi.org/10.1016/j.gca.2009.02.032

Grange, M.L., Nemchin, A.A., Timms, N., Pidgeon, R.T., Meyer, C., 2011. Complex magmatic and impact history prior to 4.1Ga recorded in zircon from Apollo 17 South Massif aphanitic breccia 73235. Geochimica et Cosmochimica Acta 75, 2213–2232. https://doi.org/10.1016/j.gca.2011.01.036

Grange, M.L., Pidgeon, R.T., Nemchin, A.A., Timms, N.E., Meyer, C., 2013. Interpreting U–Pb data from primary and secondary features in lunar zircon. Geochimica et Cosmochimica Acta 101, 112–132. https://doi.org/10.1016/j.gca.2012.10.013

Grange, M.L., Nemchin, A.A., Pidgeon, R.T., 2013. The effect of 1.9 and 1.4 Ga impact events on 4.3 Ga zircon and phosphate from an Apollo 15 melt breccia. Journal of Geophysical Research: Planets 118, 2180–2197. https://doi.org/10.1002/jgre.20167

Grieve, R.A.F., 1975. Petrology and chemistry of the impact melt at Mistastin Lake crater, Labrador. GSA Bulletin 86, 1617–1629. https://doi.org/10.1130/0016-7606(1975)86<1617:PACOTI>2.0.CO;2

Grieve, Richard A. F., 2006. Mistastin, in: Impact Structures in Canada. Earth Science Sector Natural Resources Canada, Geological Association of Canada, pp. 115–120.

Grieve, R.A.F., Therriault, A.M., 2012. Impactites: their characteristics and spatial distribution, in: Impact Cratering: Processes and Products. John Wiley & Sons, Ltd.

Grieve, R.A.F., Osinski, G.R., Tornabene, L.L., 2014. Chapter 4 - Planetary Impacts, in: Spohn, T., Breuer, D., Johnson, T.V. (Eds.), Encyclopedia of the Solar System (Third Edition). Elsevier, Boston, pp. 83–99. https://doi.org/10.1016/B978-0-12-415845-0.00004-9

Gulick, S.P.S., Barton, P.J., Christeson, G.L., Morgan, J.V., McDonald, M., Mendoza-Cervantes, K., Pearson, Z.F., Surendra, A., Urrutia-Fucugauchi, J., Vermeesch, P.M., Warner, M.R., 2008. Importance of pre-impact crustal structure for the asymmetry of the Chicxulub impact crater. Nature Geosci 1, 131–135. https://doi.org/10.1038/ngeo103

Haskin, L.A., Korotev, R.L., Rockow, K.M., Jolliff, B.L., 2010. The case for an Imbrium origin of the Apollo thorium-rich impact-melt breccias. Meteoritics & Planetary Science 33, 959–975. https://doi.org/10.1111/j.1945-5100.1998.tb01703.x

Hayne, P.O., Bandfield, J.L., Siegler, M.A., Vasavada, A.R., Ghent, R.R., Williams, J.-P., Greenhagen, B.T., Aharonson, O., Elder, C.M., Lucey, P.G., Paige, D.A., 2017. Global Regolith Thermophysical Properties of the Moon From the Diviner Lunar Radiometer Experiment. Journal of Geophysical Research: Planets 122, 2371–2400. https://doi.org/10.1002/2017JE005387

Hazen, R.M., Finger, L.W., 1979. Crystal structure and compressibility of zircon at high pressure. American Mineralogist 64, 196–201.

Head, J.W., Fassett, C.I., Kadish, S.J., Smith, D.E., Zuber, M.T., Neumann, G.A., Mazarico, E., 2010. Global Distribution of Large Lunar Craters: Implications for Resurfacing and Impactor Populations. Science 329, 1504–1507. https://doi.org/10.1126/science.1195050

Heath, M., Phillips, D., Matchan, E.L., 2020. Basalt lava flows of the intraplate Newer Volcanic Province in south-east Australia (Melbourne region): 40Ar/39Ar geochronology reveals ~8 Ma of episodic activity. Journal of Volcanology and Geothermal Research 389, 106730. https://doi.org/10.1016/j.jvolgeores.2019.106730

Herriott, T.M., Crowley, J.L., Schmitz, M.D., Wartes, M.A., Gillis, R.J., 2019. Exploring the law of detrital zircon: LA-ICP-MS and CA-TIMS geochronology of Jurassic forearc strata, Cook Inlet, Alaska, USA. Geology 47, 1044–1048. https://doi.org/10.1130/G46312.1

Hildebrand, A.R., Boynton, W.V., 1990. Proximal Cretaceous-Tertiary Boundary Impact Deposits in the Caribbean. Science 248, 843–847. https://doi.org/10.1126/science.248.4957.843

Hildebrand, A.R., Penfield, G.T., Kring, D.A., Pilkington, M., Camargo Z., A., Jacobsen, S.B., Boynton, W.V., 1991. Chicxulub Crater: A possible Cretaceous/Tertiary boundary impact crater on the Yucatán Peninsula, Mexico. Geology 19, 867–871. https://doi.org/10.1130/0091-7613(1991)019<0867:CCAPCT>2.3.CO;2

Hopkins, M.D., Mojzsis, S.J., 2015. A protracted timeline for lunar bombardment from mineral chemistry, Ti thermometry and U–Pb geochronology of Apollo 14 melt breccia zircons. Contrib Mineral Petrol 169, 1–18. https://doi.org/10.1007/s00410-015-1123-x

Hoskin, P. w. o., Black, L. p., 2000. Metamorphic zircon formation by solid-state recrystallization of protolith igneous zircon. Journal of Metamorphic Geology 18, 423–439. https://doi.org/10.1046/j.1525-1314.2000.00266.x

Howard, C.J., Hill, R.J., Reichert, B.E., 1988. Structures of ZrO2 polymorphs at room temperature by high-resolution neutron powder diffraction. Acta Cryst B 44, 116–120. https://doi.org/10.1107/S0108768187010279

Howard, B.L., Sharman, G.R., Crowley, J.L., Wersan, E.R., 2025. The leaky chronometer: Evidence for systematic cryptic Pb loss in laser ablation U-Pb dating of zircon relative to CA-TIMS. Terra Nova 37, 19–25. https://doi.org/10.1111/ter.12742

Hu, J., Sharp, T.G., 2022. Formation, preservation and extinction of high-pressure minerals in meteorites: temperature effects in shock metamorphism and shock classification. Prog Earth Planet Sci 9, 6. https://doi.org/10.1186/s40645-021-00463-2

Huber, M.S., Črne, A.E., McDonald, I., Hecht, L., Melezhik, V.A., Koeberl, C., 2014. Impact spherules from Karelia, Russia: Possible ejecta from the 2.02 Ga Vredefort impact event. Geology 42, 375–378. https://doi.org/10.1130/G35231.1

Izett, G.A., 1987. The Cretaceous-Tertiary (K-T) boundary interval, Raton Basin, Colorado and New Mexico, and its content of shock-metamorphosed minerals; implication concerning the K-T boundary impact-extinction theory (No. 87–606), Open-File Report. U.S. Geological Survey,. https://doi.org/10.3133/ofr87606

Izett, G.A., 1991. Tektites in Cretaceous-Tertiary boundary rocks on Haiti and their bearing on the Alvarez Impact Extinction Hypothesis. Journal of Geophysical Research: Planets 96, 20879–20905. https://doi.org/10.1029/91JE02249

James, S., Chandran, S.R., Aswathi, J., Padmakumar, D., Sajinkumar, K.S., 2023. Geologic, geomorphic, tectonic, and paleoclimatic controls on the distribution and preservation of Chicxulub distal ejecta: A global perspective. Earth-Science Reviews 244, 104545. https://doi.org/10.1016/j.earscirev.2023.104545

Jaret, S.J., Woerner, W.R., Phillips, B.L., Ehm, L., Nekvasil, H., Wright, S.P., Glotch, T.D., 2015. Maskelynite formation via solid-state transformation: Evidence of infrared and X-ray anisotropy. Journal of Geophysical Research: Planets 120, 570–587. https://doi.org/10.1002/2014JE004764

Jaret, S.J., Hemming, S.R., Rasbury, E.T., Thompson, L.M., Glotch, T.D., Ramezani, J., Spray, J.G., 2018. Context matters – Ar–Ar results from in and around the Manicouagan Impact

Structure, Canada: Implications for martian meteorite chronology. Earth and Planetary Science Letters 501, 78–89. https://doi.org/10.1016/j.epsl.2018.08.016

Jaumann, R., Hiesinger, H., Anand, M., Crawford, I.A., Wagner, R., Sohl, F., Jolliff, B.L., Scholten, F., Knapmeyer, M., Hoffmann, H., Hussmann, H., Grott, M., Hempel, S., Köhler, U., Krohn, K., Schmitz, N., Carpenter, J., Wieczorek, M., Spohn, T., Robinson, M.S., Oberst, J., 2012. Geology, geochemistry, and geophysics of the Moon: Status of current understanding. Planetary and Space Science, Scientific Preparations For Lunar Exploration 74, 15–41. https://doi.org/10.1016/j.pss.2012.08.019

Jolliff, B.L., Gillis, J.J., Haskin, L.A., Korotev, R.L., Wieczorek, M.A., 2000. Major lunar crustal terranes: Surface expressions and crust-mantle origins. Journal of Geophysical Research: Planets 105, 4197–4216. https://doi.org/10.1029/1999JE001103

Jourdan, F., Renne, P.R., Reimold, W.U., 2007. The problem of inherited 40Ar* in dating impact glass by the 40Ar/39Ar method: Evidence from the Tswaing impact crater (South Africa). Geochimica et Cosmochimica Acta 71, 1214–1231. https://doi.org/10.1016/j.gca.2006.11.013

Jourdan, F., Renne, P.R., Reimold, W.U., 2009. An appraisal of the ages of terrestrial impact structures. Earth and Planetary Science Letters 286, 1–13. https://doi.org/10.1016/j.epsl.2009.07.009

Jourdan, F., Moynier, F., Koeberl, C., Eroglu, S., 2011. 40Ar/39Ar age of the Lonar crater and consequence for the geochronology of planetary impacts. Geology 39, 671–674. https://doi.org/10.1130/G31888.1

Jourdan, F., 2012. The 40Ar/39Ar dating technique applied to planetary sciences and terrestrial impacts. Australian Journal of Earth Sciences 59, 199–224. https://doi.org/10.1080/08120099.2012.644404

Joy, K.H., Snape, J.F., Nemchin, A.A., Tartèse, R., Martin, D.M., Whitehouse, M.J., Vishnyakov, V., Pernet-Fisher, J.F., Kring, D.A., 2020. Timing of geological events in the lunar highlands recorded in shocked zircon-bearing clasts from Apollo 16. Royal Society Open Science 7, 200236. https://doi.org/10.1098/rsos.200236

Kalleson, E., Corfu, F., Dypvik, H., 2009. U–Pb systematics of zircon and titanite from the Gardnos impact structure, Norway: Evidence for impact at 546 Ma? Geochimica et Cosmochimica Acta 73, 3077–3092. https://doi.org/10.1016/j.gca.2009.02.020

Kamo, S.L., Krogh, T.E., 1995. Chicxulub crater source for shocked zircon crystals from the Cretaceous-Tertiary boundary layer, Saskatchewan: Evidence from new U-Pb data. Geology 23, 281–284. https://doi.org/10.1130/0091-7613(1995)023<0281:CCSFSZ>2.3.CO;2

Kamo, S.L., Reimold, W.U., Krogh, T.E., Colliston, W.P., 1996. A 2.023 Ga age for the Vredefort impact event and a first report of shock metamorphosed zircons in pseudotachylitic breccias

and Granophyre. Earth and Planetary Science Letters 144, 369–387. https://doi.org/10.1016/S0012-821X(96)00180-X

Kamo, S.L., Lana, C., Morgan, J.V., 2011. U–Pb ages of shocked zircon grains link distal K–Pg boundary sites in Spain and Italy with the Chicxulub impact. Earth and Planetary Science Letters 310, 401–408. https://doi.org/10.1016/j.epsl.2011.08.031

Kayama, M., Gucsik, A., Nishido, H., Ninagawa, K., Tsuchiyama, A., 2009. Cathodoluminescence and Raman Spectroscopic Characterization of Experimentally Shocked Plagioclase. American Institute of Physics Conference Proceedings 1163, 86–95. https://doi.org/10.1063/1.3222897

Keller, G., Adatte, T., Berner, Z., Harting, M., Baum, G., Prauss, M., Tantawy, A., Stueben, D., 2007. Chicxulub impact predates K–T boundary: New evidence from Brazos, Texas. Earth and Planetary Science Letters 255, 339–356. https://doi.org/10.1016/j.epsl.2006.12.026

Kelley, S.P., Sherlock, S.C., 2012. The geochronology of impact craters, in: Impact Cratering: Processes and Products. John Wiley & Sons, Ltd.

Kelly, N.M., Flowers, R.M., Metcalf, J.R., Mojzsis, S.J., 2018. Late accretion to the Moon recorded in zircon (U–Th)/He thermochronometry. Earth and Planetary Science Letters 482, 222–235. https://doi.org/10.1016/j.epsl.2017.11.009

Kenny, G.G., Morales, L.F., Whitehouse, M.J., Petrus, J.A., Kamber, B.S., 2017. The formation of large neoblasts in shocked zircon and their utility in dating impacts. Geology 45, 1003–1006. https://doi.org/10.1130/G39328.1

Kenny, G.G., Schmieder, M., Whitehouse, M.J., Nemchin, A.A., Morales, L.F.G., Buchner, E., Bellucci, J.J., Snape, J.F., 2019. A new U-Pb age for shock-recrystallised zircon from the Lappajärvi impact crater, Finland, and implications for the accurate dating of impact events. Geochimica et Cosmochimica Acta 245, 479–494. https://doi.org/10.1016/j.gca.2018.11.021

Keppie, J.D., Dostal, J., Norman, M., Urrutia-Fucugauchi, J., Grajales-Nishimura, M., 2011. Study of melt and a clast of 546 Ma magmatic arc rocks in the 65 Ma Chicxulub bolide breccia, northern Maya block, Mexico: western limit of Ediacaran arc peripheral to northern Gondwana. International Geology Review 53, 1180–1193. https://doi.org/10.1080/00206810903545527

Kesson, S.E., 1975. Experimental investigation of reaction coronas on olivine in Apollo 14 high-grade breccias. Earth and Planetary Science Letters 28, 65–68. https://doi.org/10.1016/0012-821X(75)90074-6

Kring, D.A., 2005. Hypervelocity collisions into continental crust composed of sediments and an underlying crystalline basement: comparing the Ries (~24 km) and Chicxulub (~180 km) impact craters. Geochemistry 65, 1–46. https://doi.org/10.1016/j.chemer.2004.10.003

Kring, D.A., Claeys, P., Gulick, S.P.S., Morgan, J.V., Collins, G.S., 2017. Chicxulub and the Exploration of Large Peak-Ring Impact Craters through Scientific Drilling. GSAT 4–8. https://doi.org/10.1130/GSATG352A.1

Kring, D.A., Tikoo, S.M., Schmieder, M., Riller, U., Rebolledo-Vieyra, M., Simpson, S.L., Osinski, G.R., Gattacceca, J., Wittmann, A., Verhagen, C.M., Cockell, C.S., Coolen, M.J.L., Longstaffe, F.J., Gulick, S.P.S., Morgan, J.V., Bralower, T.J., Chenot, E., Christeson, G.L., Claeys, P., Ferrière, L., Gebhardt, C., Goto, K., Green, S.L., Jones, H., Lofi, J., Lowery, C.M., Ocampo-Torres, R., Perez-Cruz, L., Pickersgill, A.E., Poelchau, M.H., Rae, A.S.P., Rasmussen, C., Sato, H., Smit, J., Tomioka, N., Urrutia-Fucugauchi, J., Whalen, M.T., Xiao, L., Yamaguchi, K.E., 2020. Probing the hydrothermal system of the Chicxulub impact crater. Science Advances 6, eaaz3053. https://doi.org/10.1126/sciadv.aaz3053

Krogh, T. E., Kamo, S.L., Bohor, B.F., 1993. Fingerprinting the K/T impact site and determining the time of impact by U-Pb dating of single shocked zircons from distal ejecta. Earth and Planetary Science Letters 119, 425–429. https://doi.org/10.1016/0012-821X(93)90150-8

Krogh, Thomas E., Kamo, S.L., Sharpton, V.L., Marin, L.E., Hildebrands, A.R., 1993. U–Pb ages of single shocked zircons linking distal K/T ejecta to the Chicxulub crater. Nature 366, 731–734. https://doi.org/10.1038/366731a0

Krogstad, E.J., Walker, R.J., 1994. High closure temperatures of the U-Pb system in large apatites from the Tin Mountain pegmatite, Black Hills, South Dakota, USA. Geochimica et Cosmochimica Acta 58, 3845–3853. https://doi.org/10.1016/0016-7037(94)90367-0

Kuiper, K.F., Deino, A., Hilgen, F.J., Krijgsman, W., Renne, P.R., Wijbrans, J.R., 2008. Synchronizing Rock Clocks of Earth History. Science 320, 500–504. https://doi.org/10.1126/science.1154339

Kumar, Y., Tripathi, S., Sengupta, P., Jha, S.N., Nand, M., Trivedi, A., Sagdeo, A., Sharma, A., Tiwari, M.K., Sathe, V.G., Arya, A., 2024. Local Structure, Structural, Vibrational, and Optical Properties of Natural Zircon. physica status solidi (b) 261, 2400032. https://doi.org/10.1002/pssb.202400032

Kusaba, K., Syono, Y., Kikuchi, M., Fukuoka, K., 1985. Shock behavior of zircon: phase transition to scheelite structure and decomposition. Earth and Planetary Science Letters 72, 433–439. https://doi.org/10.1016/0012-821X(85)90064-0

Lee, J.K.W., Williams, I.S., Ellis, D.J., 1997. Pb, U and Th diffusion in natural zircon. Nature 390, 159–162. https://doi.org/10.1038/36554

Lee, J.K.W., 2015. Ar–Ar and K–Ar Dating, in: Jack Rink, W., Thompson, J.W. (Eds.), Encyclopedia of Scientific Dating Methods, Encyclopedia of Earth Sciences Series. Springer Netherlands, Dordrecht, pp. 58–73. https://doi.org/10.1007/978-94-007-6304-3_40

Leroux, H., Reimold, W.U., Koeberl, C., Hornemann, U., Doukhan, J.-C., 1999. Experimental shock deformation in zircon: a transmission electron microscopic study. Earth and Planetary Science Letters 169, 291–301. https://doi.org/10.1016/S0012-821X(99)00082-5

Lovera, O.M., Richter, F.M., Harrison, T.M., 1989. The 40Ar/39Ar thermochronometry for slowly cooled samples having a distribution of diffusion domain sizes - Lovera - 1989 - Journal of Geophysical Research: Solid Earth - Wiley Online Library. Journal of Geophysical Research: Solid Earth 94, 17917–17935. https://doi.org/10.1029/JB094iB12p17917

Mader, M.M., Osinski, G.R., 2018. Impactites of the Mistastin Lake impact structure: Insights into impact ejecta emplacement. Meteoritics & Planetary Science 53, 2492–2518. https://doi.org/10.1111/maps.13173

Mak, E.K., York, D., Grieve, R.A.F., Dence, M.R., 1976. The age of the Mistastin Lake crater, Labrador, Canada. Earth and Planetary Science Letters 31, 345–357. https://doi.org/10.1016/0012-821X(76)90116-3

Marchand, M., Crocket, J.H., 1974. The Mistastin Lake pluton and meteorite crater, northern Labrador. Presented at the Geological Association of Canada/Mineral Association of Canada Joint Annual Meeting, St. John's, Newfoundland, p. 58.

Marchi, S., Bottke, W.F., Cohen, B.A., Wünnemann, K., Kring, D.A., McSween, H.Y., De Sanctis, M.C., O'Brien, D.P., Schenk, P., Raymond, C.A., Russell, C.T., 2013. High-velocity collisions from the lunar cataclysm recorded in asteroidal meteorites. Nature Geosci 6, 303–307. https://doi.org/10.1038/ngeo1769

Margot, J.-L., Campbell, D.B., Jurgens, R.F., Slade, M.A., 1999. The topography of Tycho Crater. Journal of Geophysical Research: Planets 104, 11875–11882. https://doi.org/10.1029/1998JE900047

Marion, C.L., 2009. Geology, distribution and geochemistry of impact melt at the Mistastin lake impact crater, Labrador (masters). Memorial University of Newfoundland.

Marion, C.L., Sylvester, P.J., 2010. Composition and heterogeneity of anorthositic impact melt at Mistastin Lake crater, Labrador. Planetary and Space Science, Exploring other worlds by exploring our own: The role of terrestrial analogue studies in planetary exploration 58, 552–573. https://doi.org/10.1016/j.pss.2009.09.018

Mark, D.F., Lindgren, P., Fallick, A.E., 2014. A high-precision 40Ar/39Ar age for hydrated impact glass from the Dellen impact, Sweden. Geological Society, London, Special Publications 378, 349–366. https://doi.org/10.1144/SP378.22

Matchan, E.L., Phillips, D., Traine, E., Zhu, D., 2018. 40Ar/39Ar ages of alkali feldspar xenocrysts constrain the timing of intraplate basaltic volcanism. Quaternary Geochronology 47, 14–28. https://doi.org/10.1016/j.quageo.2018.04.009

McDougall, I., Harrison, T.M., 1999. Geochronology and Thermochronology by the 40Ar/39Ar Method. Oxford University Press.

Melosh, H.J., 1989. Impact cratering : a geologic process. New York : Oxford University Press ; Oxford : Clarendon Press.

Melosh, J., 2012. The contact and compression stage of impact cratering, in: Impact Cratering: Processes and Products. John Wiley & Sons, Ltd.

Mercer, C.M., Young, K.E., Weirich, J.R., Hodges, K.V., Jolliff, B.L., Wartho, J.-A., van Soest, M., 2015. Refining lunar impact chronology through high spatial resolution 40Ar/39Ar dating of impact melts | Science Advances. Science Advances 1. https://doi.org/DOI: 10.1126/sciadv.1400050

Merle, R.E., Nemchin, A.A., Grange, M.L., Whitehouse, M.J., Pidgeon, R.T., 2014. High resolution U-Pb ages of Ca-phosphates in Apollo 14 breccias: Implications for the age of the Imbrium impact. Meteoritics & Planetary Science 49, 2241–2251. https://doi.org/10.1111/maps.12395

Merle, R.E., Nemchin, A.A., Whitehouse, M.J., Pidgeon, R.T., Grange, M.L., Snape, J.F., Thiessen, F., 2017. Origin and transportation history of lunar breccia 14311. Meteoritics & Planetary Science 52, 842–858. https://doi.org/10.1111/maps.12835

Meyer, C., Williams, I.S., Compston, W., 1989. Workshop on Moon in Transition: Apollo 14, KREEP, and Evolved Lunar Rocks. Zircon-containing Rock Fragments within Apollo 14 Breccia Indicate Serial Magmatism from 4350 to 4000 Million Years 75–78.

Meyer, C., Williams, I.S., Compston, W., 1996. Uranium-lead ages for lunar zircons: Evidence for a prolonged period of granophyre formation from 4.32 to 3.88 Ga. Meteoritics & Planetary Science 31, 370–387. https://doi.org/10.1111/j.1945-5100.1996.tb02075.x

Meyer, C., 2008. 14311, in: The Lunar Sample Compendium. NASA.

Michael, G., Basilevsky, A., Neukum, G., 2018. On the history of the early meteoritic bombardment of the Moon: Was there a terminal lunar cataclysm? Icarus 302, 80–103. https://doi.org/10.1016/j.icarus.2017.10.046

Min, K., Mundil, R., Renne, P.R., Ludwig, K.R., 2000. A test for systematic errors in 40Ar/39Ar geochronology through comparison with U/Pb analysis of a 1.1-Ga rhyolite. Geochimica et Cosmochimica Acta 64, 73–98. https://doi.org/10.1016/S0016-7037(99)00204-5

Montalvo, S.D., Reddy, S.M., Saxey, D.W., Rickard, W.D.A., Fougerouse, D., Quadir, Z., Johnson, T.E., 2019. Nanoscale constraints on the shock-induced transformation of zircon to reidite. Chemical Geology 507, 85–95. https://doi.org/10.1016/j.chemgeo.2018.12.039

Morbidelli, A., Lunine, J.I., O'Brien, D.P., Raymond, S.N., Walsh, K.J., 2012. Building Terrestrial Planets. Annu. Rev. Earth Planet. Sci. 40, 251–275. https://doi.org/10.1146/annurev-earth-042711-105319

Morgan, J., Warner, M., the Chicxulub Working Group, Brittan, J., Buffler, R., Camargo, A., Christeson, G., Denton, P., Hildebrand, A., Hobbs, R., Macintyre, H., Mackenzie, G., Maguire, P., Marin, L., Nakamura, Y., Pilkington, M., Sharpton, V., Snyder, D., Suarez, G., Trejo, A., 1997. Size and morphology of the Chicxulub impact crater. Nature 390, 472–476. https://doi.org/10.1038/37291

Morgan, J.V., Gulick, S.P.S., Bralower, T., Chenot, E., Christeson, G., Claeys, P., Cockell, C., Collins, G.S., Coolen, M.J.L., Ferrière, L., Gebhardt, C., Goto, K., Jones, H., Kring, D.A., Le Ber, E., Lofi, J., Long, X., Lowery, C., Mellett, C., Ocampo-Torres, R., Osinski, G.R., Perez-Cruz, L., Pickersgill, A., Poelchau, M., Rae, A., Rasmussen, C., Rebolledo-Vieyra, M., Riller, U., Sato, H., Schmitt, D.R., Smit, J., Tikoo, S., Tomioka, N., Urrutia-Fucugauchi, J., Whalen, M., Wittmann, A., Yamaguchi, K.E., Zylberman, W., 2016. The formation of peak rings in large impact craters. Science 354, 878–882. https://doi.org/10.1126/science.aah6561

Morozova, I., 2015. Strength Study of Zircon Under High Pressure (M.Sc.). The University of Western Ontario (Canada), Canada -- Ontario, CA.

Moser, D.E., Cupelli, C.L., Barker, I.R., Flowers, R.M., Bowman, J.R., Wooden, J., Hart, J.R., 2011. New zircon shock phenomena and their use for dating and reconstruction of large impact structures revealed by electron nanobeam (EBSD, CL, EDS) and isotopic U–Pb and (U–Th)/He analysis of the Vredefort domeThis article is one of a series of papers published in this Special Issue on the theme of Geochronology in honour of Tom Krogh. Canadian Journal of Earth Sciences 48, 117–139. https://doi.org/10.1139/E11-011

Murakami, T., Chakoumakos, B.C., Ewing, R.C., Lumpkin, G.R., Weber, W.J., 1991. Alpha-decay event damage in zircon. American Mineralogist 76, 1510–1532.

Nasdala, L., Irmer, G., Wolf, D., 1995. The degree of metamictization in zircon; a Raman spectroscopic study. European Journal of Mineralogy 7, 471–478.

Naumov, M.V., 2002. Impact-Generated Hydrothermal Systems: Data from Popigai, Kara, and Puchezh-Katunki Impact Structures, in: Plado, J., Pesonen, L.J. (Eds.), Impacts in Precambrian Shields. Springer, Berlin, Heidelberg, pp. 117–171. https://doi.org/10.1007/978-3-662-05010-1_6

Naumov, M.V., 2005. Principal features of impact-generated hydrothermal circulation systems: mineralogical and geochemical evidence. Geofluids 5, 165–184. https://doi.org/10.1111/j.1468-8123.2005.00092.x

Nemchin, A.A., Whitehouse, M.J., Pidgeon, R.T., Meyer, C., 2006. Oxygen isotopic signature of 4.4–3.9 Ga zircons as a monitor of differentiation processes on the Moon. Geochimica et Cosmochimica Acta 70, 1864–1872. https://doi.org/10.1016/j.gca.2005.12.009

Nemchin, A.A., Pidgeon, R.T., Whitehouse, M.J., Vaughan, J.P., Meyer, C., 2008. SIMS U–Pb study of zircon from Apollo 14 and 17 breccias: Implications for the evolution of lunar KREEP. Geochimica et Cosmochimica Acta 72, 668–689. https://doi.org/10.1016/j.gca.2007.11.009

Nemchin, A.A., Pidgeon, R.T., Healy, D., Grange, M.L., Whitehouse, M.J., Vaughan, J., 2010. The comparative behavior of apatite-zircon U-Pb systems in Apollo 14 breccias: Implications for the thermal history of the Fra Mauro Formation. Meteoritics & Planetary Science 44, 1717–1734. https://doi.org/10.1111/j.1945-5100.2009.tb01202.x

Nemchin, A., 2015. Uranium–Lead, Extraterrestrial, Planetary Materials, in: Jack Rink, W., Thompson, J.W. (Eds.), Encyclopedia of Scientific Dating Methods, Encyclopedia of Earth Sciences Series. Springer Netherlands, Dordrecht, pp. 890–894. https://doi.org/10.1007/978-94-007-6304-3_255

Norman, M.D., Duncan, R.A., Huard, J.J., 2006. Identifying impact events within the lunar cataclysm from 40Ar–39Ar ages and compositions of Apollo 16 impact melt rocks. Geochimica et Cosmochimica Acta, A Special Issue Dedicated to Larry A. Haskin 70, 6032–6049. https://doi.org/10.1016/j.gca.2006.05.021

Osinski, G., Grieve, R.A.F., Tornabene, L.L., 2012. Excavation and impact ejecta emplacement, in: Impact Cratering: Processes and Products. John Wiley & Sons, Ltd.

Osinski, G., Pierazzo, E., 2012. Impact cratering: processes and products, in: Impact Cratering: Processes and Products. John Wiley & Sons, Ltd.

Osinski, G.R., Grieve, R.A.F., Bleacher, J.E., Neish, C.D., Pilles, E.A., Tornabene, L.L., 2018. Igneous rocks formed by hypervelocity impact. Journal of Volcanology and Geothermal Research 353, 25–54. https://doi.org/10.1016/j.jvolgeores.2018.01.015

Osinski, G.R., Grieve, R.A.F., Ferrière, L., Losiak, A., Pickersgill, A.E., Cavosie, A.J., Hibbard, S.M., Hill, P.J.A., Bermudez, J.J., Marion, C.L., Newman, J.D., Simpson, S.L., 2022. Impact Earth: A review of the terrestrial impact record. Earth-Science Reviews 232, 104112. https://doi.org/10.1016/j.earscirev.2022.104112

Ostertag, R., 1983. Shock experiments on feldspar crystals. Journal of Geophysical Research: Solid Earth 88, B364–B376. https://doi.org/10.1029/JB088iS01p0B364

Paces, J.B., Miller Jr., J.D., 1993. Precise U-Pb ages of Duluth Complex and related mafic intrusions, northeastern Minnesota: Geochronological insights to physical, petrogenetic, paleomagnetic, and tectonomagmatic processes associated with the 1.1 Ga Midcontinent Rift

System. Journal of Geophysical Research: Solid Earth 98, 13997–14013. https://doi.org/10.1029/93JB01159

Parrish, R., 2015. Uranium–Lead Dating, in: Jack Rink, W., Thompson, J.W. (Eds.), Encyclopedia of Scientific Dating Methods, Encyclopedia of Earth Sciences Series. Springer Netherlands, Dordrecht, pp. 848–857. https://doi.org/10.1007/978-94-007-6304-3_193

Pickersgill, A.E., Osinski, G.R., Flemming, R.L., 2015. Shock effects in plagioclase feldspar from the Mistastin Lake impact structure, Canada. Meteoritics & Planetary Science 50, 1546–1561. https://doi.org/10.1111/maps.12495

Pickersgill, A.E., Mark, D.F., Lee, M.R., Osinski, G.R., 2020. 40Ar/39Ar systematics of melt lithologies and target rocks from the Gow Lake impact structure, Canada. Geochimica et Cosmochimica Acta 274, 317–332. https://doi.org/10.1016/j.gca.2020.01.025

Pidgeon, R.T., Nemchin, A.A., van Bronswijk, W., Geisler, T., Meyer, C., Compston, W., Williams, I.S., 2007. Complex history of a zircon aggregate from lunar breccia 73235. Geochimica et Cosmochimica Acta 71, 1370–1381. https://doi.org/10.1016/j.gca.2006.11.021

Pidgeon, R.T., Nemchin, A.A., Kamo, S.L., 2011. Comparison of structures in zircons from lunar and terrestrial impactites. Can. J. Earth Sci. 48, 107–116. https://doi.org/10.1139/E10-037

Pidgeon, R.T., Merle, R.E., Grange, M.L., Nemchin, A.A., Whitehouse, M.J., 2016. Annealing of radiation damage in zircons from Apollo 14 impact breccia 14311: Implications for the thermal history of the breccia. Meteoritics & Planetary Science 51, 155–166. https://doi.org/10.1111/maps.12572

Pierazzo, E., Melosh, J., 2012. Environmental effects of impact events, in: Impact Cratering: Processes and Products. John Wiley & Sons, Ltd.

Pike, R.J., 1980. Control of crater morphology by gravity and target type: Mars, Earth, Moon. Presented at the Lunar and Planetary Science Conference XI, pp. 2159–2189.

Pillmore, C.L., Flores, R.M., 1987. Stratigraphy and depositional environments of the Cretaceous-Tertiary boundary clay and associated rocks, Raton basin, New Mexico and Colorado, in: Fassett, J.E., Rigby, J.K., Jr. (Eds.), The Cretaceous-Tertiary Boundary in the San Juan and Raton Basins, New Mexico and Colorado. Geological Society of America, p. 0. https://doi.org/10.1130/SPE209-p111

Pinto, J.A., Warme, J.E., 2007. Alamo Event, Nevada: Crater stratigraphy and impact breccia Realms, in: Evans, K.R., Horton, J.W., Jr., King, D.T., Jr., Morrow, J.R. (Eds.), The Sedimentary Record of Meteorite Impacts. Geological Society of America, p. 0. https://doi.org/10.1130/2008.2437(07)

Plan, A., Kenny, G.G., Erickson, T.M., Lindgren, P., Alwmark, C., Holm-Alwmark, S., Lambert, P., Scherstén, A., Söderlund, U., 2021. Exceptional preservation of reidite in the Rochechouart impact structure, France: New insights into shock deformation and phase transition of zircon. Meteoritics & Planetary Science 56, 1795–1828. https://doi.org/10.1111/maps.13723

Rasmussen, B., Fletcher, I.R., Muhling, J.R., 2008. Pb/Pb geochronology, petrography and chemistry of Zr-rich accessory minerals (zirconolite, tranquillityite and baddeleyite) in mare basalt 10047. Geochimica et Cosmochimica Acta 72, 5799–5818. https://doi.org/10.1016/j.gca.2008.09.010

Rasmussen, C., Stockli, D.F., Ross, C.H., Pickersgill, A., Gulick, S.P., Schmieder, M., Christeson, G.L., Wittmann, A., Kring, D.A., Morgan, J.V., 2019. U-Pb memory behavior in Chicxulub's peak ring — Applying U-Pb depth profiling to shocked zircon. Chemical Geology 525, 356–367. https://doi.org/10.1016/j.chemgeo.2019.07.029

Rasmussen, C., Stockli, D.F., Erickson, T.M., Schmieder, M., 2020. Spatial U-Pb age distribution in shock-recrystallized zircon – A case study from the Rochechouart impact structure, France. Geochimica et Cosmochimica Acta 273, 313–330. https://doi.org/10.1016/j.gca.2020.01.017

Rautman, C.A., Herrin, J.M., Cooper, S.P., Basinski, P.M., Olsson, W.A., Arnold, B.W., Broadhead, R.F., Knight, C.D., Keefe, R.G., McKinney, C., Holm, G., Holland, J.F., Larson, R., Engler, T.W., Lorenz, J.C., 2004. Natural gas production problems : solutions, methodologies, and modeling. (No. SAND2004-4859). Sandia National Laboratories (SNL), Albuquerque, NM, and Livermore, CA (United States). https://doi.org/10.2172/919653

Reddy, S.M., Timms, N.E., Pantleon, W., Trimby, P., 2007. Quantitative characterization of plastic deformation of zircon and geological implications. Contrib Mineral Petrol 153, 625–645. https://doi.org/10.1007/s00410-006-0174-4

Reimold, W.U., Gibson, R.L., 1996. Geology and evolution of the Vredefort impact structure, South Africa. Journal of African Earth Sciences 23, 125–162. https://doi.org/10.1016/S0899-5362(96)00059-0

Ross, C., Stockli, D.F., Gulick, S.P.S., Kaskes, P., Smit, J., Artemieva, N.A., 2021. Finding a Specific Needle in a Haystack: Tracing Ejected Zircon from the Chicxulub Impact in K-Pg Boundary Sections, in: 6. Presented at the Geological Society of America. https://doi.org/doi:10.1130/abs/2021AM-370733

Ross, C.H., Stockli, D.F., Rasmussen, C., Gulick, S.P.S., de Graaff, S.J., Claeys, P., Zhao, J., Xiao, L., Pickersgill, A.E., Schmieder, M., Kring, D.A., Wittmann, A., Morgan, J.V., 2021. Evidence of Carboniferous arc magmatism preserved in the Chicxulub impact structure. GSA Bulletin 134, 241–260. https://doi.org/10.1130/B35831.1

Salguero-Hernández, E., Pérez-Cruz, L., Urrutia-Fucugauchi, J., 2020. Seismic attribute analysis of Chicxulub impact crater. Acta Geophys. 68, 627–640. https://doi.org/10.1007/s11600-020-00442-z

Salje, E.K.H., Chrosch, J., Ewing, R.C., 1999. Is "metamictization" of zircon a phase transition? American Mineralogist 84, 1107–1116. https://doi.org/10.2138/am-1999-7-813

Sanders, R.E., Heizler, M.T., Goodwin, L.B., 2006. 40Ar/39Ar thermochronology constraints on the timing of Proterozoic basement exhumation and fault ancestry, southern Sangre de Cristo Range, New Mexico. GSA Bulletin 118, 1489–1506. https://doi.org/10.1130/B25857.1

Sañudo-Wilhelmy, S.A., Flegal, A.R., 1994. Temporal variations in lead concentrations and isotopic composition in the Southern California Bight. Geochimica et Cosmochimica Acta 58, 3315–3320. https://doi.org/10.1016/0016-7037(94)90060-4

Schaen, A.J., Jicha, B.R., Hodges, K.V., Vermeesch, P., Stelten, M.E., Mercer, C.M., Phillips, D., Rivera, T.A., Jourdan, F., Matchan, E.L., Hemming, S.R., Morgan, L.E., Kelley, S.P., Cassata, W.S., Heizler, M.T., Vasconcelos, P.M., Benowitz, J.A., Koppers, A.A.P., Mark, D.F., Niespolo, E.M., Sprain, C.J., Hames, W.E., Kuiper, K.F., Turrin, B.D., Renne, P.R., Ross, J., Nomade, S., Guillou, H., Webb, L.E., Cohen, B.A., Calvert, A.T., Joyce, N., Ganerød, M., Wijbrans, J., Ishizuka, O., He, H., Ramirez, A., Pfänder, J.A., Lopez-Martínez, M., Qiu, H., Singer, B.S., 2020. Interpreting and reporting 40Ar/39Ar geochronologic data. GSA Bulletin 133, 461–487. https://doi.org/10.1130/B35560.1

Schmieder, M., Jourdan, F., 2013. The Lappajärvi impact structure (Finland): Age, duration of crater cooling, and implications for early life. Geochimica et Cosmochimica Acta 112, 321–339. https://doi.org/10.1016/j.gca.2013.02.015

Schmieder, M., Tohver, E., Jourdan, F., Denyszyn, S., Haines, P., 2015. Zircons from the Acraman impact melt rock (South Australia): Shock metamorphism, U–Pb and 40Ar/39Ar systematics, and implications for the isotopic dating of impact events. Geochimica et Cosmochimica Acta 161, 71–100. https://doi.org/10.1016/j.gca.2015.04.021

Schmieder, M., Shaulis, B.J., Lapen, T.J., Kring, D.A., 2017. U–Th–Pb systematics in zircon and apatite from the Chicxulub impact crater, Yucatán, Mexico. Geological Magazine 155, 1330–1350. https://doi.org/10.1017/S0016756817000255

Schmieder, M., Kennedy, T., Jourdan, F., Buchner, E., Reimold, W.U., 2018. A high-precision 40Ar/39Ar age for the Nördlinger Ries impact crater, Germany, and implications for the accurate dating of terrestrial impact events. Geochimica et Cosmochimica Acta 220, 146–157. https://doi.org/10.1016/j.gca.2017.09.036

Schmieder, M., Kring, D., 2020. Earth's Impact Events Through Geologic Time: A List of Recommended Ages for Terrestrial Impact Structures and Deposits | Astrobiology. Astrobiology 20, 91–141.

Schmitz, M.D., Bowring, S.A., 2001. U-Pb zircon and titanite systematics of the Fish Canyon Tuff: an assessment of high-precision U-Pb geochronology and its application to young volcanic rocks. Geochimica et Cosmochimica Acta 65, 2571–2587. https://doi.org/10.1016/S0016-7037(01)00616-0

Schulte, P., Speijer, R., Mai, H., Kontny, A., 2006. The Cretaceous–Paleogene (K–P) boundary at Brazos, Texas: Sequence stratigraphy, depositional events and the Chicxulub impact. Sedimentary Geology 184, 77–109. https://doi.org/10.1016/j.sedgeo.2005.09.021

Schulte, P., Alegret, L., Arenillas, I., Arz, J.A., Barton, P.J., Bown, P.R., Bralower, T.J., Christeson, G.L., Claeys, P., Cockell, C.S., Collins, G.S., Deutsch, A., Goldin, T.J., Goto, K., Grajales-Nishimura, J.M., Grieve, R.A.F., Gulick, S.P.S., Johnson, K.R., Kiessling, W., Koeberl, C., Kring, D.A., MacLeod, K.G., Matsui, T., Melosh, J., Montanari, A., Morgan, J.V., Neal, C.R., Nichols, D.J., Norris, R.D., Pierazzo, E., Ravizza, G., Rebolledo-Vieyra, M., Reimold, W.U., Robin, E., Salge, T., Speijer, R.P., Sweet, A.R., Urrutia-Fucugauchi, J., Vajda, V., Whalen, M.T., Willumsen, P.S., 2010. The Chicxulub Asteroid Impact and Mass Extinction at the Cretaceous-Paleogene Boundary. Science 327, 1214–1218. https://doi.org/10.1126/science.1177265

Schwarz, W.H., Lippolt, H.J., 2014. 40Ar-39Ar step-heating of impact glasses from the Nördlinger Ries impact crater—Implications on excess argon in impact melts and tektites. Meteoritics & Planetary Science 49, 1023–1036. https://doi.org/10.1111/maps.12309

Schwarz, W.H., Hanel, M., Trieloff, M., 2020. U-Pb dating of zircons from an impact melt of the Nördlinger Ries crater. Meteoritics & Planetary Science 55, 312–325. https://doi.org/10.1111/maps.13437

Scoon, J.H., 1972. Chemical analyses of lunar samples. Presented at the Proceedings of the Third Lunar Science Conference, pp. 1335–1336.

Sharman, G.R., Malkowski, M.A., 2024. Modeling apparent Pb loss in zircon U–Pb geochronology. Geochronology 6, 37–51. https://doi.org/10.5194/gchron-6-37-2024

Sharpton, V.L., Marín, L.E., Schuraytz, B.C., Spudis, P.D., Ryder, G., 1994. Constraints on Excavation and Mixing During the Chicxulub Impact Event. Presented at the 25th Lunar and Planetary Science Conference, pp. 1255–1256.

Sharpton, V.L., Marin, L.E., Carney, J.D., Lee, S., Ryder, G., Schuraytz, B.C., Sikora, P., Spudis, P.D., 1996. A Model of the Chicxulub Impact Basin Based on Evaluation of Geophysical Data, Well Logs, and Drill Core Samples (No. LPI-Contrib-873).

Short, N.M., 1970. Progressive Shock Metamorphism of Quartzite Ejecta from the Sedan Nuclear Explosion Crater. The Journal of Geology 78, 705–732. https://doi.org/10.1086/627572

Simonds, C.H., Phinney, W.C., Warner, J.L., McGee, P.E., Geeslin, J., Brown, R.W., Rhodes, J.M., 1977. Apollo 14 revisited, or breccias aren't so bad after all.

Singleton, A.C., Osinski, G.R., McCausland, P.J.A., Moser, D.E., 2011. Shock-induced changes in density and porosity in shock-metamorphosed crystalline rocks, Haughton impact structure, Canada. Meteoritics & Planetary Science 46, 1774–1786. https://doi.org/10.1111/j.1945-5100.2011.01290.x

Smit, J., 1990. Meteorite impact, extinctions and the Cretaceous-Tertiary Boundary. Geologie en Mijnbouw 69, 187–204.

Smit, J., 1999. The Global Stratigraphy of the Cretaceous-Tertiary Boundary Impact Ejecta. Annual Review of Earth and Planetary Sciences 27, 75–113. https://doi.org/10.1146/annurev.earth.27.1.75

Snape, J.F., Nemchin, A.A., Grange, M.L., Bellucci, J.J., Thiessen, F., Whitehouse, M.J., 2016. Phosphate ages in Apollo 14 breccias: Resolving multiple impact events with high precision U–Pb SIMS analyses. Geochimica et Cosmochimica Acta 174, 13–29. https://doi.org/10.1016/j.gca.2015.11.005

Spencer, C.J., Kirkland, C.L., Taylor, R.J.M., 2016. Strategies towards statistically robust interpretations of in situ U–Pb zircon geochronology. Geoscience Frontiers 7, 581–589. https://doi.org/10.1016/j.gsf.2015.11.006

Spray, J.G., Thompson, L.M., Biren, M.B., O'Connell-Cooper, C., 2010. The Manicouagan impact structure as a terrestrial analogue site for lunar and martian planetary science. Planetary and Space Science, Exploring other worlds by exploring our own: The role of terrestrial analogue studies in planetary exploration 58, 538–551. https://doi.org/10.1016/j.pss.2009.09.010

Stadermann, F.J., Heusser, E., Jessberger, E.K., Lingner, S., Stöffler, D., 1991. The case for a younger Imbrium basin: New 40Ar-39Ar ages of Apollo 14 rocks. Geochimica et Cosmochimica Acta 55, 2339–2349. https://doi.org/10.1016/0016-7037(91)90108-H

Stöffler, D., 1971. Progressive metamorphism and classification of shocked and brecciated crystalline rocks at impact craters. Journal of Geophysical Research (1896-1977) 76, 5541–5551. https://doi.org/10.1029/JB076i023p05541

Stöffler, D., Knöll, H.-D., 1977. Composition and origin of plagioclase, pyroxene, and olivine clasts of lunar breccias 14006, 14063, 14066, 14311, 14320, and 14321. Presented at the Proceedings of the Eighth Lunar Science Conference, pp. 1849–1867.

Stöffler, D., Ryder, G., Ivanov, B.A., Artemieva, N.A., Cintala, M.J., Grieve, R.A.F., 2006. Cratering History and Lunar Chronology. Reviews in Mineralogy and Geochemistry 60, 519–596. https://doi.org/10.2138/rmg.2006.60.05

Stöffler, D., Hamann, C., Metzler, K., 2018. Shock metamorphism of planetary silicate rocks and sediments: Proposal for an updated classification system. Meteoritics & Planetary Science 53, 5–49. https://doi.org/10.1111/maps.12912

Storzer, D., Wagner, G.A., 1977. Fission Track Dating of Meteorite Impacts. Meteoritics 12, 368–369.

Swisher, C.C., Grajales-Nishimura, J.M., Montanari, A., Margolis, S.V., Claeys, P., Alvarez, W., Renne, P., Cedillo-Pardoa, E., Maurrasse, F.J.-M.R., Curtis, G.H., Smit, J., McWilliams, M.O., 1992. Coeval 40Ar/39Ar Ages of 65.0 Million Years Ago from Chicxulub Crater Melt Rock and Cretaceous-Tertiary Boundary Tektites. Science 257, 954–958. https://doi.org/10.1126/science.257.5072.954

Sylvester, P.J., Crowley, J.L., Schmitz, M.D., 2013. U-Pb zircon age of Mistastin Lake crater, Labrador, Canada - implications for high-precision dating of small impact melt sheets and the end Eocene extinction, in: Mineralogical Magazine. Presented at the Goldschmidt, p. 2295.

Sylvester, P.J., Souders, A.K., Liu, R., 2022. Significance of U-Pb detrital zircon geochronology for mudstone provenance. Geology 50, 670–675. https://doi.org/10.1130/G49684.1

Szumila, I., Trail, D., Erickson, T., Simon, J.I., Wielicki, M.M., Lapen, T., Nakajima, M., Fries, M., Bell, E.A., 2023. Microstructural changes and Pb mobility during the zircon to reidite transformation: Implications for planetary impact chronology. American Mineralogist 108, 1516–1529. https://doi.org/10.2138/am-2022-8604

Taylor, S.R., 1982. Planetary science : a lunar perspective. Publishers Production International.

Taylor, J.R., 1982. An introduction to error analysis: the study of uncertainties in physical measurements. University science books, Mill Valley, CA.

Taylor, G.J., 2009. Ancient Lunar Crust: Origin, Composition, and Implications. Elements 5, 17–22. https://doi.org/10.2113/gselements.5.1.17

Thiessen, F., Nemchin, A.A., Snape, J.F., Bellucci, J.J., Whitehouse, M.J., 2018. Apollo 12 breccia 12013: Impact-induced partial Pb loss in zircon and its implications for lunar geochronology. Geochimica et Cosmochimica Acta 230, 94–111. https://doi.org/10.1016/j.gca.2018.03.023

Thomas, J.B., Bodnar, R.J., Shimizu, N., Chesner, C.A., 2003. Melt Inclusions in Zircon. Reviews in Mineralogy and Geochemistry 53, 63–87. https://doi.org/10.2113/0530063

Timms, N.E., Kinny, P.D., Reddy, S.M., Evans, K., Clark, C., Healy, D., 2011. Relationship among titanium, rare earth elements, U–Pb ages and deformation microstructures in zircon: Implications for Ti-in-zircon thermometry. Chemical Geology 280, 33–46. https://doi.org/10.1016/j.chemgeo.2010.10.005

Timms, N.E., Reddy, S.M., Healy, D., Nemchin, A.A., Grange, M.L., Pidgeon, R.T., Hart, R., 2012. Resolution of impact-related microstructures in lunar zircon: A shock-deformation mechanism map. Meteoritics & Planetary Science 47, 120–141. https://doi.org/10.1111/j.1945-5100.2011.01316.x

Timms, N.E., Erickson, T.M., Pearce, M.A., Cavosie, A.J., Schmieder, M., Tohver, E., Reddy, S.M., Zanetti, M.R., Nemchin, A.A., Wittmann, A., 2017. A pressure-temperature phase diagram for zircon at extreme conditions. Earth-Science Reviews 165, 185–202. https://doi.org/10.1016/j.earscirev.2016.12.008

Timms, N.E., Erickson, T.M., Zanetti, M.R., Pearce, M.A., Cayron, C., Cavosie, A.J., Reddy, S.M., Wittmann, A., Carpenter, P.K., 2017. Cubic zirconia in >2370 °C impact melt records Earth's hottest crust. Earth and Planetary Science Letters 477, 52–58. https://doi.org/10.1016/j.epsl.2017.08.012

Timms, N.E., Healy, D., Erickson, T.M., Nemchin, A.A., Pearce, M.A., Cavosie, A.J., 2018. Role of Elastic Anisotropy in the Development of Deformation Microstructures in Zircon, in: Microstructural Geochronology. American Geophysical Union (AGU), pp. 183–202. https://doi.org/10.1002/9781119227250.ch8

Timms, N.E., Pearce, M.A., Erickson, T.M., Cavosie, A.J., Rae, Auriol S. P., Wheeler, J., Wittmann, Axel, Ferrière, Ludovic, Poelchau, Michael H., Tomioka, Naotaka, Collins, G.S., Gulick, Sean P. S., Rasmussen, Cornelia, Morgan, Joanna V., Gulick, S. P. S., Morgan, J. V., Chenot, E., Christeson, G.L., Claeys, P., Cockell, C.S., Coolen, M.J.L., Ferrière, L., Gebhardt, C., Goto, K., Green, S., Jones, H., Kring, D.A., Lofi, J., Lowery, C.M., Ocampo-Torres, R., Perez-Cruz, L., Pickersgill, A.E., Poelchau, M. H., Rae, A. S. P., Rasmussen, C., Rebolledo-Vieyra, M., Riller, U., Sato, H., Smit, J., Tikoo, S.M., Tomioka, N., Urrutia-Fucugauchi, J., Whalen, M.T., Wittmann, A., Xiao, L., Yamaguchi, K.E., IODP-ICDP Expedition 364 Scientists, 2019. New shock microstructures in titanite (CaTiSiO5) from the peak ring of the Chicxulub impact structure, Mexico. Contrib Mineral Petrol 174, 38. https://doi.org/10.1007/s00410-019-1565-7

Tohver, E., Lana, C., Cawood, P.A., Fletcher, I.R., Jourdan, F., Sherlock, S., Rasmussen, B., Trindade, R.I.F., Yokoyama, E., Souza Filho, C.R., Marangoni, Y., 2012. Geochronological constraints on the age of a Permo–Triassic impact event: U–Pb and 40Ar/39Ar results for the 40 km Araguainha structure of central Brazil. Geochimica et Cosmochimica Acta 86, 214–227. https://doi.org/10.1016/j.gca.2012.03.005

Tolometti, G.D., Erickson, T.M., Osinski, G.R., Cayron, C., Neish, C.D., 2022. Hot rocks: Constraining the thermal conditions of the Mistastin Lake impact melt deposits using zircon grain microstructures. Earth and Planetary Science Letters 584, 117523. https://doi.org/10.1016/j.epsl.2022.117523

Trail, D., Barboni, M., McKeegan, K.D., 2020. Evidence for diverse lunar melt compositions and mixing of the pre-3.9 Ga crust from zircon chemistry. Geochimica et Cosmochimica Acta 284, 173–195. https://doi.org/10.1016/j.gca.2020.06.018

Trop, J.M., Benowitz, J., Cole, R.B., O'Sullivan, P., 2019. Cretaceous to Miocene magmatism, sedimentation, and exhumation within the Alaska Range suture zone: A polyphase

reactivated terrane boundary. Geosphere 15, 1066–1101. https://doi.org/10.1130/GES02014.1

Tuttle, O.F., Bowen, N.L. (Eds.), 1958. Origin of Granite in the Light of Experimental Studies in the System NaAlSi3O8–KAlSi3O8–SiO2–H2O, in: Origin of Granite in the Light of Experimental Studies in the System NaAlSi3O8–KAlSi3O8–SiO2–H2O. Geological Society of America, p. 0. https://doi.org/10.1130/MEM74-p1

Valley, J.W., Spicuzza, M.J., Ushikubo, T., 2014. Correlated δ18O and [Ti] in lunar zircons: a terrestrial perspective for magma temperatures and water content on the Moon. Contrib Mineral Petrol 167, 956. https://doi.org/10.1007/s00410-013-0956-4

Vanderliek, D.M., Becker, H., Rocholl, A., 2021. Impact-related crystallization and modification of small zircons in Apollo 15 and 16 impactites at 4.2 Ga. Earth and Planetary Science Letters 576, 117216. https://doi.org/10.1016/j.epsl.2021.117216

Vermeesch, P., 2018. IsoplotR: A free and open toolbox for geochronology. Geoscience Frontiers, SPECIAL ISSUE: Frontiers in geoscience:A tribute to Prof. Xuanxue Mo 9, 1479–1493. https://doi.org/10.1016/j.gsf.2018.04.001

Walkden, G., Parker, J., Kelley, S., 2002. A Late Triassic Impact Ejecta Layer in Southwestern Britain. Science 298, 2185–2188. https://doi.org/10.1126/science.1076249

Wanless, R.K., Stevens, R.D., Lachance, G.R., Delabio, R.M.D., 1974. Age Determinations and Geological Studies K-Ar Isotopic Ages, Report 12. Geological Survey of Canada 145–148.

Warren, P.H., Taylor, G.J., Keil, K., Kallemeyn, G.W., Shirley, D.N., Wasson, J.T., 1983. Seventh Foray: Whitlockite-rich lithologies, a diopside-bearing troctolitic anorthosite, Ferroan anorthosites, and KREEP. Journal of Geophysical Research: Solid Earth 88, B151–B164. https://doi.org/10.1029/JB088iS01p0B151

Watson, E.B., Harrison, T.M., 2005. Zircon Thermometer Reveals Minimum Melting Conditions on Earliest Earth. Science 308, 841–844. https://doi.org/10.1126/science.1110873

Waychunas, G., Kempe, U., 2024. Activators in Minerals and the Role of Electronic Defects. Elements 20, 293–298. https://doi.org/10.2138/gselements.20.5.293

Weber, W.J., 1990. Radiation-induced defects and amorphization in zircon. Journal of Materials Research 5, 2687–2697. https://doi.org/10.1557/JMR.1990.2687

Weber, W.J., Ewing, R.C., Wang, L.-M., 1994. The radiation-induced crystalline-to-amorphous transition in zircon. Journal of Materials Research 9, 688–698. https://doi.org/10.1557/JMR.1994.0688

Wiedenbeck, M., Hanchar, J.M., Peck, W.H., Sylvester, P., Valley, J., Whitehouse, M., Kronz, A., Morishita, Y., Nasdala, L., Fiebig, J., Franchi, I., Girard, J.-P., Greenwood, R. c., Hinton, R.,

Kita, N., Mason, P. r. d., Norman, M., Ogasawara, M., Piccoli, P. m., Rhede, D., Satoh, H., Schulz-Dobrick, B., Skår, O., Spicuzza, Mj., Terada, K., Tindle, A., Togashi, S., Vennemann, T., Xie, Q., Zheng, Y.-F., 2004. Further Characterisation of the 91500 Zircon Crystal. Geostandards and Geoanalytical Research 28, 9–39. https://doi.org/10.1111/j.1751-908X.2004.tb01041.x

Wittmann, A., Kenkmann, T., Schmitt, R.T., Stöffler, D., 2006. Shock-metamorphosed zircon in terrestrial impact craters. Meteoritics & Planetary Science 41, 433–454. https://doi.org/10.1111/j.1945-5100.2006.tb00472.x

Wittmann, A., Schmitt, R.T., Kring, D.A., Reimold, W.U., Povenmire, H., 2009. The ICDP-USGS Deep Drilling Project in the Chesapeake Bay Impact Structure: Results from the Eyreville Core Holes. Geological Society of America.

Wittmann, A., Cavosie, A.J., Timms, N.E., Ferrière, L., Rae, A., Rasmussen, C., Ross, C., Stockli, D., Schmieder, M., Kring, D.A., Zhao, J., Xiao, L., Morgan, J.V., Gulick, S.P.S., 2021. Shock impedance amplified impact deformation of zircon in granitic rocks from the Chicxulub impact crater. Earth and Planetary Science Letters, 117201 575, 1–13. https://doi.org/10.1016/j.epsl.2021.117201

Woodhead, J.A., Rossman, G.R., Silver, L.T., 1991. The metamictization of zircon: Radiation dose-dependent structural characteristics. American Mineralogist 76, 74–82.

Wopenka, B., Jolliff, B.L., Zinner, E., Kremser, D.T., 1996. Trace element zoning and incipient metamictization in a lunar zircon; application of three microprobe techniques. American Mineralogist 81, 902–912. https://doi.org/10.2138/am-1996-7-813

Xie, T., Osinski, G.R., Shieh, S.R., 2020. Raman study of shock features in plagioclase feldspar from the Mistastin Lake impact structure, Canada. Meteoritics & Planetary Science 55, 1471–1490. https://doi.org/10.1111/maps.13523

Xie, T., Osinski, G.R., Shieh, S.R., 2021. Raman study of shock effects in lunar anorthite from the Apollo missions. Meteoritics & Planetary Science 56, 1633–1651. https://doi.org/10.1111/maps.13728

Yin, F., Dai, D., 2020. A Study of Shock-Metamorphic Features of Feldspars from the Xiuyan Impact Crater. Minerals 10, 231. https://doi.org/10.3390/min10030231

Young, K., 2014. The use of terrestrial analogs in preparing for planetary surface exploration: sampling and radioisotopic dating of impactites and deployment of in situ analytical technologies. Arizona State University.

Zhang, M., Salje, E.K.H., Farnan, I., Graeme-Barber, A., Daniel, P., Ewing, R.C., Clark, A.M., Leroux, H., 2000. Metamictization of zircon: Raman spectroscopic study. Journal of Physics: Condensed Matter 12, 1915–1925.

Zhang, B., Lin, Y., Moser, D.E., Hao, J., Shieh, S.R., Bouvier, A., 2019. Imbrium Age for Zircons in Apollo 17 South Massif Impact Melt Breccia 73155. Journal of Geophysical Research: Planets 124, 3205–3218. https://doi.org/10.1029/2019JE005992

Zhang, B., Lin, Y., Moser, D.E., Hao, J., Liu, Y., Zhang, J., Barker, I.R., Li, Q., Shieh, S.R., Bouvier, A., 2021. Radiogenic Pb mobilization induced by shock metamorphism of zircons in the Apollo 72255 Civet Cat norite clast. Geochimica et Cosmochimica Acta 302, 175–192. https://doi.org/10.1016/j.gca.2021.03.012

Zhao, J., Xiao, L., Xiao, Z., Morgan, J.V., Osinski, G.R., Neal, C.R., Gulick, S.P.S., Riller, U., Claeys, P., Zhao, S., Prieur, N.C., Nemchin, A., Yu, S., IODP 364 Science Party, 2021. Shock-deformed zircon from the Chicxulub impact crater and implications for cratering process. Geology 49, 755–760. https://doi.org/10.1130/G48278.1

Zhao, Jiawei, Zhang, X., Xiao, L., Cavosie, A.J., Timms, N.E., Nemchin, A., Xiao, Z., Hu, W., Chang, Y., Shu, J., He, Q., Zhao, S., Wang, J., Zhao, Jiannan, 2024. Nanoscale constraints on the nucleation and evolution of granular zircon from reidite in impactites at the Chicxulub impact structure. Earth and Planetary Science Letters 626, 118507. https://doi.org/10.1016/j.epsl.2023.118507

Appendices
Appendix A – $^{40}Ar/^{39}Ar$ data tables

Table A1: Overview of $^{40}Ar/^{39}Ar$ analyses (uncertainties are reported at 2σ)

Analysis parameters					Integrated age		Weighted average age			
Sample	**Mass for $^{40}Ar/^{39}Ar$ (g)**	**J value**	**Intercalibration factor**	**Standard**	**Age**	**Steps**	**Age**	**Steps**	**MSWD**	**$\%^{39}Ar$ release**
MM10-016	9.16	0.0028513 ± 1.3641E-06	0.9989243 ± 0.0031467	NM-324J	39.132 ± 0.092 Ma	30	38.20 ± 0.04 Ma	6	2.0	35.8
MM09-035	12.38	0.0026204 ± 1.4122E-06	0.9989243 ± 0.0031467	NM-324J	50.33 ± 0.12 Ma	35	37.95 ± 0.063 Ma	5	10	28.7
MM09-021b	11.07	0.0027728 ±1.53E-06	0.9989243 ± 0.0031467	NM-324J	762.39 ± 0.94 Ma	33	n/a	n/a	n/a	n/a
MM10-028	11.45	0.0026204 ± 1.4122E-06	0.9989243 ± 0.0031467	NM-324J	527.69 ± 0.74 Ma	34	n/a	n/a	n/a	n/a
2021-3163	2.95	0.0027504 ± 1.2727E-06	0.9975774 ± 0.0025217	NM-324G	1342.25 ± 0.92 Ma	35	n/a	n/a	n/a	n/a
CM09-05_1	4.44	0.0023264 ± 9.95E-07	0.9987184 ± 0.0026753	NM-324B	241.68 ± 0.32 Ma	9	78.93 ± 0.84 Ma	4	33	87.2
CM09-05_2	3.2	0.0023913 ± 1.22E-06	0.9964695 ± 0.002263	NM-324B	147.06 ± 0.20 Ma	10	80.22 ± 0.55 Ma	4	18	83.4
CM09-05_3	2.22	0.0044115 ± 1.13E-06	0.9978471 ± 0.0014232	NM-327M	102.95 ± 0.12 Ma	13	78.84 ± 0.42 Ma	7	7	85.5
CM09-05_4	2.42	0.0044136 ± 1.06E-06	0.9978471 ± 0.0014232	NM-327M	81.420 ± 0.09 Ma	13	77.42 ± 0.24 Ma	4	3	60.3

Table A2: $^{40}Ar/^{39}Ar$ geochronology data

Sample	**$^{40}Ar/^{39}Ar$**	**$^{37}Ar/^{39}Ar$**	**$^{36}Ar/^{39}Ar$ (10^{-3})**	**$^{39}Ar_K$ (fA)**	**K/Ca**	**$^{40}Ar^*$ (%)**	**Total ^{39}Ar released (%)**	**Age (Ma)**	**± 2σ**	**Temperature (°C)**	**Step time (minutes)**
Sample MM10-016 – Shocked and baked granite											
MM10-016A	86.88	0.1702	280.7	13.78	3.06	4.5	2.9	20.42	2.78	450	10
MM10-016B	8.836	0.1068	4.402	12.30	4.88	85.4	5.5	38.96	0.12	450	20
MM10-016C	7.824	0.1077	1.489	10.98	4.84	94.5	7.9	38.19	0.10	500	10

MM10-016D	7.634	0.0884	0.7707	21.92	5.89	97.1	12.6	38.29	0.05	500	20
MM10-016E	7.508	0.0657	0.3749	22.37	7.94	98.6	17.3	38.23	0.05	550	10
MM10-016F	7.481	0.0526	0.2819	38.32	9.92	98.9	25.5	38.23	0.03	550	20
MM10-016G	7.447	0.0484	0.1724	34.34	10.79	99.4	32.8	38.22	0.03	600	10
MM10-016H	7.426	0.0546	0.1511	51.24	9.55	99.5	43.7	38.15	0.02	600	20
MM10-016I	7.392	0.0651	0.1139	38.22	8.00	99.6	51.8	38.04	0.03	650	10
MM10-016J	7.390	0.0664	0.1310	48.11	7.85	99.6	62.0	38.00	0.02	650	20
MM10-016K	7.365	0.0868	0.1344	29.91	6.01	99.6	68.4	37.88	0.03	700	10
MM10-016L	7.362	0.1056	0.1695	33.75	4.93	99.4	75.6	37.82	0.03	700	20
MM10-016M	7.358	0.1469	0.2014	19.88	3.54	99.4	79.8	37.77	0.05	750	10
MM10-016N	7.388	0.1472	0.2889	19.68	3.54	99.0	84.0	37.79	0.05	750	20
MM10-016O	7.415	0.2032	0.3872	11.18	2.56	98.7	86.4	37.80	0.08	800	10
MM10-016P	7.465	0.2259	0.5572	11.42	2.30	98.0	88.8	37.81	0.08	800	20
MM10-016Q	7.505	0.3072	0.6913	7.00	1.69	97.6	90.3	37.85	0.13	850	10
MM10-016R	7.613	0.2839	0.9835	7.70	1.83	96.5	91.9	37.95	0.12	850	20
MM10-016S	7.704	0.2618	1.185	4.65	1.99	95.7	92.9	38.10	0.19	900	10
MM10-016T	7.891	0.3154	1.660	5.18	1.65	94.1	94.0	38.37	0.18	900	20
MM10-016U	8.128	0.3763	2.093	3.19	1.38	92.8	94.7	38.95	0.28	950	10
MM10-016V	8.664	0.2845	3.422	3.14	1.83	88.6	95.4	39.66	0.29	950	20

MM10-016W	9.438	0.4507	4.647	2.02	1.15	85.8	95.8	41.82	0.46	1000	10
MM10-016X	10.65	0.3727	7.741	2.04	1.40	78.8	96.2	43.29	0.53	1000	20
MM10-016Y	11.48	0.1051	7.895	1.51	4.95	79.8	96.6	47.17	0.70	1050	10
MM10-016Z	13.28	0.1535	11.37	1.55	3.39	74.8	96.9	51.15	0.75	1050	20
MM10-016AA	12.62	0.1337	9.217	1.73	3.89	78.5	97.3	50.98	0.66	1100	10
MM10-016AB	16.91	0.0889	12.52	5.23	5.86	78.2	98.4	67.71	0.35	1250	5
MM10-016AC	55.28	0.0784	118.1	6.27	6.65	36.9	99.7	103.51	1.28	1500	5
MM10-016AD	45.97	-0.1801	88.47	1.34	—	43.1	100.0	100.57	1.89	1650	4
MM09-035 – Shocked and baked granite											
MM09-035A	217.8	0.1050	712.3	12.20	4.96	3.4	1.6	34.79	6.39	450	10
MM09-035B	10.82	0.0540	7.918	23.02	9.66	78.4	4.7	40.24	0.11	450	20
MM09-035C	8.516	0.0407	1.532	19.41	12.82	94.7	7.2	38.29	0.06	500	10
MM09-035D	8.185	0.0405	0.6763	37.81	12.89	97.6	12.2	37.92	0.03	500	20
MM09-035E	8.069	0.0355	0.3411	36.92	14.73	98.8	17.1	37.84	0.03	550	10
MM09-035F	8.061	0.0307	0.2302	61.18	17.01	99.2	25.2	37.95	0.02	550	20
MM09-035G	8.062	0.0304	0.1554	50.05	17.23	99.5	31.8	38.06	0.02	600	10
MM09-035H	8.037	0.0327	0.1370	68.69	16.01	99.5	40.8	37.97	0.02	600	20
MM09-035I	8.016	0.0317	0.1275	46.06	16.48	99.6	46.9	37.89	0.02	650	10
MM09-035J	8.016	0.0346	0.1314	52.71	15.09	99.6	53.9	37.88	0.02	650	20
MM09-035K	8.001	0.0384	0.1516	29.59	13.59	99.5	57.8	37.79	0.03	700	10

MM09-035L	8.038	0.0452	0.3068	33.35	11.56	98.9	62.2	37.74	0.03	700	20
MM09-035M	8.017	0.0512	0.2511	18.88	10.19	99.1	64.7	37.73	0.05	750	10
MM09-035N	8.065	0.0367	0.3431	19.73	14.23	98.8	67.3	37.82	0.05	750	20
MM09-035O	8.112	0.0696	0.4143	11.51	7.49	98.6	68.8	37.96	0.07	800	10
MM09-035P	8.203	0.0381	0.5732	13.10	13.73	98.0	70.6	38.15	0.07	800	20
MM09-035Q	8.281	0.0303	0.6602	8.57	17.24	97.7	71.7	38.39	0.11	850	10
MM09-035R	8.433	0.0215	0.8891	10.57	24.39	96.9	73.1	38.78	0.09	850	20
MM09-035S	8.744	0.0136	0.9551	7.36	38.82	96.8	74.1	40.15	0.12	900	10
MM09-035T	9.038	0.0017	1.271	8.93	340.55	95.8	75.2	41.09	0.11	900	20
MM09-035U	11.51	-0.0035	7.137	5.34	—	81.7	75.9	44.54	0.22	950	11
MM09-035V	9.847	0.0223	1.592	9.78	23.46	95.2	77.2	44.44	0.11	950	20
MM09-035W	10.89	0.0242	1.647	7.85	21.66	95.5	78.3	49.24	0.14	1000	10
MM09-035X	11.02	0.0137	2.325	8.88	38.42	93.8	79.4	48.90	0.13	1000	20
MM09-035Y	11.70	0.0168	1.735	10.83	31.23	95.6	80.9	52.89	0.11	1050	10
MM09-035Z	12.19	0.0132	2.178	12.72	39.78	94.7	82.5	54.55	0.11	1050	20
MM09-035AA	13.29	0.0009	1.622	19.13	672.25	96.4	85.1	60.44	0.08	1100	10
MM09-035AB	16.59	0.0159	2.528	23.00	32.97	95.5	88.1	74.48	0.08	1100	20
MM09-035AC	21.86	0.0067	3.229	30.43	79.18	95.6	92.1	97.63	0.08	1100	60
MM09-035AD	27.69	0.0093	5.442	26.81	57.08	94.2	95.7	121.04	0.11	1100	120

MM09-035AE	32.15	0.0122	10.77	20.47	43.40	90.1	98.4	133.92	0.18	1100	240
MM09-035AF	32.52	-0.0913	9.079	3.16	—	91.7	98.8	137.74	0.79	1200	10
MM09-035AG	30.55	0.0401	11.52	2.89	13.03	88.9	99.2	125.81	0.83	1250	5
MM09-035AH	79.66	0.2355	172.0	5.04	2.21	36.2	99.8	133.41	2.75	1500	5
MM09-035AI	90.35	0.2567	169.7	1.22	2.03	44.5	100.0	183.53	3.12	1650	4
MM09-021b – Shocked anorthosite											
MM09-021bA	72.32	0.4505	152.9	7.98	1.15	37.6	8.1	133.01	1.60	450	10
MM09-021bB	41.69	0.2876	4.670	5.41	1.81	96.7	13.6	194.09	0.63	450	20
MM09-021bC	49.02	0.4653	5.486	3.28	1.12	96.8	17.0	226.29	1.12	500	10
MM09-021bD	56.89	0.4993	5.034	4.70	1.04	97.5	21.8	261.84	0.93	500	20
MM09-021bE	92.24	0.6968	5.128	3.62	0.75	98.4	25.5	411.17	1.79	550	10
MM09-021bF	99.30	0.9938	4.091	5.57	0.52	98.9	31.1	440.97	1.26	550	20
MM09-021bG	130.9	1.179	2.968	4.54	0.44	99.4	35.8	564.38	2.01	600	10
MM09-021bH	143.6	1.010	2.215	6.51	0.51	99.6	42.4	611.93	1.42	600	20
MM09-021bI	180.4	1.090	1.913	4.61	0.48	99.7	47.1	741.38	2.33	650	10
MM09-021bJ	203.8	1.079	2.001	6.07	0.48	99.8	53.3	818.98	1.90	650	20
MM09-021bK	232.8	1.308	2.474	4.06	0.40	99.7	57.4	910.53	3.06	700	10
MM09-021bL	245.7	1.476	2.539	4.98	0.35	99.7	62.5	949.77	2.55	700	20
MM09-021bM	264.1	1.714	2.608	3.31	0.30	99.8	65.8	1004.89	4.03	750	10
MM09-021bN	267.8	2.029	3.359	3.87	0.26	99.7	69.8	1015.18	3.82	750	20

MM09-021bO	284.5	2.353	3.710	2.47	0.22	99.7	72.3	1063.40	5.42	800	10
MM09-021bP	290.2	2.170	5.272	2.60	0.24	99.5	74.9	1078.05	5.46	800	20
MM09-021bQ	296.5	2.076	6.145	1.58	0.25	99.4	76.5	1094.89	8.79	850	10
MM09-021bR	305.6	2.253	7.879	1.64	0.23	99.3	78.2	1118.79	8.60	850	20
MM09-021bS	303.0	2.212	6.565	1.02	0.23	99.4	79.3	1112.67	13.79	900	10
MM09-021bT	300.1	2.020	9.099	1.20	0.26	99.2	80.5	1102.56	12.21	900	20
MM09-021bU	301.2	2.020	7.626	0.76	0.26	99.3	81.3	1106.73	18.89	950	10
MM09-021bV	304.9	2.253	10.01	0.90	0.23	99.1	82.2	1115.13	15.32	950	20
MM09-021bW	305.3	2.285	7.141	0.59	0.23	99.4	82.8	1118.62	24.00	1000	10
MM09-021bX	312.9	1.942	10.94	0.68	0.27	99.0	83.5	1136.12	22.00	1000	20
MM09-021bY	316.9	3.517	9.011	0.50	0.15	99.3	84.0	1150.05	28.61	1050	10
MM09-021bZ	309.7	2.890	12.98	0.60	0.18	98.8	84.6	1126.47	24.26	1050	20
MM09-021bAA	337.4	2.966	15.60	0.38	0.17	98.7	85.0	1199.16	39.57	1100	10
MM09-021bAB	329.6	3.310	15.15	0.57	0.16	98.7	85.6	1179.15	25.66	1100	20
MM09-021bAC	349.7	3.962	28.03	1.06	0.13	97.7	86.6	1222.74	14.92	1100	60
MM09-021bAD	356.8	4.522	45.89	1.38	0.11	96.3	88.1	1227.87	11.05	1100	120
MM09-021bAE	346.0	4.670	23.07	1.29	0.11	98.1	89.4	1217.52	12.05	1200	10
MM09-021bAF	333.6	7.588	9.499	8.71	0.07	99.3	98.2	1197.86	1.79	1500	5
MM09-021bAG	248.7	5.129	23.75	1.73	0.10	97.4	100.0	942.93	7.23	1650	4
MM10-028 – Anorthosite											

MM10-028A	66.94	0.7262	202.7	6.67	0.72	10.6	7.5	34.75	2.09	450	10
MM10-028B	13.99	0.7697	13.95	5.78	0.68	71.0	14.0	48.43	0.30	450	20
MM10-028C	11.59	0.9267	6.317	3.68	0.56	84.6	18.2	47.83	0.33	500	10
MM10-028D	12.03	1.231	5.767	4.78	0.42	86.7	23.5	50.86	0.28	500	20
MM10-028E	13.11	1.504	5.769	3.56	0.35	88.0	27.6	56.15	0.37	550	10
MM10-028F	16.98	1.956	8.324	4.25	0.27	86.5	32.3	71.23	0.37	550	20
MM10-028G	22.44	2.636	9.876	3.05	0.20	88.0	35.8	95.20	0.60	600	10
MM10-028H	31.05	3.388	12.53	3.90	0.15	89.0	40.2	131.94	0.65	600	20
MM10-028I	41.86	4.569	11.73	3.02	0.11	92.6	43.6	182.76	1.06	650	10
MM10-028J	51.41	4.866	10.94	3.98	0.11	94.5	48.0	226.28	0.95	650	20
MM10-028K	64.12	5.305	8.037	3.12	0.10	97.0	51.6	285.00	1.48	700	10
MM10-028L	78.60	4.593	6.421	4.04	0.11	98.1	56.1	346.98	1.37	700	20
MM10-028M	102.4	4.468	4.680	3.26	0.12	99.0	59.8	444.12	2.16	750	10
MM10-028N	120.4	4.167	3.916	3.63	0.12	99.3	63.9	513.45	2.28	750	20
MM10-028O	138.3	4.398	3.674	2.63	0.12	99.5	66.8	579.45	3.32	800	10
MM10-028P	149.2	3.996	4.213	2.83	0.13	99.4	70.0	617.83	3.05	800	20
MM10-028Q	169.5	3.680	5.541	2.09	0.14	99.2	72.4	686.53	4.66	850	10
MM10-028R	173.1	3.380	3.929	2.04	0.15	99.5	74.7	700.03	4.84	850	20
MM10-028S	192.3	3.311	2.695	1.28	0.16	99.7	76.1	765.08	7.95	900	10

MM10-028T	207.6	3.064	5.320	1.38	0.17	99.4	77.6	811.73	8.27	900	20
MM10-028U	230.9	3.490	5.890	1.09	0.15	99.4	78.9	883.98	10.76	950	10
MM10-028V	249.0	3.735	5.396	1.46	0.14	99.5	80.5	939.02	8.67	950	20
MM10-028W	256.0	3.877	3.844	1.17	0.13	99.7	81.8	961.17	11.18	1000	10
MM10-028X	265.5	3.911	7.259	1.48	0.13	99.3	83.5	985.80	8.97	1000	20
MM10-028Y	297.2	5.160	8.314	0.93	0.10	99.3	84.6	1075.53	15.29	1050	10
MM10-028Z	304.7	5.329	12.76	1.15	0.10	98.9	85.8	1092.62	13.08	1050	20
MM10-028AA	387.5	8.362	23.63	0.85	0.06	98.4	86.8	1300.47	18.52	1100	10
MM10-028AB	396.7	7.502	27.65	1.17	0.07	98.1	88.1	1319.30	13.86	1100	20
MM10-028AC	418.2	7.806	38.72	2.16	0.07	97.4	90.6	1362.90	8.39	1100	60
MM10-028AD	427.7	7.544	54.08	2.78	0.07	96.4	93.7	1374.55	5.99	1100	120
MM10-028AE	432.6	7.480	79.13	3.31	0.07	94.7	97.4	1368.55	5.21	1100	240
MM10-028AF	472.0	12.75	37.38	0.66	0.04	97.9	98.2	1491.00	26.74	1200	10
MM10-028AG	467.4	9.813	31.32	0.51	0.05	98.2	98.7	1482.20	33.81	1250	5
MM10-028AH	416.3	7.625	46.89	1.12	0.07	96.8	100.0	1352.61	16.47	1650	4
2021-3163 – Mangerite											
2021-3163A	747.9	-0.2091	228.6	1.14	—	91.0	0.3	1930.51	22.46	450	10
2021-3163B	301.7	0.0339	19.53	1.08	15.40	98.1	0.6	1090.18	14.19	450	20
2021-3163C	365.8	0.2598	15.90	0.90	2.00	98.7	0.8	1262.80	18.55	500	10
2021-3163D	349.3	-0.2356	9.843	1.33	—	99.2	1.2	1224.89	12.51	500	20

2021-3163E	397.2	-0.1372	11.57	1.29	—	99.1	1.6	1343.18	14.03	550	10
2021-3163F	354.8	-0.0022	5.265	1.96	—	99.6	2.1	1242.67	8.37	550	20
2021-3163G	406.6	-0.0443	7.891	1.96	—	99.4	2.6	1368.40	9.54	600	10
2021-3163H	370.4	-0.0510	3.268	2.91	—	99.7	3.4	1283.53	6.41	600	20
2021-3163I	390.3	-0.0821	5.572	2.65	—	99.6	4.1	1330.83	6.57	650	10
2021-3163J	367.4	-0.0866	2.560	3.66	—	99.8	5.1	1276.41	4.83	650	20
2021-3163K	384.2	-0.1949	4.284	3.27	—	99.7	6.0	1316.59	5.53	700	10
2021-3163L	373.1	-0.0424	2.006	4.37	—	99.8	7.2	1291.02	3.92	700	20
2021-3163M	379.5	-0.0808	4.209	3.84	—	99.7	8.2	1305.20	4.56	750	10
2021-3163N	370.0	-0.0478	2.319	4.82	—	99.8	9.5	1283.11	3.57	750	20
2021-3163O	385.4	-0.0225	4.625	4.06	—	99.6	10.6	1319.54	4.33	800	10
2021-3163P	374.0	-0.0024	2.852	4.77	—	99.8	11.9	1292.69	3.76	800	20
2021-3163Q	399.1	-0.1065	7.495	4.20	—	99.4	13.1	1350.57	4.35	850	10
2021-3163R	379.8	-0.0534	4.252	4.73	—	99.7	14.3	1305.97	3.81	850	20
2021-3163S	407.1	-0.0466	9.448	4.68	—	99.3	15.6	1368.44	3.78	900	10
2021-3163T	390.7	0.0085	6.104	5.74	62.08	99.5	17.1	1331.36	2.98	900	20
2021-3163U	408.6	-0.0788	9.529	7.14	—	99.3	19.1	1372.03	2.67	950	10
2021-3163V	391.3	-0.0440	5.732	8.97	—	99.6	21.5	1333.17	2.08	950	20
2021-3163W	407.0	-0.0008	8.057	11.74	—	99.4	24.7	1369.31	1.60	1000	10

2021-3163X	391.0	-0.0031	5.036	14.20	—	99.6	28.5	1333.04	1.31	1000	20
2021-3163Y	406.6	0.0077	6.971	21.17	69.24	99.5	34.3	1369.01	0.94	1050	10
2021-3163Z	401.1	0.0329	6.028	24.88	15.89	99.6	41.0	1356.55	0.80	1050	20
2021-3163AA	404.1	0.0187	5.605	34.70	28.00	99.6	50.4	1364.02	0.59	1100	10
2021-3163AB	404.6	0.0109	4.903	51.07	48.51	99.6	64.2	1365.85	0.47	1100	20
2021-3163AC	405.9	0.0100	4.445	53.28	53.06	99.7	78.6	1369.27	0.45	1100	60
2021-3163AD	410.6	0.0198	5.977	31.69	26.53	99.6	87.2	1379.39	0.69	1100	120
2021-3163AE	418.7	0.0548	11.31	24.67	9.51	99.2	93.9	1394.79	0.83	1100	240
2021-3163AF	423.4	0.0164	4.676	5.29	32.09	99.7	95.3	1410.26	3.47	1200	10
2021-3163AG	416.2	-0.0054	3.621	4.05	—	99.7	96.4	1394.23	4.46	1250	5
2021-3163AH	422.7	0.1993	6.234	7.43	2.61	99.6	98.4	1407.84	2.62	1500	5
2021-3163AI	426.2	0.2346	9.344	5.85	2.22	99.4	100	1413.81	3.18	1650	4
Sample	**$^{40}Ar/^{39}Ar$**	**$^{37}Ar/^{39}Ar$**	**$^{36}Ar/^{39}Ar$ (10^{-3})**	**$^{39}Ar_K$ (fA)**	**K/Ca**	**$^{40}Ar^*$ (%)**	**Total ^{39}Ar released (%)**	**Age (Ma)**	**± 2σ**	**Power (Watts)**	
CM09-05 subsample 1 – Impact glass											
CM09-05_1B	55.89	2.352	2.316	0.45	2.21E-01	99.1	0.6	222.24	12.39	1.3	
CM09-05_1C	176.7	2.139	0.3355	0.64	2.43E-01	100.0	1.5	631.43	22.71	1.6	
CM09-05_1D	1728.4	2.281	2.605	1.41	2.28E-01	100.0	3.4	2955.54	29.82	1.9	
CM09-05_1E	247.2	2.298	1.019	2.27	2.26E-01	100.0	6.5	832.30	7.99	2.2	
CM09-05_1F	25.87	2.351	0.5518	4.67	2.21E-01	100.1	12.8	107.27	0.62	3.0	

CM09-05_1G	19.04	2.349	0.6867	26.38	2.21E-01	100.0	48.6	79.43	0.10	5.0
CM09-05_1H	18.97	2.349	0.7043	12.64	2.21E-01	99.9	65.8	79.14	0.19	7.0
CM09-05_1I	18.61	2.340	0.8787	10.86	2.22E-01	99.7	80.5	77.44	0.21	10.0
CM09-05_1J	18.81	2.324	1.050	14.36	2.23E-01	99.4	100.0	78.06	0.18	15.0
CM09-05 subsample 2 – Impact glass										
CM09-05_2A	43.77	3.129	18.01	0.07	1.66E-01	88.4	0.1	162.41	41.21	0.8
CM09-05_2B	22.26	2.424	2.322	0.41	2.14E-01	97.8	0.9	93.06	3.65	1.3
CM09-05_2C	91.40	2.142	1.263	0.64	2.42E-01	99.8	2.1	361.64	8.07	1.6
CM09-05_2D	387.9	2.397	1.723	1.88	2.17E-01	99.9	5.7	1202.01	8.08	1.9
CM09-05_2E	69.51	2.254	0.8260	2.21	2.30E-01	99.9	9.8	281.69	2.05	2.2
CM09-05_2F	19.79	2.321	0.6660	3.56	2.24E-01	100.0	16.6	84.74	0.43	3.0
CM09-05_2G	18.65	2.334	0.7299	13.84	2.22E-01	99.9	42.7	79.89	0.11	5.0
CM09-05_2H	18.70	2.329	0.7541	15.43	2.23E-01	99.8	71.8	80.07	0.10	7.0
CM09-05_2I	18.92	2.312	0.7503	7.74	2.25E-01	99.9	86.5	81.02	0.20	10.0
CM09-05_2J	19.02	2.316	0.8532	7.17	2.24E-01	99.7	100.0	81.30	0.21	15.0
CM09-05 subsample 3 – Impact glass										
CM09-05_3A	45.19	1.884	100.4	0.09	2.76E-01	34.7	0.1	122.54	25.09	0.5
CM09-05_3B	13.32	2.263	6.566	0.47	2.30E-01	86.8	0.9	91.17	3.81	0.8
CM09-05_3C	10.81	2.258	1.886	1.70	2.30E-01	96.5	3.7	82.45	0.93	1.3
CM09-05_3D	87.02	2.263	1.082	1.66	2.29E-01	99.8	6.3	594.72	5.29	1.6

CM09-05_3E	40.17	2.328	0.9011	2.10	2.23E-01	99.8	9.7	298.53	2.11	1.9
CM09-05_3F	10.09	2.333	0.7632	2.98	2.23E-01	99.6	14.5	79.54	0.48	2.2
CM09-05_3G	9.982	2.359	0.7016	6.78	2.20E-01	99.8	25.5	78.84	0.23	2.6
CM09-05_3H	9.933	2.383	0.6689	10.35	2.18E-01	100.0	42.2	78.55	0.16	3.0
CM09-05_3I	9.915	2.361	0.7177	10.95	2.20E-01	99.8	59.9	78.29	0.15	3.5
CM09-05_3J	10.01	2.366	0.7185	7.39	2.20E-01	99.8	71.9	79.00	0.23	4.0
CM09-05_3K	10.12	2.361	0.7686	4.72	2.20E-01	99.7	79.5	79.76	0.33	6.0
CM09-05_3L	10.16	2.374	0.8683	3.22	2.19E-01	99.4	84.7	79.81	0.51	10.0
CM09-05_3M	10.08	2.364	0.7546	9.45	2.20E-01	99.7	100.0	79.51	0.18	15.0
CM09-05 subsample 4 – Impact glass										
CM09-05_4A	39.09	2.258	83.26	0.23	2.30E-01	37.5	0.3	114.96	9.39	0.5
CM09-05_4B	14.43	2.215	13.16	1.38	2.35E-01	74.3	2.2	84.70	1.30	0.8
CM09-05_4C	13.86	2.283	2.643	3.95	2.27E-01	95.7	7.7	104.26	0.48	1.3
CM09-05_4D	13.02	2.323	1.062	2.93	2.24E-01	99.0	11.7	101.43	0.65	1.6
CM09-05_4E	12.35	2.325	0.9396	3.66	2.23E-01	99.3	16.8	96.57	0.46	1.9
CM09-05_4F	9.772	2.348	0.7568	7.31	2.21E-01	99.7	26.9	77.11	0.21	2.2
CM09-05_4G	9.802	2.358	0.7580	11.03	2.20E-01	99.7	42.1	77.35	0.15	2.6
CM09-05_4H	9.838	2.349	0.8793	14.00	2.21E-01	99.3	61.5	77.35	0.12	3.0
CM09-05_4I	9.923	2.360	0.9942	11.25	2.20E-01	99.0	77.1	77.75	0.14	3.5
CM09-05_4J	10.43	2.333	2.707	4.82	2.23E-01	94.1	83.7	77.73	0.36	4.0

CM09-05_4K	9.989	2.327	0.9290	3.39	2.23E-01	99.1	88.4	78.39	0.44	6.0
CM09-05_4L	10.06	2.334	1.169	4.19	2.23E-01	98.5	94.2	78.42	0.37	10.0
CM09-05_4M	10.31	2.327	0.9871	4.19	2.23E-01	99.0	100.0	80.77	0.37	15.0

Argon isotopic ratios corrected for blank, radioactive decay, and mass discrimination, not corrected for interfering reactions.
Uncertainties quoted for individual analyses include analytical uncertainty only, without interfering reaction or J uncertainties.
Integrated age calculated by summing isotopic measurements of all steps.
Plateau age is inverse-variance-weighted mean of selected steps.
Plateau age uncertainty is inverse-variance-weighted mean uncertainty (Taylor, 1982) times root MSWD where MSWD>1.
Plateau uncertainty is weighted uncertainty of Taylor (1982).
Isotopic abundances after Steiger and Jäger (1977).
" – " No detectable ^{37}Ar thus K/Ca undefined.
Weight percent K_2O calculated from ^{39}Ar signal, sample weight, and instrument sensitivity.
Ages calculated relative to FC-2 Fish Canyon Tuff sanidine interlaboratory standard at 28.201 Ma.
$\lambda^{40}K_{total}$ = 5.463E-10

Appendix B – Supporting Figures from Kamestastin Impact Structure Study (Chapter 2)

Images of Sampling Locations



Figure B1: Image of outcrop site where sample 2021-3163 was collected. This is a mangerite outcrop inside the impact crater near the west rim of the impact structure.



Figure B2: Image of field site where sample MM09-021b was collected. This site hosts shocked anorthosite and is from the central uplift region of the impact structure on Horseshoe Island.



Figure B3: Image of collection site of sample MM09-035. This site hosts shocked and baked granite rock. The locality is near Coté Creek and is part of an inner terrace portion of the impact structure.



Figure B4: Sample outcrop for sample MM10-016. This sample site is primarily shocked and baked sample material found near the Coté Creek region. This sample site is considered to be part of an inner terrace of the impact structure.



Figure B5: Outcrop that hosted sample MM10-028. This site consists of anorthositic material and is located near the Piccadilly Creek region. This site is considered to be part of an inner terrace of the impact structure.

Thin section images

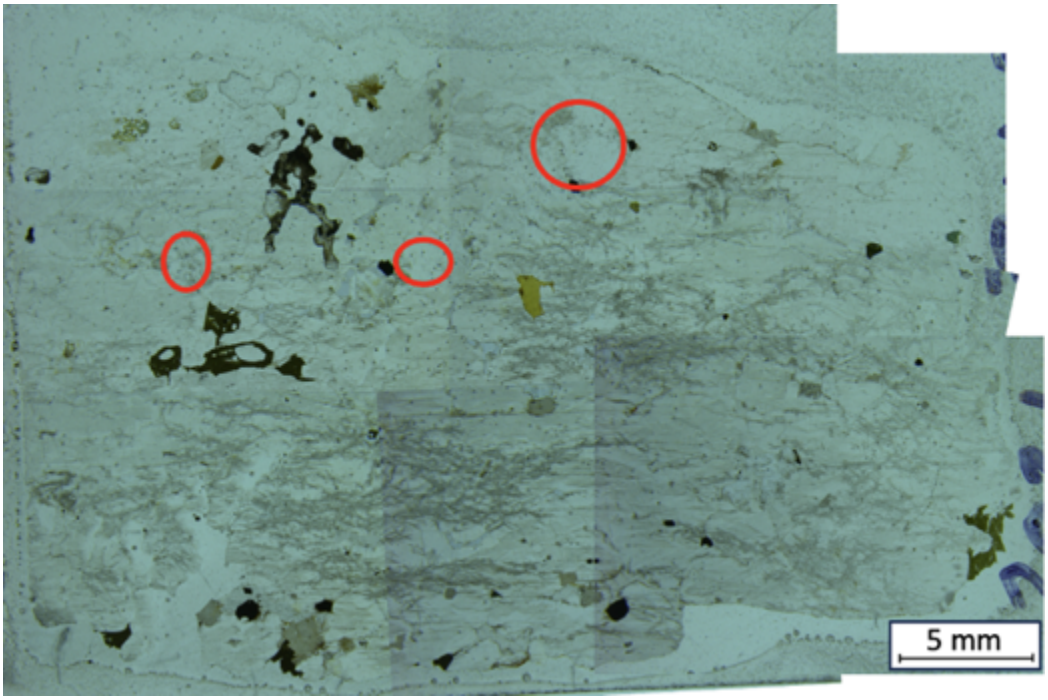

Figure B6: Thin section of sample 2021-3163 under plane polarized light. This rock is classified as a mangerite and was found near the west rim of the impact structure within the crater rim. Plagioclase feldspar crystals that were targeted for Raman analyses are circled in red.

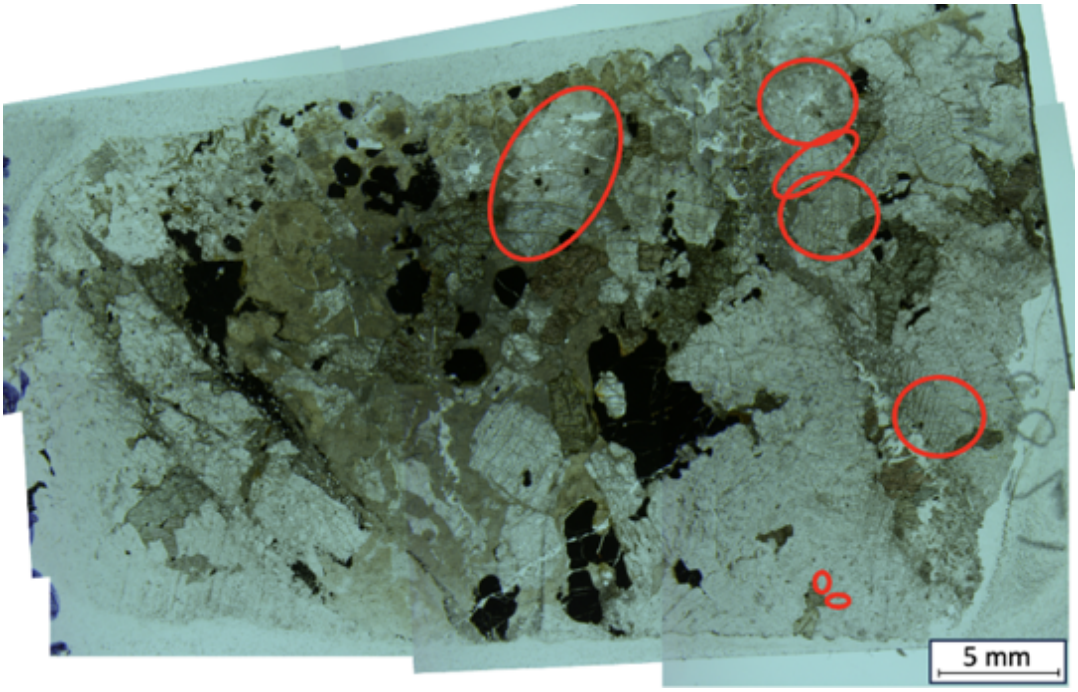

Figure B7: Thin section of sample MM09-021b under plane polarized light. This sample is shocked anorthosite from the central uplift of the impact structure on Horseshoe Island. The regions circled in green are plagioclase feldspar crystals and diaplectic glass that were targeted for Raman analyses.

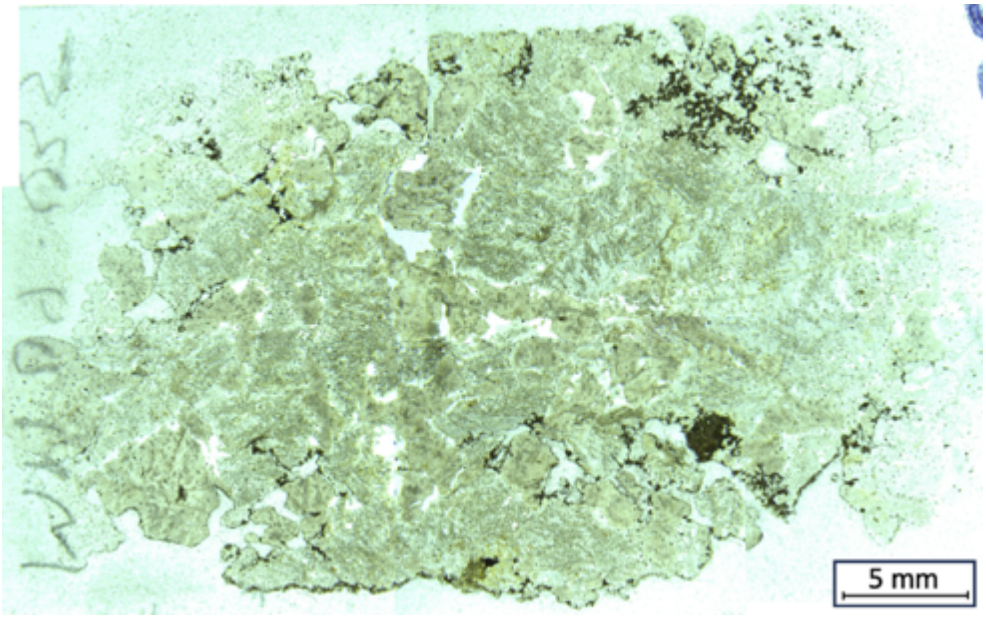

Figure B8: Thin section of sample MM09-035 under plane polarized light. This sample is shocked and baked granite from an inner terrace of the impact structure.

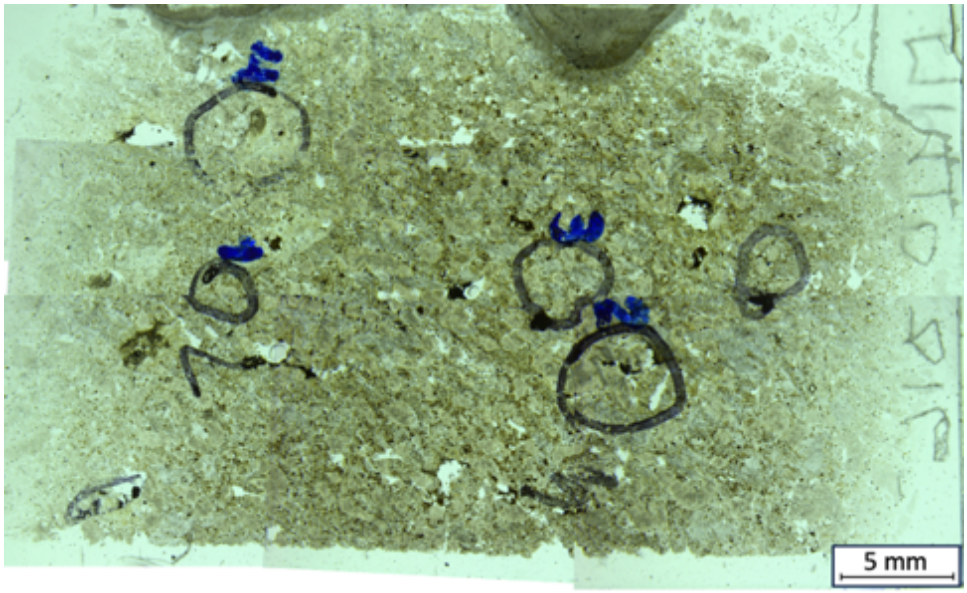

Figure B9: Thin section of sample MM10-016 under plane polarized light. This sample is shocked and baked granite from an inner terrace of the impact structure.

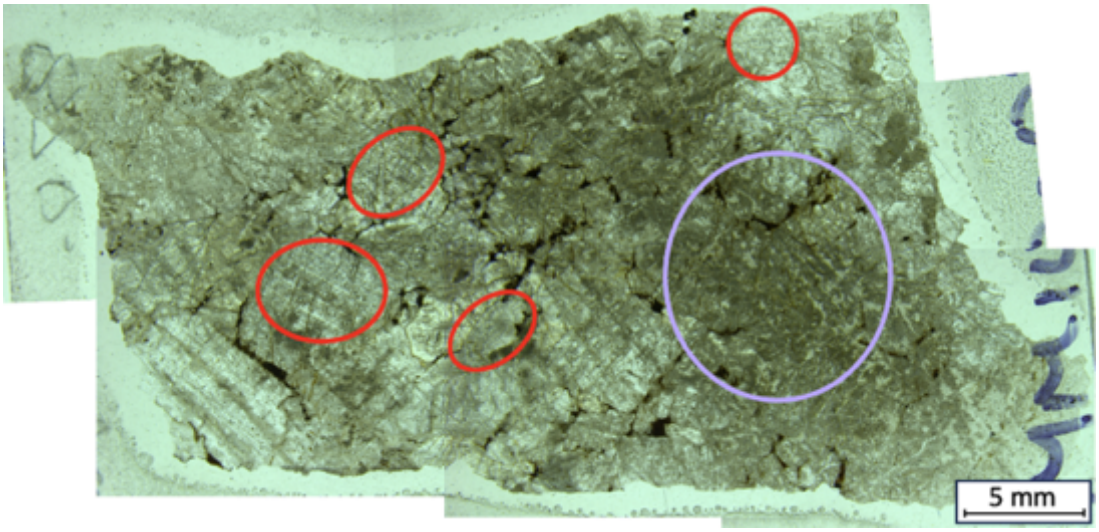

Figure B10: Thin section of sample MM10-028 under plane polarized light. This is an anorthosite rock from an inner terrace of the impact structure. Regions circled in red are plagioclase feldspar crystals that were targeted for Raman analyses. The region circled in purple is a hydrothermally altered region of this sample that we targeted for Raman analyses.

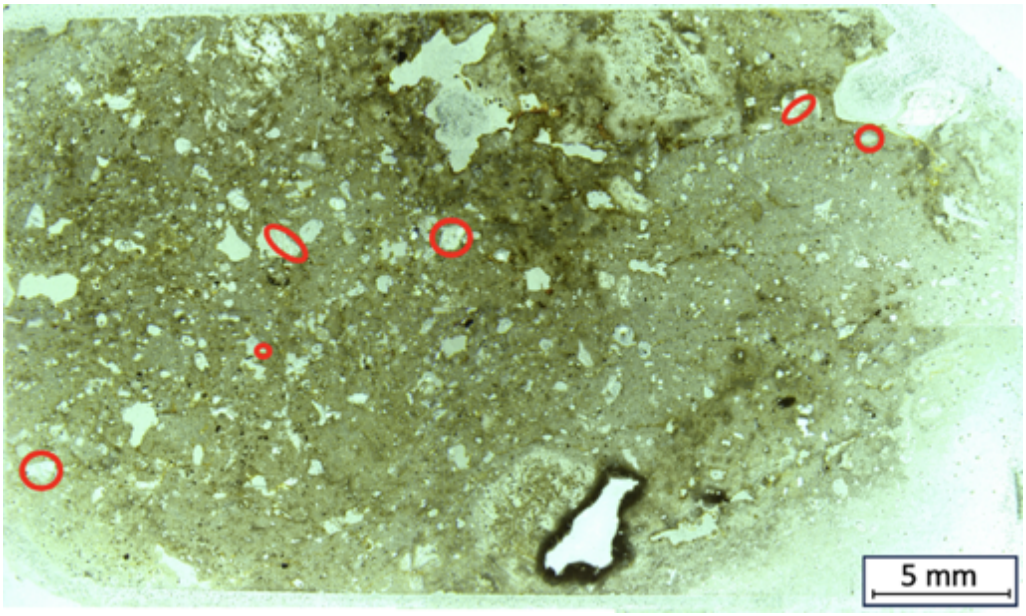

Figure B11: Thin section of sample MM09-035- under plane polarized light. This is a shocked and baked granite from an inner terrace of the impact structure. The plagioclase feldspar crystals that were targeted for Raman analyses are circled in red.

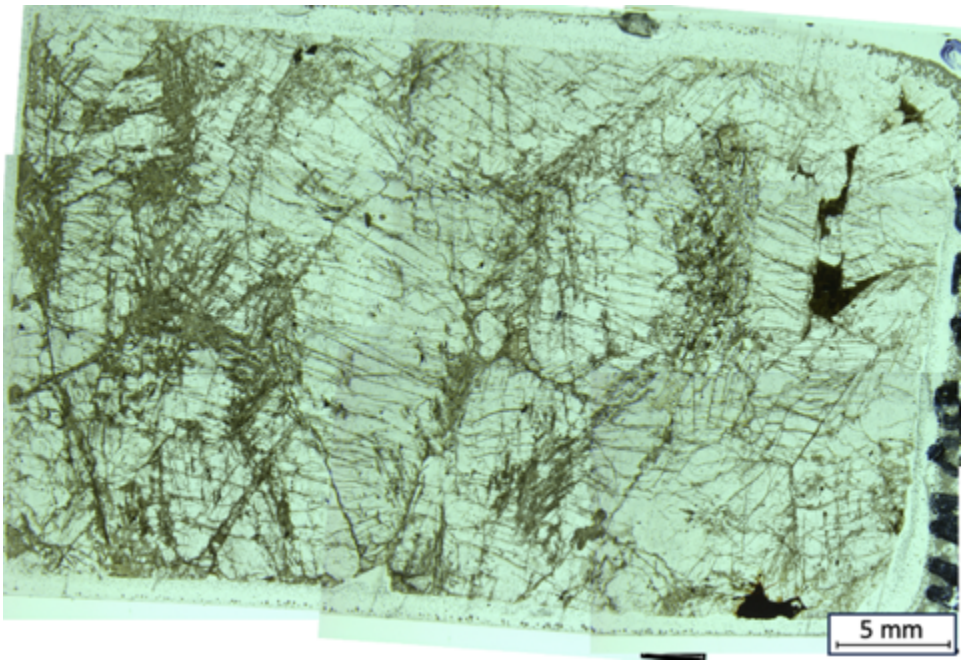

Figure B12: Thin section of sample MM09-035 D under plane polarized light. This is a shocked and baked granite from an inner terrace of the impact structure.

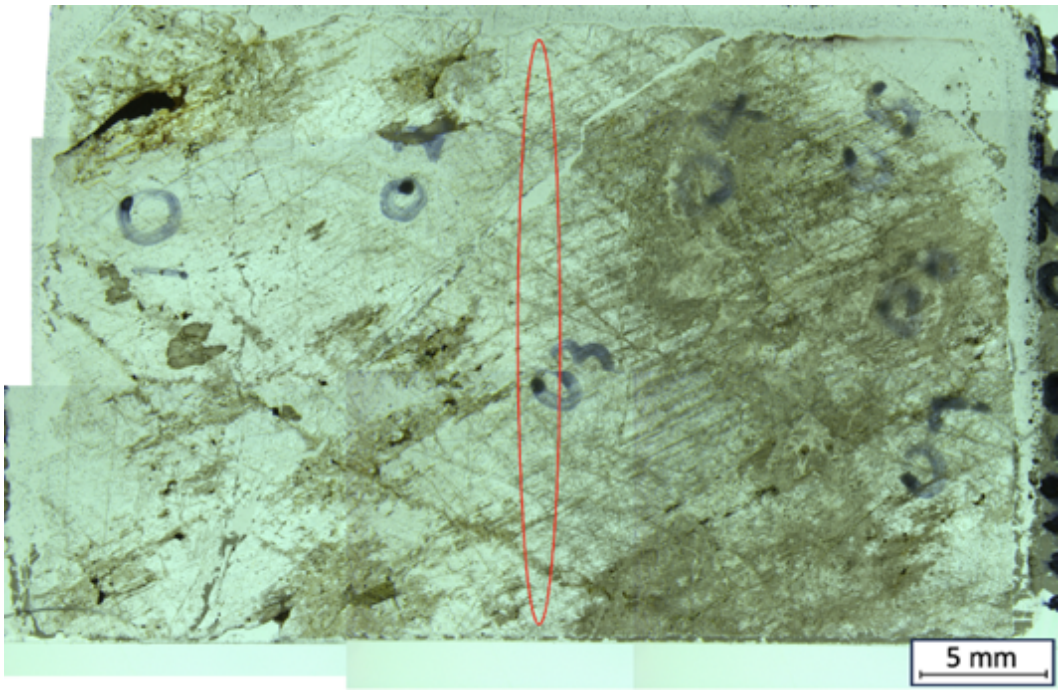

Figure B13: Thin section of sample MM09-035 F under plane polarized light. This is a shocked and baked granite from an inner terrace of the impact structure. Nearly the entirety of this thin section consists of one large plagioclase crystal and a transect of Raman analyses was taken across this sample in the region circled in red.

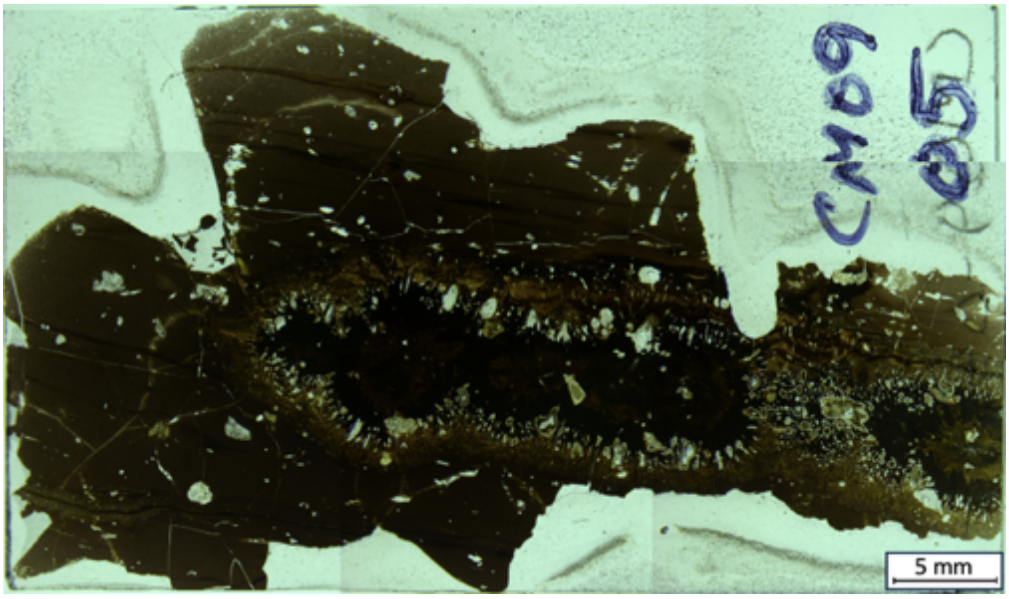

Figure B14: Thin section of sample CM09-05 under plane polarized light. This glass sample is from an inner terrace of the impact structure. The glass is clast rich and in the center of the thin section consists of a series of phyllosilicates and infilled amygdules.

Raman spectra of plagioclase from each sample

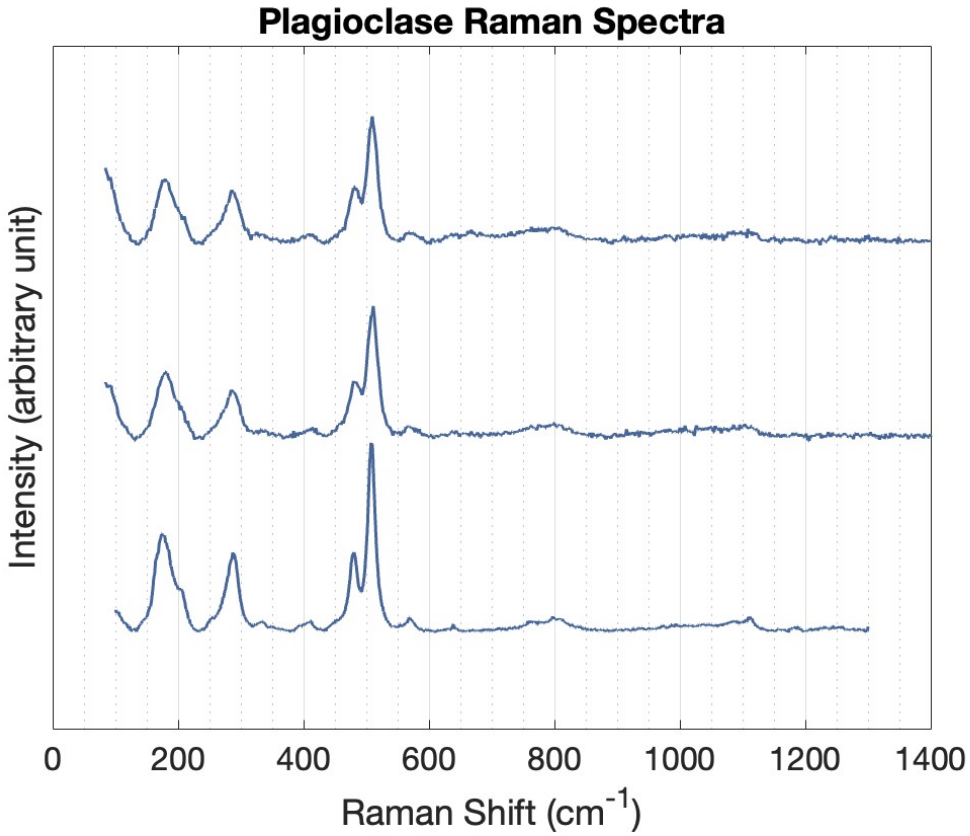

Figure B15: Representative Raman spectra from each of the three plagioclase crystals analyzed via Raman in sample 2021-3163. These samples were classified as shock stages S1 and S2.

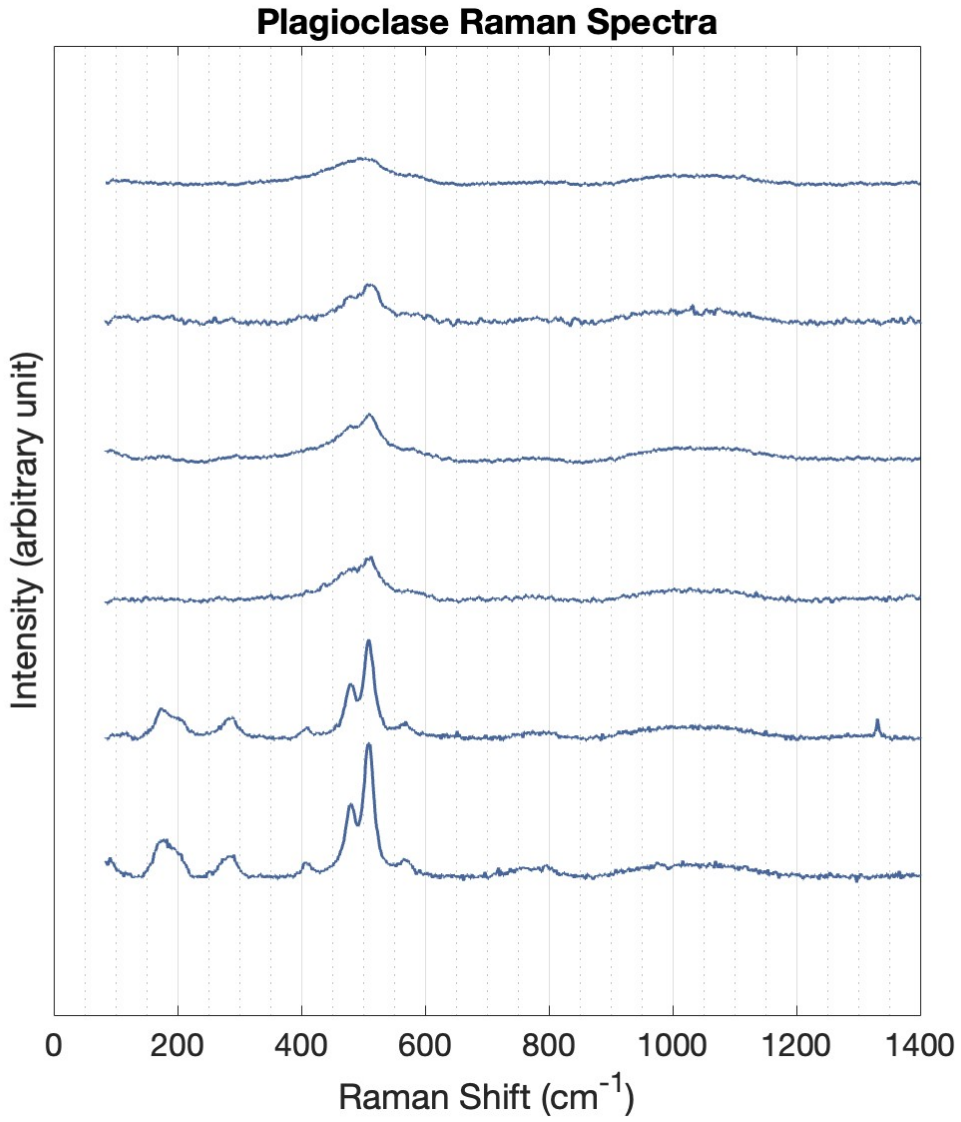

Figure B16: Representative Raman spectra from each of the six plagioclase crystals analyzed via Raman in sample MM09-021b. These samples were classified as shock stages S3 and S4.

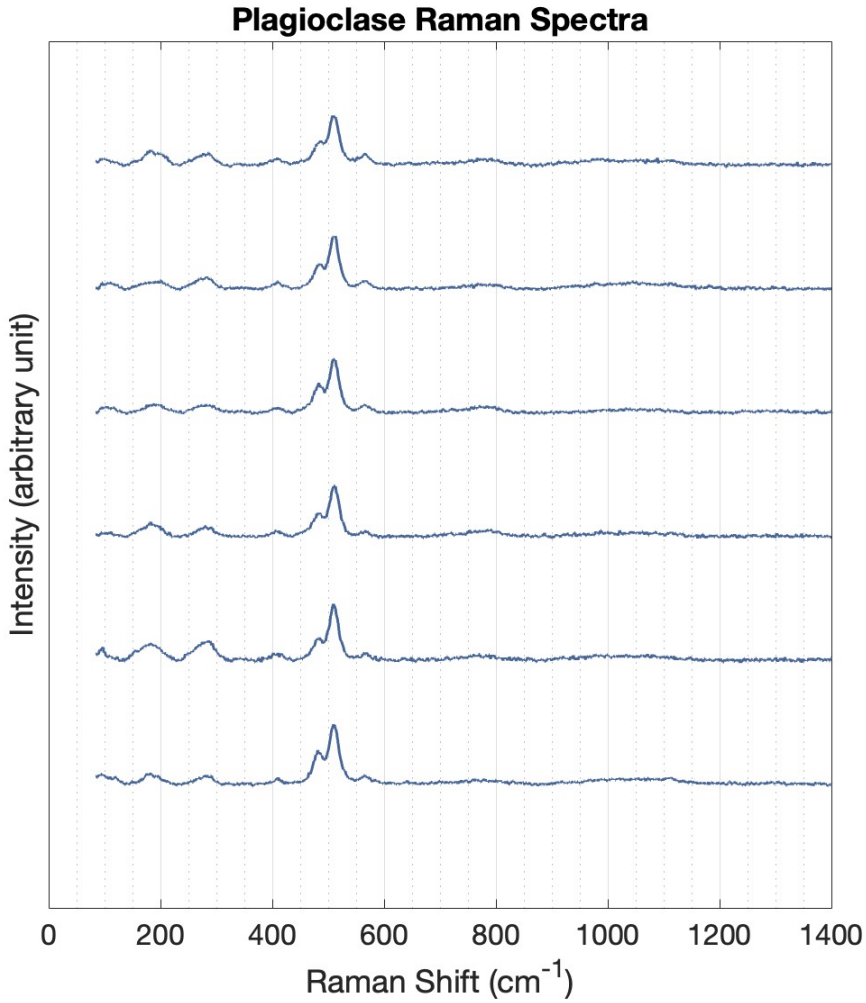

Figure B17: Representative Raman spectra from each of the six plagioclase crystals analyzed via Raman in sample MM09-035. These samples were classified as shock stages S2 and S3.

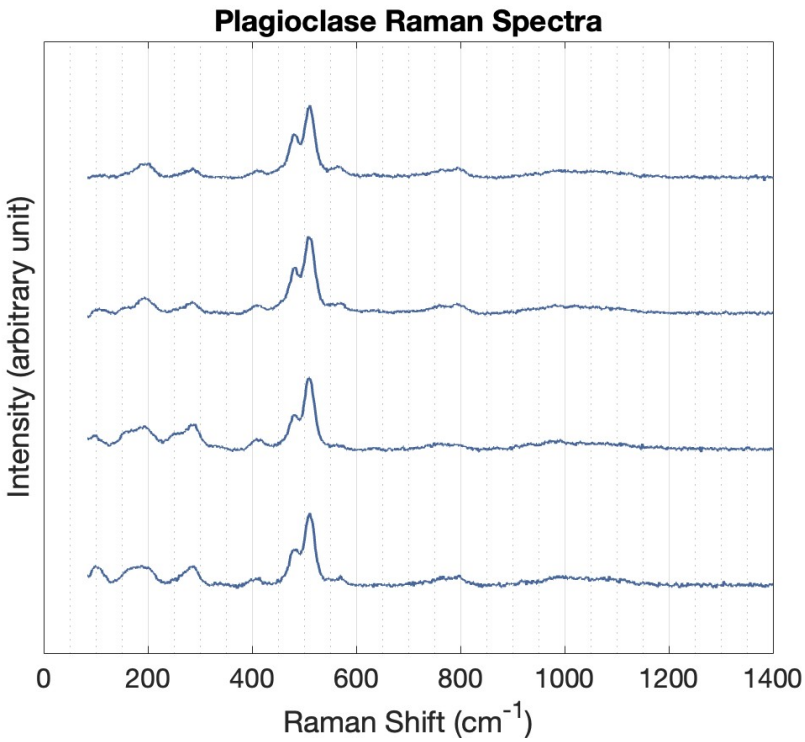

Figure B18: Representative Raman spectra from each of the four plagioclase crystals analyzed via Raman in sample MM10-028. These samples were classified as shock stage S3.

Raman spectra of hydrothermal minerals

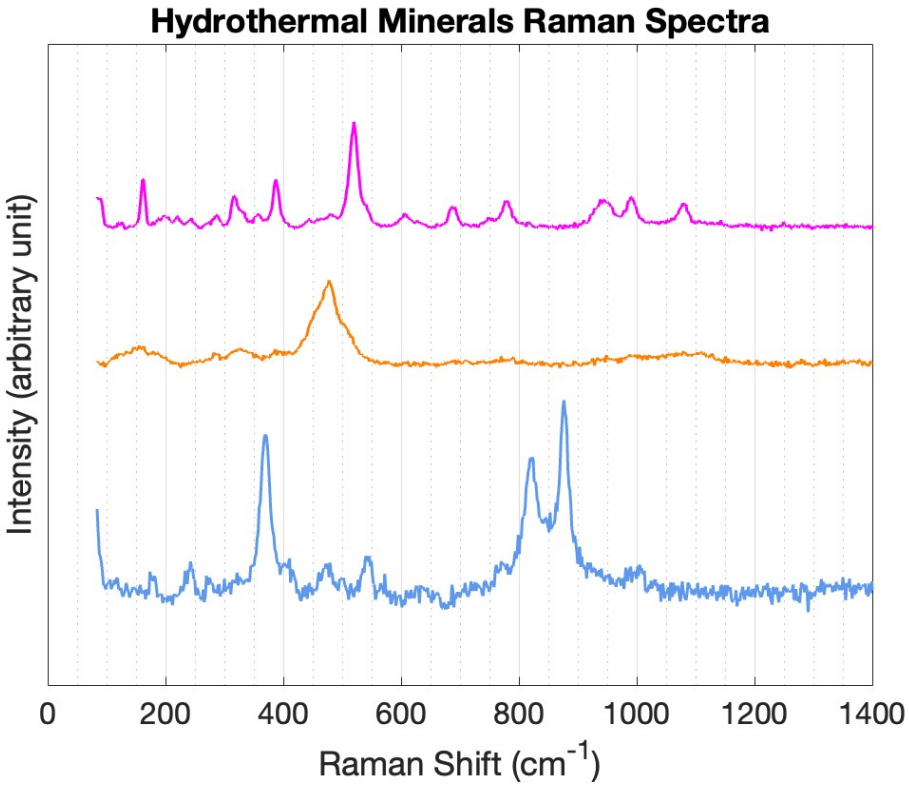

Figure B19: Raman spectra from a visually altered region of sample MM10-028. Spectra were identified as grossular (blue), chabazite (orange), and prehnite (pink) and are interpreted to be hydrothermal in origin.

Full age spectra (unzoomed)

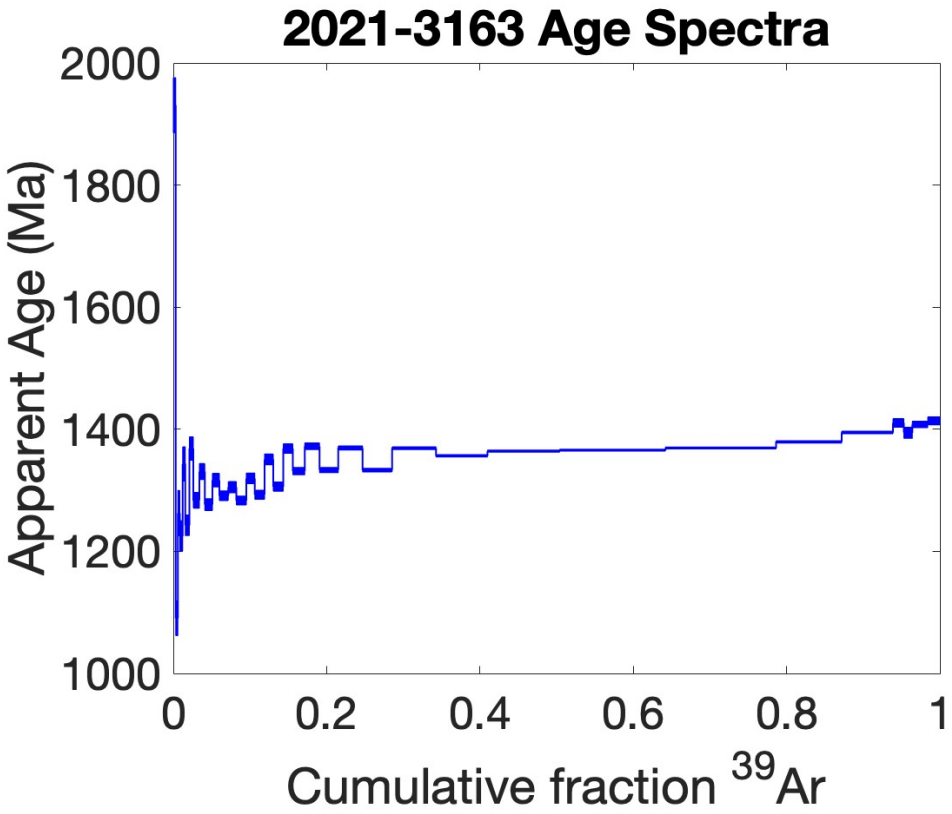

Figure B20: Full scale $^{40}Ar/^{39}Ar$ age spectra from sample 2021-3163. Age spectra figure presented in the main manuscript is zoomed into a narrower age range for ease of viewing.

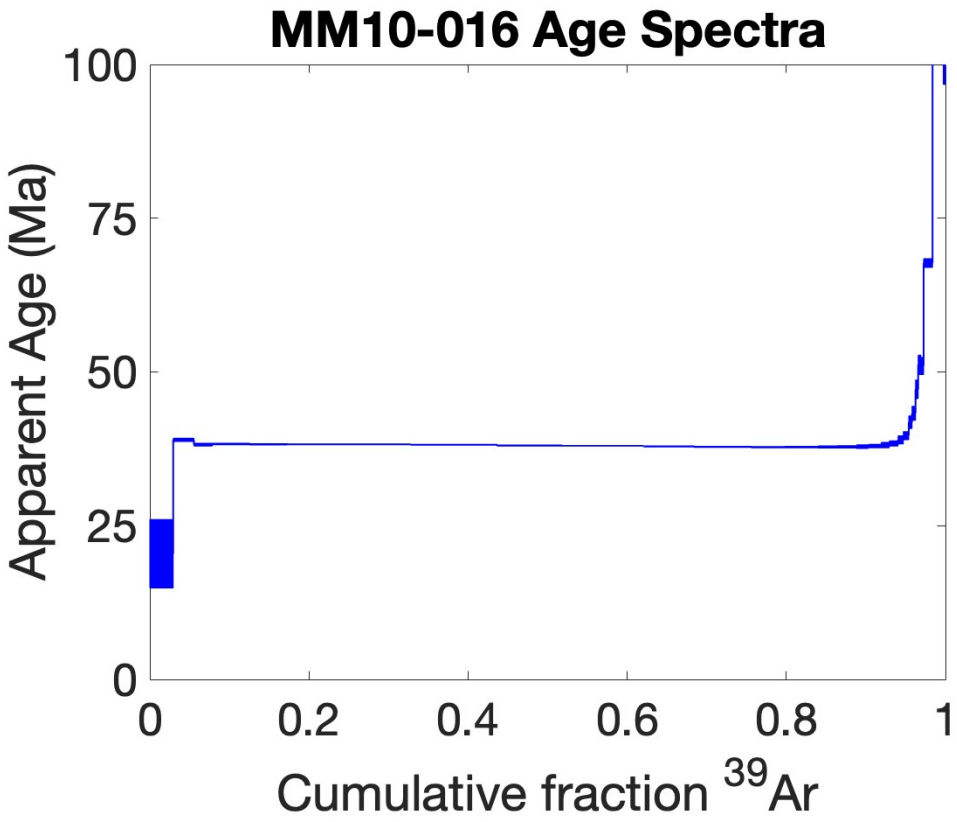

Figure B21: Full scale $^{40}Ar/^{39}Ar$ age spectra from sample MM10-016. Age spectra figure presented in the main manuscript is zoomed into a narrower age range for ease of viewing.

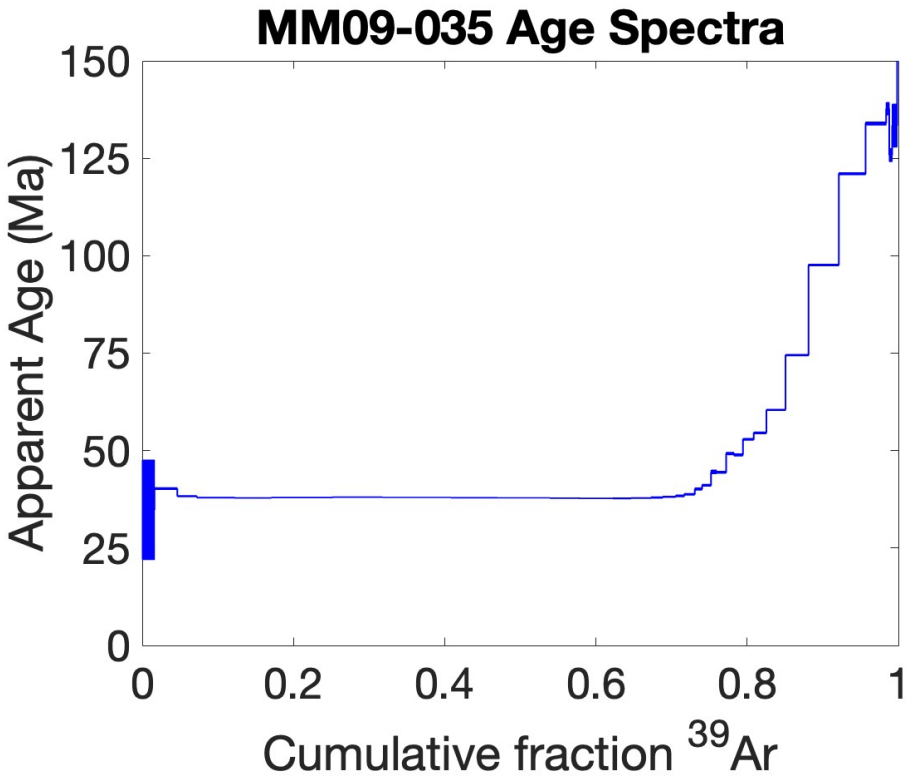

Figure B22: Full scale $^{40}Ar/^{39}Ar$ age spectra from sample MM09-035. Age spectra figure presented in the main manuscript is zoomed into a narrower age range for ease of viewing.

Glass age spectra

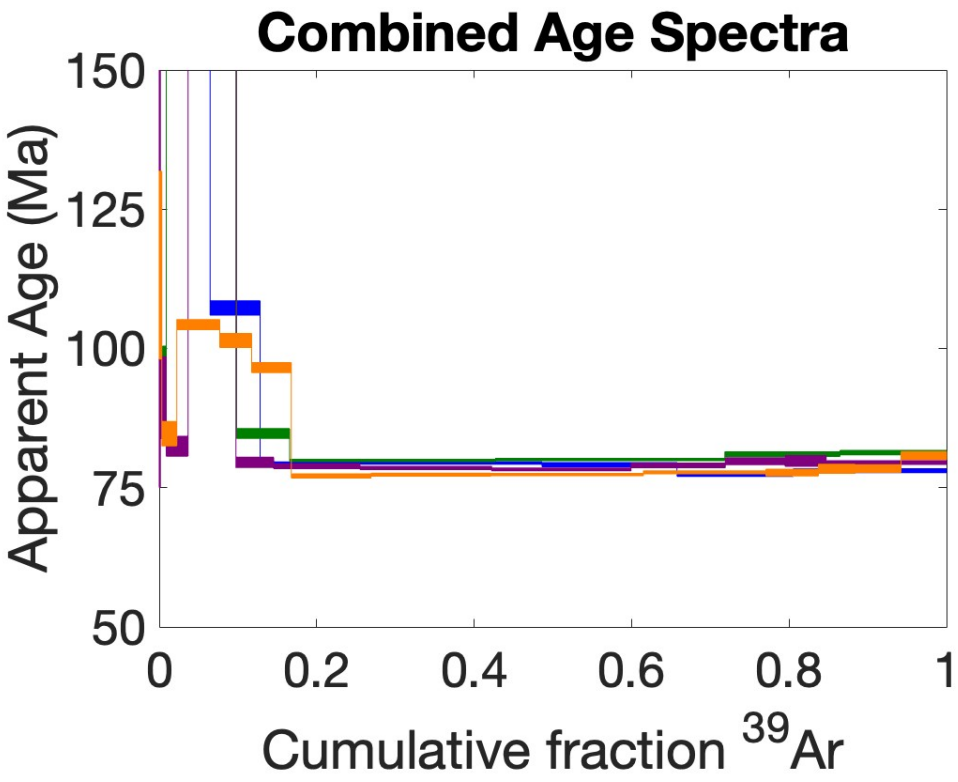

Figure B23: Combined $^{40}Ar/^{39}Ar$ age spectra of the four impact glass analyses from sample CM09-05. These ages depict geologically meaningless ages as these do not represent the age of the impact nor the age of the target rock material. The plateau ages range from 77.42 ± 0.12 Ma to 80.22 ± 0.28 Ma. All samples present older ages initially as excess Ar is degassed during low-temperature steps before reaching a flat gas release pattern during the latter, higher temperature/high laser power steps.

Overview of Geochronology Impact Age Determinations of the Kamestastin Lake Impact Structure

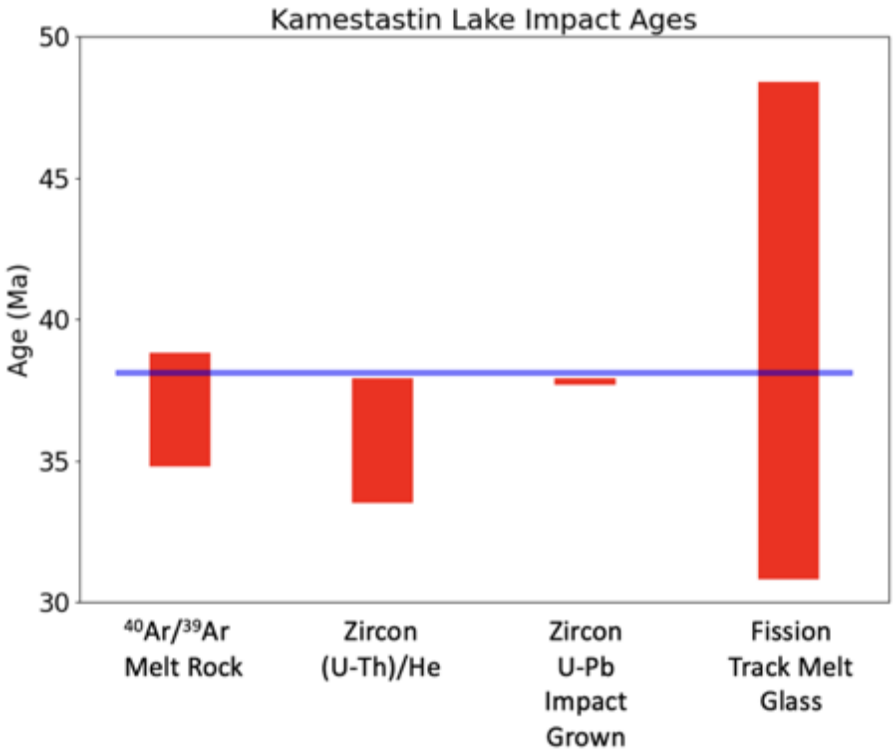

Figure B24: Overview of the geochronology completed at the Kamestastin Lake impact structure. Red bars represent the "best" Kamestastin Lake impact age determination and their uncertainties for each of these studies. The blue line is the age of the Kamestastin Lake impact determined in this study (38.12 ± 0.07 Ma (2σ)). All uncertainties are reported as 2σ. Spot analysis $^{40}Ar/^{39}Ar$ on glass melts and conventional (U-Th)/He zircon ages are calculated from Young, 2014; U-Pb is from Sylvester et al., 2013; and Fission Track is from Storzer and Wagner, 1977.

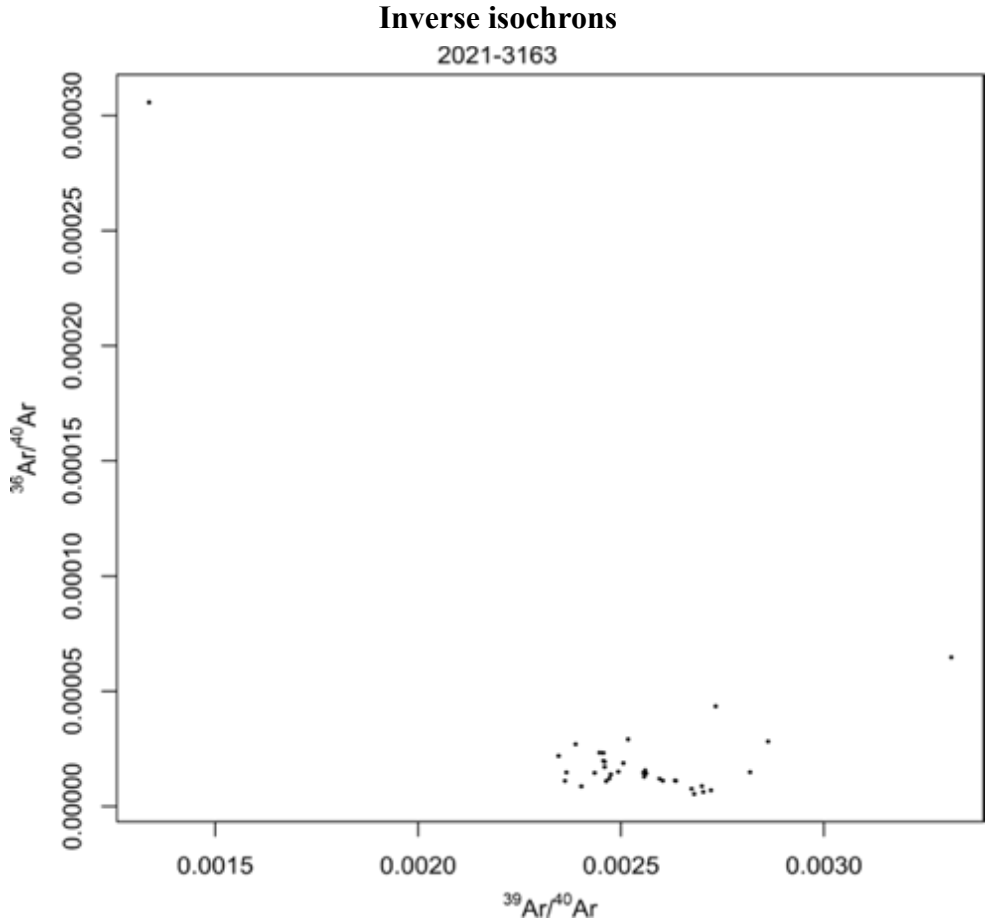

Figure B25: Inverse isochron for sample 2021-3163 (unshocked mangerite).

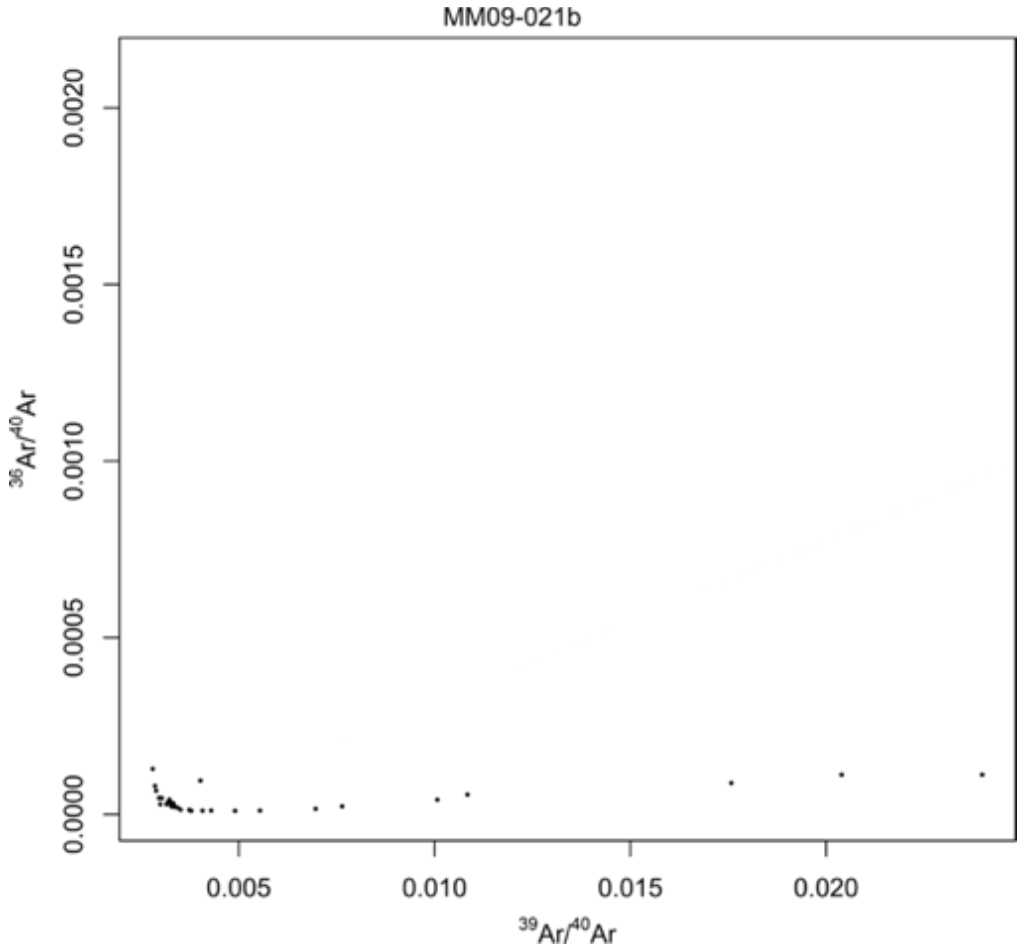

Figure B26: Inverse isochron for sample MM09-021b (shocked anorthosite).

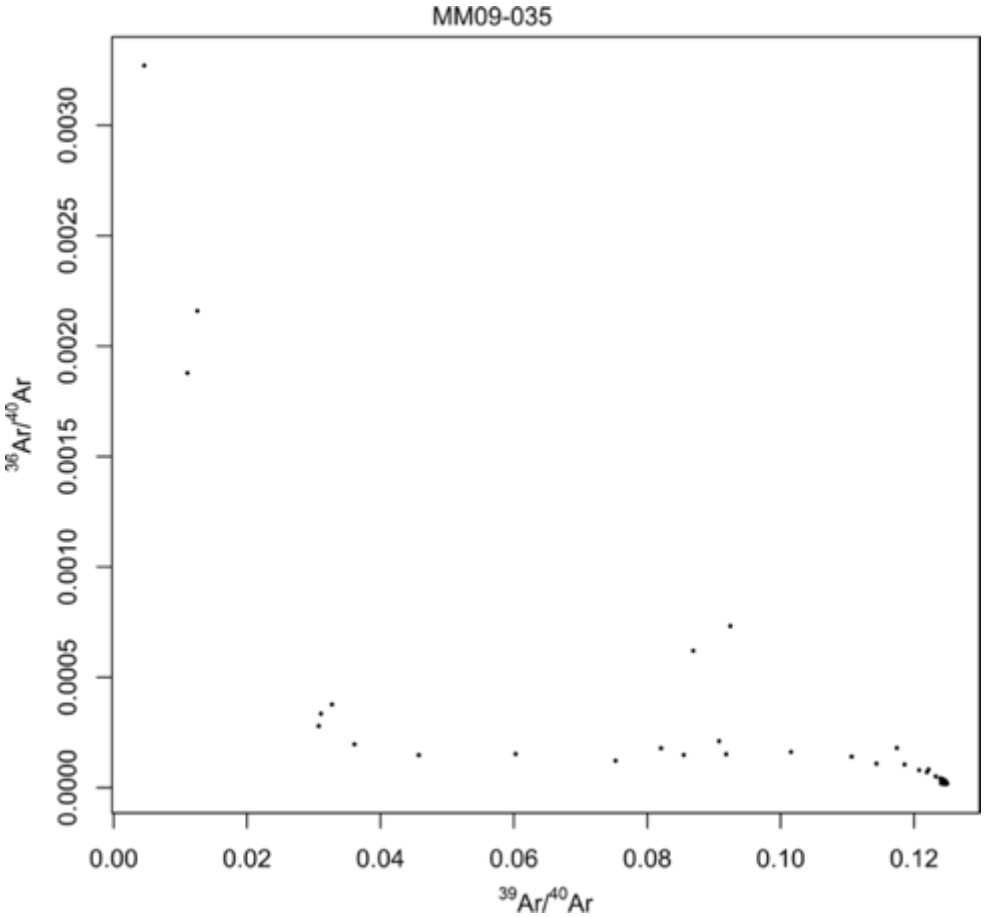

Figure B27: Inverse isochron for sample MM09-035 (shocked and baked granite).

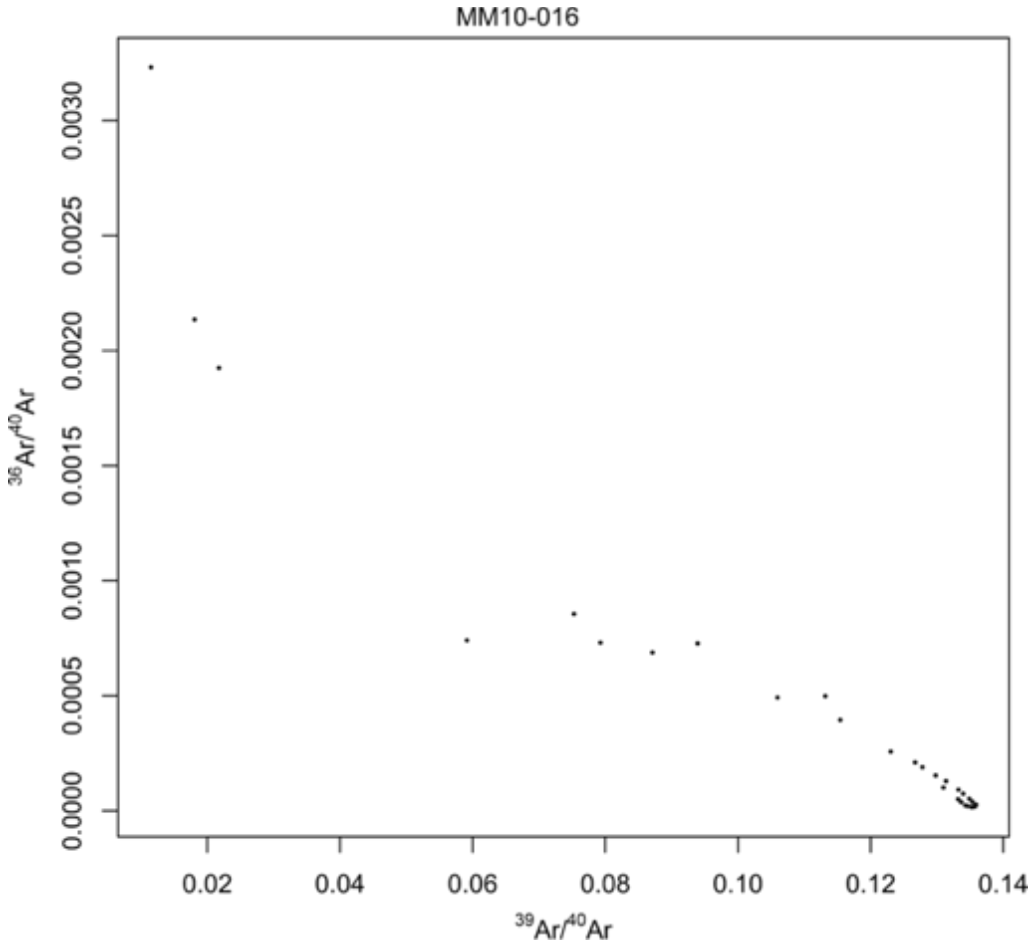

Figure B28: Inverse isochron for sample MM10-016 (shocked and baked granite).

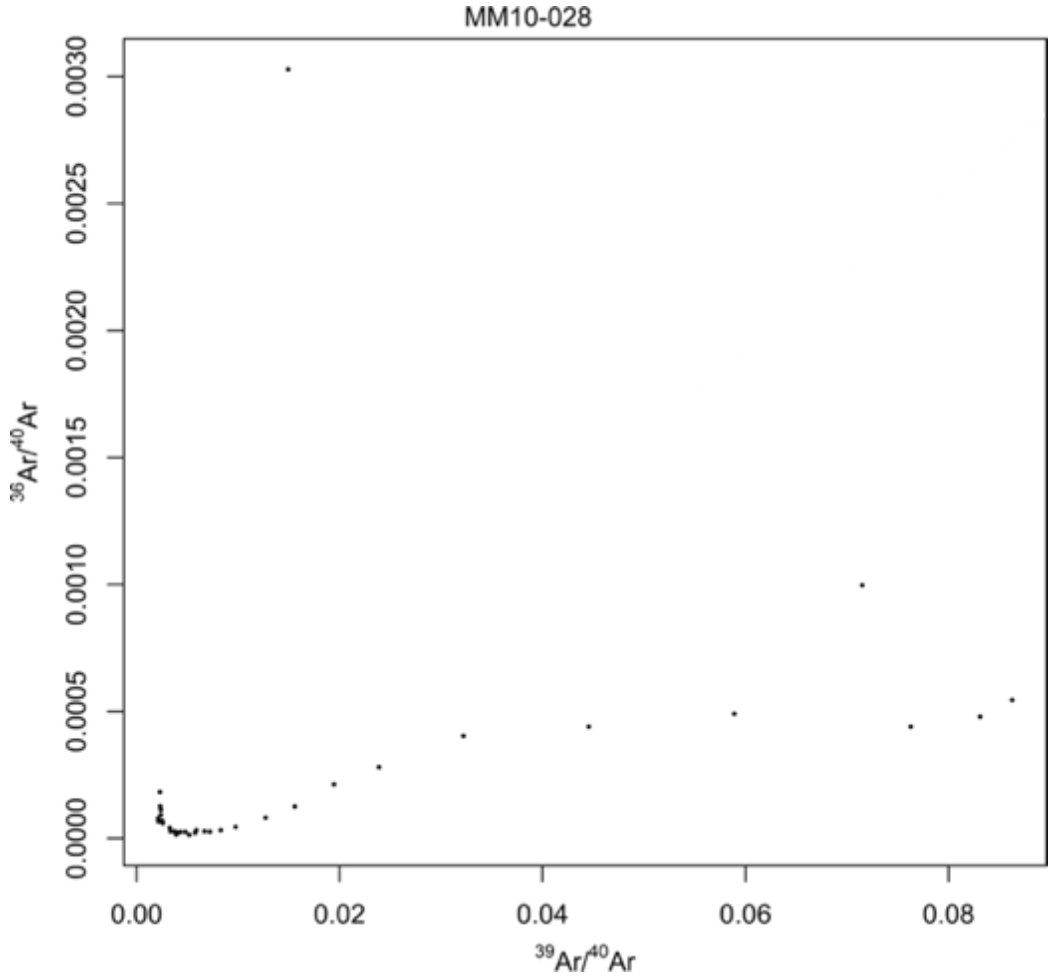

Figure B29: Inverse isochron for sample MM10-028 (anorthosite).

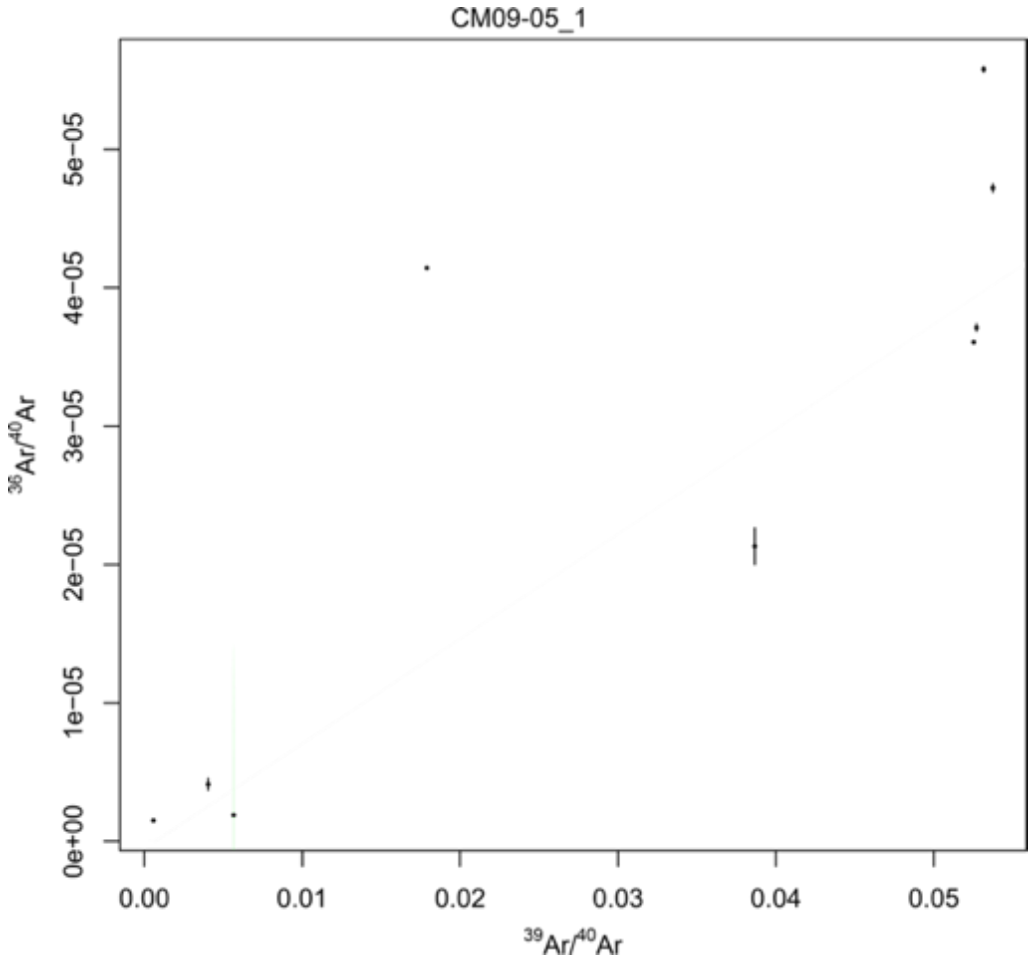

Figure B30: Inverse isochron for sample CM09-05_1 (impact glass).

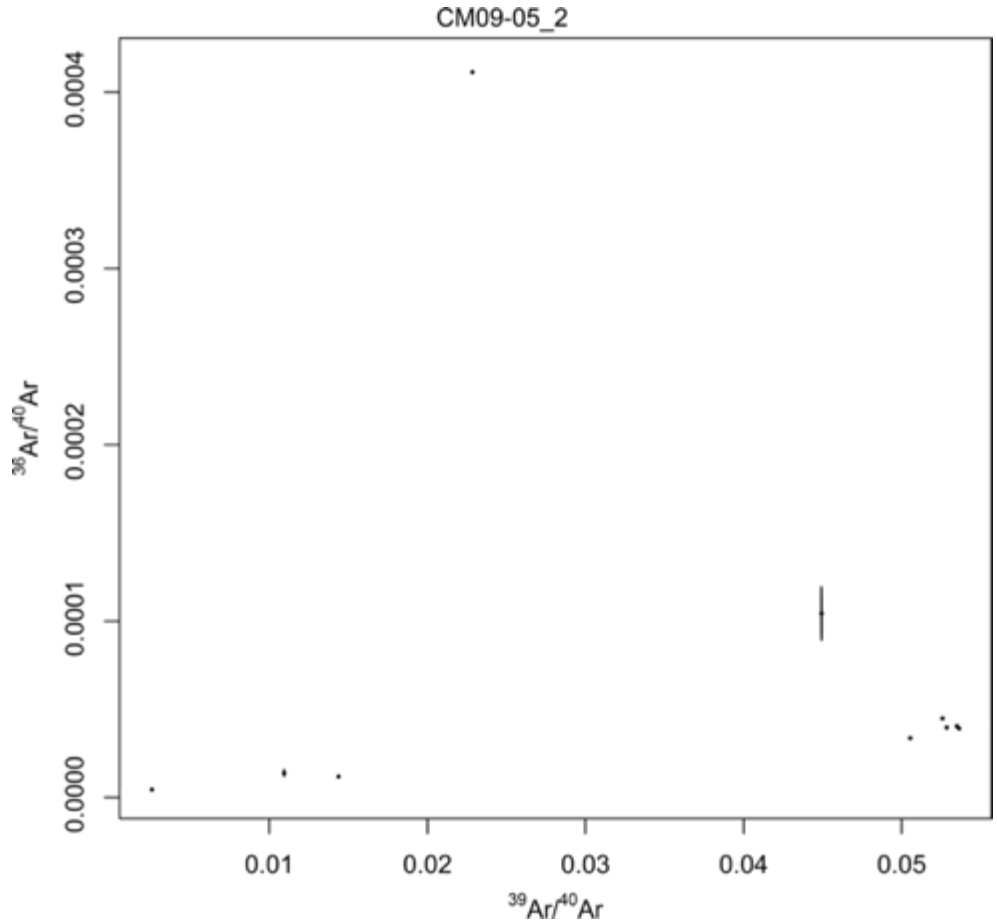

Figure B31: Inverse isochron for sample CM09-05_2 (impact glass).

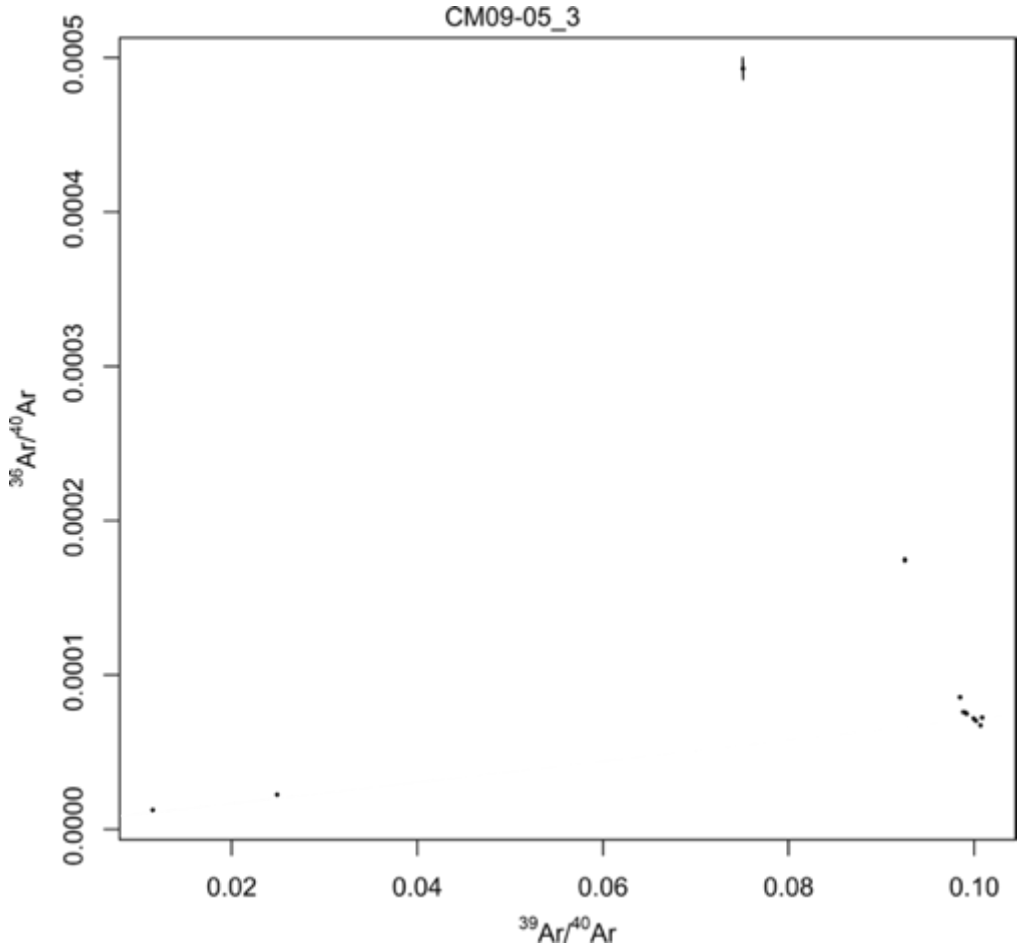

Figure B32: Inverse isochron for sample CM09-05_3 (impact glass).

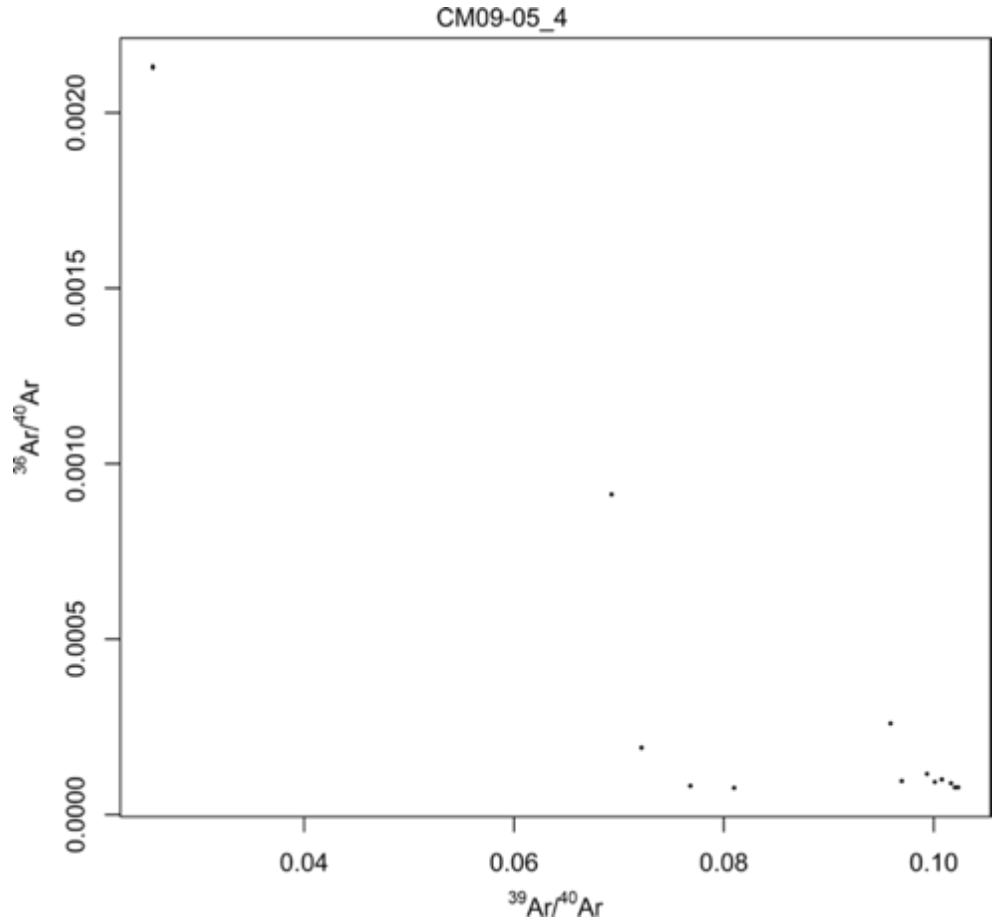

Figure B33: Inverse isochron for sample CM09-05_4 (impact glass).

Appendix C – Diffusion Parameter and Fractional Loss Calculations for Granite Clasts

In this section, we explain our diffusion parameter and fractional loss calculations used to constrain the possible temperature-time histories of the granite clasts that yielded impact ages. The calculations followed the methods in McDougall and Harrison (1999) and Lovera et al. (1989), however, we include an overview of our calculation for completeness. Also included in this section are the Arrhenius plot (Figure C1) and a table of the diffusion parameters and potential temperature-time histories suggested by the fractional loss calculations (Table C1).

Step 1:
The log (D/r^2) for the mth laboratory heating step (assuming plane sheet) can be calculated using equations 5.30 (eq. 1) and 5.31 (eq. 2) from McDougall and Harrison (1999).

$$(eq.1)\ \ log\left(\frac{D}{r^2}\right)_m = log\left(\frac{\Delta\zeta_m}{\Delta t_m}\right)$$

$$(eq.2)\ \ \Delta\zeta_m = \{\frac{\pi}{4}(f_m^2 - f_{m-1}^2) \qquad f_m \leq 0.6\ \ -\frac{4}{\pi^2} ln\left[\frac{(1-f_m)}{(1-f_{m-1})}\right] \qquad f_m > 0.6$$

Where f_m is the fraction of ^{39}Ar released and Dt_m is the duration of heating in the mth laboratory heating step. An Arrhenius plot is then produced using the calculated $\log(D/r^2)$ value and associated temperature for that laboratory heating step.

Step 2:
A hypothetical or idealized release of a single diffusion domain can be plotted on the Arrhenius plot using a modified version of equation 5.23 (eq. 3) from McDougall and Harrison (1999).

$$(eq.3)\frac{D}{r^2} = log\ log\ \frac{D_0}{r^2} - \frac{E_a}{2.303R}\frac{1}{T}$$

Where R is the gas constant (8.314 J / mol·K or 1.939 x 10^{-3} kcal / mol·K) and T is in Kelvin. This equation takes the form of a line where the activation energy (E_a) and the frequency factor ($\log(D_0/r^2)$) is the intercept. Writing this equation in terms of D/r^2 instead of D allows for Arrhenius relationships to be derived without knowing the exact diffusion domain size (r). The MDD program by Lovera et al. (1989) uses this relationship to determine the best fit for the least retentive diffusion domain (i.e., lowest temperature steps). We used this relationship to manually determine frequency factors for the lowest temperature steps assuming crystalline plagioclase and the highest temperature steps assuming crystalline orthoclase.

Below is an Arrhenius plot for the two granite clast samples and the modeled plagioclase and orthoclase phases (Lovera et al. 1989; Cassata and Renne, 2013).

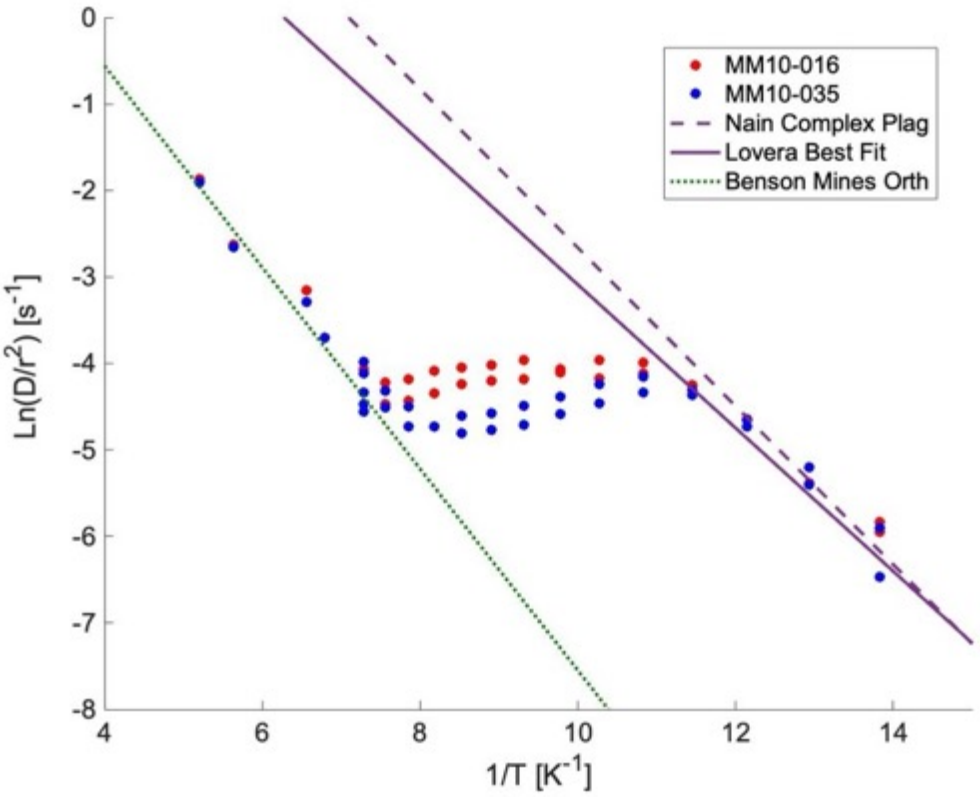

Figure C1: Arrhenius plot for granite clasts along with potential diffusion parameters for plagioclase and orthoclase phases. Lovera best fit was determined using the MDD program of Lovera et al. (1989) and Nain Complex plagioclase and Benson Mines orthoclase utilize activations measured energies from Cassata et al. (2013) and our best fit for frequency factors.

Step 3:

To determine the fraction of gas loss (*f*) from each phase during a pulse heating event (or single gas loss event), we used the approximation equation for a plane sheet in Table 5.1 from McDougall and Harrison (1999). Since we were interested in near-total gas loss, we used the following equation:

$$(eq.4)\ f = 1 - \left(\frac{8}{\pi^2}\right) exp\left(\frac{-\pi}{4}\frac{D}{r^2}t\right)$$

Where D/r^2 is calculated using eq. 3, the assumed activation energy and frequency factor, and the temperature (T) of the heating event. The equation can be solved for the time of heating (t).

$$(eq.5)\ t = \left(\frac{-4}{\pi}\right)\left(\frac{r^2}{D}\right) ln\left[\left(\frac{\pi^2}{8}\right)(1-f)\right]$$

The following table includes a summary of the diffusion parameters used for the fractional loss calculations and the resulting temperature-time (T-t) constraints.

Table C1: Summary of diffusion parameter and T-t results

Name	Type	E_a (kcal/mol)	$\log(D_0/r^2)$	t_{loss} @1150°C	t_{loss} @1450°C	t_{loss} @2000°C	Reference
Lovera Fit	Best Fit	37	5.2	40 Mins	76 Secs	2 Secs	Lovera et al. 1989
Nain Complex Plag	An 49 Ab48 Or 3	40.9	6.5	11 Mins	15 Secs	28 Secs	Cassata & Renne, 2013
Benson Mines Orth	An 0 Ab 3 Or 97	52	4.1	40 Days	7.6 Hours	2.35 Mins	Cassata & Renne, 2013

Appendix C References

Cassata, W.S., Renne, P.R., 2013. Systematic variations of argon diffusion in feldspars and implications for thermochronometry. Geochimica et Cosmochimica Acta 112, 251–287. https://doi.org/10.1016/j.gca.2013.02.030

Lovera, O.M., Richter, F.M., Harrison, T.M., 1989. The 40Ar/39Ar thermochronometry for slowly cooled samples having a distribution of diffusion domain sizes - Lovera - 1989 - Journal of Geophysical Research: Solid Earth - Wiley Online Library. Journal of Geophysical Research: Solid Earth 94, 17917–17935. https://doi.org/10.1029/JB094iB12p17917

McDougall, I., Harrison, T.M., 1999. Geochronology and Thermochronology by the 40Ar/39Ar Method. Oxford University Press.

Storzer, D., Wagner, G.A., 1977. Fission Track Dating of Meteorite Impacts. Meteoritics 12, 368–369.

Sylvester, P.J., Crowley, J.L., Schmitz, M.D., 2013. U-Pb zircon age of Mistastin Lake crater, Labrador, Canada - implications for high-precision dating of small impact melt sheets and the end Eocene extinction, in: Mineralogical Magazine. Presented at the Goldschmidt, p. 2295.

Young, K., 2014. The use of terrestrial analogs in preparing for planetary surface exploration: sampling and radioisotopic dating of impactites and deployment of in situ analytical technologies. Arizona State University.

Appendix D – U-Pb, Ti-in-zircon thermometry, and U concentration data tables

Table D1: U-Pb geochronology data from Chicxulub zircons

Sample	$^{206}Pb/^{238}U$ age (Ma)	± 1σ	$^{207}Pb/^{206}Pb$ age (Ma)	± 1σ	$^{206}Pb^*/^{238}U$	± 1σ	$^{207}Pb^*/^{206}Pb^*$	± 1σ	$^{204}Pb/^{206}Pb$	± 1σ	^{206}Pb (counts)	% ^{206}Pb radiogenic	Microtexture at SIMS spot (X = multiple textures)
M1	1850	41.9	1763	80.4	3.32E-01	8.66E-03	1.08E-01	4.75E-03	9.78E-04	2.60E-04	1.83E+03	98.16	Unshocked
M2	80.3	5.6	800.3	1710	1.25E-02	8.80E-04	6.58E-02	5.36E-02	1.46E-02	2.17E-03	1.62E+02	72.4	FRIGN X
M2b	570.8	19.5	499.3	735.0	9.26E-02	3.31E-03	5.72E-02	1.91E-02	4.60E-03	9.46E-04	2.55E+02	91.32	Unshocked
M3	88.0	6.9	-1.0	0.1	1.38E-02	1.09E-03	1.34E-02	5.44E-02	1.37E-02	2.01E-03	1.99E+02	74.27	Unshocked
M4	246.1	9.8	48.5	1570	3.89E-02	1.58E-03	4.70E-02	3.08E-02	9.29E-03	1.20E-03	2.96E+02	82.47	Unshocked
M5	337.6	9.4	180.1	522.0	5.38E-02	1.54E-03	4.97E-02	1.11E-02	4.31E-03	5.13E-04	5.14E+02	91.88	Unshocked
M6	528.2	16.7	473.0	834.0	8.54E-02	2.82E-03	5.65E-02	2.13E-02	6.26E-03	9.10E-04	3.50E+02	88.19	Unshocked
M7	1658	36.5	1665	38.7	2.93E-01	7.32E-03	1.02E-01	2.14E-03	6.39E-04	7.75E-05	3.05E+03	98.79	Unshocked
M8	1708	42.9	1790	106.0	3.03E-01	8.67E-03	1.09E-01	6.34E-03	1.98E-03	3.61E-04	5.95E+02	96.28	Unshocked
M9	86.4	4.4	-1.0	0.0	1.35E-02	6.89E-04	3.05E-02	2.69E-02	1.07E-02	1.12E-03	1.57E+02	79.92	Unshocked
M10	318.8	10.0	94.4	465.0	5.07E-02	1.62E-03	4.79E-02	9.41E-03	3.41E-03	5.13E-04	9.35E+02	93.57	Granular X
M11	1533	60.9	1673	326.0	2.69E-01	1.20E-02	1.03E-01	1.81E-02	6.54E-03	8.37E-04	1.74E+02	87.68	Unshocked
M12	481.6	25.6	686.7	877.0	7.76E-02	4.27E-03	6.24E-02	2.56E-02	7.71E-03	1.02E-03	1.39E+02	85.46	FRIGN X
M12b	497.2	28.1	614.7	1480	8.02E-02	4.71E-03	6.03E-02	4.13E-02	8.85E-03	2.03E-03	1.50E+02	83.32	Unshocked
M13	510.6	14.6	433.3	495.0	8.24E-02	2.45E-03	5.55E-02	1.23E-02	3.90E-03	6.68E-04	4.44E+02	92.65	Unshocked
M14	171.7	11.6	1404	941.0	2.70E-02	1.84E-03	8.90E-02	4.37E-02	1.15E-02	1.90E-03	8.47E+01	78.35	Unshocked

M15	119.4	12.4	-1.0	0.1	1.87E-02	1.96E-03	1.34E-02	8.34E-02	2.07E-02	2.93E-03	4.66E+01	60.89	Metamict
M16	569.9	23.2	725.7	909.0	9.24E-02	3.93E-03	6.35E-02	2.72E-02	7.60E-03	1.26E-03	3.54E+02	85.67	Unshocked
M17	483.4	30.6	-1.0	0.0	7.79E-02	5.12E-03	4.59E-02	4.60E-02	1.04E-02	2.14E-03	1.51E+02	80.44	Plastic
M19	515.8	24.7	351.2	1200	8.33E-02	4.15E-03	5.35E-02	2.84E-02	8.61E-03	1.27E-03	1.12E+02	83.77	Plastic
M20	237.5	11.1	610.6	1100	3.75E-02	1.79E-03	6.02E-02	3.07E-02	1.29E-02	1.09E-03	2.83E+02	75.77	Reidite X
M20b	211.0	7.9	521.0	856.0	3.33E-02	1.26E-03	5.78E-02	2.25E-02	8.13E-03	9.91E-04	3.18E+02	84.66	Reidite X
M21	105.4	2.5	55.4	296.0	1.65E-02	3.92E-04	4.71E-02	5.85E-03	1.53E-03	3.20E-04	5.36E+02	97.12	Unshocked
M22	361.3	12.8	699.1	540.0	5.76E-02	2.09E-03	6.27E-02	1.59E-02	3.77E-03	8.23E-04	2.71E+02	92.88	Shock twin X
M22b	109.6	9.3	-1.0	0.1	1.71E-02	1.46E-03	3.94E-02	7.49E-02	1.51E-02	2.95E-03	8.21E+01	71.61	FRIGN
M23	928.2	32.6	1794	425.0	1.55E-01	5.84E-03	1.10E-01	2.56E-02	8.08E-03	1.14E-03	1.97E+02	84.75	Unshocked
M24	74.7	2.8	1306	610.0	1.17E-02	4.36E-04	8.46E-02	2.66E-02	7.29E-03	9.44E-04	1.69E+02	86.26	FRIGN
M25	1044	24.4	1031	73.9	1.76E-01	4.45E-03	7.36E-02	2.69E-03	5.03E-04	1.33E-04	5.34E+02	99.05	Unshocked
M26	585.3	13.0	534.6	74.9	9.51E-02	2.21E-03	5.81E-02	1.99E-03	5.97E-04	9.16E-05	2.93E+03	98.87	Plastic X
M27	425.2	22.4	-1.0	0.0	6.82E-02	3.71E-03	4.34E-02	3.17E-02	8.79E-03	1.49E-03	1.67E+02	83.42	Plastic X
M28	82.5	3.3	77.0	1390	1.29E-02	5.14E-04	4.76E-02	2.79E-02	6.63E-03	1.29E-03	2.14E+02	87.49	Unshocked
M28b	81.6	2.0	-1.0	0.0	1.27E-02	3.10E-04	3.79E-02	6.06E-03	1.96E-03	3.52E-04	4.72E+02	96.3	Unshocked
M29	554.9	13.7	859.2	191.0	8.99E-02	2.31E-03	6.77E-02	6.24E-03	1.97E-03	2.23E-04	7.35E+02	96.29	Unshocked
M30	438.6	13.3	683.4	256.0	7.04E-02	2.20E-03	6.23E-02	7.47E-03	2.80E-03	3.05E-04	5.60E+02	94.72	Plastic
M31	143.0	12.1	-1.0	0.1	2.24E-02	1.92E-03	2.57E-02	6.54E-02	1.56E-02	2.58E-03	8.03E+01	70.58	FRIGN

M32	1788	34.9	1709	21.9	3.20E-01	7.14E-03	1.05E-01	1.25E-03	3.38E-04	4.48E-05	7.23E+03	99.36	Unshocked
M33	505.4	27.4	450.6	1630	8.16E-02	4.60E-03	5.60E-02	4.12E-02	9.45E-03	1.75E-03	1.22E+02	82.19	Plastic
M34	201.9	6.6	-1.0	0.0	3.18E-02	1.06E-03	4.60E-02	1.58E-02	5.06E-03	7.60E-04	4.45E+02	90.46	FRIGNX
M34b	220.6	9.3	-1.0	0.0	3.48E-02	1.50E-03	3.65E-02	2.90E-02	9.73E-03	1.23E-03	2.81E+02	81.65	UnshockedX
M35	393.4	11.0	528.8	262.0	6.29E-02	1.81E-03	5.80E-02	6.92E-03	1.84E-03	3.30E-04	4.45E+02	96.53	Plastic
M36	1438	43.9	1742	25.9	2.50E-01	8.51E-03	1.07E-01	1.50E-03	5.30E-04	6.81E-05	2.26E+03	99	Unshocked
M37	74.9	13.9	-1.0	-0.2	1.17E-02	2.18E-03	-3.56E-02	-1.55E-01	3.38E-02	2.95E-03	7.42E+01	36.19	Unshocked
M38	490.4	10.9	467.5	220.0	7.90E-02	1.82E-03	5.64E-02	5.60E-03	1.75E-03	3.07E-04	1.22E+03	96.71	Unshocked
M39	570.0	18.5	957.0	461.0	9.25E-02	3.14E-03	7.10E-02	1.60E-02	4.18E-03	6.50E-04	3.77E+02	92.11	Unshocked
M40	542.7	15.3	600.4	331.0	8.78E-02	2.57E-03	5.99E-02	9.16E-03	3.22E-03	4.36E-04	5.05E+02	93.94	Unshocked
M41	63.9	8.4	3238	468.0	9.96E-03	1.32E-03	2.59E-01	7.68E-02	2.10E-02	3.62E-03	4.45E+01	60.31	FRIGNX
M41b	82.0	6.2	1719	855.0	1.28E-02	9.78E-04	1.05E-01	4.90E-02	1.47E-02	2.16E-03	5.90E+01	72.33	FRIGN
M51	1395	31.7	1406	88.8	2.42E-01	6.11E-03	8.91E-02	4.13E-03	1.17E-03	1.83E-04	1.49E+03	97.8	Unshocked
M52	76.1	9.2	-1.0	0.1	1.19E-02	1.44E-03	3.88E-02	9.54E-02	2.47E-02	2.82E-03	5.98E+01	53.47	Unshocked
M53	1721	39.4	1708	84.2	3.06E-01	7.99E-03	1.05E-01	4.79E-03	1.11E-03	2.37E-04	1.13E+03	97.9	Unshocked
M54	466.1	17.8	594.4	454.0	7.50E-02	2.97E-03	5.98E-02	1.25E-02	3.76E-03	6.58E-04	3.86E+02	92.9	Plastic
M55	536.6	14.9	422.7	210.0	8.68E-02	2.51E-03	5.53E-02	5.19E-03	1.12E-03	2.78E-04	2.72E+02	97.88	Unshocked
M56	483.5	33.2	1109	1180	7.79E-02	5.55E-03	7.65E-02	4.50E-02	1.07E-02	2.16E-03	1.04E+02	79.91	Plastic
M57	461.7	12.4	589.9	255.0	7.42E-02	2.06E-03	5.96E-02	7.02E-03	2.37E-03	3.69E-04	5.88E+02	95.53	Plastic

M58	224.6	7.4	483.0	678.0	3.55E-02	1.18E-03	5.68E-02	1.74E-02	6.69E-03	7.14E-04	3.68E+02	87.39	Granular X
M58b	260.5	9.9	256.8	838.0	4.12E-02	1.60E-03	5.14E-02	1.87E-02	6.94E-03	8.28E-04	3.56E+02	86.92	Plastic
M59	527.8	14.5	760.7	332.0	8.53E-02	2.45E-03	6.46E-02	1.02E-02	3.38E-03	5.14E-04	3.30E+02	93.63	Plastic
M60	444.9	15.4	649.8	548.0	7.15E-02	2.56E-03	6.13E-02	1.56E-02	5.42E-03	8.37E-04	1.45E+02	89.78	Unshocked
M62	464.0	14.4	334.5	446.0	7.46E-02	2.41E-03	5.31E-02	1.05E-02	4.30E-03	4.80E-04	3.90E+02	91.88	Plastic
M67	141.8	13.6	1771	1320	2.22E-02	2.15E-03	1.08E-01	7.81E-02	1.79E-02	2.72E-03	6.22E+01	66.19	FRIGN
M67b	96.2	17.2	-1.0	0.2	1.50E-02	2.71E-03	2.04E-02	1.57E-01	2.84E-02	4.06E-03	4.02E+01	46.48	FRIGN
M68	455.1	10.9	684.9	255.0	7.32E-02	1.81E-03	6.23E-02	7.45E-03	2.41E-03	3.46E-04	3.71E+02	95.46	Plastic
M70	71.9	9.0	-1.0	0.1	1.12E-02	1.41E-03	2.27E-02	9.46E-02	2.68E-02	2.47E-03	8.34E+01	49.49	FRIGN
M70b	127.2	8.7	-1.0	0.0	1.99E-02	1.38E-03	1.63E-02	4.61E-02	1.42E-02	1.70E-03	1.91E+02	73.32	FRIGN X
M76	295.3	19.7	769.8	1590.0	4.69E-02	3.20E-03	6.49E-02	4.90E-02	1.39E-02	1.91E-03	1.54E+02	73.87	FRIGN X
M76b	159.5	36.1	-1.0	-0.2	2.51E-02	5.74E-03	-1.30E-01	-2.27E-01	3.22E-02	4.54E-03	7.44E+01	39.27	FRIGN X
M77	347.0	17.1	763.6	348.0	5.53E-02	2.79E-03	6.47E-02	1.07E-02	3.70E-03	4.92E-04	2.80E+02	93.02	FRIGN X
M81	442.0	13.0	550.0	409.0	7.10E-02	2.16E-03	5.85E-02	1.10E-02	3.22E-03	4.98E-04	3.80E+02	93.92	Plastic
M84	381.3	9.7	615.3	128.0	6.09E-02	1.59E-03	6.03E-02	3.57E-03	1.10E-03	1.78E-04	1.50E+03	97.93	FRIGN X
M88	77.3	8.3	-1.0	0.1	1.21E-02	1.31E-03	3.30E-02	8.50E-02	1.78E-02	3.38E-03	8.06E+01	66.49	FRIGN X
M88b	76.9	5.4	999.3	1700	1.20E-02	8.51E-04	7.25E-02	6.05E-02	1.40E-02	2.19E-03	7.15E+01	73.63	FRIGN X
M89	117.9	9.5	986.9	1690	1.85E-02	1.50E-03	7.20E-02	5.99E-02	1.31E-02	2.59E-03	7.84E+01	75.23	FRIGN
M90	443.4	29.7	871.4	1700	7.12E-02	4.93E-03	6.81E-02	5.57E-02	1.41E-02	2.19E-03	1.70E+02	73.46	Plastic

M91	244.1	22.8	-1.0	0.1	3.86E-02	3.67E-03	4.15E-02	7.78E-02	2.15E-02	2.42E-03	6.84E+01	59.43	Plastic
M91b	449.6	27.2	1841	764.0	7.22E-02	4.53E-03	1.13E-01	4.75E-02	1.23E-02	1.86E-03	9.68E+01	76.89	Plastic
M93	166.4	5.0	318.3	410.0	2.62E-02	7.94E-04	5.28E-02	9.50E-03	3.44E-03	5.00E-04	2.83E+02	93.51	FRIGN
M99	546.7	18.3	622.2	205.0	8.85E-02	3.09E-03	6.05E-02	5.74E-03	1.86E-03	2.18E-04	7.29E+02	96.49	Plastic
M100	421.8	11.2	768.3	192.0	6.76E-02	1.85E-03	6.48E-02	5.90E-03	1.23E-03	3.07E-04	2.43E+02	97.68	Plastic
M100b	411.2	11.9	707.4	247.0	6.59E-02	1.97E-03	6.30E-02	7.30E-03	1.58E-03	4.44E-04	2.60E+02	97.02	Plastic
M98	421.5	19.6	581.5	1060	6.76E-02	3.25E-03	5.94E-02	2.89E-02	8.09E-03	1.26E-03	2.17E+02	84.74	Plastic
M97	562.8	15.9	762.3	302.0	9.12E-02	2.69E-03	6.46E-02	9.26E-03	2.25E-03	4.11E-04	2.49E+02	95.77	Unshocked
M96	1812	48.1	1739	184.0	3.25E-01	9.88E-03	1.06E-01	1.07E-02	3.09E-03	5.87E-04	9.89E+02	94.18	Unshocked
M92	529.5	15.0	512.6	298.0	8.56E-02	2.52E-03	5.76E-02	7.82E-03	2.58E-03	3.57E-04	7.78E+02	95.13	Unshocked
M85	333.7	10.7	142.3	1050	5.31E-02	1.75E-03	4.89E-02	2.18E-02	1.02E-02	9.38E-04	2.83E+02	80.75	Unshocked
M80	335.7	13.2	1100	609.0	5.35E-02	2.16E-03	7.62E-02	2.32E-02	6.32E-03	1.12E-03	2.08E+02	88.09	Unshocked
M72	1677	38.1	1696	40.9	2.97E-01	7.67E-03	1.04E-01	2.30E-03	6.17E-04	1.19E-04	1.95E+03	98.84	Unshocked
M72b	1731	37.6	1726	33.2	3.08E-01	7.63E-03	1.06E-01	1.91E-03	5.34E-04	8.23E-05	2.06E+03	98.99	Unshocked
M69	497.3	20.1	135.3	998.0	8.02E-02	3.37E-03	4.87E-02	2.07E-02	8.49E-03	8.42E-04	2.23E+02	83.98	Unshocked
M69b	208.0	20.9	276.5	3410	3.28E-02	3.35E-03	5.18E-02	7.71E-02	2.77E-02	1.91E-03	2.13E+02	47.76	Unshocked
M42	80.3	8.4	793.4	2730	1.25E-02	1.32E-03	6.56E-02	8.55E-02	1.90E-02	3.02E-03	7.97E+01	64.14	FRIGN
M42b	114.1	6.6	-1.0	0.0	1.79E-02	1.04E-03	3.13E-02	4.57E-02	1.47E-02	1.44E-03	1.50E+02	72.26	FRIGN X
M45	527.8	21.7	879.4	668.0	8.53E-02	3.65E-03	6.84E-02	2.21E-02	5.59E-03	1.04E-03	9.64E+01	89.47	Shock twins X

M45b	395.3	11.4	407.3	766.0	6.32E-02	1.88E-03	5.49E-02	1.88E-02	5.34E-03	1.01E-03	2.20E+02	89.94	Shock twins X
M102	126.9	4.4	-1.0	0.0	1.99E-02	6.94E-04	4.30E-02	2.09E-02	7.01E-03	9.76E-04	3.29E+02	86.78	Plastic
M102b	84.4	4.3	-1.0	0.0	1.32E-02	6.80E-04	2.51E-02	4.76E-02	1.56E-02	1.54E-03	1.24E+02	70.64	Granular X
M109	591.6	25.2	1715	499.0	9.61E-02	4.28E-03	1.05E-01	2.85E-02	7.42E-03	1.14E-03	1.06E+02	86.01	Plastic
M111	518.4	14.5	533.8	443.0	8.38E-02	2.44E-03	5.81E-02	1.18E-02	3.70E-03	5.96E-04	5.15E+02	93.03	Plastic
M112	102.0	6.2	-1.0	0.1	1.60E-02	9.80E-04	1.35E-02	5.57E-02	1.66E-02	1.96E-03	1.15E+02	68.75	FRIGN
M113	48.7	7.3	1930	1980	7.59E-03	1.15E-03	1.18E-01	1.30E-01	2.86E-02	3.19E-03	5.41E+01	46.07	FRIGN X
M114	387.1	18.4	341.9	1530	6.19E-02	3.03E-03	5.33E-02	3.60E-02	1.09E-02	1.40E-03	1.50E+02	79.36	Plastic
M118	505.4	12.1	444.8	136.0	8.16E-02	2.02E-03	5.58E-02	3.41E-03	1.87E-03	1.80E-04	1.07E+03	96.48	Unshocked
M119	552.2	12.4	493.9	229.0	8.94E-02	2.09E-03	5.71E-02	5.92E-03	1.50E-03	3.13E-04	1.64E+03	97.17	Plastic
M120	99.8	5.3	1469	783.0	1.56E-02	8.32E-04	9.21E-02	3.80E-02	1.11E-02	1.74E-03	1.00E+02	79.14	FRIGN X
M120b	136.3	4.6	227.1	860.0	2.14E-02	7.31E-04	5.07E-02	1.89E-02	5.91E-03	9.94E-04	1.12E+02	88.86	FRIGN X
M121	104.9	12.4	-1.0	0.1	1.64E-02	1.95E-03	3.55E-02	9.01E-02	2.07E-02	3.34E-03	1.21E+02	60.88	FRIGN X
M121b	405.1	14.3	879.2	583.0	6.49E-02	2.37E-03	6.84E-02	1.93E-02	6.20E-03	7.73E-04	3.88E+02	88.3	Shock twin X
M122	94.0	5.5	355.0	1820	1.47E-02	8.58E-04	5.36E-02	4.31E-02	1.36E-02	1.65E-03	9.48E+01	74.3	FRIGN
M122b	193.9	6.1	1620	390.0	3.05E-02	9.71E-04	9.98E-02	2.09E-02	8.18E-03	7.86E-04	2.50E+02	84.56	FRIGN X
M123	118.9	19.9	1421	2630	1.86E-02	3.14E-03	8.98E-02	1.23E-01	3.70E-02	2.49E-03	1.15E+02	30.24	Reidite X
M124	87.7	5.2	-1.0	0.0	1.37E-02	8.18E-04	3.70E-02	4.05E-02	1.22E-02	1.64E-03	1.25E+02	76.93	FRIGN
R13b	77.3	4.8	342.5	1990	1.21E-02	7.57E-04	5.33E-02	4.69E-02	1.35E-02	2.07E-03	1.20E+02	74.49	FRIGN

R13	333.2	9.5	670.5	312.0	5.30E-02	1.55E-03	6.19E-02	9.04E-03	2.81E-03	4.84E-04	4.36E+02	94.7	Plastic
R13c	129.9	4.7	296.6	955.0	2.04E-02	7.50E-04	5.23E-02	2.19E-02	8.74E-03	9.33E-04	1.89E+02	83.52	FRIGN
R5	102.7	5.7	2350	412.0	1.61E-02	8.90E-04	1.50E-01	3.63E-02	1.00E-02	1.41E-03	1.09E+02	81.07	FRIGN X
R6	119.8	5.3	1536	523.0	1.88E-02	8.40E-04	9.54E-02	2.65E-02	1.02E-02	1.20E-03	1.34E+02	80.77	FRIGN
R11	65.8	6.9	926.9	2350	1.03E-02	1.08E-03	7.00E-02	7.99E-02	2.56E-02	2.60E-03	7.66E+01	51.78	FRIGN

* = corrected for common Pb
Calibration line slope: 0.59
Calibration line intercept: 1.69

Table D2: U-Pb geochronology data from Apollo 14311,58 zircons

Sample	**$^{207}Pb/^{206}Pb$ age (Ma)**	**± 1σ**	**$^{206}Pb/^{238}U$ age (Ma)**	**± 1σ**	**$^{206}Pb^*/^{238}U$**	**± 1σ**	**$^{207}Pb^*/^{206}Pb^*$**	**± 1σ**	**$^{204}Pb/^{206}Pb$**	**± 1σ**	**^{206}Pb (counts)**	**% ^{206}Pb radiogenic**	**Microtexture at SIMS spot**
M_M1_Z2	4104	19	4061	75	8.78E-01	2.19E-02	4.56E-01	5.84E-03	1.56E-04	3.45E-05	1.66E+03	99.71	Unshocked
M_M1_Z4	4235	37	4414	90	9.83E-01	2.77E-02	4.98E-01	1.26E-02	1.88E-05	5.94E-06	7.36E+03	99.96	Partially metamict
M_M1_Z3	4310	9	4294	84	9.47E-01	2.54E-02	5.24E-01	3.32E-03	5.40E-05	1.46E-05	3.23E+03	99.9	Metamict
M_M1_Z5	4298	9	4173	109	9.11E-01	3.24E-02	5.20E-01	3.12E-03	1.36E-04	3.53E-05	1.39E+03	99.74	Fracture
M_M1_Z6	4263	32	4267	90	9.39E-01	2.70E-02	5.07E-01	1.09E-02	6.95E-05	1.88E-05	3.22E+03	99.87	Unshocked
M_M1_Z7	4314	8	4399	79	9.79E-01	2.43E-02	5.25E-01	2.92E-03	1.29E-04	2.91E-05	2.54E+03	99.76	Unshocked
S_M2_Z2	4242	5	4214	116	9.23E-01	3.47E-02	5.00E-01	1.57E-03	2.39E-05	1.60E-05	5.24E+03	99.96	Metamict
S_M2_Z3	4340	9	4229	93	9.27E-01	2.77E-02	5.35E-01	3.38E-03	1.81E-05	9.68E-06	8.91E+03	99.97	Metamict

S_M2_Z5	4107	7	4429	149	9.88E-01	4.61E-02	4.57E-01	2.02E-03	5.42E-05	1.46E-05	4.85E+03	99.9	Metamict
S_M2_Z6	4248	10	4495	125	1.01E+00	3.90E-02	5.02E-01	3.52E-03	1.75E-04	4.55E-05	1.57E+03	99.67	Unshocked
S_M2_Z7	3933	4	4084	77	8.84E-01	2.25E-02	4.06E-01	1.05E-03	3.99E-05	1.26E-05	4.58E+03	99.92	Metamict
S_M2_Z16	3933	8	3928	85	8.39E-01	2.43E-02	4.07E-01	2.20E-03	7.49E-05	3.00E-05	6.00E+03	99.86	Granular and metamict
S_M2_Z17	4347	23	4464	204	9.99E-01	6.33E-02	5.37E-01	8.55E-03	1.88E-04	5.95E-05	9.70E+02	99.65	Unshocked
S_M2_Z18	4342	6	4776	136	1.10E+00	4.43E-02	5.36E-01	2.26E-03	4.38E-05	1.24E-05	5.26E+03	99.92	Metamict
S_M2_Z19	4312	15	4440	119	9.91E-01	3.68E-02	5.25E-01	5.44E-03	6.08E-05	2.80E-05	4.42E+03	99.89	Partially metamict
S_M2_Z20	4306	7	4375	116	9.71E-01	3.55E-02	5.23E-01	2.38E-03	6.11E-05	2.40E-05	2.51E+03	99.88	Unshocked
S_M2_Z21	4306	5	4354	95	9.65E-01	2.88E-02	5.23E-01	1.90E-03	9.13E-05	2.64E-05	2.43E+03	99.83	Unshocked
S_M2_Z22	4089	53	3377	381	6.88E-01	9.98E-02	4.51E-01	1.62E-02	5.66E-03	8.49E-04	1.47E+02	89.32	Unshocked
S_M2_Z23	4259	7	4416	101	9.84E-01	3.10E-02	5.06E-01	2.36E-03	2.37E-05	9.48E-06	4.86E+03	99.96	Metamict
S_M2_Z24	4275	4	4452	79	9.95E-01	2.43E-02	5.12E-01	1.28E-03	1.34E-05	4.33E-06	1.30E+04	99.97	Metamict
S_M2_Z25	4321	6	4490	110	1.01E+00	3.43E-02	5.28E-01	2.32E-03	5.79E-05	1.65E-05	4.01E+03	99.89	Partially metamict
S_M2_Z26	4329	7	4504	101	1.01E+00	3.15E-02	5.31E-01	2.52E-03	1.01E-04	2.25E-05	3.78E+03	99.81	Unshocked
M_M1_Z8	4279	18	4257	129	9.35E-01	3.86E-02	5.13E-01	6.28E-03	2.05E-04	4.48E-05	1.87E+03	99.61	Unshocked
M_M1_Z9	4050	42	3623	168	7.54E-01	4.56E-02	4.40E-01	1.23E-02	4.92E-04	1.08E-04	7.81E+02	99.07	Unshocked
M_M1_Z10	4127	12	4237	82	9.29E-01	2.46E-02	4.63E-01	3.84E-03	7.02E-05	2.11E-05	3.26E+03	99.87	Unshocked
M_M1_Z11	4319	9	4354	111	9.65E-01	3.38E-02	5.27E-01	3.33E-03	9.13E-05	2.88E-05	2.09E+03	99.83	Unshocked
M_M1_Z12	4324	7	4336	109	9.59E-01	3.31E-02	5.29E-01	2.43E-03	8.81E-05	2.63E-05	2.38E+03	99.83	Unshocked

M_M1_Z13	4031	28	3642	115	7.60E-01	3.15E-02	4.34E-01	8.25E-03	6.31E-04	1.76E-04	4.85E+02	98.81	Unshocked
M_M1_Z14	4236	7	4237	90	9.30E-01	2.68E-02	4.98E-01	2.29E-03	1.09E-04	2.94E-05	2.65E+03	99.79	Unshocked
M_M1_Z15	3929	14	3825	140	8.10E-01	3.92E-02	4.05E-01	3.65E-03	5.51E-04	1.00E-04	1.02E+03	98.96	Unshocked
M_M1_Z16	4254	3	4277	68	9.42E-01	2.04E-02	5.05E-01	1.15E-03	1.22E-05	4.15E-06	1.30E+04	99.98	Metamict
M_M1_Z17	4285	21	4456	125	9.96E-01	3.87E-02	5.15E-01	7.33E-03	3.33E-04	7.86E-05	1.01E+03	99.37	Unshocked
M_M1_Z18	4345	20	4220	169	9.24E-01	5.05E-02	5.37E-01	7.25E-03	2.70E-04	7.47E-05	9.10E+02	99.49	Unshocked
M_M1_Z19	4313	5	4205	116	9.20E-01	3.47E-02	5.25E-01	1.86E-03	4.98E-05	2.13E-05	4.58E+03	99.91	Metamict
M_M1_Z20	4326	10	4180	113	9.12E-01	3.35E-02	5.30E-01	3.71E-03	6.69E-05	2.41E-05	5.55E+03	99.87	Metamict
M_M1_Z21	4248	7	4383	73	9.74E-01	2.22E-02	5.02E-01	2.33E-03	7.37E-05	1.92E-05	3.68E+03	99.86	Partially metamict
M_M1_Z23	4347	7	4535	145	1.02E+00	4.54E-02	5.37E-01	2.71E-03	9.71E-05	2.72E-05	2.41E+03	99.82	Unshocked
M_M1_Z24	4299	12	4153	83	9.05E-01	2.45E-02	5.20E-01	4.14E-03	1.26E-04	3.46E-05	1.93E+03	99.76	Unshocked
M_M1_Z26	3970	8	4015	85	8.64E-01	2.46E-02	4.17E-01	2.09E-03	8.73E-05	1.95E-05	4.29E+03	99.84	Metamict
M_M1_Z27	4258	7	4372	103	9.70E-01	3.15E-02	5.06E-01	2.38E-03	7.67E-05	2.72E-05	2.41E+03	99.86	Unshocked
M_M1_Z28	4246	5	4195	76	9.17E-01	2.27E-02	5.02E-01	1.66E-03	3.54E-05	1.04E-05	6.01E+03	99.93	Metamict
M_M1_Z29	3920	13	3867	154	8.22E-01	4.34E-02	4.03E-01	3.51E-03	5.19E-04	1.34E-04	9.75E+02	99.02	Unshocked
M_M1_Z30	4340	4	4405	100	9.80E-01	3.06E-02	5.35E-01	1.34E-03	5.87E-05	1.43E-05	5.24E+03	99.89	Metamict
M_M1_Z31	4019	29	4069	179	8.80E-01	5.21E-02	4.31E-01	8.23E-03	3.82E-04	1.05E-04	7.32E+02	99.28	Unshocked
M_M1_Z32	3987	9	3981	71	8.54E-01	2.04E-02	4.21E-01	2.65E-03	7.58E-06	2.29E-06	2.73E+04	99.99	Metamict
M_M1_Z33	4072	24	4060	94	8.77E-01	2.74E-02	4.46E-01	7.18E-03	1.28E-04	3.50E-05	2.92E+03	99.76	Unshocked

M_M1_Z34	4244	5	4438	90	9.91E-01	2.77E-02	5.01E-01	1.74E-03	2.29E-05	6.23E-06	1.10E+04	99.96	Metamict
M_M1_Z35	4305	9	4392	97	9.77E-01	2.97E-02	5.22E-01	3.33E-03	8.61E-05	2.66E-05	2.26E+03	99.84	Unshocked
M_M1_Z36	4031	29	3892	197	8.29E-01	5.59E-02	4.34E-01	8.39E-03	4.36E-04	1.17E-04	8.81E+02	99.18	Unshocked
M_M1_Z38	4339	6	4291	146	9.46E-01	4.39E-02	5.35E-01	2.17E-03	1.71E-04	3.81E-05	2.19E+03	99.68	Unshocked
M_M1_Z39	4169	9	4097	77	8.88E-01	2.24E-02	4.76E-01	2.79E-03	1.00E-04	2.78E-05	2.41E+03	99.81	Unshocked
M_M1_Z41	4369	23	4366	175	9.69E-01	5.36E-02	5.46E-01	8.55E-03	3.95E-04	1.02E-04	1.58E+03	99.26	Unshocked
M_M1_Z42	4222	14	4261	163	9.37E-01	4.90E-02	4.94E-01	4.69E-03	4.39E-04	8.71E-05	1.23E+03	99.17	Unshocked
M_M1_Z43	4335	3	4529	123	1.02E+00	3.87E-02	5.33E-01	1.26E-03	1.32E-04	2.93E-05	2.86E+03	99.75	Unshocked
M_M1_Z44	4024	34	4106	196	8.91E-01	5.74E-02	4.32E-01	9.69E-03	1.90E-04	5.03E-05	1.40E+03	99.64	Unshocked
M_M1_Z45	4348	5	4338	118	9.60E-01	3.58E-02	5.38E-01	1.87E-03	1.01E-04	2.75E-05	2.47E+03	99.81	Unshocked
M_M1_Z46	4279	8	4258	141	9.36E-01	4.24E-02	5.13E-01	2.78E-03	1.10E-04	3.19E-05	1.99E+03	99.79	Unshocked
M_M1_Z47	3930	14	3925	129	8.38E-01	3.68E-02	4.06E-01	3.78E-03	3.19E-04	7.52E-05	1.05E+03	99.4	Unshocked
M_M1_Z48	4273	10	4265	80	9.38E-01	2.42E-02	5.11E-01	3.62E-03	1.83E-05	5.86E-06	9.81E+03	99.97	Metamict
M_M1_Z49	4128	9	4044	102	8.73E-01	2.98E-02	4.63E-01	2.78E-03	1.31E-04	3.02E-05	2.67E+03	99.75	Unshocked
M_M1_Z50	3952	8	4077	121	8.82E-01	3.54E-02	4.12E-01	2.17E-03	1.73E-04	4.38E-05	1.67E+03	99.67	Unshocked
M_M1_Z51	4038	32	4341	95	9.61E-01	2.89E-02	4.36E-01	9.38E-03	2.41E-05	1.17E-05	4.67E+03	99.95	Partially metamict
M_M2_Z9	4000	55	4029	180	8.68E-01	5.20E-02	4.25E-01	1.56E-02	1.27E-04	7.65E-05	8.99E+02	99.76	Unshocked
M_M2_Z10@1	4169	44	4315	145	9.53E-01	4.39E-02	4.76E-01	1.42E-02	2.58E-04	1.14E-04	4.07E+02	99.51	Unshocked
M_M2_Z10@2	3939	19	4053	242	8.75E-01	7.03E-02	4.08E-01	5.14E-03	1.09E-03	2.49E-04	3.40E+02	97.95	Unshocked

M_M2_Z11	3946	13	3791	95	8.01E-01	2.64E-02	4.10E-01	3.44E-03	8.95E-05	4.10E-05	9.82E+02	99.83	Unshocked
M_M2_Z12@1	4277	24	4107	112	8.91E-01	3.30E-02	5.12E-01	8.17E-03	9.56E-05	3.53E-05	1.69E+03	99.82	Unshocked
M_M2_Z12@2	4208	16	4265	117	9.38E-01	3.51E-02	4.89E-01	5.20E-03	3.56E-04	6.04E-05	1.81E+03	99.33	Unshocked
M_M2_Z13	3907	49	4394	157	9.77E-01	4.80E-02	4.00E-01	1.29E-02	1.13E-04	6.77E-05	8.08E+02	99.79	Unshocked
M_M2_Z14	4336	5	4399	100	9.79E-01	3.08E-02	5.33E-01	1.72E-03	1.91E-05	9.28E-06	4.10E+03	99.96	Partially metamict
M_M2_Z17	4226	10	4220	143	9.25E-01	4.28E-02	4.95E-01	3.40E-03	2.03E-04	4.14E-05	2.14E+03	99.62	Unshocked
M_M2_Z18	4326	9	4315	86	9.53E-01	2.60E-02	5.30E-01	3.19E-03	3.21E-05	1.54E-05	3.40E+03	99.94	Metamict
Zrsm90	4346	22	4334	175	9.59E-01	5.31E-02	5.37E-01	8.13E-03	1.60E-04	5.09E-05	2.55E+03	99.7	Unshocked
Zrsm91	3956	14	3922	79	8.38E-01	2.24E-02	4.13E-01	3.74E-03	1.89E-04	5.44E-05	1.17E+03	99.64	Unshocked
Zrsm92@1	4365	9	4371	63	9.70E-01	1.93E-02	5.44E-01	3.28E-03	7.07E-05	1.82E-05	3.97E+03	99.87	Unshocked
Zrsm92@2	4366	7	4345	64	9.62E-01	1.95E-02	5.44E-01	2.71E-03	7.82E-05	2.35E-05	4.07E+03	99.85	Unshocked
Zrsm93	4237	40	4081	132	8.83E-01	3.86E-02	4.99E-01	1.36E-02	1.11E-04	5.74E-05	6.88E+02	99.79	Unshocked
Zrsm94	3981	23	4147	106	9.03E-01	3.14E-02	4.20E-01	6.30E-03	3.10E-04	8.09E-05	1.07E+03	99.42	Unshocked
Zrsm95	4005	33	4028	203	8.68E-01	5.89E-02	4.27E-01	9.33E-03	5.54E-04	1.68E-04	5.46E+02	98.96	Unshocked
Zrsm96@1	3948	17	3978	87	8.54E-01	2.49E-02	4.10E-01	4.76E-03	2.73E-04	6.47E-05	1.22E+03	99.48	Unshocked
Zrsm96@2	3979	23	3944	112	8.44E-01	3.19E-02	4.19E-01	6.55E-03	2.24E-04	6.00E-05	1.16E+03	99.58	Unshocked
Zrsm97	4044	31	4069	106	8.80E-01	3.10E-02	4.38E-01	9.08E-03	1.54E-04	6.86E-05	7.84E+02	99.71	Unshocked
Zrsm98	3973	28	4000	71	8.60E-01	2.03E-02	4.18E-01	7.75E-03	3.09E-04	6.92E-05	1.20E+03	99.42	Unshocked
Zrsm99	4093	45	4166	98	9.09E-01	2.91E-02	4.52E-01	1.37E-02	3.43E-04	1.33E-04	7.75E+02	99.35	Unshocked

Zrsm100	4130	43	4136	107	8.99E-01	3.15E-02	4.64E-01	1.34E-02	1.35E-04	3.75E-05	2.01E+03	99.75	Unshocked
Zrsm101	4363	5	4335	54	9.59E-01	1.65E-02	5.43E-01	1.67E-03	2.51E-05	7.55E-06	8.24E+03	99.95	Metamict
Zrsm102	3945	14	4066	113	8.79E-01	3.28E-02	4.10E-01	3.74E-03	1.68E-04	5.33E-05	1.10E+03	99.68	Unshocked
Zrsm103	3980	11	4014	118	8.64E-01	3.40E-02	4.20E-01	3.19E-03	2.46E-04	6.87E-05	9.95E+02	99.54	Unshocked
Zrsm104	3969	19	3979	66	8.54E-01	1.90E-02	4.16E-01	5.28E-03	1.87E-04	5.98E-05	1.20E+03	99.65	Unshocked
Zrsm106 @1	4265	9	4245	80	9.32E-01	2.40E-02	5.08E-01	3.13E-03	1.20E-04	3.61E-05	1.71E+03	99.77	Unshocked
Zrsm106 @2	4098	17	3949	178	8.45E-01	5.08E-02	4.54E-01	5.17E-03	1.10E-04	3.43E-05	2.58E+03	99.79	Unshocked
Zrsm107	4283	34	4510	97	1.01E+00	3.02E-02	5.15E-01	1.19E-02	8.23E-05	1.79E-05	4.82E+03	99.84	Partially metamict
Zrsm108 @1	4281	5	4221	79	9.25E-01	2.36E-02	5.14E-01	1.70E-03	1.26E-04	4.98E-05	1.78E+03	99.76	Unshocked
Zrsm108 @2	4115	13	4170	130	9.10E-01	3.85E-02	4.59E-01	3.94E-03	2.58E-04	6.44E-05	1.15E+03	99.51	Plastic
Zrsm109 @1	4014	29	4050	108	8.74E-01	3.15E-02	4.29E-01	8.18E-03	1.62E-04	6.16E-05	9.16E+02	99.7	Unshocked
Zrsm109 @2	4066	37	3987	68	8.56E-01	1.95E-02	4.44E-01	1.11E-02	2.20E-04	6.64E-05	9.32E+02	99.58	Unshocked
Zrsm110 @1	4165	22	4070	101	8.80E-01	2.94E-02	4.75E-01	7.16E-03	2.36E-04	6.33E-05	1.22E+03	99.55	Plastic
Zrsm110 @2	4255	6	4387	74	9.75E-01	2.25E-02	5.05E-01	1.96E-03	1.23E-04	4.40E-05	1.78E+03	99.77	Fracture
Zrsm111	4238	8	4149	53	9.03E-01	1.57E-02	4.99E-01	2.58E-03	3.28E-05	1.15E-05	5.04E+03	99.94	Metamict
Zrsm112	3965	18	3905	83	8.33E-01	2.35E-02	4.15E-01	4.98E-03	9.47E-05	3.87E-05	1.21E+03	99.82	Unshocked
Zrsm113	3953	14	3969	104	8.51E-01	2.98E-02	4.12E-01	3.82E-03	1.07E-04	4.32E-05	1.18E+03	99.8	Unshocked
Zrsm114	3957	16	3981	105	8.54E-01	3.01E-02	4.13E-01	4.38E-03	1.69E-04	5.10E-05	1.19E+03	99.68	Unshocked
Zrsm115	4344	10	4486	65	1.01E+00	2.01E-02	5.36E-01	3.69E-03	4.13E-05	1.50E-05	4.46E+03	99.92	Partially metamict

Zrsm116	4169	45	4136	57	9.00E-01	1.68E-02	4.76E-01	1.43E-02	6.04E-05	2.07E-05	5.18E+03	99.89	Partially metamict
M_M2_Z19@1	4312	12	4691	151	1.07E+00	4.84E-02	5.25E-01	4.30E-03	6.18E-05	3.57E-05	9.97E+02	99.88	Unshocked
M_M2_Z19@2	4344	14	4441	119	9.92E-01	3.68E-02	5.36E-01	5.03E-03	8.67E-05	3.06E-05	1.73E+03	99.84	Unshocked
M_M2_Z21@1	4349	6	4426	65	9.87E-01	1.99E-02	5.38E-01	2.10E-03	7.08E-06	4.90E-06	5.39E+03	99.99	Metamict
M_M2_Z21@2	4358	6	4401	68	9.79E-01	2.08E-02	5.41E-01	2.34E-03	3.76E-06	3.68E-06	5.20E+03	99.99	Metamict
M_M2_Z22	4080	5	4154	64	9.05E-01	1.88E-02	4.48E-01	1.49E-03	5.69E-06	2.33E-06	2.26E+04	99.99	Metamict
M_M2_Z23	3838	85	4173	188	9.11E-01	5.57E-02	3.82E-01	2.15E-02	1.69E-03	4.88E-04	1.59E+02	96.82	Unshocked
M_M2_Z24	3978	13	3913	100	8.35E-01	2.84E-02	4.19E-01	3.59E-03	1.42E-04	5.00E-05	1.04E+03	99.73	Unshocked
M_M2_Z25	3954	24	3889	99	8.28E-01	2.80E-02	4.12E-01	6.49E-03	1.33E-04	5.09E-05	1.10E+03	99.75	Unshocked
Zrlg76@1	3982	12	3951	73	8.46E-01	2.10E-02	4.20E-01	3.45E-03	3.01E-05	2.13E-05	1.23E+03	99.94	No EBSD
Zrlg76@2	3952	17	4014	63	8.64E-01	1.81E-02	4.12E-01	4.69E-03	1.03E-04	3.92E-05	1.24E+03	99.81	No EBSD
Zrlg77@1	3983	17	3850	122	8.17E-01	3.45E-02	4.20E-01	4.85E-03	3.01E-05	2.13E-05	1.20E+03	99.94	Unshocked
Zrlg77@2	3951	18	4157	92	9.06E-01	2.71E-02	4.11E-01	4.86E-03	1.08E-04	4.10E-05	1.22E+03	99.8	Unshocked
Zrlg78@1	3968	17	3966	71	8.50E-01	2.03E-02	4.16E-01	4.58E-03	1.10E-04	5.10E-05	1.22E+03	99.79	Unshocked
Zrlg78@2	3979	18	3884	82	8.27E-01	2.33E-02	4.19E-01	5.08E-03	6.71E-04	1.00E-04	1.24E+03	98.74	Unshocked
Zrlg79@1	3963	10	4008	131	8.62E-01	3.77E-02	4.15E-01	2.66E-03	9.32E-05	3.80E-05	1.19E+03	99.82	Unshocked
Zrlg79@2	3957	13	4064	96	8.78E-01	2.80E-02	4.13E-01	3.50E-03	6.21E-05	3.09E-05	1.19E+03	99.88	Unshocked
Zrlg80@1	4192	64	4146	153	9.03E-01	4.51E-02	4.84E-01	2.08E-02	1.09E-03	1.61E-04	1.01E+03	97.95	Unshocked
Zrlg80@2	4165	59	4124	124	8.96E-01	3.66E-02	4.75E-01	1.90E-02	1.10E-03	1.44E-04	9.91E+02	97.94	Unshocked

Zrlg81@1	4130	13	4070	101	8.80E-01	2.94E-02	4.64E-01	4.12E-03	4.91E-05	2.84E-05	1.14E+03	99.91	Unshocked
Zrlg81@2	4136	14	4035	120	8.70E-01	3.48E-02	4.66E-01	4.48E-03	2.85E-04	7.63E-05	9.23E+02	99.46	Unshocked
Zrlg82@1	3976	31	3977	95	8.53E-01	2.72E-02	4.18E-01	8.65E-03	3.14E-05	2.98E-05	1.16E+03	99.94	Unshocked
Zrlg82@2	3954	18	4131	78	8.98E-01	2.28E-02	4.12E-01	4.85E-03	1.56E-04	5.17E-05	1.07E+03	99.71	Unshocked
Zrlg83@1	4368	10	4397	96	9.78E-01	2.96E-02	5.45E-01	3.61E-03	3.44E-05	1.41E-05	3.18E+03	99.94	Unshocked
Zrlg83@2	4371	9	4315	66	9.53E-01	2.01E-02	5.46E-01	3.28E-03	1.91E-05	1.09E-05	7.07E+03	99.96	Metamict
Zrlg84@1	4271	17	4119	64	8.95E-01	1.89E-02	5.10E-01	5.72E-03	7.83E-05	2.99E-05	1.64E+03	99.85	Plastic
Zrlg84@2	4208	19	4322	116	9.55E-01	3.52E-02	4.89E-01	6.11E-03	1.08E-04	3.60E-05	1.72E+03	99.8	Plastic
Zrlg84@3	4240	12	4260	53	9.37E-01	1.59E-02	5.00E-01	4.12E-03	1.11E-04	3.51E-05	1.68E+03	99.79	Plastic
Zrlg85@1	4108	67	4075	153	8.82E-01	4.46E-02	4.57E-01	2.07E-02	5.54E-04	1.28E-04	8.03E+02	98.95	Unshocked
Zrlg85@2	4234	85	3956	105	8.47E-01	3.01E-02	4.98E-01	2.86E-02	3.51E-04	1.01E-04	9.67E+02	99.34	Unshocked
Zrlg86@1	3964	18	3799	65	8.03E-01	1.81E-02	4.15E-01	5.00E-03	4.81E-04	8.26E-05	1.32E+03	99.09	Unshocked
Zrlg86@2	3973	11	3884	69	8.27E-01	1.95E-02	4.18E-01	2.99E-03	1.87E-04	5.17E-05	1.30E+03	99.65	Unshocked
Zrlg87	4381	12	4197	80	9.18E-01	2.37E-02	5.50E-01	4.37E-03	3.40E-05	1.64E-05	3.25E+03	99.94	Unshocked
Zrlg88@1	4193	67	4236	144	9.29E-01	4.31E-02	4.84E-01	2.20E-02	3.68E-04	9.19E-05	8.04E+02	99.31	Unshocked
Zrlg88@2	4052	36	4155	123	9.05E-01	3.63E-02	4.40E-01	1.05E-02	2.69E-04	5.88E-05	1.84E+03	99.49	Shock twin
Zrlg88@3	4025	51	4361	132	9.67E-01	4.03E-02	4.32E-01	1.49E-02	1.00E-03	2.60E-04	5.85E+02	98.11	Shock twin

* = corrected for common Pb
Calibration for zircons M_M1_Z2 through M_M2_Z18
Calibration line slope: 0.046
Calibration line intercept: 0.320

Calibration for zircons Zrsm90 through Zrlg88@3
Calibration line slope: 0.065
Calibration line intercept: 0.240

Table D3: Apollo 14311,58 Ti-in-zircon thermometry

Sample	Ti (ppm)	Ti-Temperature (°C)	$^{57}Fe/^{94}Zr_2O_{16}$
Zrsm90	122	1065	1.84E-02
Zrsm91	117	1058	1.42E-02
Zrsm92@1	40	907	1.37E-02
Zrsm92@2	50	934	1.35E-02
Zrsm93	65	969	1.55E-02
Zrsm94	130	1075	1.45E-02
Zrsm95	230	1176	3.09E-02
Zrsm96@1	140	1088	2.11E-02
Zrsm96@2	118	1060	1.48E-02
Zrsm97	54	945	1.48E-02
Zrsm98	123	1066	1.30E-02
Zrsm99	77	994	1.40E-02
Zrsm100	187	1138	1.39E-02
Zrsm101	51	937	1.46E-02
Zrsm102	97	1029	1.37E-02
Zrsm103	100	1034	1.36E-02
Zrsm104	138	1085	1.73E-02
Zrsm106@1	119	1061	1.46E-02
Zrsm106@2	358	1266	1.30E-02
Zrsm107	79	998	1.40E-02
Zrsm108@1	124	1067	1.40E-02
Zrsm108@2	112	1051	1.34E-02
Zrsm109@1	47	927	1.38E-02
Zrsm109@2	47	927	1.35E-02
Zrsm110@1	114	1054	1.24E-02
Zrsm110@2	115	1055	1.35E-02
Zrsm111	104	1040	1.41E-02
Zrsm112	87	1013	1.66E-02
Zrsm113	99	1032	1.41E-02
Zrsm114	113	1053	1.46E-02
Zrsm115	34	887	1.41E-02
Zrsm116	63	967	1.47E-02

M_M2_Z19@1	217	1165	2.48E-02
M_M2_Z19@2	83	1006	1.54E-02
M_M2_Z21@1	33	882	1.06E-02
M_M2_Z21@2	47	926	1.18E-02
M_M2_Z22	263	1202	1.28E-02
M_M2_Z23	629	1397	5.55E-02
M_M2_Z24	84	1008	1.16E-02
M_M2_Z25	99	1031	1.30E-02
Zrlg76@1	97	1029	1.10E-02
Zrlg76@2	101	1035	1.15E-02
Zrlg77@1	102	1037	1.21E-02
Zrlg77@2	93	1023	1.20E-02
Zrlg78@1	88	1013	1.16E-02
Zrlg78@2	99	1032	1.23E-02
Zrlg79@1	103	1038	1.16E-02
Zrlg79@2	111	1050	1.20E-02
Zrlg80@1	78	997	1.28E-02
Zrlg80@2	84	1008	1.29E-02
Zrlg81@1	40	907	1.55E-02
Zrlg81@2	42	913	1.29E-02
Zrlg82@1	123	1067	1.42E-02
Zrlg82@2	104	1040	1.34E-02
Zrlg83@1	98	1030	1.17E-02
Zrlg83@2	108	1046	1.30E-02
Zrlg84@1	156	1107	1.41E-02
Zrlg84@2	136	1083	1.36E-02
Zrlg84@3	136	1083	1.34E-02
Zrlg85@1	157	1107	1.38E-02
Zrlg85@2	163	1114	1.76E-02
Zrlg86@1	117	1058	1.29E-02
Zrlg86@2	113	1052	1.24E-02
Zrlg87	186	1137	1.32E-02
Zrlg88@1	136	1083	1.17E-02
Zrlg88@2	1064	1541	1.29E-02
Zrlg88@3	104	1040	1.24E-02

Table D4: U concentrations, alpha dose, and amorphization fraction for Apollo 14311,58 zircons

Sample	U ppm	Alpha dose (alpha event/gram) (10^{18})	Amorphization percentage
M_M1_Z2	38	0.94	17.1
M_M1_Z4	172	4.37	58.2
M_M1_Z3	73	1.83	30.6
M_M1_Z5	34	0.88	16.2
M_M1_Z6	82	2.10	34.3
M_M1_Z7	61	1.63	27.8
S_M2_Z2	120	3.06	45.7
S_M2_Z3	203	5.37	65.8
S_M2_Z5	133	3.83	53.5
S_M2_Z6	35	0.93	17.0
S_M2_Z7	117	2.62	40.8
S_M2_Z16	187	4.31	57.8
S_M2_Z17	20	0.50	9.4
S_M2_Z18	119	3.22	47.5
S_M2_Z19	108	2.88	43.8
S_M2_Z20	58	1.50	25.9
S_M2_Z21	56	1.48	25.6
S_M2_Z22	13	0.31	6.0
S_M2_Z23	116	3.10	46.2
S_M2_Z24	285	7.78	78.9
S_M2_Z25	91	2.42	38.4
S_M2_Z26	87	2.37	37.7
M_M1_Z8	44	1.14	20.4
M_M1_Z9	17	0.41	7.8
M_M1_Z10	87	2.17	35.2
M_M1_Z11	50	1.34	23.5
M_M1_Z12	57	1.49	25.8
M_M1_Z13	11	0.26	5.2
M_M1_Z14	68	1.77	29.8
M_M1_Z15	27	0.63	11.9
M_M1_Z16	328	8.89	83.1
M_M1_Z17	26	0.66	12.3

M_M1_Z18	22	0.56	10.6
M_M1_Z19	150	4.03	55.3
M_M1_Z20	149	3.96	54.7
M_M1_Z21	89	2.20	35.6
M_M1_Z23	58	1.56	26.8
M_M1_Z24	49	1.24	22.0
M_M1_Z26	121	3.01	45.3
M_M1_Z27	62	1.58	27.1
M_M1_Z28	147	3.66	51.9
M_M1_Z29	29	0.68	12.7
M_M1_Z30	127	3.60	51.3
M_M1_Z31	19	0.45	8.6
M_M1_Z32	708	16.70	96.5
M_M1_Z33	71	1.69	28.6
M_M1_Z34	283	7.43	77.4
M_M1_Z35	57	1.96	32.4
M_M1_Z36	24	0.58	11.0
M_M1_Z38	54	1.40	24.4
M_M1_Z39	60	1.53	26.4
M_M1_Z41	36	0.98	17.8
M_M1_Z42	32	0.85	15.6
M_M1_Z43	66	1.76	29.7
M_M1_Z44	46	1.17	20.8
M_M1_Z45	60	1.59	27.2
M_M1_Z46	50	1.33	23.3
M_M1_Z47	28	0.66	12.4
M_M1_Z48	238	5.68	67.9
M_M1_Z49	76	1.94	32.2
M_M1_Z50	44	1.01	18.3
M_M1_Z51	110	2.63	40.9
M_M2_Z9	21	0.51	9.7
M_M2_Z10@1	10	0.26	5.0
M_M2_Z10@2	8	0.20	3.9
M_M2_Z11	28	0.66	12.3
M_M2_Z12@1	48	1.28	22.6

M_M2_Z12@2	47	1.23	21.8
M_M2_Z13	21	0.50	9.5
M_M2_Z14	100	2.68	41.5
M_M2_Z17	59	1.53	26.3
M_M2_Z18	105	2.82	43.1
Zrsm90	70	1.84	30.8
Zrsm91	34	0.82	15.1
Zrsm92@1	105	2.83	43.2
Zrsm92@2	104	2.75	42.3
Zrsm93	20	0.50	9.5
Zrsm94	32	0.78	14.4
Zrsm95	13	0.31	6.0
Zrsm96@1	34	0.81	15.0
Zrsm96@2	36	0.87	16.0
Zrsm97	24	0.56	10.6
Zrsm98	33	0.80	14.7
Zrsm99	20	0.52	9.9
Zrsm100	55	1.41	24.6
Zrsm101	203	5.66	67.7
Zrsm102	31	0.73	13.6
Zrsm103	28	0.68	12.7
Zrsm104	33	0.80	14.8
Zrsm106@1	45	1.21	21.6
Zrsm106@2	96	2.51	39.5
Zrsm107	124	3.21	47.4
Zrsm108@1	44	1.17	20.8
Zrsm108@2	29	0.75	13.9
Zrsm109@1	24	0.57	10.8
Zrsm109@2	25	0.59	11.2
Zrsm110@1	32	0.86	15.7
Zrsm110@2	44	1.18	21.0
Zrsm111	129	3.44	49.8
Zrsm112	33	0.80	14.7
Zrsm113	34	0.81	14.9
Zrsm114	33	0.78	14.5

Zrsm115	112	2.85	43.4
Zrsm116	141	3.55	50.9
M_M2_Z19@1	45	1.23	21.9
M_M2_Z19@2	47	1.31	23.0
M_M2_Z21@1	132	3.56	50.9
M_M2_Z21@2	124	3.36	48.9
M_M2_Z22	610	15.70	95.7
M_M2_Z23	20	0.48	9.1
M_M2_Z24	33	0.78	14.5
M_M2_Z25	32	0.76	14.1
Zrlg76@1	31	0.75	14.0
Zrlg76@2	32	0.77	14.4
Zrlg77@1	31	0.76	14.1
Zrlg77@2	31	0.73	13.6
Zrlg78@1	33	0.78	14.5
Zrlg78@2	33	0.80	14.8
Zrlg79@1	32	0.77	14.2
Zrlg79@2	32	0.78	14.4
Zrlg80@1	27	0.68	12.8
Zrlg80@2	25	0.66	12.3
Zrlg81@1	29	0.75	13.9
Zrlg81@2	24	0.62	11.6
Zrlg82@1	32	0.76	14.1
Zrlg82@2	30	0.73	13.6
Zrlg83@1	79	2.07	34.0
Zrlg83@2	176	4.66	60.6
Zrlg84@1	42	1.13	20.2
Zrlg84@2	45	1.23	21.7
Zrlg84@3	42	1.11	19.9
Zrlg85@1	20	0.50	9.6
Zrlg85@2	26	0.67	12.5
Zrlg86@1	36	0.86	15.8
Zrlg86@2	35	0.84	15.4
Zrlg87	77	2.11	34.4
Zrlg88@1	19	0.49	9.4

Zrlg88@2	45	1.16	20.8
Zrlg88@3	14	0.33	6.4

Appendix E – Chicxulub zircon images (excluding unshocked grains)

C1-grain 1

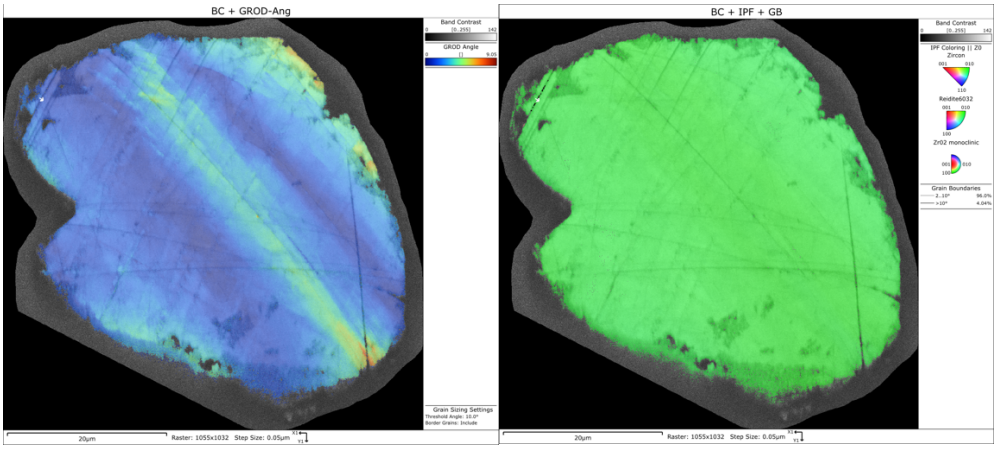

C1-grain 2

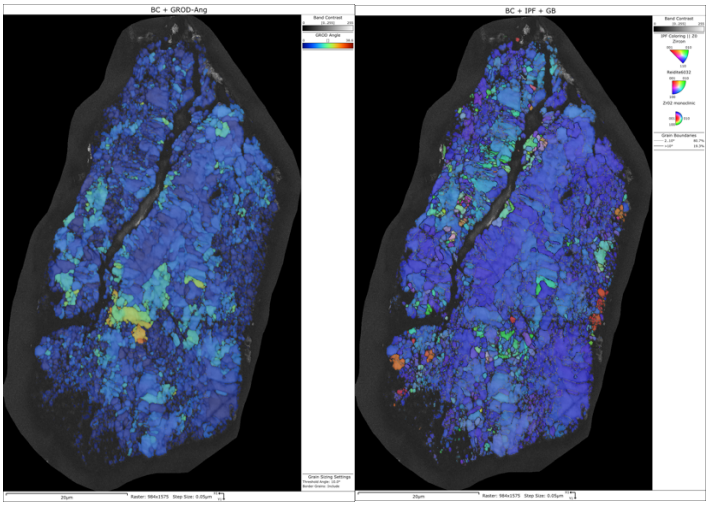

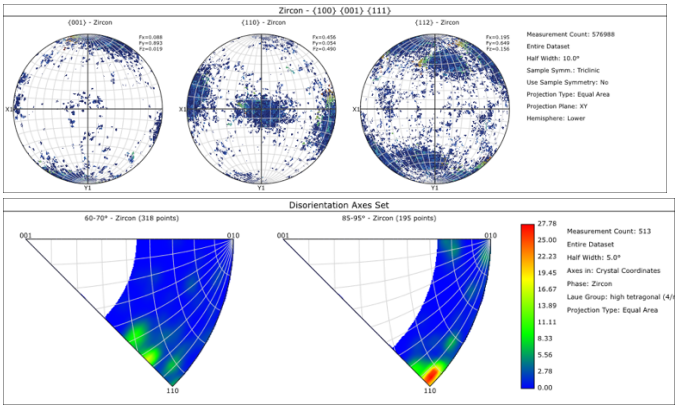

M2

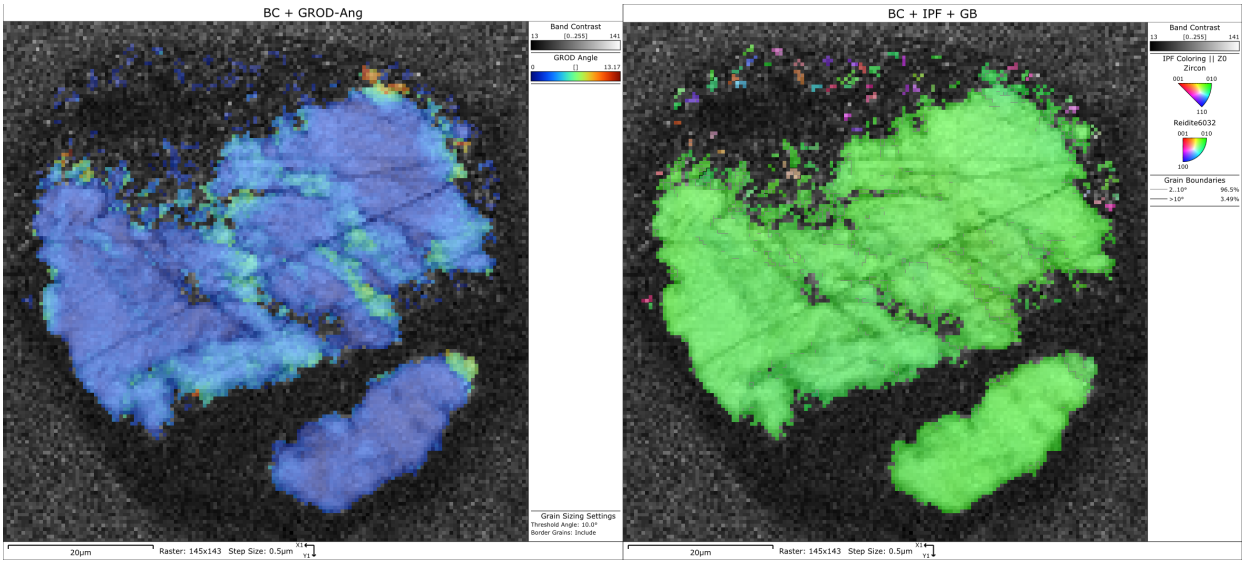
BC + GROD-Ang
Band Contrast
GROD Angle
Grain Sizing Settings
Threshold Angle: 10.0°
Border Grains: Include
20µm
Raster: 145x143 Step Size: 0.5µm
BC + IPF + GB
Band Contrast
IPF Coloring || Z0
Zircon
Reidite6032
Grain Boundaries
2..10° 96.5%
>10° 3.49%
20µm
Raster: 145x143 Step Size: 0.5µm

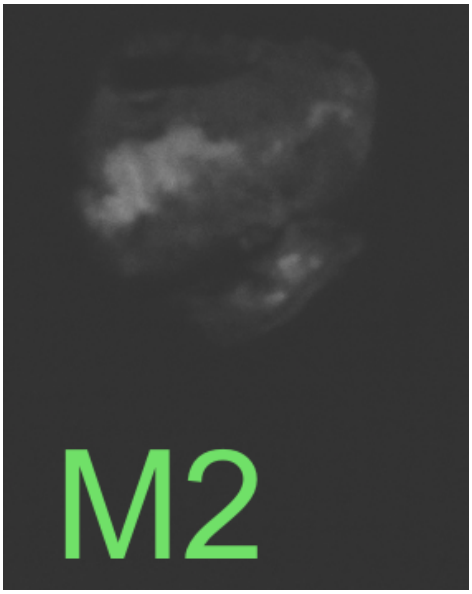
M2

M10

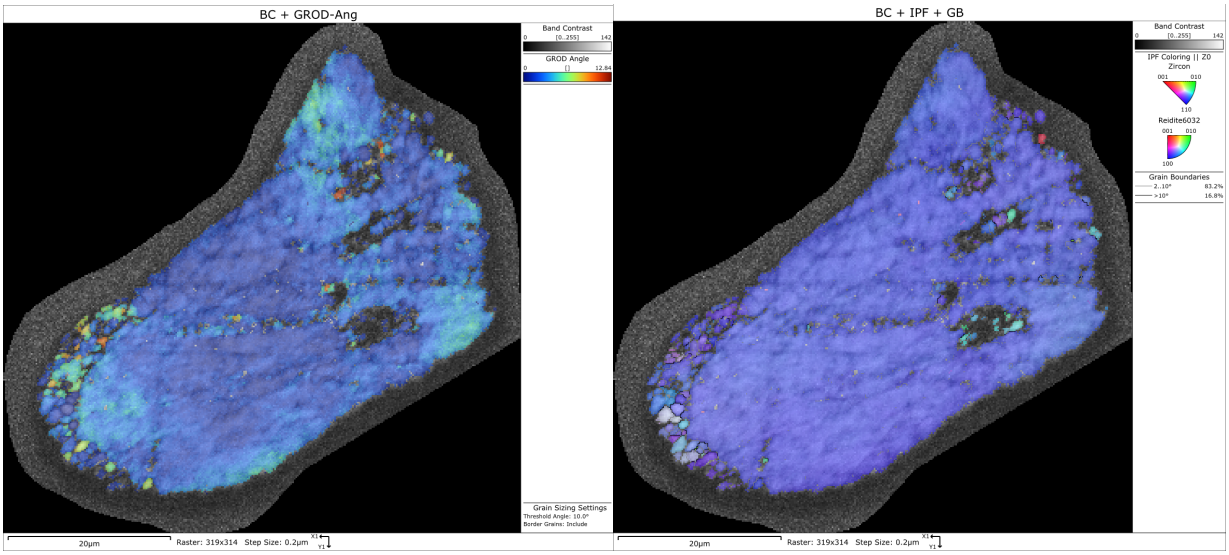
BC + GROD-Ang
Band Contrast
GROD Angle
Grain Sizing Settings
20µm
Raster: 319x314 Step Size: 0.2µm
BC + IPF + GB
Band Contrast
IPF Coloring || Z0
Zircon
Reidite6032
Grain Boundaries
20µm
Raster: 319x314 Step Size: 0.2µm

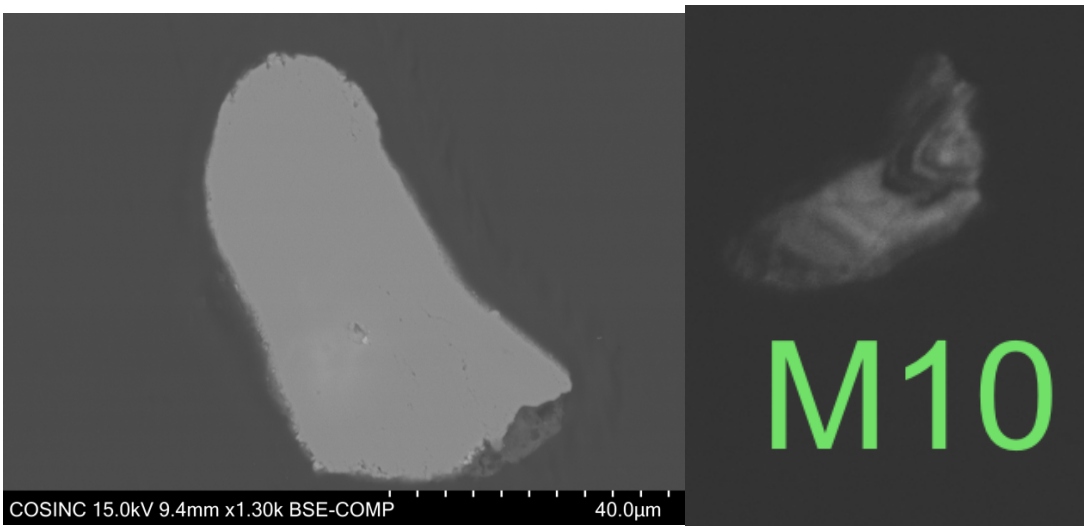
COSINC 15.0kV 9.4mm x1.30k BSE-COMP
40.0µm
M10

M12

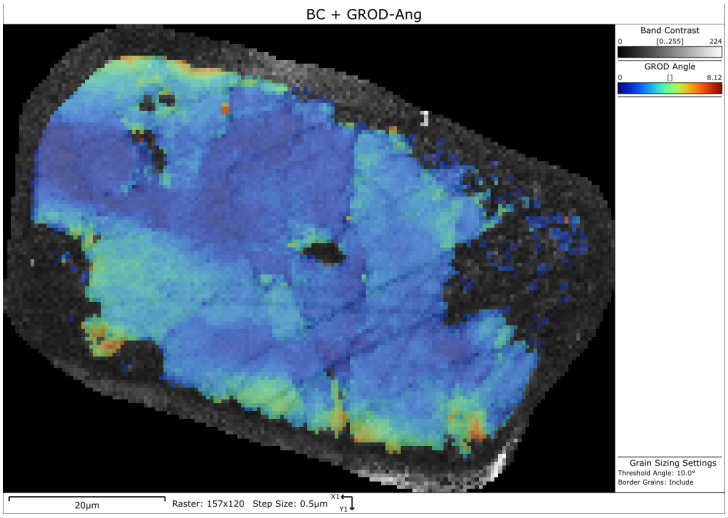
BC + GROD-Ang
Band Contrast
0 [0..255] 224
GROD Angle
0 [] 8.12
Grain Sizing Settings
Threshold Angle: 10.0°
Border Grains: Include
20µm
Raster: 157x120 Step Size: 0.5µm

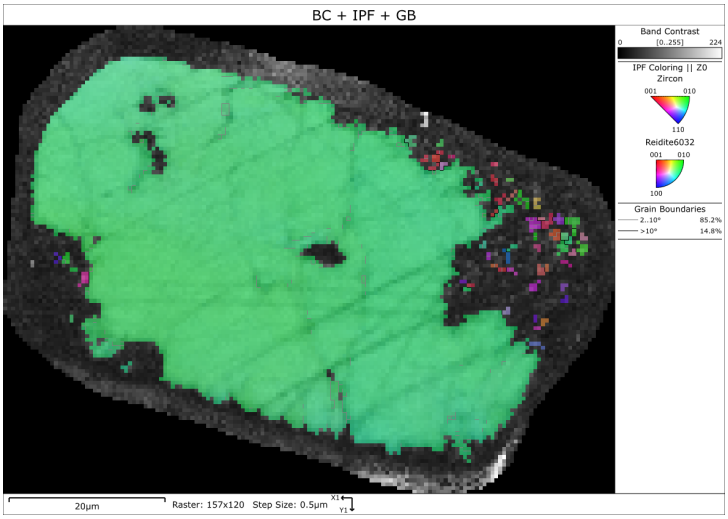
BC + IPF + GB
Band Contrast
0 [0..255] 224
IPF Coloring || Z0
Zircon
001 010
110
Reidite6032
001 010
100
Grain Boundaries
2..10° 85.2%
>10° 14.8%
20µm
Raster: 157x120 Step Size: 0.5µm

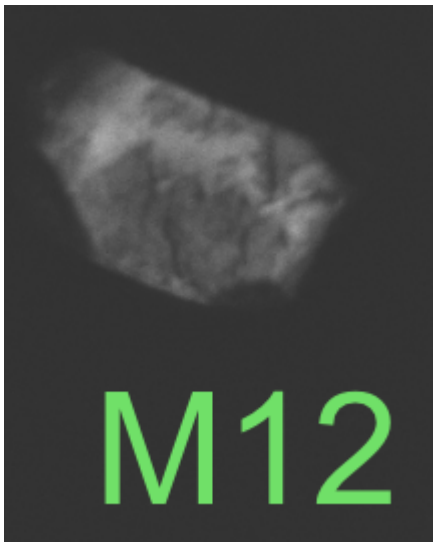
M12

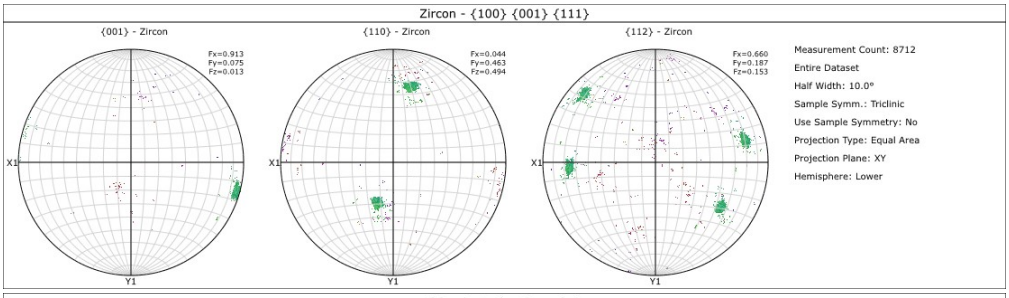
Zircon - {100} {001} {111}
{001} - Zircon
Fx=0.913
Fy=0.075
Fz=0.013
{110} - Zircon
Fx=0.044
Fy=0.463
Fz=0.494
{112} - Zircon
Fx=0.660
Fy=0.187
Fz=0.153
X1
Y1
Measurement Count: 8712
Entire Dataset
Half Width: 10.0°
Sample Symm.: Triclinic
Use Sample Symmetry: No
Projection Type: Equal Area
Projection Plane: XY
Hemisphere: Lower

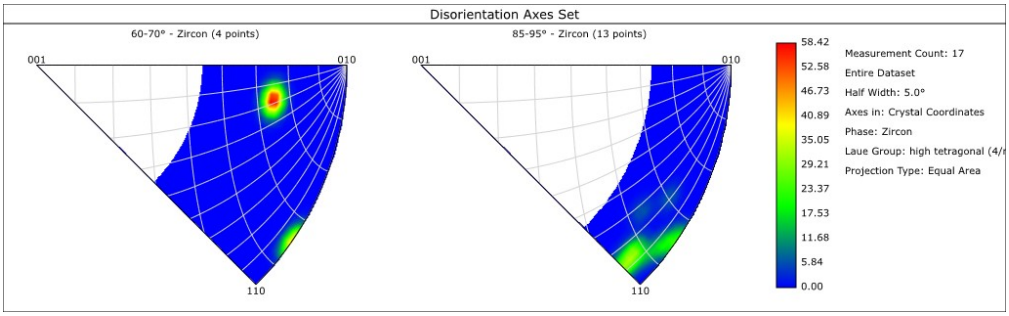
Disorientation Axes Set
60-70° - Zircon (4 points)
85-95° - Zircon (13 points)
001
010
110
58.42
52.58
46.73
40.89
35.05
29.21
23.37
17.53
11.68
5.84
0.00
Measurement Count: 17
Entire Dataset
Half Width: 5.0°
Axes in: Crystal Coordinates
Phase: Zircon
Laue Group: high tetragonal (4/
Projection Type: Equal Area

M15

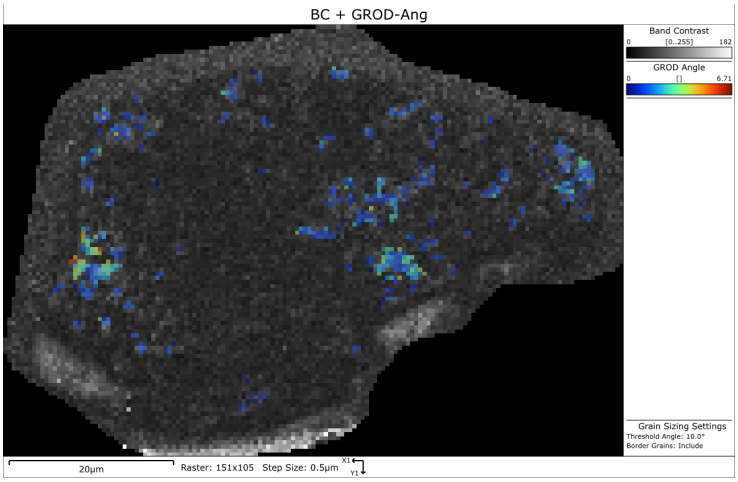
BC + GROD-Ang
Band Contrast
0 [0..255] 182
GROD Angle
0 [] 6.71
Grain Sizing Settings
Threshold Angle: 10.0°
Border Grains: Include
20µm
Raster: 151x105 Step Size: 0.5µm

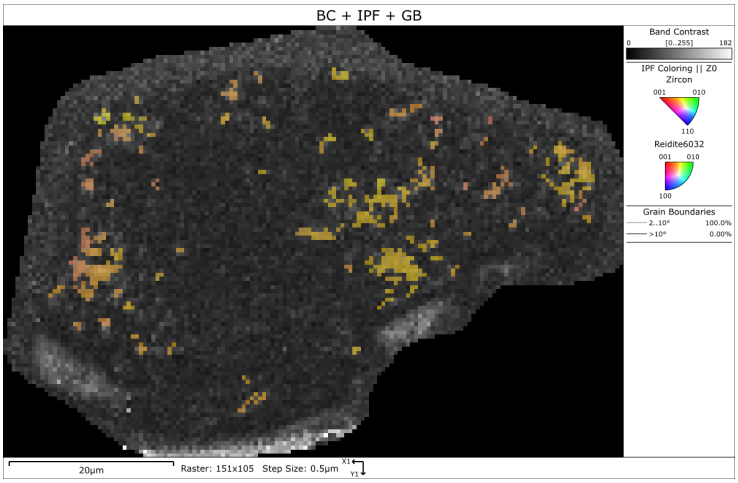
BC + IPF + GB
Band Contrast
0 [0..255] 182
IPF Coloring || Z0
Zircon
001 010
110
Reidite6032
001 010
100
Grain Boundaries
2..10° 100.0%
>10° 0.00%
20µm
Raster: 151x105 Step Size: 0.5µm

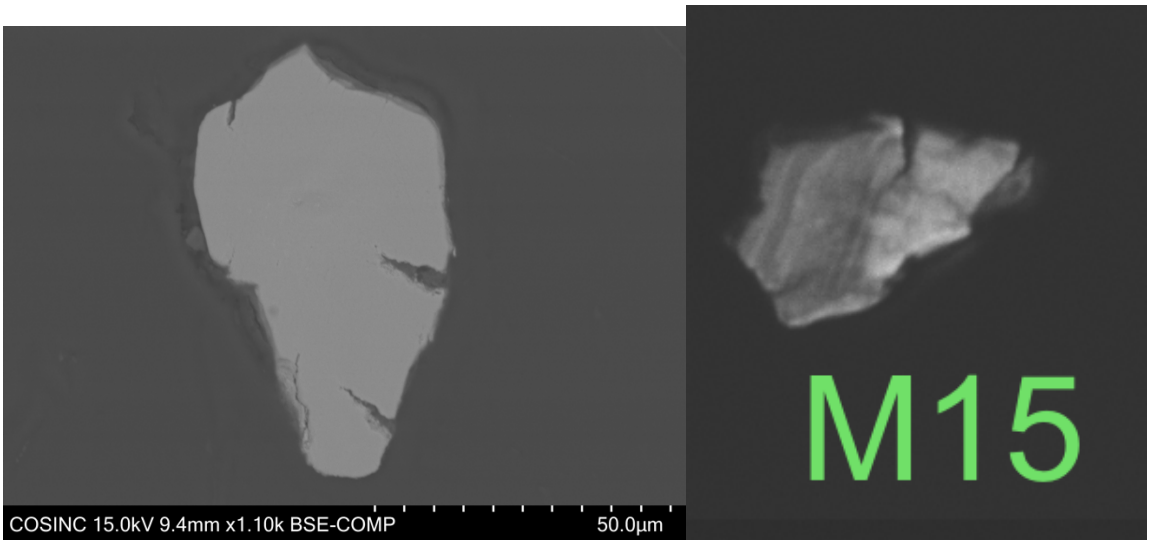
COSINC 15.0kV 9.4mm x1.10k BSE-COMP
50.0µm
M15

M17

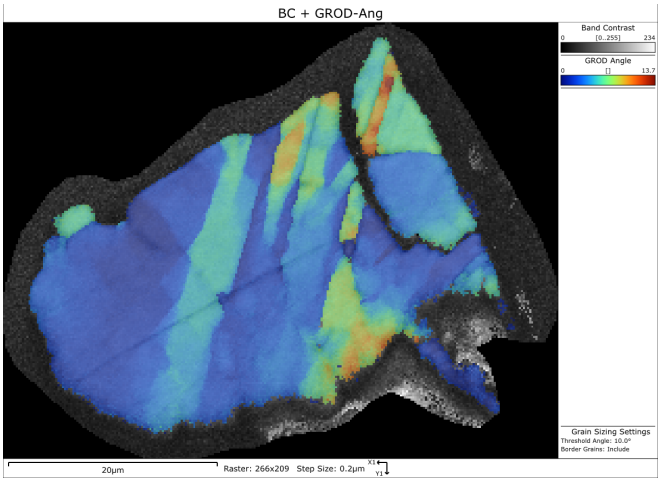
BC + GROD-Ang
Band Contrast
0 [0..255] 234
GROD Angle
0 [] 13.7
Grain Sizing Settings
Threshold Angle: 10.0°
Border Grains: Include
20µm
Raster: 266x209 Step Size: 0.2µm

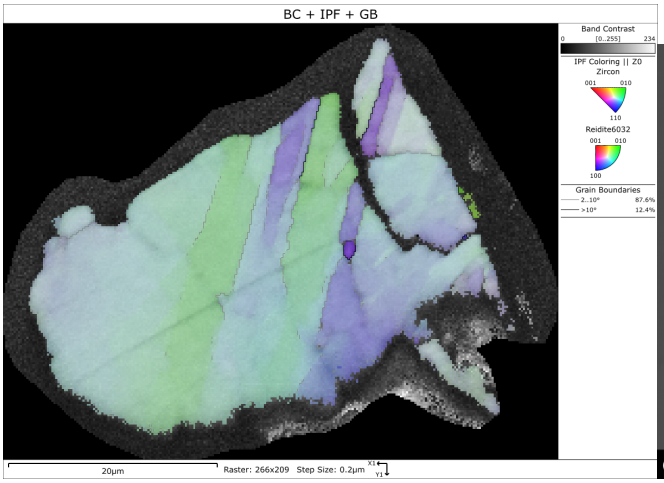
BC + IPF + GB
Band Contrast
0 [0..255] 234
IPF Coloring || Z0
Zircon
001 010
110
Reidite6032
001 010
100
Grain Boundaries
2..10° 87.6%
>10° 12.4%
20µm
Raster: 266x209 Step Size: 0.2µm

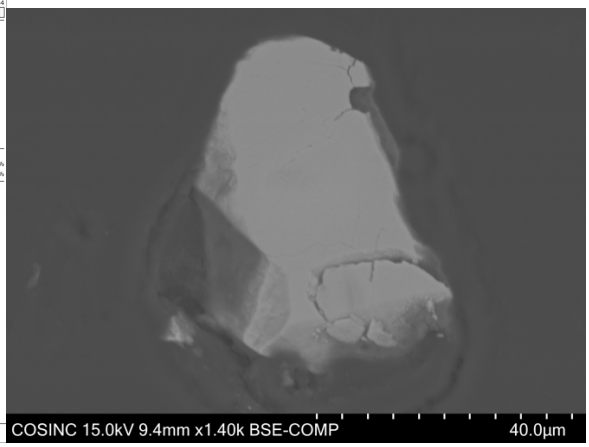
COSINC 15.0kV 9.4mm x1.40k BSE-COMP
40.0µm

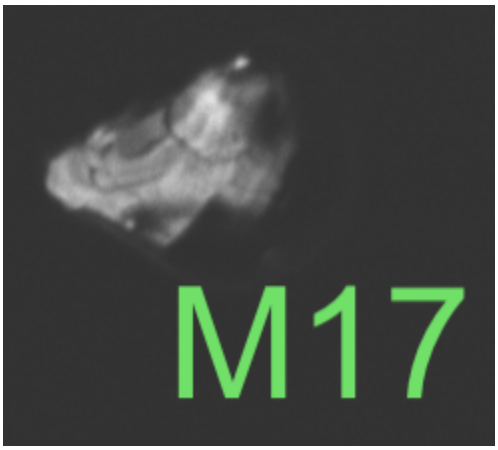
M17

M19

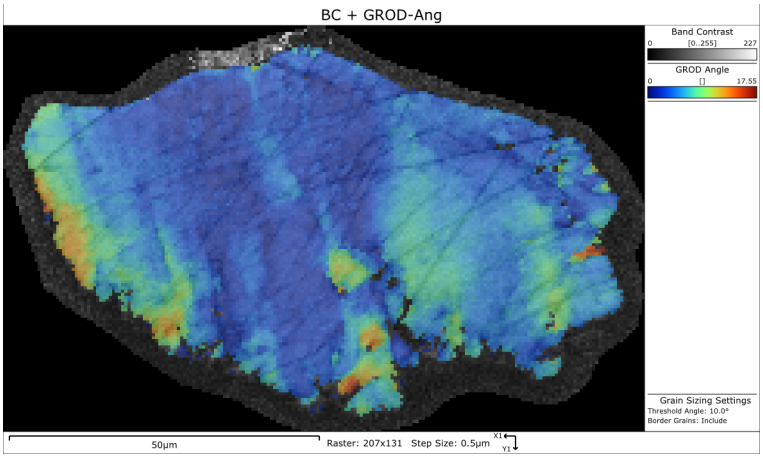
BC + GROD-Ang
Band Contrast
0
[0..255]
227
GROD Angle
0
[]
17.55
Grain Sizing Settings
Threshold Angle: 10.0°
Border Grains: Include
50µm
Raster: 207x131 Step Size: 0.5µm
X1
Y1

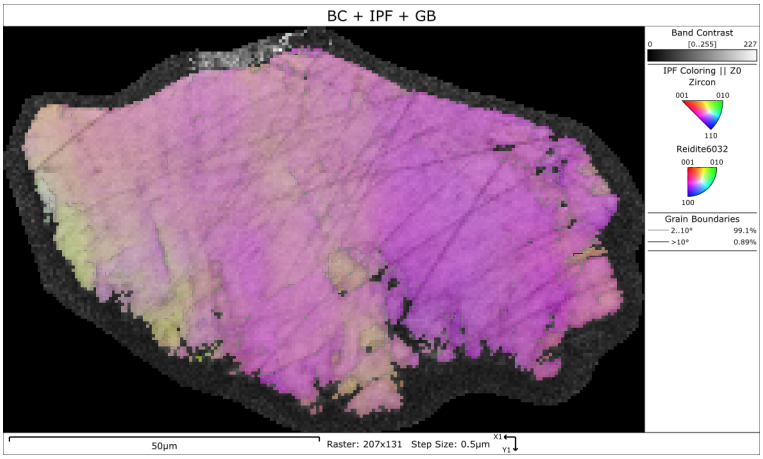
BC + IPF + GB
Band Contrast
0
[0..255]
227
IPF Coloring || Z0
Zircon
001
010
110
Reidite6032
001
010
100
Grain Boundaries
2..10°
99.1%
>10°
0.89%
50µm
Raster: 207x131 Step Size: 0.5µm
X1
Y1

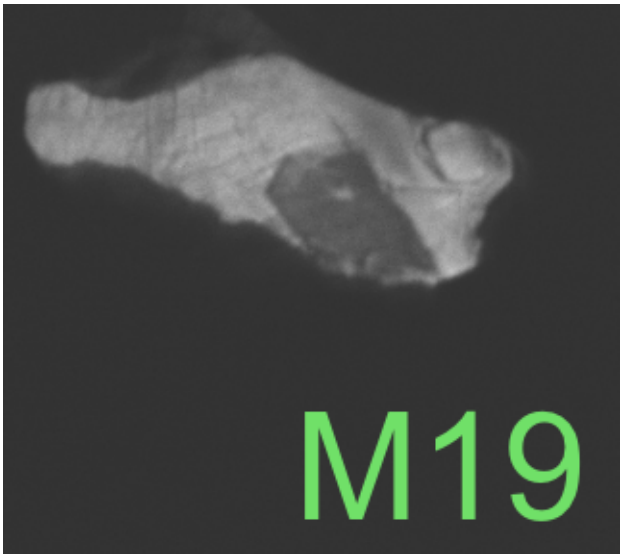
M19

M20

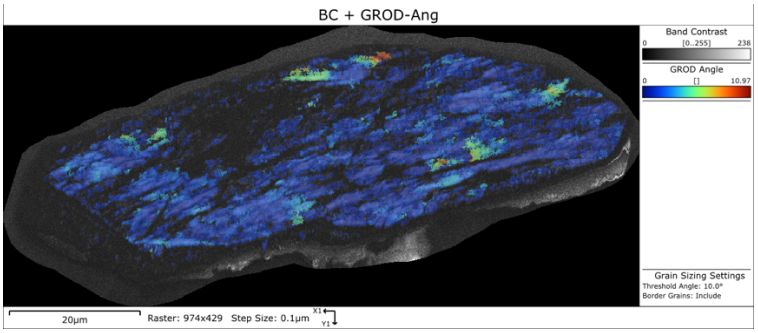
BC + GROD-Ang
Band Contrast
0 [0..255] 238
GROD Angle
0 [] 10.97
Grain Sizing Settings
Threshold Angle: 10.0°
Border Grains: Include
20µm
Raster: 974x429 Step Size: 0.1µm

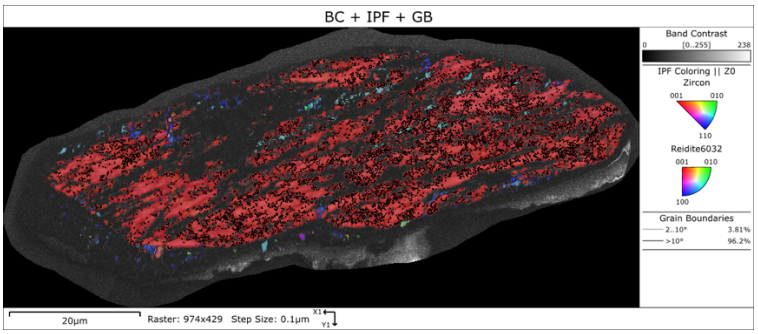
BC + IPF + GB
Band Contrast
0 [0..255] 238
IPF Coloring || Z0
Zircon
001 010
110
Reidite6032
001 010
100
Grain Boundaries
2..10° 3.81%
>10° 96.2%
20µm
Raster: 974x429 Step Size: 0.1µm

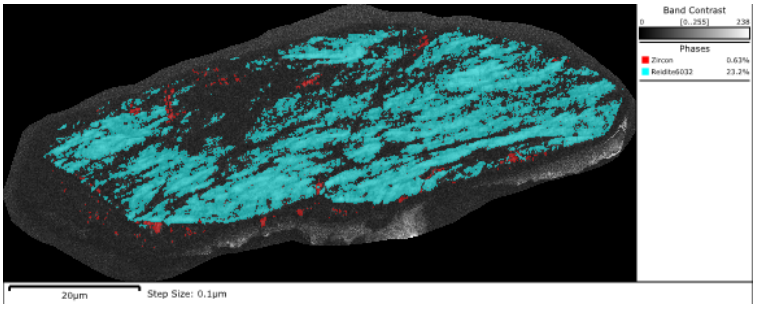
Band Contrast
0 [0..255] 238
Phases
Zircon 0.63%
Reidite6032 23.2%
20µm
Step Size: 0.1µm

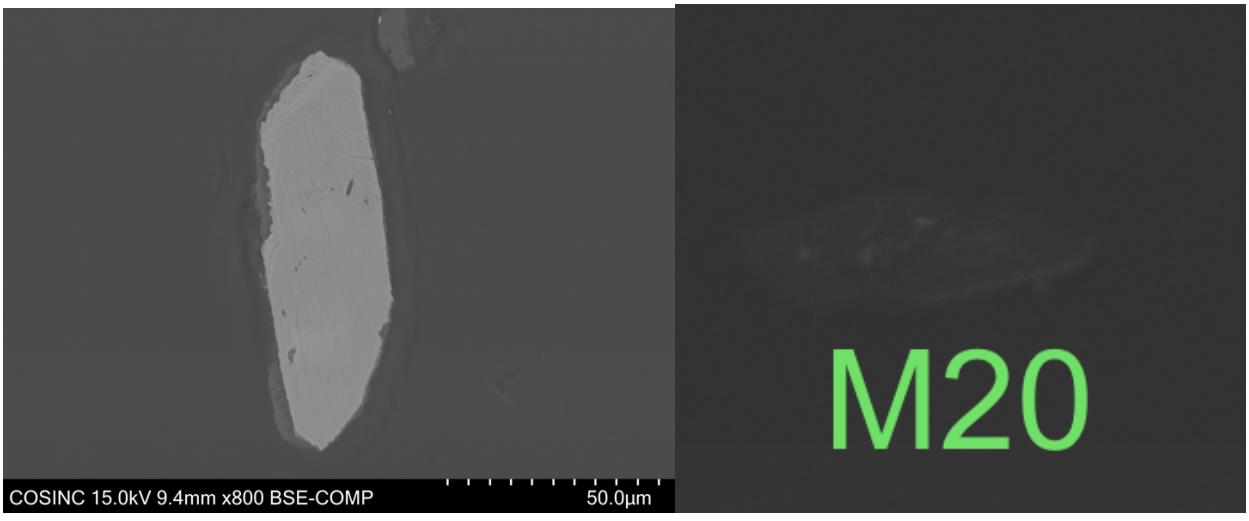
M20
COSINC 15.0kV 9.4mm x800 BSE-COMP
50.0µm

M22

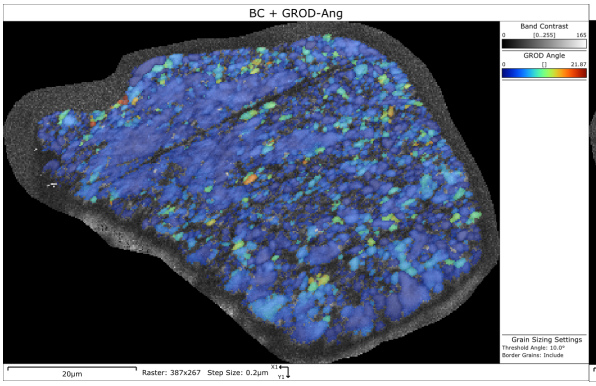
BC + GROD-Ang
Band Contrast
GROD Angle
Grain Sizing Settings
20µm
Raster: 387x267 Step Size: 0.2µm

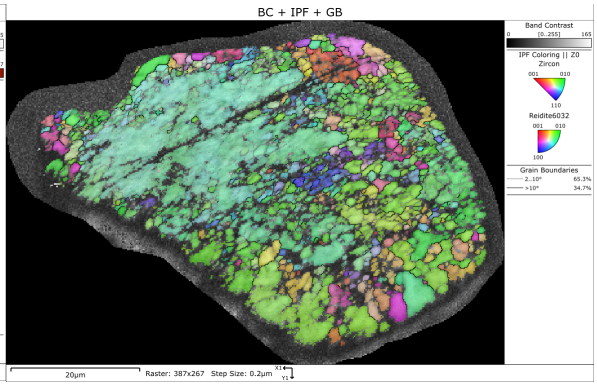
BC + IPF + GB
Band Contrast
IPF Coloring || Z0
Zircon
Reldite6032
Grain Boundaries
20µm
Raster: 387x267 Step Size: 0.2µm

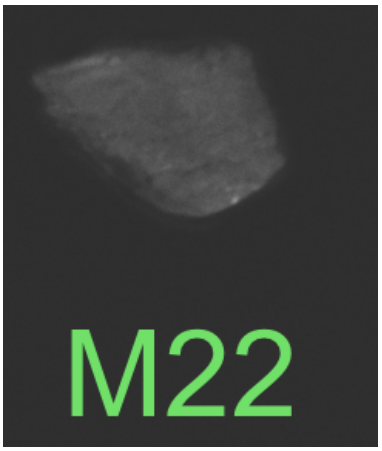
M22

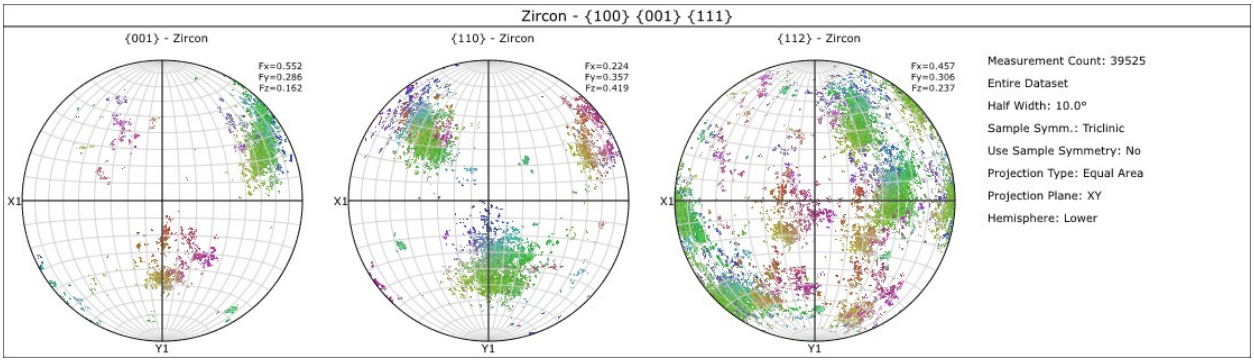
Zircon - {100} {001} {111}
{001} - Zircon
Fx=0.552
Fy=0.286
Fz=0.162
{110} - Zircon
Fx=0.224
Fy=0.357
Fz=0.419
{112} - Zircon
Fx=0.457
Fy=0.306
Fz=0.237
X1
Y1
Measurement Count: 39525
Entire Dataset
Half Width: 10.0°
Sample Symm.: Triclinic
Use Sample Symmetry: No
Projection Type: Equal Area
Projection Plane: XY
Hemisphere: Lower

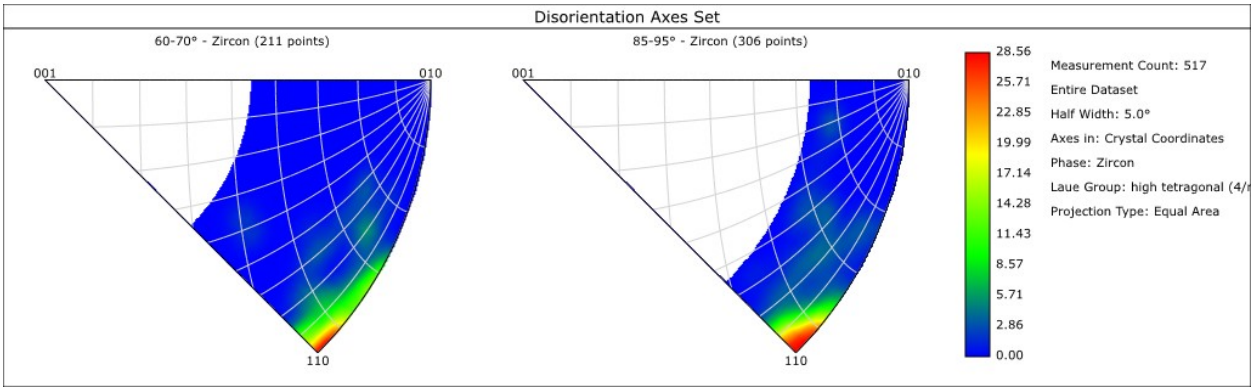
Disorientation Axes Set
60-70° - Zircon (211 points)
85-95° - Zircon (306 points)
001
010
110
28.56
25.71
22.85
19.99
17.14
14.28
11.43
8.57
5.71
2.86
0.00
Measurement Count: 517
Entire Dataset
Half Width: 5.0°
Axes in: Crystal Coordinates
Phase: Zircon
Laue Group: high tetragonal (4/
Projection Type: Equal Area

M24

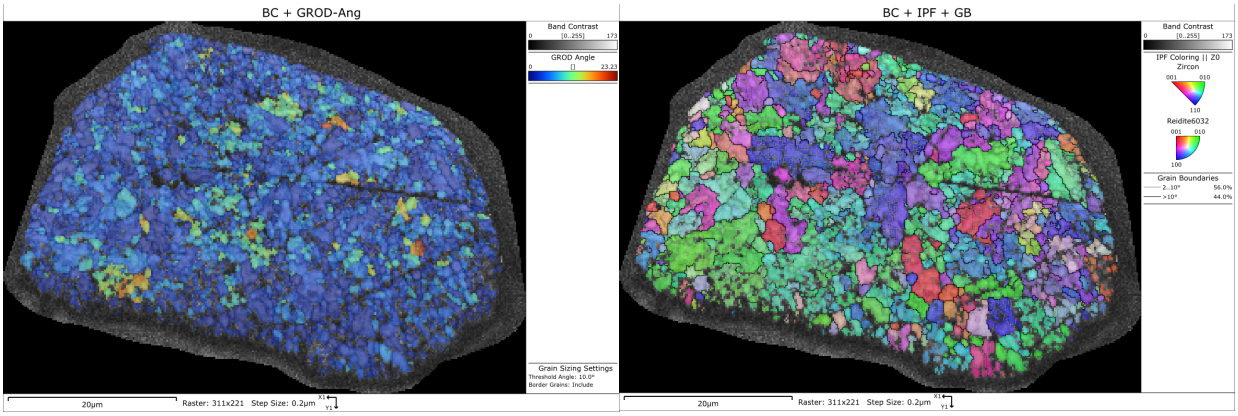
BC + GROD-Ang
Band Contrast
GROD Angle
Grain Sizing Settings
20µm
Raster: 311x221 Step Size: 0.2µm
BC + IPF + GB
Band Contrast
IPF Coloring || Z0
Zircon
Reidite6032
Grain Boundaries
20µm
Raster: 311x221 Step Size: 0.2µm


M24

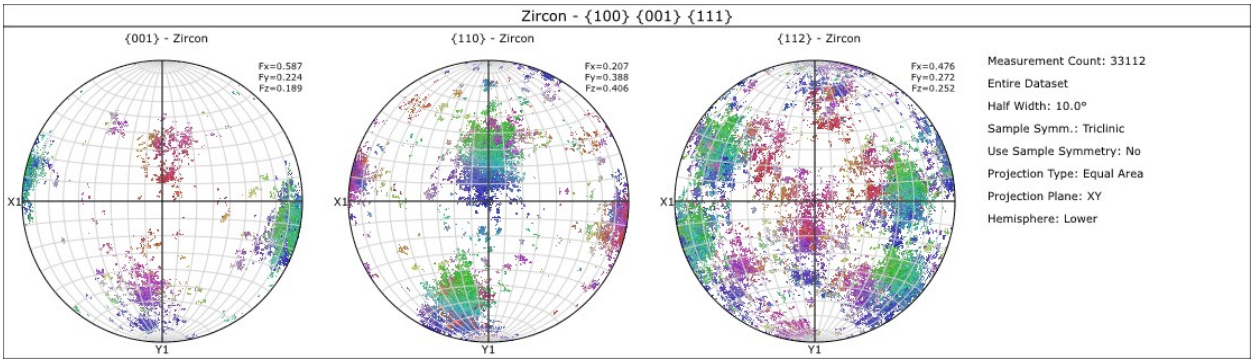
Zircon - {100} {001} {111}
{001} - Zircon
Fx=0.587
Fy=0.224
Fz=0.189
{110} - Zircon
Fx=0.207
Fy=0.388
Fz=0.406
{112} - Zircon
Fx=0.476
Fy=0.272
Fz=0.252
X1
Y1
Measurement Count: 33112
Entire Dataset
Half Width: 10.0°
Sample Symm.: Triclinic
Use Sample Symmetry: No
Projection Type: Equal Area
Projection Plane: XY
Hemisphere: Lower

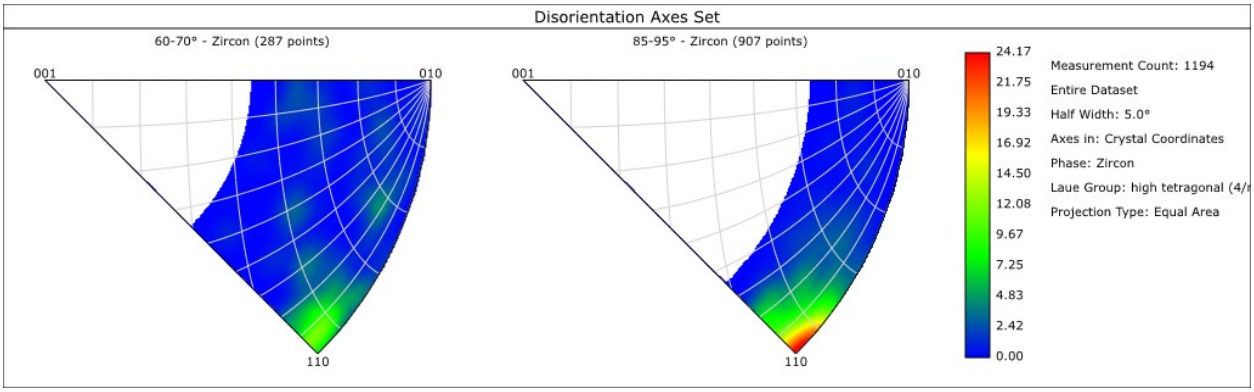
Disorientation Axes Set
60-70° - Zircon (287 points)
85-95° - Zircon (907 points)
001
010
110
24.17
21.75
19.33
16.92
14.50
12.08
9.67
7.25
4.83
2.42
0.00
Measurement Count: 1194
Entire Dataset
Half Width: 5.0°
Axes in: Crystal Coordinates
Phase: Zircon
Projection Type: Equal Area

M26

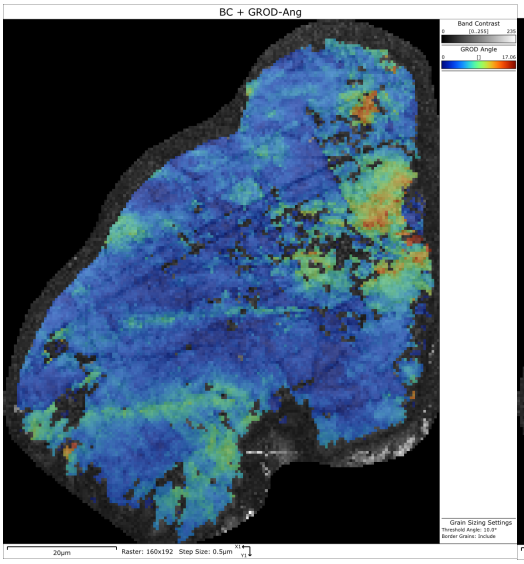
BC + GROD-Ang
Band Contrast
GROD Angle
Grain Sizing Settings
20μm
Raster: 160x192 Step Size: 0.5μm

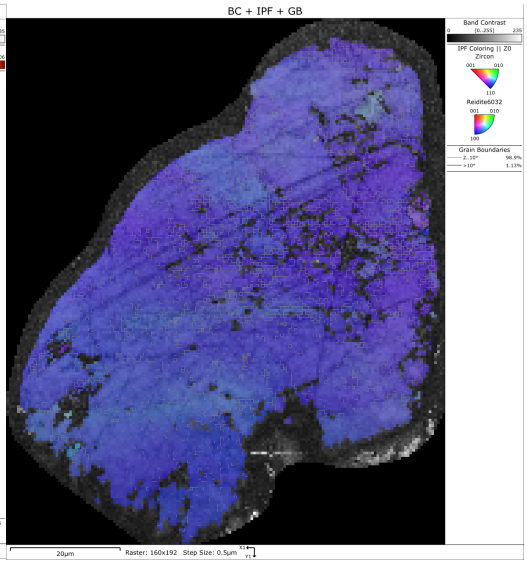
BC + IPF + GB
Band Contrast
IPF Coloring || Z0
Zircon
Reidite6032
Grain Boundaries
20μm
Raster: 160x192 Step Size: 0.5μm

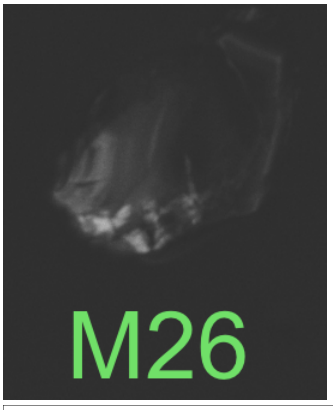
M26

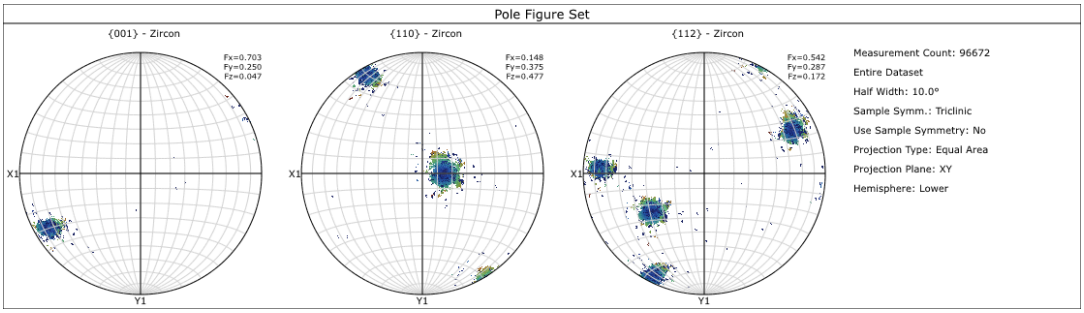
Pole Figure Set
{001} - Zircon
Fx=0.703
Fy=0.250
Fz=0.047
{110} - Zircon
Fx=0.148
Fy=0.375
Fz=0.477
{112} - Zircon
Fx=0.542
Fy=0.287
Fz=0.172
X1
Y1
Measurement Count: 96672
Entire Dataset
Half Width: 10.0°
Sample Symm.: Triclinic
Use Sample Symmetry: No
Projection Type: Equal Area
Projection Plane: XY
Hemisphere: Lower

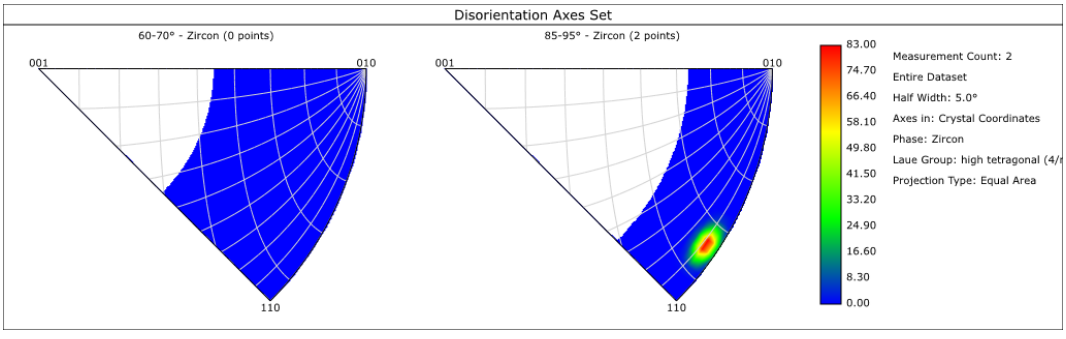
Disorientation Axes Set
60-70° - Zircon (0 points)
85-95° - Zircon (2 points)
001
010
110
83.00
74.70
66.40
58.10
49.80
41.50
33.20
24.90
16.60
8.30
0.00
Measurement Count: 2
Entire Dataset
Half Width: 5.0°
Axes in: Crystal Coordinates
Phase: Zircon
Projection Type: Equal Area

M27

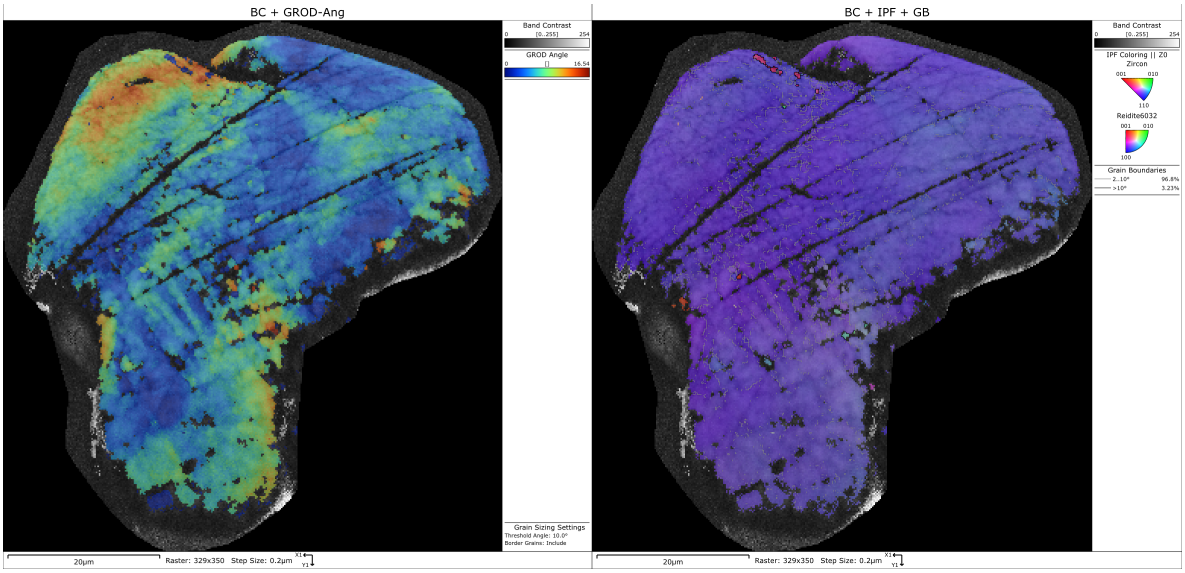
BC + GROD-Ang
Band Contrast
GROD Angle
Grain Sizing Settings
20µm
Raster: 329x350 Step Size: 0.2µm
BC + IPF + GB
Band Contrast
IPF Coloring || Z0
Zircon
Reidite6032
Grain Boundaries
20µm
Raster: 329x350 Step Size: 0.2µm


M27

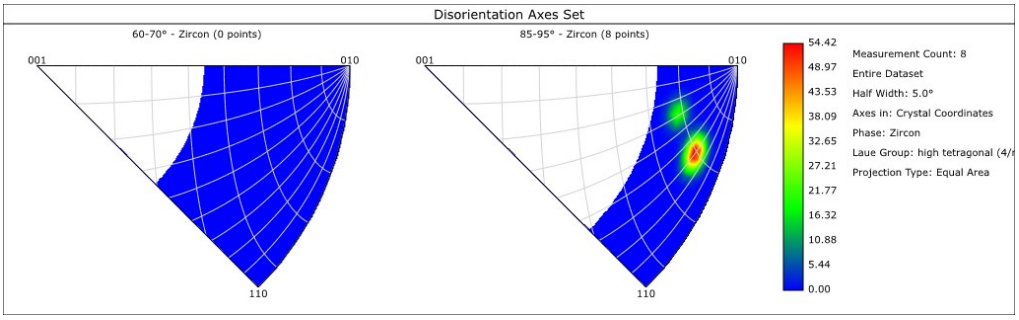
Disorientation Axes Set
60-70° - Zircon (0 points)
85-95° - Zircon (8 points)
001
010
110
54.42
48.97
43.53
38.09
32.65
27.21
21.77
16.32
10.88
5.44
0.00
Measurement Count: 8
Entire Dataset
Half Width: 5.0°
Axes in: Crystal Coordinates
Phase: Zircon
Projection Type: Equal Area

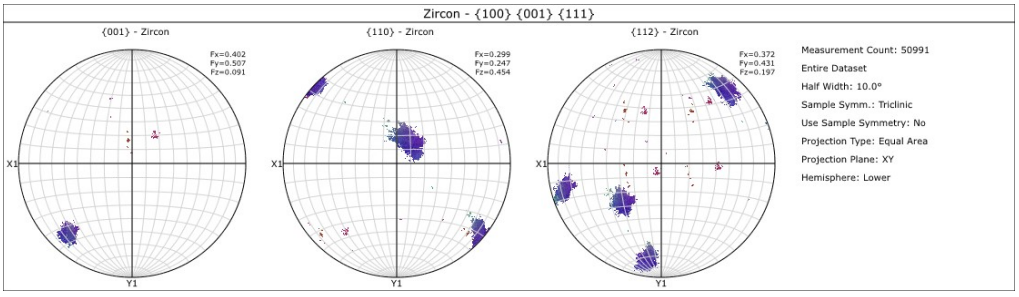
Zircon - {100} {001} {111}
{001} - Zircon
{110} - Zircon
{112} - Zircon
Measurement Count: 50991
Entire Dataset
Half Width: 10.0°
Sample Symm.: Triclinic
Use Sample Symmetry: No
Projection Type: Equal Area
Projection Plane: XY
Hemisphere: Lower

M30

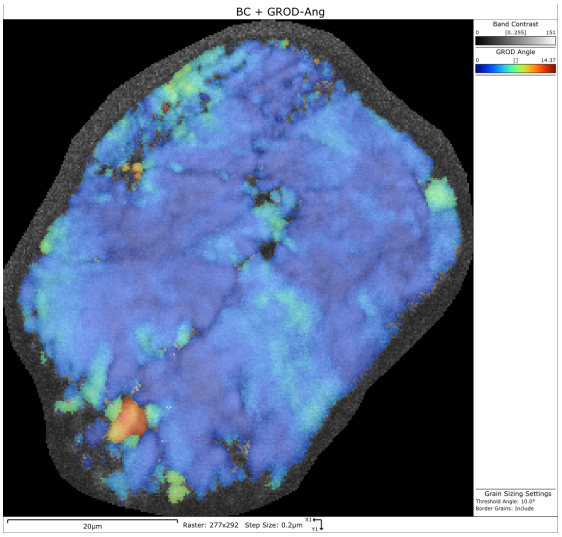
BC + GROD-Ang
Band Contrast
GROD Angle
Grain Sizing Settings
20µm
Raster: 277x292 Step Size: 0.2µm

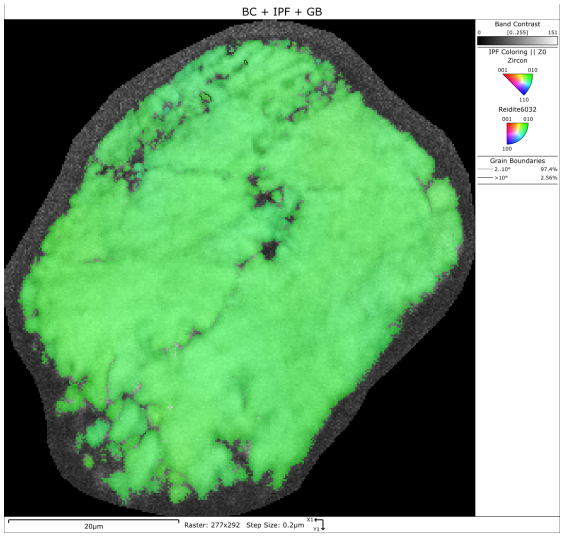
BC + IPF + GB
Band Contrast
IPF Coloring || Z0
Zircon
Reidite032
Grain Boundaries
20µm
Raster: 277x292 Step Size: 0.2µm

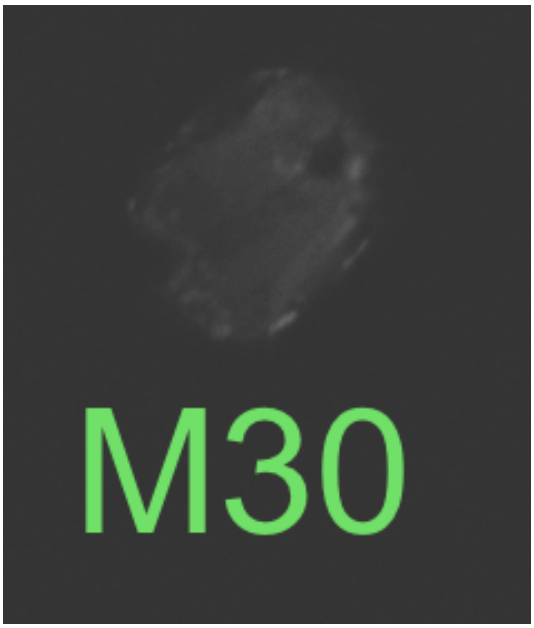
M30

M31

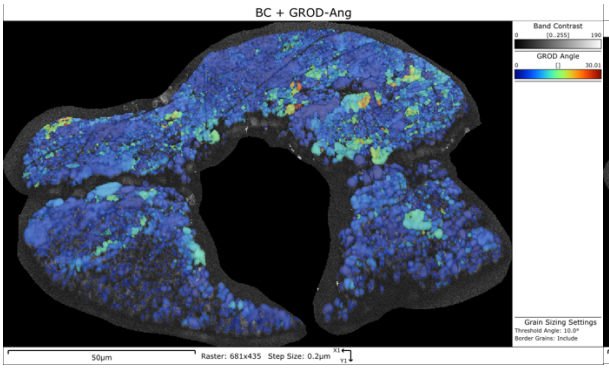
BC + GROD-Ang
Band Contrast
GROD Angle
Grain Sizing Settings
50µm
Raster: 681x435 Step Size: 0.2µm

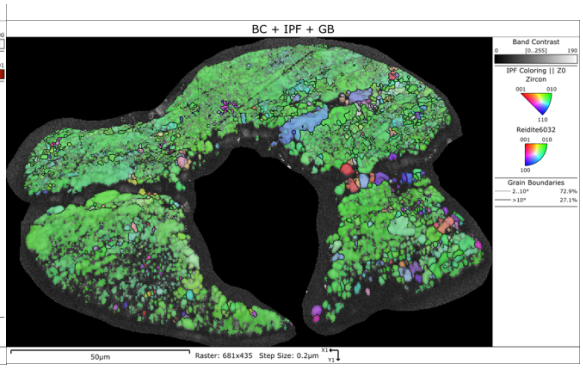
BC + IPF + GB
Band Contrast
IPF Coloring || Z0
Zircon
Reidite6032
Grain Boundaries
50µm
Raster: 681x435 Step Size: 0.2µm

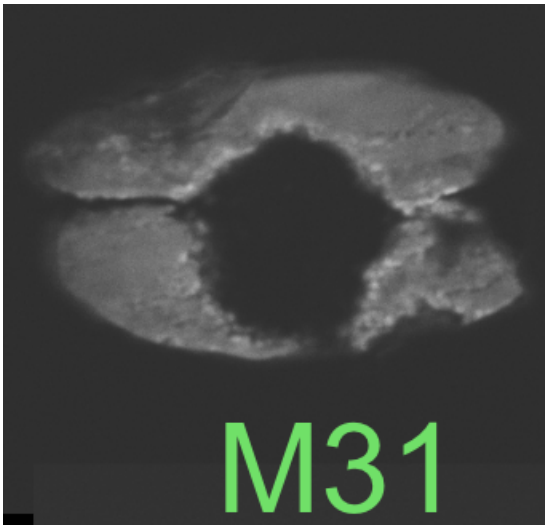
M31

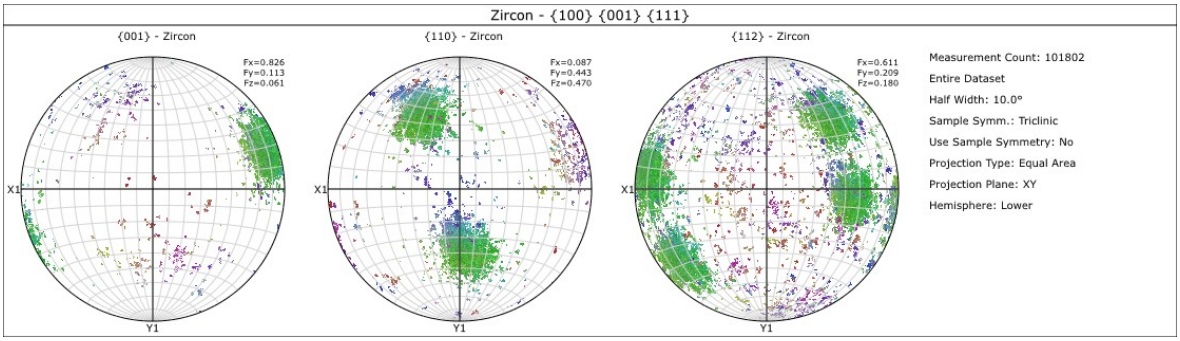
Zircon - {100} {001} {111}
{001} - Zircon
Fx=0.826
Fy=0.113
Fz=0.061
{110} - Zircon
Fx=0.087
Fy=0.443
Fz=0.470
{112} - Zircon
Fx=0.611
Fy=0.209
Fz=0.180
X1
Y1
Measurement Count: 101802
Entire Dataset
Half Width: 10.0°
Sample Symm.: Triclinic
Use Sample Symmetry: No
Projection Type: Equal Area
Projection Plane: XY
Hemisphere: Lower

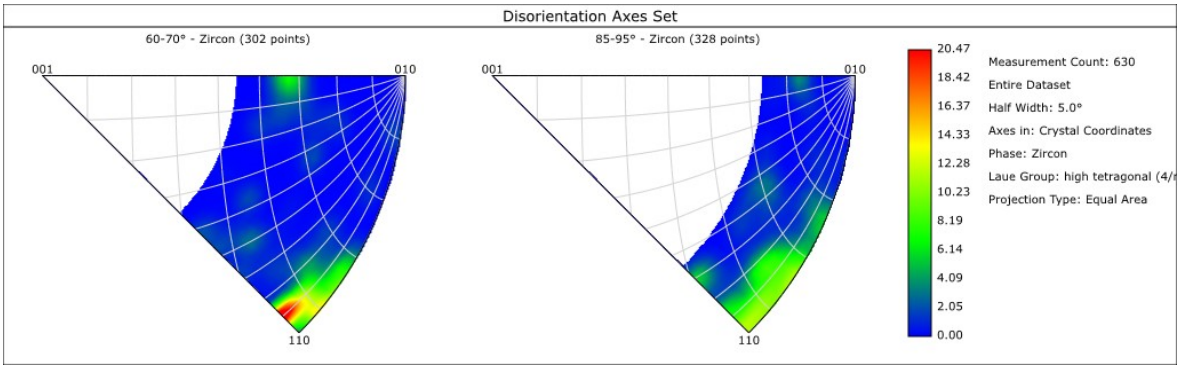
Disorientation Axes Set
60-70° - Zircon (302 points)
85-95° - Zircon (328 points)
001
010
110
20.47
18.42
16.37
14.33
12.28
10.23
8.19
6.14
4.09
2.05
0.00
Measurement Count: 630
Entire Dataset
Half Width: 5.0°
Axes in: Crystal Coordinates
Phase: Zircon
Projection Type: Equal Area

M33

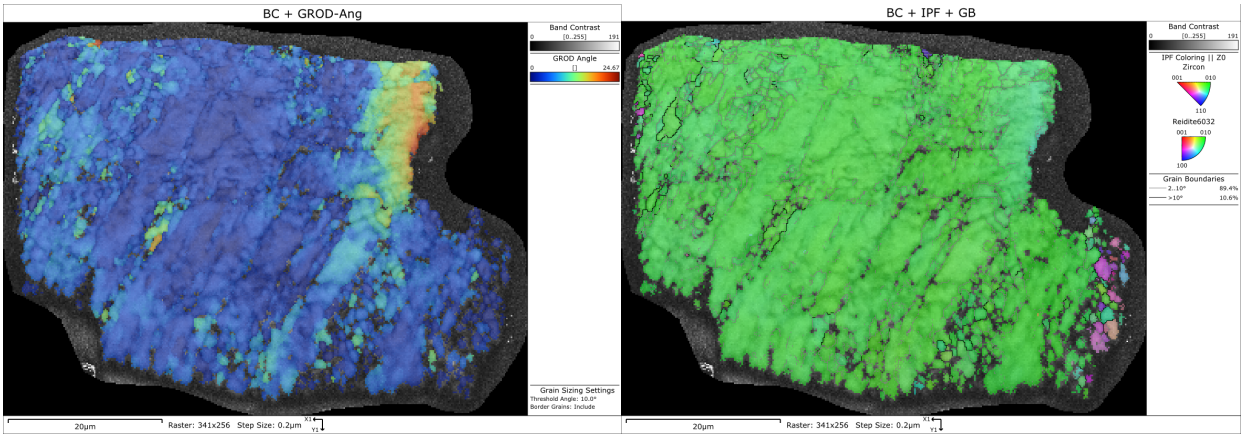
BC + GROD-Ang
Band Contrast
GROD Angle
Grain Sizing Settings
20µm
Raster: 341x256 Step Size: 0.2µm
BC + IPF + GB
Band Contrast
IPF Coloring || Z0
Zircon
Reidite6032
Grain Boundaries
20µm
Raster: 341x256 Step Size: 0.2µm

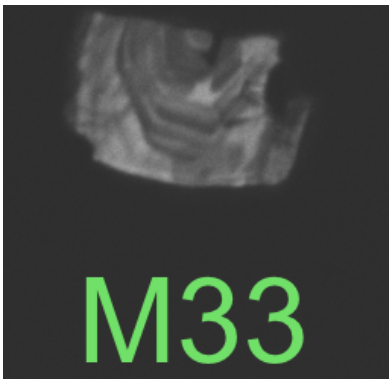
M33

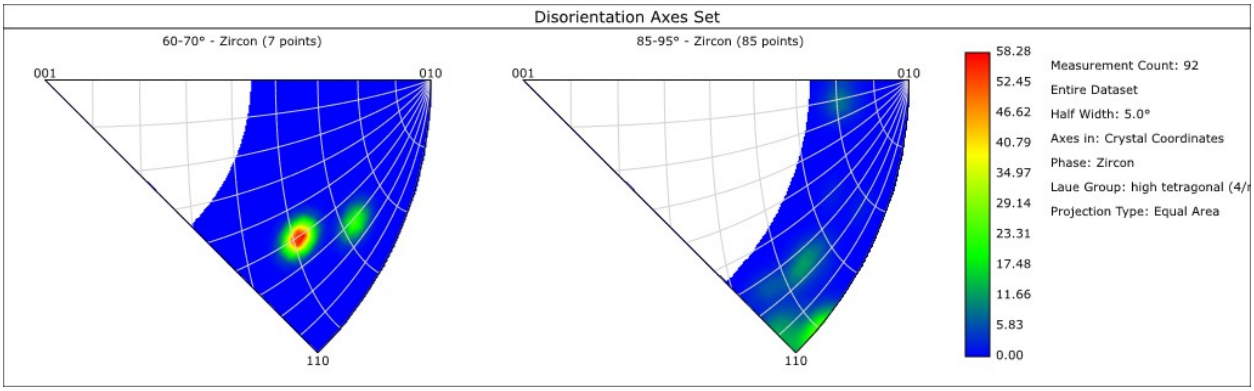
Disorientation Axes Set
60-70° - Zircon (7 points)
85-95° - Zircon (85 points)
001
010
110
58.28
52.45
46.62
40.79
34.97
29.14
23.31
17.48
11.66
5.83
0.00
Measurement Count: 92
Entire Dataset
Half Width: 5.0°
Axes in: Crystal Coordinates
Phase: Zircon
Projection Type: Equal Area

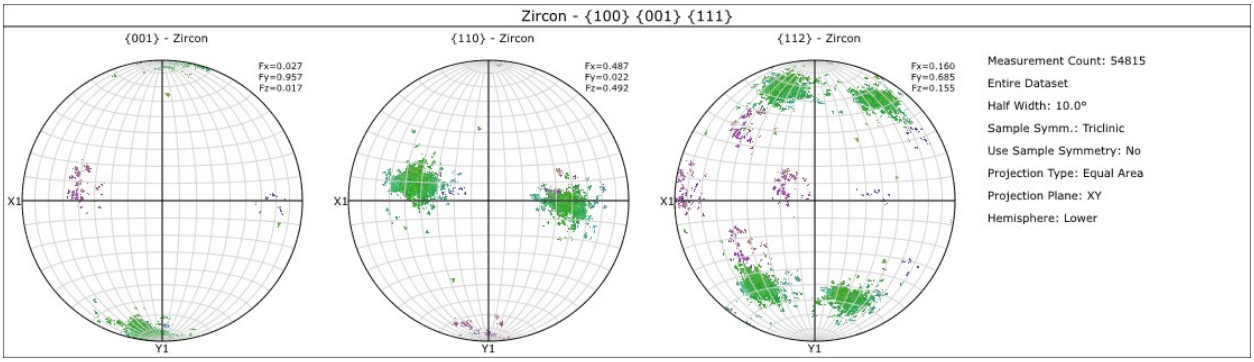
Zircon - {100} {001} {111}
{001} - Zircon
{110} - Zircon
{112} - Zircon
Fx=0.027
Fy=0.957
Fz=0.017
Fx=0.487
Fy=0.022
Fz=0.492
Fx=0.160
Fy=0.685
Fz=0.155
X1
Y1
Measurement Count: 54815
Entire Dataset
Half Width: 10.0°
Sample Symm.: Triclinic
Use Sample Symmetry: No
Projection Type: Equal Area
Projection Plane: XY
Hemisphere: Lower

M34

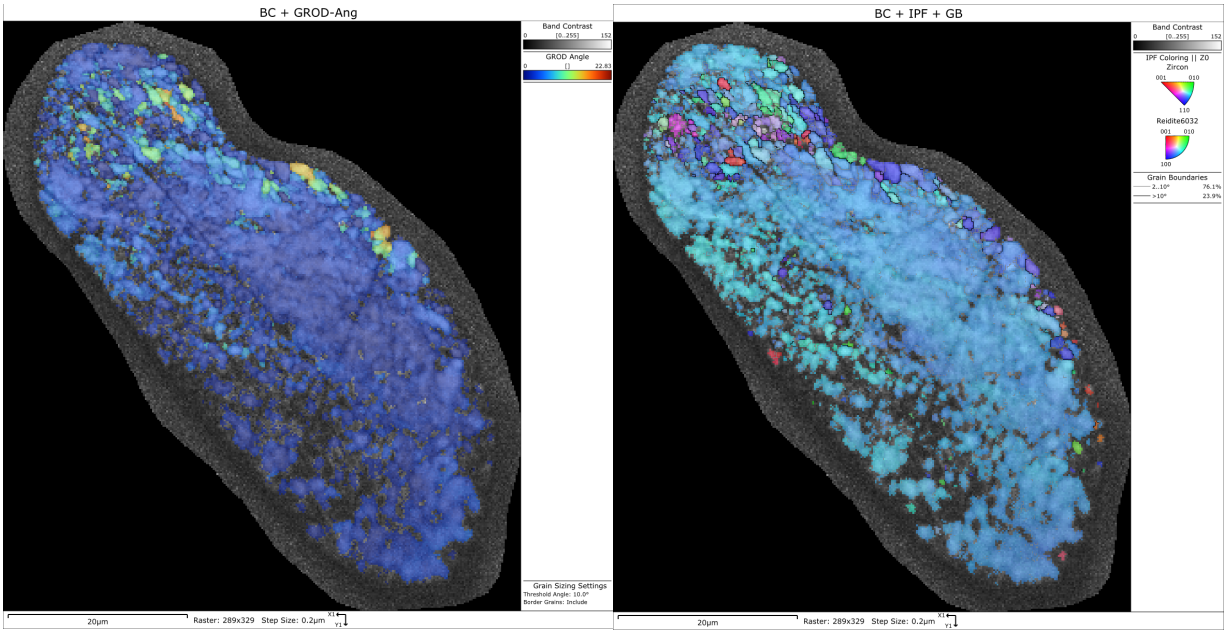
BC + GROD-Ang
Band Contrast
GROD Angle
Grain Sizing Settings
Threshold Angle: 10.0°
Border Grains: Include
20µm
Raster: 289x329 Step Size: 0.2µm
BC + IPF + GB
Band Contrast
IPF Coloring || Z0
Zircon
Reidite6032
Grain Boundaries
2..10° 76.1%
>10° 23.9%
20µm
Raster: 289x329 Step Size: 0.2µm

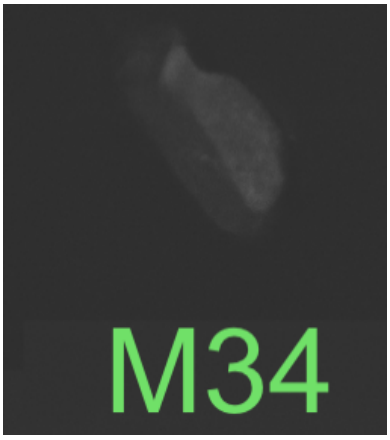
M34

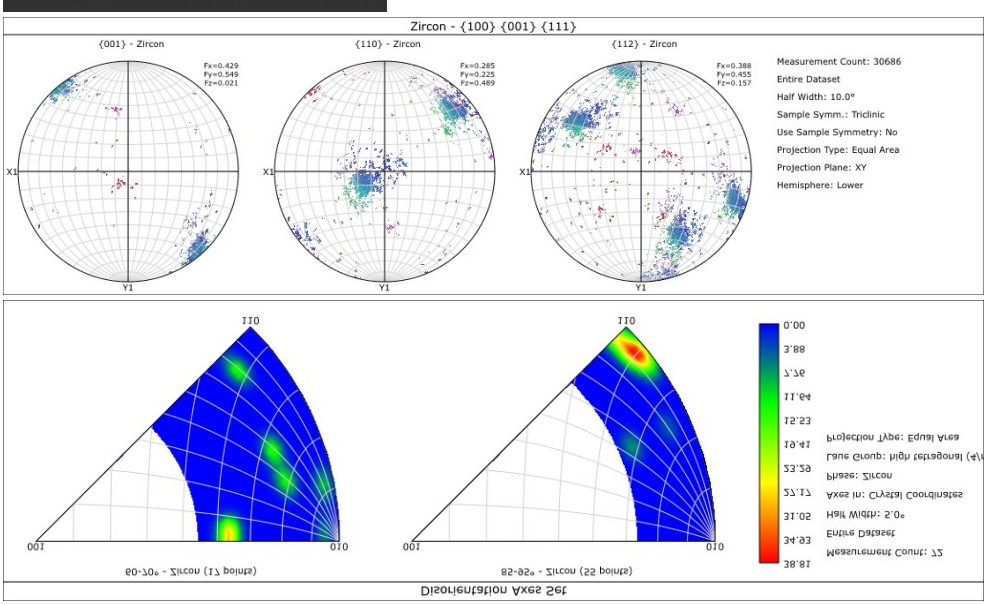
Zircon - {100} {001} {111}
{001} - Zircon
Fx=0.429
Fy=0.549
Fz=0.021
{110} - Zircon
Fx=0.285
Fy=0.225
Fz=0.489
{112} - Zircon
Fx=0.388
Fy=0.455
Fz=0.157
Measurement Count: 30686
Entire Dataset
Half Width: 10.0°
Sample Symm.: Triclinic
Use Sample Symmetry: No
Projection Type: Equal Area
Projection Plane: XY
Hemisphere: Lower
Disorientation Axes Set

M35

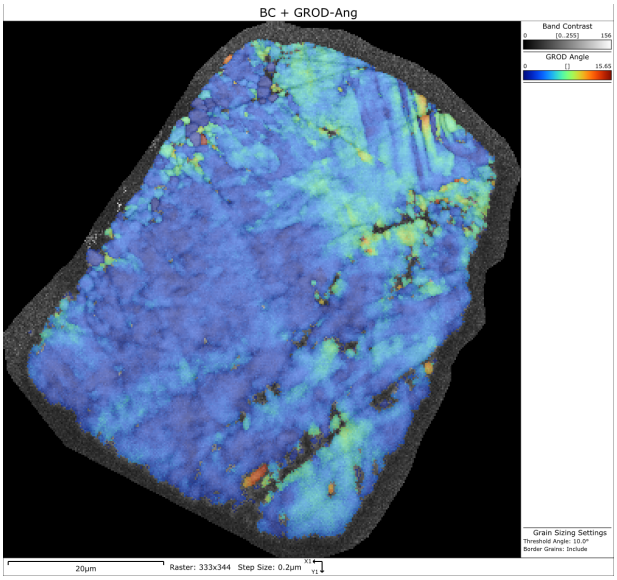
BC + GROD-Ang
Band Contrast
GROD Angle
Grain Sizing Settings
20µm
Raster: 333x344 Step Size: 0.2µm

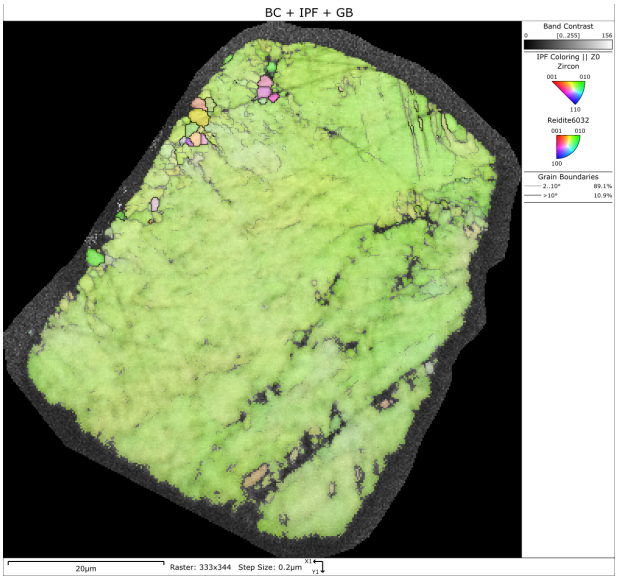
BC + IPF + GB
Band Contrast
IPF Coloring || Z0
Zircon
Reidite6032
Grain Boundaries
20µm
Raster: 333x344 Step Size: 0.2µm

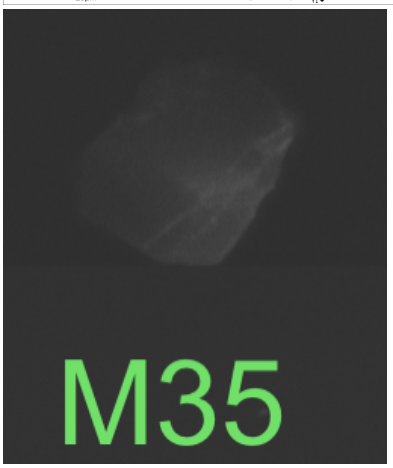
M35

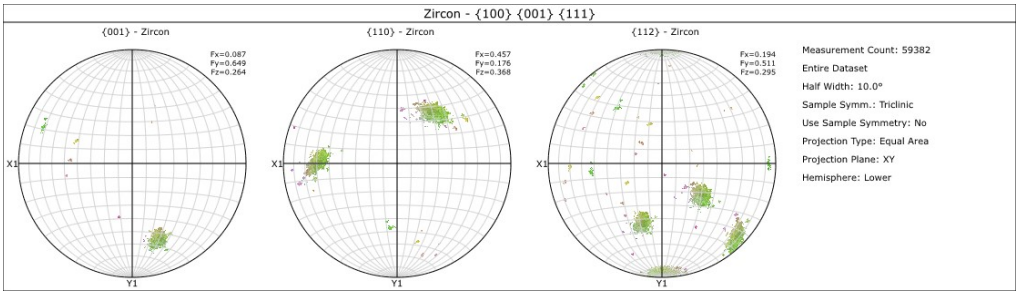
Zircon - {100} {001} {111}
{001} - Zircon
{110} - Zircon
{112} - Zircon
Measurement Count: 59382
Entire Dataset
Half Width: 10.0°
Sample Symm.: Triclinic
Use Sample Symmetry: No
Projection Type: Equal Area
Projection Plane: XY
Hemisphere: Lower

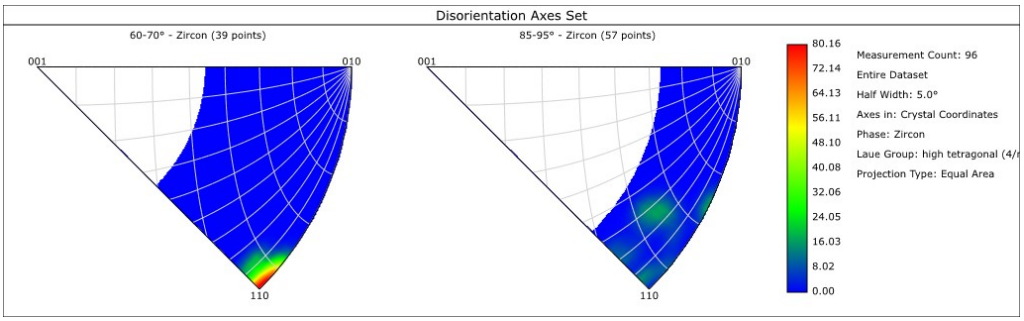
Disorientation Axes Set
60-70° - Zircon (39 points)
85-95° - Zircon (57 points)
001
010
110
80.16
72.14
64.13
56.11
48.10
40.08
32.06
24.05
16.03
8.02
0.00
Measurement Count: 96
Entire Dataset
Half Width: 5.0°
Axes in: Crystal Coordinates
Phase: Zircon
Projection Type: Equal Area

M39

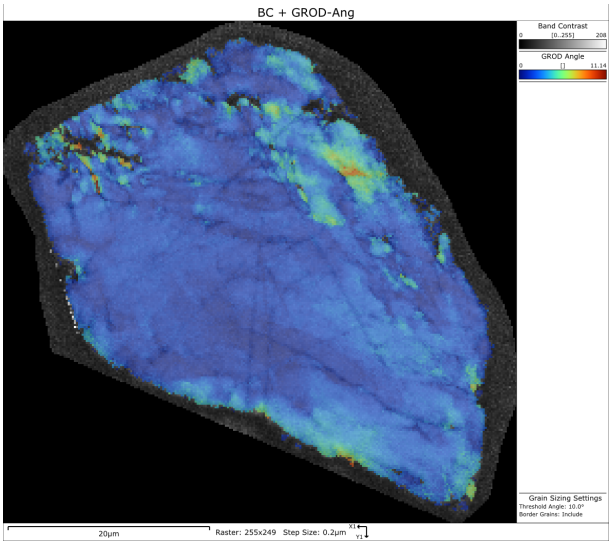
BC + GROD-Ang
Band Contrast
GROD Angle
Grain Sizing Settings
20µm
Raster: 255x249 Step Size: 0.2µm

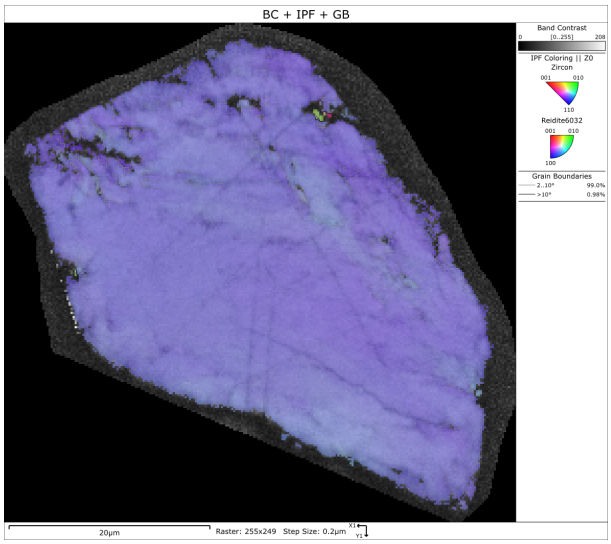
BC + IPF + GB
Band Contrast
IPF Coloring || Z0
Zircon
Reidite6032
Grain Boundaries
20µm
Raster: 255x249 Step Size: 0.2µm


M39

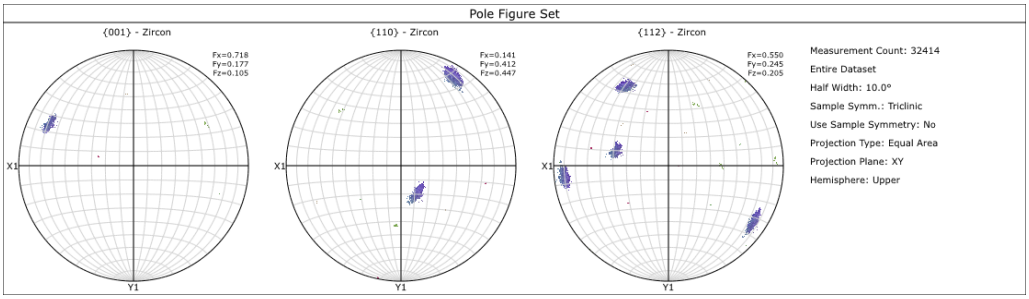
Pole Figure Set
{001} - Zircon
Fx=0.718
Fy=0.177
Fz=0.105
{110} - Zircon
Fx=0.141
Fy=0.412
Fz=0.447
{112} - Zircon
Fx=0.550
Fy=0.245
Fz=0.205
Measurement Count: 32414
Entire Dataset
Half Width: 10.0°
Sample Symm.: Triclinic
Use Sample Symmetry: No
Projection Type: Equal Area
Projection Plane: XY
Hemisphere: Upper

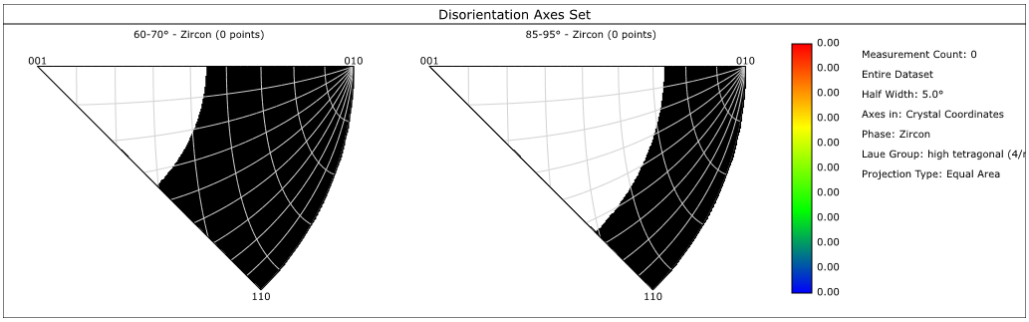
Disorientation Axes Set
60-70° - Zircon (0 points)
85-95° - Zircon (0 points)
001
010
110
Measurement Count: 0
Entire Dataset
Half Width: 5.0°
Axes in: Crystal Coordinates
Phase: Zircon
Projection Type: Equal Area

M41

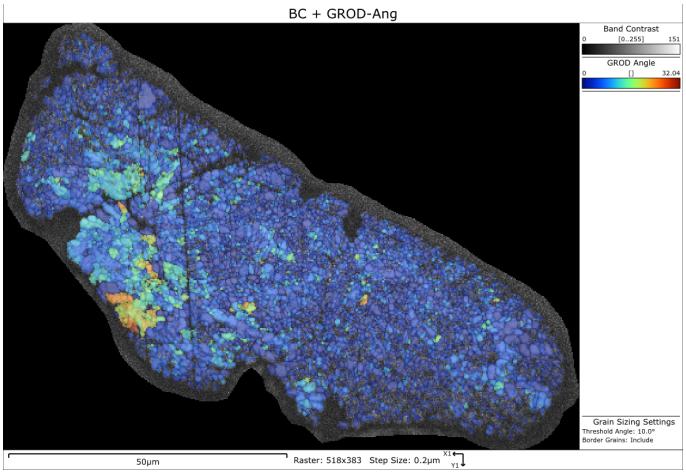
BC + GROD-Ang
Band Contrast
GROD Angle
Grain Sizing Settings
50µm
Raster: 518x383 Step Size: 0.2µm

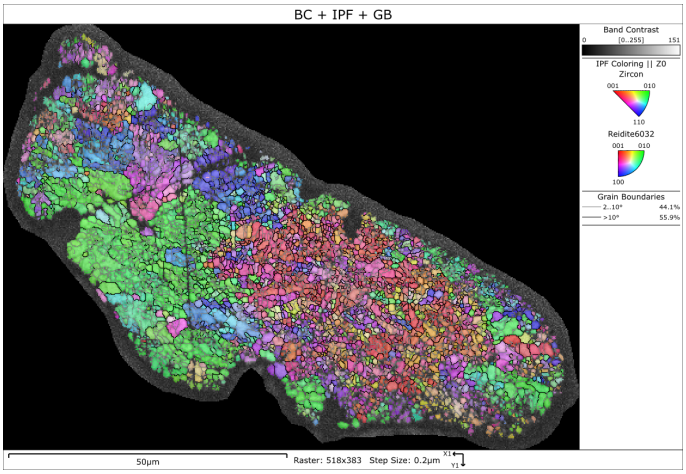
BC + IPF + GB
Band Contrast
IPF Coloring || Z0
Zircon
Reidite6032
Grain Boundaries
50µm
Raster: 518x383 Step Size: 0.2µm

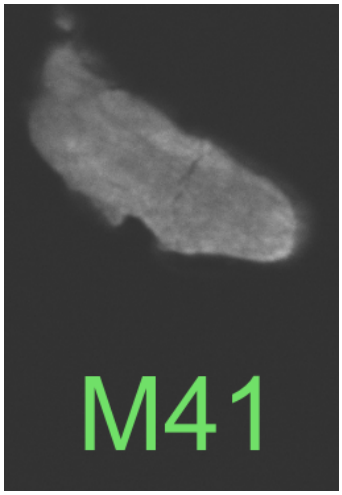
M41

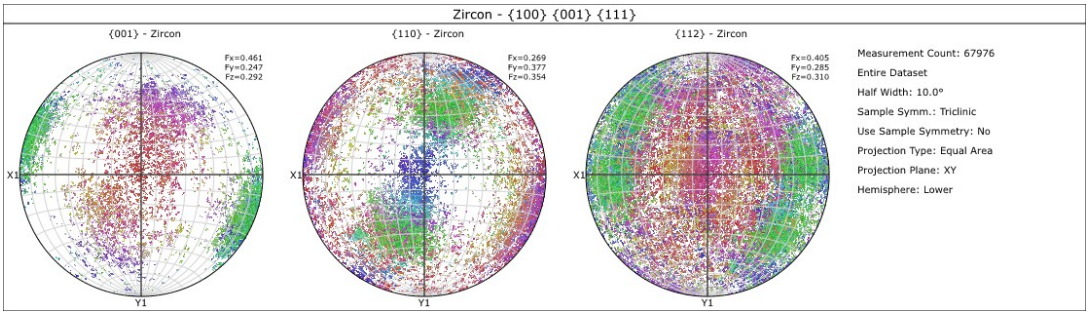
Zircon - {100} {001} {111}
{001} - Zircon
{110} - Zircon
{112} - Zircon
Measurement Count: 67976
Entire Dataset
Half Width: 10.0°
Sample Symm.: Triclinic
Use Sample Symmetry: No
Projection Type: Equal Area
Projection Plane: XY
Hemisphere: Lower

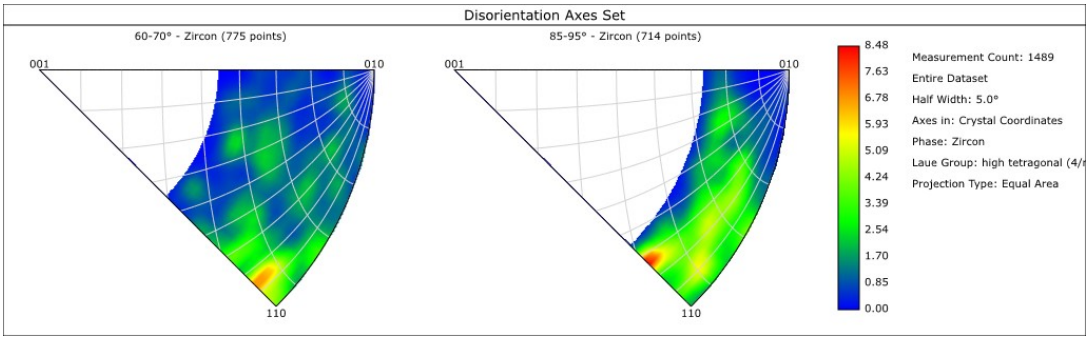
Disorientation Axes Set
60-70° - Zircon (775 points)
85-95° - Zircon (714 points)
Measurement Count: 1489
Entire Dataset
Half Width: 5.0°
Axes in: Crystal Coordinates
Phase: Zircon
Projection Type: Equal Area

M42

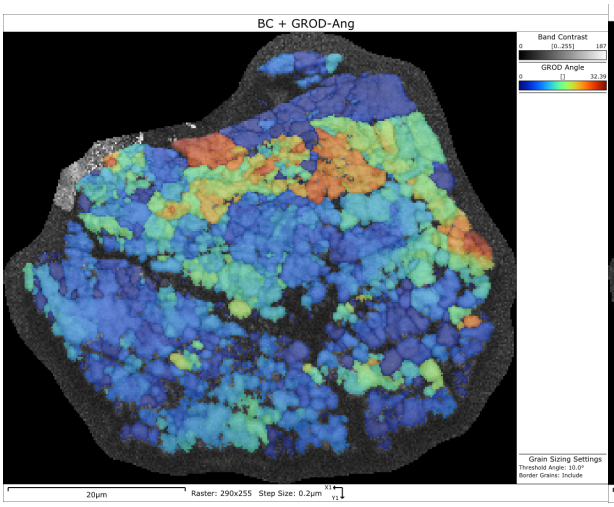
BC + GROD-Ang
Band Contrast
GROD Angle
Grain Sizing Settings
20µm
Raster: 290x255 Step Size: 0.2µm

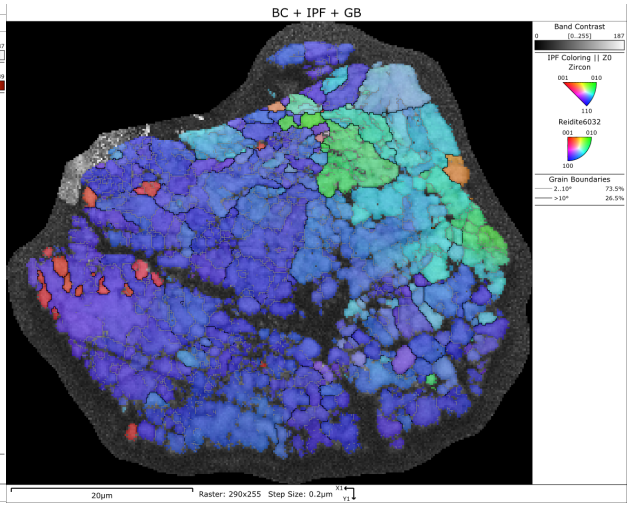
BC + IPF + GB
Band Contrast
IPF Coloring || Z0
Zircon
Reidite6032
Grain Boundaries
20µm
Raster: 290x255 Step Size: 0.2µm

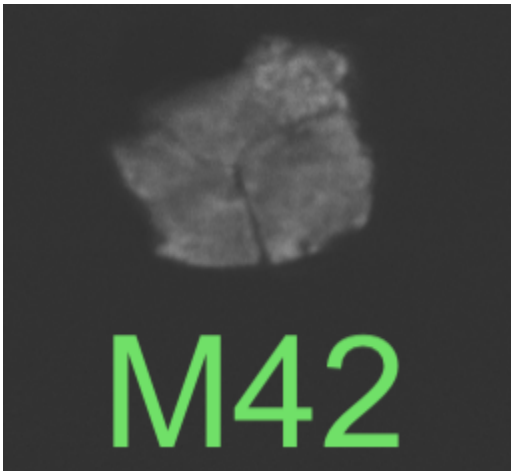
M42

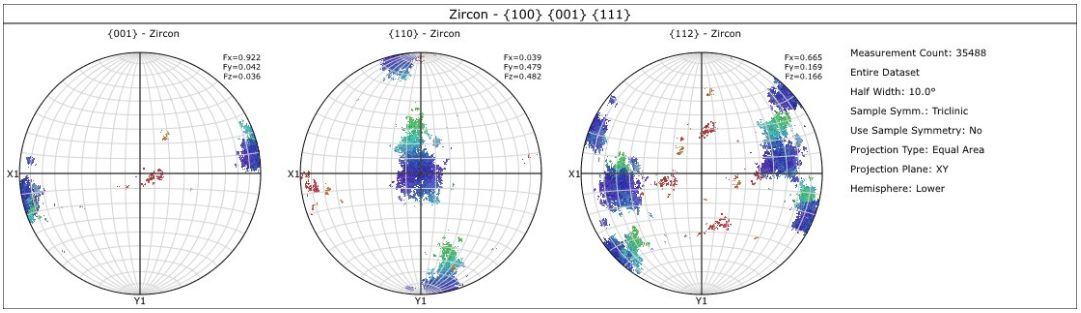
Zircon - {100} {001} {111}
{001} - Zircon
{110} - Zircon
{112} - Zircon
Fx=0.922
Fy=0.042
Fz=0.036
Fx=0.039
Fy=0.479
Fz=0.482
Fx=0.665
Fy=0.169
Fz=0.166
Measurement Count: 35488
Entire Dataset
Half Width: 10.0°
Sample Symm.: Triclinic
Use Sample Symmetry: No
Projection Type: Equal Area
Projection Plane: XY
Hemisphere: Lower

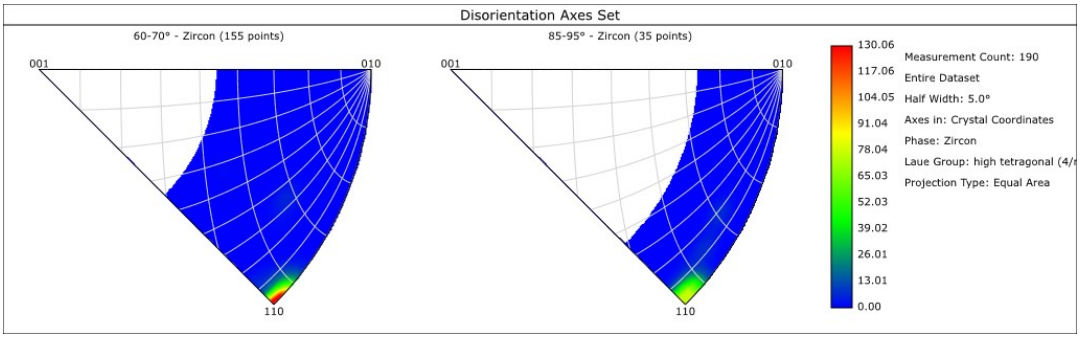
Disorientation Axes Set
60-70° - Zircon (155 points)
85-95° - Zircon (35 points)
001
010
110
130.06
117.06
104.05
91.04
78.04
65.03
52.03
39.02
26.01
13.01
0.00
Measurement Count: 190
Entire Dataset
Half Width: 5.0°
Axes in: Crystal Coordinates
Phase: Zircon
Projection Type: Equal Area

M45

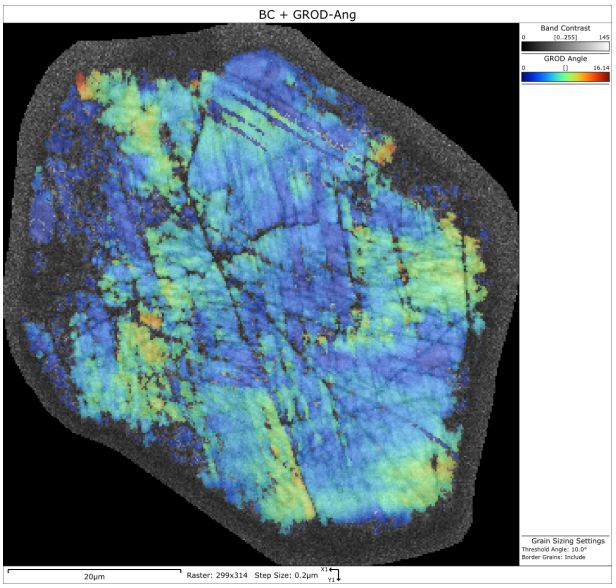
BC + GROD-Ang
Band Contrast
GROD Angle
Grain Sizing Settings
20µm
Raster: 299x314 Step Size: 0.2µm

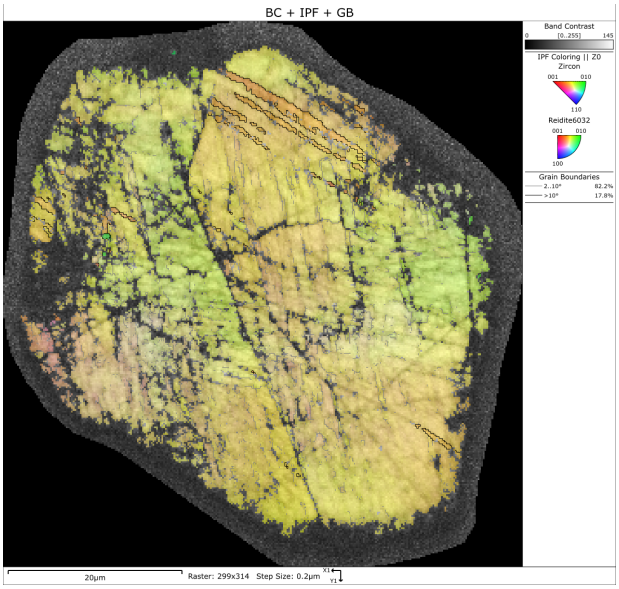
BC + IPF + GB
Band Contrast
IPF Coloring || Z0
Zircon
Reidite6032
Grain Boundaries
20µm
Raster: 299x314 Step Size: 0.2µm

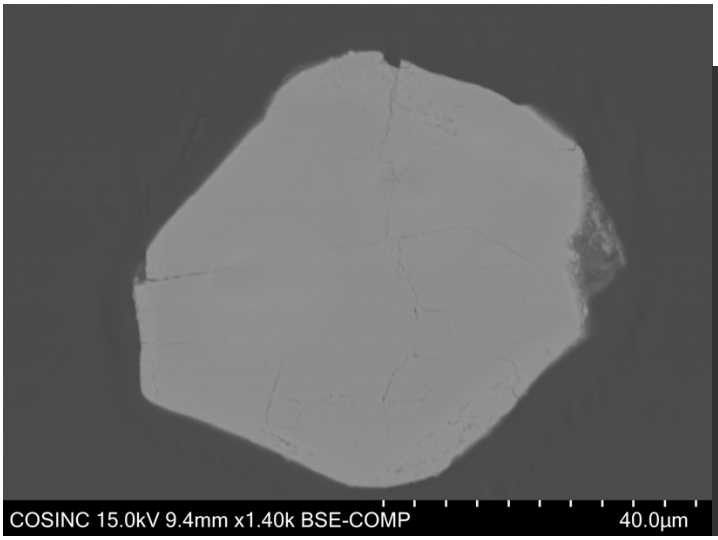
COSINC 15.0kV 9.4mm x1.40k BSE-COMP
40.0µm

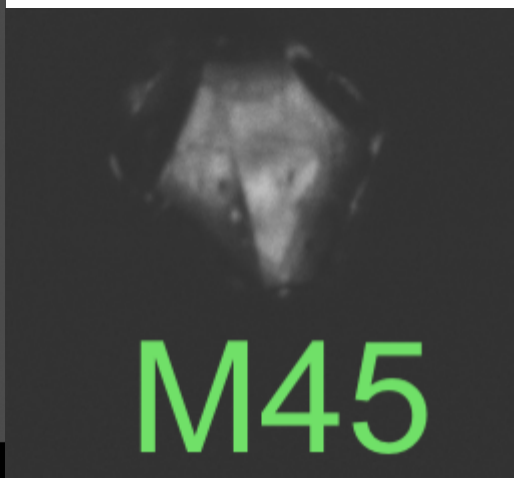
M45

M47

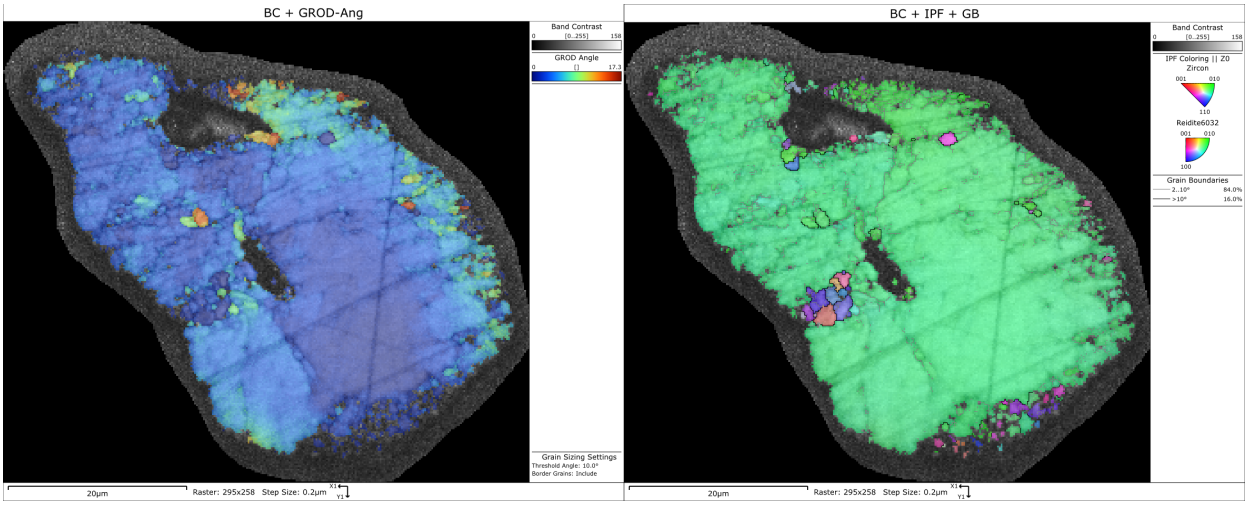
BC + GROD-Ang
Band Contrast
GROD Angle
Grain Sizing Settings
20µm
Raster: 295x258 Step Size: 0.2µm
BC + IPF + GB
Band Contrast
IPF Coloring || Z0
Zircon
Reidite6032
Grain Boundaries
20µm
Raster: 295x258 Step Size: 0.2µm

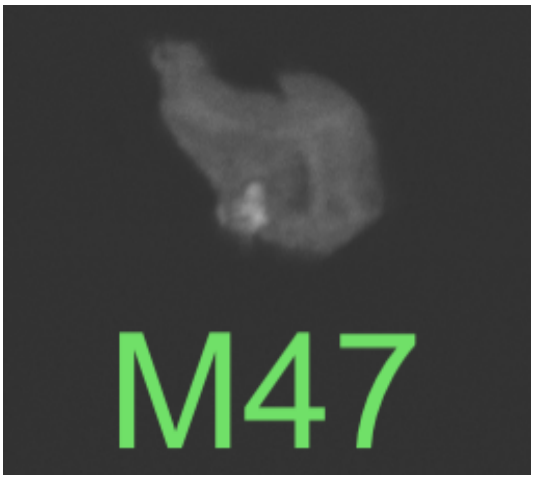
M47

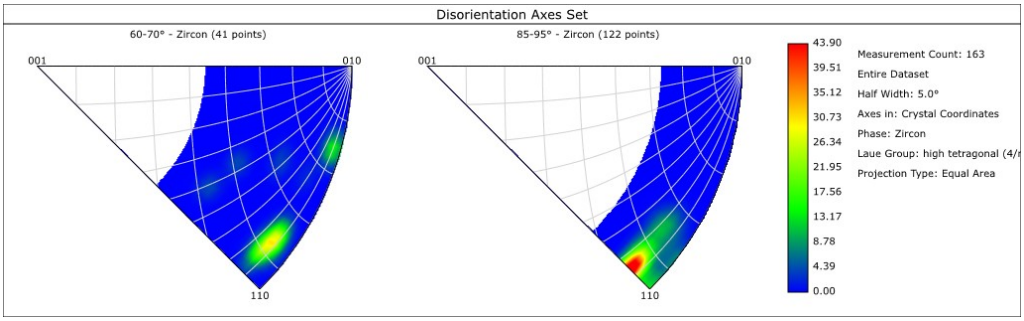
Disorientation Axes Set
60-70° - Zircon (41 points)
85-95° - Zircon (122 points)
001
010
110
43.90
39.51
35.12
30.73
26.34
21.95
17.56
13.17
8.78
4.39
0.00
Measurement Count: 163
Entire Dataset
Half Width: 5.0°
Axes in: Crystal Coordinates
Phase: Zircon
Projection Type: Equal Area

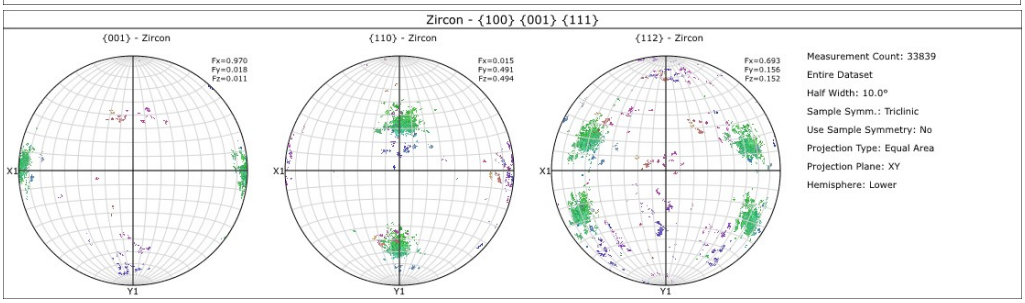
Zircon - {100} {001} {111}
{001} - Zircon
{110} - Zircon
{112} - Zircon
Measurement Count: 33839
Entire Dataset
Half Width: 10.0°
Sample Symm.: Triclinic
Use Sample Symmetry: No
Projection Type: Equal Area
Projection Plane: XY
Hemisphere: Lower

M54

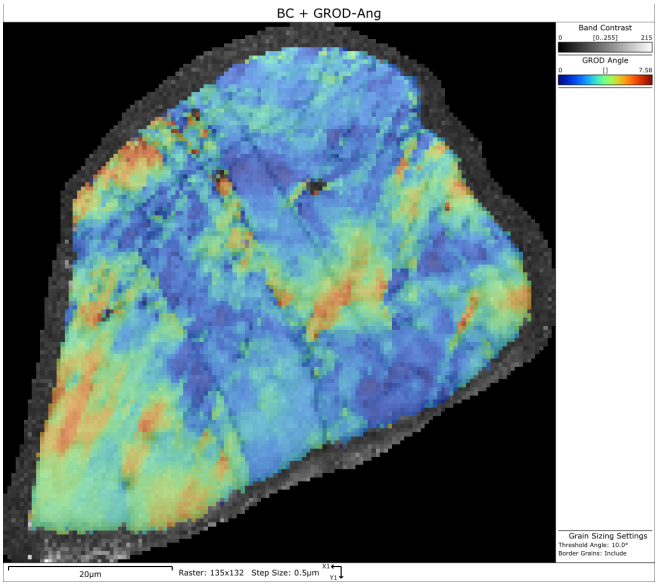
BC + GROD-Ang
Band Contrast
0 [0..255] 215
GROD Angle
0 [] 7.58
Grain Sizing Settings
Threshold Angle: 10.0°
Border Grains: Include
20µm
Raster: 135x132 Step Size: 0.5µm

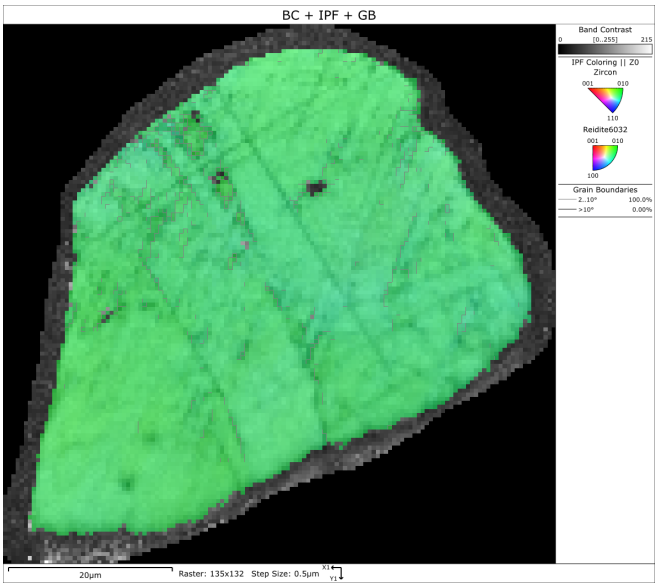
BC + IPF + GB
Band Contrast
0 [0..255] 215
IPF Coloring || Z0
Zircon
001 010
110
Reidite6032
001 010
100
Grain Boundaries
2..10° 100.0%
>10° 0.00%
20µm
Raster: 135x132 Step Size: 0.5µm

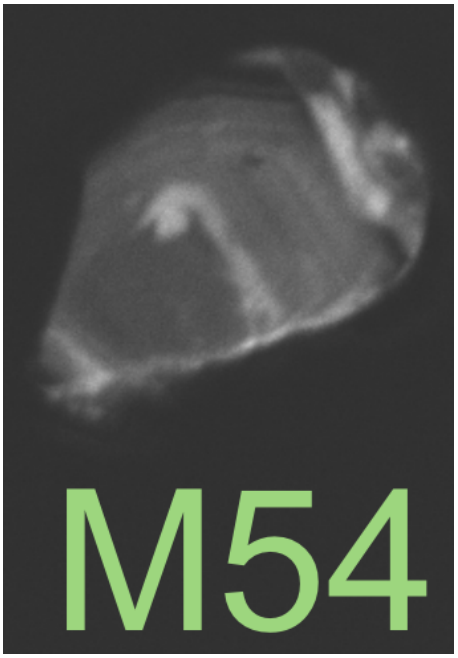
M54

M56

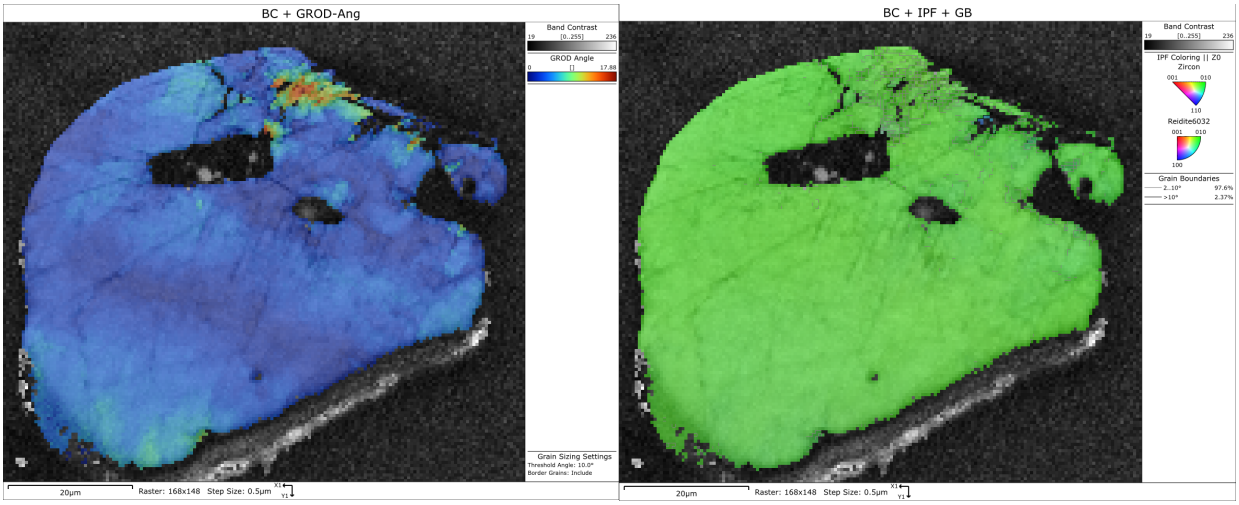
BC + GROD-Ang
Band Contrast
GROD Angle
Grain Sizing Settings
20µm
Raster: 168x148 Step Size: 0.5µm
BC + IPF + GB
Band Contrast
IPF Coloring || Z0
Zircon
Reidite6032
Grain Boundaries
20µm
Raster: 168x148 Step Size: 0.5µm

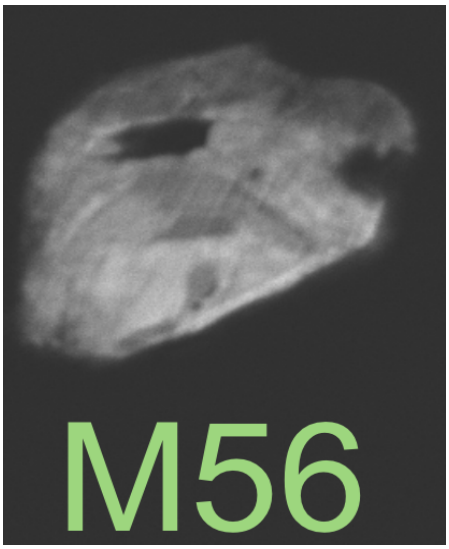
M56

M57

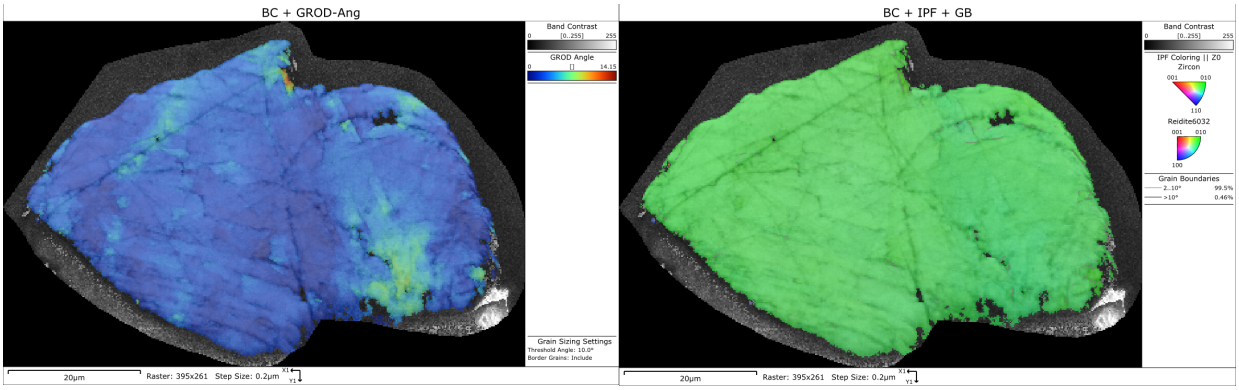
BC + GROD-Ang
Band Contrast
GROD Angle
Grain Sizing Settings
20µm
Raster: 395x261 Step Size: 0.2µm
BC + IPF + GB
Band Contrast
IPF Coloring || Z0
Zircon
Reidite6032
Grain Boundaries
20µm
Raster: 395x261 Step Size: 0.2µm

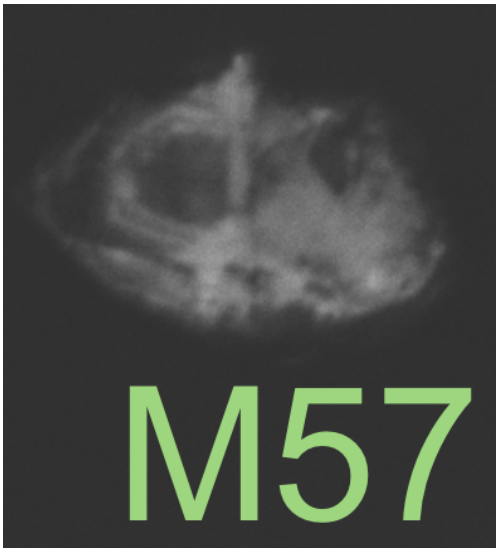
M57

M58

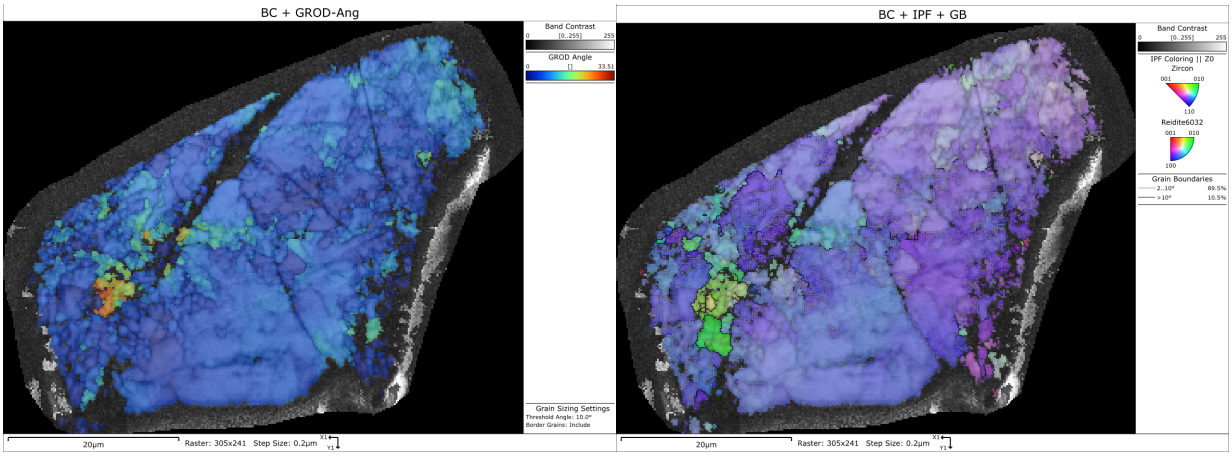
BC + GROD-Ang
Band Contrast
GROD Angle
Grain Sizing Settings
20µm
Raster: 305x241 Step Size: 0.2µm
BC + IPF + GB
Band Contrast
IPF Coloring || Z0
Zircon
Reidite6032
Grain Boundaries
20µm
Raster: 305x241 Step Size: 0.2µm

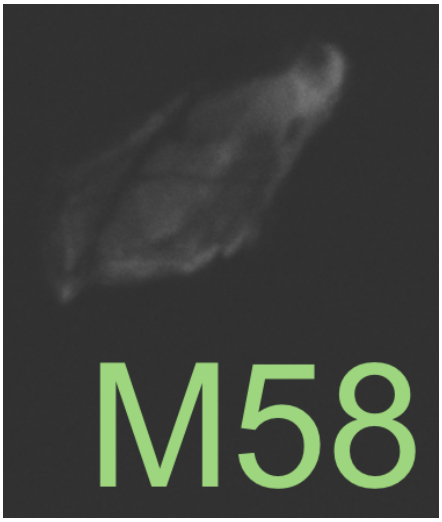
M58

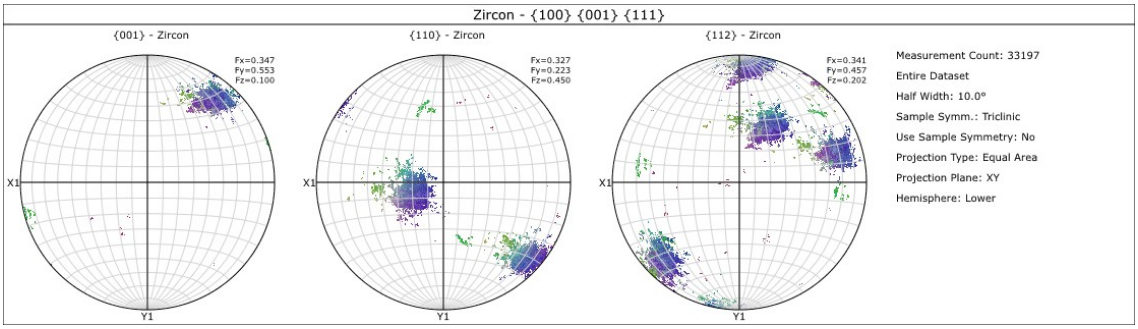
Zircon - {100} {001} {111}
{001} - Zircon
Fx=0.347
Fy=0.553
Fz=0.100
{110} - Zircon
Fx=0.327
Fy=0.223
Fz=0.450
{112} - Zircon
Fx=0.341
Fy=0.457
Fz=0.202
X1
Y1
Measurement Count: 33197
Entire Dataset
Half Width: 10.0°
Sample Symm.: Triclinic
Use Sample Symmetry: No
Projection Type: Equal Area
Projection Plane: XY
Hemisphere: Lower

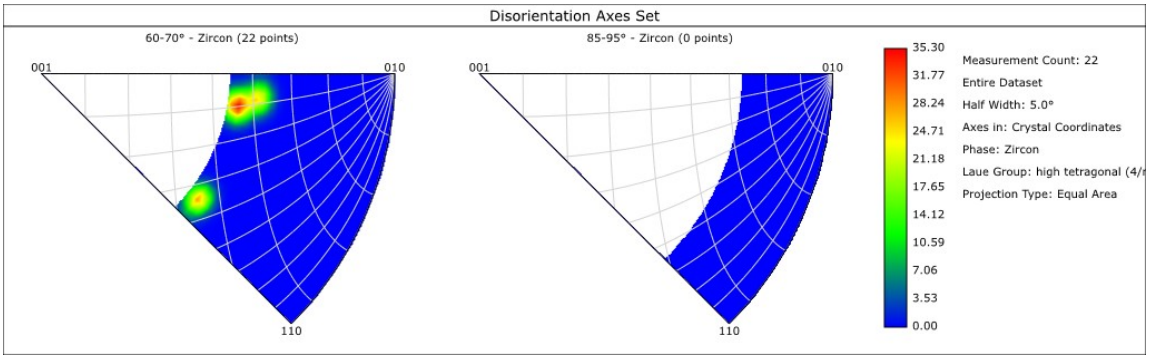
Disorientation Axes Set
60-70° - Zircon (22 points)
85-95° - Zircon (0 points)
001
010
110
35.30
31.77
28.24
24.71
21.18
17.65
14.12
10.59
7.06
3.53
0.00
Measurement Count: 22
Entire Dataset
Half Width: 5.0°
Axes in: Crystal Coordinates
Phase: Zircon
Laue Group: high tetragonal (4/
Projection Type: Equal Area

M59

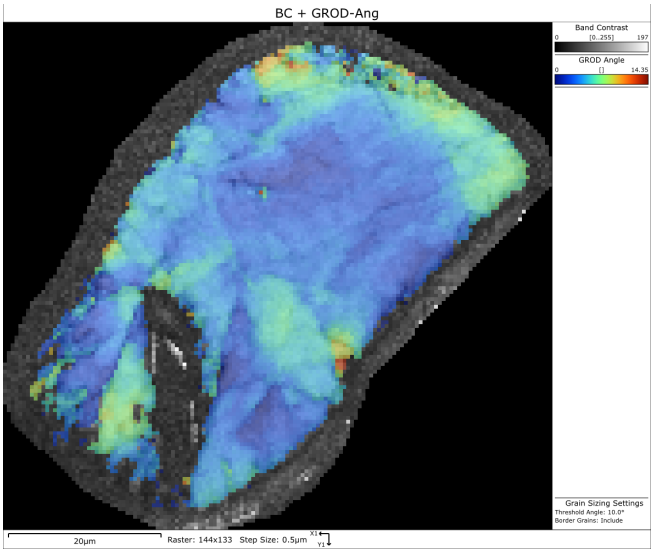
BC + GROD-Ang
Band Contrast
0 [0..255] 197
GROD Angle
0 [] 14.35
Grain Sizing Settings
Threshold Angle: 10.0°
Border Grains: Include
20µm
Raster: 144x133 Step Size: 0.5µm
X1
Y1

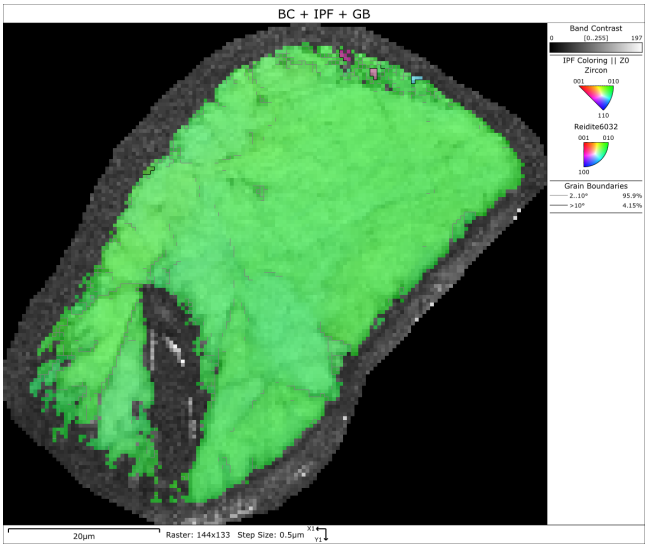
BC + IPF + GB
Band Contrast
0 [0..255] 197
IPF Coloring || Z0
Zircon
001 010
110
Reidite6032
001 010
100
Grain Boundaries
2..10° 95.9%
>10° 4.15%
20µm
Raster: 144x133 Step Size: 0.5µm
X1
Y1

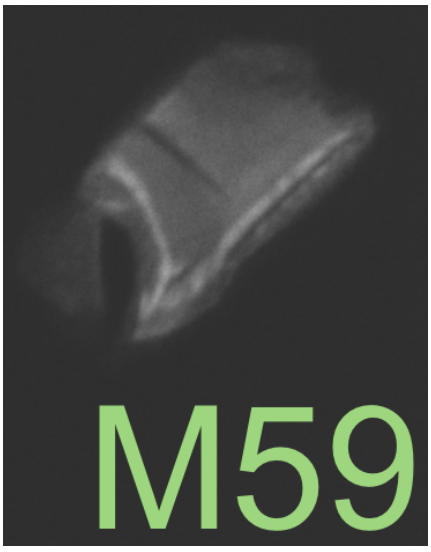
M59

M60

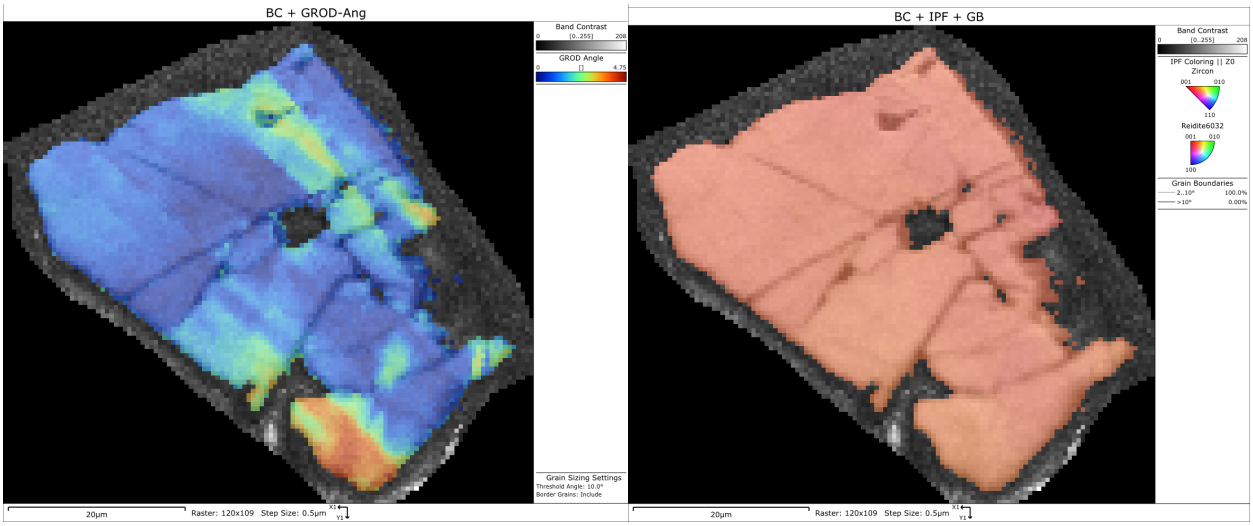
BC + GROD-Ang
Band Contrast
GROD Angle
Grain Sizing Settings
20µm
Raster: 120x109 Step Size: 0.5µm
BC + IPF + GB
Band Contrast
IPF Coloring || Z0
Zircon
Reidite6032
Grain Boundaries
20µm
Raster: 120x109 Step Size: 0.5µm

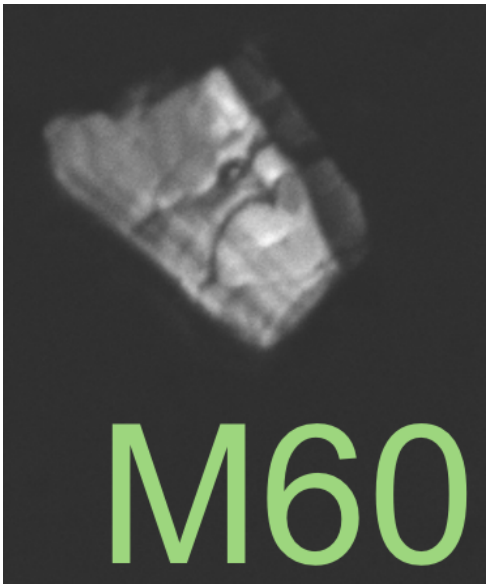
M60

M62

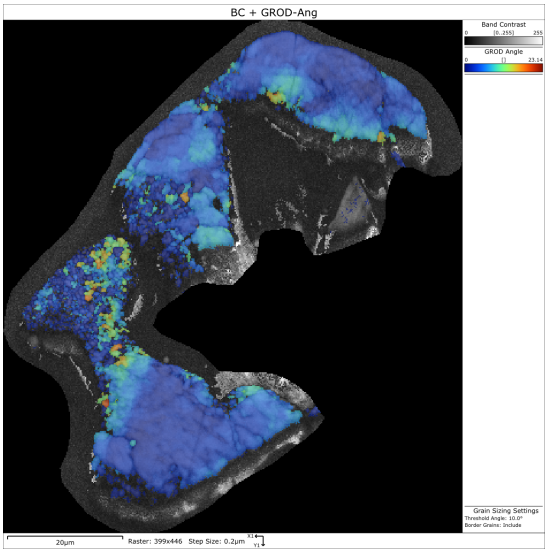
BC + GROD-Ang
Band Contrast
GROD Angle
Grain Sizing Settings
20μm
Raster: 399x446 Step Size: 0.2μm

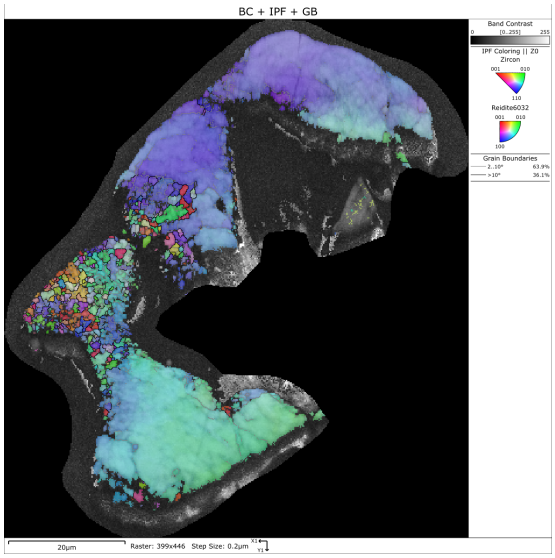
BC + IPF + GB
Band Contrast
IPF Coloring || Z0
Zircon
Reidite6032
Grain Boundaries
20μm
Raster: 399x446 Step Size: 0.2μm

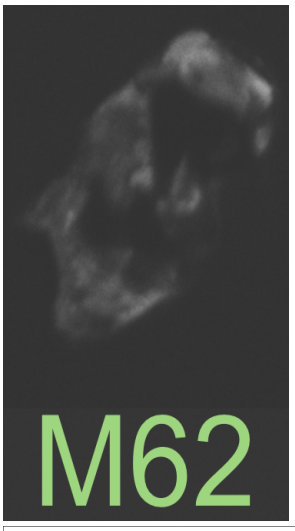
M62

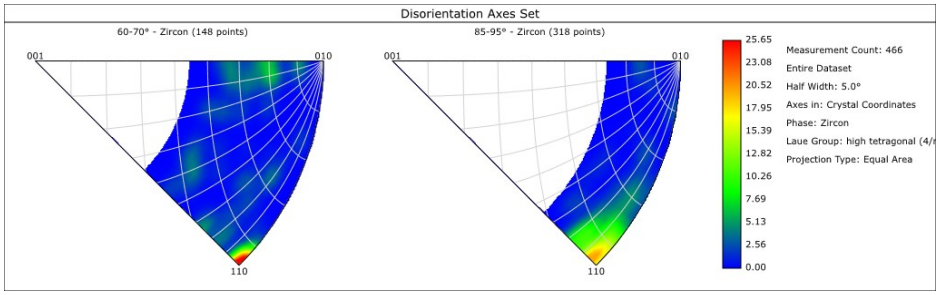
Disorientation Axes Set
60-70° - Zircon (148 points)
85-95° - Zircon (318 points)
001
010
110
25.65
23.08
20.52
17.95
15.39
12.82
10.26
7.69
5.13
2.56
0.00
Measurement Count: 466
Entire Dataset
Half Width: 5.0°
Axes in: Crystal Coordinates
Phase: Zircon
Projection Type: Equal Area

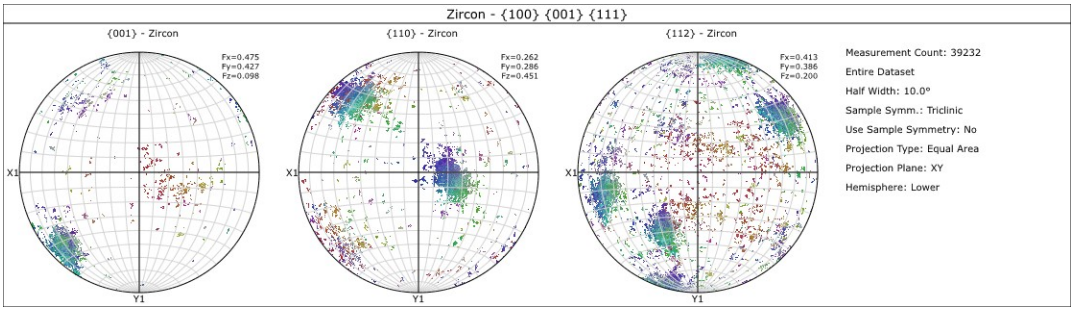
Zircon - {100} {001} {111}
{001} - Zircon
{110} - Zircon
{112} - Zircon
Fx=0.475
Fy=0.427
Fz=0.098
Fx=0.262
Fy=0.286
Fz=0.451
Fx=0.413
Fy=0.386
Fz=0.200
X1
Y1
Measurement Count: 39232
Entire Dataset
Half Width: 10.0°
Sample Symm.: Triclinic
Use Sample Symmetry: No
Projection Type: Equal Area
Projection Plane: XY
Hemisphere: Lower

M67

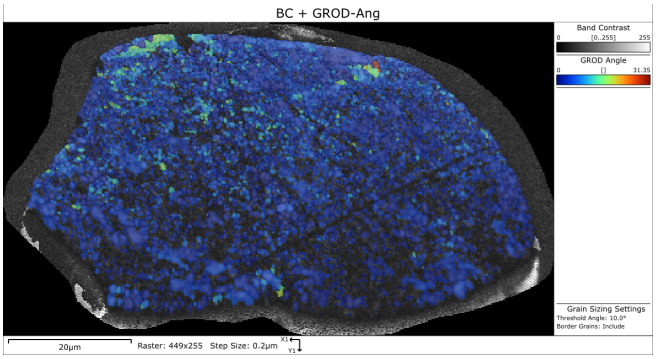
BC + GROD-Ang
Band Contrast
GROD Angle
Grain Sizing Settings
20µm
Raster: 449x255 Step Size: 0.2µm

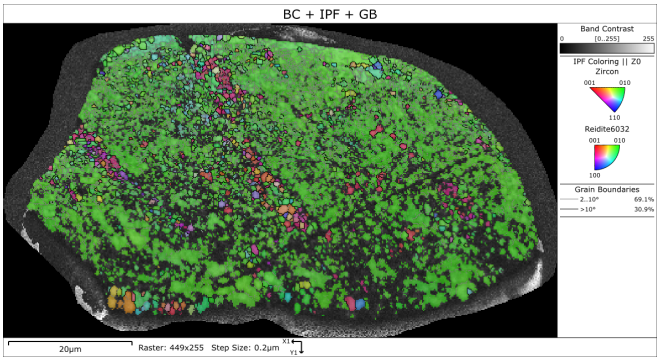
BC + IPF + GB
Band Contrast
IPF Coloring || Z0
Zircon
Reidite6032
Grain Boundaries
20µm
Raster: 449x255 Step Size: 0.2µm

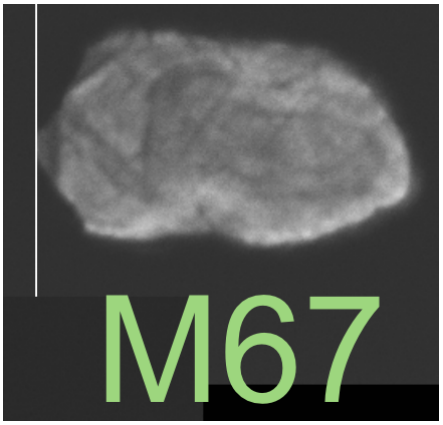
M67

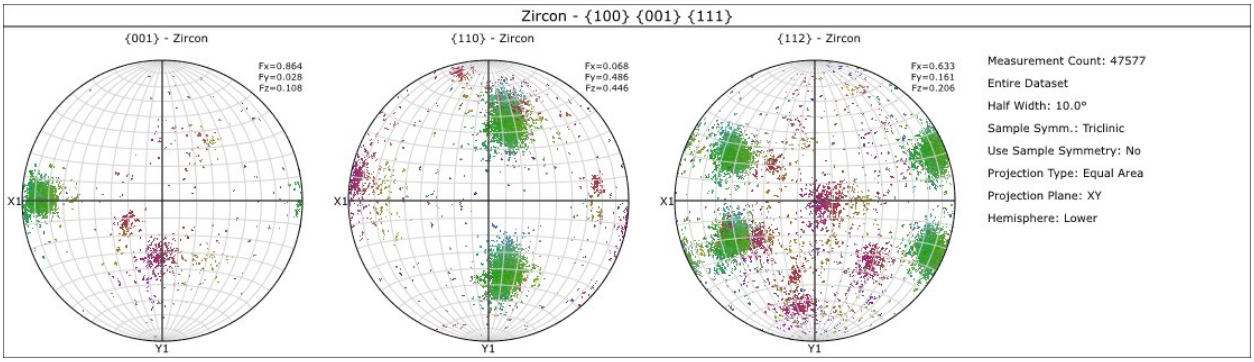
Zircon - {100} {001} {111}
{001} - Zircon
Fx=0.864
Fy=0.028
Fz=0.108
{110} - Zircon
Fx=0.068
Fy=0.486
Fz=0.446
{112} - Zircon
Fx=0.633
Fy=0.161
Fz=0.206
Measurement Count: 47577
Entire Dataset
Half Width: 10.0°
Sample Symm.: Triclinic
Use Sample Symmetry: No
Projection Type: Equal Area
Projection Plane: XY
Hemisphere: Lower

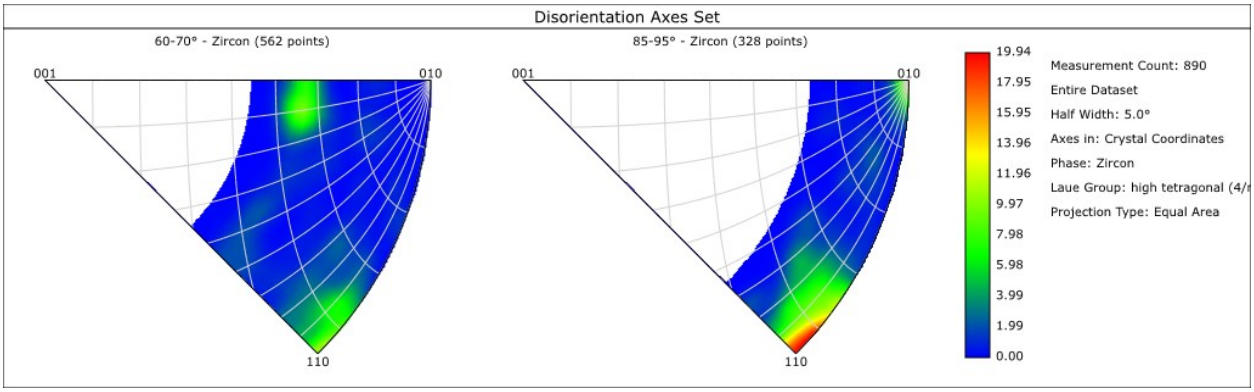
Disorientation Axes Set
60-70° - Zircon (562 points)
85-95° - Zircon (328 points)
001
010
110
19.94
17.95
15.95
13.96
11.96
9.97
7.98
5.98
3.99
1.99
0.00
Measurement Count: 890
Entire Dataset
Half Width: 5.0°
Axes in: Crystal Coordinates
Phase: Zircon
Projection Type: Equal Area

M68

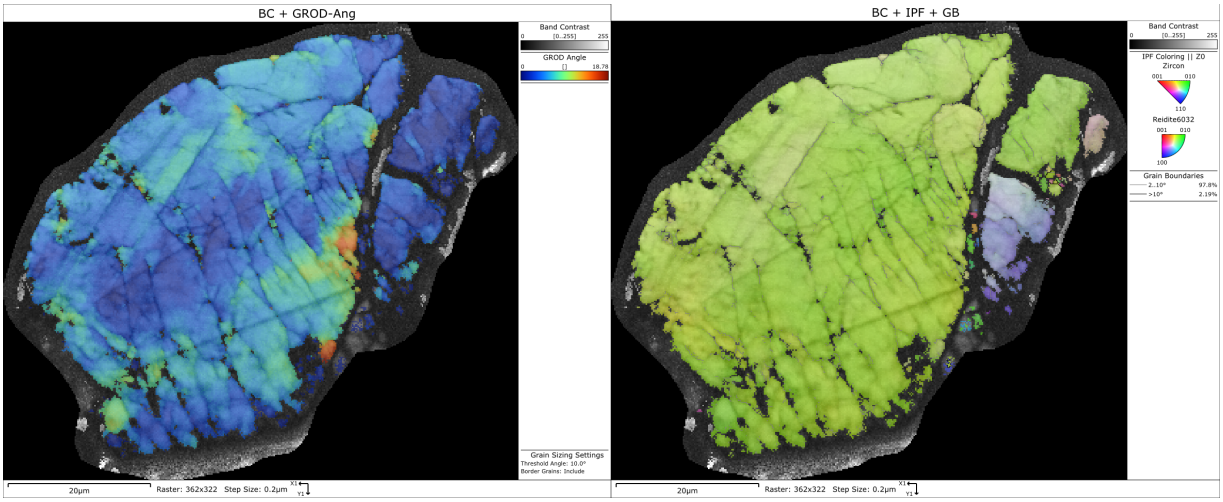
BC + GROD-Ang
Band Contrast
GROD Angle
Grain Sizing Settings
20µm
Raster: 362x322 Step Size: 0.2µm
BC + IPF + GB
Band Contrast
IPF Coloring || Z0
Zircon
Reidite6032
Grain Boundaries
20µm
Raster: 362x322 Step Size: 0.2µm

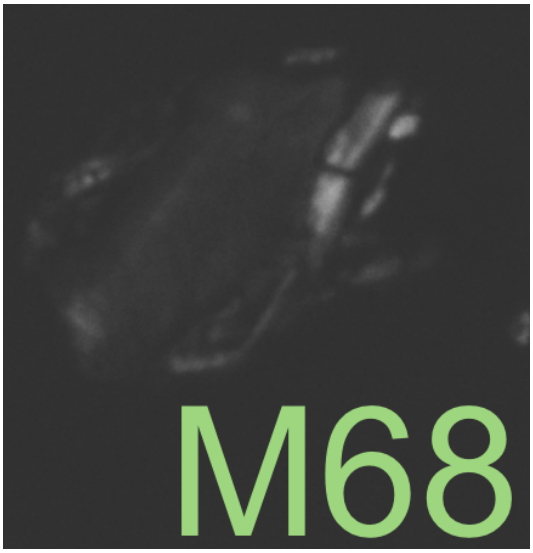
M68

M70

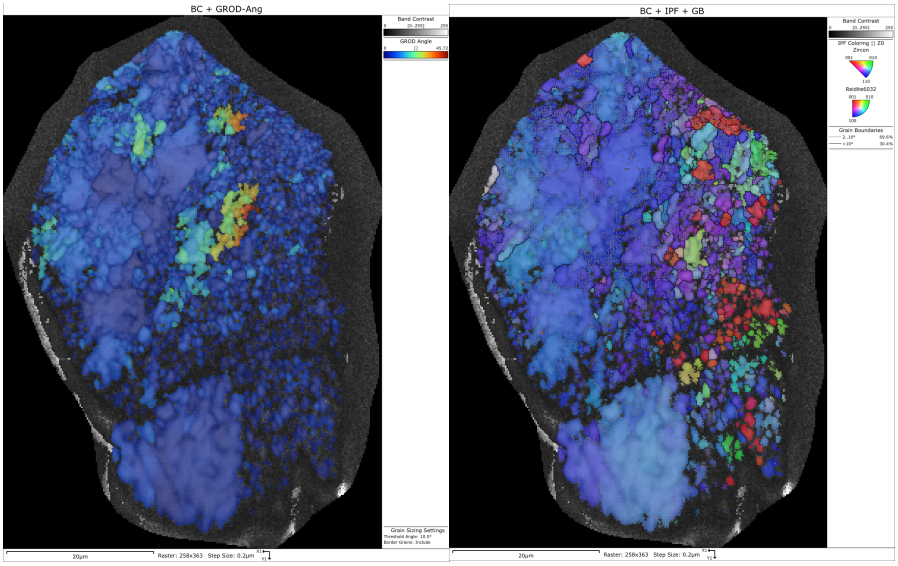
BC + GROD-Ang
BC + IPF + GB

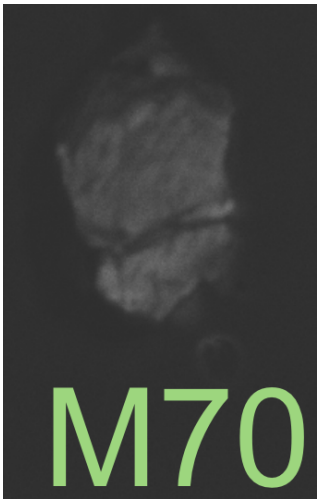
M70

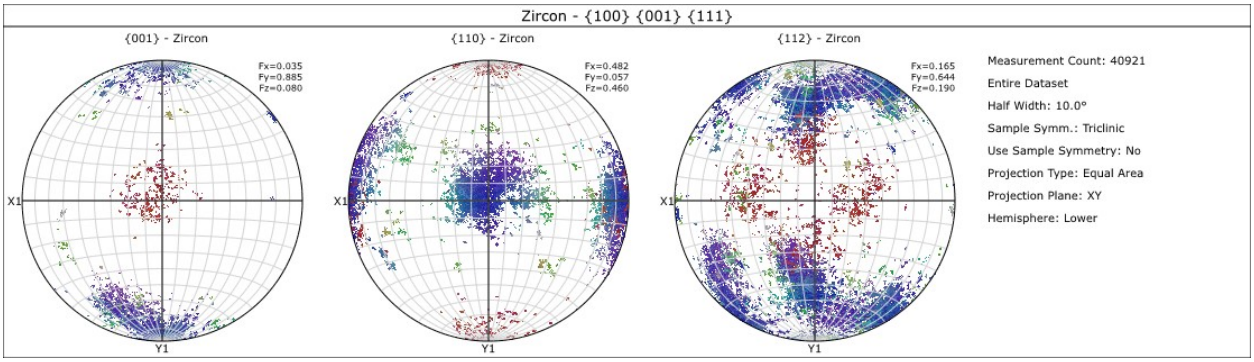
Zircon - {100} {001} {111}
{001} - Zircon
Fx=0.035
Fy=0.885
Fz=0.080
{110} - Zircon
Fx=0.482
Fy=0.057
Fz=0.460
{112} - Zircon
Fx=0.165
Fy=0.644
Fz=0.190
X1
Y1
Measurement Count: 40921
Entire Dataset
Half Width: 10.0°
Sample Symm.: Triclinic
Use Sample Symmetry: No
Projection Type: Equal Area
Projection Plane: XY
Hemisphere: Lower

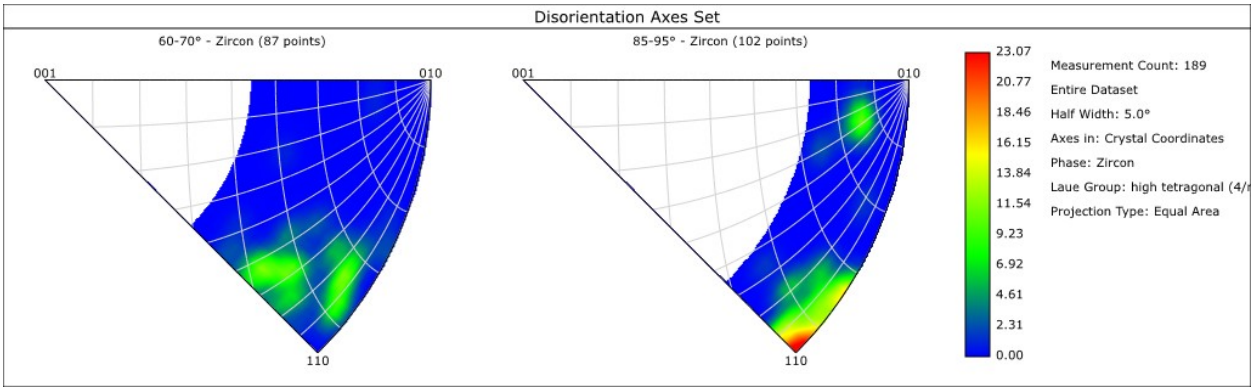
Disorientation Axes Set
60-70° - Zircon (87 points)
85-95° - Zircon (102 points)
001
010
110
23.07
20.77
18.46
16.15
13.84
11.54
9.23
6.92
4.61
2.31
0.00
Measurement Count: 189
Entire Dataset
Half Width: 5.0°
Axes in: Crystal Coordinates
Phase: Zircon
Projection Type: Equal Area

M76

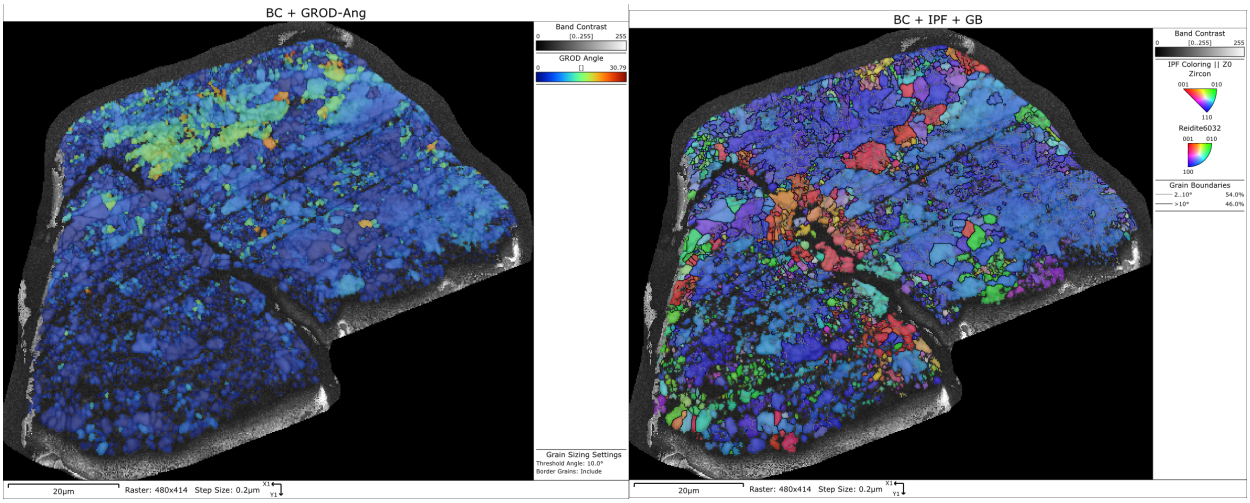
BC + GROD-Ang
Band Contrast
GROD Angle
Grain Sizing Settings
20µm
Raster: 480x414 Step Size: 0.2µm
BC + IPF + GB
Band Contrast
IPF Coloring || Z0
Zircon
Reidite6032
Grain Boundaries
20µm
Raster: 480x414 Step Size: 0.2µm

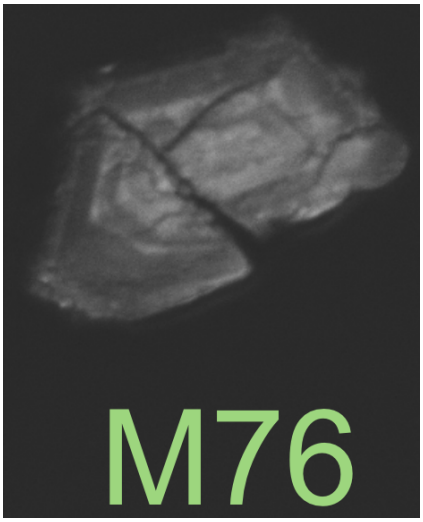
M76

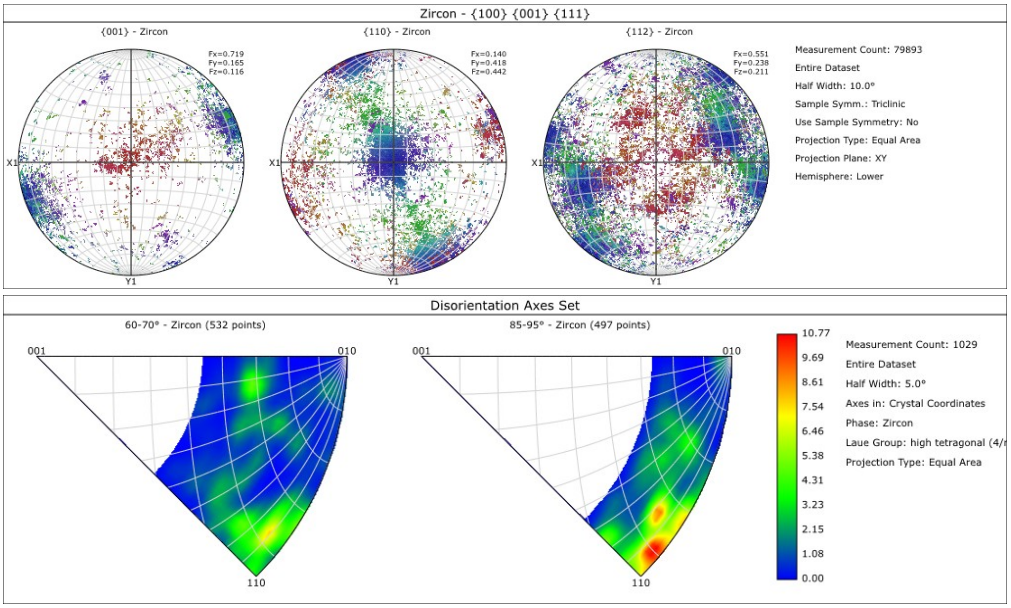
Zircon - {100} {001} {111}
{001} - Zircon
Fx=0.719
Fy=0.165
Fz=0.116
{110} - Zircon
Fx=0.140
Fy=0.418
Fz=0.442
{112} - Zircon
Fx=0.551
Fy=0.238
Fz=0.211
Measurement Count: 79893
Entire Dataset
Half Width: 10.0°
Sample Symm.: Triclinic
Use Sample Symmetry: No
Projection Type: Equal Area
Projection Plane: XY
Hemisphere: Lower
Disorientation Axes Set
60-70° - Zircon (532 points)
85-95° - Zircon (497 points)
001
010
110
10.77
9.69
8.61
7.54
6.46
5.38
4.31
3.23
2.15
1.08
0.00
Measurement Count: 1029
Entire Dataset
Half Width: 5.0°
Axes in: Crystal Coordinates
Phase: Zircon
Projection Type: Equal Area

M77

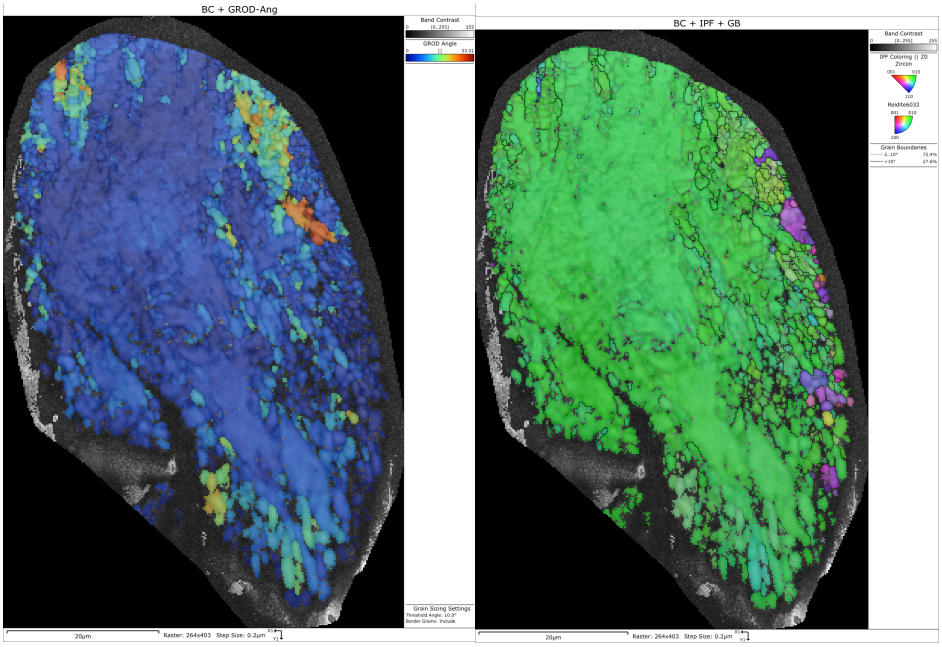
BC + GROD-Ang
BC + IPF + GB

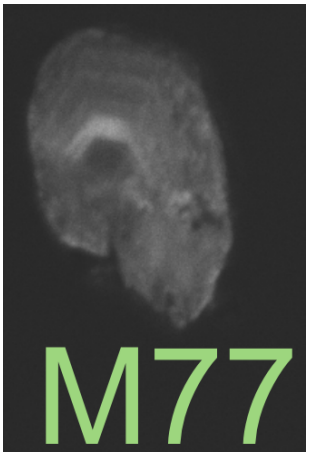
M77

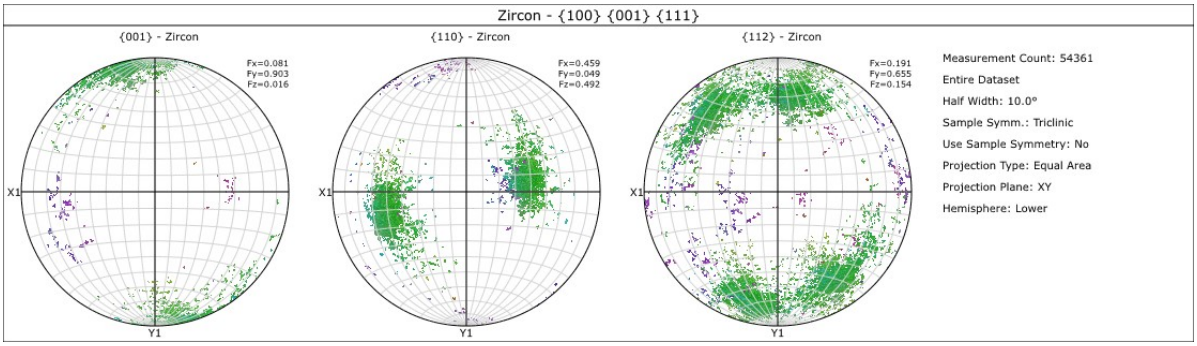
Zircon - {100} {001} {111}
{001} - Zircon
Fx=0.081
Fy=0.903
Fz=0.016
{110} - Zircon
Fx=0.459
Fy=0.049
Fz=0.492
{112} - Zircon
Fx=0.191
Fy=0.655
Fz=0.154
Measurement Count: 54361
Entire Dataset
Half Width: 10.0°
Sample Symm.: Triclinic
Use Sample Symmetry: No
Projection Type: Equal Area
Projection Plane: XY
Hemisphere: Lower

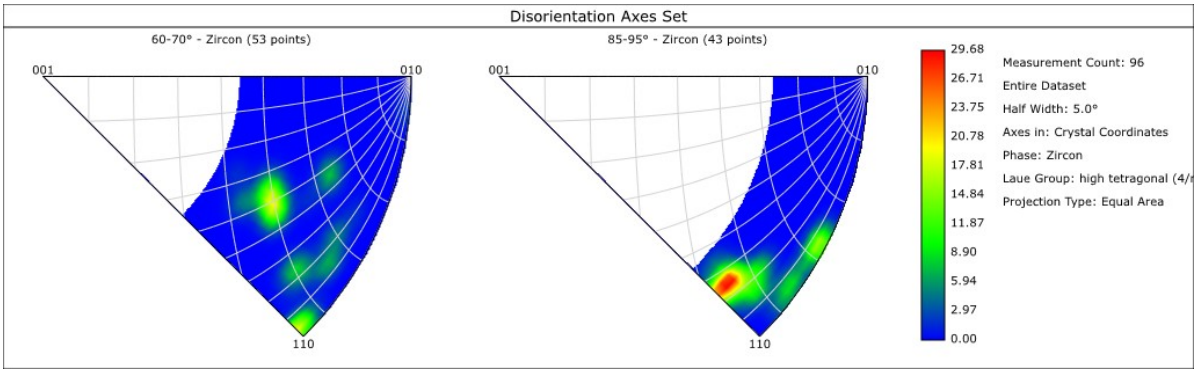
Disorientation Axes Set
60-70° - Zircon (53 points)
85-95° - Zircon (43 points)
001
010
110
29.68
26.71
23.75
20.78
17.81
14.84
11.87
8.90
5.94
2.97
0.00
Measurement Count: 96
Entire Dataset
Half Width: 5.0°
Axes in: Crystal Coordinates
Phase: Zircon
Projection Type: Equal Area

M79

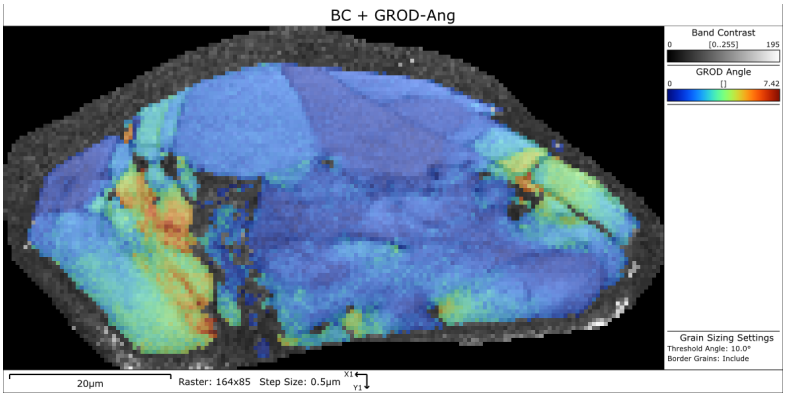
BC + GROD-Ang
Band Contrast
0 [0..255] 195
GROD Angle
0 [] 7.42
Grain Sizing Settings
Threshold Angle: 10.0°
Border Grains: Include
20µm
Raster: 164x85 Step Size: 0.5µm
X1
Y1

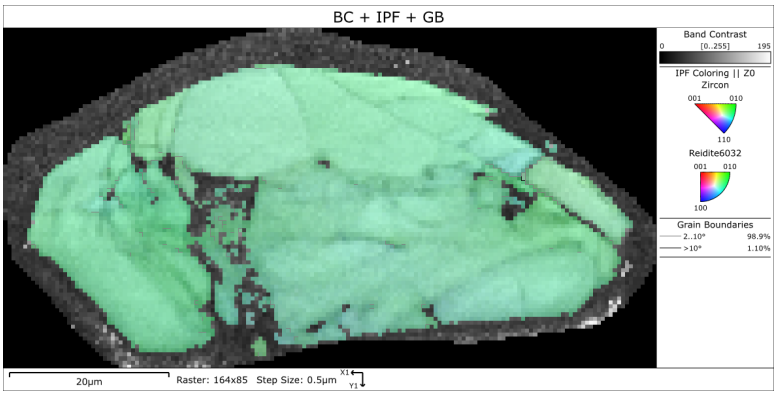
BC + IPF + GB
Band Contrast
0 [0..255] 195
IPF Coloring || Z0
Zircon
001 010
110
Reidite6032
001 010
100
Grain Boundaries
2..10° 98.9%
>10° 1.10%
20µm
Raster: 164x85 Step Size: 0.5µm
X1
Y1


M79

M81

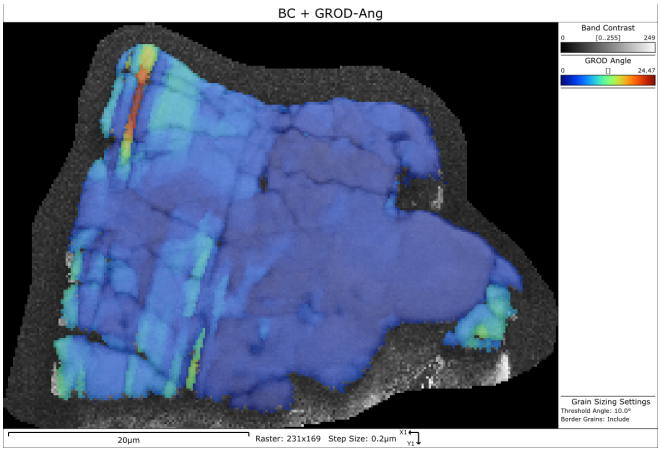
BC + GROD-Ang
Band Contrast
0 [0..255] 249
GROD Angle
0 24.47
Grain Sizing Settings
Threshold Angle: 10.0°
Border Grains: Include
20µm
Raster: 231x169 Step Size: 0.2µm

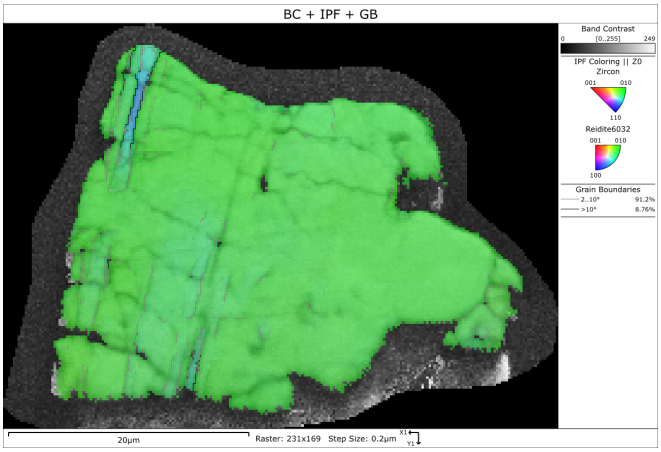
BC + IPF + GB
Band Contrast
0 [0..255] 249
IPF Coloring || Z0
Zircon
001 010
110
Reidite6032
001 010
100
Grain Boundaries
2..10° 91.2%
>10° 8.76%
20µm
Raster: 231x169 Step Size: 0.2µm

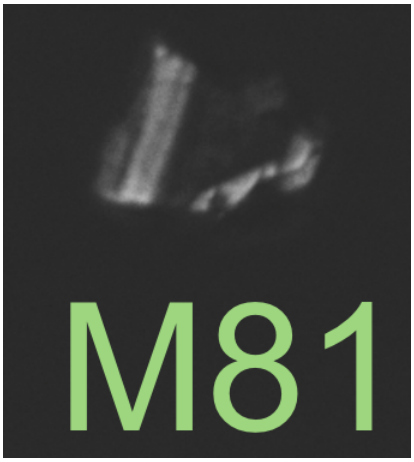
M81

M83

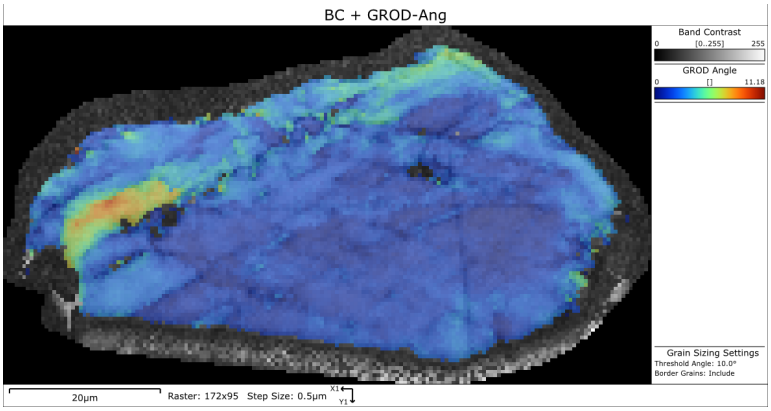
BC + GROD-Ang
Band Contrast
0 [0..255] 255
GROD Angle
0 [] 11.18
Grain Sizing Settings
Threshold Angle: 10.0°
Border Grains: Include
20µm
Raster: 172x95 Step Size: 0.5µm

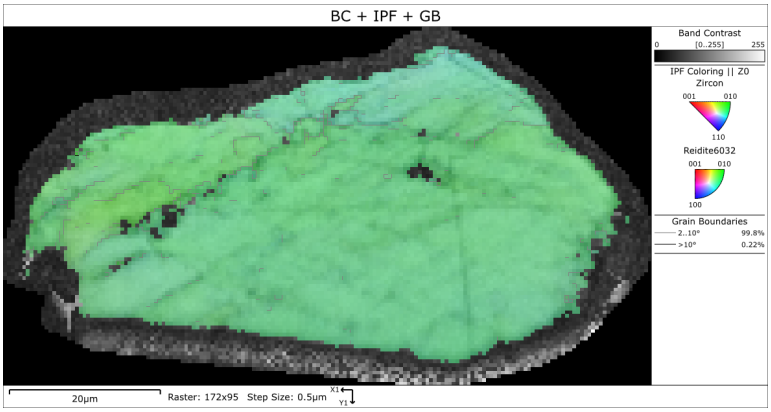
BC + IPF + GB
Band Contrast
0 [0..255] 255
IPF Coloring || Z0
Zircon
001 010
110
Reidite6032
001 010
100
Grain Boundaries
2..10° 99.8%
>10° 0.22%
20µm
Raster: 172x95 Step Size: 0.5µm

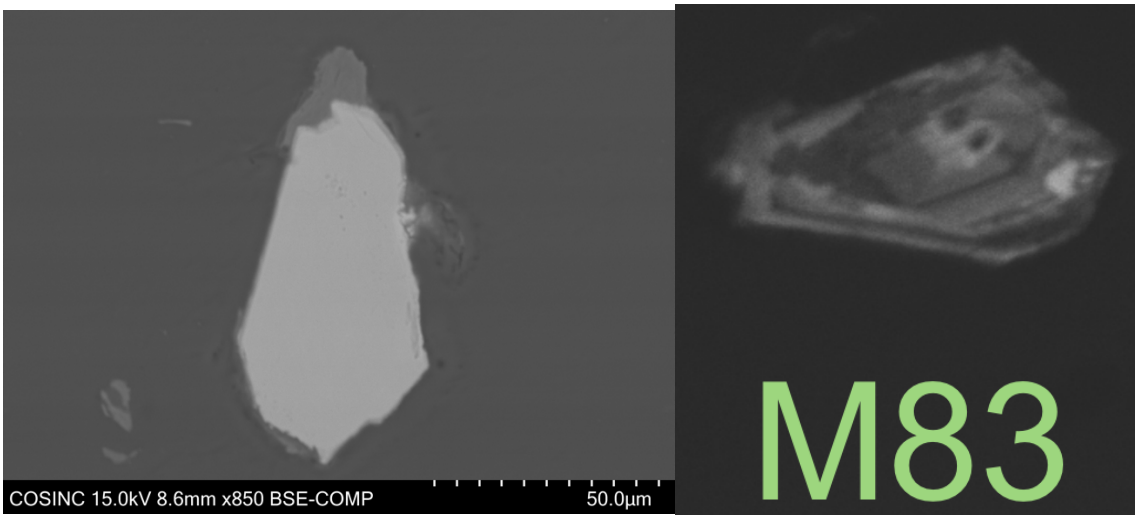
COSINC 15.0kV 8.6mm x850 BSE-COMP
50.0µm
M83

M84

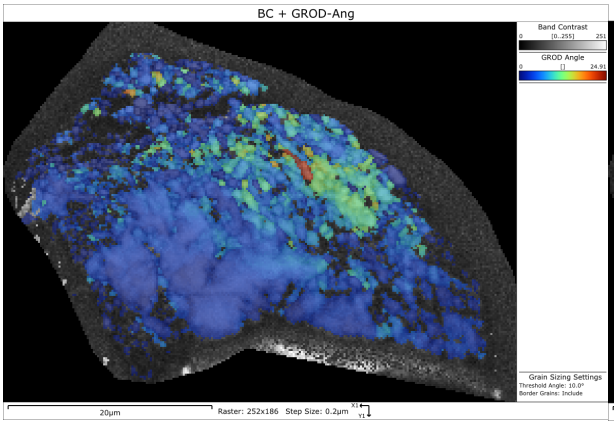
BC + GROD-Ang
Band Contrast
GROD Angle
Grain Sizing Settings
20µm
Raster: 252x186 Step Size: 0.2µm

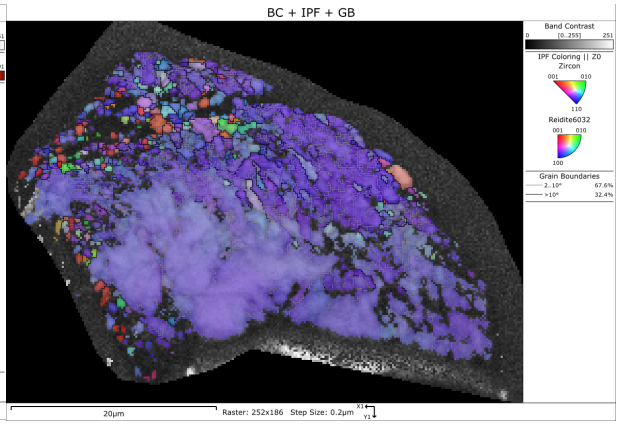
BC + IPF + GB
Band Contrast
IPF Coloring || Z0
Zircon
Reidite6032
Grain Boundaries
20µm
Raster: 252x186 Step Size: 0.2µm


M84

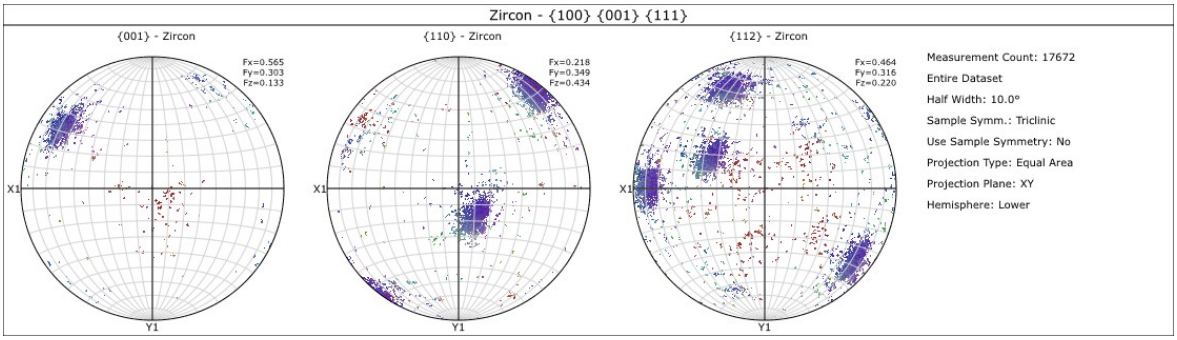
Zircon - {100} {001} {111}
{001} - Zircon
Fx=0.565
Fy=0.303
Fz=0.133
{110} - Zircon
Fx=0.218
Fy=0.349
Fz=0.434
{112} - Zircon
Fx=0.464
Fy=0.316
Fz=0.220
Measurement Count: 17672
Entire Dataset
Half Width: 10.0°
Sample Symm.: Triclinic
Use Sample Symmetry: No
Projection Type: Equal Area
Projection Plane: XY
Hemisphere: Lower

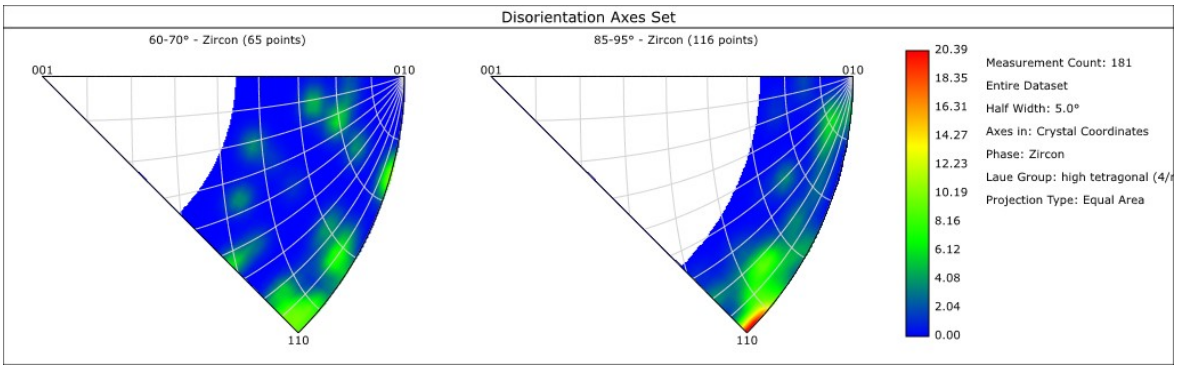
Disorientation Axes Set
60-70° - Zircon (65 points)
85-95° - Zircon (116 points)
001
010
110
20.39
18.35
16.31
14.27
12.23
10.19
8.16
6.12
4.08
2.04
0.00
Measurement Count: 181
Entire Dataset
Half Width: 5.0°
Axes in: Crystal Coordinates
Phase: Zircon
Projection Type: Equal Area

M88

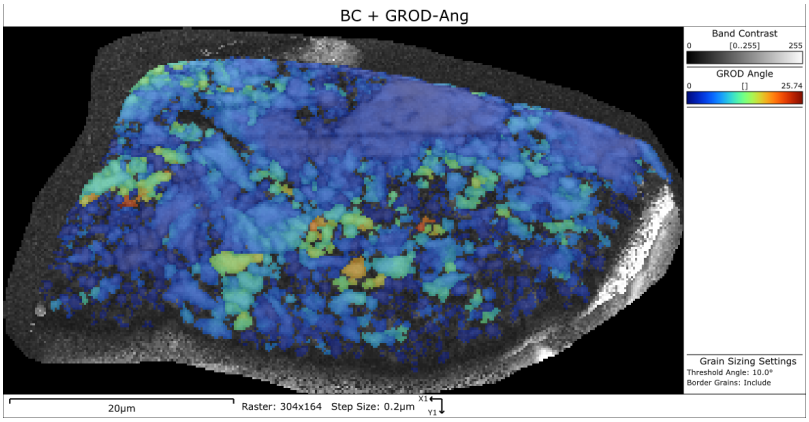
BC + GROD-Ang
Band Contrast
0 [0..255] 255
GROD Angle
0 [] 25.74
Grain Sizing Settings
Threshold Angle: 10.0°
Border Grains: Include
20µm
Raster: 304x164 Step Size: 0.2µm

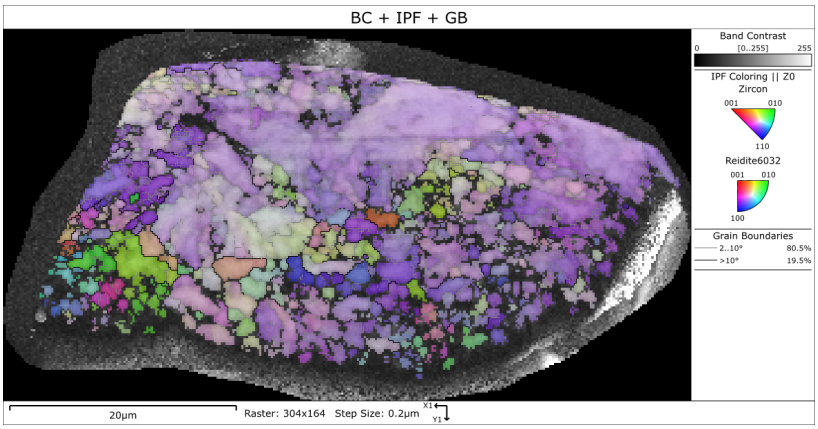
BC + IPF + GB
Band Contrast
0 [0..255] 255
IPF Coloring || Z0
Zircon
001 010
110
Reidite6032
001 010
100
Grain Boundaries
2..10° 80.5%
>10° 19.5%
20µm
Raster: 304x164 Step Size: 0.2µm

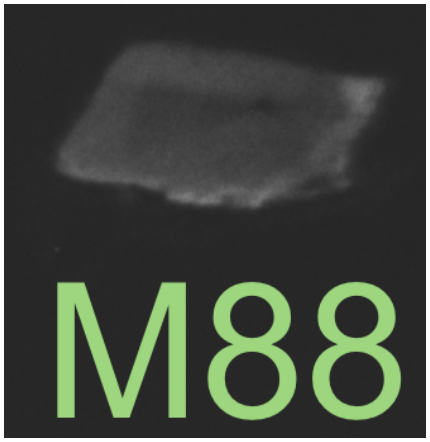
M88

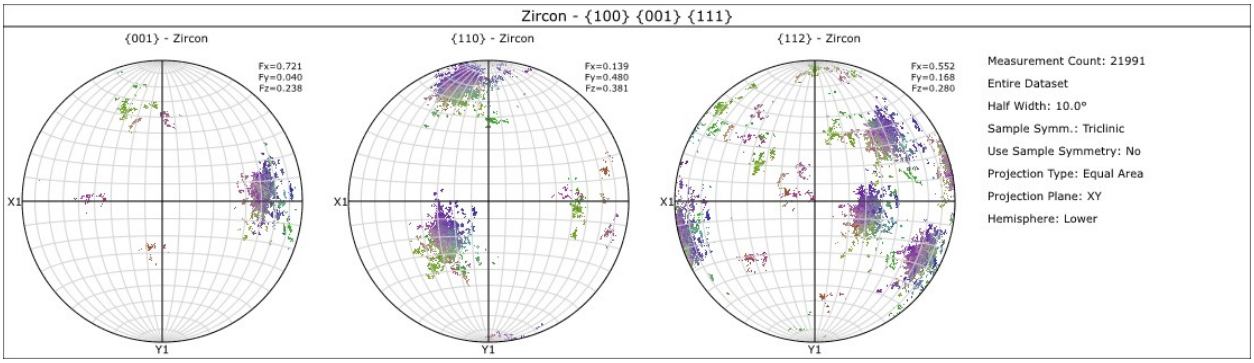
Zircon - {100} {001} {111}
{001} - Zircon
Fx=0.721
Fy=0.040
Fz=0.238
{110} - Zircon
Fx=0.139
Fy=0.480
Fz=0.381
{112} - Zircon
Fx=0.552
Fy=0.168
Fz=0.280
Measurement Count: 21991
Entire Dataset
Half Width: 10.0°
Sample Symm.: Triclinic
Use Sample Symmetry: No
Projection Type: Equal Area
Projection Plane: XY
Hemisphere: Lower

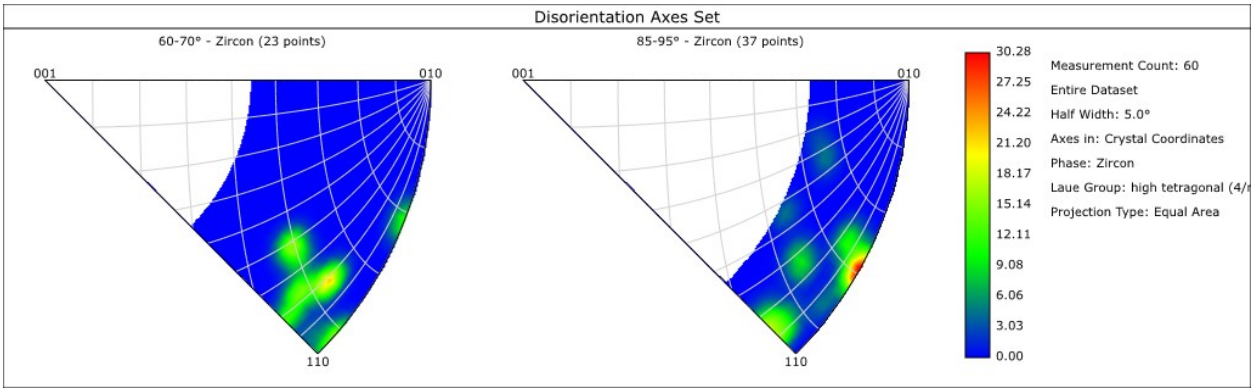
Disorientation Axes Set
60-70° - Zircon (23 points)
85-95° - Zircon (37 points)
001
010
110
30.28
27.25
24.22
21.20
18.17
15.14
12.11
9.08
6.06
3.03
0.00
Measurement Count: 60
Entire Dataset
Half Width: 5.0°
Axes in: Crystal Coordinates
Phase: Zircon
Projection Type: Equal Area

M89

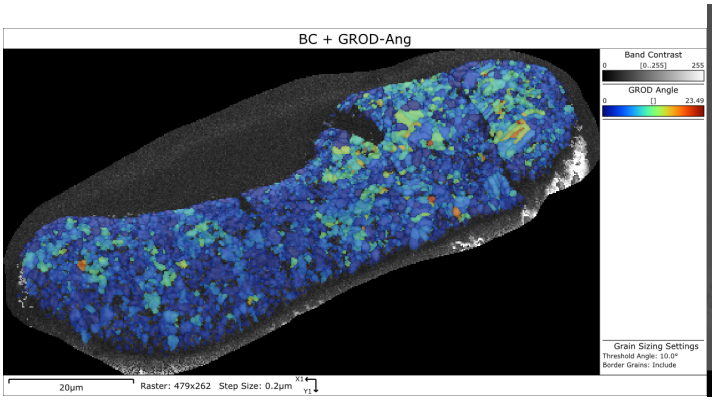
BC + GROD-Ang
Band Contrast
GROD Angle
Grain Sizing Settings
20µm
Raster: 479x262 Step Size: 0.2µm

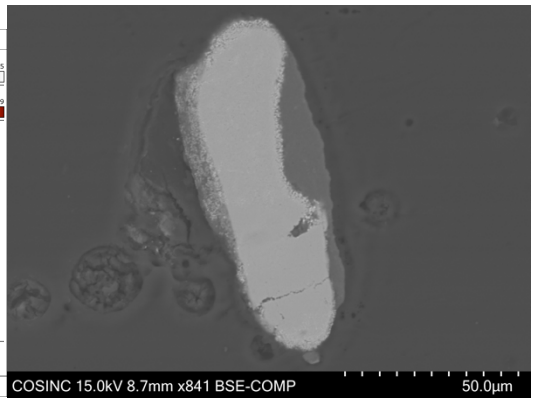
COSINC 15.0kV 8.7mm x841 BSE-COMP
50.0µm

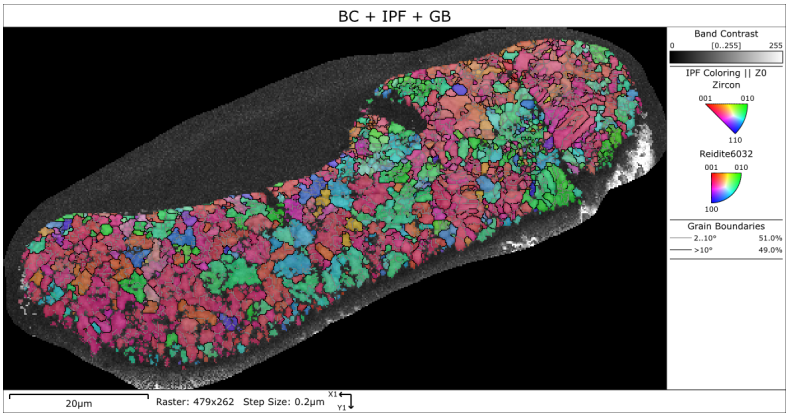
BC + IPF + GB
Band Contrast
IPF Coloring || Z0
Zircon
Reidite6032
Grain Boundaries
20µm
Raster: 479x262 Step Size: 0.2µm

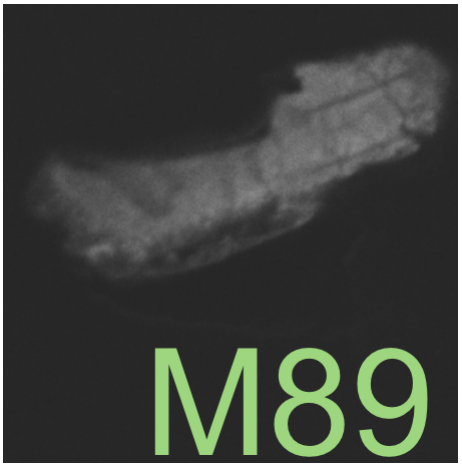
M89

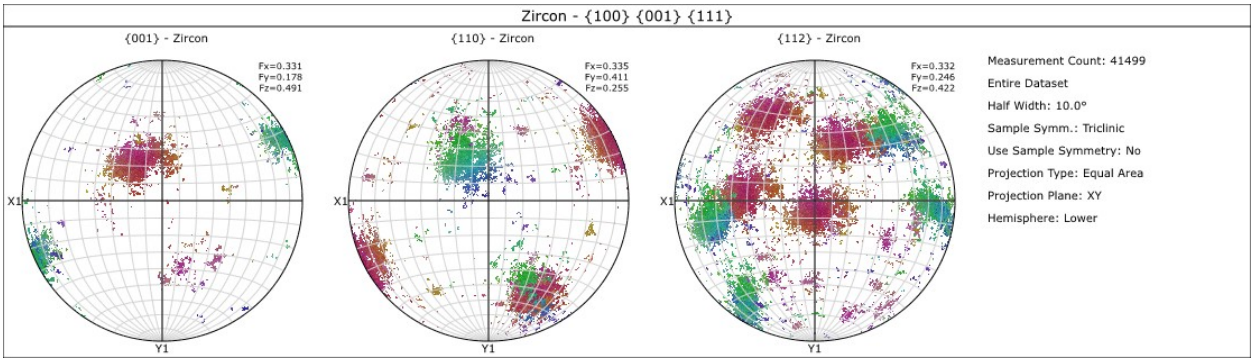
Zircon - {100} {001} {111}
{001} - Zircon
Fx=0.331
Fy=0.178
Fz=0.491
{110} - Zircon
Fx=0.335
Fy=0.411
Fz=0.255
{112} - Zircon
Fx=0.332
Fy=0.246
Fz=0.422
Measurement Count: 41499
Entire Dataset
Half Width: 10.0°
Sample Symm.: Triclinic
Use Sample Symmetry: No
Projection Type: Equal Area
Projection Plane: XY
Hemisphere: Lower

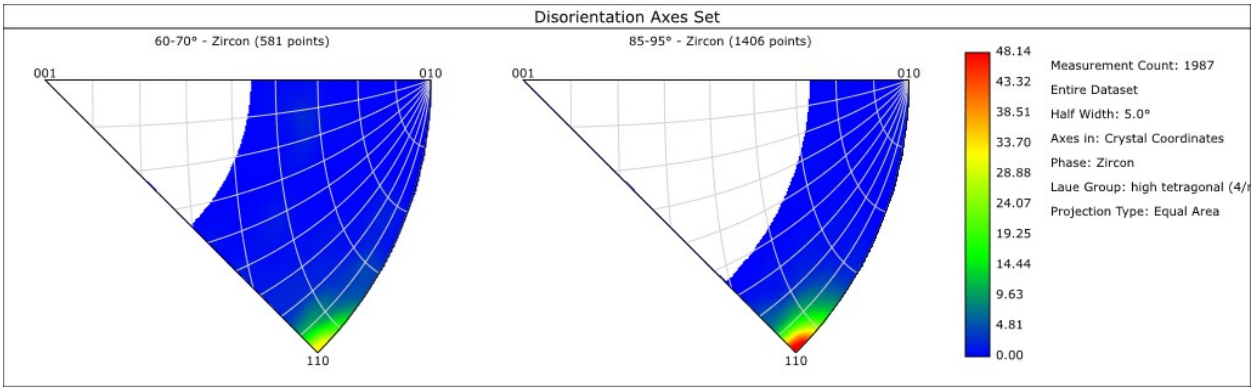
Disorientation Axes Set
60-70° - Zircon (581 points)
85-95° - Zircon (1406 points)
001
010
110
48.14
43.32
38.51
33.70
28.88
24.07
19.25
14.44
9.63
4.81
0.00
Measurement Count: 1987
Entire Dataset
Half Width: 5.0°
Axes in: Crystal Coordinates
Phase: Zircon
Projection Type: Equal Area

M90

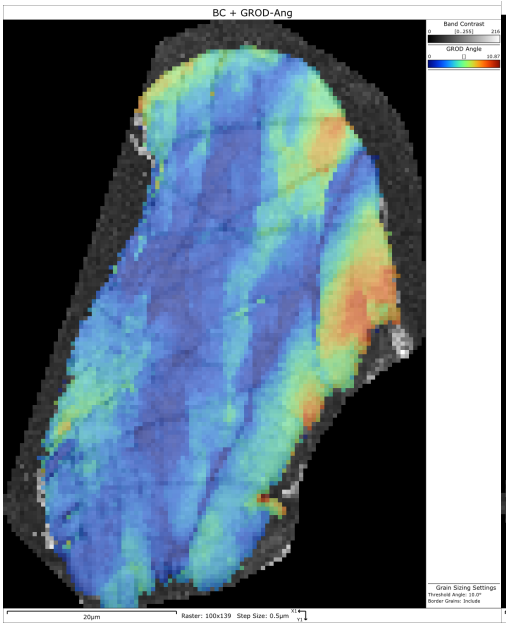
BC + GROD-Ang
Band Contrast
GROD Angle
Grain Sizing Settings
20µm
Raster: 100x139 Step Size: 0.5µm

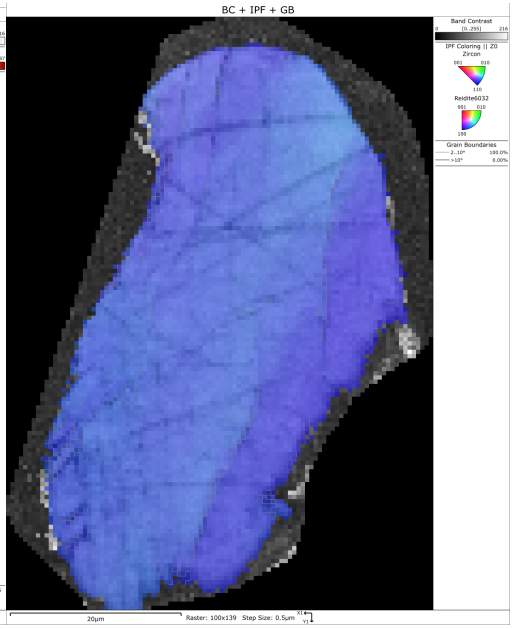
BC + IPF + GB
Band Contrast
IPF Coloring || Z0
Zircon
Reidite6032
Grain Boundaries
20µm
Raster: 100x139 Step Size: 0.5µm

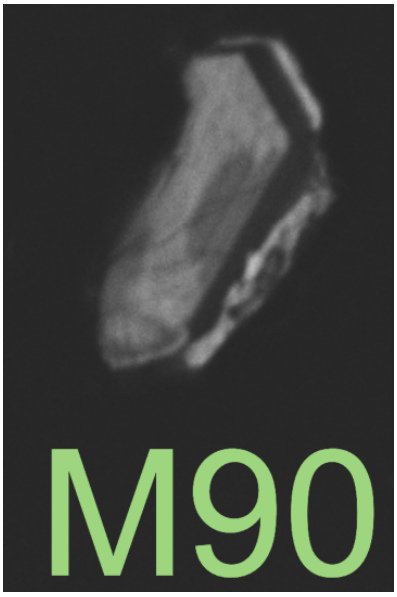
M90

M91

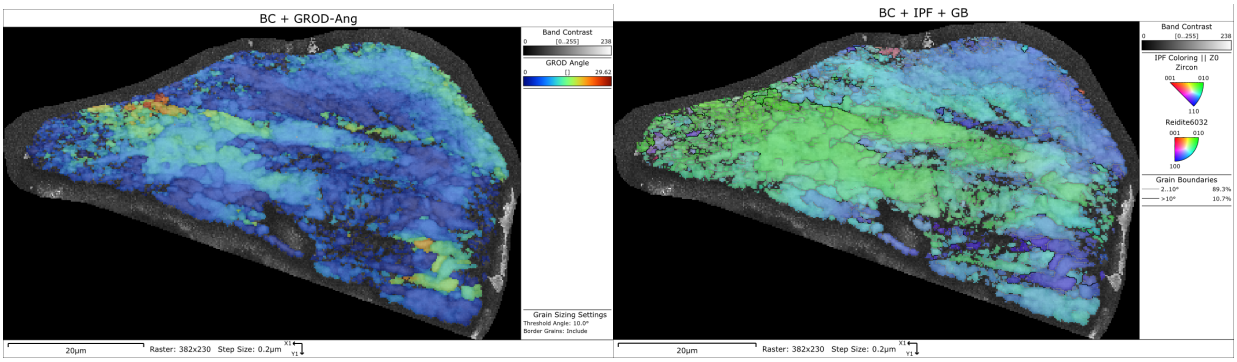
BC + GROD-Ang
Band Contrast
GROD Angle
Grain Sizing Settings
20µm
Raster: 382x230 Step Size: 0.2µm
BC + IPF + GB
Band Contrast
IPF Coloring || Z0
Zircon
Reidite6032
Grain Boundaries
20µm
Raster: 382x230 Step Size: 0.2µm

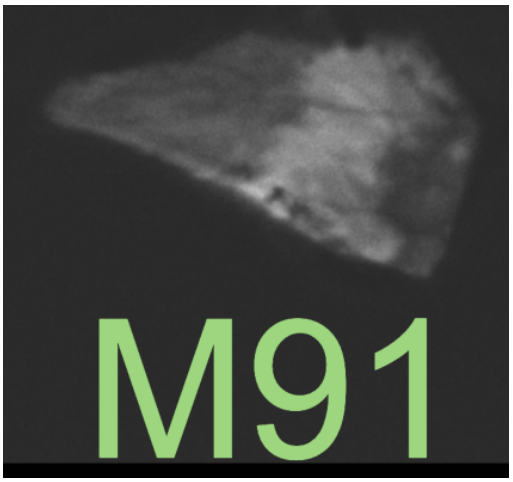
M91

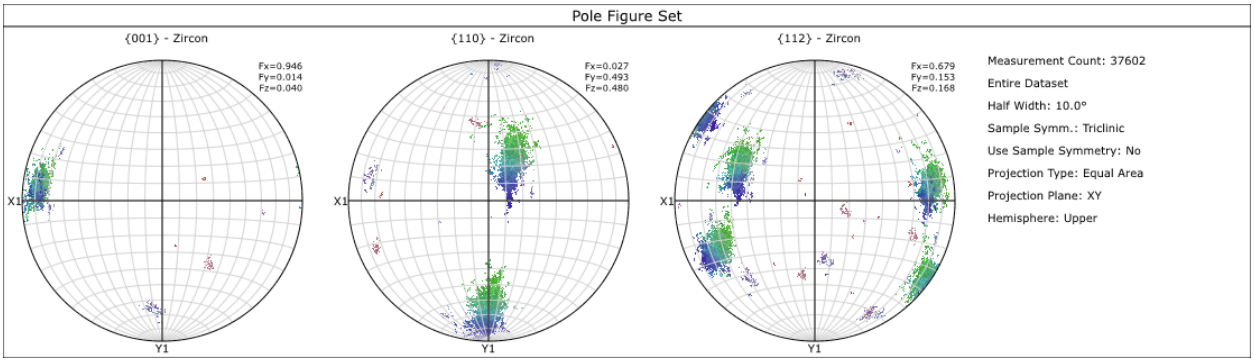
Pole Figure Set
{001} - Zircon
Fx=0.946
Fy=0.014
Fz=0.040
{110} - Zircon
Fx=0.027
Fy=0.493
Fz=0.480
{112} - Zircon
Fx=0.679
Fy=0.153
Fz=0.168
X1
Y1
Measurement Count: 37602
Entire Dataset
Half Width: 10.0°
Sample Symm.: Triclinic
Use Sample Symmetry: No
Projection Type: Equal Area
Projection Plane: XY
Hemisphere: Upper

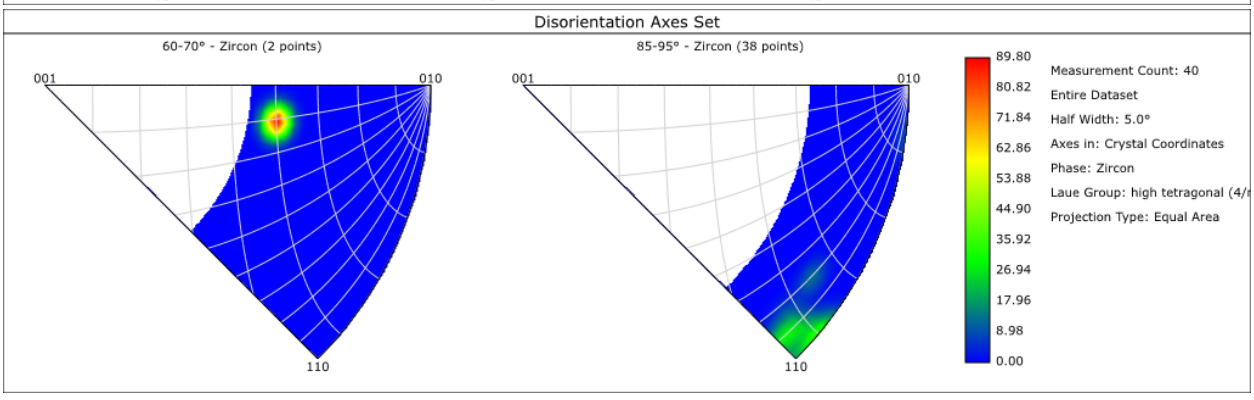
Disorientation Axes Set
60-70° - Zircon (2 points)
85-95° - Zircon (38 points)
001
010
110
89.80
80.82
71.84
62.86
53.88
44.90
35.92
26.94
17.96
8.98
0.00
Measurement Count: 40
Entire Dataset
Half Width: 5.0°
Axes in: Crystal Coordinates
Phase: Zircon
Projection Type: Equal Area

M93

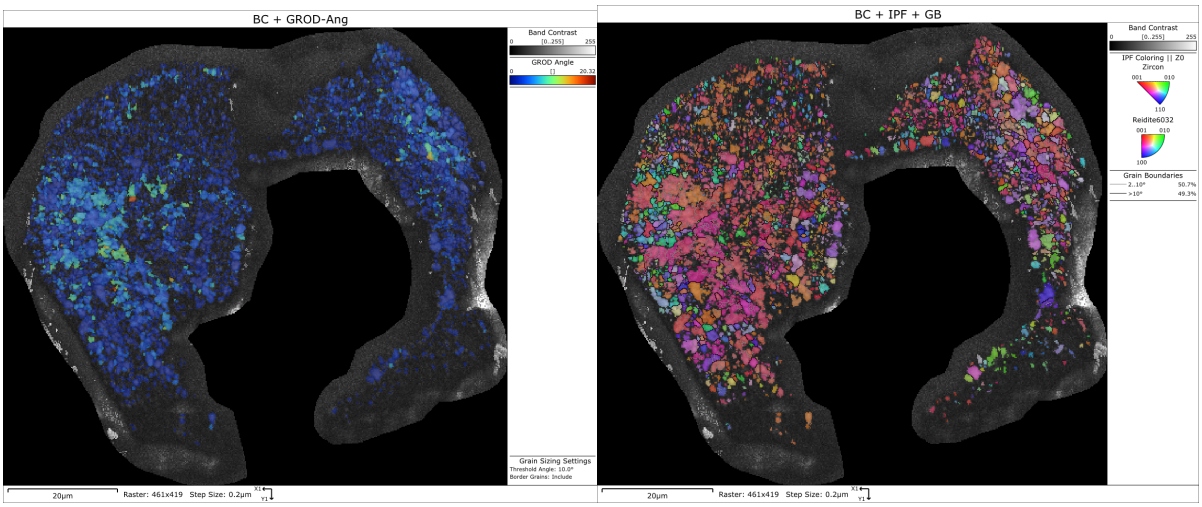
BC + GROD-Ang
Band Contrast
GROD Angle
Grain Sizing Settings
20µm
Raster: 461x419 Step Size: 0.2µm
BC + IPF + GB
Band Contrast
IPF Coloring || Z0
Zircon
Reidite6032
Grain Boundaries
20µm
Raster: 461x419 Step Size: 0.2µm


M93

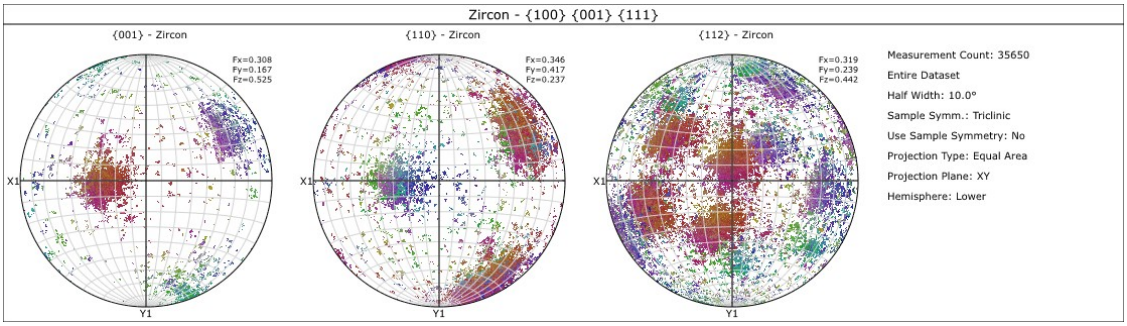
Zircon - {100} {001} {111}
{001} - Zircon
Fx=0.308
Fy=0.167
Fz=0.525
{110} - Zircon
Fx=0.346
Fy=0.417
Fz=0.237
{112} - Zircon
Fx=0.319
Fy=0.239
Fz=0.442
X1
Y1
Measurement Count: 35650
Entire Dataset
Half Width: 10.0°
Sample Symm.: Triclinic
Use Sample Symmetry: No
Projection Type: Equal Area
Projection Plane: XY
Hemisphere: Lower

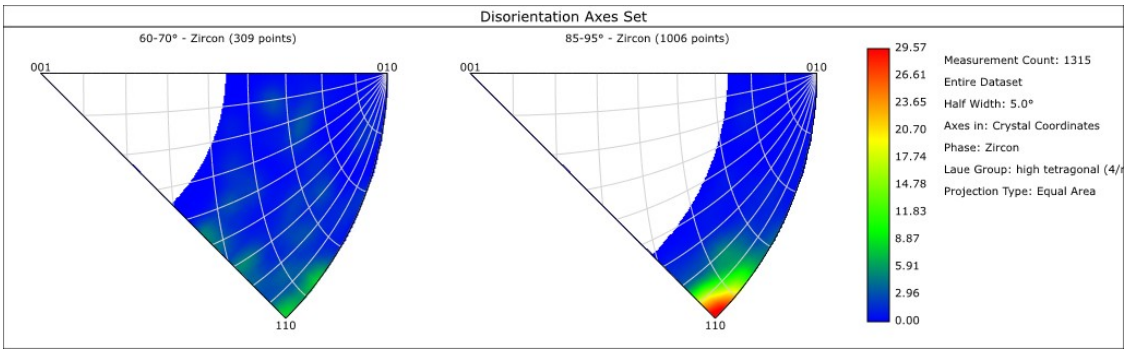
Disorientation Axes Set
60-70° - Zircon (309 points)
85-95° - Zircon (1006 points)
001
010
110
29.57
26.61
23.65
20.70
17.74
14.78
11.83
8.87
5.91
2.96
0.00
Measurement Count: 1315
Entire Dataset
Half Width: 5.0°
Axes in: Crystal Coordinates
Phase: Zircon
Projection Type: Equal Area

M98

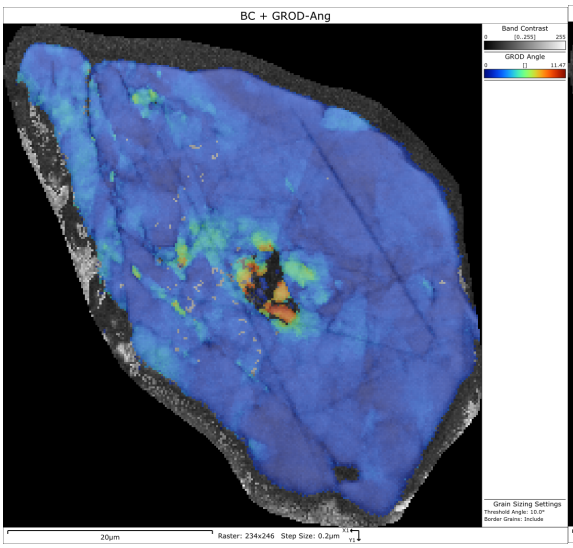
BC + GROD-Ang
Band Contrast
[0..255]
GROD Angle
Grain Sizing Settings
20µm
Raster: 234x246 Step Size: 0.2µm

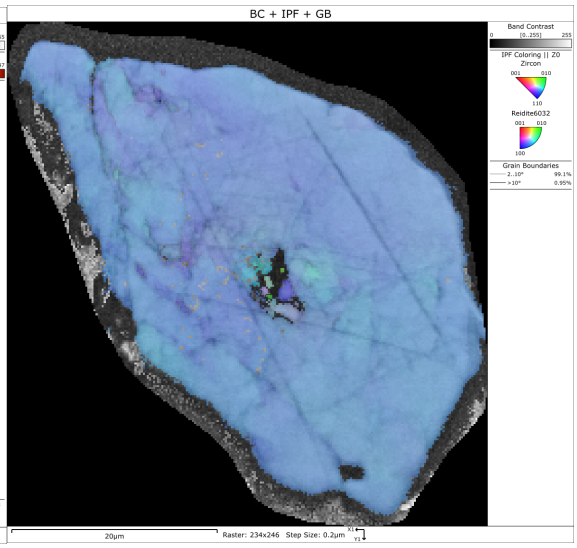
BC + IPF + GB
Band Contrast
[0..255]
IPF Coloring || Z0
Zircon
Reidite6032
Grain Boundaries
20µm
Raster: 234x246 Step Size: 0.2µm

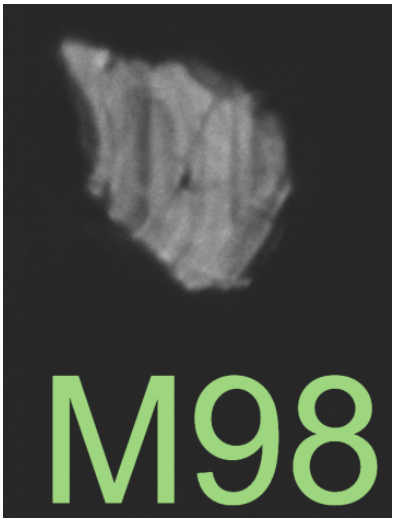
M98

M99

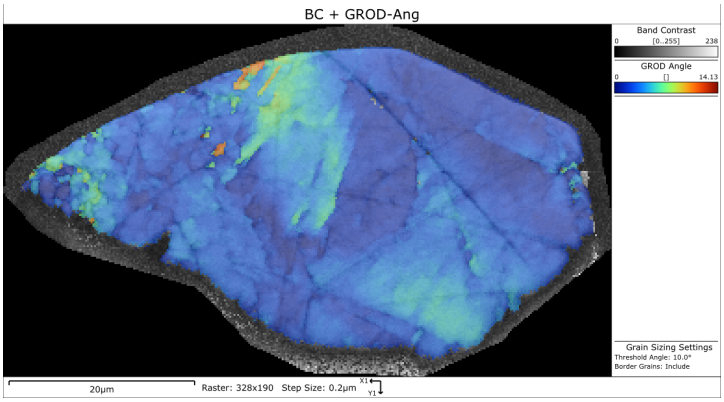
BC + GROD-Ang
Band Contrast
GROD Angle
Grain Sizing Settings
20µm
Raster: 328x190 Step Size: 0.2µm

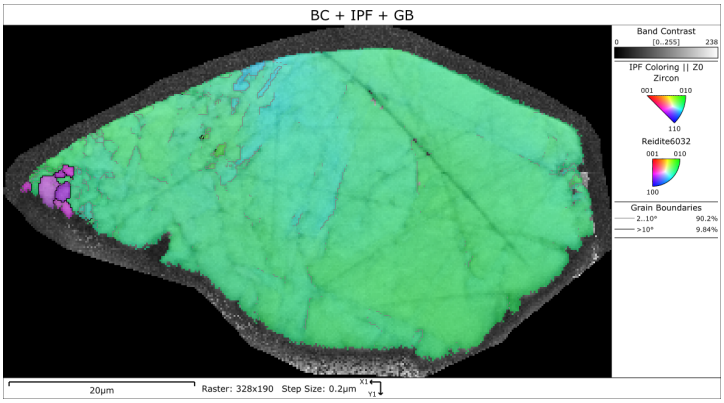
BC + IPF + GB
Band Contrast
IPF Coloring || Z0
Zircon
Reidite6032
Grain Boundaries
20µm
Raster: 328x190 Step Size: 0.2µm

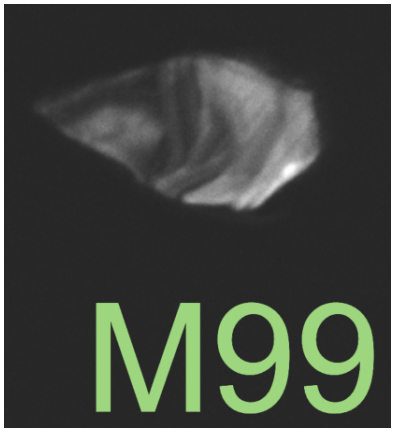
M99

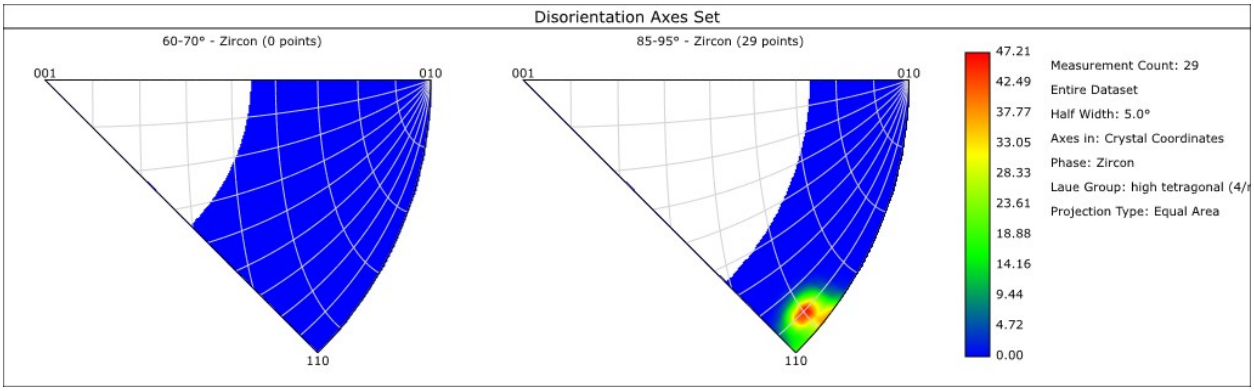
Disorientation Axes Set
60-70° - Zircon (0 points)
85-95° - Zircon (29 points)
001
010
110
47.21
42.49
37.77
33.05
28.33
23.61
18.88
14.16
9.44
4.72
0.00
Measurement Count: 29
Entire Dataset
Half Width: 5.0°
Axes in: Crystal Coordinates
Phase: Zircon
Projection Type: Equal Area

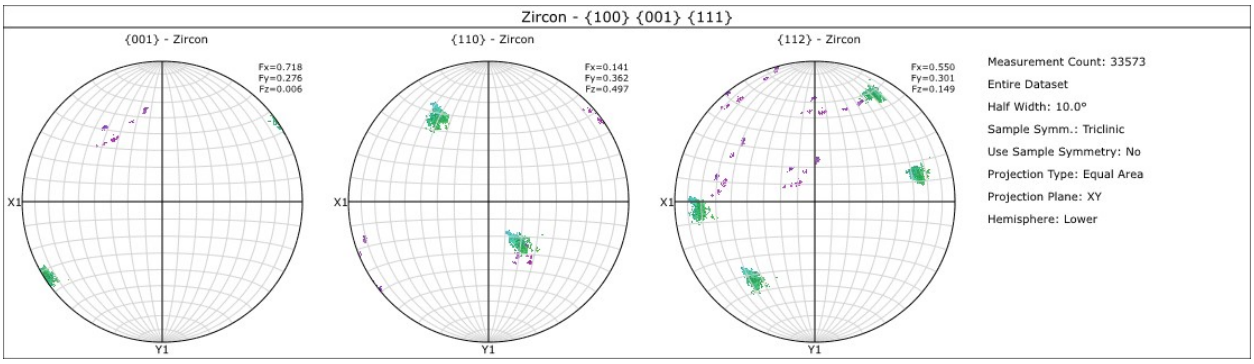
Zircon - {100} {001} {111}
{001} - Zircon
{110} - Zircon
{112} - Zircon
Fx=0.718
Fy=0.276
Fz=0.006
Fx=0.141
Fy=0.362
Fz=0.497
Fx=0.550
Fy=0.301
Fz=0.149
X1
Y1
Measurement Count: 33573
Entire Dataset
Half Width: 10.0°
Sample Symm.: Triclinic
Use Sample Symmetry: No
Projection Type: Equal Area
Projection Plane: XY
Hemisphere: Lower

M100

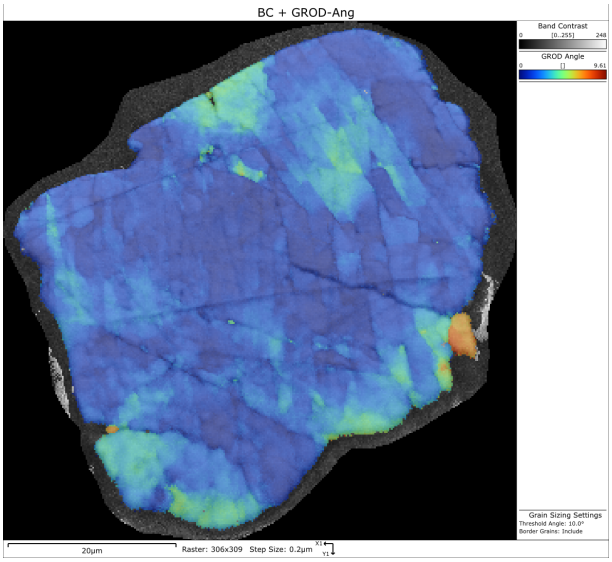
BC + GROD-Ang
Band Contrast
GROD Angle
Grain Sizing Settings
20µm
Raster: 306x309 Step Size: 0.2µm

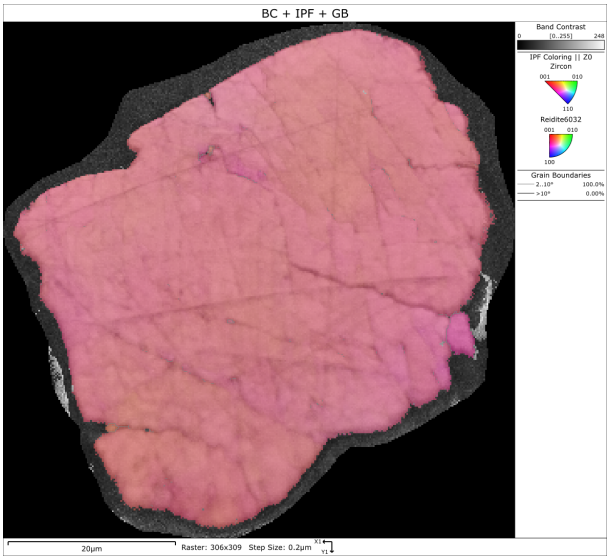
BC + IPF + GB
Band Contrast
IPF Coloring || Z0
Zircon
Reidite6032
Grain Boundaries
20µm
Raster: 306x309 Step Size: 0.2µm

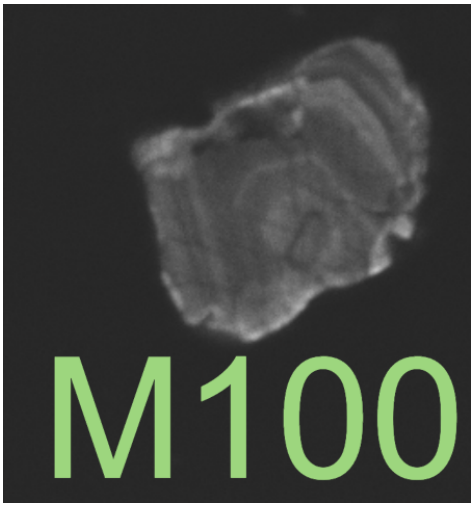
M100

M102

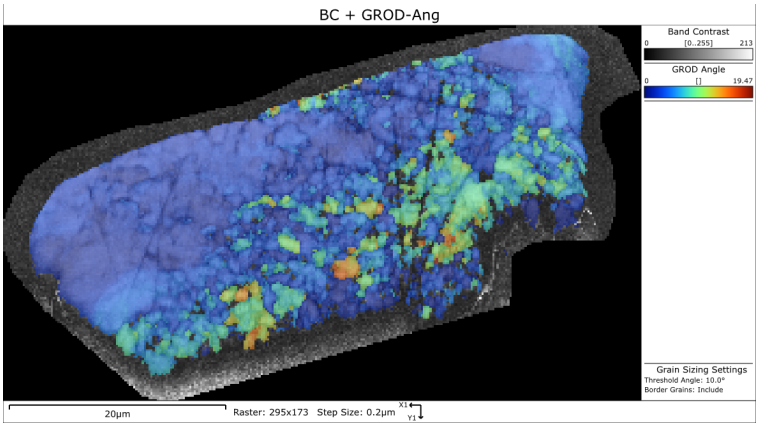
BC + GROD-Ang
Band Contrast
0 [0..255] 213
GROD Angle
0 [] 19.47
Grain Sizing Settings
Threshold Angle: 10.0°
Border Grains: Include
20µm
Raster: 295x173 Step Size: 0.2µm

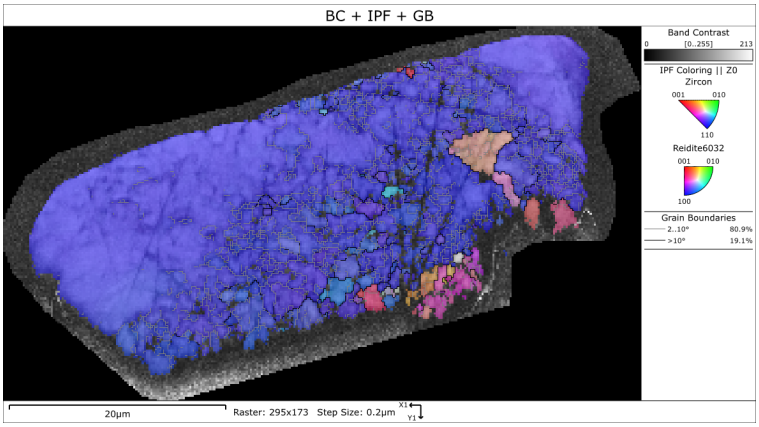
BC + IPF + GB
Band Contrast
0 [0..255] 213
IPF Coloring || Z0
Zircon
001 010
110
Reidite6032
001 010
100
Grain Boundaries
2..10° 80.9%
>10° 19.1%
20µm
Raster: 295x173 Step Size: 0.2µm

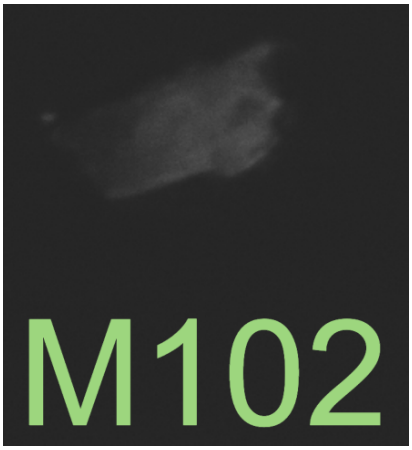
M102

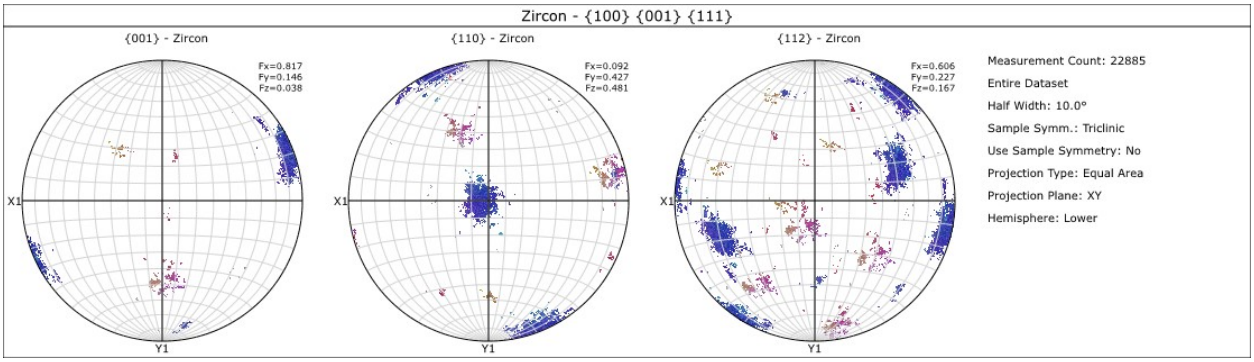
Zircon - {100} {001} {111}
{001} - Zircon
Fx=0.817
Fy=0.146
Fz=0.038
{110} - Zircon
Fx=0.092
Fy=0.427
Fz=0.481
{112} - Zircon
Fx=0.606
Fy=0.227
Fz=0.167
X1
Y1
Measurement Count: 22885
Entire Dataset
Half Width: 10.0°
Sample Symm.: Triclinic
Use Sample Symmetry: No
Projection Type: Equal Area
Projection Plane: XY
Hemisphere: Lower

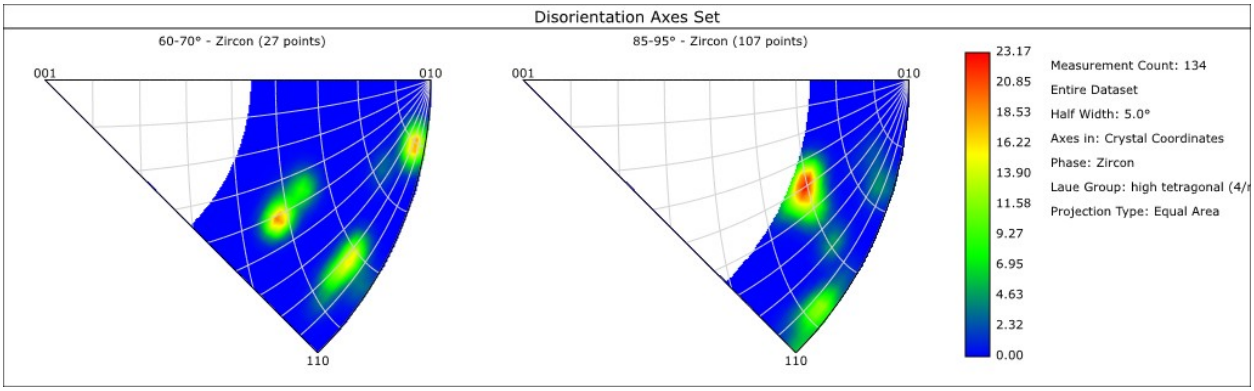
Disorientation Axes Set
60-70° - Zircon (27 points)
85-95° - Zircon (107 points)
001
010
110
23.17
20.85
18.53
16.22
13.90
11.58
9.27
6.95
4.63
2.32
0.00
Measurement Count: 134
Entire Dataset
Half Width: 5.0°
Axes in: Crystal Coordinates
Phase: Zircon
Laue Group: high tetragonal (4/
Projection Type: Equal Area

M104

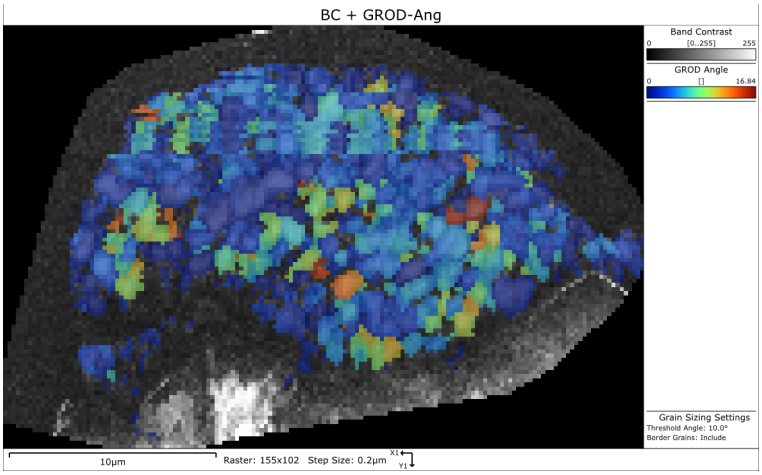
BC + GROD-Ang
Band Contrast
0 [0..255] 255
GROD Angle
0 [] 16.84
Grain Sizing Settings
Threshold Angle: 10.0°
Border Grains: Include
10µm
Raster: 155x102 Step Size: 0.2µm

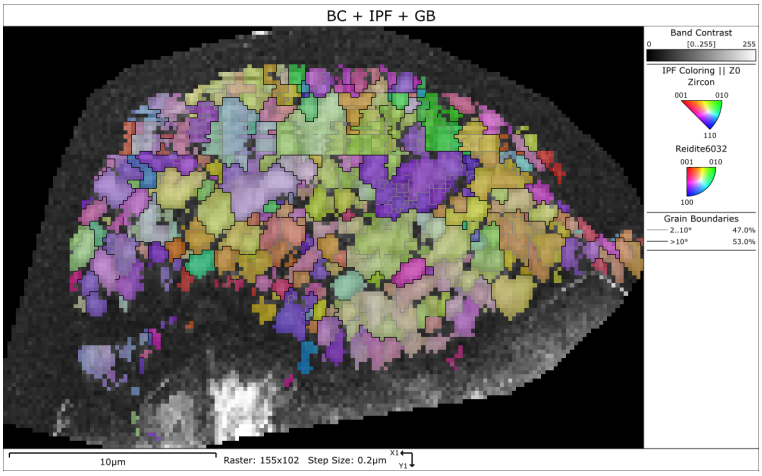
BC + IPF + GB
Band Contrast
0 [0..255] 255
IPF Coloring || Z0
Zircon
001 010
110
Reidite6032
001 010
100
Grain Boundaries
2..10° 47.0%
>10° 53.0%
10µm
Raster: 155x102 Step Size: 0.2µm


M104

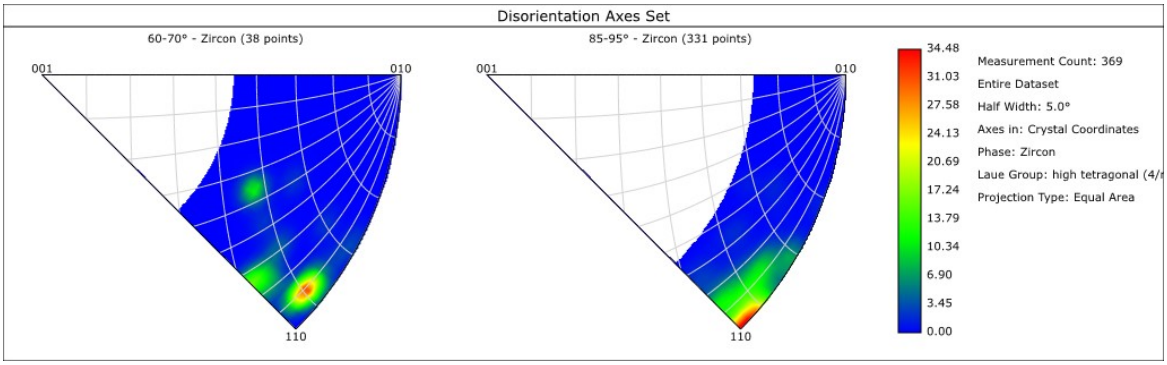
Disorientation Axes Set
60-70° - Zircon (38 points)
85-95° - Zircon (331 points)
001
010
110
34.48
31.03
27.58
24.13
20.69
17.24
13.79
10.34
6.90
3.45
0.00
Measurement Count: 369
Entire Dataset
Half Width: 5.0°
Axes in: Crystal Coordinates
Phase: Zircon
Projection Type: Equal Area

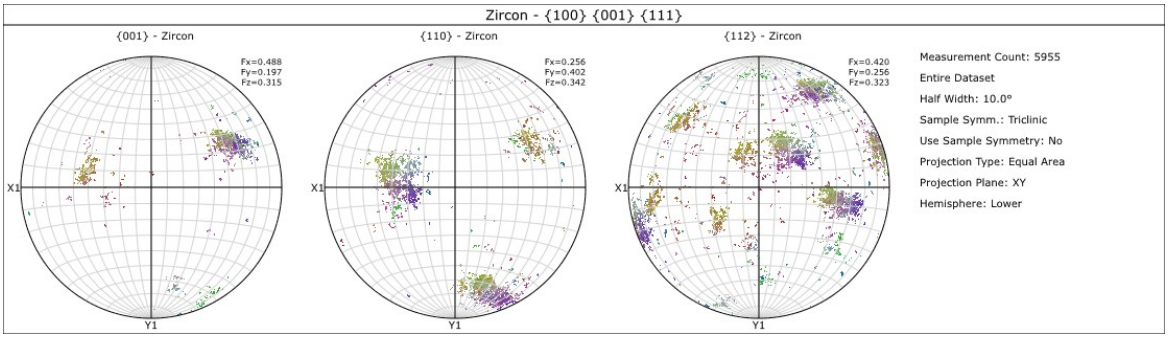
Zircon - {100} {001} {111}
{001} - Zircon
{110} - Zircon
{112} - Zircon
Fx=0.488
Fy=0.197
Fz=0.315
Fx=0.256
Fy=0.402
Fz=0.342
Fx=0.420
Fy=0.256
Fz=0.323
X1
Y1
Measurement Count: 5955
Entire Dataset
Half Width: 10.0°
Sample Symm.: Triclinic
Use Sample Symmetry: No
Projection Type: Equal Area
Projection Plane: XY
Hemisphere: Lower

M109

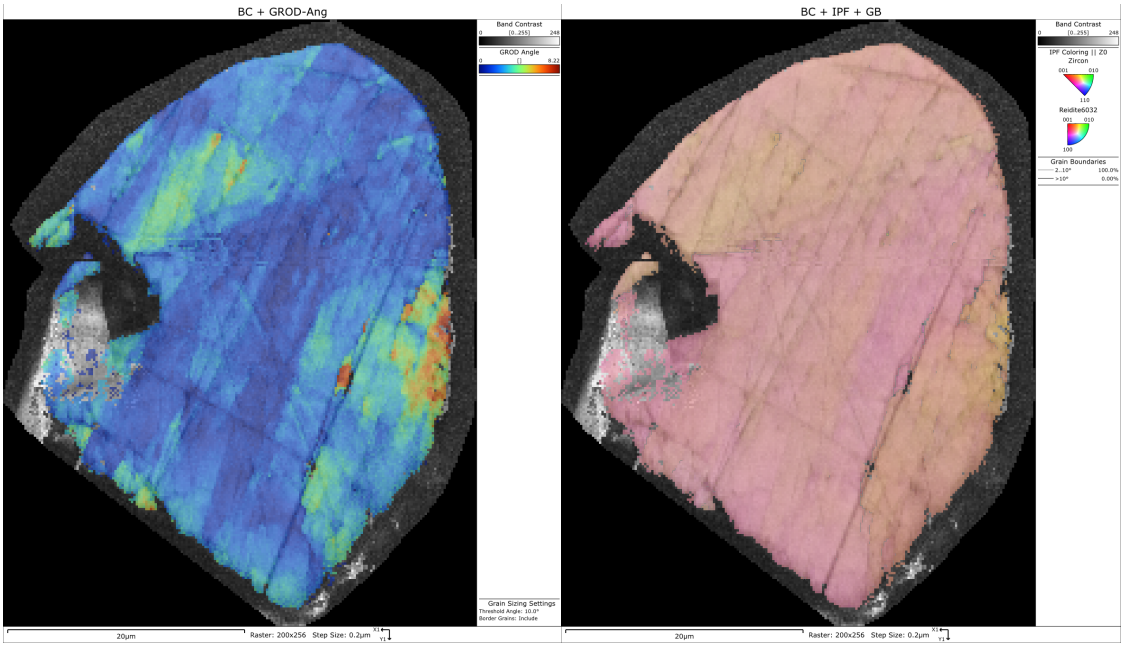
BC + GROD-Ang
Band Contrast
[0..255]
GROD Angle
Grain Sizing Settings
Threshold Angle: 10.0°
Border Grains: Include
20µm
Raster: 200x256 Step Size: 0.2µm
BC + IPF + GB
Band Contrast
[0..255]
IPF Coloring || Z0
Zircon
Reidite6032
Grain Boundaries
2..10°
>10°
100.0%
0.00%
20µm
Raster: 200x256 Step Size: 0.2µm

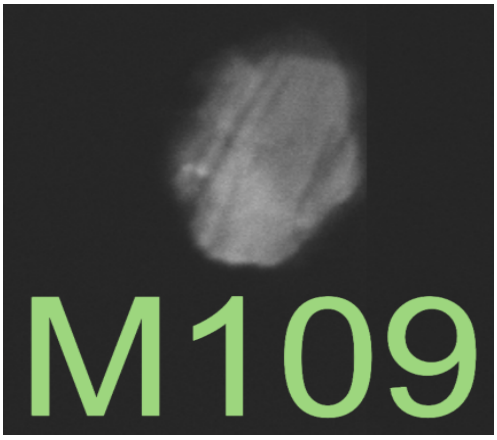
M109

M111

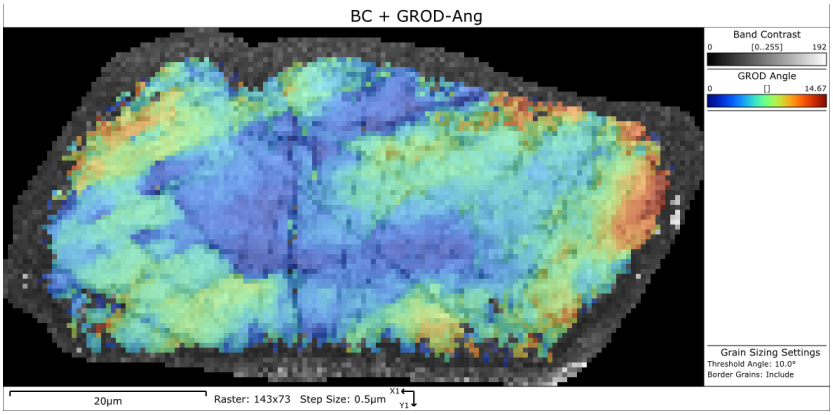
BC + GROD-Ang
Band Contrast
0 [0..255] 192
GROD Angle
0 [] 14.67
Grain Sizing Settings
Threshold Angle: 10.0°
Border Grains: Include
20µm
Raster: 143x73 Step Size: 0.5µm
X1
Y1

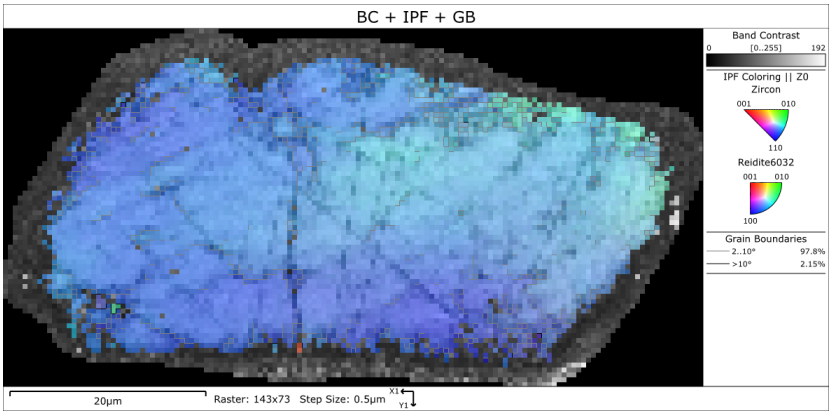
BC + IPF + GB
Band Contrast
0 [0..255] 192
IPF Coloring || Z0
Zircon
001 010
110
Reidite6032
001 010
100
Grain Boundaries
2..10° 97.8%
>10° 2.15%
20µm
Raster: 143x73 Step Size: 0.5µm
X1
Y1

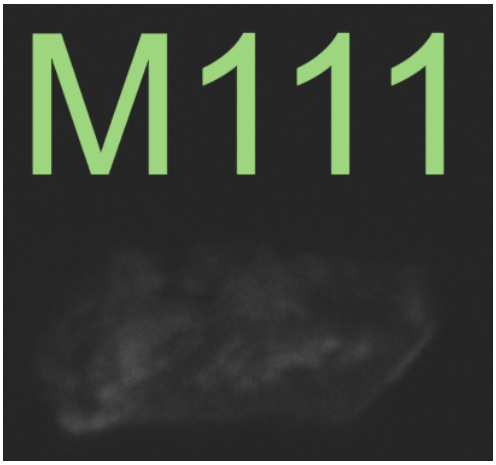
M111

M112

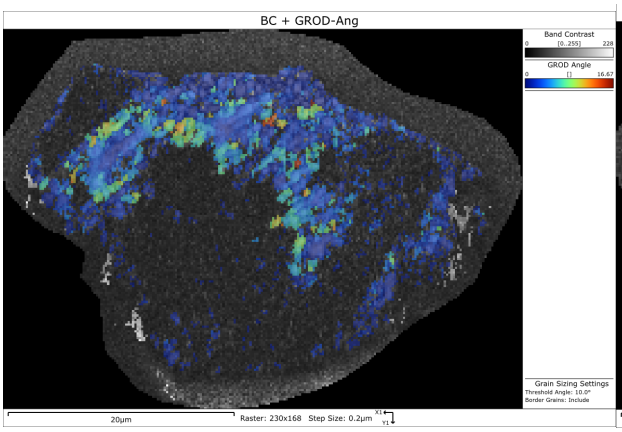
BC + GROD-Ang
Band Contrast
GROD Angle
Grain Sizing Settings
20µm
Raster: 230x168 Step Size: 0.2µm

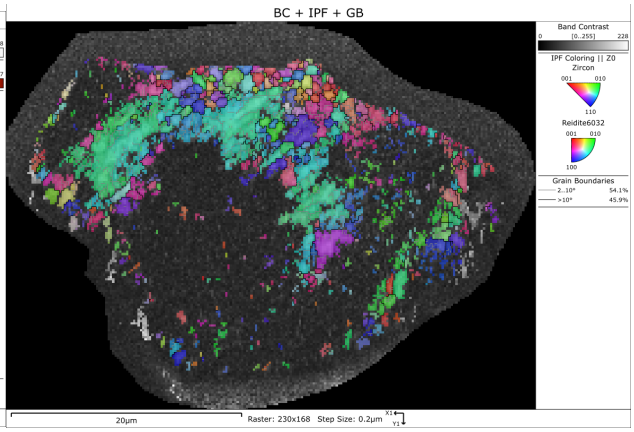
BC + IPF + GB
Band Contrast
IPF Coloring || Z0
Zircon
Reidite6032
Grain Boundaries
20µm
Raster: 230x168 Step Size: 0.2µm


M112

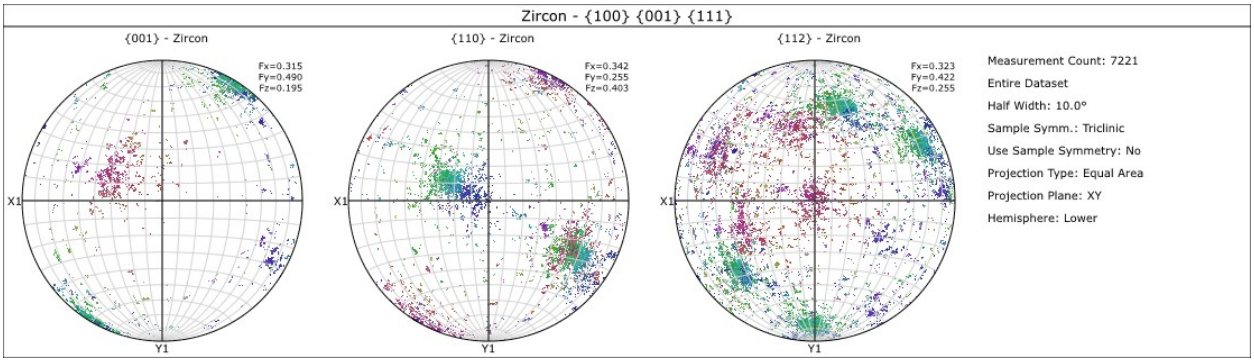
Zircon - {100} {001} {111}
{001} - Zircon
Fx=0.315
Fy=0.490
Fz=0.195
{110} - Zircon
Fx=0.342
Fy=0.255
Fz=0.403
{112} - Zircon
Fx=0.323
Fy=0.422
Fz=0.255
X1
Y1
Measurement Count: 7221
Entire Dataset
Half Width: 10.0°
Sample Symm.: Triclinic
Use Sample Symmetry: No
Projection Type: Equal Area
Projection Plane: XY
Hemisphere: Lower

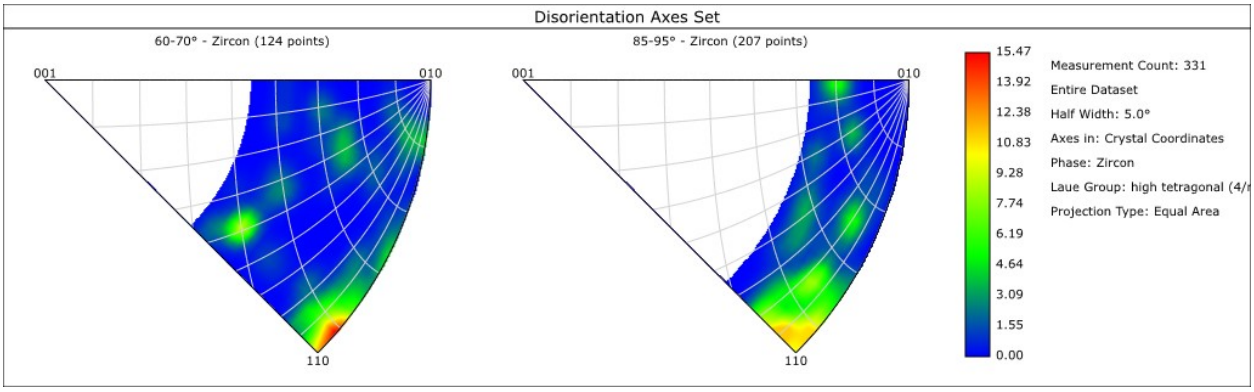
Disorientation Axes Set
60-70° - Zircon (124 points)
85-95° - Zircon (207 points)
001
010
110
15.47
13.92
12.38
10.83
9.28
7.74
6.19
4.64
3.09
1.55
0.00
Measurement Count: 331
Entire Dataset
Half Width: 5.0°
Axes in: Crystal Coordinates
Phase: Zircon
Laue Group: high tetragonal (4/
Projection Type: Equal Area

M113

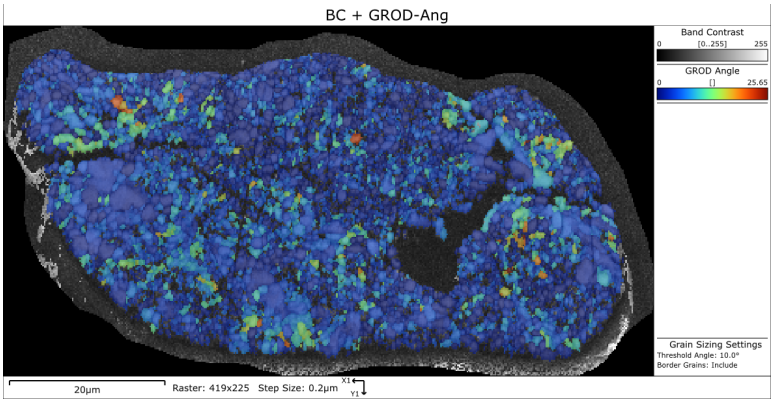
BC + GROD-Ang
Band Contrast
0 [0..255] 255
GROD Angle
0 [] 25.65
Grain Sizing Settings
Threshold Angle: 10.0°
Border Grains: Include
20µm
Raster: 419x225 Step Size: 0.2µm

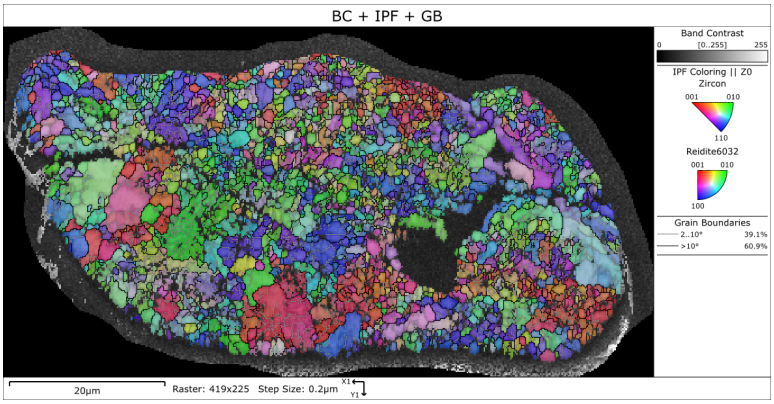
BC + IPF + GB
Band Contrast
0 [0..255] 255
IPF Coloring || Z0
Zircon
001 010
110
Reidite6032
001 010
100
Grain Boundaries
2..10° 39.1%
>10° 60.9%
20µm
Raster: 419x225 Step Size: 0.2µm

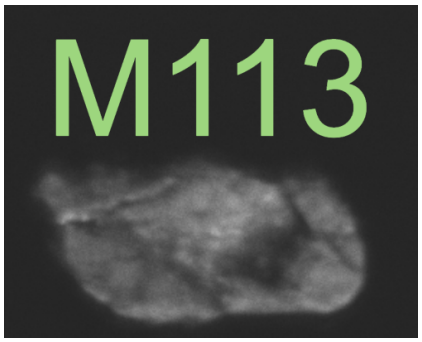
M113

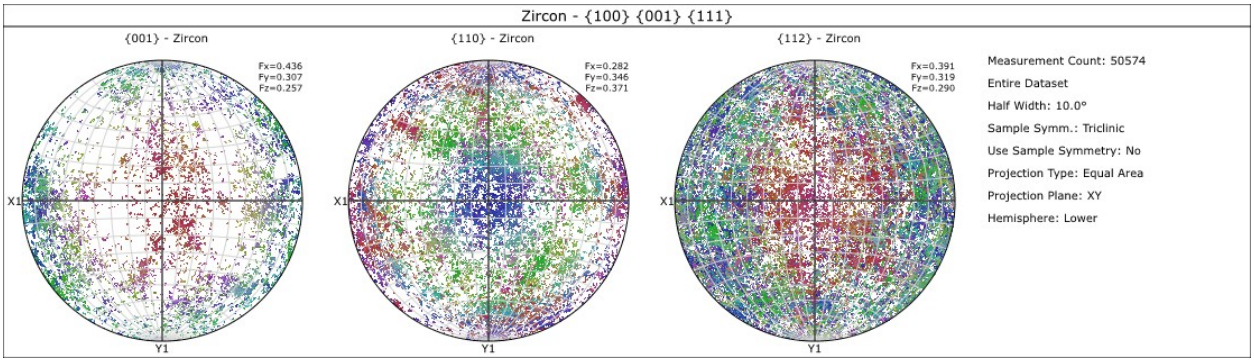
Zircon - {100} {001} {111}
{001} - Zircon
Fx=0.436
Fy=0.307
Fz=0.257
{110} - Zircon
Fx=0.282
Fy=0.346
Fz=0.371
{112} - Zircon
Fx=0.391
Fy=0.319
Fz=0.290
X1
Y1
Measurement Count: 50574
Entire Dataset
Half Width: 10.0°
Sample Symm.: Triclinic
Use Sample Symmetry: No
Projection Type: Equal Area
Projection Plane: XY
Hemisphere: Lower

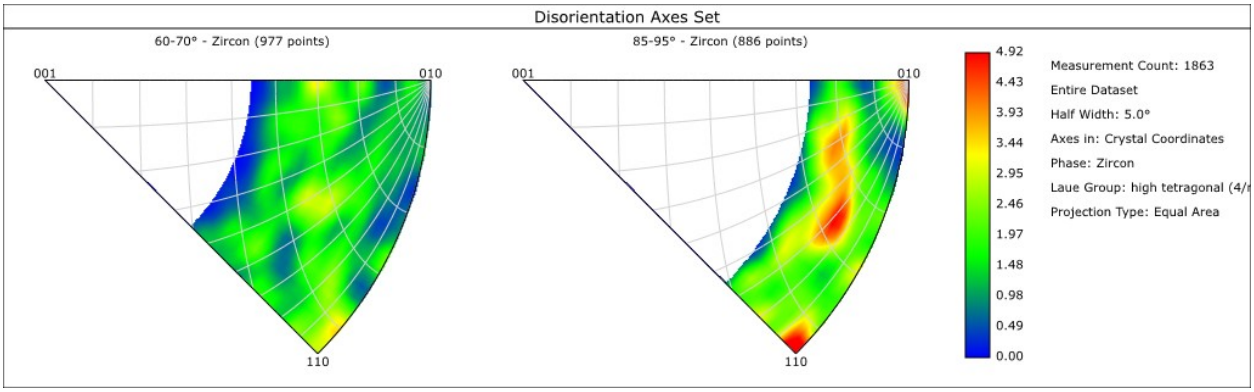
Disorientation Axes Set
60-70° - Zircon (977 points)
85-95° - Zircon (886 points)
001
010
110
4.92
4.43
3.93
3.44
2.95
2.46
1.97
1.48
0.98
0.49
0.00
Measurement Count: 1863
Entire Dataset
Half Width: 5.0°
Axes in: Crystal Coordinates
Phase: Zircon
Laue Group: high tetragonal (4/
Projection Type: Equal Area

M114

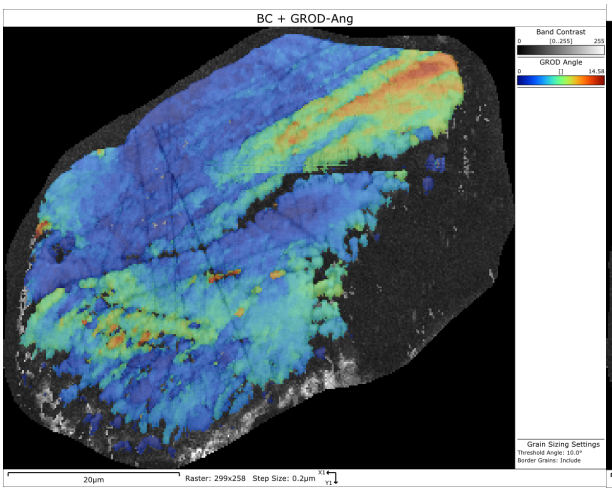
BC + GROD-Ang
Band Contrast
[0..255]
GROD Angle
Grain Sizing Settings
Threshold Angle: 10.0°
Border Grains: Include
20µm
Raster: 299x258 Step Size: 0.2µm

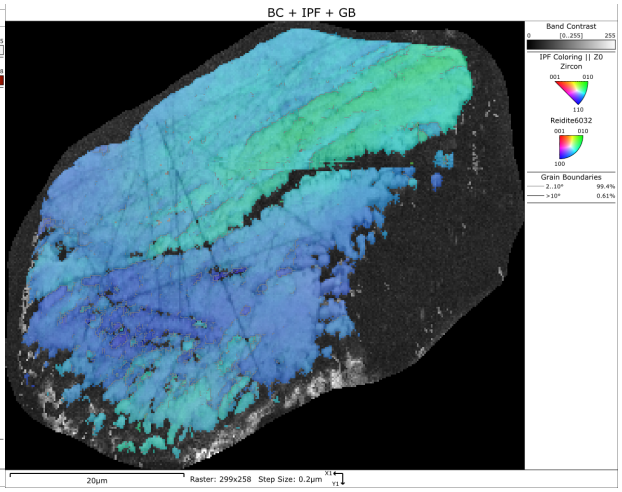
BC + IPF + GB
Band Contrast
[0..255]
IPF Coloring || Z0
Zircon
Reidite6032
Grain Boundaries
20µm
Raster: 299x258 Step Size: 0.2µm

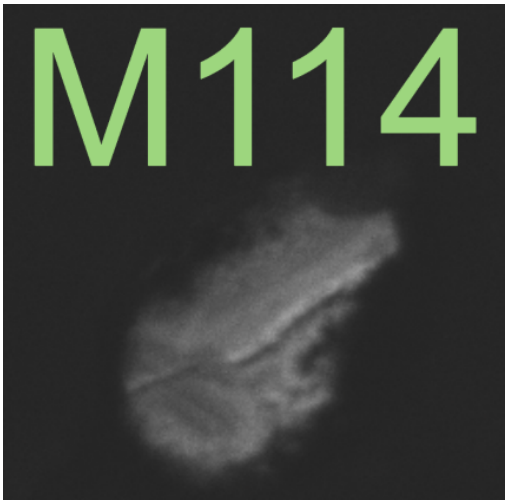
M114

M115

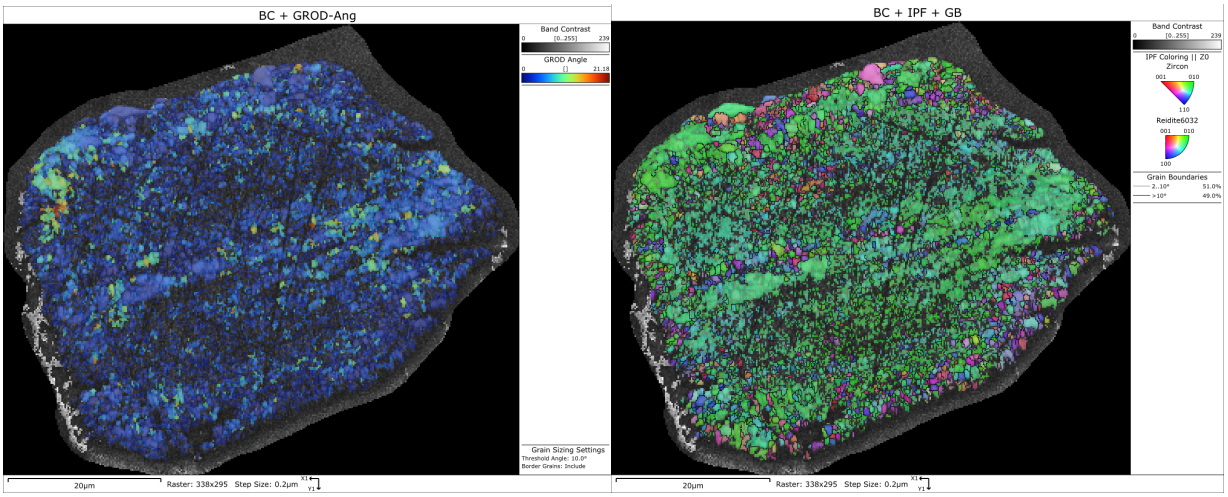
BC + GROD-Ang
Band Contrast
GROD Angle
Grain Sizing Settings
20µm
Raster: 338x295 Step Size: 0.2µm
BC + IPF + GB
Band Contrast
IPF Coloring || Z0
Zircon
Reidite6032
Grain Boundaries
20µm
Raster: 338x295 Step Size: 0.2µm

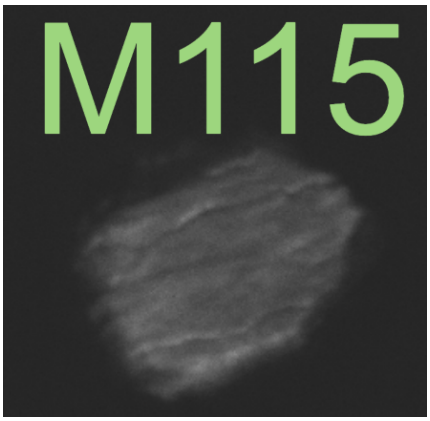
M115

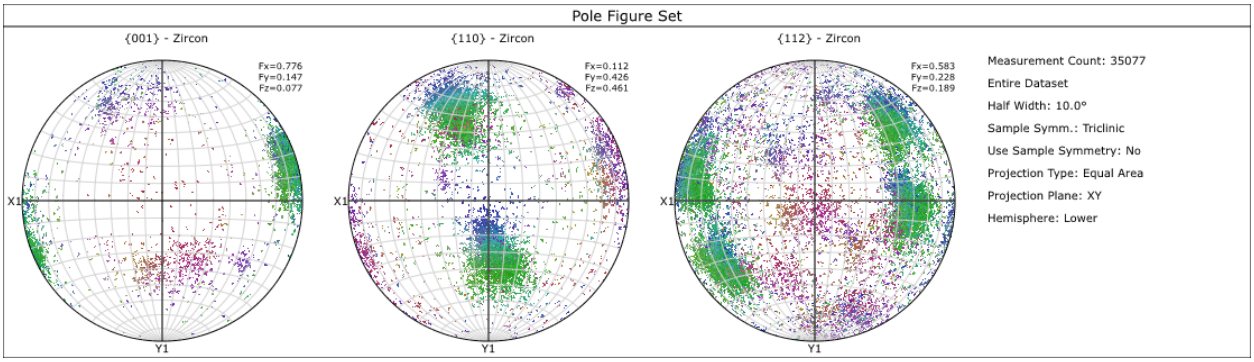
Pole Figure Set
{001} - Zircon
Fx=0.776
Fy=0.147
Fz=0.077
{110} - Zircon
Fx=0.112
Fy=0.426
Fz=0.461
{112} - Zircon
Fx=0.583
Fy=0.228
Fz=0.189
X1
Y1
Measurement Count: 35077
Entire Dataset
Half Width: 10.0°
Sample Symm.: Triclinic
Use Sample Symmetry: No
Projection Type: Equal Area
Projection Plane: XY
Hemisphere: Lower

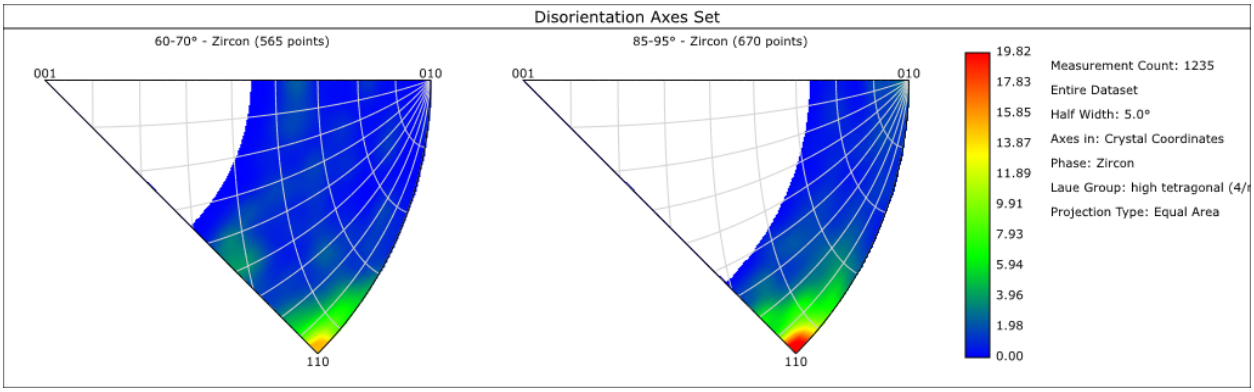
Disorientation Axes Set
60-70° - Zircon (565 points)
85-95° - Zircon (670 points)
001
010
110
19.82
17.83
15.85
13.87
11.89
9.91
7.93
5.94
3.96
1.98
0.00
Measurement Count: 1235
Entire Dataset
Half Width: 5.0°
Axes in: Crystal Coordinates
Phase: Zircon
Laue Group: high tetragonal (4/
Projection Type: Equal Area

M118

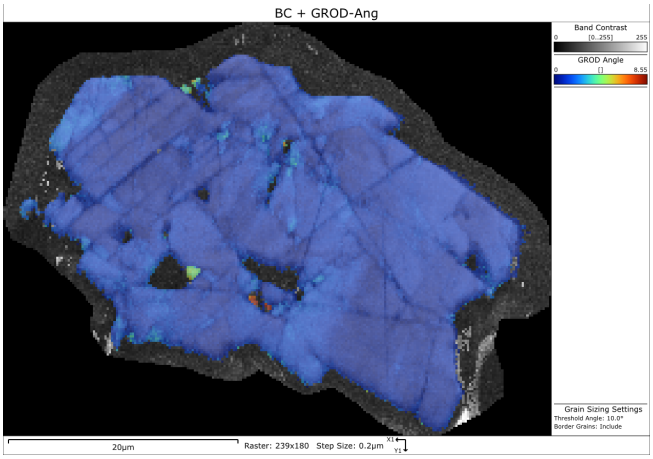
BC + GROD-Ang
Band Contrast
0 [0..255] 255
GROD Angle
0 [] 8.55
Grain Sizing Settings
Threshold Angle: 10.0°
Border Grains: Include
20µm
Raster: 239x180 Step Size: 0.2µm

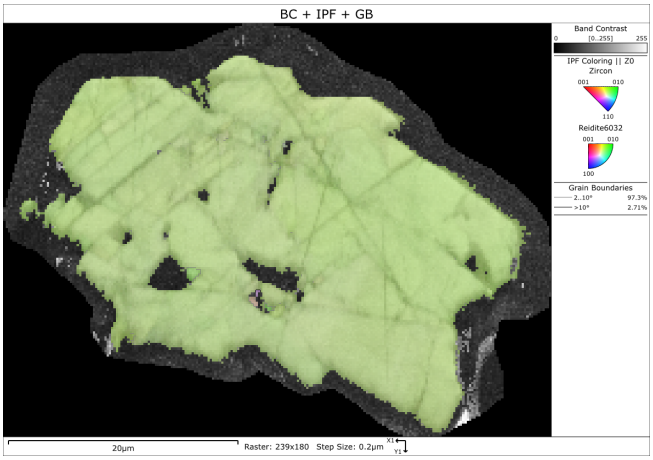
BC + IPF + GB
Band Contrast
0 [0..255] 255
IPF Coloring || Z0
Zircon
001 010
100
Reidite6032
001 010
100
Grain Boundaries
2..10° 97.3%
>10° 2.71%
20µm
Raster: 239x180 Step Size: 0.2µm

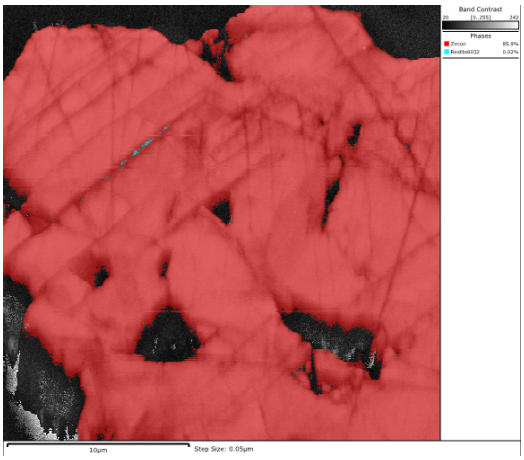
Band Contrast
Phases
10µm
Step Size: 0.05µm

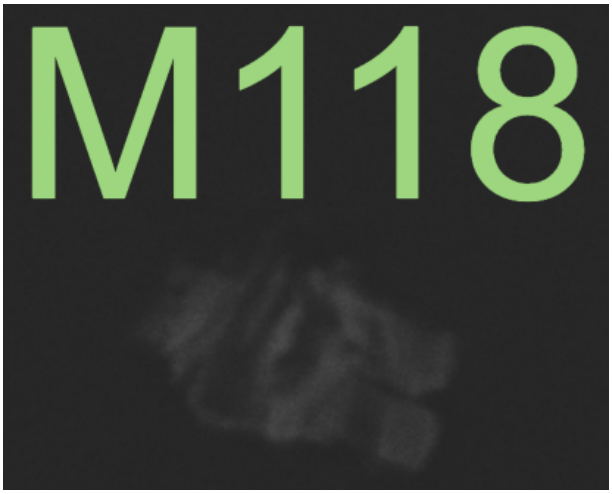
M118

M119

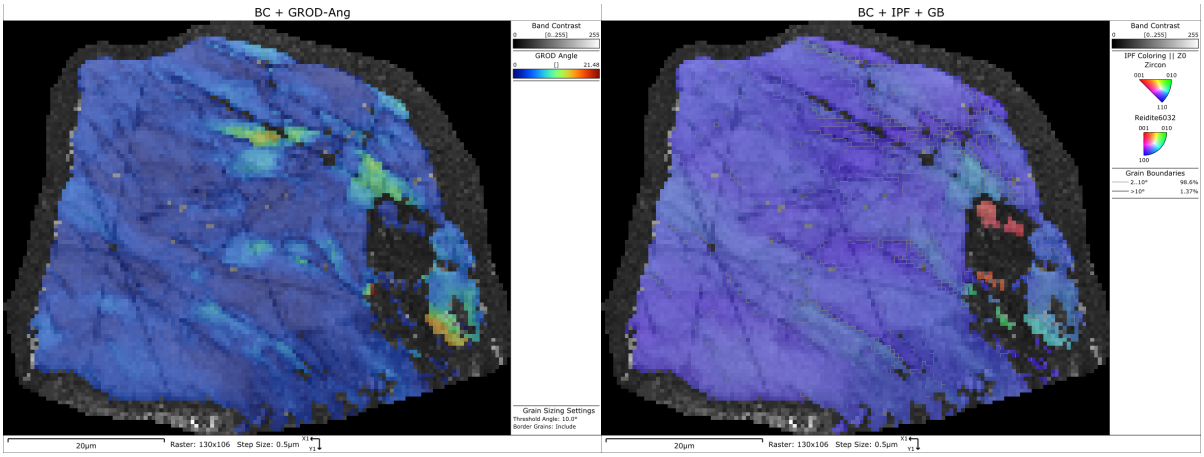
BC + GROD-Ang
Band Contrast
GROD Angle
Grain Sizing Settings
20µm
Raster: 130x106 Step Size: 0.5µm
BC + IPF + GB
Band Contrast
IPF Coloring || ZO
Zircon
Reidite6032
Grain Boundaries
20µm
Raster: 130x106 Step Size: 0.5µm

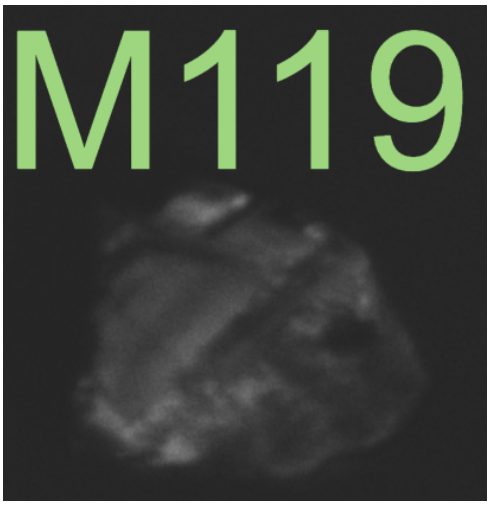
M119

M120

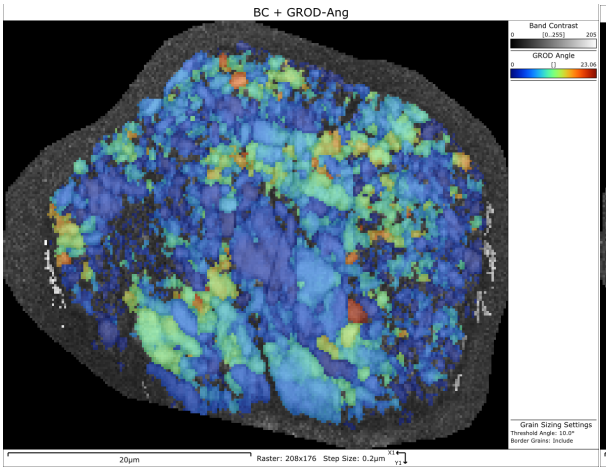
BC + GROD-Ang
Band Contrast
GROD Angle
Grain Sizing Settings
20µm
Raster: 208x176 Step Size: 0.2µm

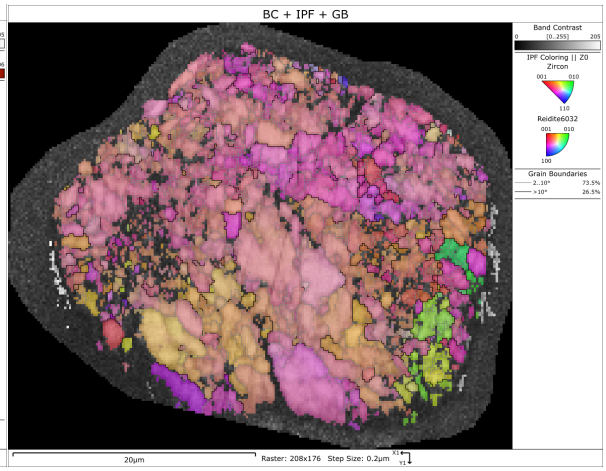
BC + IPF + GB
Band Contrast
IPF Coloring || Z0
Zircon
Reidite6032
Grain Boundaries
20µm
Raster: 208x176 Step Size: 0.2µm


M120

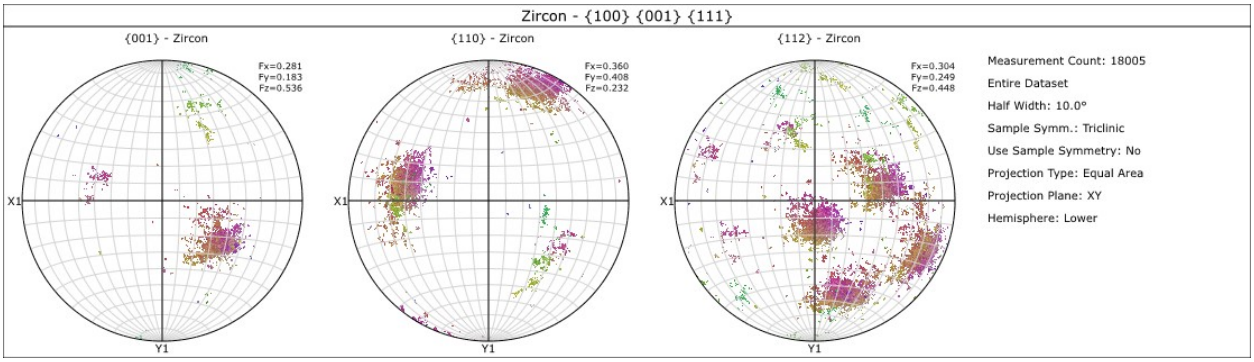
Zircon - {100} {001} {111}
{001} - Zircon
Fx=0.281
Fy=0.183
Fz=0.536
{110} - Zircon
Fx=0.360
Fy=0.408
Fz=0.232
{112} - Zircon
Fx=0.304
Fy=0.249
Fz=0.448
X1
Y1
Measurement Count: 18005
Entire Dataset
Half Width: 10.0°
Sample Symm.: Triclinic
Use Sample Symmetry: No
Projection Type: Equal Area
Projection Plane: XY
Hemisphere: Lower

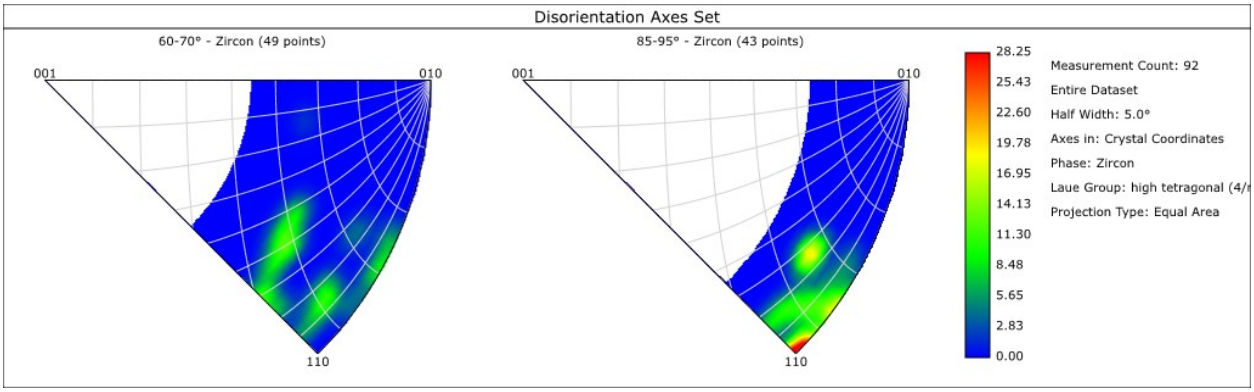
Disorientation Axes Set
60-70° - Zircon (49 points)
85-95° - Zircon (43 points)
001
010
110
28.25
25.43
22.60
19.78
16.95
14.13
11.30
8.48
5.65
2.83
0.00
Measurement Count: 92
Entire Dataset
Half Width: 5.0°
Axes in: Crystal Coordinates
Phase: Zircon
Projection Type: Equal Area

M121

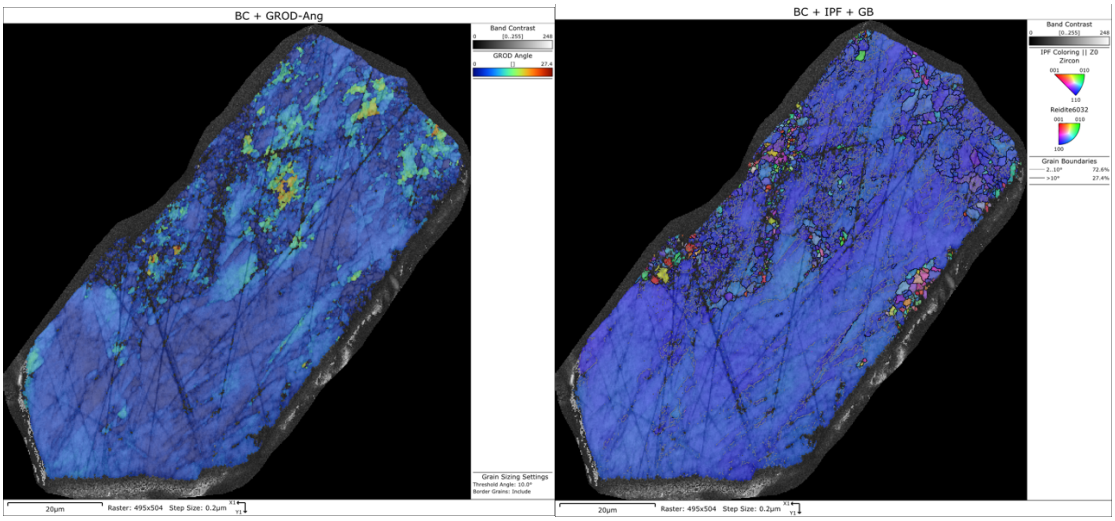
BC + GROD-Ang
Band Contrast
GROD Angle
Grain Sizing Settings
20µm
Raster: 495x504 Step Size: 0.2µm
BC + IPF + GB
Band Contrast
IPF Coloring || Z0
Zircon
Reidite6032
Grain Boundaries
20µm
Raster: 495x504 Step Size: 0.2µm

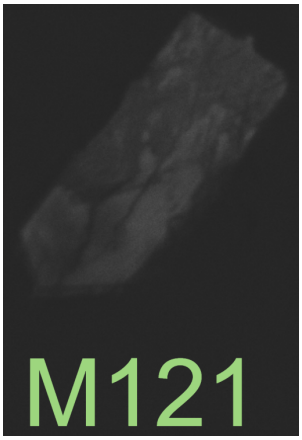
M121

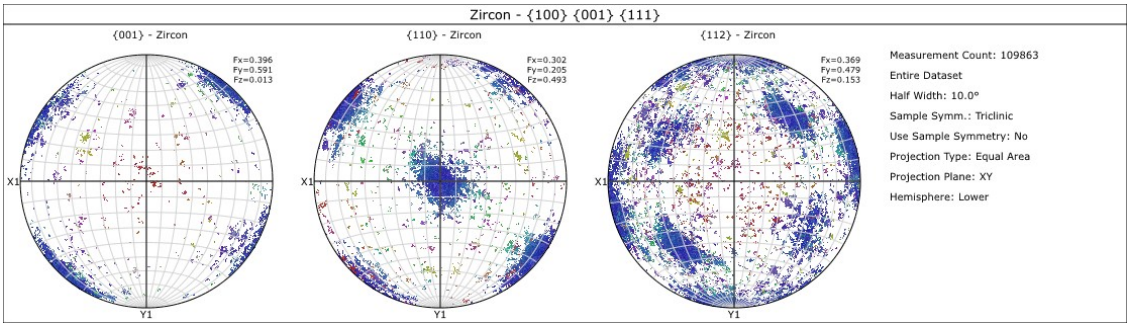
Zircon - {100} {001} {111}
{001} - Zircon
Fx=0.396
Fy=0.591
Fz=0.013
{110} - Zircon
Fx=0.302
Fy=0.205
Fz=0.493
{112} - Zircon
Fx=0.369
Fy=0.479
Fz=0.153
X1
Y1
Measurement Count: 109863
Entire Dataset
Half Width: 10.0°
Sample Symm.: Triclinic
Use Sample Symmetry: No
Projection Type: Equal Area
Projection Plane: XY
Hemisphere: Lower

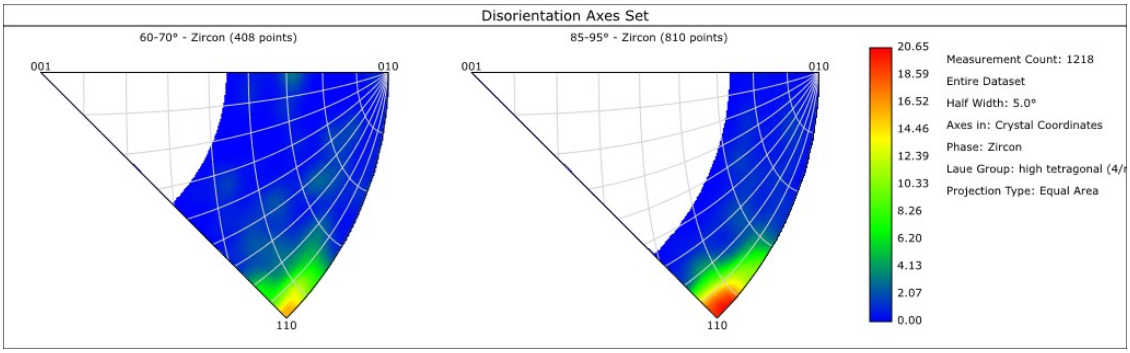
Disorientation Axes Set
60-70° - Zircon (408 points)
85-95° - Zircon (810 points)
001
010
110
20.65
18.59
16.52
14.46
12.39
10.33
8.26
6.20
4.13
2.07
0.00
Measurement Count: 1218
Entire Dataset
Half Width: 5.0°
Axes in: Crystal Coordinates
Phase: Zircon
Projection Type: Equal Area

M122

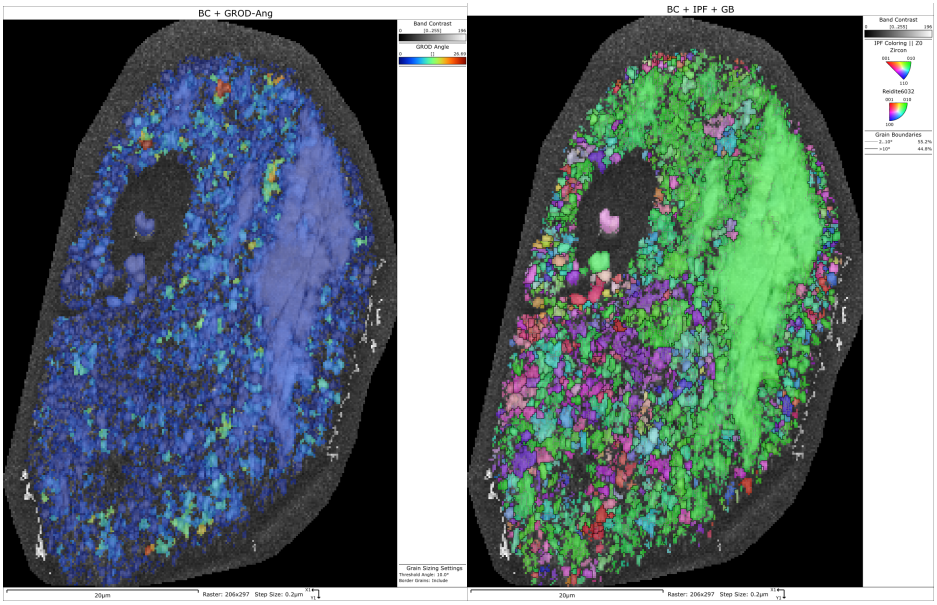
BC + GROD-Ang
BC + IPF + GB

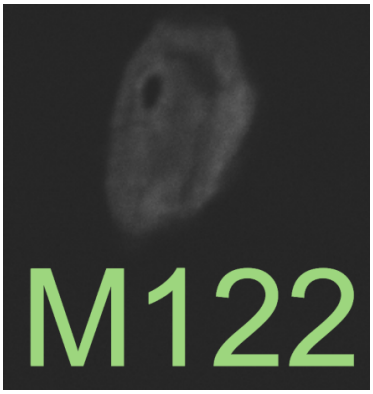
M122

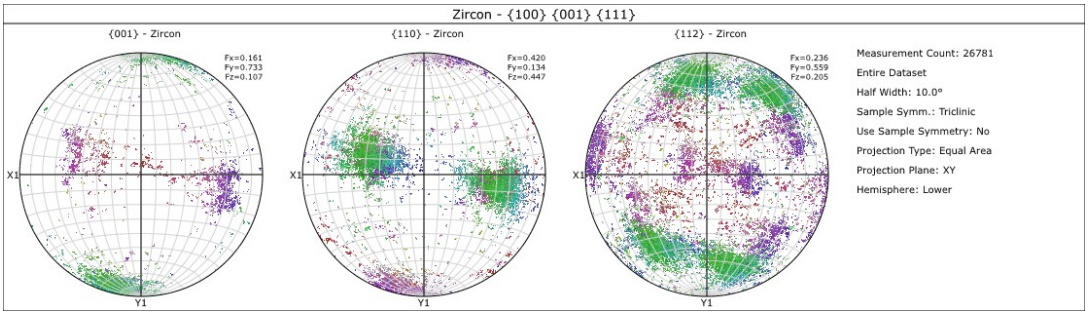
Zircon - {100} {001} {111}
{001} - Zircon
{110} - Zircon
{112} - Zircon
Measurement Count: 26781
Entire Dataset
Half Width: 10.0°
Sample Symm.: Triclinic
Use Sample Symmetry: No
Projection Type: Equal Area
Projection Plane: XY
Hemisphere: Lower

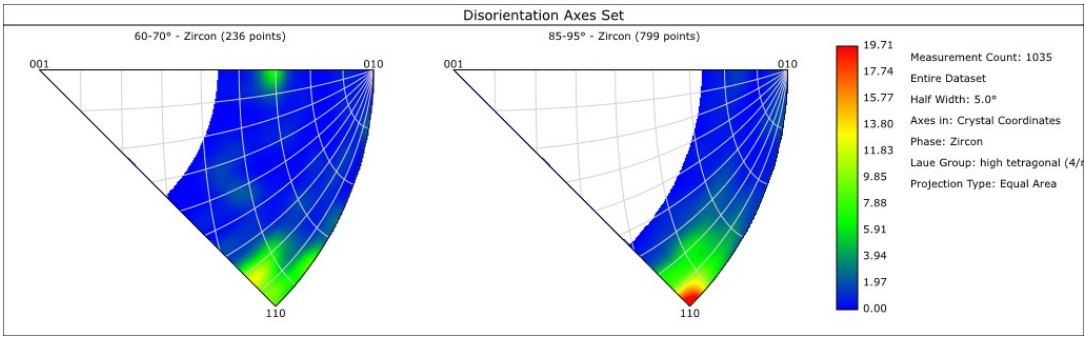
Disorientation Axes Set
60-70° - Zircon (236 points)
85-95° - Zircon (799 points)
001
010
110
19.71
17.74
15.77
13.80
11.83
9.85
7.88
5.91
3.94
1.97
0.00
Measurement Count: 1035
Entire Dataset
Half Width: 5.0°
Axes in: Crystal Coordinates
Phase: Zircon
Projection Type: Equal Area

M123

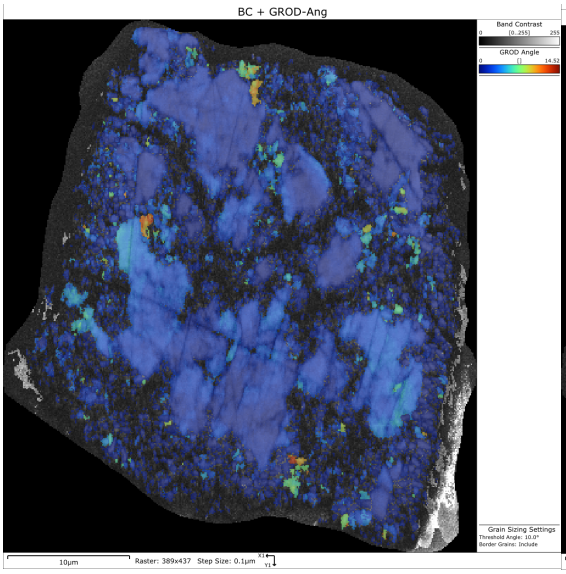
BC + GROD-Ang
Band Contrast
GROD Angle
Grain Sizing Settings
10µm
Raster: 389x437 Step Size: 0.1µm

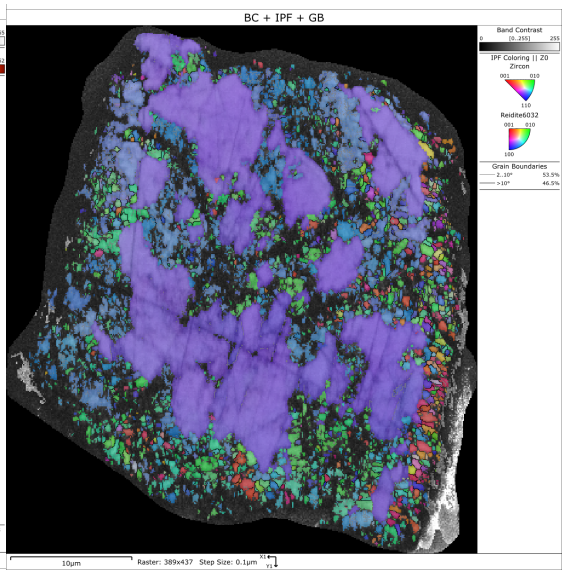
BC + IPF + GB
Band Contrast
IPF Coloring || Z0
Zircon
Reidite6032
Grain Boundaries
10µm
Raster: 389x437 Step Size: 0.1µm

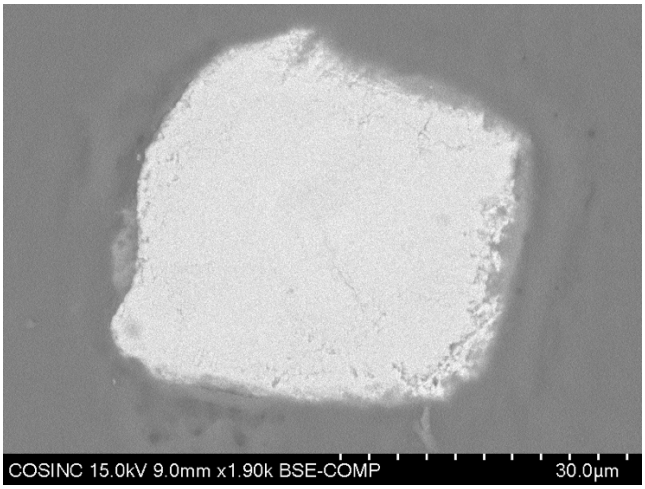
COSINC 15.0kV 9.0mm x1.90k BSE-COMP
30.0µm

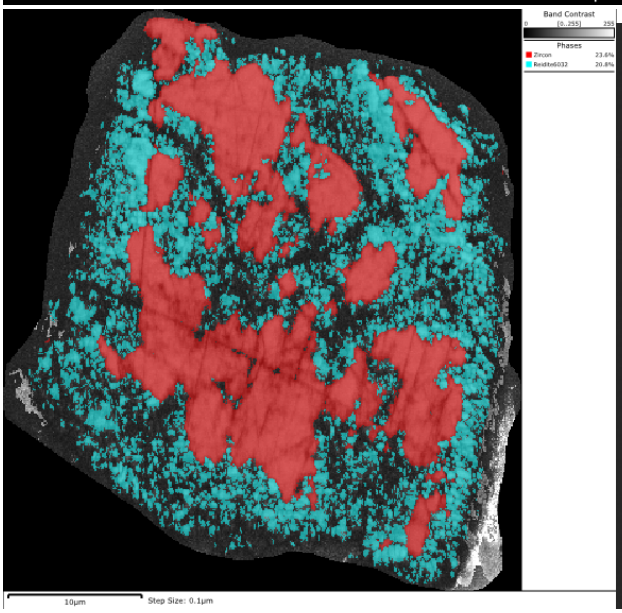
Band Contrast
Phases
Zircon
Reidite6032
10µm
Step Size: 0.1µm


M123

M124

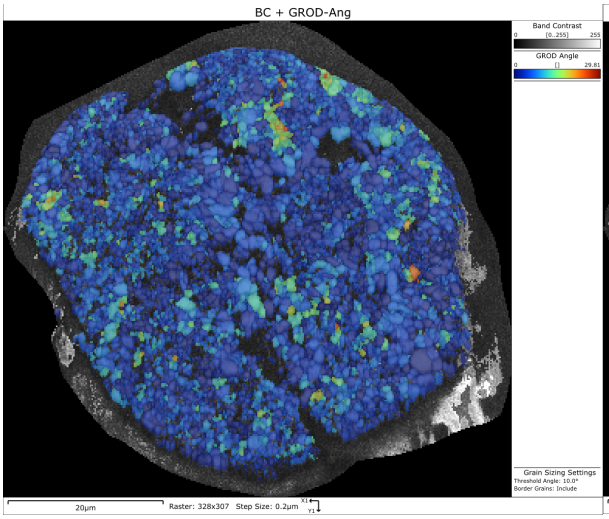
BC + GROD-Ang
Band Contrast
GROD Angle
Grain Sizing Settings
20µm
Raster: 328x307 Step Size: 0.2µm

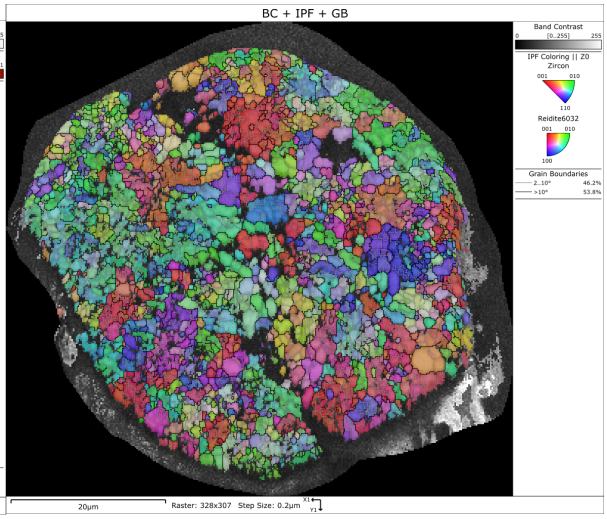
BC + IPF + GB
Band Contrast
IPF Coloring || Z0
Zircon
Reidite6032
Grain Boundaries
20µm
Raster: 328x307 Step Size: 0.2µm

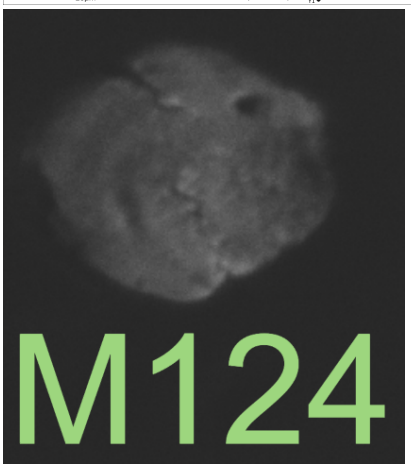
M124

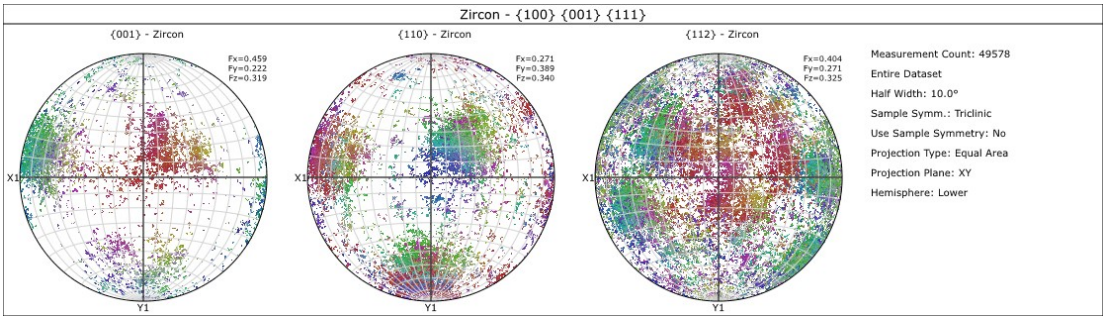
Zircon - {100} {001} {111}
{001} - Zircon
Fx=0.459
Fy=0.222
Fz=0.319
{110} - Zircon
Fx=0.271
Fy=0.389
Fz=0.340
{112} - Zircon
Fx=0.404
Fy=0.271
Fz=0.325
Measurement Count: 49578
Entire Dataset
Half Width: 10.0°
Sample Symm.: Triclinic
Use Sample Symmetry: No
Projection Type: Equal Area
Projection Plane: XY
Hemisphere: Lower

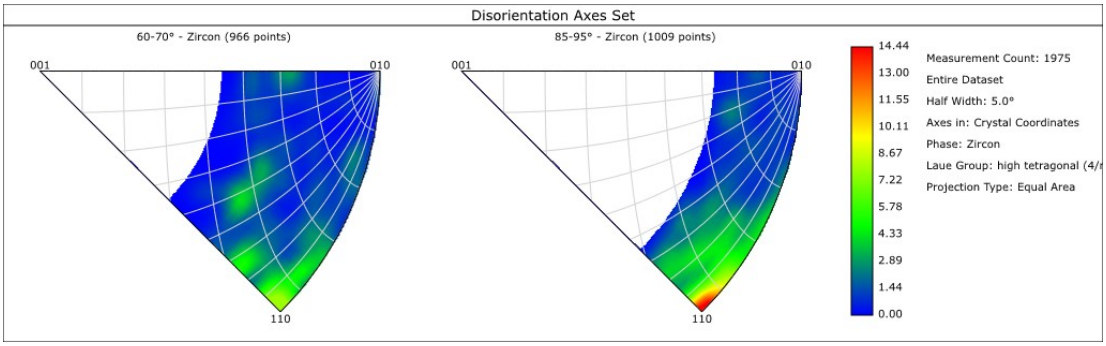
Disorientation Axes Set
60-70° - Zircon (966 points)
85-95° - Zircon (1009 points)
001
010
110
14.44
13.00
11.55
10.11
8.67
7.22
5.78
4.33
2.89
1.44
0.00
Measurement Count: 1975
Entire Dataset
Half Width: 5.0°
Axes in: Crystal Coordinates
Phase: Zircon
Projection Type: Equal Area

M125

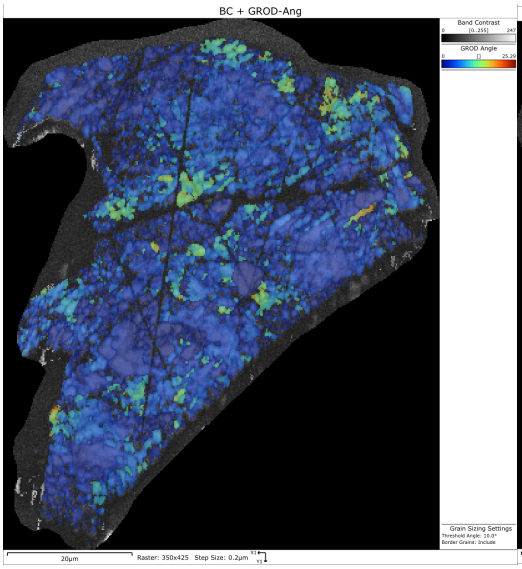
BC + GROD-Ang
Band Contrast
GROD Angle
Grain Sizing Settings
Raster: 350x425 Step Size: 0.2µm

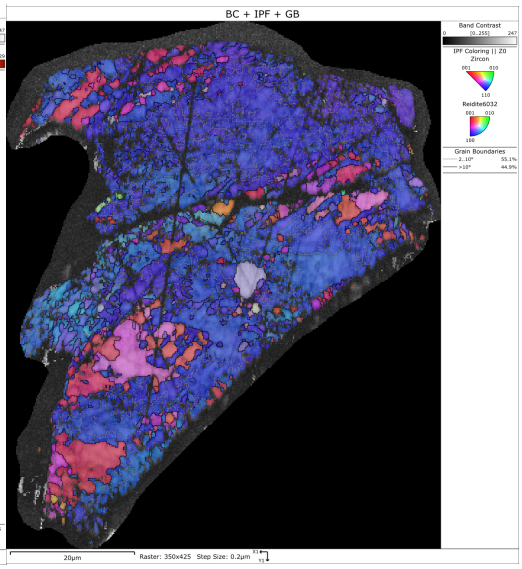
BC + IPF + GB
Band Contrast
IPF Coloring || ZD
Zircon
Reidite6032
Grain Boundaries
Raster: 350x425 Step Size: 0.2µm


M125

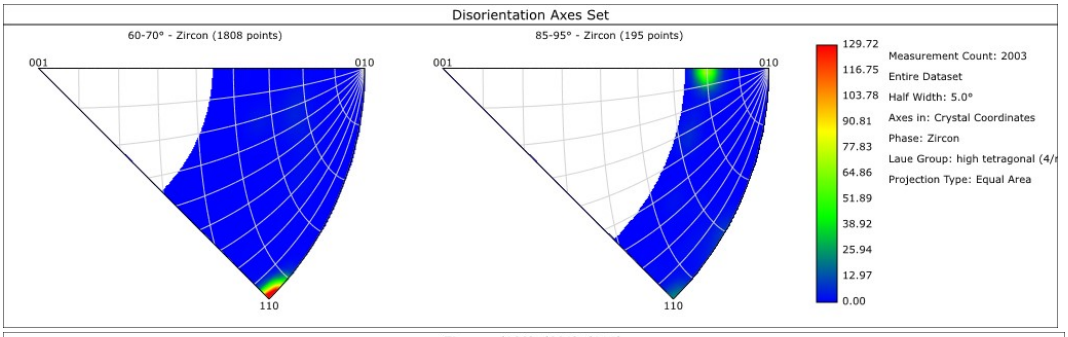
Disorientation Axes Set
60-70° - Zircon (1808 points)
85-95° - Zircon (195 points)
001
010
110
129.72
116.75
103.78
90.81
77.83
64.86
51.89
38.92
25.94
12.97
0.00
Measurement Count: 2003
Entire Dataset
Half Width: 5.0°
Axes in: Crystal Coordinates
Phase: Zircon
Projection Type: Equal Area

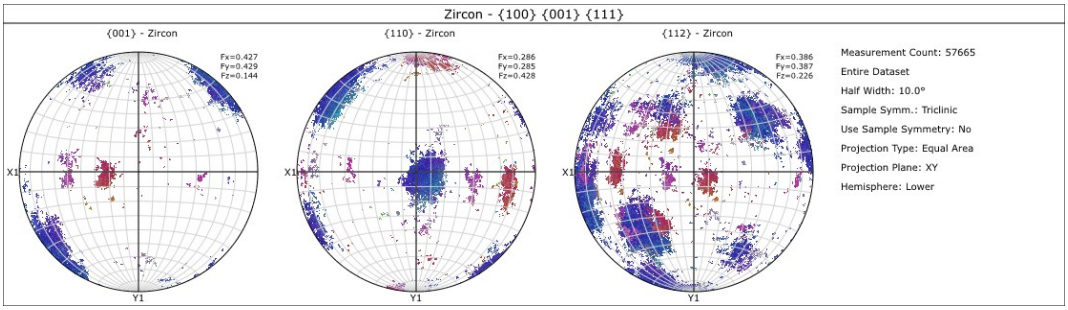
Zircon - {100} {001} {111}
{001} - Zircon
{110} - Zircon
{112} - Zircon
Fx=0.427
Fy=0.429
Fz=0.144
Fx=0.286
Fy=0.285
Fz=0.428
Fx=0.386
Fy=0.387
Fz=0.226
X1
Y1
Measurement Count: 57665
Entire Dataset
Half Width: 10.0°
Sample Symm.: Triclinic
Use Sample Symmetry: No
Projection Type: Equal Area
Projection Plane: XY
Hemisphere: Lower

M126

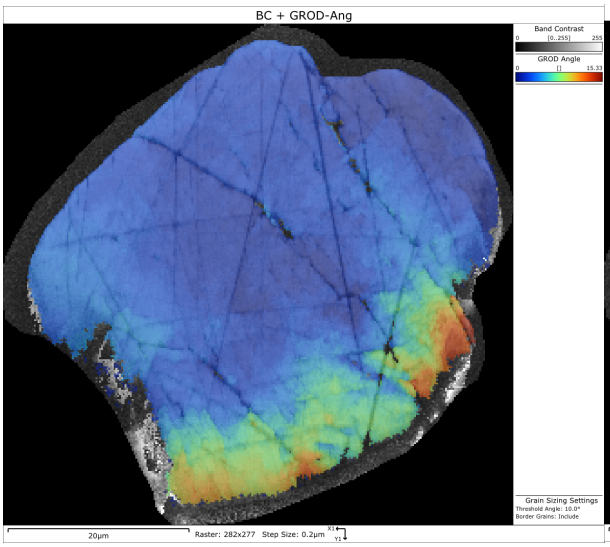
BC + GROD-Ang
Band Contrast
GROD Angle
Grain Sizing Settings
20µm
Raster: 282x277 Step Size: 0.2µm

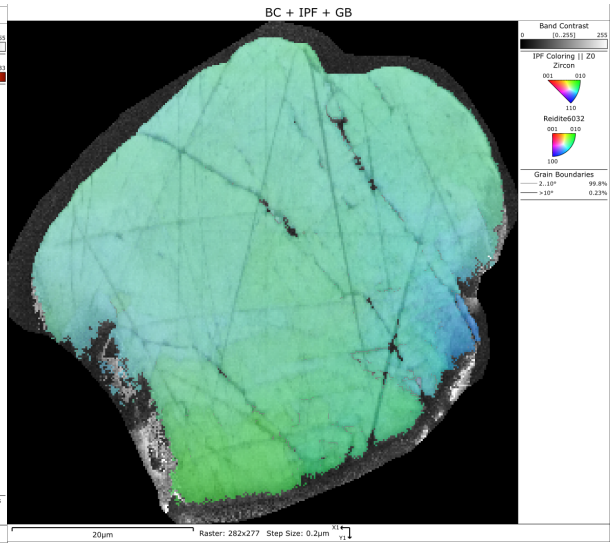
BC + IPF + GB
Band Contrast
IPF Coloring || Z0
Zircon
Reidite6032
Grain Boundaries
20µm
Raster: 282x277 Step Size: 0.2µm

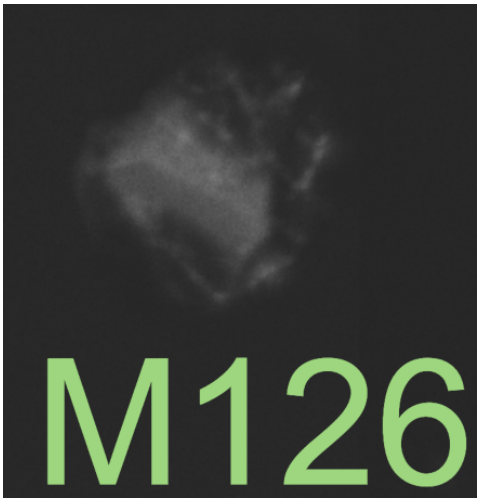
M126

M128

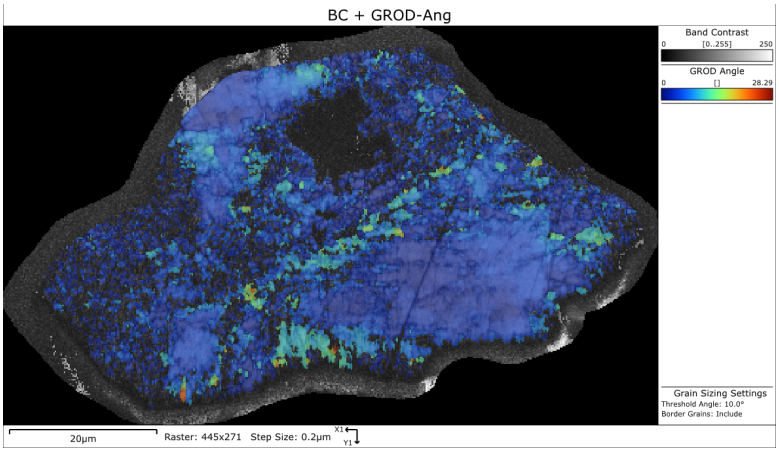
BC + GROD-Ang
Band Contrast
0 [0..255] 250
GROD Angle
0 [] 28.29
Grain Sizing Settings
Threshold Angle: 10.0°
Border Grains: Include
20µm
Raster: 445x271 Step Size: 0.2µm

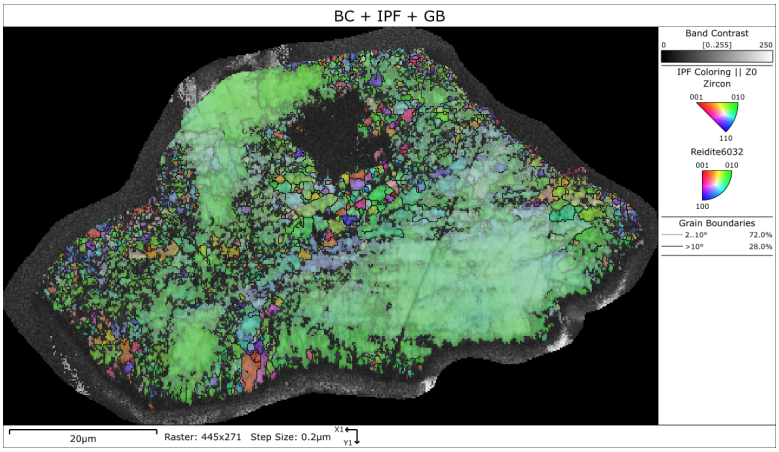
BC + IPF + GB
Band Contrast
0 [0..255] 250
IPF Coloring || Z0
Zircon
001 010
110
Reidite6032
001 010
100
Grain Boundaries
2..10° 72.0%
>10° 28.0%
20µm
Raster: 445x271 Step Size: 0.2µm

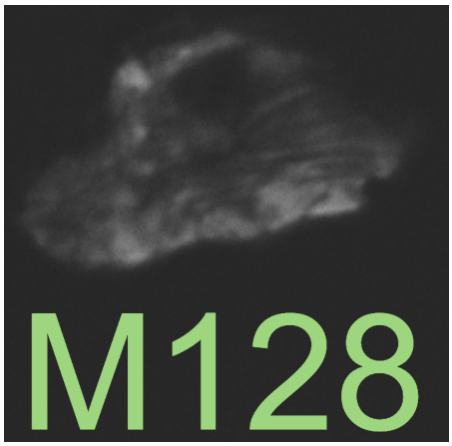
M128

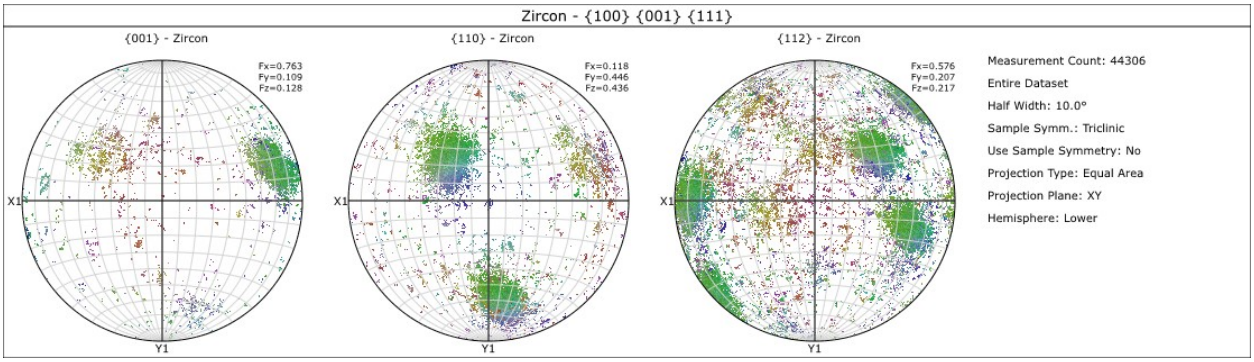
Zircon - {100} {001} {111}
{001} - Zircon
Fx=0.763
Fy=0.109
Fz=0.128
{110} - Zircon
Fx=0.118
Fy=0.446
Fz=0.436
{112} - Zircon
Fx=0.576
Fy=0.207
Fz=0.217
X1
Y1
Measurement Count: 44306
Entire Dataset
Half Width: 10.0°
Sample Symm.: Triclinic
Use Sample Symmetry: No
Projection Type: Equal Area
Projection Plane: XY
Hemisphere: Lower

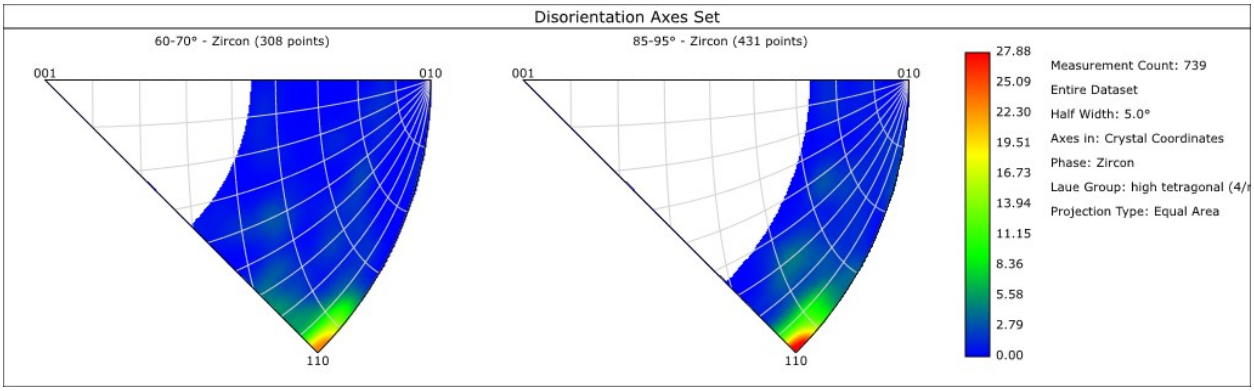
Disorientation Axes Set
60-70° - Zircon (308 points)
85-95° - Zircon (431 points)
001
010
110
27.88
25.09
22.30
19.51
16.73
13.94
11.15
8.36
5.58
2.79
0.00
Measurement Count: 739
Entire Dataset
Half Width: 5.0°
Axes in: Crystal Coordinates
Phase: Zircon
Laue Group: high tetragonal (4/
Projection Type: Equal Area

M129

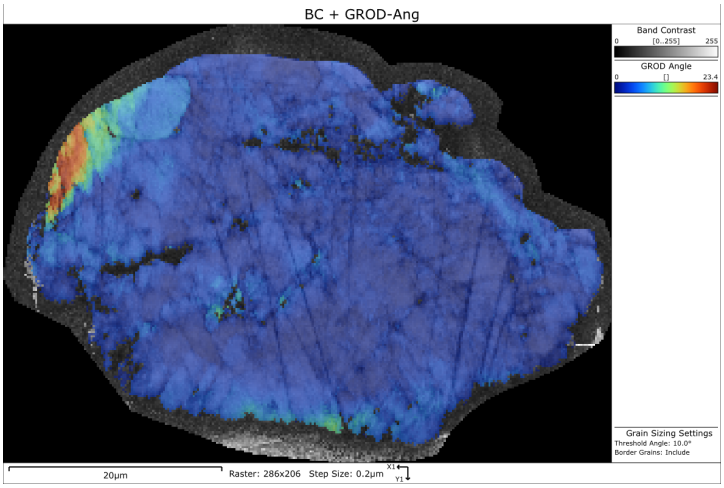
BC + GROD-Ang
Band Contrast
0 [0..255] 255
GROD Angle
0 [] 23.4
Grain Sizing Settings
Threshold Angle: 10.0°
Border Grains: Include
20µm
Raster: 286x206 Step Size: 0.2µm

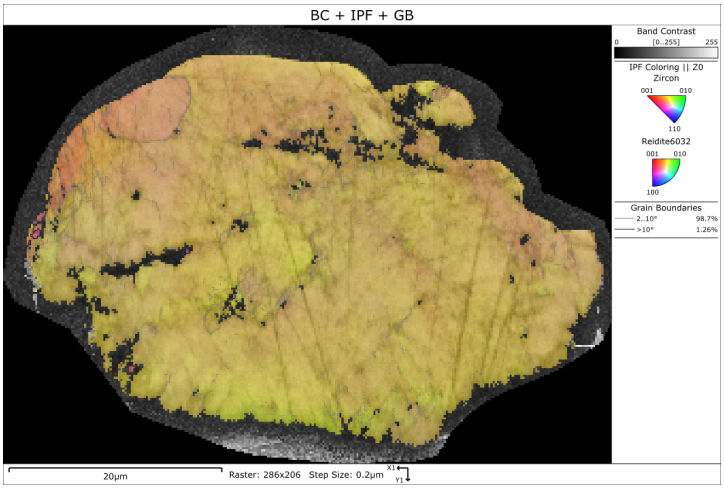
BC + IPF + GB
Band Contrast
0 [0..255] 255
IPF Coloring || Z0
Zircon
001 010
110
Reidite6032
001 010
100
Grain Boundaries
2..10° 98.7%
>10° 1.26%
20µm
Raster: 286x206 Step Size: 0.2µm

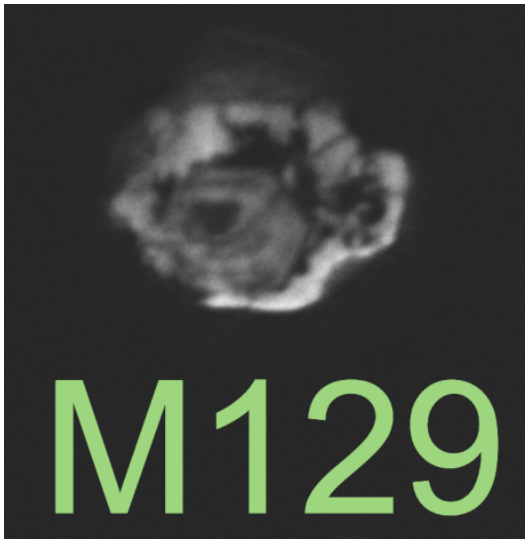
M129

M132

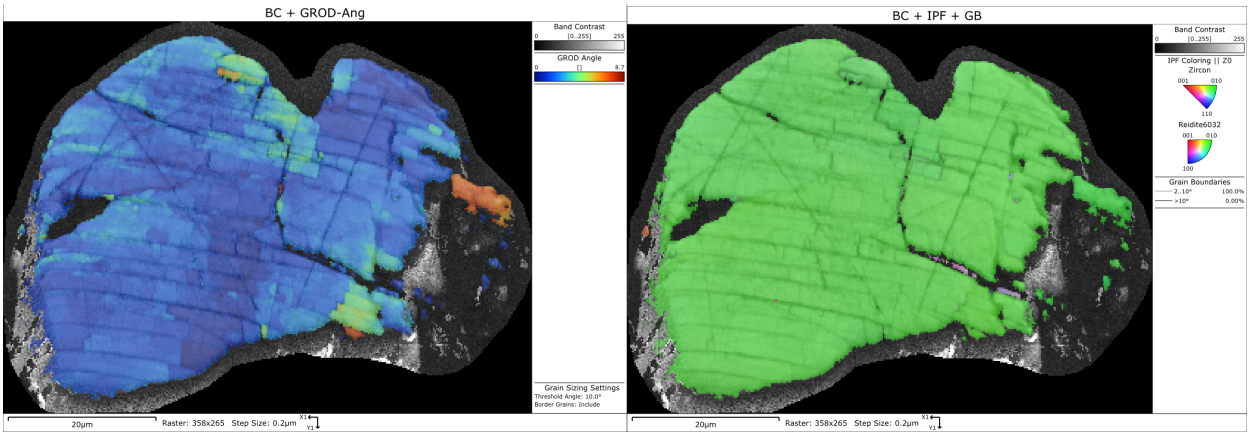
BC + GROD-Ang
Band Contrast
GROD Angle
Grain Sizing Settings
20µm
Raster: 358x265 Step Size: 0.2µm
BC + IPF + GB
Band Contrast
IPF Coloring || Z0
Zircon
Reidite6032
Grain Boundaries
20µm
Raster: 358x265 Step Size: 0.2µm

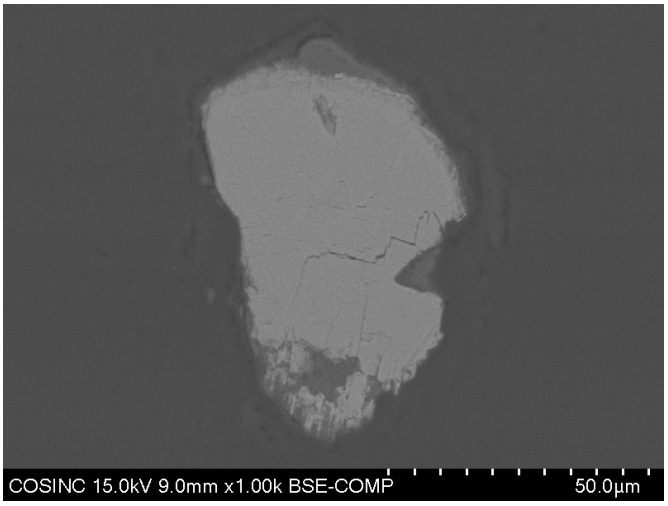
COSINC 15.0kV 9.0mm x1.00k BSE-COMP
50.0µm

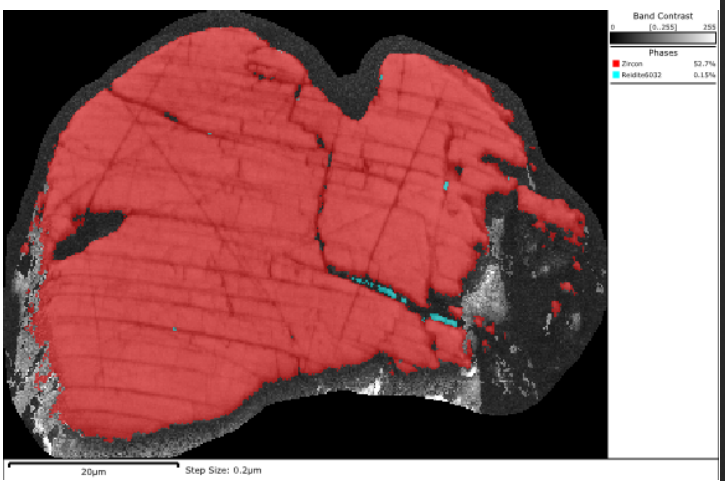
Band Contrast
Phases
Zircon
Reidite6032
20µm
Step Size: 0.2µm

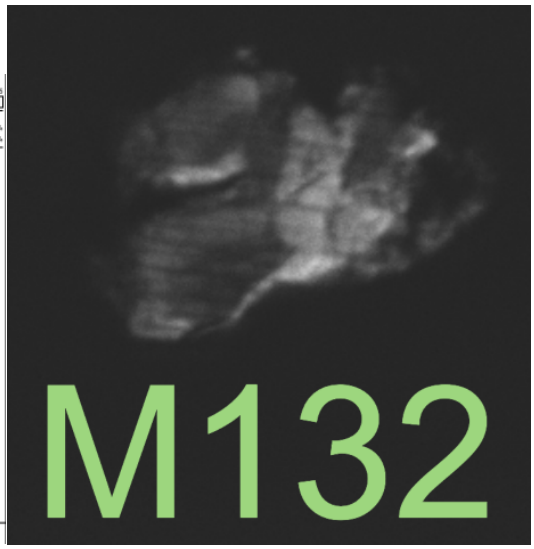
M132

M133

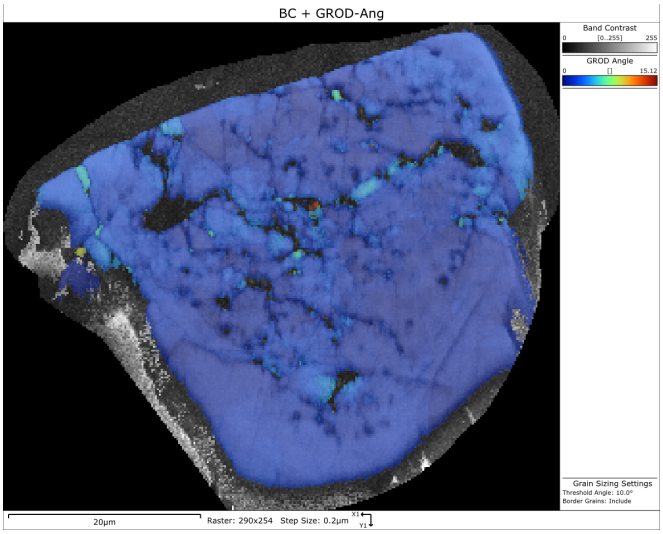
BC + GROD-Ang
Band Contrast
0 [0..255] 255
GROD Angle
0 [] 15.12
Grain Sizing Settings
Threshold Angle: 10.0°
Border Grains: Include
20µm
Raster: 290x254 Step Size: 0.2µm

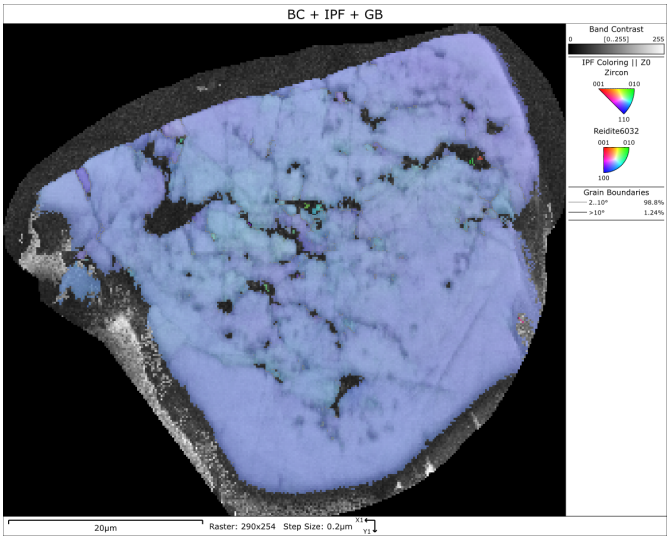
BC + IPF + GB
Band Contrast
0 [0..255] 255
IPF Coloring || Z0
Zircon
001 010
110
Reldite6032
001 010
100
Grain Boundaries
2..10° 98.8%
>10° 1.24%
20µm
Raster: 290x254 Step Size: 0.2µm


M133

M137

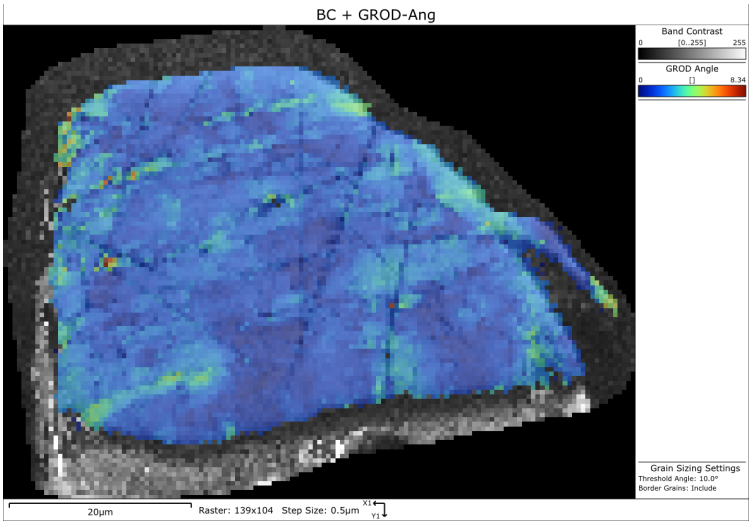
BC + GROD-Ang
Band Contrast
0 [0..255] 255
GROD Angle
0 [] 8.34
Grain Sizing Settings
Threshold Angle: 10.0°
Border Grains: Include
20µm
Raster: 139x104 Step Size: 0.5µm

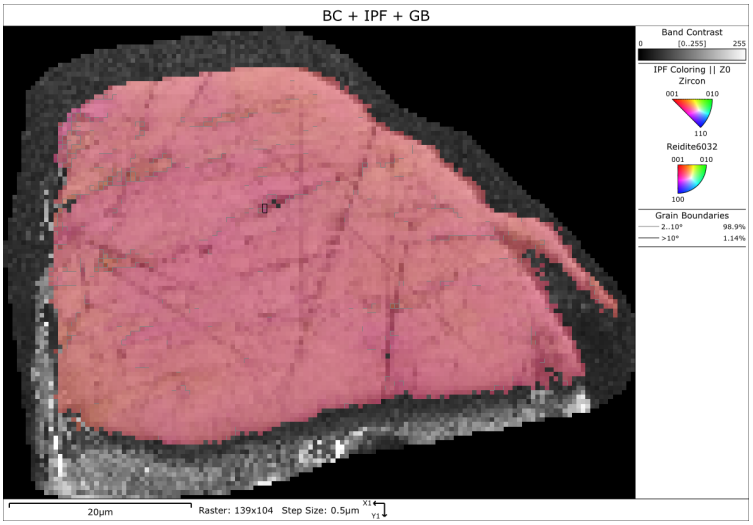
BC + IPF + GB
Band Contrast
0 [0..255] 255
IPF Coloring || Z0
Zircon
001 010
110
Reidite6032
001 010
100
Grain Boundaries
2..10° 98.9%
>10° 1.14%
20µm
Raster: 139x104 Step Size: 0.5µm

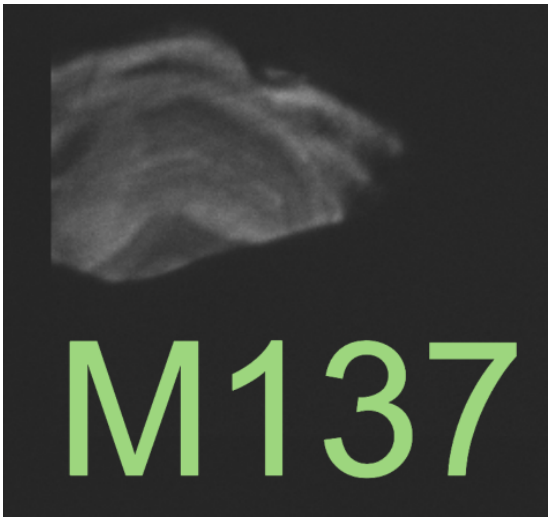
M137

M138

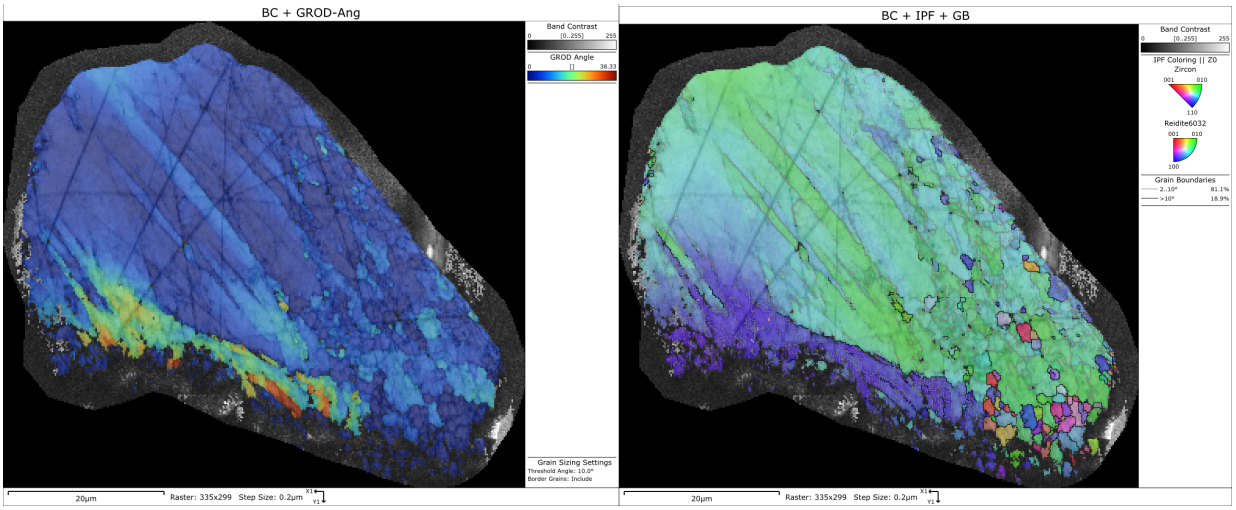
BC + GROD-Ang
Band Contrast
GROD Angle
Grain Sizing Settings
20µm
Raster: 335x299 Step Size: 0.2µm
BC + IPF + GB
Band Contrast
IPF Coloring || Z0 Zircon
Reidite6032
Grain Boundaries
20µm
Raster: 335x299 Step Size: 0.2µm

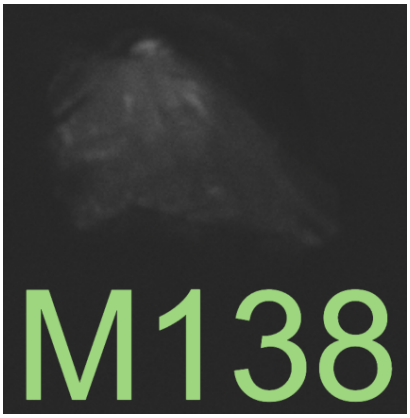
M138

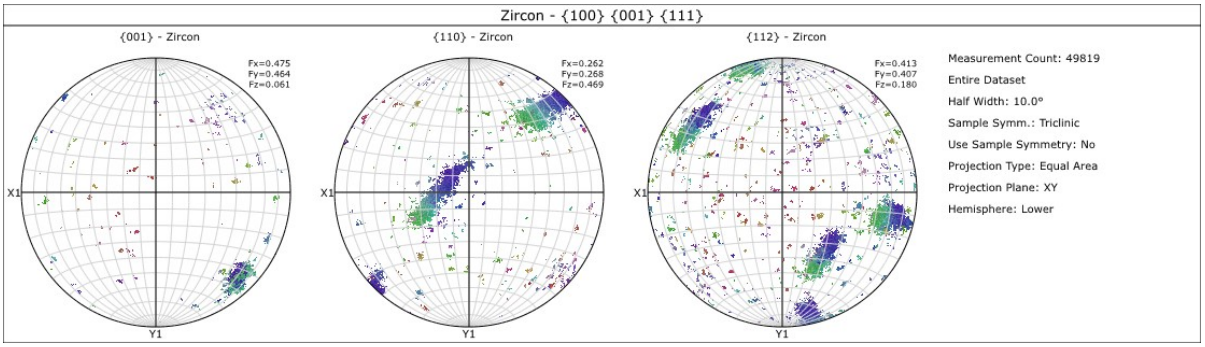
Zircon - {100} {001} {111}
{001} - Zircon
Fx=0.475
Fy=0.464
Fz=0.061
{110} - Zircon
Fx=0.262
Fy=0.268
Fz=0.469
{112} - Zircon
Fx=0.413
Fy=0.407
Fz=0.180
X1
Y1
Measurement Count: 49819
Entire Dataset
Half Width: 10.0°
Sample Symm.: Triclinic
Use Sample Symmetry: No
Projection Type: Equal Area
Projection Plane: XY
Hemisphere: Lower

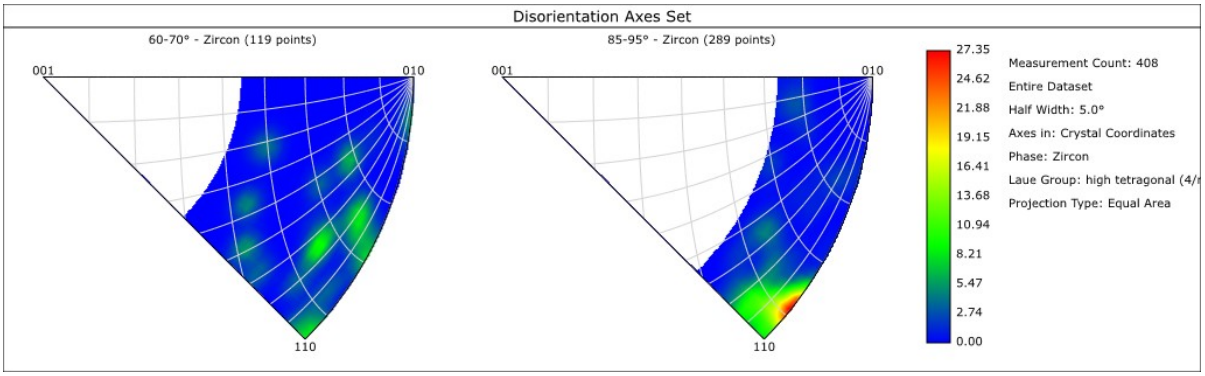
Disorientation Axes Set
60-70° - Zircon (119 points)
85-95° - Zircon (289 points)
001
010
110
27.35
24.62
21.88
19.15
16.41
13.68
10.94
8.21
5.47
2.74
0.00
Measurement Count: 408
Entire Dataset
Half Width: 5.0°
Axes in: Crystal Coordinates
Phase: Zircon
Laue Group: high tetragonal (4/
Projection Type: Equal Area

M139

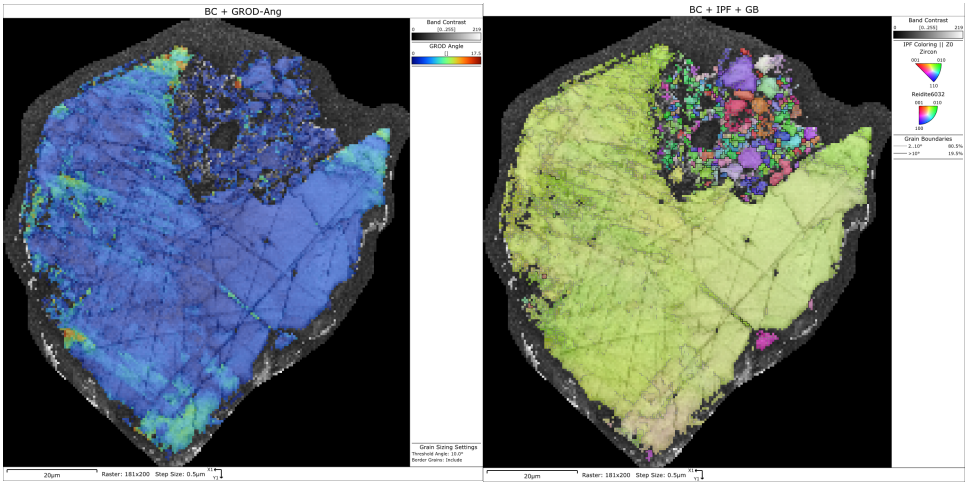
BC + GROD-Ang
BC + IPF + GB

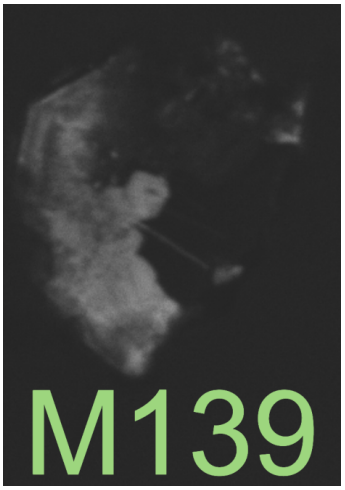
M139

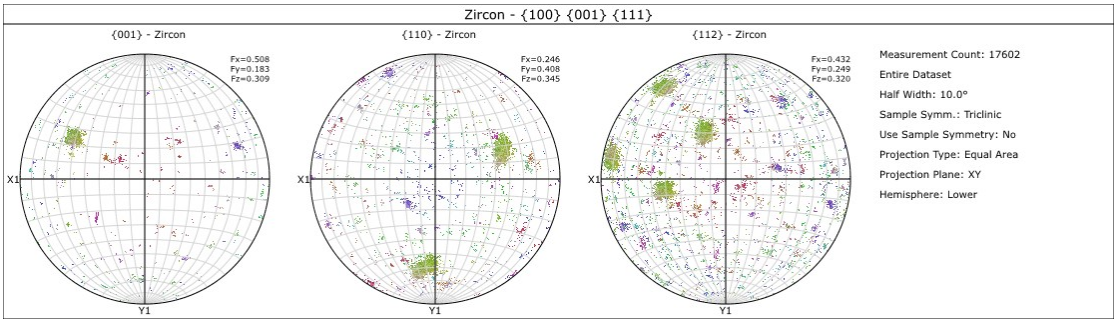
Zircon - {100} {001} {111}
{001} - Zircon
{110} - Zircon
{112} - Zircon
Measurement Count: 17602
Entire Dataset
Half Width: 10.0°
Sample Symm.: Triclinic
Use Sample Symmetry: No
Projection Type: Equal Area
Projection Plane: XY
Hemisphere: Lower

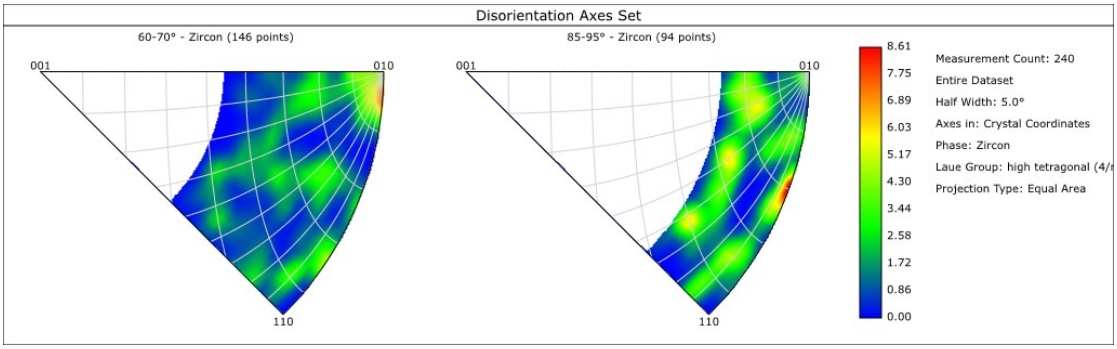
Disorientation Axes Set
60-70° - Zircon (146 points)
85-95° - Zircon (94 points)
Measurement Count: 240
Entire Dataset
Half Width: 5.0°
Axes in: Crystal Coordinates
Phase: Zircon
Projection Type: Equal Area

M140

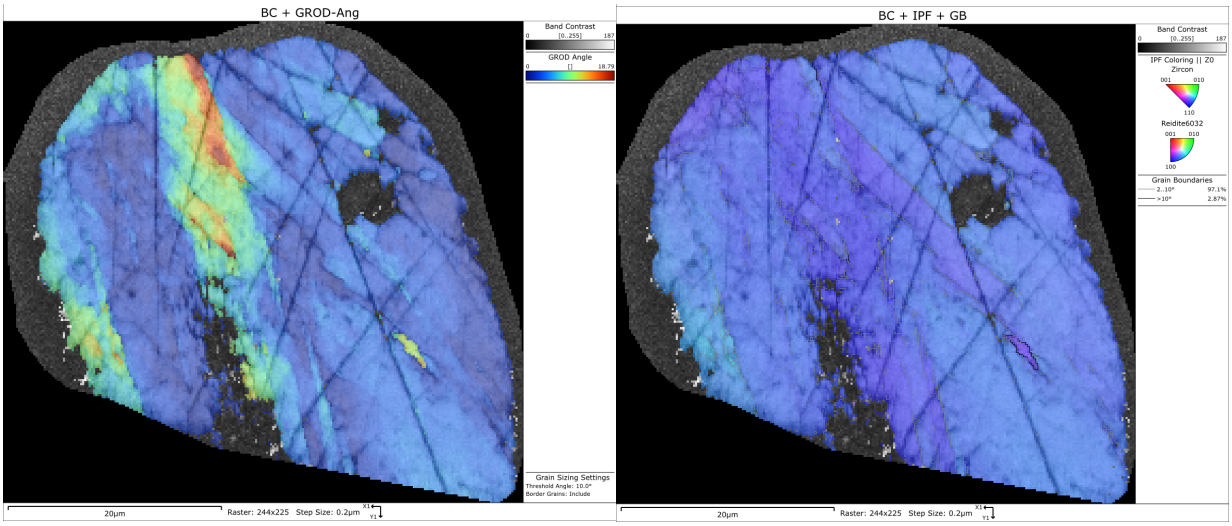
BC + GROD-Ang
Band Contrast
0 [0..255] 187
GROD Angle
0 [] 18.79
Grain Sizing Settings
Threshold Angle: 10.0°
Border Grains: Include
20µm
Raster: 244x225 Step Size: 0.2µm
BC + IPF + GB
Band Contrast
0 [0..255] 187
IPF Coloring || Z0
Zircon
001 010
110
Reidite6032
001 010
100
Grain Boundaries
2..10° 97.1%
>10° 2.87%
20µm
Raster: 244x225 Step Size: 0.2µm

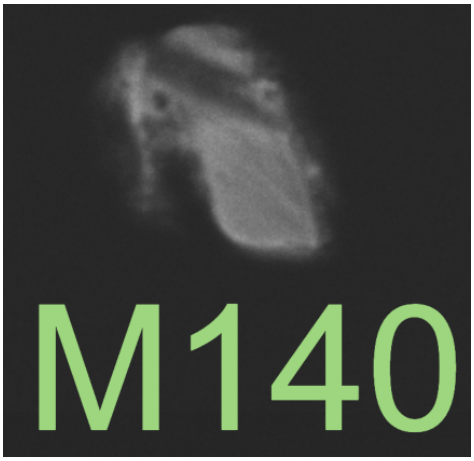
M140

M141

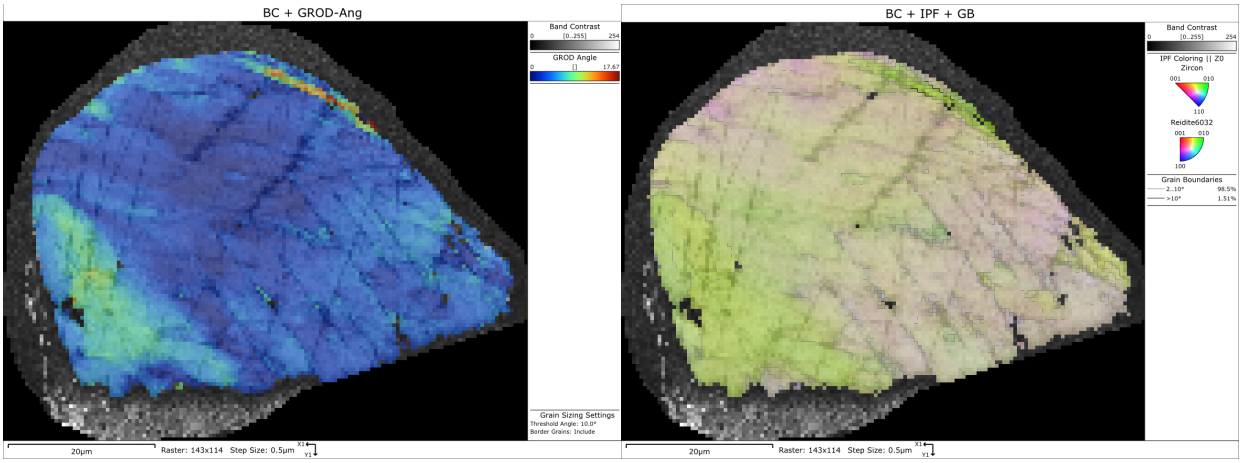
BC + GROD-Ang
Band Contrast
GROD Angle
Grain Sizing Settings
20µm
Raster: 143x114 Step Size: 0.5µm
BC + IPF + GB
Band Contrast
IPF Coloring || Z0
Zircon
Reidite6032
Grain Boundaries
20µm
Raster: 143x114 Step Size: 0.5µm

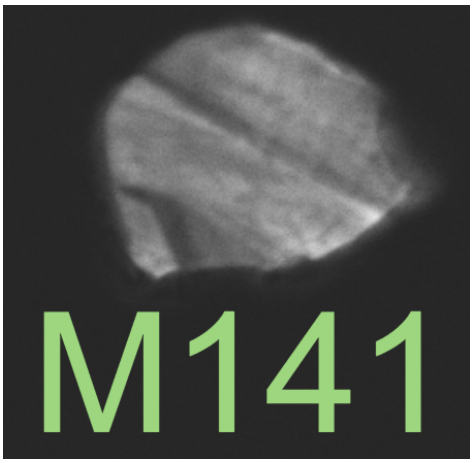
M141

M142

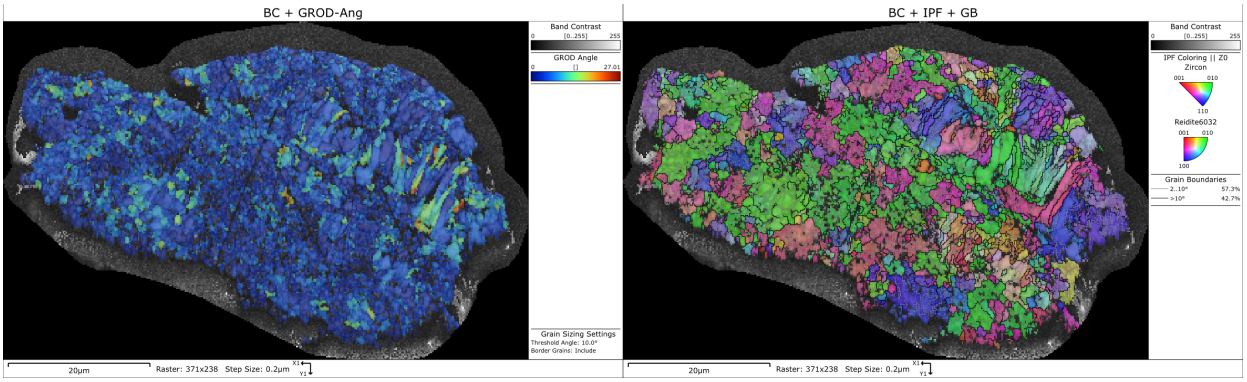
BC + GROD-Ang
Band Contrast
GROD Angle
Grain Sizing Settings
20µm
Raster: 371x238 Step Size: 0.2µm
BC + IPF + GB
Band Contrast
IPF Coloring || Z0
Zircon
Reidite6032
Grain Boundaries
20µm
Raster: 371x238 Step Size: 0.2µm

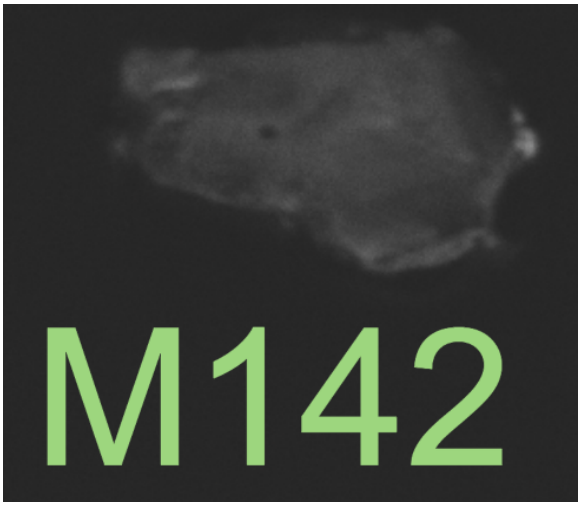
M142

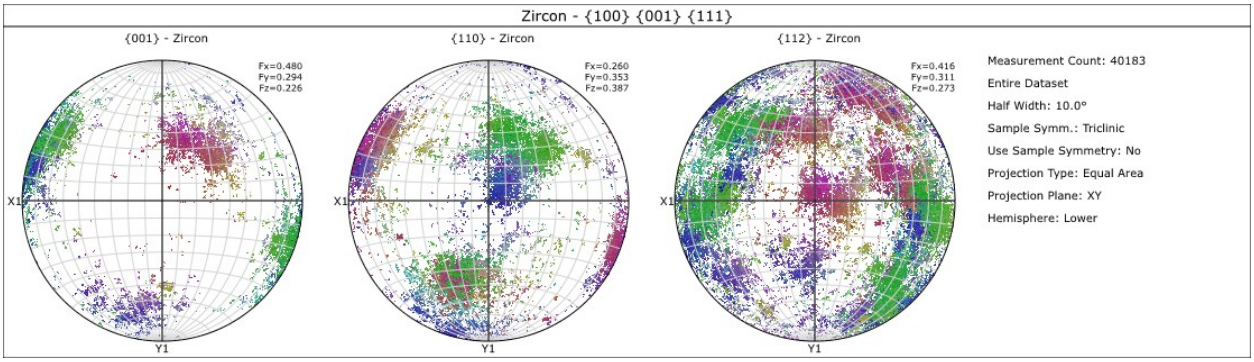
Zircon - {100} {001} {111}
{001} - Zircon
Fx=0.480
Fy=0.294
Fz=0.226
{110} - Zircon
Fx=0.260
Fy=0.353
Fz=0.387
{112} - Zircon
Fx=0.416
Fy=0.311
Fz=0.273
X1
Y1
Measurement Count: 40183
Entire Dataset
Half Width: 10.0°
Sample Symm.: Triclinic
Use Sample Symmetry: No
Projection Type: Equal Area
Projection Plane: XY
Hemisphere: Lower

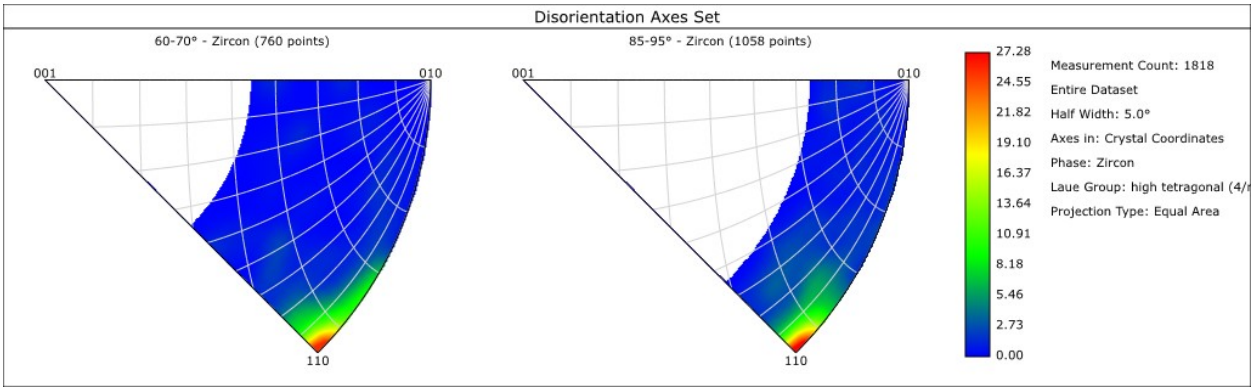
Disorientation Axes Set
60-70° - Zircon (760 points)
85-95° - Zircon (1058 points)
001
010
110
27.28
24.55
21.82
19.10
16.37
13.64
10.91
8.18
5.46
2.73
0.00
Measurement Count: 1818
Entire Dataset
Half Width: 5.0°
Axes in: Crystal Coordinates
Phase: Zircon
Projection Type: Equal Area

M143

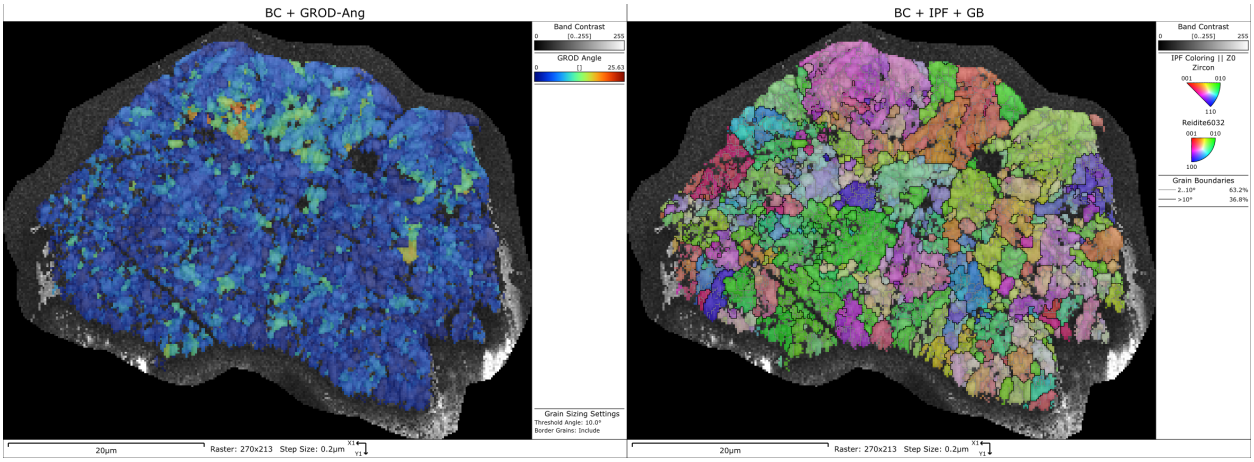
BC + GROD-Ang
Band Contrast
GROD Angle
Grain Sizing Settings
20µm
Raster: 270x213 Step Size: 0.2µm
BC + IPF + GB
Band Contrast
IPF Coloring || Z0
Zircon
Reidite6032
Grain Boundaries
20µm
Raster: 270x213 Step Size: 0.2µm

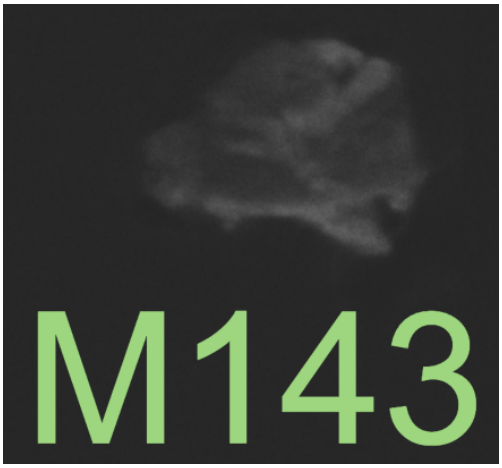
M143

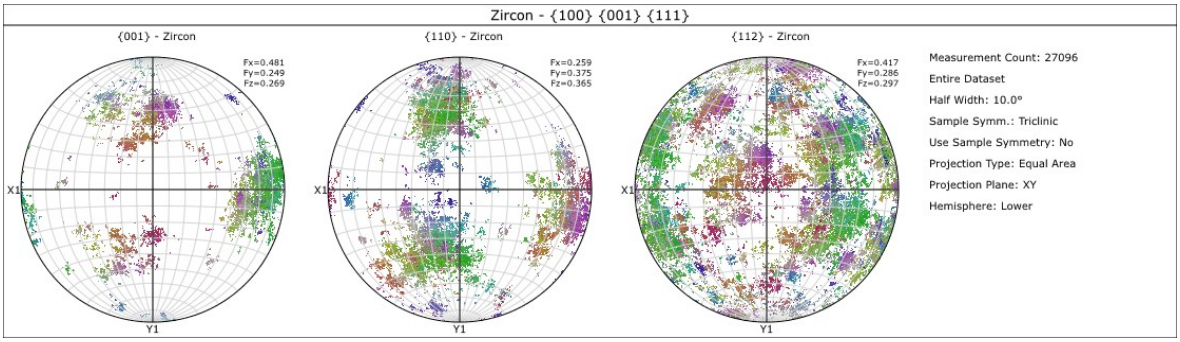
Zircon - {100} {001} {111}
{001} - Zircon
Fx=0.481
Fy=0.249
Fz=0.269
{110} - Zircon
Fx=0.259
Fy=0.375
Fz=0.365
{112} - Zircon
Fx=0.417
Fy=0.286
Fz=0.297
X1
Y1
Measurement Count: 27096
Entire Dataset
Half Width: 10.0°
Sample Symm.: Triclinic
Use Sample Symmetry: No
Projection Type: Equal Area
Projection Plane: XY
Hemisphere: Lower

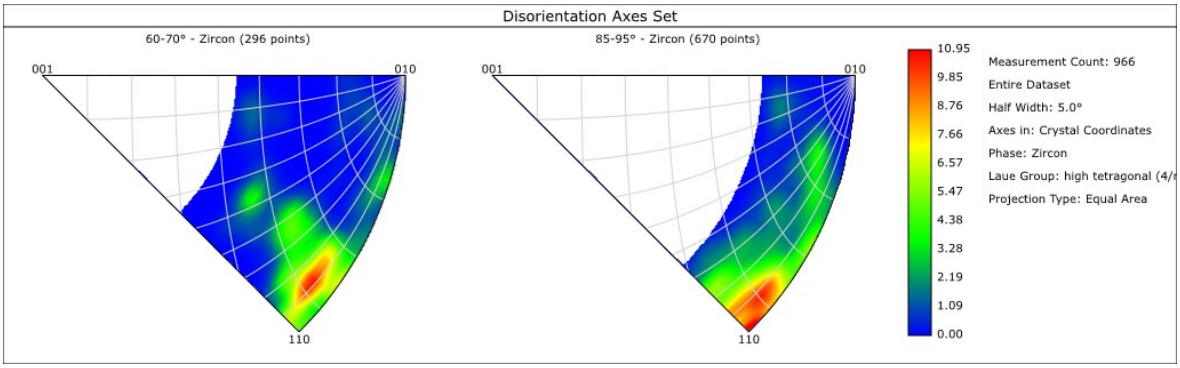
Disorientation Axes Set
60-70° - Zircon (296 points)
85-95° - Zircon (670 points)
001
010
110
10.95
9.85
8.76
7.66
6.57
5.47
4.38
3.28
2.19
1.09
0.00
Measurement Count: 966
Entire Dataset
Half Width: 5.0°
Axes in: Crystal Coordinates
Phase: Zircon
Laue Group: high tetragonal (4/
Projection Type: Equal Area

M144

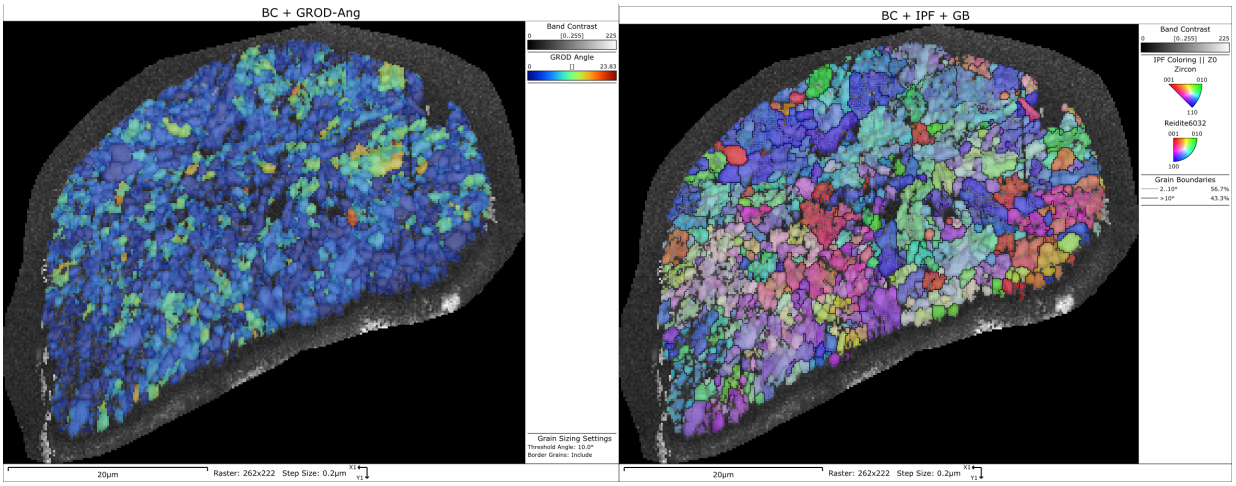
BC + GROD-Ang
Band Contrast
GROD Angle
Grain Sizing Settings
20µm
Raster: 262x222 Step Size: 0.2µm
BC + IPF + GB
Band Contrast
IPF Coloring || Z0 Zircon
Reidite6032
Grain Boundaries
20µm
Raster: 262x222 Step Size: 0.2µm

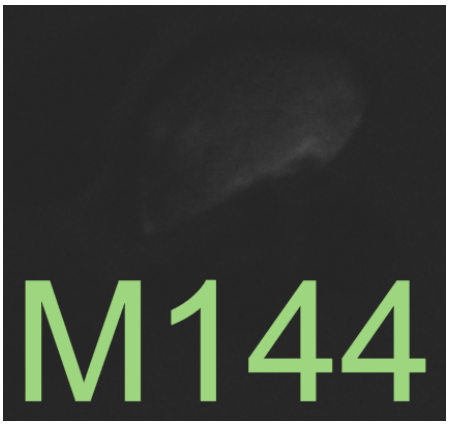
M144

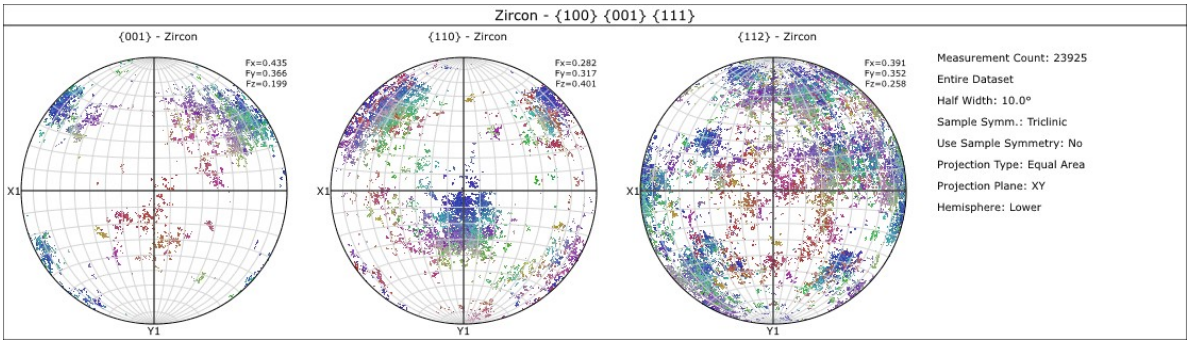
Zircon - {100} {001} {111}
{001} - Zircon
Fx=0.435
Fy=0.366
Fz=0.199
{110} - Zircon
Fx=0.282
Fy=0.317
Fz=0.401
{112} - Zircon
Fx=0.391
Fy=0.352
Fz=0.258
X1
Y1
Measurement Count: 23925
Entire Dataset
Half Width: 10.0°
Sample Symm.: Triclinic
Use Sample Symmetry: No
Projection Type: Equal Area
Projection Plane: XY
Hemisphere: Lower

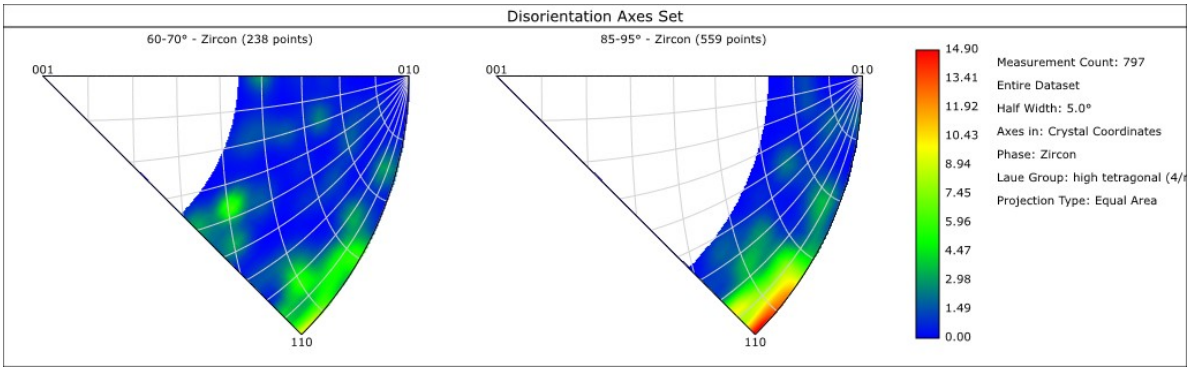
Disorientation Axes Set
60-70° - Zircon (238 points)
85-95° - Zircon (559 points)
001
010
110
14.90
13.41
11.92
10.43
8.94
7.45
5.96
4.47
2.98
1.49
0.00
Measurement Count: 797
Entire Dataset
Half Width: 5.0°
Axes in: Crystal Coordinates
Phase: Zircon
Projection Type: Equal Area

M146

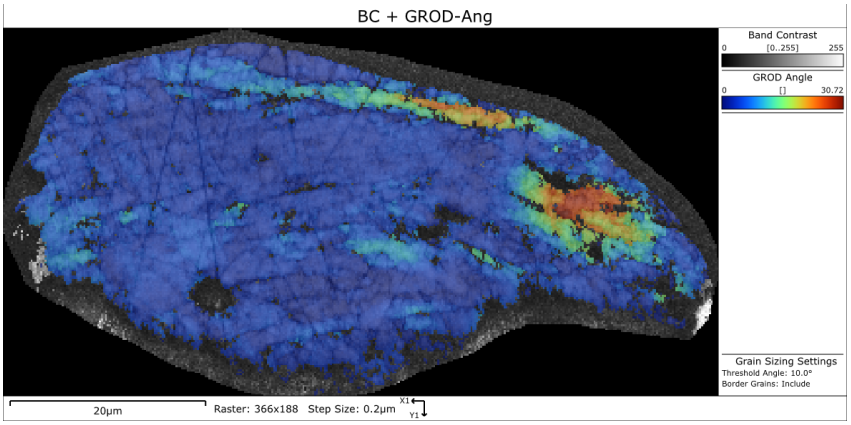
BC + GROD-Ang
Band Contrast
0 [0..255] 255
GROD Angle
0 [] 30.72
Grain Sizing Settings
Threshold Angle: 10.0°
Border Grains: Include
20µm
Raster: 366x188 Step Size: 0.2µm
X1
Y1

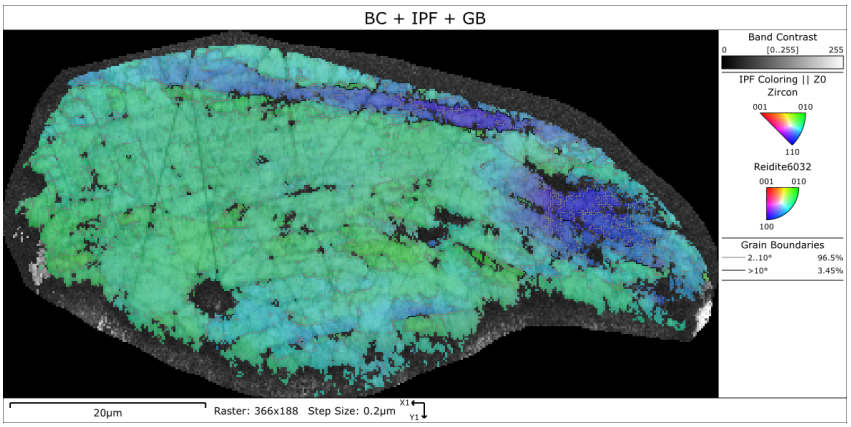
BC + IPF + GB
Band Contrast
0 [0..255] 255
IPF Coloring || Z0
Zircon
001 010
110
Reidite6032
001 010
100
Grain Boundaries
2..10° 96.5%
>10° 3.45%
20µm
Raster: 366x188 Step Size: 0.2µm
X1
Y1

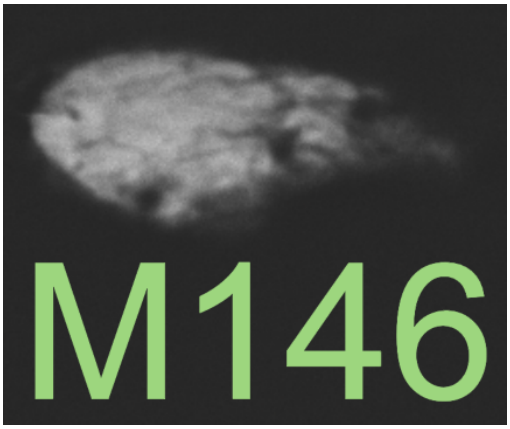
M146

M149

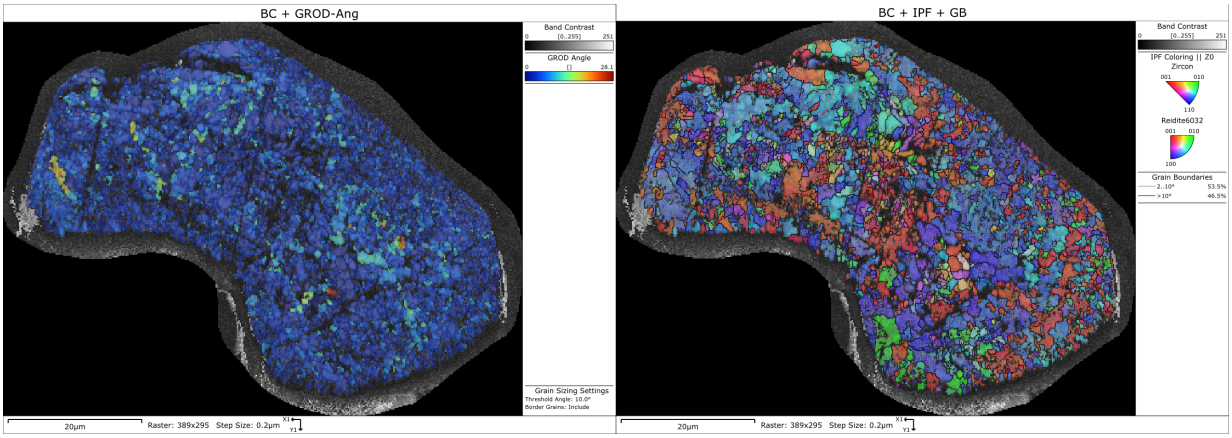
BC + GROD-Ang
Band Contrast
GROD Angle
Grain Sizing Settings
20µm
Raster: 389x295 Step Size: 0.2µm
BC + IPF + GB
Band Contrast
IPF Coloring || Z0
Zircon
Reidite6032
Grain Boundaries
20µm
Raster: 389x295 Step Size: 0.2µm


M149

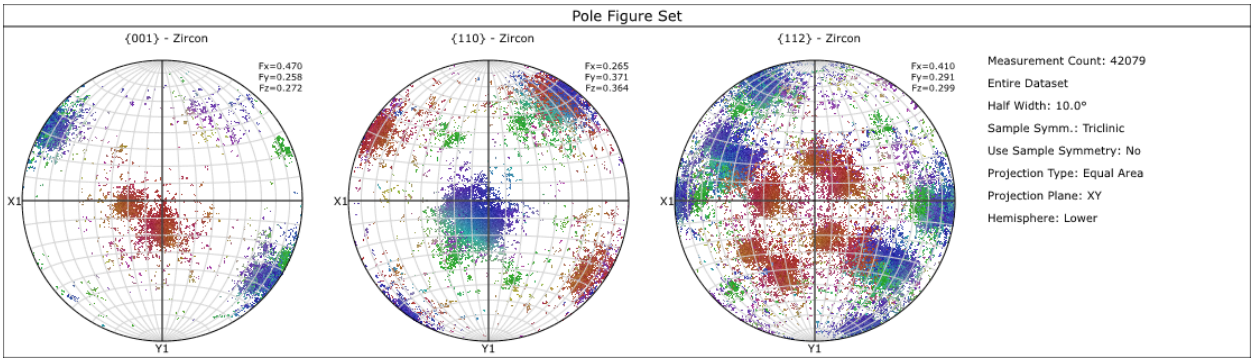
Pole Figure Set
{001} - Zircon
Fx=0.470
Fy=0.258
Fz=0.272
{110} - Zircon
Fx=0.265
Fy=0.371
Fz=0.364
{112} - Zircon
Fx=0.410
Fy=0.291
Fz=0.299
X1
Y1
Measurement Count: 42079
Entire Dataset
Half Width: 10.0°
Sample Symm.: Triclinic
Use Sample Symmetry: No
Projection Type: Equal Area
Projection Plane: XY
Hemisphere: Lower

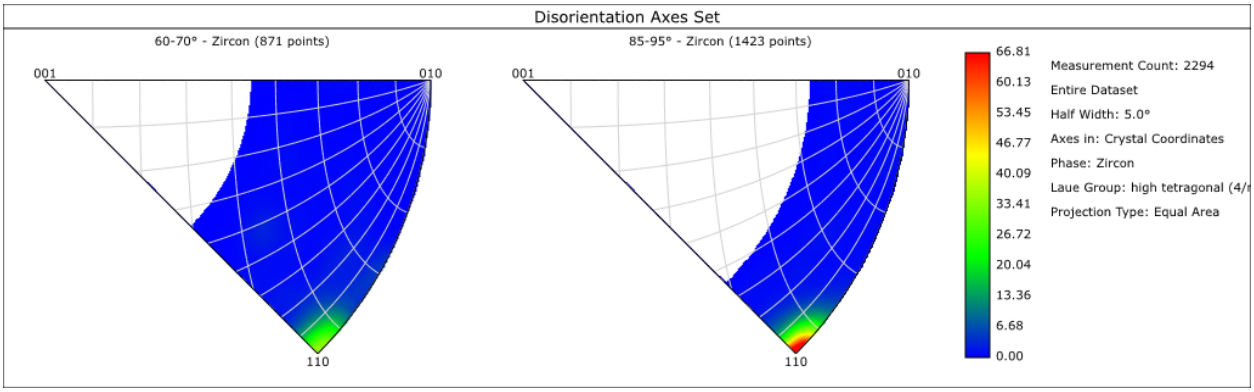
Disorientation Axes Set
60-70° - Zircon (871 points)
85-95° - Zircon (1423 points)
001
010
110
66.81
60.13
53.45
46.77
40.09
33.41
26.72
20.04
13.36
6.68
0.00
Measurement Count: 2294
Entire Dataset
Half Width: 5.0°
Axes in: Crystal Coordinates
Phase: Zircon
Projection Type: Equal Area

M152

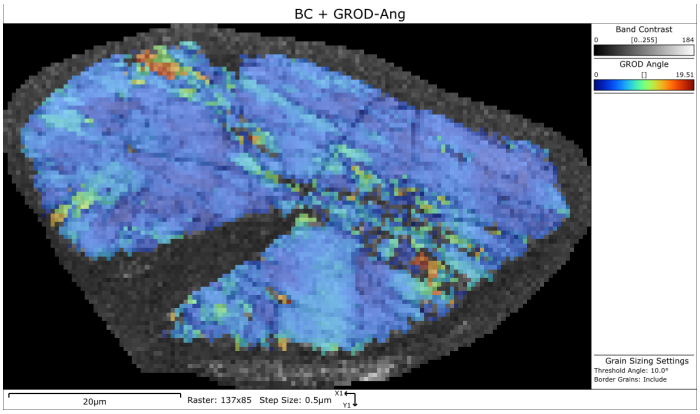
BC + GROD-Ang
Band Contrast
0 [0..255] 184
GROD Angle
0 [] 19.51
Grain Sizing Settings
Threshold Angle: 10.0°
Border Grains: Include
20µm
Raster: 137x85 Step Size: 0.5µm

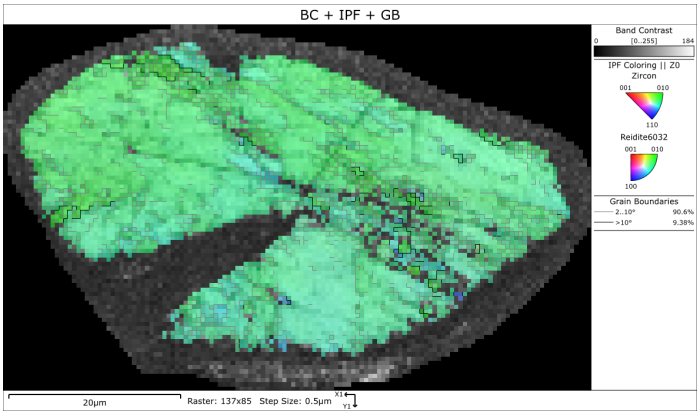
BC + IPF + GB
Band Contrast
0 [0..255] 184
IPF Coloring || Z0
Zircon
001 010
110
Reidite6032
001 010
100
Grain Boundaries
2..10° 90.6%
>10° 9.38%
20µm
Raster: 137x85 Step Size: 0.5µm


M152

M153

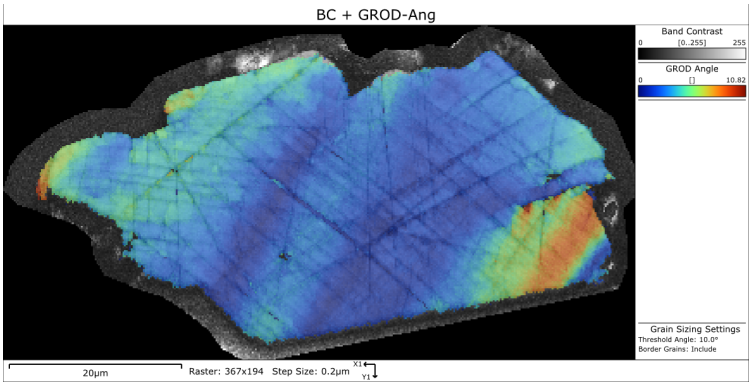
BC + GROD-Ang
Band Contrast
0 [0..255] 255
GROD Angle
0 [] 10.82
Grain Sizing Settings
Threshold Angle: 10.0°
Border Grains: Include
20µm
Raster: 367x194 Step Size: 0.2µm

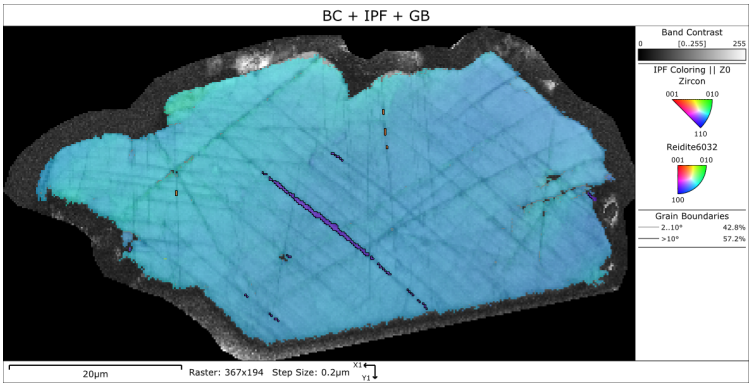
BC + IPF + GB
Band Contrast
0 [0..255] 255
IPF Coloring || Z0
Zircon
001 010
110
Reidite6032
001 010
100
Grain Boundaries
2..10° 42.8%
>10° 57.2%
20µm
Raster: 367x194 Step Size: 0.2µm


M153

M156

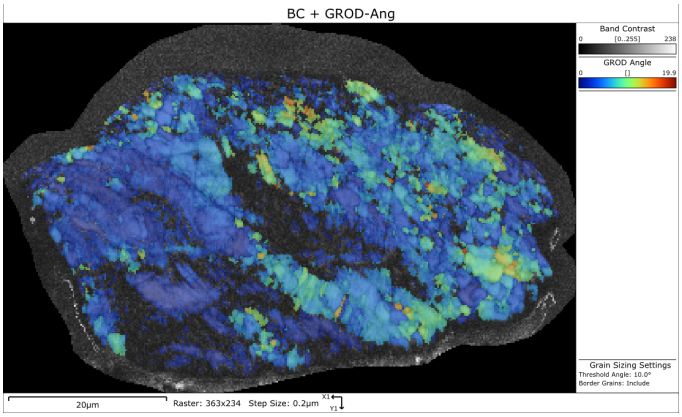
BC + GROD-Ang
Band Contrast
GROD Angle
Grain Sizing Settings
20µm
Raster: 363x234 Step Size: 0.2µm

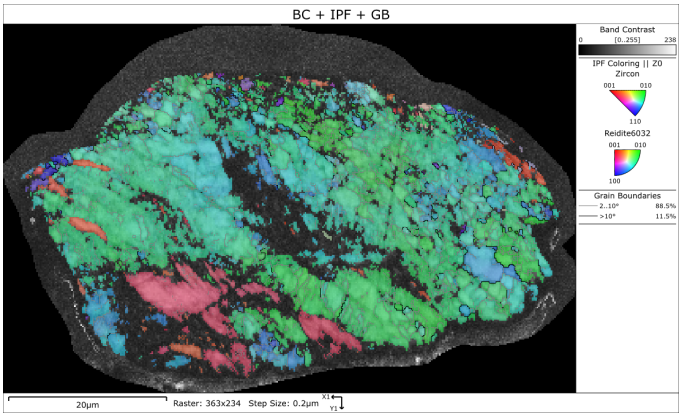
BC + IPF + GB
Band Contrast
IPF Coloring || Z0
Zircon
Reidite6032
Grain Boundaries
20µm
Raster: 363x234 Step Size: 0.2µm

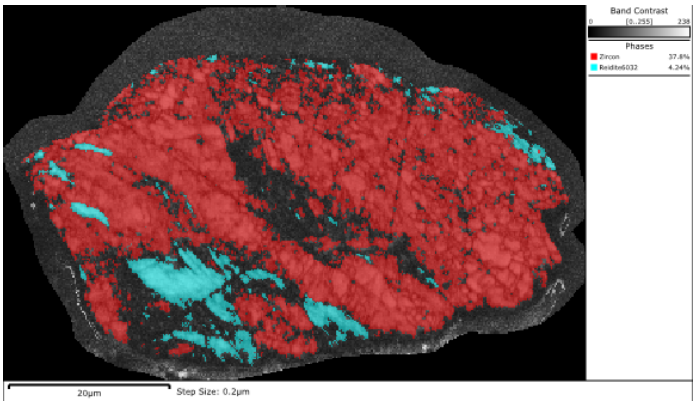
Band Contrast
Phases
20µm
Step Size: 0.2µm

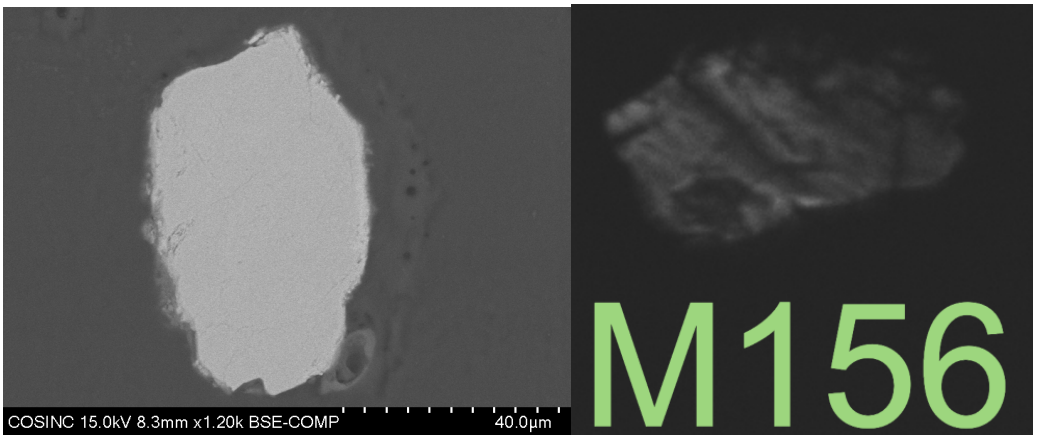
COSINC 15.0kV 8.3mm x1.20k BSE-COMP
40.0µm
M156

M160

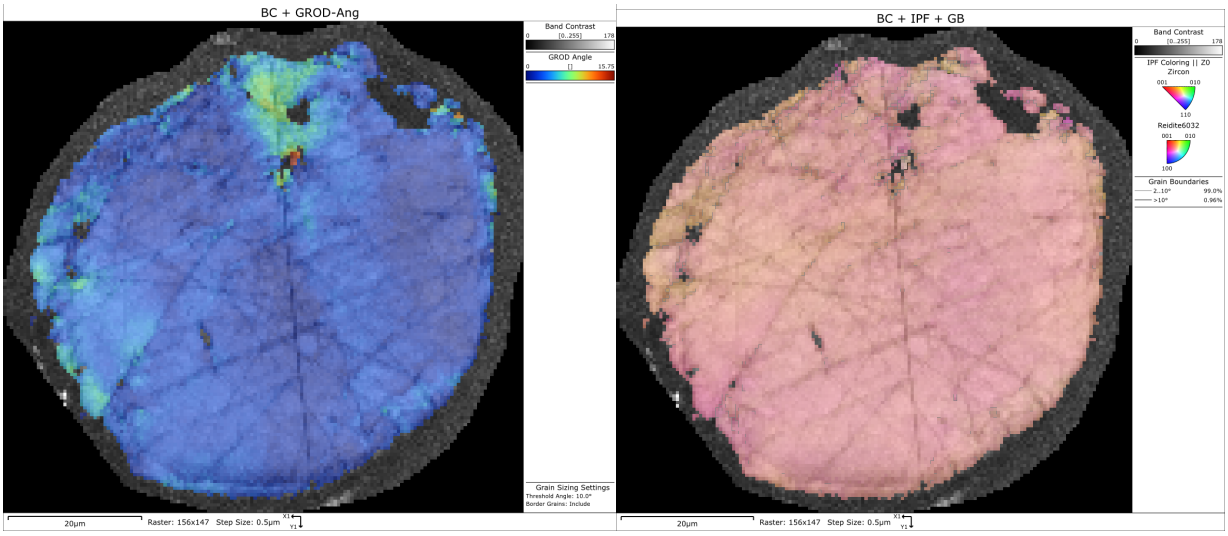
BC + GROD-Ang
Band Contrast
GROD Angle
Grain Sizing Settings
20µm
Raster: 156x147 Step Size: 0.5µm
BC + IPF + GB
Band Contrast
IPF Coloring || ZO
Zircon
Reidite6032
Grain Boundaries
20µm
Raster: 156x147 Step Size: 0.5µm

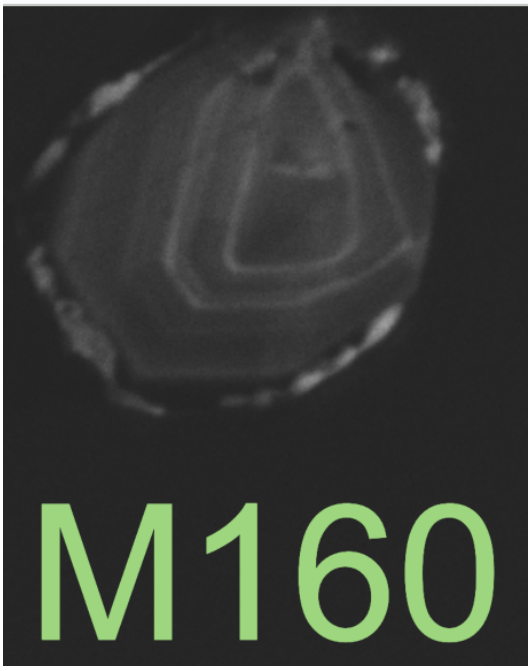
M160

M161

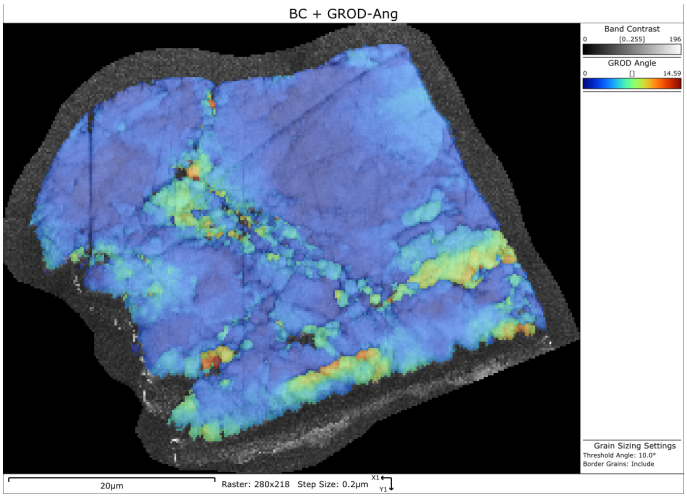
BC + GROD-Ang
Band Contrast
0 [0..255] 196
GROD Angle
0 [] 14.59
Grain Sizing Settings
Threshold Angle: 10.0°
Border Grains: Include
20µm
Raster: 280x218 Step Size: 0.2µm

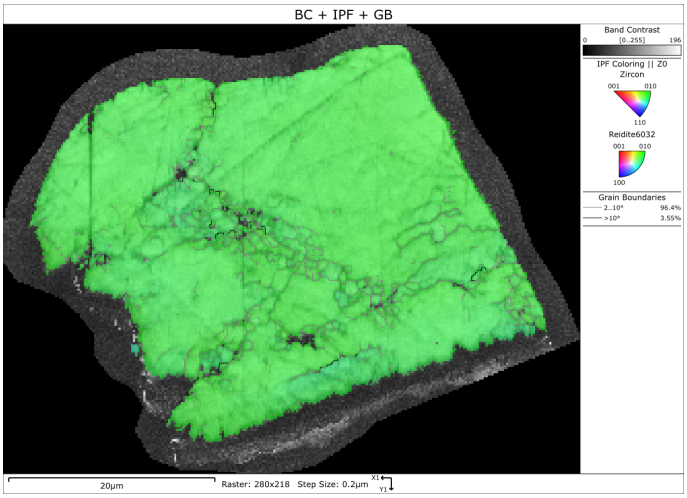
BC + IPF + GB
Band Contrast
0 [0..255] 196
IPF Coloring || Z0
Zircon
001 010
110
Reidite6032
001 010
100
Grain Boundaries
2..10° 96.4%
>10° 3.55%
20µm
Raster: 280x218 Step Size: 0.2µm


M161

M163

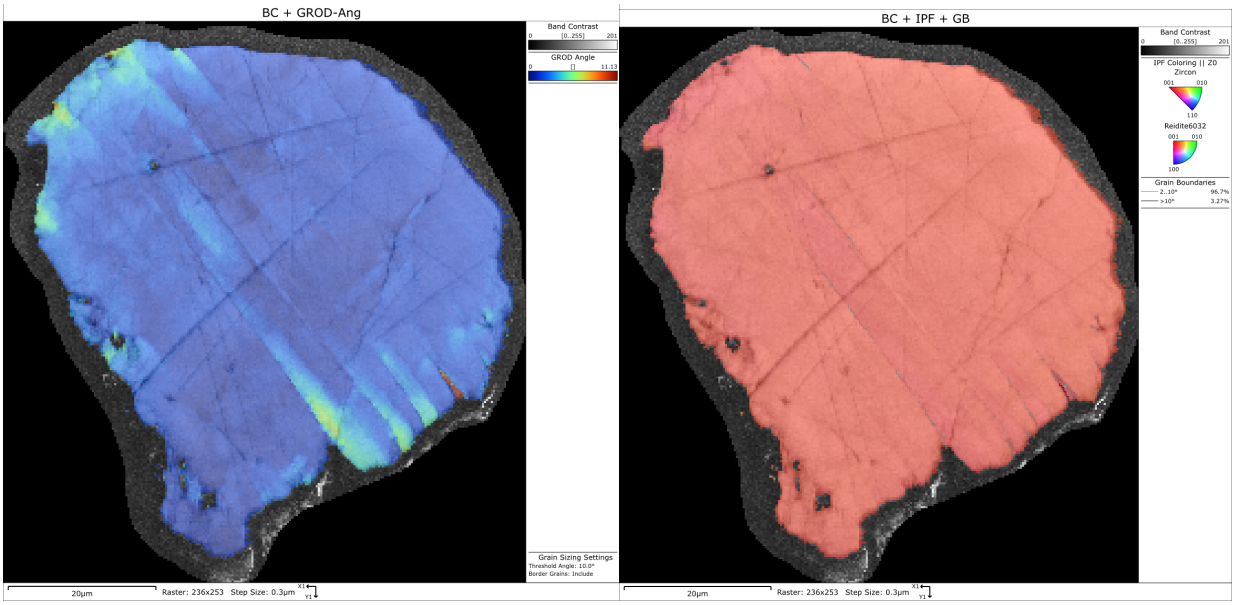
BC + GROD-Ang
Band Contrast
GROD Angle
Grain Sizing Settings
20µm
Raster: 236x253 Step Size: 0.3µm
BC + IPF + GB
Band Contrast
IPF Coloring || Z0
Zircon
Reidite6032
Grain Boundaries
20µm
Raster: 236x253 Step Size: 0.3µm


M163

M164

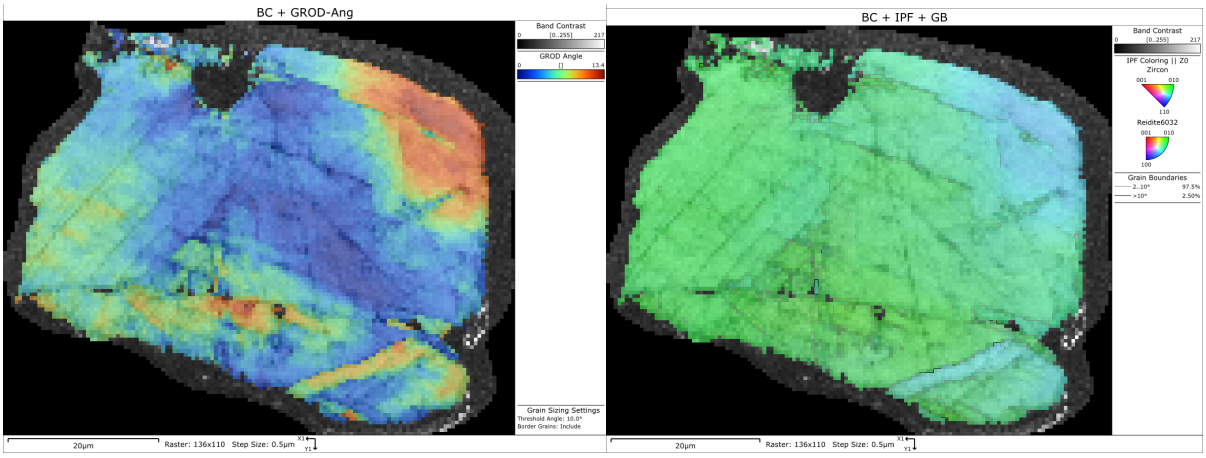
BC + GROD-Ang
Band Contrast
GROD Angle
Grain Sizing Settings
20µm
Raster: 136x110 Step Size: 0.5µm
BC + IPF + GB
Band Contrast
IPF Coloring || Z0
Zircon
Reidite6032
Grain Boundaries
20µm
Raster: 136x110 Step Size: 0.5µm

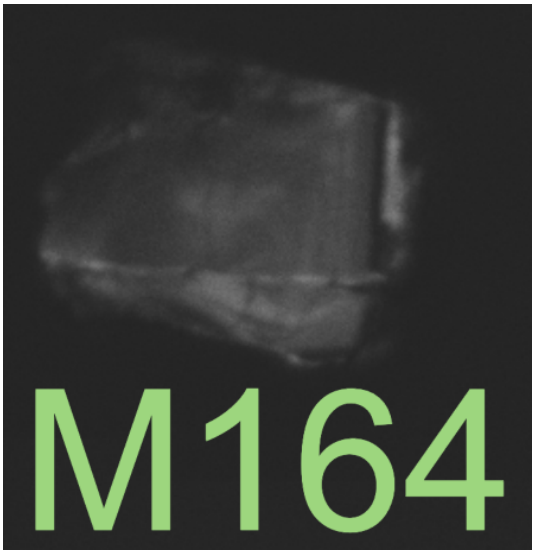
M164

M165

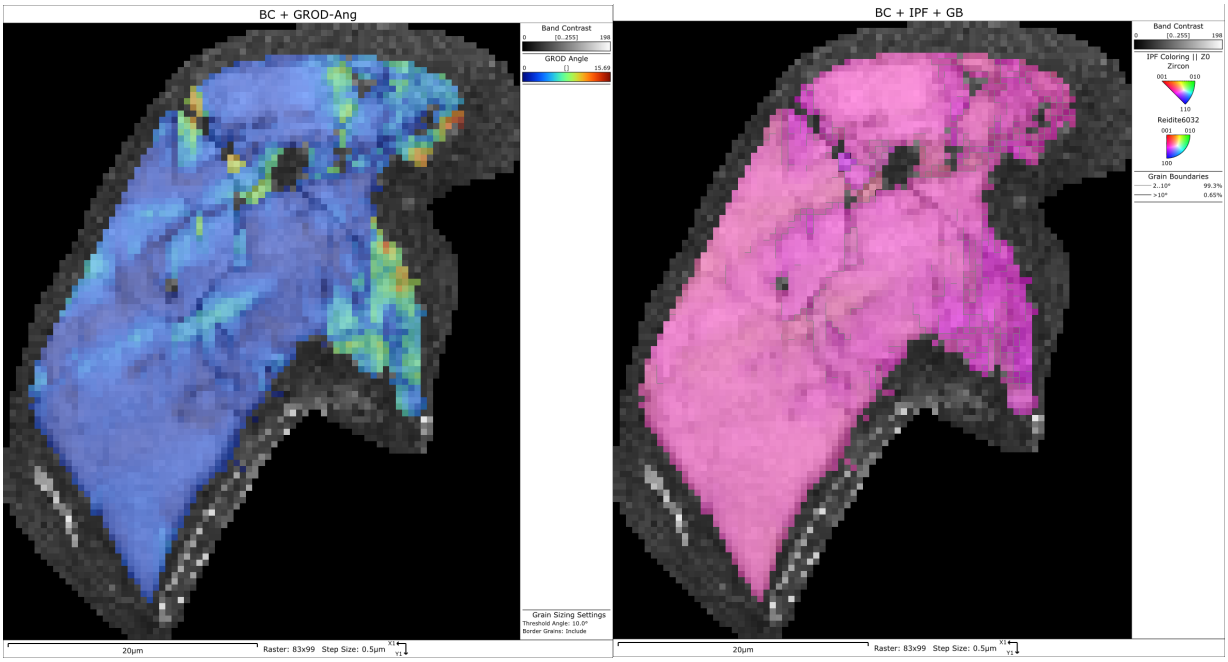
BC + GROD-Ang
Band Contrast
GROD Angle
Grain Sizing Settings
20µm
Raster: 83x99 Step Size: 0.5µm
BC + IPF + GB
Band Contrast
IPF Coloring || Z0
Zircon
Reidite6032
Grain Boundaries
20µm
Raster: 83x99 Step Size: 0.5µm

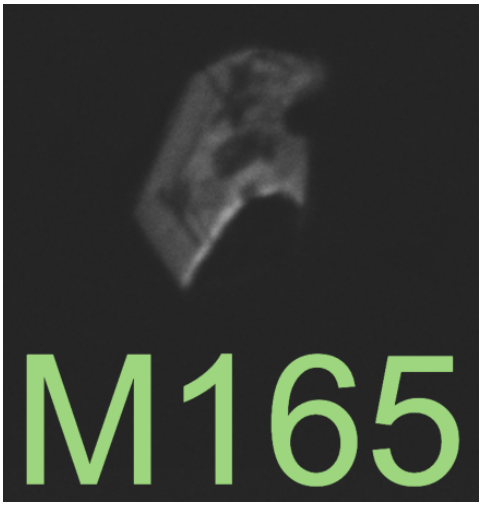
M165

M166

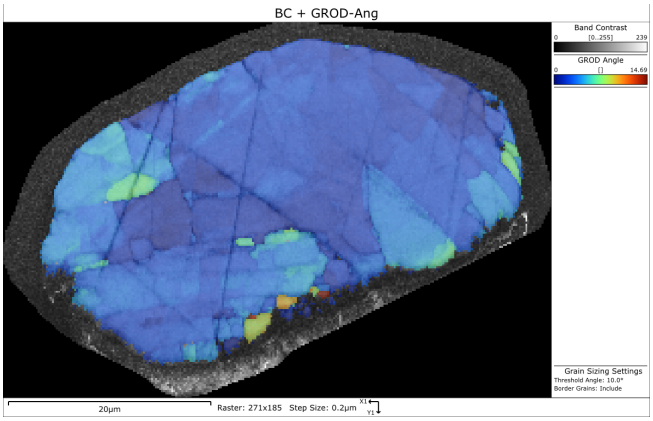
BC + GROD-Ang
Band Contrast
0 [0..255] 239
GROD Angle
0 [] 14.69
Grain Sizing Settings
Threshold Angle: 10.0°
Border Grains: Include
20µm
Raster: 271x185 Step Size: 0.2µm

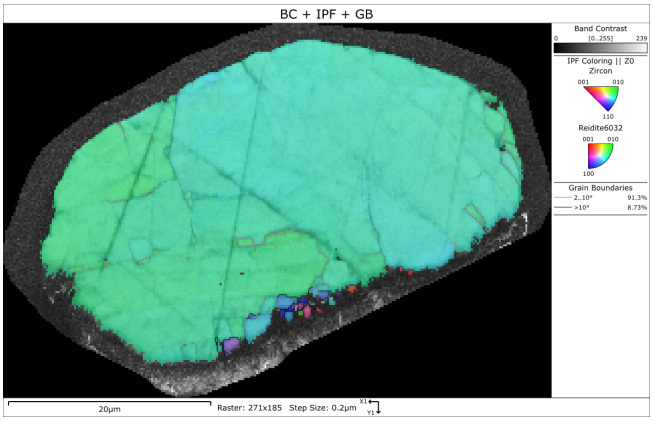
BC + IPF + GB
Band Contrast
0 [0..255] 239
IPF Coloring || Z0
Zircon
001 010
110
Reidite6032
001 010
100
Grain Boundaries
2..10° 91.3%
>10° 8.73%
20µm
Raster: 271x185 Step Size: 0.2µm

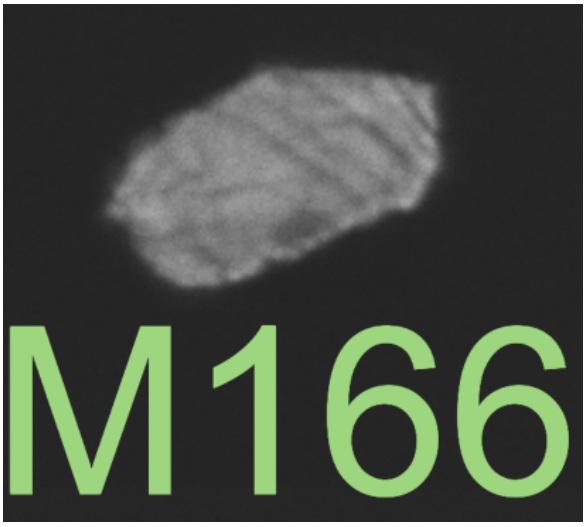
M166

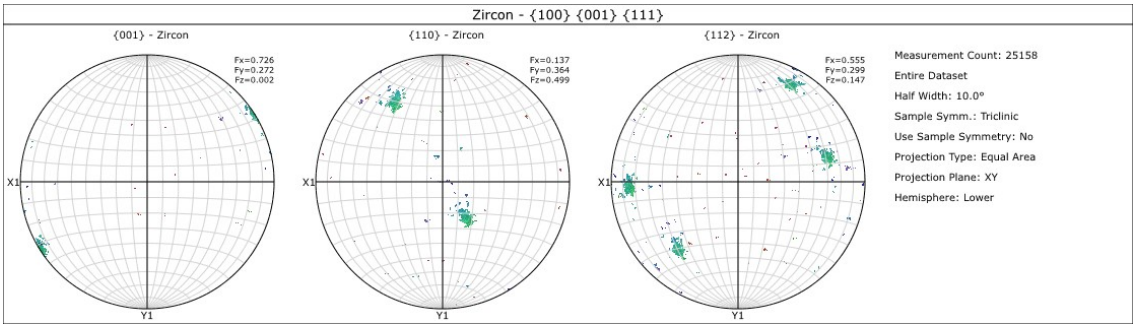
Zircon - {100} {001} {111}
{001} - Zircon
Fx=0.726
Fy=0.272
Fz=0.002
{110} - Zircon
Fx=0.137
Fy=0.364
Fz=0.499
{112} - Zircon
Fx=0.555
Fy=0.299
Fz=0.147
X1
Y1
Measurement Count: 25158
Entire Dataset
Half Width: 10.0°
Sample Symm.: Triclinic
Use Sample Symmetry: No
Projection Type: Equal Area
Projection Plane: XY
Hemisphere: Lower

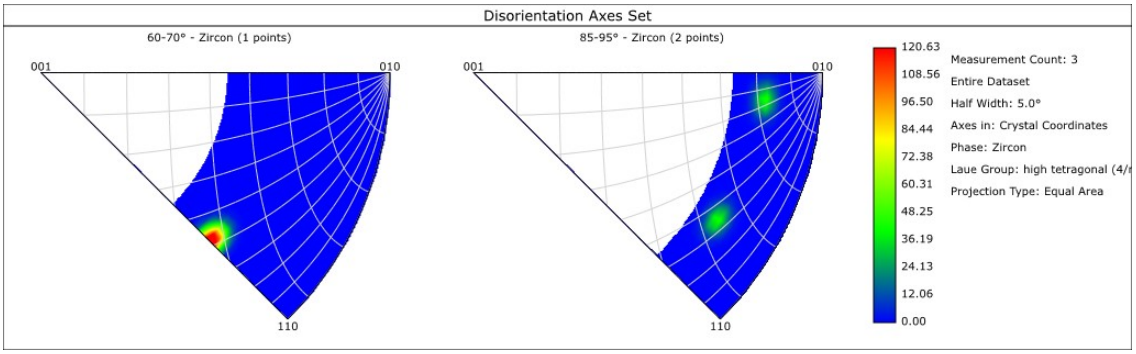
Disorientation Axes Set
60-70° - Zircon (1 points)
85-95° - Zircon (2 points)
001
010
110
120.63
108.56
96.50
84.44
72.38
60.31
48.25
36.19
24.13
12.06
0.00
Measurement Count: 3
Entire Dataset
Half Width: 5.0°
Axes in: Crystal Coordinates
Phase: Zircon
Projection Type: Equal Area

M168

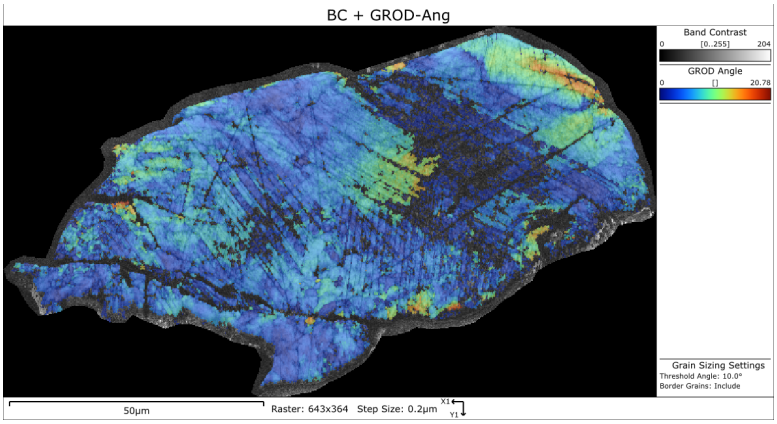
BC + GROD-Ang
Band Contrast
0 [0..255] 204
GROD Angle
0 [] 20.78
Grain Sizing Settings
Threshold Angle: 10.0°
Border Grains: Include
50µm
Raster: 643x364 Step Size: 0.2µm

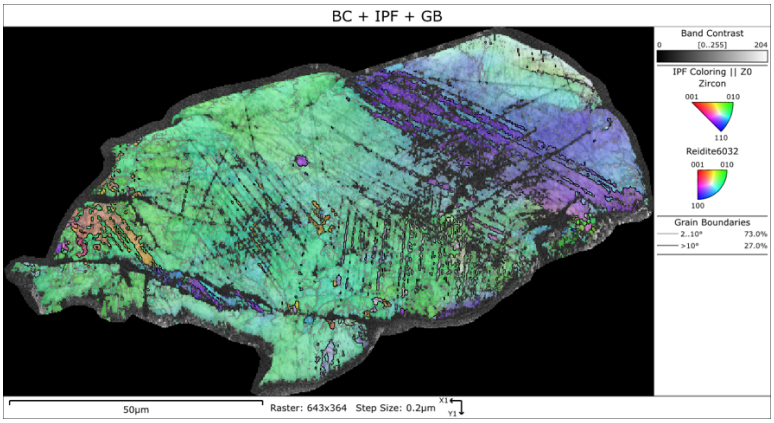
BC + IPF + GB
Band Contrast
0 [0..255] 204
IPF Coloring || Z0
Zircon
001 010
110
Reidite6032
001 010
100
Grain Boundaries
2..10° 73.0%
>10° 27.0%
50µm
Raster: 643x364 Step Size: 0.2µm

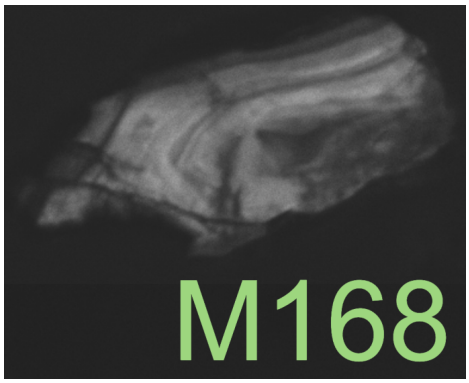
M168

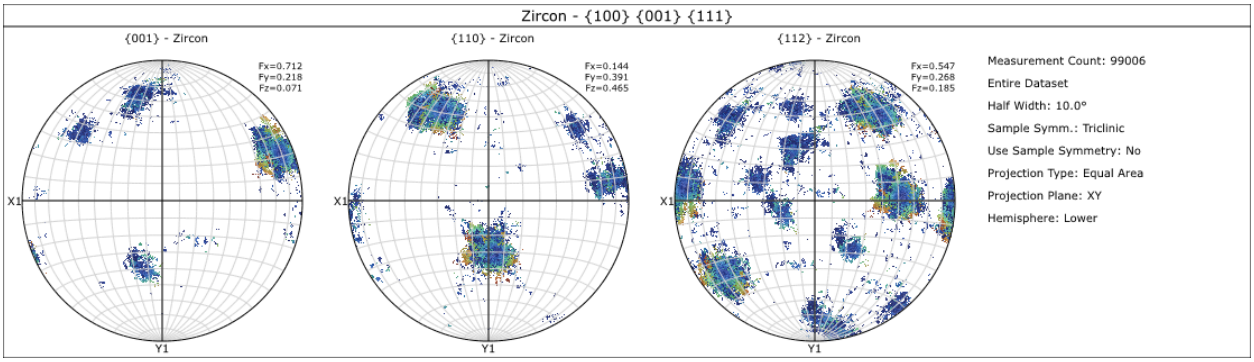
Zircon - {100} {001} {111}
{001} - Zircon
Fx=0.712
Fy=0.218
Fz=0.071
{110} - Zircon
Fx=0.144
Fy=0.391
Fz=0.465
{112} - Zircon
Fx=0.547
Fy=0.268
Fz=0.185
X1
Y1
Measurement Count: 99006
Entire Dataset
Half Width: 10.0°
Sample Symm.: Triclinic
Use Sample Symmetry: No
Projection Type: Equal Area
Projection Plane: XY
Hemisphere: Lower

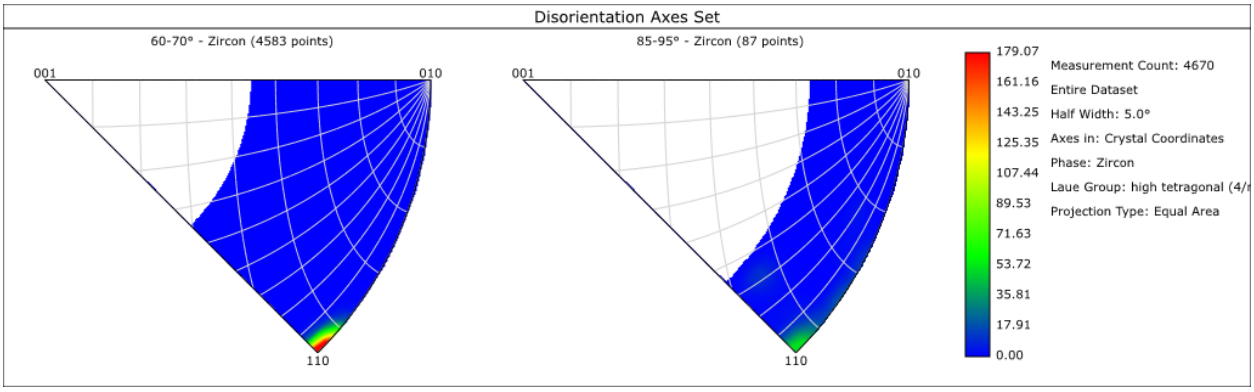
Disorientation Axes Set
60-70° - Zircon (4583 points)
85-95° - Zircon (87 points)
001
010
110
179.07
161.16
143.25
125.35
107.44
89.53
71.63
53.72
35.81
17.91
0.00
Measurement Count: 4670
Entire Dataset
Half Width: 5.0°
Axes in: Crystal Coordinates
Phase: Zircon
Laue Group: high tetragonal (4/
Projection Type: Equal Area

M170

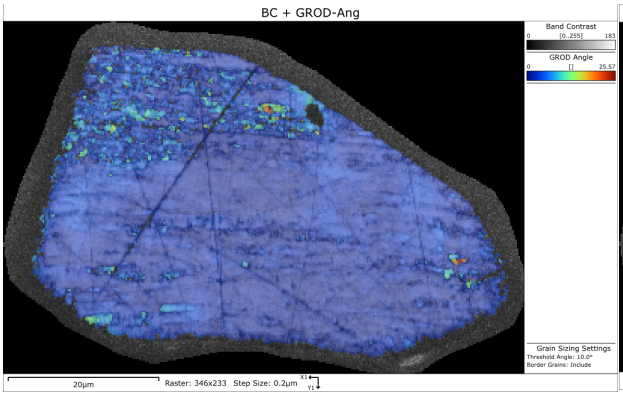
BC + GROD-Ang
Band Contrast
GROD Angle
Grain Sizing Settings
20µm
Raster: 346x233 Step Size: 0.2µm

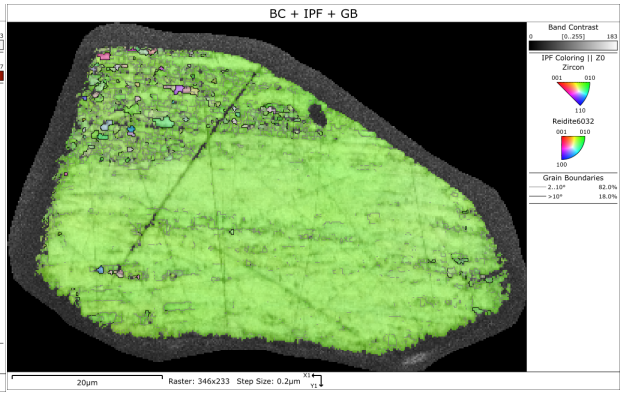
BC + IPF + GB
Band Contrast
IPF Coloring || Z0
Zircon
Reidite6032
Grain Boundaries
20µm
Raster: 346x233 Step Size: 0.2µm

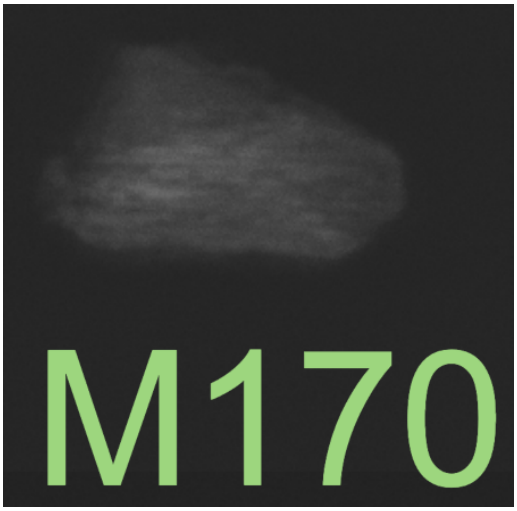
M170

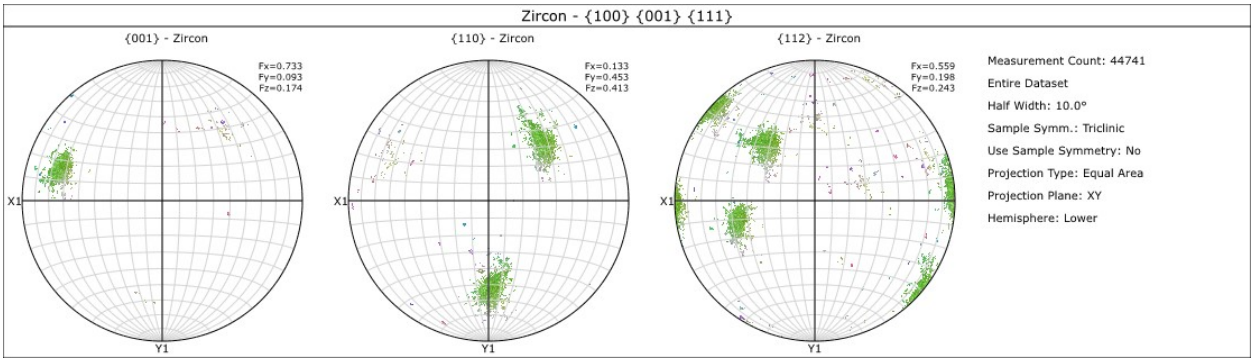
Zircon - {100} {001} {111}
{001} - Zircon
Fx=0.733
Fy=0.093
Fz=0.174
{110} - Zircon
Fx=0.133
Fy=0.453
Fz=0.413
{112} - Zircon
Fx=0.559
Fy=0.198
Fz=0.243
X1
Y1
Measurement Count: 44741
Entire Dataset
Half Width: 10.0°
Sample Symm.: Triclinic
Use Sample Symmetry: No
Projection Type: Equal Area
Projection Plane: XY
Hemisphere: Lower

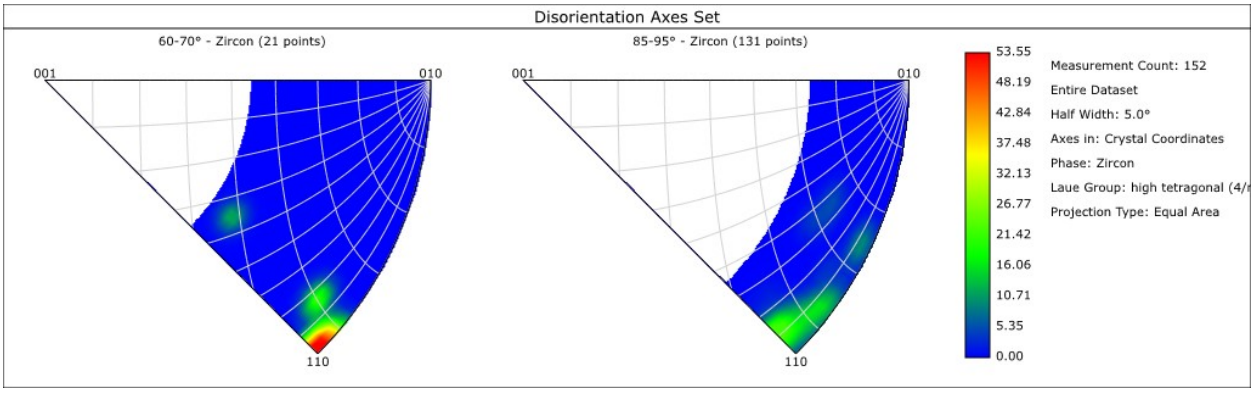
Disorientation Axes Set
60-70° - Zircon (21 points)
85-95° - Zircon (131 points)
001
010
110
53.55
48.19
42.84
37.48
32.13
26.77
21.42
16.06
10.71
5.35
0.00
Measurement Count: 152
Entire Dataset
Half Width: 5.0°
Axes in: Crystal Coordinates
Phase: Zircon
Laue Group: high tetragonal (4/
Projection Type: Equal Area

M171

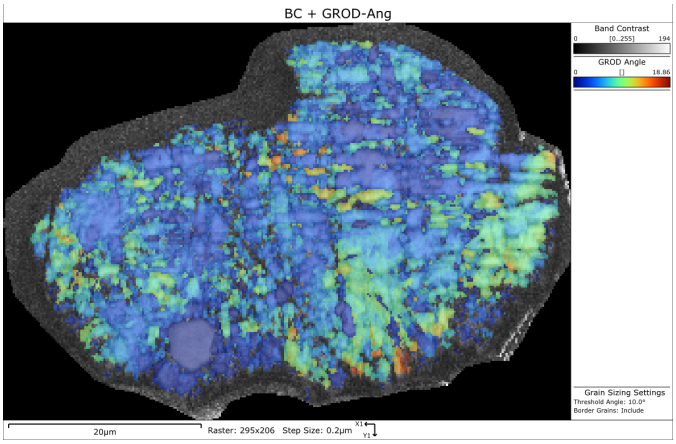
BC + GROD-Ang
Band Contrast
GROD Angle
Grain Sizing Settings
20µm
Raster: 295x206 Step Size: 0.2µm

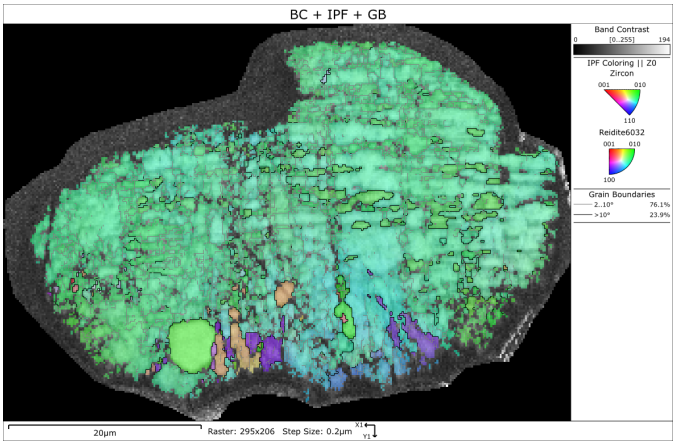
BC + IPF + GB
Band Contrast
IPF Coloring || Z0
Zircon
Reidite6032
Grain Boundaries
20µm
Raster: 295x206 Step Size: 0.2µm


M171

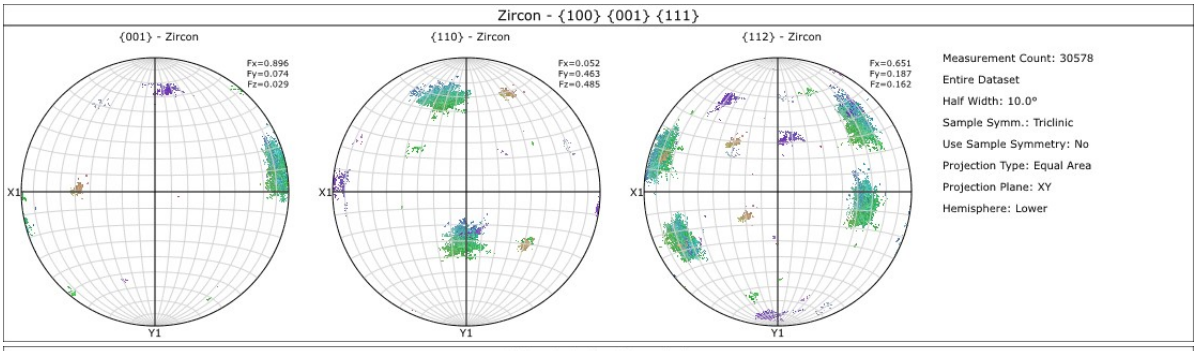
Zircon - {100} {001} {111}
{001} - Zircon
{110} - Zircon
{112} - Zircon
Measurement Count: 30578
Entire Dataset
Half Width: 10.0°
Sample Symm.: Triclinic
Use Sample Symmetry: No
Projection Type: Equal Area
Projection Plane: XY
Hemisphere: Lower

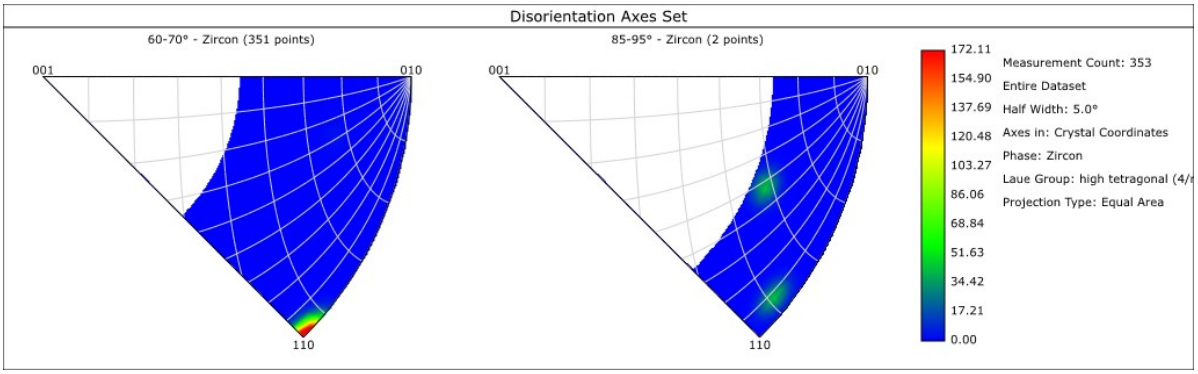
Disorientation Axes Set
60-70° - Zircon (351 points)
85-95° - Zircon (2 points)
001
010
110
Measurement Count: 353
Entire Dataset
Half Width: 5.0°
Axes in: Crystal Coordinates
Phase: Zircon
Projection Type: Equal Area

M175

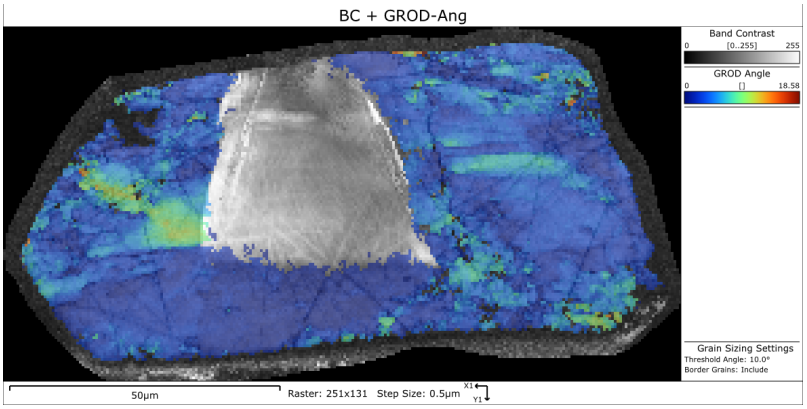
BC + GROD-Ang
Band Contrast
0 [0..255] 255
GROD Angle
0 [] 18.58
Grain Sizing Settings
Threshold Angle: 10.0°
Border Grains: Include
50µm
Raster: 251x131 Step Size: 0.5µm
X1
Y1

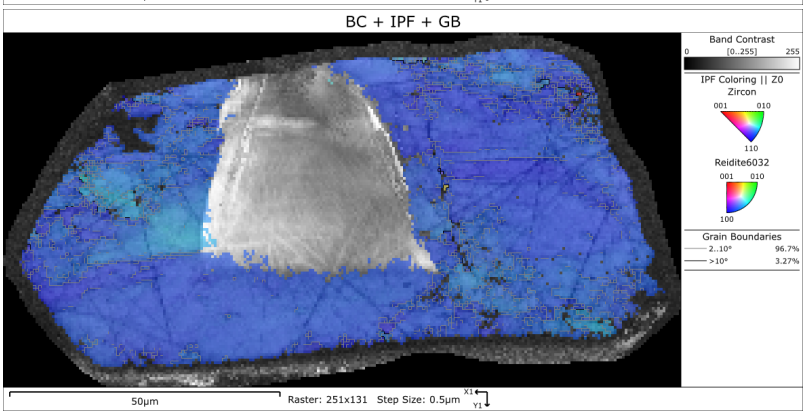
BC + IPF + GB
Band Contrast
0 [0..255] 255
IPF Coloring || Z0
Zircon
001 010
110
Reidite6032
001 010
100
Grain Boundaries
2..10° 96.7%
>10° 3.27%
50µm
Raster: 251x131 Step Size: 0.5µm
X1
Y1

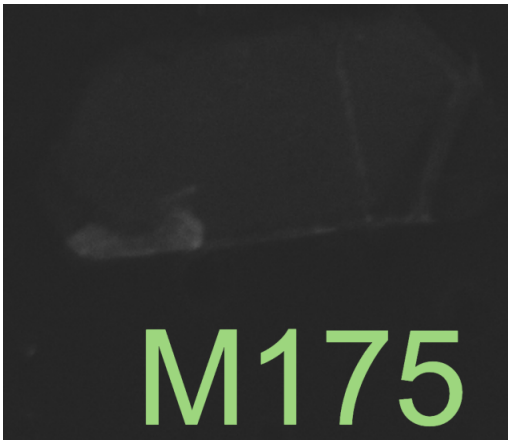
M175

M177

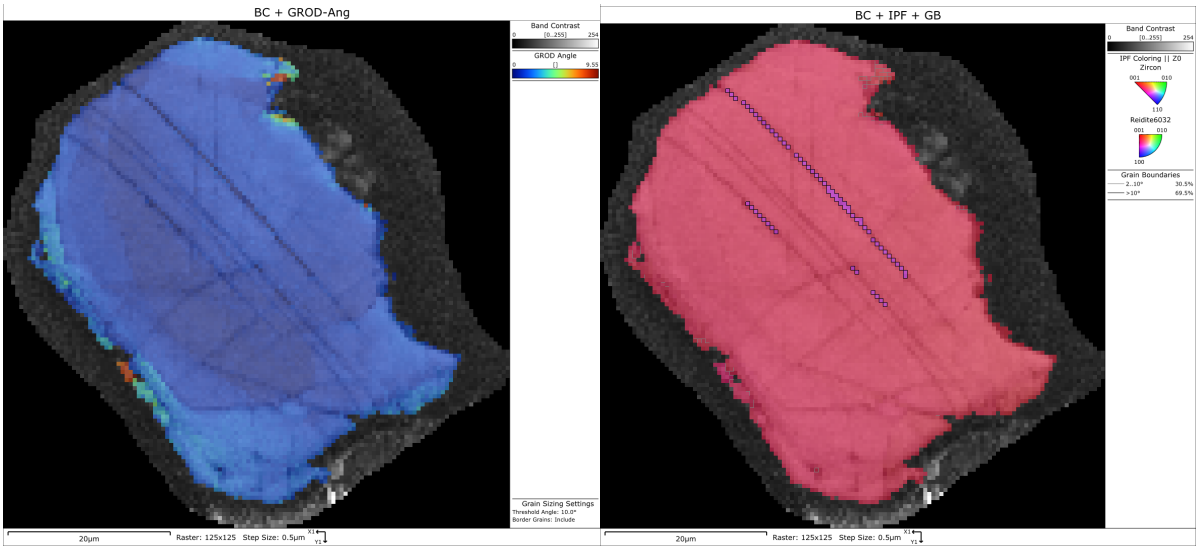
BC + GROD-Ang
Band Contrast
GROD Angle
Grain Sizing Settings
20µm
Raster: 125x125 Step Size: 0.5µm
BC + IPF + GB
Band Contrast
IPF Coloring || Z0
Zircon
Reidite6032
Grain Boundaries
20µm
Raster: 125x125 Step Size: 0.5µm

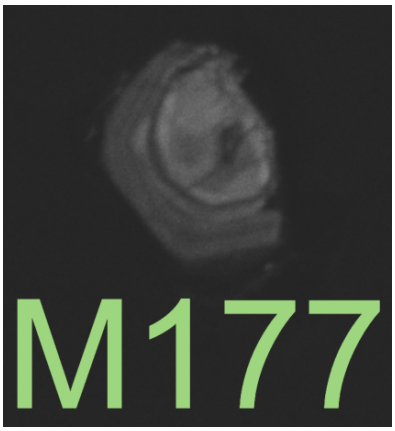
M177

M178

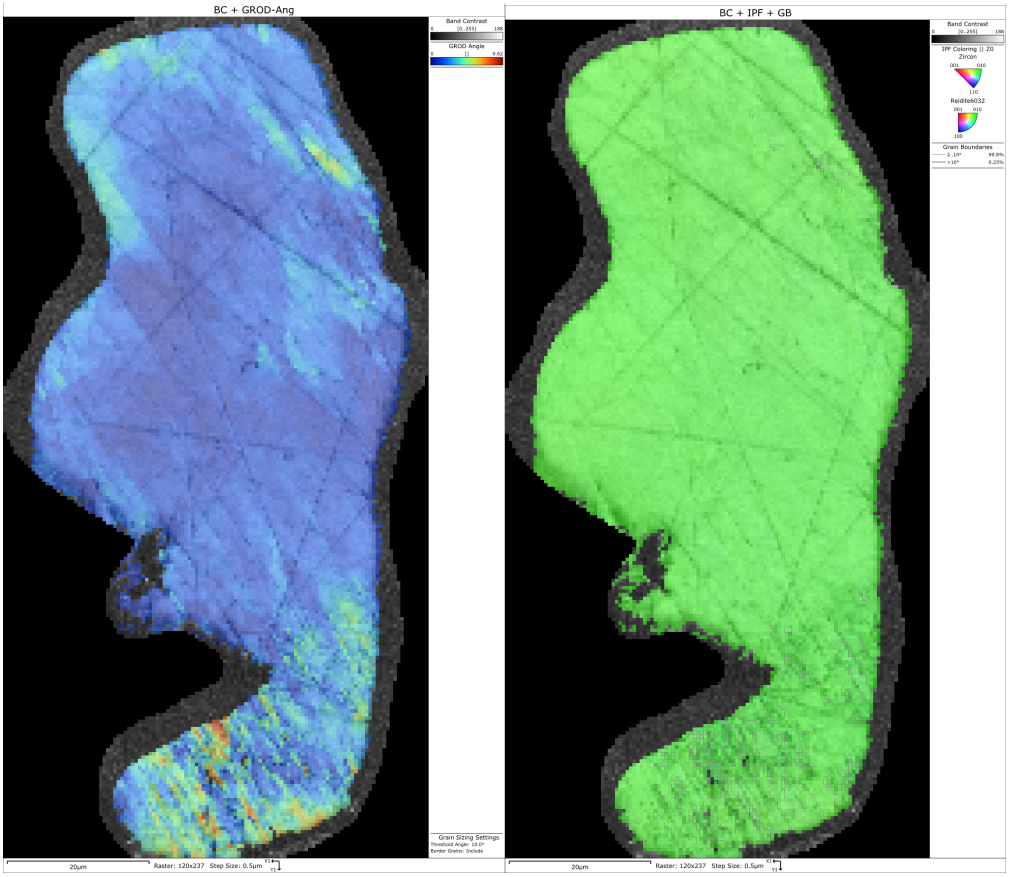
BC + GROD-Ang
Band Contrast
GROD Angle
Grain Sizing Settings
20μm
Raster: 120x237 Step Size: 0.5μm
BC + IPF + GB
Band Contrast
IPF Coloring || Z0
Zircon
Reidite6032
Grain Boundaries
20μm
Raster: 120x237 Step Size: 0.5μm

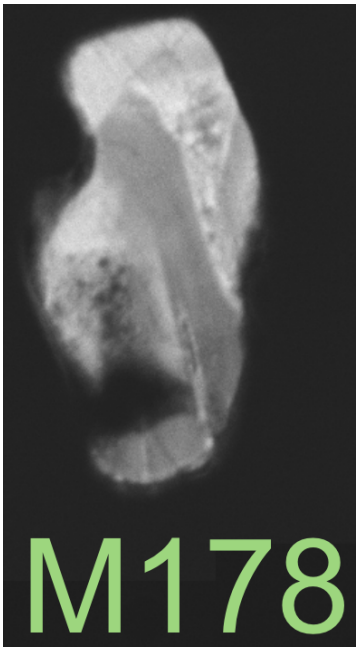
M178

M179

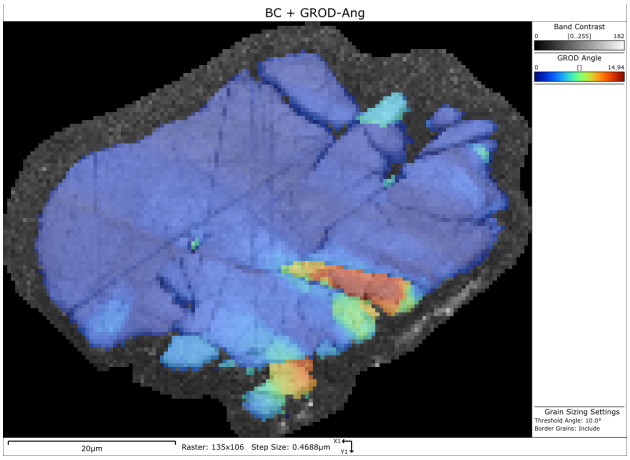
BC + GROD-Ang
Band Contrast
0 [0..255] 182
GROD Angle
0 [°] 14.94
Grain Sizing Settings
Threshold Angle: 10.0°
Border Grains: Include
20µm
Raster: 135x106 Step Size: 0.4688µm

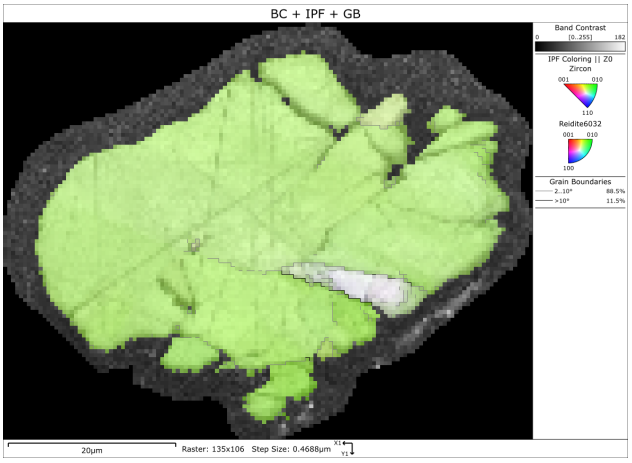
BC + IPF + GB
Band Contrast
0 [0..255] 182
IPF Coloring || Z0
Zircon
001 010
110
Reidite6032
001 010
100
Grain Boundaries
2..10° 88.5%
>10° 11.5%
20µm
Raster: 135x106 Step Size: 0.4688µm

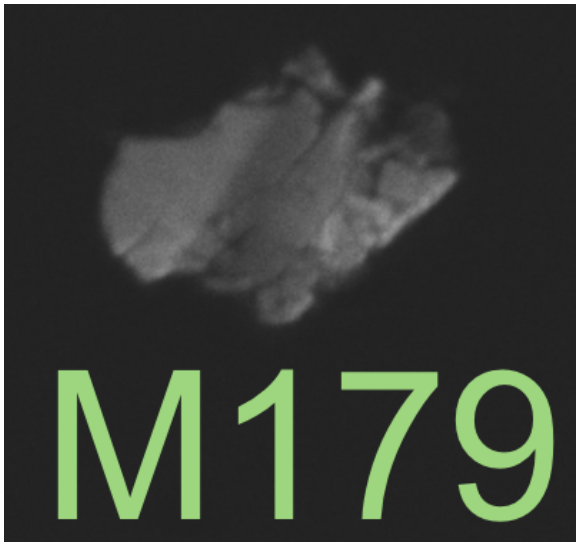
M179

M181

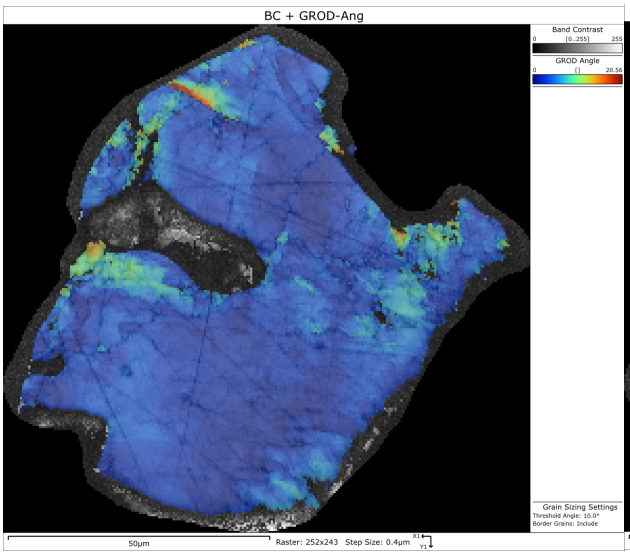
BC + GROD-Ang
Band Contrast
0 [0..255] 255
GROD Angle
0 [] 20.56
Grain Sizing Settings
Threshold Angle: 10.0°
Border Grains: Include
50µm
Raster: 252x243 Step Size: 0.4µm

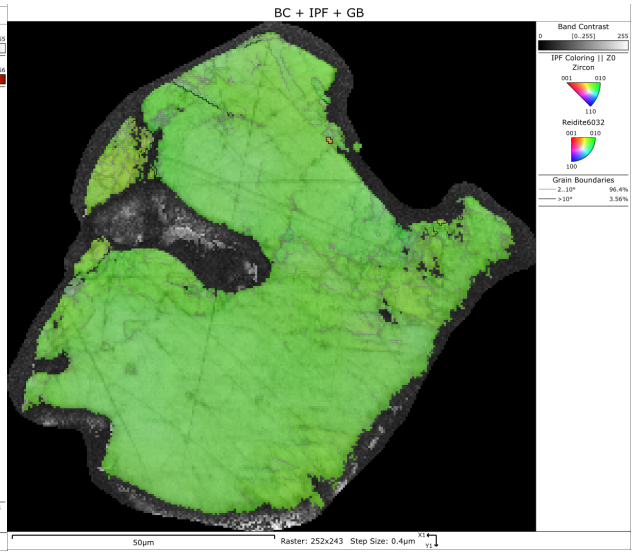
BC + IPF + GB
Band Contrast
0 [0..255] 255
IPF Coloring || Z0
Zircon
001 010
110
Reidite6032
001 010
100
Grain Boundaries
2..10° 96.4%
>10° 3.56%
50µm
Raster: 252x243 Step Size: 0.4µm

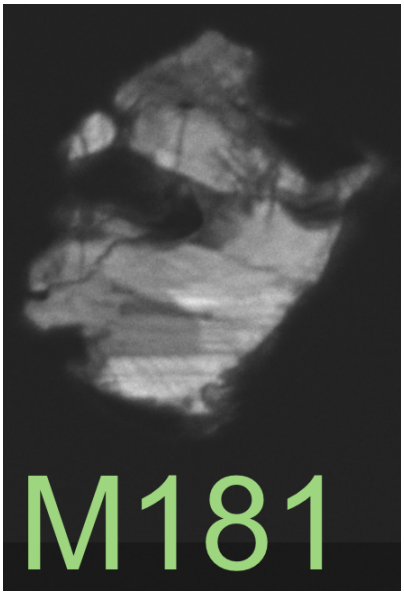
M181

M182

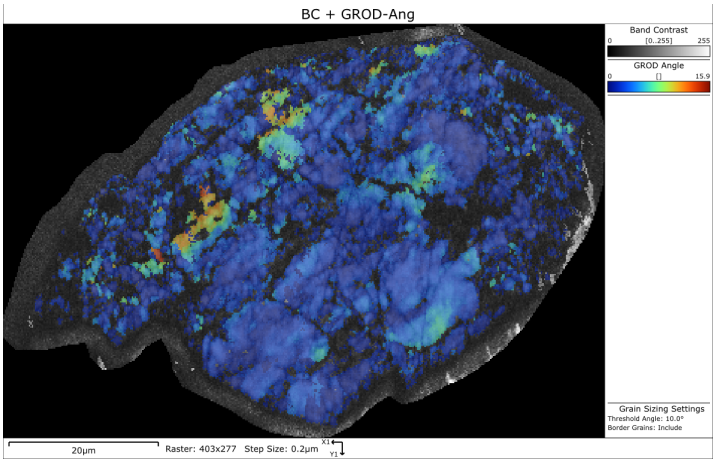
BC + GROD-Ang
Band Contrast
[0..255]
GROD Angle
Grain Sizing Settings
Threshold Angle: 10.0°
Border Grains: Include
20µm
Raster: 403x277 Step Size: 0.2µm

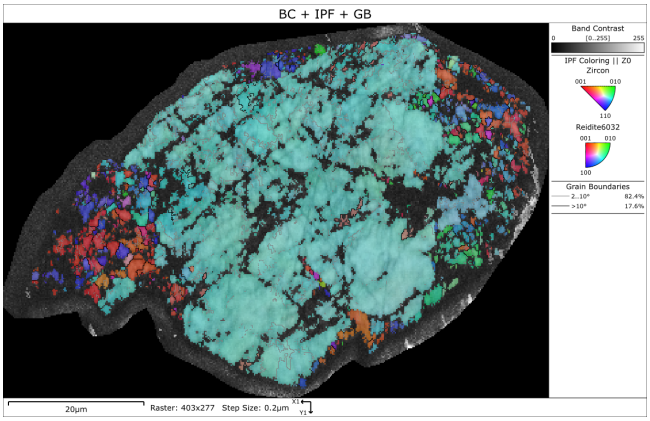
BC + IPF + GB
Band Contrast
IPF Coloring || Z0
Zircon
Reidite6032
Grain Boundaries
20µm
Raster: 403x277 Step Size: 0.2µm

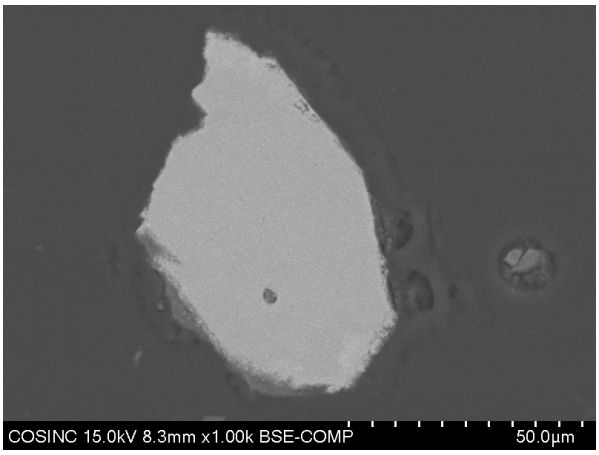
COSINC 15.0kV 8.3mm x1.00k BSE-COMP
50.0µm

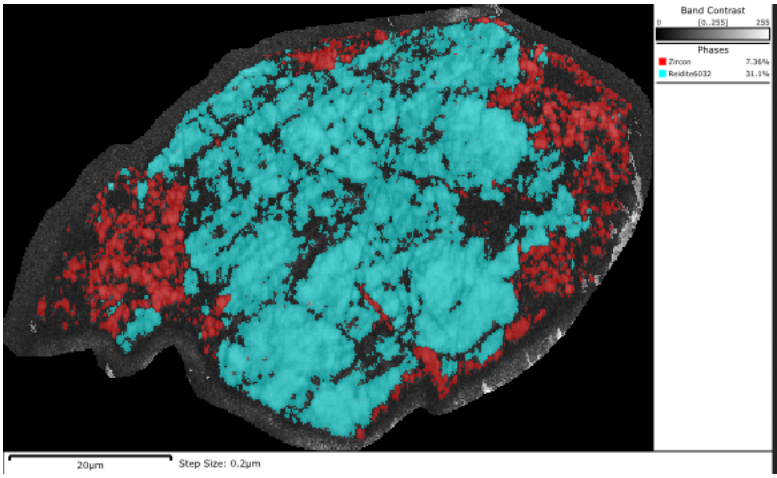
Band Contrast
Phases
Zircon
Reidite6032
20µm
Step Size: 0.2µm

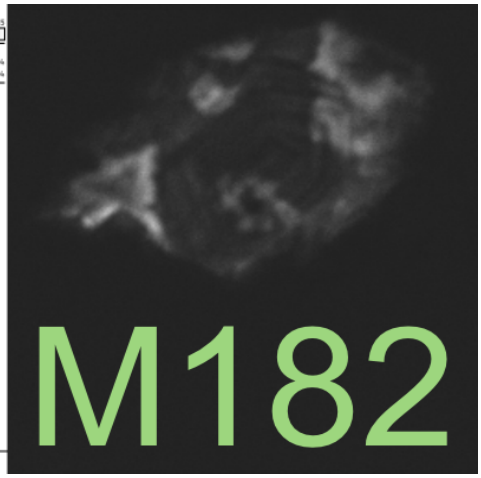
M182

M183

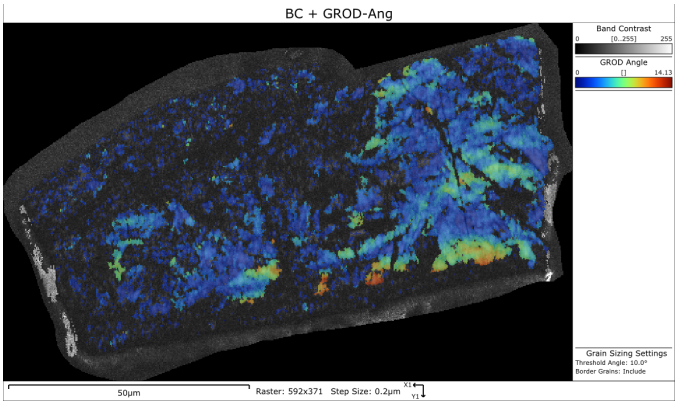
BC + GROD-Ang
Band Contrast
GROD Angle
Grain Sizing Settings
50µm
Raster: 592x371 Step Size: 0.2µm

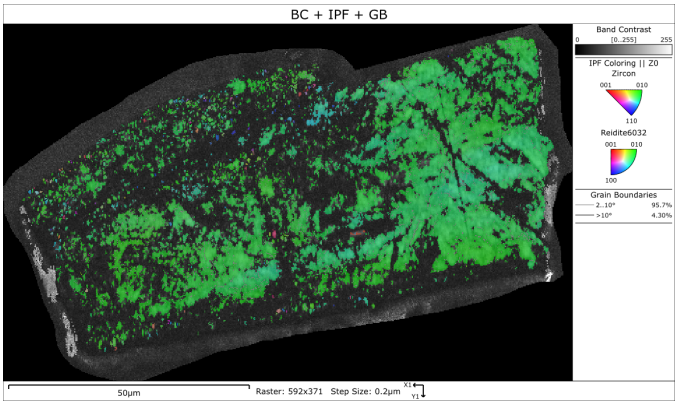
BC + IPF + GB
Band Contrast
IPF Coloring || Z0
Zircon
Reidite6032
Grain Boundaries
50µm
Raster: 592x371 Step Size: 0.2µm

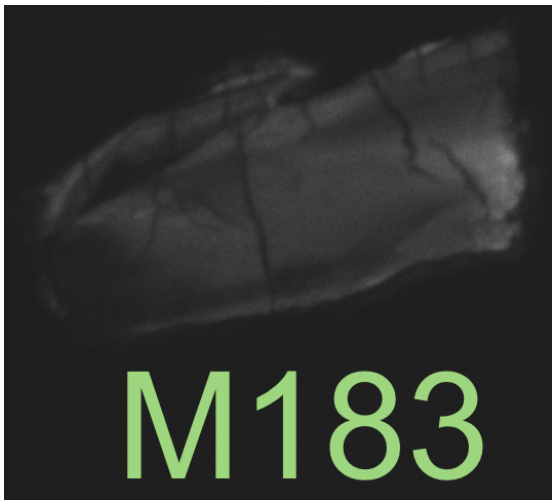
M183

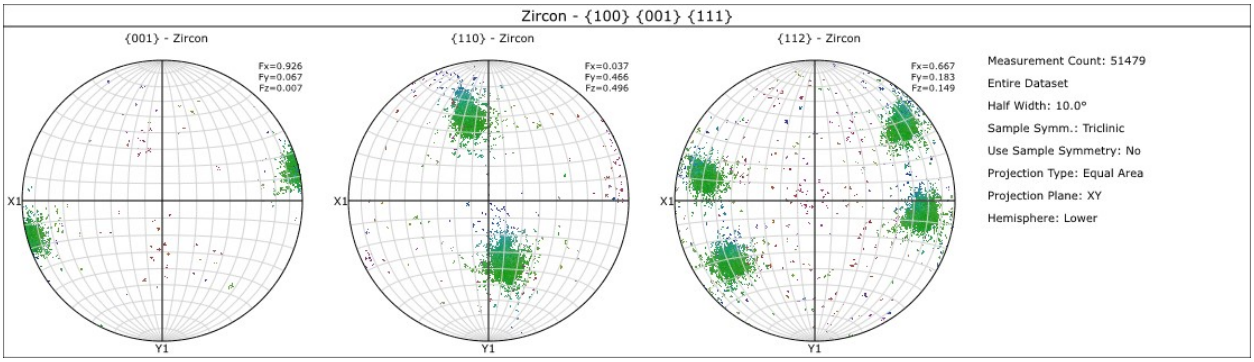
Zircon - {100} {001} {111}
{001} - Zircon
Fx=0.926
Fy=0.067
Fz=0.007
{110} - Zircon
Fx=0.037
Fy=0.466
Fz=0.496
{112} - Zircon
Fx=0.667
Fy=0.183
Fz=0.149
X1
Y1
Measurement Count: 51479
Entire Dataset
Half Width: 10.0°
Sample Symm.: Triclinic
Use Sample Symmetry: No
Projection Type: Equal Area
Projection Plane: XY
Hemisphere: Lower

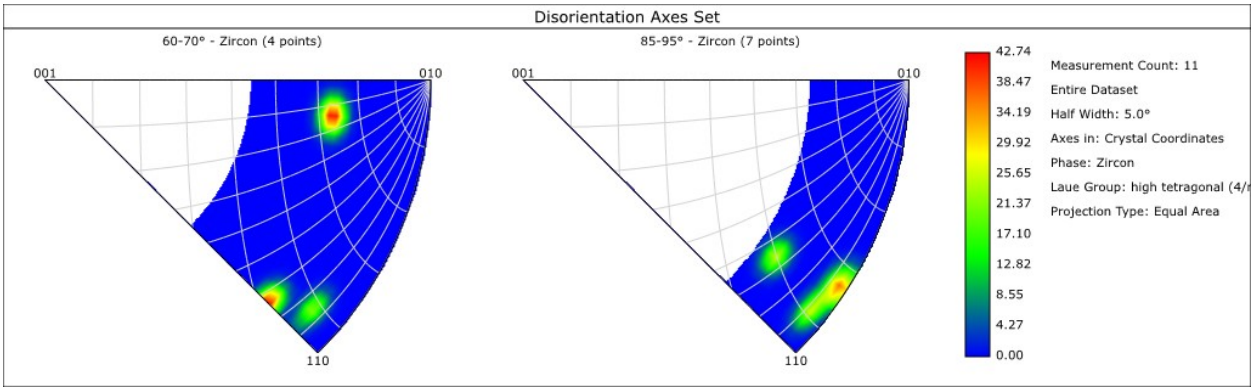
Disorientation Axes Set
60-70° - Zircon (4 points)
85-95° - Zircon (7 points)
001
010
110
42.74
38.47
34.19
29.92
25.65
21.37
17.10
12.82
8.55
4.27
0.00
Measurement Count: 11
Entire Dataset
Half Width: 5.0°
Axes in: Crystal Coordinates
Phase: Zircon
Laue Group: high tetragonal (4/
Projection Type: Equal Area

M186

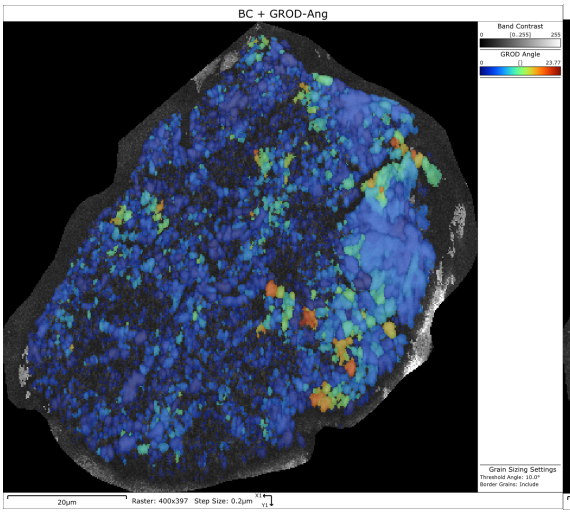
BC + GROD-Ang
Band Contrast
GROD Angle
Grain Sizing Settings
20µm
Raster: 400x397 Step Size: 0.2µm

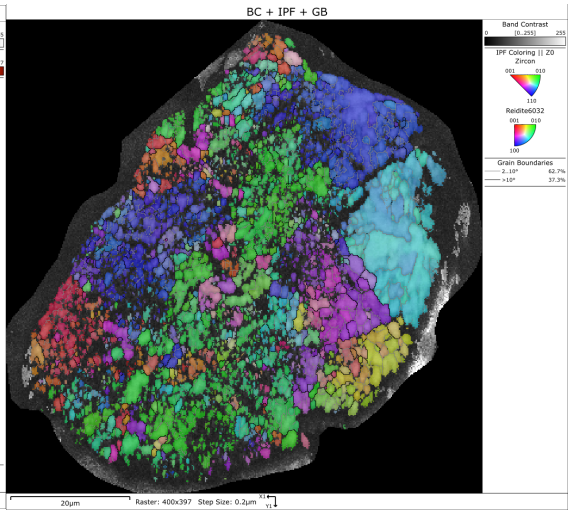
BC + IPF + GB
Band Contrast
IPF Coloring || Z0
Zircon
Reidite6032
Grain Boundaries
20µm
Raster: 400x397 Step Size: 0.2µm

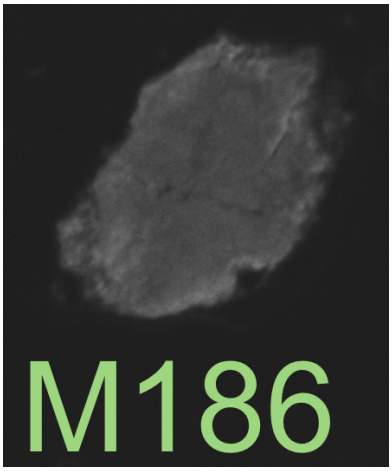
M186

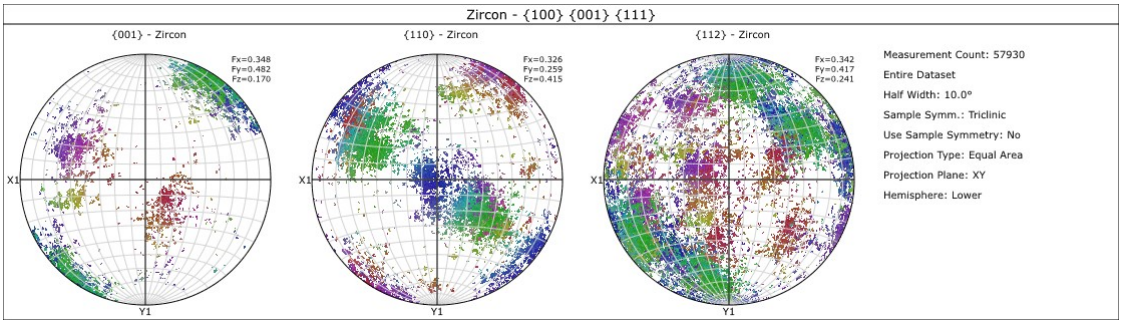
Zircon - {100} {001} {111}
{001} - Zircon
{110} - Zircon
{112} - Zircon
Fx=0.348
Fy=0.482
Fz=0.170
Fx=0.326
Fy=0.259
Fz=0.415
Fx=0.342
Fy=0.417
Fz=0.241
X1
Y1
Measurement Count: 57930
Entire Dataset
Half Width: 10.0°
Sample Symm.: Triclinic
Use Sample Symmetry: No
Projection Type: Equal Area
Projection Plane: XY
Hemisphere: Lower

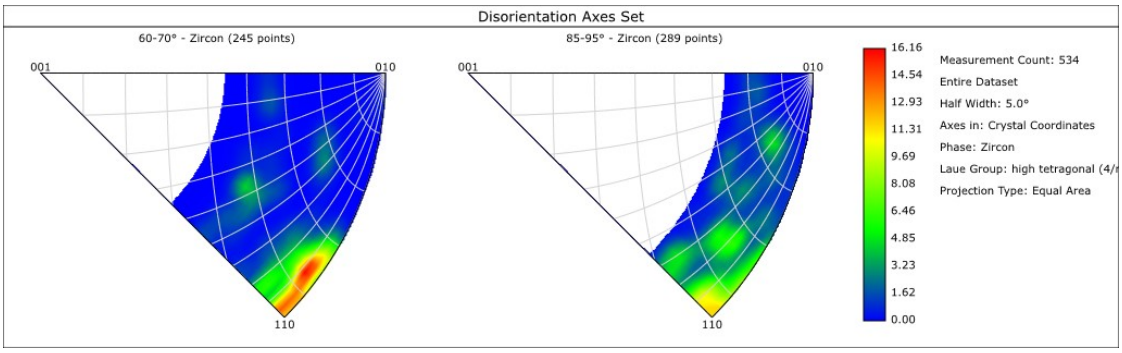
Disorientation Axes Set
60-70° - Zircon (245 points)
85-95° - Zircon (289 points)
001
010
110
16.16
14.54
12.93
11.31
9.69
8.08
6.46
4.85
3.23
1.62
0.00
Measurement Count: 534
Entire Dataset
Half Width: 5.0°
Axes in: Crystal Coordinates
Phase: Zircon
Laue Group: high tetragonal (4/
Projection Type: Equal Area

M187

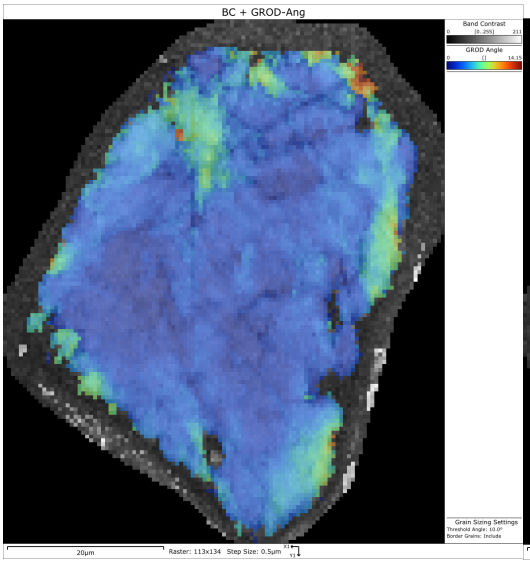
BC + GROD-Ang
Band Contrast
GROD Angle
Grain Sizing Settings
20μm
Raster: 113x134 Step Size: 0.5μm

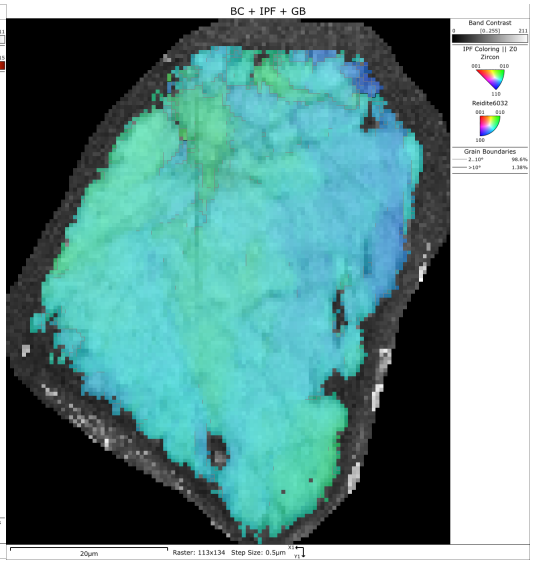
BC + IPF + GB
Band Contrast
IPF Coloring || Z0
Zircon
Reidite6032
Grain Boundaries
20μm
Raster: 113x134 Step Size: 0.5μm

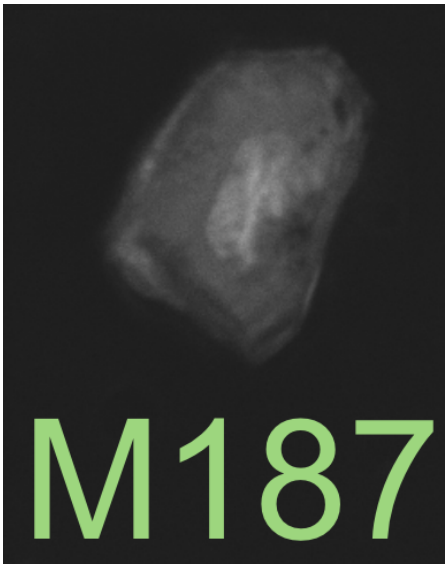
M187

M190

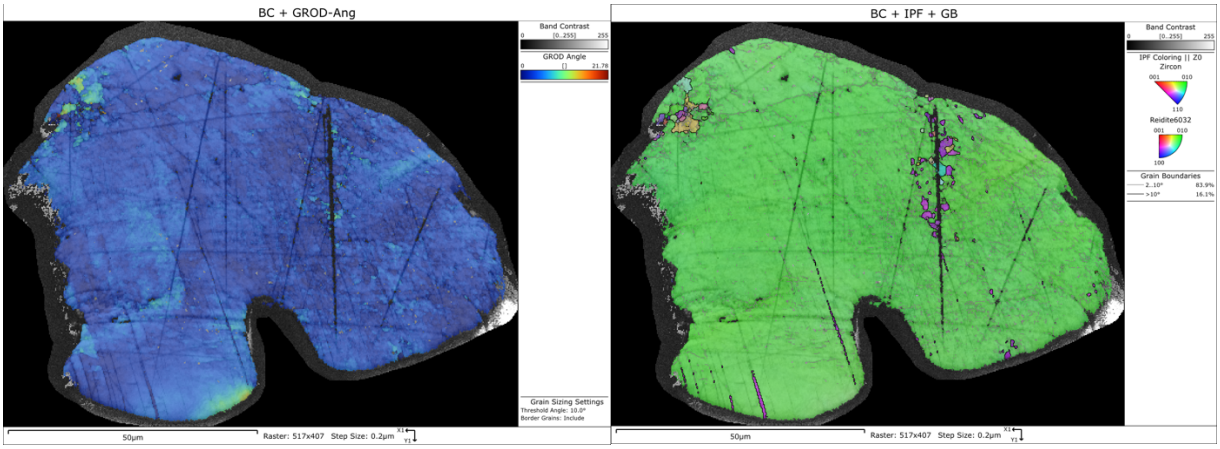
BC + GROD-Ang
Band Contrast
GROD Angle
Grain Sizing Settings
50µm
Raster: 517x407 Step Size: 0.2µm
BC + IPF + GB
Band Contrast
IPF Coloring || Z0
Zircon
Reidite6032
Grain Boundaries
50µm
Raster: 517x407 Step Size: 0.2µm

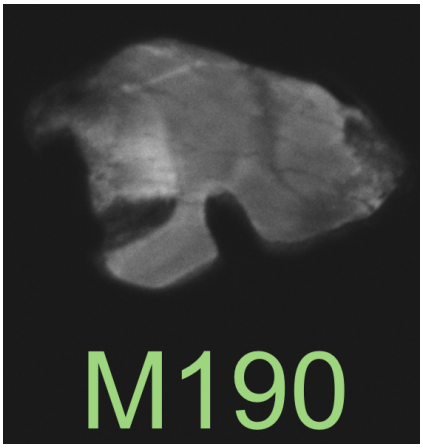
M190

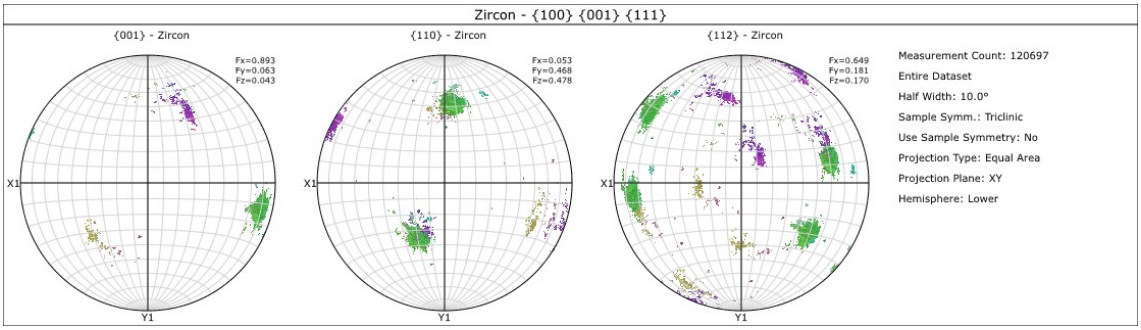
Zircon - {100} {001} {111}
{001} - Zircon
Fx=0.893
Fy=0.063
Fz=0.043
{110} - Zircon
Fx=0.053
Fy=0.468
Fz=0.478
{112} - Zircon
Fx=0.649
Fy=0.181
Fz=0.170
X1
Y1
Measurement Count: 120697
Entire Dataset
Half Width: 10.0°
Sample Symm.: Triclinic
Use Sample Symmetry: No
Projection Type: Equal Area
Projection Plane: XY
Hemisphere: Lower

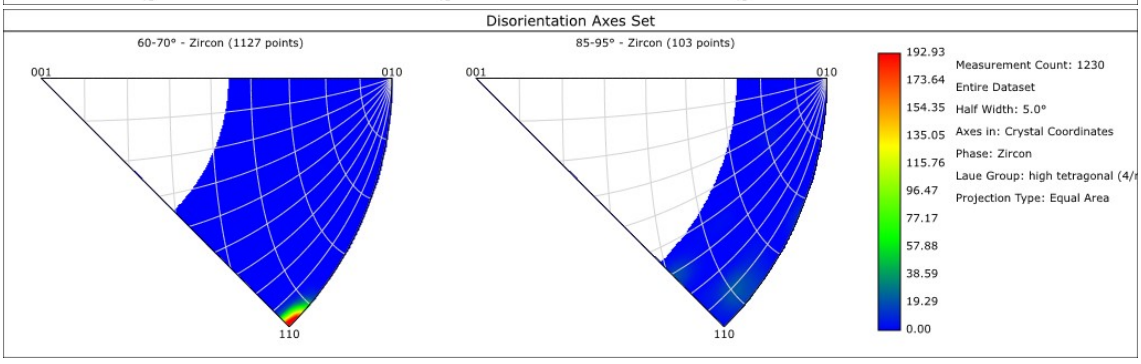
Disorientation Axes Set
60-70° - Zircon (1127 points)
85-95° - Zircon (103 points)
001
010
110
192.93
173.64
154.35
135.05
115.76
96.47
77.17
57.88
38.59
19.29
0.00
Measurement Count: 1230
Entire Dataset
Half Width: 5.0°
Axes in: Crystal Coordinates
Phase: Zircon
Projection Type: Equal Area

M195

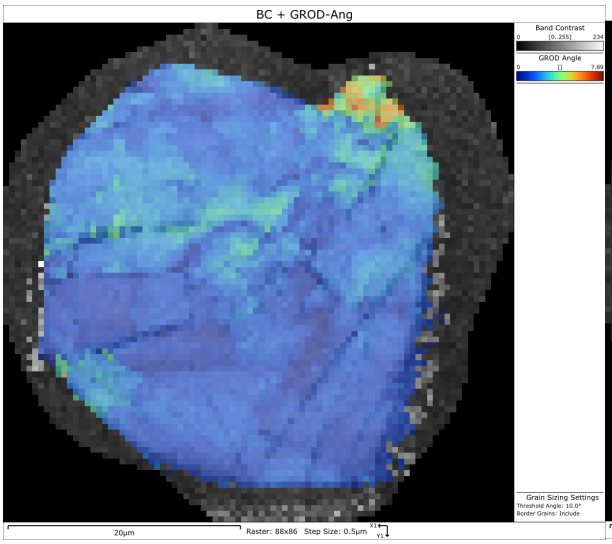
BC + GROD-Ang
Band Contrast
GROD Angle
Grain Sizing Settings
20µm
Raster: 88x86 Step Size: 0.5µm

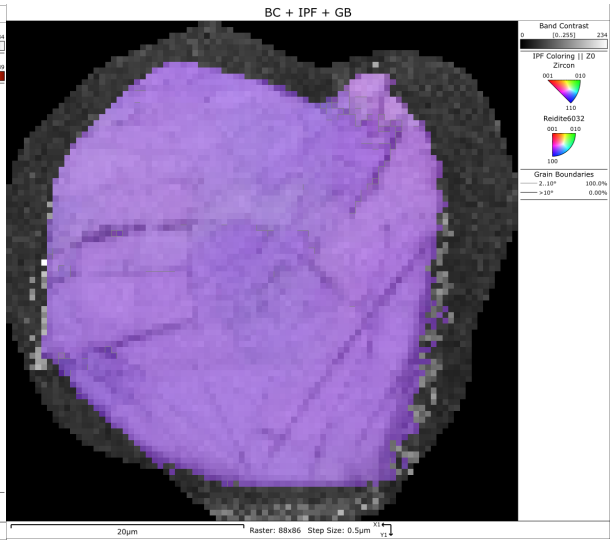
BC + IPF + GB
Band Contrast
IPF Coloring || Z0
Zircon
Reidite6032
Grain Boundaries
20µm
Raster: 88x86 Step Size: 0.5µm

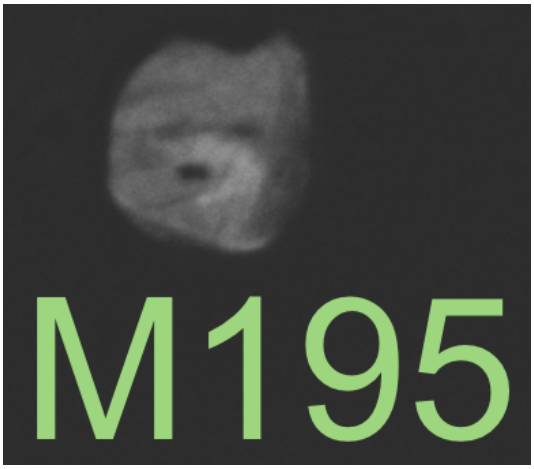
M195

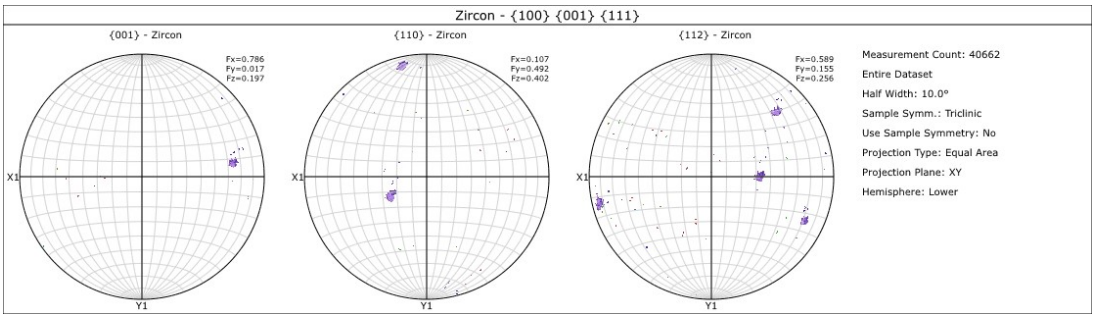
Zircon - {100} {001} {111}
{001} - Zircon
Fx=0.786
Fy=0.017
Fz=0.197
{110} - Zircon
Fx=0.107
Fy=0.492
Fz=0.402
{112} - Zircon
Fx=0.589
Fy=0.155
Fz=0.256
X1
Y1
Measurement Count: 40662
Entire Dataset
Half Width: 10.0°
Sample Symm.: Triclinic
Use Sample Symmetry: No
Projection Type: Equal Area
Projection Plane: XY
Hemisphere: Lower

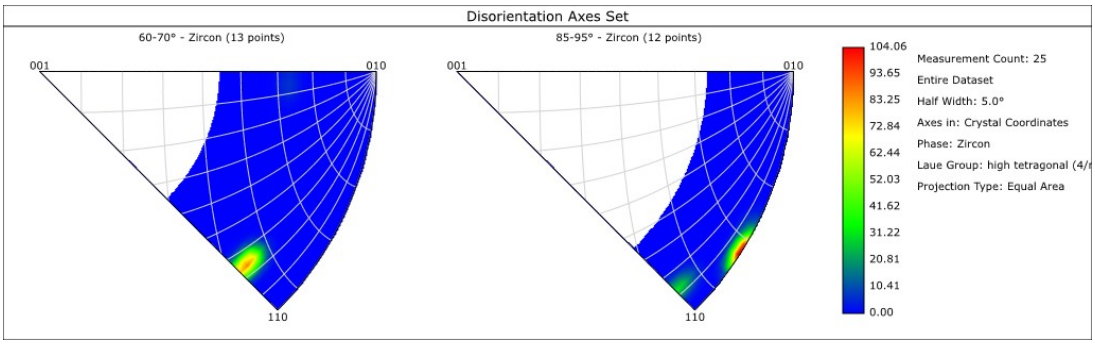
Disorientation Axes Set
60-70° - Zircon (13 points)
85-95° - Zircon (12 points)
001
010
110
104.06
93.65
83.25
72.84
62.44
52.03
41.62
31.22
20.81
10.41
0.00
Measurement Count: 25
Entire Dataset
Half Width: 5.0°
Axes in: Crystal Coordinates
Phase: Zircon
Projection Type: Equal Area

M196

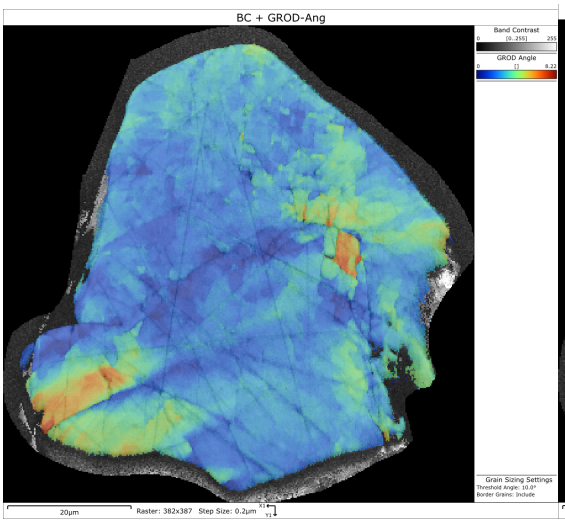
BC + GROD-Ang
Band Contrast
GROD Angle
Grain Sizing Settings
20μm
Raster: 382x387 Step Size: 0.2μm

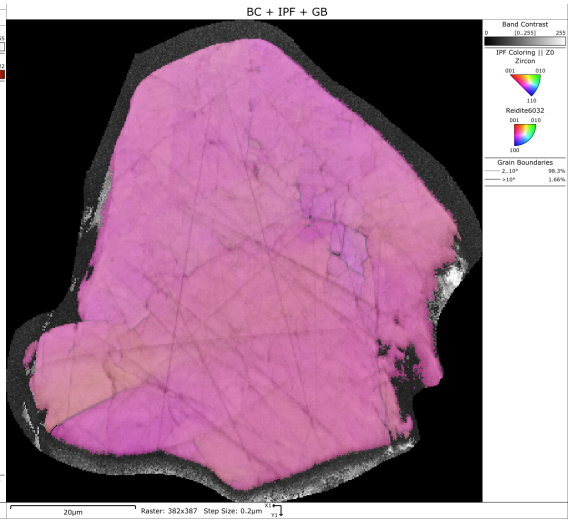
BC + IPF + GB
Band Contrast
IPF Coloring || Z0
Zircon
Reidite6032
Grain Boundaries
20μm
Raster: 382x387 Step Size: 0.2μm

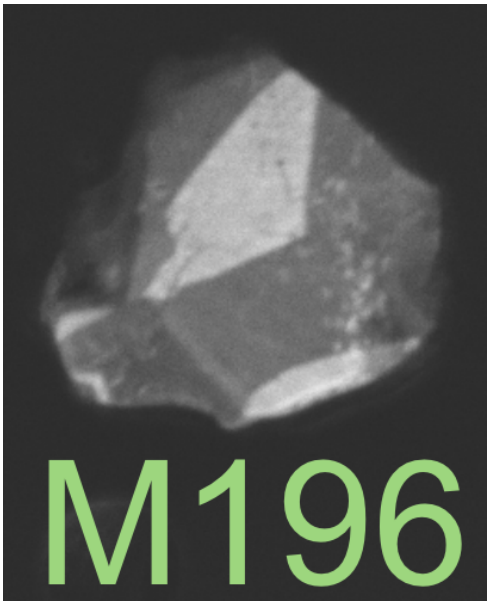
M196

M197

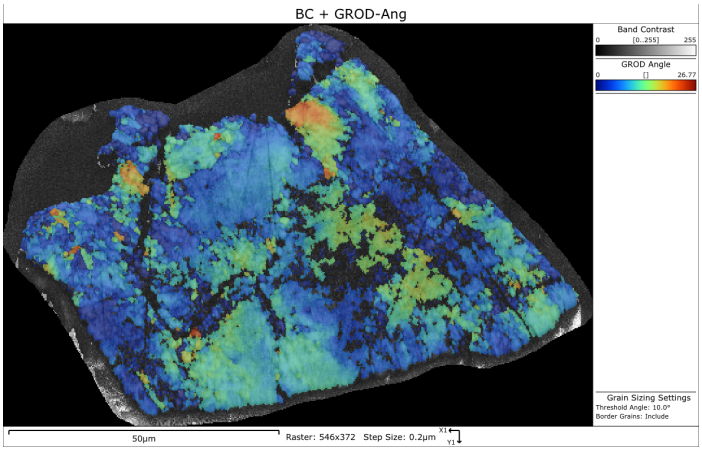
BC + GROD-Ang
Band Contrast
0 [0..255] 255
GROD Angle
0 [] 26.77
Grain Sizing Settings
Threshold Angle: 10.0°
Border Grains: Include
50µm
Raster: 546x372 Step Size: 0.2µm

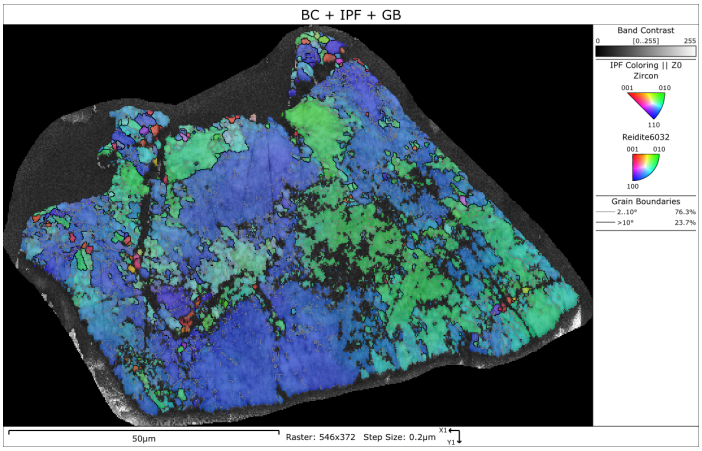
BC + IPF + GB
Band Contrast
0 [0..255] 255
IPF Coloring || Z0
Zircon
001 010
110
Reidite6032
001 010
100
Grain Boundaries
2..10° 76.3%
>10° 23.7%
50µm
Raster: 546x372 Step Size: 0.2µm

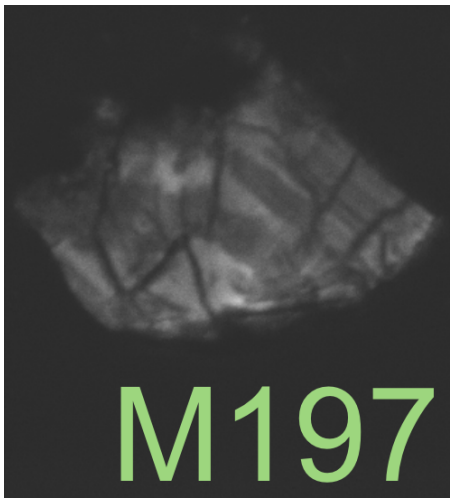
M197

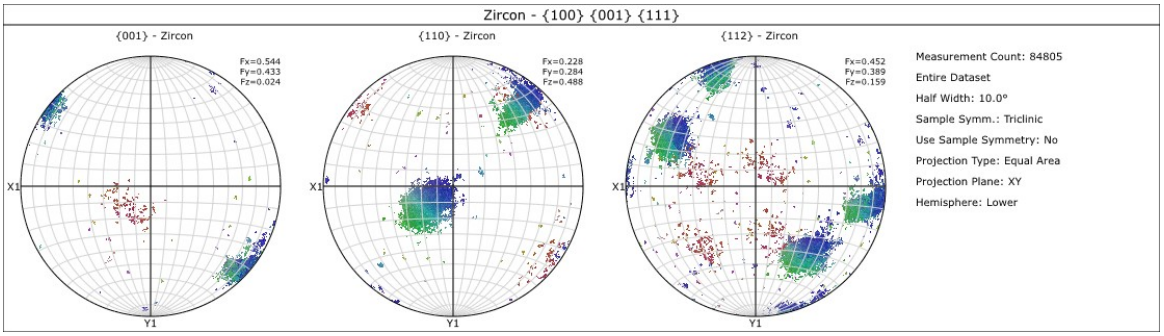
Zircon - {100} {001} {111}
{001} - Zircon
Fx=0.544
Fy=0.433
Fz=0.024
{110} - Zircon
Fx=0.228
Fy=0.284
Fz=0.488
{112} - Zircon
Fx=0.452
Fy=0.389
Fz=0.159
Measurement Count: 84805
Entire Dataset
Half Width: 10.0°
Sample Symm.: Triclinic
Use Sample Symmetry: No
Projection Type: Equal Area
Projection Plane: XY
Hemisphere: Lower

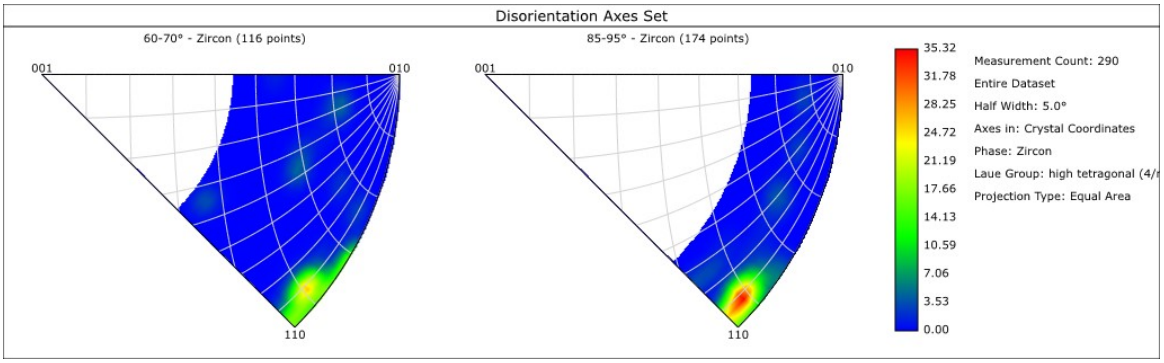
Disorientation Axes Set
60-70° - Zircon (116 points)
85-95° - Zircon (174 points)
001
010
110
35.32
31.78
28.25
24.72
21.19
17.66
14.13
10.59
7.06
3.53
0.00
Measurement Count: 290
Entire Dataset
Half Width: 5.0°
Axes in: Crystal Coordinates
Phase: Zircon
Projection Type: Equal Area

M198

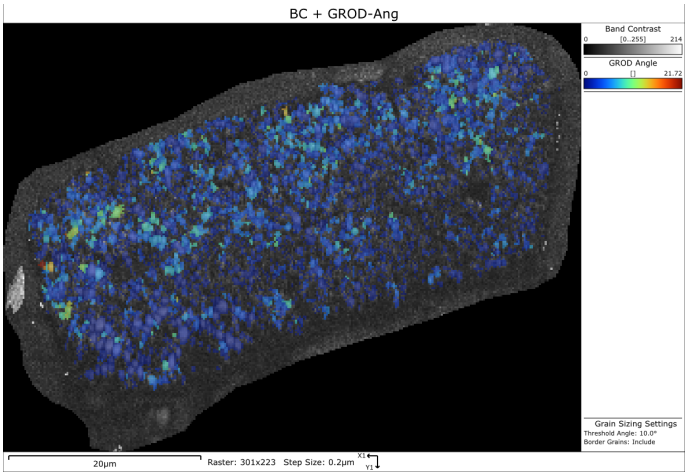
BC + GROD-Ang
Band Contrast
GROD Angle
Grain Sizing Settings
20µm
Raster: 301x223 Step Size: 0.2µm

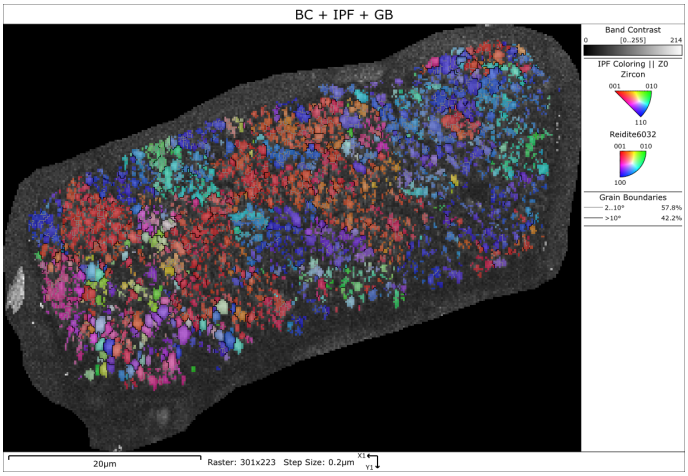
BC + IPF + GB
Band Contrast
IPF Coloring || Z0
Zircon
Reidite6032
Grain Boundaries
20µm
Raster: 301x223 Step Size: 0.2µm

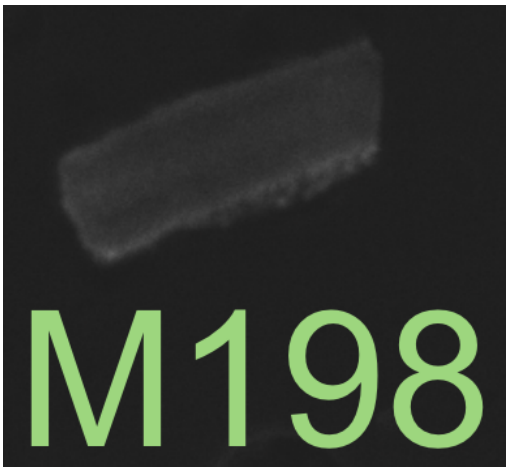
M198

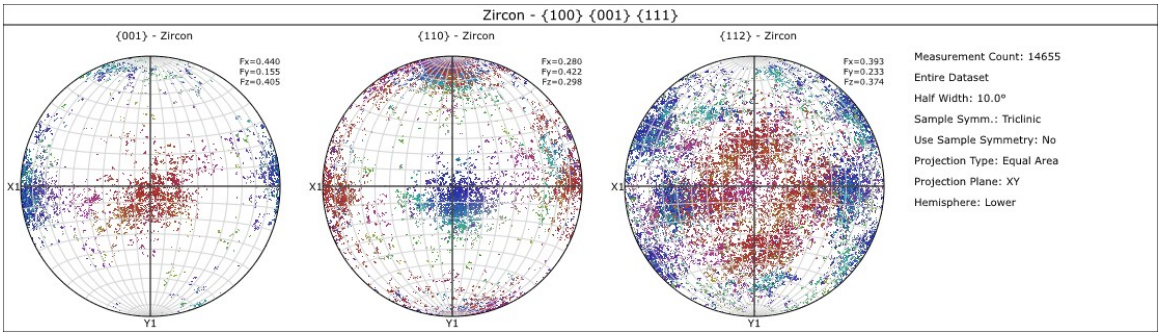
Zircon - {100} {001} {111}
{001} - Zircon
{110} - Zircon
{112} - Zircon
Measurement Count: 14655
Entire Dataset
Half Width: 10.0°
Sample Symm.: Triclinic
Use Sample Symmetry: No
Projection Type: Equal Area
Projection Plane: XY
Hemisphere: Lower

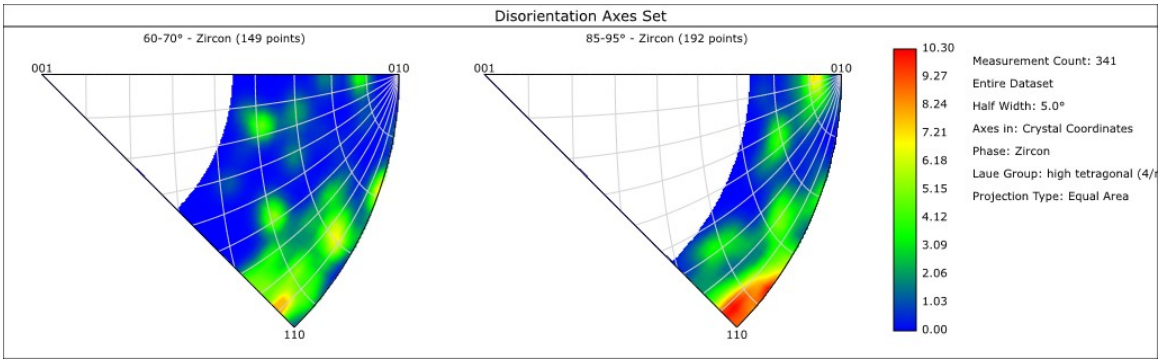
Disorientation Axes Set
60-70° - Zircon (149 points)
85-95° - Zircon (192 points)
001
010
110
10.30
9.27
8.24
7.21
6.18
5.15
4.12
3.09
2.06
1.03
0.00
Measurement Count: 341
Entire Dataset
Half Width: 5.0°
Axes in: Crystal Coordinates
Phase: Zircon
Projection Type: Equal Area

M199

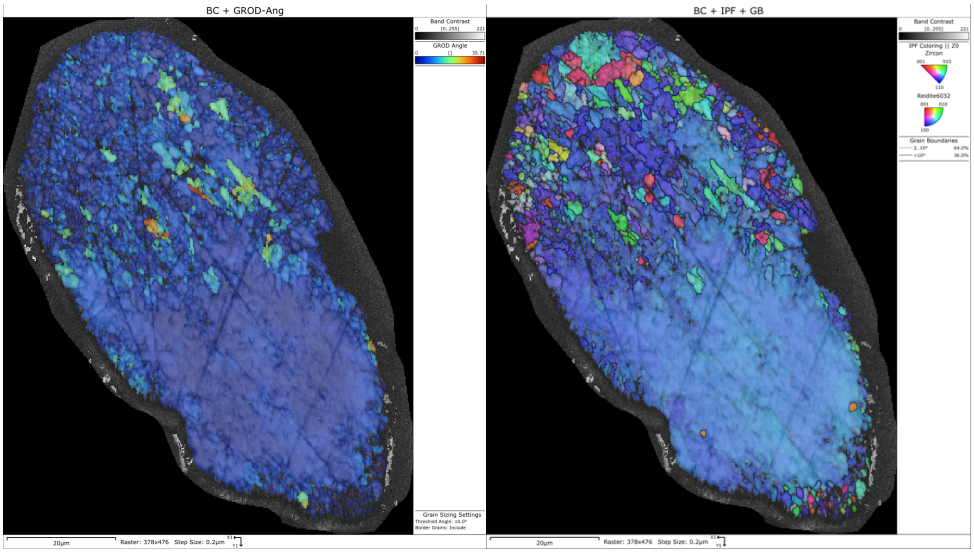
BC + GROD-Ang
BC + IPF + GB

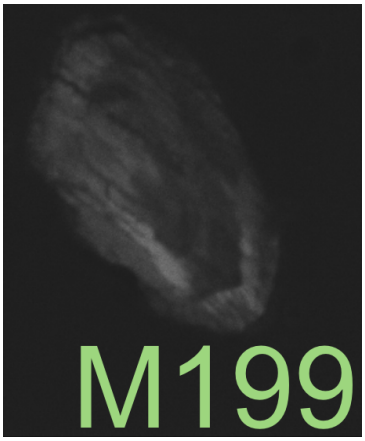
M199

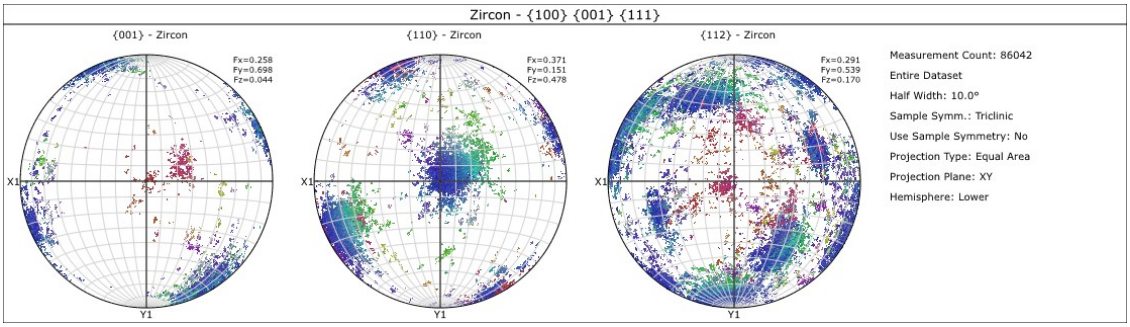
Zircon - {100} {001} {111}
{001} - Zircon
Fx=0.258
Fy=0.698
Fz=0.044
{110} - Zircon
Fx=0.371
Fy=0.151
Fz=0.478
{112} - Zircon
Fx=0.291
Fy=0.539
Fz=0.170
X1
Y1
Measurement Count: 86042
Entire Dataset
Half Width: 10.0°
Sample Symm.: Triclinic
Use Sample Symmetry: No
Projection Type: Equal Area
Projection Plane: XY
Hemisphere: Lower

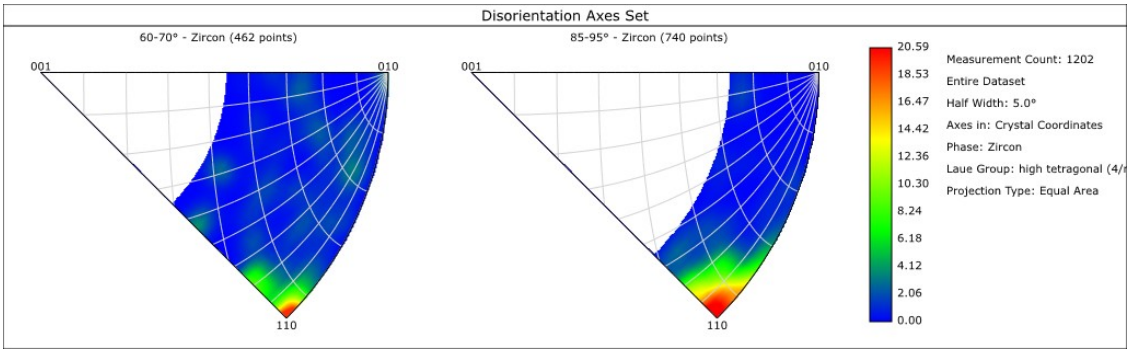
Disorientation Axes Set
60-70° - Zircon (462 points)
85-95° - Zircon (740 points)
001
010
110
20.59
18.53
16.47
14.42
12.36
10.30
8.24
6.18
4.12
2.06
0.00
Measurement Count: 1202
Entire Dataset
Half Width: 5.0°
Axes in: Crystal Coordinates
Phase: Zircon
Projection Type: Equal Area

M201

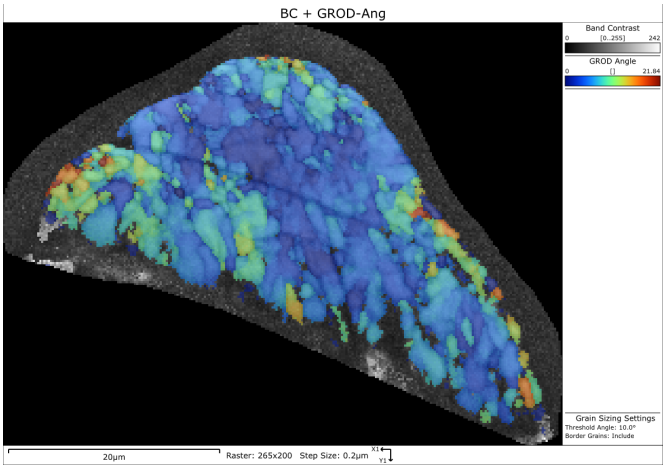
BC + GROD-Ang
Band Contrast
GROD Angle
Grain Sizing Settings
20µm
Raster: 265x200 Step Size: 0.2µm

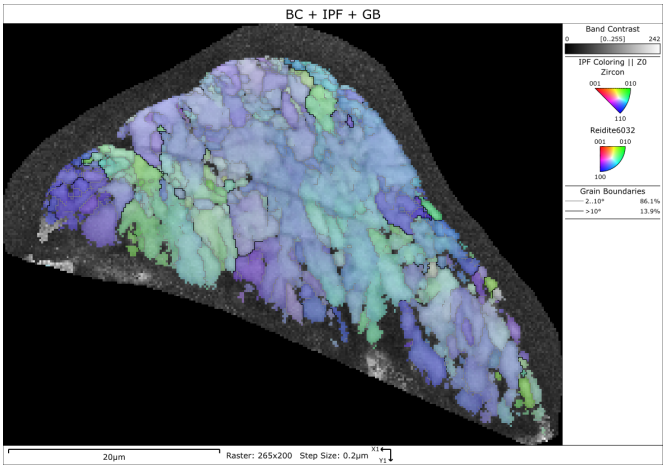
BC + IPF + GB
Band Contrast
IPF Coloring || Z0
Zircon
Reidite6032
Grain Boundaries
20µm
Raster: 265x200 Step Size: 0.2µm


M201

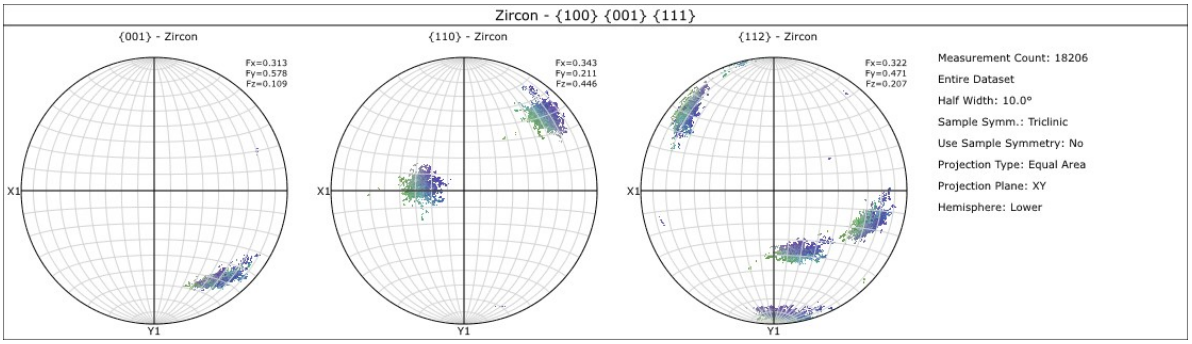
Zircon - {100} {001} {111}
{001} - Zircon
{110} - Zircon
{112} - Zircon
Measurement Count: 18206
Entire Dataset
Half Width: 10.0°
Sample Symm.: Triclinic
Use Sample Symmetry: No
Projection Type: Equal Area
Projection Plane: XY
Hemisphere: Lower

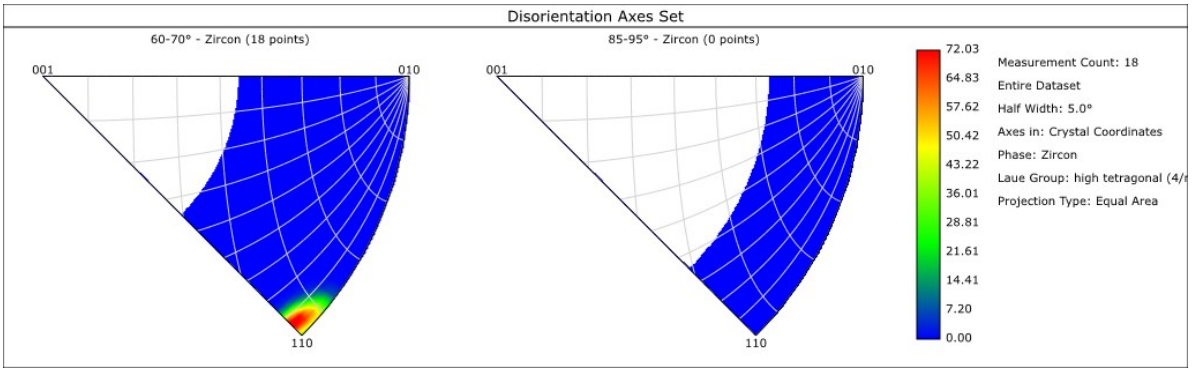
Disorientation Axes Set
60-70° - Zircon (18 points)
85-95° - Zircon (0 points)
001
010
110
72.03
64.83
57.62
50.42
43.22
36.01
28.81
21.61
14.41
7.20
0.00
Measurement Count: 18
Entire Dataset
Half Width: 5.0°
Axes in: Crystal Coordinates
Phase: Zircon
Projection Type: Equal Area

M202

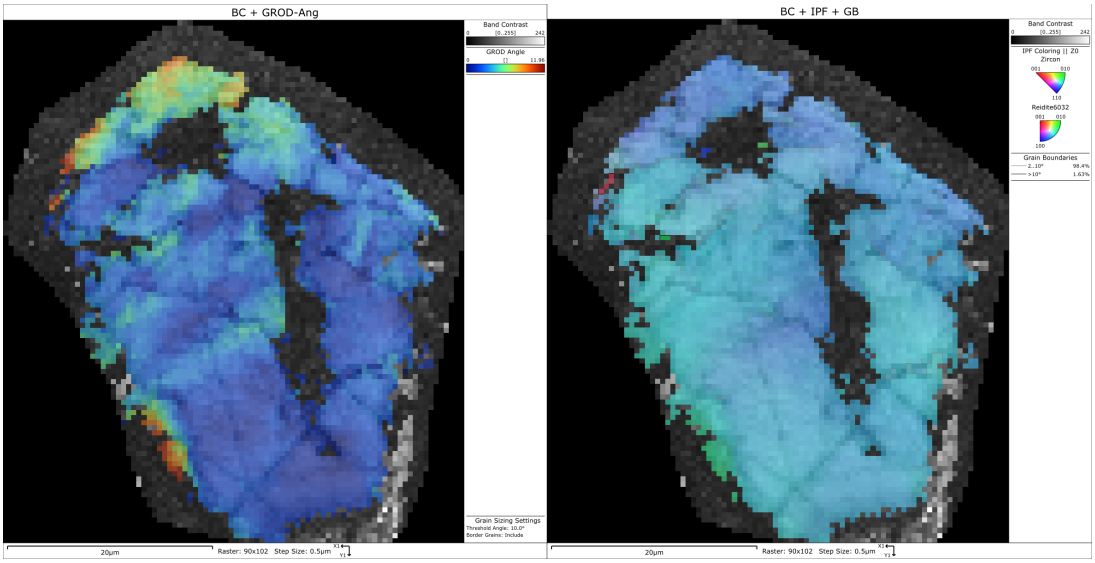
BC + GROD-Ang
Band Contrast
GROD Angle
Grain Sizing Settings
20μm
Raster: 90x102 Step Size: 0.5μm
BC + IPF + GB
Band Contrast
IPF Coloring || Z0
Zircon
Reidite6032
Grain Boundaries
20μm
Raster: 90x102 Step Size: 0.5μm


M202

M205

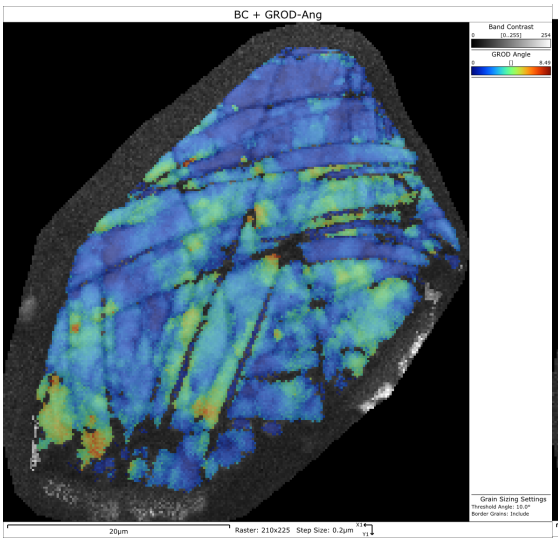
BC + GROD-Ang
Band Contrast
GROD Angle
Grain Sizing Settings
20µm
Raster: 210x225 Step Size: 0.2µm

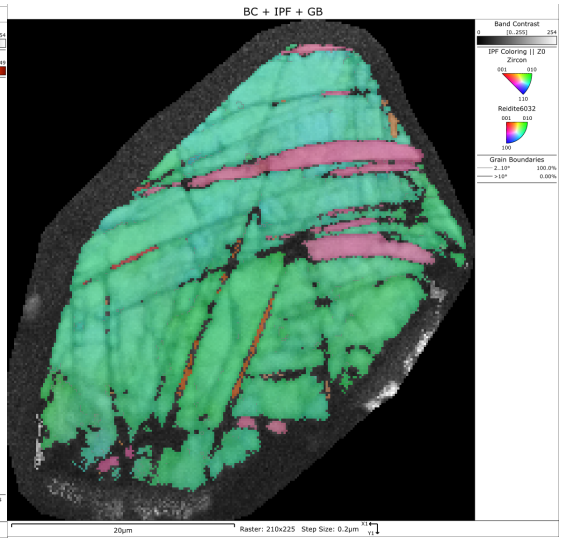
BC + IPF + GB
Band Contrast
IPF Coloring | ZO
Zircon
Reidite6032
Grain Boundaries
20µm
Raster: 210x225 Step Size: 0.2µm

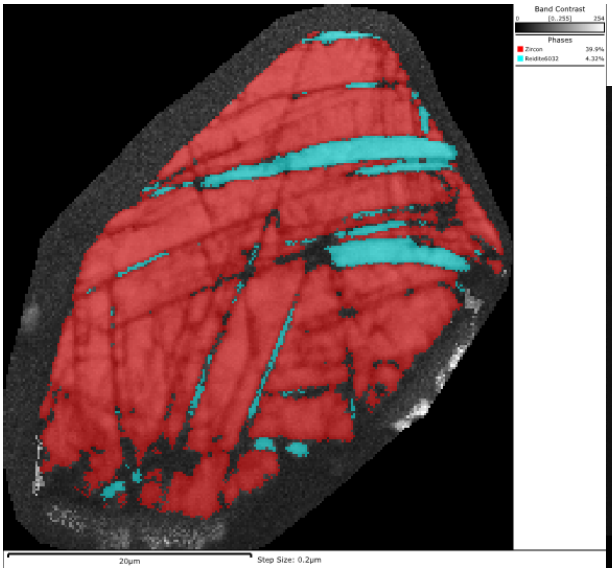
Band Contrast
Phases
Zircon 39.9%
Reidite6032 4.32%
20µm
Step Size: 0.2µm

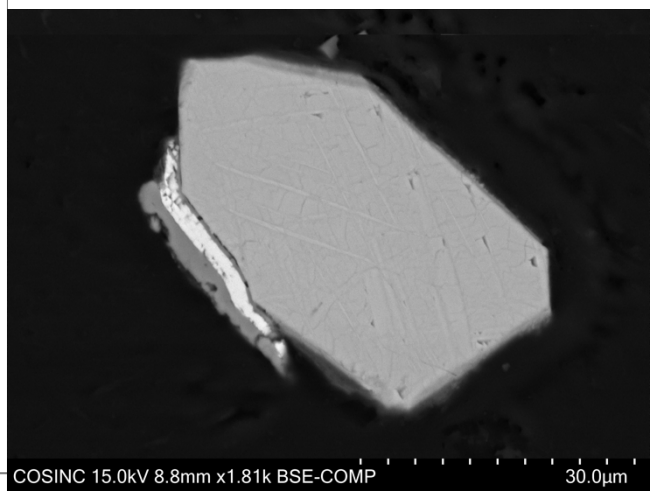
COSINC 15.0kV 8.8mm x1.81k BSE-COMP
30.0µm

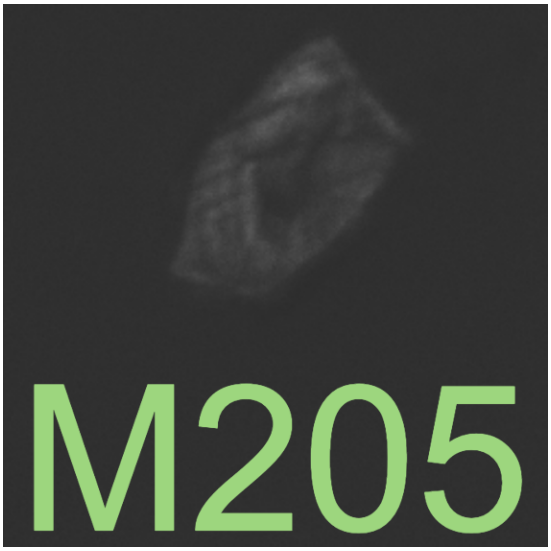
M205

M208

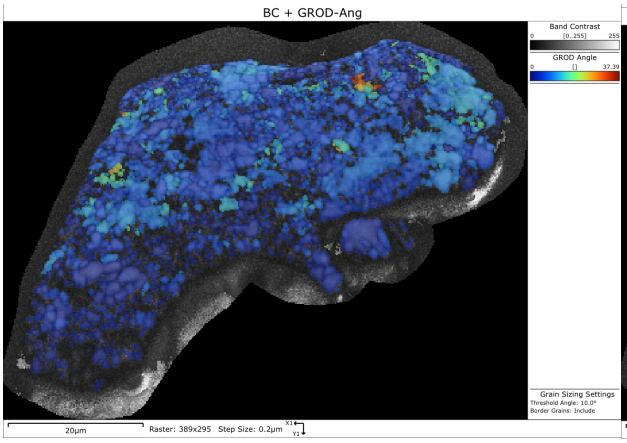
BC + GROD-Ang
Band Contrast
GROD Angle
Grain Sizing Settings
20µm
Raster: 389x295 Step Size: 0.2µm

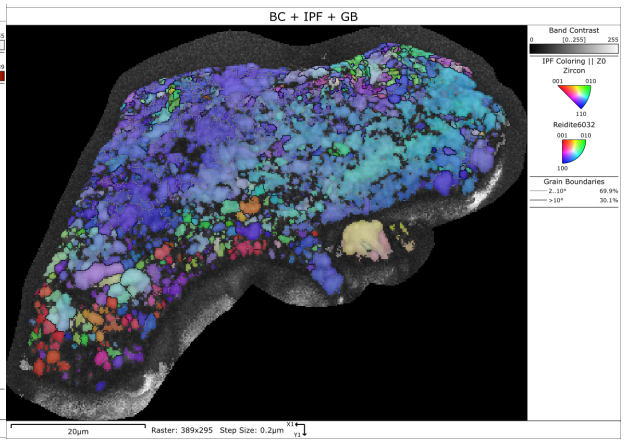
BC + IPF + GB
Band Contrast
IPF Coloring || Z0
Zircon
Reidite6032
Grain Boundaries
20µm
Raster: 389x295 Step Size: 0.2µm

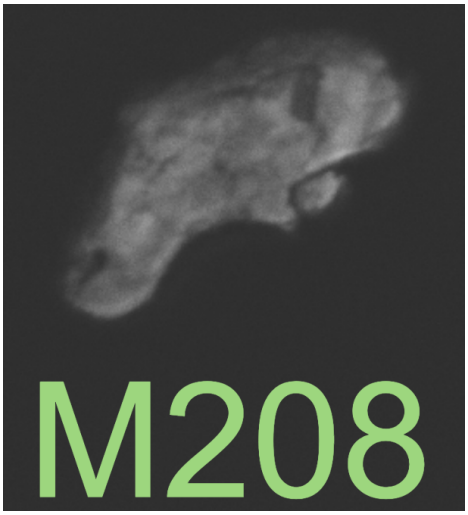
M208

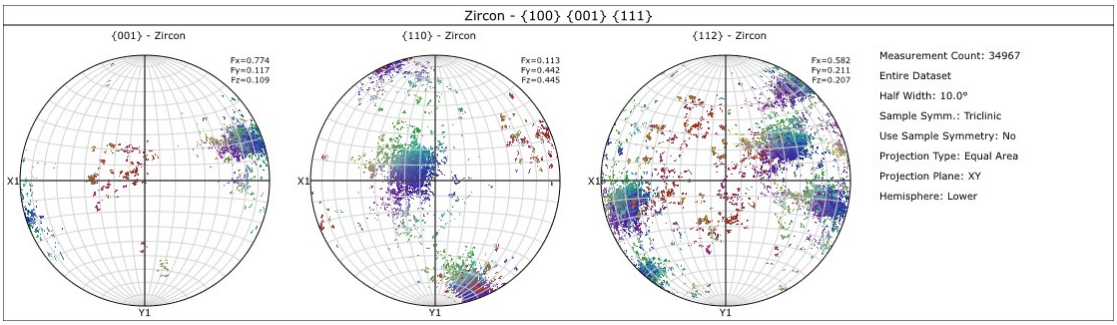
Zircon - {100} {001} {111}
{001} - Zircon
Fx=0.774
Fy=0.117
Fz=0.109
{110} - Zircon
Fx=0.113
Fy=0.442
Fz=0.445
{112} - Zircon
Fx=0.582
Fy=0.211
Fz=0.207
Measurement Count: 34967
Entire Dataset
Half Width: 10.0°
Sample Symm.: Triclinic
Use Sample Symmetry: No
Projection Type: Equal Area
Projection Plane: XY
Hemisphere: Lower

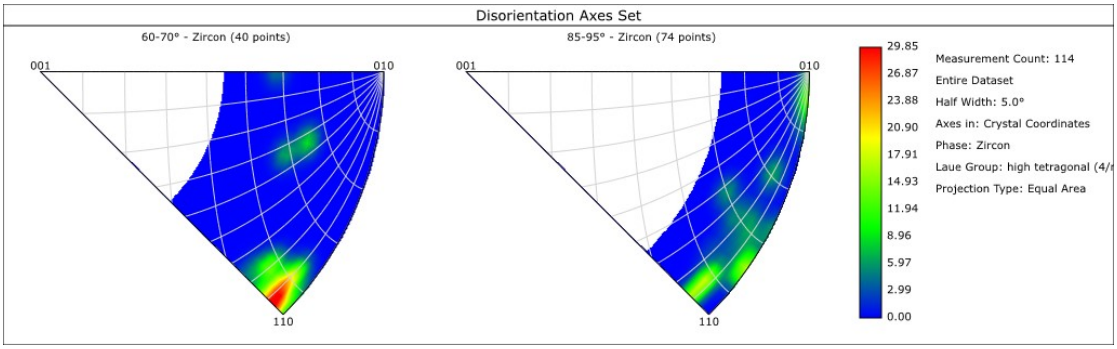
Disorientation Axes Set
60-70° - Zircon (40 points)
85-95° - Zircon (74 points)
001
010
110
29.85
26.87
23.88
20.90
17.91
14.93
11.94
8.96
5.97
2.99
0.00
Measurement Count: 114
Entire Dataset
Half Width: 5.0°
Axes in: Crystal Coordinates
Phase: Zircon
Projection Type: Equal Area

M209

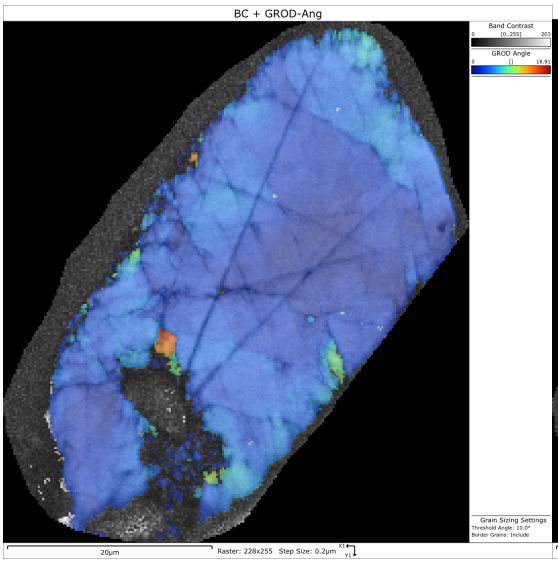
BC + GROD-Ang
Band Contrast
GROD Angle
Grain Sizing Settings
20µm
Raster: 228x255 Step Size: 0.2µm

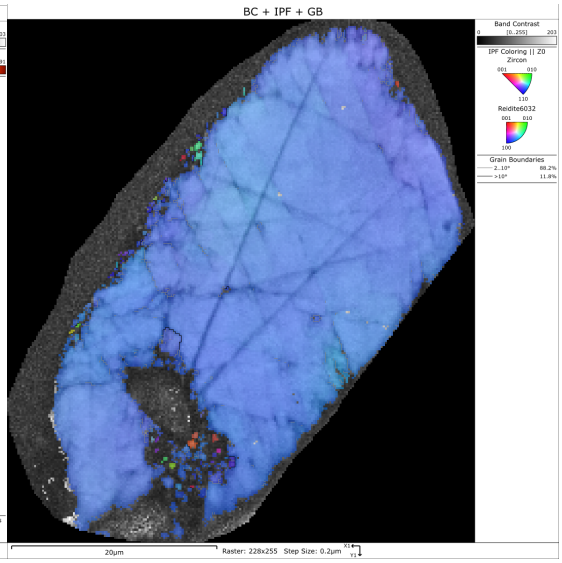
BC + IPF + GB
Band Contrast
IPF Coloring | Z0
Zircon
Reidite6032
Grain Boundaries
20µm
Raster: 228x255 Step Size: 0.2µm

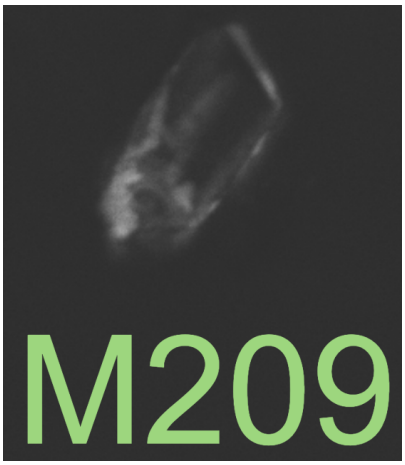
M209

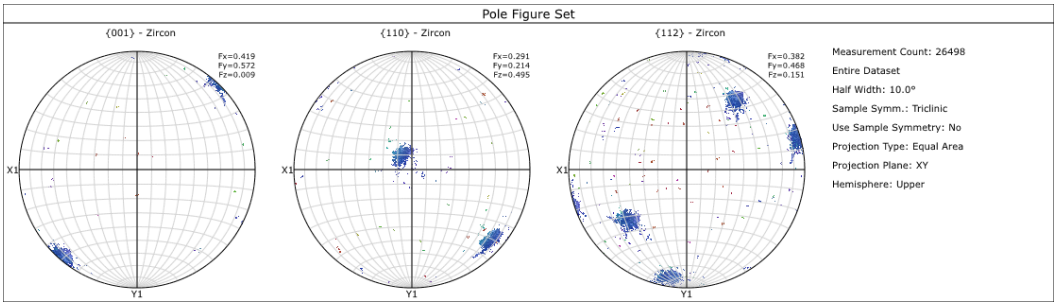
Pole Figure Set
{001} - Zircon
Fx=0.419
Fy=0.572
Fz=0.009
{110} - Zircon
Fx=0.291
Fy=0.214
Fz=0.495
{112} - Zircon
Fx=0.382
Fy=0.468
Fz=0.151
X1
Y1
Measurement Count: 26498
Entire Dataset
Half Width: 10.0°
Sample Symm.: Triclinic
Use Sample Symmetry: No
Projection Type: Equal Area
Projection Plane: XY
Hemisphere: Upper

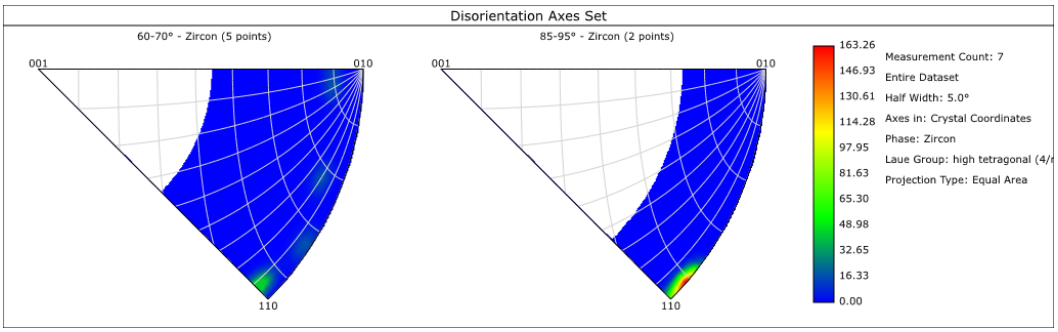
Disorientation Axes Set
60-70° - Zircon (5 points)
85-95° - Zircon (2 points)
001
010
110
163.26
146.93
130.61
114.28
97.95
81.63
65.30
48.98
32.65
16.33
0.00
Measurement Count: 7
Entire Dataset
Half Width: 5.0°
Axes in: Crystal Coordinates
Phase: Zircon
Projection Type: Equal Area

M210

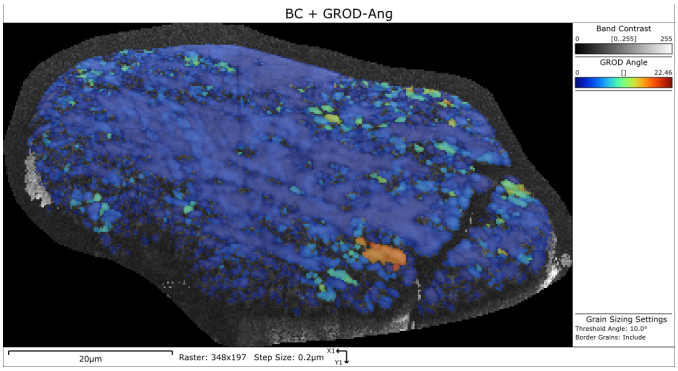
BC + GROD-Ang
Band Contrast
GROD Angle
Grain Sizing Settings
20µm
Raster: 348x197 Step Size: 0.2µm

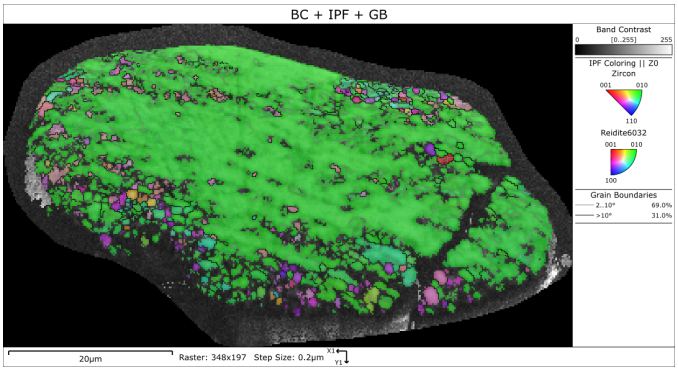
BC + IPF + GB
Band Contrast
IPF Coloring || Z0
Zircon
Reidite6032
Grain Boundaries
20µm
Raster: 348x197 Step Size: 0.2µm

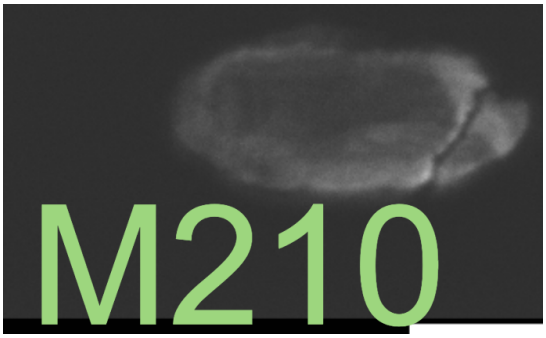
M210

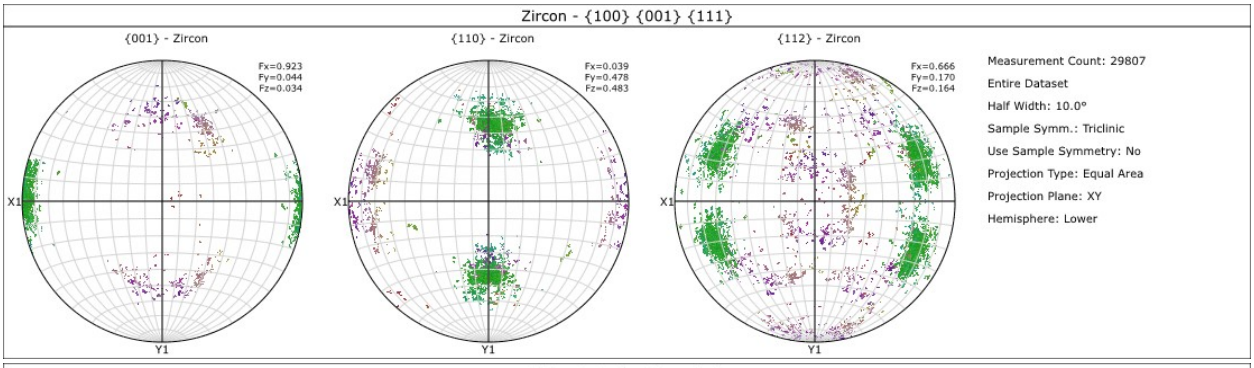
Zircon - {100} {001} {111}
{001} - Zircon
Fx=0.923
Fy=0.044
Fz=0.034
{110} - Zircon
Fx=0.039
Fy=0.478
Fz=0.483
{112} - Zircon
Fx=0.666
Fy=0.170
Fz=0.164
Measurement Count: 29807
Entire Dataset
Half Width: 10.0°
Sample Symm.: Triclinic
Use Sample Symmetry: No
Projection Type: Equal Area
Projection Plane: XY
Hemisphere: Lower

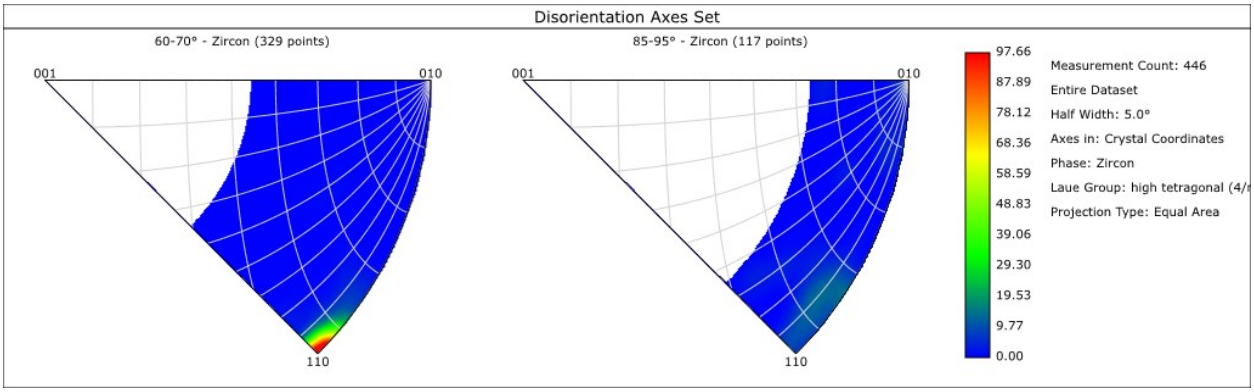
Disorientation Axes Set
60-70° - Zircon (329 points)
85-95° - Zircon (117 points)
001
010
110
97.66
87.89
78.12
68.36
58.59
48.83
39.06
29.30
19.53
9.77
0.00
Measurement Count: 446
Entire Dataset
Half Width: 5.0°
Axes in: Crystal Coordinates
Phase: Zircon
Projection Type: Equal Area

R4

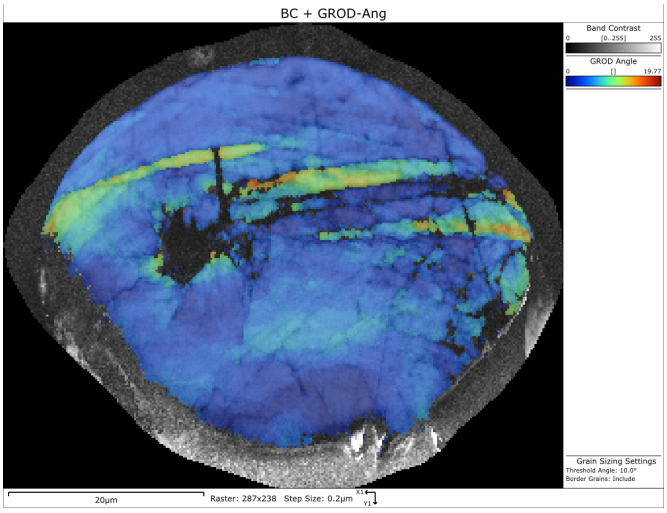
BC + GROD-Ang
Band Contrast
0 [0..255] 255
GROD Angle
0 [] 19.77
Grain Sizing Settings
Threshold Angle: 10.0°
Border Grains: Include
20µm
Raster: 287x238 Step Size: 0.2µm
X1
Y1

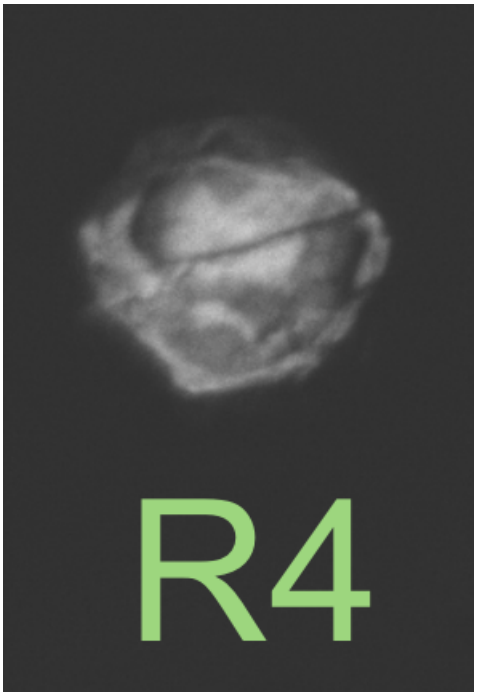
R4

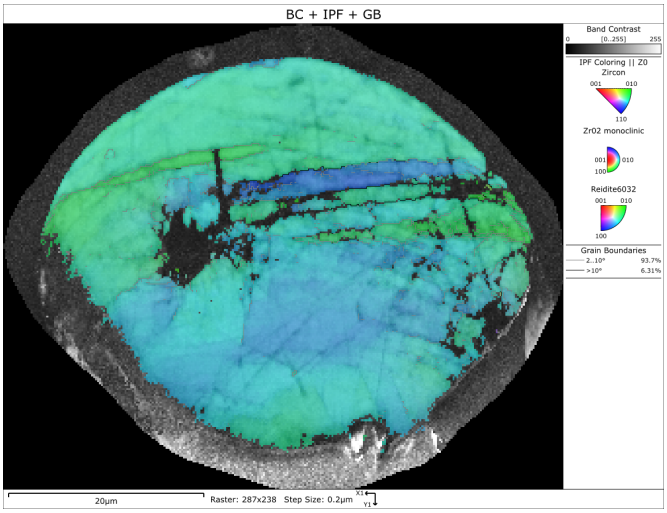
BC + IPF + GB
Band Contrast
0 [0..255] 255
IPF Coloring || Z0
Zircon
001 010
110
ZrO2 monoclinic
001 010
100
Reidite6032
001 010
100
Grain Boundaries
2..10° 93.7%
>10° 6.31%
20µm
Raster: 287x238 Step Size: 0.2µm
X1
Y1

R5

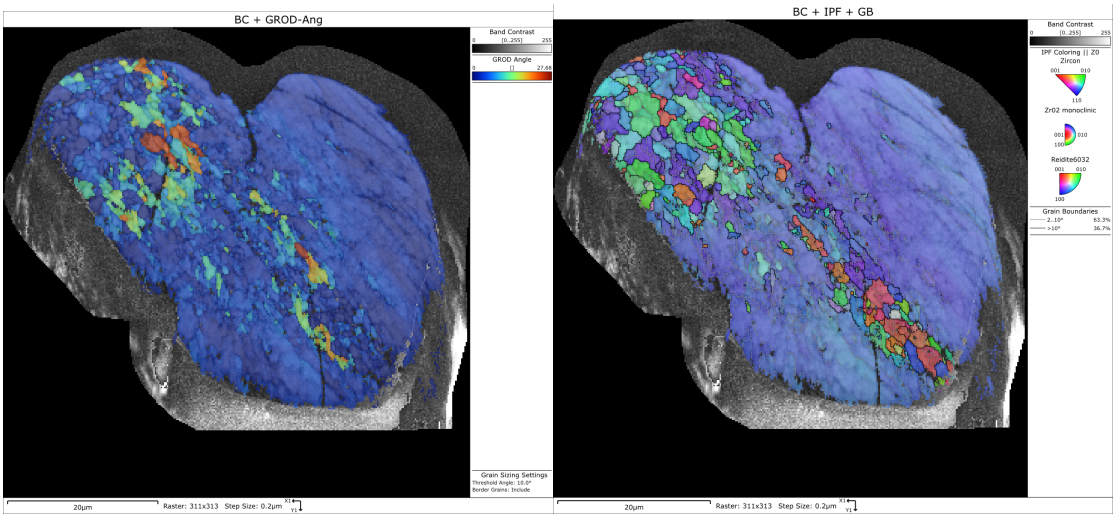
BC + GROD-Ang
Band Contrast
GROD Angle
Grain Sizing Settings
20µm
Raster: 311x313 Step Size: 0.2µm
BC + IPF + GB
Band Contrast
IPF Coloring || Z0
Zircon
Zr02 monoclinic
Reidite6032
Grain Boundaries
20µm
Raster: 311x313 Step Size: 0.2µm

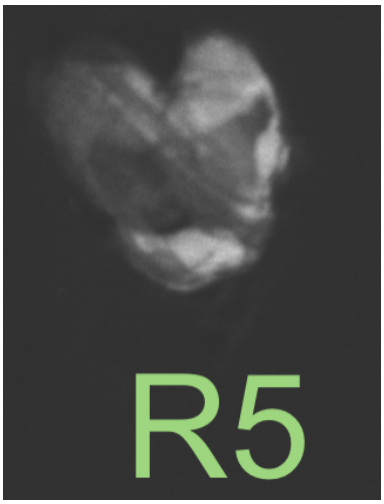
R5

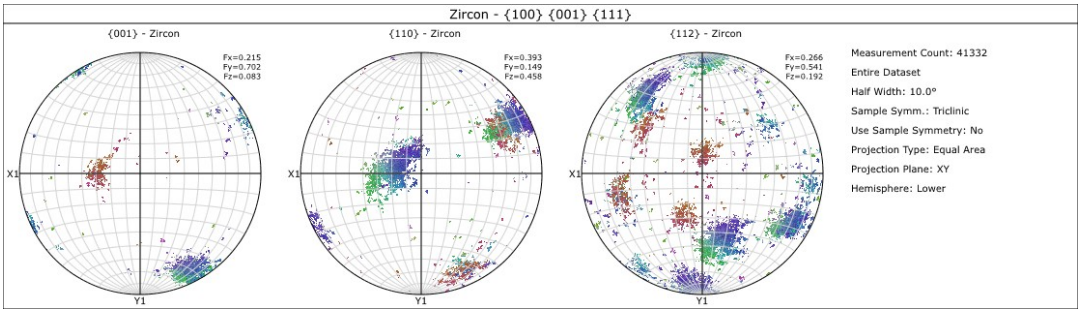
Zircon - {100} {001} {111}
{001} - Zircon
Fx=0.215
Fy=0.702
Fz=0.083
{110} - Zircon
Fx=0.393
Fy=0.149
Fz=0.458
{112} - Zircon
Fx=0.266
Fy=0.541
Fz=0.192
X1
Y1
Measurement Count: 41332
Entire Dataset
Half Width: 10.0°
Sample Symm.: Triclinic
Use Sample Symmetry: No
Projection Type: Equal Area
Projection Plane: XY
Hemisphere: Lower

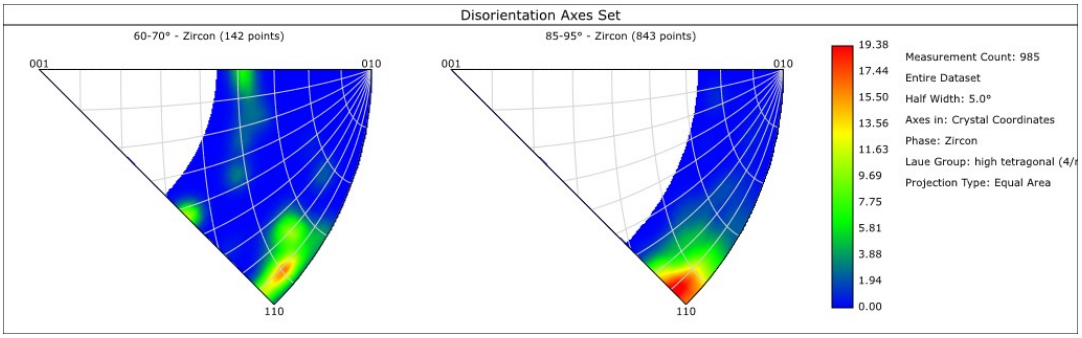
Disorientation Axes Set
60-70° - Zircon (142 points)
85-95° - Zircon (843 points)
001
010
110
19.38
17.44
15.50
13.56
11.63
9.69
7.75
5.81
3.88
1.94
0.00
Measurement Count: 985
Entire Dataset
Half Width: 5.0°
Axes in: Crystal Coordinates
Phase: Zircon
Projection Type: Equal Area

R6

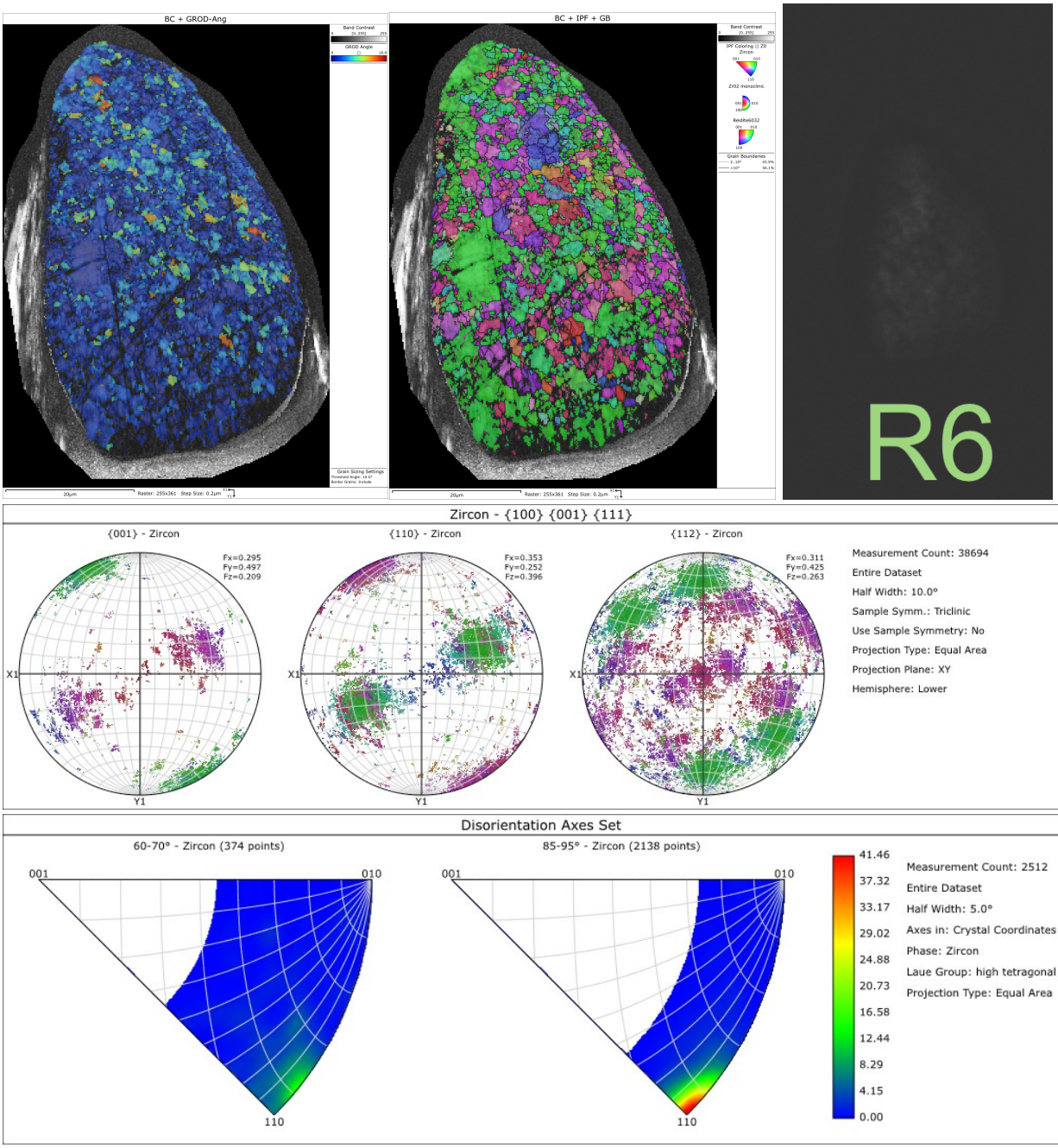
BC + GROD-Ang
BC + IPF + GB
R6
Zircon - {100} {001} {111}
{001} - Zircon
Fx=0.295
Fy=0.497
Fz=0.209
{110} - Zircon
Fx=0.353
Fy=0.252
Fz=0.396
{112} - Zircon
Fx=0.311
Fy=0.425
Fz=0.263
Measurement Count: 38694
Entire Dataset
Half Width: 10.0°
Sample Symm.: Triclinic
Use Sample Symmetry: No
Projection Type: Equal Area
Projection Plane: XY
Hemisphere: Lower
Disorientation Axes Set
60-70° - Zircon (374 points)
85-95° - Zircon (2138 points)
001
010
110
41.46
37.32
33.17
29.02
24.88
20.73
16.58
12.44
8.29
4.15
0.00
Measurement Count: 2512
Entire Dataset
Half Width: 5.0°
Axes in: Crystal Coordinates
Phase: Zircon
Projection Type: Equal Area

R9

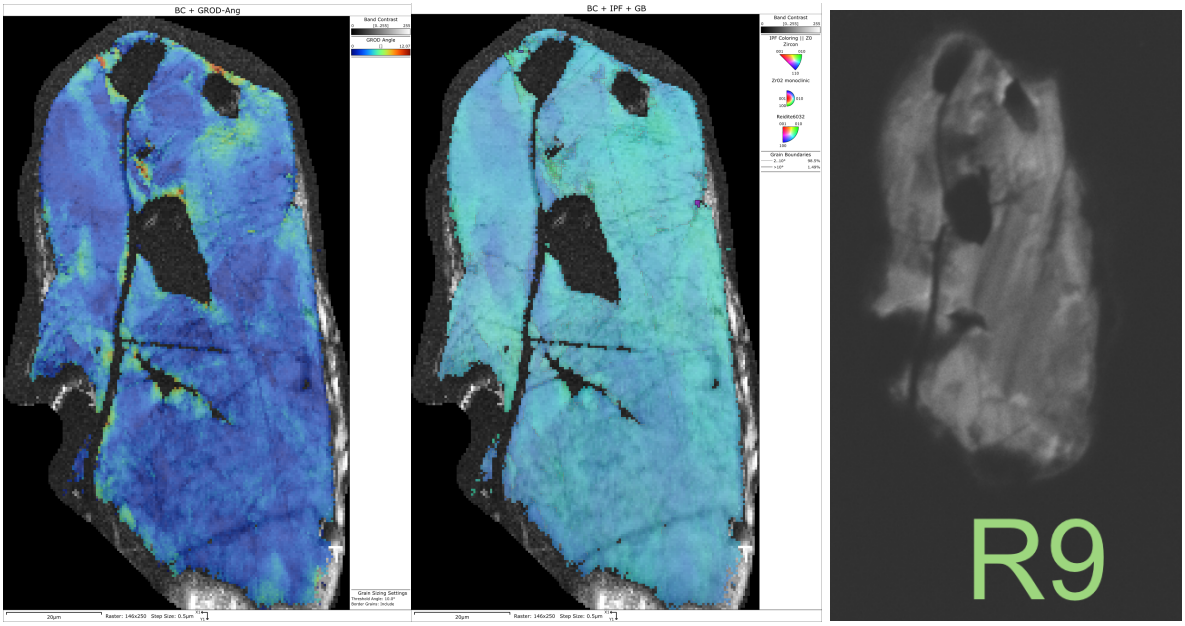

R10

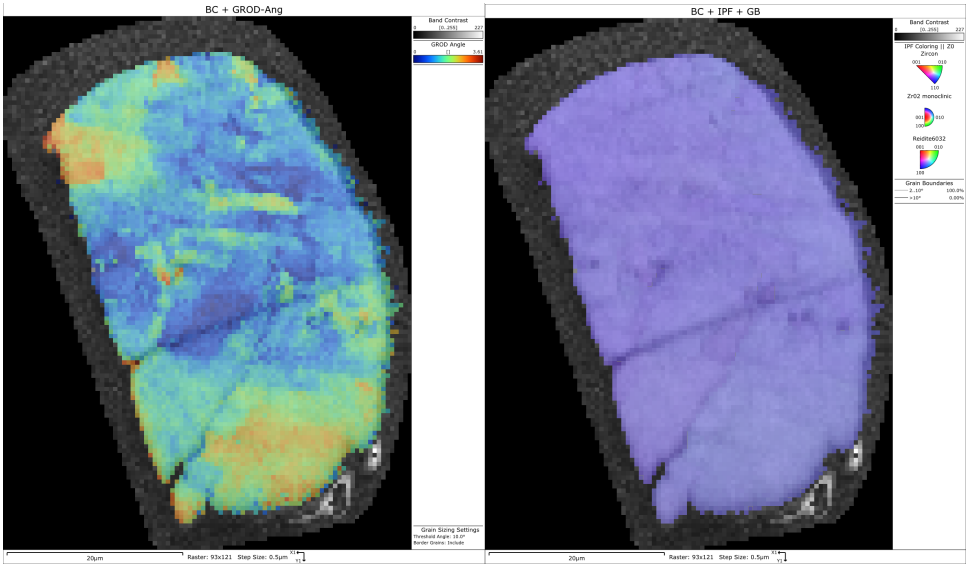
BC + GROD-Ang
Band Contrast
GROD Angle
Grain Sizing Settings
20µm
Raster: 93x121 Step Size: 0.5µm
BC + IPF + GB
Band Contrast
IPF Coloring || ZO
ZrO2 monoclinic
Grain Boundaries
20µm
Raster: 93x121 Step Size: 0.5µm

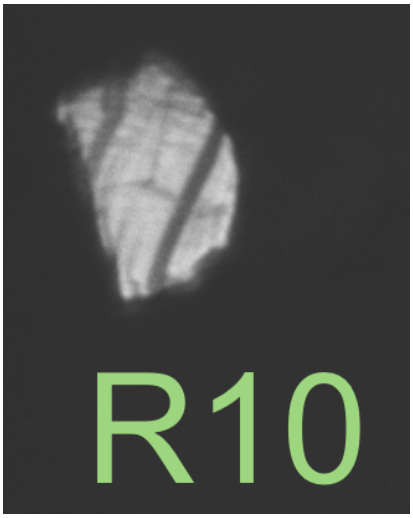
R10

R11

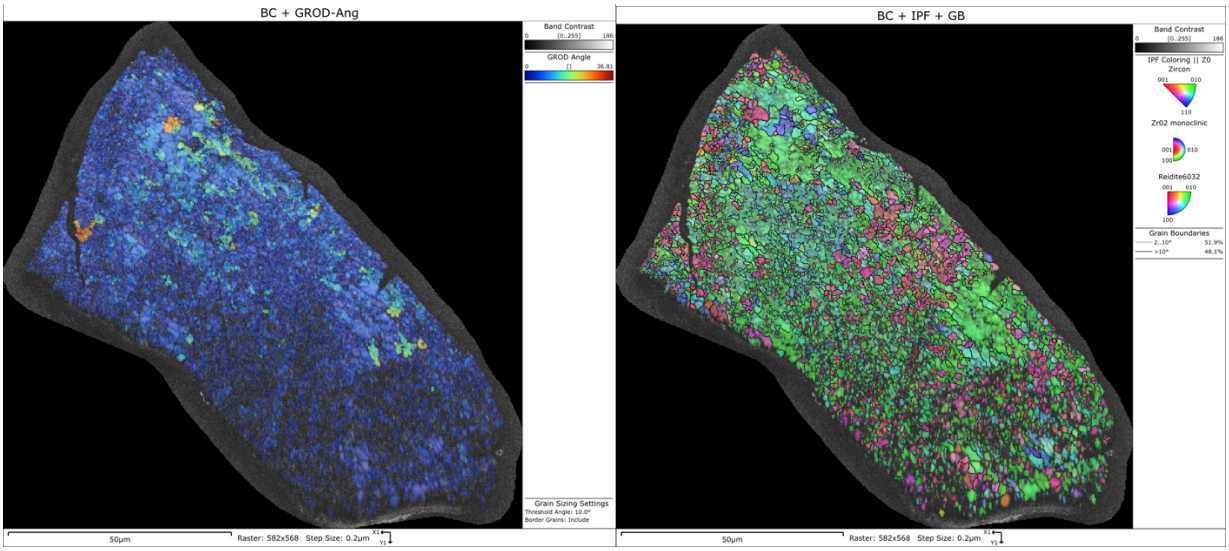
BC + GROD-Ang
Band Contrast
GROD Angle
Grain Sizing Settings
50µm
Raster: 582x568 Step Size: 0.2µm
BC + IPF + GB
Band Contrast
IPF Coloring || Z0
Zircon
ZrO2 monoclinic
Reidite6032
Grain Boundaries
50µm
Raster: 582x568 Step Size: 0.2µm

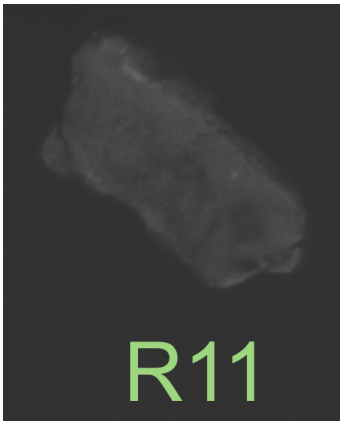
R11

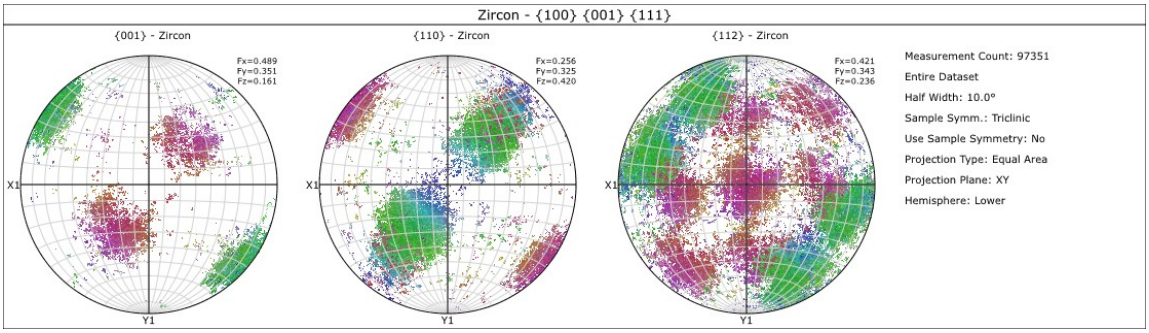
Zircon - {100} {001} {111}
{001} - Zircon
Fx=0.489
Fy=0.351
Fz=0.161
{110} - Zircon
Fx=0.256
Fy=0.325
Fz=0.420
{112} - Zircon
Fx=0.421
Fy=0.343
Fz=0.236
Measurement Count: 97351
Entire Dataset
Half Width: 10.0°
Sample Symm.: Triclinic
Use Sample Symmetry: No
Projection Type: Equal Area
Projection Plane: XY
Hemisphere: Lower
X1
Y1

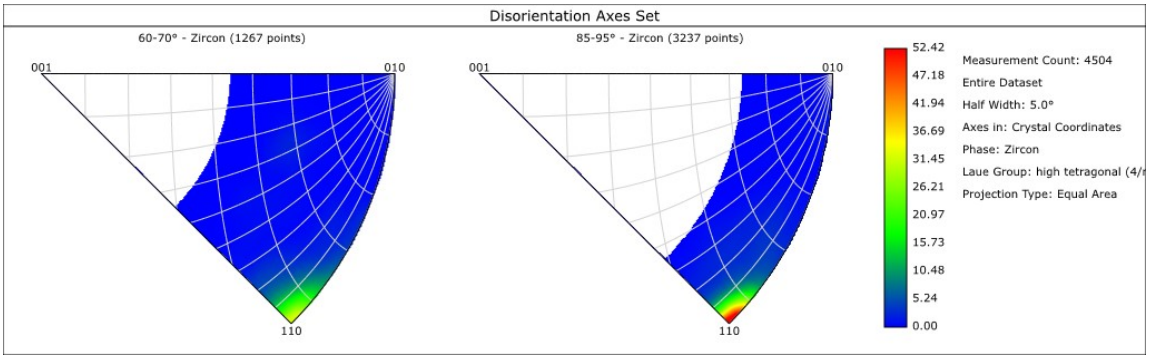
Disorientation Axes Set
60-70° - Zircon (1267 points)
85-95° - Zircon (3237 points)
001
010
110
52.42
47.18
41.94
36.69
31.45
26.21
20.97
15.73
10.48
5.24
0.00
Measurement Count: 4504
Entire Dataset
Half Width: 5.0°
Axes in: Crystal Coordinates
Phase: Zircon
Projection Type: Equal Area

R13

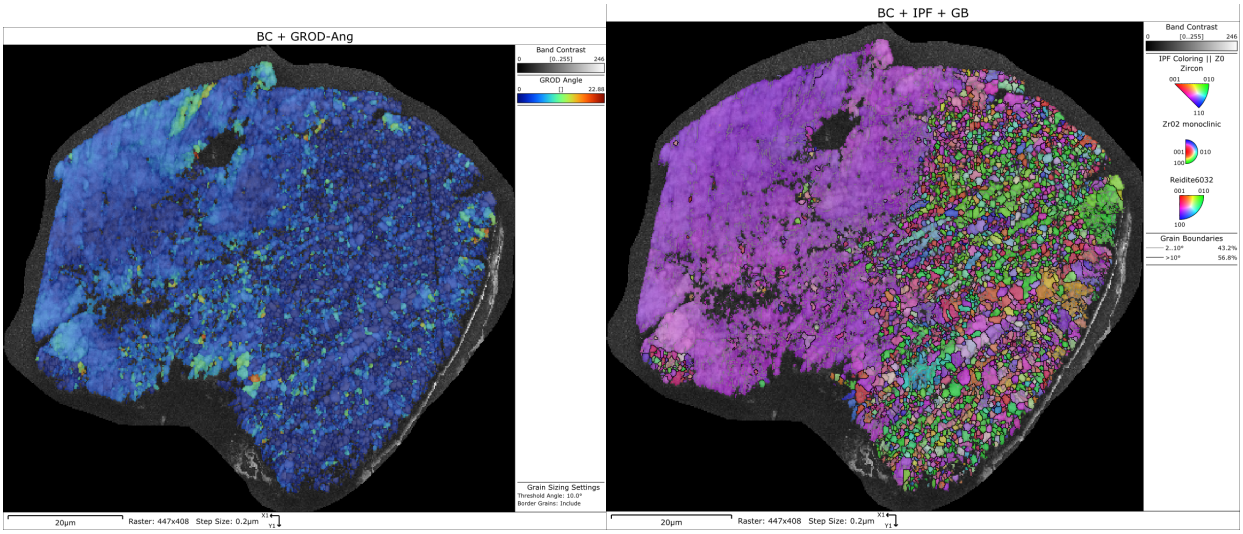
BC + GROD-Ang
Band Contrast
GROD Angle
Grain Sizing Settings
20µm
Raster: 447x408 Step Size: 0.2µm
BC + IPF + GB
Band Contrast
IPF Coloring || Z0
Zircon
Zr02 monoclinic
Reidite6032
Grain Boundaries
20µm
Raster: 447x408 Step Size: 0.2µm

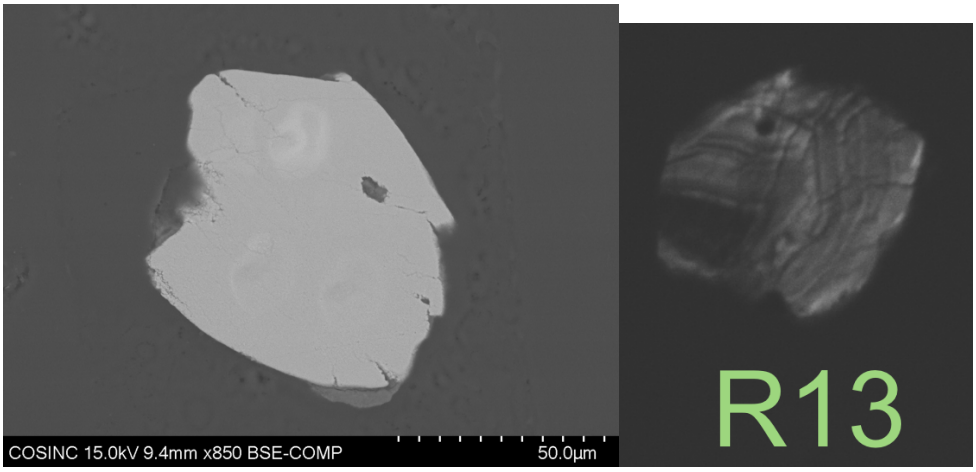
COSINC 15.0kV 9.4mm x850 BSE-COMP
50.0µm
R13

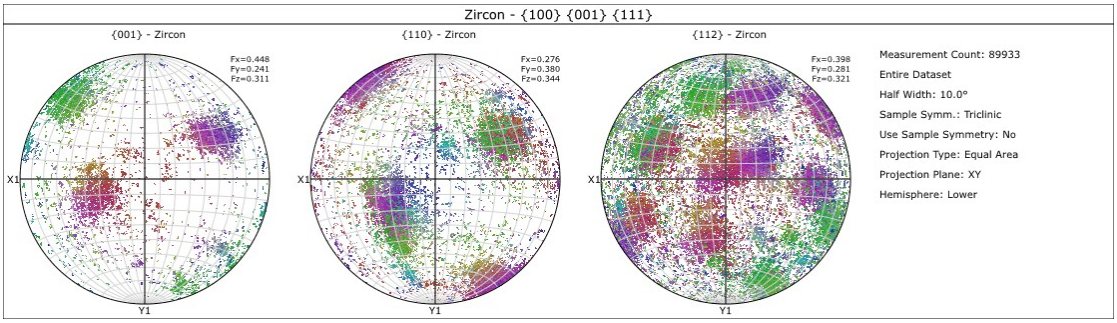
Zircon - {100} {001} {111}
{001} - Zircon
{110} - Zircon
{112} - Zircon
Fx=0.448
Fy=0.241
Fz=0.311
Fx=0.276
Fy=0.380
Fz=0.344
Fx=0.398
Fy=0.281
Fz=0.321
X1
Y1
Measurement Count: 89933
Entire Dataset
Half Width: 10.0°
Sample Symm.: Triclinic
Use Sample Symmetry: No
Projection Type: Equal Area
Projection Plane: XY
Hemisphere: Lower

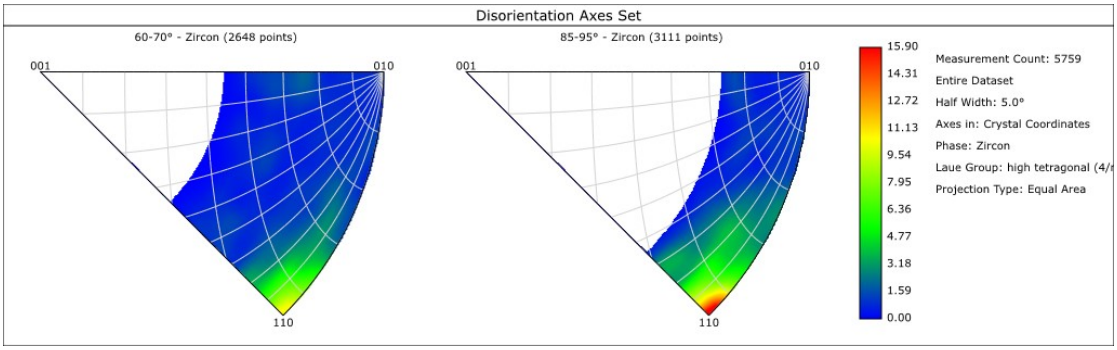
Disorientation Axes Set
60-70° - Zircon (2648 points)
85-95° - Zircon (3111 points)
001
010
110
15.90
14.31
12.72
11.13
9.54
7.95
6.36
4.77
3.18
1.59
0.00
Measurement Count: 5759
Entire Dataset
Half Width: 5.0°
Axes in: Crystal Coordinates
Phase: Zircon
Projection Type: Equal Area

Appendix F – Apollo 14311,58 zircon images

Zrlg77

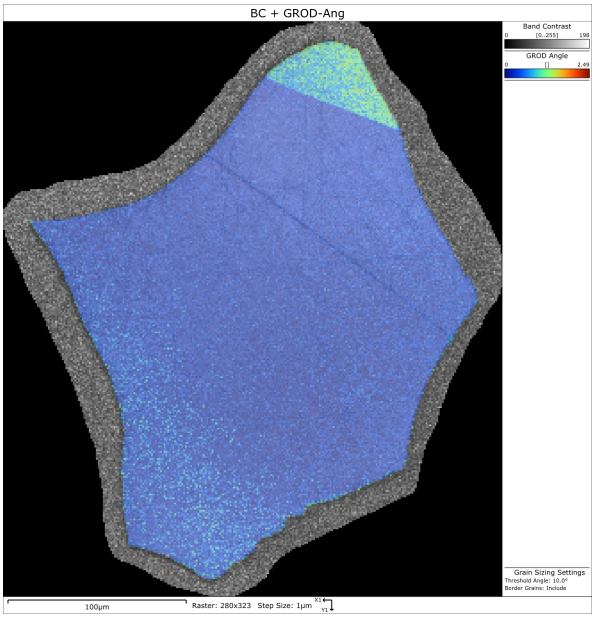

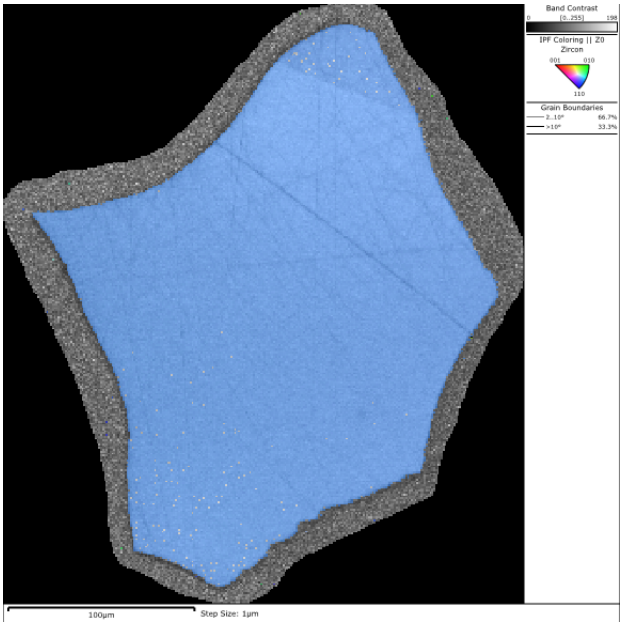

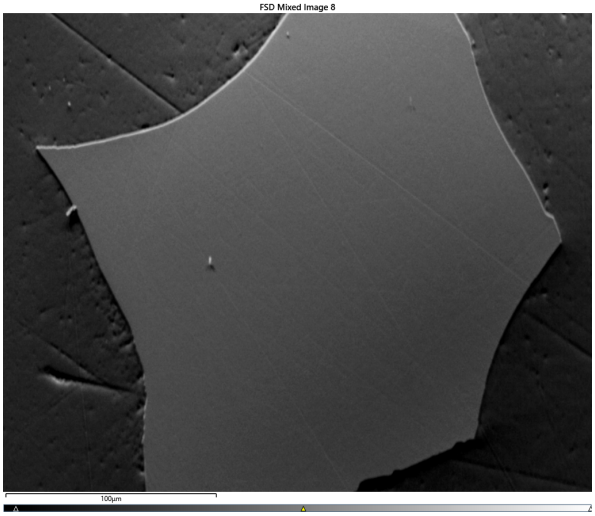

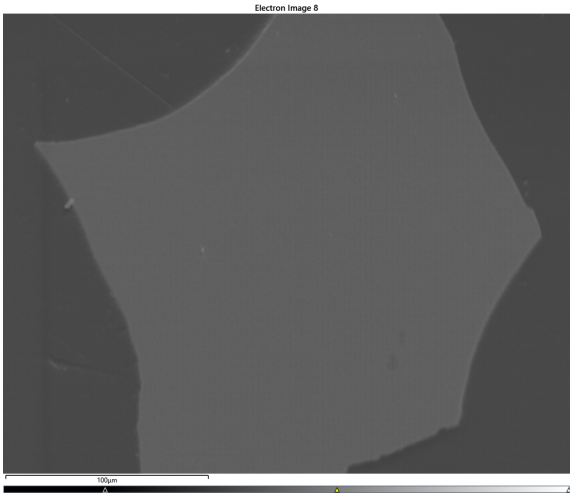

Zrlg78

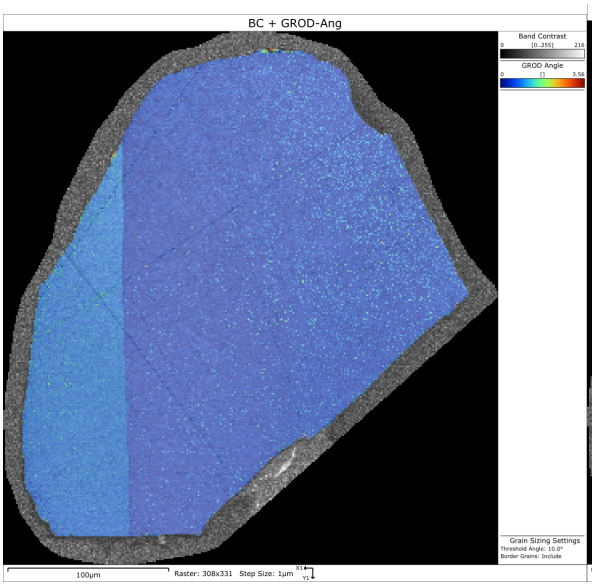
BC + GROD-Ang
Band Contrast
GROD Angle
Grain Sizing Settings
100µm
Raster: 308x331 Step Size: 1µm

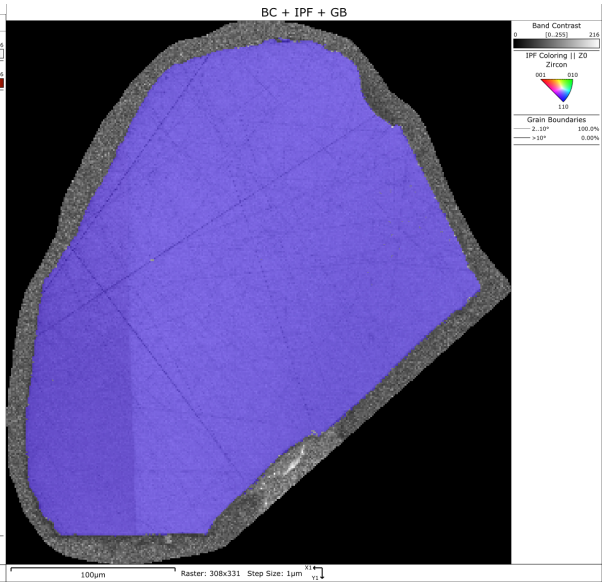
BC + IPF + GB
Band Contrast
IPF Coloring || Z0
Zircon
Grain Boundaries
100µm
Raster: 308x331 Step Size: 1µm

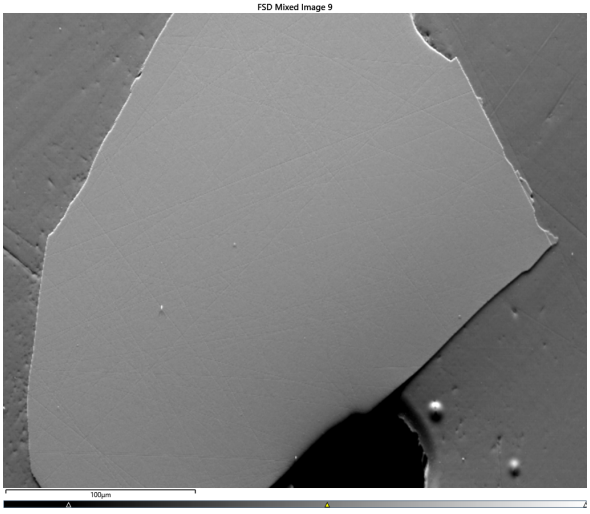
FSD Mixed Image 9
100µm

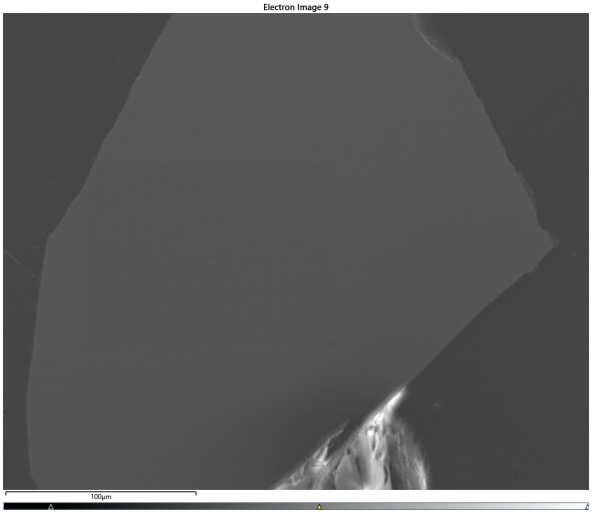
Electron Image 9
100µm

Zrlg79

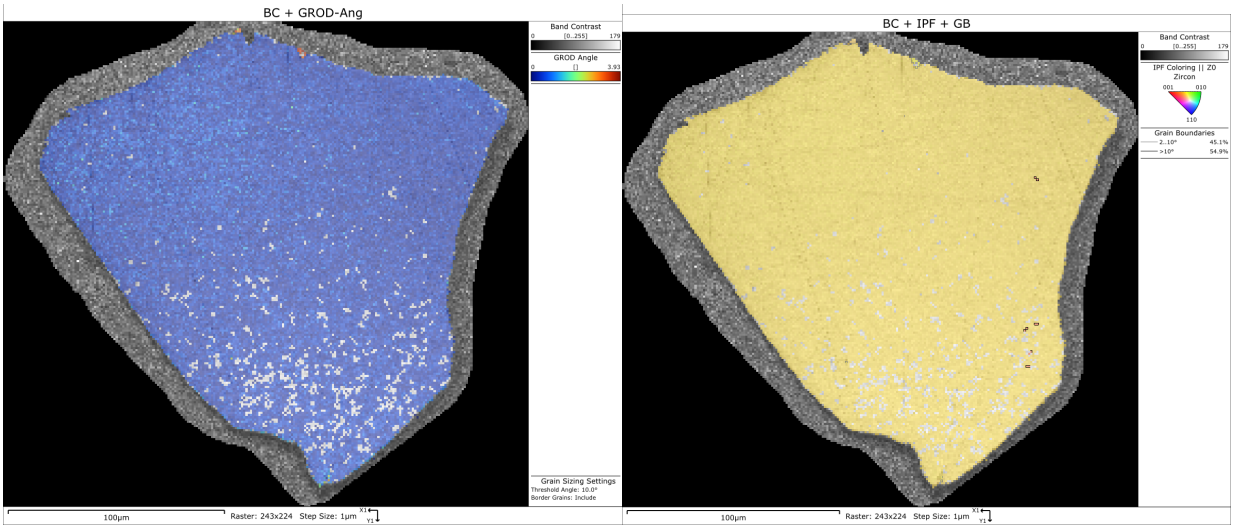
BC + GROD-Ang
Band Contrast
GROD Angle
Grain Sizing Settings
100µm
Raster: 243x224 Step Size: 1µm
BC + IPF + GB
Band Contrast
IPF Coloring || Z0
Zircon
Grain Boundaries
100µm
Raster: 243x224 Step Size: 1µm

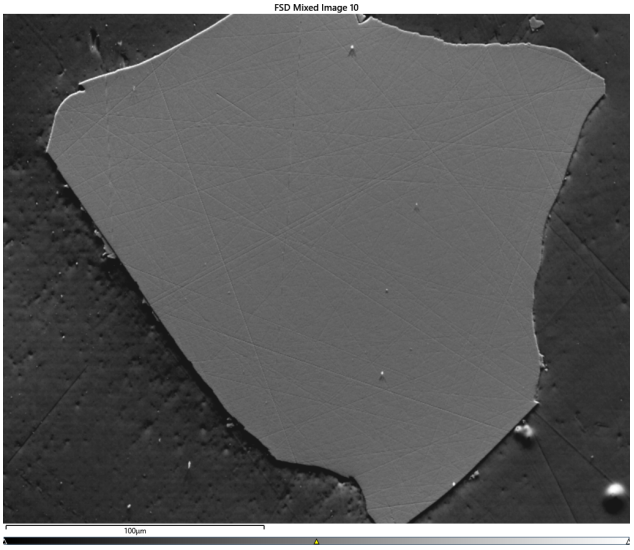
FSD Mixed Image 10
100µm

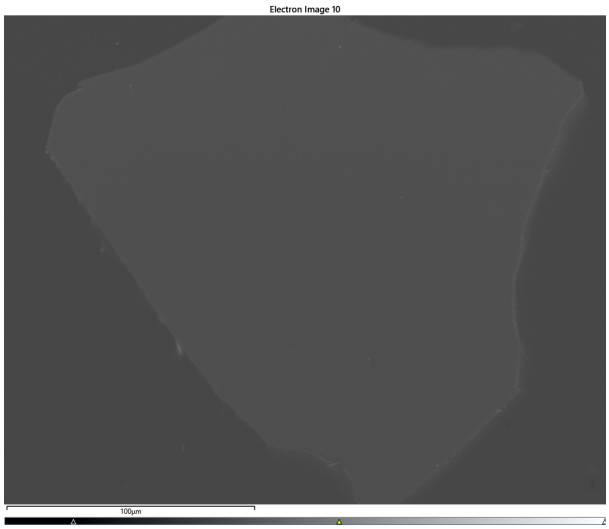
Electron Image 10
100µm

Zrlg80

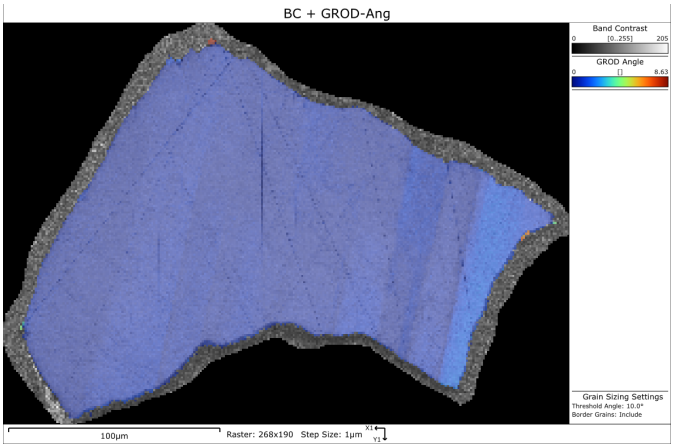
BC + GROD-Ang
Band Contrast
0 [0..255] 205
GROD Angle
0 [] 8.63
Grain Sizing Settings
Threshold Angle: 10.0°
Border Grains: Include
100µm
Raster: 268x190 Step Size: 1µm

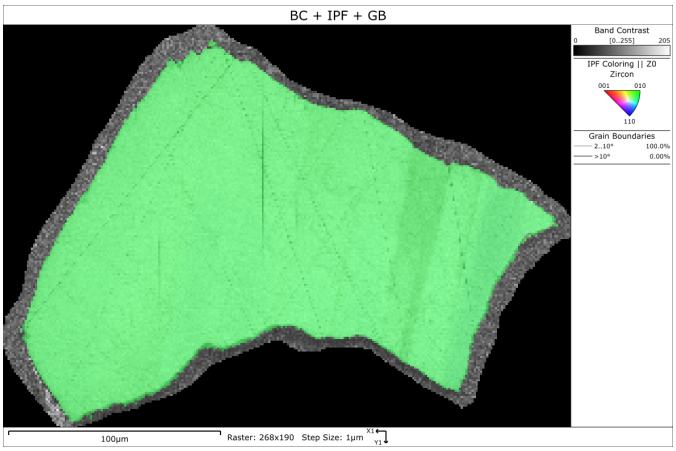
BC + IPF + GB
Band Contrast
0 [0..255] 205
IPF Coloring || Z0
Zircon
001 010
110
Grain Boundaries
2..10° 100.0%
>10° 0.00%
100µm
Raster: 268x190 Step Size: 1µm

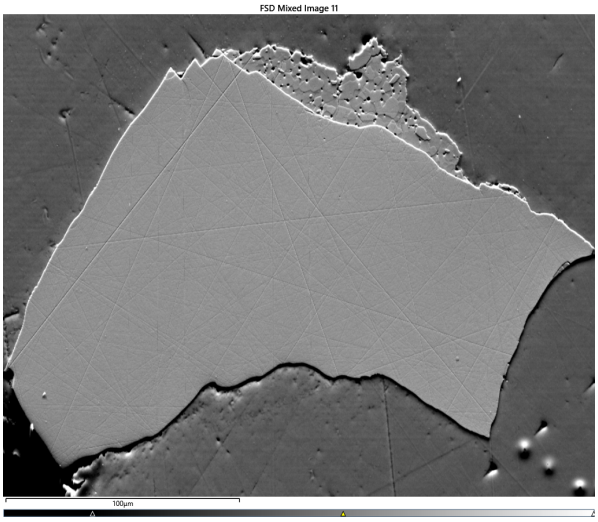
FSD Mixed Image 11
100µm

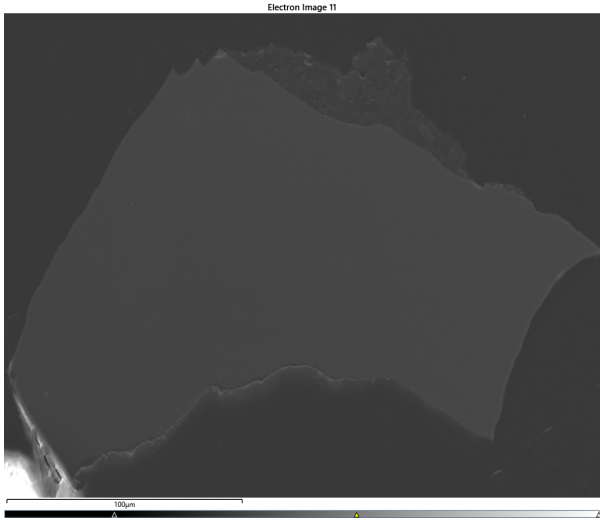
Electron Image 11
100µm

Zrlg81

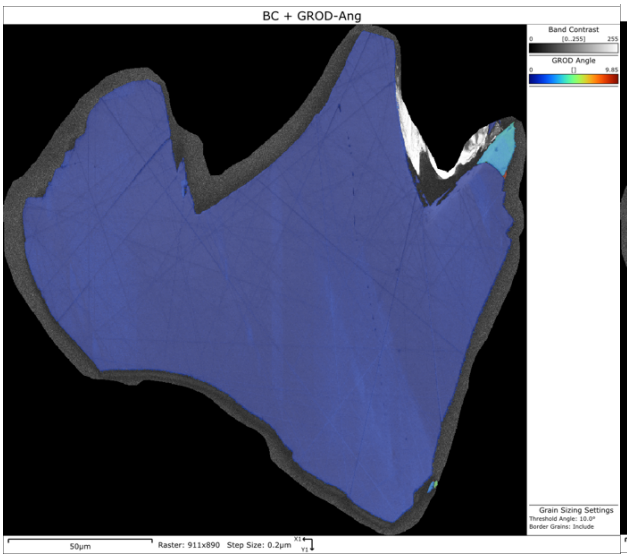
BC + GROD-Ang
Band Contrast
GROD Angle
Grain Sizing Settings
50µm
Raster: 911x890 Step Size: 0.2µm

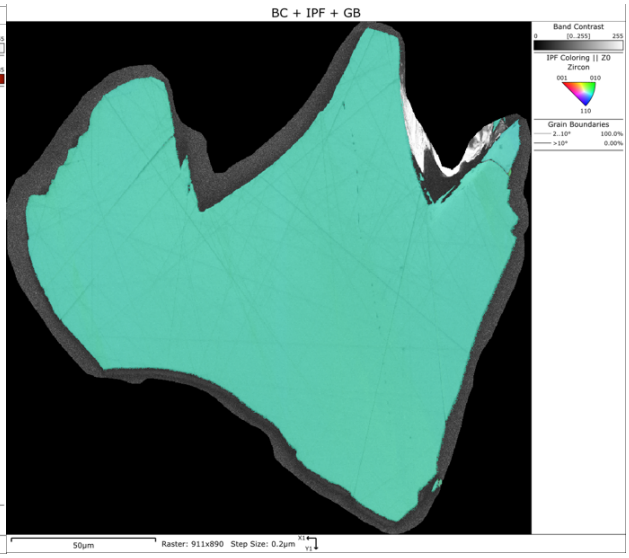
BC + IPF + GB
Band Contrast
IPF Coloring || Z0
Zircon
Grain Boundaries
50µm
Raster: 911x890 Step Size: 0.2µm

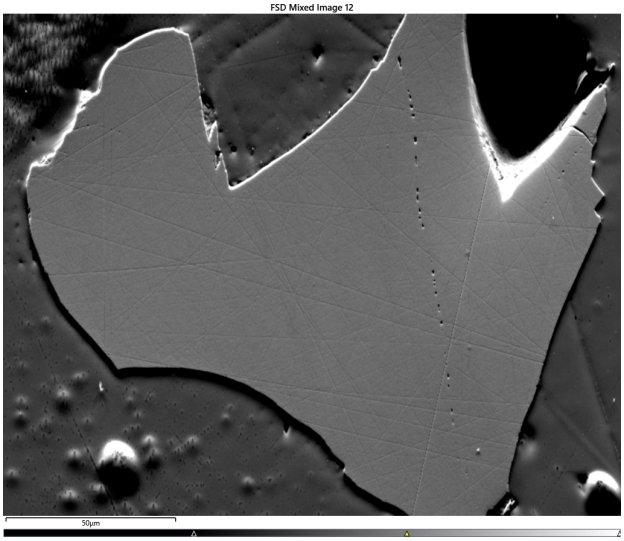
FSD Mixed Image 12
50µm

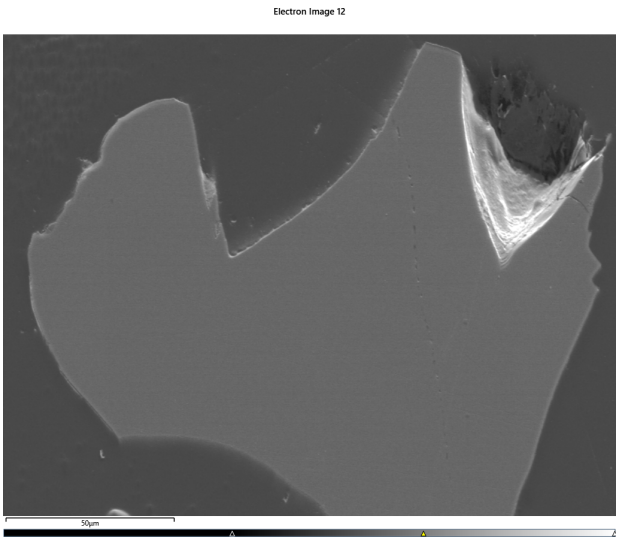
Electron Image 12
50µm

Zrlg82

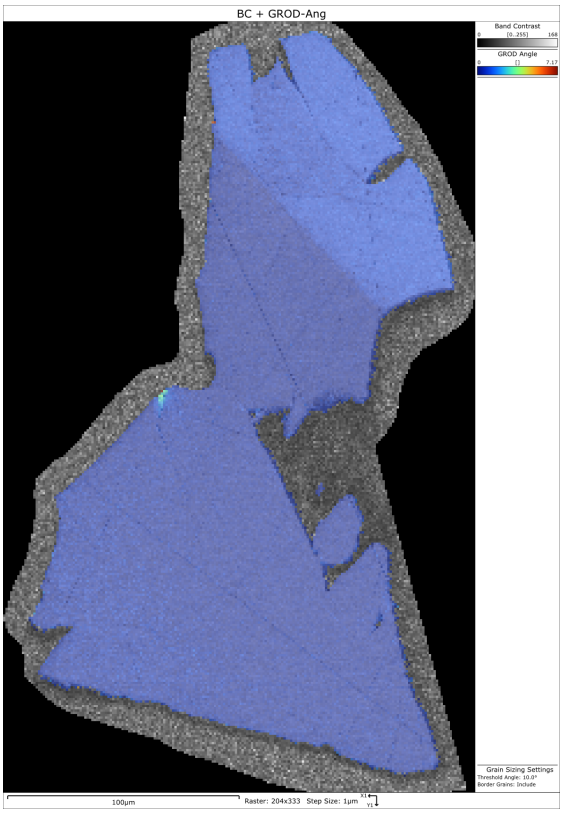
BC + GROD-Ang
Band Contrast
GROD Angle
Grain Sizing Settings
100µm
Raster: 204x333 Step Size: 1µm

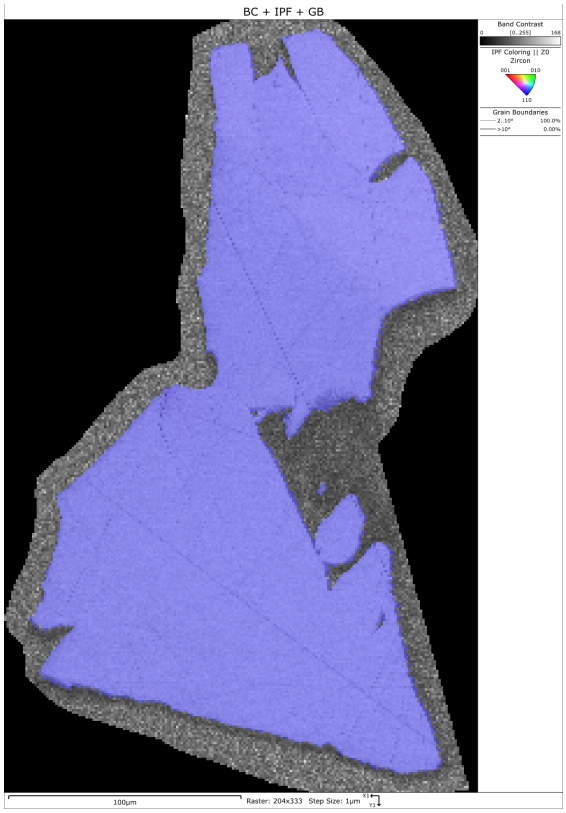
BC + IPF + GB
Band Contrast
IPF Coloring || Z0
Zircon
Grain Boundaries
100µm
Raster: 204x333 Step Size: 1µm

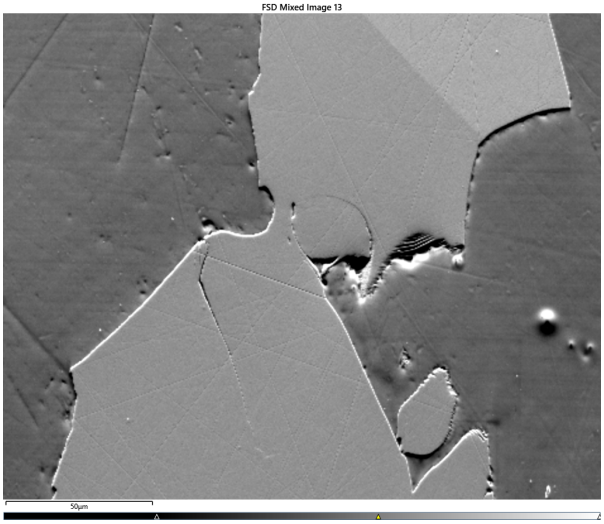
FSD Mixed Image 13
50µm

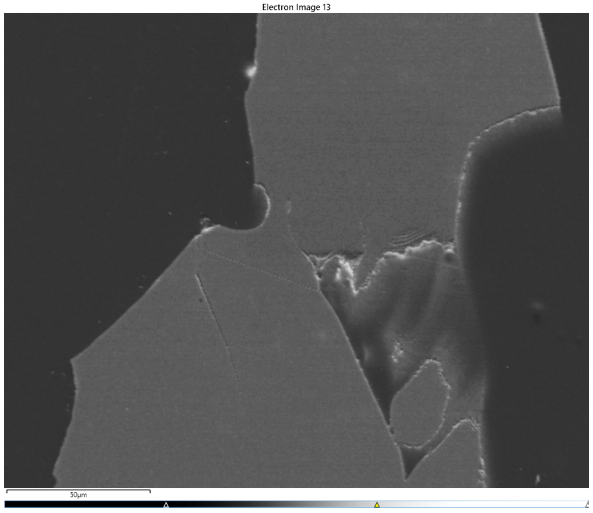
Electron Image 13
50µm

Zrlg83

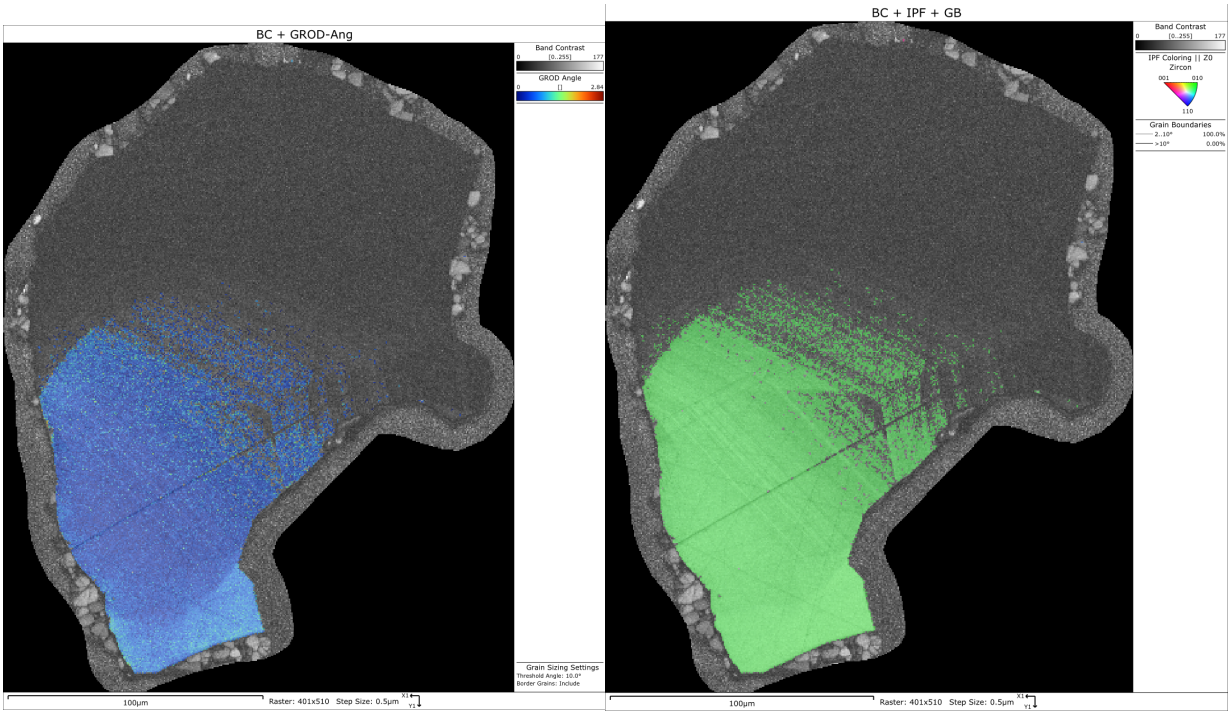
BC + GROD-Ang
Band Contrast
GROD Angle
Grain Sizing Settings
100µm
Raster: 401x510 Step Size: 0.5µm
BC + IPF + GB
Band Contrast
IPF Coloring || Z0
Zircon
Grain Boundaries
100µm
Raster: 401x510 Step Size: 0.5µm

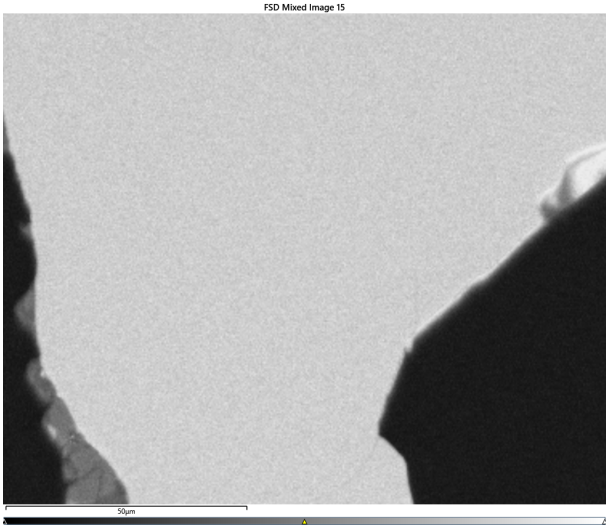
FSD Mixed Image 15
50µm

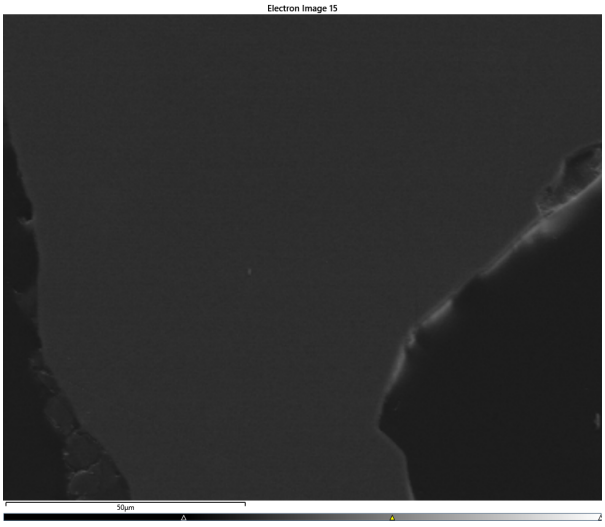
Electron Image 15
50µm

Zrlg84

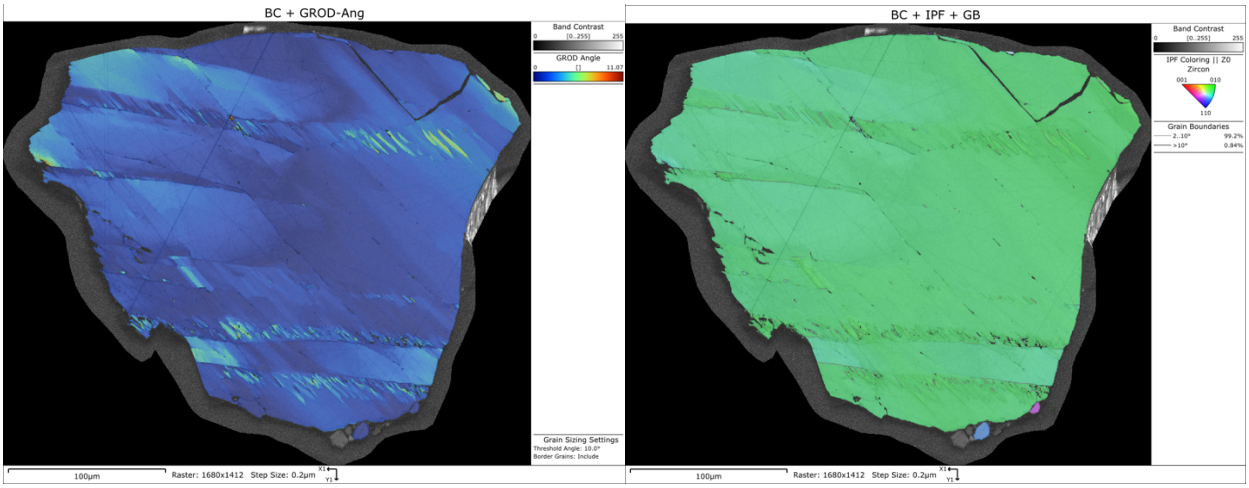
BC + GROD-Ang
Band Contrast
GROD Angle
Grain Sizing Settings
100µm
Raster: 1680x1412 Step Size: 0.2µm
BC + IPF + GB
Band Contrast
IPF Coloring || Z0
Zircon
Grain Boundaries
100µm
Raster: 1680x1412 Step Size: 0.2µm

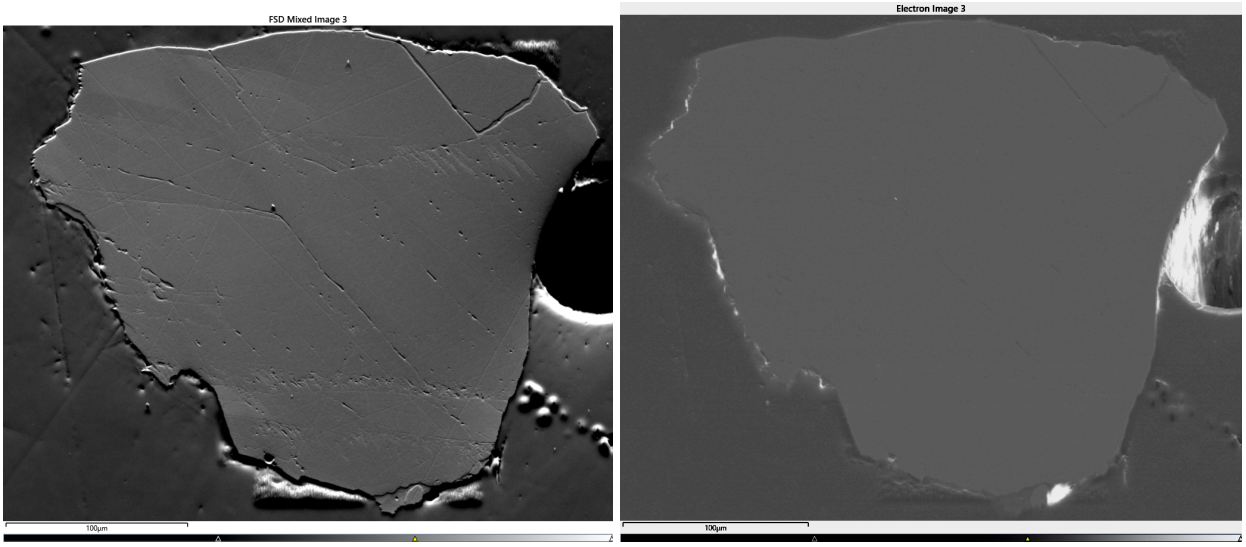
FSD Mixed Image 3
100µm
Electron Image 3
100µm

Zrlg85

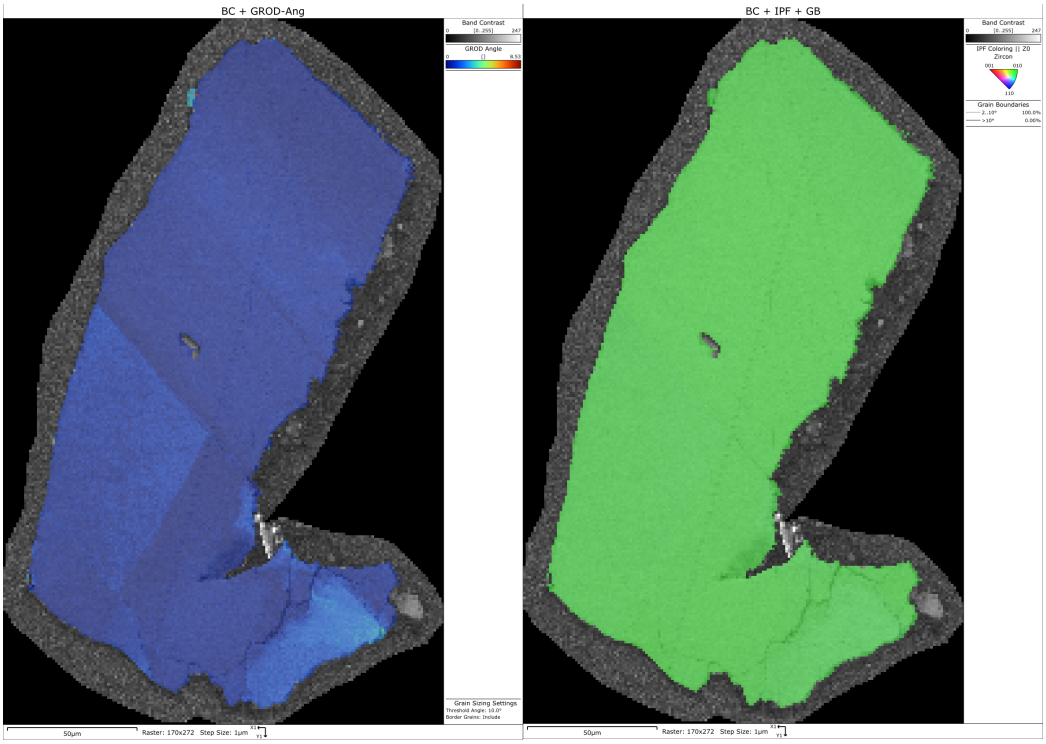
BC + GROD-Ang
Band Contrast
GROD Angle
Grain Sizing Settings
50µm
Raster: 170x272 Step Size: 1µm
BC + IPF + GB
Band Contrast
IPF Coloring || Z0
Zircon
Grain Boundaries
50µm
Raster: 170x272 Step Size: 1µm

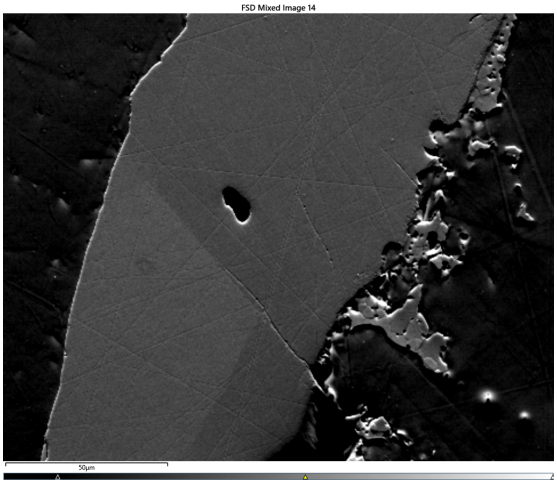
FSD Mixed Image 14
50µm

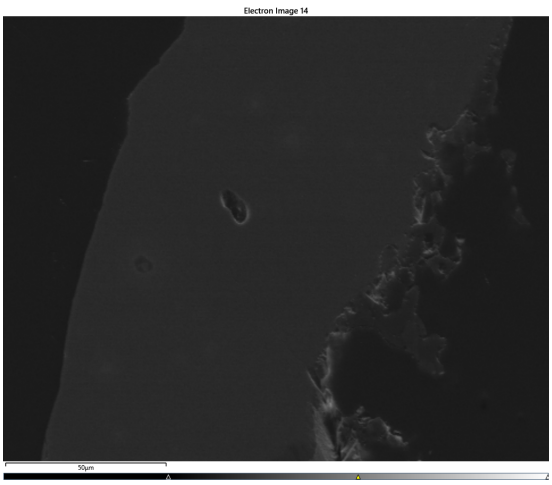
Electron Image 14
50µm

Zrlg86

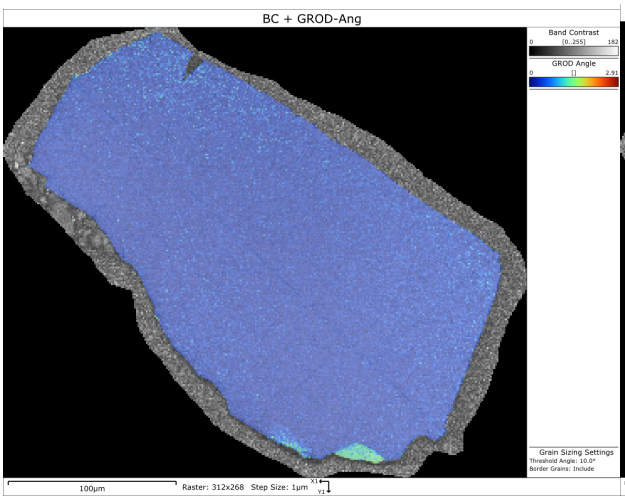
BC + GROD-Ang
Band Contrast
[0..255]
GROD Angle
Grain Sizing Settings
100µm
Raster: 312x268 Step Size: 1µm

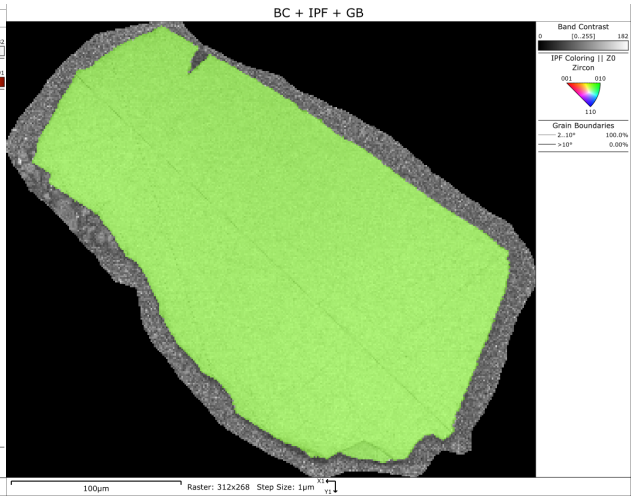
BC + IPF + GB
Band Contrast
IPF Coloring || Z0
Zircon
Grain Boundaries
100µm
Raster: 312x268 Step Size: 1µm

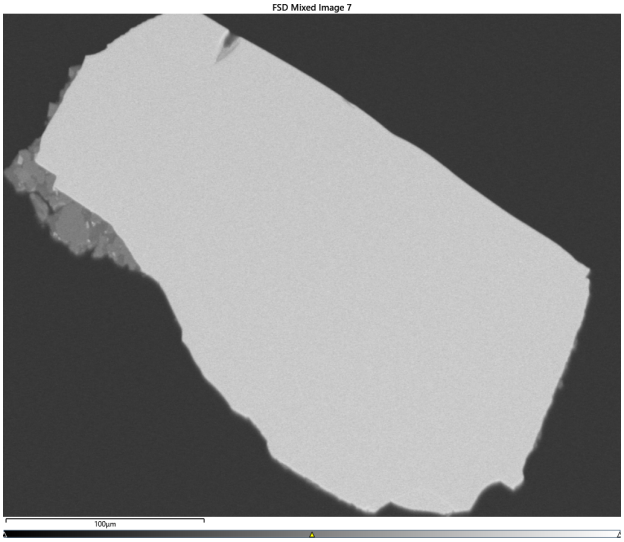
FSD Mixed Image 7
100µm

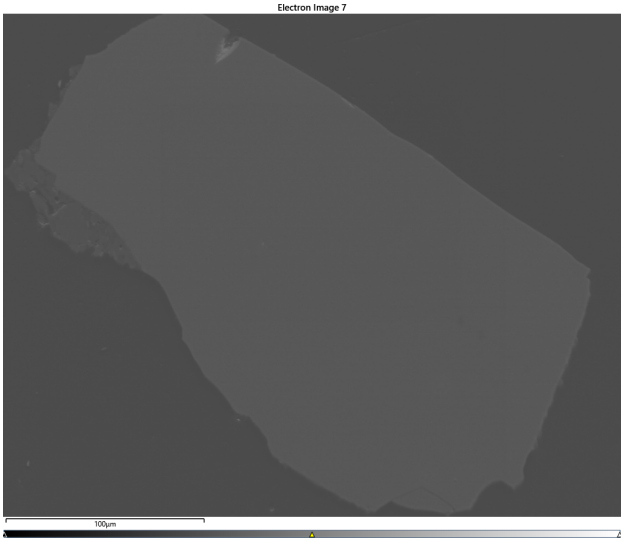
Electron Image 7
100µm

Zrlg87

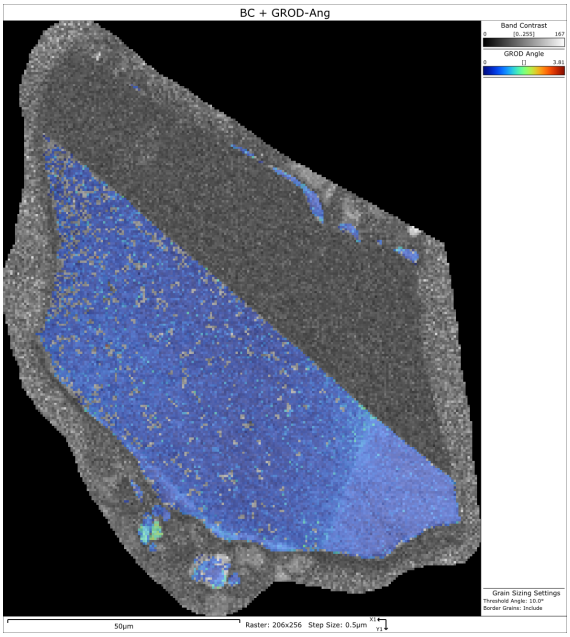
BC + GROD-Ang
Band Contrast
GROD Angle
Grain Sizing Settings
50µm
Raster: 206x256 Step Size: 0.5µm

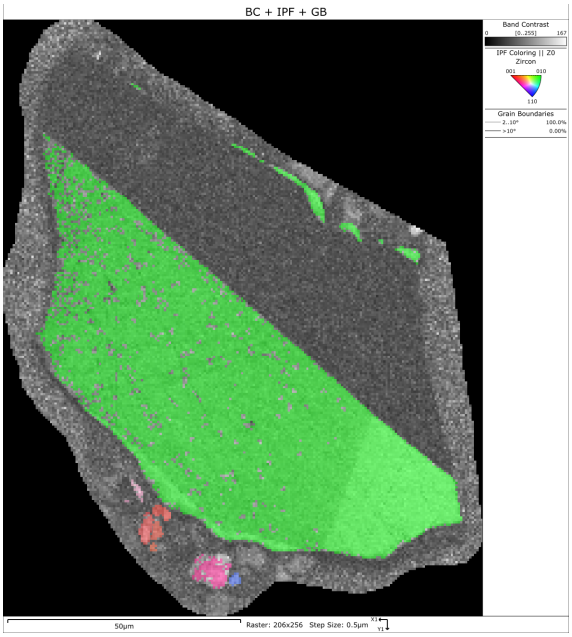
BC + IPF + GB
Band Contrast
IPF Coloring || Z0
Zircon
Grain Boundaries
50µm
Raster: 206x256 Step Size: 0.5µm

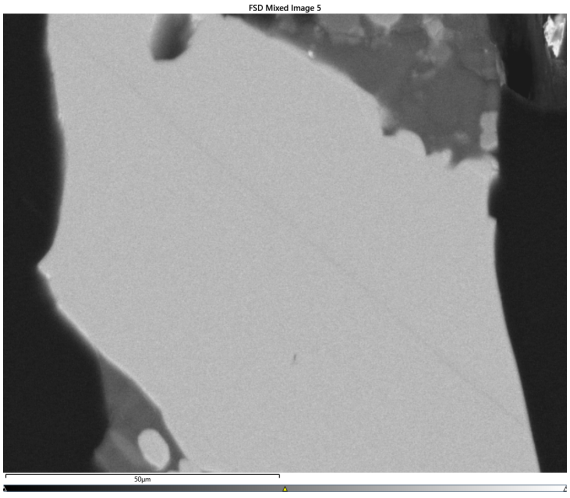
FSD Mixed Image 5
50µm

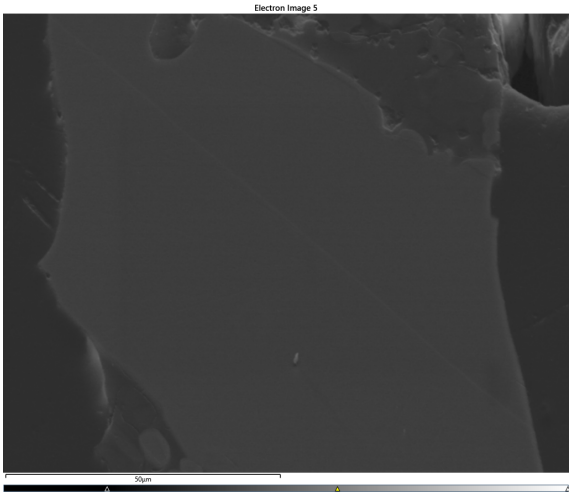
Electron Image 5
50µm

Zrlg88

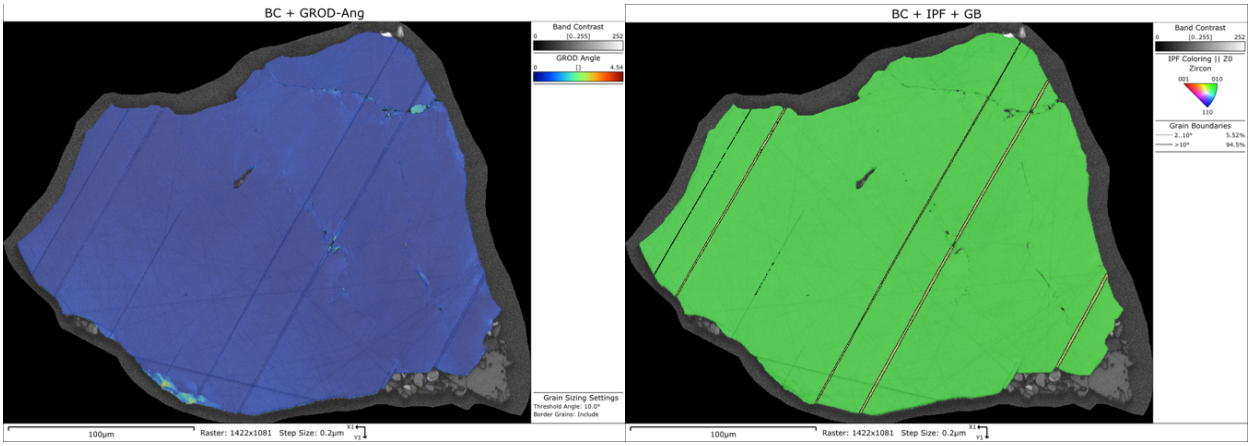
BC + GROD-Ang
Band Contrast
GROD Angle
Grain Sizing Settings
100µm
Raster: 1422x1081 Step Size: 0.2µm
BC + IPF + GB
Band Contrast
IPF Coloring || Z0
Zircon
Grain Boundaries
100µm
Raster: 1422x1081 Step Size: 0.2µm

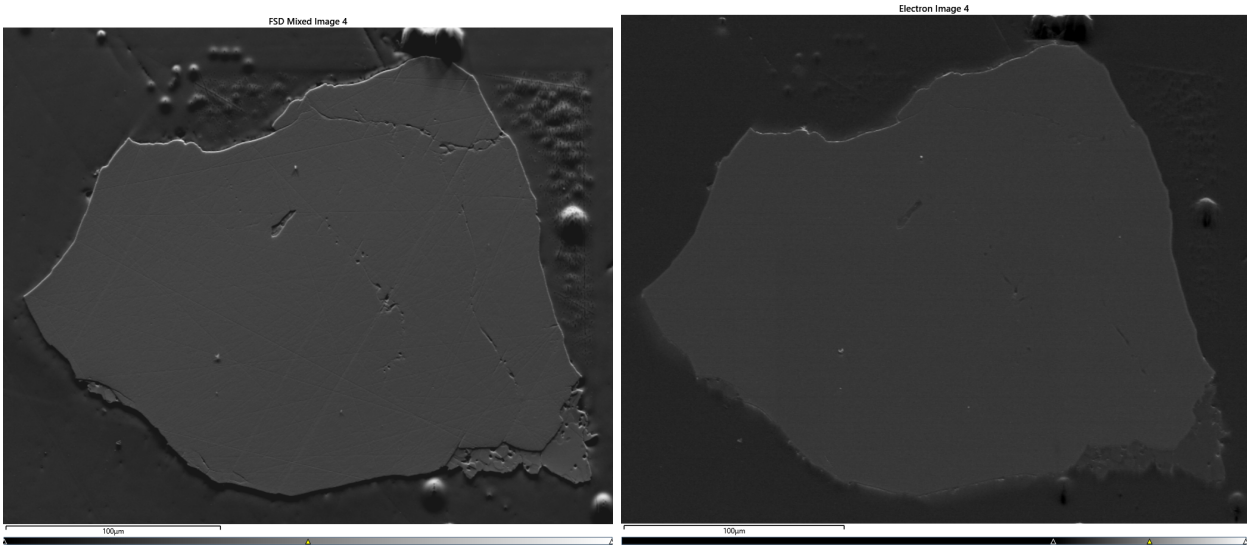
FSD Mixed Image 4
100µm
Electron Image 4
100µm

Zrsm90

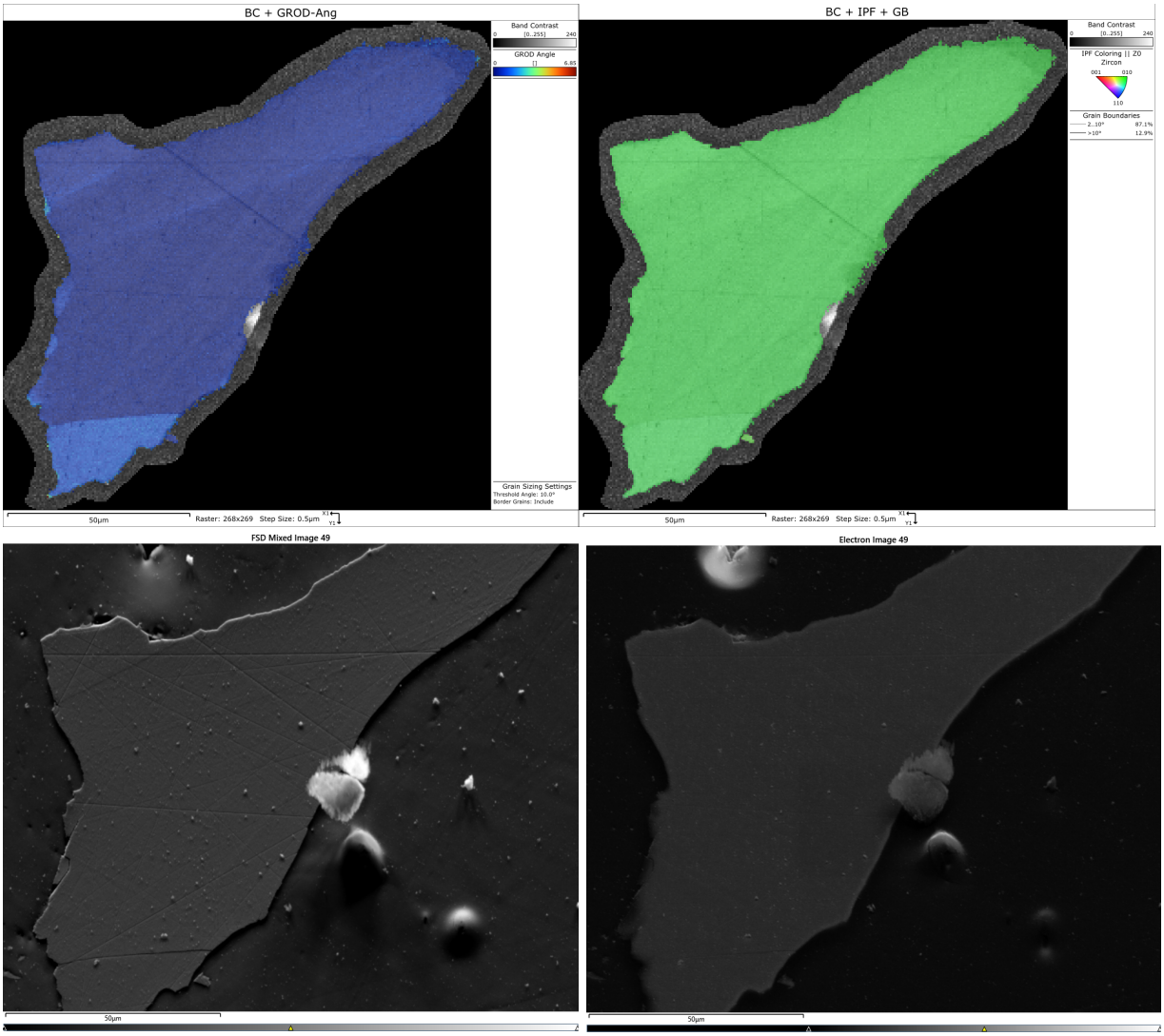
BC + GROD-Ang
Band Contrast
GROD Angle
Grain Sizing Settings
50µm
Raster: 268x269 Step Size: 0.5µm
BC + IPF + GB
Band Contrast
IPF Coloring || Z0
Zircon
Grain Boundaries
50µm
Raster: 268x269 Step Size: 0.5µm
FSD Mixed Image 49
50µm
Electron Image 49
50µm

Zrsm91

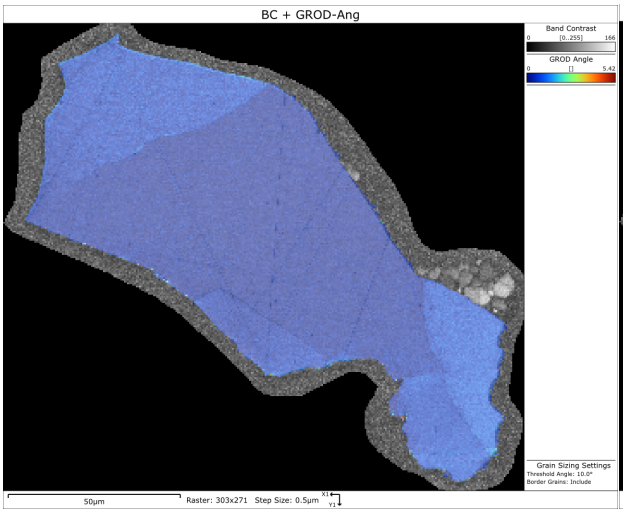
BC + GROD-Ang
Band Contrast
[0..255]
GROD Angle
Grain Sizing Settings
50µm
Raster: 303x271 Step Size: 0.5µm

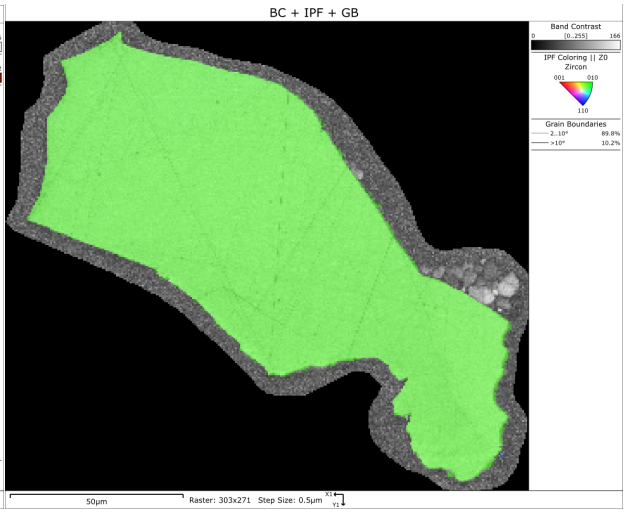
BC + IPF + GB
Band Contrast
[0..255]
IPF Coloring || Z0
Zircon
Grain Boundaries
50µm
Raster: 303x271 Step Size: 0.5µm

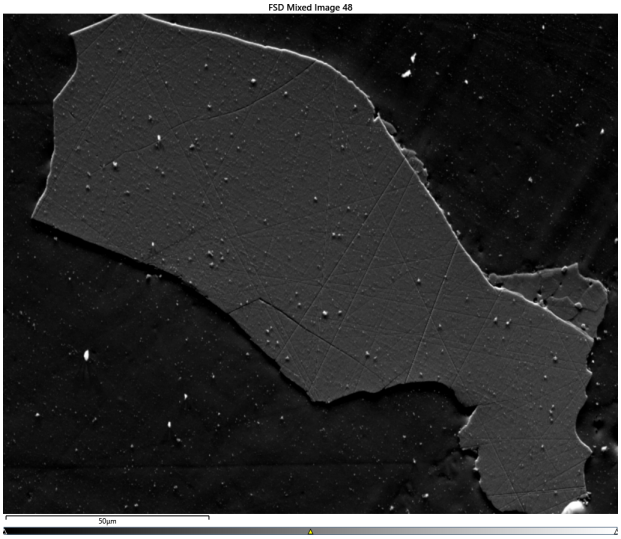
FSD Mixed Image 48
50µm

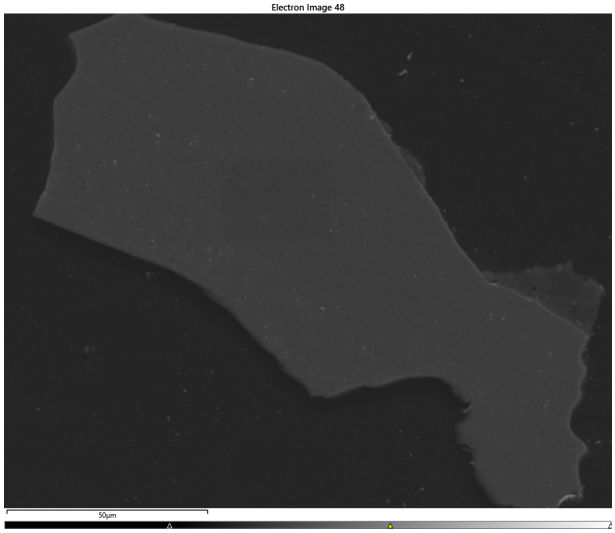
Electron Image 48
50µm

Zrsm92

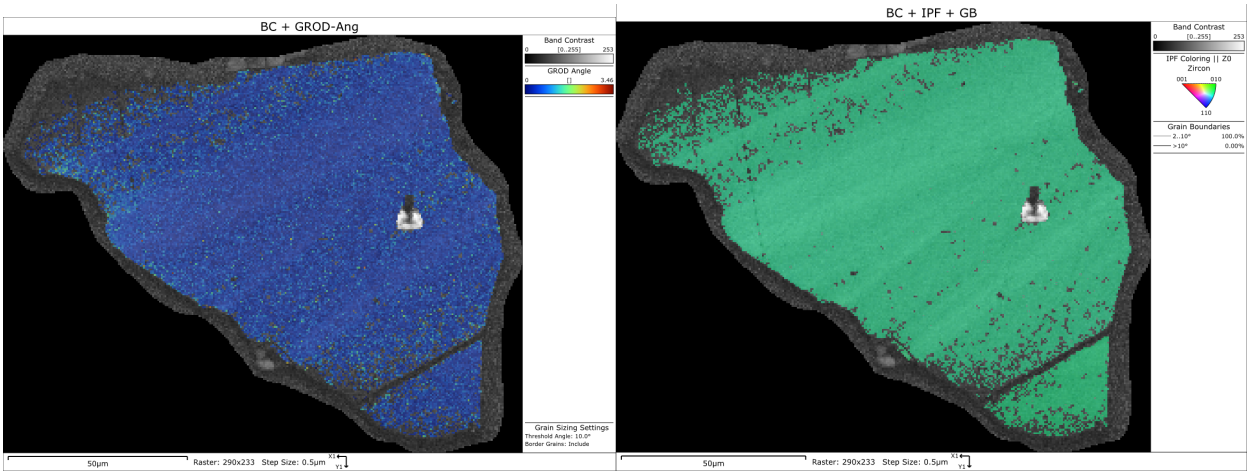
BC + GROD-Ang
Band Contrast
0 [0..255] 253
GROD Angle
0 [] 3.46
Grain Sizing Settings
Threshold Angle: 10.0°
Border Grains: Include
50µm
Raster: 290x233 Step Size: 0.5µm
BC + IPF + GB
Band Contrast
0 [0..255] 253
IPF Coloring || Z0
Zircon
001 010
110
Grain Boundaries
2..10° 100.0%
>10° 0.00%
50µm
Raster: 290x233 Step Size: 0.5µm

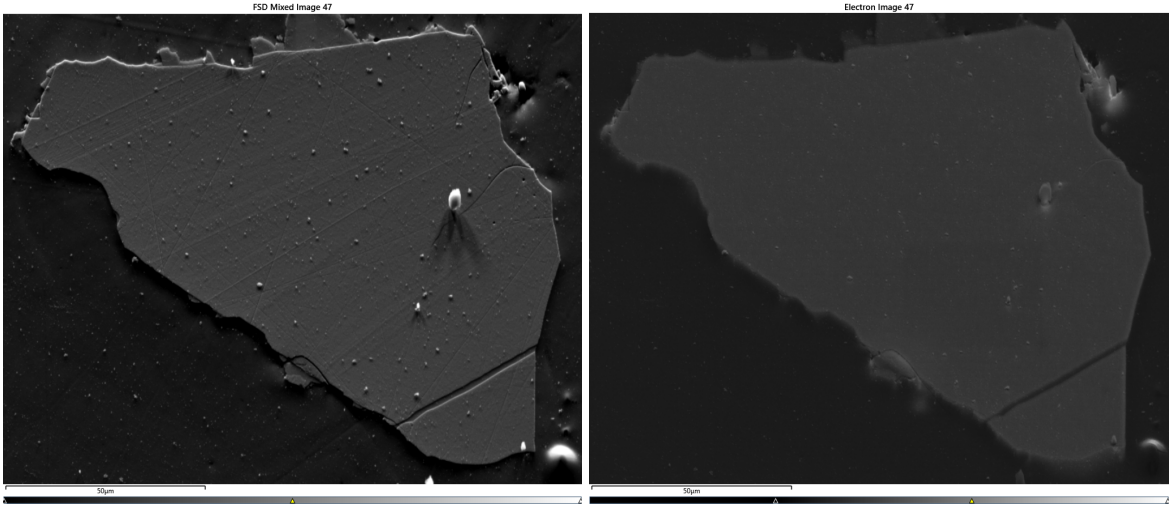
FSD Mixed Image 47
50µm
Electron Image 47
50µm

Zrsm93

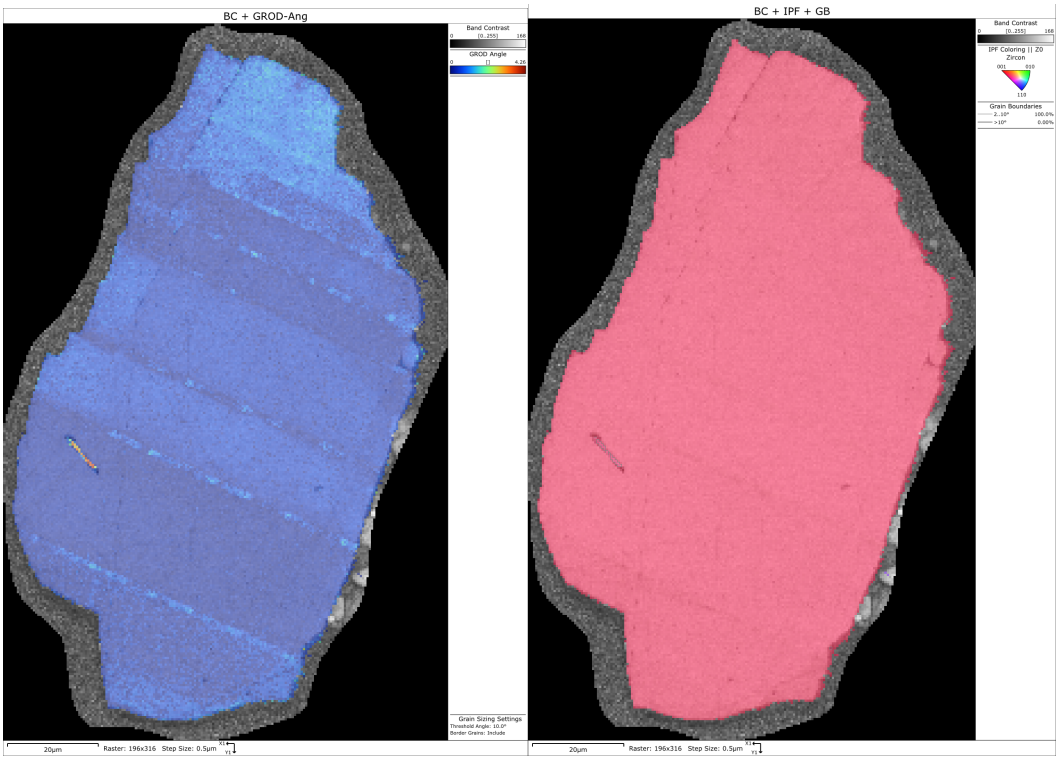
BC + GROD-Ang
Band Contrast
GROD Angle
Grain Sizing Settings
20µm
Raster: 196x316 Step Size: 0.5µm
BC + IPF + GB
Band Contrast
IPF Coloring || Z0
Zircon
Grain Boundaries
20µm
Raster: 196x316 Step Size: 0.5µm

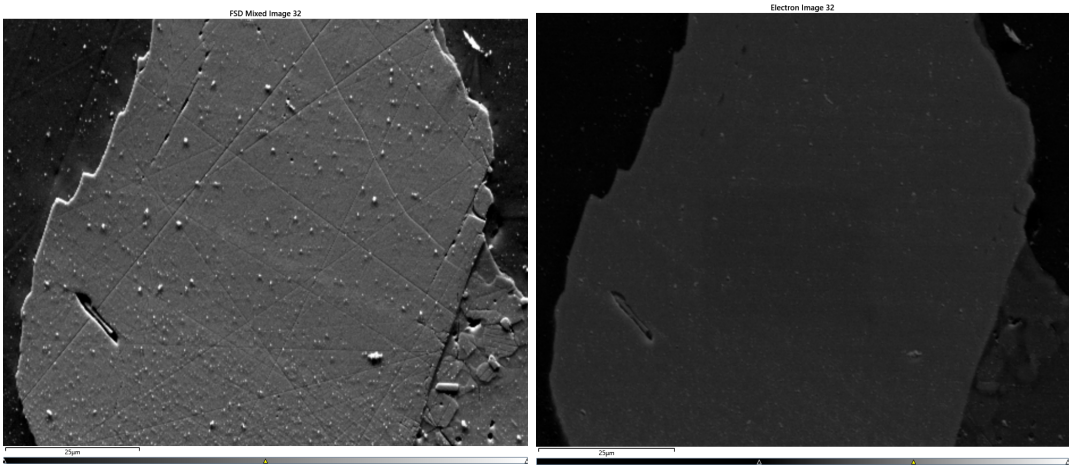
FSD Mixed Image 32
25µm
Electron Image 32
25µm

Zrsm94

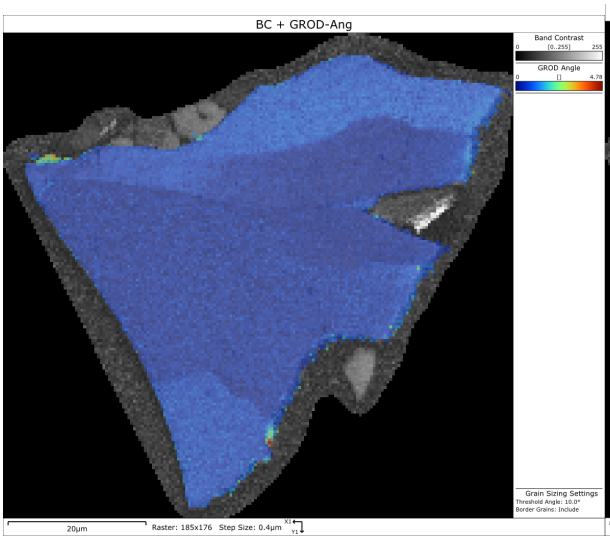
BC + GROD-Ang
Band Contrast
GROD Angle
Grain Sizing Settings
20µm
Raster: 185x176 Step Size: 0.4µm

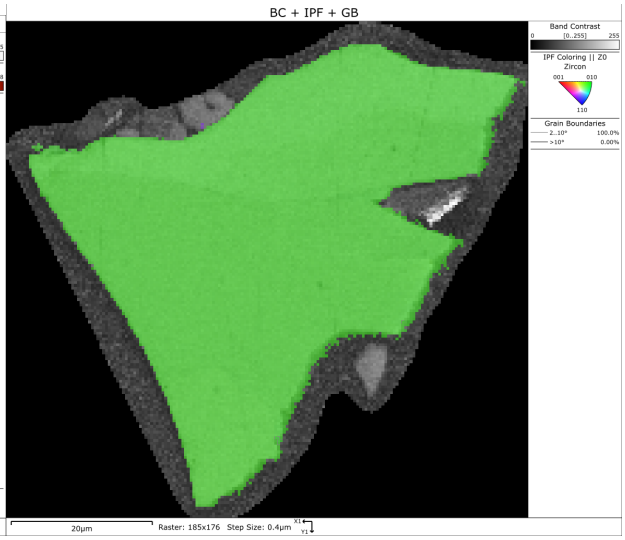
BC + IPF + GB
Band Contrast
IPF Coloring || Z0
Zircon
Grain Boundaries
20µm
Raster: 185x176 Step Size: 0.4µm

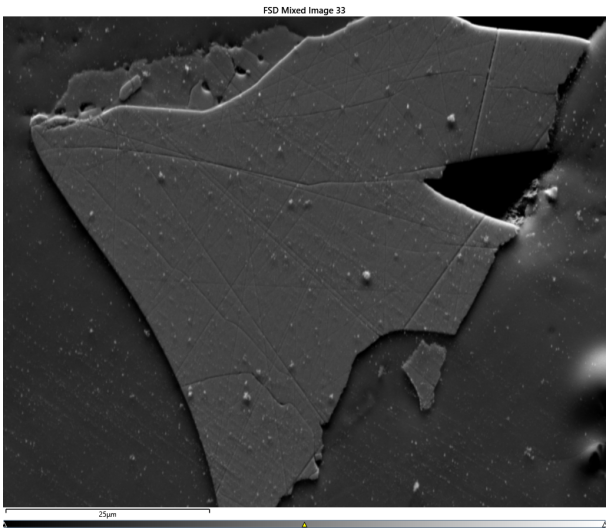
FSD Mixed Image 33
25µm

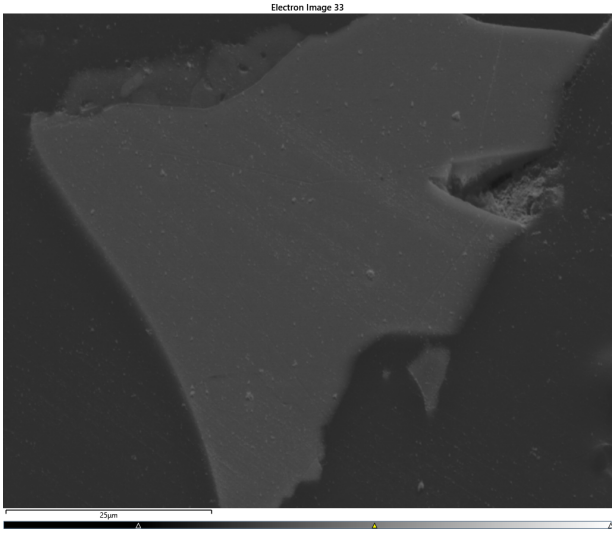
Electron Image 33
25µm

Zrsm95

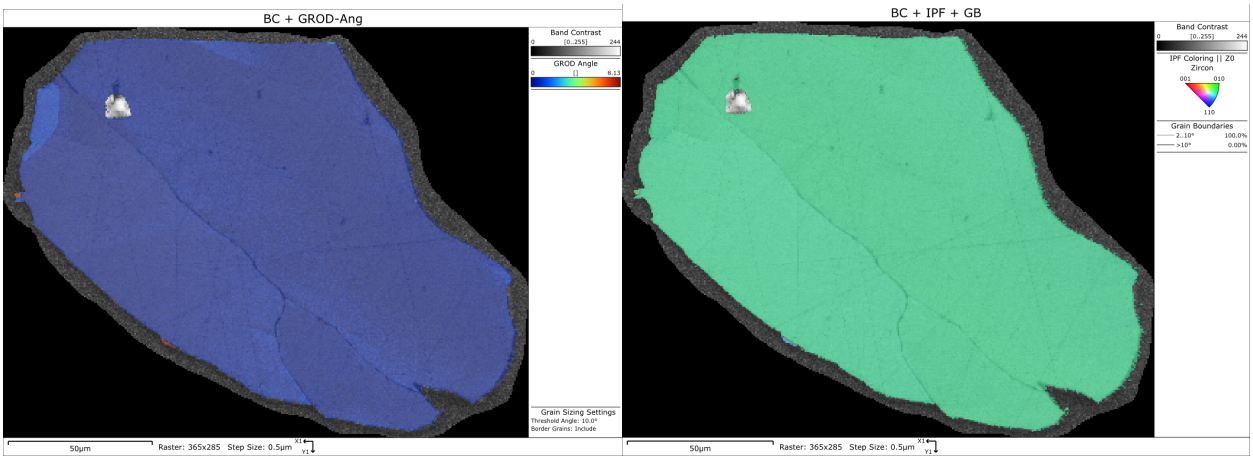
BC + GROD-Ang
Band Contrast
GROD Angle
Grain Sizing Settings
50µm
Raster: 365x285 Step Size: 0.5µm
BC + IPF + GB
Band Contrast
IPF Coloring || Z0
Zircon
Grain Boundaries
50µm
Raster: 365x285 Step Size: 0.5µm

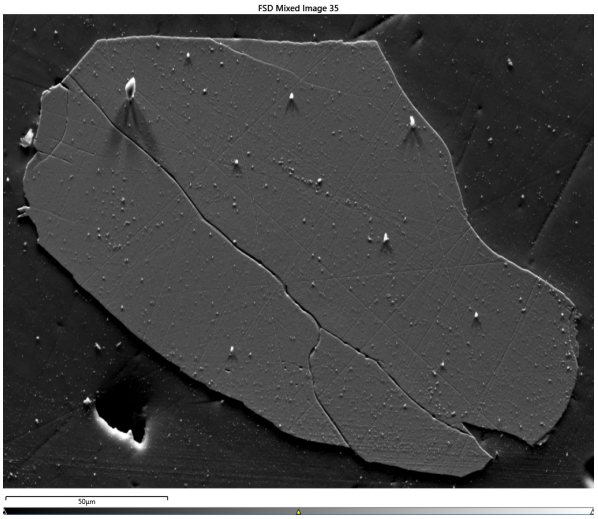
FSD Mixed Image 35
50µm

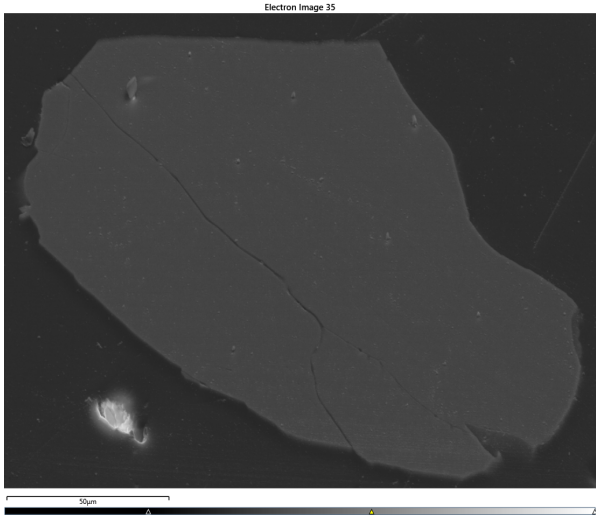
Electron Image 35
50µm

Zrsm96

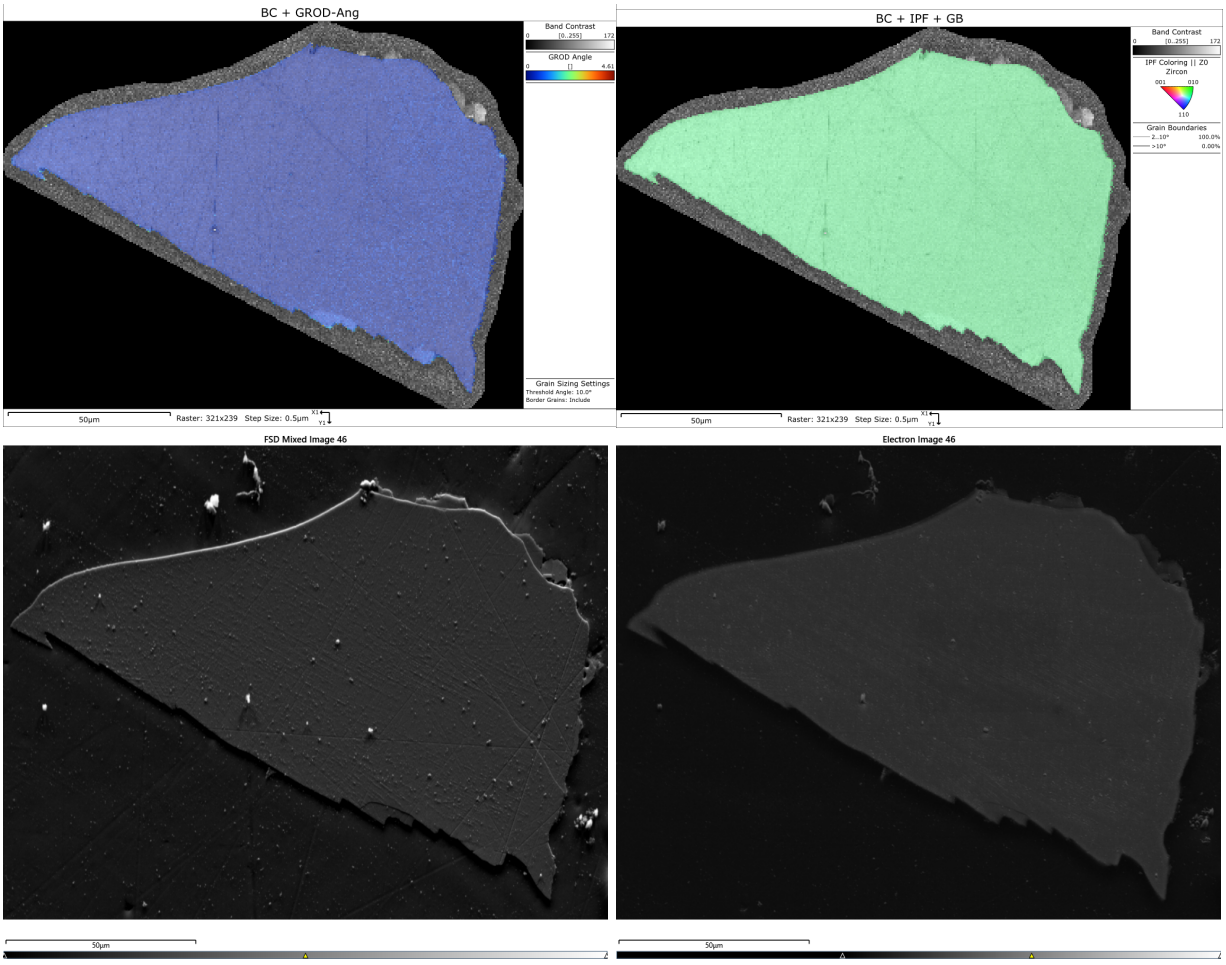
BC + GROD-Ang
Band Contrast
0 [0..255] 172
GROD Angle
0 [] 4.61
Grain Sizing Settings
Threshold Angle: 10.0°
Border Grains: Include
50µm
Raster: 321x239 Step Size: 0.5µm
BC + IPF + GB
Band Contrast
0 [0..255] 172
IPF Coloring || Z0
Zircon
001 010
110
Grain Boundaries
2..10° 100.0%
>10° 0.00%
50µm
Raster: 321x239 Step Size: 0.5µm
FSD Mixed Image 46
50µm
Electron Image 46
50µm

Zrsm97

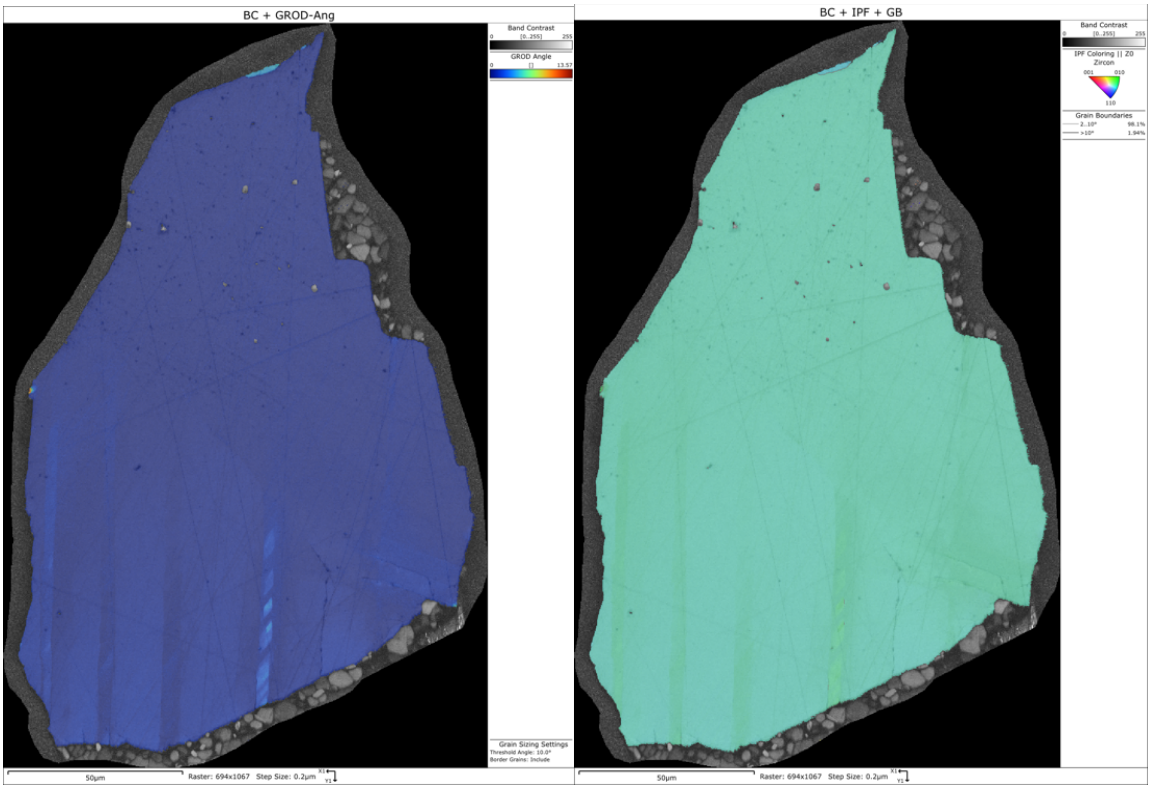
BC + GROD-Ang
Band Contrast
GROD Angle
Grain Sizing Settings
50µm
Raster: 694x1067 Step Size: 0.2µm
BC + IPF + GB
Band Contrast
IPF Coloring || Z0
Zircon
Grain Boundaries
50µm
Raster: 694x1067 Step Size: 0.2µm

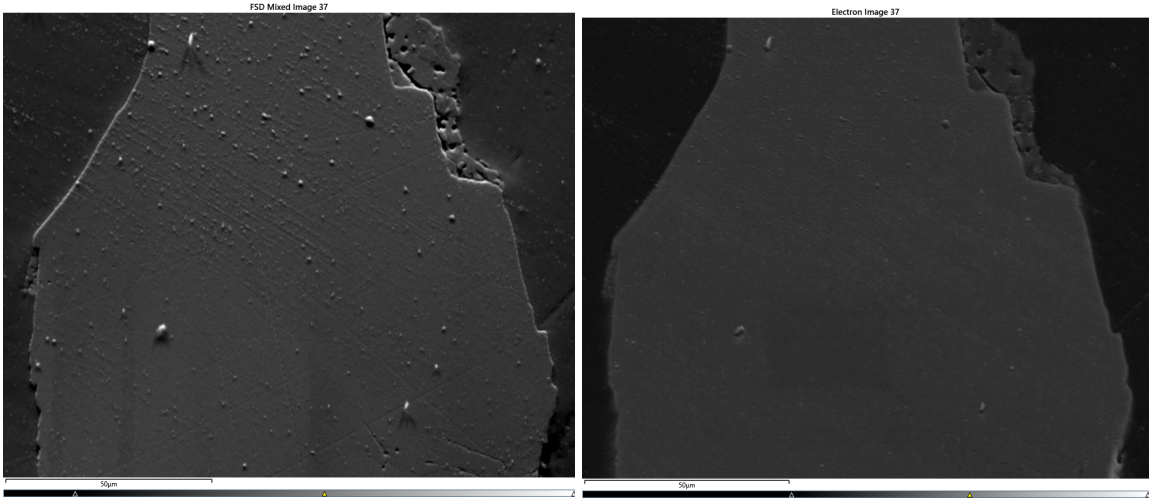
FSD Mixed Image 37
50µm
Electron Image 37
50µm

Zrsm98

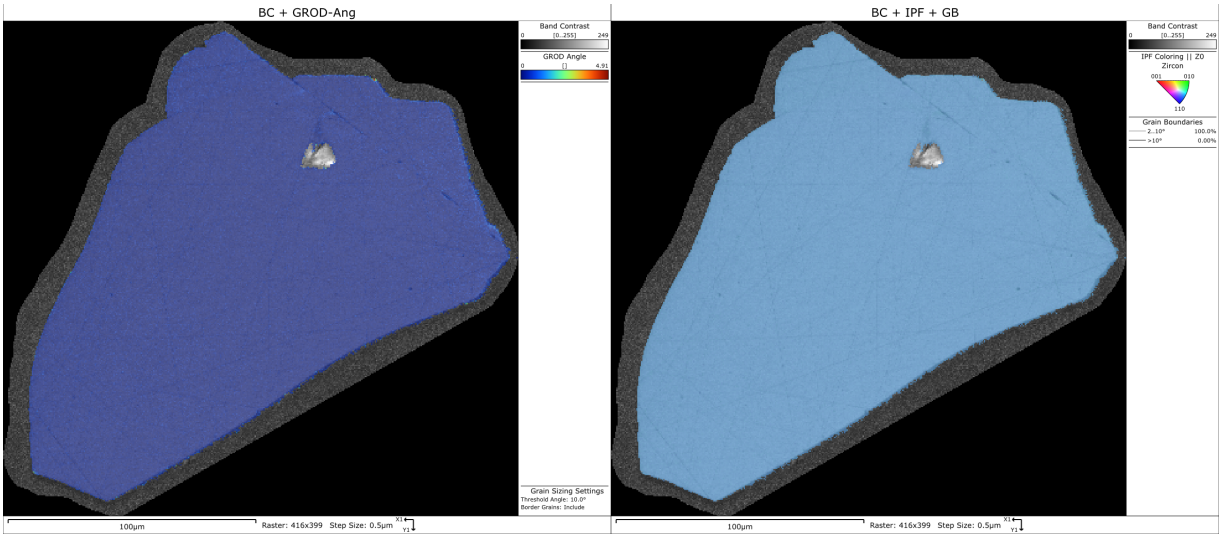
BC + GROD-Ang
Band Contrast
0 [0..255] 249
GROD Angle
0 [] 4.91
Grain Sizing Settings
Threshold Angle: 10.0°
Border Grains: Include
100µm
Raster: 416x399 Step Size: 0.5µm
BC + IPF + GB
Band Contrast
0 [0..255] 249
IPF Coloring || Z0
Zircon
001
010
110
Grain Boundaries
2..10° 100.0%
>10° 0.00%
100µm
Raster: 416x399 Step Size: 0.5µm

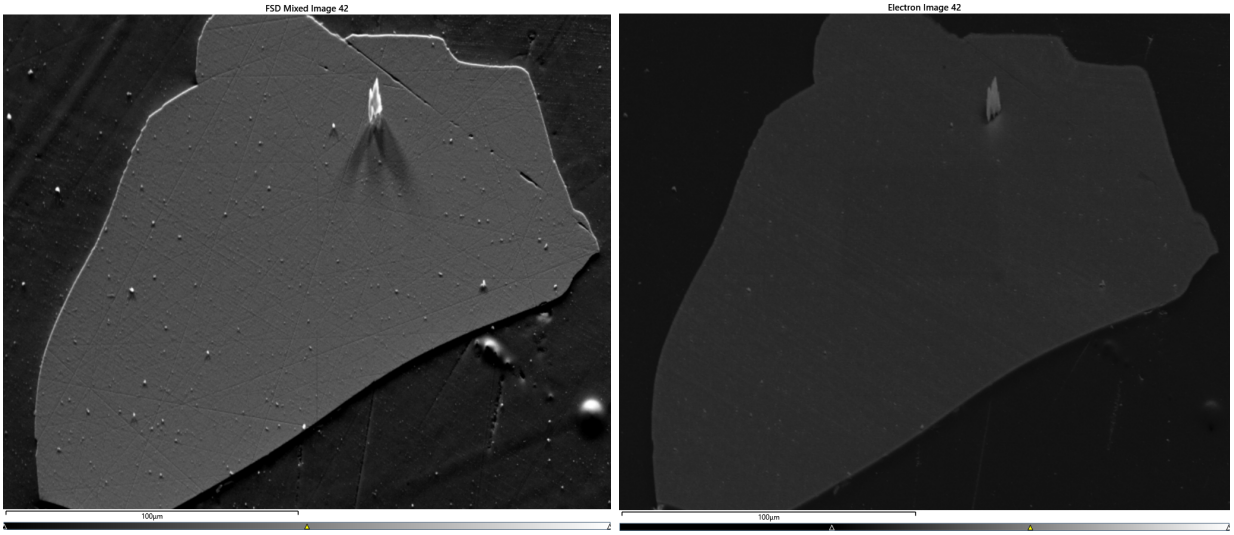
FSD Mixed Image 42
100µm
Electron Image 42
100µm

Zrsm99

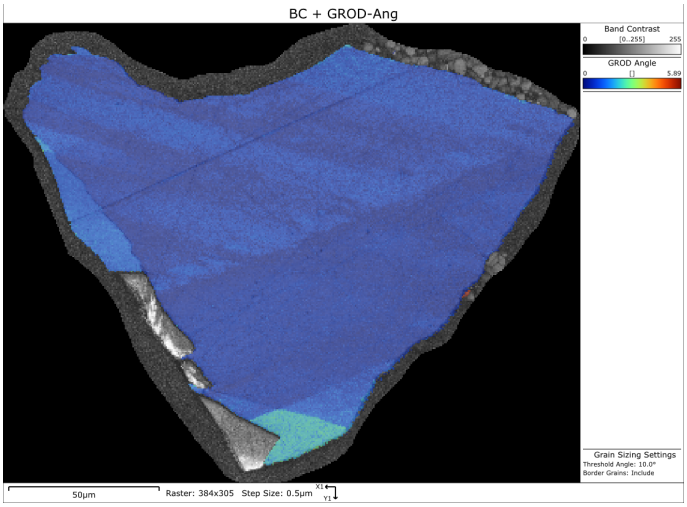
BC + GROD-Ang
Band Contrast
0 [0..255] 255
GROD Angle
0 [] 5.89
Grain Sizing Settings
Threshold Angle: 10.0°
Border Grains: Include
50µm
Raster: 384x305 Step Size: 0.5µm

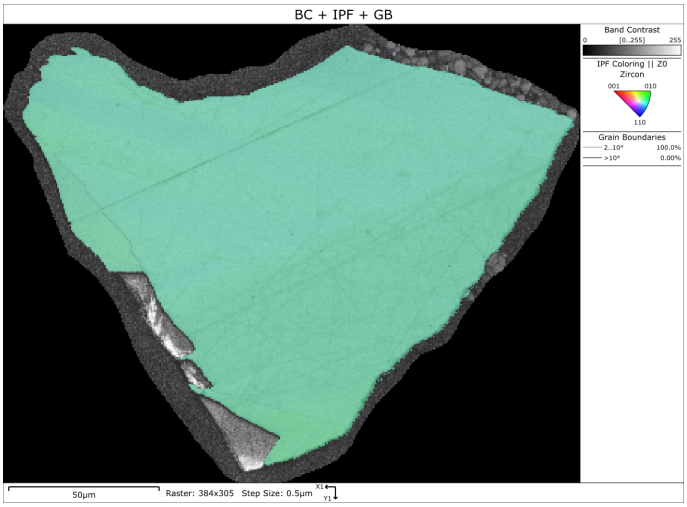
BC + IPF + GB
Band Contrast
0 [0..255] 255
IPF Coloring || Z0
Zircon
001 010
110
Grain Boundaries
2..10° 100.0%
>10° 0.00%
50µm
Raster: 384x305 Step Size: 0.5µm

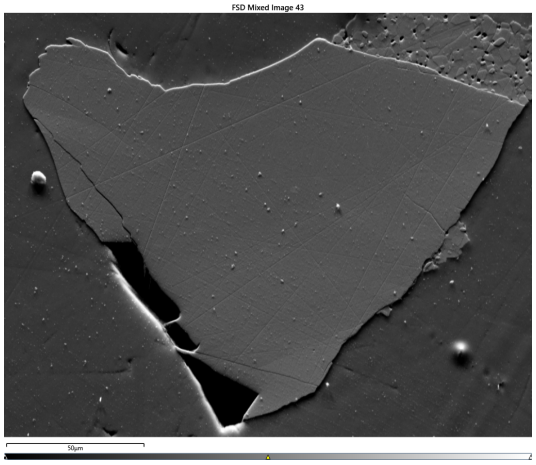
FSD Mixed Image 43
50µm

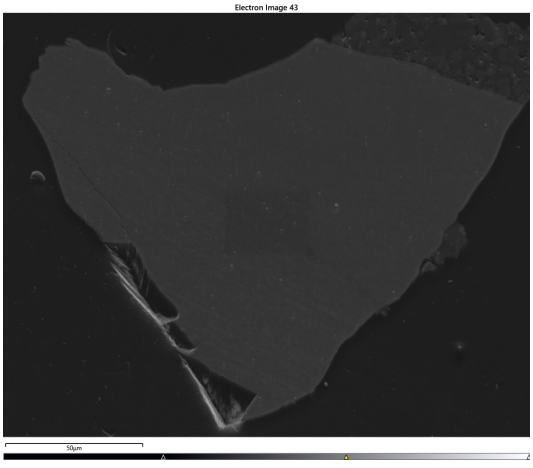
Electron Image 43
50µm

Zrsm100

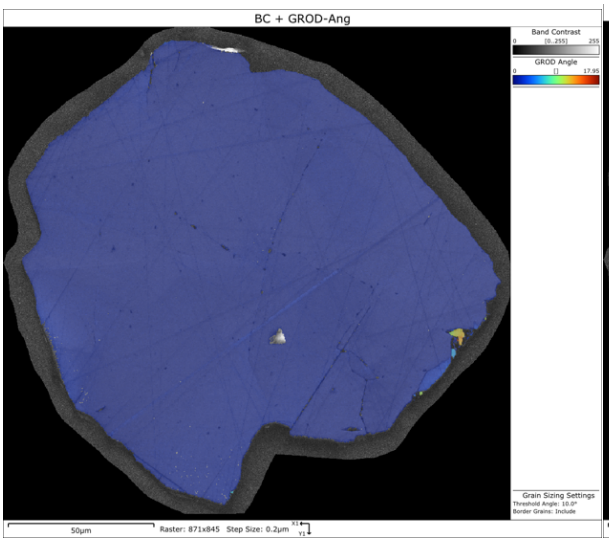
BC + GROD-Ang
Band Contrast
GROD Angle
Grain Sizing Settings
50µm
Raster: 871x845 Step Size: 0.2µm

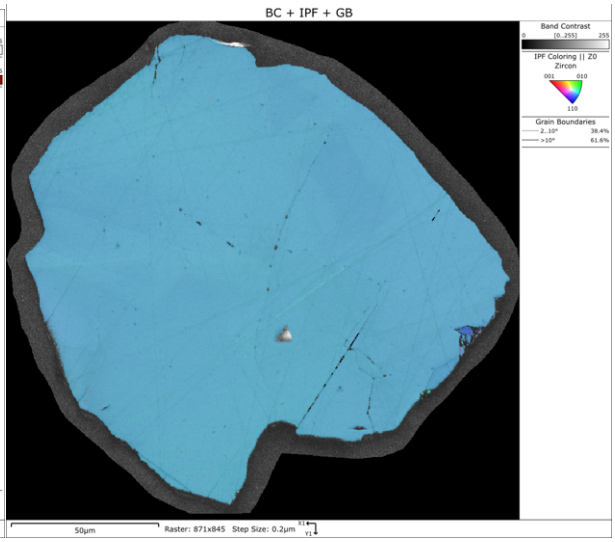
BC + IPF + GB
Band Contrast
IPF Coloring || Z0
Zircon
Grain Boundaries
50µm
Raster: 871x845 Step Size: 0.2µm

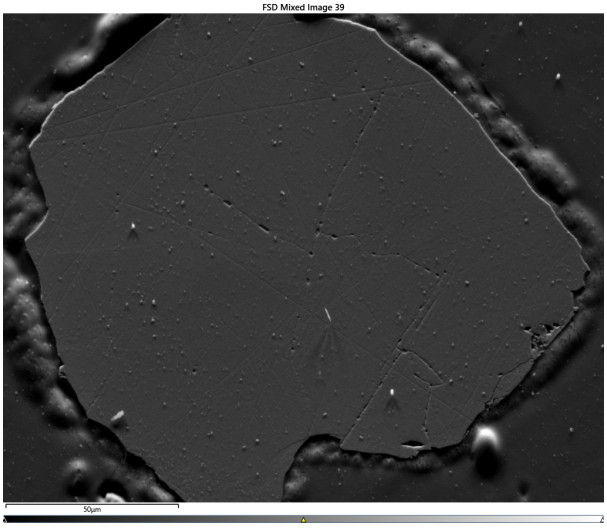
FSD Mixed Image 39
50µm

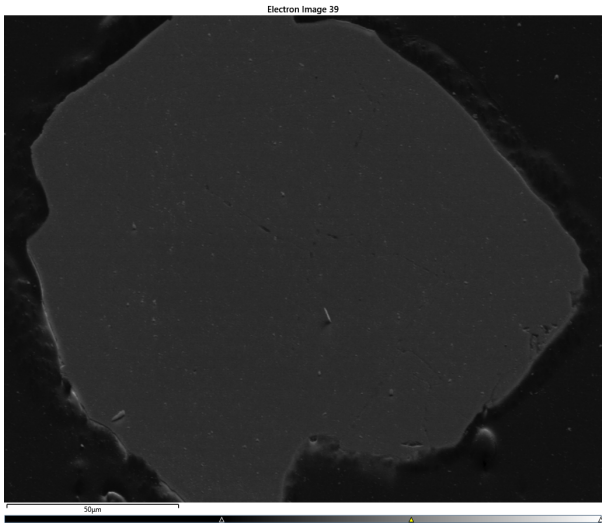
Electron Image 39
50µm

Zrsm101

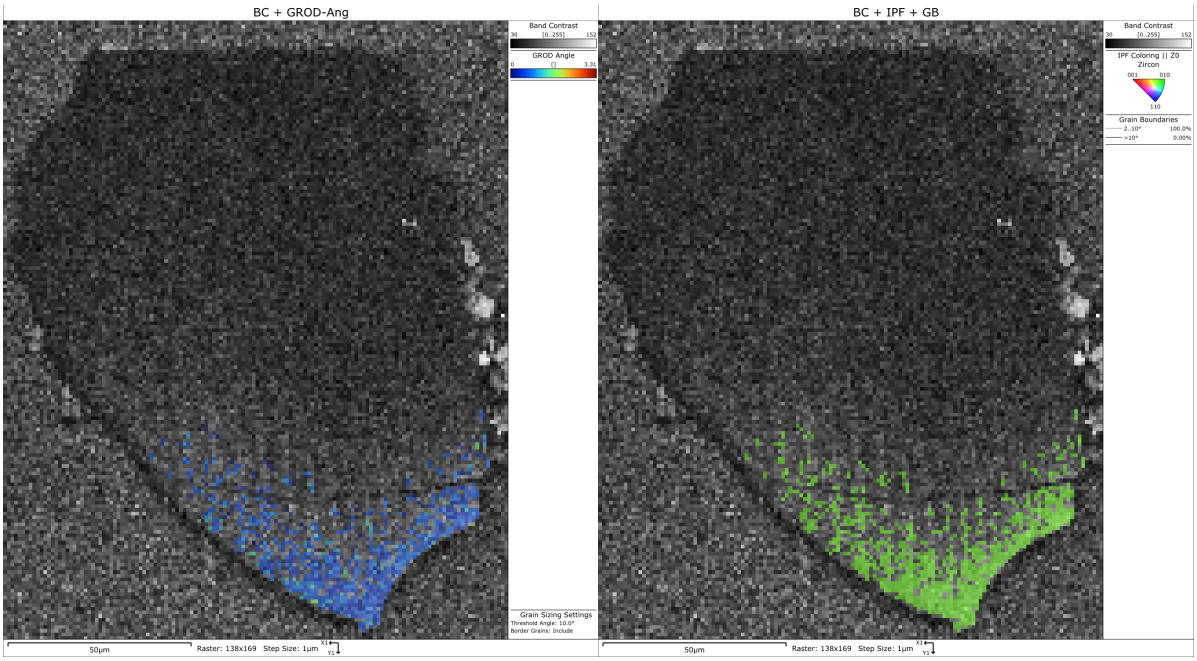
BC + GROD-Ang
Band Contrast
GROD Angle
Grain Sizing Settings
50µm
Raster: 138x169 Step Size: 1µm
BC + IPF + GB
Band Contrast
IPF Coloring || Z0
Zircon
Grain Boundaries
50µm
Raster: 138x169 Step Size: 1µm

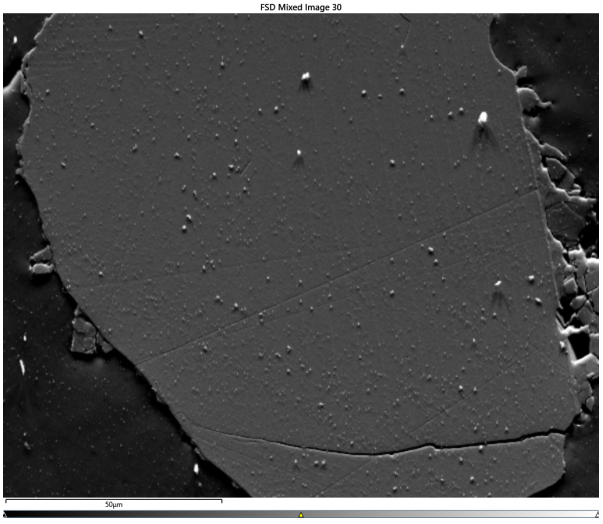
FSD Mixed Image 30
50µm

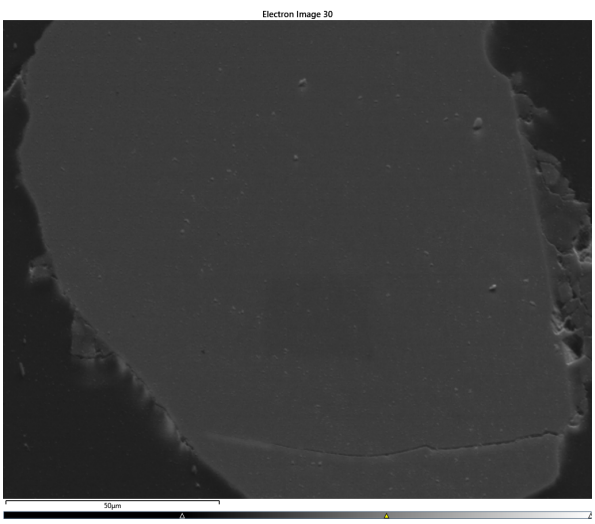
Electron Image 30
50µm

Zrsm102

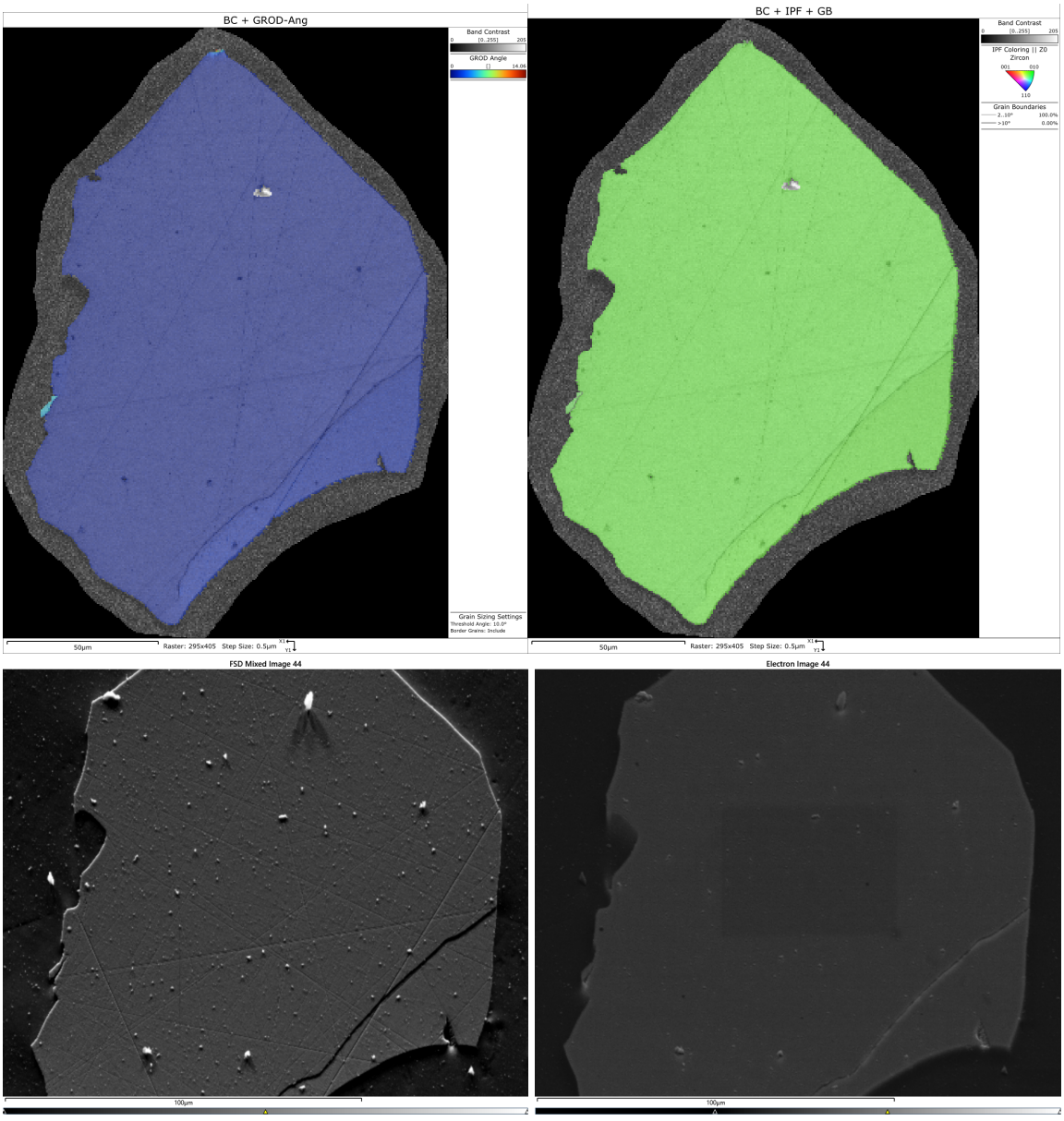
BC + GROD-Ang
Band Contrast
GROD Angle
Grain Sizing Settings
50µm
Raster: 295x405 Step Size: 0.5µm
BC + IPF + GB
Band Contrast
IPF Coloring || Z0
Zircon
Grain Boundaries
50µm
Raster: 295x405 Step Size: 0.5µm
FSD Mixed Image 44
100µm
Electron Image 44
100µm

Zrsm103

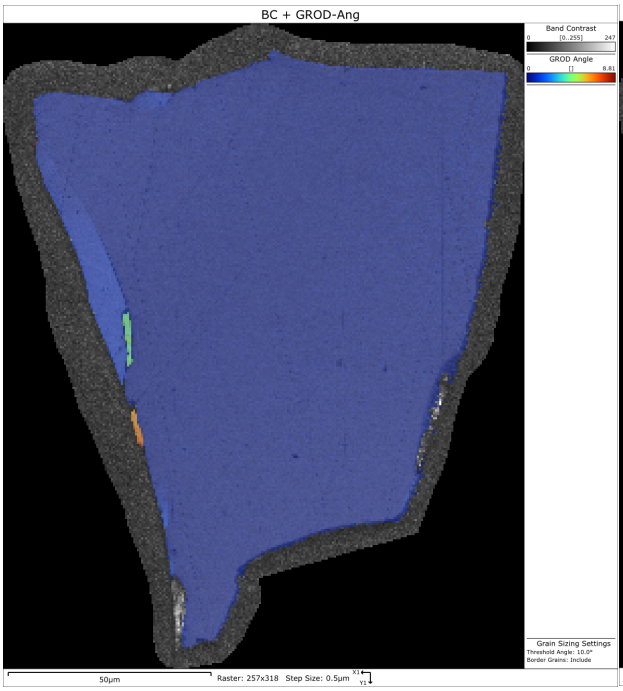
BC + GROD-Ang
Band Contrast
0 [0..255] 247
GROD Angle
0 [] 8.83
Grain Sizing Settings
Threshold Angle: 10.0°
Border Grains: Include
50µm
Raster: 257x318 Step Size: 0.5µm

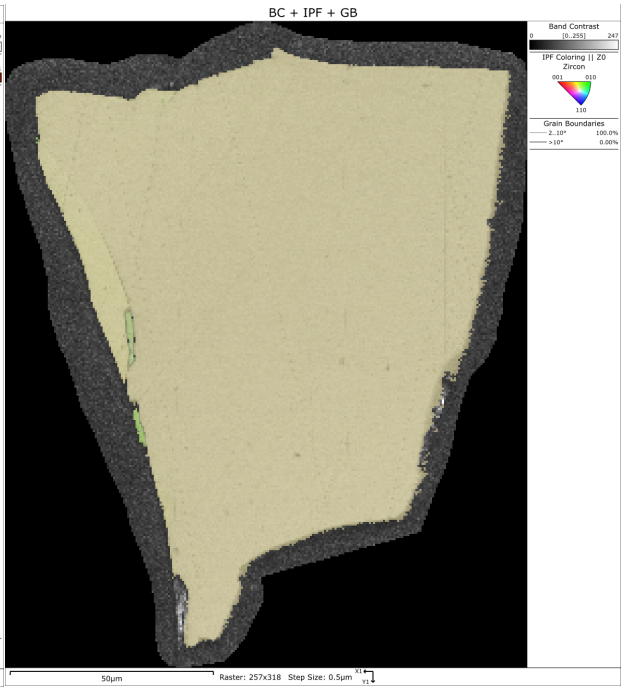
BC + IPF + GB
Band Contrast
0 [0..255] 247
IPF Coloring || Z0
Zircon
001 010
110
Grain Boundaries
2..10° 100.0%
>10° 0.00%
50µm
Raster: 257x318 Step Size: 0.5µm

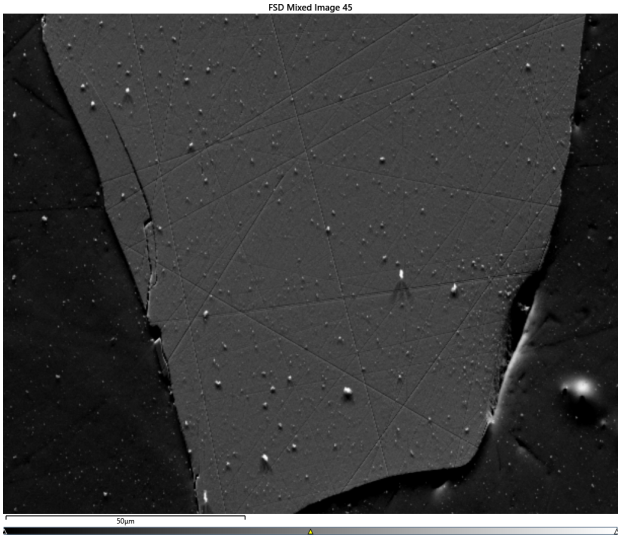
FSD Mixed Image 45
50µm

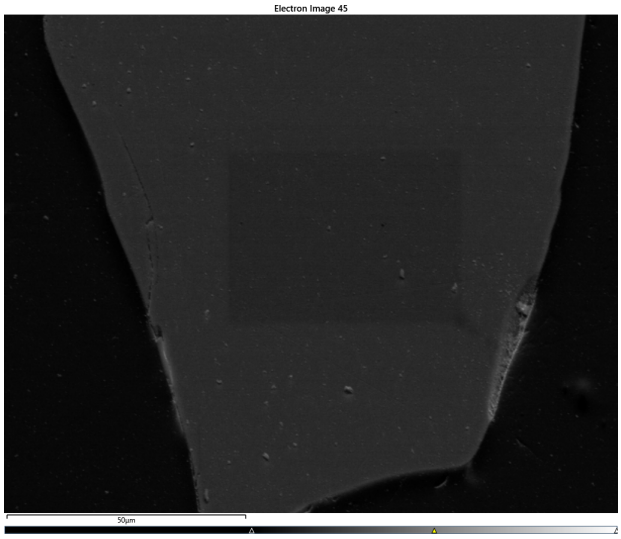
Electron Image 45
50µm

Zrsm104

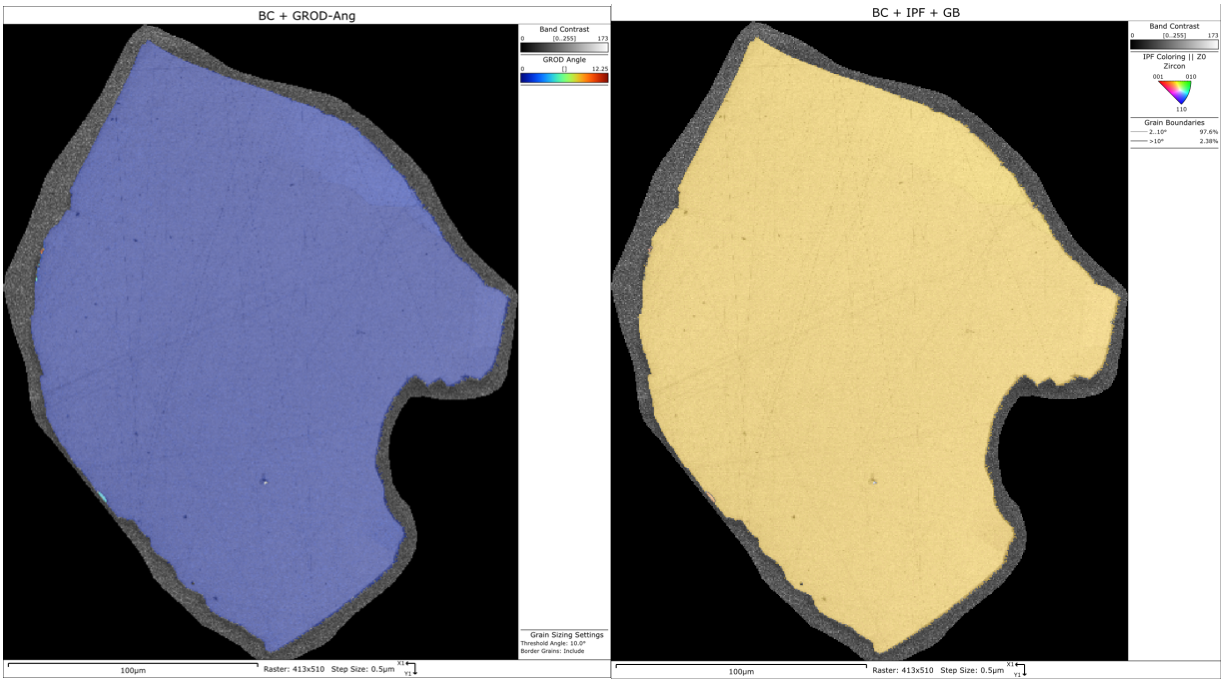
BC + GROD-Ang
Band Contrast
GROD Angle
Grain Sizing Settings
100µm
Raster: 413x510 Step Size: 0.5µm
BC + IPF + GB
Band Contrast
IPF Coloring || Z0
Zircon
Grain Boundaries
100µm
Raster: 413x510 Step Size: 0.5µm

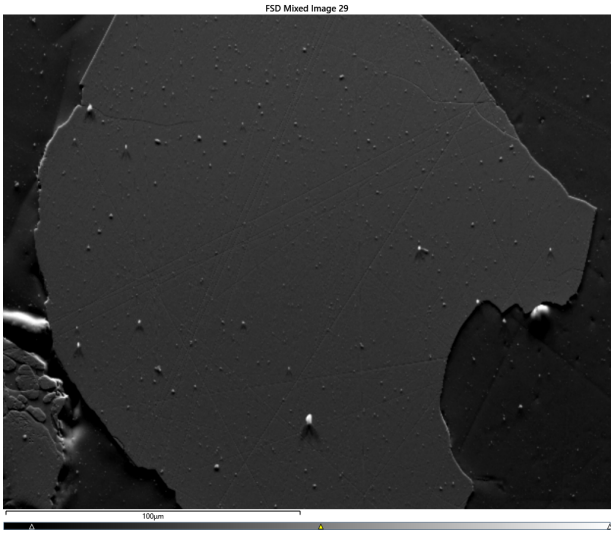
FSD Mixed Image 29
100µm

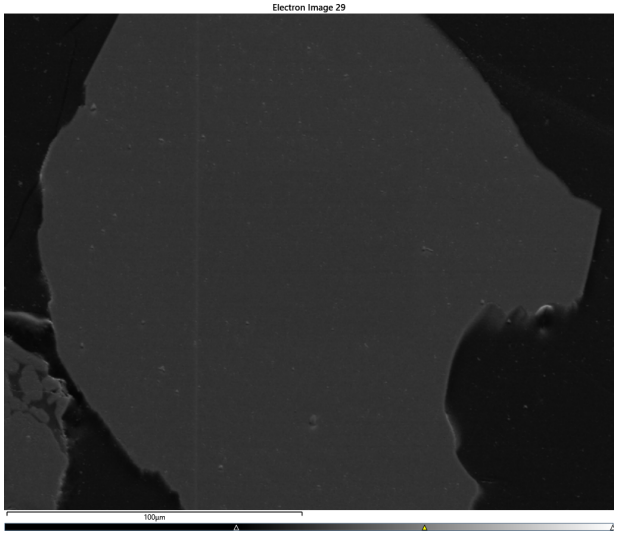
Electron Image 29
100µm

Zrsm106

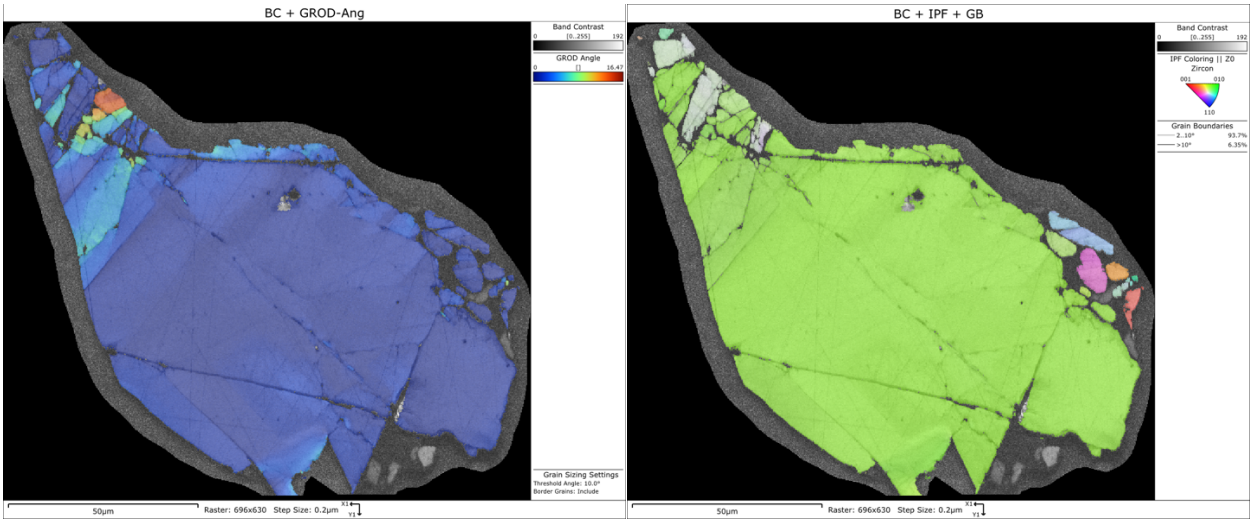
BC + GROD-Ang
Band Contrast
GROD Angle
Grain Sizing Settings
50µm
Raster: 696x630 Step Size: 0.2µm
BC + IPF + GB
Band Contrast
IPF Coloring || Z0
Zircon
Grain Boundaries
50µm
Raster: 696x630 Step Size: 0.2µm

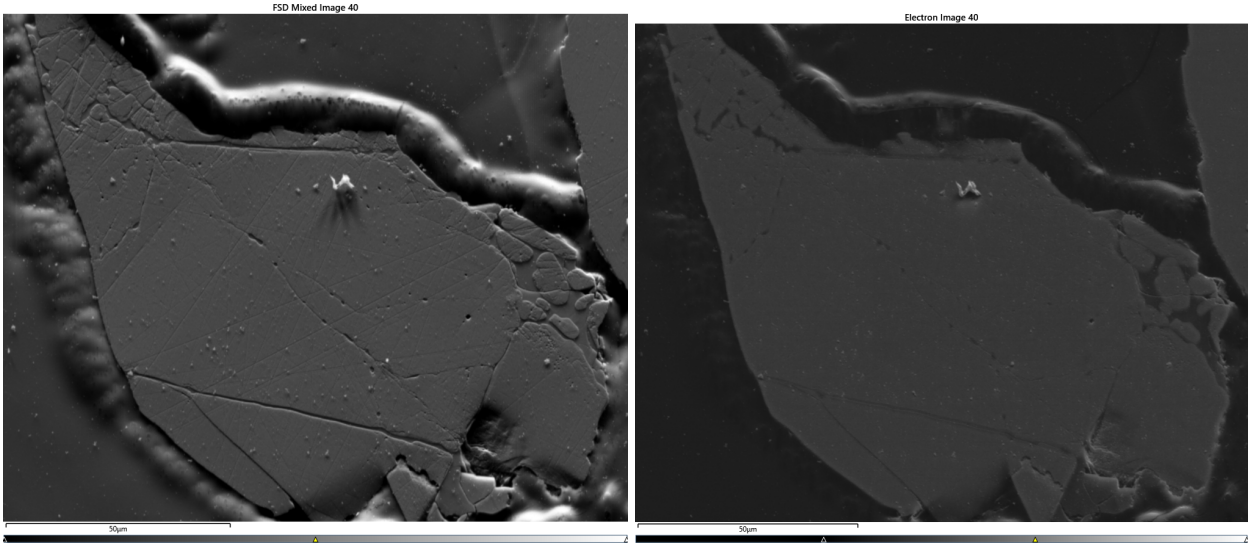
FSD Mixed Image 40
50µm
Electron Image 40
50µm

Zrsm107

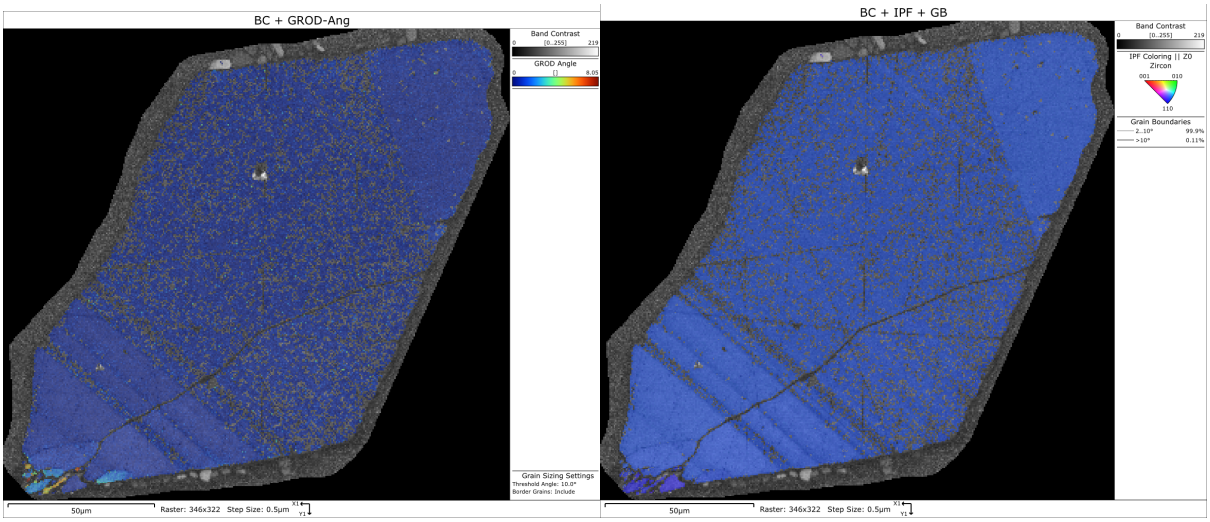
BC + GROD-Ang
Band Contrast
GROD Angle
Grain Sizing Settings
50µm
Raster: 346x322 Step Size: 0.5µm
BC + IPF + GB
Band Contrast
IPF Coloring || Z0
Zircon
Grain Boundaries
50µm
Raster: 346x322 Step Size: 0.5µm

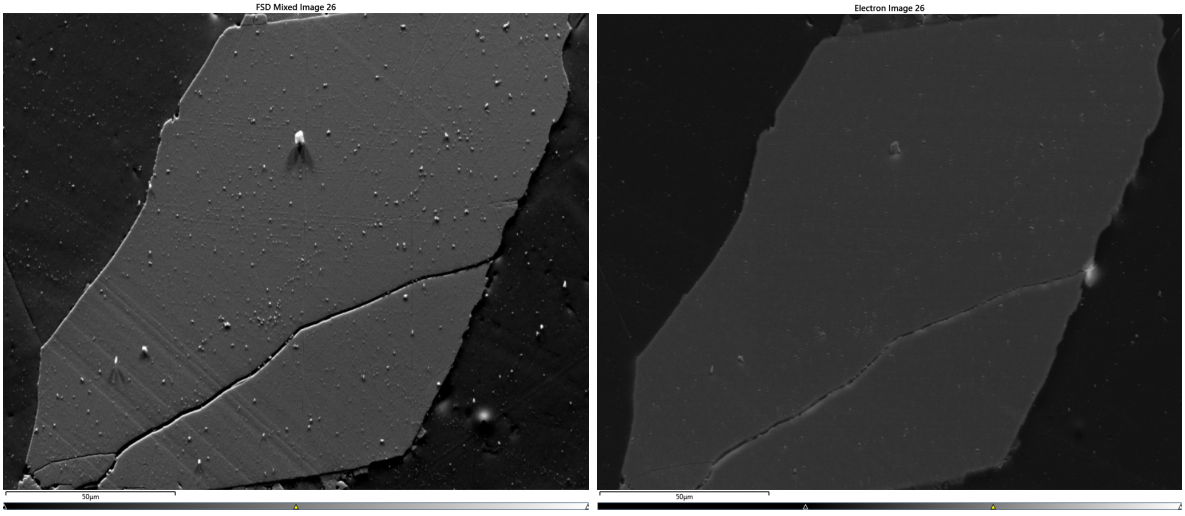
FSD Mixed Image 26
50µm
Electron Image 26
50µm

Zrsm108

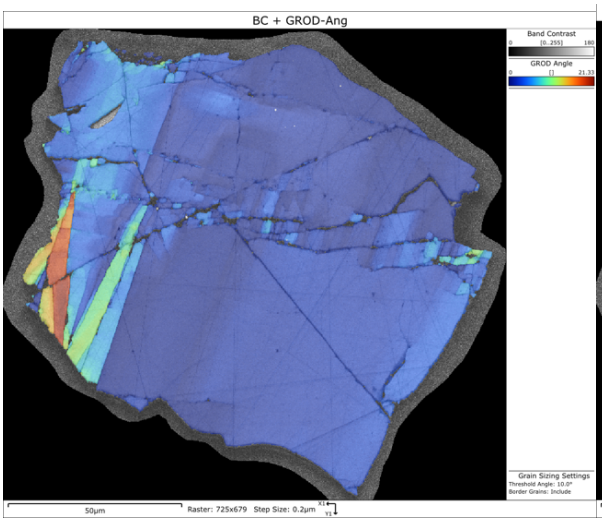
BC + GROD-Ang
Band Contrast
GROD Angle
Grain Sizing Settings
50µm
Raster: 725x679 Step Size: 0.2µm

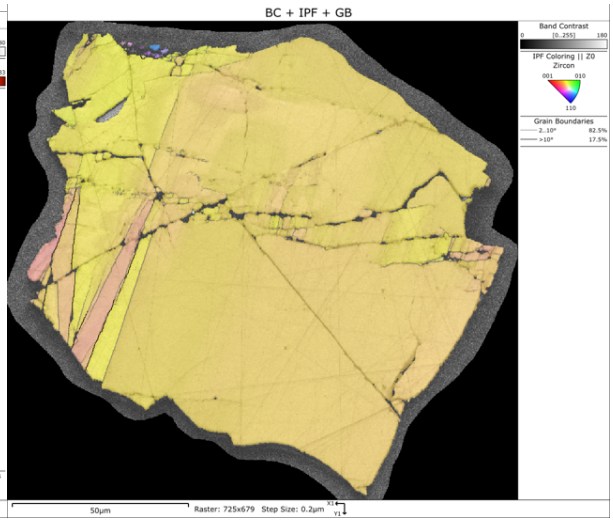
BC + IPF + GB
Band Contrast
IPF Coloring || Z0
Zircon
Grain Boundaries
50µm
Raster: 725x679 Step Size: 0.2µm

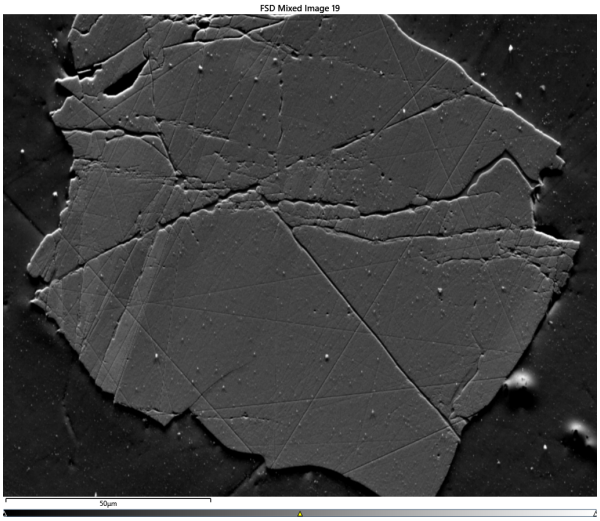
FSD Mixed Image 19
50µm

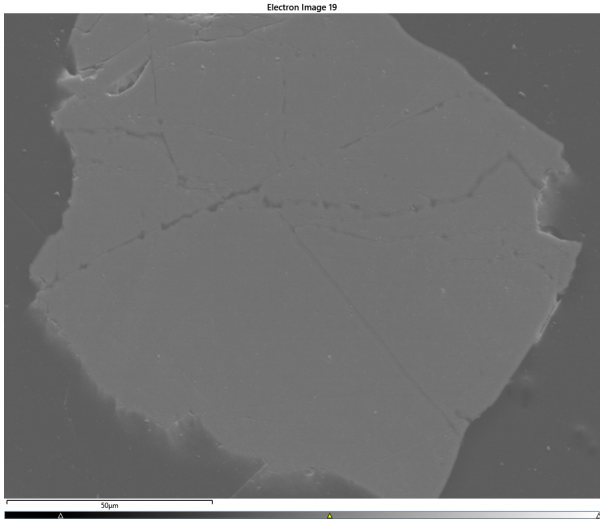
Electron Image 19
50µm

Zrsm109

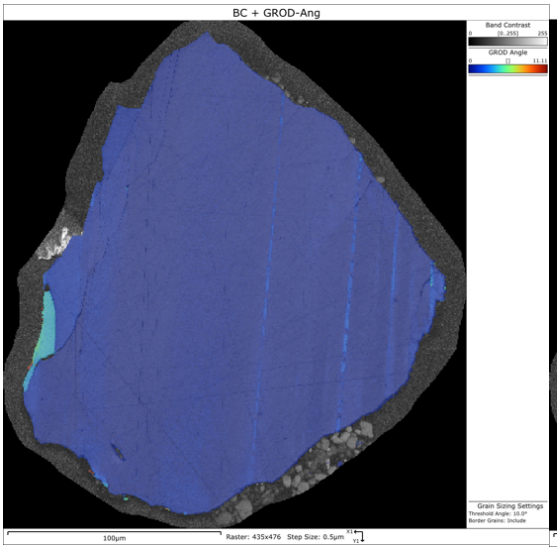
BC + GROD-Ang
Band Contrast
GROD Angle
Grain Sizing Settings
100µm
Raster: 435x476 Step Size: 0.5µm

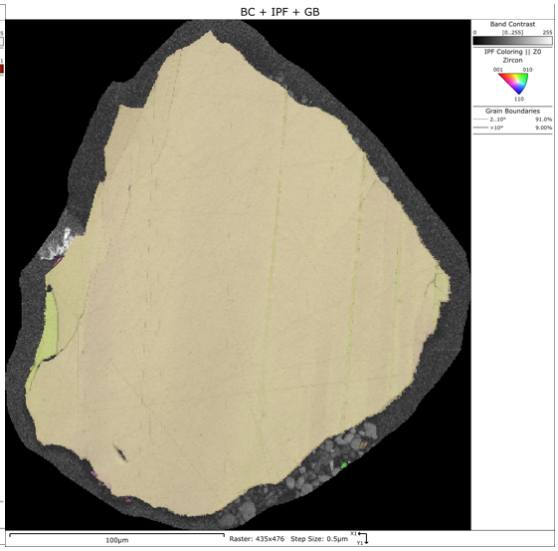
BC + IPF + GB
Band Contrast
IPF Coloring || Z0
Zircon
Grain Boundaries
100µm
Raster: 435x476 Step Size: 0.5µm

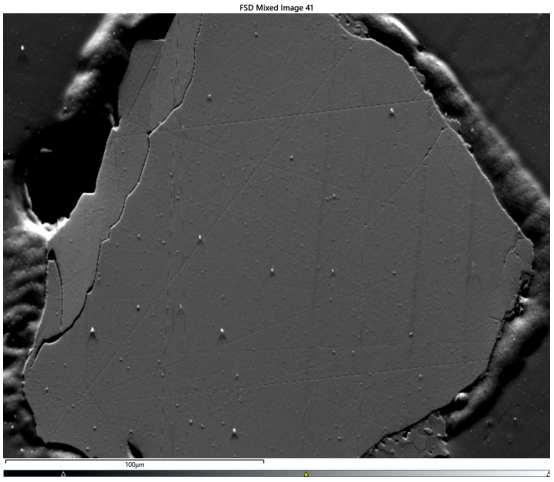
FSD Mixed Image 41
100µm

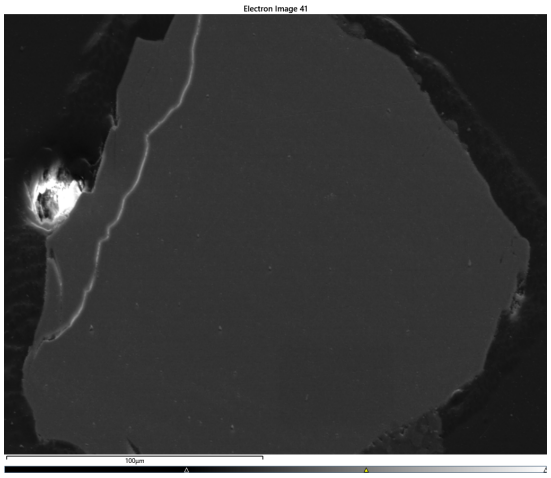
Electron Image 41
100µm

Zrsm110

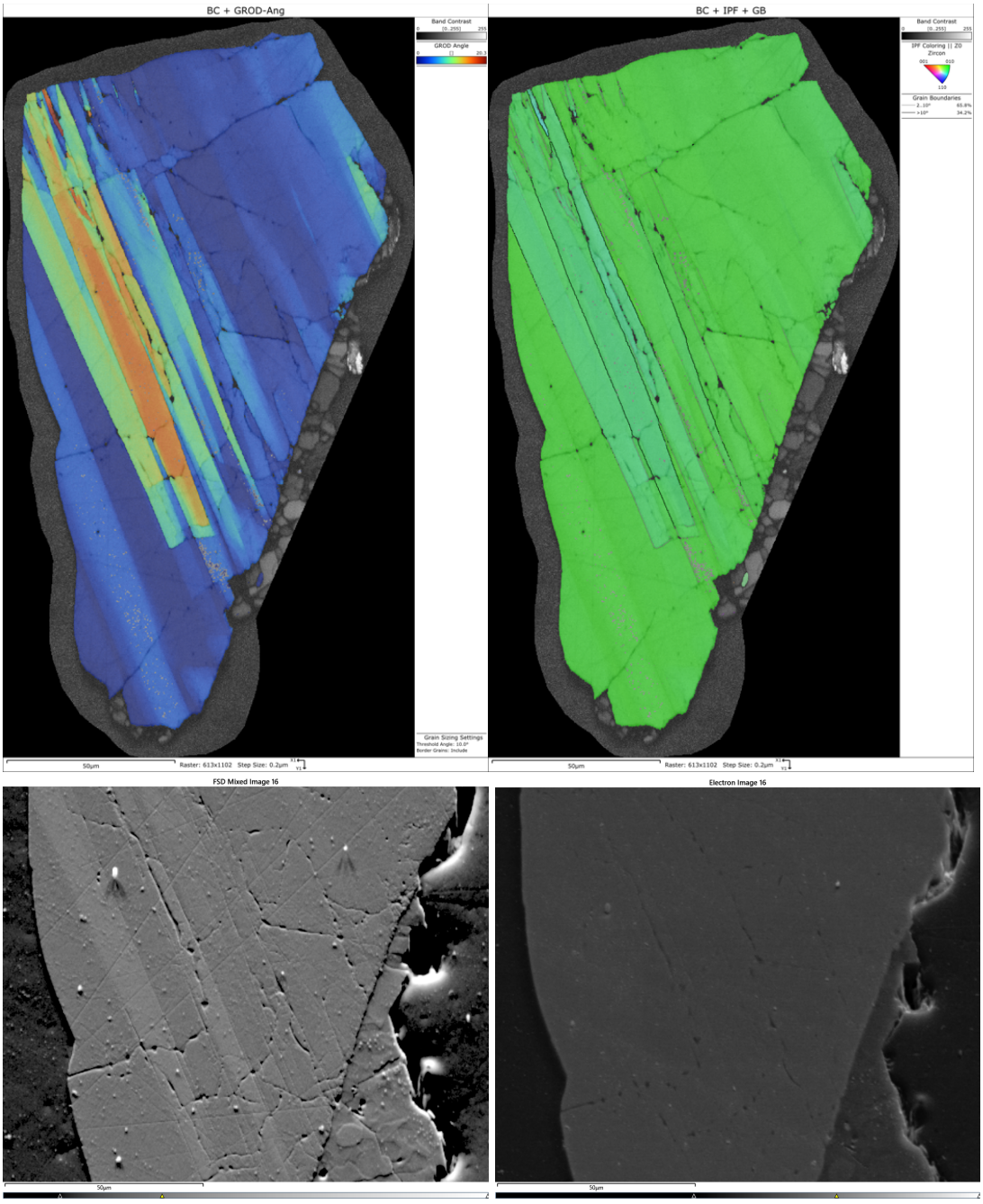
BC + GROD-Ang
Band Contrast
GROD Angle
Grain Sizing Settings
50µm
Raster: 613x1102 Step Size: 0.2µm
BC + IPF + GB
Band Contrast
IPF Coloring || Z0
Zircon
Grain Boundaries
50µm
Raster: 613x1102 Step Size: 0.2µm
FSD Mixed Image 16
50µm
Electron Image 16
50µm

Zrsm111

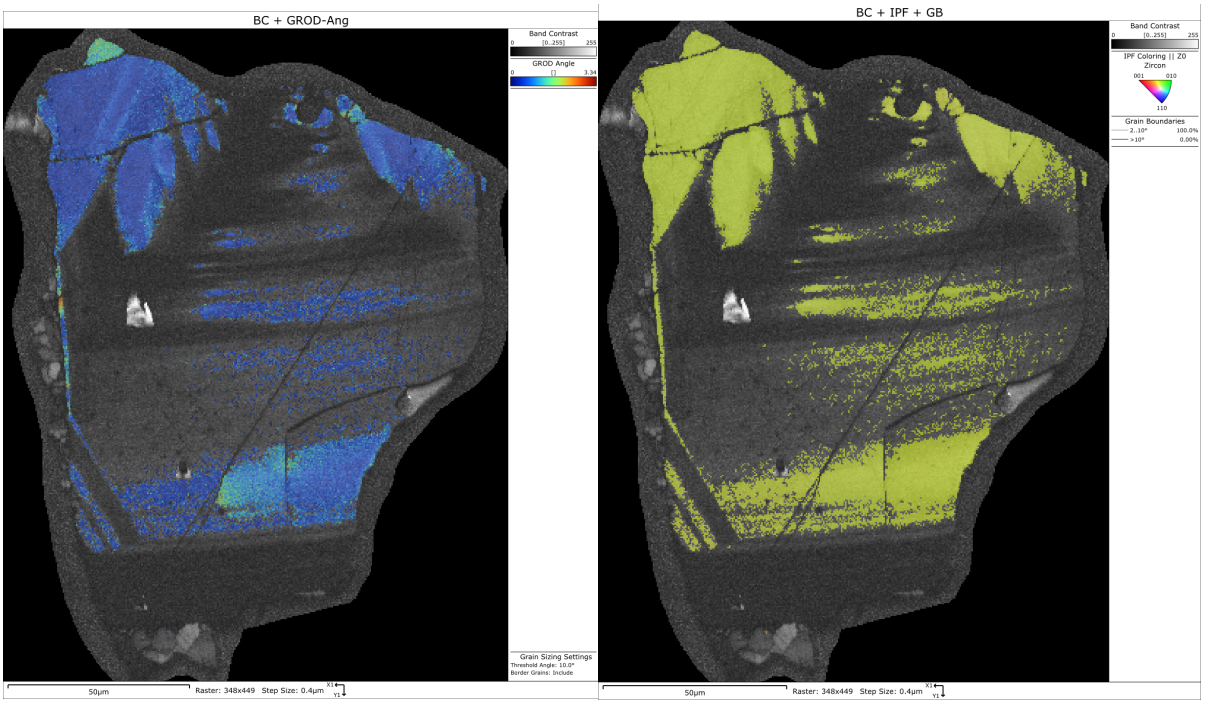
BC + GROD-Ang
Band Contrast
GROD Angle
Grain Sizing Settings
50µm
Raster: 348x449 Step Size: 0.4µm
BC + IPF + GB
Band Contrast
IPF Coloring || ZO
Zircon
Grain Boundaries
50µm
Raster: 348x449 Step Size: 0.4µm

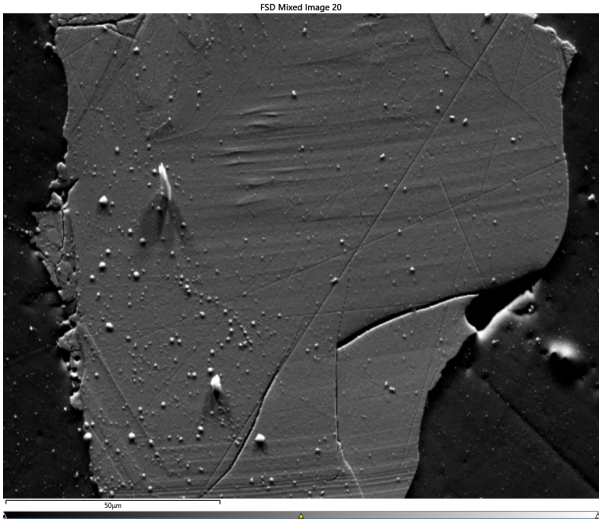
FSD Mixed Image 20
50µm

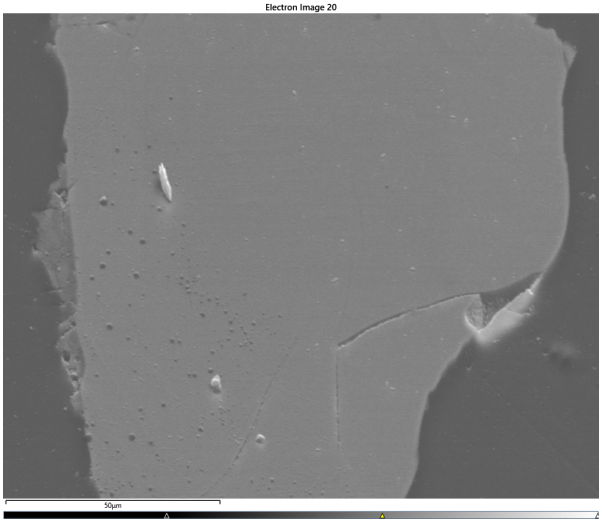
Electron Image 20
50µm

Zrsm112

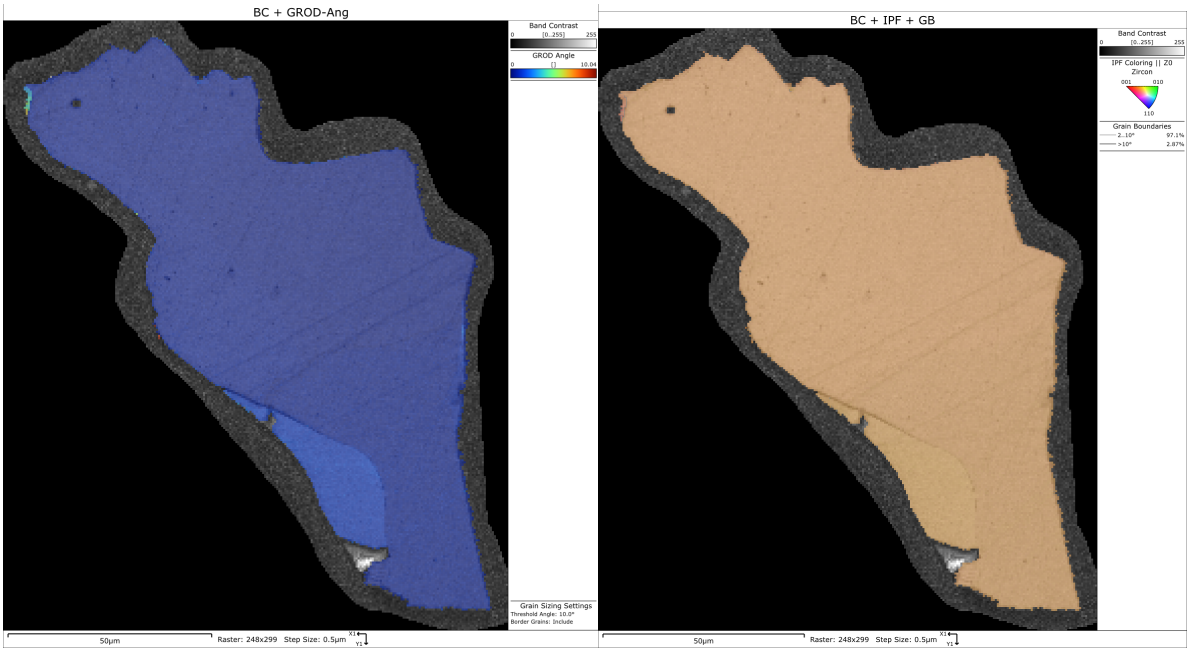
BC + GROD-Ang
Band Contrast
GROD Angle
Grain Sizing Settings
50µm
Raster: 248x299 Step Size: 0.5µm
BC + IPF + GB
Band Contrast
IPF Coloring || Z0
Zircon
Grain Boundaries
50µm
Raster: 248x299 Step Size: 0.5µm

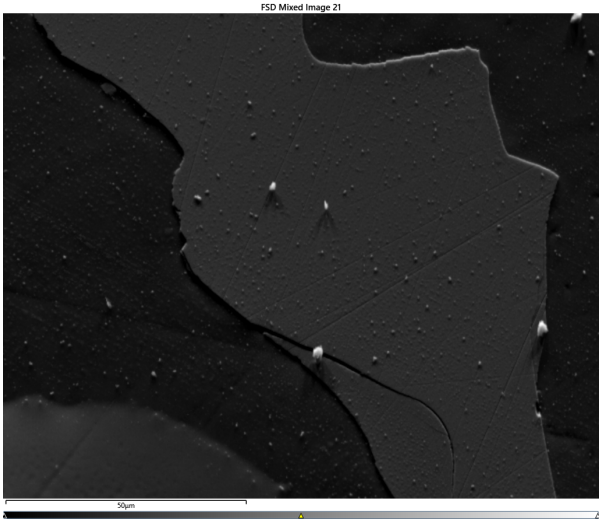
FSD Mixed Image 21
50µm

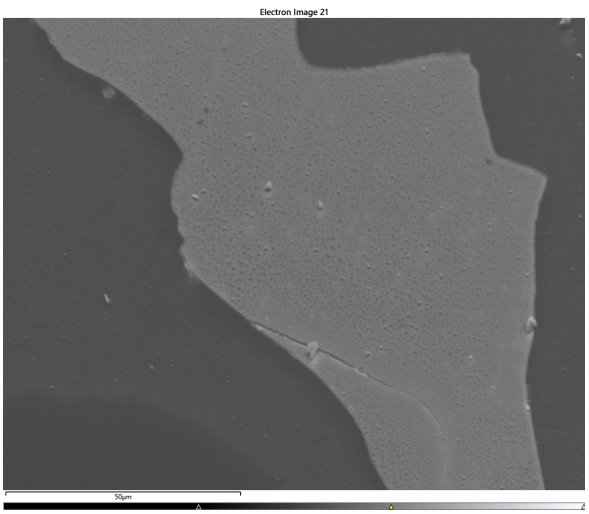
Electron Image 21
50µm

Zrsm113

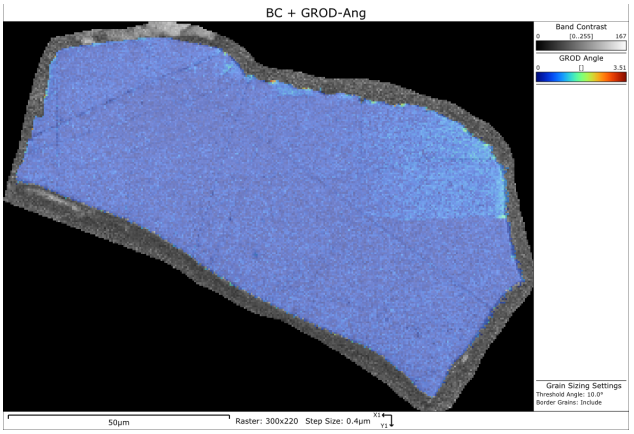
BC + GROD-Ang
Band Contrast
0 [0..255] 167
GROD Angle
0 [] 3.51
Grain Sizing Settings
Threshold Angle: 10.0°
Border Grains: Include
50µm
Raster: 300x220 Step Size: 0.4µm

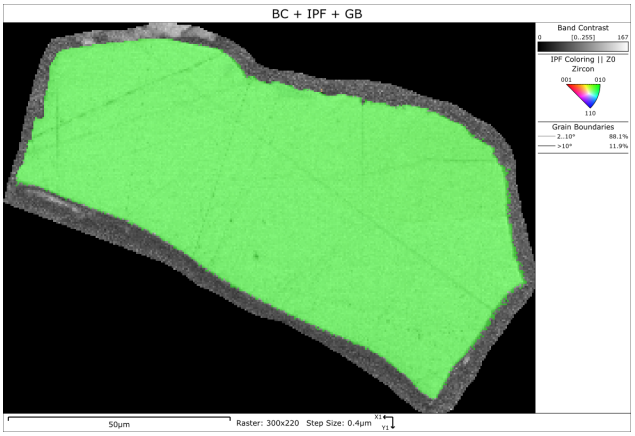
BC + IPF + GB
Band Contrast
0 [0..255] 167
IPF Coloring || Z0
Zircon
001 010
110
Grain Boundaries
2..10° 88.1%
>10° 11.9%
50µm
Raster: 300x220 Step Size: 0.4µm

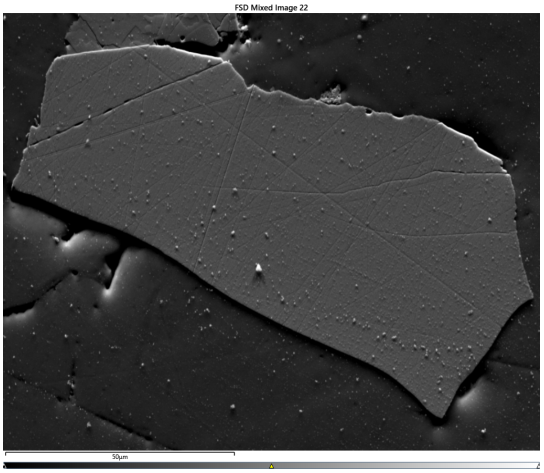
FSD Mixed Image 22
50µm

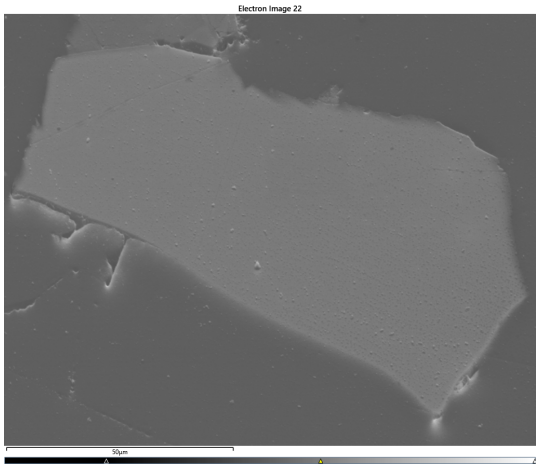
Electron Image 22
50µm

Zrsm114

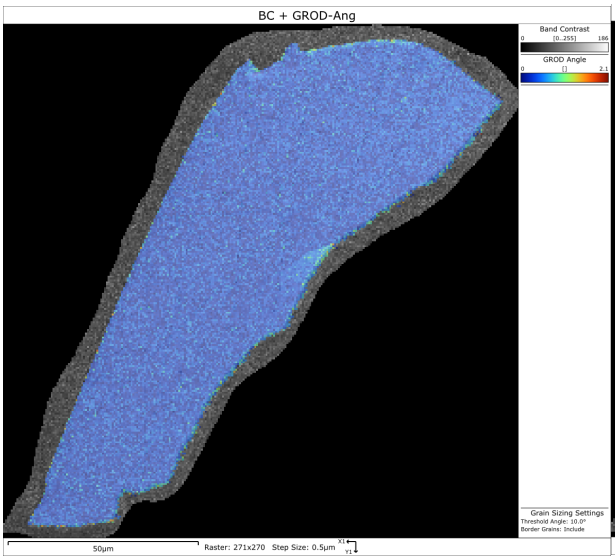
BC + GROD-Ang
Band Contrast
[0..255]
GROD Angle
Grain Sizing Settings
50µm
Raster: 271x270 Step Size: 0.5µm

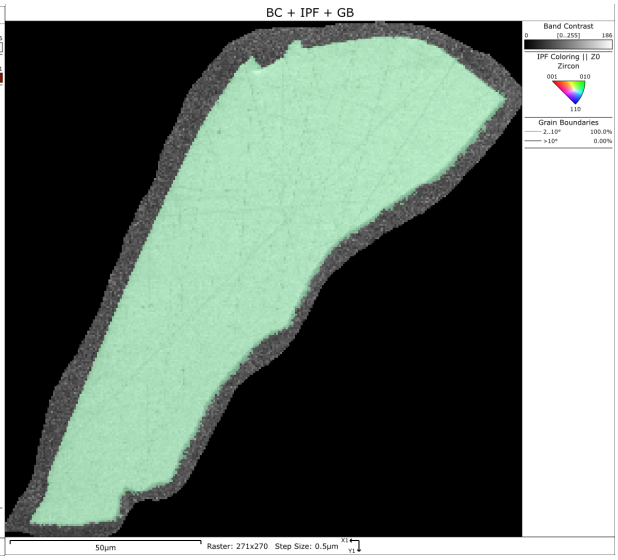
BC + IPF + GB
Band Contrast
[0..255]
IPF Coloring || Z0
Zircon
Grain Boundaries
50µm
Raster: 271x270 Step Size: 0.5µm

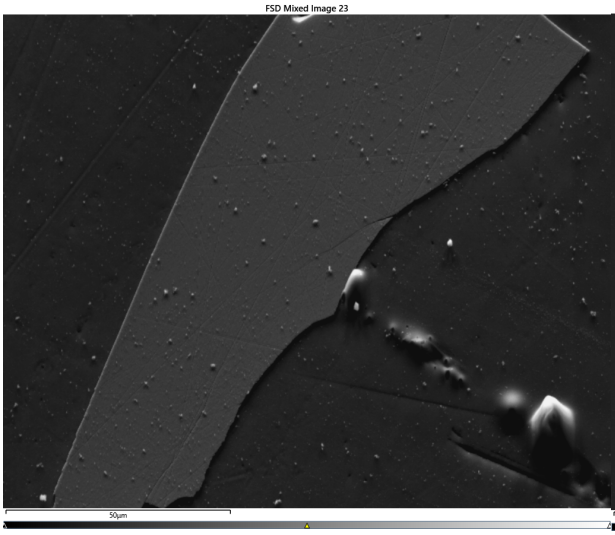
FSD Mixed Image 23
50µm

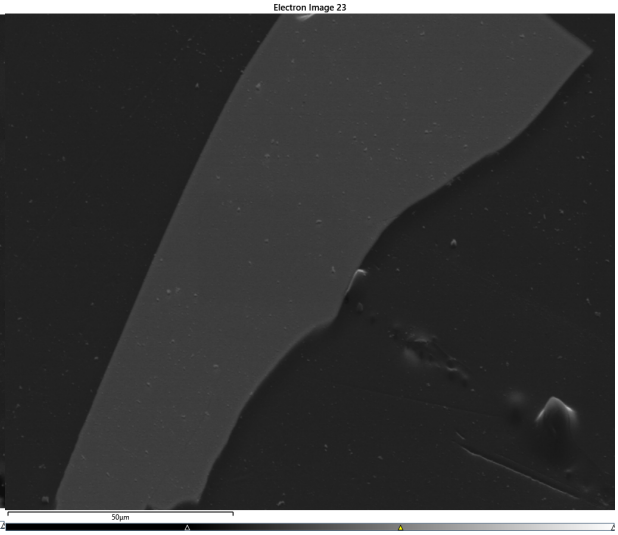
Electron Image 23
50µm

Zrsm115

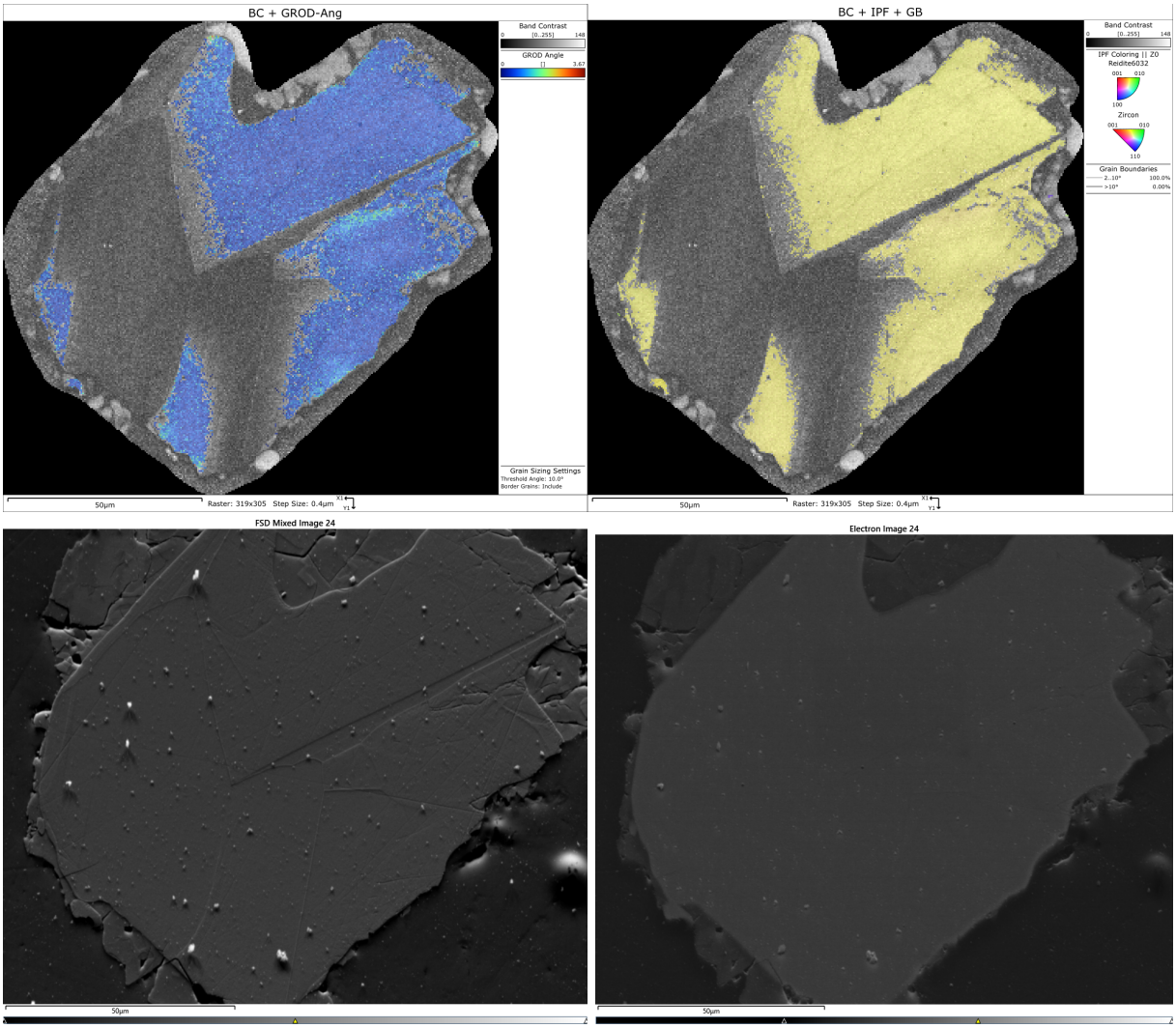
BC + GROD-Ang
Band Contrast
GROD Angle
Grain Sizing Settings
50µm
Raster: 319x305 Step Size: 0.4µm
BC + IPF + GB
Band Contrast
IPF Coloring || ZO
Reichte6032
Zircon
Grain Boundaries
50µm
Raster: 319x305 Step Size: 0.4µm
FSD Mixed Image 24
50µm
Electron Image 24
50µm

Zrsm116

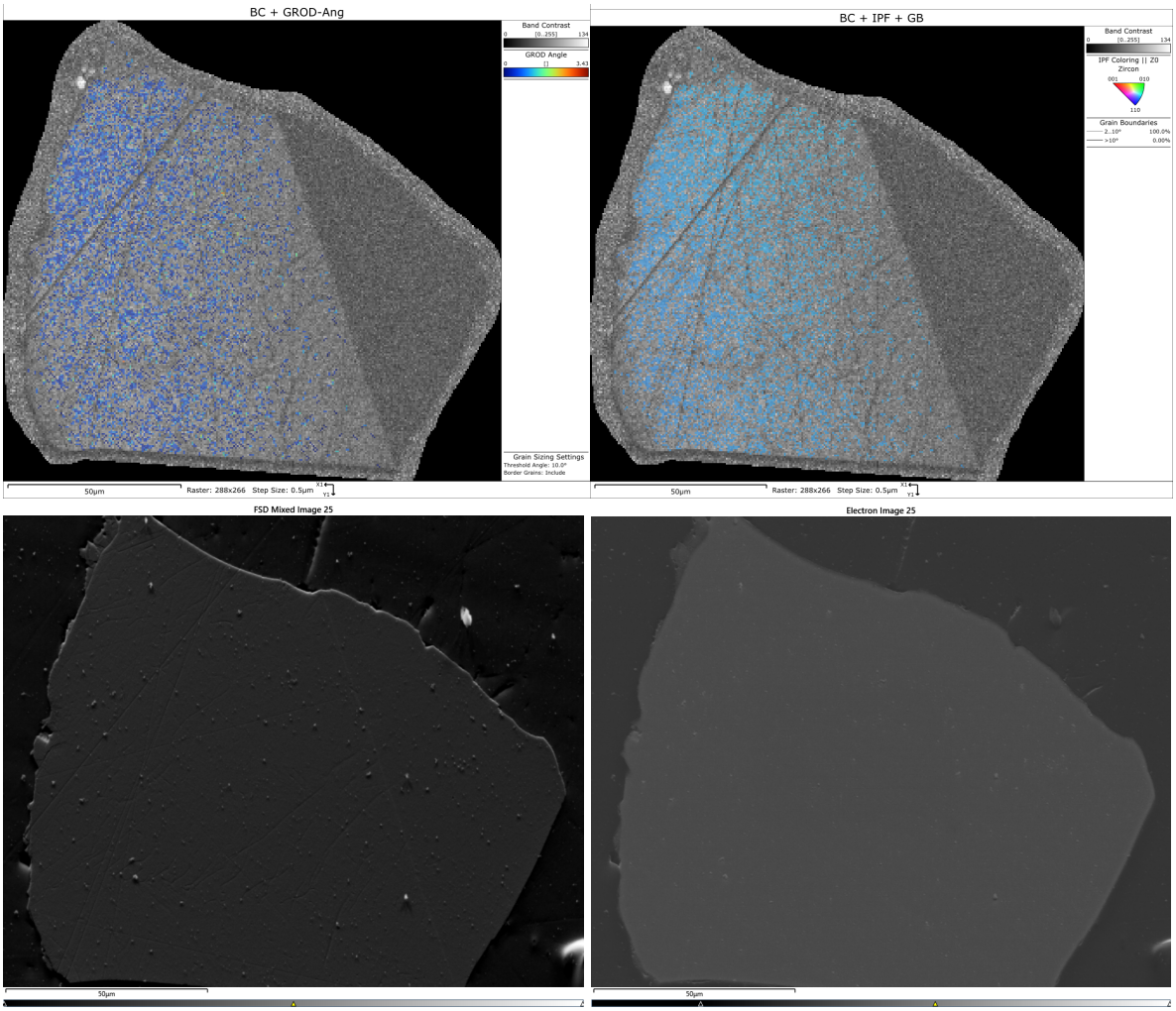
BC + GROD-Ang
Band Contrast
GROD Angle
Grain Sizing Settings
50µm
Raster: 288x266 Step Size: 0.5µm
BC + IPF + GB
Band Contrast
IPF Coloring || Z0
Zircon
Grain Boundaries
50µm
Raster: 288x266 Step Size: 0.5µm
FSD Mixed Image 25
50µm
Electron Image 25
50µm

M_M1_2

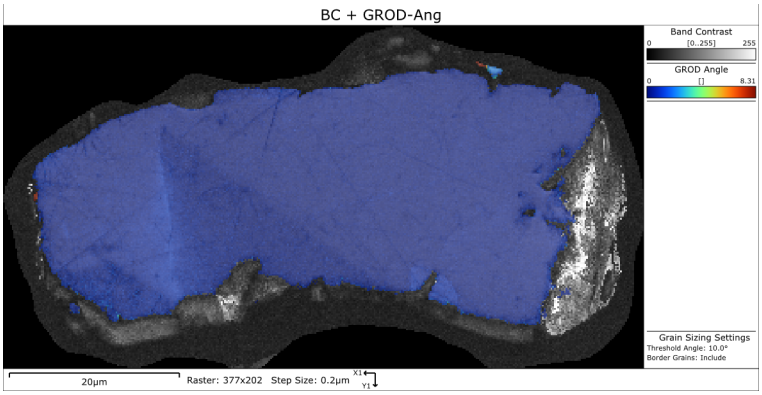
BC + GROD-Ang
Band Contrast
0 [0..255] 255
GROD Angle
0 [] 8.31
Grain Sizing Settings
Threshold Angle: 10.0°
Border Grains: Include
20µm
Raster: 377x202 Step Size: 0.2µm

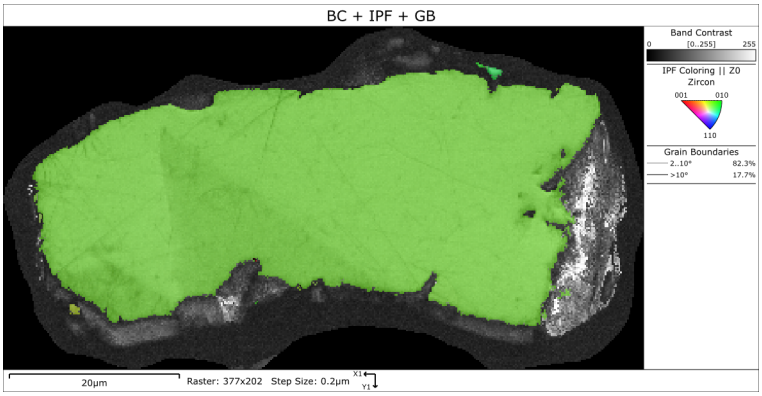
BC + IPF + GB
Band Contrast
0 [0..255] 255
IPF Coloring || Z0
Zircon
001 010
110
Grain Boundaries
2..10° 82.3%
>10° 17.7%
20µm
Raster: 377x202 Step Size: 0.2µm

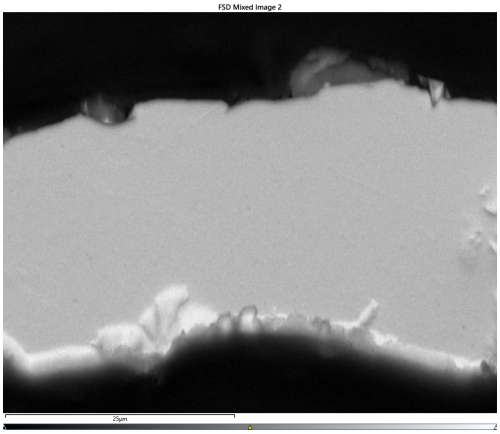
FSD Mixed Image 2

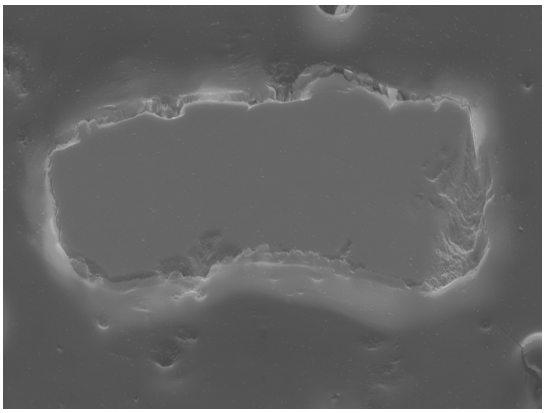

M_M1_3

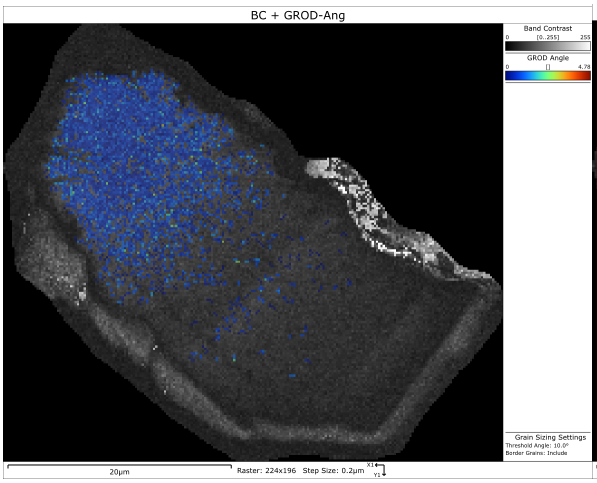
BC + GROD-Ang
Band Contrast
GROD Angle
Grain Sizing Settings
20µm
Raster: 224x196 Step Size: 0.2µm

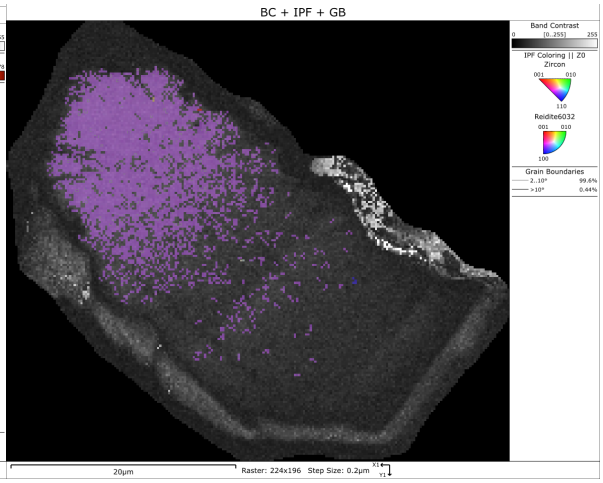
BC + IPF + GB
Band Contrast
IPF Coloring || Z0
Zircon
Reidite6032
Grain Boundaries
20µm
Raster: 224x196 Step Size: 0.2µm

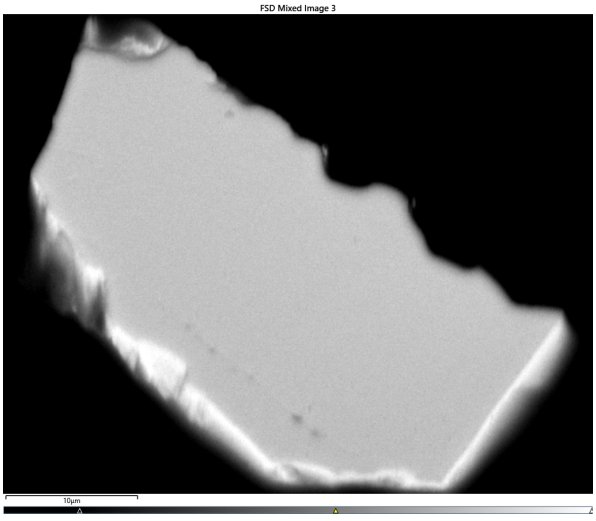
FSD Mixed Image 3
10µm

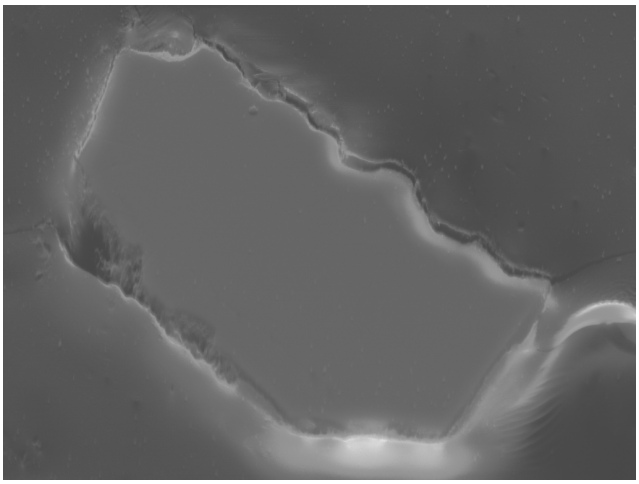

M_M1_4

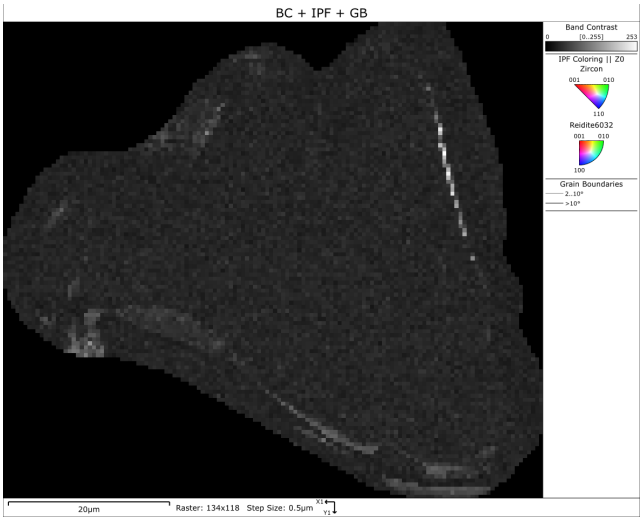
BC + IPF + GB
Band Contrast
0 [0..255] 253
IPF Coloring || Z0
Zircon
001 010
110
Reidite6032
001 010
100
Grain Boundaries
2..10°
>10°
20µm
Raster: 134x118 Step Size: 0.5µm
X1
Y1

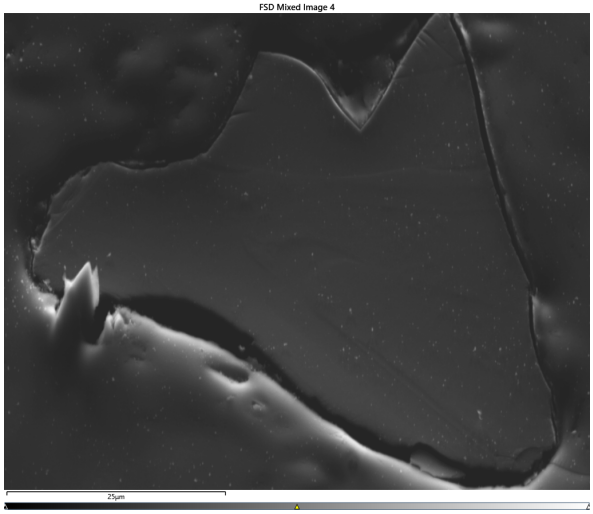
FSD Mixed Image 4
25µm

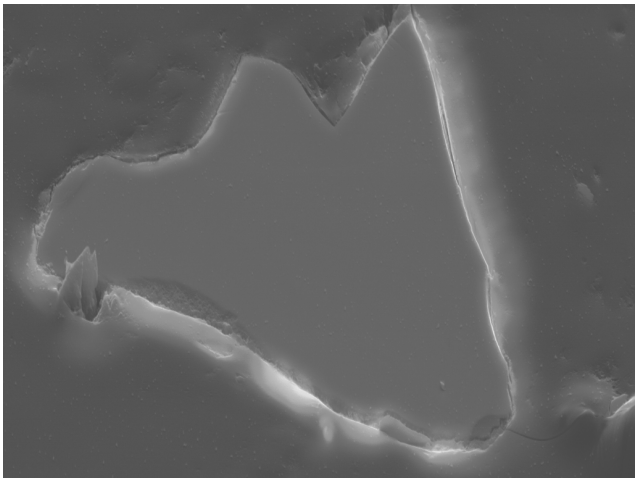

M_M1_5

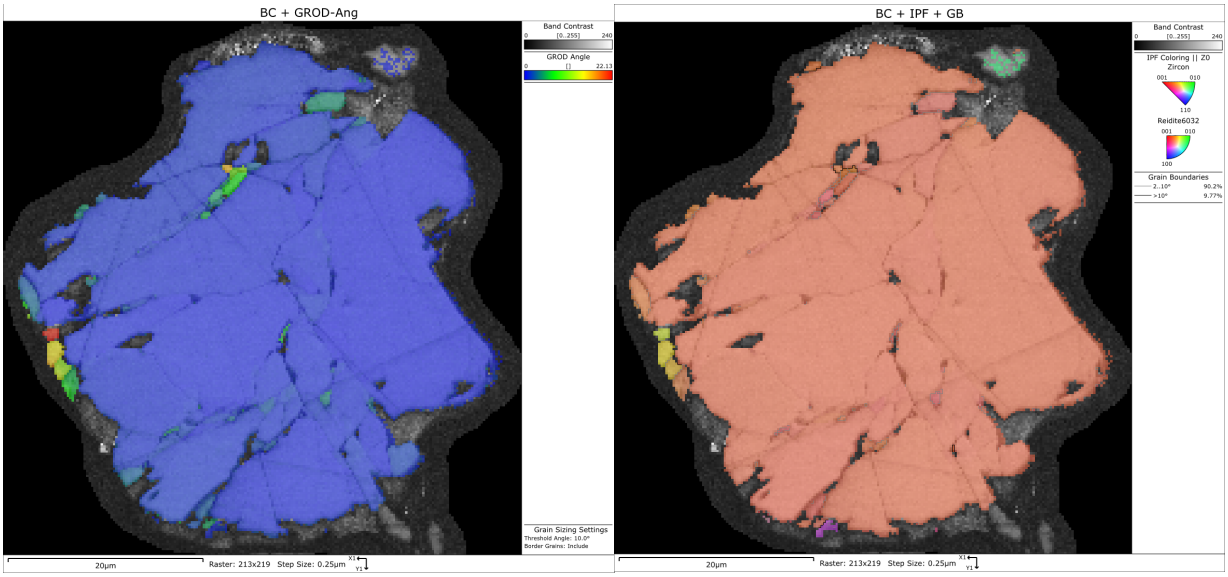
BC + GROD-Ang
Band Contrast
GROD Angle
Grain Sizing Settings
20µm
Raster: 213x219 Step Size: 0.25µm
BC + IPF + GB
Band Contrast
IPF Coloring || Z0
Zircon
Reidite6032
Grain Boundaries
20µm
Raster: 213x219 Step Size: 0.25µm

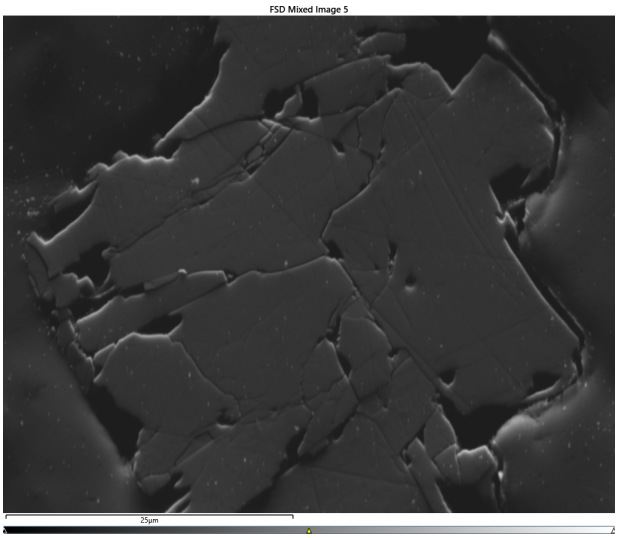
FSD Mixed Image 5
25µm

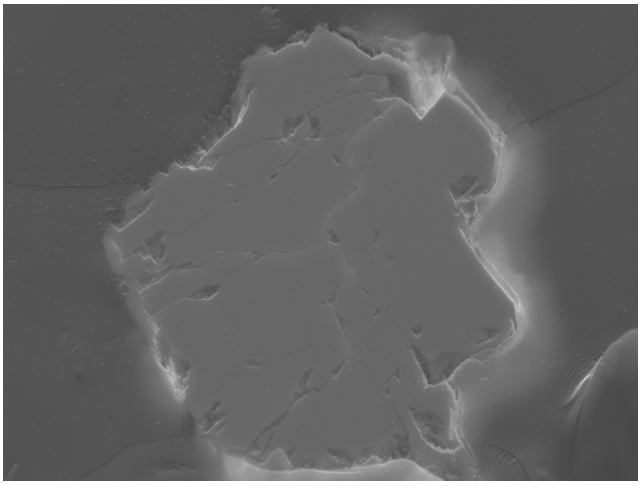

M_M1_6

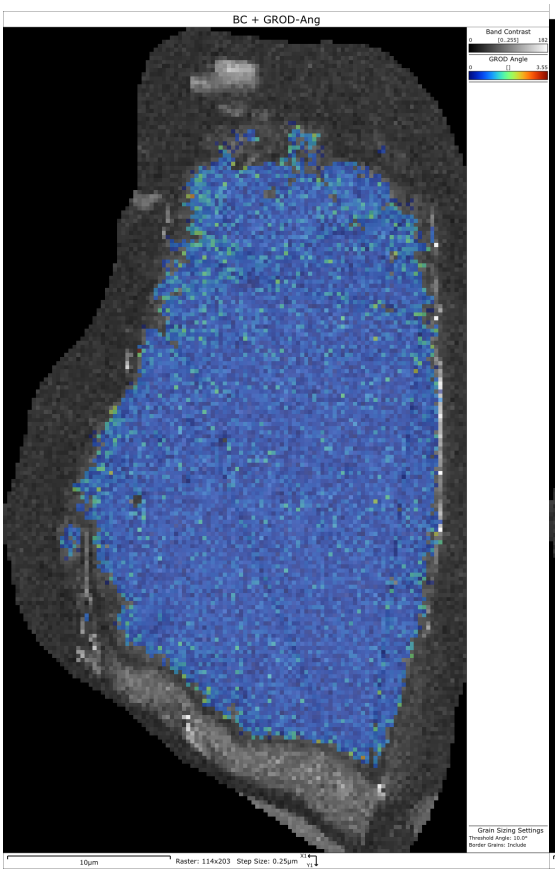
BC + GROD-Ang
Band Contrast
GROD Angle
Grain Sizing Settings
10µm
Raster: 114x203 Step Size: 0.25µm

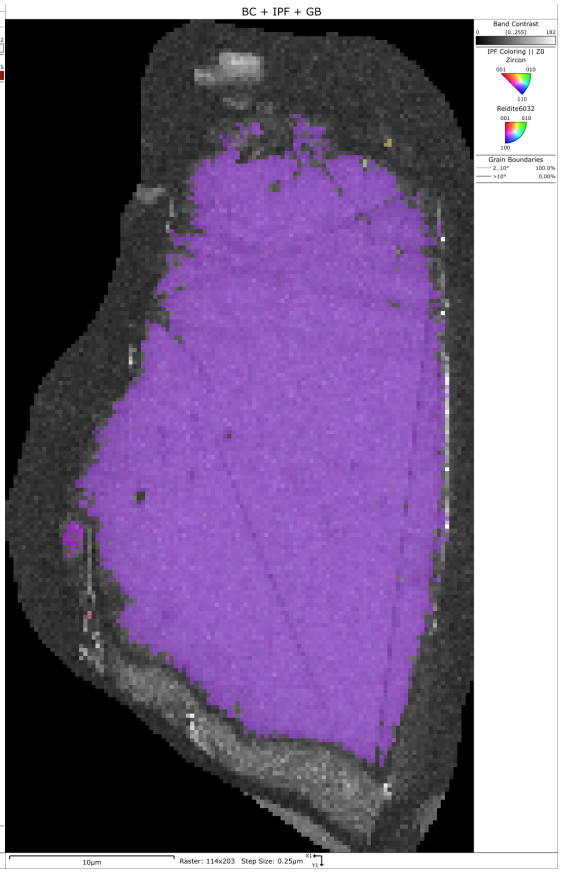
BC + IPF + GB
Band Contrast
IPF Coloring || ZD
Zircon
Reidfit6032
Grain Boundaries
10µm
Raster: 114x203 Step Size: 0.25µm

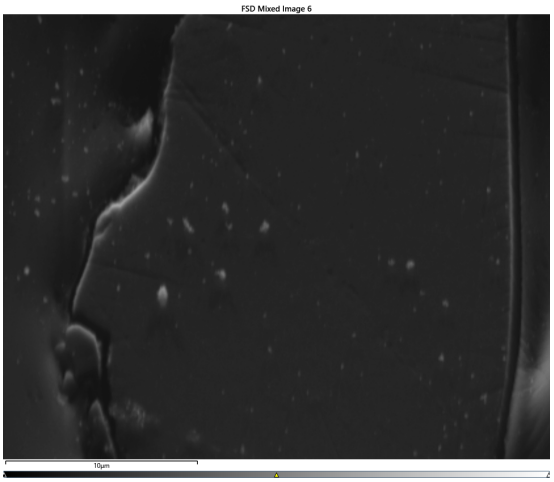
FSD Mixed Image 6
10µm

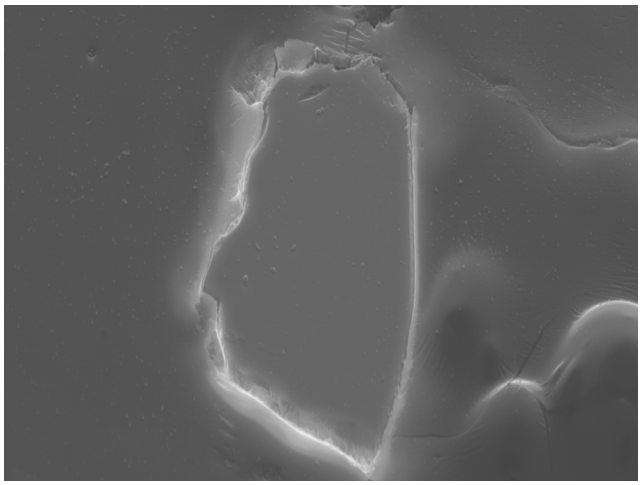

M_M1_7

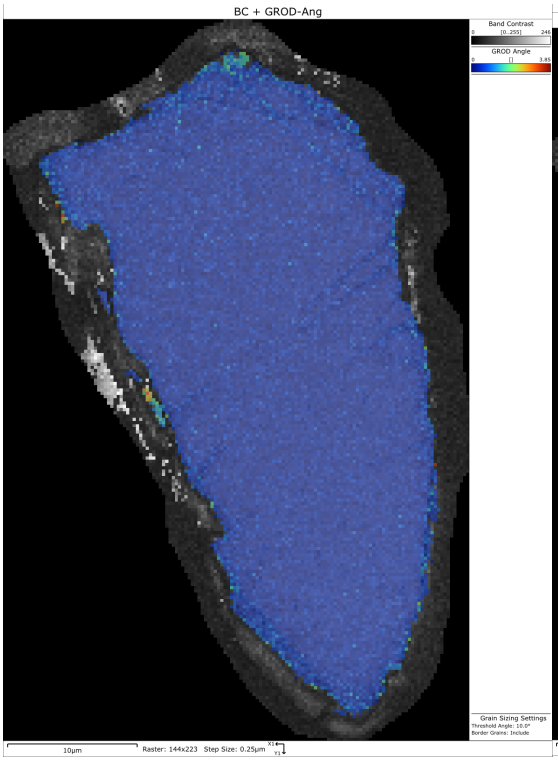
BC + GROD-Ang
Band Contrast
GROD Angle
Grain Sizing Settings
10µm
Raster: 144x223 Step Size: 0.25µm

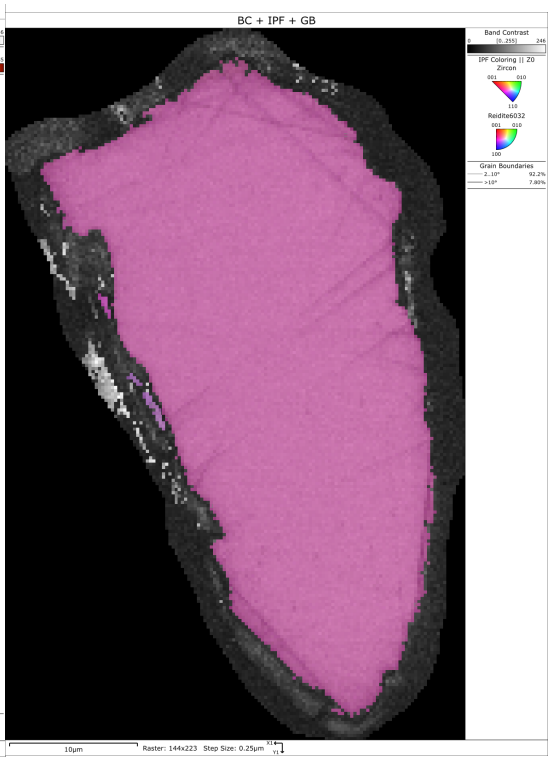
BC + IPF + GB
Band Contrast
IPF Coloring || Z0
Zircon
Reidite6032
Grain Boundaries
10µm
Raster: 144x223 Step Size: 0.25µm

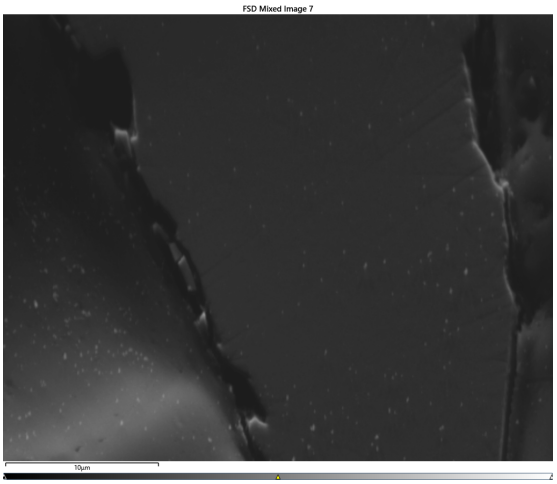
FSD Mixed Image 7
10µm

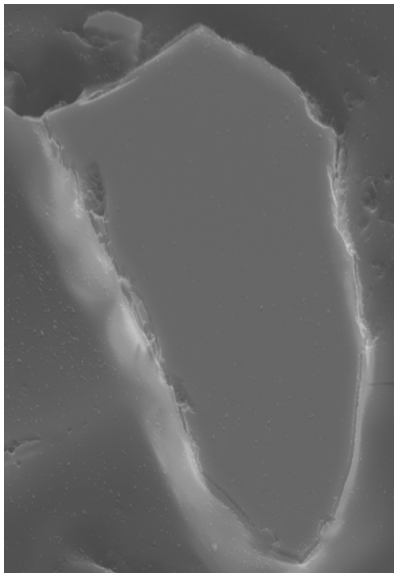

M_M1_8

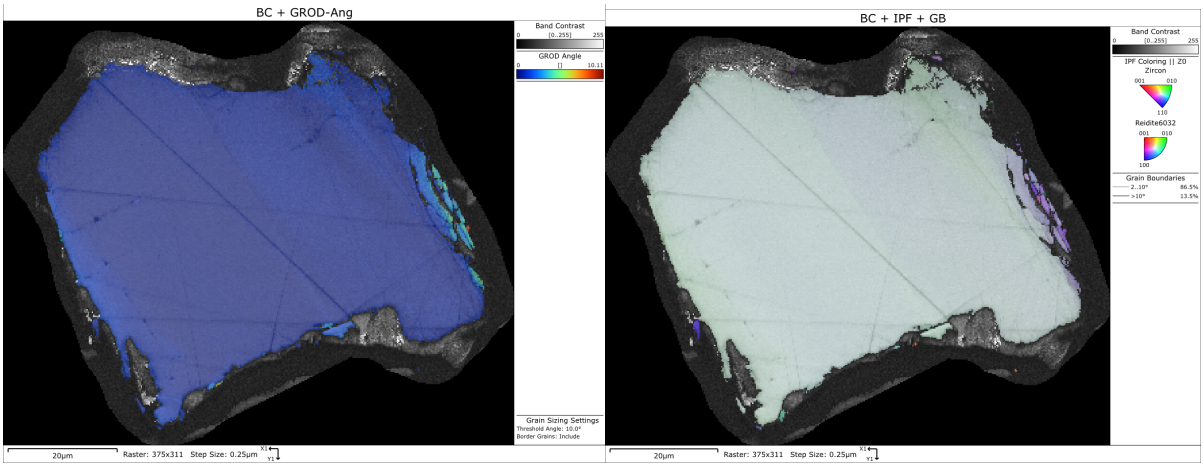
BC + GROD-Ang
Band Contrast
GROD Angle
Grain Sizing Settings
20µm
Raster: 375x311 Step Size: 0.25µm
BC + IPF + GB
Band Contrast
IPF Coloring || Z0
Zircon
Reidite6032
Grain Boundaries
20µm
Raster: 375x311 Step Size: 0.25µm

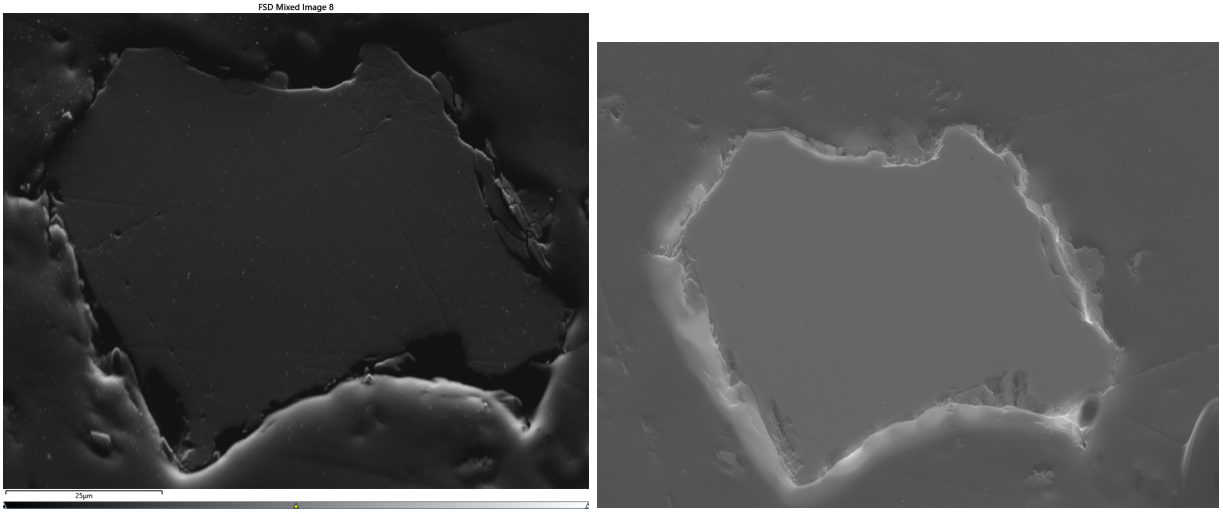
FSD Mixed Image 8
25µm

M_M1_9

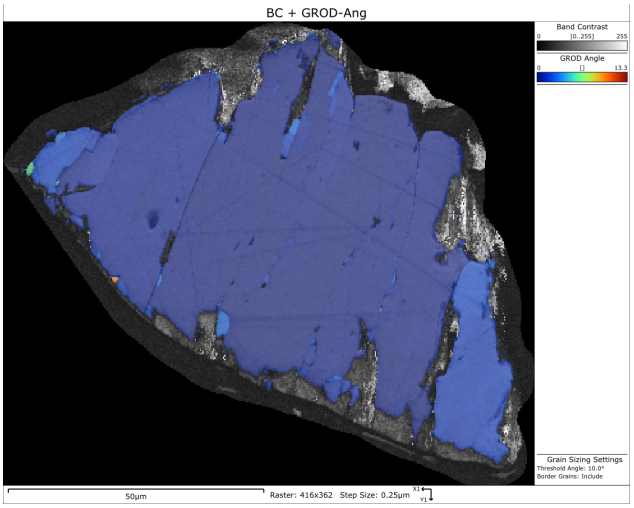
BC + GROD-Ang
Band Contrast
0 [0..255] 255
GROD Angle
0 [] 13.3
Grain Sizing Settings
Threshold Angle: 10.0°
Border Grains: Include
50µm
Raster: 416x362 Step Size: 0.25µm

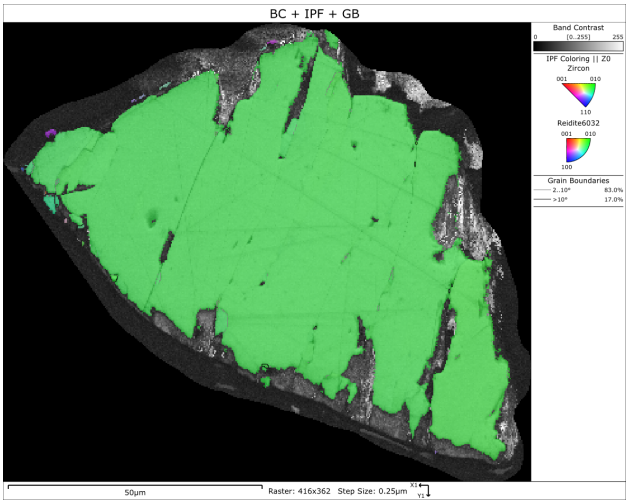
BC + IPF + GB
Band Contrast
0 [0..255] 255
IPF Coloring || Z0
Zircon
001 010
110
Reidite60J32
001 010
100
Grain Boundaries
2..10° 83.0%
>10° 17.0%
50µm
Raster: 416x362 Step Size: 0.25µm

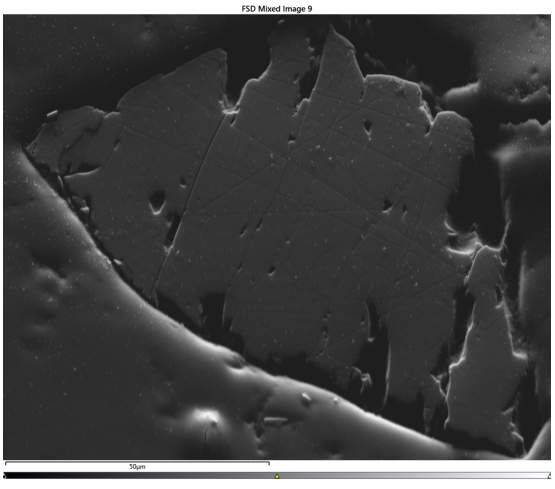
FSD Mixed Image 9
50µm

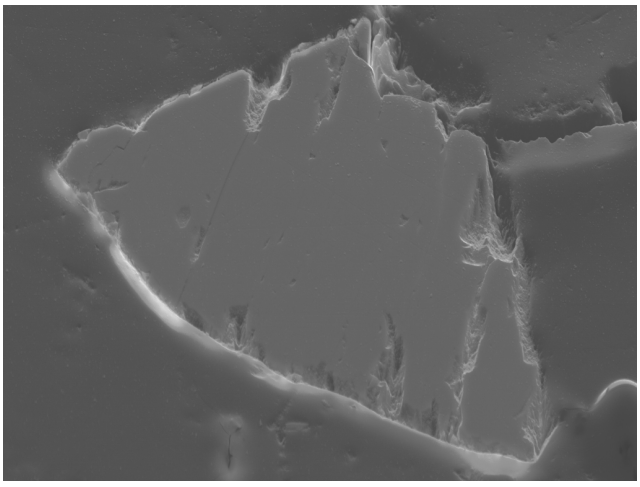

M_M1_10

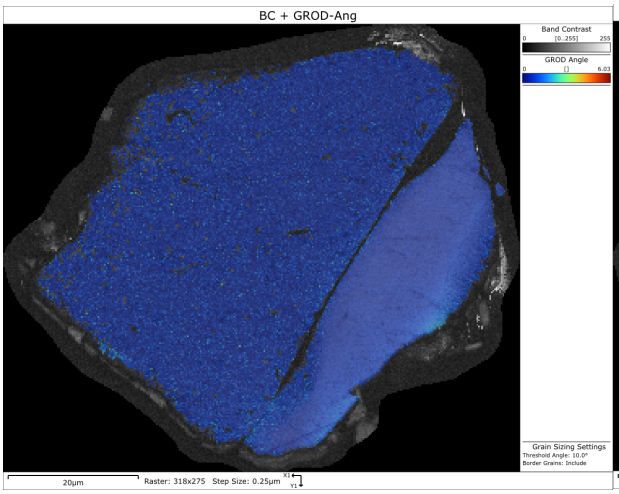
BC + GROD-Ang
Band Contrast
[0..255]
GROD Angle
Grain Sizing Settings
20µm
Raster: 318x275 Step Size: 0.25µm

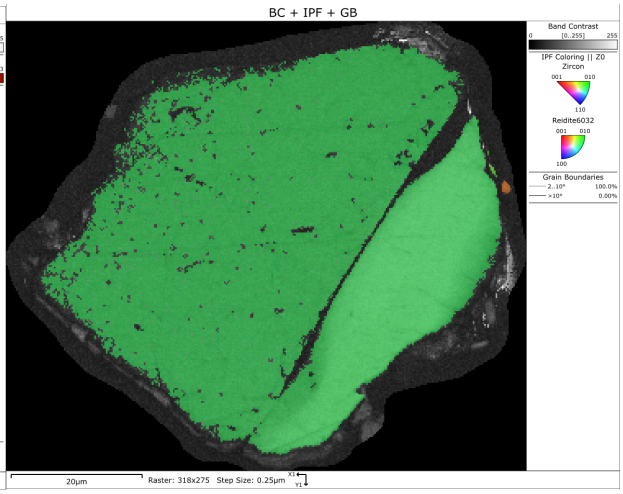
BC + IPF + GB
Band Contrast
IPF Coloring || Z0
Zircon
Reidite6032
Grain Boundaries
20µm
Raster: 318x275 Step Size: 0.25µm

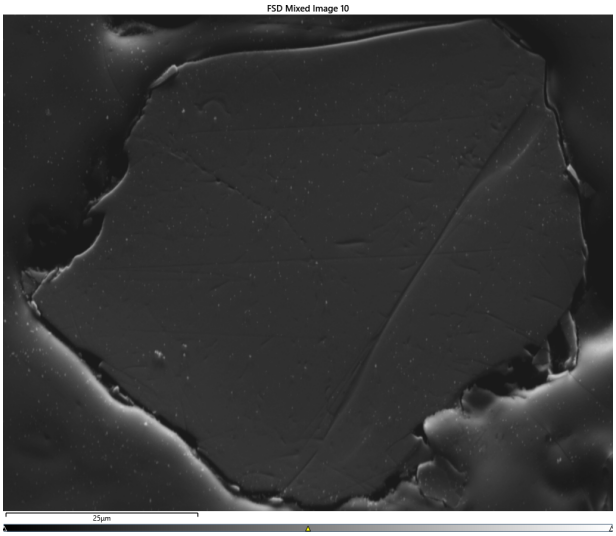
FSD Mixed Image 10
25µm

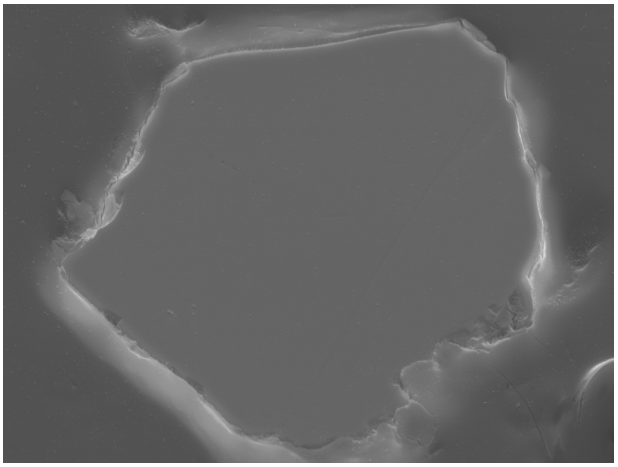

M_M1_11

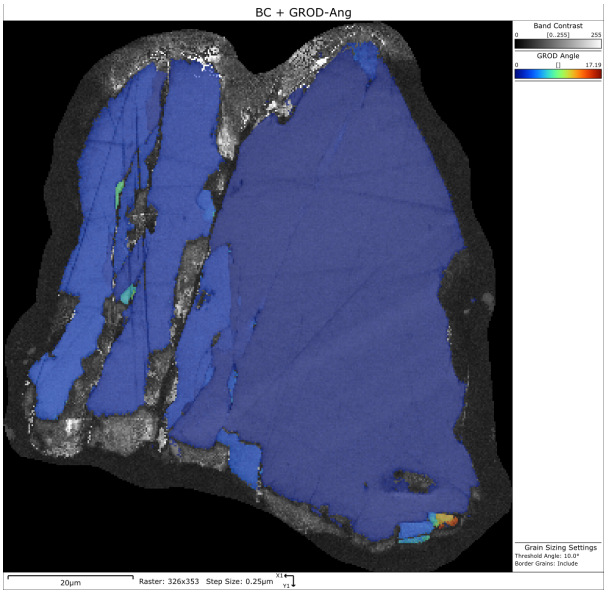
BC + GROD-Ang
Band Contrast
GROD Angle
Grain Sizing Settings
20µm
Raster: 326x353 Step Size: 0.25µm

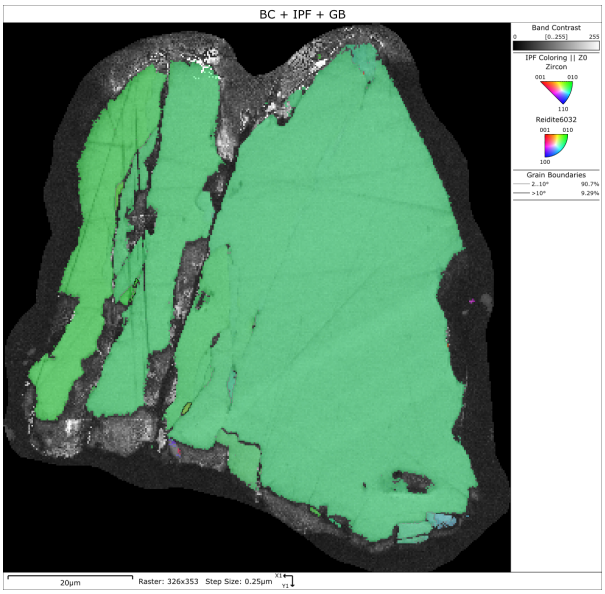
BC + IPF + GB
Band Contrast
IPF Coloring || Z0
Zircon
Reidite6032
Grain Boundaries
20µm
Raster: 326x353 Step Size: 0.25µm

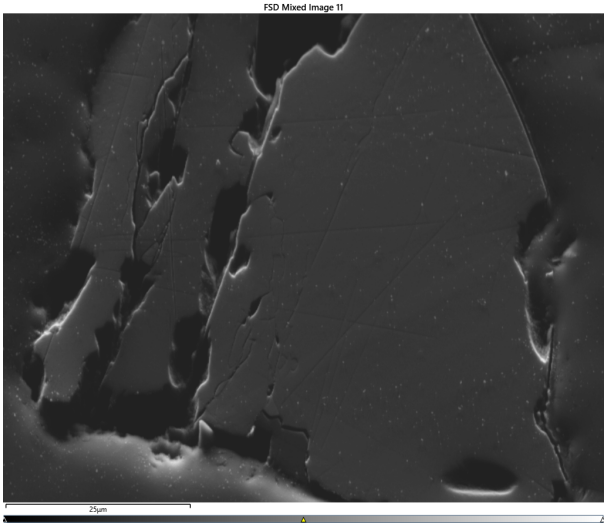
FSD Mixed Image 11
25µm

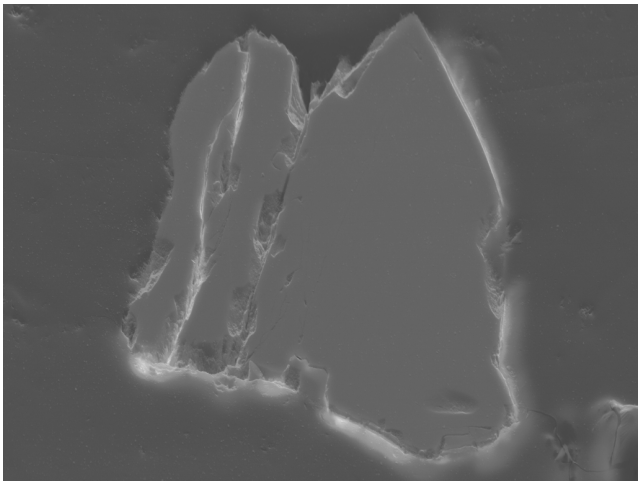

M_M1_12

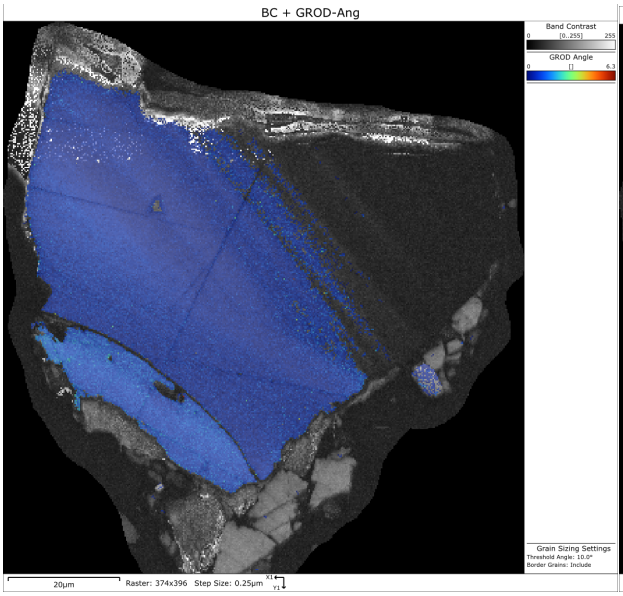
BC + GROD-Ang
Band Contrast
[0..255]
GROD Angle
Grain Sizing Settings
20µm
Raster: 374x396 Step Size: 0.25µm

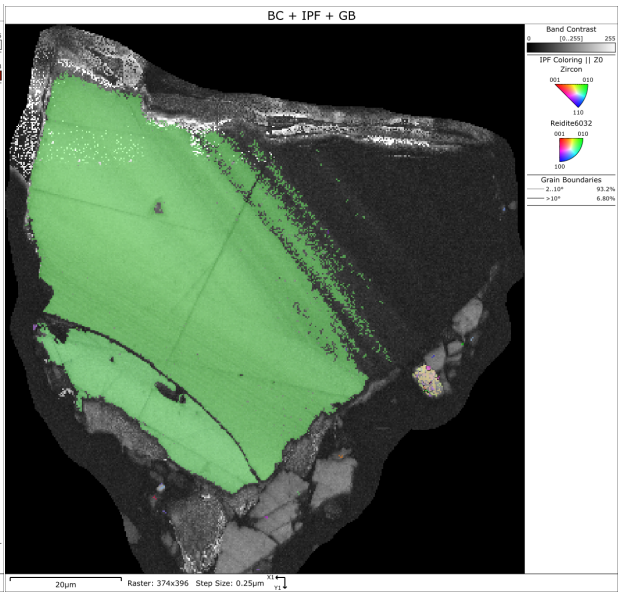
BC + IPF + GB
Band Contrast
[0..255]
IPF Coloring || Z0
Zircon
Reidite6032
Grain Boundaries
20µm
Raster: 374x396 Step Size: 0.25µm

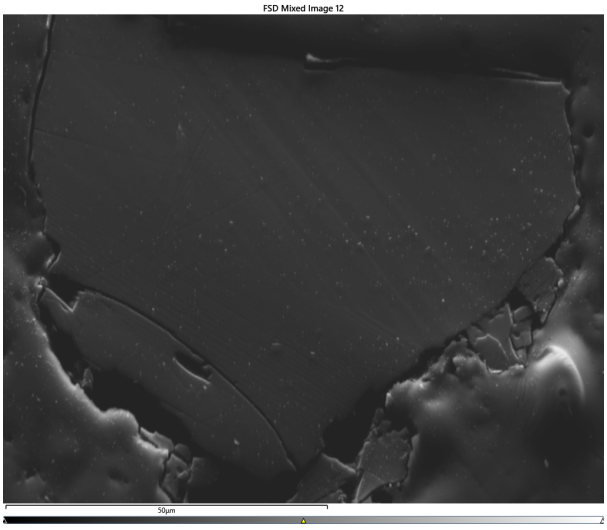
FSD Mixed Image 12
50µm

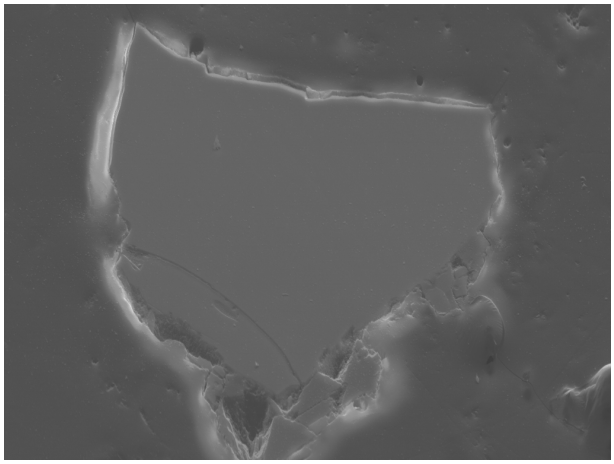

M_M1_13

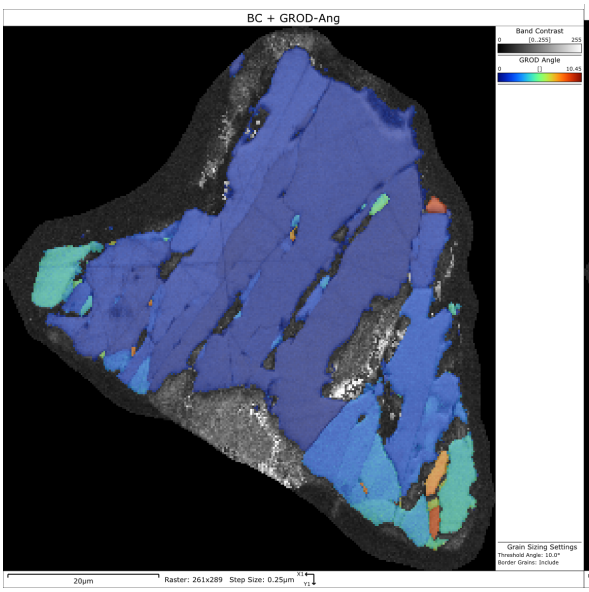
BC + GROD-Ang
Band Contrast
[0..255]
GROD Angle
Grain Sizing Settings
20µm
Raster: 261x289 Step Size: 0.25µm

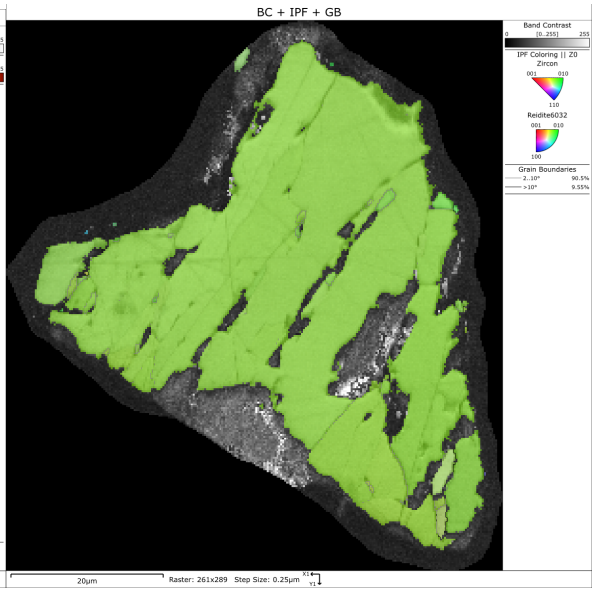
BC + IPF + GB
Band Contrast
[0..255]
IPF Coloring || Z0
Zircon
Reidite6032
Grain Boundaries
20µm
Raster: 261x289 Step Size: 0.25µm

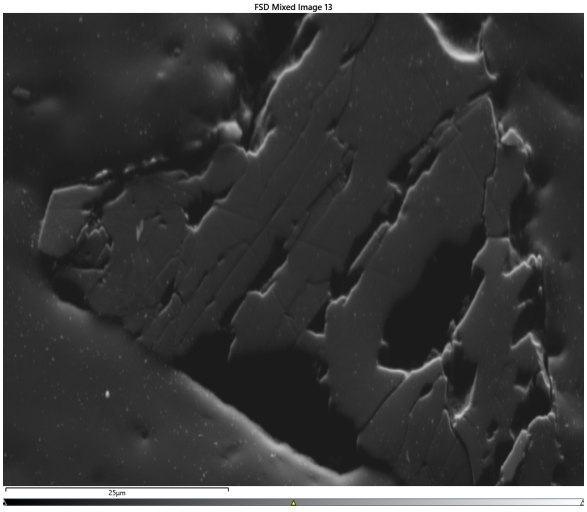
FSD Mixed Image 13
25µm

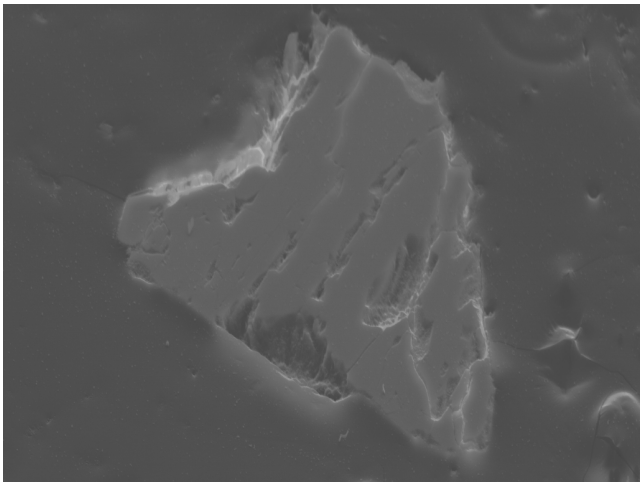

M_M1_14

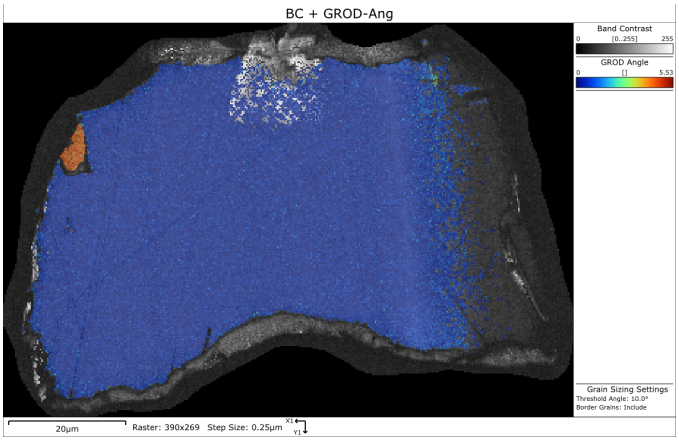
BC + GROD-Ang
Band Contrast
0 [0..255] 255
GROD Angle
0 [] 5.53
Grain Sizing Settings
Threshold Angle: 10.0°
Border Grains: Include
20µm
Raster: 390x269 Step Size: 0.25µm

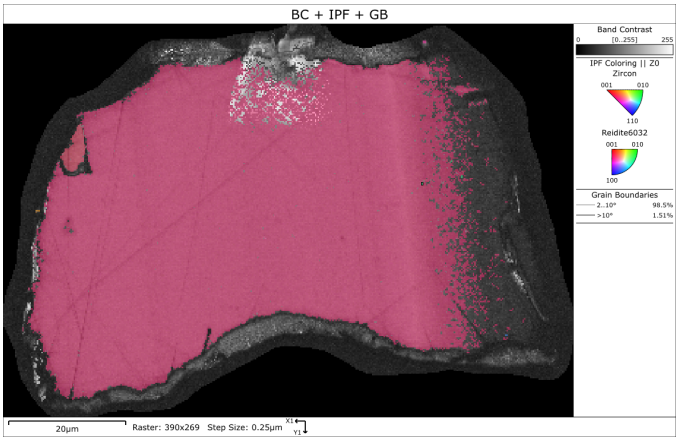
BC + IPF + GB
Band Contrast
0 [0..255] 255
IPF Coloring || Z0
Zircon
001 010
110
Reidite6032
001 010
100
Grain Boundaries
2..10° 98.5%
>10° 1.51%
20µm
Raster: 390x269 Step Size: 0.25µm

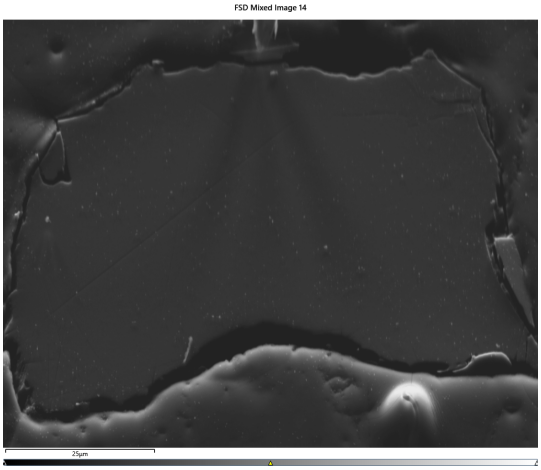
FSD Mixed Image 14
25µm

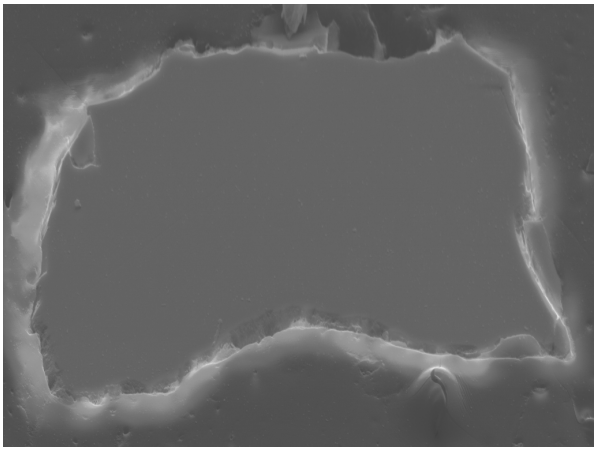

M_M1_15

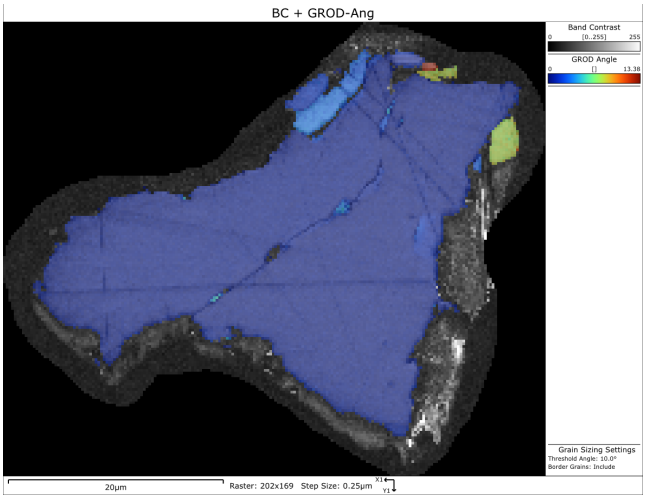
BC + GROD-Ang
Band Contrast
0 [0..255] 255
GROD Angle
0 [] 13.38
Grain Sizing Settings
Threshold Angle: 10.0°
Border Grains: Include
20µm
Raster: 202x169 Step Size: 0.25µm
X1
Y1

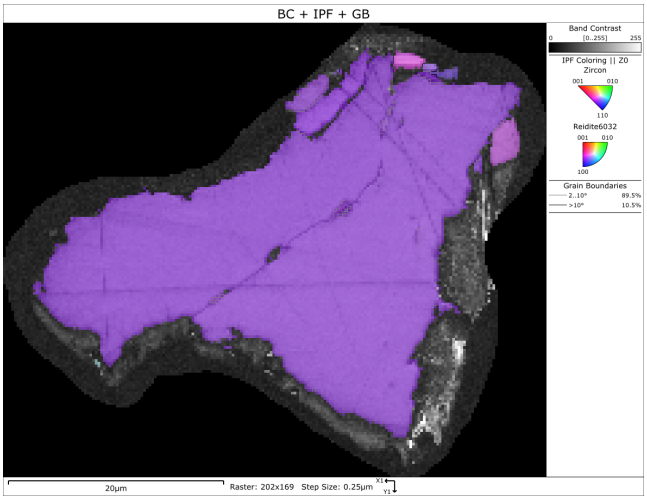
BC + IPF + GB
Band Contrast
0 [0..255] 255
IPF Coloring || Z0
Zircon
001 010
110
Reidite6032
001 010
100
Grain Boundaries
2..10° 89.5%
>10° 10.5%
20µm
Raster: 202x169 Step Size: 0.25µm
X1
Y1

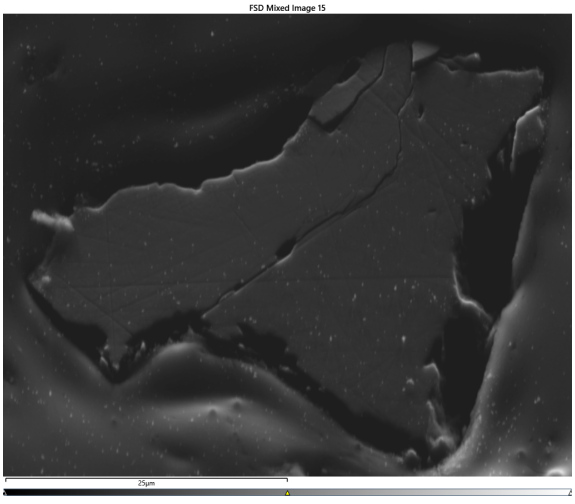
FSD Mixed Image 15
25µm

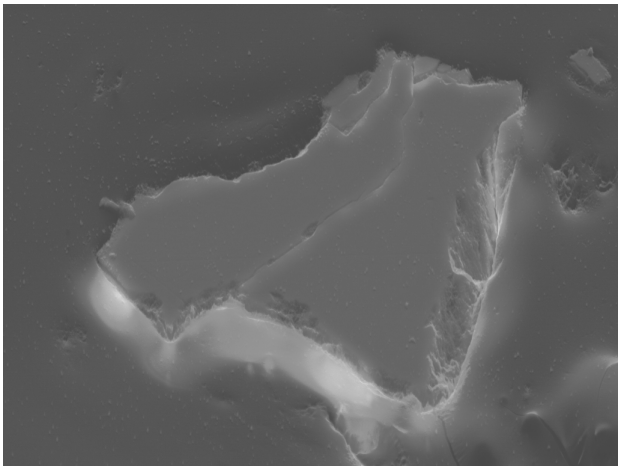

M_M1_16

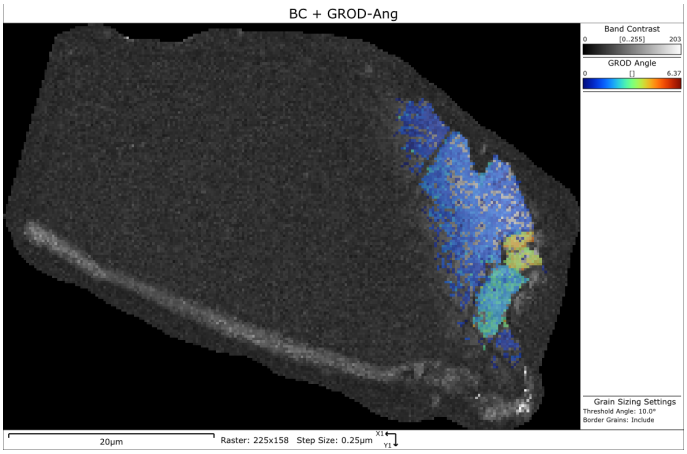
BC + GROD-Ang
Band Contrast
0 [0..255] 203
GROD Angle
0 [] 6.37
Grain Sizing Settings
Threshold Angle: 10.0°
Border Grains: Include
20µm
Raster: 225x158 Step Size: 0.25µm
X1
Y1

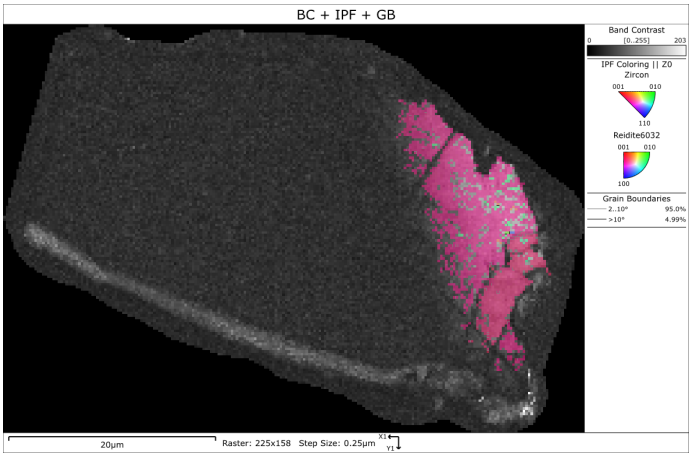
BC + IPF + GB
Band Contrast
0 [0..255] 203
IPF Coloring || Z0
Zircon
001 010
110
Reidite6032
001 010
100
Grain Boundaries
2..10° 95.0%
>10° 4.99%
20µm
Raster: 225x158 Step Size: 0.25µm
X1
Y1

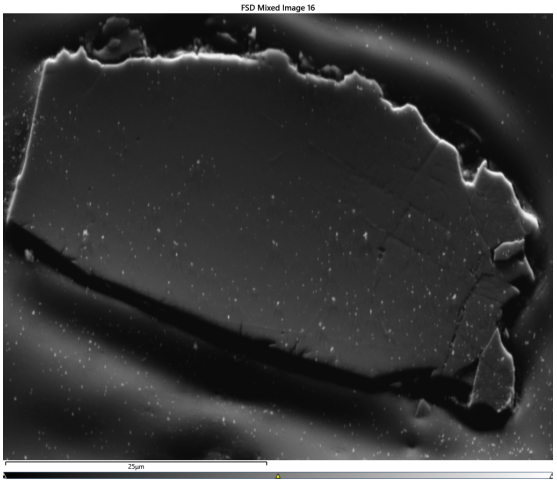
FSD Mixed Image 16
25µm

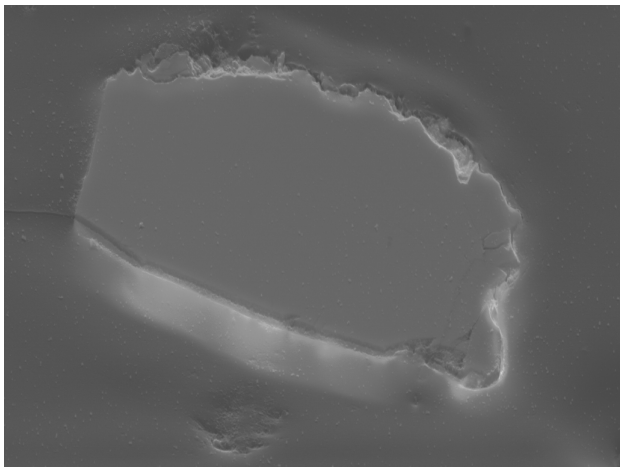

M_M1_17

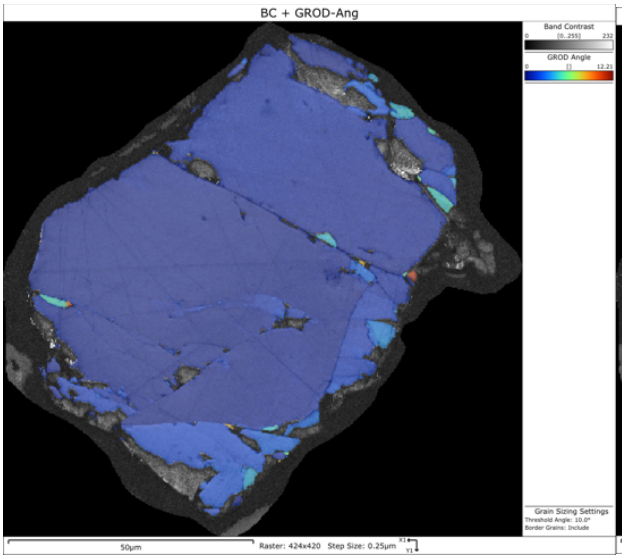
BC + GROD-Ang
Band Contrast
GROD Angle
Grain Sizing Settings
50µm
Raster: 424x420 Step Size: 0.25µm

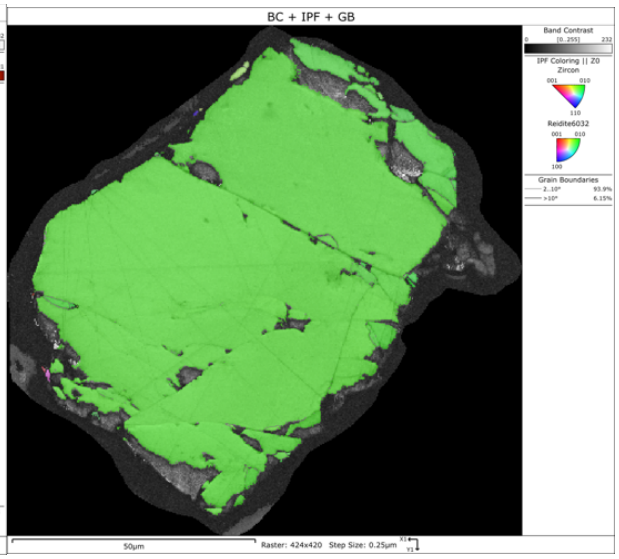
BC + IPF + GB
Band Contrast
IPF Coloring || Z0
Zircon
Reidite6032
Grain Boundaries
50µm
Raster: 424x420 Step Size: 0.25µm

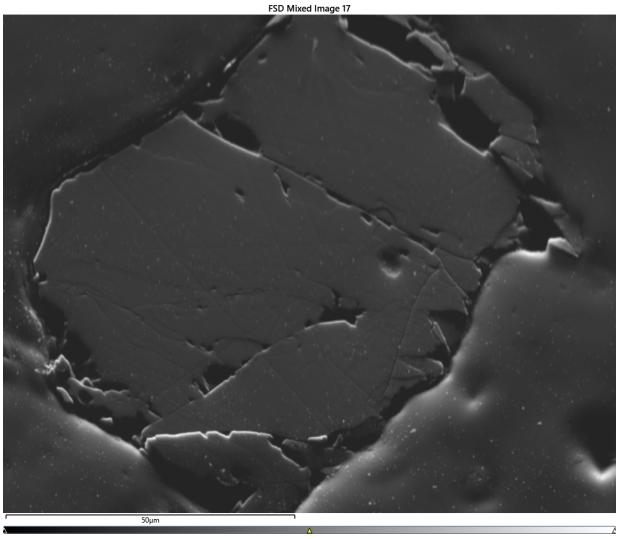
FSD Mixed Image 17
50µm

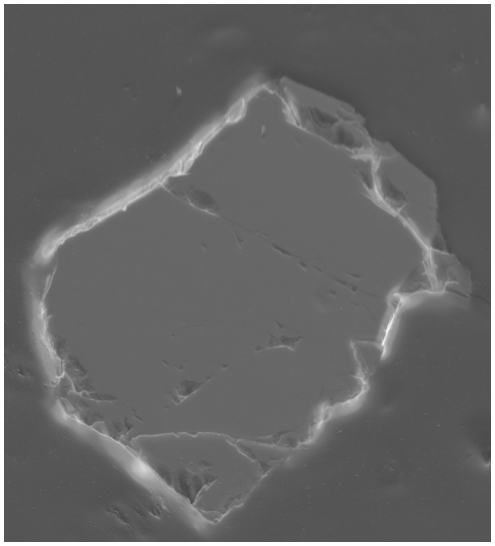

M_M1_18

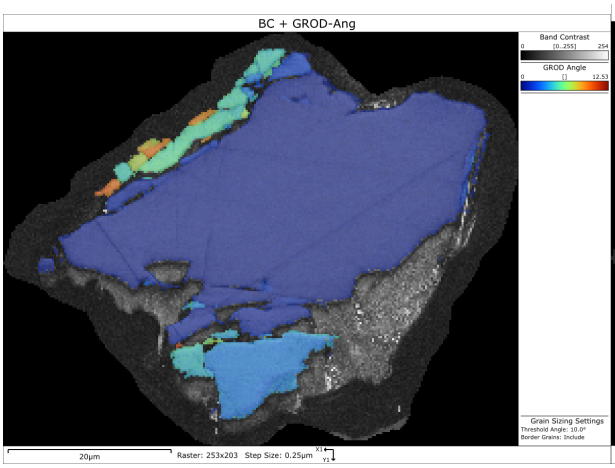
BC + GROD-Ang
Band Contrast
GROD Angle
Grain Sizing Settings
20µm
Raster: 253x203 Step Size: 0.25µm

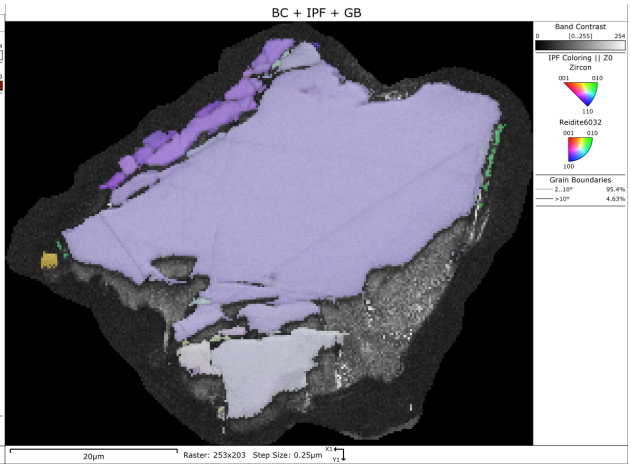
BC + IPF + GB
Band Contrast
IPF Coloring || Z0
Zircon
Reidite6032
Grain Boundaries
20µm
Raster: 253x203 Step Size: 0.25µm

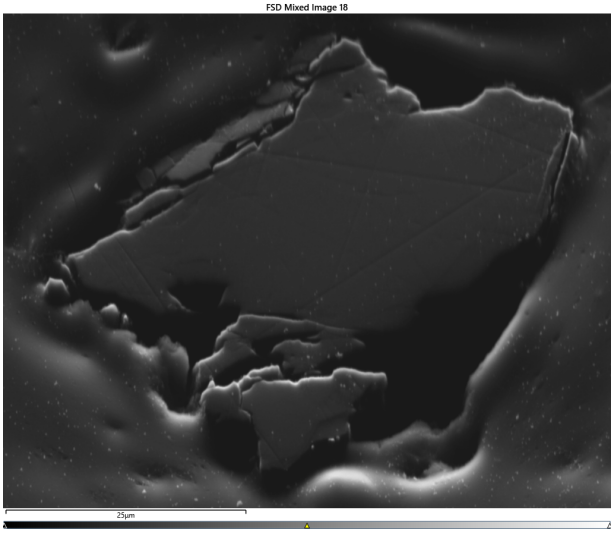
FSD Mixed Image 18
25µm

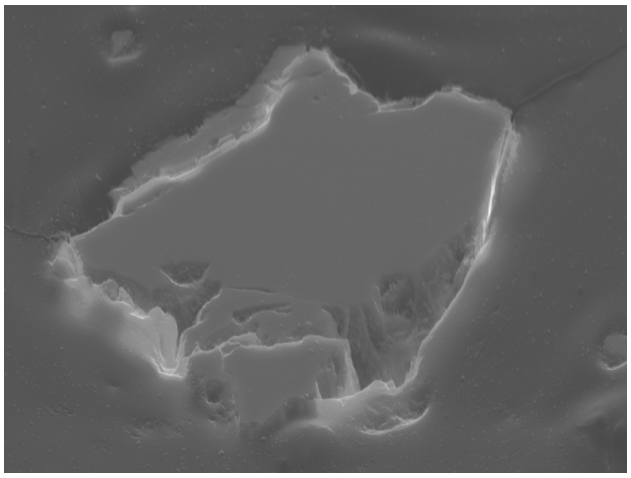

M_M1_19

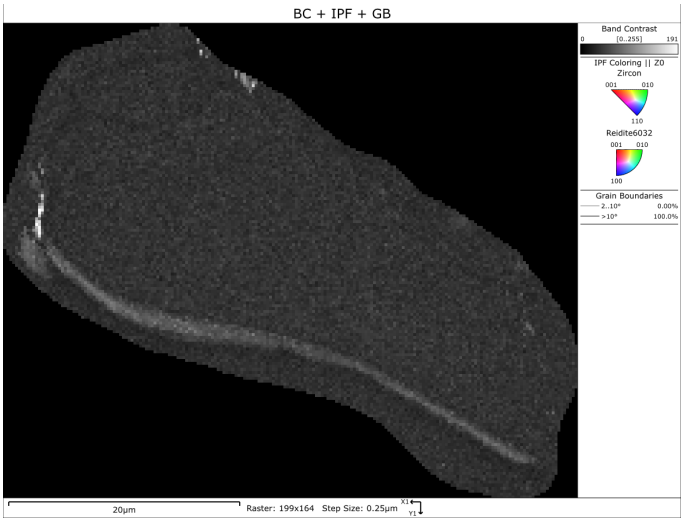
BC + IPF + GB
Band Contrast
0 [0..255] 191
IPF Coloring || Z0
Zircon
001 010
110
Reidite6032
001 010
100
Grain Boundaries
2..10° 0.00%
>10° 100.0%
20µm
Raster: 199x164 Step Size: 0.25µm
X1
Y1

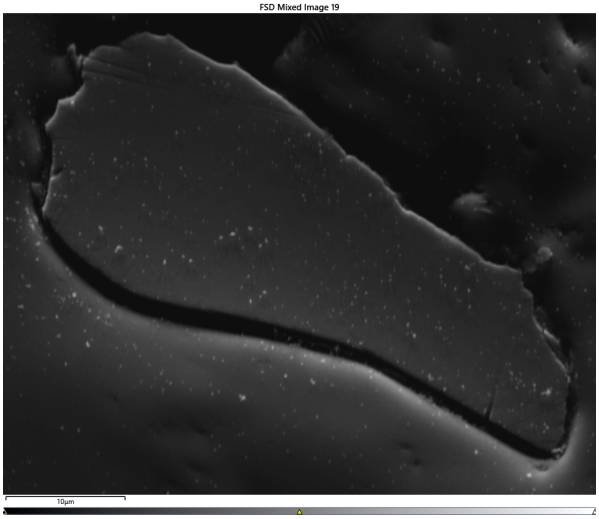
FSD Mixed Image 19
10µm

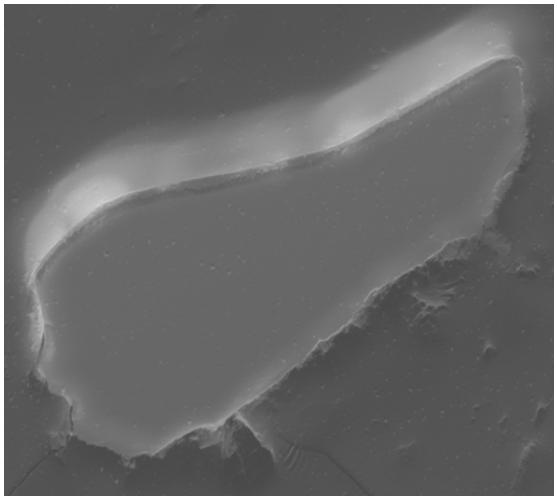

M_M1_20

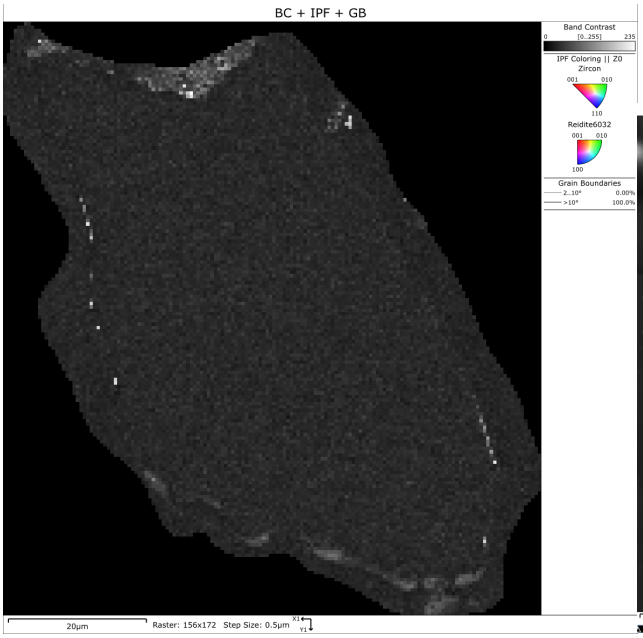
BC + IPF + GB
Band Contrast
[0..255]
IPF Coloring || Z0
Zircon
Reidite6032
Grain Boundaries
2..10°
>10°
0.00%
100.0%
20µm
Raster: 156x172 Step Size: 0.5µm

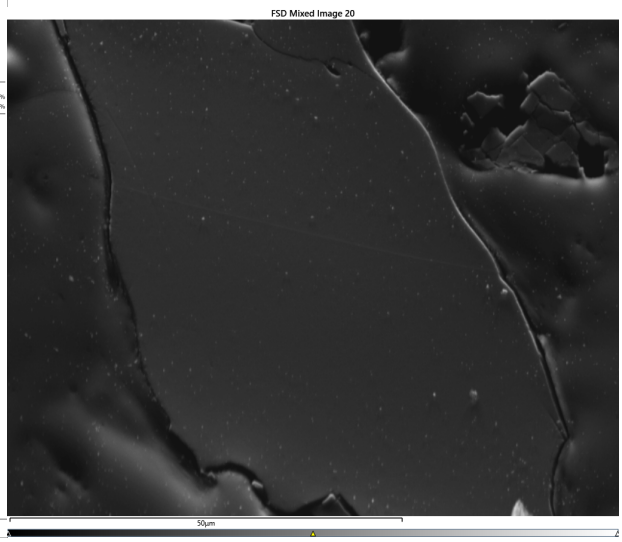
FSD Mixed Image 20
50µm

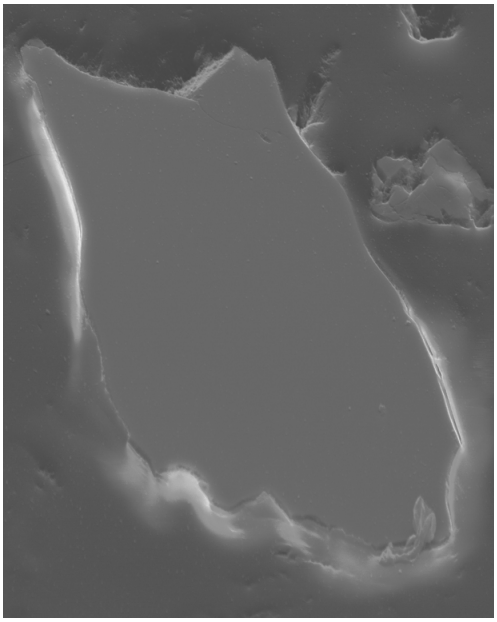

M_M1_21

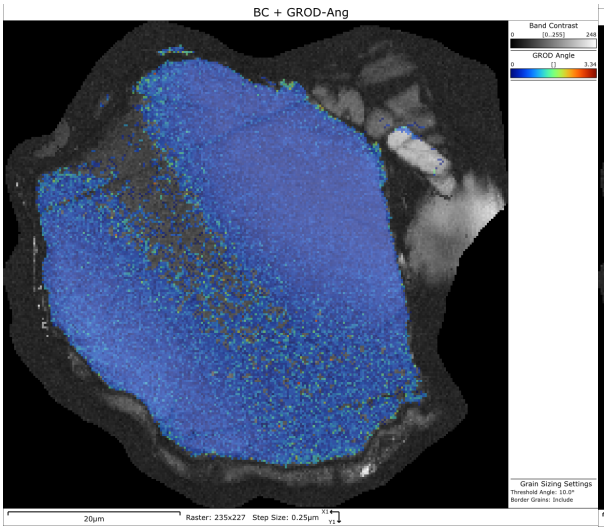
BC + GROD-Ang
Band Contrast
GROD Angle
Grain Sizing Settings
20µm
Raster: 235x227 Step Size: 0.25µm

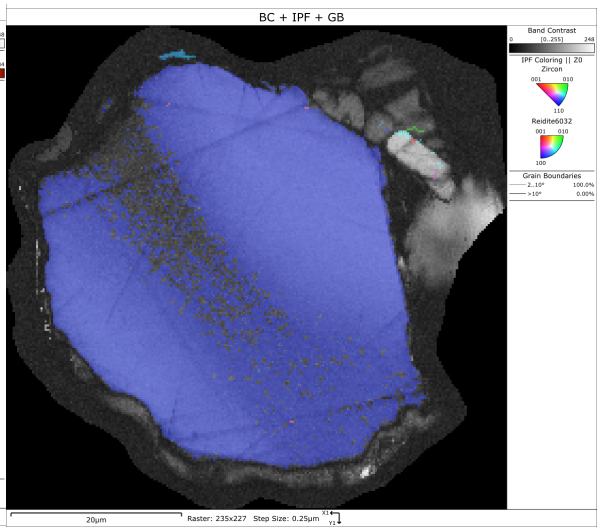
BC + IPF + GB
Band Contrast
IPF Coloring || Z0
Zircon
Reidite6032
Grain Boundaries
20µm
Raster: 235x227 Step Size: 0.25µm

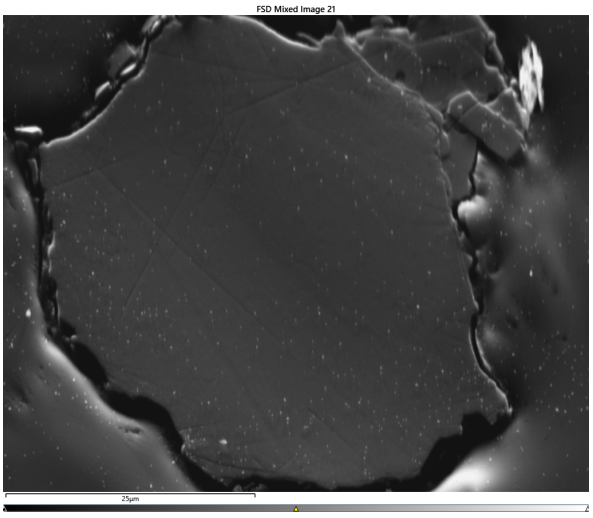
FSD Mixed Image 21
25µm

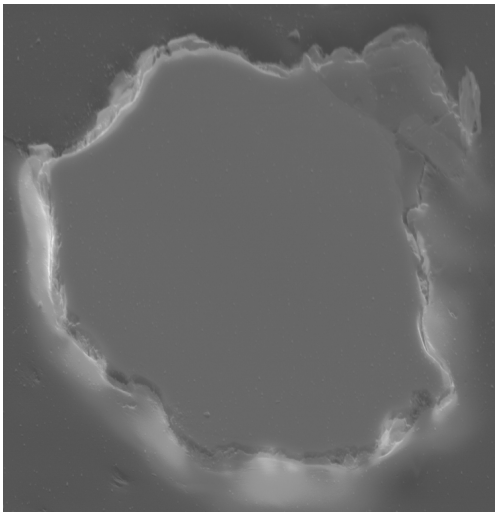

M_M1_23

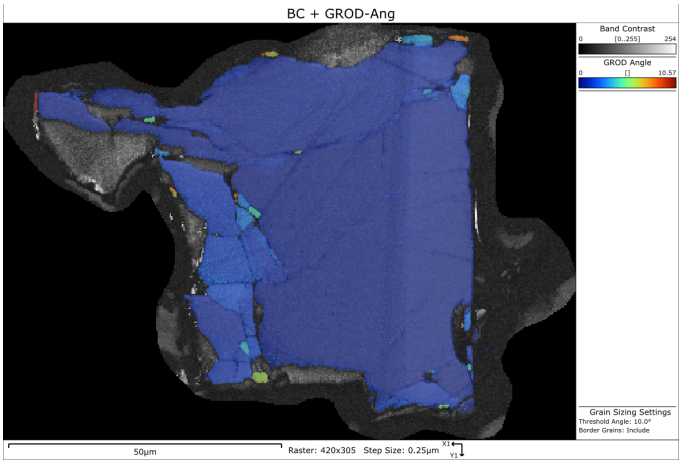
BC + GROD-Ang
Band Contrast
0 [0..255] 254
GROD Angle
0 [] 10.57
Grain Sizing Settings
Threshold Angle: 10.0°
Border Grains: Include
50µm
Raster: 420x305 Step Size: 0.25µm

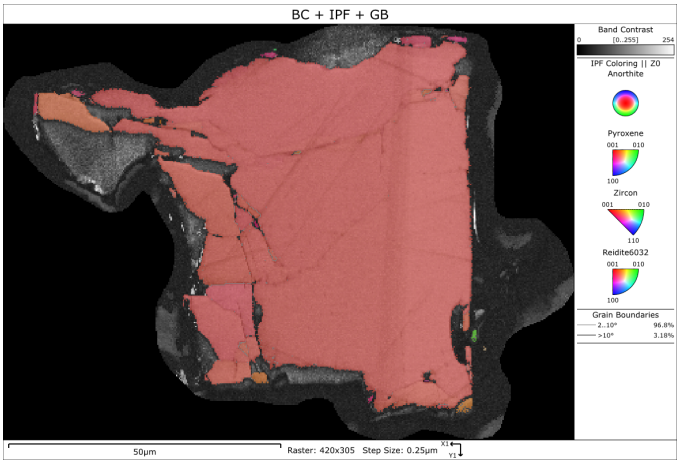
BC + IPF + GB
Band Contrast
0 [0..255] 254
IPF Coloring || Z0
Anorthite
Pyroxene
001 010
100
Zircon
001 010
110
Reidite6032
001 010
100
Grain Boundaries
2..10° 96.8%
>10° 3.18%
50µm
Raster: 420x305 Step Size: 0.25µm

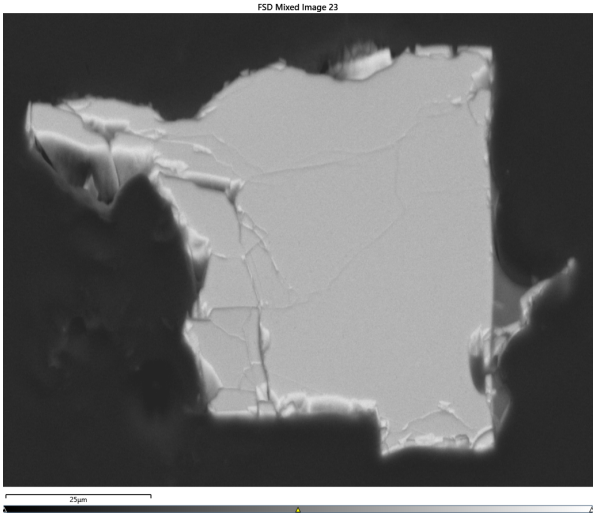
FSD Mixed Image 23
25µm

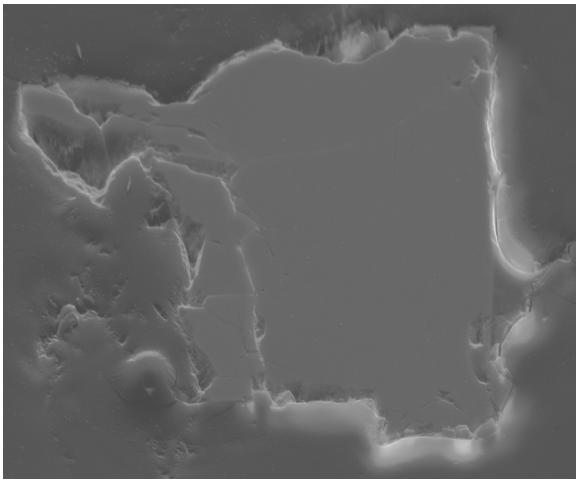

M_M1_24

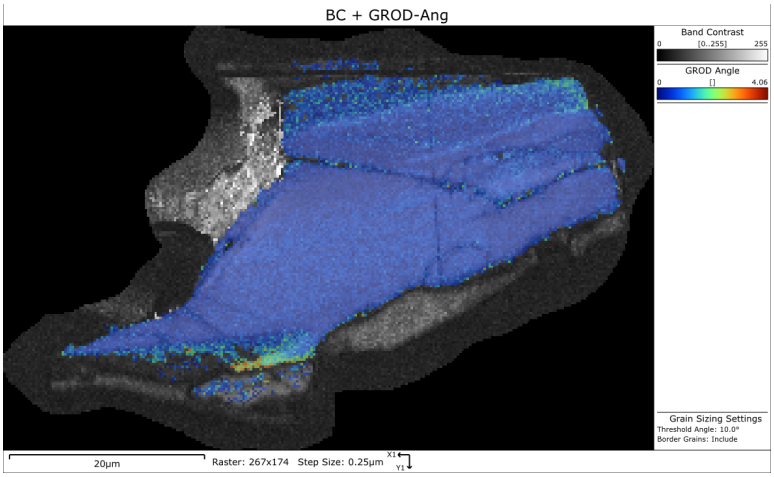
BC + GROD-Ang
Band Contrast
0 [0..255] 255
GROD Angle
0 [] 4.06
Grain Sizing Settings
Threshold Angle: 10.0°
Border Grains: Include
20µm
Raster: 267x174 Step Size: 0.25µm

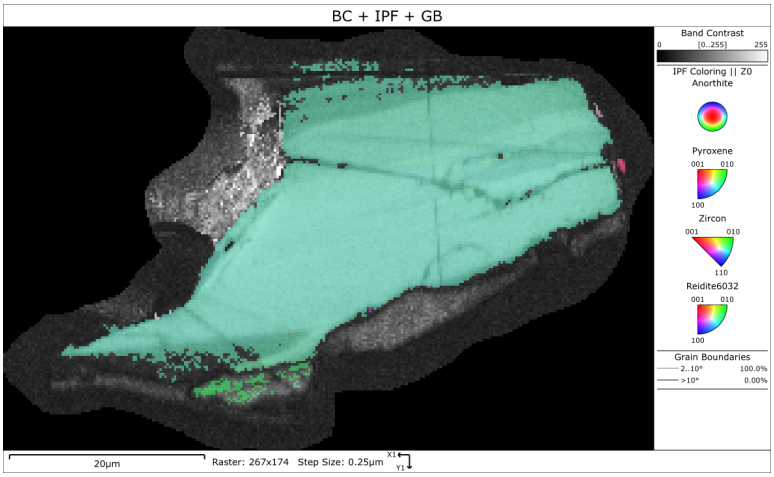
BC + IPF + GB
Band Contrast
0 [0..255] 255
IPF Coloring || Z0
Anorthite
Pyroxene
001 010
100
Zircon
001 010
110
Reidite6032
001 010
100
Grain Boundaries
2..10° 100.0%
>10° 0.00%
20µm
Raster: 267x174 Step Size: 0.25µm

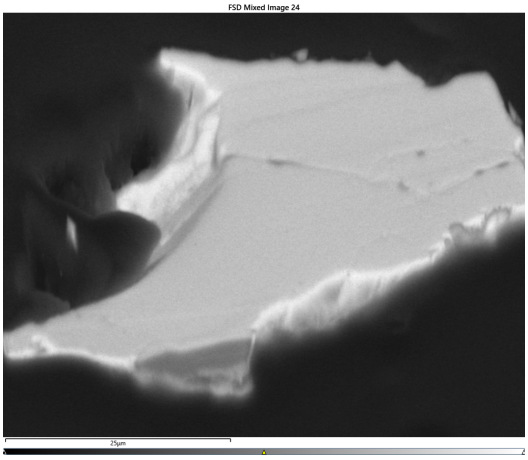
FSD Mixed Image 24

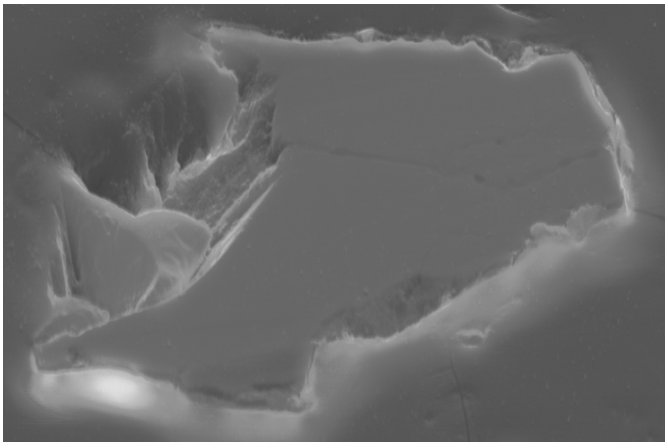

M_M1_26

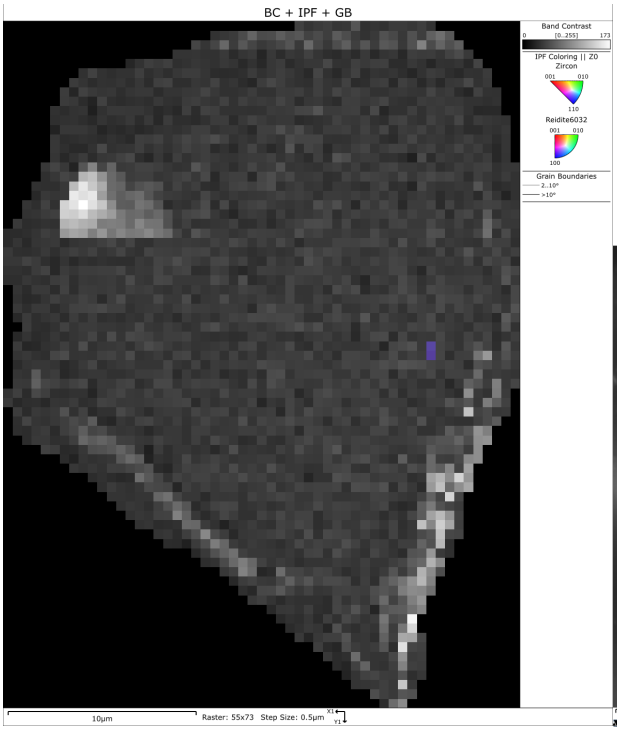
BC + IPF + GB
Band Contrast
0 [0..255] 173
IPF Coloring || ZO
Zircon
001 010
110
Reidite6032
001 010
100
Grain Boundaries
2..10°
>10°
10µm
Raster: 55x73 Step Size: 0.5µm
X1
Y1

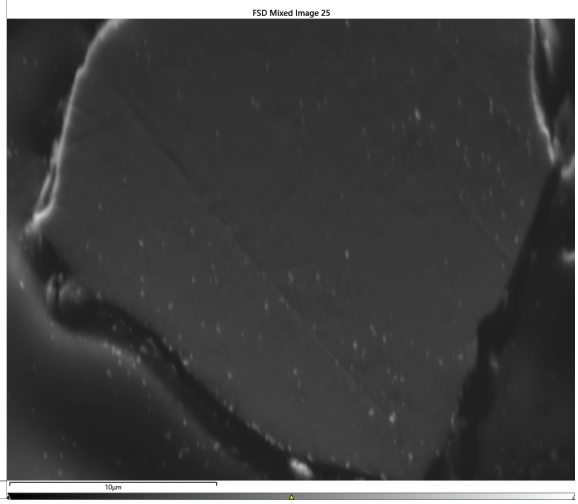
FSD Mixed Image 25
10µm

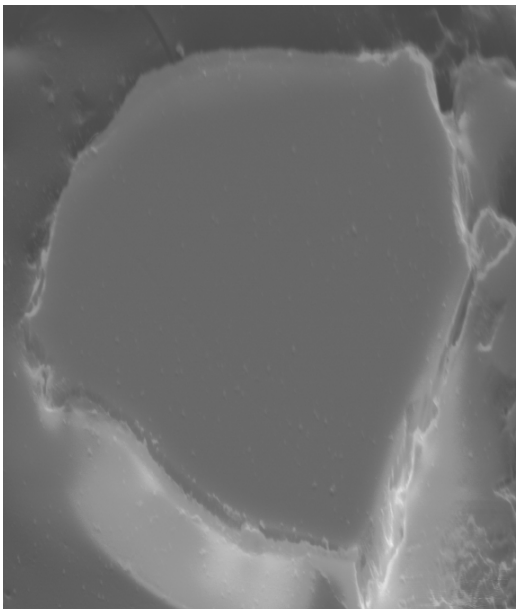

M_M1_27

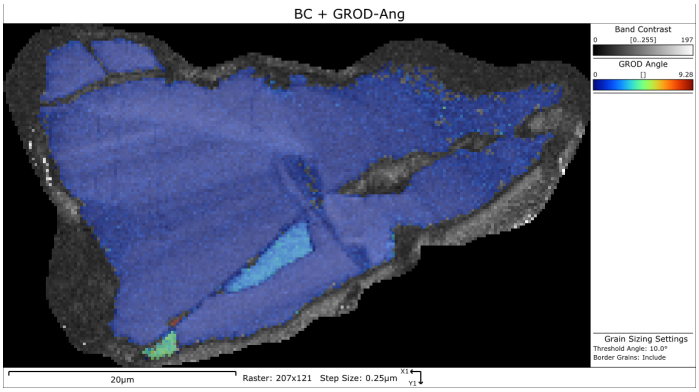
BC + GROD-Ang
Band Contrast
0 [0..255] 197
GROD Angle
0 [] 9.28
Grain Sizing Settings
Threshold Angle: 10.0°
Border Grains: Include
20µm
Raster: 207x121 Step Size: 0.25µm
X1
Y1

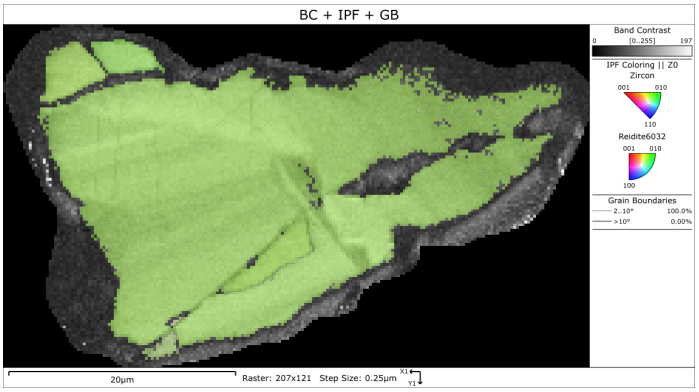
BC + IPF + GB
Band Contrast
0 [0..255] 197
IPF Coloring || Z0
Zircon
001 010
110
Reidite6032
001 010
100
Grain Boundaries
2..10° 100.0%
>10° 0.00%
20µm
Raster: 207x121 Step Size: 0.25µm
X1
Y1

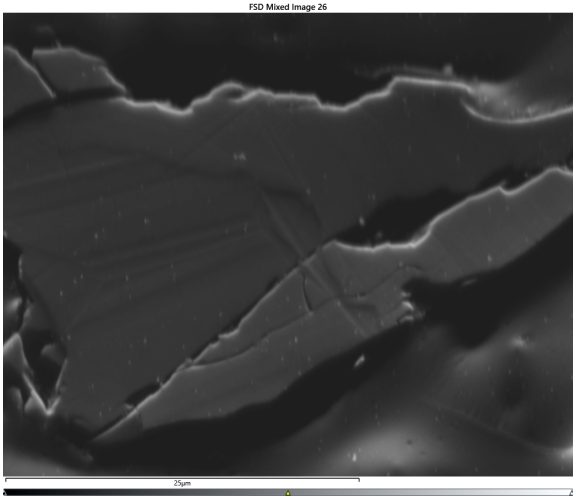
FSD Mixed Image 26
25µm

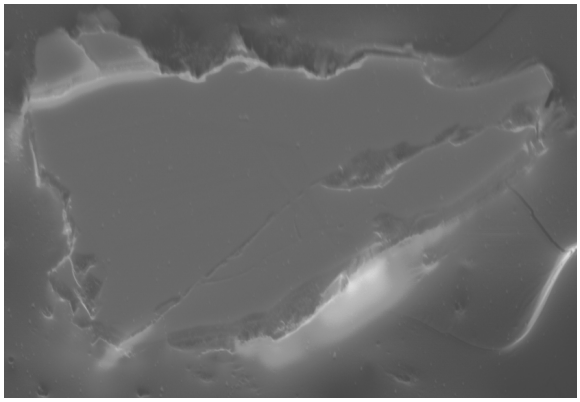

M_M1_28

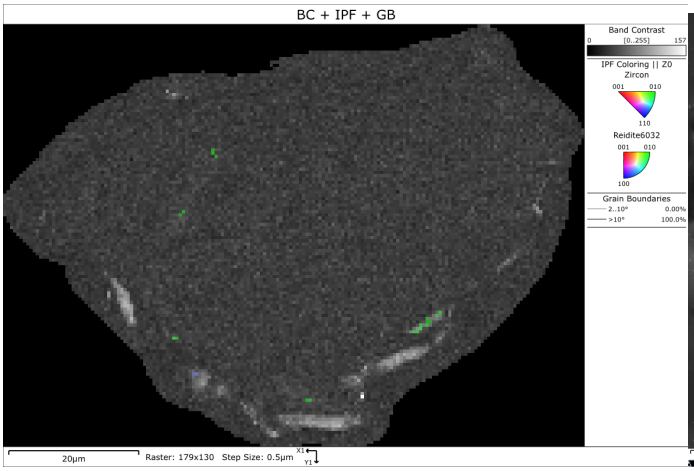
BC + IPF + GB
Band Contrast
0 [0..255] 157
IPF Coloring || Z0
Zircon
001 010
110
Reidite6032
001 010
100
Grain Boundaries
2..10° 0.00%
>10° 100.0%
20µm
Raster: 179x130 Step Size: 0.5µm

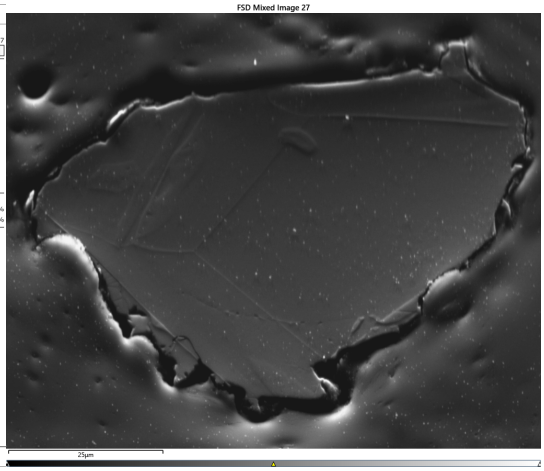
FSD Mixed Image 27
25µm

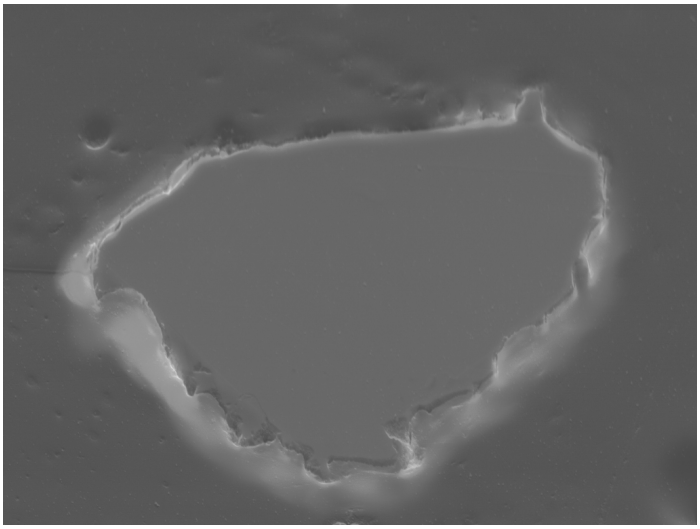

M_M1_29

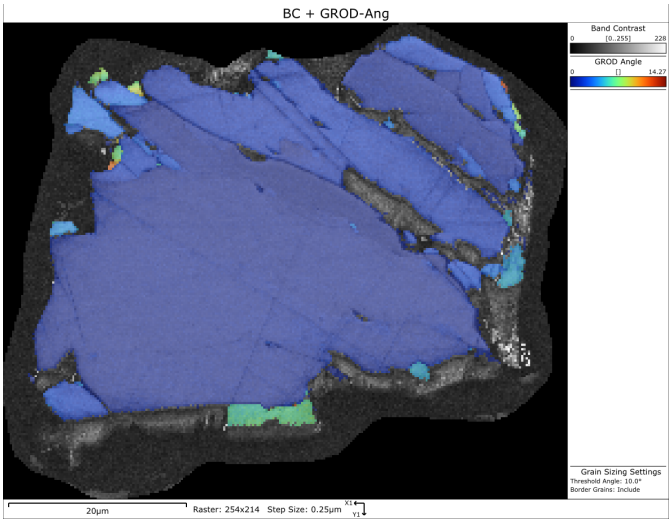
BC + GROD-Ang
Band Contrast
0 [0..255] 228
GROD Angle
0 [] 14.27
Grain Sizing Settings
Threshold Angle: 10.0°
Border Grains: Include
20µm
Raster: 254x214 Step Size: 0.25µm

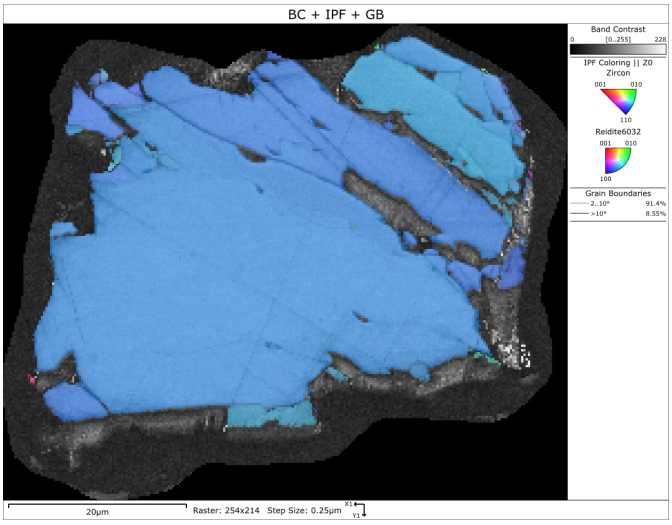
BC + IPF + GB
Band Contrast
0 [0..255] 228
IPF Coloring || Z0
Zircon
001 010
110
Reidite6032
001 010
100
Grain Boundaries
2..10° 91.4%
>10° 8.55%
20µm
Raster: 254x214 Step Size: 0.25µm

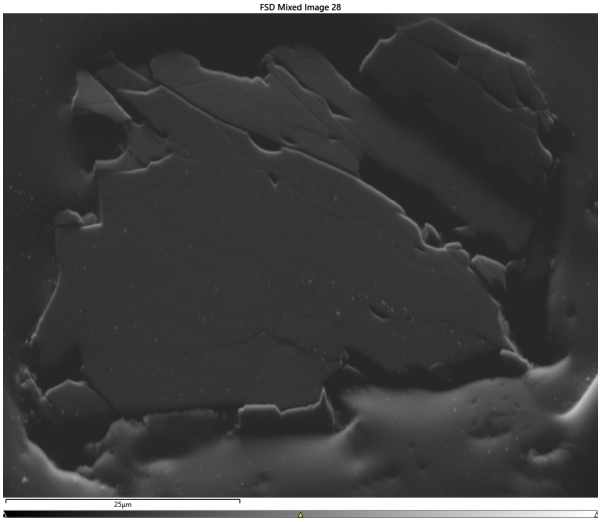
FSD Mixed Image 28
25µm

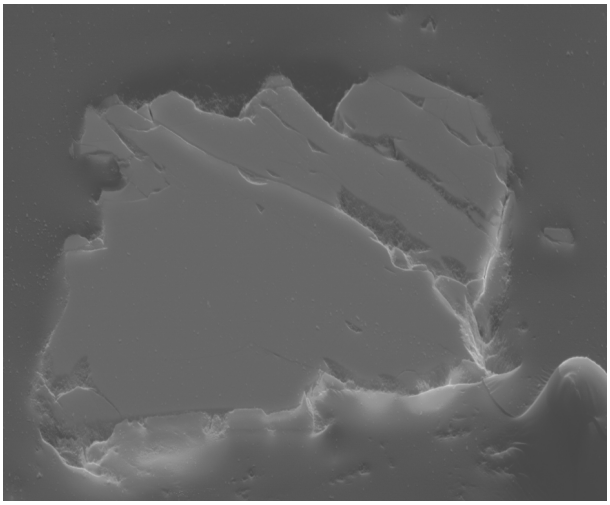

M_M1_30

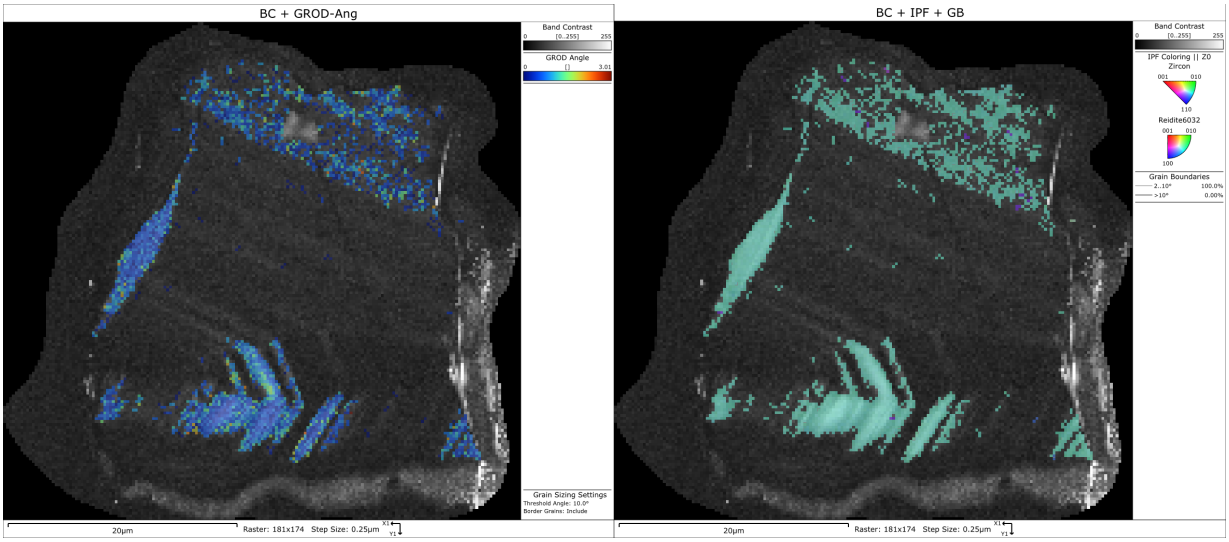
BC + GROD-Ang
Band Contrast
GROD Angle
Grain Sizing Settings
20µm
Raster: 181x174 Step Size: 0.25µm
BC + IPF + GB
Band Contrast
IPF Coloring || Z0
Zircon
Reidite6032
Grain Boundaries
20µm
Raster: 181x174 Step Size: 0.25µm

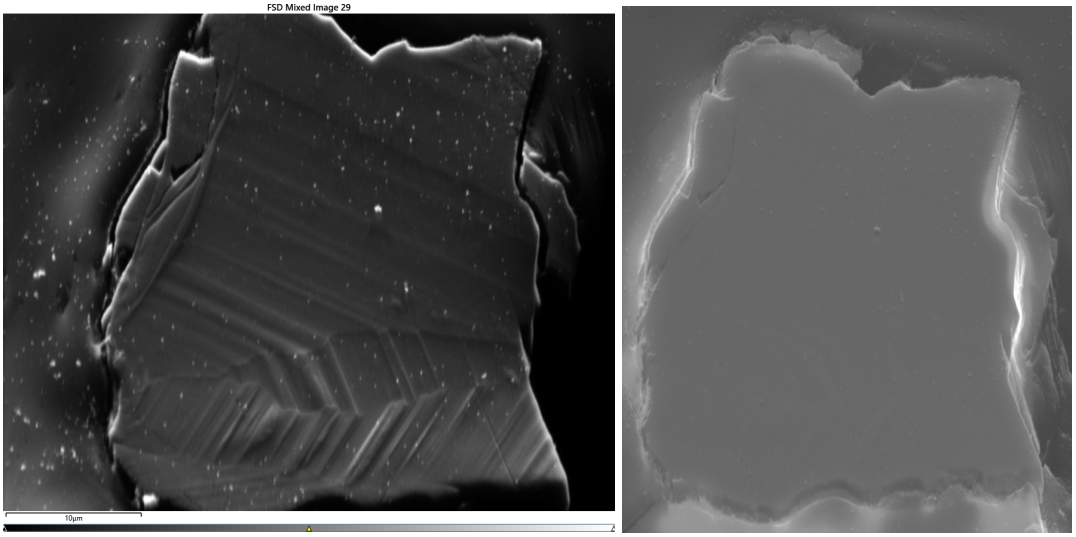
FSD Mixed Image 29
10µm

M_M1_31

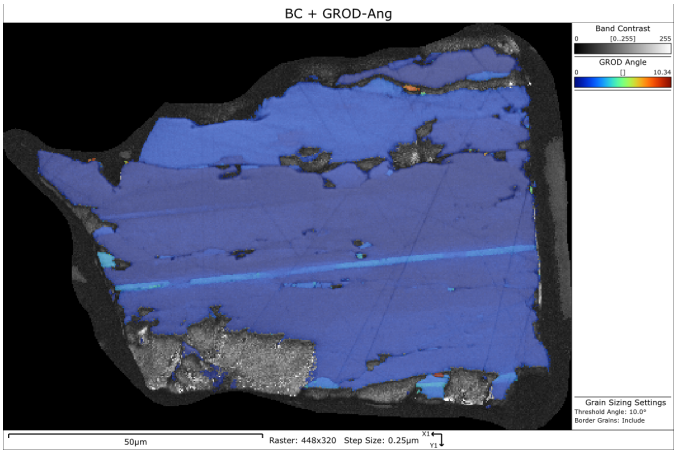
BC + GROD-Ang
Band Contrast
0 [0..255] 255
GROD Angle
0 [] 10.34
Grain Sizing Settings
Threshold Angle: 10.0°
Border Grains: Include
50µm
Raster: 448x320 Step Size: 0.25µm

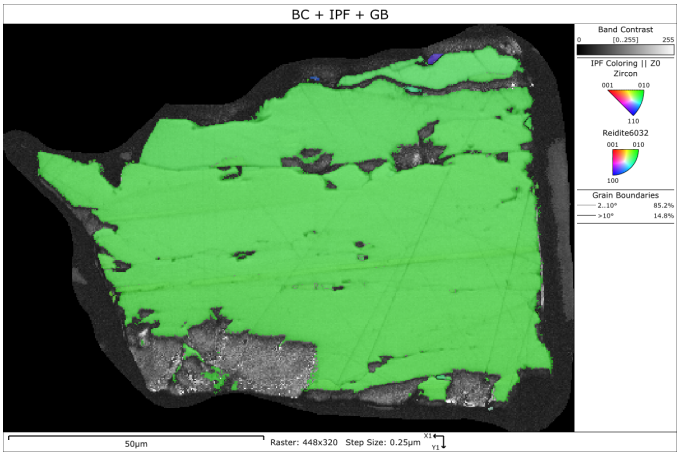
BC + IPF + GB
Band Contrast
0 [0..255] 255
IPF Coloring || Z0
Zircon
001 010
110
Reidite6032
001 010
100
Grain Boundaries
2..10° 85.2%
>10° 14.8%
50µm
Raster: 448x320 Step Size: 0.25µm

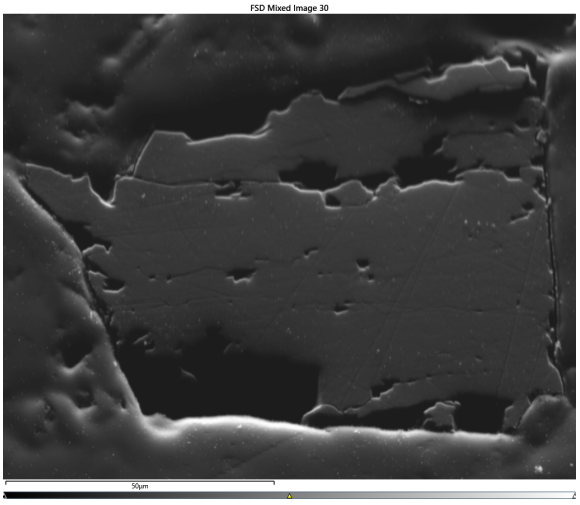
FSD Mixed Image 30
50µm

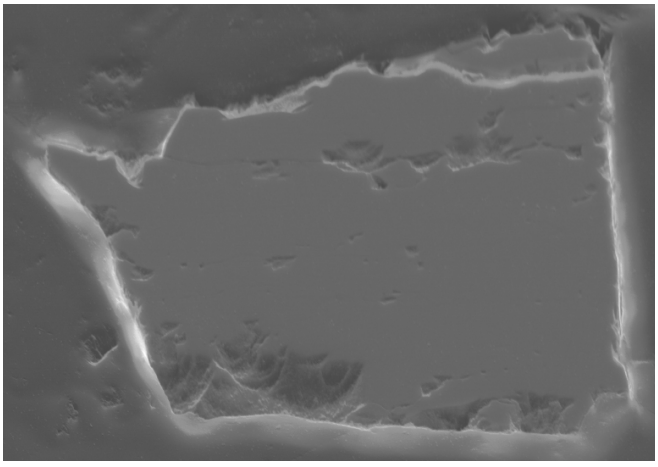

M_M1_32

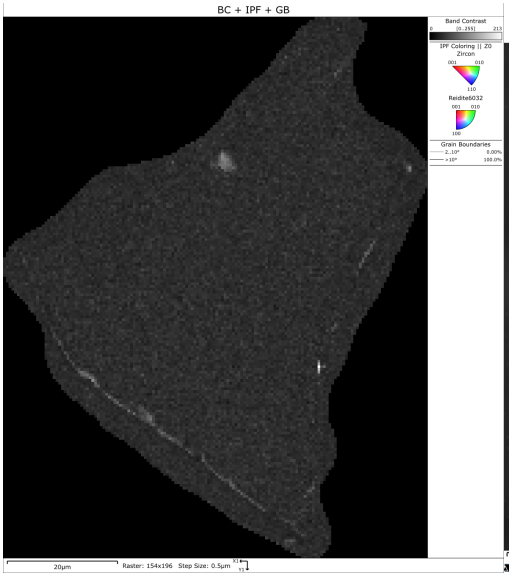
BC + IPF + GB
Band Contrast
IPF Coloring || Z0
Zircon
Reidite6032
Grain Boundaries
20µm
Raster: 154x196 Step Size: 0.5µm

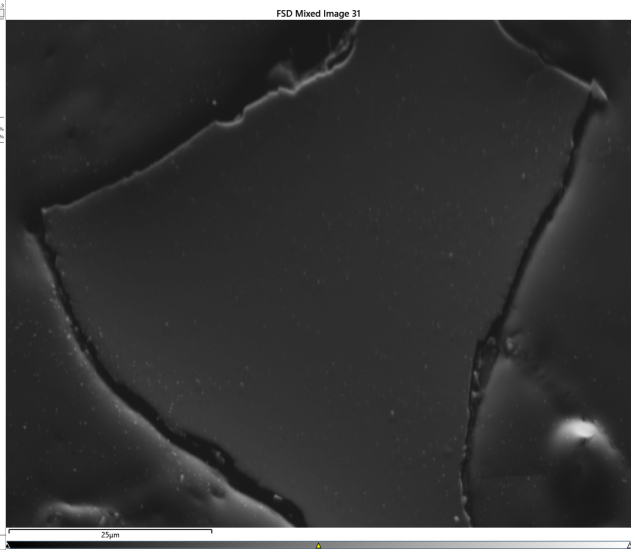
FSD Mixed Image 31
25µm

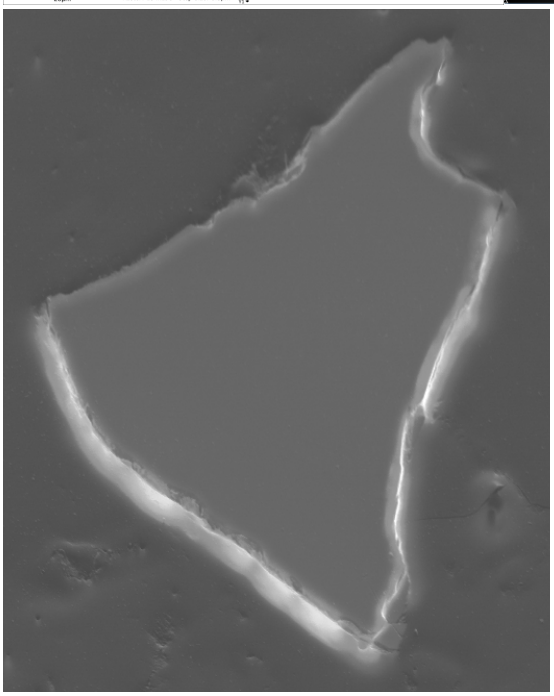

M_M1_33

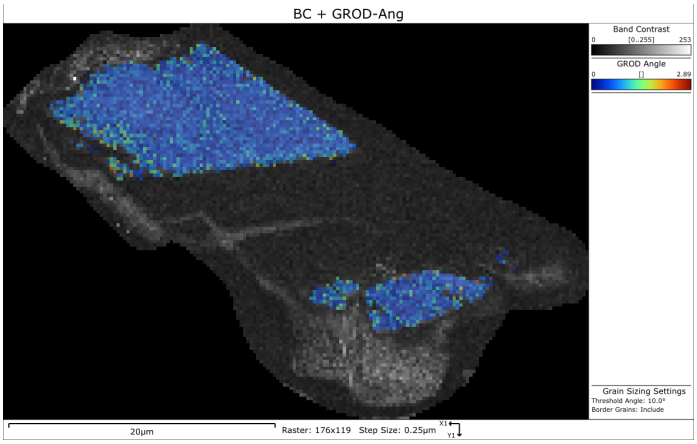
BC + GROD-Ang
Band Contrast
0 [0..255] 253
GROD Angle
0 [] 2.89
Grain Sizing Settings
Threshold Angle: 10.0°
Border Grains: Include
20µm
Raster: 176x119 Step Size: 0.25µm

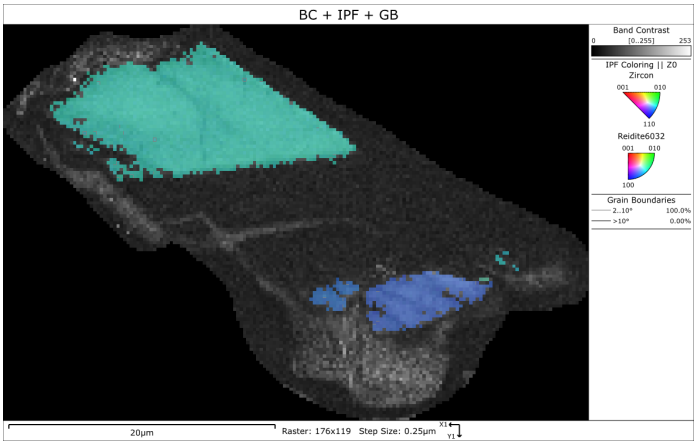
BC + IPF + GB
Band Contrast
0 [0..255] 253
IPF Coloring || Z0
Zircon
001 010
110
Reidite6032
001 010
100
Grain Boundaries
2..10° 100.0%
>10° 0.00%
20µm
Raster: 176x119 Step Size: 0.25µm

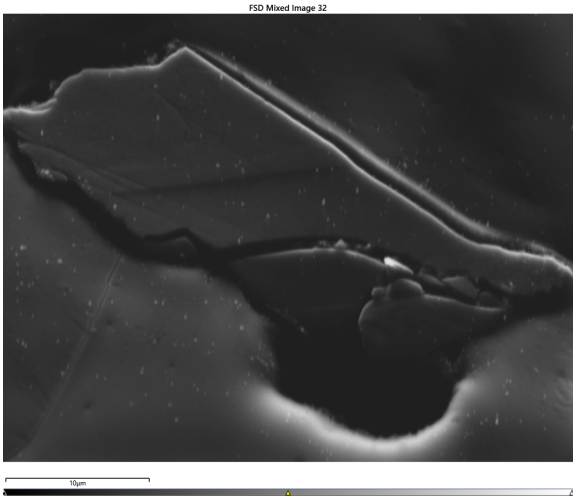
FSD Mixed Image 32
10µm

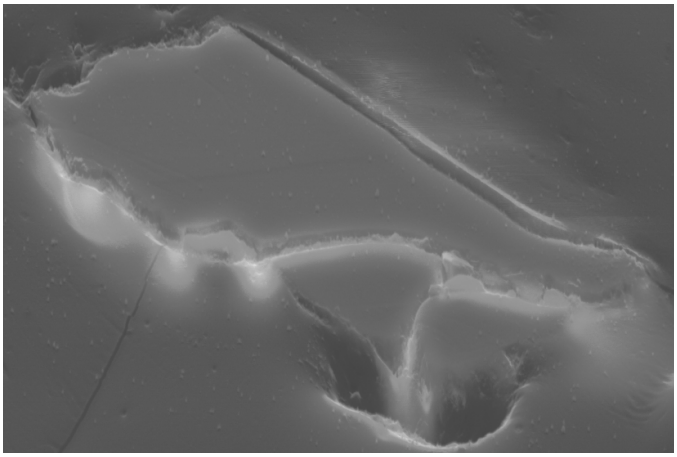

M_M1_34

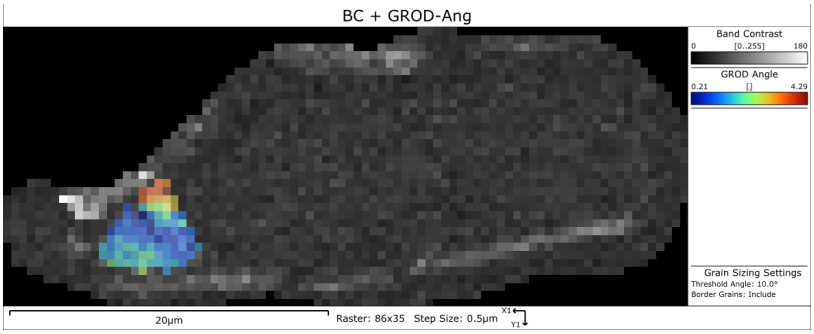
BC + GROD-Ang
Band Contrast
0 [0..255] 180
GROD Angle
0.21 [] 4.29
Grain Sizing Settings
Threshold Angle: 10.0°
Border Grains: Include
20µm
Raster: 86x35 Step Size: 0.5µm
X1
Y1

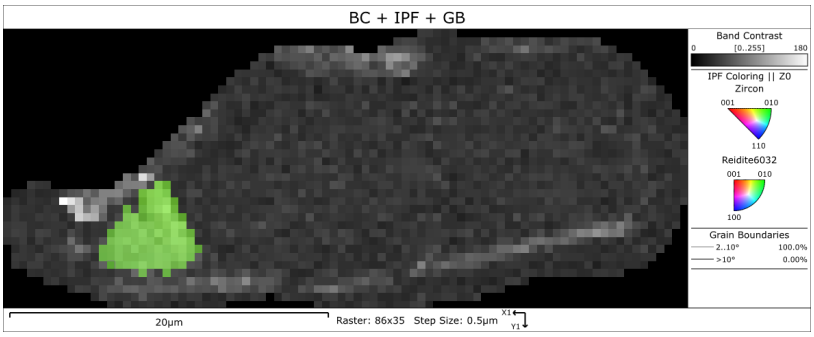
BC + IPF + GB
Band Contrast
0 [0..255] 180
IPF Coloring || Z0
Zircon
001 010
110
Reidite6032
001 010
100
Grain Boundaries
2..10° 100.0%
>10° 0.00%
20µm
Raster: 86x35 Step Size: 0.5µm
X1
Y1

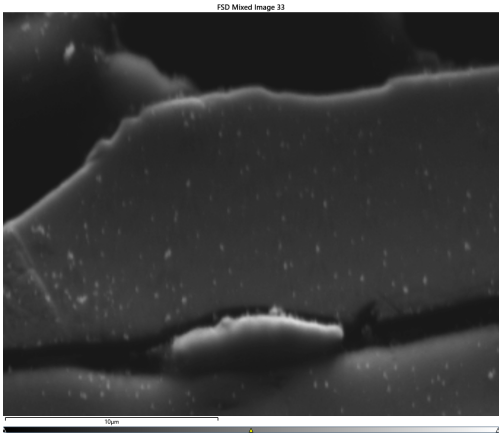
FSD Mixed Image 33

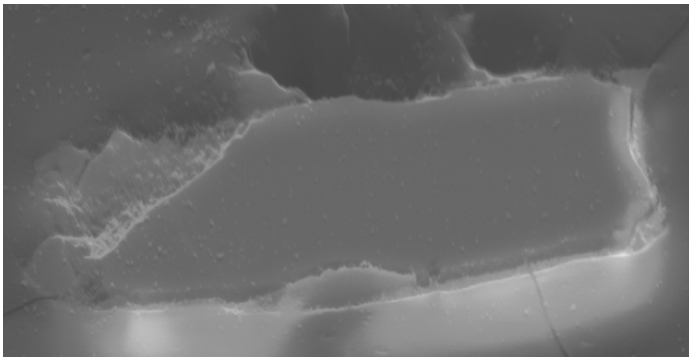

M_M1_35

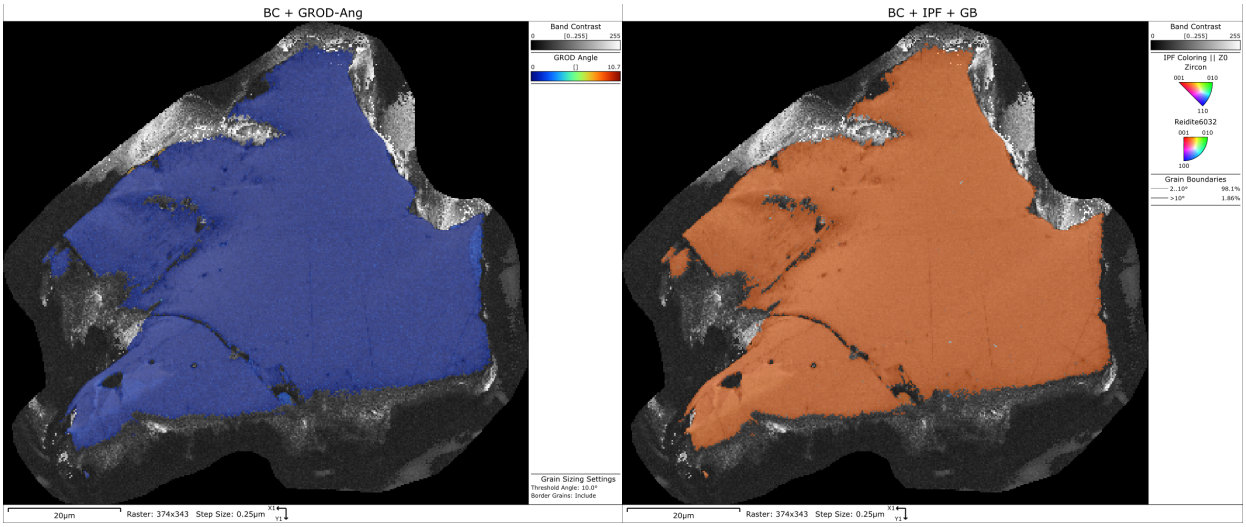
BC + GROD-Ang
Band Contrast
GROD Angle
Grain Sizing Settings
20µm
Raster: 374x343 Step Size: 0.25µm
BC + IPF + GB
Band Contrast
IPF Coloring || Z0
Zircon
Reidite6032
Grain Boundaries
2..10°
98.1%
>10°
1.86%
20µm
Raster: 374x343 Step Size: 0.25µm

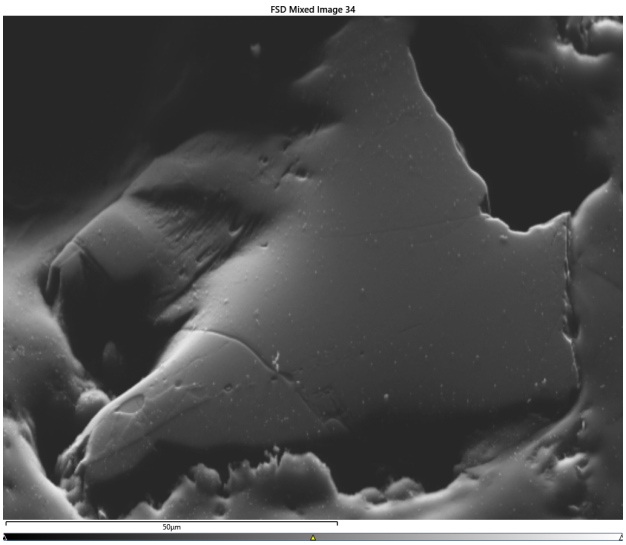
FSD Mixed Image 34
50µm

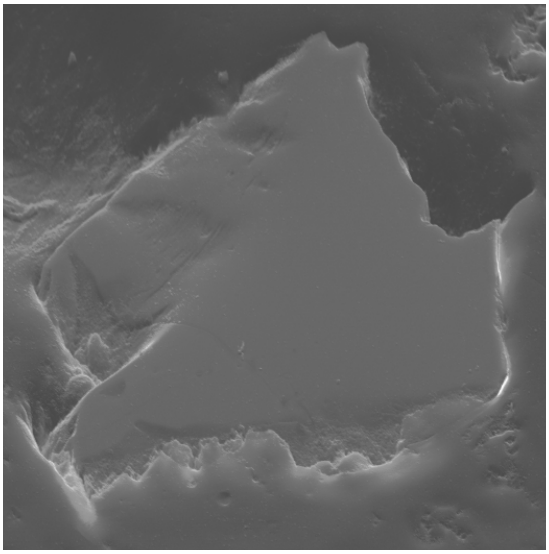

M_M1_36

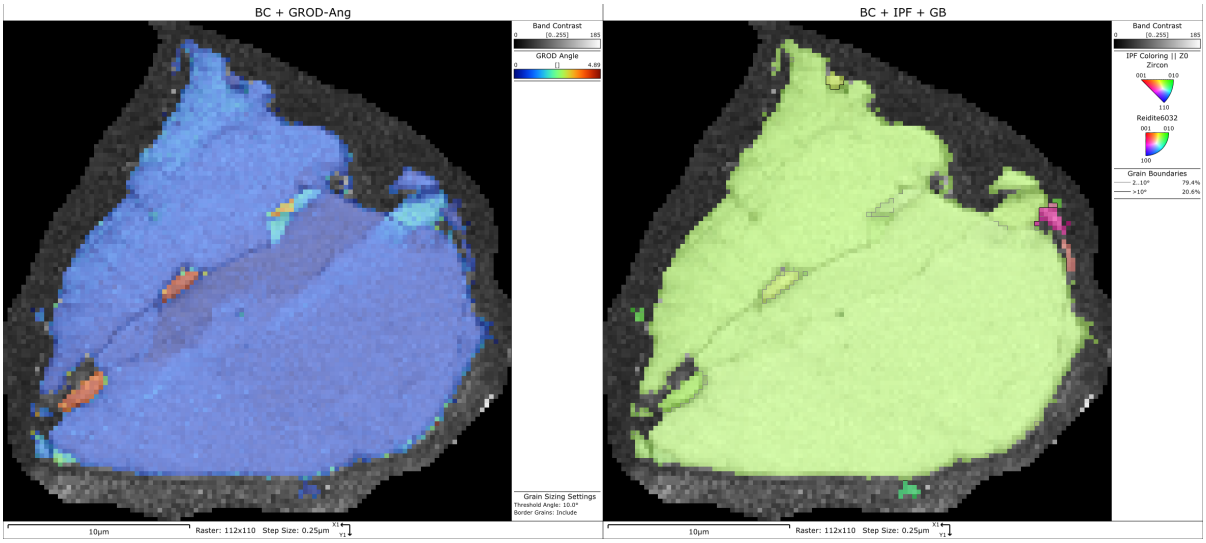
BC + GROD-Ang
Band Contrast
GROD Angle
Grain Sizing Settings
10µm
Raster: 112x110 Step Size: 0.25µm
BC + IPF + GB
Band Contrast
IPF Coloring || Z0
Zircon
Reidite6032
Grain Boundaries
10µm
Raster: 112x110 Step Size: 0.25µm

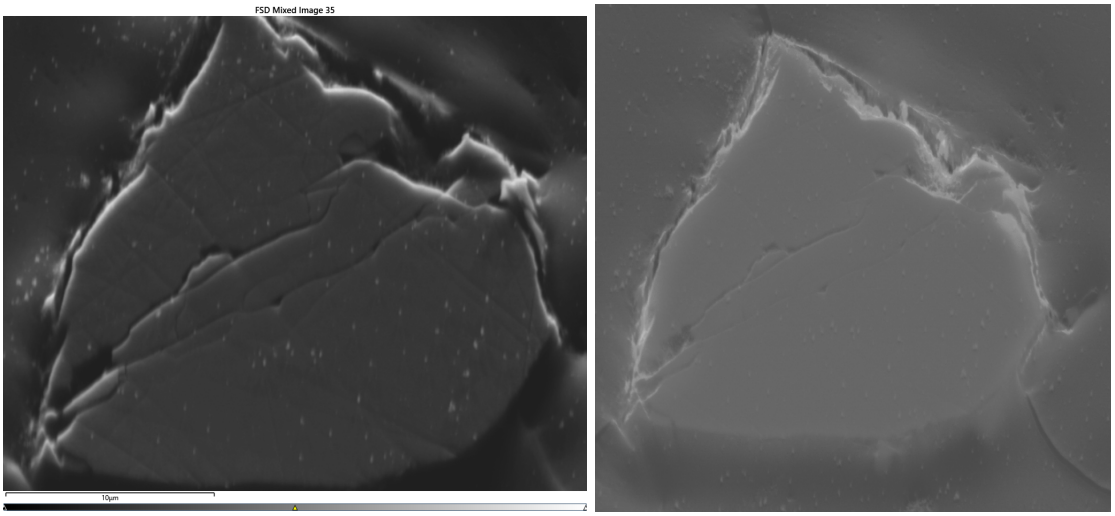
FSD Mixed Image 35
10µm

M_M1_37

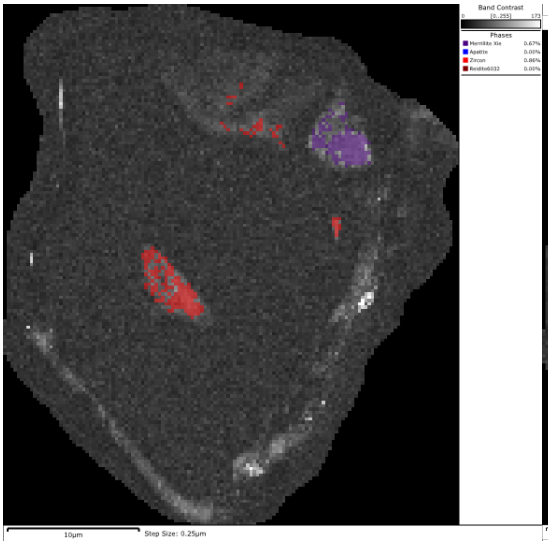
Band Contrast
Phases
Merrillite Xie 0.67%
Apatite 0.00%
Zircon 0.86%
Reidite6032 0.00%
10µm
Step Size: 0.25µm

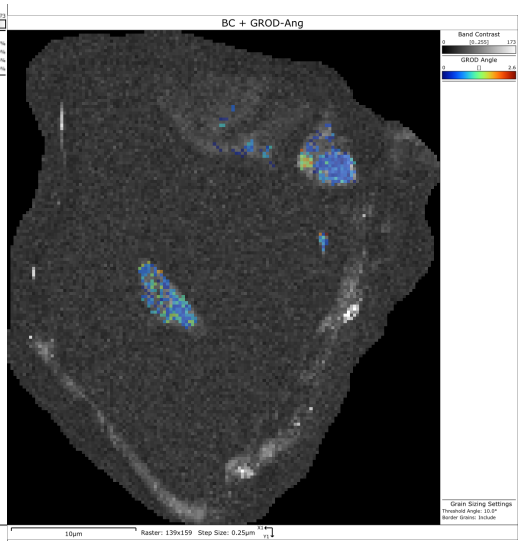
BC + GROD-Ang
Band Contrast
GROD Angle
Grain Sizing Settings
10µm
Raster: 139x159 Step Size: 0.25µm

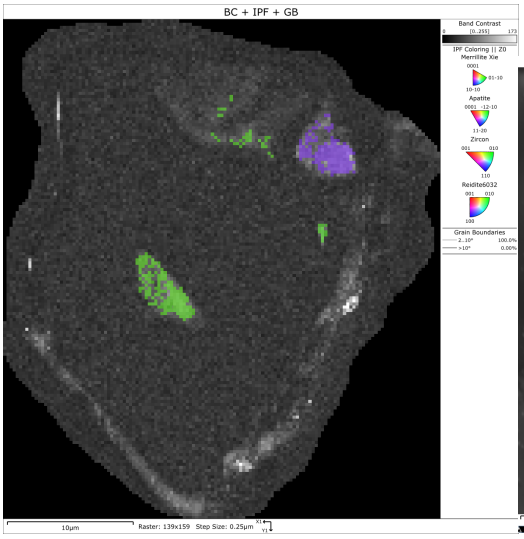
BC + IPF + GB
Band Contrast
IPF Coloring || Z0
Merrillite Xie
Apatite
Zircon
Reidite6032
Grain Boundaries
10µm
Raster: 139x159 Step Size: 0.25µm

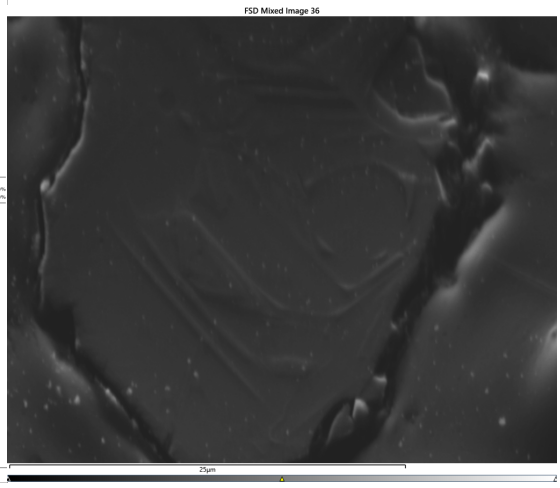
FSD Mixed Image 36
25µm

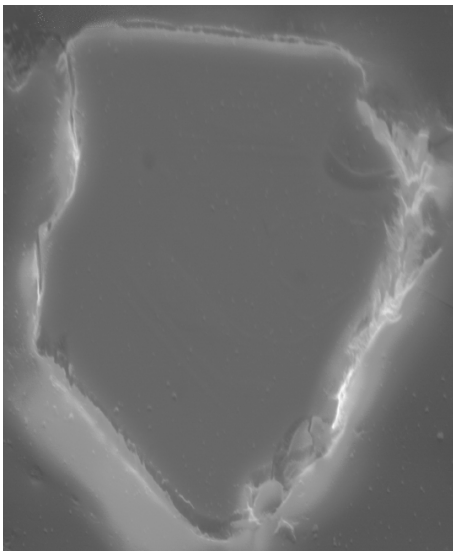

M_M1_38

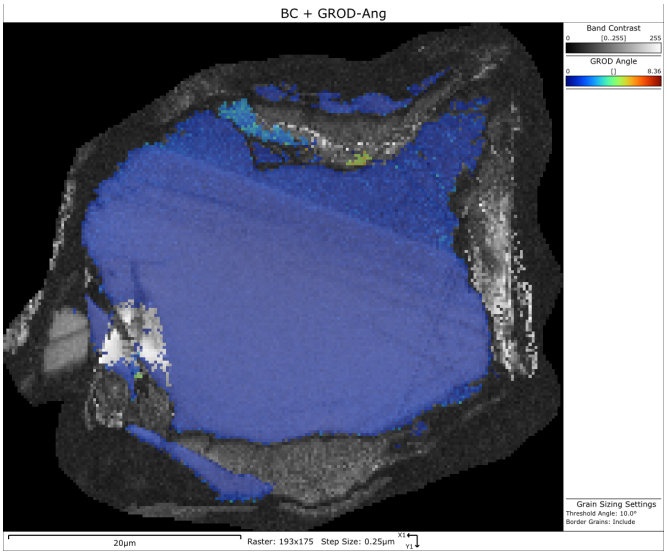
BC + GROD-Ang
Band Contrast
0 [0..255] 255
GROD Angle
0 [] 8.36
Grain Sizing Settings
Threshold Angle: 10.0°
Border Grains: Include
20µm
Raster: 193x175 Step Size: 0.25µm

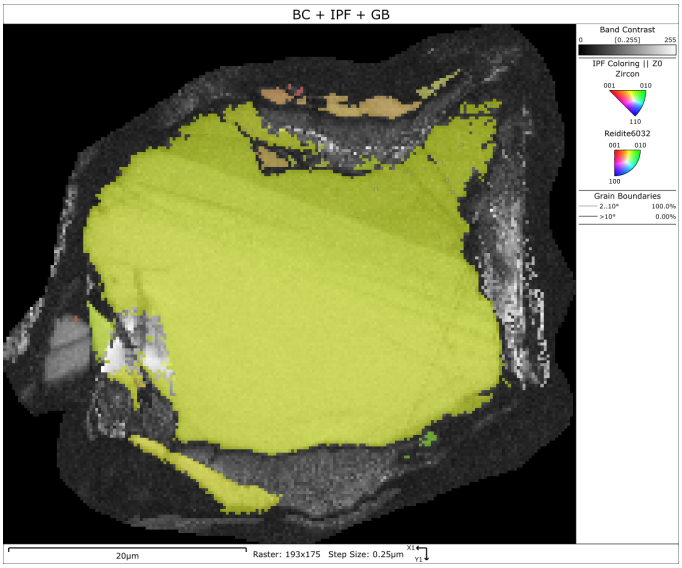
BC + IPF + GB
Band Contrast
0 [0..255] 255
IPF Coloring || Z0
Zircon
001 010
110
Reidite6032
001 010
100
Grain Boundaries
2..10° 100.0%
>10° 0.00%
20µm
Raster: 193x175 Step Size: 0.25µm

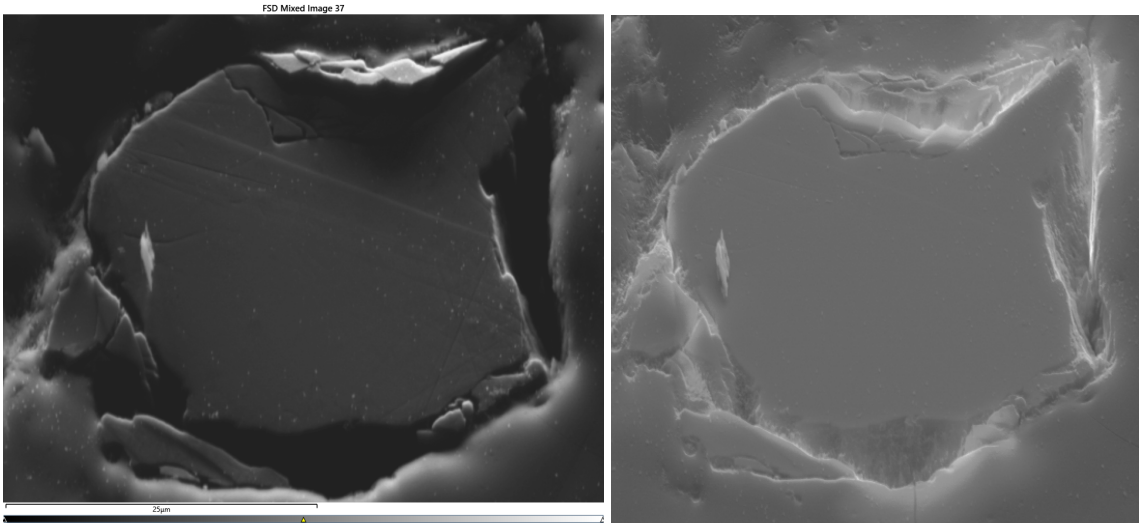
FSD Mixed Image 37
25µm

M_M1_39

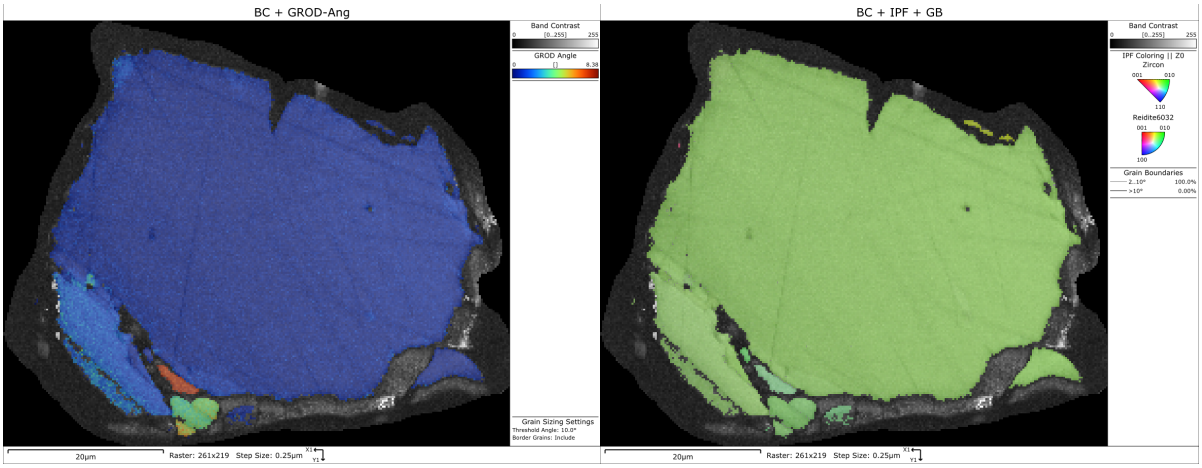
BC + GROD-Ang
Band Contrast
GROD Angle
Grain Sizing Settings
20µm
Raster: 261x219 Step Size: 0.25µm
BC + IPF + GB
Band Contrast
IPF Coloring || Z0
Zircon
Reidite6032
Grain Boundaries
20µm
Raster: 261x219 Step Size: 0.25µm

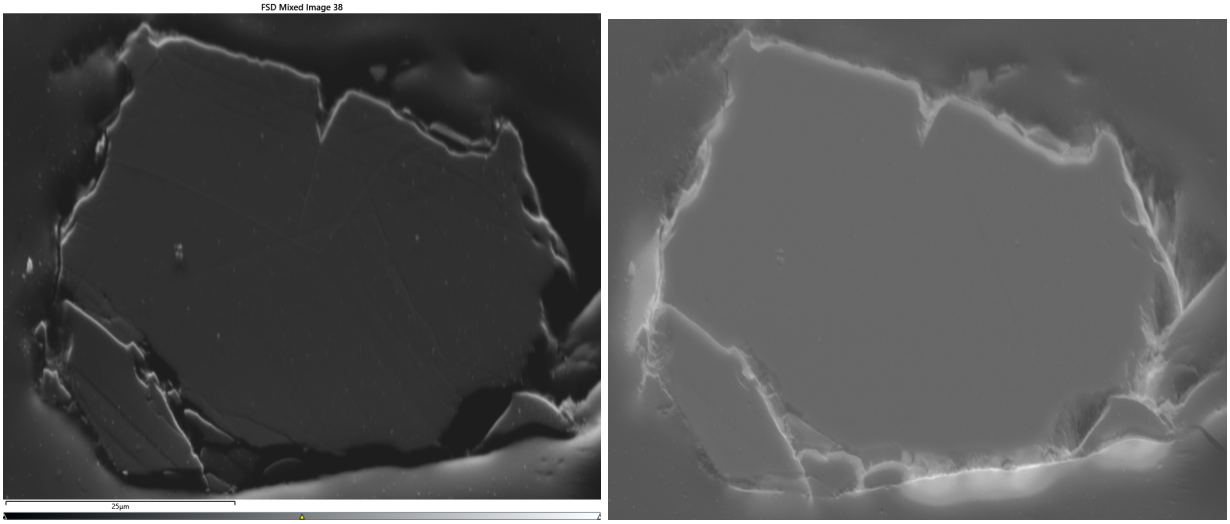
FSD Mixed Image 38
25µm

M_M1_41

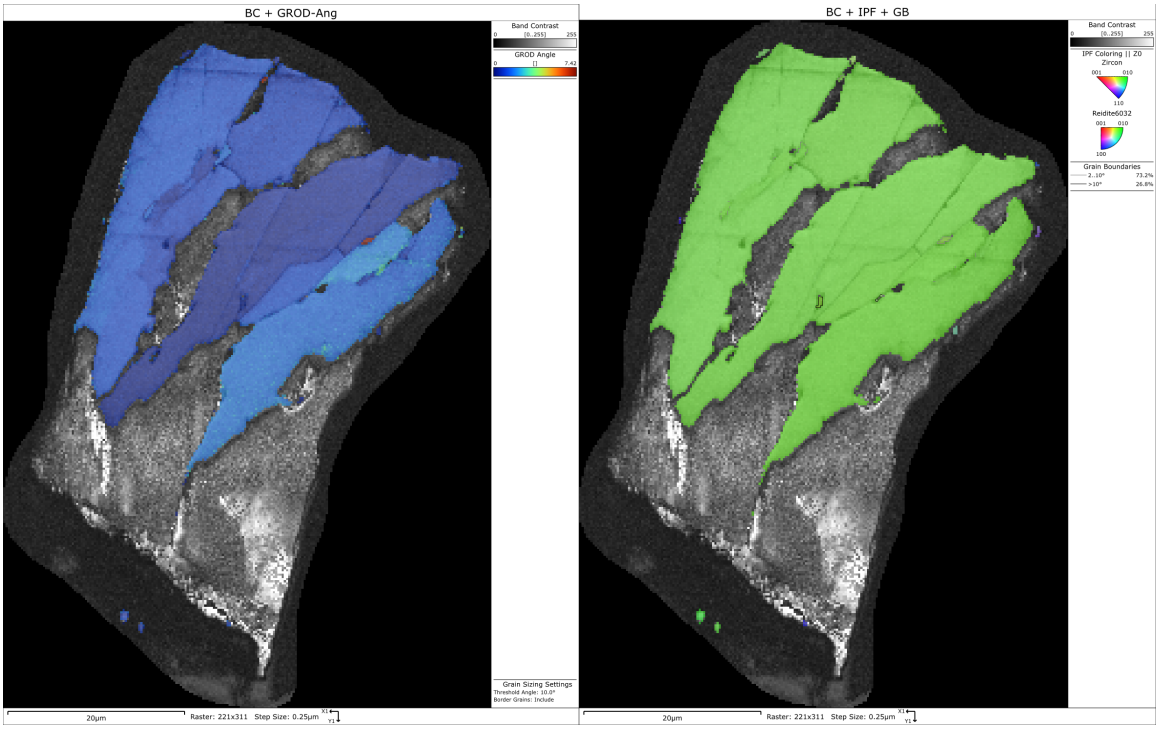
BC + GROD-Ang
Band Contrast
GROD Angle
Grain Sizing Settings
20µm
Raster: 221x311 Step Size: 0.25µm
BC + IPF + GB
Band Contrast
IPF Coloring || Z0
Zircon
Reidite6032
Grain Boundaries
20µm
Raster: 221x311 Step Size: 0.25µm

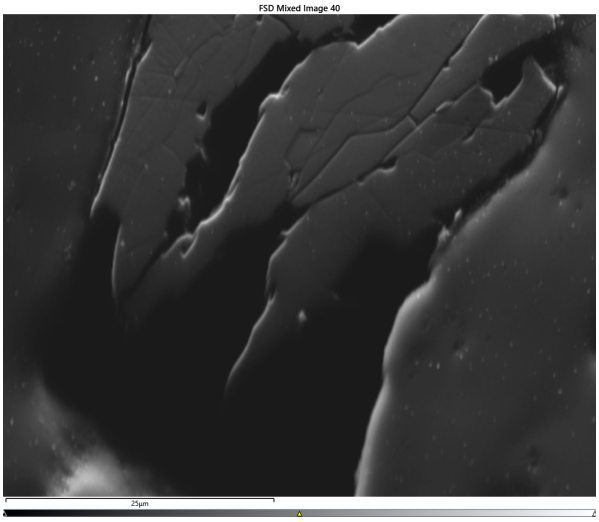
FSD Mixed Image 40
25µm

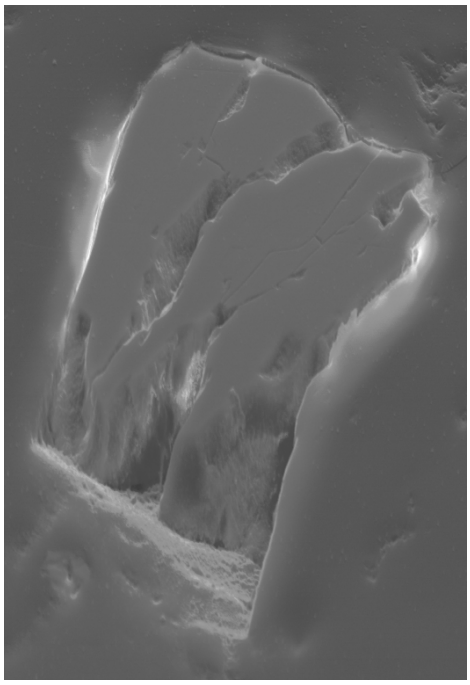

M_M1_42

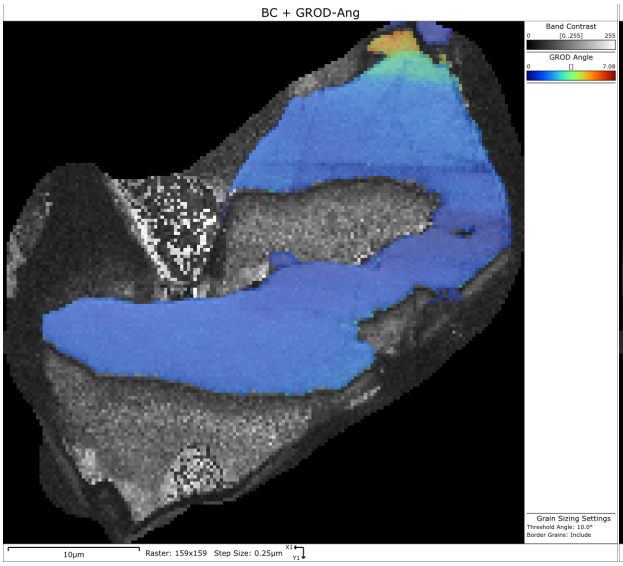
BC + GROD-Ang
Band Contrast
GROD Angle
Grain Sizing Settings
10µm
Raster: 159x159 Step Size: 0.25µm

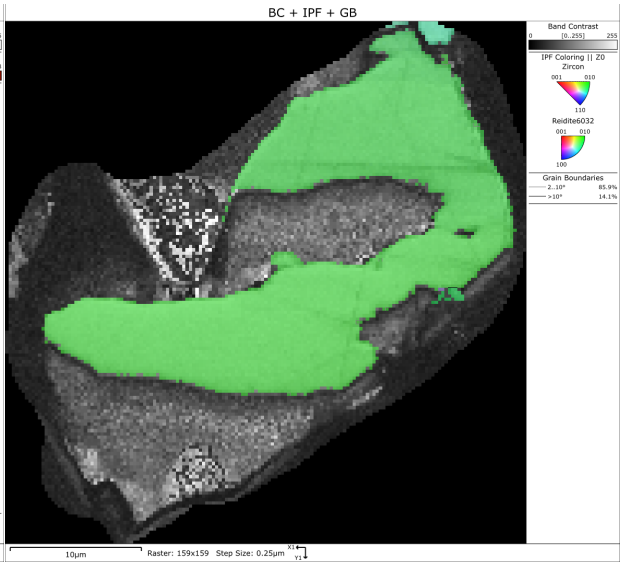
BC + IPF + GB
Band Contrast
IPF Coloring || Z0
Zircon
Reidite6032
Grain Boundaries
10µm
Raster: 159x159 Step Size: 0.25µm

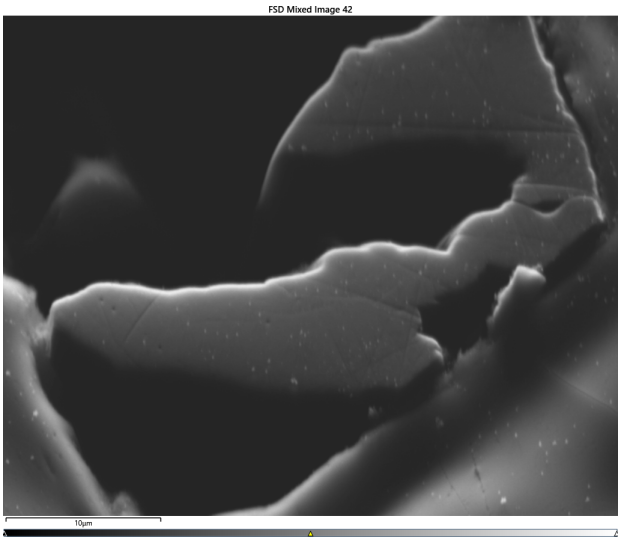
FSD Mixed Image 42
10µm

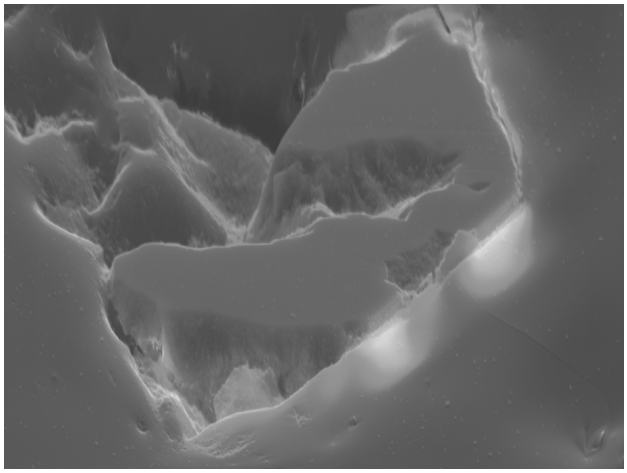

M_M1_43

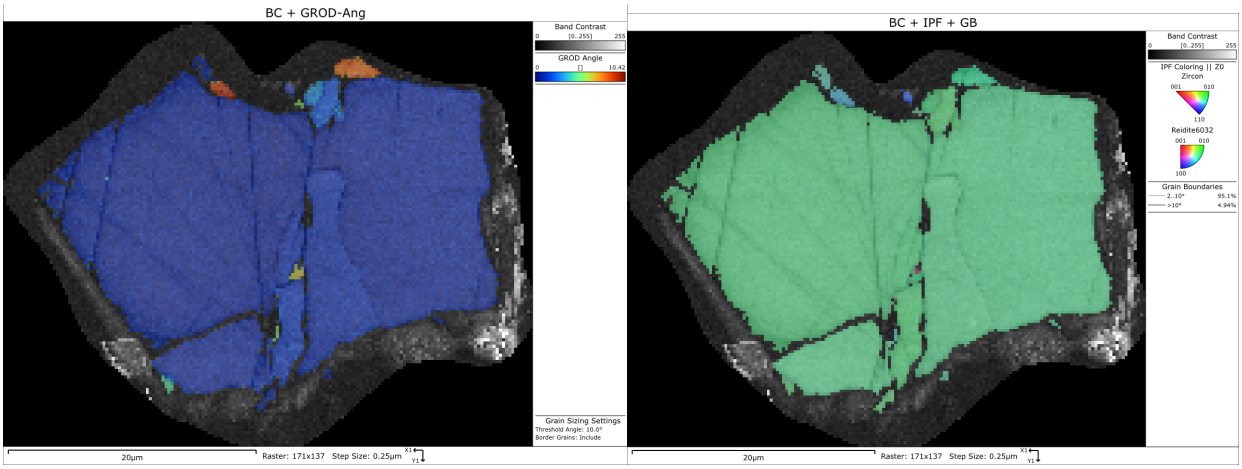
BC + GROD-Ang
Band Contrast
GROD Angle
Grain Sizing Settings
20µm
Raster: 171x137 Step Size: 0.25µm
BC + IPF + GB
Band Contrast
IPF Coloring || Z0
Zircon
Reidite6032
Grain Boundaries
20µm
Raster: 171x137 Step Size: 0.25µm

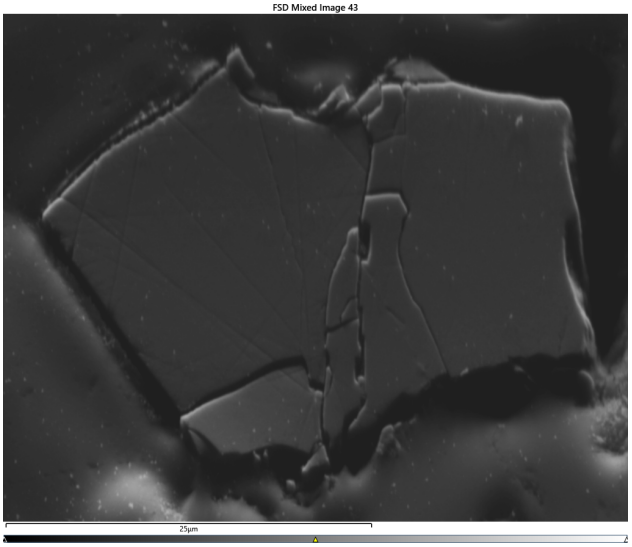
FSD Mixed Image 43
25µm

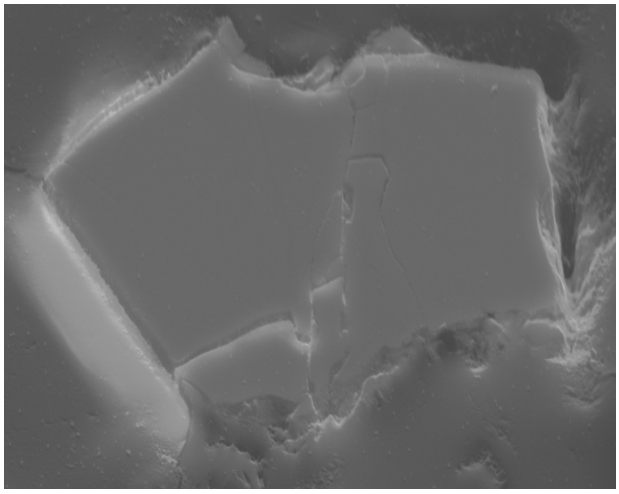

M_M1_44

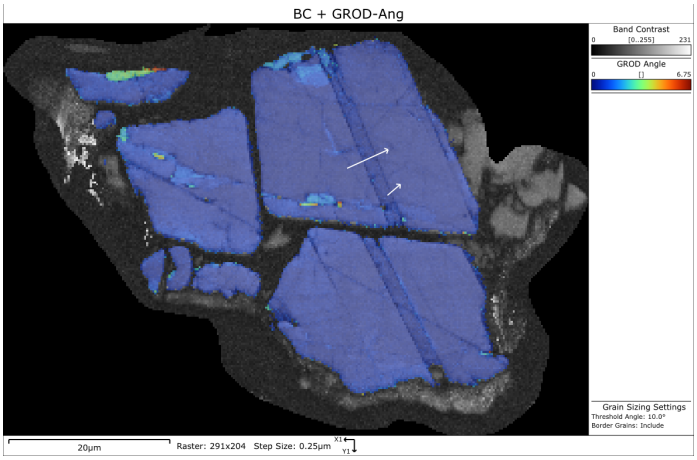
BC + GROD-Ang
Band Contrast
0 [0..255] 231
GROD Angle
0 [] 6.75
Grain Sizing Settings
Threshold Angle: 10.0°
Border Grains: Include
20µm
Raster: 291x204 Step Size: 0.25µm

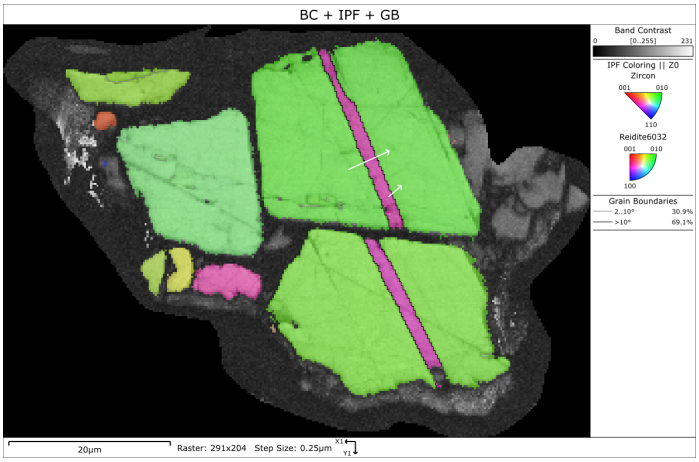
BC + IPF + GB
Band Contrast
0 [0..255] 231
IPF Coloring || Z0
Zircon
001 010
110
Reidite6032
001 010
100
Grain Boundaries
2..10° 30.9%
>10° 69.1%
20µm
Raster: 291x204 Step Size: 0.25µm

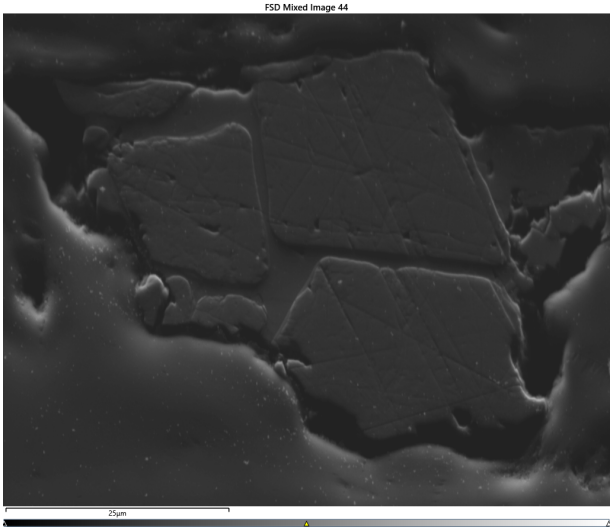
FSD Mixed Image 44
25µm

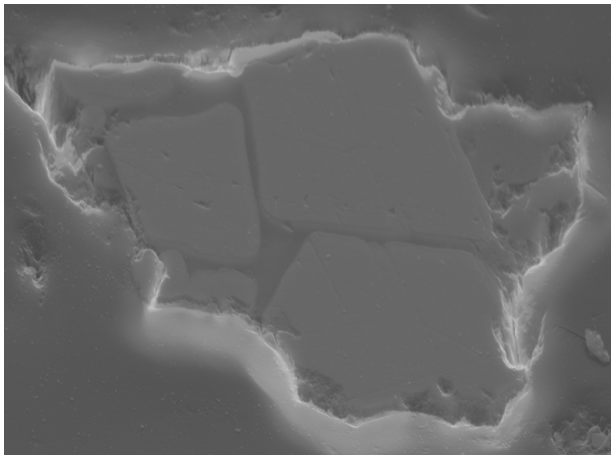

M_M1_45

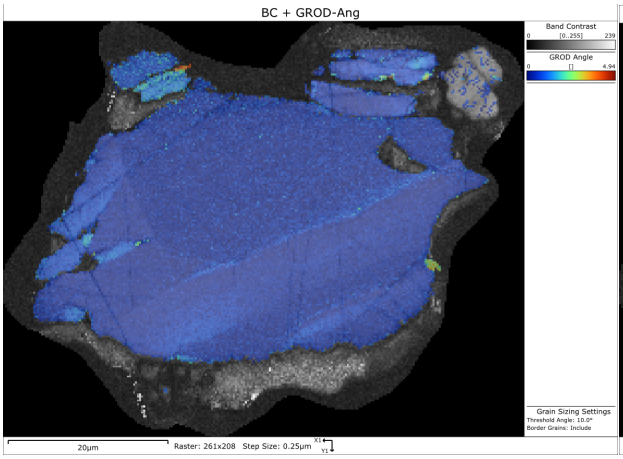
BC + GROD-Ang
Band Contrast
0 [0..255] 239
GROD Angle
0 [] 4.94
Grain Sizing Settings
Threshold Angle: 10.0°
Border Grains: Include
20µm
Raster: 261x208 Step Size: 0.25µm

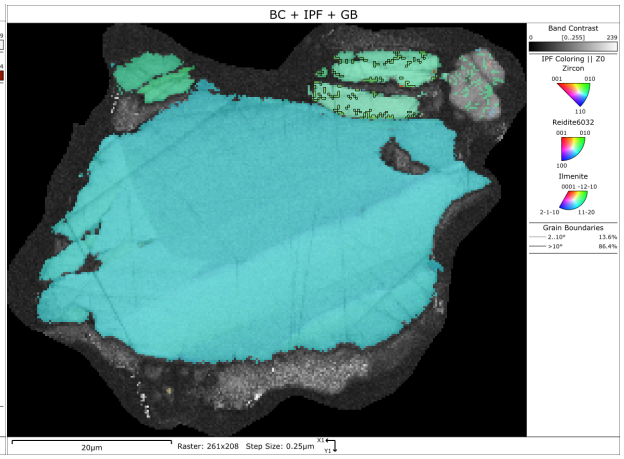
BC + IPF + GB
Band Contrast
0 [0..255] 239
IPF Coloring || Z0
Zircon
001 010
110
Reidite6032
001 010
100
Ilmenite
0001 -12-10
2-1-10 11-20
Grain Boundaries
2..10° 13.6%
>10° 86.4%
20µm
Raster: 261x208 Step Size: 0.25µm

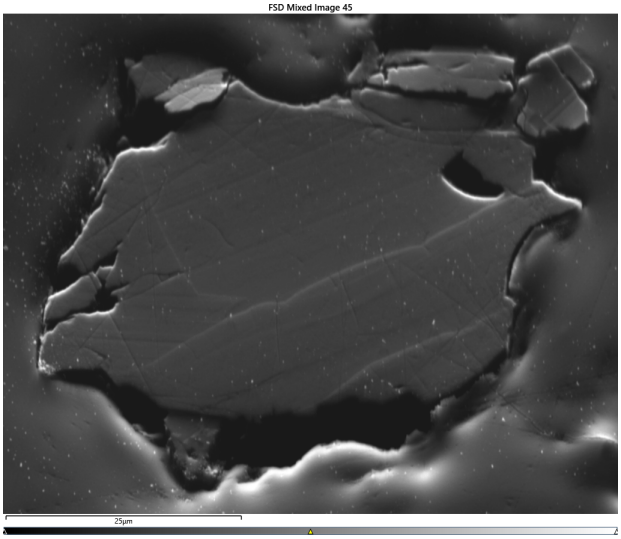
FSD Mixed Image 45
25µm

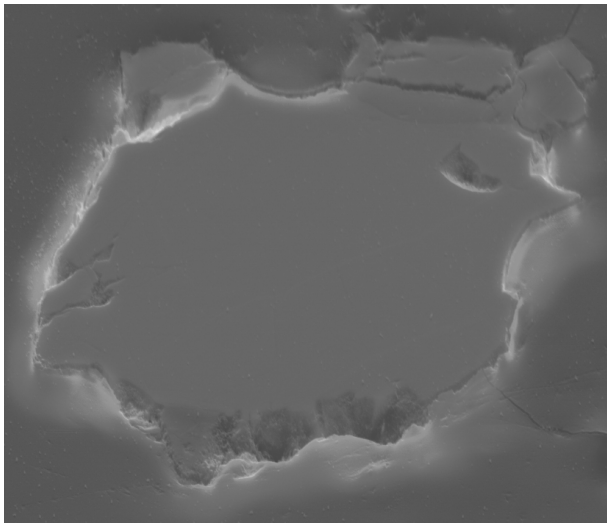

M_M1_46

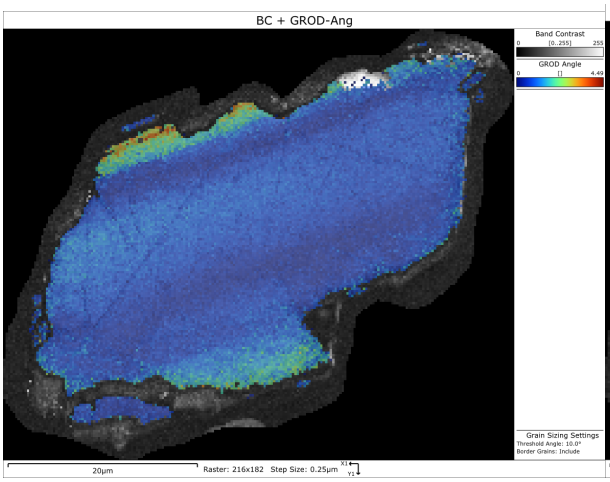
BC + GROD-Ang
Band Contrast
GROD Angle
Grain Sizing Settings
20µm
Raster: 216x182 Step Size: 0.25µm

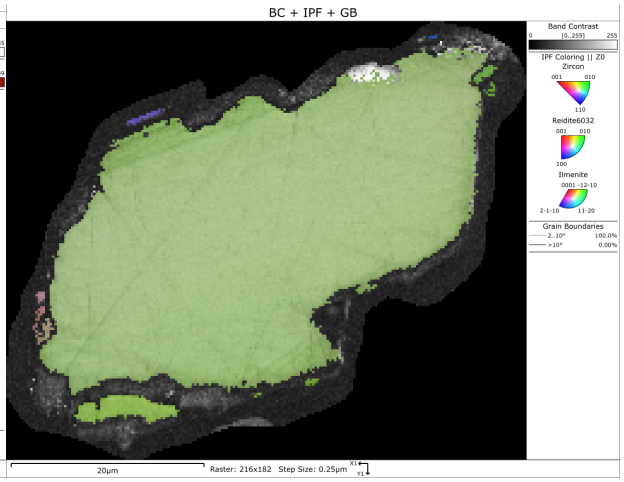
BC + IPF + GB
Band Contrast
IPF Coloring || Z0
Zircon
Reidite6032
Ilmenite
Grain Boundaries
20µm
Raster: 216x182 Step Size: 0.25µm

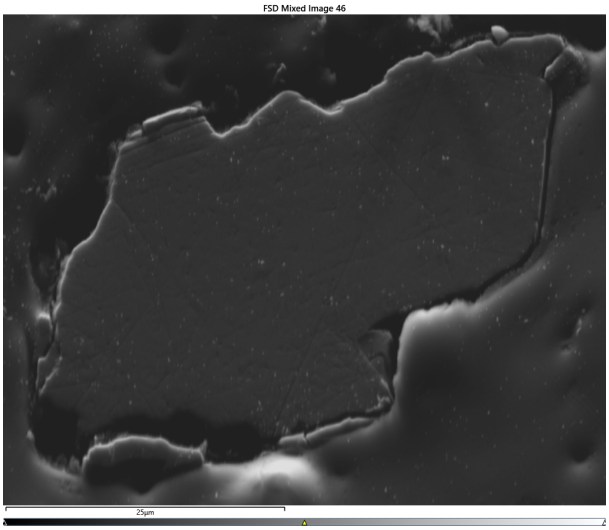
FSD Mixed Image 46
25µm

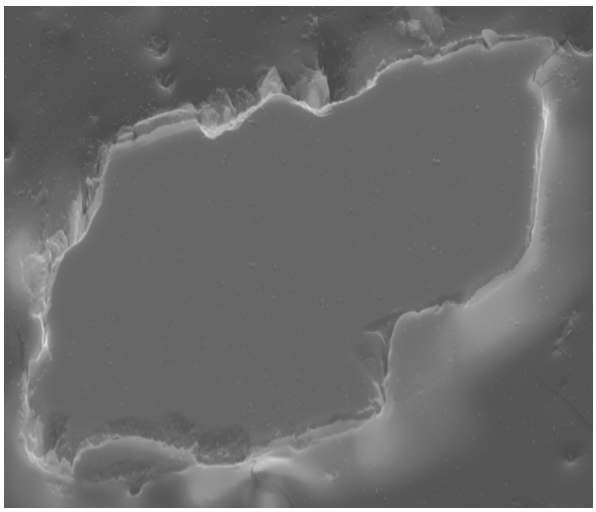

M_M1_47

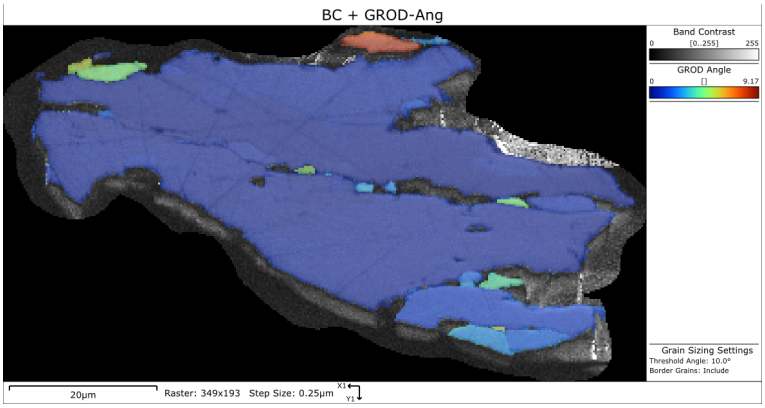
BC + GROD-Ang
Band Contrast
0 [0..255] 255
GROD Angle
0 [] 9.17
Grain Sizing Settings
Threshold Angle: 10.0°
Border Grains: Include
20µm
Raster: 349x193 Step Size: 0.25µm
X1
Y1

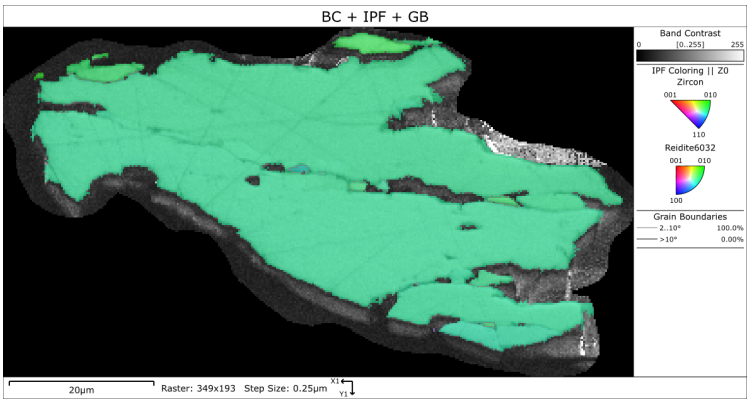
BC + IPF + GB
Band Contrast
0 [0..255] 255
IPF Coloring || Z0
Zircon
001 010
110
Reidite6032
001 010
100
Grain Boundaries
2..10° 100.0%
>10° 0.00%
20µm
Raster: 349x193 Step Size: 0.25µm
X1
Y1

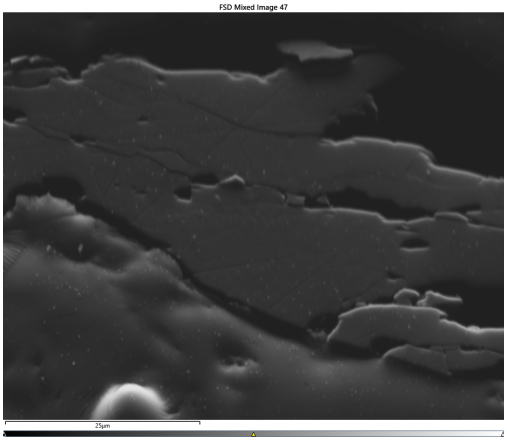
FSD Mixed Image 47
25µm

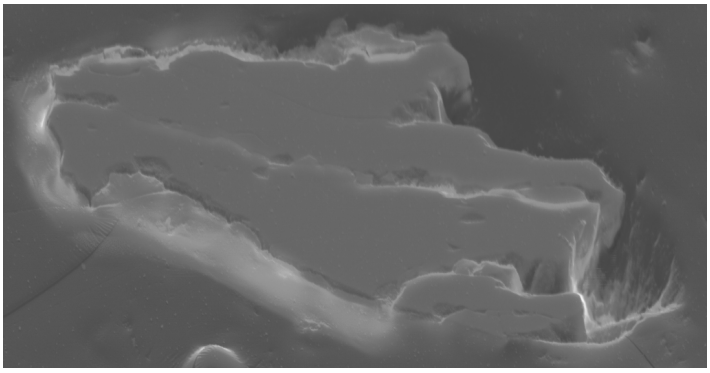

M_M1_48

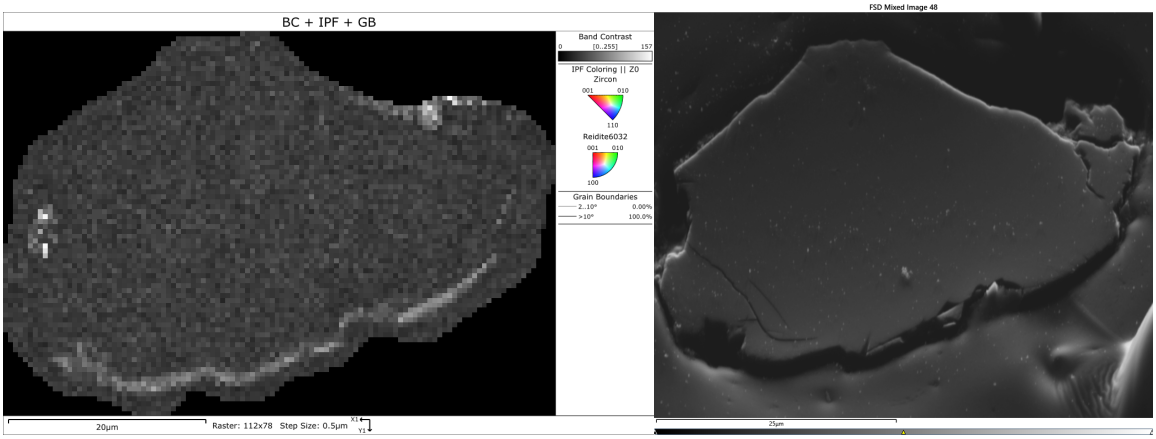
BC + IPF + GB
Band Contrast
0 [0..255] 157
IPF Coloring || Z0
Zircon
001 010
110
Reidite6032
001 010
100
Grain Boundaries
2..10° 0.00%
>10° 100.0%
20µm
Raster: 112x78 Step Size: 0.5µm
FSD Mixed Image 48
25µm

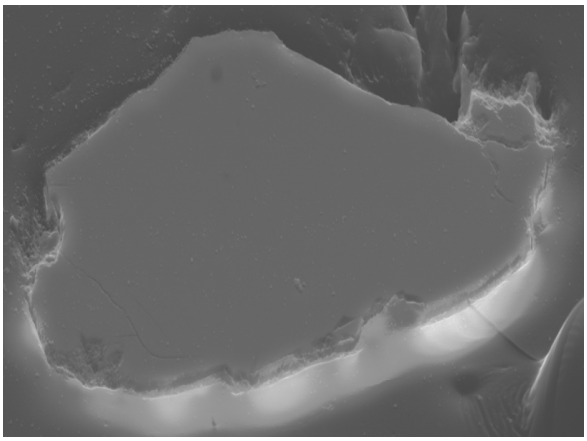

M_M1_49

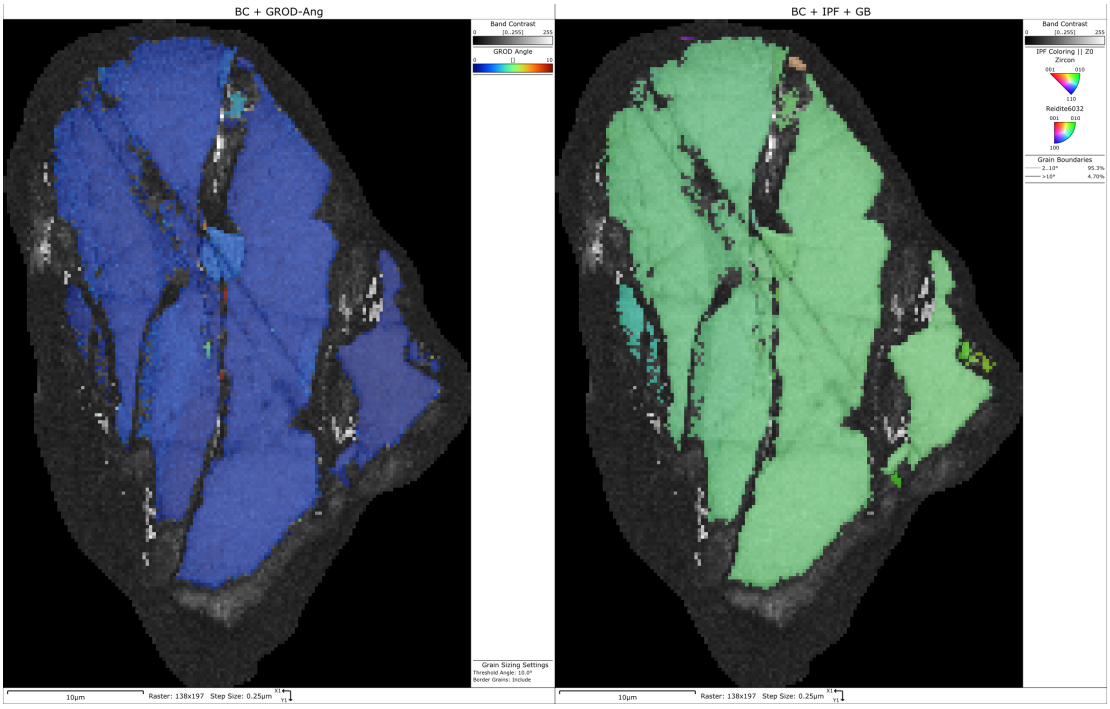
BC + GROD-Ang
Band Contrast
GROD Angle
Grain Sizing Settings
10µm
Raster: 138x197 Step Size: 0.25µm
BC + IPF + GB
Band Contrast
IPF Coloring || Z0
Zircon
Reidite6032
Grain Boundaries
10µm
Raster: 138x197 Step Size: 0.25µm

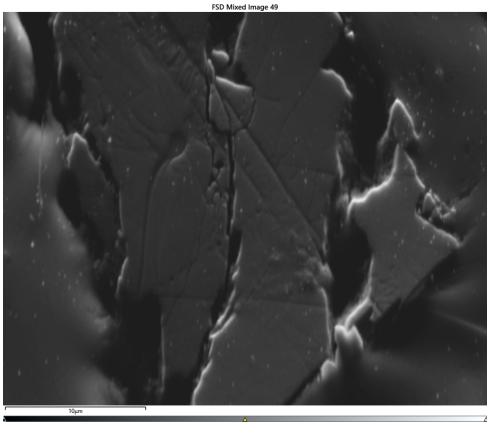
FSD Mixed Image 49
10µm

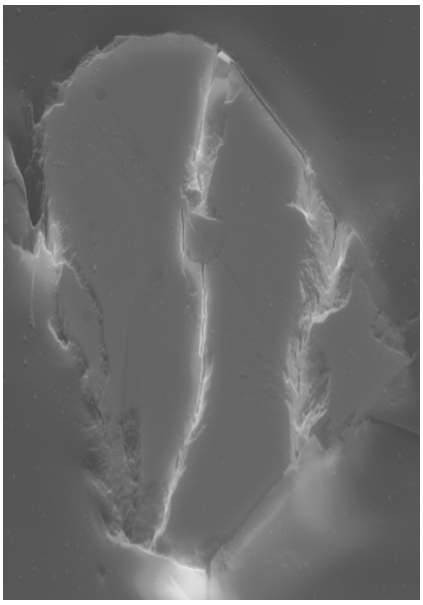

M_M1_50

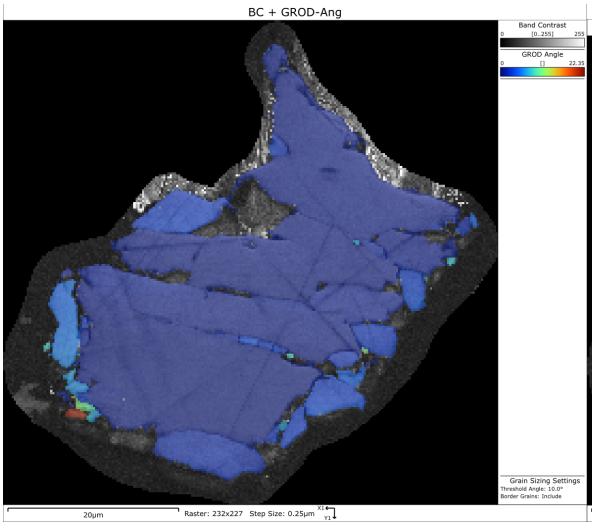
BC + GROD-Ang
Band Contrast
GROD Angle
Grain Sizing Settings
20µm
Raster: 232x227 Step Size: 0.25µm

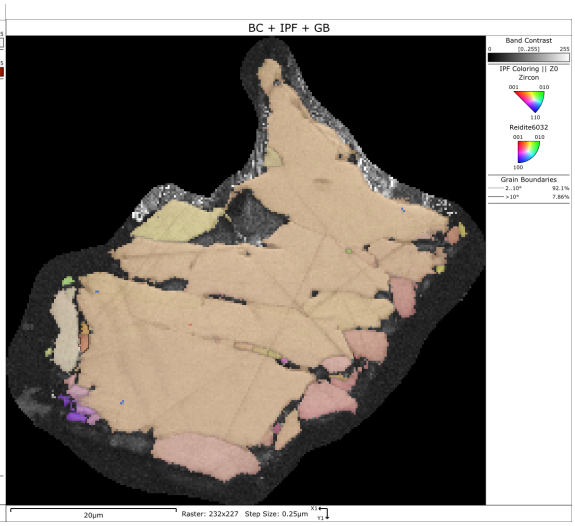
BC + IPF + GB
Band Contrast
IPF Coloring || Z0
Zircon
Reidite6032
Grain Boundaries
20µm
Raster: 232x227 Step Size: 0.25µm

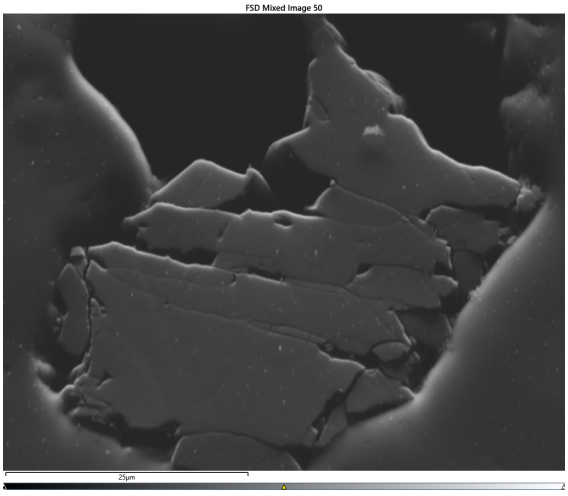
FSD Mixed Image 50
25µm

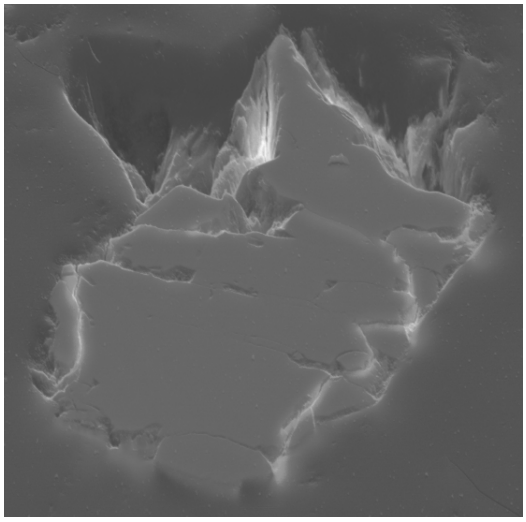

M_M1_51

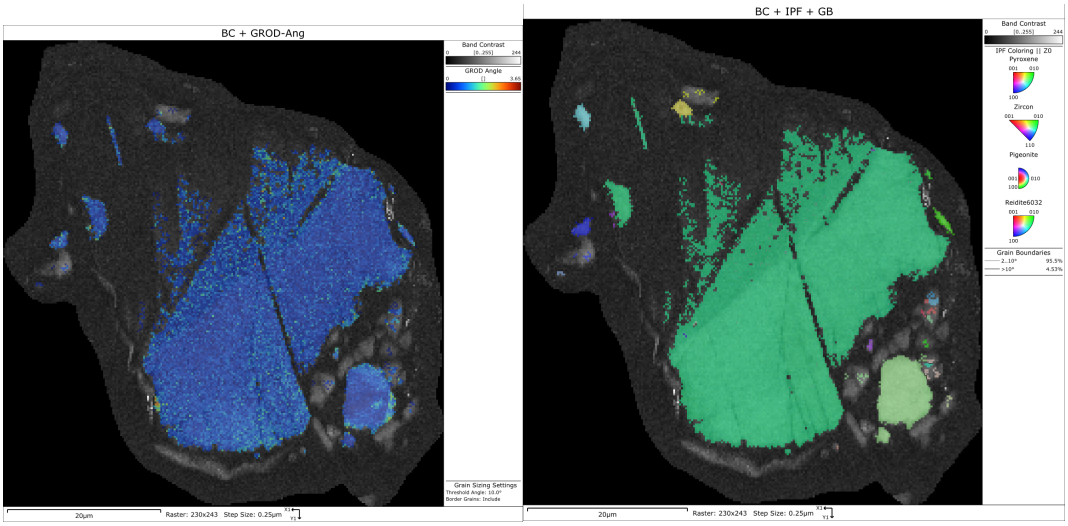
BC + GROD-Ang
Band Contrast
GROD Angle
Grain Sizing Settings
20µm
Raster: 230x243 Step Size: 0.25µm
BC + IPF + GB
Band Contrast
IPF Coloring || Z0
Pyroxene
Zircon
Pigeonite
Reidite6032
Grain Boundaries
20µm
Raster: 230x243 Step Size: 0.25µm

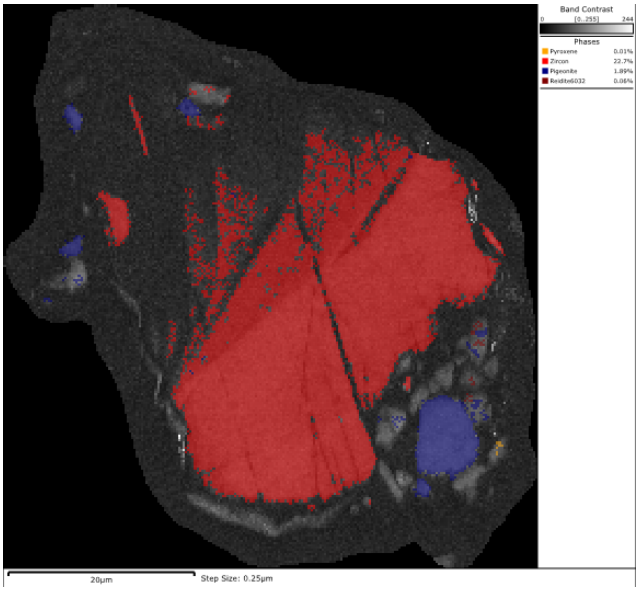
Band Contrast
Phases
Pyroxene 0.01%
Zircon 22.7%
Pigeonite 1.89%
Reidite6032 0.06%
20µm
Step Size: 0.25µm

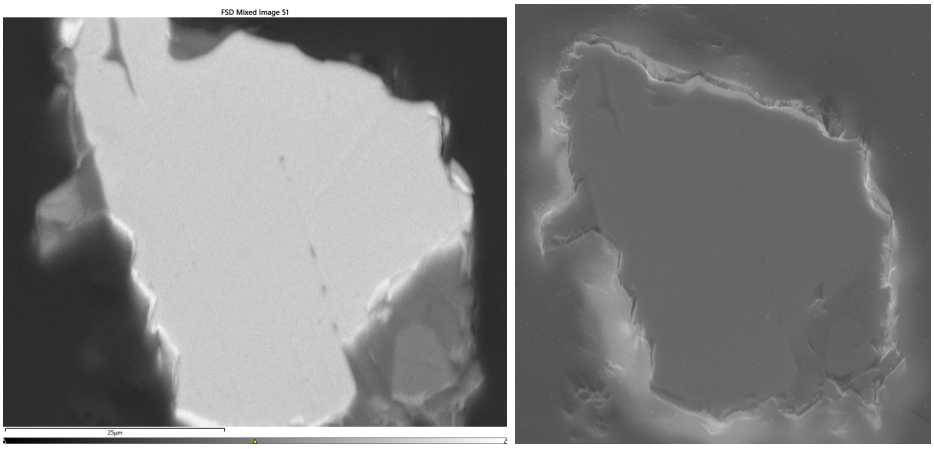
FSD Mixed Image 51
25µm

S_M2_2

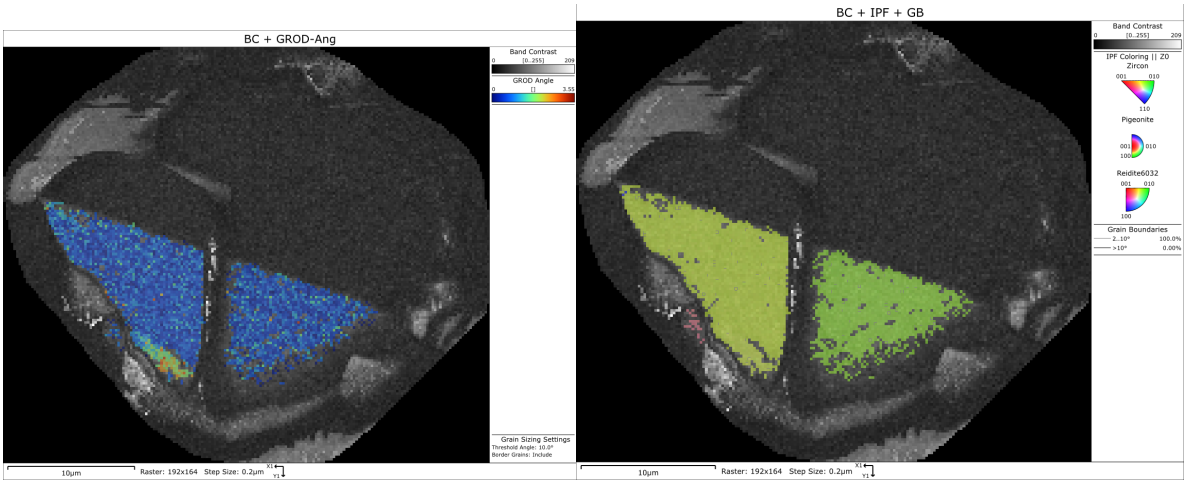
BC + GROD-Ang
Band Contrast
GROD Angle
Grain Sizing Settings
10µm
Raster: 192x164 Step Size: 0.2µm
BC + IPF + GB
Band Contrast
IPF Coloring || Z0
Zircon
Pigeonite
Reidite6032
Grain Boundaries
10µm
Raster: 192x164 Step Size: 0.2µm

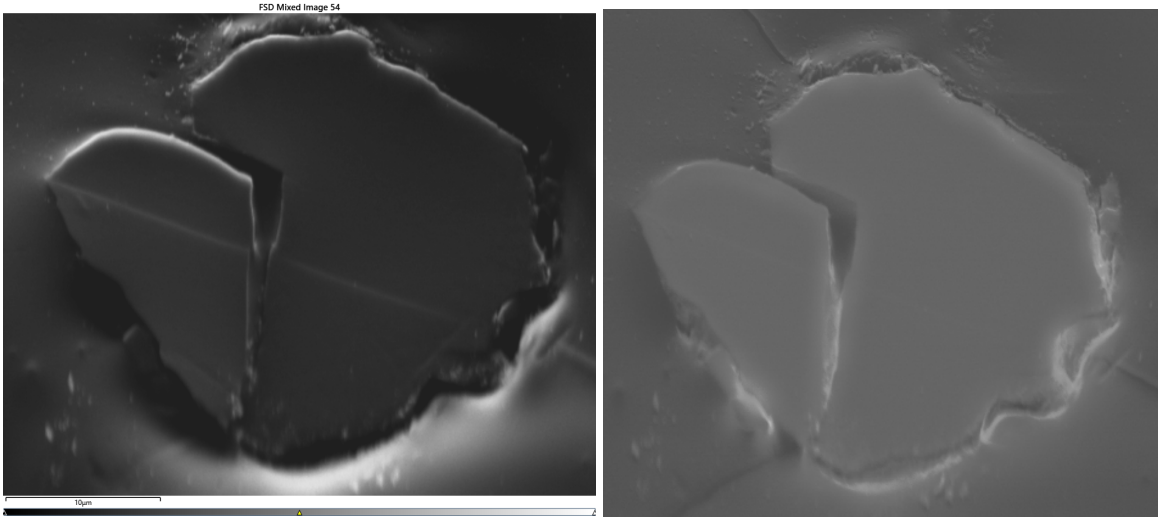
FSD Mixed Image S4
10µm

S_M2_3

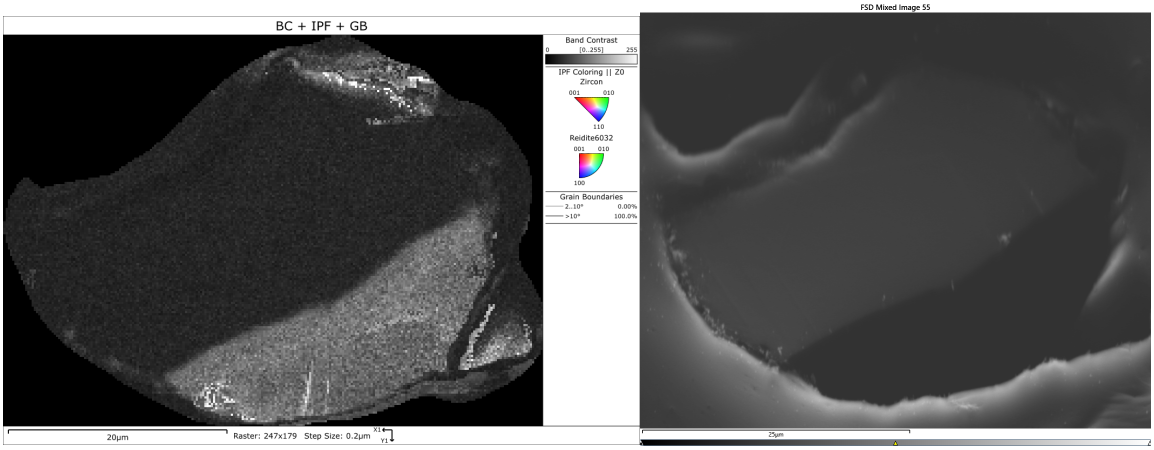
BC + IPF + GB
Band Contrast
0 [0..255] 255
IPF Coloring || Z0
Zircon
001 010
110
Reidite6032
001 010
100
Grain Boundaries
2..10° 0.00%
>10° 100.0%
20µm
Raster: 247x179 Step Size: 0.2µm
X1
Y1
FSD Mixed Image 55
25µm

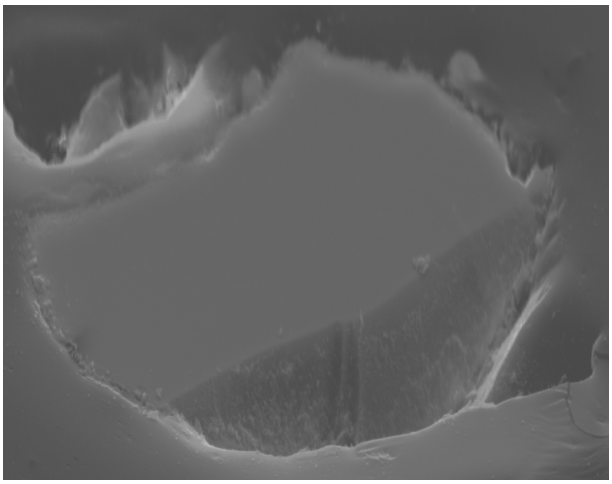

S_M2_5

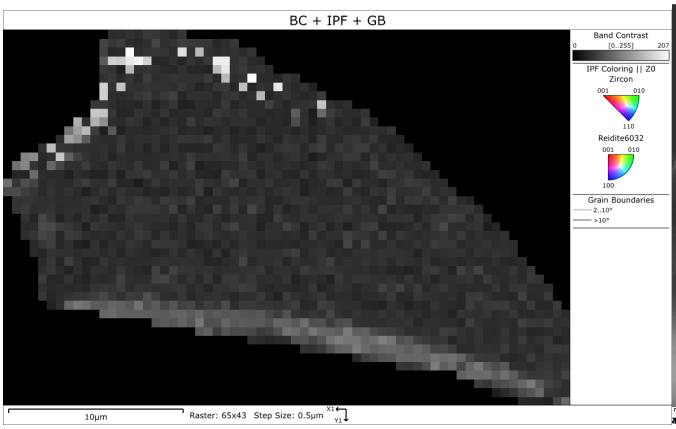
BC + IPF + GB
Band Contrast
0
[0..255]
207
IPF Coloring || Z0
Zircon
001
010
110
Reidite6032
001
010
100
Grain Boundaries
2..10°
>10°
10µm
Raster: 65x43 Step Size: 0.5µm
X1
Y1

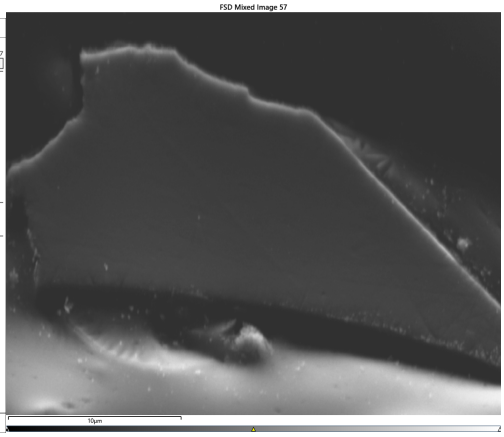
FSD Mixed Image 57
10µm

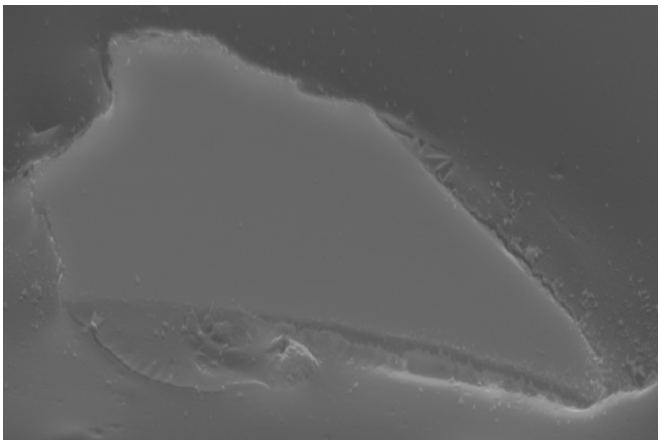

S_M2_6

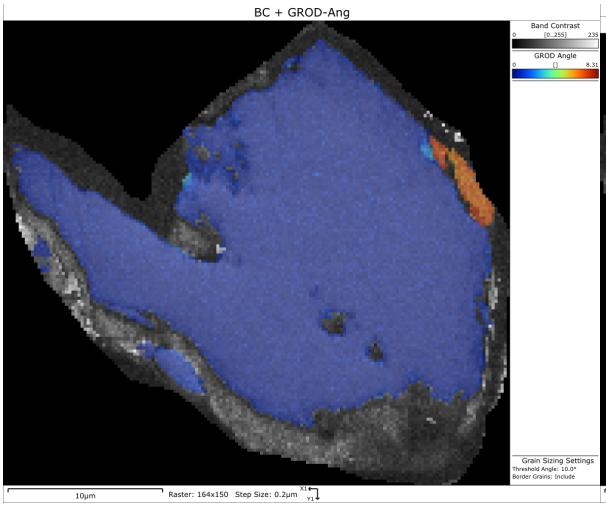
BC + GROD-Ang
Band Contrast
GROD Angle
Grain Sizing Settings
10µm
Raster: 164x150 Step Size: 0.2µm

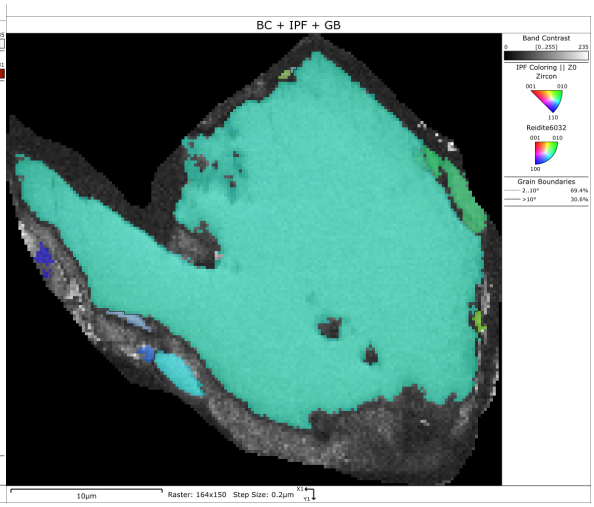
BC + IPF + GB
Band Contrast
IPF Coloring || Z0
Zircon
Reidite6032
Grain Boundaries
10µm
Raster: 164x150 Step Size: 0.2µm

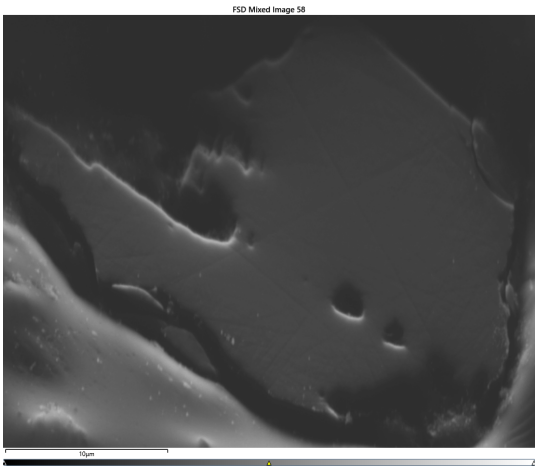
FSD Mixed Image 58
10µm

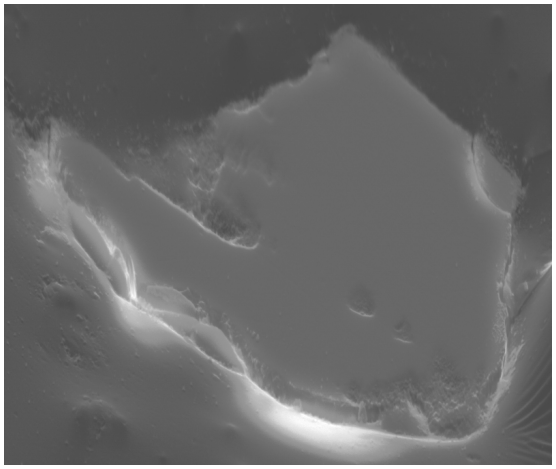

S_M2_7

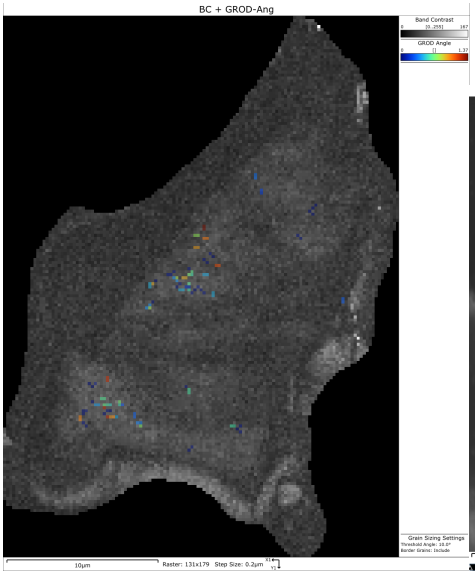
BC + GROD-Ang
Band Contrast
GROD Angle
10µm
Raster: 131x179 Step Size: 0.2µm

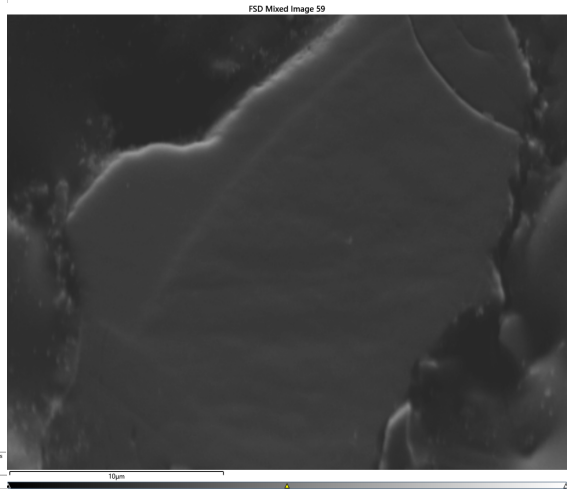
FSD Mixed Image 59
10µm

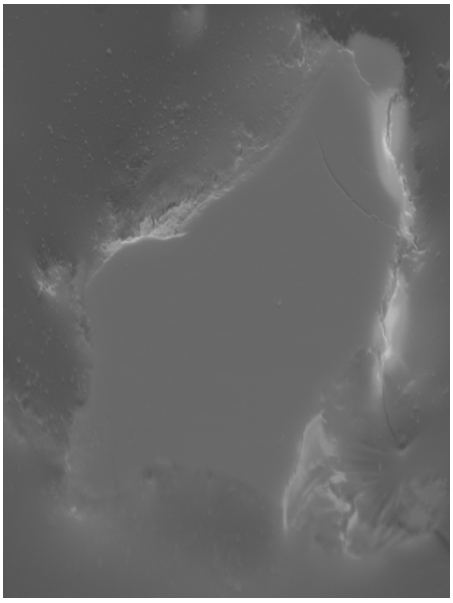

S_M2_8

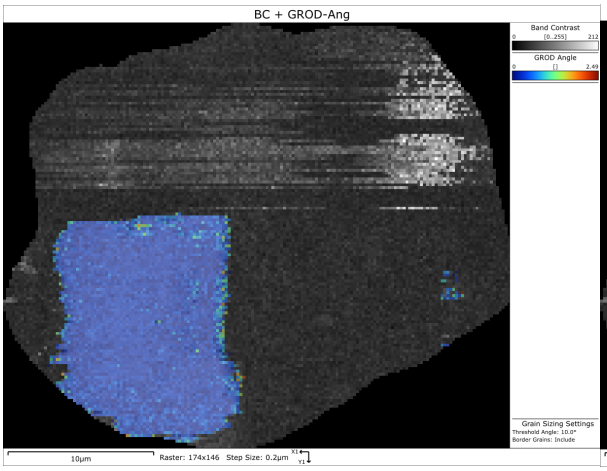
BC + GROD-Ang
Band Contrast
GROD Angle
Grain Sizing Settings
10µm
Raster: 174x146 Step Size: 0.2µm

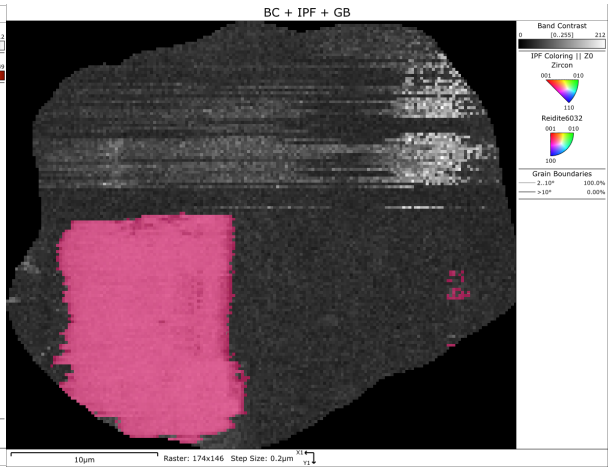
BC + IPF + GB
Band Contrast
IPF Coloring || Z0
Zircon
Reidite6032
Grain Boundaries
10µm
Raster: 174x146 Step Size: 0.2µm

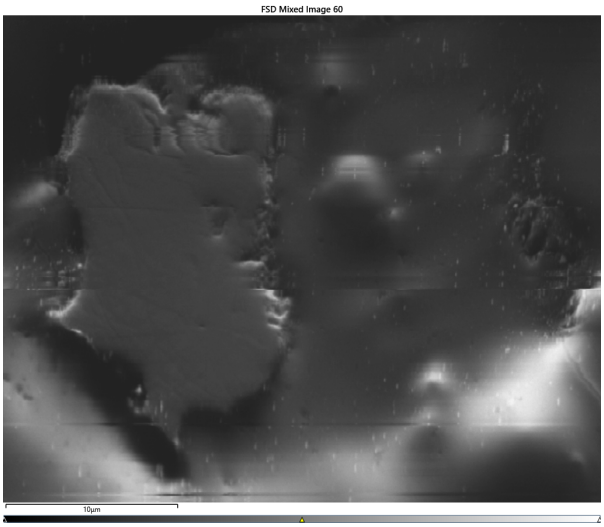
FSD Mixed Image 60
10µm

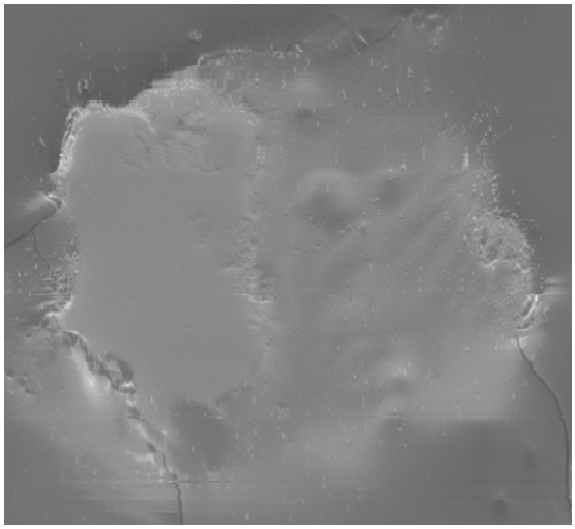

S_M2_16

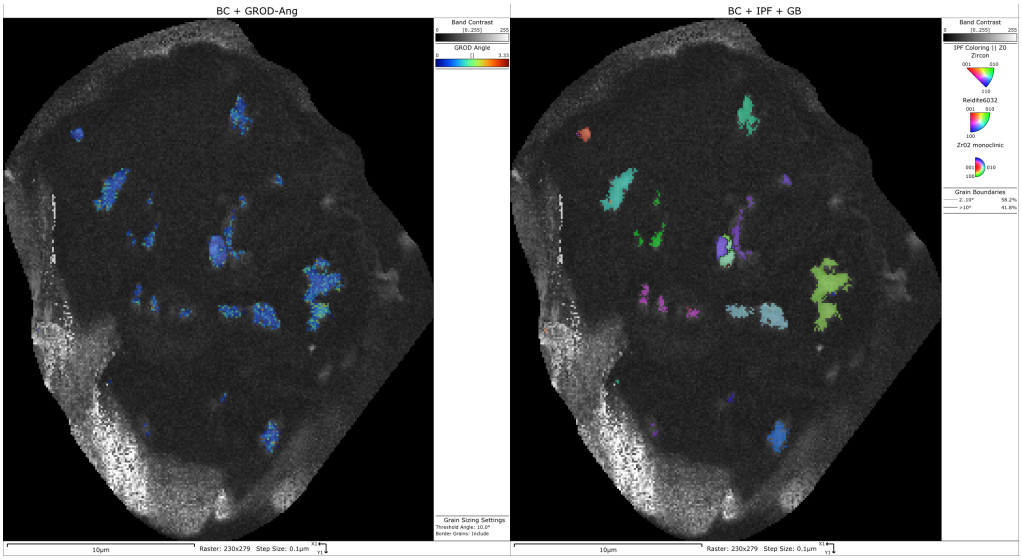
BC + GROD-Ang
Band Contrast
GROD Angle
Grain Sizing Settings
10µm
Raster: 230x279 Step Size: 0.1µm
BC + IPF + GB
Band Contrast
IPF Coloring || Z0
Zircon
Reidite6032
Zr02 monoclinic
Grain Boundaries
10µm
Raster: 230x279 Step Size: 0.1µm

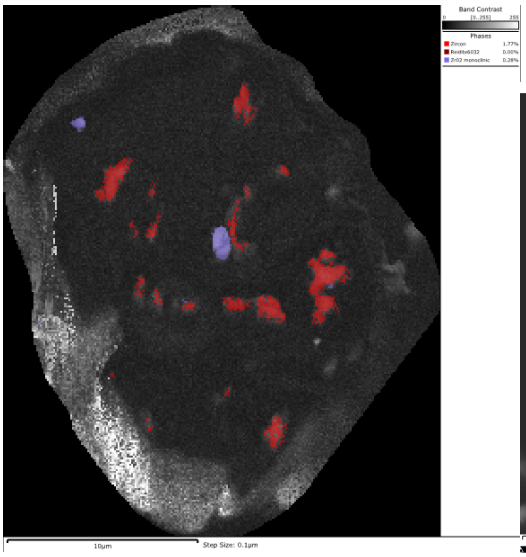
Band Contrast
Phases
Zircon 1.77%
Reidite6032 0.00%
Zr02 monoclinic 0.28%
10µm
Step Size: 0.1µm

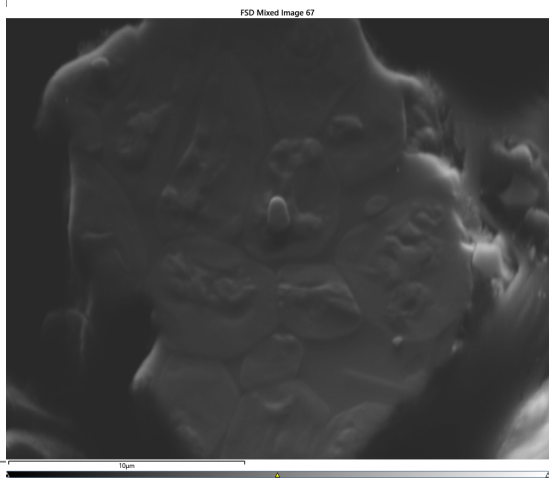
FSD Mixed Image 67
10µm

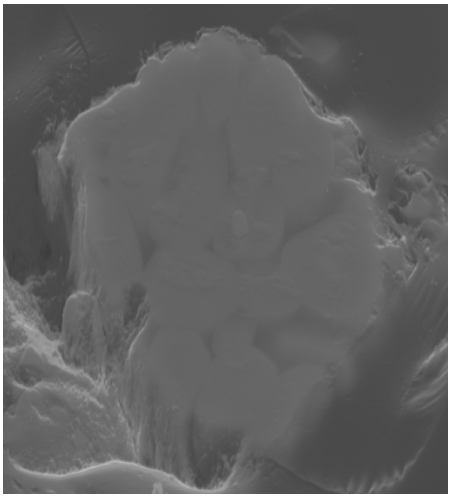

S_M2_17

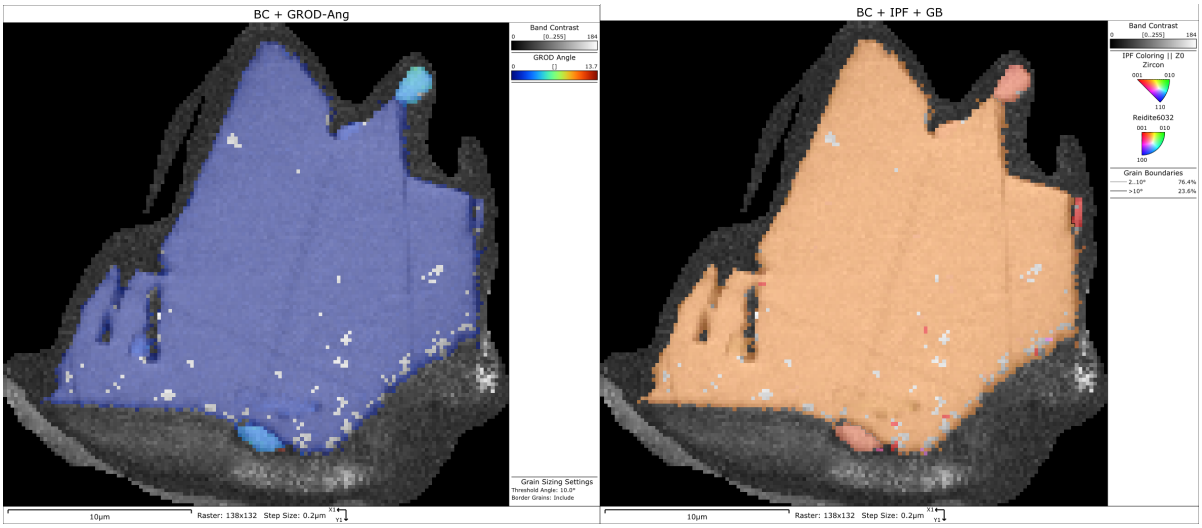
BC + GROD-Ang
Band Contrast
GROD Angle
Grain Sizing Settings
10µm
Raster: 138x132 Step Size: 0.2µm
BC + IPF + GB
Band Contrast
IPF Coloring || Z0
Zircon
Reidite6032
Grain Boundaries
10µm
Raster: 138x132 Step Size: 0.2µm

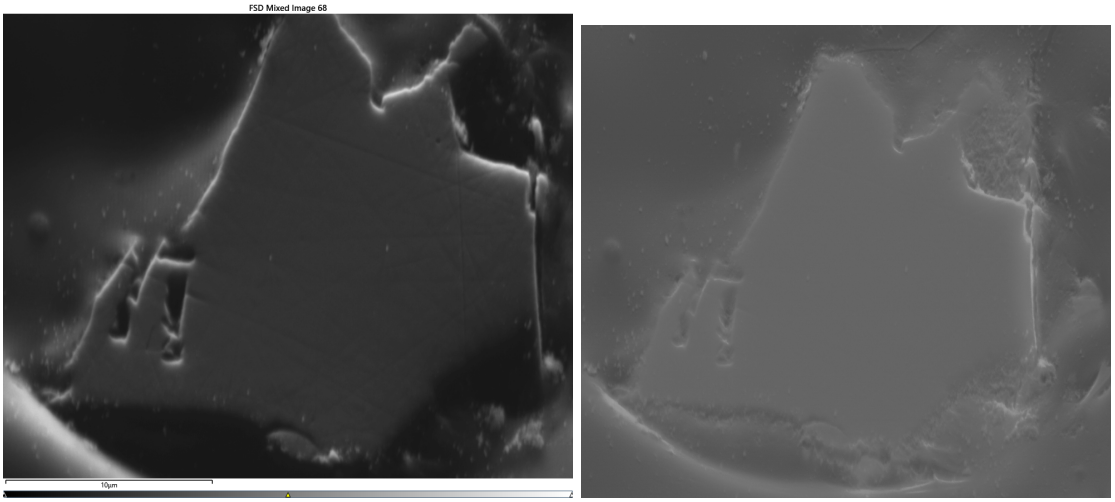
FSD Mixed Image 68
10µm

S_M2_18

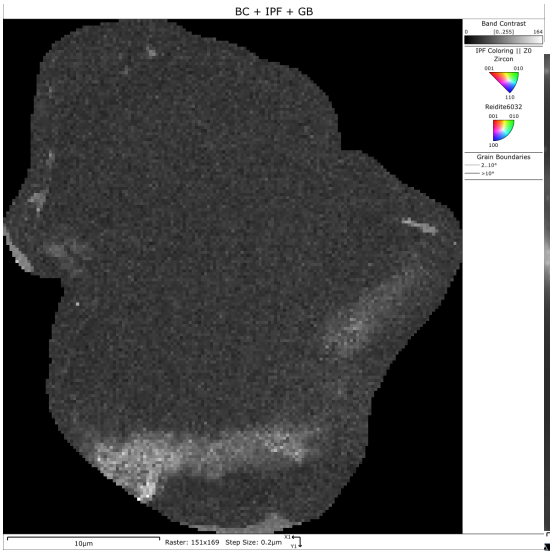
BC + IPF + GB
Band Contrast
IPF Coloring || Z0
Zircon
Reidite6032
Grain Boundaries
10µm
Raster: 151x169 Step Size: 0.2µm

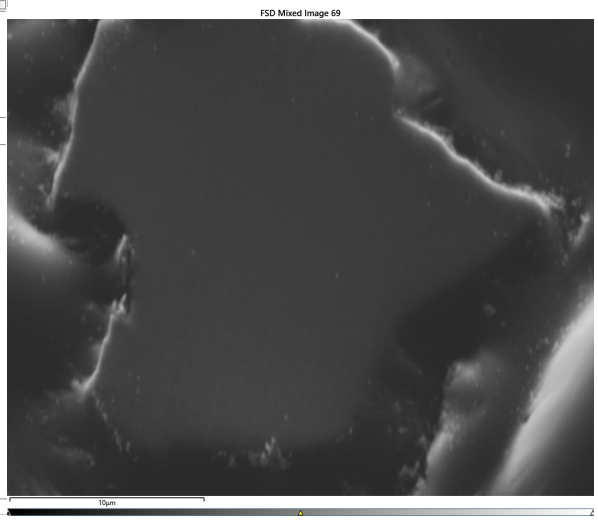
FSD Mixed Image 69
10µm

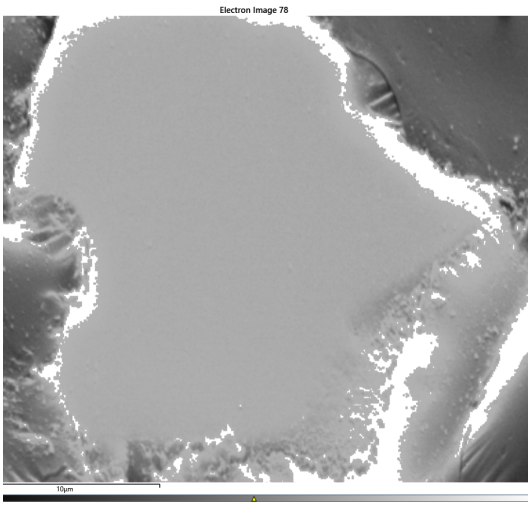
Electron Image 78
10µm

S_M2_19

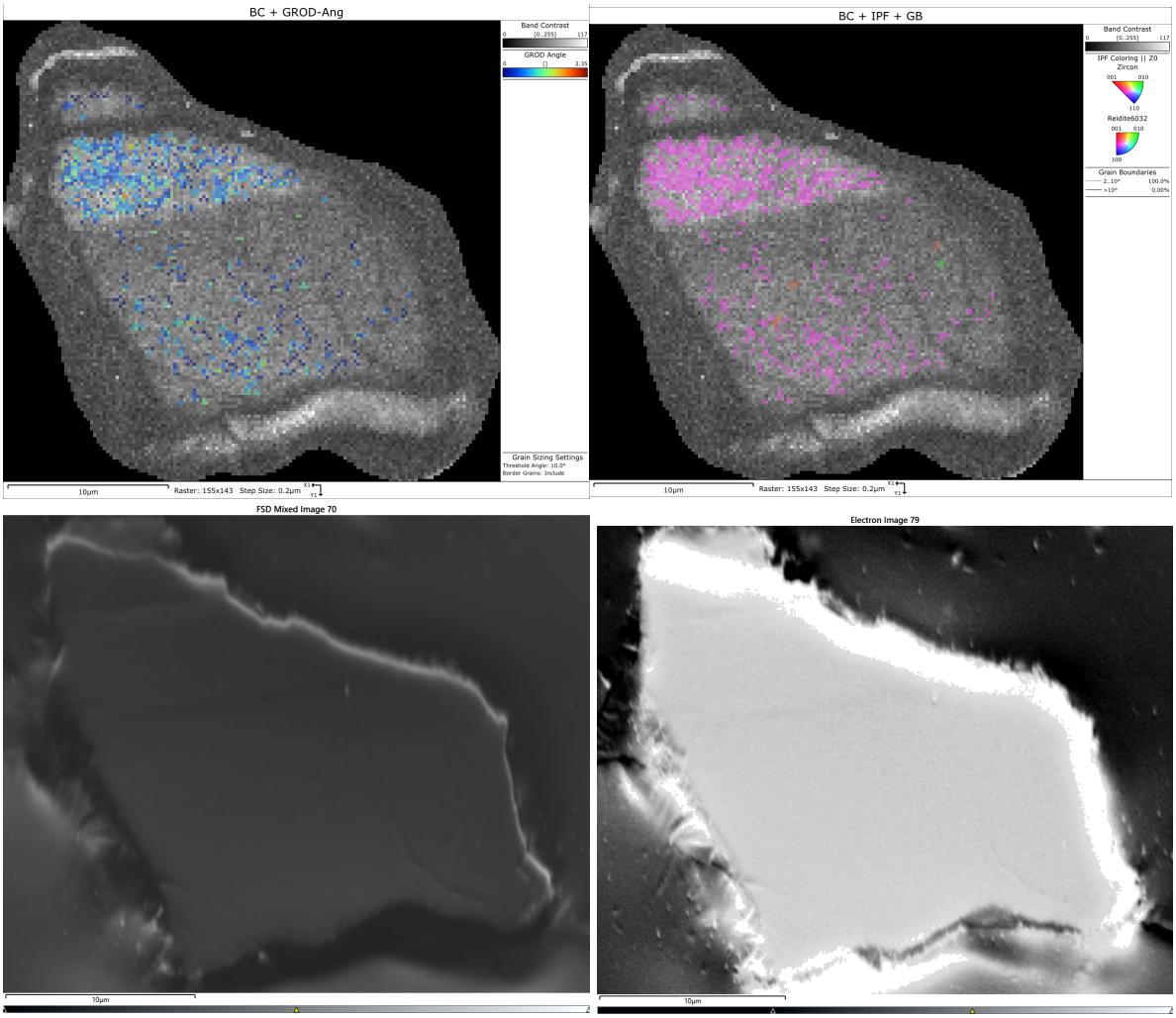
BC + GROD-Ang
Band Contrast
GROD Angle
Grain Sizing Settings
10µm
Raster: 155x143 Step Size: 0.2µm
BC + IPF + GB
Band Contrast
IPF Coloring || Z0
Zircon
Reidite6032
Grain Boundaries
10µm
Raster: 155x143 Step Size: 0.2µm
FSD Mixed Image 70
10µm
Electron Image 79
10µm

S_M2_20

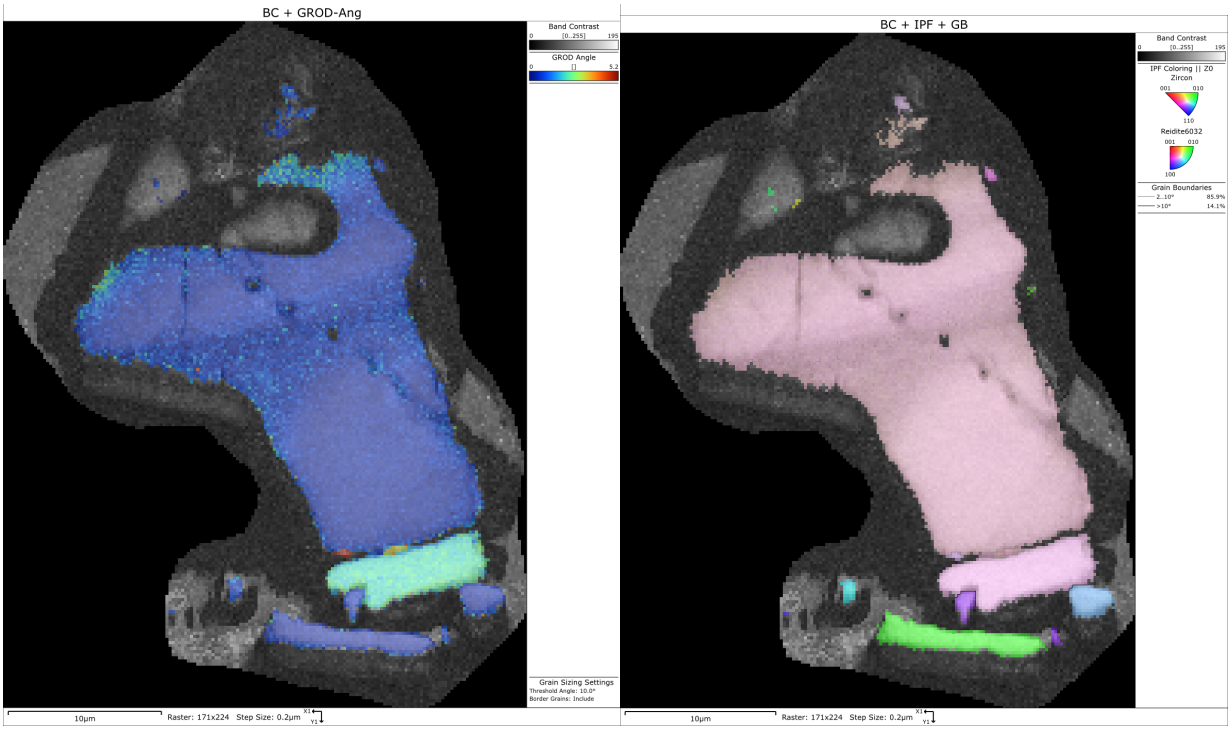
BC + GROD-Ang
Band Contrast
GROD Angle
Grain Sizing Settings
10µm
Raster: 171x224 Step Size: 0.2µm
BC + IPF + GB
Band Contrast
IPF Coloring || ZO
Zircon
Reidite6032
Grain Boundaries
10µm
Raster: 171x224 Step Size: 0.2µm

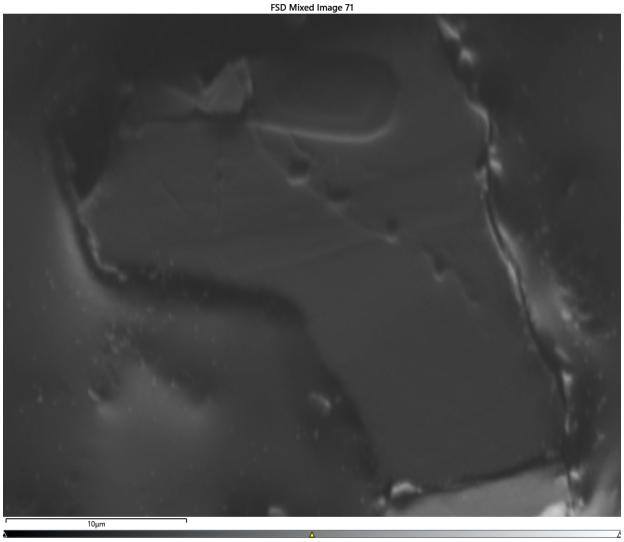
FSD Mixed Image 71
10µm

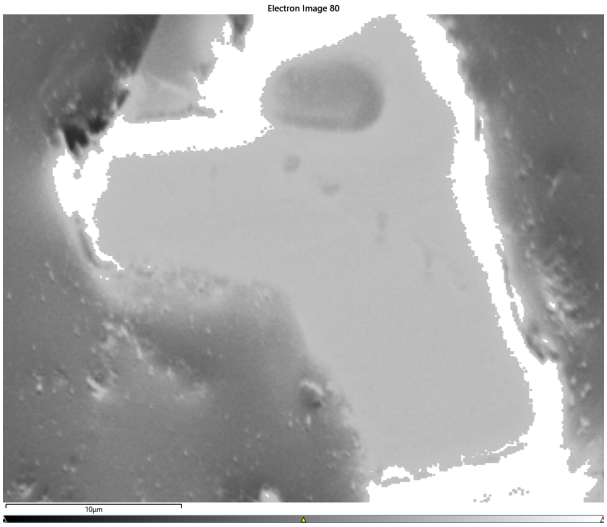
Electron Image 80
10µm

S_M2_21

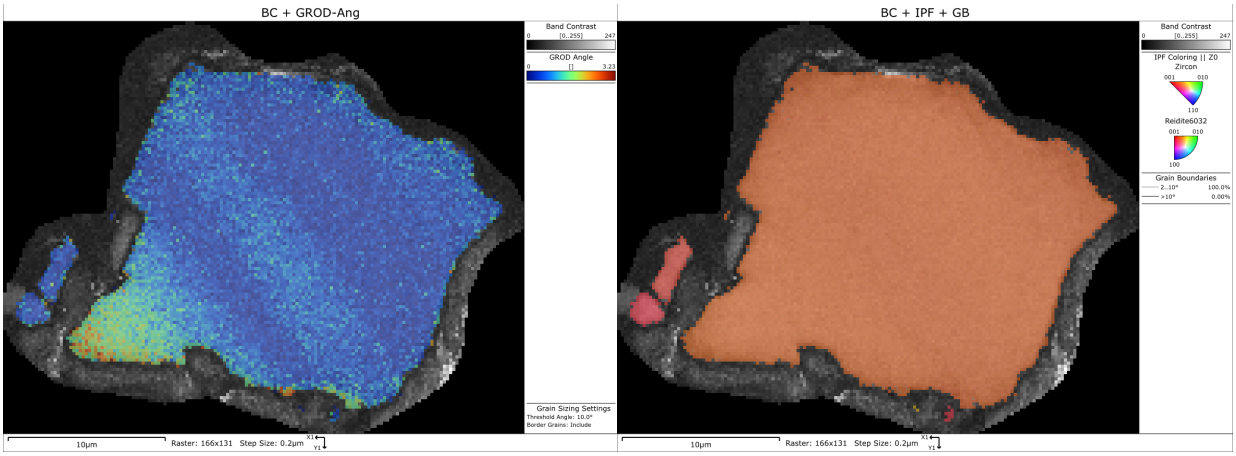
BC + GROD-Ang
Band Contrast
GROD Angle
Grain Sizing Settings
10µm
Raster: 166x131 Step Size: 0.2µm
BC + IPF + GB
Band Contrast
IPF Coloring || Z0
Zircon
Reidite6032
Grain Boundaries
10µm
Raster: 166x131 Step Size: 0.2µm

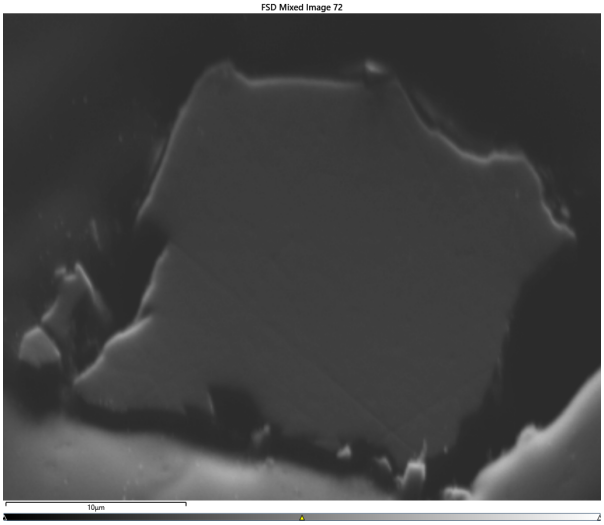
FSD Mixed Image 72
10µm


Electron Image 81
10µm

S_M2_22

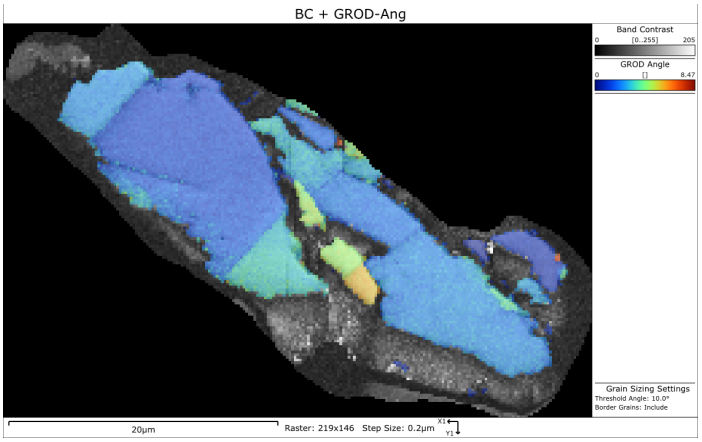
BC + GROD-Ang
Band Contrast
0 [0..255] 205
GROD Angle
0 [] 8.47
Grain Sizing Settings
Threshold Angle: 10.0°
Border Grains: Include
20µm
Raster: 219x146 Step Size: 0.2µm

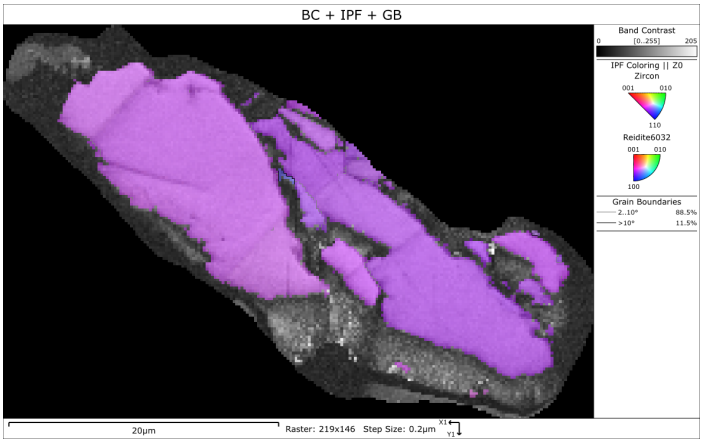
BC + IPF + GB
Band Contrast
0 [0..255] 205
IPF Coloring || Z0
Zircon
001 010
110
Reidite6032
001 010
100
Grain Boundaries
2..10° 88.5%
>10° 11.5%
20µm
Raster: 219x146 Step Size: 0.2µm

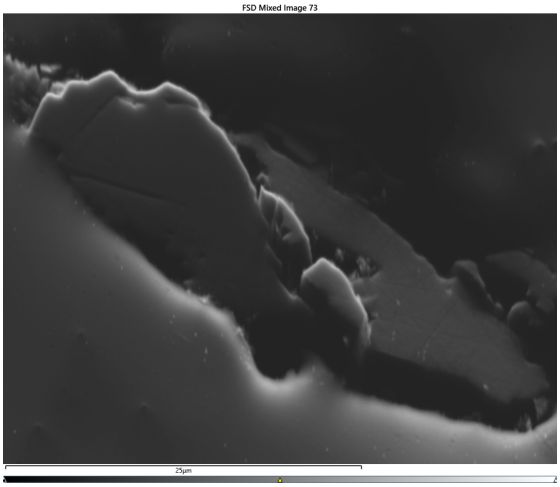
FSD Mixed Image 73
25µm

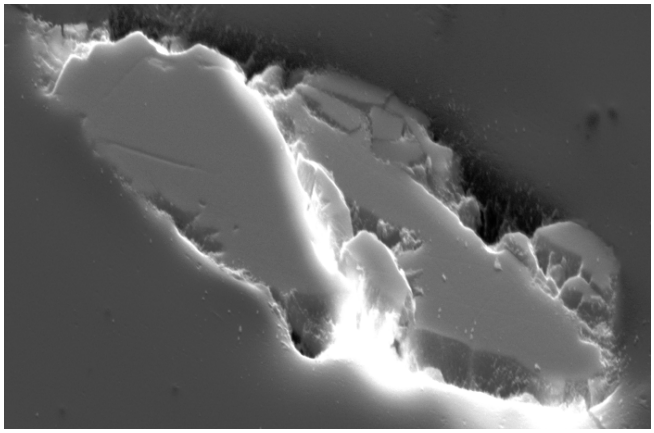

S_M2_23

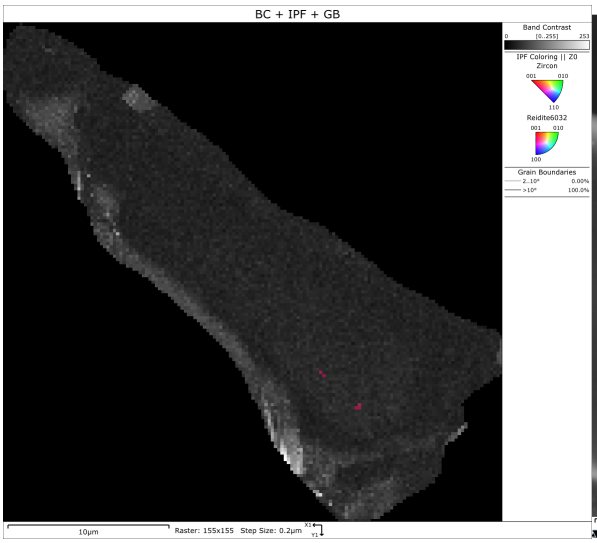
BC + IPF + GB
Band Contrast
IPF Coloring || Z0
Zircon
Reidite6032
Grain Boundaries
10µm
Raster: 155x155 Step Size: 0.2µm

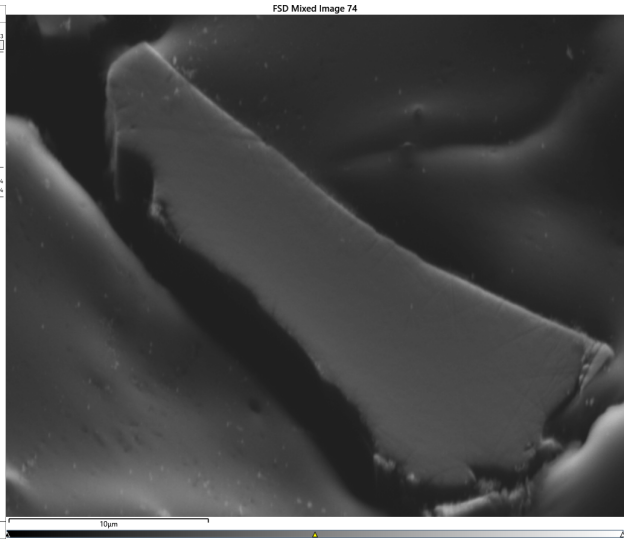
FSD Mixed Image 74
10µm

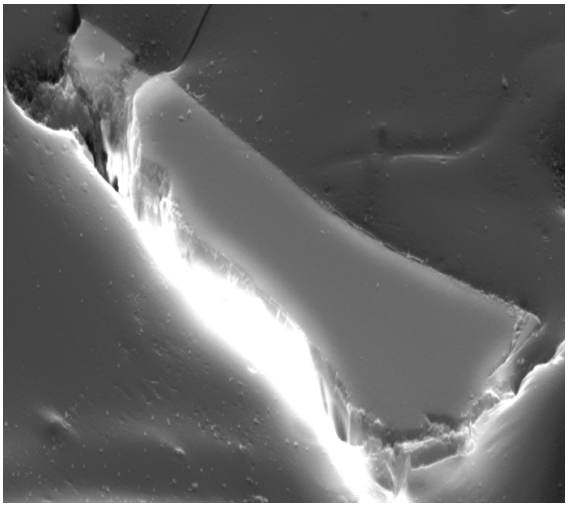

S_M2_24

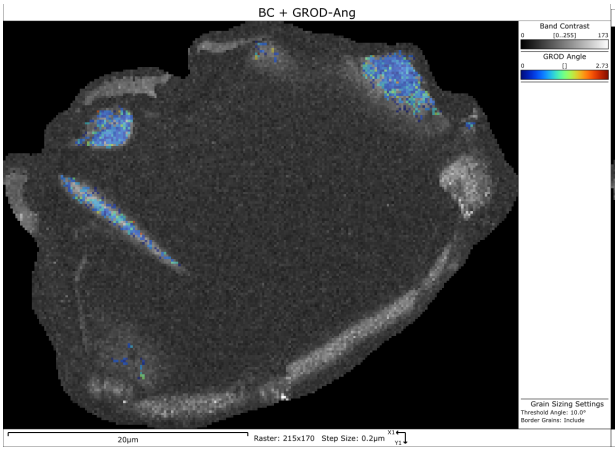
BC + GROD-Ang
Band Contrast
0 [0..255] 173
GROD Angle
0 [] 2.73
Grain Sizing Settings
Threshold Angle: 10.0°
Border Grains: Include
20µm
Raster: 215x170 Step Size: 0.2µm

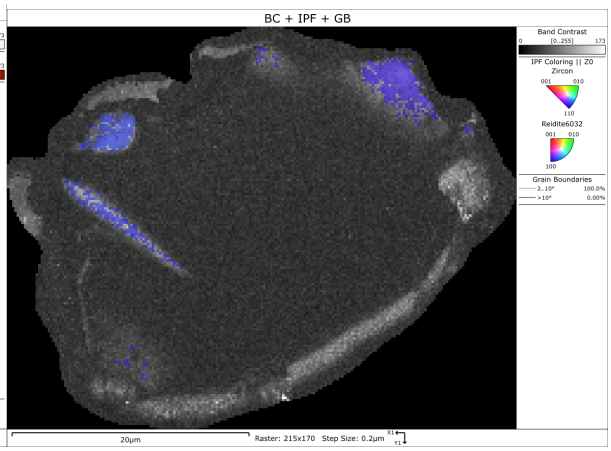
BC + IPF + GB
Band Contrast
0 [0..255] 173
IPF Coloring || Z0
Zircon
001 010
110
Reidite6032
001 010
100
Grain Boundaries
2..10° 100.0%
>10° 0.00%
20µm
Raster: 215x170 Step Size: 0.2µm

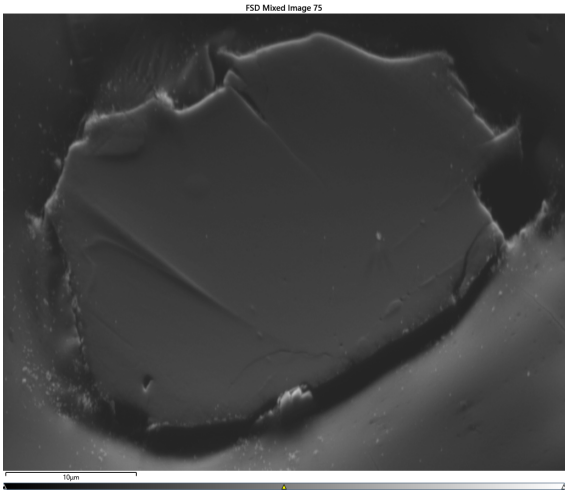
FSD Mixed Image 75
10µm

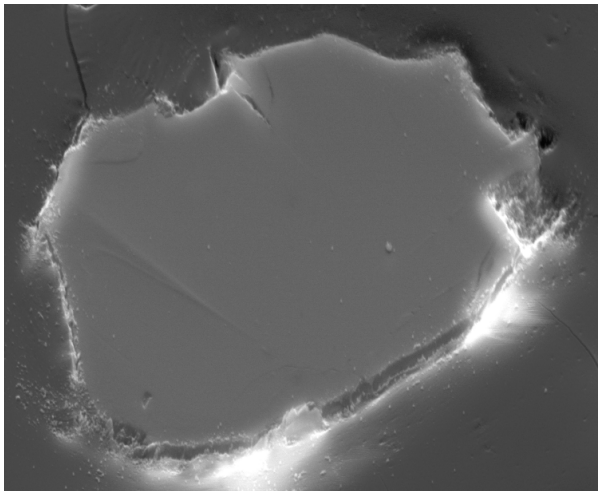

S_M2_25

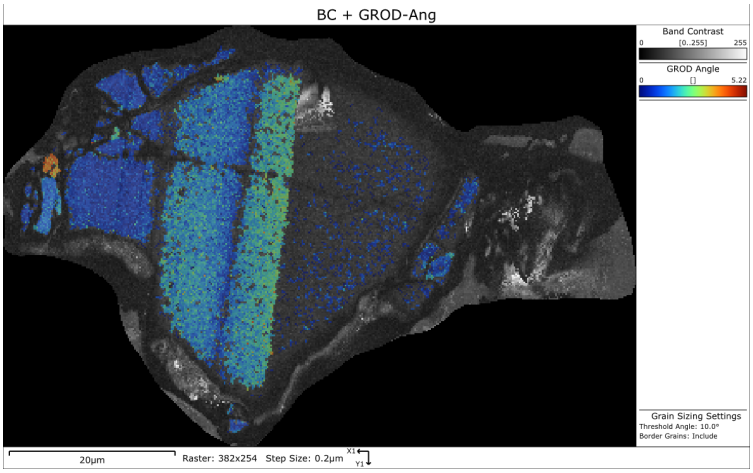
BC + GROD-Ang
Band Contrast
0 [0..255] 255
GROD Angle
0 [] 5.22
Grain Sizing Settings
Threshold Angle: 10.0°
Border Grains: Include
20µm
Raster: 382x254 Step Size: 0.2µm

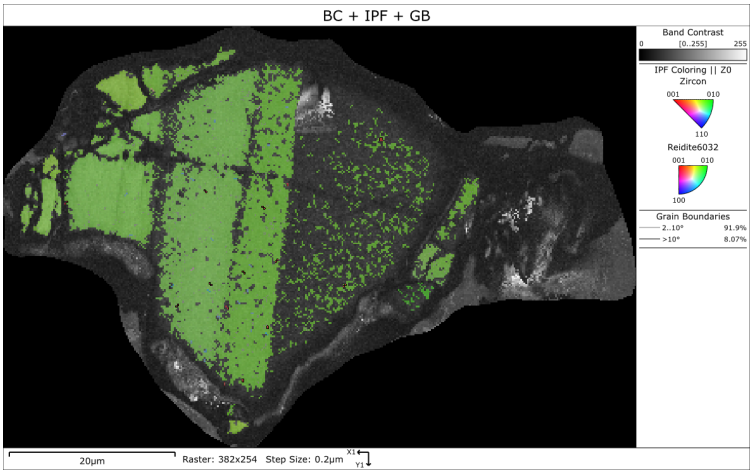
BC + IPF + GB
Band Contrast
0 [0..255] 255
IPF Coloring || Z0
Zircon
001 010
110
Reidite6032
001 010
100
Grain Boundaries
2..10° 91.9%
>10° 8.07%
20µm
Raster: 382x254 Step Size: 0.2µm

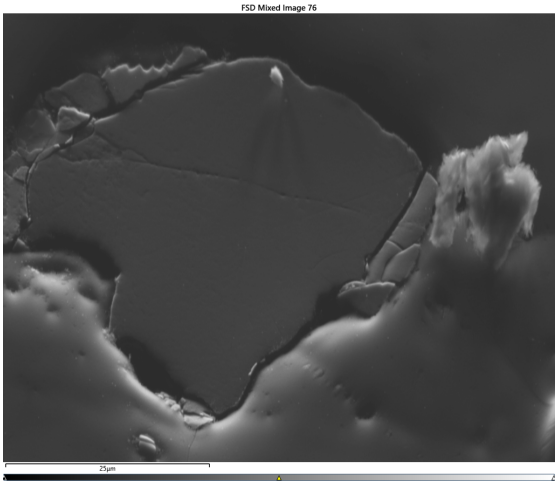
FSD Mixed Image 76
25µm

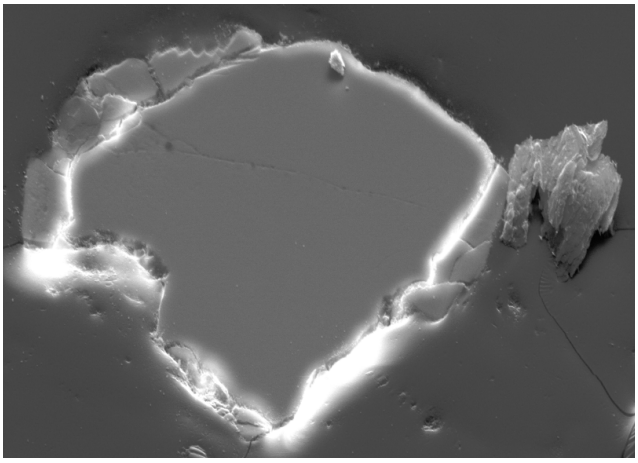

S_M2_26

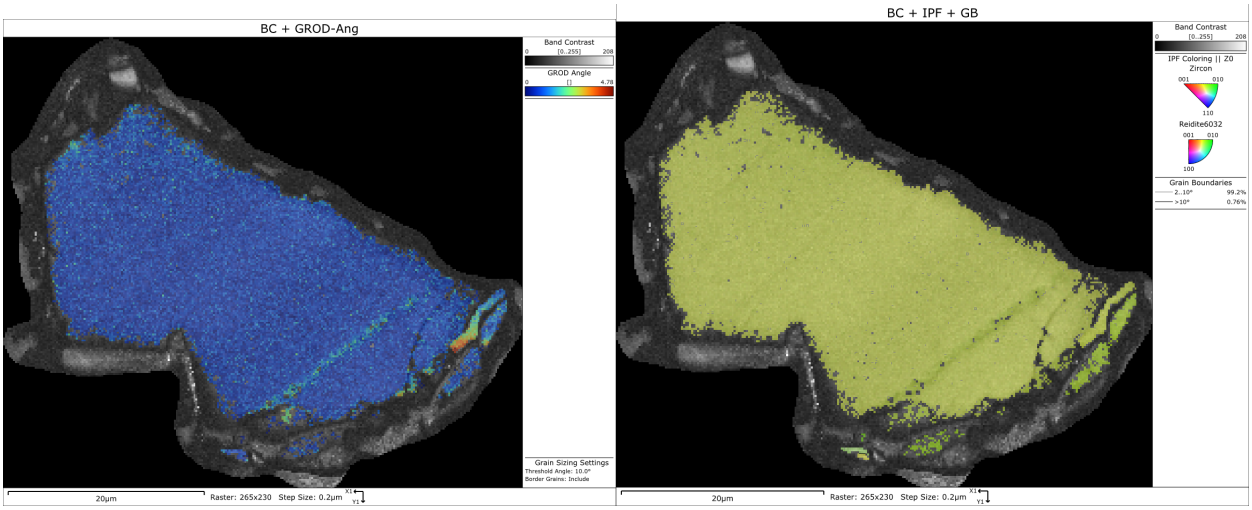
BC + GROD-Ang
Band Contrast
0 [0..255] 208
GROD Angle
0 [] 4.78
Grain Sizing Settings
Threshold Angle: 10.0°
Border Grains: Include
20µm
Raster: 265x230 Step Size: 0.2µm
BC + IPF + GB
Band Contrast
0 [0..255] 208
IPF Coloring || Z0
Zircon
001 010
110
Reidite6032
001 010
100
Grain Boundaries
2..10° 99.2%
>10° 0.76%
20µm
Raster: 265x230 Step Size: 0.2µm

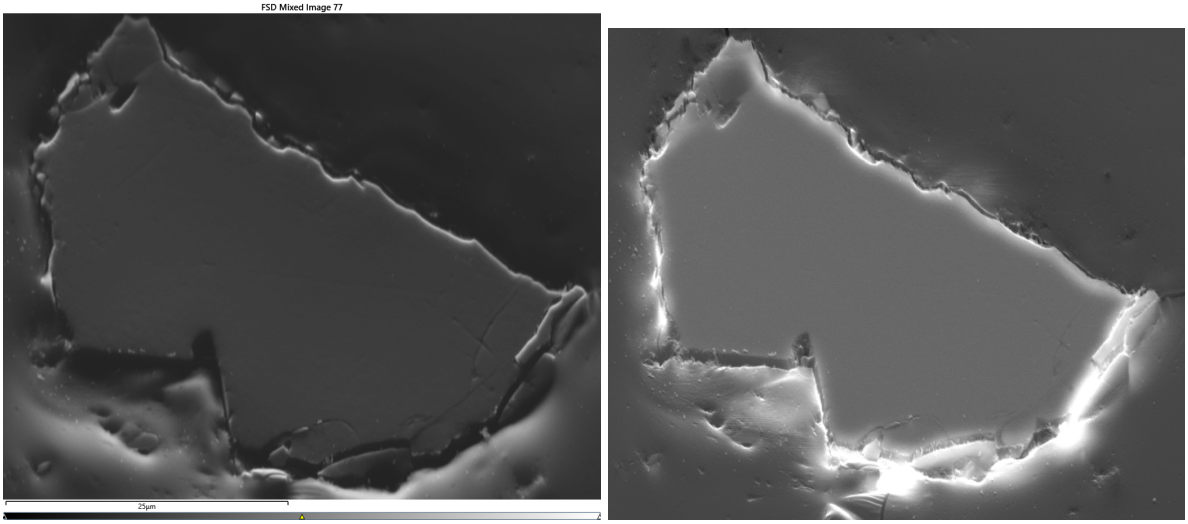
FSD Mixed Image 77
25µm

M_M2_5

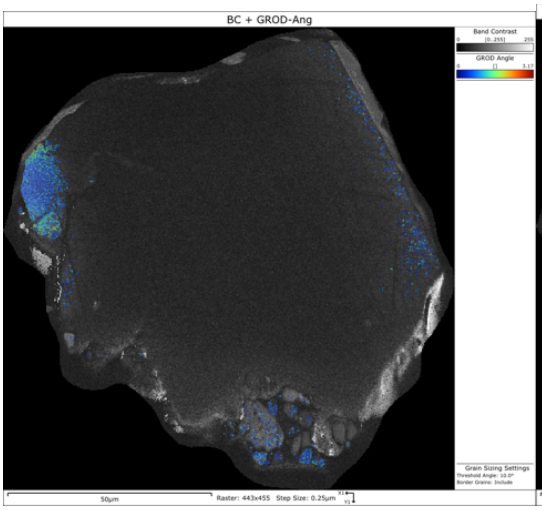
BC + GROD-Ang
Band Contrast
GROD Angle
Grain Sizing Settings
50µm
Raster: 443x455 Step Size: 0.25µm

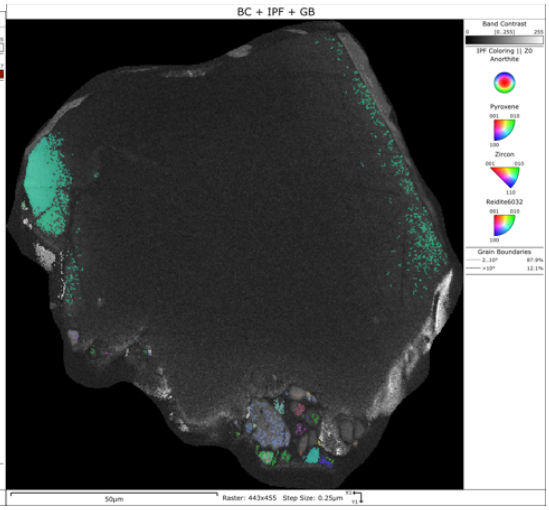
BC + IPF + GB
Band Contrast
IPF Coloring || Z0
Anorthite
Pyroxene
Zircon
Reidite6032
Grain Boundaries
50µm
Raster: 443x455 Step Size: 0.25µm

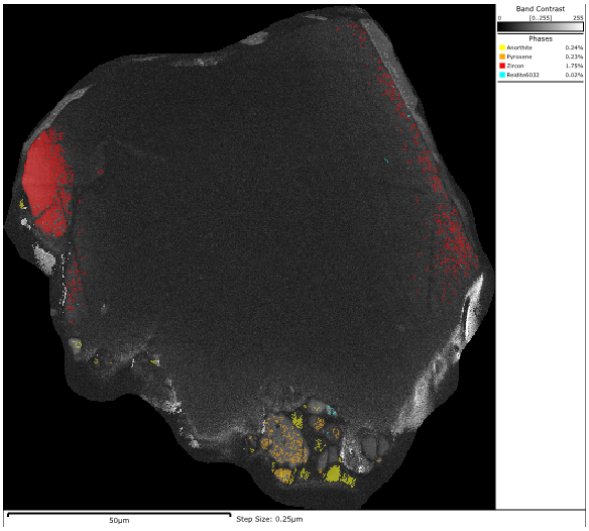
Band Contrast
Phases
Anorthite 0.24%
Pyroxene 0.23%
Zircon 1.75%
Reidite6032 0.02%
50µm
Step Size: 0.25µm

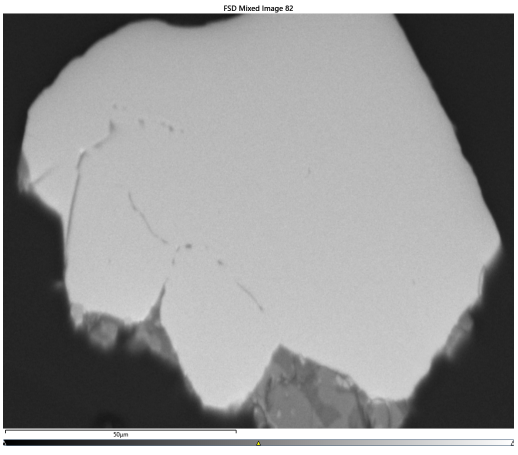
FSD Mixed Image 82
50µm

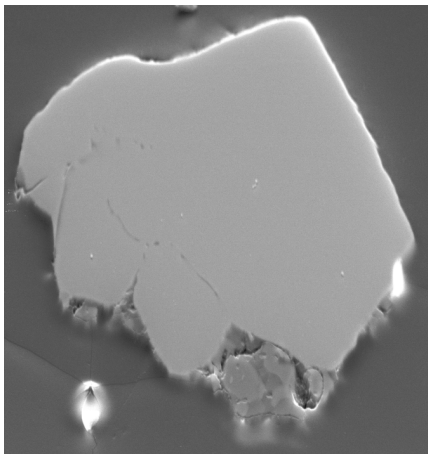

M_M2_9

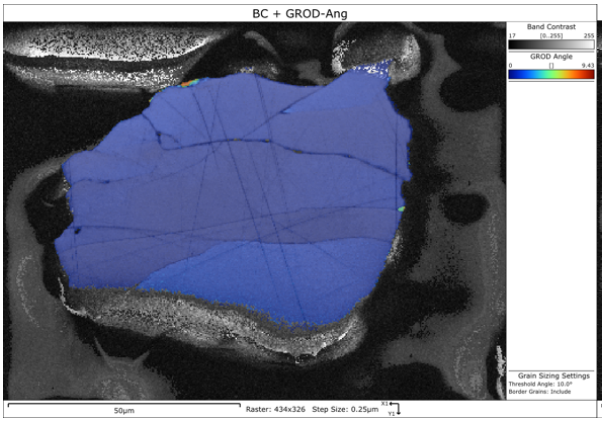

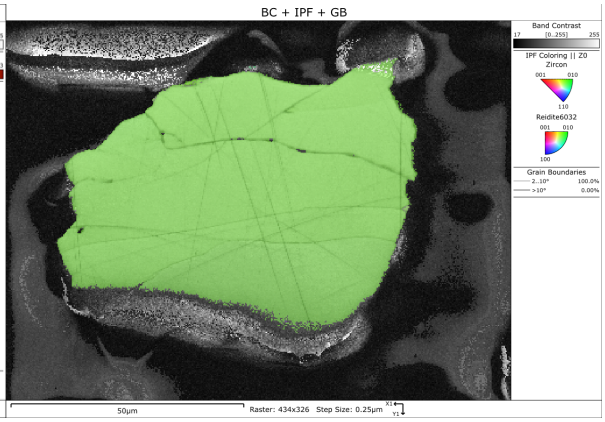

FSD Mixed Image 86

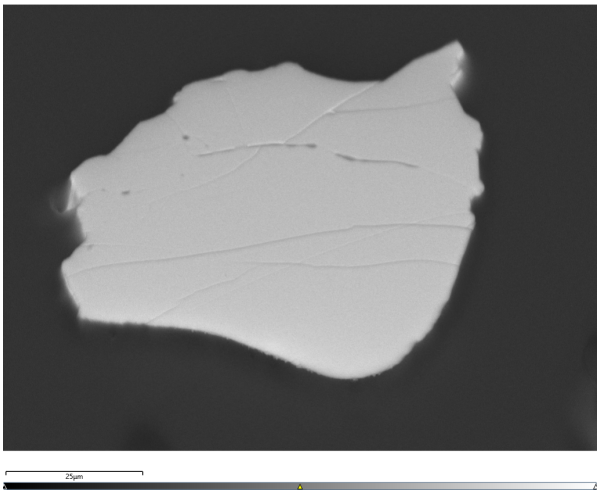

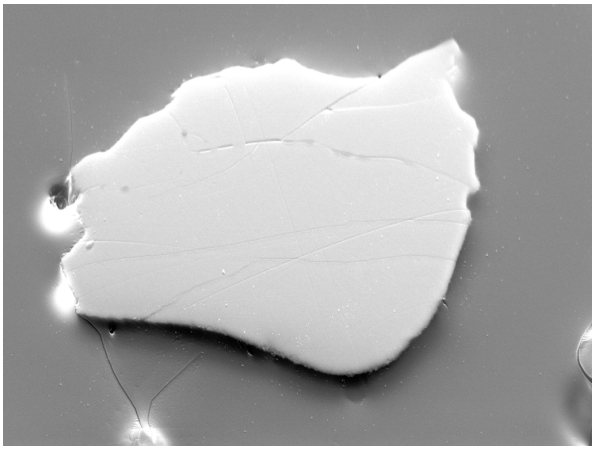

M_M2_10

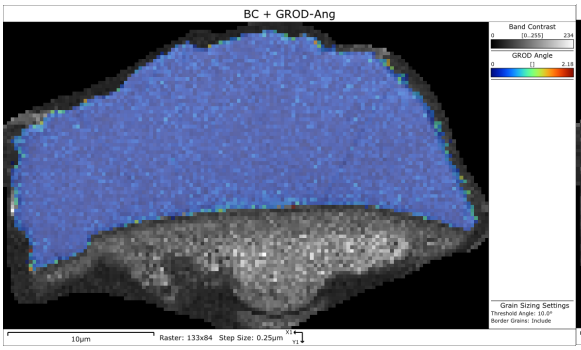
BC + GROD-Ang
Band Contrast
GROD Angle
Grain Sizing Settings
10µm
Raster: 133x84 Step Size: 0.25µm

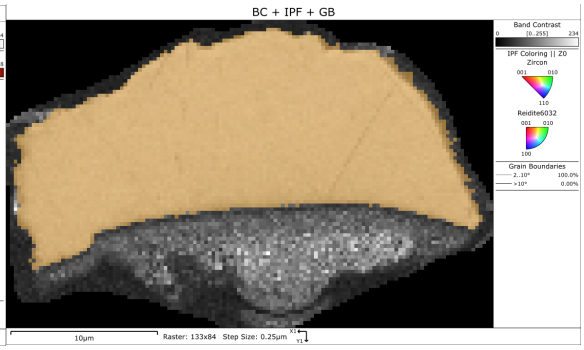
BC + IPF + GB
Band Contrast
IPF Coloring || Z0
Zircon
Reidite6032
Grain Boundaries
10µm
Raster: 133x84 Step Size: 0.25µm

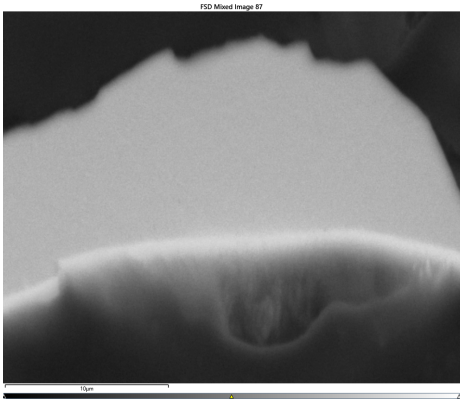
FSD Mixed Image 87

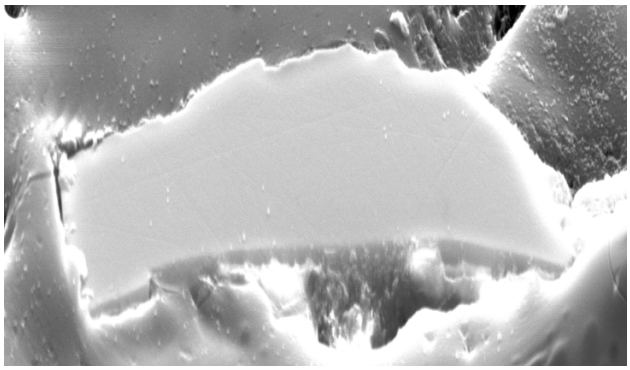

M_M2_11

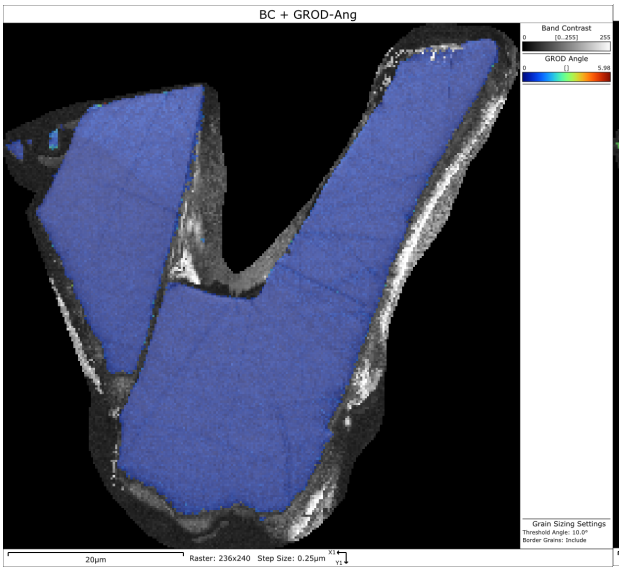
BC + GROD-Ang
Band Contrast
GROD Angle
Grain Sizing Settings
20µm
Raster: 236x240 Step Size: 0.25µm

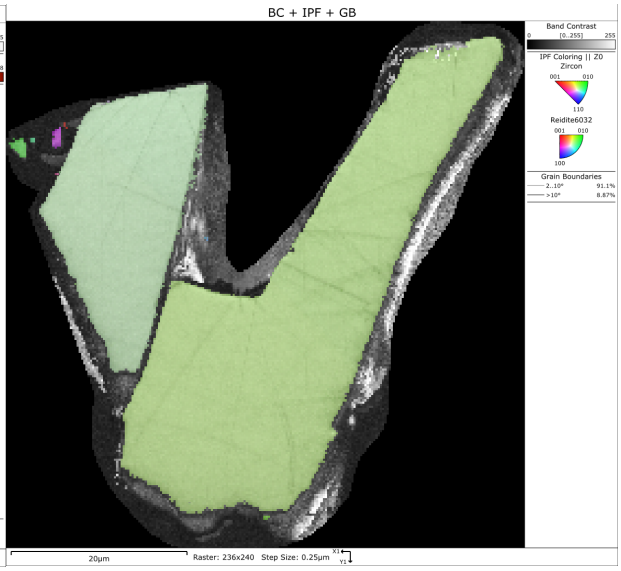
BC + IPF + GB
Band Contrast
IPF Coloring || Z0
Zircon
Reidite6032
Grain Boundaries
20µm
Raster: 236x240 Step Size: 0.25µm

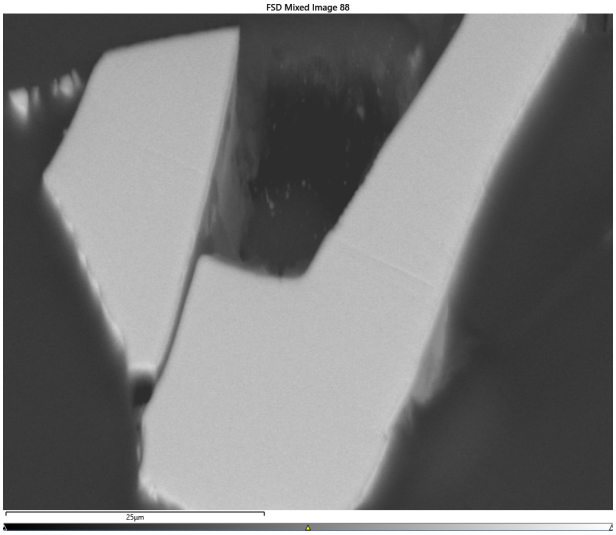
FSD Mixed Image 88
25µm

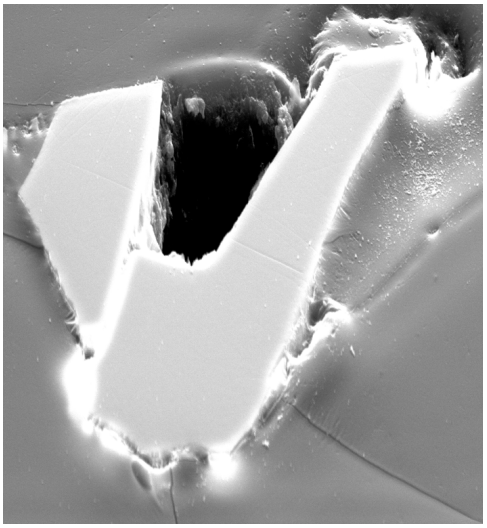

M_M2_12

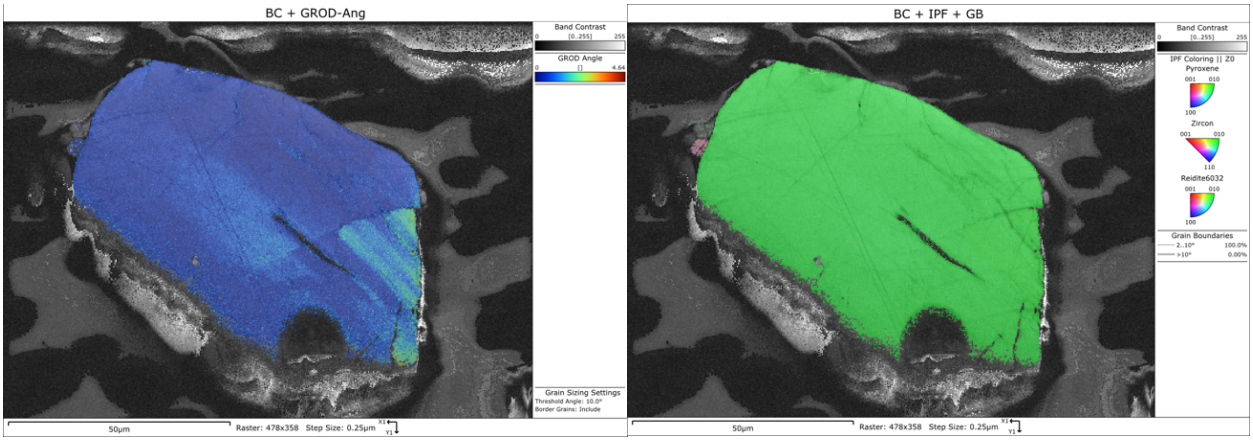

FSD Mixed Image 89

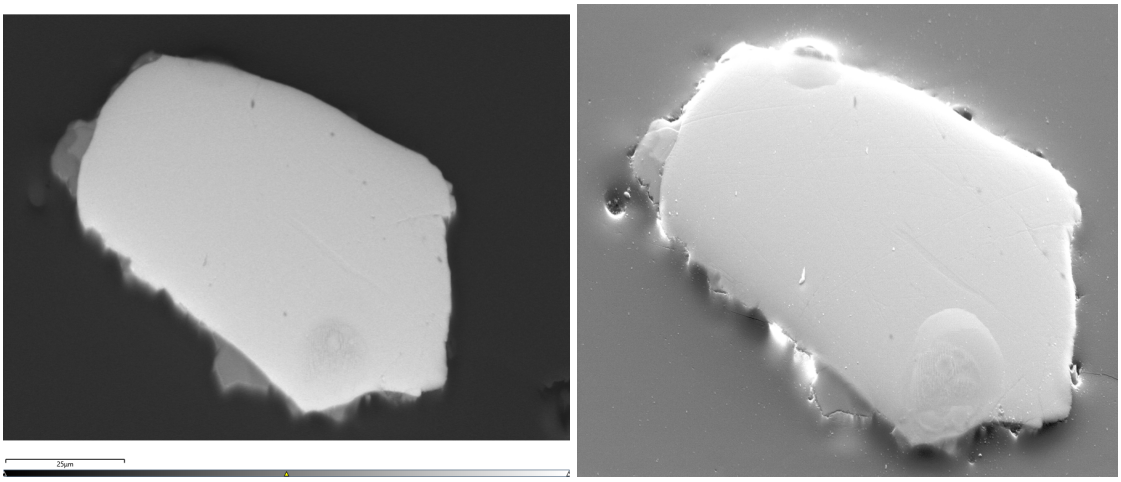

M_M2_13

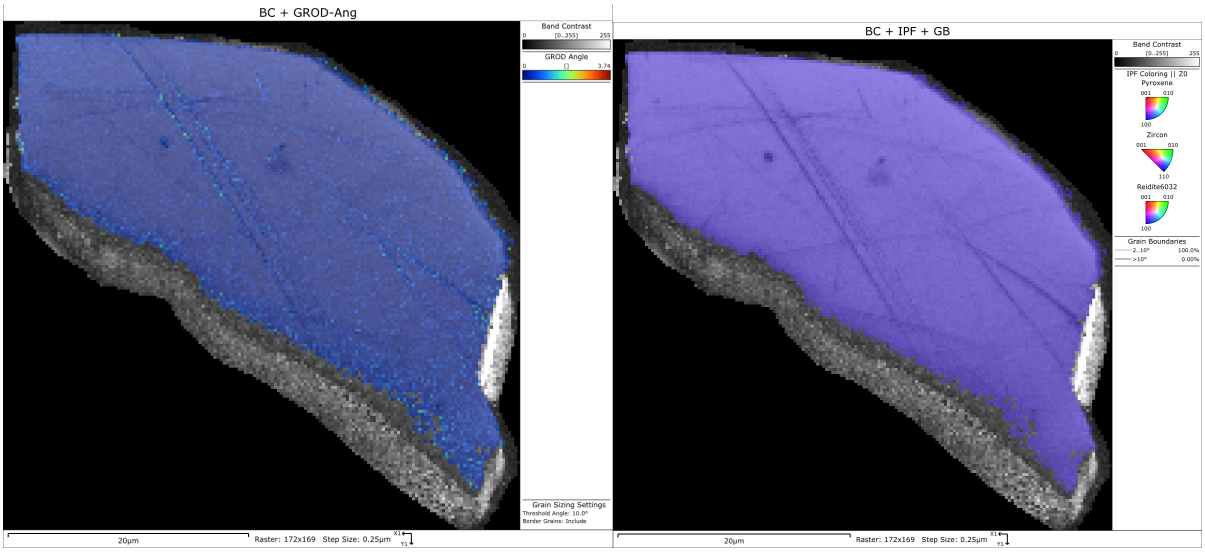
BC + GROD-Ang
Band Contrast
GROD Angle
Grain Sizing Settings
20µm
Raster: 172x169 Step Size: 0.25µm
BC + IPF + GB
Band Contrast
IPF Coloring || Z0
Pyroxene
Zircon
Reidite6032
Grain Boundaries
20µm
Raster: 172x169 Step Size: 0.25µm

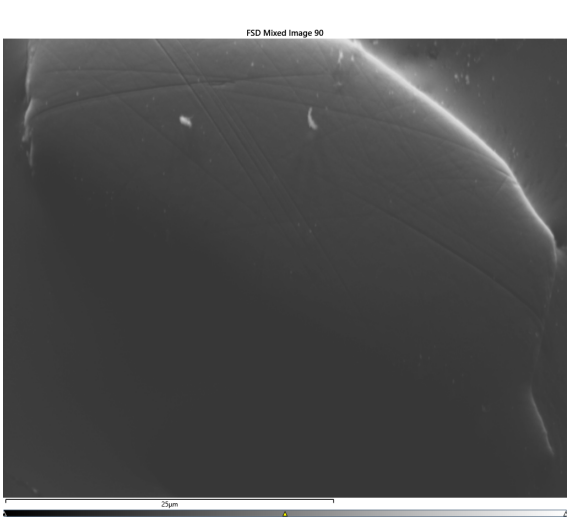
FSD Mixed Image 90
25µm

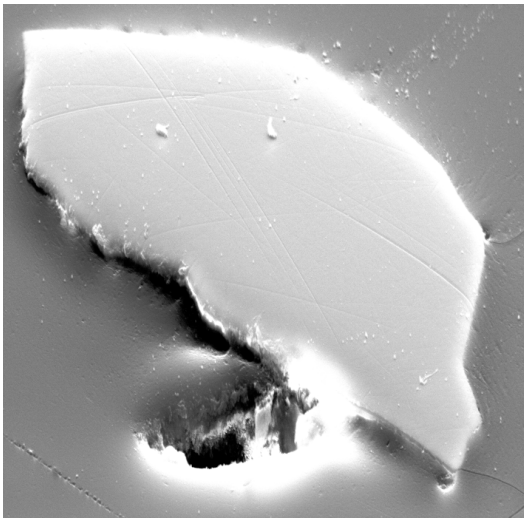

M_M2_14

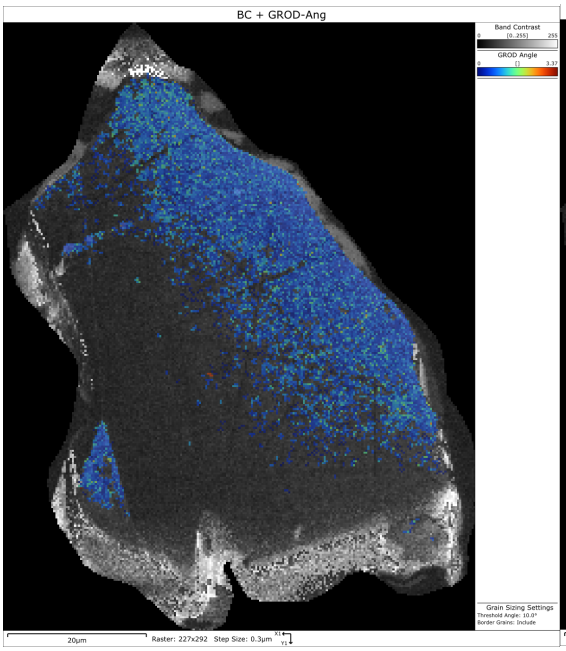
BC + GROD-Ang
Band Contrast
GROD Angle
Grain Sizing Settings
20µm
Raster: 227x292 Step Size: 0.3µm

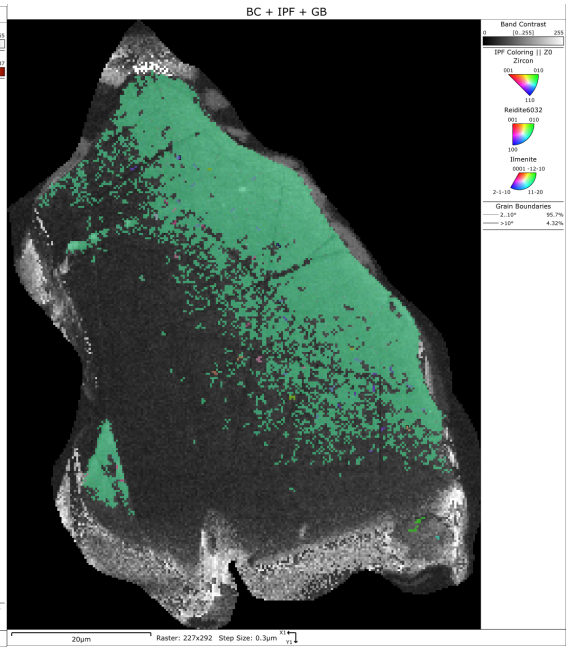
BC + IPF + GB
Band Contrast
IPF Coloring || Z0
Zircon
Reidfe6032
Ilmenite
Grain Boundaries
20µm
Raster: 227x292 Step Size: 0.3µm

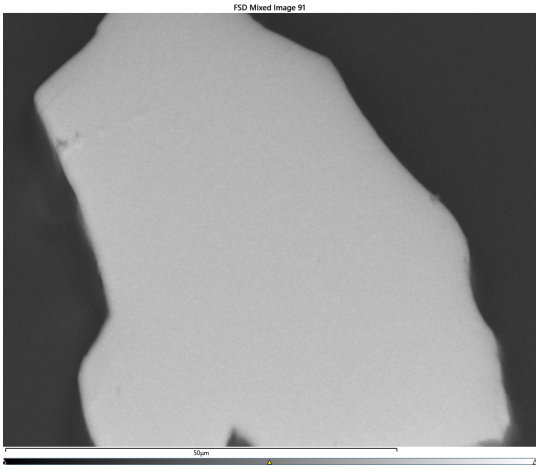
FSD Mixed Image 91
50µm

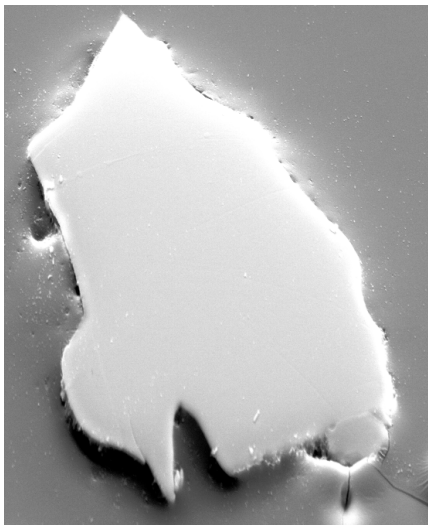

M_M2_15

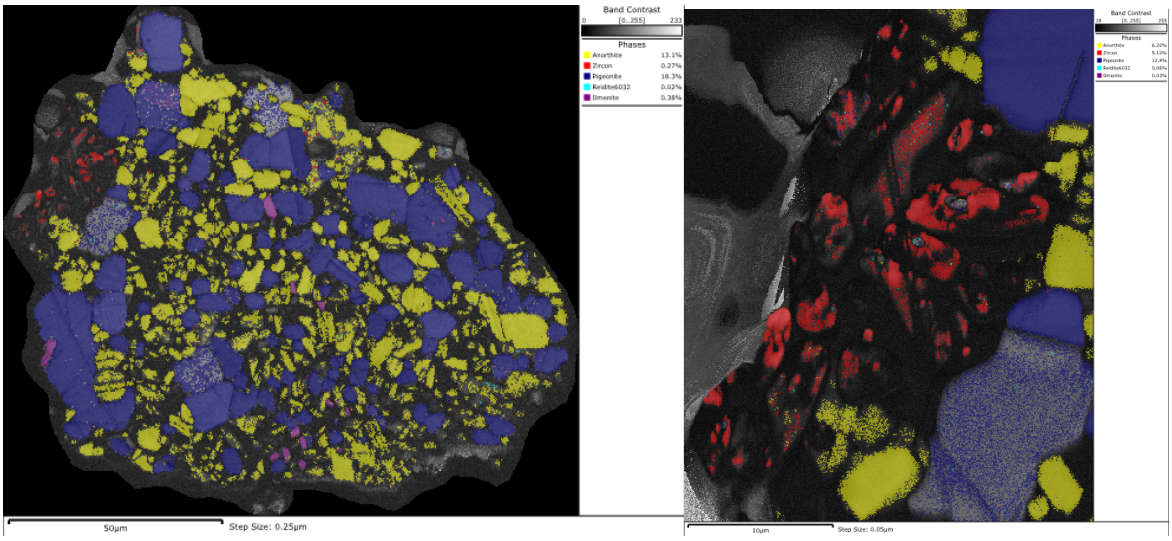
Band Contrast
Phases
Anorthite 13.1%
Zircon 0.27%
Pigeonite 18.3%
Rediite6032 0.02%
Ilmenite 0.38%
50µm
Step Size: 0.25µm
Band Contrast
Phases
Anorthite 6.20%
Zircon 5.10%
Pigeonite 12.4%
Rediite6032 0.06%
Ilmenite 0.03%
10µm
Step Size: 0.05µm

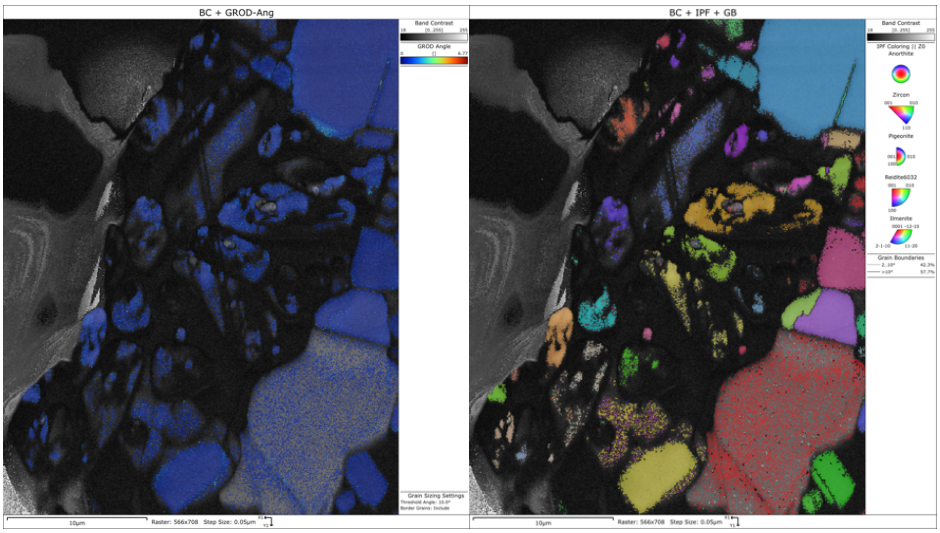
BC + GROD-Ang
Band Contrast
GROD Angle
Grain Sizing Settings
10µm
Raster: 566x708 Step Size: 0.05µm
BC + IPF + GB
Band Contrast
IPF Coloring || ZO
Anorthite
Zircon
Pigeonite
Rediite6032
Ilmenite
Grain Boundaries
10µm
Raster: 566x708 Step Size: 0.05µm

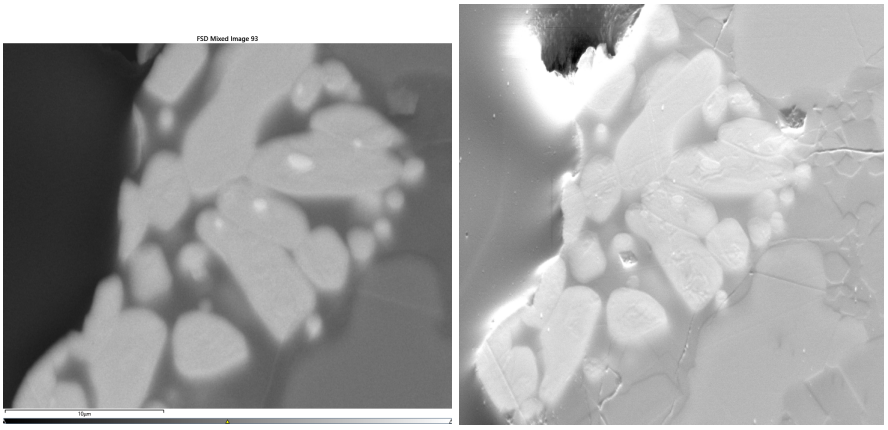
FSD Mixed Image 93
10µm

M_M2_17

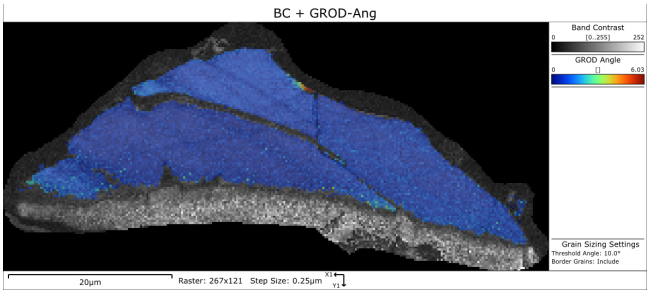
BC + GROD-Ang
Band Contrast
0 [0..255] 252
GROD Angle
0 [] 6.03
Grain Sizing Settings
Threshold Angle: 10.0°
Border Grains: Include
20µm
Raster: 267x121 Step Size: 0.25µm

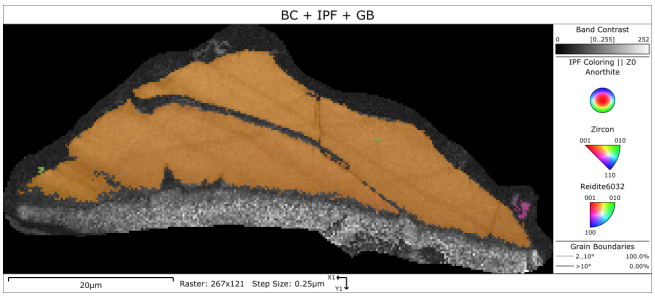
BC + IPF + GB
Band Contrast
0 [0..255] 252
IPF Coloring || Z0
Anorthite
Zircon
001 010
110
Reidite6032
001 010
100
Grain Boundaries
2..10° 100.0%
>10° 0.00%
20µm
Raster: 267x121 Step Size: 0.25µm

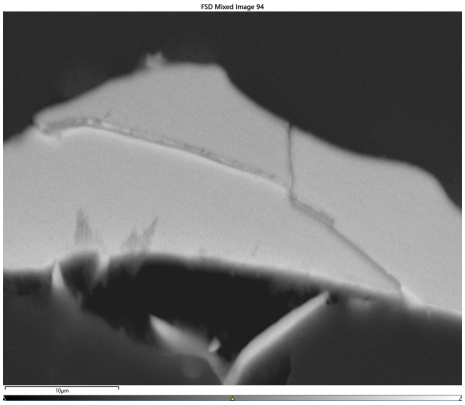
FSD Mixed Image 94

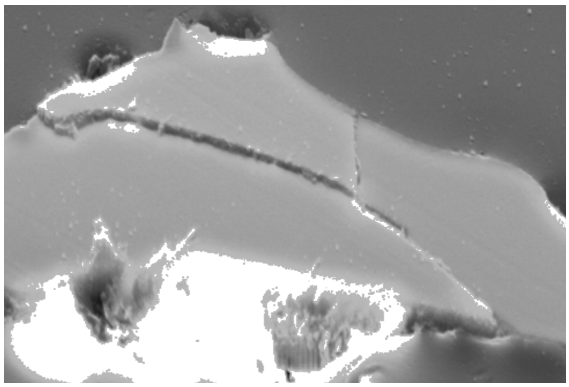

M_M2_18

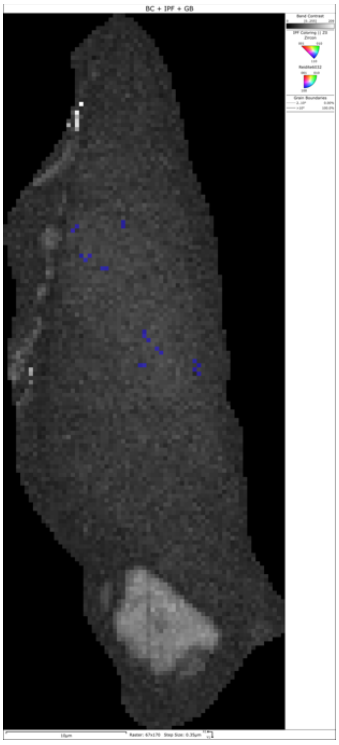

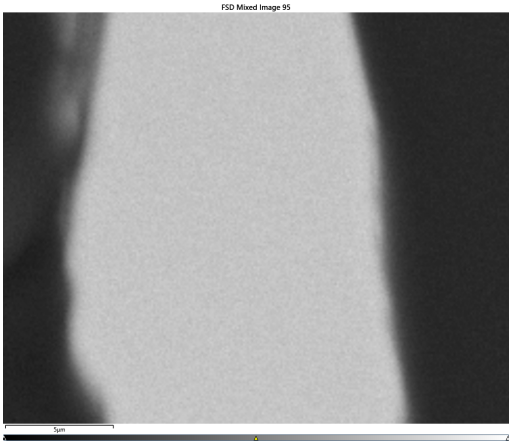

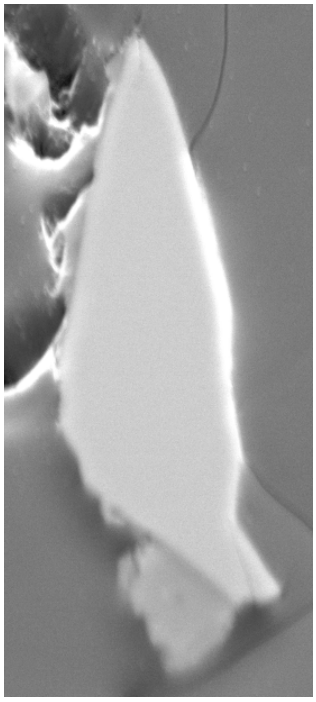

M_M2_19

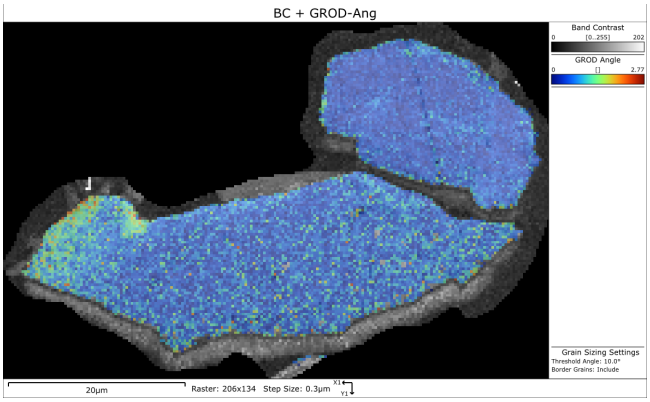
BC + GROD-Ang
Band Contrast
0 [0..255] 202
GROD Angle
0 [] 2.77
Grain Sizing Settings
Threshold Angle: 10.0°
Border Grains: Include
20µm
Raster: 206x134 Step Size: 0.3µm

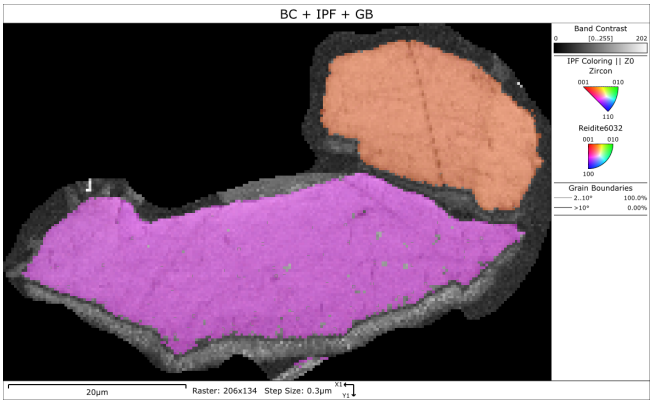
BC + IPF + GB
Band Contrast
0 [0..255] 202
IPF Coloring || Z0
Zircon
001 010
110
Reidite6032
001 010
100
Grain Boundaries
2..10° 100.0%
>10° 0.00%
20µm
Raster: 206x134 Step Size: 0.3µm

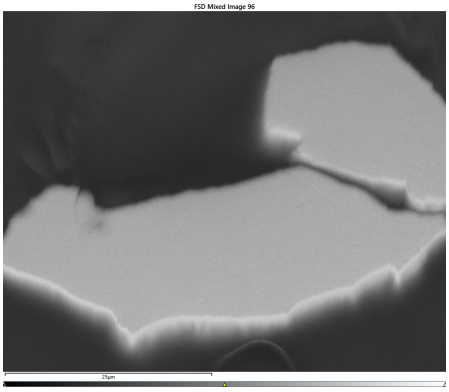
FSD Mixed Image 96

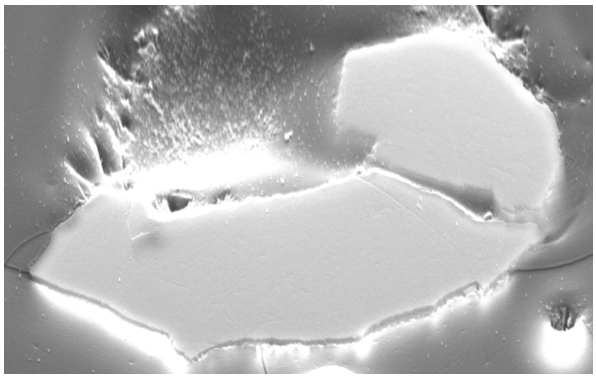

M_M2_20

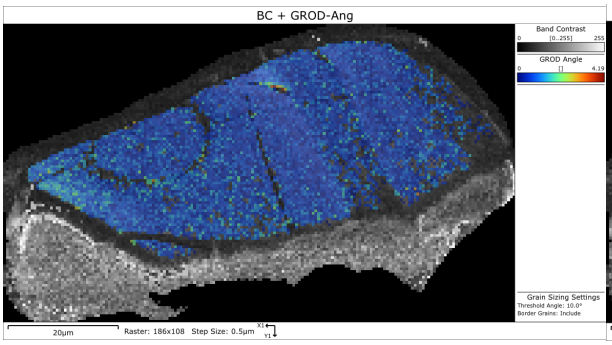
BC + GROD-Ang
Band Contrast
GROD Angle
Grain Sizing Settings
20µm
Raster: 186x108 Step Size: 0.5µm

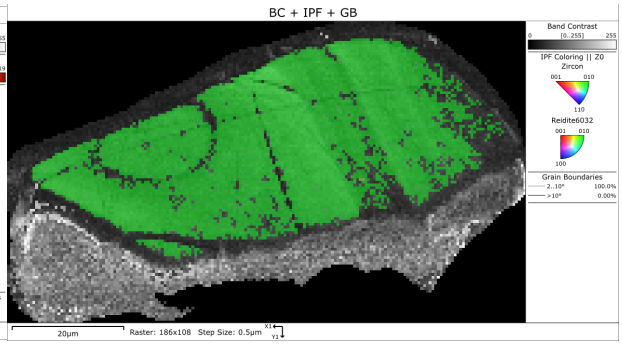
BC + IPF + GB
Band Contrast
IPF Coloring || Z0
Zircon
Reidite6032
Grain Boundaries
20µm
Raster: 186x108 Step Size: 0.5µm

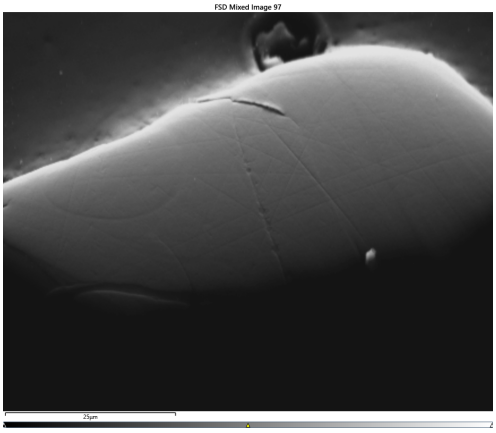
FSD Mixed Image 97

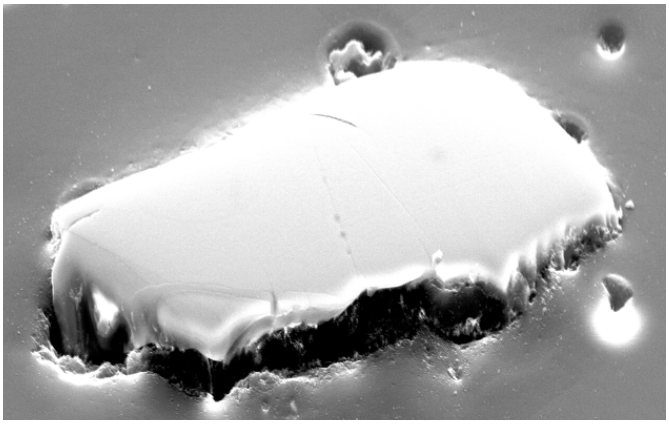

M_M2_21

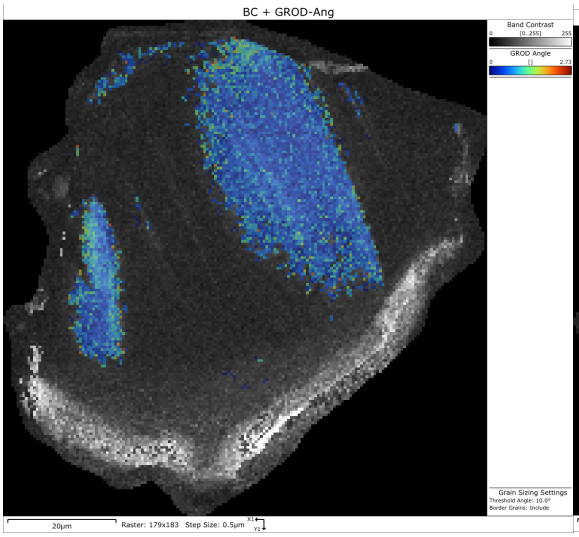
BC + GROD-Ang
Band Contrast
GROD Angle
Grain Sizing Settings
20µm
Raster: 179x183 Step Size: 0.5µm

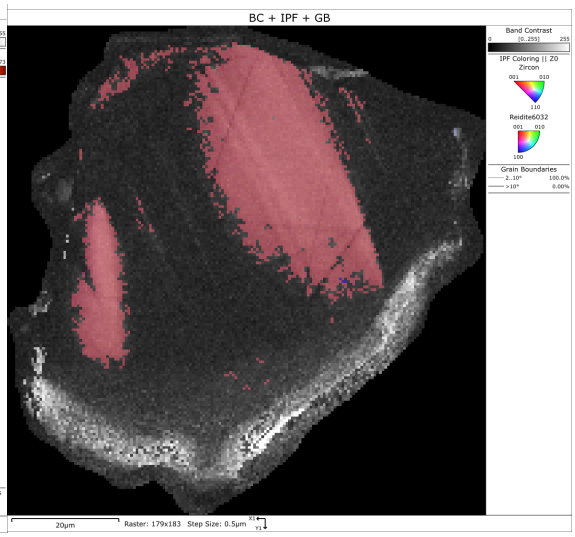
BC + IPF + GB
Band Contrast
IPF Coloring || Z0
Zircon
Reidite6032
Grain Boundaries
20µm
Raster: 179x183 Step Size: 0.5µm

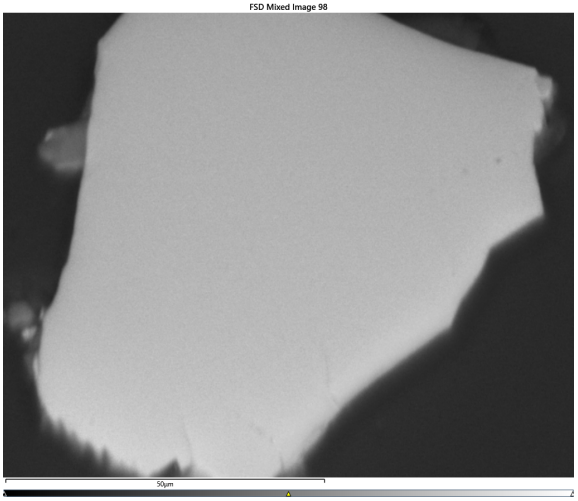
FSD Mixed Image 98
50µm

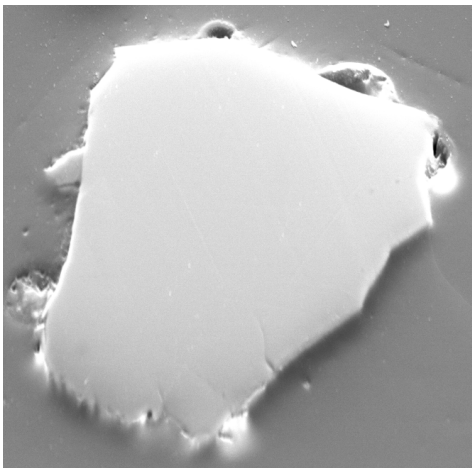

M_M2_22

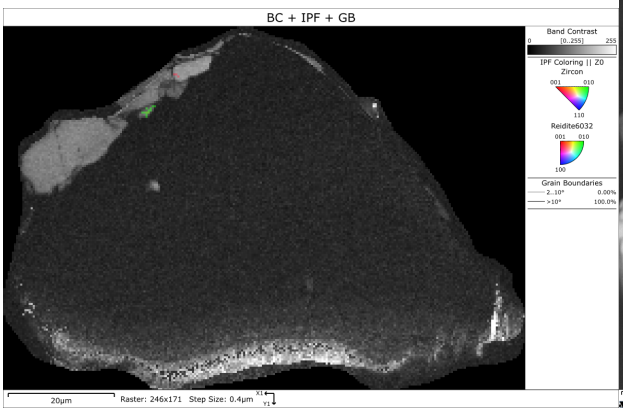
BC + IPF + GB
Band Contrast
0
[0..255]
255
IPF Coloring || Z0
Zircon
001
010
110
Reidite6032
001
010
100
Grain Boundaries
2..10°
0.00%
>10°
100.0%
20µm
Raster: 246x171 Step Size: 0.4µm

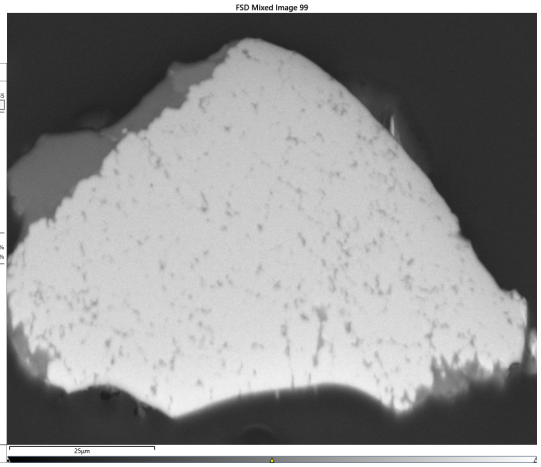
FSD Mixed Image 99
25µm

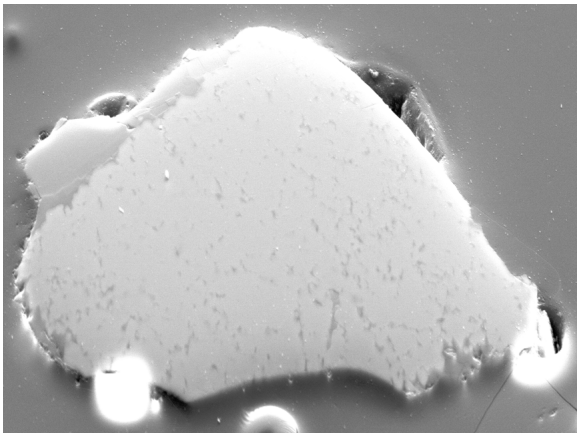

M_M2_23

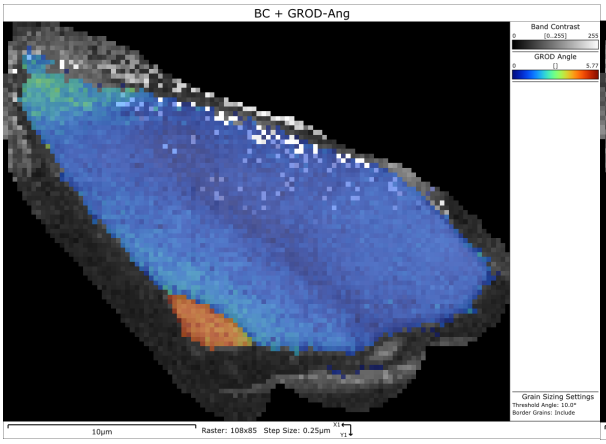
BC + GROD-Ang
Band Contrast
GROD Angle
Grain Sizing Settings
10µm
Raster: 108x85 Step Size: 0.25µm

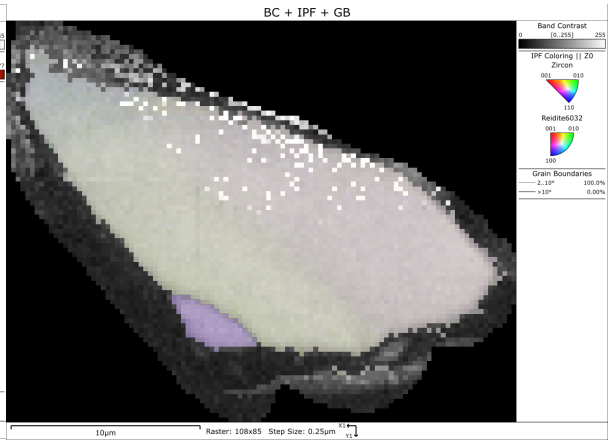
BC + IPF + GB
Band Contrast
IPF Coloring || Z0
Zircon
Reidite6032
Grain Boundaries
10µm
Raster: 108x85 Step Size: 0.25µm

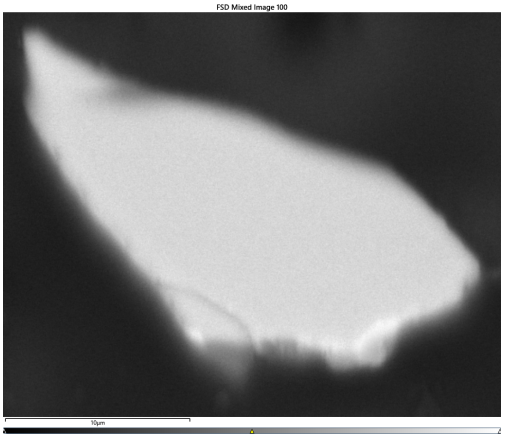
FSD Mixed Image 100

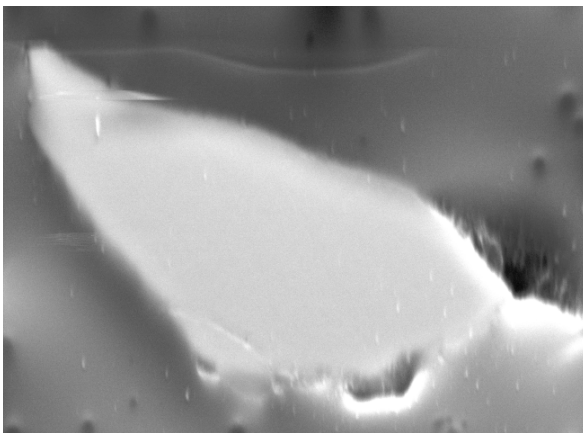

M_M2_24

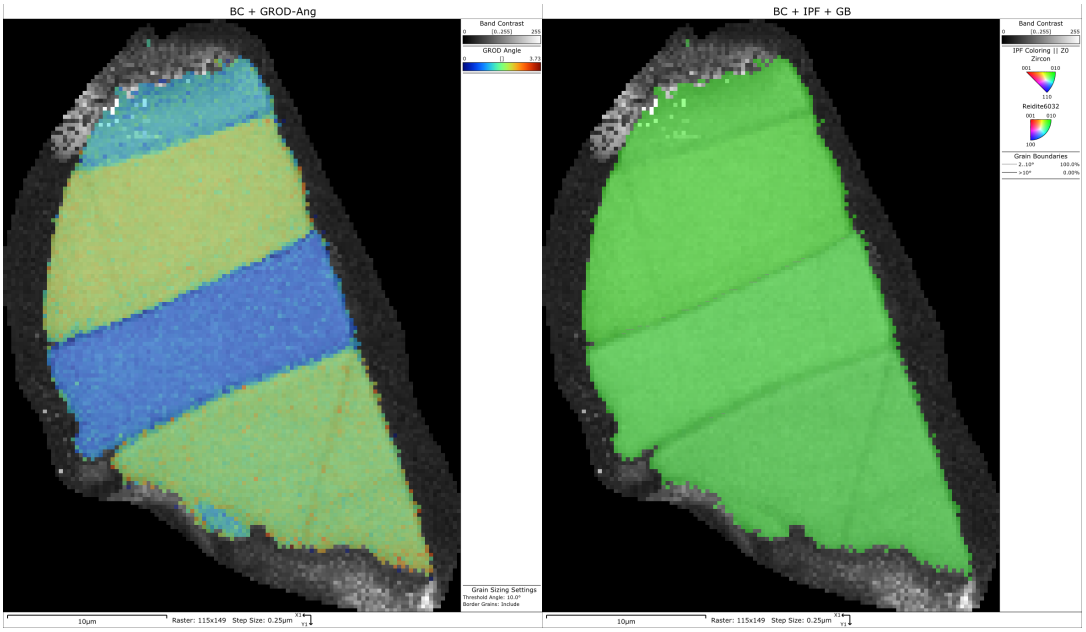
BC + GROD-Ang
Band Contrast
GROD Angle
Grain Sizing Settings
10µm
Raster: 115x149 Step Size: 0.25µm
BC + IPF + GB
Band Contrast
IPF Coloring || Z0
Zircon
Reidite6032
Grain Boundaries
10µm
Raster: 115x149 Step Size: 0.25µm

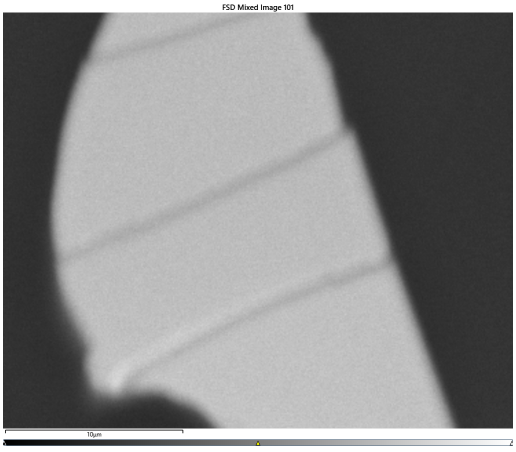
FSD Mixed Image 101
10µm

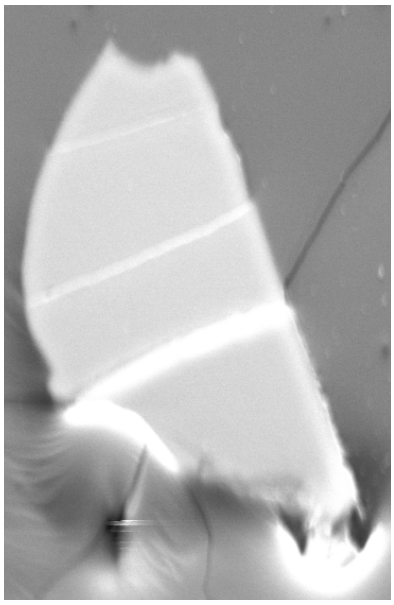

M_M2_25

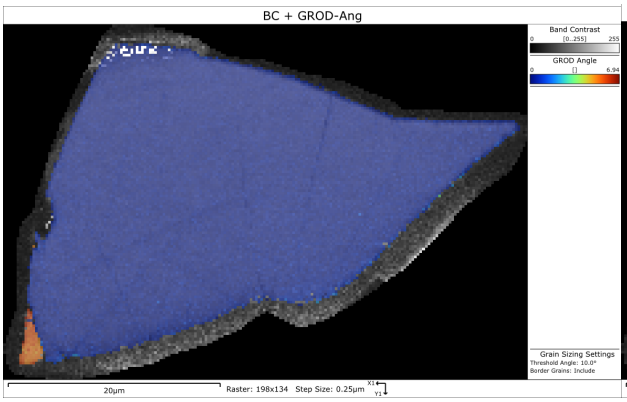
BC + GROD-Ang
Band Contrast
[0..255]
GROD Angle
Grain Sizing Settings
20µm
Raster: 198x134 Step Size: 0.25µm

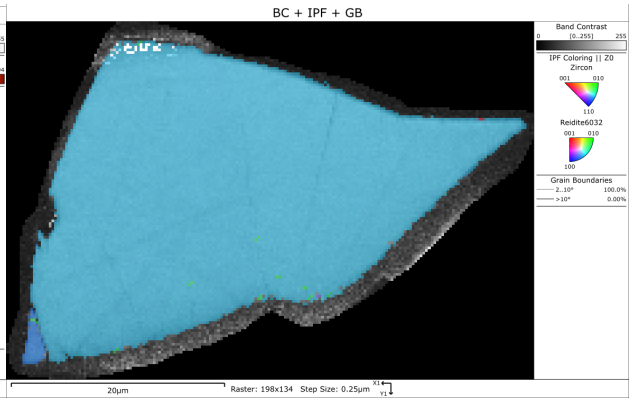
BC + IPF + GB
Band Contrast
[0..255]
IPF Coloring || Z0
Zircon
Reidite6032
Grain Boundaries
2..10°
>10°
20µm
Raster: 198x134 Step Size: 0.25µm

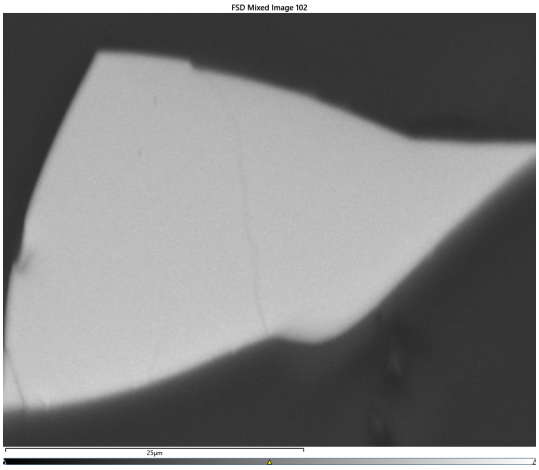
FSD Mixed Image 102
25µm

